THE JOURNAL
OF
CHEMICAL PHYSICS

VOLUME 34, NUMBER 3 MARCH, 1961

Radiolysis of Aqueous Solutions Highly Enriched in O^{18}

MICHAEL ANBAR AND SHMUEL GUTTMANN

Isotope Department, Weizmann Institute of Science, Rehovoth, Israel

AND

GABRIEL STEIN

Department of Physical Chemistry, Hebrew University, Jerusalem, Israel

(Received July 22, 1960)

Solutions of $H_2O_2^{16,16}$ in water highly enriched in O^{18} were irradiated with x rays and protons. The effects of H_2O_2 concentration, *p*H, bromide and nitrite ions, on the yield of the isotopic species $H_2O_2^{16,18}$ and $H_2O_2^{18,18}$, were investigated. The "molecular" H_2O_2 is formed with a G value of 0.3 in neutral solutions. The formation of $H_2O_2^{16,18}$ is attributed to the attack of $O^{18}H$ radicals on $H_2O_2^{16,16}$. The evolved $O_2^{16,18}$ may be regarded as a product of a parallel reaction. The yield of $O_2^{16,18}$ is dependent on an exchange reaction between HO_2 and H_2O_2. Specific effects due to added NO_2^- and high concentrations of Br^- are discussed.

ONE of the fundamental questions in the radiation chemistry of aqueous solutions is the mode of formation of the so-called "molecular products" H_2O_2 and H_2.[1] The question, whether these are formed as the result of the interaction of the primary radicals H and OH produced in reaction (1)

$$HOH \rightarrow H+OH \qquad (1)$$

by the reactions

$$H+H \rightarrow H_2 \qquad (2)$$

$$OH+OH \rightarrow H_2O_2, \qquad (3)$$

or alternatively, whether at least part of these "molecular products" are formed through another distinct mechanism,[2] still remains open. Such an alternative process may be the interaction of excited water molecules, H_2O^*, with normal ones,

$$H_2O^*+H_2O \rightarrow H_2O_2+H_2. \qquad (4)$$

In the first case, in the presence of radical capturing agents, the molecular products would correspond merely to that portion of the radicals which the added scavengers failed to capture from inside the tracks. In the second, one may expect radical scavengers to influence at least part of the molecular products in a manner which would be significantly different from their effects on the products of radical precursors. Since the discovery of the molecular products, by Allen, decisive evidence could not be obtained in favor of a distinct molecular mechanism, though evidence from the isotope fractionation effect on the H_2 evolved, supported it.[2,3] Recently Mahlman[4,5] obtained evidence showing that part of the H_2 originates in a distinct molecular process.

In the present paper we present our experimental results on the radiolysis of water solution in which the oxygen of the water was almost wholly O^{18}. To this water, up to $3M$ H_2O_2 was added, the oxygen of which was almost wholly O^{16}; H_2O_2 does not appreciably exchange its oxygen with water and acts, consequently, both as a scavenger and as a carrier for H_2O_2 originating from the irradiated system. The high concentration of $H_2O_2^{16,16}$ added, protected the relatively small amount of hydrogen peroxide formed during irradiation, so that the isotopic composition and the quantity of species such as $H_2O_2^{18,18}$ and $H_2O_2^{16,18}$ (scrambled hydrogen peroxide) thus formed could be determined. The effects of other scavengers, such as Br^- or NO_2^- on the formation of $H_2O_2^{18,18}$ and $H_2O_2^{16,18}$ were then followed. The isotopic composition of the O_2 formed during irradiation and the utilization of O_2, initially

[1] A. O. Allen, Discussions Faraday Soc. **12**, 79 (1952).
[2] P. Kelley, T. Rigg, and J. Weiss, Chem. & Ind. (London) **1954**, 129.
[3] J. Jortner and G. Stein, Intern. J. Appl. Radiation and Isotopes **7**, 198 (1960).
[4] H. A. Mahlman, J. Chem. Phys. **31**, 993 (1959).
[5] H. A. Mahlman, J. Chem. Phys. **32**, 601 (1960).

Copyright © 1961 by the American Institute of Physics

present, for the formation of H_2O_2 could also be determined. The high isotopic purity of the H_2O^{18} used, was essential in obtaining clear-cut results as it enabled us to distinguish between $H_2O_2^{18,18}$ originating from the water alone and $H_2O_2^{16,18}$ originating both from H_2O_2 and the solvent.

Others have used similar isotope techniques previously. Thus Hart, Gordon, and Hutchison[6] investigated the $O^{16}O^{18}$–H_2O^{16} exchange in water, and the formation[7] of H_2O_2 in H_2O^{16} in the presence of $O^{16}O^{18}$. Backhurst, Johnson, Scholes, and Weiss[8] used water enriched in O^{18} to elucidate the problem of molecular H_2O_2 formation. The use of highly enriched H_2O^{18} enables us to extend the work of these authors.

EXPERIMENTAL

Materials

The O^{18} labeled water was between 92–97 atom % O^{18}, obtained from the Isotope Distillation Plant of the Weizmann Institute, Rehovoth. It contained practically 100 atom % deuterium and was thus nearly pure D_2O^{18}. To simplify formulas we shall refer to this water as H_2O^{18}. The H_2O_2 was Fisher's 50% (stabilized with phosphoric acid) and Merck's Perhydrol 30% (free of stabilizer). Identical results were obtained with both reagents. The $O_2^{18,18}$ was obtained by alkaline electrolysis with Pt electrodes of enriched water and was 95 atom % O^{18}. The various *p*H values were obtained by using BDH 100% phosphoric acid, Merck's analytical quality anhydrous KH_2PO_4, Baker's Analyzed anhydrous Na_3PO_4, Baker's Analyzed hydrated $Na_2B_4O_7$, which was desiccated to the anhydrous solid by drying at 70°C in vacuum, Baker's Analyzed NaOH and BDH Analar H_2SO_4, NaBr was Baker's Analyzed. The *p*H values were determined by a METROHM type El48c instrument using a type U combined microelectrode, which has a minimal error in alkaline solutions.

Irradiations

Irradiations were carried out using a G.E. Maximar x-ray set of 200 kVp, 0.5 and 1-ml samples were used in sealed Pyrex glass ampules fitted with breakoff tips. To minimize thermal decomposition the ampules were cleaned before use by soaking for 24 hr in concentrated Analar HNO_3, followed by soaking and a large number of rinsings in triple distilled water, then drying in a vacuum oven at 70°C. The dose rate was 1.1×10^4 rad/min^{-1} (6.9×10^{17} ev/ml^{-1}/min^{-1}). Identical control samples were treated at all stages of the procedure, except for the irradiation.

Proton irradiations were carried out in Teflon irradiation cells with polyethylene windows of 1.6 mg/cm^2 thickness containing 0.5 ml of solution. Unevacuated solutions were used, which were freed of dissolved air by passing helium through the solution; 2.3-Mev protons generated by a Van de Graaff accelerator were used, emitted through a quartz window of 0.1 mg/cm^2. At an effective energy of 1.5 Mev absorbed in the solution, 10–60 μamp sec were delivered during 1.5 to 3 min. Thus, approximately $2–9\times10^{20}$ ev were absorbed per sample. In these experiments only the isotopic composition of the H_2O_2 was determined.

Analysis

After irradiation, the irradiated and unirradiated samples, respectively, were opened in a vacuum by breaking the seal with a magnetic hammer. The quantity of O_2 evolved was determined. It was then sealed into a separate ampule for mass spectrometric analysis. In an aliquot of the solution the H_2O_2 concentration was determined iodometrically. The remainder was decomposed in a vacuum system over Pt black. The evolved oxygen in this procedure comes only from the H_2O_2 and there is no induced oxygen exchange between differently labeled H_2O_2 molecules during the decomposition.[9] The quantity of evolved O_2 was determined and the gas sealed into a separate ampule for mass spectrometry. The mass spectrometric analysis was performed on a CEC model 21–401 mass spectrometer. In our case the isotopic abundance was determined for each of the different masses 32 to 36. Masses 28 (N_2) and 40 (A) were determined to check for air contamination. Each value of isotope analysis reported is the average of 2–4 separate experiments.

In all experiments ordinary H_2O_2 was used, in which the natural abundance of O^{18} is 0.2 atom %. Oxygen originating from ordinary H_2O_2 contained consequently, 0.4% of $O^{16}O^{18}$; $O^{18}O^{18}$ due to natural abundance has only the negligible value of 4×10^{-4}%. The H_2O^{18} used by us contained 3 to 8 atom % of O^{16}, and consequently O_2 originating from water contained 6 to 16% of $O^{16}O^{18}$, and only of the order of 0.35% $O^{16}O^{16}$. Allowance for these factors was made in all our calculations.

RESULTS

Irradiations With X-rays

Effect of Varying pH

With $H_2O_2^{16,16}$ as the only added scavenger present, the *p*H was varied. All solutions were initially free of O_2. The results of the experiments in the presence of 1M H_2O_2 added initially, are summarized in Table I. The contribution of the thermal decomposition was large, especially around *p*H 12, where, as Erdey[10] has shown, its velocity shows a marked maximum. How-

[6] E. J. Hart, S. Gordon, and D. A. Hutchison, J. Am. Chem. Soc. **75**, 6165 (1953).
[7] E. J. Hart, S. Gordon, and D. A. Hutchison, J. chim. phys. **52**, 570 (1955).
[8] J. D. Backhurst, G. R. A. Johnson, G. Scholes, and J. Weiss, Nature **183**, 176 (1959).
[9] M. Anbar (to be published).
[10] L. Erdey, Acta Chim. Acad. Sci. Hung. **3**, 95 (1953).

TABLE I. $H_2O_2^{16,18}$ solution in H_2O^{18} (95% O^{18}) irradiated by 200-kev x rays.

Ions present	pH	Initial H_2O_2 mole/liter	Dose M rads	$G_{H_2O_2}$ decomp'n.	$G_{H_2O_2}^{18,18}$	$G_{H_2O_2}^{16,18}$	$R=\frac{G_{H_2O_2}^{18,18}}{G_{H_2O_2}^{16,18}}$	$G_{O_2}^{18,18}$	$G_{O_2}^{16,18}$
$SO_4^=$ H^+	0.3	0.83	2.0	4	0.54	0.52	1.04	...	0.58
$SO_4^=$ H^+	0.65	0.80	2.0	6	0.59	0.58	1.02	...	0.56
$H_2PO_4^-$ Na^+	1.65	1.05	1.33	25	0.43	0.57	0.75	...	0.59
$H_2PO_4^-$ Na^+	2.70	1.00	2.0	19	0.48	0.63	0.76	0.012	0.35
$H_2PO_4^-$ Na^+	3.90	0.80	1.0	25	0.48	0.51	0.93	0.010	0.28
$HPO_4^=$ Na^+	6.2	0.85	2.0	40	0.51	0.48	1.07	0.023	0.43
$HPO_4^=$ Na^+	7.8	0.75	2.0	21	0.45	0.37	1.21	0.007	0.26
$HPO_4^=$ Na^+	8.0	1.35	1.35	25	0.41	0.53	0.77	...	0.42
$HPO_4^=$ Na^+	8.0	0.80	2.0	27	0.44	0.43	1.02	0.005	0.37
Borate Na^+	9.2	1.15	1.33	26	0.40	0.45	0.89	...	0.35
Borate Na^+	10.2	0.76	2.0	43	0.43	0.39	1.10	0.026	0.19
$HPO_4^=$ Na^+	10.1	1.15	1.33	75	0.38	0.37	1.02	0.012	0.16
$HPO_4^=$ Na^+	10.95	1.10	1.33	120	0.32	0.47	0.68	0.017	0.21
$PO_4^=$ Na^+	12.0	0.77	1.0	48	0.36	0.42	0.86	0.020	0.23
$PO_4^=$ Na^+	12.2	1.10	1.33	49	0.20	0.60	0.33	0.009	0.15
$PO_4^=$ Na^+	13.0	0.75	2.0	16	0.21	0.46	0.46	0.019	0.05
$PO_4^=$ Na^+	13.0	0.66	1.33	15	0.27	0.21	1.28	0.003	0.12
OH^- Na^+	13.1	1.10	1.33	26	0.17	0.72	0.24	...	0.13
OH^- Na^+	13.2	0.80	2.0	19	0.19	0.19	0.58	0.004	0.23
OH^- Na^+	13.3	0.75	4.0	19	0.19	0.26	0.73	0.010	0.15
OH^- Na^+	13.8	0.80	2.0	6	0.20	0.73	0.27	0.017	0.18

TABLE II. Effect of H_2O_2 concentration on radiation yields (x rays).

pH	H_2O_2 mole/liter	$G_{H_2O_2}^{18,18}$	$G_{H_2O_2}^{16,18}$	$R=\frac{G_{H_2O_2}^{18,18}}{G_{H_2O_2}^{16,18}}$	$G_{O_2}^{18,18}$	$G_{O_2}^{16,18}$
1.65	0.08	0.71	0.26	2.73	0.033	0.75
1.95	0.24	0.72	0.41	1.75	...	0.66
1.65	0.36	0.54	0.44	1.23	0.004	0.50
1.95	0.80	0.48	0.51	0.93	0.010	0.28
1.65	1.05	0.43	0.57	0.75	...	0.39
1.95	3.24	0.33	0.51	0.65	...	0.14
13.6	0.08	0.34	0.31	0.10	0.064	0.52
13.4	0.35	0.24	0.30	0.80	0.010	0.20
13.4	0.80	0.19	0.33	0.58	0.004	0.23
13.1	1.30	0.14	0.35	0.40	...	0.04

ever, as this yields only $O_2^{16,16}$ originating from H_2O_2 alone, the yield of $O_2^{16,18}$ and $O_2^{18,18}$ containing oxygen originating from the water (evolved through radiolysis) could be accurately determined. The results include, in addition to the absolute values of $G_{H_2O_2}^{18,18}$ and $G_{H_2O_2}^{16,18}$ also R, the ratio of these values from the same experiment; R will be less affected by variations in total dose and concentration between different experiments, than the absolute G values will be. Our experiments were carried out at temperatures between 25° and 35°C. Changes in temperature had considerable effect on the thermal decomposition, which has an activation energy[11] of 12–13 kcal/mole, but only a very small effect on the radiolysis (activation energy[11] of the order of 2–3 kcal/mole).

It may be seen from Table I that the change in the total dose of irradiation by a factor of four had little effect on the $G_{H_2O_2}^{18,18}$ and $G_{H_2O_2}^{16,18}$.

In the pH dependence of the yield of $H_2O_2^{16,18}$ the experimental scatter is large in the alkaline region. However, when using these results together with those for the pH dependence of the yield of $H_2O_2^{18,18}$, Fig. 1 is obtained showing R, in which errors are largely canceled out. In the acid and neutral region the results are also much more consistent for the separate G values as well. The results show that $G_{H_2O_2}^{18,18}$ and $G_{H_2O_2}^{16,18}$ as well as their ratio R, are nearly constant throughout the acid and neutral pH region, but are very significantly affected in a dissimilar manner as the pH rises above 9.

In Fig. 2 the pH dependence of the yield of $O_2^{16,18}$ evolved during irradiation is shown. The yield of $O_2^{18,18}$ is more than an order of magnitude smaller than that of $O_2^{16,18}$, and the results are thus not accurate. On the other hand, the yield of $O_2^{16,18}$ shows a significant decrease at pH 2–3 and a further decrease at pH 9–10.

Effect of Varying H_2O_2 Concentration

The H_2O_2 is itself a scavenger for both the H and OH radicals. Its reaction with HO^{18} may yield part or all of the $H_2O_2^{16,18}$ observed. In order to ascertain the role

[11] V. Y. Chernikh, S. Y. Pshzhetsky, and G. S. Tyurikov, Trans. All-Union Conf. Rad. Chem. Moscow, 1958, p. 48.

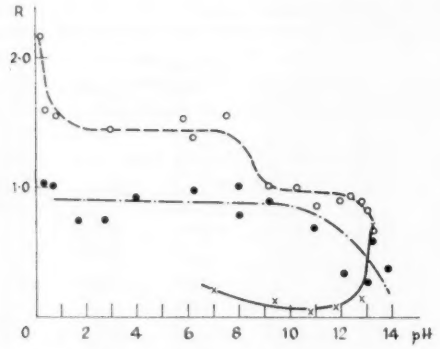

FIG. 1. The effect of pH on the ratio between the yield of $H_2O_2^{18,18}$ and $H_2O_2^{16,18}$, $R=G_{H_2O_2}^{18,18}/G_{H_2O_2}^{16,18}$ [●= (no) added ions; ○=Br^- added; X=NO_2^- added].

of H_2O_2 as a scavenger, and its role in the processes leading to O_2 evolution, the experiments reported in Table II were carried out, at varying initial H_2O_2 concentrations and at constant pH values, one in the alkaline region. The results are shown in Fig. 3.

Effect of Added Br^-–Cl^-–$SO_4^=$, Rb^+, *and* Cs^+

Bromide ions react efficiently with OH radicals, according to

$$OH+Br^-\rightarrow OH^-+Br, \qquad (5)$$

and have been used previously[12] to elucidate some aspects of the reaction mechanism in the radiolysis of aqueous solutions. Owing to its high atomic number, the radiation dose absorbed in bromide-containing solutions will be higher. This effect may be approximately imitated by adding Rb^+ instead of Br^- as the heavy ion; Rb^+ will not act as a scavenger for OH radicals, and its main effect (apart from general ionic effects on reaction rates) will be due to its high atomic number. The differential effect between Br^-- and Rb^+-containing solutions may be attributed to the specific effects of Br^- as an easily ionized negative ion and as a radical scavenger for OH. The results are shown in Table IIIa and b, showing the effect of Rb^+, Cs^+, Cl^-, $SO_4^=$ as well as of Br^- ions are under various conditions, so that the specific effects due to each can be observed. In Fig. 1 the effect of Br^- on R is shown.

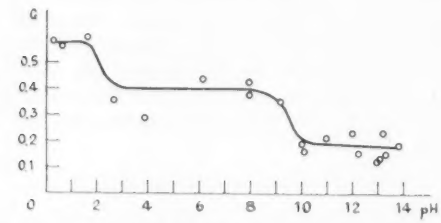

FIG. 2. The effect of pH on the radiation yield of $O_2^{16,18}$.

[12] T. J. Sworski, J. Am. Chem. Soc. **76**, 4687 (1954).

Effect of Added NO_2^-

While Br^- is an excellent scavenger for OH radicals, its high atomic number and specific chemical nature introduce new effects when it is used in higher concentrations. These effects are most useful in revealing new aspects of the reactions involved, as we shall discuss further. However, to interpret them it is desirable to be able to attribute the various effects to the right cause.

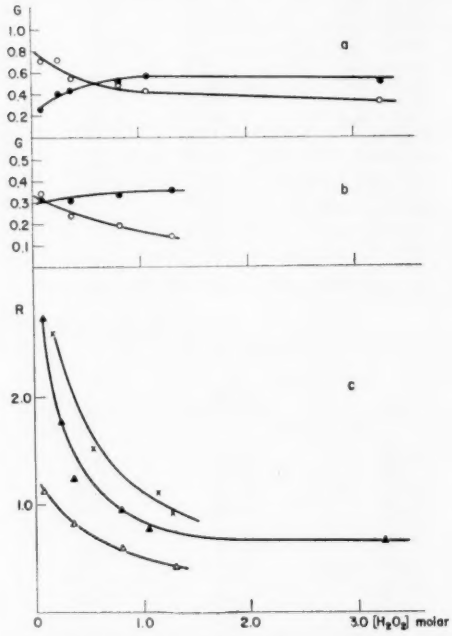

FIG. 3. The effect of H_2O_2 concentration on the radiation yield of $H_2O_2^{18,18}$, $H_2O_2^{16,18}$ and on their ratio, (a) x rays at pH=1.6–1.9, ○=$G_{H_2O_2}^{18,18}$, ●=$G_{H_2O_2}^{16,18}$, (b) x rays at pH=13, ○=$G_{H_2O_2}^{18,18}$, ●=$G_{H_2O_2}^{16,18}$, (c) $R=G_{H_2O_2}^{18,18}/G_{H_2O_2}^{16,18}$, ▲=x rays at pH=1.6–1.9, Δ=x rays at pH=13, X=protons at pH=1.0.

With this in view, added NO_2^- ions were used as scavengers. These react according to

$$OH+NO_2^-\rightarrow OH^-+NO_2, \qquad (6)$$

also eliminating OH radicals from solution; NO_2^- is not of high atomic number and will not change the absorbed dose significantly. The chemical nature of the product NO_2 causes new chemical effects, dissimilar to those observed with Br^-. The results are shown in Table IV.

Irradiations in the Presence of $O_2^{18,18}$

It was found that if mixtures of dry $O_2^{18,18}$ and $O_2^{16,16}$ are irradiated with x rays, complete isotopic equilibrium is obtained when the gas, at total pressures of the order of 20 mm is placed in an ampule, in the

TABLE IIIa. $H_2O_2^{16,16}$ solutions in H_2O^{18} (95% O^{18}) in presence of bromide ions irradiated by 200-kev x rays.

pH	Br^- mole/liter	H_2O_2 mole/liter	Dose M rads	$G_{H_2O_2}$ decomp'n.	$G_{H_2O_2}^{18,18}$	$G_{H_2O_2}^{16,18}$	$R=\frac{G_{H_2O_2}^{18,18}}{G_{H_2O_2}^{16,18}}$	$G_{O_2}^{18,18}$	$G_{O_2}^{16,18}$
0.20	1.0	0.73	1.33	32	0.65	0.30	2.17	0.065	0.19
0.35	1.0	0.80	2.0	24	0.79	0.46	1.61	0.070	0.21
0.78	0.1	0.76	1.33	35	0.42	0.27	1.56	0.021	0.05
1.60	1.0	0.84	2.0	13	0.79	0.25	3.2	0.055	0.15
2.90	0.3	0.84	1.33	12	0.45	0.31	1.45	...	0.43
2.95	0.1	0.72	1.33	11	0.44	0.35	1.26	...	0.21
2.95	3.0	0.75	1.33	22	0.31	0.24	1.29	0.007	0.38
3.25	1.0	0.72	1.33	6	0.42	0.34	1.23	...	0.21
5.8	1.0	0.83	2.0	30	0.41	0.27	1.53	0.023	0.47
6.2	1.0	0.76	2.0	25	0.42	0.30	1.30	0.020	0.52
7.5	1.0	0.76	2.0	32	0.43	0.28	1.56	0.024	0.12
9.3	1.0	1.15	1.33	110	0.46	0.45	1.02	0.045	0.19
10.2	1.0	1.10	1.33	120	0.44	0.44	1.00	0.042	0.30
11.1	1.0	1.15	1.33	41	0.45	0.53	1.85	0.020	0.12
12.2	1.0	0.76	1.0	26	0.42	0.47	0.89	0.014	0.20
12.4	1.0	0.68	2.0	40	0.37	0.39	0.94	0.039	0.08
12.8	0.1	0.80	2.0	28	0.34	0.38	0.89	0.018	0.05
13.0	1.0	0.75	2.0	50	0.45	0.55	0.83	0.045	0.20
13.0	3.0	0.68	1.33	21	0.41	0.49	0.83	0.015	0.13
13.3	1.0	0.80	2.0	28	0.42	0.72	0.58	0.012	0.09

TABLE IIIb. The effect of various ions on $G_{H_2O_2}^{18,18}$ and $G_{H_2O_2}^{16,18}$ (concentrations in mole/liter).

pH	$[H_2O_2]$	$[Br^-]$	$[Cl^-]$	$[Rb^+]$	$[Cs^+]$	$[SO_4^=]$	$[Na^+]$	$G_{H_2O_2}^{18,18}$	$G_{H_2O_2}^{16,18}$
		0	0	0	0	0	0	0.48	0.63
3	0.8	1.0	0	0	0	0	1.0	0.44	0.32
		0	1.0	0	0	0	1.0	0.37	0.53
		0	1.0	1.0	0	0	0	1.52	1.24
0.5	0.8	0	0	0	0	0.8	0	0.54	0.52
		1.0	0	0	0	0.8	1.0	0.78	0.46
		0	0	1.0	0	1.9	0	2.42	2.37
13	0.8	0	0	0	0	0.1	0	0.19	0.5
		1.0	0	0	0	0	2.0	0.45	0.55
		0	0	0	1.0	1.0	1.0	1.61	2.16

TABLE IV. $H_2O_2^{16,16}$ solutions irradiated by presence of 0.2M $NaNO_2$ in H_2O^{18} (95% O^{18}) by 200-kev x rays.

pH	$[H_2O_2]$ mole/liter	Dose M rad	$G_{H_2O_2}$ decomp'n.	$G_{H_2O_2}^{18,18}$	$G_{H_2O_2}^{16,18}$	$R=\frac{G_{H_2O_2}^{18,18}}{G_{H_2O_2}^{16,18}}$	$G_{O_2}^{16,18}$	$G_{O_2}^{16,18}$
6.95	1.20	1.33	8	0.42	2.0	0.21	0.010	0.23
9.35	1.10	1.33	75	0.35	2.7	0.13	0.019	0.10
10.85	1.10	1.33	95	0.40	8.2	0.05	0.021	0.15
11.8	1.10	1.33	49	0.15	2.0	0.08	...	0.12
12.8	1.10	1.33	22	0.15	1.25	0.12	...	0.02
13.3	0.67	1.33	19	0.19	0.27	0.70	...	0.02

field of radiation in which aqueous solutions under the same condition would have received a dose of 0.3*M* rad. If however, some water is present in the ampule, no equilibrium could be detected after the same dose, or after a sixfold increase in the dose. Thus, it seems that water vapor effectively breaks the chains carried by O atoms and ozone which are responsible for the high rate of radiation-induced exchange in dry gas. Thanks to this effect it is possible in our case to follow the extent of change in isotopic composition, introduced into the gas through radiation chemical reactions in the liquid phase. The radiation induced exchange between $O_2^{18,18}$ initially added, with $H_2O_2^{16,16}$ in H_2O^{16} solution was investigated. The results are presented in Table V.

Irradiations with Protons

Using protons instead of x rays as the ionizing radiations, we are able to observe the effect of changing LET on the different products, and the effects of various additives and *p*H on these yields. The results are summarized in Table VI.

TABLE V. Radiation induced exchange of O_2 with H_2O_2 (phosphate buffered solutions of $H_2O_2^{16,16}$ in H_2O^{18} in presence of $O_2^{18,18}$).

Dose M rad	...[a]	1.0	2.0	...[a]	2.0
pH	2.7	2.7	2.7	12.0	12.0
H_2O_2 initial	1.0	1.0	1.0	0.74	0.74
H_2O_2 final	1.0	0.98	0.92	0.26	0.14
O_2 initial mm Hg	240	240	240	200	200
O_2 initial μ moles	120	120	120	200	200
O_2 final μ moles	121	123	129	237	289
H_2O_2 isotopic composition					
$O_2^{18,18}$ corrected	0.007	0.124	0.163	1.32	6.30
$O_2^{16,18}$ scrambled	0.012	0.01	0.02	0.50	0.38
Yield $H_2O_2^{18,18}$ μ moles	0.07	1.22	1.56	6.6	27.7
Yield $H_2O_2^{16,18}$ μ moles	0.12	0.09	0.22	2.5	1.7
$G_{H_2O_2}^{18,18b}$		1.23	0.81		10.5
$G_{H_2O_2}^{16,18b}$		...	...		...

[a] Thirty-six hours of thermal exchange at 10°C.
[b] Corrected for $H_2O_2^{18,18}$ and $H_2O_2^{16,18}$ formed by thermal exchange.

Irradiation with a Tesla Discharge

In an attempt to see whether the ratio between excitation and radical production from water, can be influenced, some experiments were carried out in which 1M $H_2O_2^{16,16}$ solutions in H_2O^{18} were exposed to the discharge from a Tesla coil. The solutions containing air, were in cylindrical glass cells with thin Mylar windows at both ends. The cells were placed between a flat copper electrode fitted to the top of the Tesla coil and a similar earthed one. The results are shown in Table VII.

DISCUSSION

The use of almost pure H_2O^{18} enables us to extend the work of previous investigators in this field, since the system may be studied in the presence of very large amounts of added $H_2O_2^{16,16}$. Hydrogen peroxide does not exchange appreciably with H_2O^{18}, the upper limit of exchange in alkali being $t_{\frac{1}{2}}$ 10^7 sec, and in acid $t_{\frac{1}{2}}$ 10^8 sec.[9] Since hydrogen peroxide reacts with the radiation produced intermediates,

$$H_2O_2+H\rightarrow H_2O+HO \qquad (7)$$

$$H_2O_2+OH\rightarrow H_2O+HO_2, \qquad (8)$$

it protects the small amount of H_2O_2 formed through radiolysis, replacing them by the less reactive HO_2 radicals. The presence of high concentrations of H_2O_2 will also prevent the exchange of OH radicals with water. Reactions (7) and (8) are schematic only, since the actual nature of the reacting species depends on the pH.

The HO_2 radical itself dissociates into H^+ and O_2^-, its pK being[13] about 3. Of significance also is the pH dependence of H_2O_2 itself,[14] with a pK of 12 and of the OH radical, the pK of which is 79. The pH-dependent reactions of H and its equivalents will influence the total decomposition of H_2O_2, but will not directly influence the isotopic composition of the H_2O_2 formed.

The results in Table I show that in the presence of 1M H_2O_2 both $H_2O_2^{18,18}$ and $H_2O_2^{16,18}$ are formed with G values which are of the same order of magnitude. Let us assume that $H_2O_2^{18,18}$ may be formed in two processes, a molecular process, for example, reaction (4), with the appropriate isotope labeling,

$$H_2O^{18*}+H_2O^{18}\rightarrow H_2O_2^{18,18}+H_2, \qquad (4a)$$

and in a radical recombination process,

$$HO^{18}+HO^{18}\rightarrow H_2O_2^{18,18}. \qquad (3a)$$

In acid solutions the yield of $H_2O_2^{18,18}$ is not reduced below a constant limiting value of $g=0.3$ by increasing H_2O_2 from 1M to 3M. Under these conditions $H_2O_2^{16,18}$ does not continue to grow above a constant value, which implies that all OH radicals formed, are captured by H_2O_2. If reaction (3a) does occur at all under these conditions, at least a constant portion of the HO^{18} radicals appear to be unusually and unexplicably inaccessible. The results appear to favor a reaction like (4a).

Regarding the formation of $H_2O_2^{16,18}$, several possibilities exist. One of these would be the existence of a reaction in which OH radicals enter a displacement reaction with H_2O_2, according to

$$OH^{18}+HO^{16}-O^{16}H\rightarrow HO^{18}-O^{16}H+OH^{16}. \qquad (9)$$

The likelihood of such a process is considerable and our isotope technique permits us to determine its extent when it occurs in competition with reaction (8), which gives a net decomposition with or without isotopic exchange. If we assume $G_{OH}\sim 3$, about 10% of all OH radicals will react according to reaction (9).

There is also the possibility that part of the $H_2O_2^{16,18}$ is due to the "molecular" reactions,

$$H_2O^{18*}+H_2O_2^{16,16}\rightarrow H_2O_2^{16,18}+H_2O^{16} \qquad (10a)$$

$$H_2O_2^{16,16*}+H_2O^{18}\rightarrow H_2O_2^{16,18}+H_2O^{16}. \qquad (10b)$$

The extent of these reactions, if they do occur at all cannot be estimated at this stage.

Regarding the pH dependence of the yield of $H_2O_2^{18,18}$ and $H_2O_2^{16,18}$, we see that this is almost unaffected by changes in pH between pH=0.5 and pH=9. Above pH=9, $G_{H_2O_2}^{16,18}$ begins to decrease, $G_{H_2O_2}^{16,18}$ to increase. We have no definite proof for any mechanism to account for this, but can suggest likely causes.

First, the two processes may be interconnected, and above pH=9, H_2O^* the excited water molecule, may yield more OH radicals than H_2O_2 via reaction (4a). This may be due to the dissociation constant of H_2O^* which may be higher than that of normal H_2O. A change of the dissociation constant with excitation has

[13] N. Uri, Chem. Revs. **50**, 375 (1952).
[14] W. C. Schumb, C. N. Satterfield, and R. L. Wentworth, *Hydrogen Peroxide* (Reinhold Publishing Corporation, New York, 1955), p. 392 (pK: 11.75).

TABLE VI. $H_2O_2^{16,16}$ solutions in H_2O^{18} (93% O^{18}) irradiated by 1.95 mev protons; window absorption, −0.45 mev, energy dose rate, 4×10^{17} ev/sec.

pH	H_2O_2 mole/liter	Ion added	Ions mole/liter	Dose ev$\times10^{20}$	$G_{H_2O_2}$	$G_{H_2O_2^{18,18}}$	$G_{H_2O_2^{16,18}}$	$R=\frac{G_{H_2O_2^{18,18}}}{G_{H_2O_2^{16,18}}}$
1.0	0.19	$SO_4^{=}$	0.1	1.9	5	1.61	0.62	2.58
1.0	0.54	$SO_4^{=}$	0.1	1.9	11	1.05	0.70	1.52
1.0	1.14	$Cl^- Li^+$	1.0	1.9	19	0.64	0.58	1.10
1.0	1.28	$SO_4^{=}$	0.1	1.9	13	0.74	0.81	0.91
1.0	1.20	Cl^-K^+	1.0	1.9	31	0.74	0.65	1.13
1.0	1.18	Cl^-Cs^+	1.0	1.9	16	0.66	0.61	1.08
1.0	1.18	$Br^- Na^+$	0.4	1.9	6	0.33	0.24	1.37
1.0	1.12	$Br^- Na^+$	1.0	1.9	22	0.19	0.15	1.27
2.4	0.78	$H_2PO_4^- Na^+$	0.1	9.1[a]	6	0.31	0.36	0.83
2.4	0.80	$Br^- Na^+$	1.0	9.1[a]	12	0.053	0.031	1.72
4.5	1.20	$H_2PO_4^- Na^+$	0.1	1.9	15	0.71	0.87	0.83
6.0	1.22	$H_2PO_4^- Na^+$	0.1	1.9	31	0.62	0.74	0.84
7.0	1.18	$NO_2^- Na^+$	0.3	1.9	10	0.54	1.44	0.40
10.7	1.20	OH^-Na^+	0.1	1.9	47	0.71	0.68	1.04
12.5	1.26	$OH^- Na^+$	0.1	1.9	22	0.19	0.35	0.54
13.0	1.2	$OH^- Na^+$	1.0	1.9	30	0.17	0.29	0.59
13.0	1.25	$NO_2^- Na^+$	0.2	1.9	50	0.19	0.30	0.63
13.0	0.98	$Br^- Na^+$	1.0	1.9	15	0.23	0.33	0.70

[a] Experiments at tenfold dose rate.

been postulated previously.[15] Alternatively, reaction of H_2O^* with OH^- ions may lead to a similar effect if it results in a catalysed formation of H+OH radicals. We have no independent support for these suggestions.

The two effects may also be due to independent causes, thus the increase of $G_{H_2O_2^{16,18}}$ may be due to the fact that above pH=9, OH dissociates into O^- and H^+; OH radicals will mainly decompose H_2O_2 according to (8), and only partly react as in (9). For O^- the likelihood of hydrogen abstraction from H_2O_2 will be less, and displacement of OH, or its equivalent from the molecule, easier. This would require that as $G_{H_2O_2^{16,18}}$ increases, the total decomposition of H_2O_2 should decrease, which indeed appears to be true. We are engaged[16] on an investigation on the radiation stability of alkaline H_2O_2 solutions, in which a decrease in the radiation induced decomposition of H_2O_2 in alkali is observed. If this is the cause of the increase in the yield of $H_2O_2^{16,18}$ we have to assume that OH^- deactivated H_2O^* without any free radical formation.

Another source of $H_2O_2^{16,18}$ might have been a radiation induced scrambling between $H_2O_2^{16,16}$ and $H_2O_2^{18,18}$ either directly or via HO_2. To test this point we carried out experiments in which at pH=5 a mixture of $H_2O_2^{16,16}$ and $H_2O_2^{18,18}$ with total $(H_2O_2)=0.03$M and total % $O^{18}=17.3$ was irradiated in H_2O^{16}. It was found that the residual H_2O_2 had an identical isotopic composition while the O_2 evolved showed only 0.4% $O_2^{16,18}$ which originated from two different molecules of H_2O_2. Thus, no scrambing (e.g., through HO_2) occurs under these conditions.

We shall now examine these conclusions in the light of the results obtained in the presence of various additives. The addition of bromide introduces several effects. Already at very much lower concentrations[12] than the one employed by us, Br^- is a very efficient scavenger for OH. Because of the high atomic number of Br^- the absorbed dose will increase. The effect of the atomic number alone is obtained by adding under similar conditions Rb^+ or Cs^+ instead of Br^-. We see that the addition of these, increases the yield of both $H_2O_2^{18,18}$ and $H_2O_2^{16,18}$ leaving their *ratio* nearly unaffected. The addition of Br^-, on the other hand, *decreases* both $H_2O_2^{18,18}$ and $H_2O_2^{16,18}$ and at the same time changes their ratio appreciably, particularly in acid solutions. This effect cannot be attributed merely to radical scavenging by Br^-. At much lower concentrations Br^- alone, if no H_2O_2 were present, would scavenge practically all OH radicals.[12] As it was previously indicated, H_2O_2 alone at 1M concentration will also be an effective scavenger, thus Br^- will be expected to compete with H_2O_2 for the radicals, and consequently a decrease in the yield of $H_2O_2^{16,18}$ formed

TABLE VII. Spark discharge induced formation of $H_2O_2^{18,18}$ and $H_2O_2^{16,18}$ (initial H_2O_2 concentration = 0.2 mole/liter).

pH	Br^-	Dec'n yield mole O_2	H_2O_2 formed from H_2O moles	yield $H_2O_2^{18,18}$ moles	yield $H_2O_2^{16,18}$ moles	R
1.30			0.412	0.326	0.173	1.9
1.30			.606	0.508	0.184	2.7
0.90	1.03		0.055	0.055	0.002	25
4.15		15	0.242	0.216	0.053	4.1
6.83		5	0.146	0.122	0.047	2.6
8.50		20	0.071	0.061	0.020	3.0
13.0		25	0.0117	0.009	0.006	1.5

[15] C. Reid, *Excited States in Chemistry and Biology* (Butterworths Scientific Publications, Ltd., London, 1957), p. 68.

[16] I. Burak and G. Stein (to be published).

by reaction (9) is expected. Br^- also diminishes the yield of $H_2O_2^{18,18}$, though to a smaller extent than that of $H_2O_2^{16,18}$. The effect of Br^- may be explained if we assume that Br^- effectively competes with water for the available radiation energy, thus decreasing the yield of both H_2O^* and of OH, and giving Br atoms instead. In addition, if H_2O^+ is formed, then the process

$$H_2O^+ + Br^- \rightarrow H_2O^* + Br \qquad (11)$$

may compete with

$$H_2O^+ + aq \rightarrow OH + H^+aq. \qquad (12)$$

Using NO_2^-, the effect of high atomic number is eliminated; NO_2^- can be used in neutral and basic solutions only, owing to its interaction with H_2O_2 in acid medium. NO_2^- does not affect the yield of $H_2O_2^{18,18}$, but *increases* very considerably that of $H_2O_2^{16,18}$. This is in agreement with the assumption that $H_2O_2^{18,18}$ is due to a molecular process and thus it is unaffected by OH radical scavengers. The increase in $H_2O_2^{16,18}$ is due to a specific effect of NO_2^-.

The formation of $H_2O_2^{16,18}$ may be explained as follows, OH radicals react with NO_2^-,

$$NO_2^- + OH \rightarrow NO_2 + OH^-, \qquad (13)$$

NO_2 thus formed may react with H_2O_2 forming

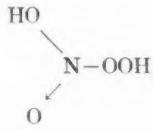

a peroxide of N(IV) acid. This may eventually be oxidized to pernitric acid (O_2NOOH). Due to the inductive effect of the $-NO_2$ group the O—O bond of the peroxide may be polarized to allow a nucleophilic substitution of $-O-OH^{16,16}$ by O^{18} from the water forming an exchanged peroxide; on hydrolysis $H_2O_2^{16,18}$ will be formed. It was found indeed that both NO_2 and HNO_3 induce an exchange between H_2O_2 and water.[9]

Regarding the $O_2^{18,18}$ and $O_2^{16,18}$ evolved during irradiation, the amount of $O_2^{18,18}$ is very small and permits only a qualitative indication of any trend with *p*H. The yield of $O_2^{16,18}$ is considerable and shows well defined changes with change of *p*H. The first decrease, between *p*H 2–3 may be connected with the dissociation of HO_2, the second between *p*H 9–10, perhaps with that of OH. There appears to be no correlation between $G_{H_2O_2}^{16,18}$ and $G_{O_2}^{16,18}$. Whereas $G_{O2}^{16,18}$ decreases with increasing H_2O_2 concentration, $G_{H_2O_2}^{16,18}$ increases; the *p*H dependence of $G_{O_2}^{16,18}$ is also different from that of $G_{H_2O_2}^{16,18}$. It may be suggested that the precursor of $O_2^{16,18}$ is scavenged by H_2O_2. This would indicate a mechanism in which the intermediate HO_2 radical, which eventually yields O_2, becomes isotopically "scrambled" at some stage.

The following may be a possible explanation which appears to offer a solution for the observed facts. The results already indicated that OH radicals exchange with H_2O_2 to a considerable extent, as in reaction (9). It may be suggested that in reaction (8), in which HO_2 is formed, the activated state is

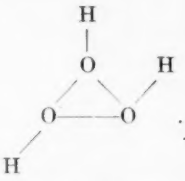

From this, scrambled $H_2O_2^{16,18}$ may result with a yield of about 10%, according to

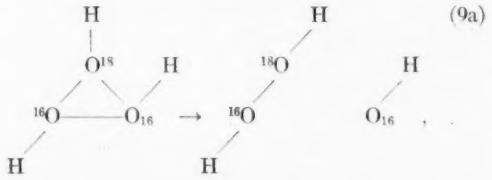

(9a)

while from the same symmetrical transition state the HO_2 radical may also evolve scrambled,

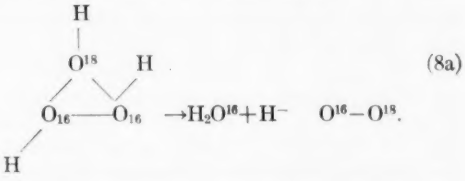

(8a)

There remains the experimental fact that with increasing $H_2O_2^{16,16}$ concentration, $G_{O_2}^{16,18}$ decreases while $G_{H_2O_2}^{16,18}$ increases. This may be due to the exchange reaction

$$HO_2^{16,18} + H_2O_2^{16,16} \rightarrow H_2O_2^{16,18} + HO_2^{16,16}. \qquad (14)$$

This exchange may be catalysed by alkalinity via reaction [(14a) and (14b)]

$$O_2^{(16,18)-} + H_2O_2^{16,16} \rightarrow O_2^{(16,16)-} + H_2O_2^{16,18} \qquad (14a)$$

$$O_2^{(16,18)-} + HO_2^{(16,16)-} \rightarrow O_2^{(16,16)-} + HO_2^{(16,18)-}. \qquad (14b)$$

On the other hand O^- may show a smaller tendency to form scrambled $HO_2^{16,18}$. These factors may account for the *p*H dependence of $G_{O_2}^{16,18}$.

In order to confirm this hypothesis on $O_2^{16,18}$ formation, experiments were carried out in presence of Cu^{++} which is an efficient scavenger for HO_2[17] and would thus compete with reaction (14),

$$HO_2 + Cu^{++} \rightarrow O_2 + H^+ + Cu^+. \qquad (15)$$

It was found that $G_{O_2}^{16,18}$ increased considerably in the

[17] W. G. Barb, J. H. Baxendale, P. George, and K. R. Hargrave, Trans. Faraday Soc. **47**, 642 (1951).

presence of Cu^{++} whereas no effect on $G_{H_2O_2}{}^{18,18}$ or $G_{H_2O_2}{}^{16,18}$ could be detected.

The experiments with protons support the conclusion of the x-ray experiments. Protons will form OH radicals much more closely spaced. Thus the recombination of two HO^{18} radicals to give $H_2O_2{}^{18,18}$ is favored, and only higher concentrations of $H_2O_2{}^{16,16}$ may compete with this radical process. On increasing initial $H_2O_2{}^{16,16}$ concentration, a substantial decrease in $G_{H_2O_2}{}^{18,18}$ and an increase in $G_{H_2O_2}{}^{16,18}$ was observed accordingly. Under these conditions of total absorption, there is no effect of Br^- on the absorbed dose. Thus, only the effect of Br^- is the competition with H_2O for the available energy. In proton irradiated solutions Br^- lowers both the yields of $H_2O_2{}^{18,18}$ and $H_2O_2{}^{16,18}$ considerably, which may be due to reaction (13) alone. On the other hand, the addition of Cs^+ has no effect at all in this case. NO_2^- shows a similar effect to that demonstrated on x-ray irradiated solutions.

The results obtained in the presence of initially added $O_2{}^{18,18}$ to x-ray irradiated solutions of $H_2O_2{}^{16,16}$ in H_2O^{16}, show two different mechanisms of exchange between O_2 and aqueous H_2O_2. The results in Table V show the existence of a thermal exchange process leading to the formation of both $H_2O_2{}^{18,18}$ and $H_2O_2{}^{16,18}$ from $O_2{}^{18,18}$. The effect of radiation produces $H_2O_2{}^{18,18}$ *only*. In alkaline solution the amount formed is some tenfold higher than in acid solution. This would be consistent with the assumption of Hart, Gordon, and Hutchison[7] that O^- (the anion of OH) may transfer its electron to O_2 yielding O_2^-, which will give H_2O_2 in good yield without leading to the formation of any scrambled O_2 or H_2O_2.

CONCLUSION

The experiments in this study provide strong evidence in favor of a distinct molecular mechanism leading to the formation of H_2O_2 in irradiated solutions. The effects of scavengers and of changes in *p*H on the yield of H_2O_2 formed directly from H_2O, are significantly different from their influence on the products of free radical precursors. The results regarding the molecular yield of H_2O_2 are consistent with those of Mahlman[5] on the formation of "molecular" H_2. They are also consistent with the results of Schwartz,[18] but for the interpretation. In a very careful investigation of the effects of varying concentrations of different scavengers on the yield of H_2 and H_2O_2, he claimed that when the concentrations of the scavengers are "normalized" to allow for their different efficiencies as scavengers, their influence on the yield of both H_2 and H_2O_2 can be derived from a theoretical curve, on the assumption that the only precursors of importance are free radicals. A careful consideration of the results of Schwartz proves that at high concentrations of scavengers, the experimental results differ significantly from the theoretical values. This can be explained both for H_2 and H_2O_2 by assuming that a residue of their free radical precursors is not accessible to scavengers. While the G value for "molecular" H_2 is only of the order of 0.1, we find for $g_{molecular}$ of H_2O_2 a value of the order of 0.3–0.4, in neutral and acid solution. Thus, some of the conclusions of Backhurst, Johnson, Scholes, and Weiss[8] are confirmed.

The discrepancy between the residual yields of H_2 and H_2O_2 is probably real and due to the fact that reaction (4) only describes the process schematically. Part of the excited H_2O may yield H_2O_2 with another water molecule, with the simultaneous formation of two H atoms. The results of the proton irradiations do not support the participation of two excited water molecules in reaction (4).

---

[18] H. A. Schwartz, J. Am. Chem. Soc. **77**, 4960 (1955).

Kinetics of Coordinate Bond Formation. IV. Kinetic Isotope Effect in the Reaction NH_3+BF_3

G. B. KISTIAKOWSKY AND C. E. KLOTS*

Gibbs Chemical Laboratory, Harvard University, Cambridge, Massachusetts

(Received September 15, 1960)

An isotopic rate ratio, $k'/k=1.91\pm0.10$, has been measured at room temperature for the reactions NH_3 $(ND_3)+BF_3=NH_3BF_3(ND_3BF_3)$. A set of vibrational frequencies for the transition states is deduced which explains the observation by attributing to the transition state a large degree of charge transfer stabilization and a negligible activation energy.

THE modified technique of the spherical "diffusion flame" of Polanyi has been successfully applied to the kinetics of fast gaseous reactions of the general type[1]

$$N(CH_3)_3+BF_3\rightarrow(CH_3)_3NBF_3.$$

The theory of the temperature pattern has been shown to be correct to a high degree of accuracy, and ranges of the critical flame parameters deduced which afford maximum reliability.[2] The results[3] may, therefore, be treated with a fair degree of confidence. They reveal, however, a surprising dependence of the rate upon the complexity of the amine. The increase of the rate constant for the association step with increasing size of the Lewis base is in contradiction with classical notions of bimolecular steric factors,[4] yet the results have since been substantiated in other laboratories.[5,6] Consequently, a small activation energy has been postulated for the ammonia reaction, which would then be lessened by the greater inductive and dispersion forces to be expected with the higher amines. However, experimental efforts have failed to reveal any temperature dependence of the rate constant.[3]

In order to gain more information about the reaction coordinates of such associations, we have undertaken the measurement of the isotopic rate ratio for the reactions

$$NH_3+BF_3=NH_3BF_3$$

$$ND_3+BF_3=ND_3BF_3.$$

The result, when interpreted by means of the transition state theory, offers some insight into the secondary structural changes occurring during the course of the reaction.

EXPERIMENTAL

A vacuum system and Pyrex reactor similar to those previously described[1] were employed in these measurements. The reactants, NH_3 or ND_3, and BF_3, both mixed with nitrogen carrier gas flowed through capillaries into the reactor. The ammonia species were mixed with the carrier gas just before entering the reaction zone, and always served as the atmosphere.

The boron trifluoride-nitrogen mixture entered the reactor by means of a small nozzle whose tip was located in the center of the reactor. The desired steady state pressure in the reaction zone was then set by adjusting the pumping speed of a Cenco Megavac pump. A liquid nitrogen trap, located between the reactor and pump, collected the unreacted ammonia, which was always present in a stoichiometric excess. The reactor was thermostated by means of a motor stirred water bath. All measurements were done in the vicinity of room temperature.

The capillary flow rates had previously been measured in terms of their driving pressures, so that the rate of influx of each species was known. The ratio of the NH_3 to ND_3 flow rates was further checked by collecting these gases in a liquid nitrogen trap just beyond the reaction zone before the boron trifluoride flow was turned on. When cracked with a hot platinum wire, this mixture yielded N_2, H_2, HD, and D_2 gases which were then analyzed with a previously calibrated Consolidated-Nier isotope ratio 21-201 mass spectrometer.

REACTANTS

Prepurified nitrogen, for use as a carrier gas, was admitted to the system through a drying column of magnesium perchlorate. Anhydrous ammonia and boron trifluoride from the Matheson Company were used without further purification. The deuterated ammonia was prepared by distilling D_2O, obtained from Stewart Oxygen Company, through magnesium nitride, in the standard fashion.[7] The nitride had been prepared in an iron furnace at 900°C and subsequently handled in a dry box. The ammonia so obtained was cracked and found, upon analysis, to be 98.5% deuterated.

CALCULATIONS

The raw data from these experiments consist of hydrogen-deuterium ratios in ammonia before and after passage through the reaction zone, and the flow

* Present address: Department of Physics, Amherst College, Amherst, Massachusetts.

[1] D. Garvin, V. P. Guinn, and G. B. Kistiakowsky, Discussions Faraday Soc. **17**, 32 (1954).
[2] F. T. Smith, J. Chem. Phys. **22**, 1605 (1954).
[3] G. B. Kistakowsky and R. Williams, J. Chem. Phys. **23**, 334 (1955).
[4] C. E. H. Bawn, Trans. Faraday Soc. **31**, 1536 (1935).
[5] J. Daen and R. A. Marcus, J. Chem. Phys. **26**, 162 (1957).
[6] S. H. Bauer (private communication).
[7] A. Smits, G. J. Muller, and F. A. Kroger, Z. physik Chem. (Leipzig) **B38**, 177 (1938).

TABLE I. Experimental Data.

Run	2	3	4	5	6	7	8	10	11	12
Time (hr)	4	3	1.5	2.5	2.5	2.5	2.0	2.0	2.0	2.0
Pressure (mm)	0.55	0.53	1.00	1.03	2.20	0.270	0.270	0.270	1.00	2.28
$\bar{H}$[a]	1.35	3.91	2.26	2.26	2.24	2.24	2.24	2.24	2.24	2.22
$\bar{D}$	0.797	4.30	1.91	1.91	1.91	1.87	1.87	1.86	1.86	1.84
$\bar{A}$	0.792	0.792	0.790	0.790	0.790	0.789	0.789	7.89	7.89	7.88
$\bar{N}$	5.01	5.00	5.00	4.95	4.90	4.90	7.33	4.02	3.52	3.50
r_0	1.73	0.920	1.21	1.21	1.21	1.22	1.22	1.22	1.23	1.23
r	1.31	0.856	1.08	1.07	1.09	1.085	1.07	1.07	1.07	1.07
k'/k	1.98	2.08	1.77	1.86	1.69	1.80	1.93	1.93	2.02	1.92

[a] $\bar{H}$—Influx, NH_3, moles/sec$\times 10^8$
$\bar{D}$—Influx, ND_3, moles/sec$\times 10^8$
$\bar{A}$—Influx, BF_3, moles/sec$\times 10^6$
$\bar{N}$—Influx, N_2 moles/sec$\times 10^6$
r_0—$\bar{H}_0/\bar{D}_0$
r—$\bar{H}_t/\bar{D}_t$.

rates of all gas species into the reactor. Since we equate the total rate of ammonia consumption with the rate of influx of the BF_3, we then know the flow rate of each species from the reactor, and thus the steady-state concentration of each species before and after passage through the flame.

There is some ambiguity as to the correct relationship between the above parameters and the rate constant ratio of interest. If we define the experimental rate constant, k_e', of the reaction $NH_3+BF_3\rightarrow NH_3BF_3$, in a small volume element by

$$-d(NH_3)/dt=k_e'(BF_3)(NH_3), \qquad (1)$$

then the integral of the left-hand side over the entire reactor is clearly equal to the difference between the flow rates of the NH_3 species into and out of the flame, which we denote by $\bar{H}_0$, $\bar{D}_0$ and $\bar{H}_t$, $\bar{D}_t$, respectively. We may remove k_e' from the integral of the right-hand side, since it can depend only on the total pressure, a constant for the reactor. Smith[8] has suggested that (NH_3) is also constant throughout the flame, being equal to the exit concentration. We may thus write

$$\bar{H}_0-\bar{H}_t=k_e'(NH_3)_t\int^v(BF_3)d\tau \qquad (2)$$

and, upon similar considerations of the ND_3 species,

$$D_0-D_t=k_e(ND_3)_t\int^v(BF_3)d\tau. \qquad (3)$$

On dividing (2) by (3), we obtain

$$(\bar{H}_0-\bar{H}_t)/(\bar{D}_0-\bar{D}_t)=(k_e'/k_e)(\bar{H}_t/\bar{D}_t), \qquad (4)$$

so that the rate constant ratio can be evaluated from the flow rates without consideration of the flame pattern.

One may object, however, to the use of the reactor exit concentrations throughout the reaction zone since, in these experiments, a liquid nitrogen trap immediately followed the reactor, in which the gaseous concentrations would be zero. An alternative expression, but one closely related to (4), and based on the notion of mass flow through the reactor, was, therefore, adopted. Integration of (1) as the volume element moves through the reaction zone gives

$$\ln\bar{H}_t/\bar{H}_0=k_e'\int_0^t(BF_3)dt. \qquad (5)$$

Division by the corresponding equation for the deuterated species produces

$$\ln\bar{H}_t/\bar{H}_0=(k_e'/k_e)\ln\bar{D}_t/\bar{D}_0, \qquad (6)$$

the usual expression for competitive isotopic reactions.[9] Upon expansion of the logarithmic terms of Eq. (6), one obtains Eq. (4) in the limit of infinitesimal depletion of the atmospheric reactants. The consistency of our results in the case of larger depletions will provide some support for the use of Eq. (6) exclusively.

The present method assumes, of course, that both reactions are irreversible. Smith has indeed shown the equilibrium constant for the reaction $NH_3+BF_3=NH_3-BF_3$ to be immeasurably large ($>5\times 10^9$ cm^3/mole).

RESULTS

The pertinent data, together with the results of Eq. (6), are given in Table I. Since no significant trend

[8] F. T. Smith and G. B. Kistiakowsky, J. Chem. Phys. **31**, 621 (1959).

[9] J. Bigeleisen and M. Wolfsberg, Advances in Chem. Phys. (1958).

TABLE II. Reactant and transition state frequencies (cm^{-1}).

NH_3	ND_3	NH_3—BF_3	ND_3—BF_3
(*a*) 3336	2419	3000	2175
(*a*) 950	749	1100	867
(*e*) 3413	2555	3072	2300
(*e*) 1627	1191	1540	1110
(*a*) ...	...	840	830
(*a*) ...	...	610	600
(*e*) ...	...	1330	1320
(*e*) ...	...	485	475
(*e*) ...	...	320	266
(*e*) ...	...	121	111

with respect to pressure or mass flow is obvious, a simple average was used to yield a final value of $k'/k = 1.91 \pm 0.11$. Of particular interest is the result of run No. 2 where some 35% of the atmospheric reactant was depleted. If Eq. (4) instead of (6) had been the correct method of interpretation, then this run would have given a lower result for k'/k. In fact, it is slightly higher than the average value suggesting that our treatment was indeed the correct one.

DISCUSSION

A simple collision model is obviously unable to account for a kinetic isotope effect of the observed size. So also is the transition state theory as applied to radical combinations,[10] invoking the notion of an extremely loose transition complex. It is necessary to consider a more rigid model. To do this we shall employ the Bigeleisen formalism in which the rate ratio may be expressed solely in terms of the vibrational frequencies of the reactants and their transition states.[9] The frequencies of the ammonia species are well known,[11] whereas those of the complexes can only be guessed. For this purpose we have found it useful to consider the fundamental frequencies of the molecules CH_3CF_3 and CD_3CF_3,[12,13] which are isoelectronic with the transition states in question, and of several BF_3 complexes.[14,15] Most of the normal vibrations would seem to undergo little change during reaction; furthermore many of them are nearly classical, thus contributing little to the isotope effect. Of overwhelming importance are the high frequencies associated with the N-H motions. In order to reproduce the experimental rate ratio, it was necessary to postulate a roughly 20% decrease in their force constants in the transition state. There is some evidence that this is completely reasonable. Applying Badger's Rule[16] to the increased bond length of NH_4^+,[17] for example, suggests that its valence bond force constants may be 35% less than those of NH_3.

The frequencies postulated, then, for the transition states are given in Table II. No claim is made that they are other than qualitatively correct. They do demonstrate, however, that the experimental result can be rationalized, at least, by means of transition state theory and chemical analogy, since their substitution into the isotopic rate constant ratio expression[9] leads to the value 1.84 in satisfactory agreement with observation.

These frequencies are further capable of reproducing the absolute rate constants of several reactions studied previously if one chooses reasonable moments of inertia and postulates a vanishingly small activation energy for the reaction. Further details of this calculation may be found elsewhere.[18] This result is important since it suggests that the charge transfer process, first postulated for this type of reaction by Mulliken,[19] provides an extremely low energy pathway in spite of the necessary secondary structural changes. The increasing N—H bond distances and subsequent isotope effect are probably symptomatic of the spreading of the formal positive charge as it appears on the nitrogen atom. The stabilization is apparently operative, however, only within a small solid angle of relative orientation, for the symmetry reasons discussed by Mulliken, and as evidenced by the low collisional yields. Presumably, then, the lower ionization potentials and larger polarizabilities of the heavier amines permit a greater degree of orientational freedom without encountering significant repulsive forces.

[10] E. Gorin, Acta Physicochim. U.R.S.S. **9**, 691 (1938).
[11] G. Herzberg, *Spectra of Diatomic Molecules* (D. Van Nostrand Company, Inc., Princeton, New Jersey, 1950).
[12] J. R. Nielsen, H. H. Claasen, and D. C. Smith, J. Chem. Phys. **18**, 1471 (1950).
[13] W. F. Edgell (private communication).
[14] A. Shepp and S. H. Bauer, J. Am. Chem. Soc. **76**, 265 (1954).
[15] S. H. Bauer, J. Am. Chem. Soc. **59**, 1804 (1937).
[16] R. M. Badger, J. Chem. Phys. **3**, 710 (1935).
[17] H. S. Gutowsky, G. E. Pake, and R. Bersohn, J. Chem. Phys. **22**, 643 (1954).
[18] C. E. Klots, thesis, Harvard University, 1959.
[19] R. S. Mulliken, J. Am. Chem. Soc. **74**, 811 (1952).

Kinetics of Coordinate Bond Formation. V. Kinetics of the Reaction $P(CH_3)_3+BF_3$

G. B. KISTIAKOWSKY AND C. E. KLOTS*

Gibbs Chemical Laboratory, Harvard University, Cambridge, Massachusetts

(Received September 15, 1960)

The temperature pattern method in dilute spherical diffusion flames has been applied to the reaction of boron trifluoride with trimethyl phosphorus. The bimolecular rate constant indicates this to be the fastest association reaction yet studied with this technique. Expectations as to the effect of the reverse reaction on the temperature pattern are qualitatively confirmed. The origin of steric factors in coordinate bond formation is briefly discussed.

INTRODUCTION

THE utility of the dilute spherical diffusion reaction technique has been successfully demonstrated for simple association reactions.[1] Its extension to more complicated kinetic situations would, therefore, seem desirable. Exploratory work by Smith[2] has shown that the reversibility of a bimolecular association process should affect the reaction pattern in a particularly straightforward manner. The present work was undertaken to test his results and thus to evaluate the diffusion reaction technique as a source of thermodynamic data. The reaction

$$P(CH_3)_3+BF_3=F_3BP(CH_3)_3 \qquad (1)$$

seemed ideal for such purposes. Thermodynamic data at 100°C suggest that the adduct will be only slightly dissociated at room temperature.[3] Furthermore the kinetics of the forward reaction should be of interest in elucidating the effect of molecular properties on the rates of such processes.

EXPERIMENTAL

A vacuum system similar to that of previous work was used.[4] One notable improvement, however, consisted of fitting the brass lid to the Pyrex reactor by means of a large O-ring seal. Upon evacuation, external pressure held the lid tight, permitting the entire reactor to be immersed in its water bath.

The thermocouple wires were 90% Pt–10% Ir, and 60% Au–40% Pd, giving a thermal emf of 47 μv/°C. They were mounted in a Teflon plug and sealed to the copper leads in a brass block in thermal contact with the reactor wall. The thermocouple mount entered the reactor through an O-ring seal in the lid, which remained vacuum tight during positioning of the thermocouple in the flame. Signals were fed to a Liston-Becker dc breaker amplifier and displayed on a G-10 graphic recorder. With proper shielding the noise level could be kept to less than 5×10^{-9} v, providing a resolution of about 10^{-4} degrees.

In a series of runs, the reservoir pressure of trimethyl phosphorus, which always served as the atmospheric gas, was successively lowered while the total reactor pressure was kept constant. By this means, the effect of the reverse reaction could be separated from a kinetic interpretation of the temperature profile. All measurements were made in the horizontal plane containing the center of the flame, and were done in the vicinity of room temperature.

Prepurified nitrogen, for use as a carrier gas, was admitted to the vacuum system through a drying column of $MgClO_4$. Boron trifluoride from a Matheson Company cylinder was used without further purification. The trimethyl phosphorus was prepared by a standard Grignard technique,[5] distilled into the system, and its infrared spectrum checked for purity.

CALCULATIONS

Knowledge of the reactor concentration of the trimethyl phosphorus depends on the calculation of its capillary flow-rate and, consequently, of its viscosity. Correcting the molecular diameter of trimethyl amine for increased bond distances,[6] and adopting Garvin's value for the viscosity of the amine,[7] we deduce coefficient of 76×10^{-6} poise for the phosphorus compound. Binary diffusion coefficients for $P(CH_3)_3$ BF_3 and BF_3 in nitrogen were calculated using molecular diameters of 7.06 A[8] and 4.74 A,[9] respectively. These values, although approximate, should be at least as accurate as the experimental data warrant.

The reaction temperature measurements were treated essentially in the manner prescribed by Smith. In practice, however, it was not necessary to apply the corrections he derived for distortion of the reaction by

* Present address: Department of Physics, Amherst College, Amherst, Massachusetts.

[1] G. B. Kistiakowsky and R. Williams, J. Chem. Phys. **23**, 334 (1955).

[2] F. T. Smith and G. B. Kistiakowsky, J. Chem. Phys. **31**, 621 (1959).

[3] H. C. Brown, J. Chem. Soc. **1956**, 1248.

[4] D. Garvin, V. Guinn, and G. B. Kistiakowsky, Discussions Faraday Soc. **17**, 32 (1954).

[5] A. B. Burg and R. I. Wagner, J. Am. Chem. Soc. **75**, 3872 (1953).

[6] L. S. Bartell and L. O. Brockway, J. Chem. Phys. **32**, 512 (1960).

[7] D. Garvin and G. B. Kistiakowsky, J. Chem. Phys. **20**, 105 (1952).

[8] The diameter of *t*-butyl amine; see work cited in footnote 1.

[9] *Landolt-Bornstein, Zahlenwerte und Functionen* (Springer-Verlag, Berlin, Germany, 1951), 6th ed., Vol. 1, pp. 369, 373.

TABLE I. Experimental Data.

	2	3	4	5	6	7	8
P—pressure (mm Hg)	0.251	0.251	0.251	0.251	0.128	0.128	0.128
M—total flow (moles/sec$\times 10^7$)	8.08	7.67	7.50	7.45	7.44	6.69	6.63
A—BF_3 flow (moles/sec$\times 10^7$)	8.46	8.40	8.39	8.40	8.38	8.30	8.30
b_{00}—partial pressure $P(CH_3)_3$ (mm$\times 10^2$)	0.228	2.98	2.58	1.15	1.73	1.45	0.887
c^2—mm^{-2}	0.55	1.10	0.891	0.848	0.146	0.117	0.0955
T—°C.	29	29	29	29	27	27	27
k_p—(cc/mole sec)	←	1.2×10^{13}	→		←	7.9×10^{12}	—
K_{eq}—(atm$\times 10^{-4}$)	←	3.6×10^{4}	→		←	1.6×10^{5}	—

	9	10	11	12	13	14	15	16	17	18	19
P	0.128	0.455	0.455	0.455	0.455	0.455	0.455	0.088	0.088	0.088	0.088
M	6.56	8.19	8.17	8.11	8.10	8.10	8.07	8.04	8.03	8.00	7.97
A	8.32	9.11	9.11	9.11	9.11	9.09	9.08	9.07	9.07	9.06	9.06
b_{00}	0.463	0.340	0.58	0.88	1.28	1.54	0.340	2.69	2.02	1.42	0 87
c^2	0.0676	0.125	0.168	0.182	0.294	0.344	0.090	0.144	0.125	0.098	0.075
T	27	27	27	27	27	27	27	28	28	28	28
k_p	→	←		7.6×10^{12}		→	←		7.6×10^{12}		→
K_{eq}	→	←		6.2×10^{5}		→	←		1.1×10^{5}		→

the outer cylindrical wall. The kinetics of the present system were such that the reaction diameters were always too small to include such boundary effects. By assuming, then, a pattern of the form

$$T=T_0+A/r-B-Ce^{-cr}/r, \tag{2}$$

one may extract c, the parameter of interest, defined by

$$c^2=(k_pZ_{\infty}/D_y)+(k_p/D_wK_{eq}). \tag{3}$$

Here k_p and K_{eq} are the forward rate constant and equilibrium constant of reaction (1), Z_{∞} the concentration of the atmospheric gas, and D_y and D_w the diffusion coefficients of BF_3 and $P(CH_3)_3BF_3$. Since k_p is defined such that

$$1/k_p=1/k_1+k_{-1}/k_1k_2(M),$$

a simple Lindeman plot of its pressure dependence yields k_1 the kinetic parameter of particular interest.

RESULTS AND DISCUSSION

Pertinent data are recorded in Table I. From them the values of $K_{eq}=8\times 10^4$ (atm)$^{-1}$ and $k_1=1.4$ (± 0.2)$\times 10^{13}$ cc/mole sec may be deduced. In both cases the contributing values were weighted in inverse proportion to the standard deviation associated with each point.[10] This procedure makes little use of values obtained at the highest pressure, and consequently smallest reaction zone diameter, where the scatter was quite large. Such behavior is not surprising since it is under just these conditions that jet flow, atmospheric depletion, and Joule-Thompson effects would cause the assumptions of the theoretical model to break down.

From thermodynamic data at 100°C one may independently calculate K_{eq} to be 7.1×10^3 (atm)$^{-1}$, in

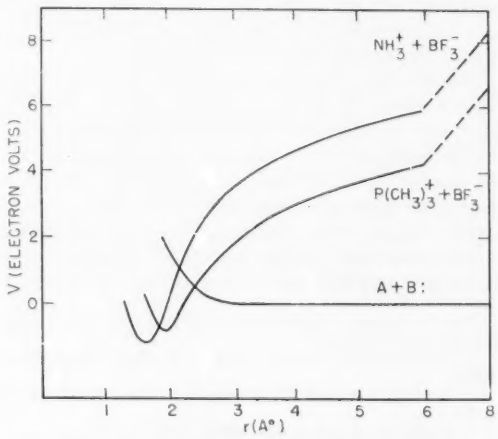

FIG. 1. Zero-order potential energy curves involved in coordinate bond formation. The upper curves follow a simple electrostatic potential form at larger intermolecular distances.

[10] J. M. Cameron, *Fundamental Formulas of Physics*, edited by D. H. Menzel (Prentice-Hall, Inc., Englewood Cliffs, New Jersey, 1955).

somewhat poor agreement with our value (3). In order to reconcile the two, one would have to postulate for the reaction that $\Delta H = -26.3$ kcal/mole rather than -18.9 kcal/mole. The dispersion among the several values of K_{eq} at the various pressures is also disappointing. Thus, although the reaction parameter in question obviously bears some relation to the equilibrium constant, its identification as such may not be completely justified.

Results of the Lindeman plot are somewhat more satisfactory. By assuming that k_2 takes its maximum value of the collisional frequency (which, although wrong, is the only concrete assumption possible), a lifetime ($\tau = 1/k_{-1}$) of the excited adduct $P(CH_3)_3$ of 1.5×10^{-6} sec may be calculated. This is comparable with the corresponding values for trimethylamine and dimethylamine (1), and is consistent with the notion that lifetimes of excited molecules are determined by the number of available degrees of freedom.

The primary rate constant $k_1 = 1.4 \times 10^{13}$ cc/mole sec is of considerable interest, representing the fastest association process yet studied with the flame technique. This is equivalent to reaction in roughly every fifteen collisions. Figure 1 shows, after Mulliken,[11] the probable zero-order potential energy curves involved in the present reaction and that of NH_3, corresponding to particularly unfavorable relative orientations.[12] The energy humps in both cases are probably negligible when reaction partners are more ideally oriented.[13] Therefore, the potential surface involving trimethyl phosphorus must remain attractive through a larger solid angle of off-axis collisions, affording its transition state greater flexibility than its ammonia counterpart. Ionization potentials of the other amines studied with the diffusion flame[14] then suggest potential curves of intermediate character, correlating with their observed kinetic behavior.

---

[11] R. S. Mulliken, J. Am. Chem. Soc. **74,** 811 (1952).

[12] Assuming an ionization potential of 8.18 ev for trimethyl phosphorus, based on those of PH_3, NH_3, and $N(CH_3)_3$. See work cited in footnote 14.

[13] G. B. Kistiakowsky and C. E. Klots, J. Chem. Phys. **34,** 712 (1961).

[14] F. H. Field and J. L. Franklin, *Electron Impact Phenomena* (Academic Press, Inc., New York, 1957).

Quadrupole Relaxation Effects in Nuclear Magnetic Double Resonance

JOHN D. BALDESCHWIELER

Department of Chemistry, Harvard University, Cambridge, Massachusetts

(Received July 11, 1960)

The effects of quadrupole relaxation on the relative linewidths of the double resonance spectrum of a molecule in the liquid state are considered. Only the special case is considered for which the broadening of individual components by quadrupole relaxation is not great enough to lead to complete collapse of a spin-multiplet. It is assumed that line separation is large compared to linewidth. The calculations are illustrated for the ammonia molecule.

I. INTRODUCTION

IN nuclear magnetic double resonance experiments, transitions between nuclear energy levels in a magnetic field are studied in the presence of two oscillatory fields. For a molecule that contains two types of nuclei whose magnetogyric ratios are different, the experiment is usually performed by applying a strong oscillatory field $\mathbf{H}_2$ near the resonance frequency of one nucleus, while transitions of the other nucleus are studied with a weak oscillatory field $\mathbf{H}_1$. The field $\mathbf{H}_2$ is assumed strong in the sense that $\gamma_2^2 H_2^2 T_1 T_2 \sim 1$, and $\mathbf{H}_1$ is weak in the sense that $\gamma_1^2 H_1^2 T_1 T_2 \ll 1$.[1] Saturation effects with the field $\mathbf{H}_2$ may be important, while those with $\mathbf{H}_1$ can be neglected. In the treatment that follows it is assumed that $\mathbf{H}_1$ is small enough that only the first-order terms in the time-dependent perturbation theory need be considered.

For a molecule that contains two types of nuclei, the resonance signal of one nucleus is split into a multiplet by an interaction of the form $J_{12}\mathbf{I}_1 \cdot \mathbf{I}_2$,[2,3] where J_{12} is the coupling constant between the spins of nuclei 1 and 2. When the spectrum is studied near the resonance frequency of nucleus 1, for example, with a single weak field $\mathbf{H}_1$, the selection rules for the allowed transitions may be written, $\Delta m_1 = \pm 1$, $\Delta m_2 = 0$.[4] The effect of applying a second strong field $\mathbf{H}_2$ near the resonance frequency of nucleus 2 is to change the selection rules to approximately: $\Delta m_1 = \pm 1$, $\Delta m_2 = 0, \pm 1, \pm 2, \cdots$. Thus in a double resonance experiment, a variety of new features appear that depend on the frequency and intensity of the fields $\mathbf{H}_1$ and $\mathbf{H}_2$.

The use of double resonance was first suggested by Bloch.[5] Bloom and Schoolery[6] gave an approximate treatment for the case of two spins of $\frac{1}{2}$ each, and tested the theory on F^{19} and P^{31} in Na_2PO_3F. A full description of the effect of double resonance on a general spin system was given by Bloch[7] and extended by Rempel.[8] A general treatment of the double resonance problem has also been given by Tomita.[9,10]

Anderson[11] applied double resonance techniques to determine the strength of an oscillatory field as suggested by Bloch.[7] He further showed that the technique could be used to decouple the spins of protons with different chemical shifts. For nuclei with spin greater than $\frac{1}{2}$, the possibility of relaxation through the interaction of the nuclear quadrupole moment with the field gradient at the nucleus often leads to a very short spin-lattice relaxation time T_1. Spin-multiplets arising from interaction with the high-spin nucleus are thus broadened. Double resonance has been used to effectively decouple nuclei such as N^{14}, B^{10}, and B^{11} from protons as an aid in the analysis of the proton resonance spectra.[12–17] A double resonance technique has been applied by Anderson, Pipkin, and Baird[18] in the determination of the ratio of the N^{14} and N^{15} magnetogyric ratios.

The effect of quadrupole relaxation on the relative widths of NMR spin-multiplets has been discussed by Pople.[19] He shows that the relative widths of various components of a spin-multiplet depend on the spin of the nucleus giving rise to the multiplet, and the particular state m_2 that gives rise to each component of the multiplet. Since the usual selection rules are $\Delta m_1 = \pm 1$, $\Delta m_2 = 0$, each component in a spin multiplet of transitions of nucleus 1 can be associated with a given state m_2 of nucleus 2. The effect of quadrupole relaxation on relative linewidth predicted by Pople[11] is in agreement with the spectrum of $N^{14}H_3$ reported by Ogg and Ray.[20,21]

[1] J. A. Pople, W. G. Schneider, and H. J. Bernstein, *High-resolution Nuclear Magnetic Resonance* (McGraw-Hill Book Company, Inc., New York, 1959), p. 31.
[2] H. S. Gutowsky and D. W. McCall, Phys. Rev. **82**, 748 (1951).
[3] E. L. Hahn and D. E. Maxwell, Phys. Rev. **84**, 1246 (1951).
[4] Footnote 1, p. 109.
[5] F. Bloch, Phys. Rev. **94**, 496 (1954).
[6] A. L. Bloom and J. N. Shoolery, Phys. Rev. **97**, 1261 (1955).
[7] F. Bloch, Phys. Rev. **102**, 104 (1956).
[8] R. C. Rempel, Phys. Rev. **109**, 831 (1958).
[9] K. Tomita, Progr. Theoret. Phys. (Kyoto) **19**, 541 (1958).
[10] K. Tomita, Progr. Theoret. Phys. (Kyoto) **20**, 743 (1958).
[11] W. A. Anderson, Phys. Rev. **102**, 151 (1956).
[12] V. Royden, Phys. Rev. **96**, 543 (1954).
[13] L. H. Piette, J. D. Ray, and R. A. Ogg, J. Mol. Spectroscopy **2**, 66 (1958).
[14] R. A. Ogg and J. D. Ray, Discussions Faraday Soc. **19**, 239 (1955).
[15] J. N. Shoolery, Discussions Faraday Soc. **19**, 215 (1955).
[16] R. A. Ogg, J. Chem. Phys. **22**, 1933 (1954).
[17] L. H. Piette, thesis, Department of Chemistry, Stanford University, Palo Alto, California, 1958.
[18] L. W. Anderson, F. M. Pipkin, and J. C. Baird, Phys. Rev. **116**, 87 (1959).
[19] J. A. Pople, Mol. Phys. **1**, 168 (1958).
[20] R. A. Ogg and J. D. Ray, J. Chem. Phys. **26**, 1339 (1957).
[21] R. A. Ogg and J. D. Ray, J. Chem. Phys. **26**, 1515 (1957).

Pople[19] considers only the usual NMR conditions for which $\Delta m_2=0$. In this paper, the treatment of Pople[19] is extended to show the effects of quadrupole relaxation on the variety of features observed in a double resonance experiment. The application of the results is illustrated for $N^{14}H_3$. Only the special case is considered for which the broadening of individual components by quadrupole relaxation is not great enough to lead to the complete collapse of the spin-multiplet. It is assumed that the line spacings are large compared with linewidth, or equivalently that T_1 and T_2 are long. In this work, as in the work of Pople,[19] it is assumed that T_1 and T_2 are equal. This is true for the special case for which the molecules are tumbling very rapidly as in a liquid at high temperature. If T_1 and T_2 are not equal, the complete treatment of Bloch[7] must be employed. Comparison of the measured relative linewidths for NH_3[20,21] with the theory of Pople[19] indicates that the assumption that T_1 equals T_2 is probably justified for NH_3 at room temperature.

II. THEORY OF DOUBLE RESONANCE

The static magnetic field is assumed to lie in the positive z direction so that $\mathbf{H}_0=H_0\hat{k}$. The fields $\mathbf{H}_1$ and $\mathbf{H}_2$ oscillate along the x axis, where $\mathbf{H}_1=2H_1\cos\omega_1 t\hat{i}$ and $\mathbf{H}_2=2H_2\cos\omega_2 t\hat{i}$. It is assumed that each oscillating field can be described as a pair of counter-rotating fields, and that only the component rotating with frequency $-\omega_1$, or $-\omega_2$ is effective in inducing transitions. The error involved in this procedure is negligible when the oscillatory fields are small in comparison with the static field.[22,23] In nuclear double resonance, as in the usual NMR experiment, the amplitudes of both the weak and strong oscillatory fields are small in comparison with H_0. The total magnetic field can then be given as

$$\mathbf{H}=H_0\hat{k}+(H_1\cos\omega_1 t+H_2\cos\omega_2 t)\hat{i}-(H_1\sin\omega_1 t+H_2\sin\omega_2 t)\hat{j}. \quad (1)$$

The Hamiltonian for a molecule in the liquid state in field $\mathbf{H}$ in the laboratory coordinate system is

$$\mathcal{H}=\mathcal{H}^0+\mathcal{H}'+\mathcal{H}'' \quad (2)$$

$$\mathcal{H}^0=\sum_i \nu_{0i}I_z(i)+\sum_{i<j}J_{ij}I_z(i)I_z(j) \quad (3)$$

$$\mathcal{H}'=\tfrac{1}{2}\sum_{i<j}J_{ij}[I_+(i)I_-(j)+I_-(i)I_+(j)]+\sum_i \nu_{2i}[I_x(i)\cos\omega_2 t-I_y(i)\sin\omega_2 t] \quad (4)$$

$$\mathcal{H}''=\sum_i \nu_{1i}[I_x(i)\cos\omega_1 t-I_y(i)\sin\omega_1 t], \quad (5)$$

where

$$\nu_{0i}=-\gamma_i H_0/2\pi,$$

$$\nu_{1i}=-\gamma_i H_1/2\pi,$$

$$\nu_{2i}=-\gamma_i H_2/2\pi,$$

γ_i = magnetogyric ratio of nucleus i including the chemical shift

$$I_\pm(i)=I_x(i)\pm I_y(i).$$

J_{ij} = spin-spin coupling constant between nuclei i and j, cps. The Hamiltonian is given in units of cycles per second, and the summations are carried out over the spins i and j of the molecule. In the laboratory system, the Schrödinger equation is

$$i\hbar\dot{\Psi}=\mathcal{H}\Psi. \quad (6)$$

Since the Hamiltonian is time dependent, it is not possible to obtain time-independent solutions to Eq. (6). However, the time dependence in $\mathcal{H}'$ can be removed if the Schrödinger equation is written in a coordinate system that rotates with the angular velocity, $-\omega_2\hat{k}$. The operator for a finite rotation $-\omega_2\hat{k}t$ can be written

$$u=\exp(-i\omega_2 I_z t). \quad (7)$$

If the wave function in the rotating coordinate system is defined as $\Psi_R=u\Psi$, the Schrödinger equation can be written in the rotating coordinate system[24]:

$$i\hbar\dot{\Psi}_R=\mathcal{H}_R\Psi_R \quad (8)$$

$$\mathcal{H}_R=\mathcal{H}_R{}^0+\mathcal{H}_R{}'+\mathcal{H}_R{}'' \quad (9)$$

$$\mathcal{H}_R{}^0=\sum_i A_i I_z(i)+\sum_{i<j}J_{ij}I_z(i)I_z(j) \quad (10)$$

$$\mathcal{H}_R{}'=\tfrac{1}{2}\sum_{i<j}J_{ij}[I_+(i)I_-(j)+I_-(i)I_+(j)]+\sum_i \nu_{2i}I_x(i) \quad (11)$$

$$\mathcal{H}_R{}''(t)=\sum_i \nu_{1i}[I_x(i)\cos(\omega_1-\omega_2)t-I_y(i)\sin(\omega_1-\omega_2)t], \quad (12)$$

where $A_i=(\nu_{0i}+\omega_2/2\pi)$.

In the rotating coordinate system, the time dependence of the Hamiltonian remains only in $\mathcal{H}_R{}''(t)$. If it is assumed that $\mathcal{H}_R{}''(t)$ is small with respect to $(\mathcal{H}_R{}^0+\mathcal{H}_R{}')$, then the solution to Eq. (8) can be approximated using first-order perturbation theory. The unperturbed Hamiltonian $(\mathcal{H}_R{}^0+\mathcal{H}_R{}')$ can be solved for its stationary eigenvalues E_R, and its normalized eigenfunctions ψ_R

$$(\mathcal{H}_R{}^0+\mathcal{H}_R{}')\psi_R=E_R\psi_R. \quad (13)$$

The time-dependent perturbation, to first order, then gives the transition probability per unit time, P_{mn}

[22] F. Bloch and A. Siegert, Phys. Rev. **57**, 522 (1940).
[23] N. F. Ramsey, Phys. Rev. **100**, 1191 (1955).
[24] I. I. Rabi, N. F. Ramsey, and J. Schwinger, Rev. Modern Phys. **26**, 167 (1954).

between states ψ_{Rm} and ψ_{Rn}. The transition probability per unit time is proportional to

$$|\langle m|\mathcal{H}''|n\rangle|^2\rho[(\omega_1-\omega_2)-\omega],$$

where $\omega=(E_{Rm}-E_{Rn})2\pi$, and the function ρ indicates that the transition probability is large when $\omega_1-\omega_2$ is close to ω. The frequency, $\omega_1/2\pi$ at which a transition is observed in the lab system is given by

$$\omega_1/2\pi=E_{Rm}-E_{Rn}+\omega_2/2\pi. \tag{14}$$

The calculation of the frequencies and relative intensities of absorptions for double resonance requires diagonalization of the Hamiltonian $(\mathcal{H}_R{}^0+\mathcal{H}_R{}')$ in the space of the spin functions for a given molecule. This process is of course considerably simplified by writing the basis functions in a manner consistent with the symmetry of the molecule.[25] The diagonalization of the Hamiltonian may often be approximated by the perturbation technique of Anderson,[11] or by simply neglecting small off-diagonal elements. In these calculations as in the work of Bloom and Shoolery,[6] the effects of changes in level populations on the intensities of signals have been neglected.

III. QUADRUPOLE EFFECTS

The special case to be considered is that for which the broadening of individual components of a spin multiplet is not great enough to lead to the complete collapse of the multiplet. It is assumed that a nucleus of spin $\frac{1}{2}$ (low-spin nucleus), is coupled with a nucleus of spin greater than $\frac{1}{2}$ (high-spin nucleus) by spin-spin interaction. A given component of a multiplet in the double resonance experiment cannot be associated with a given state m_2 of the high-spin nucleus, even when the magnetogyric ratios of the two spins are quite different. The width of a component depends on the lifetime of the high-spin nucleus in both states ψ_{Rm} and ψ_{Rn} associated with a given transition, where the states ψ_{Rm} and ψ_{Rn} are some linear combination of the basis functions.

Following the work of Pople,[19] it is assumed that mechanisms other than quadrupole relaxation for spin-lattice relaxation are negligible. It is further assumed that the line broadening is small compared to the multiplet separation. From Pople,[19] the transition probability P_{mk} between two states ψ_{Rm} and ψ_{Rk} due to the quadrupole operator F is

$$P_{mk}=2\hbar^{-2}|\langle m|F|k\rangle|^2\tau_c, \tag{15}$$

where τ_c is the correlation time for molecular motion, the matrix element is averaged over all orientations, and it is assumed that $\tau_c\omega_1\ll 1$.[26] The operator F is written as the scalar product,

$$F=Q\cdot\nabla E=\sum_{-2}^{2}(-1)^M Q_M(\nabla E)_{-M}, \tag{16}$$

where Q and ∇E are spherical tensor operators of second rank representing the nuclear electric quadrupole moment and the electric field gradient at the nucleus.

The solution to Eq. (8) may be written in the basis of the ϕ_i functions as

$$R^\dagger(\mathcal{H}_R{}^0+\mathcal{H}_R{}')R=E_R, \tag{17}$$

where the matrix R, representing a finite rotation of the coordinate system, is defined by

$$\psi_R=R\phi \tag{18}$$

and the functions ϕ_i are the basis spin functions consistent with the symmetry of the molecule.[25] The quadrupole operator in the same basis is then $R^\dagger FR$. In the work of Pople,[19] the functions ϕ_i were written as the product of functions associated with the low-spin nucleus and the simple spin functions for the high-spin nucleus. In the double resonance experiment the simple spin functions are mixed by the transformation R. It is thus necessary to show the effect of R on the matrix elements P_{mk}.

The operator F is the scalar product of two second rank spherical tensor operators, since the angular dependence of both Q and ∇E is contained in spherical harmonics of the form $Y_M{}^L(\cos\theta,\phi)$.[27] The scalar product given in Eq. (16) is then just a special case of the spherical-harmonic addition theorem.[28]

$$Y_0{}^L(\cos\theta,\phi)=\left(\frac{4\pi}{2L+1}\right)^{\frac{1}{2}}\sum_M Y_M{}^{*L}(\cos\theta_1,\phi_1)\,Y_M{}^L \times(\cos\theta_2,\phi_2). \tag{19}$$

The scalar product is thus proportional to the spherical harmonic $Y_0{}^L$. The behavior of the spherical harmonics or irreducible tensor operators under rotations is given by Rose as[29]

$$R^\dagger Y_M{}^L R=\sum_{M'}D_{M'M}{}^L Y_{M'}{}^L, \tag{20}$$

where $D_{M'M}{}^L$ is the $(2L+1)$ dimensional representation of the rotation group. Since the rows and columns of $D_{M'M}{}^L$ are orthonormal, the matrix elements P_{mk} are invariant under R and the matrix element is averaged over all orientations;

$$\hbar^2P_{mk}/2\tau_c=|\langle m|F|k\rangle|^2=|\langle i|R^\dagger FR|j\rangle|^2 =|\langle i|F|j\rangle|^2, \tag{21}$$

where $m=i$, $k=j$, m and k represent ψ_m and ψ_k, and

[25] E. B. Wilson, J. Chem. Phys. **27**, 60 (1957).
[26] See work cited in footnote 1, p. 216.
[27] R. V. Pound, Phys. Rev. **79**, 685 (1950).
[28] M. E. Rose, *Elementary Theory of Angular Momentum* (John Wiley & Sons, Inc., New York, 1957), p. 60.
[29] See work cited in footnote 28, p. 77.

TABLE I. Basis functions, diagonal elements, and eigenvalues for $N^{14}H_3$.

M_H	M_N		ϕ_i	$H_{Rmm}{}^0$	E_R
$\frac{3}{2}$	1	A_1	$\alpha\alpha\alpha(+)$	$A_N+\frac{3}{2}A_H+\frac{3}{2}J_{NH}$	$\frac{3}{2}A_H+l$
	0	A_1	$\alpha\alpha\alpha(0)$	$\frac{3}{2}A_H$	$\frac{3}{2}A_H$
	-1	A_1	$\alpha\alpha\alpha(-)$	$-A_N+\frac{3}{2}A_H-\frac{3}{2}J_{NH}$	$\frac{3}{2}A_H-l$
$\frac{1}{2}$	1	A_1	$(1/3)^{\frac{1}{2}}(\beta\alpha\alpha+\alpha\beta\alpha+\alpha\alpha\beta)(+)$	$A_N+\frac{1}{2}A_H+\frac{1}{2}J_{NH}$	$\frac{1}{2}A_H+m$
	0	A_1	$(1/3)^{\frac{1}{2}}(\beta\alpha\alpha+\alpha\beta\alpha+\alpha\alpha\beta)(0)$	$\frac{1}{2}A_H$	$\frac{1}{2}A_H$
	-1	A_1	$(1/3)^{\frac{1}{2}}(\beta\alpha\alpha+\alpha\beta\alpha+\alpha\alpha\beta)(-)$	$-A_N+\frac{1}{2}A_H-\frac{1}{2}J_{NH}$	$\frac{1}{2}A_H-m$
$\frac{1}{2}$	1	E_a	$(1/6)^{\frac{1}{2}}(2\beta\alpha\alpha-\alpha\beta\alpha-\alpha\alpha\beta)(+)$	$A_N+\frac{1}{2}A_H+\frac{1}{2}J_{NH}$	$\frac{1}{2}A_H+m$
	0	E_a	$(1/6)^{\frac{1}{2}}(2\beta\alpha\alpha-\alpha\beta\alpha-\alpha\alpha\beta)(0)$	$\frac{1}{2}A_H$	$\frac{1}{2}A_H$
	-1	E_a	$(1/6)^{\frac{1}{2}}(2\beta\alpha\alpha-\alpha\beta\alpha-\alpha\alpha\beta)(-)$	$-A_N+\frac{1}{2}A_H-\frac{1}{2}J_{NH}$	$\frac{1}{2}A_H-m$
$\frac{1}{2}$	1	E_b	$(1/2)^{\frac{1}{2}}(+\alpha\beta\alpha-\alpha\alpha\beta)(+)$	$A_N+\frac{1}{2}A_H+\frac{1}{2}J_{NH}$	$\frac{1}{2}A_H+m$
	0	E_b	$(1/2)^{\frac{1}{2}}(+\alpha\beta\alpha-\alpha\alpha\beta)(0)$	$\frac{1}{2}A_H$	$\frac{1}{2}A_H$
	-1	E_b	$(1/2)^{\frac{1}{2}}(+\alpha\beta\alpha-\alpha\alpha\beta)(-)$	$-A_N+\frac{1}{2}A_H-\frac{1}{2}J_{NH}$	$\frac{1}{2}A_H-m$
$-\frac{1}{2}$	1	E_a	$(1/6)^{\frac{1}{2}}(2\alpha\beta\beta-\beta\alpha\beta-\beta\beta\alpha)(+)$	$A_N-\frac{1}{2}A_H-\frac{1}{2}J_{NH}$	$-\frac{1}{2}A_H+n$
	0	E_a	$(1/6)^{\frac{1}{2}}(2\alpha\beta\beta-\beta\alpha\beta-\beta\beta\alpha)(0)$	$-\frac{1}{2}A_H$	$-\frac{1}{2}A_H$
	-1	E_a	$(1/6)^{\frac{1}{2}}(2\alpha\beta\beta-\beta\alpha\beta-\beta\beta\alpha)(-)$	$-A_N-\frac{1}{2}A_H+\frac{1}{2}J_{NH}$	$-\frac{1}{2}A_H-n$
$-\frac{1}{2}$	1	E_b	$(1/2)^{\frac{1}{2}}(\beta\alpha\beta-\beta\beta\alpha)(+)$	$A_N-\frac{1}{2}A_H-\frac{1}{2}J_{NH}$	$-\frac{1}{2}A_H+n$
	0	E_b	$(1/2)^{\frac{1}{2}}(\beta\alpha\beta-\beta\beta\alpha)(0)$	$-\frac{1}{2}A_H$	$-\frac{1}{2}A_H$
	-1	E_b	$(1/2)^{\frac{1}{2}}(\beta\alpha\beta-\beta\beta\alpha)(-)$	$-A_N-\frac{1}{2}A_H+\frac{1}{2}J_{NH}$	$-\frac{1}{2}A_H-n$
$-\frac{1}{2}$	1	A_1	$(1/3)^{\frac{1}{2}}(\alpha\beta\beta+\beta\alpha\beta+\beta\beta\alpha)(+)$	$A_N-\frac{1}{2}A_H-\frac{1}{2}J_{NH}$	$-\frac{1}{2}A_H+n$
	0	A_1	$(1/3)^{\frac{1}{2}}(\alpha\beta\beta+\beta\alpha\beta+\beta\beta\alpha)(0)$	$-\frac{1}{2}A_H$	$-\frac{1}{2}A_H$
	-1	A_1	$(1/3)^{\frac{1}{2}}(\alpha\beta\beta+\beta\alpha\beta+\beta\beta\alpha)(-)$	$-A_N-\frac{1}{2}A_H+\frac{1}{2}J_{NH}$	$-\frac{1}{2}A_H-n$
$-\frac{3}{2}$	1	A_1	$\beta\beta\beta(+)$	$A_N-\frac{3}{2}A_H-\frac{3}{2}J_{NH}$	$-\frac{3}{2}A_H+0$
	0	A_1	$\beta\beta\beta(0)$	$-\frac{3}{2}A_H$	$-\frac{3}{2}A_H$
	-1	A_1	$\beta\beta\beta(-)$	$-A_N-\frac{3}{2}A_H+\frac{3}{2}J_{NH}$	$-\frac{3}{2}A_H-o$

i and j represent ϕ_i and ϕ_j. Since P is invariant under R, the matrix elements P_{mk} can be calculated in the simplest set of basis functions.

The inverse lifetime $1/\tau_m$ of a given state m is then given by $\sum_k{}' P_{mk}$, where the sum is over all the states, k, to which m can relax by quadrupole transitions. Then for a dipole transition between two states m and n, the inverse lifetime $1/\tau_n$ of the state n is given by $\sum_l{}' P_{nl}$, and the effective inverse spin-lattice relaxation time $1/T_1$ is

$$1/T_1=1/\tau_m+1/\tau_n. \tag{22}$$

Since a variety of transitions are allowed in the double resonance experiment, the relative values of $1/T_1$ must be calculated for each transition type.

IV. SAMPLE CALCULATION FOR AMMONIA

For the C_{3v} symmetry of NH_3, the basis functions ϕ_i can be constructed from the spin product functions following the procedure of Wilson.[25] These are given in Table I. The functions α and β represent the proton spin functions with z components of spin of $+\frac{1}{2}$ and $-\frac{1}{2}$, respectively, and $(+)$, (0), and $(-)$ represent N^{14} spin functions with z components of spin of $+1$, 0, and -1. The total z component of the proton spins is given under M_H, while that of the nitrogen is given under M_N. The irreducible representation Γ of the group C_{3v} to which each function belongs is also given.

The stationary parts of the Hamiltonian can be written:

$$\mathcal{H}_R{}^0=A_N I_z(N)+\sum_i A_H I_z(H)+\sum_i J_{NH} I_z(N) I_z(H) \tag{23}$$

$$\mathcal{H}_R{}'=\tfrac{1}{2}\sum_i J_{NH}[I_+(N) I_-(H)+I_-(N) I_+(H)]$$
$$+v_{2N} I_x(N)+\sum_i v_{2H} I_x(H), \tag{24}$$

TABLE II. Relative intensity and inverse relaxation time for N^{14} wavefunctions.

Transition type	Relative intensity	$1/T_1$
$\langle a' \mid a \rangle$	$\frac{1}{4}[1+\cos(\theta_m-\theta_l)]^2$	3
$\langle b' \mid a \rangle$	$\frac{1}{2}\sin^2(\theta_m-\theta_l)$	5/2
$\langle c' \mid a \rangle$	$\frac{1}{4}[1-\cos(\theta_m-\theta_l)]^2$	3
$\langle a' \mid b \rangle$	$\frac{1}{2}\sin^2(\theta_m-\theta_l)$	5/2
$\langle b' \mid b \rangle$	$\cos^2(\theta_m-\theta_l)$	2
$\langle c' \mid b \rangle$	$\frac{1}{2}\sin^2(\theta_m-\theta_l)$	5/2
$\langle a' \mid c \rangle$	$\frac{1}{4}[1-\cos(\theta_m-\theta_l)]^2$	3
$\langle b' \mid c \rangle$	$\frac{1}{2}\sin^2(\theta_m-\theta_l)$	5/2
$\langle c' \mid c \rangle$	$\frac{1}{4}[1+\cos(\theta_m-\theta_l)]^2$	3

where the summations are over the three equivalent protons. It can be shown that terms in the coupling of the equivalent protons, J_{HH} do not enter in the expressions for the frequency or intensity of allowed transitions.[30] These have thus been omitted from Eqs. (23) and (24).

The matrix elements of $\mathcal{H}_R^0$ and $\mathcal{H}_R'$ can be written down from well-known rules.[31] The diagonal elements in $\mathcal{H}_R^0$ for the basis functions, ϕ_i, are given in Table I. Since terms in J_{HH} have not been included in Eq. (24), there are no diagonal elements in $\mathcal{H}_R'$. Since only terms in I_z occur in Eq. (23), there are no off-diagonal elements in $\mathcal{H}_R^0$. It can be shown by the perturbation technique of Anderson[11] that off-diagonal terms in J_{NH} and ν_{2H} can be neglected. The only important off diagonal elements are then those arising from $\nu_{2N}I_x(N)$. In the approximation that off-diagonal terms in J_{NH} and ν_{2H} are negligible, the only states that can interact are those connected by off-diagonal elements in $I_x(N)$. These are simply the states (+), (0); and (0), (−); with a given function of proton spins. The magnitude of these off-diagonal elements is $\sqrt{2}\nu_{2N}/2$. The complete Hamiltonian matrix thus consists of eight 3-by-3 blocks of elements along the diagonal. The secular determinant for the first block is

$$\begin{vmatrix} W_1-E_R & \sqrt{2}\nu_{2N}/2 & 0 \\ \sqrt{2}\nu_{2N}/2 & W_2-E_R & \sqrt{2}\nu_{2N}/2 \\ 0 & \sqrt{2}\nu_{2N}/2 & W_3-E_R \end{vmatrix}=0, \qquad (25)$$

where $W_1=A_N+\frac{3}{2}A_H+\frac{3}{2}J_{NH}$, $W_2=\frac{3}{2}A_H$, and $W_3=-A_N+\frac{3}{2}A_H-\frac{3}{2}J_{NH}$. The 3-by-3 secular determinants of the form of Eq. (25) can be solved to give the values of E_R given in Table I. The new constants introduced are

$$l=[(A_N+\tfrac{3}{2}J_{NH})^2+\nu_{2N}^2]^{\frac{1}{2}}$$
$$m=[(A_N+\tfrac{1}{2}J_{NH})^2+\nu_{2N}^2]^{\frac{1}{2}}$$
$$n=[(A_N-\tfrac{1}{2}J_{NH})^2+\nu_{2N}^2]^{\frac{1}{2}}$$
$$o=[(A_N-\tfrac{3}{2}J_{NH})^2+\nu_{2N}^2]^{\frac{1}{2}}.$$

The proper linear combinations of the ϕ_i functions to give the ψ_R functions are also found from Eq. (25).

$$\psi_{Rm}=\sum_i R_{mi}\phi_i, \qquad (26)$$

where the R_{mi} satisfy $\sum_j \mathcal{H}_{Rij}R_{mj}=E_{Rm}R_{mi}$. The constants R_{mi} are thus proportional to the co-factors of any row of the determinant in Eq. (25). The values of R_{mi} are fixed by requiring R to be unitary. The eigenfunctions for the first block in the secular equation can be written:

$$\psi_a=(\alpha\alpha\alpha)[\tfrac{1}{2}(1+\cos\theta_l)(+)-\sqrt{2}/2\sin\theta_l(0)+\tfrac{1}{2}(1-\cos\theta_l)(-)] \qquad (27)$$

$$\psi_b=(\alpha\alpha\alpha)[-1/\sqrt{2}\sin\theta_l(+)-\cos\theta_l(0)+1/\sqrt{2}(\sin\theta_l)(-)]$$

$$\psi_c=(\alpha\alpha\alpha)[\tfrac{1}{2}(1-\cos\theta_l)(+)+\sqrt{2}/2\sin\theta_l(0)+\tfrac{1}{2}(1+\cos\theta_l)(-)], \qquad (27)$$

where

$$\theta_l=\cos^{-1}(A_N+\tfrac{3}{2}J_{NH})/l$$
$$\theta_m=\cos^{-1}(A_N+\tfrac{1}{2}J_{NH})/m$$
$$\theta_n=\cos^{-1}(A_N-\tfrac{1}{2}J_{NH})/n$$
$$\theta_0=\cos^{-1}(A_N-\tfrac{3}{2}J_{NH})/o.$$

The eigenfunctions for the other blocks in the secular equation will be similar functions in the angles θ_m, θ_n, and θ_0. The convenient abbreviation $\psi_a=\phi(M_H,\Gamma)\phi_a(\theta_l)$ will be used to describe the complete wave function where the letter a, b, or c indicates the type of nitrogen spin function from Eq. (27), and $\phi(M_H,\Gamma)$ is the proton spin function of the Γ representation with total z component M_H.

Since only transitions at the proton resonance frequency are being studied, only those transitions are allowed for which $\Delta M_H=\pm 1$. Furthermore, transitions are only allowed between states belonging to the same irreducible representation. The transition probability is proportional to terms of the type

$$|\langle\phi(M_H,\Gamma)\mid\sum_i I_+(i)+I_-(i)\mid\phi(M_H\pm1,\Gamma)\rangle|^2\,|\langle\phi_a'(\theta_l)\mid\phi_a(\theta_m)\rangle|^2.$$

For transitions involving $\Delta M_H=\pm 1$, the functions $\phi_{a'}(\theta_l)$ are not in general orthogonal to any of the $\phi_a(\theta_m)$. Thus for each transition with $\Delta M_H=\pm 1$, there

[30] See work cited in footnote 1, p. 115.
[31] See work cited in footnote 28, p. 27.

TABLE III. ΔE_R values for allowed transitions.

Transition type	$(\frac{3}{2}, A_1)\leftarrow(\frac{1}{2}, A_1)$	$(\frac{1}{2}, A_1)\leftarrow(-\frac{1}{2}, A_1)$ $(\frac{1}{2}, E_a)\leftarrow(-\frac{1}{2}, E_a)$ $(\frac{1}{2}, E_b)\leftarrow(-\frac{1}{2}, E_b)$	$(-\frac{1}{2}, A_1)\leftarrow(-\frac{3}{2}, A_1)$
$\langle a' \mid a \rangle$	$-A_H+m-l$	$-A_H+n-m$	$-A_H+o-n$
$\langle b' \mid a \rangle$	$-A_H-l$	$-A_H-m$	$-A_H-n$
$\langle c' \mid a \rangle$	$-A_H-m-l$	$-A_H-n-m$	$-A_H-o-n$
$\langle a' \mid b \rangle$	$-A_H+m$	$-A_H+n$	$-A_H+o$
$\langle b' \mid b \rangle$	$-A_H$	$-A_H$	$-A_H$
$\langle c' \mid b \rangle$	$-A_H-m$	$-A_H-n$	$-A_H-o$
$\langle a' \mid c \rangle$	$-A_H+m+l$	$-A_H+n+m$	$-A_H+o+n$
$\langle b' \mid c \rangle$	$-A_H+l$	$-A_H+m$	$-A_H+n$
$\langle c' \mid c \rangle$	$-A_H-m+l$	$-A_H-n+m$	$-A_H-o+n$
Relative transition probability	1	2	1

will be nine components involving all the combinations of the $\phi_{a'}(\theta_l)$ and the $\phi_a(\theta_m)$. The relative intensities of these components will depend on terms of the type,

$$|\langle \phi_{a'}(\theta_l) \mid \phi_a(\theta_m) \rangle|^2.$$

These are given in Table II for the constants θ_l and θ_m. Similar terms occur for the other values of θ. The calculation of the remainder of the transition moment follows the usual rules.[31] The values of ΔE_R for the allowed transitions are given in Table III. Transitions of the type $(\frac{1}{2}, A_1)\leftarrow(-\frac{1}{2}, A_1)$, $(\frac{1}{2}, E_a)\leftarrow(-\frac{1}{2}, E_a)$, and $(\frac{1}{2}, E_b)\leftarrow(-\frac{1}{2}, E_b)$ are degenerate, and are indicated together in Table III. The relative intensities of the various transitions can be found by multiplying the appropriate term of the type $|\langle a' \mid a \rangle|^2$ from Table II by the factors indicated in the last row of Table III. These factors are obtained by summing terms of the type, $|\langle (M_H, \Gamma) \mid \sum_i I_+(i)+I_-(i) \mid (M_H \pm 1, \Gamma) \rangle|^2$, over the various degenerate transitions of each type.

Considerable simplification results for certain special cases. For example, if the frequency ω_2 of the field $\mathbf{H}_2$ is exactly equal to the resonance frequency of nitrogen, ν_{0N}, then A_N equals zero, and the constants $m=n$ and $1=o$. Then only thirteen different values of ΔE_R can be found. In the limit as ν_{2N} approaches zero, the spectrum reduces to the familiar triplet structure. In the limit as ν_{2N} becomes very large, the constants l, m, n, and o become equal, and the angles θ_l, θ_m, θ_n and θ_0 become equal. Thus only transitions of the types $\langle a' \mid a \rangle$, $\langle b' \mid b \rangle$, and $\langle c' \mid c \rangle$ are allowed, and the spectrum reduces to a single component at $\Delta E_R = -A_H$. In this limit the nitrogen spin is "decoupled" from the proton spins.

Since the matrix elements for quadrupole relaxation are invariant under R, the values of P_{mk} are calculated with the simplest set of basis functions, the ϕ_i. The relative values of the inverse lifetime, $1/\tau_m$, where m is a, b, or c must be the same as those given by Pople.[19]

$$1/\tau_a : 1/\tau_b : 1/\tau_c = \tfrac{3}{2} : 1 : \tfrac{3}{2}. \quad (28)$$

The relative values of $1/T_1$ are then found from Eq. (22). These are given for the various transition types in Table II. The relative values of $1/T_1$ now give the ratios of the broadening of the various components for protons coupled to N^{14} in a double resonance experiment.

V. CONCLUSIONS

The extension of the work of Pople[19] to the double resonance problem is straightforward. Double resonance is a powerful technique both for studying the details of spin interactions in molecules, and for the analysis of complex NMR spectra. These calculations suggest that the relative linewidths may be useful in assigning the features in a double resonance spectrum. A detailed study of linewidth can, of course, give information on the quadrupole coupling, the correlation times for molecular motion, and the molecular symmetry.

Oxygen Isotope Fractionation between Calcium Carbonate and Water*

ROBERT N. CLAYTON

Enrico Fermi Institute for Nuclear Studies, and Department of Chemistry, University of Chicago, Chicago, Illinois

(Received June 6, 1960)

A technique is described for the total extraction of oxygen from calcium carbonate for isotopic analysis. This permits recalculation of previously published data to yield absolute values of equilibrium constants for the oxygen isotope exchange reaction between calcite and water. The equilibrium constant varies with temperature according to the empirical relationship $\ln K = 2730\ T^{-2} - 0.00256$ over the temperature range 273°–1023°K.

INTRODUCTION

SINCE the early work of Urey[1] and his co-workers, the study of variations in stable isotope abundances has received increasing attention in the field of geochemistry. The relative abundances of the isotopes of a light element vary in natural materials as a result of isotopic fractionation in the processes which produced these materials. The purpose of the stable isotopic investigations on rocks and minerals is to deduce quantitative information about the conditions under which the mineral phases were crystallized, and about the sources of their constituents.

Most of the stable isotope fractionation in nature appears to be the result of exchange reactions occurring at or near equilibrium. For example, water vapor over the oceans is near isotopic equilibrium with liquid ocean water[2]; calcium carbonate deposited by a marine organism has an O^{18}/O^{16} ratio determined by the equilibrium fractionation between $CaCO_3$ and water[3]; minerals in hydrothermal veins are often crystallized in equilibrium with one another and with the fluid phase from which they were precipitated.[4]

Quantitative interpretation of the observed fractionations in natural systems requires knowledge of the various isotopic exchange equilibrium constants over a wide range of temperatures. Such measurements have been made in only one system of geological interest: calcium carbonate (calcite) and water.

The earliest work in this system is that of McCrea,[5] who measured variations in O^{18}/O^{16} of calcite precipitated inorganically from aqueous solutions at temperatures from $-1°$ to $+80°$C. He developed a chemical procedure for extraction of oxygen from carbonates by reaction with 100% H_3PO_4 to produce carbon dioxide. The carbon dioxide thus formed is suitable for isotopic analysis of carbon, and for measurements of variations in O^{18}/O^{16} of the carbonate. The procedure cannot be used to determine the absolute O^{18}/O^{16} of the carbonate, since the reaction yields stoichiometrically only two-thirds of the oxygen, which is fractionated from the original oxygen by a factor α (constant at constant temperature):

$$CaCO_3 + 2H^+ \rightarrow Ca^{++} + CO_2 + H_2O$$

$$\alpha = \frac{(O^{18}/O^{16})_{CO_2}}{(O^{18}/O^{16})_{CaCO_3}}.$$

Since a measurement of α was not available at the time of McCrea's work, he was able to determine only the temperature coefficient of the equilibrium constant K for the reaction:

$$\tfrac{1}{3}\,CaCO_{3(s)}{}^{16} + H_2O_{(l)}{}^{18} \rightleftarrows \tfrac{1}{3}\,CaCO_{3(s)}{}^{18} + H_2O_{(l)}{}^{16}$$

$$K = \frac{(O^{18}/O^{16})_{CaCO_3}}{(O^{18}/O^{16})_{H_2O}}$$

assuming random distribution of the various isotopic species of carbonate ion. For McCrea's purpose, the establishment of an oxygen isotope "thermometer" for ocean phenomena, the temperature coefficient was all that was needed.

Epstein *et al.*[3] measured variations in O^{18}/O^{16} ratio of calcite deposited by marine organisms in the formation of their shells. The data cover the range from $+7°$ to $+30°$C, and are in substantial agreement with McCrea's experimental results.

Measurements at higher temperatures were made by Clayton,[6] who recrystallized calcite in water in a high-pressure apparatus at temperatures from 190°C to 750°C, the upper limit of stability of calcite in water.[7] On a graph of $\ln K$ vs $1/T^2$, all the data of Clayton and of Epstein *et al.*[3] fall on a single straight line (see footnote 6, Fig. 2). Since it is known theoretically[8] that isotopic exchange equilibrium constants are proportional to $1/T^2$ in the high-temperature limit, this straight line was extrapolated to infinite temperature, giving a value for α, the analytical fractionation for extraction of CO_2 from $CaCO_3$. The value determined was $\alpha = 1.00750$ at 25°C.

* This work was supported in part by a grant from the National Science Foundation.

[1] H. C. Urey, J. Chem. Soc. **1947**, 562.

[2] S. Epstein and T. Mayeda, Geochim. et Cosmochim. Acta **4**, 213 (1953).

[3] S. Epstein, R. Buchsbaum, H. A. Lowenstam, and H. C. Urey, Bull. Geol. Soc. Am. **64**, 1315 (1953).

[4] R. N. Clayton and S. Epstein, J. Geol. **66**, 352 (1958).

[5] J. M. McCrea, J. Chem. Phys. **18**, 849 (1950).

[6] R. N. Clayton, J. Chem. Phys. **30**, 1246 (1959).

[7] P. J. Wyllie and O. F. Tuttle, J. Petrology **1**, 1 (1960).

[8] J. Bigeleisen and M. G. Mayer, J. Chem. Phys. **15**, 261 (1947).

This value of α is in disagreement with the estimate of 1.01000 made by Clayton and Epstein.[4] They determined the O^{18}/O^{16} ratio of CO_2 liberated from $MnCO_3$ by the phosphoric acid procedure, and the total O^{18}/O^{16} by carbon reduction of $MnCO_3$ by a technique not applicable to $CaCO_3$. The assumption was then made that the value of α determined for $MnCO_3$ applied also to $CaCO_3$. It was clear, however, that a direct measurement of α for $CaCO_3$ was necessary. Such a measurement requires a chemical procedure for complete extraction of the oxygen from calcium carbonate.

EXPERIMENTAL PROCEDURE

A procedure was devised for the total extraction of oxygen from calcium carbonate. It is based on the reaction

$$6\,CaCO_3+4BrF_3\rightarrow 6CaF_2+2Br_2+6CO_2+3O_2.$$

This reaction was found to proceed cleanly and quantitatively at 125°C with no observable production of CF_4 or COF_2 or any other oxygen-containing compounds.

The procedure was similar to that described by Tudge[9] for extraction of oxygen from phosphates. A sample of 20–40 mg of calcium carbonate was weighed into a Kel-F reaction tube attached to a vacuum system of monel construction. After evacuation, about 30 cc NTP of reagent was frozen into the tube. The reagent was a mixture of unknown proportions of BrF_3 and BrF_5. It contained no measurable oxygen. The stoichiometric excess of reagent was about 5:1. The reaction tube was heated in a furnace for two hours, and the product gas extracted through a trap cooled to the freezing point of ethyl alcohol, −112°C. At this temperature, bromine and excess BrF_5 and BrF_3 were condensed, but CO_2 and O_2 were not.

The oxygen-carbon dioxide mixture was collected by means of a Toepler pump and its volume determined. Carbon dioxide was removed from the mixture by circulating the gas through a trap at liquid nitrogen temperature. The volume of carbon dioxide was determined and the gas was analyzed isotopically.

TABLE I. Total oxygen isotope analysis of calcite.

δ_{CO_2}	δ_{O_2}	Total δ_{CaCO_3}
−0.34	−29.18	−9.95
−2.80	−24.12	−9.91
−0.61	−28.58	−9.93
+0.16	−30.14	−9.94
−0.53	−28.88	−9.98
−1.16	−27.88	−10.07
	Average	−9.96‰

[9] A. P. Tudge, Geochim. et Cosmochim. Acta **18**, 81 (1960).

TABLE II. Experimental equilibrium constants for $CaCO_{3(s)}$—$H_2O_{(l)}$.

Temp. °C	$10^6\,T^{-2}$	ln$K$	K
7[a]	12.74	0.03220	1.03273
9	12.59	0.03175	1.03226
11	12.38	0.03138	1.03188
12	12.29	0.03093	1.03141
14.5	12.08	0.03042	1.03089
15	12.04	0.03024	1.03071
17	11.87	0.03000	1.03045
19	11.71	0.02925	1.02968
21	11.55	0.02901	1.02943
21.5	11.51	0.02882	1.02924
29.5	10.91	0.02733	1.02771
190[b]	4.67	0.00947	1.00951
190	4.67	0.01023	1.01028
240	3.80	0.00772	1.00775
240	3.80	0.00808	1.00811
360	2.52	0.00489	1.00490
460	1.86	0.00249	1.00249
462	1.85	0.00188	1.00188
466	1.83	0.00228	1.00228
472	1.80	0.00242	1.00242
552	1.47	0.00128	1.00128
552	1.47	0.00163	1.00163
646	1.16	0.00078	1.00078
716	0.98	0.00009	1.00009
750	0.96	0.00035	1.00035

[a] Data from 7°–30°C from Epstein *et al.* (footnote 3).
[b] Data from 190°–750°C from Clayton (footnote 6).

The oxygen fraction was converted to carbon dioxide by passing it over a piece of carbon heated to a very dull red by a radio-frequency induction furnace. Carbon dioxide was removed in a cold trap as it was formed. The oxygen was circulated over the carbon until it had all reacted, as shown by a thermocouple vacuum gauge. The reaction is quantitative and isotopically reproducible. The volume of carbon dioxide formed was measured and the gas was analyzed isotopically.

The isotopic analyses were done using a 6-inch, 60° sector, double-collecting mass spectrometer.[10] Relative values of O^{18}/O^{16} were determined to ±0.1‰, and are reported as deviations from a standard in parts per thousand:

$$\delta=\left[\frac{(O^{18}/O^{16})_{\text{sample}}}{(O^{18}/O^{16})_{\text{standard}}}-1\right]1000.$$

All data have been corrected for mass spectrometer mixing and C^{13} variations, according to the formulas given by Craig.[11]

The two gases produced by BrF_3 reacting with $CaCO_3$ were found to differ considerably in isotopic composition. The carbon dioxide fraction has an O^{18}/O^{16} ratio close to that of the acid-liberated carbon dioxide, whereas the oxygen fraction has an O^{18}/O^{16} ratio almost 30% lighter. The isotopic composition of each frac-

[10] C. R. McKinney, J. M. McCrea, S. Epstein, H. A. Allen, and H. Urey, Rev. Sci. Instr. **21**, 724 (1950).
[11] H. Craig, Geochim. et Cosmochim. Acta **12**, 133 (1957).

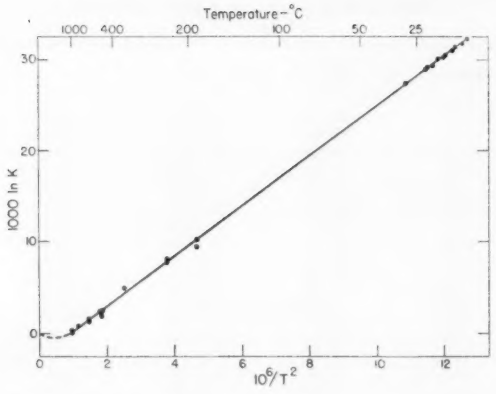

FIG. 1. Experimental equilibrium constants for $CaCO_{3(s)}-H_2O_{(l)}$.

tion varied by one or two per mil from run to run, but the total isotopic composition of the oxygen plus carbon dioxide was very reproducible. The C^{13}/C^{12} ratio of the carbon dioxide fraction was found to be identical with that in acid-liberated carbon dioxide.

RESULTS

The results of six analyses of a single calcite sample are shown in Table I.

Analyzed relative to the same standard, the mean of three samples of CO_2 produced by phosphoric acid treatment of the sample was $\delta=-0.07‰$,

$$\left[\frac{(O^{18}/O^{16})_{CaCO_3}}{(O^{18}/O^{16})_{CO_2}}-1\right]1000=-9.89$$

then

$$\alpha=\frac{(O^{18}/O^{16})_{CO_2}}{(O^{18}/O^{16})_{CaCO_3}}=1.00999$$

and

$$\ln\alpha=0.00994.$$

Using this value of α, the data of Clayton[6] and of Epstein *et al.*[3] have been recalculated to give absolute values of the exchange equilibrium constant. Table II shows the experimental values of K, and in Fig. 1, $\ln K$ is plotted against the reciprocal of the square of the absolute temperature.

DISCUSSION

There is a "crossover" in the isotopic fractionation between calcite and water, occurring at 750°C. It was ignorance of this effect which led to the incorrect extrapolation to infinite temperature in the earlier determination of α for the acid reaction with carbonates.[6] The crossover is not unusual in isotope exchange reactions,[1] and will occur when the phase which concentrates the lighter isotope at low temperatures has higher vibrational frequencies than the phase concentrating the heavier isotope. In particular, for exchange reactions involving water, most other oxygen compounds concentrate O^{18} relative to water at room temperature, and these will all show a crossover at higher temperature.

The equilibrium constant at 25°C for isotopic exchange between calcite and liquid water is 1.02855 and an empirical equation which fits the experimental data over the range 0°–750°C is

$$\ln K=2730T^{-2}-0.00256.$$

Studies in Molecular Structure. III. Populations Analyses for Selected First-Row Diatomic Molecules*

SERAFIN FRAGA AND BERNARD J. RANSIL

Laboratory of Molecular Structure and Spectra, Department of Physics, The University of Chicago, Chicago, Illinois

(Received August 15, 1960)

Electronic population analyses for selected diatomic molecules of the first row of the periodic table are tabulated. The tentative value of population analyses in relation to accuracy of approximation is discussed briefly.

BACKGROUND

THE idea of electronic population analysis was proposed by R. S. Mulliken in 1955 and the theory developed (in terms of LCAO MO molecular wave functions) in a close succession of four papers.[1] Analyses of a few diatomic molecules, for which limited LCAO MO functions were available at the time, were presented and discussed, correlating bonding and antibonding character of the various molecular orbitals and the total overlap population, with known chemical behavior.

Although plausible correlations have been made, the general validity and predictive value of such analyses has remained open to question since their proposal. Nonetheless, the simplicity of the underlying ideas has had widespread appeal, which no doubt goes far to account for their wide acceptance and use since publication. Population analyses should be used with considerable caution and reserve until their significance has been thoroughly explored. A theoretical demonstration from first principles would be most desirable. However, just as acceptable would be demonstrations involving families of compounds, wherein the trend in the computed population indices can be shown to parallel the trend in chemical behavior, e.g., change in binding energies, ionization potentials, electronegativities, electron affinities, dipole moments, force constants, and the like, as the periodic table is spanned laterally or vertically. Such correlation has necessarily awaited the mass calculation of wave functions, a technical problem that has only recently been solved. The analyses in the Appendix are the first body of data available for checking the meaningfulness of population analyses. However, care must be exercised in their use for the following reason.

The wave functions were calculated in a single determinant *limited* LCAO MO approximation [which means that only inner and valence-shell Slater type orbitals (STO's) were used]. These functions give a good account of some properties (e.g., total energies, ionization potentials, certain of the spectroscopic constants), poorer account of others (e.g., dipole moments quadrupole moments, the remaining spectroscopic constants), but (for readily understandable reasons) an unsatisfactory dissociation energy.

Improvement of these functions would consist (according to present ideas), (1) of expanding the basis set sufficiently so that (with or without ζ variation) a close to accurate analytical solution to the Hartree-Fock equation is obtained; (2) inclusion of configuration interaction (CI).

Setting aside the problem of CI and how it affects the interpretation of population analysis, the effect of expanding the basis set on the atomic and overlap populations requires exploration. In all probability the various indices (bonding and antibonding character of each MO, the net populations and overlap population) change as the function is improved by basis set expansion and ζ variation. However, we do not know how significant the change may be. Meager information exists for H_2 (where a close-to-accurate—using the criterion of total energy—molecular Hartree-Fock function is available); for a few hydrides where a larger basis set was employed, i.e., $1s$, $2s$, $2p\sigma$ and $2p\pi$, for both hydrogen and the other component atom, though not yet large enough to provide a good approximation to a molecular Hartree-Fock function; and for LiH and HF using Hartree-Fock AO's.[2]

Consequently any comparisons or correlations made with these functions must be considered tentative until such a time as accurate analytical molecular functions are available for comparison.

DEFINITIONS

The reader is directed to the basic papers for an extensive treatment of the basic theory and its application. It is sufficient for our purposes that a summary of definitions corresponding to a single LCAO MO electron configuration be given here.

k, l ≡ indices denoting atoms k and l

r, s ≡ indices denoting orthonormal AO's χ_r and χ_s on atoms k or l

* This work was assisted by the National Science Foundation and by the Office of Ordnance Research under contract with the University of Chicago.

[1] R. S. Mulliken, J. Chem. Phys. **23**, 1833, 1841, 2338, 2343 (1955). Overlap and "net" atomic populations had already been in use for some time; see R. S. Mulliken, Revs. Modern Phys. **41**, 66 (1932); J. Chem. Phys. **3**, 573 (1935), Eqs. (38), (39), and (42).

[2] A. M. Karo, J. Chem. Phys. **31**, 182 (1959).

$S \equiv$ overlap integral $S = \int_0^\infty \chi_r \chi_s dV$

$i \equiv$ index denoting molecular orbital (MO) ϕ_i

$C_{ir_k}, C_{is_l} \equiv$ MO coefficients

$N(i) \equiv$ number of electrons in MO ϕ_i

$n(i; r_k, s_l) = 2N(i) C_{ir_k} C_{is_l} S_{r_k s_l} \equiv$ partial overlap population

$$n(i; k, l) = \sum_r \sum_s n(i; r_k, s_l)$$
$$n(r_k, s_l) = \sum_i n(i; r_k, s_l)$$
$$n(k, l) = \sum_r \sum_s n(r_k, s_l)$$
$$n(i) = \sum_{r_k, s_l} n(i; r_k, s_l)$$

Subtotal overlap populations corresponding to various ways of breakdown of the total overlap population, n

$$n = \sum_i n(i) = \sum_{k,l} n(k, l) = \sum_{r_k, s_l} n(r_k, s_l) \equiv \text{total overlap populations}$$

$$N(i; r_k) = N(i) C_{ir_k} (C_{ir_k} + \sum_{l \neq k} C_{is_l} S_{r_k s_l})$$

$\equiv$ partial gross population in MO ϕ_i and AO χ_{r_k}

$N(i; k) = \sum_r N(i; r_k) \equiv$ subtotal in MO ϕ_i on atom k

$N(k) = \sum_i N(i; k) = \sum_r N(r_k)$

$\equiv$ total gross population on atom k

$N(i) = \sum_{r,k} N(i; r_k) = \sum_k N(i; k)$

$\equiv$ electron population in MO ϕ_i, an integer

$N(r_k) = \sum_i N(i; r_k)$

$\equiv$ total gross population in AO χ_{r_k}

$N = \sum_i N(i) = \sum_{r,k} N(r_k)$

$\equiv$ total electron population.

THEOREMS[3]

(1) Overlap populations which represent sums over all MO's [e.g., $n(r_k, s_l)$, $n(k, l)$, and n] are invariant with respect to any orthogonal transformation among the *occupied* LCAO MO's in the given configuration.

(2) Similarly $N(r_k)$, $N(k)$, and N are invariant with respect to orthogonal transformation of the occupied MO's.

NOTATION AND CONVENTION OF TABLES

The tables contain gross atomic and overlap populations for the LCAO MO diatomic wave functions reported earlier in I and II.[4] All previous conventions and notation related to construction of these functions hold here, with one exception. *The wave functions were tabulated in terms of nonorthogonal STO's; but the atomic and overlap populations given here are calculated using orthogonal STO's.* This was done because the individual $n(i; r_k)$, $n(i; r_k, s_l)$, etc., are *not* invariant under the transformation from nonorthogonal to orthogonal basis set, and it is preferable to work with orthogonal partial populations.

A lengthy discussion of these results tabulated in the Appendix, in terms of $s \rightarrow p$ promotion, polarity, bonding and antibonding character, covalent and ionic bond character, is in preparation.

ACKNOWLEDGMENTS

The authors are indebted to Tracy Kinyon for invaluable and extensive supporting desk calculations. They gratefully acknowledge the use of computer facilities and the continuous cheerful cooperation of the computer staff at Wright Patterson Air Force Base, Dayton, Ohio. The authors are also indebted to Professor R. S. Mulliken for reading and commenting on the manuscript during its preparation.

[3] See C. W. Scherr, J. Chem. Phys. **23**, 569 (1955), for invariance theorems in Appendix II.

[4] B. J. Ransil, Revs. Modern Phys. **32**, 239, 245 (1960).

APPENDIX

TABLE Ia. Gross atomic populations in LiH (R_e=3.015 a.u.).

	ϕ_i	$1s_{Li}$	$2s_{Li}$	$2p\sigma_{Li}$	$1s_H$	$N(i;$ Li)	$N(i;$ H)	$N(i)$
Slater	1σ	1.998	0.001	0.000	0.001	1.999	0.001	2
	2σ	0.002	0.407	0.282	1.309	0.691	1.309	2
	Totals $N(r_k)$	2.000	0.408	0.282	1.310	2.690	1.310	4
Best atom	1σ	1.998	0.001	0.000	0.001	1.999	0.001	2
	2σ	0.002	0.406	0.279	1.313	0.687	1.313	2
	Totals $N(r_k)$	2.000	0.407	0.279	1.314	2.686	1.314	4
Best limited MO	1σ	1.998	0.001	0.000	0.001	1.999	0.001	2
	2σ	0.002	0.389	0.256	1.353	0.647	1.353	2
	Totals $N(r_k)$	2.000	0.390	0.256	1.354	2.646	1.354	4

TABLE Ib. Overlap populations in LiH.

	ϕ_i	$1s_{Li}$, $1s_H$	$2s_{Li}$, $1s_H$	$2p\sigma_{Li}$, $1s_H$	$n(i)$
Slater	1σ	0.002	0.000	0.000	0.002
	2σ	−0.020	0.408	0.351	0.739
	Totals $n(r_k, s_l)$	−0.018	0.408	0.351	0.741
Best atom	1σ	0.002	0.000	0.000	0.002
	2σ	−0.020	0.406	0.348	0.734
	Totals $n(r_k, s_l)$	−0.018	0.406	0.348	0.736
Best limited MO	1σ	0.002	0.000	0.000	0.002
	2σ	−0.022	0.414	0.332	0.724
	Totals $n(r_k, s_l)$	−0.020	0.414	0.332	0.726

TABLE IIa. Gross atomic populations in BH (R_e=2.329 a.u.).

	ϕ_i	$1s_B$	$2s_B$	$2p\sigma_B$	$1s_H$	$N(i;B)$	$N(i;H)$	$N(i)$
	1σ	2.001	0.000	0.000	−0.001	2.001	−0.001	2
	2σ	0.001	0.924	0.204	0.871	1.129	0.871	2
	3σ	0.000	0.879	0.870	0.251	1.749	0.251	2
Slater								
	Totals							
	$N(r_k)$	2.002	1.803	1.074	1.121	4.879	1.121	6
	1σ	2.001	0.000	0.000	−0.001	2.001	−0.001	2
	2σ	0.001	0.955	0.188	0.856	1.144	0.856	2
	3σ	0.000	0.826	0.921	0.253	1.747	0.253	2
Best atom								
	Totals							
	$N(r_k)$	2.002	1.781	1.109	1.108	4.892	1.108	6
	1σ	2.000	0.000	0.000	0.000	2.000	0.000	2
	2σ	0.001	0.966	0.236	0.797	1.203	0.797	2
	3σ	0.000	0.840	0.933	0.227	1.773	0.227	2
Best limited MO								
	Totals							
	$N(r_k)$	2.001	1.806	1.169	1.024	4.976	1.024	6

TABLE IIb. Overlap populations in BH.

	ϕ_i	$1s_B, 1s_H$	$2s_B, 1s_H$	$2p\sigma_B, 1s_H$	$n(i)$
	1σ	−0.003	0.000	0.000	−0.003
	2σ	−0.007	0.603	0.219	0.815
	3σ	−0.003	−0.799	0.513	−0.289
Slater					
	Totals				
	$n(r_k, s_l)$	−0.013	−0.196	0.732	0.523
	1σ	−0.002	0.000	0.000	−0.002
	2σ	−0.007	0.603	0.211	0.807
	3σ	−0.003	−0.714	0.522	−0.195
Best atom					
	Totals				
	$n(r_k, s_l)$	−0.012	−0.111	0.733	0.609
	1σ	−0.001	0.000	0.000	−0.001
	2σ	−0.005	0.540	0.232	0.767
	3σ	−0.002	−0.561	0.461	−0.102
Best limited MO					
	Totals				
	$n(r_k, s_l)$	−0.008	−0.021	0.693	0.664

TABLE IIIa. Gross atomic populations in NH[a] (R_e=1.976 a.u.).

	ϕ_i	$1s_N$	$2s_N$	$2p\sigma_N$	$2p\pi_N$	$1s_H$	$N(i;N)$	$N(i;H)$	$N(i)$
	1σ	2.000	0.001	0.000		−0.001	2.001	−0.001	2
	2σ	0.001	1.380	0.079		0.540	1.460	0.540	2
	1π				4.000		4.000	0.000	4
Slater									
	Totals								
	$N(r_k)$	2.001	1.381	0.079	4.000	0.539	7.461	0.539	8
	1σ	2.000	0.001	0.000		−0.001	2.001	−0.001	2
	2σ	0.001	1.420	0.081		0.498	1.502	0.498	2
	1π				4.000		4.000		4
Best atom									
	Totals								
	$N(r_k)$	2.001	1.421	0.081	4.000	0.497	7.503	0.497	8
	1σ	2.000	0.000	0.000		0.000	2.000	0.000	2
	2σ	0.000	1.537	0.081		0.382	1.618	0.382	2
	1π				4.000		4.000		4
Best limited MO									
	Totals								
	$N(r_k)$	2.000	1.537	0.081	4.000	0.382	7.618	0.382	8

[a] Excited $^1\Sigma^+$ state.

TABLE IIIb. Overlap populations in NH.

	ϕ_i	$1s_N, 1s_H$	$2s_N, 1s_H$	$2p\sigma_N, 1s_H$	$n(i)$
	1σ	−0.002	0.000	0.000	−0.002
	2σ	−0.003	0.536	0.077	0.610
Slater					
	Totals				
	$n(r_k, s_l)$	−0.005	0.536	0.077	0.608
	1σ	−0.001	0.000	0.000	−0.001
	2σ	−0.003	0.515	0.076	0.588
Best atom					
	Totals				
	$n(r_k, s_l)$	−0.004	0.515	0.076	0.587
	1σ	−0.001	0.000	0.000	−0.001
	2σ	−0.001	0.394	0.068	0.461
Best limited MO					
	Totals				
	$n(r_k, s_l)$	−0.002	0.394	0.068	0.460

TABLE IVa. Gross atomic populations in HF (R_e=1.733 a.u.).

	ϕ_i	$1s_F$	$2s_F$	$2p\sigma_F$	$2p\pi_F$	$1s_H$	$N(i;\mathrm{F})$	$N(i;\mathrm{H})$	$N(i)$
	1σ	2.001	0.000	0.000		−0.001	2.001	−0.001	2
	2σ	0.001	1.777	0.025		0.197	1.803	0.197	2
	3σ	0.000	0.170	1.180		0.650	1.350	0.650	2
	1π				4.000		4.000		4
Slater	Totals								
	$N(r_k)$	2.002	1.947	1.205	4.000	0.846	9.154	0.846	10
	1σ	2.000	0.000	0.000		0.000	2.000	0.000	2
	2σ	0.000	1.799	0.028		0.173	1.827	0.173	2
	3σ	0.000	0.159	1.233		0.608	1.392	0.608	2
	1π				4.000		4.000		4
Best atom	Totals								
	$N(r_k)$	2.000	1.958	1.261	4.000	0.781	9.219	0.781	10
	1σ	2.000	0.000	0.000		0.000	2.000	0.000	2
	2σ	0.000	1.794	0.026		0.180	1.820	0.180	2
	3σ	0.000	0.151	1.258		0.591	1.409	0.591	2
	1π				4.000		4.000		4
Best limited MO	Totals								
	$N(r_k)$	2.000	1.945	1.284	4.000	0.771	9.229	0.771	10

TABLE IVb. Overlap populations in HF.

	ϕ_i	$1s_F$, $1s_H$	$2s_F$, $1s_H$	$2p\sigma_F$, $1s_H$	$n(i)$
	1σ	−0.001	0.000	0.000	−0.001
	2σ	−0.001	0.275	0.017	0.291
	3σ	−0.004	−0.498	0.473	−0.029
Slater	Totals				
	$n(r_k, s_l)$	−0.006	−0.223	0.490	0.261
	1σ	−0.001	0.000	0.000	−0.001
	2σ	−0.001	0.250	0.017	0.266
	3σ	−0.003	−0.467	0.477	0.007
Best atom	Totals				
	$n(r_k, s_l)$	−0.005	−0.217	0.494	0.272
	1σ	−0.001	0.000	0.000	−0.001
	2σ	−0.001	0.247	0.019	0.265
	3σ	−0.002	−0.373	0.492	0.117
Best limited MO	Totals				
	$n(r_k, s_l)$	−0.004	−0.126	0.511	0.381

TABLE Va. Gross atomic populations in Li_2 ($R_e = 5.051$ a.u.).

	ϕ_i	$1s$	$2s$	$2p\sigma$	$N(i)$
Slater	$1\sigma_g$	1.998	0.002	0.000	2
	$1\sigma_u$	2.010	−0.006	−0.004	2
	$2\sigma_g$	0.004	1.810	0.186	2
	Totals				
	σ_g	2.002	1.812	0.186	4
	σ_u	2.010	−0.006	−0.004	2
	$N(r_k)$	4.012	1.806	0.182	6
Best atom	$1\sigma_g$	1.997	0.003	0.000	2
	$1\sigma_u$	2.009	−0.005	−0.004	2
	$2\sigma_g$	0.003	1.801	0.196	2
	Totals				
	σ_g	2.000	1.804	0.196	4
	σ_u	2.009	−0.005	−0.004	2
	$N(r_k)$	4.009	1.799	0.192	6
Best limited MO	$1\sigma_g$	1.998	0.002	0.000	2
	$1\sigma_u$	2.004	−0.003	−0.001	2
	$2\sigma_g$	0.003	1.833	0.164	2
	Totals				
	σ_g	2.001	1.835	0.164	4
	σ_u	2.004	−0.003	−0.001	2
	$N(r_k)$	4.005	1.832	0.163	6

TABLE Vb. Overlap populations in Li_2.

	ϕ_i	$1s_a, 1s_b$	$1s_a, 2s_b$ + $1s_b, 2s_a$	$1s_a, 2p\sigma_b$ + $1s_b, 2p\sigma_a$	$2s_a, 2s_b$	$2s_a, 2p\sigma_b$ + $2s_b, 2p\sigma_a$	$2p\sigma_a, 2p\sigma_b$	$n(i)$
Slater	$1\sigma_g$	0.000	0.004	0.000	0.000	0.000	0.000	0.004
	$1\sigma_u$	0.000	−0.013	−0.007	−0.002	−0.001	0.000	−0.023
	$2\sigma_g$	0.000	−0.017	−0.006	0.622	0.240	0.013	0.852
	Totals							
	σ_g	0.000	−0.013	−0.006	0.622	0.240	0.013	0.856
	σ_u	0.000	−0.013	−0.007	−0.002	−0.001	0.000	−0.023
	$n(r_k, s_l)$	0.000	−0.026	−0.013	0.620	0.239	0.013	0.833
Best atom	$1\sigma_g$	0.000	0.004	0.001	0.000	0.000	0.000	0.005
	$1\sigma_u$	0.000	−0.012	−0.007	−0.002	−0.001	0.000	−0.022
	$2\sigma_g$	0.000	−0.017	−0.007	0.626	0.249	0.013	0.864
	Totals							
	σ_g	0.000	−0.013	−0.006	0.626	0.249	0.013	0.869
	σ_u	0.000	−0.012	−0.007	−0.002	−0.001	0.000	−0.022
	$n(r_k, s_l)$	0.000	−0.025	−0.013	0.624	0.248	0.013	0.847
Best limited MO	$1\sigma_g$	0.000	0.004	0.000	0.000	0.000	0.000	0.004
	$1\sigma_u$	0.000	−0.008	−0.002	−0.001	0.000	0.000	−0.011
	$2\sigma_g$	0.000	−0.017	−0.005	0.649	0.197	0.016	0.840
	Totals							
	σ_g	0.000	−0.013	−0.005	0.649	0.197	0.016	0.844
	σ_u	0.000	−0.008	−0.002	−0.001	0.000	0.000	−0.011
	$n(r_k, s_l)$	0.000	−0.021	−0.007	0.648	0.197	0.016	0.833

TABLE VIa. Gross atomic populations in Be_2 (R=3.780 a.u.).

	ϕ_i	$1s$	$2s$	$2p\sigma$	$N(i)$
Slater	$1\sigma_g$	2.006	−0.003	−0.003	2
	$1\sigma_u$	1.998	0.002	0.000	2
	$2\sigma_g$	0.002	1.709	0.289	2
	$2\sigma_u$	−0.001	1.606	0.395	2
	Totals				
	σ_g	2.008	1.706	0.286	4
	σ_u	1.997	1.608	0.395	4
	$N(r_k)$	4.005	3.314	0.681	8
Best atom	$1\sigma_g$	1.998	0.002	0.000	2
	$1\sigma_u$	2.006	−0.003	−0.003	2
	$2\sigma_g$	0.002	1.697	0.301	2
	$2\sigma_u$	−0.001	1.614	0.387	2
	Totals				
	σ_g	2.000	1.699	0.301	4
	σ_u	2.005	1.611	0.384	4
	$N(r_k)$	4.005	3.310	0.685	8
Best limited MO	$1\sigma_g$	1.998	0.002	0.000	2
	$1\sigma_u$	2.004	−0.002	−0.002	2
	$2\sigma_g$	0.002	1.731	0.267	2
	$2\sigma_u$	−0.001	1.742	0.259	2
	Totals				
	σ_g	2.000	1.733	0.267	4
	σ_u	2.003	1.740	0.257	4
	$N(r_k)$	4.003	3.473	0.524	8

TABLE VIb. Overlap populations in Be_2.

	ϕ_i	$1s_a, 1s_b$	$1s_a, 2s_b$ + $1s_b, 2s_a$	$1s_a, 2p\sigma_b$ + $1s_b, 2p\sigma_a$	$2s_a, 2s_b$	$2s_a, 2p\sigma_b$ + $2s_b, 2p\sigma_a$	$2p\sigma_a, 2p\sigma_b$	$n(i)$
Slater	$1\sigma_g$	0.000	−0.008	−0.006	−0.001	−0.001	0.000	−0.016
	$1\sigma_u$	0.000	0.003	0.001	0.000	0.000	0.000	0.004
	$2\sigma_g$	0.000	−0.014	−0.007	0.526	0.308	0.031	0.844
	$2\sigma_u$	0.000	−0.008	0.003	−1.363	0.579	−0.042	−0.831
	Totals							
	σ_g	0.000	−0.022	−0.013	0.525	0.307	0.031	0.828
	σ_u	0.000	−0.005	0.004	−1.363	0.579	−0.042	−0.827
	$n(r_k, s_l)$	0.000	−0.027	−0.009	−0.838	0.886	−0.011	0.001
Best atom	$1\sigma_g$	0.000	0.003	0.001	0.000	0.000	0.000	0.004
	$1\sigma_u$	0.000	−0.008	−0.006	−0.001	−0.001	0.000	−0.016
	$2\sigma_g$	0.000	−0.014	−0.008	0.528	0.318	0.032	0.856
	$2\sigma_u$	0.000	−0.010	0.004	−1.443	0.575	−0.038	−0.912
	Totals							
	σ_g	0.000	−0.011	−0.007	0.528	0.318	0.032	0.860
	σ_u	0.000	−0.018	−0.002	−1.444	0.574	−0.038	−0.928
	$n(r_k, s_l)$	0.000	−0.029	−0.009	−0.916	0.892	−0.006	−0.068
Best limited MO	$1\sigma_g$	0.000	0.003	0.001	0.000	0.000	0.000	0.004
	$1\sigma_u$	0.000	−0.006	−0.003	−0.001	0.000	0.000	−0.010
	$2\sigma_g$	0.000	−0.014	−0.006	0.549	0.260	0.035	0.824
	$2\sigma_u$	0.000	−0.015	0.003	−1.671	0.404	−0.027	−1.306
	Totals							
	σ_g	0.000	−0.011	−0.005	0.549	0.260	0.035	0.828
	σ_u	0.000	−0.021	0.000	−1.672	0.404	−0.027	−1.316
	$n(r_k, s_l)$	0.000	−0.032	−0.005	−1.123	0.664	0.008	−0.488

TABLE VIIa. Gross atomic populations in C_2 (R_e=2.3475 a.u.).

	ϕ_i	$1s$	$2s$	$2p\sigma$	$2p\pi$	$N(i)$
	$1\sigma_g$	1.998	0.002	0.000		2
	$1\sigma_u$	2.006	−0.003	−0.003		2
	$2\sigma_g$	0.002	1.658	0.340		2
	$2\sigma_u$	0.000	1.489	0.511		2
	$1\pi_u$				4.000	4
Slater	Totals					
	σ_g	2.000	1.660	0.340		4
	σ_u	2.006	1.486	0.508		4
	$N(r_k)$	4.006	3.146	0.848	4.000	12
	$1\sigma_g$	1.998	0.002	0.000		2
	$1\sigma_u$	2.005	−0.003	−0.002		2
	$2\sigma_g$	0.002	1.641	0.357		2
	$2\sigma_u$	0.000	1.473	0.527		2
	$1\pi_u$				4.000	4
Best atom	Totals					
	σ_g	2.000	1.643	0.357		4
	σ_u	2.005	1.470	0.525		4
	$N(r_k)$	4.005	3.113	0.882	4.000	12
	$1\sigma_g$	1.998	0.002	0.000		2
	$1\sigma_u$	2.003	−0.002	−0.001		2
	$2\sigma_g$	0.002	1.680	0.318		2
	$2\sigma_u$	−0.001	1.660	0.341		2
	$1\pi_u$				4.000	4
Best limited MO	Totals					
	σ_g	2.000	1.682	0.318		4
	σ_u	2.002	1.658	0.340		4
	$N(r_k)$	4.002	3.340	0.658	4.000	12

TABLE VIIb. Overlap populations in C_2.

	ϕ_i	$1s_a, 1s_b$	$1s_a, 2s_b$ + $1s_b, 2s_a$	$1s_a, 2p\sigma_b$ + $1s_b, 2p\sigma_a$	$2s_a, 2s_b$	$2s_a, 2p\sigma_b$ + $2s_b, 2p\sigma_a$	$2p\sigma_a, 2p\sigma_b$	$2p\pi_a, 2p\pi_b$	$n(i)$
	$1\sigma_g$	0.000	0.003	0.001	0.000	0.000	0.000		0.004
	$1\sigma_u$	0.000	−0.007	−0.005	−0.001	−0.001	0.000		−0.014
	$2\sigma_g$	0.000	−0.015	−0.009	0.490	0.334	0.041		0.841
	$2\sigma_u$	0.000	−0.005	0.003	−1.090	0.674	−0.076		−0.494
	$1\pi_u$							0.961	0.961
Slater	Totals								
	σ_g	0.000	−0.012	−0.008	0.490	0.334	0.041		0.845
	σ_u	0.000	−0.012	−0.002	−1.091	0.673	−0.076		−0.508
	$n(r_k, s_l)$	0.000	−0.024	−0.010	−0.601	1.007	−0.035	0.961	1.298
	$1\sigma_g$	0.000	0.002	0.001	0.000	0.000	0.000		0.003
	$1\sigma_u$	0.000	−0.006	−0.005	−0.001	−0.001	0.000		−0.013
	$2\sigma_g$	0.000	−0.015	−0.010	0.486	0.351	0.042		0.854
	$2\sigma_u$	0.000	−0.005	0.003	−1.094	0.694	−0.073		−0.475
	$1\pi_u$							1.011	1.011
Best atom	Totals								
	σ_g	0.000	−0.013	−0.009	0.486	0.351	0.042		0.857
	σ_u	0.000	−0.011	−0.002	−1.095	0.693	−0.073		−0.488
	$n(r_k, s_l)$	0.000	−0.024	−0.011	−0.609	1.044	−0.031	1.011	1.380
	$1\sigma_g$	0.000	0.003	0.000	0.000	0.000	0.000		0.003
	$1\sigma_u$	0.000	−0.005	−0.002	0.000	0.000	0.000		−0.007
	$2\sigma_g$	0.000	−0.014	−0.006	0.504	0.275	0.046		0.805
	$2\sigma_u$	0.000	−0.012	0.003	−1.333	0.472	−0.051		−0.921
	$1\pi_u$							0.976	0.976
Best limited MO	Totals								
	σ_g	0.000	−0.011	−0.006	0.504	0.275	0.046		0.808
	σ_u	0.000	−0.017	0.001	−1.333	0.472	−0.051		−0.928
	$n(r_k, s_l)$	0.000	−0.028	−0.005	−0.829	0.747	−0.005	0.976	0.856

TABLE VIIIa. Gross atomic populations in N_2 (R_e=2.068 a.u.).

	ϕ_i	1s	2s	2pσ	2pπ	N(i)
Slater	$1\sigma_g$	1.998	0.002	0.000		2
	$1\sigma_u$	2.004	−0.002	−0.002		2
	$2\sigma_g$	0.002	1.502	0.496		2
	$2\sigma_u$	0.000	1.476	0.524		2
	$1\pi_u$				4.000	4
	$3\sigma_g$	0.000	0.496	1.504		2
	Totals					
	σ_g	2.000	2.000	2.000		6
	σ_u	2.004	1.474	0.522		4
	$N(r_k)$	4.004	3.474	2.522	4.000	14
Best atom	$1\sigma_g$	1.998	0.001	0.001		2
	$1\sigma_u$	2.004	−0.002	−0.002		2
	$2\sigma_g$	0.002	1.492	0.506		2
	$2\sigma_u$	0.000	1.480	0.520		2
	$1\pi_u$				4.000	4
	$3\sigma_g$	0.000	0.507	1.493		2
	Totals					
	σ_g	2.000	2.000	2.000		6
	σ_u	2.004	1.478	0.518		4
	$N(r_k)$	4.004	3.478	2.518	4.000	14
Best limited MO	$1\sigma_g$	1.999	0.001	0.000		2
	$1\sigma_u$	2.003	−0.002	−0.001		2
	$2\sigma_g$	0.002	1.501	0.497		2
	$2\sigma_u$	−0.001	1.590	0.411		2
	$1\pi_u$				4.000	4
	$3\sigma_g$	0.000	0.497	1.503		2
	Totals					
	σ_g	2.001	1.999	2.000		6
	σ_u	2.002	1.588	0.410		4
	$N(r_k)$	4.003	3.587	2.410	4.000	14

TABLE VIIIb. Overlap populations in N_2.

	ϕ_i	$1s_a, 1s_b$	$1s_a, 2s_b$ + $1s_b, 2s_a$	$1s_a, 2p\sigma_b$ + $1s_b, 2p\sigma_a$	$2s_a, 2s_b$	$2s_a, 2p\sigma_b$ + $2s_b, 2p\sigma_a$	$2p\sigma_a, 2p\sigma_b$	$2p\pi_a, 2p\pi_b$	$n(i)$
Slater	$1\sigma_g$	0.000	0.003	0.001	0.000	0.000	0.000		0.004
	$1\sigma_u$	0.000	−0.006	−0.004	−0.001	−0.001	0.000		−0.012
	$2\sigma_g$	0.000	−0.012	−0.010	0.407	0.394	0.074		0.853
	$2\sigma_u$	0.000	−0.002	0.001	−0.938	0.663	−0.091		−0.367
	$1\pi_u$							0.880	0.880
	$3\sigma_g$	0.000	0.005	−0.013	0.281	−0.824	0.467		−0.084
	Totals								
	σ_g	0.000	−0.004	−0.022	0.688	−0.430	0.541		0.773
	σ_u	0.000	−0.008	−0.003	−0.939	0.662	−0.091		−0.379
	$n(r_k, s_l)$	0.000	−0.012	−0.025	−0.251	0.232	0.450	0.880	1.274
Best atom	$1\sigma_g$	0.000	0.002	0.001	0.000	0.000	0.000		0.003
	$1\sigma_u$	0.000	−0.006	−0.004	0.000	0.000	0.000		−0.010
	$2\sigma_g$	0.000	−0.012	−0.010	0.408	0.401	0.075		0.862
	$2\sigma_u$	0.000	−0.003	0.002	−0.974	0.666	−0.086		−0.395
	$1\pi_u$							0.905	0.905
	$3\sigma_g$	0.000	0.006	−0.014	0.291	−0.844	0.462		−0.099
	Totals								
	σ_g	0.000	−0.004	−0.023	0.699	−0.443	0.537		0.766
	σ_u	0.000	−0.009	−0.002	−0.974	0.666	−0.086		−0.405
	$n(r_k, s_l)$	0.000	−0.013	−0.025	−0.275	0.223	0.451	0.905	1.266
Best limited MO	$1\sigma_g$	0.000	0.002	0.001	0.000	0.000	0.000		0.003
	$1\sigma_u$	0.000	−0.005	−0.003	0.000	0.000	0.000		−0.008
	$2\sigma_g$	0.000	−0.011	−0.008	0.421	0.344	0.082		0.828
	$2\sigma_u$	0.000	−0.007	0.003	−1.136	0.530	−0.072		−0.682
	$1\pi_u$							0.911	0.911
	$3\sigma_g$	0.000	0.003	−0.006	0.256	−0.634	0.453		0.072
	Totals								
	σ_g	0.000	−0.006	−0.013	0.677	−0.290	0.535		0.903
	σ_u	0.000	−0.012	0.000	−1.136	0.530	−0.072		−0.690
	$n(r_k, s_l)$	0.000	−0.018	−0.013	−0.459	0.240	0.463	0.911	1.124

TABLE IXa. Gross atomic populations in F_2 (R_e=2.680 a.u.).

	ϕ_i	1s	2s	2pσ	2pπ	N(i)
	$1\sigma_u$	2.000	0.000	0.000		2
	$1\sigma_g$	2.000	0.000	0.000		2
	$2\sigma_g$	0.000	1.933	0.067		2
	$2\sigma_u$	0.000	1.950	0.050		2
	$1\pi_u$				4.000	4
	$3\sigma_g$	0.000	0.067	1.933		2
	$1\pi_g$				4.000	4
Slater						
	Totals					
	σ_g	2.000	2.000	2.000	4.000	10
	σ_u	2.000	1.950	0.050	4.000	8
	$N(r_k)$	4.000	3.950	2.050	8.000	18
	$1\sigma_u$	2.000	0.000	0.000		2
	$1\sigma_g$	2.000	0.000	0.000		2
	$2\sigma_g$	0.000	1.932	0.068		2
	$2\sigma_u$	0.000	1.951	0.049		2
	$1\pi_u$				4.000	4
	$3\sigma_g$	0.000	0.068	1.932		2
	$1\pi_g$				4.000	4
Best atom						
	Totals					
	σ_g	2.000	2.000	2.000	4.000	10
	σ_u	2.000	1.951	0.049	4.000	8
	$N(r_k)$	4.000	3.951	2.049	8.000	18
	$1\sigma_u$	2.000	0.000	0.000		2
	$1\sigma_g$	2.000	0.000	0.000		2
	$2\sigma_g$	0.000	1.932	0.068		2
	$2\sigma_u$	0.000	1.949	0.051		2
	$1\pi_u$				4.000	4
	$3\sigma_g$	0.000	0.068	1.932		2
	$1\pi_g$				4.000	4
Best limited MO						
	Totals					
	σ_g	2.000	2.000	2.000	4.000	10
	σ_u	2.000	1.949	0.051	4.000	8
	$N(r_k)$	4.000	3.949	2.051	8.000	18

TABLE IXb. Overlap populations in F_2.

	ϕ_i	$1s_a, 1s_b$	$1s_a, 2s_b$ + $1s_b, 2s_a$	$1s_a, 2p\sigma_b$ + $1s_b, 2p\sigma_a$	$2s_a, 2s_b$	$2s_a, 2p\sigma_b$ + $2s_b, 2p\sigma_a$	$2p\sigma_a, 2p\sigma_b$	$2p\pi_a, 2p\pi_b$	$n(i)$
	$1\sigma_u$	0.000	0.000	0.000	0.000	0.000	0.000		0.000
	$1\sigma_g$	0.000	0.000	0.000	0.000	0.000	0.000		0.000
	$2\sigma_g$	0.000	0.000	0.000	0.198	0.065	0.005		0.268
	$2\sigma_u$	0.000	0.000	0.000	−0.253	0.064	−0.004		−0.193
	$1\pi_u$							0.180	0.180
	$3\sigma_g$	0.000	0.000	0.000	0.014	−0.130	0.296		0.180
	$1\pi_g$							−0.197	−0.197
Slater									
	Totals								
	σ_g	0.000	0.000	0.000	0.212	−0.065	0.301		0.448
	σ_u	0.000	0.000	0.000	−0.253	0.064	−0.004		−0.193
	$n(r_k, s_l)$	0.000	0.000	0.000	−0.041	−0.001	0.297	−0.017	0.238
	$1\sigma_u$	0.000	0.000	0.000	0.000	0.000	0.000		0.000
	$1\sigma_g$	0.000	0.000	0.000	0.000	0.000	0.000		0.000
	$2\sigma_g$	0.000	0.000	0.000	0.208	0.068	0.005		0.281
	$2\sigma_u$	0.000	0.000	0.000	−0.268	0.065	−0.004		−0.207
	$1\pi_u$							0.196	0.196
	$3\sigma_g$	0.000	0.000	0.000	0.015	−0.141	0.311		0.185
	$1\pi_g$							−0.217	−0.217
Best atom									
	Totals								
	σ_g	0.000	0.000	0.000	0.223	−0.073	0.316		0.466
	σ_u	0.000	0.000	0.000	−0.268	0.065	−0.004		−0.207
	$n(r_k, s_l)$	0.000	0.000	0.000	−0.045	−0.008	0.312	−0.021	0.238
	$1\sigma_u$	0.000	0.000	0.000	0.000	0.000	0.000		0.000
	$1\sigma_g$	0.000	0.000	0.000	0.000	0.000	0.000		0.000
	$2\sigma_g$	0.000	0.000	0.000	0.204	0.070	0.005		0.279
	$2\sigma_u$	0.000	0.000	0.000	−0.262	0.069	−0.004		−0.197
	$1\pi_u$							0.190	0.190
	$3\sigma_g$	0.000	0.000	0.000	0.015	−0.149	0.329		0.195
	$1\pi_g$							−0.209	−0.209
Best limited MO									
	Totals								
	σ_g	0.000	0.000	0.000	0.219	−0.079	0.334		0.474
	σ_u	0.000	0.000	0.000	−0.262	0.069	−0.004		−0.197
	$n(r_k, s_l)$	0.000	0.000	0.000	−0.043	−0.010	0.330	−0.019	0.258

TABLE Xa. Gross atomic populations for BF (R_e=2.385 a.u.).

	ϕ_i	$1s_B$	$2s_B$	$2p\sigma_B$	$2p\pi_B$	$1s_F$	$2s_F$	$2p\sigma_F$	$2p\pi_F$	$N(i;B)$	$N(i;F)$	$N(i)$
	1σ	0.000	0.000	−0.001		2.000	0.001	0.000		−0.001	2.001	2
	2σ	1.999	0.000	0.000		0.000	0.000	0.001		1.999	0.001	2
	3σ	0.001	0.090	0.104		0.001	1.764	0.040		0.195	1.805	2
	4σ	0.001	0.264	0.065		0.000	0.149	1.521		0.330	1.670	2
	5σ	0.000	1.371	0.507		0.000	0.000	0.122		1.878	0.122	2
	1π				0.545				3.455	0.545	3.455	4
Slater	Totals											
	$N(r_k)$	2.001	1.725	0.675	0.545	2.001	1.914	1.684	3.455	4.946	9.054	14
	1σ	0.000	0.000	−0.001		2.001	0.000	0.000		−0.001	2.001	2
	2σ	2.000	0.000	0.000		0.000	0.000	0.000		2.000	0.000	2
	3σ	0.001	0.078	0.084		0.000	1.791	0.046		0.163	1.837	2
	4σ	0.001	0.269	0.043		0.000	0.144	1.543		0.313	1.687	2
	5σ	0.000	1.353	0.511		0.000	0.000	0.136		1.864	0.136	2
	1π				0.523				3.477	0.523	3.477	4
Best atom	Totals											
	$N(r_k)$	2.002	1.700	0.637	0.523	2.001	1.935	1.725	3.477	4.862	9.138	14

TABLE Xb. Overlap populations in BF.

	ϕ_i	$1s_B, 1s_F$	$1s_B, 2s_F$	$1s_B, 2p\sigma_F$	$2s_B, 1s_F$	$2s_B, 2s_F$	$2s_B, 2p\sigma_F$	$2p\sigma_B, 1s_F$	$2p\sigma_B, 2s_F$	$2p\sigma_B, 2p\sigma_F$	$2p\sigma_B, 2p\pi_F$	$n(i)$
	1σ	0.000	0.000	0.000	−0.001	0.000	0.000	−0.001	0.000	0.000		−0.002
	2σ	0.000	0.000	0.000	0.000	0.000	0.000	0.000	0.000	0.000		0.000
	3σ	0.000	−0.005	−0.001	0.000	0.128	0.010	0.001	0.162	0.011		0.306
	4σ	0.000	0.002	−0.006	−0.001	−0.190	0.229	−0.001	−0.133	0.136		0.036
	5σ	0.000	0.000	0.000	0.000	−0.108	−0.198	0.000	0.076	0.119		−0.111
	1π										0.393	0.393
Slater	Totals											
	σ_T	0.000	−0.003	−0.007	−0.002	−0.170	0.041	−0.001	0.105	0.266		0.229
	$n(r_k, s_l)$	0.000	−0.003	−0.007	−0.002	−0.170	0.041	−0.001	0.105	0.266	0.393	0.622
	1σ	0.000	0.000	0.000	0.000	0.000	0.000	−0.001	0.000	0.000		−0.001
	2σ	0.000	0.000	0.000	0.000	0.000	0.000	0.000	0.000	0.000		0.000
	3σ	0.000	−0.005	−0.001	0.000	0.114	0.010	0.000	0.137	0.009		0.264
	4σ	0.000	0.002	−0.007	−0.001	−0.183	0.243	−0.001	−0.114	0.109		0.048
	5σ	0.000	0.000	−0.001	0.000	−0.091	−0.227	0.000	0.068	0.121		−0.130
	1π										0.402	0.402
Best atom	Totals											
	σ_T	0.000	−0.003	−0.009	−0.001	−0.160	0.026	−0.002	0.091	0.239		0.181
	$n(r_k, s_l)$	0.000	−0.003	−0.009	−0.001	−0.160	0.026	−0.002	0.091	0.239	0.402	0.583

TABLE XIa. Gross atomic populations in CO (R_e=2.132 a.u.).

	ϕ_i	$1s_C$	$2s_C$	$2p\sigma_C$	$2p\pi_C$	$1s_O$	$2s_O$	$2p\sigma_O$	$2p\pi_O$	$N(i;C)$	$N(i;O)$	$N(i)$
	1σ	0.000	−0.001	−0.001		2.001	0.001	0.000		−0.002	2.002	2
	2σ	2.001	0.000	0.000		0.000	−0.001	0.000		2.001	−0.001	2
	3σ	0.001	0.290	0.201		0.001	1.354	0.153		0.492	1.508	2
	4σ	0.000	0.482	−0.008		0.000	0.483	1.043		0.474	1.526	2
	5σ	0.000	0.907	0.767		0.000	0.005	0.321		1.674	0.326	2
	1π				1.250				2.750	1.250	2.750	4
Slater												
	Totals											
	$N(r_k)$	2.002	1.678	0.959	1.250	2.002	1.842	1.517	2.750	5.889	8.111	14
	1σ	0.000	0.000	−0.001		2.001	0.000	0.000		−0.001	2.001	2
	2σ	2.000	0.000	0.000		0.000	0.000	0.000		2.000	0.000	2
	3σ	0.001	0.270	0.187		0.001	1.374	0.167		0.458	1.542	2
	4σ	0.000	0.479	−0.010		0.000	0.483	1.048		0.469	1.531	2
	5σ	0.000	0.912	0.753		0.000	0.006	0.329		1.665	0.335	2
	1π				1.234				2.766	1.234	2.766	4
Best atom												
	Totals											
	$N(r_k)$	2.001	1.661	0.929	1.234	2.002	1.863	1.544	2.766	5.825	8.175	14

TABLE XIb. Overlap populations in CO.

	ϕ_i	$1s_C,1s_O$	$1s_C,2s_O$	$1s_C,2p\sigma_O$	$2s_C,1s_O$	$2s_C,2s_O$	$2s_C,2p\sigma_O$	$2p\sigma_C,1s_O$	$2p\sigma_C,2s_O$	$2p\sigma_C,2p\sigma_O$	$2p\pi_C,2p\pi_O$	$n(i)$
	1σ	0.000	0.000	0.000	−0.001	0.000	0.000	−0.002	0.000	0.000		−0.003
	2σ	0.000	−0.001	0.000	0.000	0.000	0.000	0.000	0.000	0.000		−0.001
	3σ	0.000	−0.009	−0.004	−0.002	0.293	0.067	−0.002	0.246	0.045		0.634
	4σ	0.000	0.003	−0.006	−0.003	−0.565	0.429	−0.001	−0.084	0.050		−0.177
	5σ	0.000	0.000	−0.004	0.002	0.045	−0.416	−0.002	−0.040	0.294		−0.121
	1π										0.742	0.742
Slater												
	Totals											
	σ_T	0.000	−0.007	−0.014	−0.004	−0.227	0.080	−0.007	0.122	0.389		0.332
	$n(r_k, s_l)$	0.000	−0.007	−0.014	−0.004	−0.227	0.080	−0.007	0.122	0.389	0.742	1.074
	1σ	0.000	0.000	0.000	−0.001	0.000	0.000	−0.002	0.000	0.000		−0.003
	2σ	0.000	−0.001	0.000	0.000	0.000	0.000	0.000	0.000	0.000		−0.001
	3σ	0.000	−0.010	−0.005	−0.002	0.282	0.069	−0.002	0.237	0.043		0.612
	4σ	0.000	0.004	−0.006	−0.003	−0.573	0.438	−0.001	−0.077	0.044		−0.174
	5σ	0.000	0.000	−0.005	0.002	0.051	−0.441	−0.002	−0.045	0.292		−0.148
	1π										0.771	0.771
Best atom												
	Totals											
	σ_T	0.000	−0.007	−0.016	−0.004	−0.240	0.066	−0.007	0.115	0.379		0.286
	$n(r_k, s_l)$	0.000	−0.007	−0.016	−0.004	−0.240	0.066	−0.007	0.115	0.379	0.771	1.057

TABLE XIIa. Gross atomic populations in LiF (R_e=2.85 a.u.).

	ϕ_i	$1s_{Li}$	$2s_{Li}$	$2p\sigma_{Li}$	$2p\pi_{Li}$	$1s_F$	$2s_F$	$2p\sigma_F$	$2p\pi_F$	$N(i;\mathrm{Li})$	$N(i;\mathrm{F})$	$N(i)$
	1σ	0.000	0.000	0.000		2.000	0.000	0.000		0.000	2.000	2
	2σ	1.993	0.001	0.000		0.000	0.004	0.002		1.994	0.006	2
	3σ	0.004	0.031	0.053		0.000	1.908	0.004		0.088	1.912	2
	4σ	0.003	0.031	0.021		0.000	0.014	1.931		0.055	1.945	2
	1π				0.679				3.321	0.679	3.321	4
Slater												
	Totals											
	$N(r_k)$	2.000	0.063	0.074	0.679	2.000	1.926	1.937	3.321	2.816	9.184	12
	1σ	0.000	0.000	0.000		2.000	0.000	0.000		0.000	2.000	2
	2σ	1.993	0.001	0.000		0.000	0.004	0.002		1.994	0.006	2
	3σ	0.004	0.025	0.041		0.000	1.925	0.005		0.070	1.930	2
	4σ	0.003	0.025	0.016		0.000	0.013	1.943		0.044	1.956	2
	1π				0.613				3.387	0.613	3.387	4
Best atom												
	Totals											
	$N(r_k)$	2.000	0.051	0.057	0.613	2.000	1.942	1.950	3.387	2.721	9.279	12

TABLE XIIb. Overlap populations in LiF.

	ϕ_i	$1s_A,1s_B$	$1s_A,2s_B$	$1s_A,2p\sigma_B$	$2s_A,1s_B$	$2s_A,2s_B$	$2s_A,2p\sigma_B$	$2p\sigma_A,1s_B$	$2p\sigma_A,2s_B$	$2p\sigma_A,2p\sigma_B$	$2p\pi_A,2p\pi_B$	$n(i)$
	1σ	0.000	0.000	0.000	0.000	0.000	0.000	−0.001	0.000	0.000		−0.001
	2σ	0.000	0.004	0.004	0.000	0.000	0.000	0.000	0.000	0.000		0.008
	3σ	0.000	−0.010	−0.001	0.000	0.051	0.000	0.000	0.091	0.001		0.132
	4σ	0.000	0.001	−0.015	0.000	−0.014	0.024	0.000	−0.019	0.023		0.000
	1π										0.322	0.322
Slater												
	Totals											
	σ_T	0.000	−0.005	−0.012	0.000	0.037	0.024	−0.001	0.072	0.024		0.139
	$n(r_k, s_l)$	0.000	−0.005	−0.012	0.000	0.037	0.024	−0.001	0.072	0.024	0.322	0.461
	1σ	0.000	0.000	0.000	0.000	0.000	0.000	0.000	0.000	0.000		0.000
	2σ	0.000	0.004	0.004	0.000	0.000	0.000	0.000	0.000	0.000		0.008
	3σ	0.000	−0.011	−0.001	0.000	0.042	0.000	0.000	0.074	0.001		0.105
	4σ	0.000	0.001	−0.017	0.000	−0.012	0.020	0.000	−0.015	0.020		−0.003
	1π										0.314	0.314
Best atom												
	Totals											
	σ_T	0.000	−0.006	−0.014	0.000	0.030	0.020	0.000	0.059	0.021		0.110
	$n(r_k, s_l)$	0.000	−0.006	−0.014	0.000	0.030	0.020	0.000	0.059	0.021	0.314	0.424

Intramolecular Energy Transfer in Rare Earth Chelates. Role of the Triplet State

G. A. CROSBY, R. E. WHAN, AND R. M. ALIRE

Department of Chemistry, University of New Mexico, Albuquerque, New Mexico

(Received September 29, 1960)

Results of luminescence studies on chelates of La^{3+}, Sm^{3+}, Eu^{3+}, Gd^{3+}, Tb^{3+}, Dy^{3+}, Tm^{3+}, Yb^{3+}, and Lu^{3+} are reported. It is shown that the intramolecular energy transfer efficiency is a sensitive function of the relative positions of the resonance energy levels of the ions and the metastable triplet states of the complexes. In the case of Eu^{3+} it is demonstrated that, by a proper choice of ligands, it is possible to selectively excite only the lowest resonance level of the two existing resonance levels of this ion. Coupling of the rare earth ions to the ligands is discussed, and a comparison is made between the optical properties of rare earth ions in chelates and in inorganic salts.

INTRODUCTION

INTRAMOLECULAR energy transfer in rare earth chelates under excitation by near ultraviolet light has been the subject of several investigations. The phenomenon was reported by Weissman[1] and later by Sevchenko *et al.*[2] who studied chelates of europium, samarium, and terbium with various ligands. It was found that excitation of a metal complex in the region of light absorption associated primarily with the ligands of the complex resulted in a high yield of linelike "atomic" emission characteristic of the metal ion. It was shown by Weissman[1] for europium chelates and corroborated by Crosby and Kasha[3] for ytterbium chelates that direct excitation of the metal ion was not responsible for the line emission, but that intramolecular energy transfer from the electronic states associated with the complexes to localized intra-4*f* shell energy levels of the ions was involved. In this paper we propose to establish the path of energy migration in rare earth chelates.

The similarity of the chemical properties of the lanthanides, combined with the comparative insensitivity of the 4*f* electrons to the environments of the ions, makes the chelates of the rare earths ideal systems for studying the general problem of intramolecular energy transfer to complexed metal ions.

There are two obvious methods for studying energy transfer in the rare earth chelates: (1) varying the ion bound by a given ligand, and (2) varying the ligand binding a given ion. Both approaches have been employed in this investigation. Attention is focused on the relatively bright line emitters, samarium, europium, terbium, dysprosium, thulium, and ytterbium. [A spectrographic study of all the dibenzoylmethide chelates of the trivalent rare earth ions (except promethium and cerium) has been completed (R. E. Whan and G. A. Crosby) and will be published elsewhere. This latter paper discusses in more detail the characteristics of some of the spectra involved here and contains photographs and densitometer traces of luminescences observed from this series of compounds].

EXPERIMENTAL

Preparations and Analyses

The following method of preparation was employed for all the chelates used in this investigation. A solution of the rare earth chloride (in ethanol, water, or methanol) was treated with a solution of the chelating agent in the same solvent. (Rare earth oxides were obtained from Research Chemicals, Burbank, California and the Institute for Atomic Research, Ames, Iowa). The precipitation was accomplished by the addition of piperidine. Whenever possible the chelates were recrystallized from an appropriate solvent (methanol, ethanol, or acetone) and either air dried or vacuum dried.

Analyses of the chelates were performed for metal and/or ligand and were consistent with the expected theoretical values.

Spectroscopic Measurements

For luminescence studies all chelates were dissolved at a concentration of $\sim 10^{-5} M$ in a solution of five parts ether, five parts 3-methylpentane, and two parts absolute ethanol by volume.

The 3-methylpentane (Phillips pure grade) was purified by passing it through a column of silica gel. The absolute ethanol (USI Company absolute pure ethanol, reagent grade) was distilled from $Mg(OEt)_2$. The ether (Mallinckrodt anhydrous grade) was found to exhibit no luminescence under the excitation wavelengths and exposure times employed and was used without further purification.

The solutions were frozen to clear rigid glasses at liquid N_2 temperatures and were irradiated with a General Electric, 1000 w, water cooled, high pressure AH-6 lamp equipped with a Pyrex water jacket. The spectra were recorded using a Steinheil Universal GH spectrograph equipped with three glass prisms adjusted

[1] S. I. Weissman, J. Chem. Phys. **10**, 214 (1942).
[2] A. N. Sevchenko and A. K. Trofimov, J. Exptl. Theoret. Phys. (U.S.S.R.) **21**, 220 (1951); A. N. Sevchenko and A. G. Morachevsky, Izvest. Akad. Nauk, S.S.S.R. (Ser. Fiz) **15**, 628 (1951).
[3] G. A. Crosby and M. Kasha, Spectrochim. Acta **10**, 377 (1958).

TABLE I. Filter combinations used for excitation of chelate luminescences (cf. Table II).

Compound[a]	First absorption band λ_{max} in A	Exciting light filter	Filter transmission range in A (approx)
MB_3	3200	$CuSO_4$,[b] 5840,[c] 9863	3100–4000
MD_3	3500	$CuSO_4$, 5840, 5970	3200–4000
MT_3	3300	$CuSO_4$, 5840	3000–4000
$M(AnAc)_3$	3300	$KCr(SO_4)_2$,[d] 9863, 9863	2800–3700
$M(8HQ)_3$	3700	$CuSO_4$, 5840, 5840	3000–4000
$M(2Me8HQ)_3$	3500	$CuSO_4$, 5840, 5840	3000–4000

[a] Abbreviations: M=rare earth trivalent ion, B=benzoylacetonate ion, D=dibenzoylmethide ion, T=T-tribenzoylmethide ion, AnAc=anthranilate ion, 8HQ=8-hydroxyquinolate ion, 2Me8HQ=2-methyl-8-hydroxyquinolate ion.
[b] $CuSO_4 \cdot 5H_2O$, 100 g/liter 5 cm path.
[c] Corning code number, std. thickness.
[d] $KCr(SO_4)_2 \cdot 12H_2O$, 30 g/liter 5 cm path.

for maximum aperture (approx. f3.5). Eastman 103a-F, I-L and ammonia hypersensitized I-M photographic plates were employed. The latter type was needed for photographing the Yb^{3+} line emission only. Argon and neon reference spectra were used for calibration.

The phosphorescence spectra were obtained by the use of a modified Becquerel-type phosphoroscope with a calculated resolution time of $\sim 10^{-4}$ sec. The total emission spectra were obtained using near front-surface illumination.

Filters were selected for exciting the molecules with light corresponding to the wavelengths of the lowest energy absorption bands of the complexes. Filter combinations used are listed in Table I.

Microphotometer traces of the plates were obtained using a Jarrell-Ash automatic recording microphotometer.

Absorption spectra were measured using either a Beckman model DU spectrophotometer or a Cary model 14 recording spectrophotometer. The absorption spectra were taken at 20°C in absolute ethanol.

RESULTS

The luminescence spectra obtained from all the chelates studied are classified in Table II.

As indicated in Table II, a majority of the chelates exhibited molecular band emission. This emission consisted of both fluorescence and phosphorescence; and except for the very strong line emitters, both types of band emission could be photographed. Especially for chelates of lanthanum, gadolinium, and lutetium, the phosphorescence emission was relatively strong and well defined and could be readily photographed through the phosphoroscope. In all cases the shortest wavelength phosphorescence band was assumed to be the O–O transition, and the position of this band in wave numbers is reported in Table III.

As indicated in Table III, the error in measurement of the triplet level is considerably smaller for dibenzoylmethide and benzoylacetonate chelates than for all the others reported. For every series, the band emissions from chelates of La^{3+}, Gd^{3+}, and Lu^{3+} were substantially stronger and better defined than from chelates of the other ions of the same series. It was also noticed that the Gd^{3+} chelates exhibited enhanced phosphorescence-fluorescence ratios compared to chelates of the other lanthanides.[4] Within a chelate series, significant red shifts of the phosphorescence spectra for the La^{3+}, Gd^{3+}, and Lu^{3+} compounds were observed, compared with the phosphorescences observed from chelates of other ions.

Accurate measurements of the triplet states for chelates of the other ions were hampered by several factors. In many cases interfering bright line emission from the ion precluded any measurement of the triplet at all. In other cases, the phosphorescence spectra were ill defined. For the anthranilates, there was no discernible structure at all for any chelate and only the broad band maxima have been reported.

The 8-hydroxyquinolates and 2-methyl-8-hydroxyquinolates presented special problems. They dissolved only at elevated temperatures resulting probably in increased dissociation and decomposition. The phosphorescence from the parent chelating agent was extremely weak in both cases. The phosphorescence was enhanced upon chelation with La^{3+}, Gd^{3+}, and Lu^{3+}, but it was not sufficiently intense from chelates of the other ions to obtain reliable spectra. Although very weak phosphorescences were photographed under prolonged exposures (400 μ slit, 8 hr, f3.5 optics), the measurements were discarded, since it was observed that these rare earth chelates do not obey Beer's law,

TABLE II. Classification of luminescence spectra of rare earth chelates under ultraviolet excitation.[a]

Chelate[b,c]	La	Sm	Eu	Gd	Tb	Dy	Tm	Yb	Lu
MB_3	*B*[d]	*CL*	*L*	*B*	*L*	*L*	*C*	*CB*	*B*
MD_3	*B*	*CL*	*L*	*B*	*L*	*B*	*B*	*CB*	*B*
MT_3		*CL*	*L*	*B*	*L*	*L*	*CB*		
$M(AnAc)_3$	*B*	*CB*	*C*	*B*	*CL*	*CB*	*B*	*CB*	*B*
$M(8HQ)_3$	*B*	*B*	*CL*	*B*	*B*	*B*	*B*	*CB*	*B*
$M(2Me8HQ)_3$	*B*	*B*	*CL*	*B*	*B*	*B*	*B*	*CB*	*B*

[a] Refer to Table I for excitation wavelengths.
[b] Refer to Table I for definitions of abbreviations.
[c] In some cases our preparative methods yielded solvates of the chelates listed, especially for the first half of the series (La^{3+} through Gd^{3+}). The fact that solvates were obtained is deemed unimportant since a hydroxylic glass was used in all cases, and the precise nature of the species in solution is not known.
[d] *B*=molecular fluorescence and phosphorescence band emission only. *L*=line emission characteristic of the lanthanide ion with only negligible molecular band emission. *C*=combination of both band and line emission of comparable intensity. *CL*=combination of band and line emission with lines predominating. *CB*=combination of band and line emission with bands predominating.

[4] P. Yuster and S. I. Weissman, J. Chem. Phys. **17**, 1182 (1949).

TABLE III. Triplet state energy levels for rare earth chelates.[a]

Chelate	La	Sm	Eu	Gd	Tb	Dy	Tm	Yb	Lu	Average
MB_3	21 386 ±25	21 566 ±50		21 395 ±25		21 552 ±50	21 514 ±50	21 436 ±50	21 505 ±25	21 480
MD_3	20 292 ±25	20 691 ±50	20 755 ±50	20 350 ±25		20 467 ±50	20 593 ±50	20 547 ±50	20 442 ±25	20 520
MT_3				20 695 ±25		20 833 ±150				20 765
$M(AnAc)_3$[b]	21 758 ±100	22 160 ±100	22 114 ±100	22 045 ±100	21 939 ±100	22 694 ±100	22 148 ±100	22 261 ±100	22 099 ±100	22 135
$M(8HQ)_3$	17 850 ±50			17 667 ±50					17 755 ±50	17 760
$M(2Me8HQ)_3$	17 818 ±50			17 980 ±50					18 214 ±50	18 000

[a] It is tacitly assumed in this paper that the energy levels responsible for the phosphorescence of the complexes are triplet states. As S. I. Weissman has pointed out [J. Chem. Phys. **18**, 1258 (1950)], these states are not pure triplets, but should be described by wave functions containing admixtures of ion spin states. This would complicate the nomenclature unnecessarily, and we prefer to label the metastable states as triplets. It is recognized that such considerations may prove to be of paramount importance for a quantitative interpretation of energy transfer in these systems.

[b] No discernible structure, band maxima reported.

decompose upon standing in solution, and undergo photolysis with long exposure to ultraviolet light.

Preliminary work was performed on many other chelates (salicylaldehydes and derivatives, *o*-aminophenol, hydroxybenzophenone derivatives, hydroxyquinones, etc.). Many of these were not suitable for study because preparations yielded in some cases uncertain products, some compounds were quite unstable, some were extremely insoluble, and others decomposed rapidly in the exciting light.

The data reported in Table III are believed to be reliable because the emission spectra were sufficiently well defined and/or intense and reproducible.

DISCUSSION

Comparison with Rare Earth Ion Luminescences

It has been established that the anhydrous chlorides of all the rare earth ions exhibit line fluorescence upon direct excitation of the ions with near ultraviolet light[5]; however, only Sm^{3+}, Eu^{3+}, Gd^{3+}, Tb^{3+}, and Dy^{3+} emit strongly in hydrated crystals. The emissions from coordinated Eu^{3+}, Gd^{3+}, and Tb^{3+} are especially bright, those of Sm^{3+} and Dy^{3+} somewhat weaker, while the remaining ions fluoresce only weakly or not at all.[6]

Excitation of chelates of the lanthanides in the region of the ligand absorption spectrum also results in line emission from the rare earth ions. The variations in the intensities of the line emissions from ion to ion parallel closely that observed for the hydrated inorganic salts. This can be seen clearly by perusal of the data in Table II. In particular, the luminescence from the benzoylacetonates consists of strong line emission from the Eu^{3+}, Tb^{3+}, and Dy^{3+} compounds and weaker line emission, in addition to band emission, from the chelates of Sm^{3+}, Tm^{3+}, and Yb^{3+}. (The anomalous case of gadolinium will be discussed later.) Similar behavior was observed for the dibenzoylmethides with the striking exception of the Dy^{3+} and Tm^{3+} chelates which exhibited band emission exclusively in marked contrast to the corresponding benzoylacetonates. The 8-hydroxyquinolates and the 2-methyl-8-hydroxyquinolates of only two ions, Eu^{3+} and Yb^{3+}, exhibited line emission. Especially notable in these series is the absence of bright line emission from the Tb^{3+} ion, since its emission was exceedingly intense in all other cases.

Previous investigations employing both absorption and fluorescence experiments on rare earth inorganic salts have located the principal resonance levels of the ions. These are tabulated in Table IV.

Role of the Triplet State

Basic Requirement for Energy Transfer

The lanthanide ion resonance levels from Table IV and the triplet state energy levels for the chelates listed in Table III are plotted in Fig. 1.

An explanation of the puzzling differences in the luminescence efficiencies of the rare earth ions as the ligands are varied is revealed in a comparison of the emitting (resonance) energy levels of the ions with the corresponding lowest triplet state energies of the complexes. It is immediately apparent by comparison of the relative energy level positions in Fig. 1 with the observed spectral data in Table II that the requirement for line emission from a given chelate is *the lowest triplet state energy level of the complex must be nearly equal to or must lie above the resonance energy level of the rare earth ion.*

[5] F. Varsanyi and G. H. Dieke, J. Chem. Phys. **31**, 1066 (1959).

[6] G. H. Dieke and L. A. Hall, J. Chem. Phys. **27**, 465 (1957).

TABLE IV. Resonance levels of rare earth ions.

Ion	Approximate positions of the resonance levels cm^{-1}	Reference
Sm^{3+}	17 800	H. Lammermann, Z. Physik **150,** 551 (1958).
Eu^{3+}	17 250[a] 19 020	E. V. Sayre and S. Freed, J. Chem. Phys. **24,** 1213 (1956).
Gd^{3+}	32 066	G. H. Dieke and L. Leopold, J. Opt. Soc. Am. **47,** 944 (1957).
Tb^{3+}	20 430	H. F. Geisler and K. H. Hellwege, Z. Physik **136,** 293 (1953).
Dy^{3+}	20 958	G. H. Dieke and S. Singh, J. Opt. Soc. Am. **46,** 495 (1956).
Tm^{3+}	21 222	G. A. Crosby and R. E. Whan, Naturwissenschaften **47,** 276 (1960).
	21 300	U. Johnsen, Z. Physik **152,** 454 (1958).
	20 946–21 268	H. Gobrecht, Ann. Physik **31,** 600 (1938).
Yb^{3+}	10 300	G. H. Dieke and H. M. Crosswhite, J. Opt. Soc. Am. **46,** 885 (1956).
	10 300	G. A. Crosby and M. Kasha, Spectrochim. Acta **10,** 377 (1958).

[a] This ion exhibits two well-established emitting states.

Individual Ions

In all cases, the triplet states of the chelate lie above the resonance level of the Yb^{3+} ion, and the latter exhibited line emission from all compounds.

The position of the resonance level of the Tm^{3+} ion has not been determined accurately because the ion fluoresces very weakly in most hydrated inorganic salts. Line emission was obtained from the benzoylacetonate of Tm^{3+}, and a measurement of the highest frequency line places the resonance level at[7] approximately 21 200 cm^{-1}. This agrees with measurements by other workers (See Table IV). Line emission was obtained also from the tribenzoylmethide chelate of this ion, but molecular band emission only was obtained from the other compounds studied. The triplet level of the benzoylacetonate complex lies above the resonance level, and that of the tribenzoylmethide chelate is coincident with it within experimental error. Although the triplet state of the anthranilate complex definitely lies above the Tm^{3+} resonance level, we were unable to determine whether or not Tm^{3+} lines were present because of the intense interfering molecular band emission from the complex falling in the same spectral region. This difficulty is compounded by the fact that the efficiency of energy transfer to the ions for the series of anthranilates is the lowest of all the complexes studies. This may be due to the more ionic character of the bonding.

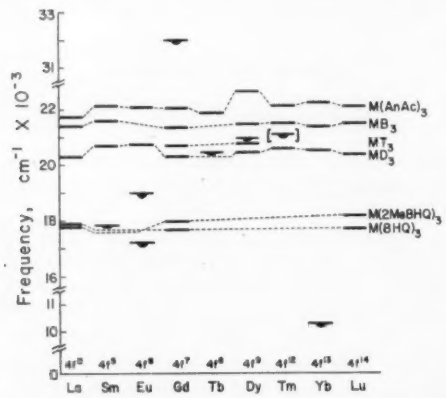

FIG. 1. Resonance levels of the ions are indicated by solid half-circles underneath the level. Measured triplet state energies for the complexes are indicated by solid lines. Dashed lines connect the energy levels for a series of chelates with the same ligand.

As reported previously, chelates of the Dy^{3+} ion show remarkable variations in luminescence properties.[8] The suggested dependence of line emission on the position of the triplet state relative to the resonance level of the ion is further substantiated by the additional results reported here. Although the triplet level of the tribenzoylmethide chelate is indicated to be below the Dy^{3+} resonance level, it is very near to the latter, and it was impossible to distinguish the relative positions more accurately.

Chelates of Tb^{3+}, one of the brightest line emitters of all the rare earths, exhibit the expected behavior. An intense green Tb^{3+} line emission is observed from all chelates having the lowest triplet level above the resonance level of the ion, and only band emission is observed from the others.

All gadolinium chelates showed intense well-defined molecular phosphorescence band emission. In the hydrated inorganic crystals this ion is reported to be the brightest emitter of all the rare earths.[9] Using our experimental apparatus we found it was energetically impossible to excite this ion directly or by energy transfer from either the singlet or triplet states, which

[7] G. A. Crosby and R. E. Whan, Naturwissenschaften **47,** 276 (1960).

[8] G. A. Crosby and R. E. Whan, J. Chem. Phys. **32,** 614 (1960).

[9] G. H. Dieke and L. Leopold, J. Opt. Soc. Am. **47,** 944 (1957).

satisfactorily accounts for the absence of any Gd^{3+} line emission.

Exceptional Case of Europium

The Eu^{3+} ion forms an exception to all the other rare earth trivalent ions in that it fluoresces strongly from two well-established resonance levels.[10] All the chelates of this ion exhibited strong line emission; however, *only* line emission originating from the *lower* resonance level at 17 250 cm^{-1} was observed from the 8-hydroxyquinolate and its 2-methyl derivative. In all the other cases, line emission originating from both resonance levels was observed. Since only the metastable triplet states for both the 8-hydroxyquinolate and the 2-methyl-8-hydroxyquinolate chelates lie between the two Eu^{3+} resonance levels, this establishes conclusively that the intramolecular energy transfer from the complex to the chelated Eu^{3+} ion is via the lowest triplet state or a nearby excited state.

Line emission was observed from Sm^{3+} chelates, whose triplet states definitely lie above the Sm^{3+} resonance level. Measurements of the phosphorescences of the 8-hydroxyquinolate and the 2-methyl-8-hydroxyquinolate chelates of La^{3+}, Gd^{3+}, and Lu^{3+} locate the triplet states close to the Sm^{3+} resonance level. Since the latter ion does not emit lines from these compounds, we place the corresponding triplets of these Sm^{3+} complexes *a posteriori* below 17 800 cm^{-1}. (Since a slight red shift occurs in the phosphorescence of the ligand parent molecules upon chelation, the triplet level of 8-hydroxyquinoline should lie very near to this value. The extremely weak phosphorescence of this molecule seems not to have been reported previously.)

Quenching

Luminescence efficiencies of the rare earth ions upon direct excitation of the ion in hydrated inorganic salts vary widely. Especially the ions praseodymium, neodymium, holmium, and erbium do not fluoresce or fluoresce very weakly. The low yield of line emission from these ions has been attributed to internal quenching through strong coupling of the ion with the crystal lattices, whereas weaker coupling with the lattice is suggested for the more efficient line emitters.[6]

In chelates a similar variation of line intensity is observed (when the triplet state is above the resonance level of the chelated ion). Since the compounds are chemically similar and relatively stable, we postulate an almost uniformly strong coupling between the ligands and the central metal ion for all chelates of the same series. High luminescence yields of lines, especially from Eu^{3+} and Tb^{3+}, indicate efficient energy transfer from the triplet state. We believe that energy transfer to the other ions is efficient also. For the latter ions, however, the energy is rapidly dissipated through existing low-lying energy levels of the ions. For the efficient emitters large energy gaps exist between the resonance levels and the lower excited states; and consequently, the radiative processes compete favorably with the nonradiative ones.[11] This is consistent with the general observation that nonradiative processes become less efficient whenever large quanta of energy must be dissipated.

These deductions are substantiated by estimates of relative quantum yields obtained from comparisons of exposure times. It was observed generally that the total yields of molecular band emission (phosphorescence and fluorescence) from chelates of La^{3+}, Gd^{3+}, and Lu^{3+}, which have no low-lying $4f$ energy levels, were markedly higher than the corresponding yields from other chelates, especially those of Pr^{3+}, Nd^{3+}, Ho^{3+}, and Er^{3+}. These latter ions possess numerous closely packed excited states which provide paths for efficient quenching of the excited states of the complexes.

Both the reported experiments and those of Yuster and Weissman show a dependence of fluorescence yields and phosphorescence yields upon the metal ion. Our experiments also demonstrate, however, that the dependence of the latter is much more pronounced than that of the former. Thus, although the total yield of molecular band emission varies markedly with change of the central ion, we attribute this change primarily to the efficiency of quenching of the triplet state.

Transfer Mechanisms

Excitation of the central metal ion by direct transfer of energy from the first excited singlet state is energetically possible, but the reported experiments show this path to be unimportant. Either the $4f$ electronic levels of the rare earth ion do not couple with the vibronic levels of the first excited singlet state, or transfer processes depending upon such coupling are not competitive with other processes which depopulate the state, i.e., vibrational internal conversion, fluorescence, and intersystem crossing to the triplet state.

Once the complex undergoes intersystem crossing to the triplet states, radiative decay is spin forbidden and thus much slower, and the nonradiative process—energy transfer to the ion—is then competitive.

A possible explanation of the mechanism of energy transfer is through vibrational coupling between the $4f$ excited states of the ion and the lowest triplet. Schematic representations of three alternatives are given in Fig. 2.

Case A represents the situation where the resonance level of the ion is definitely below the triplet state and transfer can occur from the zeroth vibrational level of the latter state to some vibronic state of the metal ion. Case B shows the similar situation regarding the relative positions of the energy levels, but crossing does not

[10] E. V. Sayre and S. Freed, J. Chem. Phys. **24**, 1213 (1956).

[11] D. S. McClure, *Solid State Physics* (Academic Press, Inc., New York, 1959), Vol. 9, p. 456. Especially Fig. 18A, B, C, and D.

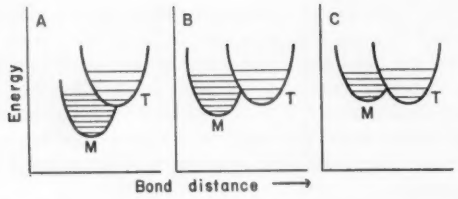

FIG. 2. Schematic representations of potential energy surfaces. *T* labels triplet state potential curve. *M* labels a 4*f* electronic level of the metal ion in the ligand environment. Horizontal lines represent vibrational spacing (schematic).

occur from the zeroth level of the triplet but from some higher vibronic level. In case C the resonance level is indicated to be slightly above the triplet state.

If case A is a valid representation of the potential energy surfaces involved, the mean lifetime of the line emission (when observed) must be equal to or greater than that of the triplet state, for as long as the triplet state is populated transfer will occur from the zeroth vibrational level to a vibronic level of the metal ion. For cases B and C, the observed lifetimes of the lines and phosphorescence bands would be independent of each other, since transfer can only occur as long as the higher vibrational levels of the triplet are populated. Once complete internal conversion to the zeroth level of the triplet occurs, energy transfer to the ion is no longer possible, and the mean lifetimes of the metal line emission and the phosphorescence band emission are independent. Qualitative observations indicate that for some chelates, the line emission is significantly shorter-lived than the phosphorescence, supporting the second alternative. Lifetime studies on complexes are being initiated in order to distinguish between these two possibilities. For two of the compounds, TmT_3 and DyT_3, case C cannot be eliminated because of the errors inherent in the measurement of the triplet state energies and the uncertainty of the exact positions of the resonance levels of the ions in the respective environments. For these two compounds the separation of the two potential well minima is certainly within 300 cm^{-1}. The participation of a higher electronic state of the complex (possibly a higher triplet or a spin-orbit component of the lowest triplet) in the energy transfer process cannot be ruled out.

Another interpretation of the intramolecular transfer phenomenon, suggested by Sponer,[12] involves a charge-transfer followed by a Förster type mechanism.[13] According to this argument a significant red shift of the phosphorescence must occur especially for the Yb^{3+} chelates in order to sensitize the emission from the ion. No significant red shifts were obtained.

The possibility of a pure Förster type mechanism seems doubtful because the necessary condition of spectral overlap of the emission of the complex and the absorption of the ion is not always fulfilled. The observation that line emission was weaker for the anthranilates, in addition to the work of Weissman on Eu^{3+} chelates,[1] shows the efficiency of the energy transfer to be dependent on the nature of the ligand-metal ion bonds. This argues strongly for a transfer mechanism involving electronic orbital overlap. An electron exchange mechanism of nonradiative energy transfer in which the total spin of the complex is conserved (such as discussed by Dexter[14]) seems appropriate.

SUMMARY

The results of spectroscopic studies on over 50 chelates of trivalent rare earth ions are reported. Luminescences from the chelates upon excitation with ultraviolet light were photographed and classified into three categories: bright line emission characteristic of the rare earth ion, molecular band emission, and a combination of line and band emission. The luminescence efficiencies of the chelated rare earth ions were found to parallel closely those observed for the hydrated inorganic salts with certain marked exceptions. Measurements of the lowest triplet state energies of the complexes were made and compared with the reported resonance levels of the ions. It is concluded that energy transfer from the electronically excited complex to the rare earth ion is via the lowest triplet state or a nearby excited state of the complex. Quenching of the excited states of the complexes by the lanthanide ion is discussed and mechanisms for the energy transfer phenomenon are presented.

ACKNOWLEDGMENTS

The research presented in this communication was sponsored by Sandia Corporation under P.O. No. 51-0244. A grant-in-aid from the Research Corporation for the initiation of these studies is gratefully acknowledged.

[12] H. Sponer, Radiation Research, Suppl. **1**, 571 (1959).

[13] Th. Förster, *Fluoreszenz organischer Verbindungen* (Vandenchoeck und Ruprecht, Göttingen, 1951), pp. 71, 83, 93, and 228.

[14] D. L. Dexter, J. Chem. Phys. **21**, 836 (1953).

THE JOURNAL OF CHEMICAL PHYSICS VOLUME 34, NUMBER 3 MARCH, 1961

Crystal Field Splitting and Covalent Bonding in Fe^{++} Silicate Garnets

PHILIP BLOOMFIELD, A. W. LAWSON, AND CHARLES REY

Institute for the Study of Metals and Department of Physics, University of Chicago, Chicago, Illinois

(Received August 3, 1960)

A point-ion model and Slater free-ion wave functions have been used to calculate the crystal field splitting of the Fe^{++} ion ^5D ground term in $Fe_3Al_2(SiO_4)_3$ garnet for various assumed charge distributions within the $(SiO_4)^{4-}$ ion. The best fit with Clark's experimental data on absorption spectra is obtained with about 50% covalent bonding between Si and O, and with an effective nuclear charge for the Fe^{++} ion about 10% less than that given by Slater's rules. This estimate of the degree of covalency is consistent with that given by Pauling. The calculated pressure dependence of the optical absorption is in satisfactory agreement with the experiments of Balchan and Drickamer.

I. INTRODUCTION

THIS paper is concerned primarily with an investigation of the charge distribution in the $(SiO_4)^{4-}$ ion of garnet crystals as calculated from the observed Fe^{++} optical absorption bands[1] by standard crystal field theory[2] neglecting electron spin. A secondary purpose is the explanation of the reported pressure dependence[3] of the absorption band.

The garnets of interest are of the type $X_3^{2+}Y_2^{3+}\cdot(SiO_4)_3^{4-}$, in which X may be Ca, Mg, or Fe, and Y is primarily Al. Such compositions occur frequently in geological formations like the minerals, grossularite, pyrope, and almandine. These garnets are cubic, belonging to the crystal class H 29.[4] In the ideal structure, they satisfy the Bragg-Pauling[5] structural rules for silicates, each divalent ion being surrounded by eight O atoms at the corners of a disphenoid, each trivalent ion being at the center of an octahedral array of O atoms, and each Si atom being the center of a regular tetrahedral array. The symmetry of the ions surrounding the Fe^{++} ion is orthorhombic (D_2).[4] For this reason, the potential of the charge array at the central atom is strongly dependent on both the inverse third and fifth powers of the distance from neighboring charges. Thus, the field depends strongly on neighbors other than nearest, and, in particular, on the charge of the Si atoms in the next-nearest shell. Since this charge in turn depends on the degree of homopolar binding with the oxygen atoms in the nearest-neighbor shell, the field, and hence the splitting responsible for the optical absorption, is critically dependent on the degree of covalency in the silicate groups.

We propose the use of the observed absorption, in conjunction with crystal field theory, to ascertain whether the point-ion model is capable of describing the observed absorption with a reasonable charge distribution in the silicate groups. This procedure is feasible because the low symmetry of the orthorhombic field completely removes the degeneracy of the Fe^{++} levels (in contrast to the more symmetric octahedral field which produces a degenerate doublet and a degenerate triplet). The five distinct levels of the ^5D ground term give rise to three allowable absorption lines. We are therefore able to examine the effect of the charge distribution within the silicate ion and to eliminate the errors associated with certain scale factors in the theory. For instance, it is relatively unimportant that the optical absorption data are inexact and for minerals whose composition is not well known.

Four major simplifications are made in the application of crystal field theory: (a) The ground state wave functions for the $3d^6$ electron configuration of the unperturbed Fe^{++} ion are expressed as linear combinations of determinants of one-electron Slater wave functions[6,7]; (b) point-ion charge distributions are used; (c) the crystal structure of the garnets is assumed ideal; (d) the magnitude of the Stark splitting is assumed small compared to the term differences in the free ion but large compared to the spin orbit splittings within the various terms.

The use of the same radial variation for all the one-electron $3d^6$ wave functions is a good approximation for Fe.[7]

The point-ion charge model for crystal field calculations has been recently discussed by Phillips,[8] who has argued that the repulsive potential of the ligand orbitals cancels, to a high degree of accuracy, the extra attractive potential obtained when point-ion ligands are replaced by distributed-charge ligands.

The distortion from ideality in garnet structures is relatively small[4] and varies from mineral to mineral. The effect of this distortion appears to be negligible compared to other errors.

The product of the effective nuclear charge and the average spacing between the Fe^{++} central ion and the

[1] Sidney P. Clark, Jr., Am. Mineralogist **42**, 732 (1957).
[2] H. A. Bethe, Ann. Physik. **3**, 133 (1929).
[3] A. S. Balchan and H. G. Drickamer, J. Appl. Phys. **30**, 1446 (1959).
[4] P. P. Ewald and C. Herman, ed., Strukturbericht **1**, 364 (1931); A. J. C. Wilson, ed., Structure Repts. **13**, 365 (1950).
[5] L. Pauling, *The Nature of the Chemical Bond* (Cornell University Press, Ithaca, New York, 1945).
[6] J. C. Slater, Phys. Rev. **36**, 57 (1930).
[7] D. Hartree, *The Calculation of Atomic Structure* (John Wiley & Sons, Inc., New York, 1955).
[8] J. C. Phillips, Phys. Chem. Solids **11**, 226 (1959).

nearest O ion can be used as an adjustable parameter; consequently, it is to be hoped that the uncertainties in these quantitatives do not affect the major conclusions of the paper.

The so-called medium-field approximation is good for elements belonging to the Fe group.

The practical effect of spin-orbit coupling is to broaden the absorption lines. The energy of the absorption lines is typically of the order of 3000–8000 cm^{-1}, while the perturbation of spin-orbit coupling is about 200 cm^{-1}. The lines will therefore have about a 10% spread.

In Sec. II, the crystal field potential is expanded in Tesseral harmonics. The matrix elements of the perturbation are calculated for a purely ionic crystal including contributions out to the eighth shell of ion neighbors.

In Sec. III, we consider the effect of a relative division of charge between Si and O within the silicate ion. The matrix elements vary linearly with this division of charge and consequently the relative energies of the absorption lines change. The best fit of the calculated relative energies to the observed energies is presumed to correspond to an assumed charge distribution approximating the actual charge distribution.

Section IV is devoted to a calculation of the pressure dependence of the absorption, and Sec. V is an appraisal of the theoretical procedures and the validity of the experimental data.

II. THEORY

The one-electron $3d$ Slater wave functions are given by,

$$\phi_{\eta M}(k) = R(r_k)\, Y_{2M}(\theta_k, \varphi_k)\eta_{Ms}(k), \tag{1}$$

where k indicates the kth electron.

The radial function is

$$R(r) = N_{3d} r^2 e^{-ar}, \tag{2}$$

where $N_{3d}^2 = (2a)^7/6!$ and $a = Z_{\text{eff}}/3$ in reciprocal atomic units. According to Slater's rules[6] the effective nuclear charge, $Z_{\text{eff}} = 6.25$.

The angular functions are the normalized Tesseral harmonics,

$$Y_{LM}(\theta, \varphi) = \{\cos M\varphi/[(1+\delta_{M0})\pi]^{\frac{1}{2}}\} P_{LM}(\theta)$$
$$Y_{L\bar{M}}(\theta,\varphi) = [\sin M\varphi/(\pi)^{\frac{1}{2}}] P_{LM}(\theta), \tag{3}$$

where $P_{LM}(\theta)$ are the normalized associated Legendre polynomials.

The spin functions are

$$\eta_{\frac{1}{2}} = \alpha = \begin{pmatrix} 1 \\ 0 \end{pmatrix},$$
$$\eta_{-\frac{1}{2}} = \beta = \begin{pmatrix} 0 \\ 1 \end{pmatrix} \tag{4}$$

In this paper we consider the splitting of the ground term under the action of the crystal field. The splitting of the configuration, $3d^6$, into the various terms is due only to the electron-electron interactions within the open $3d$ shell. Similarly, the crystal field splitting of the terms is not due to interactions with electrons of complete groups. Because we neglect spin-orbit coupling, all states of a single term have the same energy in the free atom. Under the action of the crystal field, M_S remains a good quantum number and we may divide up the 25 states of the ground term into five sets corresponding to the given M_S values. Any one of the sets may be used for our calculations. For the ground term the wave functions from the set $M_S = 2$ will be merely *single* determinants.[7]

For example, one of the wave functions for the state $M_S = 2$ is given by,

$$\Phi(^5D) = (6!)^{-\frac{1}{2}} \begin{vmatrix} \varphi_{\alpha 2}^{(1)} & \varphi_{\alpha 1}^{(1)} & \varphi_{\alpha 0}^{(1)} & \varphi_{\alpha \bar{1}}^{(1)} & \varphi_{\alpha \bar{2}}^{(1)} & \varphi_{\beta 2}^{(1)} \\ \varphi_{\alpha 2}^{(2)} & \varphi_{\alpha 1}^{(2)} & \cdot & \cdot & \cdot & \varphi_{2\beta}^{(2)} \\ \cdot & \cdot & \cdot & \cdot & \cdot & \cdot \\ \cdot & \cdot & \cdot & \cdot & \cdot & \cdot \\ \cdot & \cdot & \cdot & \cdot & \cdot & \cdot \\ \varphi_{\alpha 2}^{(6)} & \cdot & \cdot & \cdot & \cdot & \varphi_{\beta 2}^{(6)} \end{vmatrix}. \tag{5}$$

These wave functions may be represented by the main diagonal of the determinants:

$$\Phi_2 = (\alpha_2\alpha_1\alpha_0\alpha_{\bar{1}}\alpha_{\bar{2}}\beta_2)$$
$$\Phi_1 = (\alpha_2\alpha_1\alpha_0\alpha_{\bar{1}}\alpha_{\bar{2}}\beta_1)$$
$$\Phi_0 = (\alpha_2\alpha_1\alpha_0\alpha_{\bar{1}}\alpha_{\bar{2}}\beta_0)$$
$$\Phi_{\bar{1}} = (\alpha_2\alpha_1\alpha_0\alpha_{\bar{1}}\alpha_{\bar{2}}\beta_{\bar{1}})$$
$$\Phi_{\bar{2}} = (\alpha_2\alpha_1\alpha_0\alpha_{\bar{1}}\alpha_{\bar{2}}\beta_{\bar{2}}), \tag{6}$$

where the subindex on Φ labels the β-spin, one-electron function [see Eqs. (3) and (4)].

The five functions with α spin make up a complete group and so we may *calculate* the perturbation levels with the (one-electron) functions:

$$\Phi_2 = \varphi_2$$
$$\Phi_1 = \varphi_1$$
$$\Phi_0 = \varphi_0$$
$$\Phi_{\bar{1}} = \varphi_{\bar{1}}$$
$$\Phi_{\bar{2}} = \varphi_{\bar{2}}. \tag{7}$$

Each of these functions, it must be remembered, represents one state of all the six electrons.

Because each of the four rotational symmetries of D_2 forms its own class (identity, E, and 180° rotation about each axis, C_2^x, C_2^y, C_2^z, all commute with each other), the group has four one-dimensional representations (Γ_E, Γ_x, Γ_y, Γ_z, corresponding to the transformations of a scalar and the x, y, z components of a vector, respectively), and the ^5D term splits up into five distinct levels.[2] The three wave functions φ_1, $\varphi_{\overline{1}}$, $\varphi_{\overline{2}}$ transform as Γ_x, Γ_y, Γ_z, respectively, while φ_2 and φ_0 belong to the invariant representation, Γ_E. Thus we must take the *proper* linear combinations of these last two field-free eigenfunctions so as to obtain the zeroth order wave functions appropriate to the particular field.

By expressing the interaction energy by means of the Legendre expansion,

$$V(\mathbf{r})=\sum_{j=1}^{\infty}\sum_{l=0}^{\infty}\sum_{m=0}^{l}Q_j r_<^{\,l} r_>^{-l-1}P_{lm}(\theta)_i \times[a_{lm}{}^j\cos m\varphi+b_{lm}{}^j\sin m\varphi], \quad (8)$$

where $r_<(r_>)$ is the lesser (greater) of $\mathbf{r}$, $\mathbf{r}_j$, and Q_j is the charge of the field ions which are situated in a shell at distance r_j from the central Fe^{++}. The constants $a_{lm}{}^j$ and $b_{lm}{}^j$ are given by

$$a_{lm}{}^j=2(2l+1)^{-1}(2-\delta_{m0})\sum_i{}^{(j)}\cos m\varphi_i P_{lm}(\theta_i)$$

$$b_{lm}{}^j=4(2l+1)^{-1}\sum_i{}^{(j)}\sin m\varphi_i P_{lm}(\theta_i). \quad (9)$$

Here the summation is over all ions in the jth shell. In the Cartesian coordinates of the work cited in footnote 4, the constants are

$$a_{00}{}^j=\sum_i{}^{(j)}\sqrt{2}$$

$$a_{20}{}^j=\tfrac{1}{2}(2/5)^{\frac{1}{2}}\sum_i{}^{(j)}[(3z_i^2/r_{ij}^2)-1]$$

$$a_{22}{}^j=(3/5)^{\frac{1}{2}}\sum_i{}^{(j)}[(x_i^2-y_i^2)/r_j^2]$$

$$a_{40}{}^j=(\sqrt{2}/8)\sum_i{}^{(j)}[\tfrac{35}{3}(z_i^4/r_j^4)-10(z_i^2/r_j^2)+1]$$

$$a_{42}{}^j=[(5)^{\frac{1}{2}}/6]\sum_i{}^{(j)}[(x_i^2-y_i^2)/r_j^2][7(z_i^2/r_j^2)-1]$$

$$a_{44}{}^j=-[(35)^{\frac{1}{2}}/12]\sum_i{}^{(j)}[(x_i^4+y_i^4-6x_i^2y_i^2)/r_j^4]. \quad (10)$$

The matrix elements of the perturbation are then

$$V_{MM'}=\sum_{j=1}^{\infty}\sum_{l=0}^{\infty}A_l{}^j\sum_{m=0}^{l}a_{lm}{}^j\iint P_{lm}Y_{2m}Y_{2M'} \times\cos m\varphi\sin\theta\,d\theta\,d\varphi. \quad (11)$$

The constants $b_{lm}{}^j$ vanish for even l while the constants $a_{lm}{}^j$ vanish unless m and l are even because each j shell has the D_2 symmetry.

The coefficients $A_l{}^j$ which result from the radial integration are given by

$$A_l{}^j=Q_j\left\{r_j^{-l-1}\int_0^{r_j}[R(r)]^2r^{l+2}\,dr +r_j^{\,l}\int_{r_j}^{\infty}[R(r)]^2r^{-l+1}\,dr\right\}. \quad (12)$$

As a result of the angular integrations only $l=0$, 2, 4 give nonzero contributions to $V_{MM'}$; thus, the exponential terms resulting from the radial integrations are negligible and we get,

$$A_l{}^j=\frac{(l+6)!N_{3d}{}^2Q_j}{(2a)^{l+7}r_j^{\,l+1}}=[(l+6)!/6!](2ar_j)^{-l}(Q_j/r_j). \quad (13)$$

The nonzero matrix elements are then (j superindex suppressed):

$$V_{00}=\sqrt{2}^{-1}A_0a_{00}+[(10)^{\frac{1}{2}}/7]A_2a_{20}+(6/7\sqrt{2})A_4a_{40}$$

$$V_{02}=-(5)^{\frac{1}{2}}/7]A_2a_{22}+(15)^{\frac{1}{2}}/14]A_4a_{42}$$

$$V_{22}=\sqrt{2}^{-1}A_0a_{00}-[(10)^{\frac{1}{2}}/7]A_2a_{20}+(7\sqrt{2})^{-1}A_4a_{40}+\tfrac{1}{2}(\tfrac{5}{7})^{\frac{1}{2}}A_4a_{44}$$

$$V_{\overline{2}\overline{2}}=\sqrt{2}^{-1}A_0a_{00}-[(10)^{\frac{1}{2}}/7]A_2a_{20}+(7\sqrt{2})^{-1}A_4a_{40}-\tfrac{1}{2}(\tfrac{5}{7})^{\frac{1}{2}}A_4a_{44}$$

$$V_{11}=\sqrt{2}^{-1}A_0a_{00}+[(10)^{\frac{1}{2}}/14]A_2a_{20}+[(15)^{\frac{1}{2}}/14]A_2a_{22}-(4/7\sqrt{2})A_4a_{40}+[(5)^{\frac{1}{2}}/7]A_4a_{42}$$

$$V_{\overline{1}\overline{1}}=\sqrt{2}^{-1}A_0a_{00}+[(10)^{\frac{1}{2}}/14]A_2a_{20}-[(15)^{\frac{1}{2}}/14]A_2a_{22}-(4/7\sqrt{2})A_4a_{40}-[(5)^{\frac{1}{2}}/7]A_4a_{42}. \quad (14)$$

In a diagonalized scheme the matrix elements corresponding to V_{00} and V_{22} are

$$V_{\chi 1}=\tfrac{1}{2}(V_{00}+V_{22})-\tfrac{1}{2}[(V_{00}-V_{22})^2+4V_{02}{}^2]^{\frac{1}{2}}$$

$$V_{\chi 2}=\tfrac{1}{2}(V_{00}+V_{22})+\tfrac{1}{2}[(V_{00}-V_{22})^2+4V_{02}{}^2]^{\frac{1}{2}}. \quad (15)$$

It is convenient to measure distance in units of the edge of the unit cell, which for specificity we take to be 11.50 A.[4] Let $r=\beta r_1$ where r_1 is the distance to the nearest oxygen neighbors in our new units, i.e., 0.2044. In these units $a=45.25$ for our choice of cell size and scales linearly with the latter. The matrix elements, V_{00}, etc., computed in these units, are converted to electron volts by the multiplicative factor 0.663.

The contribution to A_l from the jth shell is now given by,

$$A_l{}^j=[(l+6)!/6!][Q_j/(2r_1a\beta_j)^l](\beta_jr_j)^{-1}. \quad (16)$$

In Table I, we give the type of ion in the jth shell for $j=1$ to $j=8$, the value of Q_j assuming the crystal bind-

TABLE I. The types of ions and values of β_j, Q_j, and n_j for the first eight shells surrounding a central Fe^{++} ion, assuming completely ionic bonding.

j	Ion	Q_j	n_j	β_j
1	O	−2	8	1.000
2	Si	+4	2	1.223
3	Al	+3	4	1.367
4	Si	+4	4	1.498
4′	Fe	+2	4	1.498
5	O	−2	4	1.500
6	O	−2	4	1.589
7	O	−2	4	1.769
8	O	−2	4	1.877

ing completely ionic, the number of ions n_j in the shell, and the value of β_j. The corresponding values of a_{lm} for each of these shells is given in Table II.

If the indicated summations of contributions from successive neighboring shells to V_{00}, etc. are carried out, it is found that the accrued partial sums approach an estimable asymptotic limit in a damped oscillatory fashion. This behavior is illustrated in Table III for V_{00} whose behavior is typical of the other matrix elements. The coefficient of the r_1^{-1} term converges so slowly that no reasonable estimate of the limiting value is possible. However, this coefficient is the same for all the matrix elements and merely determines the "center of gravity" of the energy levels. Differences in energy which determine the absorption frequencies are unaffected by this coefficient. The convergence of the coefficients of the r_1^{-3} and r_1^{-5} terms is sufficiently rapid to allow estimates of the limiting values satisfactory for our purposes if the first eight shells are included in the summation.

Three strong absorption lines attributable to transitions between the levels of the ^5D term are predicted by the following selection rules.

(a) Intercombinations for atoms satisfying Russell-Saunders coupling are prohibited.[9] Transitions between levels of the same multiplicity are strongly favored if allowed by selection rule (b).

(b) The direct product of the symmetry representations associated with the components of the matrix element must contain the identity representation Γ_E.[10,11]

Since the field surrounding the central Fe^{++} ion is strongly orthorhombic (D_2), there is no inversion symmetry and hence the usual selection rule for electric dipole transitions requiring the initial and final states to be of opposite parity is not applicable.[12] Both a polar vector and an axial vector transform according to the same representations in D_2, Γ_x, Γ_y, Γ_z.

Transitions from the lowest level $V_{\chi 1}$ (Γ_E) to the next three levels V_{11} (Γ_y), $V_{\Upsilon\Upsilon}$(Γ_x), $V_{\Xi\Xi}$(Γ_z) are then allowed while a transition to $V_{\chi 2}$(Γ_E) is forbidden by electric dipole *and* magnetic dipole transitions.

We anticipate the results of a detailed numerical comparison of theory and experiment, discussed in the next section, to remark that the completely ionic bonding, which we used to illustrate the theory in this section, does not give a satisfactory description of the observed behavior.

In the first place, the energy differences calculated for completely ionic binding on the basis of our estimates of a and r_1 are too low. Worse than this scaling error, however, is the fact that the separation between the predicted absorption lines is badly distorted. We note that this failure is hardly surprising in view of the extreme assumption of completely ionic bonding. In light of considerable chemical evidence,[5] it is to be expected that the $(SiO_4)^{4-}$ tetrahedra will be a charge distribution considerably different from that predicted by this model. Because the individual contributions of shells of identical ions is linearly dependent on the charge assigned to these ions, it is a relatively simple matter to adjust this charge empirically to fit the observed absorption lines. If we assume that the covalent bonding is predominantly within the $(SiO_4)^{4-}$ ions and that the positive ions assume their normal ionic valencies,[5] we may use one observed line to set the scale, one observed line to determine the degree of covalency, and the third line as a check on the validity of our model. This procedure is carried out in the next section.

III. ENERGY LEVELS AS A FUNCTION OF COVALENCY

The form of the undiagonalized matrix elements V_{pq} is

$$V_{pq}=C/r_1+D_{pq}/r_1^3+E_{pq}/r_1^5. \tag{17}$$

The omission of subscripts on C is a reminder of the fact that C is the same for all the matrix elements and

TABLE II. Values of the coefficients a_{lm} for various shells.

j	$a_{00}/\sqrt{2}$	$(5/2)^{\frac{1}{2}}a_{20}$	$(5/3)^{\frac{1}{2}}a_{22}$	$(3/\sqrt{2})a_{40}$	$(1/5)^{\frac{1}{2}}a_{42}$	$(5/7)^{\frac{1}{2}}a_{44}$
1	8	−0.266	0.297	0.401	−0.834	1.254
2	2	2.000	0.000	2.000	0.000	0.000
3	4	−0.800	0.000	−0.800	0.000	1.067
4	4	−1.000	2.667	−0.514	0.074	−0.324
4′	4	−1.000	−2.667	−0.514	−0.074	−0.324
5	4	−0.068	2.440	−1.515	0.510	−0.474
6	4	−1.672	−2.905	0.731	0.299	−0.269
7	4	3.272	0.348	1.832	0.299	−0.0004
8	4	0.342	0.579	−1.690	0.167	0.550

[9] G. Herzberg, *Atomic Spectra and Atomic Structure* (Dover Publications, New York, 1944).
[10] L. D. Landau and E. M. Lifshitz, *Quantum Mechanics* (Addison-Wesley Publishing Company, Inc., Reading, Massachusetts, 1958).
[11] C. Kittel and J. M. Luttinger, Phys. Rev. **73**, 162 (1948).
[12] R. K. Verma, J. Geophys. Research **65**, 757 (1960).

TABLE III. The coefficients of the terms r_1^{-1}, r_1^{-3}, and r_1^{-5} in the matrix elements V_{00} illustrate the nature of the oscillatory convergence of the partial sum to an estimated limit.

j	$\sqrt{2}^{-1}a_{00}{}^jA_0{}^j$	$\Sigma_j\sqrt{2}^{-1}a_{00}{}^jA_0{}^j$	$[(10)^{\frac{1}{2}}/7]a_{20}{}^jA_2{}^j$	$\Sigma_j[(10)^{\frac{1}{2}}/7]a_{20}{}^jA_2{}^j$	$(3\sqrt{2}/7)a_{40}{}^jA_4{}^j$	$\Sigma_j(3\sqrt{2}/7)a_{40}{}^jA_4{}^j$
1	−16.00	−16.00	1.04×10^{-3}	1.04×10^{-3}	-1.72×10^{-5}	-1.72×10^{-5}
2	6.54	−9.46	8.54	9.58	6.27	4.55
3	8.78	−0.68	−1.70	7.88	−2.15	2.40
4	10.68	10.00	−2.32	5.55	−0.58	1.81
4′	5.34	15.33	−1.16	4.39	−0.29	1.52
5	−5.33	10.00	0.68	4.47	0.86	2.38
6	−5.03	4.97	1.63	6.09	−0.31	2.07
7	−4.52	0.45	−2.31	3.79	−0.45	1.61
8	−4.24	−3.79	−0.20	3.59	0.30	1.91
		(...)		(3.8)		(1.9)

consequently has no effect on the absorption frequencies. The values of D_{pq} and E_{pq} vary linearly with the assumed charge distribution between the Si and O ions. We express this distribution through Q, the charge on the Si ion. If it is assumed that Q is +4 and that the charge on the O ions is −2, the bonding is completely ionic. If $Q=-4$ for the Si ion, the binding is completely covalent. The values of these quantities for $Q=+4$ and $Q=-4$, computed for $r_1/11.50$ A$=0.2044$ and $Z_{\text{eff}}=6.25$, are given in Table IV. Using Eq. (17), we may easily compute the matrix elements V_{11}, V_{22}, etc. which vary in the manner shown in Fig. 1, where the dashed curves correspond to $Z_{\text{eff}}=6.25$ and the solid curves to $Z_{\text{eff}}=5.20$.

The computed absorption energies correspond to the differences $(V_{11}-V_{\chi1})$, $(V_{\bar2\bar2}-V_{\chi1})$, and $(V_{\bar1\bar1}-V_{\chi1})$, i.e., the allowed transitions from the lowest level $V_{\chi1}$ to the accessible levels within the ^5D ground term. These absorption energies are plotted in Fig. 2 as a function of Q for the same two choices of Z_{eff} used in Fig. 1. The horizontal lines in Fig. 2 represent the absorption energies experimentally determined by Clark.[1] They correspond to the three lowest and most intense peaks in the absorption spectrum. The complete set of observed peaks is given in Table V.

In accordance with the program outlined in the introduction, we now seek to determine for what value of Q, if any, the calculated and observed absorption lines agree within the experimental error. An inspection of Fig. 2 suggests that agreement might be achieved for some value of Z_{eff} intermediate to the two values used in our sample calculations in the neighborhood of

TABLE IV. The coefficients D_{pq} and E_{pq} and the matrix elements V_{pq} in electron volts for the extreme values of the charge Q on the silicon ion. Calculated for $a=45.25$ and $r_1=0.2044$.

	$Q=-4$	
$D_{00}-6.0\times10^{-3}$	$E_{00}-5.4\times10^{-5}$	$V_{00}-0.86$
$D_{02}+5.3$	$E_{02}-0.2$	$V_{02}+0.62$
$D_{11}-7.6$	$E_{11}+4.8$	$V_{11}-0.79$
$D_{\bar1\bar1}+1.6$	$E_{\bar1\bar1}+3.4$	$V_{\bar1\bar1}+0.28$
$D_{22}+6.0$	$E_{22}+1.0$	$V_{22}+0.73$
$D_{\bar2\bar2}+6.0$	$E_{\bar2\bar2}-2.8$	$V_{\bar2\bar2}+0.63$
	$Q=+4$	
$D_{00}+2.5\times10^{-3}$	$E_{00}+1.3\times10^{-5}$	$V_{00}+0.33$
$D_{02}-0.8$	$E_{02}+4.4$	$V_{02}+0.03$
$D_{11}+1.9$	$E_{11}+4.2$	$V_{11}+0.35$
$D_{\bar1\bar1}+0.6$	$E_{\bar1\bar1}-5.8$	$V_{\bar1\bar1}-0.10$
$D_{22}-2.5$	$E_{22}-4.7$	$V_{22}-0.43$
$D_{\bar2\bar2}-2.5$	$E_{\bar2\bar2}+5.0$	$V_{\bar2\bar2}-0.15$

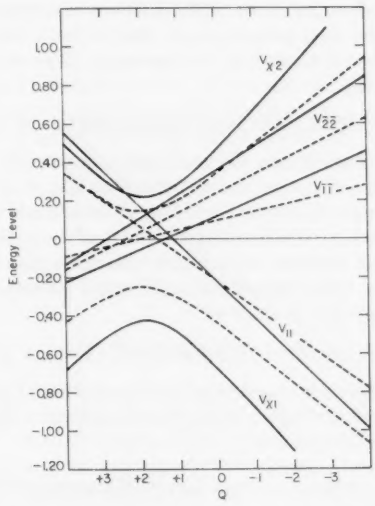

FIG. 1. Diagonalized matrix elements as function of Q for $Z_{\text{eff}}=6.25$ (dashed curves), $Z_{\text{eff}}=5.20$ (solid curves), and $r_1=0.2044$.

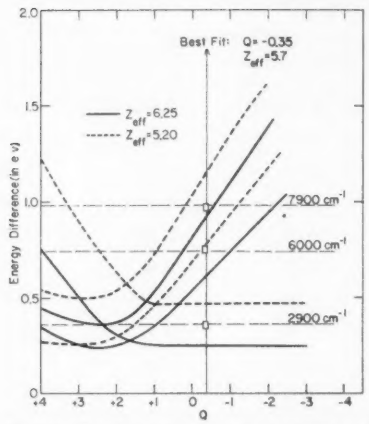

FIG. 2. Variation of absorption energies with Q for $Z_{eff}=6.25$ (dashed curves), $Z_{eff}=5.20$ (solid curves), and $r_1=0.2044$.

$Q=0$. A more precise analysis is aided by the observation that agreement with the 2900 cm^{-1} absorption line is only possible with $Z_{eff}=5.72$ for any value of $Q\gtrsim 1$.

Using the fact that this value of Z_{eff} is an average of the two values of Z_{eff} used in the calculations, by interpolation we find two new curves for the absorption lines of higher energy. These curves come the closest to intersecting the horizontal lines simultaneously at $Q=-0.35$ (marked by the vertical line). The intersections are within the squares in Fig. 2. In view of the fact that the observed lines have a width of approximately 10%, the agreement between experimental and theoretical values must be considered eminently satisfactory. The value $Q=-0.35$ corresponds to 54% covalent bonding in agreement with Pauling's estimate of 50%. All these estimates should be taken *cum grano salis* in view of both the experimental and theoretical uncertainties discussed in the following.

IV. THE PRESSURE DEPENDENCE OF ΔE_1

The dependence of the highest observable energy difference ΔE_1 (resulting from an allowed transition between levels within the ^5D term) on pressure has been measured by Balchan and Drickamer.[3] It is, therefore, of some interest to estimate this dependence theoretically. The logarithmic derivative of the energy difference ΔE_1 is given by

$$\partial \ln\Delta E_1/\partial \ln R=(\Delta E_1)^{-1}(\partial/\partial \ln R)(V_{\bar{2}\bar{2}}-V_{x1}). \quad (18)$$

This derivative may be easily evaluated from Eqs. (17), (15), and the values of D_{pq} and E_{pq} given in Table IV. We find,

$$\partial \ln\Delta E_1/\partial \ln R=-3-(2/\Delta E_1)r_1^{-5}\{E_{\bar{2}\bar{2}}-E_{00}-E_{22}+\tfrac{1}{4}[(V_{00}-V_{22})(E_{00}-E_{22})+4V_{02}E_{02}]\times[(V_{00}-V_{22})^2+4V_{02}^2]^{-\frac{1}{2}}\}. \quad (19)$$

For $Q=0$, the numerical value of this derivative is 3.82.

To compare this estimate with experiment, it is necessary to know the compressibility of garnet. Unfortunately, this quantity is not known for the sample studied by Balchan and Drickamer. Measurements of the volume compressibility and the elastic constants of a variety of garnets of different compositions are available. The exact composition of Balchan and Drickamer's sample is not known but is specified as almandine from Gore Mountain, Essex County, New Jersey. Bridgman[13] has measured the volume of a sample of approximately the same composition to 40 kbars. Because the compressibility measurements are least accurate at low pressures, and because the pressure distribution in the quasi-hydrostatic stress used in the optical experiments is most uncertain in the same region, we have chosen to make our comparison by using the slope of V vs P, and ΔE vs P, near 40 kbars, the highest pressures for which the two experiments overlap. In this way, we find $\partial \ln\Delta E/\partial \ln r_1=3.92\pm 10\%$ in excellent, and possibly fortuitous, agreement with the theoretical estimate.

V. DISCUSSION

In this section, we address attention to the validity of our model and its application to the particular mineralogical data available.

As remarked in the Introduction, a justification of the point-ion model has been discussed by Phillips. It is perhaps too early to say that this justification is the final word, particularly for systems as complex as the garnets, but in any case it is the only approach which can be used with facility.

It may easily be shown that $3p$ states are not mixed with $3d$ states by the field with D_2 symmetry. Furthermore, the $4s$ electrons are stripped from the iron atom by charge transfer to the O^- atom. An estimate of the effect of mixing with wave functions of excited free ion states indicates that errors from this source are not important.

TABLE V. Observed[1] absorption energies for various garnets.

Almandine	Pyrope	Grossularite
2900 cm^{-1}	2900 cm^{-1}	2800 cm^{-1}
6000	6000	5000
7900	7900	8000
12 100	12 100	11 300
14 400	14 300	
17 600	17 600	
20 000	20 000	
21 500		

[13] P. W. Bridgman, Proc. Am. Acad. Arts Sci. **76**, 55 (1948).

The assumption of ideality for the garnet structure, i.e., silicate ions with a regular tetrahedral arrangement, should not be serious because the major dependence of the energy levels on r_1 has already been absorbed in the scale parameter $(2a\beta_i r_1)$. The remaining dependence on r_1 is a scale factor which varies as r_1^{-1}. As a typical example we cite grossularite, for which, ideally, $r_1=0.2044$. Actually, the eight nearest O^{--} neighbors are not all exactly equidistant; four have $r_1=0.199$ and four have $r_1=0.196$. Taking the maximum difference from the ideal value of r_1 as a measure of the error, we should not introduce an uncertainty of more than 0.75% by this assumption.

The value of the lattice constant varies with composition which is, at best, uncertain. The maximum variation in this quantity is from about 11.5 to 12.0 A. For the same reasons given in the preceding paragraph, the uncertainty in composition should not introduce an error of more than 5%.

We have assumed that all the covalency effects are confined to the silicate ion $(SiO_4)^{4-}$. Actually a certain amount of covalency will exist in the bonding between the Fe^{++} and Al^{3+} ions and the O^{--} ions. Pauling[5] estimates these effects to be less than 5%; it is quite possibly less.

Taking into account all these sources of error, including the uncertainty in the estimate of the asymptotic values of the oscillatory coefficients, we believe the calculation is good to about 10%.

It is heartening that the three lowest lines observed in all the minerals are the most strongly absorbed. No other absorption of comparable oscillator strength is observed. The absorption lines near 12 000 and 14 000 cm^{-1} may be due to other ions such as Mn^{++} or Fe^{3+} impurities, particularly since, in various different samples of pyrope, Clark found a significant variation in the strength of the absorption. The lines of higher energy which are more weakly absorbed could be transitions to states of other multiplicity weakly allowed owing to the perturbing effects of spin-orbit coupling and vibronic effects. We shall make no effort to give a detailed analysis of these lines.

We turn now to a consideration of the calculation on the effect of pressure. In our previous discussion, we have avoided being specific about the compositions of some of the minerals. The almandine garnet used by Clark was of Indian origin whereas that used by Bridgman was from Gore Mountain, Essex County, New Jersey. The chemical analysis of Clark's sample is given in Table VI where it is compared with those for two typical Gore Mountain samples studied by Levin.[14] No analysis is available for the sample used by Balchan and Drickamer.

Despite the wide variations in composition, we believe that the relative independence of the absorption lines found by Clark on chemical composition (see Table V) lends some confidence to our comparison of theory and experiment. Similarly, Bridgman[13] has remarked on the striking similarity of compressibility data obtained on various garnet samples. Verma[12] and Ramachandra Rao[15] have measured the velocity of sound and thus deduced the elastic constants for a variety of garnets. Their data indicate a relatively strong dependence of these quantities on composition. However, it would appear that a large part of this variation is associated with the different masses of the varying constituents which accordingly affect the density. For this reason, we feel justified in our procedure of using Bridgman's data in analyzing the pressure dependence of ΔE_1.

TABLE VI. Compositional comparison of various almandine garnets.[9]

	Indian	Gore Mt. CT	Gore Mt. XH
SiO_2	37.69%	41.30%	39.29%
TiO_2	0.07	0.15	0.05
Al_2O_3	20.62	19.78	22.12
Fe_2O_3	4.30	1.80	0.73
FeO	30.80	17.80	19.63
MnO	1.97	0.49	0.38
MgO	4.40	10.60	11.48
CaO	...	6.98	6.16
H_2O	0.36	0.54	0.03
Total	100.21%	99.44%	99.87%

Finally, it would be noted that in our theoretical estimates of the pressure dependence of ΔE_1, two further assumptions have been made. First, we have assumed that changes in ideality are unimportant. We believe that errors from these distortions are second order. Second, we have made the more *blatant* assumption that Z_{eff} is independent of pressure. This assumption is tantamount to assuming that overlap (or, more correctly, changes in overlap) have no effect.

It is unfortunate that data on more homogeneous samples are not available. It would be desirable to obtain such data to provide a more convincing test of the assumptions made in this calculation. Indeed if this calculation stimulates further experimental work on this and similar systems, it will have served a useful purpose.

VI. SUMMARY

The point-ion model for crystal field calculations gives some insight into the charge distribution in a partially covalent crystal if the crystal field splitting of atomic levels is calculated for various charge distributions. Such a calculation has been carried out for

[14] S. B. Levin, Bull. Geol. Soc. Am. **61**, 519 (1956).

[15] B. Ramachandra Rao, Proc. Indian Acad. Sci. **A22**, 194 (1945).

the Fe^{++} ion in the garnet structure, using the frequency of one of three absorption bands for the empirical determination of the critical theoretical parameter, a, and the ratio of the remaining lines to select the most plausible distribution of ionic charge. The results are consistent with the conclusions of Pauling concerning the degree of covalency in the silicate ion. The calculated pressure dependence of the optical absorption agrees within experimental error with the data of Balchan and Drickamer if one assumes that the charge distribution, i.e., the degree of covalency, is independent of pressure.

ACKNOWLEDGMENTS

The authors would like to acknowledge helpful discussions with Professor R. S. Mulliken and Professor Willard Stout. The authors would also like to acknowledge the support of both the Office of Naval Research and the Industrial Sponsors of the Division of Physical Sciences of the University of Chicago.

THE JOURNAL OF CHEMICAL PHYSICS VOLUME 34, NUMBER 3 MARCH, 1961

Anomalous Relaxation of Hyperfine Components in Electron Spin Resonance. II*

JAN W. H. SCHREURS† AND GEORGE K. FRAENKEL

Department of Chemistry, Columbia University, New York

(Received August 1, 1960)

A detailed study has been made of the linewidth and peak height of each of the five components in the electron spin resonance spectrum of the *p*-benzosemiquinone ion as a function of microwave power at X-band frequencies. Studies were also made of the spectrum of the peroxylamine disulfonate ion as a function of power. A 20% variation in the linewidths from one hyperfine component to another was found in the *p*-benzosemiquinone ion spectrum, and a 13% variation in the saturation parameters (T_1). The average value for the linewidth parameter at low power for the *p*-benzosemiquinone ion was found to be $(1/T_2) = 1.11\times10^{6}$ sec^{-1}, and the reciprocal of the average value of the saturation parameter was found to be about $(1/T_1) = 0.74\times10^{6}$ sec^{-1}. No variation in linewidths or saturation parameters among the three hyperfine components in the peroxylamine disulfonate ion spectrum was found, and the results were $T_2 = 2.5\times10^{-7}$ sec, and $T_1 = 3.3\times10^{-7}$ sec. The variation in the linewidth of the *p*-benzosemiquinone ion can be accurately represented by a quadratic equation in m_J, the field-direction component of the total nuclear spin angular momentum, and the form of this equation is in excellent agreement with the linewidth predicted for a relaxation mechanism arising from an anisotropic intramolecular dipolar interaction between the unpaired electron and the four protons in the molecule, as well as a rotational relaxation of the anisotropic g tensor. Good quantitative agreement between theory and experiment is obtained for the coefficient of m_J^2 in the equation for $(1/T_2)$ if the rotational correlation time is taken to be $\tau_c = 7\times10^{-11}$ sec, a value which is consistent with the molecular dimensions. The dependence of the saturation parameters on m_J is also in qualitative agreement with the theory, but quantitative discrepancies are found which have not been explained.

I. INTRODUCTION

THE conventional theory of the electron spin resonance spectra of free radicals in solution predicts that the hyperfine components should each have intensities proportional to the degeneracy of the nuclear spin states and should each have the same linewidth and saturation behavior. It was shown in a previous article,[1] however, that there actually is a variation in widths and saturation parameters from one component to another. These data raise interesting questions about the mechanisms which produce line broadening and relaxation, and about the theory of saturation in complex multilevel systems. The present work was undertaken to obtain a quantitative description of the line shape, linewidth, and saturation behavior for comparison with recently formulated theories.[2,3] Measurements are presented on the spectrum of the *p*-benzosemiquinone ion and, for comparison purposes, the peroxylamine disulfonate ion.

If the line shape of a component is Lorentzian, the linewidth and peak height presumably depend on microwave power in a well-known manner. The width (δ_i) between points of extreme slope (on a magnetic field scale) for the ith component is[1]

$$\delta_i = (2/\sqrt{3}\gamma T_{2i})\,(1+\gamma^2 H_1^2 T_{1i} T_{2i})^{\frac{1}{2}}, \qquad (1.1)$$

and the peak height p_i, normalized for the degeneracy of the component, is

$$p_i = (1/c)\,T_{2i}(1+\gamma^2 H_1^2 T_{1i} T_{2i})^{-1}. \qquad (1.2)$$

The normalized peak height is the observed peak height of a component divided by the degree of de-

* This research was supported in part by the U. S. Air Force through the Office of Scientific Research.

† Present address: National Research Council, Ottawa, Canada.

[1] J. W. H. Schreurs, G. E. Blomgren, and G. K. Fraenkel, J. Chem. Phys. **32**, 1861 (1960).

[2] M. J. Stephen and G. K. Fraenkel, J. Chem. Phys. **32**, 1435 (1960).

[3] D. Kivelson, J. Chem. Phys. **33**, 1094 (1960).

generacy of the component D_i. In these equations T_{1i} and T_{2i} are the spin-lattice (longitudinal) and transverse relaxation times, respectively, of the ith component; H_1 is the rf magnetic field; γ is the gyromagnetic ratio of the electron; and c is a constant which depends on the number of unpaired spins, the frequency at which the measurements are performed, and the sensitivity of the spectrometer. The notation T_{1i} and terminology "spin-lattice relaxation time" are used for conventional reasons. The physical significance of T_{1i} in the present application is that of a saturation parameter, not a relaxation time.[1,2] The saturation parameter Ω_i is related to T_{1i} by

$$T_{1i}=D_i\Omega_i. \tag{1.3}$$

It follows from Eq. (1.1) that a plot of the square of the width vs microwave power should give the straight line

$$\delta_i^2=(4/3\gamma^2)(1/T_{2i})^2+(\tfrac{4}{3})H_1^2(T_{1i}/T_{2i}). \tag{1.4}$$

From the intercept of this straight line, the transverse relaxation time T_{2i} can be computed, and from the slope the ratio of relaxation times T_{1i}/T_{2i} can be found. The spin-lattice relaxation time T_{1i} can then be obtained by multiplying this ratio by the measured values of T_{2i}. From Eq. (1.2) the reciprocal of the peak height should also give a straight line,

$$(1/p_i)=(c/T_{2i})+c\gamma^2H_1^2T_{1i}. \tag{1.5}$$

If the experimental observations are properly described by Eqs. (1.1) and (1.2), the experimentally determined ratio of the intercept of Eq. (1.5) to the square root of the intercept of Eq. (1.4) for the ith hyperfine component should be a constant independent of i with the value $(\frac{1}{2})\sqrt{3}\gamma c$, and thus the value of c can be determined from an average of the measurements on all the components. With c known, the experimentally determined slope of Eq. (1.5) can be used to obtain the spin-lattice relaxation time T_{1i}. The ratios of slope to intercept obtained from experimental fits for the ith component to either Eq. (1.4) or (1.5) should both have the same value, namely $\gamma^2T_{1i}T_{2i}$.

II. EXPERIMENTAL

A modified version of the X-band crystal superheterodyne spectrometer described by Hirshon and Fraenkel was employed.[4] Power was varied without changing the detection sensitivity by using a two-attenuator arrangement, one preceding the magic tee bridge connected to the spectrometer cavity, and one following the output of this bridge. When the power was lowered by increasing the attenuation of the first attenuator, the attenuation of the second attenuator was decreased by a corresponding amount.[5] A Varian type V-153C klystron was employed to provide power into the spectrometer cavity.

A silver-plated brass rectangular reflection cavity operating in the TE_{102} mode was used. The sample was contained in a 1.4-mm i.d. thin-walled melting-point capillary tube inserted through small holes in the center of the broad face of the cavity. With this type of sample placement, the rf magnetic field over the sample is constant over the length of the capillary, and the variation over the cross section is about 1%.[1] The resonant frequency of the cavity was $\nu_0\cong 9214$ Mc, the volume was $V_c=10.70$ cm^3, and the ratio of length to width was $(c/a)=2.014$. If the rf magnetic field perpendicular to the external steady field causing the Zeeman splitting is written as $H=2H_1\cos\omega t$, the expression for H_1^2 becomes[1]

$$H_1^2=4.05\times10^{-7}Q_{LE}P_{\text{inc}}, \tag{2.1}$$

where Q_{LE} is the loaded Q of the cavity with the sample in place in the absence of magnetic absorption, and P_{inc} is the power incident on the cavity in milliwatts. In Eq. (2.1), H_1 is expressed in oersteds. The numerical values in Eq. (2.1) are only valid when, as in the present experiments, the reflection coefficient of the cavity is very small compared to unity. The incident power could be adjusted from very low values up to 100 mw; it was determined by means of a bolometer.

A Varian model V-4007 electromagnet with 6-in. diam pole faces and a $2\frac{3}{4}$-in. air gap with ring-shim pole caps was employed, together with a Varian model V-2200A power supply. Field modulation at 38 cps was provided by coils wound around the pole caps and powered by an audio amplifier driven by an RC phase-shift oscillator. Considerable difficulty was encountered in obtaining sufficient field stability to study the narrow lines (approx 60 mgauss) being investigated. Careful tuning up of the power supply, the inclusion of a voltage regulator (Sorenson model 2501), the use of pressure-regulated cooling water, disassembly of the magnet followed by cleaning and honing down of burrs, as well as careful tightening on reassembly, all helped to stabilize the field. In addition, however, it was found necessary to rotate the magnet through 90° about a vertical axis to eliminate small field fluctuations which were discovered in the laboratory both inside and outside the magnet air gap even when the magnet was turned off. We have speculated that these fluctuations might have arisen from variations in the third-rail current in the Broadway-7th Avenue subway running under the street adjacent to the laboratories, but these speculations have not been checked. The current stability was found to be a few parts in 10^7 and the field stability 3 to 4 parts in 10^7 after these precautions had been taken.

The magnet was reshimmed to provide adequate field homogeneity, and the most homogeneous portion of the field was found by searching with a sample of an alcoholic solution of the 2,5-ditertiarybutyl semi-

[4] J. M. Hirshon and G. K. Fraenkel, Rev. Sci. Instr. **26**, 34 (1955).

[5] We are indebted to Dr. G. Feher for suggesting this double-attenuator procedure.

quinone ion in the spectrometer[6,7] until optimum resolution was obtained. No difference was found in the spectra observed from a sample of the *p*-benzosemiquinone ion extending the width of the cavity (10.2 mm) and a sample about 2 mm long, thus indicating that field inhomogeneity could not make an appreciable contribution to the observed linewidth. The consistency of the entire set of width measurements also indicates that field inhomogeneity is not a significant contribution to the width (see Sec. III).

Magnetic field measurements were made with a proton resonance oscillator using a small probe containing a dilute aqueous solution of Ni_2SO_4. A stability of about one part in 10^7 was obtained by locking the proton oscillator on a stable but adjustable external frequency. The frequency of the proton oscillator was determined with an electronic counter, and the microwave frequency was measured with a multiplier chain derived from a 1-Mc frequency standard.

Linewidths were measured by determining the difference in proton oscillator frequency between the points of maximum and minimum slope on the absorption line of the paramagnetic sample. The points of extreme slope were located by displaying the first derivative of the absorption on an oscilloscope. The derivative of the proton resonance signal was observed on a second oscilloscope at the same time the absorption of the paramagnetic sample was observed. The techniques used are similar to those described previously.[4,7] A correction had to be made for the finite width of the modulation amplitude. This was performed by assuming the lines to be of Lorentz shape and deriving an expression for the corrected width as a function of the ratio of the modulation amplitude to linewidth. Careful measurements were made of the modulation amplitude. The corrections varied from 4% for the narrow lines observed at low power to slightly less than 1% for the broad lines observed at high power.

Peak heights were measured by displaying the absorption line of a particular component directly on an oscilloscope using a field modulation that was large compared to the width of the component but smaller than the separation between components. At low power, the peak-height measurements were reproducible to better than 1%, and at high power to 2–3%.

The *p*-benzosemiquinone ions are rather unstable, and therefore a flow system was used to maintain a constant radical concentration in the spectrometer.[7,8] The mixing chamber of the flow system was fed from two bulbs. One bulb contained a $0.002M$ solution of *p*-benzohydroquinone in 95% ethanol and the other contained a $0.2M$ solution of NaOH made up in a solvent consisting of a mixture of 80 parts (by volume) of 95% ethanol and 20 parts water. The water was needed to dissolve Na_2CO_3 formed from absorption of atmospheric CO_2 which, if allowed to precipitate, would have clogged the capillary tubing in the flow system. The storage bulbs were connected to the mixing chamber by 0.2-mm diam. glass capillary tubing, and the mixing chamber was connected to one end of the sample tube in the spectrometer cavity (see above) by a thin Teflon tube. The other end of the sample tube was connected to a second piece of Teflon tubing and the vertical position of the end of this tube could be varied to change the flow rate and therefore the radical concentration. The concentrations of reagents and the flow rate were adjusted, in so far as possible, to obtain a linewidth which was independent of concentration. The rate of flow was such that about one drop formed every 4.1 to 4.5 sec, and during a series of measurements the drop time was held constant to 0.2 to 0.3 sec.

The concentration of *p*-benzosemiquinone ions was estimated by comparing the area of the central component of the spectrum with the area of the spectrum of a known concentration of the peroxylamine disulfonate radical $(SO_3)_2NO^{=}$ in an aqueous solution containing some Na_2CO_3. Corrections were made for the differences in the Q of the cavity in the two sets of measurements and the differences in volume of the two samples, and the measurements were made at sufficiently low power to avoid saturation. The concentration of the *p*-benzosemiquinone ions under the above conditions in the flow system was about $3\times 10^{-5}\ M$.

A sample of the *p*-benzosemiquinone ion made up in a capillary tube in an 80–20 ethanol-water solution containing NaOH, with a radical concentration adjusted to give a spectrum of about the same initial intensity as that given by the flow system, decayed in intensity by a factor of two in about 20 min.

Line shapes were studied by photographing oscilloscope presentations of the absorption spectrum of a single component, and by making strip-chart recordings of the first derivative and of the integral of the first derivative of the spectrum. The first derivative of the spectrum was obtained using small-amplitude field modulation (at 38 cps) in the usual manner with a tuned amplifier and a lock-in detector, and integration was performed electronically.

III. RESULTS, *p*-BENZOSEMIQUINONE ION

The four equivalent protons in the *p*-benzosemiquinone ion give rise to five equally spaced components which will be designated by the numbers -2, -1, 0, 1, 2. The component lines have degeneracies 1, 4, 6, 4, 1, respectively, and the -2 component is at the low-field side of the spectrum. The numbers designating the lines coincide with the value of the quantum number of the field-direction component of the total nuclear spin angular momentum m_I if the isotropic contact

[6] G. K. Fraenkel, Ann. N. Y. Acad. Sci. **67**, 546 (1957).
[7] B. Venkataraman, B. G. Segal, and G. K. Fraenkel, J. Chem. Phys. **30**, 1006 (1959).
[8] B. Venkataraman and G. K. Fraenkel, J. Am. Chem. Soc. **77**, 2707 (1955).

interaction constant a_i is negative.[9] In the following, we shall assume that the component with $m_J=-2$ occurs at the low-field end of the spectrum.

Line Shape

The lines were found to adhere very closely to a Lorentz shape at all powers studied. In Fig. 1 a tracing is shown of the absorption line of the central component ($m_J=0$) of the *p*-benzosemiquinone ion obtained by integrating the first-derivative output of a field-modulation frequency lock-in detector. The solid line represents the curve obtained from an electronic integrator, and the points are calculated from the equation of a Lorentz-shaped curve. The peak height and width at half-maximum absorption obtained from the experimental curve were taken as the two parameters needed to fit the theoretical equation to the experimental curve. For the curve in Fig. 1, the power incident on the microwave cavity was about 0.8 mw, and the loaded Q (Q_{LE}) was about 2000.

A slight bump can be observed on both sides of the curve. These bumps can be seen more clearly in Fig. 2, which is a photograph of the absorption line displayed on an oscilloscope. The "bumps" were observed under almost all conditions on all components although they became somewhat obscured at high power. No explanation of the "bumps" has been found, although it is possible that they arise from splitting caused by the natural abundance of C^{13}. A similar explanation[10] has been proposed, but not verified, for the small extra lines found in the spectrum of the semiquinone ion of duroquinone.[11] Although these "bumps" are an interesting phenomenon in themselves, it is not believed that they affect the present measurements in a significant manner.

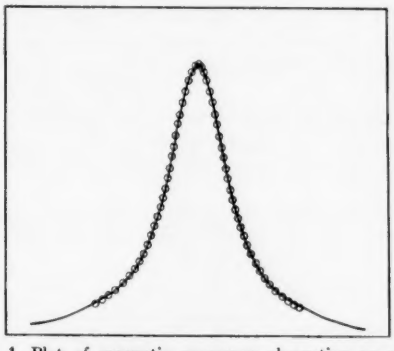

FIG. 1. Plot of magnetic resonance absorption vs magnetic field for the central component ($m_J=0$) of the *p*-benzosemiquinone ion spectrum. The solid line is the experimentally determined curve obtained from integration of the derivative of the spectrum, and the points are calculated for a Lorentz line shape.

[9] H. M. McConnell and D. B. Chesnut, J. Chem. Phys. **28**, 107 (1958).
[10] B. Venkataraman (private communication).
[11] B. Venkataraman, thesis, Columbia University, New York, 1955.

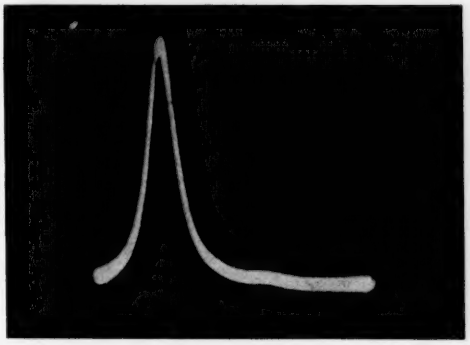

FIG. 2. Plot of magnetic resonance absorption vs magnetic field for the central component ($m_J=0$) of the *p*-benzosemiquinone ion spectrum obtained by photographing an oscilloscope presentation of the spectrum and showing "bumps" in the wings of the absorption line.

Linewidth Measurements

The linewidths of each of the five components in the spectrum of the *p*-benzosemiquinone ion were measured as a function of microwave power with the power incident on the cavity ranging from about 0.02 mw to 10 mw. The particular power at which a measurement was made was chosen at random from a predetermined set of values of power to be investigated, and the widths of all five components were measured without changing the power. The order in which the components were measured at a given power was randomized, and a second set of measurements was then made at the same power, using a different random order. A plot of the square of the width vs power for the component with $m_J=-1$ is shown in Fig. 3. Each point represents the average of two measurements, and the line is drawn by the method of least squares. No correction has been made, in Fig. 3, for the effect of overmodulation.

Figure 3, and similar plots for the other four components, show that the width measurements adhere closely to Eq. (1.4). These data also indicate that field inhomogeneity is not a limiting factor in determining the widths of the narrowest lines, for if the lines were broadened by field inhomogeneity, the points at low power would be higher than a straight line fitted to high-power points and extrapolated to zero power.

The equations obtained by least-square fits to the data for the square of the width, corrected for the finite amplitude of the field modulation, are:

$$\begin{aligned}
m_J=-2:&\quad (\delta_{-2}')^2\times10^{-3}=124.0\pm6.8+(28.87\pm1.37)\,P_{\text{inc}}\\
m_J=-1:&\quad (\delta_{-1}')^2\times10^{-3}=100.5\pm4.7+(28.76\pm0.95)\,P_{\text{inc}}\\
m_J=0:&\quad (\delta_{0}')^2\times10^{-3}=81.7\pm3.0+(29.38\pm0.61)\,P_{\text{inc}}\\
m_J=1:&\quad (\delta_{1}')^2\times10^{-3}=81.3_5\pm3.2+(28.46\pm0.66)\,P_{\text{inc}}\\
m_J=2:&\quad (\delta_{2}')^2\times10^{-3}=90.2\pm6.3+(26.52\pm1.29)\,P_{\text{inc}}.
\end{aligned}\tag{3.1}$$

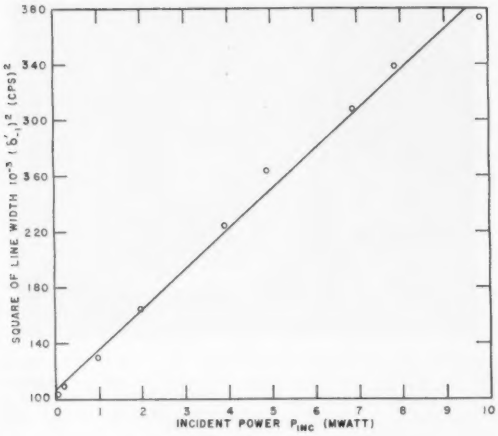

FIG. 3. Plot of the square of the linewidth between points of extreme slope $(\delta'_{-1})^2$ for the $m_J=-1$ component of the *p*-benzosemiquinone ion spectrum vs power incident on the cavity. The units of δ'_{-1} are cps of proton oscillator frequency. The rf magnetic field, in oersteds, is obtained from $H_1=0.0280(P_{\text{inc}})^{\frac{1}{2}}$ where P_{inc} is in milliwatts. The straight line is obtained from a least-squares fit, and no correction has been made for overmodulation.

In these equations, δ_{m_J}' is the width between points of extreme slope in units of cycles per second of the proton oscillator frequency, and P_{inc} is the power incident on the cavity in milliwatts. For the width measurements, the Q was $Q_{LE}=1939\pm25$. Using this value in Eq. (2.1), the rf magnetic field H_1 (in oersteds) can be calculated from $H_1^2=7.85\times10^{-4}P_{\text{inc}}$. The errors given in Eqs. (3.1) are standard deviations computed from the residual sum of squares in the least-squares fit.[12]

Measurements of width were also made with about 30 mw incident on the cavity, giving results about 15% lower than values extrapolated from Eqs. (3.1). No detailed study of high-power results was made.

Peak-Height Measurements

The heights of maximum absorption of each of the five components in the spectrum of the *p*-benzosemiquinone ion were measured as a function of power over the range from about 0.5 mw to 10 mw. The order of measurements was randomized in a manner similar to that used for the width measurements except that only one measurement of the peak height of each component was made at a particular power. A plot of the reciprocal of the height vs power for the component with $m_J=-1$ is shown in Fig. 4 together with a line fitted by the method of least squares.

The equations obtained from least-square fits to the data for the reciprocal of the normalized peak height are, in arbitrary units:

$$\begin{aligned}
m_J=-2: &\quad p_{-2}^{-1}=6.406\pm0.233+(239.7\pm4.45)\,P_{\text{inc}}\\
m_J=-1: &\quad p_{-1}^{-1}=5.990\pm0.140+(250.8\pm2.79)\,P_{\text{inc}}\\
m_J=0: &\quad p_{0}^{-1}=5.623\pm0.130+(269.1\pm2.60)\,P_{\text{inc}}\\
m_J=1: &\quad p_{1}^{-1}=5.725\pm0.112+(249.2\pm2.23)\,P_{\text{inc}}\\
m_J=2: &\quad p_{2}^{-1}=5.636\pm0.181+(243.6\pm3.61)\,P_{\text{inc}}.
\end{aligned}\tag{3.2}$$

For these measurements, the value of Q was $Q_{LE}=2206$ so that $H_1^2=8.93\times10^{-4}P_{\text{inc}}$.

Limiting Linewidths. Transverse Relaxation Times T_{2i}

The intercepts of Eqs. (3.1) for the square of the width are related to the transverse relaxation times T_{2i} by Eq. (1.4). The values of $(1/T_{2i})$ obtained in this manner are given in the second column of Table I.

The theory for the variation of linewidth from one hyperfine component to another (see Sec. V) predicts a quadratic dependence of the width on m_J. A fit of the values of $(1/T_{2i})$ to a quadratic by the method of orthogonal polynomials,[12] with the assignment of equal weight to each of the five points, gives

$$(1/T_{2m_J})=(1.036_5-0.044_5m_J+0.0376m_J^2)\times10^6\ \text{sec}^{-1}.\tag{3.3}$$

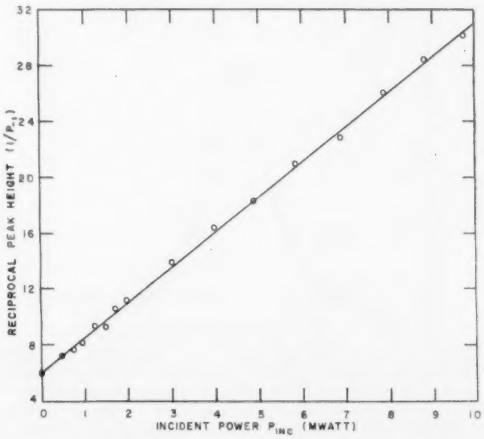

FIG. 4. Plot of the reciprocal of the peak height, p_{-1}^{-1}, for the $m_J=-1$ component of the *p*-benzosemiquinone ion spectrum vs power incident on the cavity. Arbitrary units are used for the ordinate. The rf magnetic field, in oersteds, is obtained from $H_1=0.0299(P_{\text{inc}})^{\frac{1}{2}}$ where P_{inc} is in milliwatts. The straight line is obtained from a least-squares fit.

[12] *Statistical Methods in Research and Production*, edited by Owen L. Davies (Oliver and Boyd, London, 1954), 2nd ed., pp. 141, 163; *Design and Analysis of Industrial Experiments*, edited by Owen L. Davies (Oliver and Boyd, London, 1954), pp. 344 ff.; R. A. Fisher, *Statistical Methods for Research Workers* (Oliver and Boyd, London, 1948), 10th ed.; R. A. Fisher and F. Yates, *Statistical Tables for Biological, Agricultural and Medical Research* (Oliver and Boyd, London, 1948), 3rd ed.; C. A. Bennett and N. L. Franklin, *Statistical Analysis in Chemistry and the Chemical Industry* (John Wiley & Sons, Inc., New York, 1954), pp. 254 ff., 431 ff.

The intercepts of Eqs. (3.2) for the reciprocal of the peak height are also related to $(1/T_{2i})$ within a factor determined by the experimental constant c in Eq. (1.5). The constant c was adjusted so as to give the best agreement between the intercepts of the reciprocal peak-height measurements and the values of $(1/T_{2i})$ determined from the width measurements. Thus, if we let w_{m_J} be the value of $(1/T_{2m_J})$ obtained from the width measurements (the second column of Table I), and h_{m_J} the value of the intercepts of the reciprocal of the peak-height measurements as given by Eqs. (3.2), the value of α which minimizes the expression

$$\sum_{m_J}(w_{m_J}-\alpha h_{m_J})^2 \tag{3.4}$$

gives the best estimate of $(1/c)$. The value found was $\alpha=0.1895\times10^6$. The estimates of $(1/T_{2i})$ obtained by multiplying the intercepts in Eqs. (3.2) by α are given in the third column of Table I. The equation of the quadratic which fits the adjusted intercepts of the reciprocal of the peak-height measurements is

$$(1/T_{2m_J})=(1.083-0.034m_J+0.0151m_J^2)\times10^6\ \text{sec}^{-1}. \tag{3.5}$$

The variation in linewidth from one component to another can be best evaluated by using data from both the width and peak-height measurements. Since the precision of the data on a given component is about the same for both types of measurements, the arithmetic mean of the two values has been taken and is tabulated in column four of Table I. The quadratic which fits these average values of the width is

$$(1/T_{2m_J})=(1.060-0.039m_J+0.0264m_J^2)\times10^6\ \text{sec}^{-1}, \tag{3.6}$$

and values computed from this equation are tabulated in the last column of Table I. Equation (3.6) and the points from the width and peak-height measurements are plotted in Fig. 5.

An analysis of variance indicates that both the linear and quadratic terms are of a high order of significance in the above equations. The mean standard deviation

TABLE I. Linewidth (reciprocal transverse relaxation time).

	$(1/T_{2m_J})$ $(\mu\text{sec})^{-1}$			
m_J	From width measurements	From peak-height measurements (adj.)	Average	Calculated Eq. (3.6)
−2	1.267±0.035	1.214±0.042	1.240	1.242
−1	1.140±0.027	1.135±0.027	1.137	1.125
0	1.027±0.019	1.066±0.025	1.046	1.060
1	1.021±0.020	1.085±0.021	1.053	1.047
2	1.104±0.040	1.068±0.034	1.086	1.086

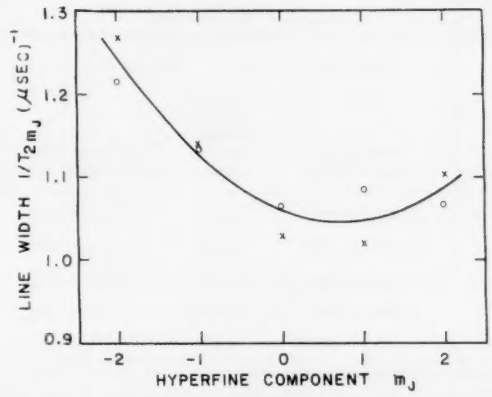

FIG. 5. Plot of linewidth parameter $(1/T_{2m_J})$ as a function of hyperfine component (m_J) for the p-benzosemiquinone ion spectrum. The magnetic field at which the absorption line of a component appears increases from left to right. x: from extrapolation to low microwave power of linewidth measurements. o: from extrapolation to low microwave power of peak-height measurements. The curve is the theoretically predicted quadratic function of m_J adjusted by a least-squares fit to the mean of the data from linewidth and peak-height measurements.

of the width measurements (estimated from the mean variance of the five intercepts given in column two of Table I) is 0.029, while the standard deviation estimated from the residual mean square from the quadratic fit is 0.019. Almost identical values hold for the estimates of width from peak-height measurements, while the standard deviation estimated from the residual for Eq. (3.6) is 0.014. With a standard deviation for the measurement of the width of a single component of 0.029, the standard deviation of the constant term in the above equations can be calculated to be 0.020, that of the coefficient of the linear term 0.009, and that of the coefficient of the quadratic term 0.008. These numbers apply to Eqs. (3.3) and (3.5), and although it is difficult to compute the precision of the coefficients in Eq. (3.6), the data appear to be consistent with the estimates that limits at the 95% confidence level for the constant term in Eq. (3.6), are less than ±0.04 (4%), limits for the coefficient of the linear term are less than ±0.02 (45%), and limits for the coefficient of the quadratic term are less than ±0.015 (60%).

Saturation Parameters. Spin-Lattice Relaxation Times T_{1i}

The slopes of Eqs. (3.1) for the square of the width are related to the ratio of relaxation times (T_{1i}/T_{2i}) by Eq. (1.4), and the values so obtained are given in the second column of Table II. The spin-lattice relaxation times T_{1i} computed by dividing the best fit for $(1/T_{2i})$ as given by Eq. (3.6) into the values of the ratio (T_{1i}/T_{2i}), are given in the third column of Table II.

When the variation in saturation parameters from one hyperfine component to another is small, the theo-

TABLE II. Relaxation times.

	T_{1m_J}/T_{2m_J}	T_{1m_J} (μsec)	
m_J	From width measurements	From width measurements (calc.)	From peak-height measurements (adj.)[a]
−2	1.526±0.071	1.229	1.660±0.031
−1	1.520±0.050	1.351	1.737±0.019
0	1.548±0.032	1.460	1.864±0.018
1	1.496±0.034	1.429	1.726±0.015
2	1.395±0.068	1.285	1.687±0.025

[a] Adjusted to fit measurements of intercepts with α of Eq. (3.4) given by $\alpha=0.1895\times10^6$.

retical equations for both T_{1i} and (T_1/T_{2i}) are quadratic in m_J. The fit to the data in column two of Table II is

$$(T_{1m_J}/T_{2m_J})=1.536-0.029m_J-0.019m_J^2. \quad (3.7)$$

The standard deviation estimated from the mean of the variances in column two of Table II is 0.054, while that estimated from the residual mean square from the quadratic fit is 0.022. Using the larger of these standard deviations to estimate the errors of the coefficients in Eq. (3.7), we find the error in the constant term is 0.04 (2.4%), the error in the linear term is 0.017 (60%), and the error in the quadratic term is 0.014 (75%). The fit to the reciprocal of the data in column three of Table II is

$$(1/T_{1m_J})=(0.690-0.011m_J+0.027m_J^2)\times10^6 \text{ sec}^{-1}. \quad (3.8)$$

The standard deviation estimated from the mean of the variances of the data in Tables I and II is 0.030, and that estimated from the residual of the fit is 0.011. Using the larger of these estimates, the errors of the coefficients in Eq. (3.8) are: for the constant term, 0.021 (3%); for the linear term, 0.010 (90%); and for the quadratic term, 0.008 (30%). A plot of the data in column two of Table II and of Eq. (3.7) is given in Fig. 6.

The slopes of Eqs. (3.2) for the reciprocal of the peak height are directly related to T_{1i} by Eq. (1.5) if the instrumental constant c is known. Using the value of c previously obtained by adjusting the intercepts of the peak-height measurements to fit the width measurements, the T_{1i}'s listed in the fourth column of Table II are obtained. The values derived in this manner from the peak-height measurements are, on the average, higher than the values derived from the width measurements by 28%. Two types of evidence indicate that this discrepancy cannot be accounted for by an error in the instrumental constant c. The first type of evidence follows from the consistency of the data. The ratio of the slope to intercept of Eqs. (3.1) for the square of the width and of Eqs. (3.2) for the reciprocal of the peak height should both give the same value, independent of c, namely a quantity proportional to $T_{1i}T_{2i}$ [see Eqs. (1.4) and (1.5)]. In fact, however, the slope-to-intercept ratio (corrected for the differences in Q_{LE}) for the peak-height measurements of the five components is, on the average, about 27% higher than the slope-to-intercept ratio for the width measurements. There is considerable scatter about this average, but the ratios involve a compounding of errors so that the scatter is not particularly significant. The second type of evidence follows from the direct observation of an oscilloscope presentation of the spectrum. Qualitative inspection of spectra at different power levels showed that the peak height decreased more rapidly with increasing power than the square of the width increased. The direction of the effect is just as if radicals were destroyed at high power, thus causing a decrease in the area and peak height over and above that arising from saturation. For dilute solutions of radicals, only the peak height and area, not the width, would be affected by a destruction of radicals.

Several tests were made in an attempt to determine the cause of this discrepancy. A direct instrumental effect seems to be unlikely because measurements on the peroxylamine disulfonate ion (see Sec. IV) are in complete agreement with Eqs. (1.1) and (1.2). The only possible instrumental effect would thus be one which was important for the narrow lines observed in the *p*-benzosemiquinone ion spectra (approx 60 mgauss) but not for the broader peroxylamine disulfonate lines (approx 225 mgauss). The discrepancy cannot arise from field inhomogeneity, because to account for the different T_1's, an inhomogeneity of the order of 15 mgauss would be required over the length

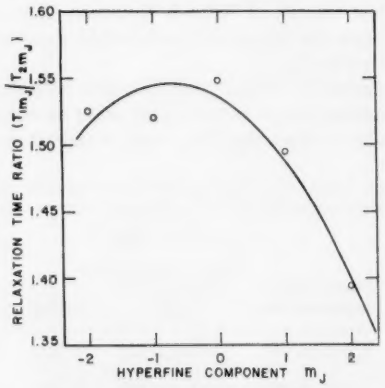

FIG. 6. Plot of the ratio of relaxation times (T_{1m_J}/T_{2m_J}) as a function of hyperfine component (m_J) for the *p*-benzosemiquinone ion as obtained from measurements of linewidth vs microwave power. The magnetic field at which the absorption line of a component appears increases from left to right. The curve is the theoretically predicted quadratic function of m_J adjusted by a least-squares fit to the data.

of the sample. An inhomogeneity of this magnitude would have been detected in the tests with a short sample and would have introduced an upward curvature in the low-power region of Figs. 3 and 4, for the square of the width and reciprocal of the peak height vs power.

An increase in room temperature of 1°C caused a decrease in radical concentration of about 3%, and it was thought that the increase in the temperature of the sample at high power arising from heating by the microwave radiation might account for the discrepancy in the T_1's. A calculation of the temperature rise showed, however, that when the flow system was used, the rise was probably less than 1°C at the highest power employed in the measurements.

The 28% difference in the absolute values of the T_1's obtained from width and peak-height measurements is not the only difficulty. Inspection of the data in column four of Table II, which are plotted as open circles in Fig. 7, shows that there is no significant linear dependence. In addition, while the mean standard deviation estimated from the variances of the data is 0.008, the standard deviation estimated from the residual of the least-squares fit to a quadratic equation is 0.015, and therefore the data cannot be adequately fitted by a quadratic. A plot of values of (T_{1i}/T_{2i}) calculated from the T_1 data in column four of Table II and the best estimate of $(1/T_{2i})$ from the last column of Table I has no significant contribution from a term in m_J^2, and shows considerable scatter about a straight line.

We are therefore forced to conclude that T_1 values obtained from the peak-height measurements are not consistent with other data, either in absolute magnitude or in variation from one hyperfine component to another. The nature of the measurements makes it highly unlikely that any systematic error could occur in the variation from one component to another, as distinct from the absolute magnitude, and we are unable to explain the discrepancies.

It should be observed, however, that there is qualitative if not quantitative agreement between T_1 values obtained from peak-height measurements and other data. Figure 7 is a plot of the T_1 data obtained from peak-height measurements (open circles) and width measurements (crosses). The plotted points for the width measurements have been adjusted to give the same value, on the average, as the data from the peak-height measurements, in order to make it possible to compare the variations from one hyperfine component to another, independent of the over-all difference in absolute values. The points from peak-height measurements in Fig. 7 show that the central component has the largest T_1, and that the T_1's for the outer components decrease systematically toward higher values of the magnitude of m_J, thus indicating that the relaxation mechanism for the central component is the weakest. Such behavior is qualitatively

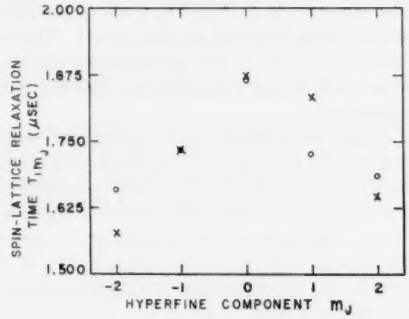

FIG. 7. Plot of the saturation parameter (T_{1m_J}) as a function of hyperfine component (m_J) for the *p*-benzosemiquinone ion. *o*: from peak-height measurements, column four, Table II. *x*: from width measurements adjusted to agree, on the average, with values from peak-height measurements by multiplying numbers in column three, Table II, by 1.30. The magnetic field at which the absorption line of a component appears increases from left to right.

consistent with the $(1/T_{2i})$ results, the T_{1i} data obtained from the width measurements, and the theory.

Effect of Oxygen

An attempt was made to determine whether dissolved oxygen could affect the linewidth. In all the experiments described above, dissolved oxygen was relied upon for the oxidation of the hydroquinone to the semiquinone, so that an experiment to test the effect of oxygen could only be made by using a different oxidizing agent. Some rough experiments were therefore made using *p*-benzoquinone as the oxidant, and degassed basic ethanolic solutions of quinhydrone were prepared and quickly examined in the spectrometer. Although many lines in addition to the ordinary five-line *p*-benzosemiquinone ion spectrum were observed,[13] the widths of the *p*-benzosemiquinone ion lines were essentially the same as for the spectrum obtained under similar conditions when an equal concentration of radical was prepared by dissolving hydroquinone in basic ethanol in the presence of oxygen. These somewhat inconclusive experiments indicate that the width is not markedly affected by dissolved oxygen.

IV. RESULTS, PEROXYLAMINE DISULFONATE

The high-field spectrum of the peroxylamine disulfonate ion, $(SO_3)_2NO^-$, consists of three equally spaced lines arising from the hyperfine interaction between the unpaired electron and the N^{14} nucleus $(I=1)$.[14,15] The lines are separated from each other by about 13 gauss. We have examined the linewidth and saturation behavior at 9.2 kMc of 9.8×10^{-4} *M* aqueous

[13] Compare the work cited in footnote 8.
[14] J. P. Lloyd and G. E. Pake, Phys. Rev. **94**, 579 (1954).
[15] G. E. Pake, J. Townsend, and S. I. Weissman, Phys. Rev. **85**, 682 (1952); J. Townsend, S. I. Weissman, and G. E. Pake, *ibid.* **89**, 606 (1953).

solutions, made 0.1M in Na_2CO_3, with up to 100 mw of microwave power incident on the cavity. The sample tube, and its location in the spectrometer cavity, were similar to that in the experiments with the p-benzosemiquinone ion.

The initial experiments were performed with the sample in a closed capillary tube, but it was found that radicals were destroyed at high power, apparently because of heating by the microwave radiation, and subsequent high-power experiments were performed using the flow system, so as to maintain a fresh supply of radical in the spectrometer. A closed capillary tube was used at low power.

No differences between either the peak heights or linewidths of the three components could be observed over the entire range of power investigated. In these measurements, a variation of a few percent would have been detectable. Similar results have been obtained at low power by C. Ryter.[16]

Only approximate measurements of the absolute values of the width and saturation parameters were made. The half-width at half-maximum absorption was found to be about 225 mgauss, corresponding to $T_2=2.5\times10^{-7}$ sec, and the spin-lattice relaxation time was found to be about $T_1=3.3\times10^{-7}$ sec. The cavity Q for these measurements was about $Q_{LE}\cong800$. A comparison of these results with studies made by Lloyd and Pake[14] and Landesman[17] at low fields will be made in Sec. V.

Approximate measurements of the spectrum displayed on the oscilloscope screen, when the power incident on the cavity was varied from 0.5 to 100 mw, showed that the square of the linewidth increased with power at the same rate as the decrease in peak height. In other words, the product $\delta_i^2 p_i$ from Eqs. (1.1) and (1.2) was a constant independent of power. An effect comparable in magnitude to that observed for the p-benzosemiquinone ion would have been easily detected. These data show that the components of the peroxylamine disulfonate spectra obey Eqs. (1.1) and (1.2), and thus no instrumental error seems to be present which affects lines a few hundred milligauss in width.

V. DISCUSSION

Theory of Linewidth

General theories from which the linewidth can be calculated have been formulated by Kubo and Tomita[18] and by Bloch.[19] We consider a molecule with spin $S=\frac{1}{2}$, and one magnetic nucleus of spin I undergoing rapid tumbling in solution. The contribution to the width from intramolecular, anisotropic, dipolar interaction, and g-tensor anisotropy, for the hyperfine component with z component of total nuclear spin angular momentum m_J can be shown to be[3]

$$(1/T_{2m_J})=(\tfrac{1}{6})(5K^0-K)m_J^2+[(\tfrac{4}{3})L^0+L]m_J+(\tfrac{4}{3})M_g^0+M_g+(\tfrac{1}{2})[K^0+(\tfrac{7}{3})K]I(I+1), \quad (5.1)$$

where

$$(K^0/K)=(L^0/L)=(M_g^0/M_g)=1+\omega^2\tau_c^2; \quad (5.2)$$

τ_c is the rotational correlation time; ω the angular frequency at which the ESR spectrum is observed; and the parameters K, L, and M_g are defined by Stephen and Fraenkel.[2] The term in K arises from the intramolecular dipolar interaction, that in M_g from the anisotropy of the g tensor, and that in L from a cross term between these two effects. Terms in K, L, and M_g are nonsecular, while those in K^0, L^0, and M_g^0 arise from essentially secular perturbations. A number of other mechanisms affect the relaxation and linewidth in a manner which does not depend on m_J.[2,3,14] For our present purposes, it is sufficient to denote the total of the transition probabilities induced by these processes with a single parameter, M', and they thus contribute a term of magnitude M' to the right-hand side of Eq. (5.1).

For a radical with several identical nuclei, the width can be computed by averaging over the degenerate nuclear spin states with a given value of m_J,[3] and for n equivalent protons one obtains

$$(1/T_{2m_J})=[K+(\tfrac{4}{3})K^0]m_J^2+[L+(\tfrac{4}{3})L^0]m_J+M_2, \quad (5.3)$$

where

$$M_2=M'+M_g+(\tfrac{4}{3})M_g^0+(n/4)[(\tfrac{7}{3})K+K^0]. \quad (5.4)$$

Theory of Saturation Parameters

The theory of Stephen and Fraenkel[2] can be used to evaluate the saturation parameters T_{1m_J} and although some of the numerical values included by these authors are applicable to the present problem, detailed evaluation of the complicated determinants required is extremely tedious. Stephen[20] has recently developed a simple diagrammatic method of evaluating the saturation parameters; it is particularly useful when some of the relaxation mechanisms are small. In terms of the relaxation mechanisms considered above, Stephen's result for the p-benzosemiquinone ion can be expressed as

$$(1/T_{1m_J})=2Km_J^2+2Lm_J+2M_1, \quad (5.5)$$

where

$$M_1=M+R, \quad (5.6)$$

and

$$R=(3K^{02}+14K^0K+8K^2)/(6K^0+14K). \quad (5.7)$$

Equation (5.5) is only valid when (K/M) and (L/M) are small compared to unity. M includes all terms in

[16] See work cited in footnote 17.
[17] A. Landesman, J. phys. Radium **20**, 937 (1959).
[18] R. Kubo and K. Tomita, J. Phys. Soc. Japan **9**, 888 (1954).
[19] F. Bloch, Phys. Rev. **102**, 104 (1956).
[20] M. J. Stephen, J. Chem. Phys. **34**, 484 (1961).

the relaxation mechanisms which are independent of m_J, and is equal to the nonsecular part of M' plus M_g in Eq. (5.4). To the approximation for which Eq. (5.5) is valid, the only relaxations which have an appreciable effect are the vertical transitions, i.e., transitions for which $\Delta m_s = \pm 1$, $\Delta m_J = 0$. From Eqs. (5.3) and (5.5),

$$(T_{1m_J}/T_{2m_J}) = (M_2/2M_1)[1+q(K^0/M_2)m_J^2 + q(L^0/M_2)m_J], \quad (5.8)$$

where

$$q = (\tfrac{4}{3}) + (1+\omega^2\tau_c^2)^{-1}[1-(M_2/M_1)]. \quad (5.9)$$

Contribution of Dipolar Relaxation

The contribution of the intramolecular, anisotropic, dipolar relaxation to the linewidth and saturation behavior is determined by the coefficient K^0 and the rotational correlation time τ_c. For the peroxylamine disulfonate ion, Weissman *et al.*[21] examined the electron resonance spectrum of a single crystal of a dilute solid solution of the ion in a diamagnetic host. The relevant part of their results can be expressed as[3]

$$(K^0/\tau_c) = 9.1\times 10^{15}\ \text{sec}^{-2} \quad (5.10)$$

if τ_c is expressed in seconds.

In order to estimate the coefficient K^0/τ_c for the *p*-benzosemiquinone ion, it is necessary to use the relation between K^0/τ_c and the expectation values of the intramolecular dipolar interaction as given by Stephen and Fraenkel.[2] We assume that the unpaired electron is in a π orbital and that its wave function can be described by a one-electron LCAO molecular orbital. The presumably small contributions from σ electrons are neglected. McConnell and Strathdee[22] have calculated the expectation value of the magnetic dipole interaction between an electron in a Slater type $2p$-π orbital and a nucleus lying in the nodal plane on the π orbital, and we make use of their result to determine the contribution from all the π orbitals in the *p*-benzosemiquinone radical. The following parameters are assumed[22]: C—C bond length, 1.397 A; C—O bond length, 1.36 A; C—H bond length, 1.084 A; Z for Slater orbital on carbon, 3.18; Z for Slater orbital on oxygen, 4.55. For the coefficients c_i in the expression for the wave function of the unpaired electron, in terms of a linear combination of $2p$-π orbitals, we take[24]: $c_2^2 = c_3^2 = c_5^2 = c_6^2 = 0.1072$, $c_1^2 = c_4^2 = 0.1071$, and $c_7^2 = c_8^2 = 0.1786$. The oxygen atoms are numbered 7 and 8 and are bonded to carbon atoms 1 and 4. For the parameters a, b, and c on which (K^0/τ_c) depends [Eqs. (3.7) of the work cited in footnote 2], we find $b=0$, and

$$(1/2\pi)g\beta_e\gamma_I a = -1.49\ \text{Mc} \quad (5.11a)$$

$$(1/2\pi)g\beta_e\gamma_I c = -(1.29+1.72i)\ \text{Mc}. \quad (5.11b)$$

The values of a, b, and c correspond to a choice of the principal axes of the g tensor such that g_1 is along a C—O bond; g_2, perpendicular to a C—O bond; and g_3, perpendicular to the plane of the ring. From Eqs. (5.11)

$$(K^0/\tau_c) = 2.72\times 10^{14}\ \text{sec}^{-2}, \quad (5.12)$$

where τ_c is expressed in seconds.[25]

Comparison with Theory, *p*-Benzosemiquinone ion

The theory of the linewidth predicts a quadratic dependence of $(1/T_{2m_J})$ on m_J, as given by Eq. (5.3), and the experimental data, as represented by Eq. (3.6), is in excellent agreement with this prediction. Data obtained from both width and peak-height measurements are essentially the same. The theory of saturation predicts that $(1/T_{1m_J})$ should also depend quadratically on m_J, as given by Eq. (5.5). The data obtained from width measurements, as represented by Eq. (3.8), is in good agreement with this prediction, but the data from peak-height measurements is not in agreement with a quadratic function. In Sec. III, it was also pointed out that the absolute magnitude of the T_1's from peak-height measurements is, on the average, 28% greater than the values obtained from the width measurements. We believe, therefore, that the data for $(1/T_{2m_J})$ is more reliable than the data for $(1/T_{1m_J})$, despite the fact that we have no *a priori* reason for believing there is a systematic error in the saturation factors which would lead to an error in the relative variation from one hyperfine component to another.

Although the data for (T_{1m_J}/T_{2m_J}) from width measurements and all the data for $(1/T_{2m_J})$ depend quadratically on m_J, the two types of measurements are not quantitatively consistent with each other and the theory. From Eqs. (5.3), (5.5), and (5.8), for $(1/T_{2m_J})$, $(1/T_{1m_J})$, and (T_{1m_J}/T_{2m_J}), respectively, it is evident that the ratio of the coefficient of the linear term to the coefficient of the square term in each of these expressions should have the same value, namely $(L^0/K^0) = (L/K)$, and this ratio should be independent of any errors in the absolute magnitude of the measurements. The experimentally determined ratios from Eqs. (3.6) and (3.7) are, respectively, -1.49 and $+1.53$, and the

[21] S. I. Weissman, T. R. Tuttle, and E. de Boer, J. Phys. Chem. **61**, 28 (1957).

[22] H. M. McConnell and J. Strathdee, Mol. Phys. **2**, 129 (1959).

[23] *Tables of Interatomic Distances and Configuration in Molecules and Ions*, edited by L. E. Sutton (The Chemical Society, London, 1958), Special Publication No. 11.

[24] G. Vincow, thesis, Columbia University, New York, 1959.

[25] The contribution to a, b, and c, of orbitals which are not atoms adjacent to the nucleus is appreciable. In the case of the benzene negative ion, for example, one obtains, using all six $2p_z$ atomic orbitals, $(1/2\pi)g\beta_e\gamma_I a = -(9.92/6) = -1.65$ Mc, $b=0$, and $(1/2\pi)g\beta_e\gamma_I c = (23.3/6) = 3.88$ Mc. If nonadjacent orbitals are neglected, the values found for these quantities are, respectively, -0.362 Mc, 0, and 2.80 Mc. Stephen and Fraenkel[2] give these latter numbers with incorrect signs, incorrectly making a positive and c negative. This change in sign affects the sign of the linear term in the linewidth. See footnote 28.

change in sign is outside the experimental error. There are certain other quantitative discrepancies between the T_1 and T_2 data which will be discussed after a more detailed examination of the agreement between the T_2 data and the theory.

A direct comparison between the theoretical and experimental values of the coefficient of m_J^2 in the expressions for $(1/T_{2m_J})$ given by Eqs. (5.3) and (3.6) could be made by using Eq. (5.12) for the calculated value of (K^0/τ_c) if the value of τ_c were known. In the absence of a reliable value of τ_c, however, we can attempt to adjust τ_c to give agreement between the experimental and theoretical results. From Eqs. (5.2), (5.3), and (5.12), using the frequency at which the measurements were performed, namely $\nu=9.21\times10^9$ sec^{-1}, it is found that a value of $\tau_c=7\times10^{-11}$ sec will fit the experimental result in Eq. (3.6), but values between 3×10^{-11} and 1.1×10^{-10} would be within the experimental errors. If the estimate of (K^0/τ_c) were in error by as much as a factor of two, values of τ_c from 1×10^{-11} to 2.5×10^{-10} would be consistent with the data. These estimates of τ_c can be compared with the rotational correlation time calculated for a spherical molecule of radius a using the expression[26]

$$\tau_c=4\pi\eta a/3kT. \tag{5.13}$$

For an 80/20 ethanol-water mixture, at room temperature, the viscosity is $\eta\cong2$ centipoises, and if $\tau_c=7\times10^{-11}$ sec, the effective radius would be $a=3.1$ A. Since the distance from the center of the p-benzosemiquinone ion to an oxygen atom is about 2.76 A, and to a hydrogen atom 2.48 A, and since the ion is undoubtedly solvated, this value of an effective radius is certainly reasonable. Although the validity of Eq. (5.13) for small, solvated, nonspherical molecules is highly questionable, it seems quite unlikely that τ_c could be as small as 10^{-11}, and a value of 2.5×10^{-10} is somewhat large.

If we take $\tau_c=7\times10^{-11}$, Eqs. (5.12) and (5.2), with $\nu=9.21\times10^9$ sec^{-1}, give $\omega\tau_c=4.05$, $K^0=1.90\times10^4$ sec^{-1}, and $K=0.109\times10^4$ sec^{-1}.

This value of K obtained from a fit to the data for $(1/T_{2m_J})$ gives for the coefficient of m_J^2 in Eq. (5.5) for $(1/T_{1m_J})$ the value 0.2×10^4 sec^{-1}, but the experimental result, from Eq. (3.8), is 2.7×10^4 sec^{-1}. In fact, one cannot obtain agreement between the coefficient of m_J^2 in the equations for $(1/T_{2m_J})$ and $(1/T_{1m_J})$ unless it is assumed that extreme motional narrowing is taking place, i.e., $\omega\tau_c\ll1$, or $\tau_c\ll1.7\times10^{-11}$. A very small τ_c is in itself unreasonable, and would require a very large value for K^0/τ_c. Thus, if we take $\omega\tau_c\ll1$, then $K=K^0$, and if K is to fit the data for $(1/T_{1m_J})$, we find $(K^0/\tau_c)=(2.7\times10^4)/2\tau_c\gg8\times10^{14}$ as compared to the estimated value in Eq. (5.12) of 2.72×10^{14}. These considerations, as well as those previously cited, tend to indicate that the T_1 data and the theory are not in as close agreement as the T_2 data.

A computation of the coefficient of the linear term in Eq. (5.3) for $(1/T_{2m_J})$ from first principles is not possible because the anisotropy in the g tensor, which is small, depends on the spin-orbit coupling, and a calculation of the spin-orbit coupling requires a knowledge of excited electronic states. If we assume that the $(1/T_2)$ data provides the most suitable estimate of the linear term, we can, however, use the experimental results to obtain the order of magnitude of the anisotropy in the g tensor. As discussed above, the experimentally determined ratio of the coefficient of the linear term to the coefficient of the quadratic term is $(L^0/K^0)=-1.49$, which gives, independent of any assumption about τ_c, but on using Eq. (5.12),

$$(L^0/\tau_c)=-4.05\times10^{14}\ \text{sec}^{-2}. \tag{5.14}$$

If τ_c is taken to be $\tau_c=7\times10^{-11}$ sec, then $L^0=-2.83\times10^4$ sec^{-1} and with $\nu=9.21\times10^9$ sec^{-1}, $L=-0.163\times10^4$ sec^{-1}. By putting the numbers from Eqs. (5.11) in Eq. (3.6) of the work cited in footnote 2 and using Eq. (5.2), we obtain

$$(L^0/\tau_c)=-11.5\times10^{-16}(g_1-g_2)-5.5\times10^{16}\times[2g_3-(g_1+g_2)], \tag{5.15}$$

where g_1, g_2, and g_3 are the principal values of the g tensor. One other piece of information is available, the isotropic g value g_s,

$$g_s=(\tfrac{1}{3})(g_1+g_2+g_3), \tag{5.16}$$

which has the value $g_s=2.0046$.[27] If one of the principal values of the g tensor were known, say g_3, the component perpendicular to the plane of the ring, a direct comparison could be made between the relaxation theory and experiment. For the benzene negative ion, in the absence of possible complications from Jahn-Teller distortion, symmetry considerations indicate that $g_3=g_0=2.0023$, the free electron value.[2] For the p-benzosemiquinone ion, it is likely that $g_3\cong g_0$. If we arbitrarily take $g_3=g_0$, Eqs. (5.14), (5.15) and (5.16), with the experimental value of g_s, give $g_1=2.0091$ and $g_2=2.0024$. Although the assumption $g_3=g_0$ causes the exact values of these numbers to be highly questionable, Eq. (5.15) and the experimental results still limit the range of reasonable possibilities for the g's.

[26] N. Bloembergen, E. M. Purcell, and R. V. Pound, Phys. Rev. **73**, 679 (1948).

[27] We are indebted to Herbert L. Strauss for the measurement of g_s. Although the precision of the measurement was good to one or two more significant figures than quoted, and reasonable efforts were made to eliminate systematic errors, the troublesome precautions required to obtain a greater accuracy than quoted were not taken. The present result agrees, within our accuracy, with that given by M. Adams, M. S. Blois, Jr., and R. H. Sands, J. Chem. Phys. **28**, 774 (1958).

Note that the sign of L^0 depends on the sign of the isotropic hyperfine interaction,[28] taken to be negative in the foregoing, and with this choice of sign, the most reasonable conclusion is that g_1 (the component of the g tensor along the line joining the oxygen atoms) is larger than the other in-plane component g_2.

The remaining terms to consider in the expressions for $(1/T_{1m_J})$ and $(1/T_{2m_J})$ are M_1 and M_2. These do not give rise to a contribution that depends on m_J. Using the above numerical evaluation of the parameters K and K^0, the contribution of K and K^0 to M_2 is 2.2×10^4 sec^{-1}. If the rather arbitrary assignment of values for g_1, g_2, and g_3 given above is used to evaluate $M_g{}^0$ from Eq. (3.8) of the work cited in footnote 2, with Eq. (5.2), one obtains $(M_g{}^0/\tau_c)=2.5\times10^{15}$ sec^{-2} if $\nu=9.21\times10^9$ sec^{-1}, and the contribution of terms in $M_g{}^0$ and M_g to M_2 is 2.6×10^5 sec^{-1}. This number must be considered at best to be only a rough estimate, but it is unlikely that a much larger value would be consistent with the measured value of g_s. The interaction between the magnetic moments of the electron and the solvent protons is part of M' and gives a contribution, which can be approximately estimated, of $M_{\text{solv}}=4\times10^4$ sec^{-1} for an 80–20 ethanol-water solution at room temperature. Another part of M' arises from the dipole-dipole interaction between free radicals which, at a radical concentration of about 3×10^{-5} M in this solvent, can be estimated to contribute about $M_{\text{rad-rad}}=0.8\times10^4$ sec^{-1}. The sum of all these contributions to M_2 is 3.1×10^5 sec^{-1}, and this is about one-third of the observed value of 1.060×10^6 sec^{-1}. The parameter M_1 would be expected to be approximately equal to M_2, although any secular contributions to M_2 would be absent in M_1, and therefore M_1 cannot be larger than M_2. In fact, neglecting the small correction term arising from R in Eq. (5.6) (estimated to be about 10^4 sec^{-1} for the above values of K and K^0), Eqs. (3.8) and (5.5) give $M_1=0.345\times10^6$ sec^{-1}, and M_1 is thus about one third of M_2. It is surprising that M_1 is so much smaller than M_2 unless the difference arises from errors in computing the effective rf field intensity in the cavity. The contribution to M_1 of the mechanisms calculated above is estimated to be about 6×10^4 sec^{-1}. One must conclude that other relaxation mechanisms make an appreciable contribution to M', but unfortunately there is insufficient evidence to make a reliable estimate of the magnitude of these effects.

[28] Because of the error in signs made by Stephen and Fraenkel in the work cited in footnote 2 (see footnote 25), their conclusions about the sign of the anisotropy for the benzene negative ion are in error. They also assumed that the departure of g_s from g_0 for the benzene negative ion (which has not been measured) was larger than now seems likely. A. Carrington, F. Dravnieks, and M. C. R. Symons, J. Chem. Soc. **1959**, 947, have recently found that g_s values for a number of positive and negative aromatic ions was 2.0028 or 2.0029. T. J. Katz and H. L. Strauss, J. Chem. Phys. **32**, 1873 (1960), have found that $g_s=2.0025$ for the mononegative ion of cyclooctatetraene. Thus (g_s-g_0) for the benzene negative ion is probably in the range from 0.0001 to 0.0005. Following the assumptions of Stephen and Fraenkel, but using the numerical values for a and c from footnote 25 in Eq. (3.6) of the work cited in footnote 2, we obtain $(L^0/\tau_c)=+0.18\times10^{14}$ sec^{-2} if $(g_s-g_0)=0.0001$ and 0.90×10^{14} if $(g_s-g_0)=0.0005$. These values are considerably smaller than, and of opposite sign to, those found for the p-benzosemiquinone ion [Eq. (5.14)]; whereas the quadratic terms are larger since, by using the values of a and c from footnote 25 in Eq. (3.5) of the work cited in footnote 2, together with Eq. (5.2), one obtains $(K^0/\tau_c)=7.79\times10^{14}$ sec^{-2} for the benzene negative ion. If $(g_s-g_0)=0.0001$, $(M_g{}^0/\tau_c)=3.4\times10^{11}$ sec^{-2} and if $(g_s-g_0)=0.0005$, then $(M_g{}^0/\tau_c)=7.9\times10^{12}$.

Comparison with Theory, Peroxylamine Disulfonate Ion

Lloyd and Pake[14] studied the linewidth and saturation of one of the low-field transitions in the spectrum of the peroxylamine disulfonate ion, namely the transition $F=\frac{3}{2}$, $m_F=-\frac{3}{2}$ to $F=\frac{3}{2}$, $m_F=-\frac{1}{2}$. The experiments were performed in fields of approximately 30 gauss at a frequency of 60 Mc. They found a half-width at half-maximum absorption intensity at low concentrations of about 300 mgauss, corresponding to $T_2=2\times10^{-7}$ sec, and a value of the spin-lattice relaxation time of $T_1=2.5\times10^{-7}$ sec. Landesman[17] determined the electron spin relaxation in this ion by studying the dynamic polarization of the solvent protons, and found the width for the transition studied by Lloyd and Pake to be 0.7 Mc or $T_2=2.3\times10^{-7}$ sec in fields of 60 gauss. Landesman also showed by a very ingenious set of experiments that the intramolecular anisotropic dipolar relaxation could not play a significant role in the relaxation.

The values of T_1 and T_2 found in the present experiments at high fields, $T_1=3.3\times10^{-7}$ sec and $T_2=2.5\times10^{-7}$ sec, are significantly higher than those found by Lloyd and Pake, but the value of T_2 is comparable to that found by Landesman. A somewhat larger value of the relaxation times at microwave frequencies is not surprising since at high frequencies there is less complete motional narrowing and the effect of the nonsecular relaxations should be reduced.

Landesman[17] and Kivelson[3] have pointed out that the large value of (K^0/τ_c) for the peroxylamine disulfonate ion [see Eq. (5.10)] should cause a dependence of linewidth on m_J that is not experimentally observed. Landesman concludes that one would have to have $\tau_c<4\times10^{-12}$ sec to obtain agreement with experiment, and our high-field measurements would require $\tau_c<10^{-11}$ sec. Molecular geometry[3] would be more consistent with a value $\tau_c>7\times10^{-11}$.

In the peroxylamine disulfonate ion, no adequate explanation has been found on the one hand for the absence of anisotropic dipolar interaction or, on the other, for the mechanism which makes the main contribution to relaxation and line broadening.

VI. CONCLUSIONS

The linewidths of the five hyperfine components in the electron resonance spectrum of the p-benzosemiquinone ion exhibit differences of as much as 20% in

the limit of low microwave power. The variation can be accurately represented by a quadratic equation in m_J, the field-direction component of the total nuclear spin angular momentum, and the form of this equation is in excellent agreement with the linewidth predicted for relaxation mechanisms arising from anisotropic intramolecular dipole interactions and anisotropy in the g tensor. Good quantitative agreement is obtained for the coefficient of m_J^2 if the rotational correlation time is taken to be $\tau_c = 7 \times 10^{-11}$, a value which is consistent with the molecular dimensions.

Saturation parameters (T_1) for the p-benzosemiquinone ion, determined from measurements of linewidth, show a variation from one hyperfine component to another of as much as 13%; the variation also is described by a quadratic equation in m_J. The data obtained for T_1 is in qualitative but not quantitative agreement with the data for T_2 and the theory, and T_1 data from width measurements is not in quantitative agreement with T_1 data from peak-height measurements. At present no explanation exists for the quantitative discrepancies in the T_1 data from the two types of measurements or for the lack of quantitative agreement between the T_1 measurements and the theory.

The major contribution to the relaxation and linebroadening mechanisms does not cause a variation from one hyperfine component to another and has only been roughly accounted for by the presently proposed mechanisms.

No variation was found among the widths or peak heights of the three hyperfine components of the peroxylamine disulfonate ion at any power studied. Neither the absence of variation in linewidth in this spectrum, which is in agreement with that of other observers, or the magnitude of the over-all line broadening and relaxation mechanisms, have been satisfactorily accounted for.

An investigation of linewidth and saturation of different radicals in a variety of solvents and over a range of temperature, as well as at different microwave frequencies, would serve to elucidate additional aspects of the significant relaxation mechanisms. The secular terms such as K^0, L^0, and M_g^0 are proportional to τ_c and should therefore vary as (η/T); the parameter L^0 should be proportional to the microwave frequency, and M_g^0 should be proportional to the square of the microwave frequency. The nonsecular terms vary, as compared to the secular terms, by the factor $(1+\omega^2\tau_c^2)^{-1}$. Systems in which chemical reaction is slow would be of interest, and specific solvent effects should be investigated.

ACKNOWLEDGMENTS

We are indebted to Mr. Herbert L. Strauss for making the g-value measurements, assisting in the linewidth measurements and for designing and constructing part of the spectrometer used. We would like to thank Dr. Michael J. Stephen for many helpful discussions of relaxation and saturation theory, and Professor Daniel Kivelson for informing us of results prior to publication.

Electrical Resistivity of Liquid Sodium, Liquid Lithium, and Dilute Liquid Sodium Solutions*

J. F. FREEDMAN

IBM Research Center, Yorktown Heights, New York

AND

W. D. ROBERTSON

Yale University, New Haven, Connecticut

(Received June 15, 1960)

The three factors of atomic size, ion core potential, and charge, which contribute to the increment in electrical resistivity produced by solutes in metallic solutions, have been separated and experimentally evaluated in liquid sodium. The results may be expressed in a semiempirical relationship defining the increment in resistivity of a monovalent solution, $\Delta\rho = 0.063 \mid \Delta \text{ Atomic Number} \mid + 0.53\ (\Delta V/V)^2$, μohm cm/at. %, where $\Delta V/V$ is the fractional difference in atomic volume of solute and solvent and the first term involves the absolute value of the difference in atomic number of sodium and the solutes lithium, potassium, cesium, rubidium, silver, and gold.

INTRODUCTION

DIFFERENCES in atomic size have long been recognized as an important factor in determining the limit of solid solubility and the stability of intermetallic compounds that are in equilibrium with a solid solution.[1] The strain energy resulting from atoms of different size in a solid solution, is calculated by the methods of elasticity theory from a model in which the hydrostatic compression or expansion of the larger or smaller solute atom, is balanced by a distributed shear stress in the surrounding lattice. This model necessarily leads to a positive free energy term, and hence to a positive energy of solution.

Diffuse scattering of x rays from liquid solutions,[2] and the relatively small changes in various thermodynamic properties that accompany transformation from solid to liquid lead to the general conclusion that properties of the liquid state of metals are similar in many respects to the corresponding properties in the solid state.[3]

The one property that changes significantly upon melting is the shear modulus, and as a result the liquid is unable to support a static shear stress. Accordingly, Lumsden[4] and Wagner[5] have suggested that a comparison of relevant thermodynamic quantities of liquid solutions (referred to their pure liquid components), and solid solutions (referred to their pure solid components) should yield satisfactory measures of the strain energy contribution to the properties of solid-solutions. Oriani[6] has pointed out, however, that in order to apply elasticity theory to estimate the fraction of the partial molar heat of solution that is due to strain energy in a solid, it is necessary first of all to decide at what radial distance r_n, away from the center of dilation, the deformation of the lattice can be considered to be elastic. The misfit energy within r_n can be thought of as arising from the small change in radius of the nth shell of neighbors when this nth shell is restricted by the imposition of lattice periodicity. Since r_n is primarily determined by electronic interactions, which may be qualitatively similar in the solid and liquid states, a misfit term may be important even in the liquid state.

The purpose of the present work is therefore to investigate the configurational state of liquids by isolating and evaluating the significance of atomic size in liquid metallic solutions in terms of electrical resistivity. Since the scattering of electrons is presumably dependent on the difference in size of the solute and solvent atoms, and also on the difference in field within the atoms, it is necessary to choose a system which minimizes the latter and maximizes the former. This is best accomplished in dilute alkali metal solutions; in particular, with sodium as the solvent and the remaining alkali metals as solutes. In this system a homogeneous, monovalent liquid solution can be obtained with a maximum difference in atomic radius of 50%, which should be large enough for direct evaluation of the effect of dilation.

The effect of solute core potential may be investigated independently with dilute solutions of silver and gold in liquid sodium. There is sufficient difference between the ion core structures of the two groups to produce a large difference in field within the solutions and, possibly, an important contribution to resistivity, in addition to the contribution associated with dilation.

*Abstracted from a thesis presented by J. F. Freedman to the Graduate Division of the School of Engineering, Yale University, in partial fulfillment of the requirements for the degree of Doctor of Engineering, 1960.

[1] F. Laves, *Theory of Alloy Phases* (American Society for Metals, Cleveland, Ohio, 1956).

[2] N. S. Gingrich, Revs. Modern Phys. **15**, 90 (1943).

[3] O. Kubaschewski, Trans. Faraday Soc. **45**, 931 (1949).

[4] J. Lumsden, *Thermodynamics of Alloys* (Institute of Metals, London, 1952).

[5] C. Wagner, Acta Met. **2**, 242 (1954).

[6] R. A. Oriani, Acta Met. **4**, 15 (1956).

TABLE I. Typical chemical analysis.

Impurity	Sodium ppm (wt)	Alloy ppm (wt)
Potassium	100	
Calcium	8	10
Barium	2	1
Copper	3	1
Iron	3	12
Magnesium	5	1
Silicon	15	50
Strontium	5	2
Chlorides	30	30
Lead	1	1
Phosphorus	1	1
Lithium	20	
Nickel	2	1
Boron	2	2
Aluminum	3	15
Molybdenum	2	2
Bismuth	10	1
Sulfur	14	15
Cadmium	5	1
Manganese	2	1
Silver	1	1
Vanadium	5	1
Chromium	5	1
Cobalt	2	5
Cesium	5	
Hydrogen	20	20
Carbon	10	10
Uranium	4	5
Cerium	2	1
Mercury	4	4
Tin	10	10
Beryllium	1	1
Titanium	10	5
Palladium	5	1
Indium	2	2

Finally, to complete the investigation of the separate factors contributing to the resistance, solute charge (i.e., a screened coulomb potential) may be evaluated by studying the change in resistance of liquid sodium produced by the addition of multivalent solutes, for example, cadmium, tin, and lead.

EXPERIMENTAL PROCEDURE

Pure sodium was obtained in hermetically sealed tins from the E. I. duPont de Nemours Company. A typical chemical analysis is given in Table I. Lithium, supplied by the Nuclear Development Corporation, was vacuum distilled to 99+% purity, the major impurity being sodium. Potassium was supplied by the Mallinckrodt Chemical Company and was of 98+% purity, the major impurity again being sodium. Rubidium and cesium were obtained from A. D. Mackay Inc., who produce it from 99.9% rubidium and/or cesium chloride and supply it sealed *in vacuo* in glass ampules. The remaining solutes were at least 99.9+% purity. A chemical analysis of a typical alloy is also given in Table I, indicating that the alloy addition and method of preparation does not increase significantly the background impurity content.

Alloys were prepared by placing weighed amounts of the component metals in a closed melting system constructed entirely of stainless steel (Fig. 1). After evacuating to 10^{-4} cm of Hg the system was filled with helium, which was purified by passing it over silica gel and through a column containing the liquid eutectic sodium-potassium alloy.

The alloy components were placed in the container, M (Fig. 1) which was heated by a glass insulated resistance heater surrounding the melting chamber. When the components were liquid, the alloy was forced under pressure of helium through the 1-μ stainless steel filter, which removed insoluble oxides, and into the length of tubing between the valves A and B. The conductivity cell was filled by opening valve B which allowed the volume of alloy contained in the side arm AB to flow into the previously evacuated cell.

The final composition of the alloy was determined by a flame photometric analysis performed at the Knolls Atomic Power Laboratory, Schenectady, on a sample obtained from dissolution in alcohol of the entire contents of the conductivity cell. This technique samples the total solute in the alloy, including any oxide smaller than 1 μ that may have passed through the filter. The estimated accuracy was $\pm 5\%$ of the value for compositions less than 0.5 at. % solute and $\pm 2\%$ of the value in the range of 0.5 to 1.0 at. % solute.

Because most electrical insulating materials normally used for conductivity measurements react with liquid sodium, the upper limit of temperature previously available for investigation was 350°C. This limitation was recently raised to over 600°C by the use of a conducting cell made of stainless steel.[7] In the

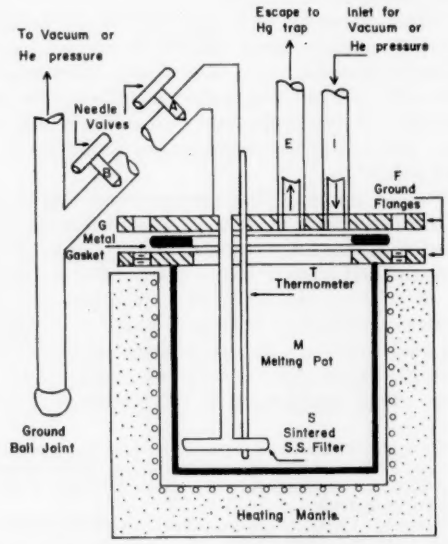

FIG. 1. Stainless steel apparatus for preparing liquid sodium alloys, filtering insoluble oxides, and transferring a measured volume to the conductivity cell.

[7] R. H. Rahiser, R. Werner, and C. B. Jackson, Mine Safety Appliance Company, Technical Report 24, June, 1953.

present work, type 304 stainless steel was chosen as the cell material because of its excellent corrosion resistant properties over this range of temperature, and its ability to be machined to sufficiently close tolerances to define the geometry of the conducting path. The cells were made by boring a longitudinal hole, 0.349 (±0.0010) in. in diam, leaving a closed end, in a 0.565-in. diam rod, 20 in. in length. The inlet end was closed by a stainless steel needle valve and attachment to the melting system was made through a stainless steel ball-joint.

The resistance of the entire cell and its contents was measured as a parallel circuit with a Kelvin bridge. Potential and current terminals were made of stainless steel with a knife edge contact seated in shallow grooves in the outer cell wall to define the length; potential terminals were separated by 9 in. and current terminals were located 1.5 in. outside the potential terminals. The precision of this method is limited only by the sensitivity of the bridge, which is 0.1% of the value measured.

Two separate furnaces were used to measure the temperature dependence of resistivity. The range from 100°C to 250°C was covered in a silicone oil bath in which the temperature could be controlled to ±0.2°C. The temperature was obtained by averaging the temperatures of two calibrated iron-constantan thermocouples attached at depths corresponding to the position of the potential contacts. The temperature gradient over the active length of the cell was less than 0.2°C. Essentially the same design was employed for the temperature range from 250°C to 550°C. However, due to excessive oxidation and decomposition of the silicone oil, an air furnace was used instead of an oil bath. By employing an aluminum core of high thermal conductivity, and electrical compensation for heat loss at the ends of the furnace, the gradient was minimized to ±2.0°C over 16 in. of the cell. The temperature at which the resistance measurement was made was obtained by averaging the values from three calibrated chromel-alumel thermocouples, one at each potential contact and one at the center of the cell.

In the high-temperature range the resistance depended on the direction of the dc current. The average of two readings, however, was in excellent agreement with the low temperature values in the range in which they overlapped. This phenomenon appears to be associated with a thermal emf created by the temperature gradient, and it corresponds exactly with previous observations of other investigators employing a dc method of measurement, for example, Scala and Robertson.[8] This interpretation is verified by the fact that the resistance did not depend on current direction in the oil bath in which the temperature gradient was essentially zero.

Since the cell was made of a conducting material it was imperative that the liquid metal "wet" the cell wall to provide a reproducible, parallel conducting path. This was accomplished by heating the filled cell to 350°C for 24 hr. The resistance of the alloy was then calculated by considering the separate resistances of the alloy and the stainless steel cell to be in parallel and, accordingly,

$$R_{\text{alloy}} = R_{ss} R_l / (R_{ss} - R_l),$$

TABLE II. Resistivity and change in resistivity ($\Delta\rho = \rho_{\text{alloy}} - \rho_{\text{Na}}$) of liquid sodium alloys.

	Sodium	Lithium	Na−0.16%Li		Na−0.65%Li	
T °C	ρ μ ohm cm	ρ μ ohm cm	ρ	$\Delta\rho$	ρ	$\Delta\rho$
100	9.44	...	9.50	0.06	9.60	0.16
150	11.10	...	11.20	0.10	11.26	0.16
200	12.90	25.06	13.02	0.12	13.08	0.18
250	14.78	26.66	14.88	0.10	14.94	0.16
300	16.78	28.28	16.88	0.10	16.96	0.18
350	18.92	29.70	19.02	0.10	19.08	0.16
400	21.12	31.04	21.22	0.10	21.30	0.18
450	23.50	32.22	23.64	0.14	23.74	0.24
500	26.00	33.44	26.14	0.14	26.26	0.26
550	28.56	34.68	28.72	0.16	28.80	0.24
600	31.36					

	Na−0.18%K		Na−0.46%K		Na−0.92%K	
T	ρ	$\Delta\rho$	ρ	$\Delta\rho$	ρ	$\Delta\rho$
100	9.60	0.16	10.06	0.62	10.24	0.80
150	11.24	0.14	11.84	0.74	12.00	0.90
200	13.06	0.16	13.66	0.76	13.80	0.90
250	14.92	0.14	15.58	0.80	15.78	1.00
300	16.92	0.14	17.62	0.84	17.90	1.12
350	19.08	0.16	19.90	0.98	20.06	1.14
400	21.30	0.18	22.20	1.08	22.38	1.26
450	23.66	0.16	24.62	1.12	24.80	1.30
500	26.14	0.14	27.18	1.18	27.32	1.32
550	28.72	0.16	29.80	1.24	30.00	1.44

	Na−0.18%Rb		Na−0.46%Rb		Na−0.71%Rb	
T	ρ	$\Delta\rho$	ρ	$\Delta\rho$	ρ	$\Delta\rho$
100	10.16	0.72	10.56	1.12	11.08	1.64
150	11.92	0.82	12.32	1.22	12.78	1.68
200	13.76	0.86	14.18	1.28	14.60	1.70
250	15.80	1.02	16.16	1.38	16.56	1.78
300	17.86	1.08	18.32	1.54	18.72	1.94
350	20.08	1.16	20.58	1.66	20.96	2.04
400	22.42	1.30	22.90	1.78	23.26	2.14
450	24.86	1.36	25.30	1.80	25.72	2.22
500	27.46	1.46	27.90	1.90	28.30	2.30
550	30.12	1.56	30.60	2.04	30.94	2.38

	Na−0.17%Cs		Na−0.35%Cs		Na−1.02%Cs	
T	ρ	$\Delta\rho$	ρ	$\Delta\rho$	ρ	$\Delta\rho$
100	10.12	0.68	11.04	1.60	12.76	3.32
150	11.84	0.74	12.74	1.64	14.44	3.34
200	13.64	0.74	14.64	1.74	16.24	3.34
250	15.60	0.82	16.60	1.82	18.18	3.40
300	17.76	0.98	18.70	1.92	20.24	3.46
350	19.90	0.98	20.94	2.02	22.46	3.54
400	22.12	1.00	23.24	2.12	24.72	3.60
450	24.48	0.98	25.70	2.20	27.14	3.64
500	27.02	1.02	28.32	2.32	29.72	3.72
550	29.60	1.04	31.00	2.44	32.46	3.90

[8] E. Scala and W. D. Robertson, J. Metals **5**, 1141 (1953).

TABLE III. Resistivity and change in resistivity ($\Delta\rho=\rho_{alloy}-\rho_{Na}$) of liquid sodium alloys.

	Na—0.5%Ag		Na—1.02%Ag		Na—1.84%Ag	
T	ρ	$\Delta\rho$	ρ	$\Delta\rho$	ρ	$\Delta\rho$
100	...	...	...	...	...	...
150	...	...	...	...	...	...
200	(13.40)	(0.50)	...	...	...	...
250	(15.64)	(0.86)	(16.50)	(1.72)	...	...
300	18.06	1.28	(19.64)	(2.86)	(20.04)	(3.26)
350	20.20	1.28	22.42	3.50	23.74	4.82
400	22.40	1.28	24.90	3.78	26.02	4.90
450	24.72	1.22	27.36	3.86	28.48	4.98
500	27.20	1.20	30.04	4.04	31.00	5.00
550	29.82	1.26	32.80	4.24	33.56	5.00

	Na—0.43%Au		Na—1.27%Au		Na—2.46%Au	
T	ρ	$\Delta\rho$	ρ	$\Delta\rho$	ρ	$\Delta\rho$
100	11.74	2.30	15.18	5.74	21.28	11.84
150	13.52	2.42	17.00	5.90	23.16	12.06
200	15.46	2.56	18.92	6.02	25.06	12.16
250	17.46	2.68	20.96	6.18	27.04	12.26
300	19.52	2.74	23.00	6.22	29.06	12.28
350	21.74	2.82	25.16	6.24	31.14	12.22
400	24.04	2.92	27.36	6.24	33.46	12.34
450	26.40	2.90	29.68	6.18	35.86	12.36
500	28.98	2.98	32.20	6.20	38.30	12.30
550	31.62	3.06	34.84	6.28	40.94	12.38

where R_{ss} is the resistance of the empty cell (approximately 10^{-3} ohms), and R_t is the total resistance of the cell filled with liquid metal (in the range of 10^{-4} ohms).

To verify the validity of the assumed parallel circuit, a glass conductivity cell was constructed from precision bore Pyrex tubing using platinum current and potential terminals that were sealed into the cell wall. The agreement between the two methods was 2.5% with the stainless steel cells always yielding a lower value of the resistivity. However, it was difficult to prevent the formation of bubbles at the wall of the glass cells, which may have been responsible for an apparent higher value of resistivity, because of the over-estimation of the cross-sectional area. It was concluded that a stainless steel conductivity cell could be used over a wider range of temperature without contaminating the contents, and that more precise results could be obtained than with the conventional nonconducting and nonwetting materials. For a given alloy (Tables II, III, and IV) the precision was limited only by the sensitivity of the bridge (0.1% of the measured value) and the temperature determination (0.2% of the measured value). In different alloys the major source of error was in the chemical analysis (a minimum of $\pm 2\%$ of the measured value).

TABLE IV. Resistivity and change in resistivity ($\Delta\rho=\rho_{alloy}-\rho_{Na}$) of liquid sodium alloys.

	Na—1.00%Cd		Na—1.10%Pb		Na—1.00%Sn	
T	ρ	$\Delta\rho$	ρ	$\Delta\rho$	ρ	$\Delta\rho$
100	14.22	4.78	...	...	...	...
150	16.10	5.00	...	...	...	...
200	18.04	5.14	25.08	12.18	...	...
250	20.08	5.30	27.22	12.44	(23.60)	(8.82)
300	22.16	5.38	29.36	12.58	27.00	10.22
350	24.42	5.50	31.54	12.62	29.20	10.28
400	26.72	5.60	34.12	13.00	31.50	10.38
450	29.12	5.62	36.70	13.20	34.06	10.56
500	31.74	5.74	39.50	13.50	36.66	10.66
550	34.68	6.12	42.32	13.76	39.50	10.94

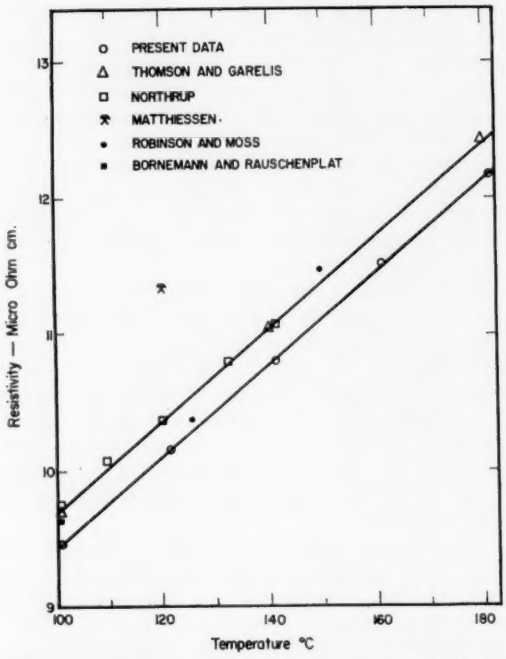

FIG. 2. Resistivity of pure liquid sodium, compared with data previously obtained.

EXPERIMENTAL RESULTS

Liquid Sodium

The present results for pure liquid sodium (Fig. 2) indicate that the resistivity is 2.6% lower than the

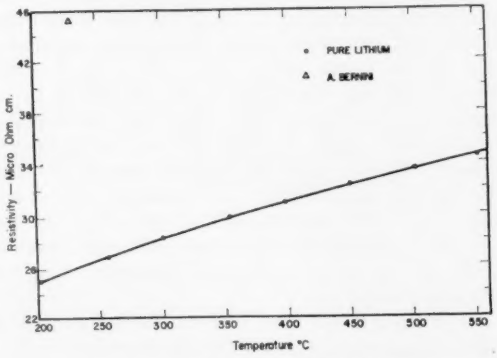

FIG. 3. Resistivity of pure liquid lithium.

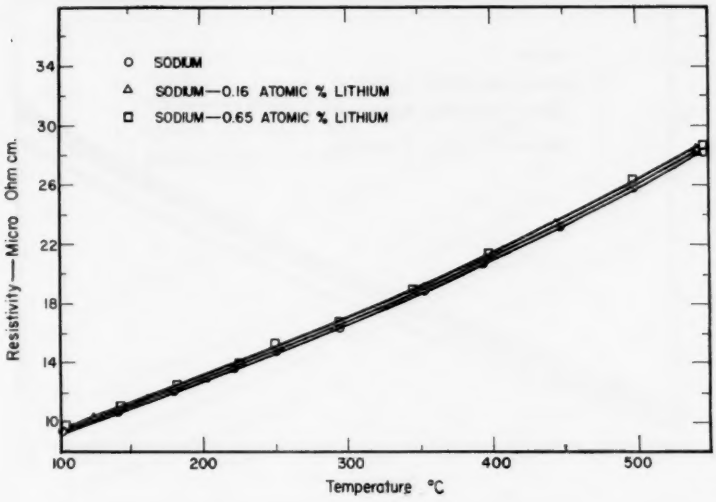

FIG. 4. Resistivity of dilute liquid sodium-lithium solutions.

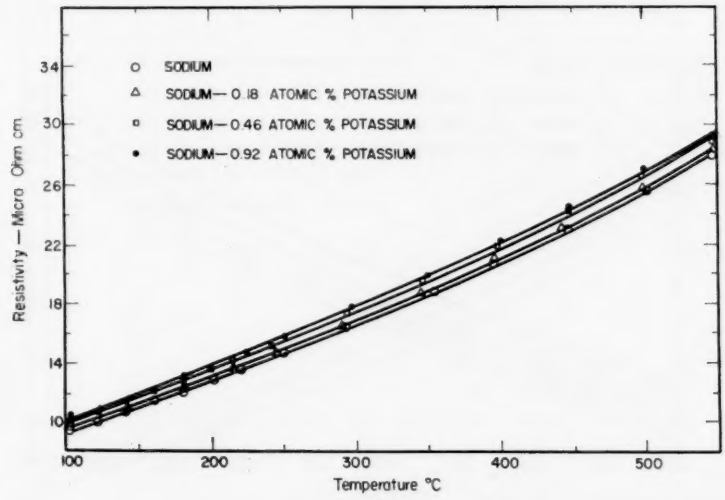

FIG. 5. Resistivity of dilute liquid sodium-potassium solutions.

average of values previously reported[7,9–15]; presumably this lower value of resistivity is due to a more accurate definition of cross section and to the purity of the sodium. The change of resistance with temperature, in the temperature range represented in Fig. 2, is essentially identical with all previous determinations; extending the range to 550°C, as shown in the following figures, clearly reveals an increasing positive curvature that is not evident in the narrower temperature range of most previous investigations.

Liquid Lithium

Only one measurement, at one temperature, of the resistivity of liquid lithium has previously been made.[16] Bridgman[17] determined the ratio of resistances, R_L/R_S, at the melting point and found the ratio to be 1.68; he also measured relative resistance as a function of pressure at two temperatures above the melting point (202.5°C and 237.4°C), but he did not determine the specific resistivity. In view of this meager collection of data it seemed important to make an absolute deter-

[9] G. W. Thompson and E. Garelis, *Physical and Thermodynamic Properties of Sodium* (Ethyl Corporation Report No. **2**, February, 1954).
[10] K. Bornemann and G. V. Rauschenplat, Metallurgie **9**, 510 (1912).
[11] L. Hackspill, Compt. rend. **151**, 305 (1911); Ann. chim. et phys., (8) **28**, 613 (1913).
[12] P. Muller, Metallurgie **7**, 730, 755 (1910).
[13] E. F. Northrup, Trans. Am. Electrochem. Soc. **20**, 200 (1911).
[14] H. Robinson and R. G. Moss, General Electric Company Report No. DF–49–GL 187 (1949).
[15] A. Matthiessen, Phil. Mag. **12**, 199 (1856); **13**, 81 (1957).
[16] A. Bernini, Ann. Physik **6**, 74 (1905).
[17] P. W. Bridgman, Proc. Am. Acad. Arts. Sci. **56**, 70 (1921).

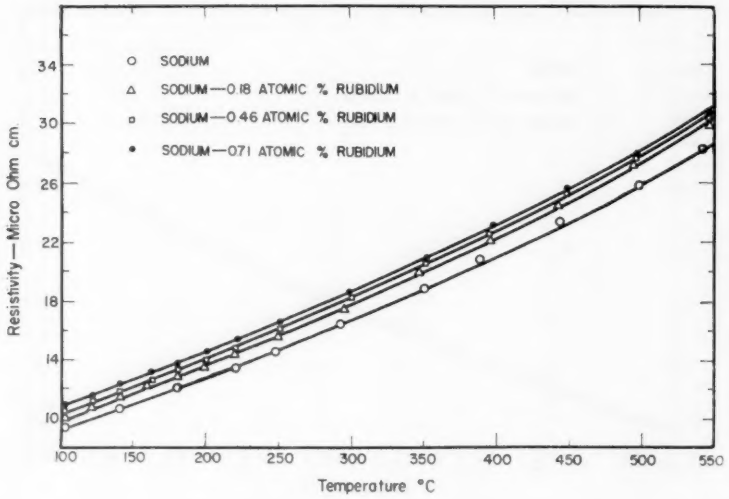

FIG. 6. Resistivity of dilute liquid sodium-rubidium solutions.

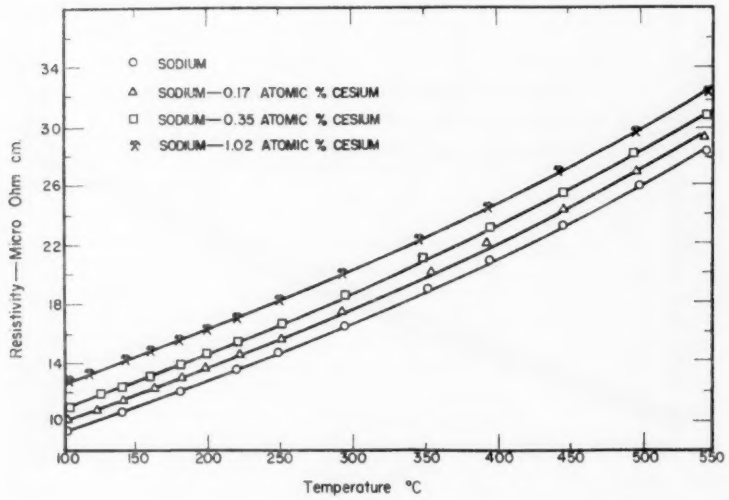

FIG. 7. Resistivity of dilute liquid sodium-cesium solutions.

mination of resistivity over an extended temperature range.

The results of two separate determinations are summarized in Fig. 3. The measured resistivity is 50% lower than that reported by Bernini[16] at one temperature. However, extrapolating the solid-state resistivity[18] to the melting point (15.2 μohm cm), and employing Bridgman's ratio of 1.68, the resistivity of the liquid at the melting point is indicated as 25.6 μohm cm, compared with the measured value of 24.0 μohm cm. Considering the limited amount of solid-state data with which to define the temperature dependence, these results are in satisfactory agreement and they provide a large measure of internal self-consistency for the more recent data, which now include the solid and liquid states and the transformation.

[18] E. Gruneisen, Ergeb. exakt. Naturwiss. **21**, 50 (1945).

Sodium-Alkali Metal Solutions

Four systems were investigated in this group: Na-Li, Na-K, Na-Rb, and Na-Cs. Except for the Na-Li system, single-phase liquid solutions are formed in these systems at all temperatures and concentrations above the melting point of sodium. Fortunately, the extent of the single-phase liquid in the monotectic Na-Li system is sufficient to encompass the compositional range required for this investigation. The data for each system are shown in Figs. 4–7, and they are also given in Table II with the precision necessary for the purpose of analyzing the temperature dependence.

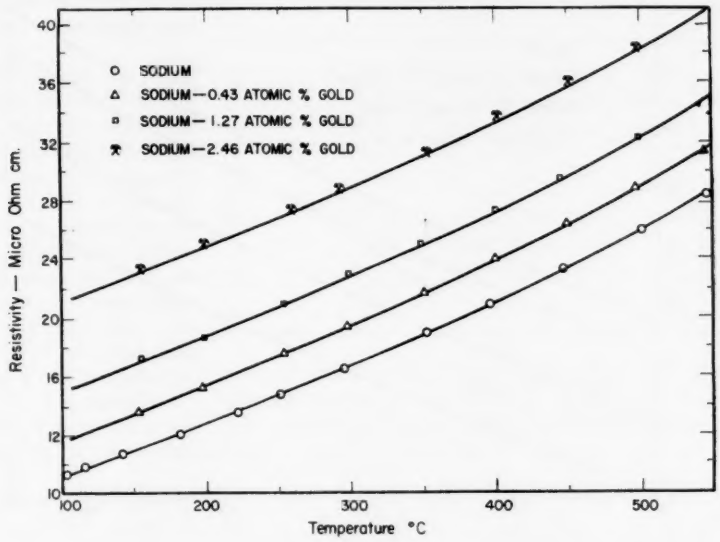

FIG. 8. Resistivity of dilute liquid sodium-gold alloys.

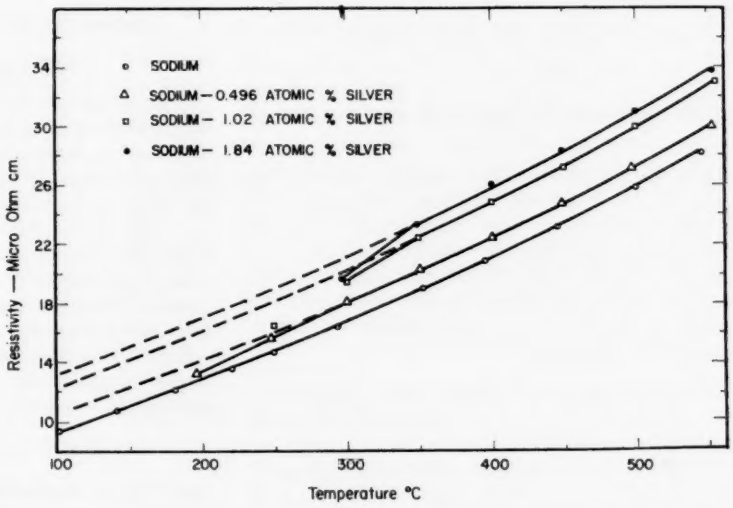

FIG. 9. Resistivity of dilute liquid sodium-silver alloys.

Solutions of Sodium Containing Silver and Gold

Because the melting points of silver and gold are above the boiling point of sodium, the previous alloying procedure could not be used. Instead, solutions were made by dissolving weighed quantities of the massive solid metals in liquid sodium contained in a previously calibrated conductivity cell, which was heated to 550°C and held at this temperature for 48 hr. The fact that a homogeneous liquid solution[19] was obtained by the procedure of dissolving massive pieces of silver or gold in liquid sodium was confirmed by (a) a residue of very fine silver or gold powder which remained after dissolving the sodium in alcohol and (b) a constant and reversible resistance which was observed over a long period of time at a constant temperature.

The resistivities of sodium solutions containing gold and silver are shown in Figs. 8 and 9, respectively, and the data are given in Table III. The deviations in the resistivity vs temperature curves for silver solutions, are consistent with the limited data defining the liquidus curve at the sodium end of the sodium-silver system.[20] Accordingly, the deviations are attributed to crossing

[19] It proved to be impossible to dissolve copper in sodium within a reasonable length of time even when the temperature was raised to 800°C.

[20] M. Hansen, *Constitution of Binary Alloys* (McGraw-Hill Book Company, Inc., New York, 1958), 2nd ed.

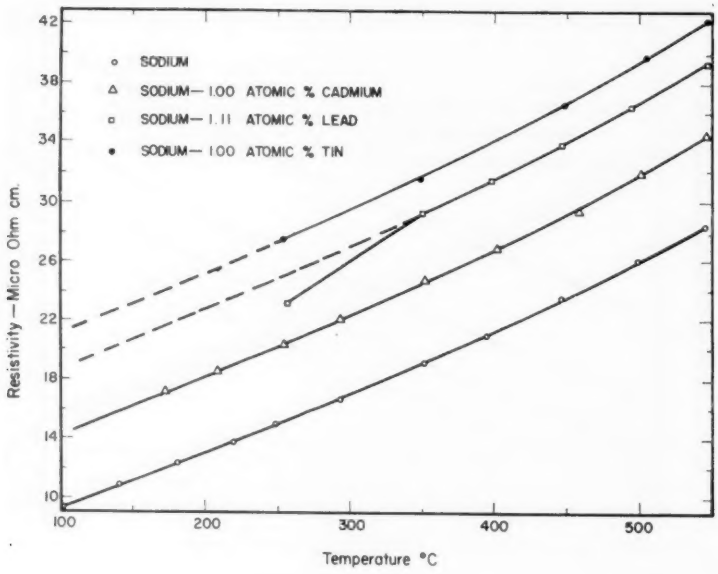

FIG. 10. Resistivity of dilute liquid sodium-cadmium, sodium-tin, and sodium-lead alloys.

the liquidus line, with a corresponding precipitation of silver.

Sodium-Cadmium, Sodium-Lead, and Sodium-Tin Solutions

Again, because of the higher melting points of these metals relative to sodium, solutions were prepared by the same technique as that employed for silver and gold solutions. The data are presented in Fig. 10 and Table IV. The deviation of resistivity from the smooth curve for Na-Pb and Na-Sn, is also associated with crossing the liquidus line and is in accord with the accepted phase diagrams.[20]

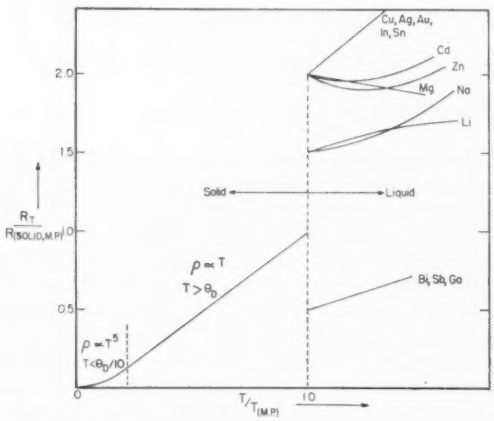

FIG. 11. A qualitative representation of the temperature dependence of resistivity of pure liquid metals, relative to the same solid materials.

DISCUSSION OF EXPERIMENTAL RESULTS

Temperature Dependence

The specific resistivity of pure liquid sodium has been extended to a relatively high temperature (550°C) and the data show an increasing positive curvature over the entire range. Over a similar range of temperature the data for pure liquid lithium exhibit a decreasing curvature. When these results are combined in a single schematic diagram with data recently obtained for other liquid metals[8,21] (Fig. 11) it is apparent that all possible combinations of temperature dependence have now been observed.

Obviously, these data cannot be immediately rationalized in terms of the following relationship[22] applying to monovalent metals in the solid state,

$$\rho = 4.78 \times 10^{-2} (T/\theta_D^2 V^{\frac{1}{3}}) (C_D/E_F)^2 \text{ ohm-cm},$$

where C_D is a constant expressing the coupling between electrons and thermal vibrations of the lattice, E_F is the Fermi energy, V is the atomic volume, and θ_D is the Debye temperature. An additional complication is Bridgman's[23] observation that the resistance of both solid and liquid lithium increases with pressure (unlike all other metals, except only calcium and strontium), and that the ratio of R_L/R_S for alkali metals is independent of pressure. It appears that it will be necessary to reconsider the whole problem of scattering of electron waves in a partially periodic structure, as a function of temperature and pressure,

[21] A. Roll and H. Motz, Z. Metallkunde **48**, 272 (1957).
[22] H. Jones, *Handbuch der Physik*, edited by S. Flugge (Springer-Verlag, Berlin, 1956), Vol. 19, Part 1, p. 226.
[23] P. W. Bridgman, Proc. Am. Acad. Arts Sci. **72**, 157 (1951).

before the temperature dependence of resistivity of the different liquid metals can be more completely and quantitatively understood.

The introduction of monovalent solutes in liquid sodium again raises questions regarding the temperature dependence of resistivity of the solutions. The data (Table II and Table V, interpolated from large scale plots) indicate that the increment in resistivity resulting from the introduction of 1 at. % of a monovalent solute into liquid sodium, is dependent on temperature. The deviation from Matthiessen's rule, $\rho=\rho_T+\rho_I$, in which the impurity contribution is assumed to be independent of temperature, varies widely and without apparent order among the different solutions. Since qualitative evidence of a deviation does not depend on an explicit knowledge of composition, the principal source of error in this investigation is not involved and the deviations from Matthiessen's rule seem to be conclusively established for liquid sodium solutions.

The fact that the "rule" is not obeyed in liquid sodium solutions is not, in itself, cause for concern. Of the assumptions underlying the simple addition of resistivities due to scattering by thermal vibrations and impurities, namely, (1) all thermal scattering is elastic, (2) the conduction electrons are "free", (3) thermal vibration does not affect the scattering potential, (4) impurity atoms do not perturb the vibration spectrum of the solvent, and (5) the effective number of electrons is not changed by the impurity; many are unjustified in varying degree even in solid solutions. The more serious problem (brought to the authors' attention by F. J. Blatt) associated with both nonlinear temperature dependence and the deviation from Matthiessen's rule, lies in the apparent impossibility of extrapolation to obtain a meaningful residual resistivity. Thus, theoretical consideration of the liquid state must be limited to the change in resistivity at the melting point, and to the partially periodic liquid state itself, without help from a hypothetical state at absolute zero.

Composition Dependence

The change in resistivity, $\Delta\rho=\rho_{\text{alloy}}-\rho_{\text{Na}}$, evaluated at 100°C, is shown in Fig. 12 as a linear function of composition. The bars through the experimental points indicate the accumulated experimental errors of $\pm 5\%$ associated with the chemical analysis and $\pm 0.5\%$ resulting from the measurement of temperature and resistance. While the scatter of data is large, the relative position of the different lines does not seem to be in serious doubt, particularly the slopes obtained from a least-squares analysis for the alkali solutes compared with those for silver and gold (summarized in Table V).

For the purpose of indicating the significance of various factors determining the resistivity of solutions, the results may be considered in terms of a model

TABLE V. Increase in resistivity of monovalent, liquid sodium solutions.

Solute	$\Delta\rho=\rho_{\text{alloy}}-\rho_{\text{Na}}$ (100°C) μ ohm cm/atm%	$\Delta\rho=\rho_{\text{alloy}}-\rho_{\text{Na}}$ (550°C) μ ohm cm/atm%	Deviation $\Delta\rho 550-\Delta\rho 100$
Li	0.28	0.52	0.24
K	1.02	1.82	0.80
Rb	2.55	4.45	1.90
Cs	3.64	4.80	1.16
Ag	2.50	3.12	0.62
Au	4.80	5.24	0.44

for solid solutions first suggested by Mott[24] and more recently developed by Arafa.[25] For a monovalent solution containing X atom fraction of solute, the resistivity may be expressed as

$$\rho\ \mu\text{ohm cm}\equiv 132V^{\frac{1}{3}}[(U_0/EF)(\bar{\mu}_B{}^2/\bar{\mu}_0{}^2)]^2X$$

The expression contains two terms which are essential to the present argument assuming that the Fermi energy, E_F is not significantly changed upon melting. (a) $\bar{\mu}_0{}^{-2}$ which describes the manner in which the charge density varies in the vicinity of a solute atom, and (b) U_0 which is the difference in energy between the lowest states in the conduction bands of the pure metals. This relationship, which has been used with some success to account for the resistivity of copper, silver, and gold solid solutions, was derived by neglecting the effect of the small differences in atomic size in the solid solutions upon the accumulation of charge around the impurity atoms. However, because of the large size differences involved in the alkali metal solutions, it is necessary to consider explicitly the change in charge density in the vicinity of the relatively large solute atoms.

Harrison[26] and Blatt[27,28] have suggested a method which they have applied to solid solutions, by which the present results may be analyzed and the effect of the size difference separated, empirically at least, from other factors. Instead of considering the scattering process in a monovalent solution in terms of physical size differences between solvent and solute, and the scattering probability as proportional to the square of a corresponding displacement; they suggest it may be more meaningful to consider the displacement of surrounding atoms in terms of the associated change in charge density. This change, due to a dilation, is measured in the present case by the ratio of the difference in atomic volume of solute and solvent to the atomic volume of the solvent $\Delta V/V$.

[24] N. F. Mott, Proc. Cambridge Phil. Soc. **32,** 281 (1936).
[25] M. K. I. Arafa, Proc. Phys. Soc. (London) **B62,** 238 (1949).
[26] W. A. Harrison, Phys. Rev. **110,** 14 (1958).
[27] F. J. Blatt, Phys. Rev. **108,** 285 (1957).
[28] F. J. Blatt, Phys. Rev. **108,** 1204 (1957).

In the absence of any displacement, the introduction of excess charge will cause scattering in proportion to the square of the excess charge both in solid solutions (Linde's Rule) and in liquid copper solutions.[8] Thus, a polyvalent impurity of valence Z in a monovalent metal introduces an apparent charge difference of

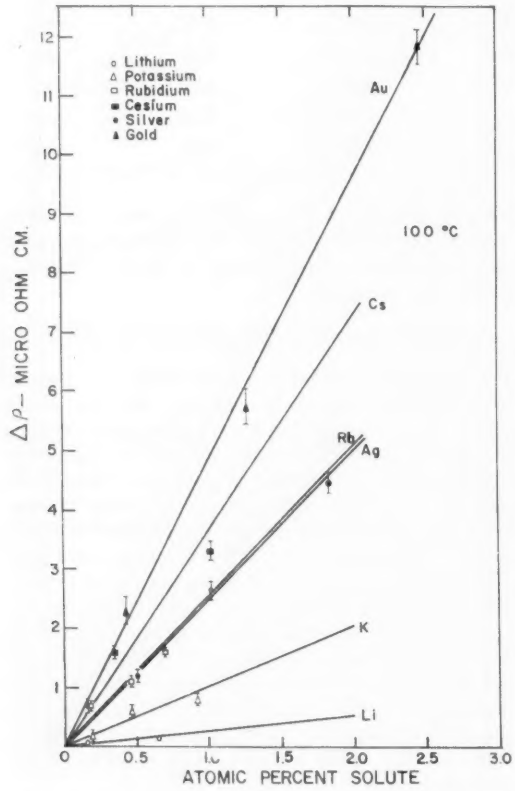

FIG. 12. Change in resistivity (ρ alloy-ρ sodium) at 100°C, as a function of solute composition.

$\Delta Z = Z - 1$ and a resistivity increment of

$$\Delta\rho = a + b(\Delta Z)^2.$$

If, in addition, the impurity also produces a dilation, the effective charge difference, ΔN becomes

$$\Delta N = Z - 1 - \Delta V/V,$$

and Linde's rule is modified to

$$\Delta\rho = a + b(\Delta N)^2.$$

In the case of a monovalent impurity in sodium,

$$\Delta\rho = a + b(\Delta V/V)^2.$$

Figure 13 shows $\Delta\rho$ for liquid sodium solutions as a function of $(\Delta V/V)^2$. The radii of the alkali metals

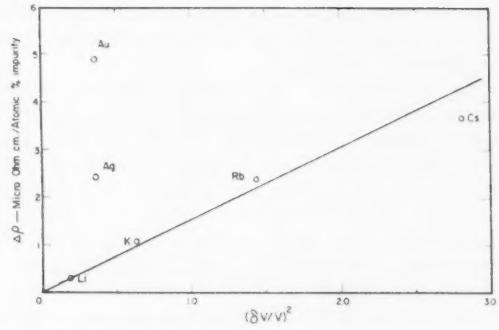

FIG. 13. Change in resistivity of liquid sodium per atomic percent solute, at 100°C, as a function of the square of the fractional difference in atomic volume of solvent and solute.

used to obtain $\Delta V/V$ (Table VI) are those of Heaton,[29] derived from recent neutron diffraction measurements on the pure liquid metals; crystal radii, corrected for eight nearest neighbors, were used for silver, gold, and the polyvalent metals.

The effect of core potential of the solute atoms is very clearly shown in Fig. 13 by the large displacement of the silver and gold, which are identical in size and charge, from the line representing the change in resistivity which was initially ascribed only to size differences between the alkali metal solutes. Therefore, since the effect of ion core properties is relatively large, it is probable that some part of the increment in resistivity produced by the alkali solutes is also due to differences in core properties, and it is clearly necessary to separate the two effects.

A semiempirical separation of the effect of the

TABLE VI. Atomic radii and effective scattering charge of solutes in liquid sodium.

Element	$r\times10^8$ cm[a]	$(\Delta V/V)$	$(\Delta V/V)^2$	$(\Delta N)^2$
Li	1.57	−0.445	0.20	0.20
Na	1.91	...	...	...
K	2.32	+0.794	0.63	0.63
Rb	2.48	+1.195	1.43	1.43
Cs	2.65	+1.675	2.81	2.81
Ag	1.40	−0.61	0.37	0.37
Au	1.40	−0.61	0.37	0.37
Cd	1.48	−0.54	0.29	2.37
Pb	1.69	−0.30	0.11	10.90
Sn	1.54	−0.48	0.23	12.10
Hg	1.50	−0.51	0.26	2.24

[a] Radii for alkali metals from neutron diffractions in liquid state,[29] all others are crystal radii corrected for 8 nearest neighbors.

[29] S. S. Sidhu, L. Heaton, and M. H. Mueller, J. Appl. Phys. **30**, 1323 (1959).

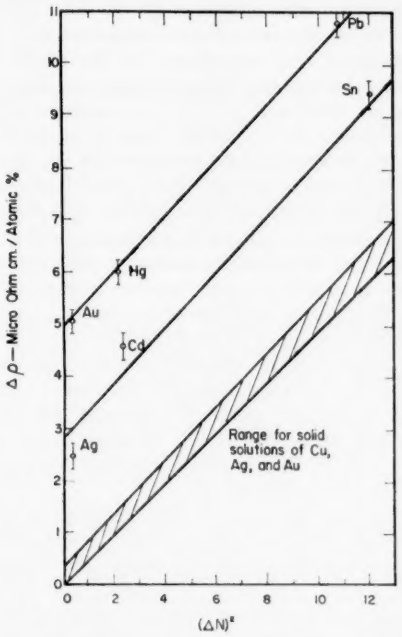

FIG. 14. The increment in resistivity, per atomic percent solute at 100°C, as a function of $(\Delta N)^2=(Z-1-\Delta V/V)^2$. The range of values for copper, silver, and gold solid-solutions correlated by Blatt,[27,28] fall within the shaded band.

differences in ion core properties from the effect of dilation on local charge density can be obtained from the modified form of Linde's expression for the charge dependence of resistivity. The constant b is taken as a measure of the localized charge difference due to the dilation alone; a is taken as a measure of the difference in ion core field between solvent and solute. Both constants can be evaluated from a consideration of the dependence of the resistivity increment on effective charge, assuming an apparent chemical valence for polyvalent solutes.

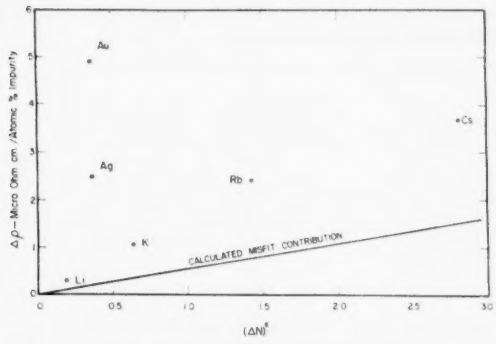

FIG. 15. The calculated misfit contribution to the resistivity of liquid sodium solutions, derived from Fig. 14, is shown as a function of ΔN^2 and compared with the measured increment in resistivity due to both misfit and the ion core field of the alkali solutes.

TABLE VII. Contributions to resistivity of liquid sodium solutions from dilation and ion core field.

Solute	$\Delta\rho$ (Total) μ ohm cm/atom%	$\Delta\rho$ (Misfit) $0.53\,(\Delta V/V)^2$	$\Delta\rho$ (Field) $\Delta\rho$ Total$-\Delta\rho$ misfit
Li	0.28	0.10	0.18
K	1.02	0.33	0.69
Rb	2.55	0.76	1.79
Cs	3.64	1.50	2.14
Ag	2.50	0.20	2.30
Au	4.80	0.20	4.60

Figure 14 shows the results of the present work, and the one previously available value for mercury in liquid sodium,[30] as a function of $(\Delta N)^2$. Included in Fig. 14 for comparative purposes is the range of data for copper, silver, and gold solid-solutions, in each other and also containing multivalent solutes, as correlated by Blatt.[27,28] It is evident that the increments in resistivity produced by solutes from the same row of the periodic table, namely silver, cadmium, and tin, from one row and gold, mercury, and lead, from another row, fall on separate, parallel lines which, it is interesting to note, are approximately parallel to the solid-state data.

The misfit contribution, obtained from the slope of the lines for liquid solutions in Fig. 14, is $\Delta\rho=0.53\,(\Delta V/V)^2$, which is shown in Fig. 15, together with the data for alkali solutes.

The magnitude of the increment in resistivity due to differences in ion core potential between sodium and the alkali solutes, is obtained by taking the difference between the total measured increment in resistivity (Fig. 15) and the derived misfit contribution. The results are given in Table VII.

Employing $\Delta\rho$ (field) and the relationship applying to monovalent solid solutions,[25] it is of some interest to calculate $U_0(\bar{\mu}_B^{-2}/\bar{\mu}_0^{-2})$ for the monovalent solutes

TABLE VIII. Calculated parameters in the expression for the resistivity of a solution.

Solute element	$U_0(\bar{\mu}_B^2/\bar{\mu}_0^2)$ ev	$(\bar{\mu}_B^2/\bar{\mu}_0^2)$
Li	0.67	1.69
K	1.32	...
Rb	2.12	...
Cs	2.32	...
Ag	2.40	1.13
Au	3.40	1.07

[30] A. L. Norbury, Trans. Faraday Soc. **16**, 570 (1921).

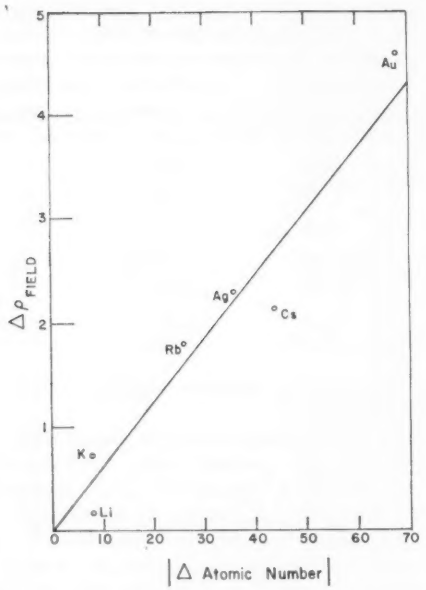

FIG. 16. Increment in resistivity due to the difference in field between solute and solvent as a function of the differences in atomic number of solute and sodium.

from the present data, and to estimate $(\bar{\mu}_B^{-2}/\bar{\mu}_0^{-2})$ from the known energies of the lowest electronic states in metallic silver,[24] gold,[24] sodium,[31] and lithium[32] (Table VIII) even though the exact interpretation to be placed upon these values is uncertain in the absence of a thorough reconsideration of the partially periodic state of liquids and liquid solutions.

Recently some consideration has been given to the problem of scattering in liquid solutions by Daniel[33] who, by employing Friedel's theory of phase shifts,[34] calculated the increment in resistivity of sodium solutions containing alkali solutes, silver, and gold, and also the Knight shift of sodium for the same solutions. The calculated change in the two properties is in excellent agreement with experiment for the alkali metal solutions; however, the corresponding calculations for solutions of silver and gold in liquid sodium indicate that the theory, in its present form, is unable to account for the experimental results when the ion core potentials of solvent and solute are greatly different.

The effect of the field differences between solvent and solute are shown in Table VII, where it is evident that the increment in resistivity increases with increasing difference in atomic number between sodium and the solutes. This increment is shown in Fig. 16 as a linear function of the absolute value of the difference in atomic number from which the constant a in the empirical relationship for the total resistivity increment may be obtained. Thus, the complete expression for the resistivity increment, per at. % of monovalent solute in liquid sodium, is $\Delta\rho = 0.063\,|\,\Delta\text{Atomic Number}\,| + 0.53(\Delta V/V)^2$ μohm cm/at. %.

In conclusion, the three factors contributing to the resistivity of a monovalent, metallic, liquid-solution, have been separated and experimentally evaluated. The fact that a separation is possible, and to some extent justified in terms of ideas and relationships developed for application to solid solutions, can be interpreted to mean that the most significant feature of the scattering process is the *difference* between the solute and the surrounding solution. The absence of long-range order in liquid solutions defines the absolute value of resistivity in the liquid state; within this state, the scattering process in liquid solutions is not primarily dependent on long-range periodicity, but on definable types of deviation from the uniformly aperiodic background of the liquid.

ACKNOWLEDGMENTS

One of the authors, J.F.F., is indebted to the Dow Chemical Company and the General Electric Foundation for the award of Fellowships. Both authors are indebted to the Atomic Energy Commission for their support of this investigation.

[31] E. Wigner and F. Seitz, Phys. Rev. **43**, 804 (1933).
[32] F. Seitz, Phys. Rev. **47**, 400 (1935).
[33] E. Daniel, J. Phys. Chem. Solids **13**, 353 (1960).
[34] J. Friedel, Advances in Phys. **3**, 446 (1954).

Analysis of Specific Heat Data for Zinc. Resolution of the Calorimetric and Elastic Θ_0 Discrepancy*

C. W. GARLAND AND J. SILVERMAN†

Department of Chemistry and Research Laboratory of Electronics, Massachusetts Institute of Technology, Cambridge, Massachusetts

(Received August 29, 1960)

The low-temperature heat capacity of zinc (in the normal state) has been expressed by $C_v=\gamma T+\alpha T^3+\beta T^5$ over the range from 0.15°K to about 8°K. The new parameters obtained are: $\gamma=1.56\times10^{-4}$ cal/deg² mole, $\alpha=1.39\times10^{-5}$ cal/deg⁴ mole, and $\beta=2.44\times10^{-7}$ cal/deg⁶ mole. The calorimetric Debye temperature, $\Theta_0{}^C$, is found to be 322°K which is in reasonable agreement with the elastic value, $\Theta_0{}^E$, of 328°K. The apparent disagreement between $\Theta_0{}^C$ and $\Theta_0{}^E$ values cited in the literature arises from the difficulty in analyzing the calorimetric data for a very anisotropic metal.

DEBYE characteristic temperatures calculated from low-temperature heat capacities, $\Theta_0{}^C$, are usually in excellent agreement[1] with those calculated from elastic constants extrapolated to 0°K, $\Theta_0{}^E$. Recently, however, discrepancies have been reported for vanadium,[2] beryllium,[3] cadmium,[4] magnesium,[5] and zinc.[6] (Except for vanadium, all of these metals have hexagonal close-packed structures.) Alers[2] has suggested that the low-temperature specific heat of vanadium has a T^3 contribution in addition to the lattice T^3 term. Warren and Ferrell[7] have postulated an electronic relaxation effect, caused by electron-phonon interactions, which would tend to make $\Theta_0{}^C>\Theta_0{}^E$, but only magnesium shows this type of disagreement. It is our feeling that these discrepancies may not be real, and that they may arise from the treatment of the low-temperature specific-heat data, especially for anisotropic metals such as zinc and cadmium.

Since zinc has been thoroughly studied, it is an excellent choice for critical evaluation. Two independent measurements of the low-temperature elastic constants[6] are in good agreement, and yield a $\Theta_0{}^E$ value of 328°±3°K. The heat capacity has been measured in considerable detail[8–12] from 0.15° to 20°K. The best specific-heat data for obtaining $\Theta_0{}^C$ are those of Keesom and Seidel,[8] who reported a value of 309°±4°K. Their data agree well with those of other observers and are presented in a table of 44 unsmoothed data points in the range 1°–4°K (in contrast with other data that are presented graphically, or as smoothed equivalent Debye Θ values).

Keesom and Seidel carried out a least-squares fit of their data for zinc (in the normal state), using the formula

$$C_v=\gamma T+\alpha T^3+\beta T^5, \tag{1}$$

in which the linear term is the usual electronic contribution, and the lattice heat capacity includes a T^5 term that is often neglected but should not be for zinc. The coefficient α is proportional to $({}_0\Theta^C)^{-3}$. They obtained the following parameters: $\gamma=(1.53\pm0.02)\ 10^{-4}$ cal/deg² mole, $\alpha=(1.58\pm0.06)\ 10^{-5}$ cal/deg⁴ mole, (or $\Theta_0{}^C=309°\pm4°$K), and $\beta=(0.93\pm0.33)\ 10^{-7}$ cal/deg⁶ mole. However, a more recent measurement at lower temperature (0.15°–1.1°K) by Phillips,[9] which should presumably give a more reliable value of the electronic term, yields $\gamma=(1.58\pm0.016)\ 10^{-4}$ cal/deg² mole.

The data of Keesom and Seidel are plotted in Fig. 1 in the form $(C_v-\gamma T)/T^3$ vs T^2. This should give a linear plot with α as the intercept and β as the slope if Eq. (1) is obeyed. In the lower half of this figure, the data are plotted with Keesom and Seidel's value of γ (closed circles), and also with Phillips' value of γ (open circles). At the low-temperature end, both sets of points show systematic deviations from a straight line, but in opposite directions. An intermediate value of γ equal to 1.56×10^{-4} cal/deg² mole (which is just outside the limit of uncertainty in the Phillips value) is assumed for the plot in the upper half of Fig. 1. This plot shows a random scatter about a straight line at the low-temperature end, but no systematic deviation. The dashed line in Fig. 1 represents the least-squares parameters of Keesom and Seidel, and the solid line is the best fit to the data plotted with $\gamma=1.56\times10^{-4}$. The other parameters for this new way of fitting the data are $\alpha=1.39\times10^{-5}$ cal/deg⁴ mole (which gives $\Theta_0{}^C=322$°K), and $\beta=2.44\times10^{-7}$ cal/deg⁶ mole. In the least-squares sense, the Keesom and Seidel parameters are obviously much better. Their parameters depend,

* This work was supported in part by the U. S. Army (Signal Corps), the U. S. Air Force (Office of Scientific Research, Air Research and Development Command); and the U. S. Navy (Office of Naval Research); and in part by the Alfred P. Sloan Foundation.

† Present address: Department of Analytical and Inorganic Chemistry, Municipal University of Amsterdam, Amsterdam, Netherlands.

[1] G. A. Alers and J. R. Neighbours, Revs. Modern Phys. **31**, 675 (1959).
[2] G. A. Alers, Phys. Rev. **119**, 1532 (1960).
[3] J. F. Smith and C. L. Arbogast, J. Appl. Phys. **31**, 99 (1960).
[4] C. W. Garland and J. Silverman, Phys. Rev. **119**, 1218 (1960).
[5] L. J. Slutsky and C. W. Garland, Phys. Rev. **107**, 972 (1957); S. Eros, U. S. Atomic Energy Commission Tech. Rept. No. 7, Case Institute of Technology, Cleveland, Ohio (December, 1959).
[6] C. W. Garland and R. Dalven, Phys. Rev. **111**, 1232 (1958); G. A. Alers and J. R. Neighbours, Phys. and Chem. Solids **7**, 58 (1958).
[7] J. L. Warren and R. A. Ferrell, Bull. Am. Phys. Soc. Ser. II, **3**, 226 (1958).
[8] G. Seidel and P. H. Keesom, Phys. Rev. **112**, 1083 (1958).
[9] N. E. Phillips, Phys. Rev. Letters **1**, 363 (1958).
[10] P. L. Smith, Phil. Mag. **46**, 744 (1955).
[11] T. M. Scrinivasan, Proc. Indian Acad. Sci. **49**, 61 (1959).
[12] W. H. Keesom and J. N. van den Ende, Proc. Koninkl. Ned. Akad. Wetenschap. **35**, 143 (1932).

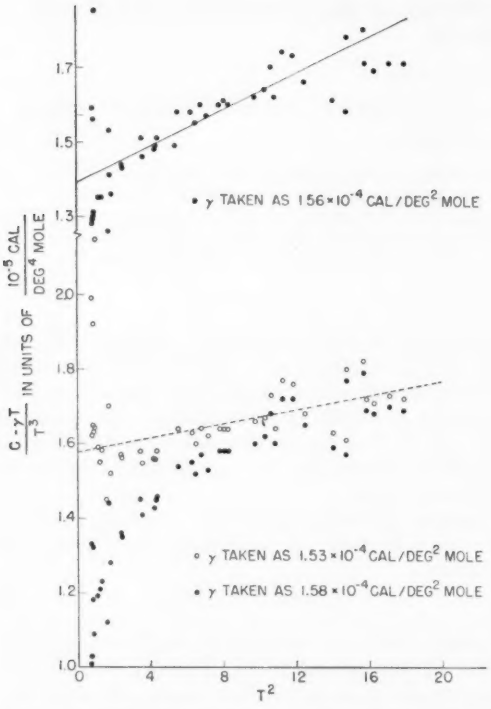
γ TAKEN AS 1.56×10⁻⁴ CAL/DEG² MOLE
γ TAKEN AS 1.53×10⁻⁴ CAL/DEG² MOLE
γ TAKEN AS 1.58×10⁻⁴ CAL/DEG² MOLE
(C_v−γT)/T³ IN UNITS OF 10⁻⁵ CAL/DEG⁴ MOLE
T²

FIG. 1. Specific-heat data of Keesom and Seidel for zinc plotted as $(C_v-\gamma T)/T^3$ vs T^2. (See text for explanation.)

however, on the assumption inherent in a least-squares treatment that the *absolute* accuracy is the same for all points throughout the temperature range covered. This means that the high-temperature points, which are rather badly scattered, dominate in determining the fit. In an average deviation sense, the two sets of parameters are quite comparable. For all of the 44 data points the average percentage difference between the measured heat capacity and that calculated from the three parameters is 1.1% for the Keesom and Seidel parameters, and 1.3% for our new parameters.

The new β value appears to be quite reasonable when we look at higher-temperature data. Figure 2 shows a plot of $(C_v-\gamma T)/T^3$ from $T^2=16°K^2$ to $400°K^2$ which includes data calculated from the smooth Θ values given by Smith[10] and the unsmoothed data of Keesom and Ende.[12] In Fig. 2 the solid and dashed lines are the same as those shown in Fig. 1. The solid line (based on the new parameters) indicates that Eq. (1) will represent the heat-capacity data for zinc from 0°K to approximately 8°K. The dashed line (based on the Keesom and Seidel parameters) would indicate that lattice heat capacity terms in higher odd powers of T are important at temperatures as low as 5°K. If this

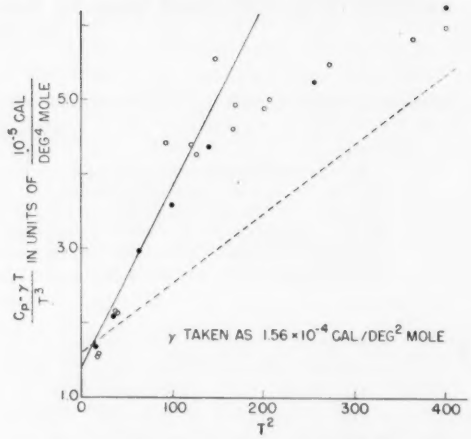

FIG. 2. $(C_v-\gamma T)/T^3$ vs T^2 in the range from 4° to 20°K. The solid and the dashed line are those shown in Fig. 1, extended to 20°K. Points represented by closed circles (●) were calculated from the smooth Θ values of Smith; the open circles (○) represent the data of Keesom and Ende.

were true, the plot in Fig. 2 should show considerable curvature at the low-temperature end.

To summarize, the new parameters γ, α, and β, chosen to represent the specific heat of zinc, seem to be preferable to those previously reported because: (1) the new γ agrees more closely with the value determined by Phillips at very low temperatures, and the data plotted in Fig. 1 show no systematic deviation at the low-temperature end when this value of γ is used; (2) the new β is in better agreement with data at higher temperatures; and (3) the new α yields 322°K for Θ_0^C, and this now agrees with Θ_0^E (328°K) within the limits of experimental error.

Thus, it would appear that there is no significant discrepancy between Θ_0^C and Θ_0^E for zinc, and that the reported apparent disagreement may be attributed to the difficulty in analyzing the low-temperature heat capacity of a very anisotropic metal. If our analysis is correct for zinc, it certainly should apply for cadmium, which is very similar to zinc in structure and elastic properties. A value of 213°±1°K has been obtained recently for Θ_0^E; the reported value[11,13] of Θ_0^C is 188°K. Thus the apparent disagreement for cadmium is much like that for zinc. Unfortunately, the very low temperature specific heat, which would provide the best value of γ, is not well known for cadmium.[14] Also, unsmoothed data in the 1°–4°K region are not available, and these are vital to the kind of analysis presented here.

[13] P. L. Smith and N. M. Wolcott, Phil. Mag. **1**, 854 (1956).
[14] B. N. Samoilov, Doklady Akad. Nauk S.S.S.R. **86**, 281 (1952).

Infrared Spectra of Alkyldiboranes. V. Tri- and Tetramethyl- and Ethyldiboranes

WALTER J. LEHMANN,* CHARLES O. WILSON, JR.,† AND I. SHAPIRO*

Chemistry Department, Hughes Tool Company—Aircraft Division, Culver City, California

and

Research Laboratory, Olin Mathieson Chemical Corporation, Pasadena, California

(Received September 12, 1960)

Frequency assignments are reported for the infrared spectra of tri- and tetramethyl- and ethyldiboranes, together with some of their boron-deuterated and B^{10} isotopic derivatives. Additionally, a Raman spectrum of tetramethyldiborane from sources in the literature is analyzed. In assigning some of the B–C stretching frequencies, use is made of the recently formulated Average Rule.

INTRODUCTION

WHILE trialkyldiboranes are relatively stable, the tetraalkyldiboranes disproportionate so rapidly, forming trialkyldiborane and trialkylborane, that it is difficult to obtain gas-phase spectra of pure tetraalkyldiboranes. For this reason, we combine the examination of the spectra of tri- and tetraalkyldiboranes.

In tetraalkyldiboranes the maximum number of alkyl groups have been introduced into the original diborane molecule, only terminal hydrogens being replaceable.[1] Since in tetramethyldiborane the BH_2B bridge has remained intact and since this molecule has the same symmetry as diborane, this alkyl compound can be used to verify assignments for bridge vibrations of diborane.[2–5] The vibrational analysis of tetramethyldiborane is facilitated by availability of its liquid-state Raman spectrum.[6]

EXPERIMENTAL

The room-temperature reaction of methyldiboranes with excess trimethylborane resulted in a mixture containing tri- and tetramethyldiboranes. The mixture was distilled through a U tube at −95°C with pumping to remove any unreacted trimethylborane and mono- and dimethyldiboranes. The condensate then was passed through a trap at −90°C, and the trimethyldiborane was collected at −95°C. The corresponding distillation temperatures for the tetra-compound were −65°C and −80°C.

Tri- and tetraethyldiboranes were obtained as by-products of the preparation of triethylborane, by reaction of ethylene and diborane in a 6:1 molar ratio.[7] Triethyldiborane was collected at −35°C after passage through a −23°C trap (slush of CCl_4). The condensate from the −23°C trap was passed through a −5°C trap with pumping. The residue in the −5°C trap was tetraethyldiborane. We found it difficult to remove all vestiges of the tetra-compounds from the triethyldiboranes because of their similar vapor pressures (0.5 and 4 mm at 0°C, respectively).[8]

Tri- and tetraalkyldiboranes at room temperature do not decompose with the evolution of hydrogen and formation of polymeric solids. However, they do disproportionate. Within several hours 1,2-dimethyldiborane and tetramethyldiborane were observed to a considerable extent in the spectrum of trimethyldiborane. After about one week 1,1-dimethyldiborane also became evident. With triethyldiborane, 1,1-diethyldiborane was visible within 24 hrs; other ethyldiboranes were difficult to detect because of overlapping absorption bands.

Tetraalkyldiboranes disproportionate even more rapidly. Within minutes, or even seconds, trialkylborane and trialkyldiborane appeared in the spectra of both tetramethyl- and tetraethyldiboranes. Within approx. one-half hour, much of the tetra-compound thus disappeared, accompanied by an appropriate increase in sample pressure, according to the equation[9]

$$3R_4B_2H_2 \leftrightarrows 2R_3B + 2R_3B_2H_3.$$

Infrared spectra were recorded on a Perkin-Elmer model 21 spectrophotometer equipped with sodium chloride optics. The spectra of tri- and tetramethyl-

* Present address: Chemistry Department, Hughes Tool Company—Aircraft Division, Culver City, California.

† Present address: National Engineering Science Company, Pasadena, California.

[1] H. I. Schlesinger and A. O. Walker, J. Am. Chem. Soc. **57**, 621 (1935).

[2] R. C. Lord and E. Nielsen, J. Chem. Phys. **19**, 1 (1951).

[3] D. A. Brown and H. C. Longuet-Higgins, J. Inorg. & Nuclear Chem. **1**, 352 (1955).

[4] R. C. Taylor and A. R. Emery, Spectrochim. Acta **10**, 419 (1958).

[5] W. J. Lehmann, J. F. Ditter, and I. Shapiro, J. Chem. Phys. **29**, 1248 (1958); also see W. J. Lehmann and J. F. Ditter, *ibid.* **31**, 549 (1959).

[6] B. Rice, J. M. Gonzalez Barredo, and T. F. Young, J. Am. Chem. Soc. **73**, 2306 (1951); also, B. Rice, T. F. Young, and J. M. Gonzalez Barredo, Anales real. soc. espan. fis. y quim. (Madrid) **48B**, 191 (1952).

[7] W. J. Lehmann, C. O. Wilson, and I. Shapiro, J. Chem. Phys. **28**, 781 (1958).

[8] H. I. Schlesinger, L. Horvitz, and A. B. Burg, J. Am. Chem. Soc. **58**, 407 (1936).

[9] For mnemonic purposes, the disproportionation process can be pictured as symmetric cleavage across the hydrogen bridge followed by disproportionation of the fragments,

$$R_4B_2H_2 \leftrightarrows 2R_2BH \leftrightarrows R_3B + RBH_2.$$

An RBH_2 fragment then combines with an R_2BH fragment to form $R_3B_2H_3$.

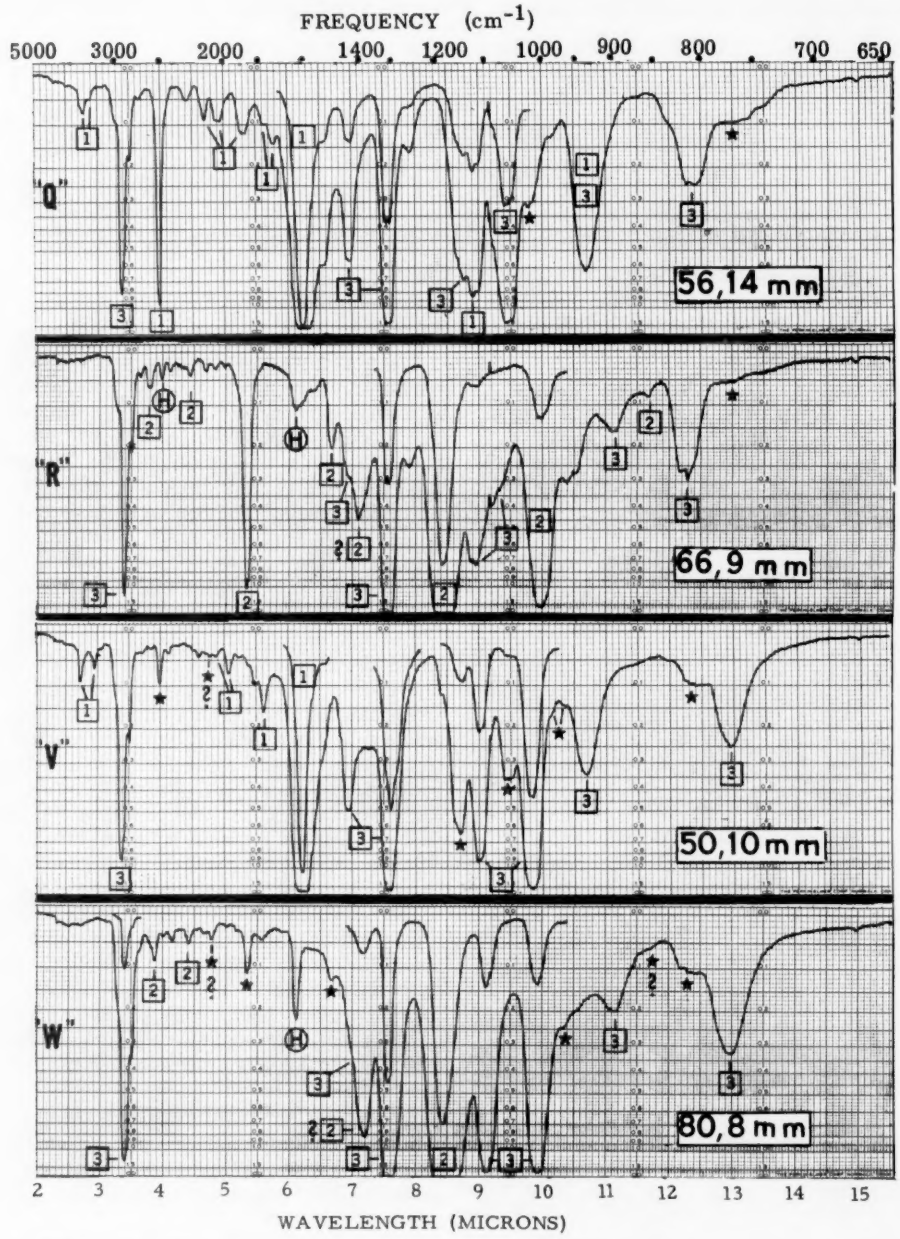

FIG. 1. Infrared spectra of tri- and tetramethyldiboranes; pressures reported for 5-cm cells.

"*Q*" – $(CH_3)_3B_2H_3$ [1] – B_2H_x (H) protium-impurity bands

"*R*" – $(CH_3)_3B_2D_3$ [2] – B_2D_x

"*V*" – $(CH_3)_4B_2H_2$ [3] – CH_3 * impurity

"*W*" – $(CH_3)_4B_2D_2$

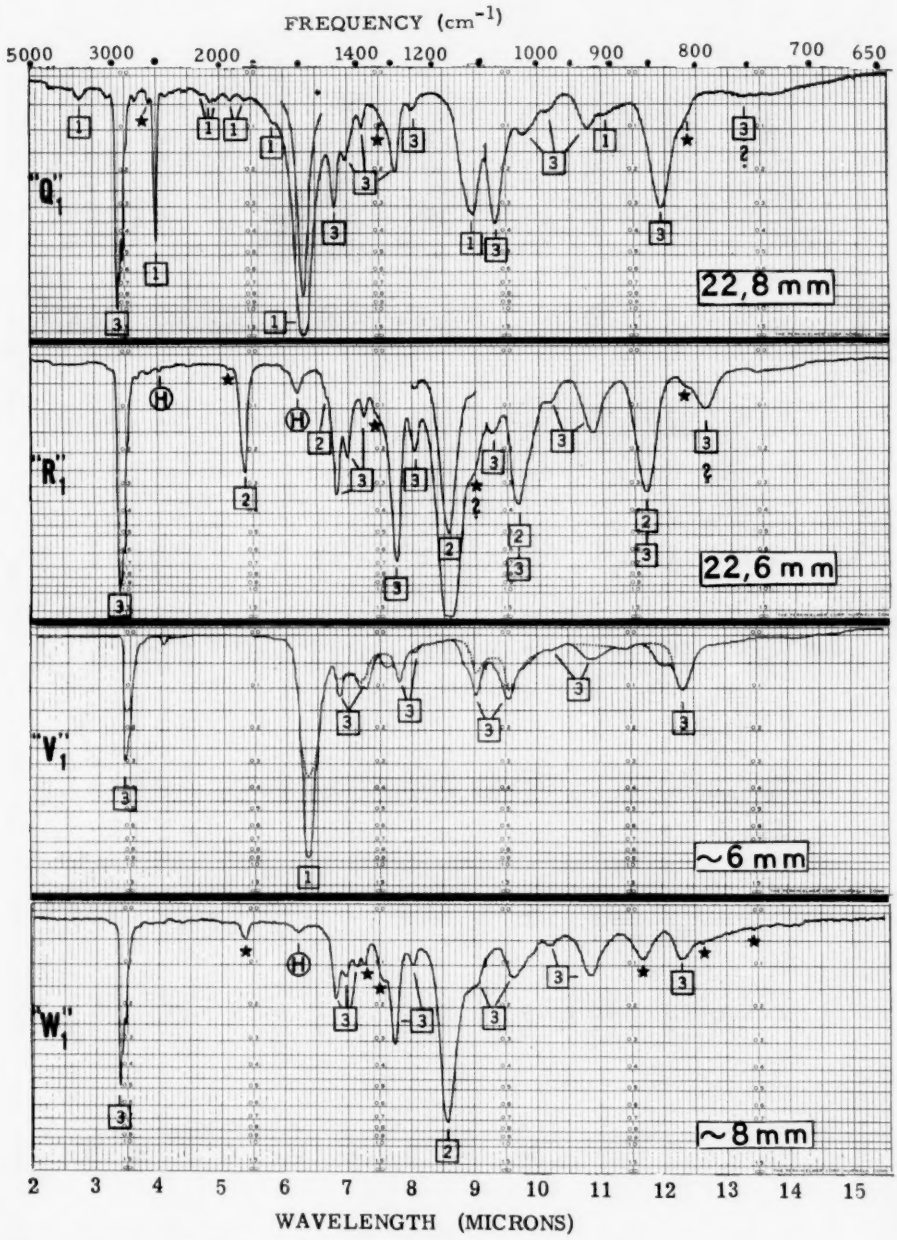

FIG. 2. Infrared spectra of tri- and tetraethyldiboranes; pressures reported for 5-cm cells.

"Q_1" – $(C_2H_5)_3B_2H_3$ [1] – B_2H_x (H) protium-impurity bands

"R_1" – $(C_2H_5)_3B_2D_3$ [2] – B_2D_x

"V_1" – $(C_2H_5)_4B_2H_2$ [3] – C_2H_5 * impurity

"W_1" – $(C_2H_5)_4B_2D_2$

TABLE I. Infrared bands of tri- and trimethyldiboranes.

"P" $(CH_3)_3B_2{}^{10}H_3$	"Q" $(CH_3)_3B_2H_3$		"R" $(CH_3)_3B_2D_3$		"U" $(CH_3)_4B_2{}^{10}H_2$	"V" $(CH_3)_4B_2H_2$		"W" $(CH_3)_4B_2D_2$		Assignments[b]
cm^{-1}	cm^{-1}	intensity[a]	cm^{-1}	intensity[a]	cm^{-1}	cm^{-1}	intensity[a]	cm^{-1}	intensity[a]	
3676	3663	sh			3676	3663	(38)			—B_2H_2 (combination)
3623	3623	(28)								—B_2H_3 (combination)
3484	3472	(18i)			3460	3448	sh			—B_2H_x (combination)
					3401	3390	(26)			—B_2H_2 (combination)
3279	3279	w								—B_2H_3 (combination)
3030	3030	sh	3030	sh	3030	3049	sh	3030	sh	
2941	2941	(320)	2950	(350)	2958	2958	(350)	2950	(300)	CH_3 stretch. asym.
						~2924	sh	~2924	sh	
2841	2841	s pip	2841	s pip	2849	2841	s pip	2849	s pip	CH_3 stretch. sym.
2740	2725	(16)	2725	(12)	2717	2688	w			
			2625	(19)				2580	(21)	—B_2D_x (combination)
						2597	w			
2506	2506	(370)	2506	(14)	2512	2506	(38)	2500	w	B—H stretch. of "P", "Q"; imp. in others
					2469	2427	(15)			
								2404	(12)	
2288	2273	(18)								
			2247	(11)				2262	(13)	—B_2D_x (combination)
					~2175	2174	(18)	2160	(9)	
			2132	(9)						
2123	2119	(27)								B—H′ sym. in-phase
					2101	2096	(18)	2096	(11)	part. imp.?
2058	2050—		2070	(9)	2049	2049	(18)			—B_2H_x
2024	—2020	(28) b								—B_2H_3
			1996	w	1976	1972	(30)	1996	w	B—H′ sym. out-of-phase in "U", "V"?
					?	1912	w	1938	(7)	
1898	1880	(40) b								B—H′ sym. out-of-phase
			1876	(300)				1876	(27)	B—D stretch. of "R"
					1828	1825	pip	1795	(11)	
1786	1780	(34i)			1786	1779	(64)			—B_2H_x
1748	1730	(48i)								B—H′ asym. out-of-phase
			1634	(30)				1637	(56)	B—H′ (single) asym. (protium imp.)
1608	1605	(2200)			1608	1605	(~2200)			B—H′ asym. in-phase
1562	1562	vwsh	1562	(20i)						
1538	1534	sh								
			1497	(53)				1499	(32)	all or part "R": B—D′ sym. in-phase

TABLE I—Continued

"P" $(CH_3)_3B_2{}^{10}H_3$	"Q" $(CH_3)_3B_2H_3$		"R" $(CH_3)_3B_2D_3$		"U" $(CH_3)_4B_2{}^{10}H_2$	"V" $(CH_3)_4B_2H_2$		"W" $(CH_3)_4B_2D_2$		Assignments[b]
cm^{-1}	cm^{-1}	intensity[a]	cm^{-1}	intensity[a]	cm^{-1}	cm^{-1}	intensity[a]	cm^{-1}	intensity[a]	
1435	1437	(190) b	1439	sh	1433	1437	(200)	~1430	sh	CH_3 def. asym.
			1404	(125)				1389	(210)	$-B_2D_x$ (combination)
1400	1400	wsh								
	1315		1318			1324				
1319	1323	(520)	1327	(670)	1318	1312	(1000)	1321	(1100)	CH_3 def. sym.
1266	1266	(60)	1266	w	1266	1260	wb			
			1183	(1650)				1186	(1750)	B—D′ asym. in-phase
					1189	1190	sh			also Me_3B
1174	1147	(260i)	1120	(200i) B	1174	1147	(260)			BC_2 stretch. asym. of "P", "Q", "R" imp. contributes in "U" and "V"
~1140	~1122	(320i) A?								BH in-plane bend.
	1110	sh			1139	1111	(400)	1096	(350)	BC_2 stretch. asym.
	1080	wsh								
~1078	~1055	(380) A?	~1075[c]	bsh	~1075	1055	(145) A			CH_3 rock. of "P", "Q", "R"
1029	1020	(120i)			1031	1017	(860)	1007	(340)	CH_3 rock. of "U", "V" and "W"
			998[d]	(300) A						BD in-plane bend.
1000	985	sh			985	985	sh			
						966	(60)	966	sh	Me_3B imp.
			962							
			950	ssh				950	sh	"R" only?
941	935	(200) A?	899	(44)	939	935	(140)	897	(50)	CH_3 rock? and BH out-of-plane bend. in "P", "Q"
						875	w			
			855	(25)						BD out-of-plane bend.
								858	sh	Me_3B imp.?
837	833	wbsh								
813	810	(78)	813	(77) A	810	806	(40)	810	(25)	BC_2 stretch. sym. of "P", "Q", "R"
777	772	bsh	770	wb	777	772	(100)	770	(80)	BC_2 stretch. sym. of "U", "V", "W"
~745	~745	(20)								
						590[e]	w			

[a] Approximate intensities expressed as absorbance$\times 10^6$ divided by cell length in centimeters and sample pressure in millimeters. Abbreviations: w=weak, s= strong, sh=shoulder, b=broad, v=very; i=apparent intensity increased by overlap with other band(s); *A*, *B*, *C*=apparent band types.

[b] B—H′ and B—D′ refer to bridge stretchings.

[c] Probably shifted by Fermi resonance from approx. 1045 cm^{-1}.

[d] Probably shifted by Fermi resonance from approx. 1030 cm^{-1}.

[e] Reported by R. D. Cowan (private communication).

TABLE II. Infrared bands of tri- and tetraethyldiboranes.

"P_1" $(C_2H_5)_3B_2{}^{10}H_3$	"Q_1" $(C_2H_5)_3B_2H_3$		"R_1" $(C_2H_5)_3B_2D_3$		"U_1" $(C_2H_5)_4B_2{}^{10}H_2$	"V_1" $(C_2H_5)_4B_2H_2$		"W_1" $(C_2H_5)_4B_2D_2$		Assignments[b]
cm^{-1}	cm^{-1}	intensity[a]	cm^{-1}	intensity[a]	cm^{-1}	cm^{-1}	intensity[a]	cm^{-1}	intensity[a]	
3597	3584	(27) b								—B_2H_x (combination)
3106	3106	(40)								
2958	2958	(870)	2950	(900)	~2958	~2958	(750)	~2958	(800)	CH_3 stretch. asym.
2932	2915	(600i)	2924	sh						CH_2 stretch. asym.
2890	2882	(480i)	2874	pip						CH_3 stretch. sym.
2849	2841	wsh	2841	wsh						CH_2 stretch. sym.
2732	2732	(40)	2725	(35)						—B_2D_3 (combination)
			2611	(30)						
...	2577	(45i)								imp. ($Et_2B_2H_4$)
2512	2500	(400)	2481	(25)						B—H stretch.
2427	2410	w								
2119	2115	w								B—H′ sym. in-phase
2053	2058	(45)								—B_2H_3
2028	2024	(40)								—B_2H_3
			1953	sh						v. sl. imp. ($Me_2B_2D_4$)
1934	1930	(40)								B—H′ sym. out-of-phase?
			1862	(230)						B—D stretch.
1859	1852	(40)								B—H′ sym. out-of-phase?
1718	1709	sh								B—H′ asym. out-of-phase
			1610	(64)				1610	(100)	B—H′ (single) (protium imp.)
1590	1582	(1600)			1582	1582	(1800)			B—H′ asym. in-phase
			1515	sh						B—D′ sym. in-phase
			1504	sh						
1473	1470	(270)	1466	(300)	~1466	~1466	(~400)	~1470	(~400)	CH_3 asym. and CH_2 def.
1433	1435	(150i)	1433	(200i)	1433	~1435	ssh	~1435	ssh	
1383	1383	(90i)	1379	(110i)	~1400	~1400	(400i)	~1400	(330i)	CH_2 def. sym.
1324	1324	bsh	1337	bsh						v. sl. Et_3B imp.
1294	1289	(180)	1287	(600)	1287	1290	(420)	1290	(800)	CH_2 wag. and/or twist.
1247	1245	(55)	1245	(180)	~1230	~1220	w	1245	w	
			1166	(1600)				1166	(1500)	B—D′ asym. in-phase
			1117	bsh						prob. Et_3B imp.
1126	1114	(290)								BH in-plane bend.
1082	1072	(330)	1081	(95i)	1131	1109	(350)	1105	(~250) sh	BC_2 stretch. asym. (in-phase for "U_1", "V_1", "W_1")
1026	1024	(100i)	1033	(280)	1058	1047	(500)	1044	(400)	CH_3 rock., and BD bend. in "R_1"

TABLE II—Continued

"P_1" $(C_2H_5)_3B_2{}^{10}H_3$		"Q_1" $(C_2H_5)_3B_2H_3$		"R_1" $(C_2H_5)_3B_2D_3$		"U_1" $(C_2H_5)_4B_2{}^{10}H_2$	"V_1" $(C_2H_5)_4B_2H_2$		"W_1" $(C_2H_5)_4B_2D_2$		Assignments[b]
cm^{-1}		cm^{-1}	intensity[a]	cm^{-1}	intensity[a]	cm^{-1}	cm^{-1}	intensity[a]	cm^{-1}	intensity[a]	
988		985	(60) sh	985	(80) bsh	~980	~980	w	~980	w	CH_3 rock.
935		928	(90)	922	(140)	~925	~920	w	~920	w	C—C stretch; and B—C_1 stretch?
913		907	sh			881	881	w?			BH out-of-plane bend.
											BC_2 stretch. sym.; BD out-of-plane bend. in "R_1"
842		838	(280)	855	(290)						BC_2 stretch. sym. out-of-phase of "U_1", "V_1", "W_1"
820		813	bwsh	813	sh	820	814	(500)	813	(250)	CH_3 rock.?
				794	(90)						v. sl. $Et_2B_2D_4$ imp.
~755		755	wb	745	w						

[a] Approximate intensities expressed as absorbance×10; divided by cell length in centimeters and sample pressure in millimeters. Abbreviations: w=weak, s=strong, sh=shoulder, b=broad, v=very; *i*=apparent intensity increased by overlap with other band(s); *A*, *B*, *C*=apparent band types.

[b] B—H′ and B—D′ refer to bridge stretchings.

diboranes containing isotopically normal boron (including boron-deuterated compounds) are reproduced in Fig. 1, those of the corresponding ethyldiboranes are shown in Fig. 2. Our measured frequencies, including those of the B^{10}-enriched compounds, are listed in Tables I and II. The labeling scheme employed in previous papers of this series[10–13] is continued.

The only significant impurities in the trialkyldiboranes are small amounts of the corresponding tetraalkyldiboranes, most obviously apparent by shoulders at approx. 770 cm^{-1} for the methyl compounds and approx. 815 cm^{-1} for the ethyl compounds. For $Et_3B_2H_3$ a minimum intensity ratio (0.88 in our chart) of the 1114 cm^{-1} to the 1072 cm^{-1} bands was a simple preliminary criterion of purity [absence of $(EtBH_2)_2$ $Et_4B_2H_2$, and Et_3B]. The tetraalkyldiboranes disproportionate so rapidly that their spectra show appreciable absorption due to trialkyldiboranes and trialkylborane. These impurities are labeled in Fig. 1. In Fig. 2 the approximate absorptions of pure $Et_4B_2H_2$ are indicated by dotted lines. In both Figures assignments to the molecular fragments $-B_2H_x$, $-B_2D_x$, and $-CH_3$ or $-C_2H_5$ are indicated by numerals [1], [2], and [3].

On the basis of the present study, it seems that compensating techniques[5] can be used to obtain spectra of pure $R_4B_2H_2$. The sample cell would be filled with a mixture of $R_4B_2H_2$ and R_3B, the latter shifting the equilibrium away from $R_3B_2H_3$. The compensating cell would then contain R_3B alone, at the appropriate partial pressure needed to cancel its effect in the spectrum.

ASSIGNMENTS

The trimethyldiborane molecule presumably has a plane of symmetry through the C_2BBC atoms, resulting in point group[14] C_s. Both vibrational species, A' and A'', are Raman and infrared active. Similarly, all vibrations of triethyldiborane are Raman and infrared active, whether or not the molecule has a symmetry plane.

Tetramethyldiborane probably contains three mutually perpendicular planes of symmetry and thus belongs to point group D_{2h}, like diborane itself. (Even if partial rotation of the methyl groups were to reduce the actual symmetry of the molecule, the following treatment would still apply as an approximation to the $C_4B_2H_2$ skeleton.) The rule of mutual exclusion for Raman and infrared activity applies, due to the presence of a center of symmetry.[14] The 20 atoms have 54

[10] W. J. Lehmann, C. O. Wilson, and I. Shapiro, J. Chem. Phys. **32**, 1088 (1960), first paper of this series.

[11] W. J. Lehmann, C. O. Wilson, and I. Shapiro, J. Chem. Phys. **32**, 1786 (1960), second paper of this series.

[12] W. J. Lehmann, C. O. Wilson, and I. Shapiro, J. Chem. Phys. **33**, 590 (1960), third paper of this series.

[13] W. J. Lehmann, C. O. Wilson, and I. Shapiro, J. Chem. Phys. **34**, 476 (1961), fourth paper of this series.

[14] G. Herzberg, *Infrared and Raman Spectra of Polyatomic Molecules* (D. Van Nostrand Company, Inc., Princeton, New Jersey, 1945).

vibrational degrees of freedom, which may be roughly classified as skeletal (18), methyl rocking (8), C—H stretching (12), CH_3 deformation (12), and methyl twisting (4). By the term "skeletal" as used here, we mean the motions of the $C_4B_2H_2$ skeleton corresponding to the 18 vibrations of the B_2H_6 molecule.[5] It is expected that many of the "nonskeletal" vibrations are accidentally degenerate. In view of the large number of possible vibrations, their probable accidental degeneracy, and the limited frequency range of the infrared spectra, no detailed vibrational analysis is attempted but rather an assignment of observed lines and bands in terms of characteristic vibrations.

Assignment of the various hydrogen stretching bands is straightforward: the C—H bands (increasing in intensity as more alkyl groups are present in the molecule)[15] at approx. 2900, B–H (terminal) at 2500, B–D at 1870, B–H′ (asymmetric in-phase bridge sketching) at 1600, and B–D′ at 1180 cm^{-1}. The B–H (and B–D) bands are now sharp peaks, since only one terminal hydrogen is present in $R_3B_2H_3$, and they lie a few wave numbers lower than in 1,2-dialkyldiboranes as a result of the added alkyl group at the other end of the molecule. Although this decrease is small, diborane derivatives differ in this respect from ethylene derivatives, where ethylenic C—H stretching frequencies seem to be unaffected by alkyl groups on the other side of the double bond.[16] The fast growth of the 2500 cm^{-1} band (due to $R_3B_2H_3$) in the spectrum of tetraalkyldiboranes is indicative of the rapid rate of disproportionation.

The weak bands at approx. 2120 cm^{-1} in $Me_3B_2{}^{10}H_3$, $Me_3B_2H_3$, $Et_3B_2{}^{10}H_3$, and $Et_3B_2H_3$ represent the B–H′ symmetric in-phase vibration. This "breathing" vibration is infrared inactive in tetramethyldiborane and probably also in tetraethyldiborane, and no infrared band is observed in these spectra. However, a weak Raman line has been reported for $Me_4B_2H_2$ (Table III),[6] and we assign this line to the B–H′ breathing vibration. The corresponding B–D′ infrared bands are found in $Me_3B_2D_3$ and $Et_3B_2D_3$ at approx. 1500 cm^{-1}.

The B–H′ symmetric out-of-phase stretching vibration is probably responsible for the band at 1880 cm^{-1} in $Me_3B_2H_3$. That frequency is apparently shifted in $Et_3B_2H_3$ to 1852 cm^{-1}, which seems somewhat low when compared to 1915 cm^{-1} for diborane[2] or 1916–1957 cm^{-1} for other ethyldiboranes;[11–13] an alternative choice is the band at 1930 cm^{-1}. In $Me_4B_2H_2$ the 1972 cm^{-1} band is a logical choice for this assignment; no band is observed in the weak spectrum of $Et_4B_2H_2$. The corresponding B–D′ bands are seemingly masked by CH deformation absorptions. (The relatively conspicuous bands at 1404 cm^{-1} in $Me_3B_2D_3$ and 1389 cm^{-1} in $Me_4B_2D_2$ are too intense and of too low frequency to be the B–D′ bands in question; they might be $-B_2D_2$ bands, even though their parallel is not found in the ethyl compounds.)

Assignment of B–H′ asymmetric out-of-phase to 1730 cm^{-1} in $Me_3B_2H_3$ and to 1709 cm^{-1} in $Et_3B_2H_3$ is consistent with the pattern established by other alkyldiboranes. In tetramethyldiborane no suitable Raman line has been reported.

In the spectra of the boron-deuterated compounds, residual protium content is responsible for a band at approx. 1620 cm^{-1}, which represents the B—H′ (single) vibration of a partially deuterated bridge.

The various internal deformation modes of the methyl and ethyl groups give rise to bands at standard positions. The CH_3 symmetric and asymmetric deformation of the methyl compounds have their absorptions at approx. 1435 (medium) and 1320 cm^{-1} (strong), respectively. Both band intensities increase with increasing degree of alkylation. The latter band appears split by 8 or 9 cm^{-1} in $Me_3B_2H_3$, $Me_3B_2D_3$ and $Me_4B_2H_2$; a similar effect has been observed in hydrocarbons when more than one methyl group is attached to the same carbon.[15] The ethyldiboranes have their CH_3 asymmetric and CH_2 deformations together at approx. 1470 (*m*) and 1435 cm^{-1} (*w*), their CH_3 symmetric deformation (*w*) at approx. 1380 (triethyldiboranes) or 1400 cm^{-1} (tetraethyldiboranes), and their CH_2 wagging and twisting modes at approx. 1290 (*s*) and 1245 cm^{-1} (*w*).

The BC_2 asymmetric stretching bands, in the 1100–1170 cm^{-1} region of the methyl compounds, are easily recognized by their large (27 cm^{-1}) B^{10}-isotope shifts. In $Me_3B_2D_3$ the band at 1120 cm^{-1} exhibits B-type contours, as expected for such a vibration. These observations are in good agreement with those[13] for $Me_2B_2H_4$, where the BC_2 vibration occurs at 1126 cm^{-1} and is shifted to 1157 cm^{-1} in $Me_2B_2{}^{10}H_4$. Similarly, in trimethylborane[17,18] the BC_3 asymmetric stretching band is found at 1156 cm^{-1} and undergoes a B^{10} shift of 29 cm^{-1}.

In ethyl compounds, the B^{10} shift of this stretching vibration is somewhat smaller, e.g., 14 cm^{-1} in triethylborane,[7] 22 cm^{-1} in 1,1-diethyldiborane;[13] furthermore, the frequencies are 10–20 cm^{-1} lower. Hence, in triethyldiboranes we assign the bands at 1072–1082 cm^{-1} to the BC_2 asymmetric stretching vibration. (The 1114–1126 cm^{-1} bands in $Et_3B_2{}^{10}H_3$ and $Et_3B_2H_3$, are assigned to BH bending—see below.) In the tetraethyl compounds the 1105–1131 cm^{-1} bands are the only logical choice for assignment to BC_2 stretching.

The BC_2 symmetric stretching vibrations, occurring in $Me_2B_2H_4$ at 829 cm^{-1} and in $Et_2B_2H_4$ at 745 cm^{-1}, can be assigned to the medium-intensity bands in the

[15] L. J. Bellamy, *The Infrared Spectra of Complex Molecules* (John Wiley & Sons, Inc., New York, 1958).
[16] E. G. Hoffmann, Ann. Chem. Liebigs **618**, 276 (1958).
[17] W. J. Lehmann, C. O. Wilson, and I. Shapiro, J. Chem. Phys. **28**, 777 (1958).
[18] W. J. Lehmann, C. O. Wilson, and I. Shapiro, J. Chem. Phys. **31**, 1071 (1959).

TABLE III. Raman spectrum[a] and infrared-active fundamentals of tetramethyldiborane.[b]

Raman spectrum		Infrared fundamentals		
cm^{-1}	Intensity[c]	cm^{-1}	Intensity[c]	Assignment[d]
2985	vs			C—H stretch. asym.
		2958	s	C—H stretch. asym.
2952	vs			C—H stretch. asym.
		~2924	sh	C—H stretch. asym.
2885	m			C—H stretch. sym.
		2841	s pip	C—H stretch. sym.
2841	m			C—H stretch. sym.
2137	w			B—H′ sym. in-phase
1987	w			combination
		1972	w	B—H′ sym. out-of-phase
		1605	vs	B—H′ asym. in-phase
1445	w			CH_3 def. asym.
		1437	ms	CH_3 def. asym.
		1324 / 1312	s	CH_3 def. sym.
		1111	s	BC_2 stretch. asym. in-phase
1100	sb			BC_2 stretch. asym. out-of-phase
		1017	s	CH_3 rock.
1003	w			CH_3 rock.
		935	m	CH_3 rock.
844	mb			BC_2 stretch. sym. in-phase
		772	m	BC_2 stretch. sym. out-of-phase
651	w			combination (274+365=639)?
516	vs			B—B stretch.
365	w			BC_2 def. or BC_2 in-plane rock.
274	vw			CH_3 twist.

[a] Spectrum obtained by Rice, Gonzales Barredo, and Young (see work cited in footnote 6).
[b] Raman and infrared activity follows the rule of mutual exclusion.
[c] Abbreviations: w=weak, m=medium, s=strong, v=very, b=broad, sh=shoulder.
[d] Assignment of present authors.

770–855 cm^{-1} region of the various tri- and tetra-compounds under discussion (see Tables I and II). In isotopically normal di-, tri-, and tetramethyldiboranes, the frequencies are 829, 810, and 772 cm^{-1}, respectively.

In tetramethyldiborane, there actually are four BC_2 stretching modes, of which only two are expected to appear in the infrared spectrum, namely the asymmetric in-phase (b_{1u}) and the symmetric out-of-phase (b_{3u}) oscillations. The other two, the asymmetric out-of-phase (b_{2g}) and the totally symmetric in-phase (a_g) vibrations, should appear only in the Raman effect.

Considering the type of boron motion, and also from analogy with such compounds as C_2F_4,[19–21] we would expect the frequency of the Raman-active, asymmetric out-of-phase vibration to differ only slightly from that of the infrared-active asymmetric in-phase mode at 1111 cm^{-1}. There is then no doubt that the strong broad Raman line (broadened by the B^{10}-isotope effect) at 1100 cm^{-1} represents the asymmetric BC_2 mode.

The totally symmetric B–C stretching frequency should appear as a fairly strong line in the Raman spectrum. To choose between the two possible candidates, 844 and 516 cm^{-1} (see Table III), we resorted to our recently formulated[22] Average Rule.

Briefly, this method involves the following principle. When all other interactions can be neglected, the average of the symmetric and asymmetric stretching frequencies of an isolated XY_2 group is equal to the single stretching frequency of an $X-Y$ group. When applied to XY_3 groups, where the asymmetric stretching frequency is doubly degenerate, the *weighted* average is used. (The asymmetric frequency is counted twice.) Strictly speaking, mean values should be obtained from *squares* of frequencies, i.e., we should use root-mean-square values. However, in view of the approximations involved, the simpler averages are usually sufficient for most purposes. This scheme has been found applicable to a large number of compounds.[22]

The averages of the symmetric and asymmetric BC_2 stretching frequencies in $Me_2B_2H_4$ and $Me_3B_2H_3$ are 978 and 979 cm^{-1}, respectively. The weighted average for Me_3B is[17,18] 996 cm^{-1}. Using 516 cm^{-1} for the a_g vibration in $Me_4B_2H_2$, we obtain the too-low average of 875 cm^{-1} for the four vibrations, while adoption of 844 cm^{-1} leads to an acceptable average of 957 cm^{-1}. Further it should be noted that the average of 808 cm^{-1}, for the in- and out-of-phase symmetric stretches (844 and 772 cm^{-1}) is close to the observed BC_2 sym-

[19] D. E. Mann, L. Fano, J. H. Meal, and T. Shimanouchi, J. Chem. Phys. **27**, 51 (1957).
[20] D. E. Mann, N. Acquista, and E. K. Plyler, J. Research Natl. Bur. Standards **52**, 67 (1954).
[21] J. R. Nielsen, H. H. Claassen, and D. C. Smith, J. Chem. Phys. **18**, 812 (1950).
[22] W. J. Lehmann, Spectroscopia Mol. **9**, 62 (1960); details will be published elsewhere.

metric stretching frequencies in $Me_3B_2H_3$ (810 cm^{-1}) and $Me_2B_2H_4$ (829 cm^{-1}).

Just a few strong bands remain to be assigned. Through correlation with other alkyldiboranes[10-12] and by noting the various B^{10} shifts, we are able to assign the band at approx. 1120 cm^{-1} to the BH in-plane bending modes in $Me_3B_2H_3$ and $Et_3B_2H_3$. The corresponding BD vibration is found at 998 and 1033 cm^{-1} in $Me_3B_2D_3$ and $Et_3B_2D_3$, respectively. The low value for $Me_3B_2D_3$ is due to resonance with the CH_3 rocking band at 1075 cm^{-1} (see following paragraph); the unperturbed frequency would lie at approx. 1030 cm^{-1}.

Methyl rocking motions account for the bands in the 1055–1078 cm^{-1} region of the trimethyldiboranes and in the 1007–1031 cm^{-1} region of the tetramethyldiboranes. Their frequencies, observed intensities, and B^{10} shifts are consistent with those in the 1,2- and 1,1-dimethyldiboranes.[12,13] The frequency in $Me_3B_2D_3$ is raised approx. 30 cm^{-1} by interaction with BD bending (see foregoing paragraph), which labels it as an *in-plane* rocking mode.

A second methyl rocking mode probably produces the bands in the 900–940 cm^{-1} region, again in agreement with such bands in all the other methyldiboranes.

In each of the tri- and tetraethyl compounds, two bands in the 980–1060 cm^{-1} region can probably be assigned to methyl rocking vibrations. In $Et_3B_2D_3$ the BD deformation is coincident with one of these. The 980 cm^{-1} rocking modes are probably coupled to some extent with C–C stretching at approx. 920 cm^{-1}. All these assignments seem compatible with similar ones in other ethyldiboranes. Bands at 755 in $Et_3B_2{}^{10}H_3$ and $Et_3B_2H_3$ and at 794 cm^{-1} in $Et_3B_2D_3$ could conceivably be CH_2 rocking bands, assigned to 794–826 cm^{-1} in other ethyldiboranes containing single ethyl groups, viz., mono- and 1,2-diethyldiborane. In none of the alkyldiboranes, including trialkyldiboranes, have we been able to assign a B–C (single) stretching frequency. These may be masked in the 950 cm^{-1} region.

Out-of-plane BH bending modes have frequencies of approx. 900–920 cm^{-1} in other alkyldiboranes. This motion is probably responsible for a weak absorption in $Et_3B_2H_3$ at 907 cm^{-1} and is masked in $Me_3B_2H_3$ by the CH_3 rocking band at 935 cm^{-1}. The corresponding BD oscillation appears at 855 cm^{-1} in $Me_3B_2D_3$ and is masked by the BC_2 symmetric stretching band in $Et_3B_2D_3$.

Most of the remaining infrared bands are due to $-B_2H_x$ and $-B_2D_x$ combinations (and/or overtones) or are labeled as impurities. Especially notable in the latter category are the prominent 1147 cm^{-1} band in $Me_4B_2H_2$ (due to $Me_3B_2H_3$ and Me_3B) and the 855 cm^{-1} band in $Et_4B_2D_2$ (due to $Et_3B_2D_3$). Other bands have already been mentioned in the "Experimental" section. The complete assignments for the infrared bands are are included in Tables I and II.

In the light of the present investigation a detailed examination of the Raman spectrum[6] of $Me_4B_2H_2$, listed in Table III, is revealing. In general, the scarcity of Raman and infrared coincidences substantiates the presence of a center of symmetry, i.e., the D_{2h} model. ($B^{10}B^{11}$ in general does not introduce much asymmetry.) The C–H stretching lines in the 2841–2985 cm^{-1} region and the CH_3 deformation at 1445 cm^{-1} are assigned in the usual manner, and the B–H′ breathing vibration at 2137 cm^{-1} and the two BC_2 stretching frequencies at 1100 and 844 cm^{-1} have already been discussed. The 1987 cm^{-1} line probably is a combination or an overtone. The 1003 cm^{-1} line is naturally assigned to methyl rocking.

B—B stretching, a totally symmetric vibration, is expected to yield a strong Raman line. In B_2H_6 and B_2D_6 this vibration is[4] at 788 and 712 cm^{-1}, while in 1,2-dimethyldiborane we have tentatively assigned 746 cm^{-1} to this mode. Thus, the very strong line at 516 cm^{-1} is a "natural" for this assignment.

Three low-frequency Raman lines remain, viz., 651, 365, and 274 cm^{-1}. In a number of compounds containing the Me_2B grouping,[17,23,24] BC_2 deformation and in-plane rocking modes have been assigned to the 300–370 cm^{-1} region, and the 365^{-1} line probably represents one of these modes. Out-of-plane wagging in those same related compounds has been assigned to the 400–520 cm^{-1} region, but we observe no such line. The line at 274 cm^{-1} can reasonably be assigned to methyl twisting.[14,25] The 651 cm^{-1} line could possibly represent a combination of the 365 and 274 cm^{-1} vibrations. Our completed assignment of the reported Raman lines is included in Table III, together with assigned infrared-active fundamentals.

ACKNOWLEDGMENT

The authors gratefully acknowledge helpful criticism by Professor D. A. Dows.

[23] H. J. Becher and J. Goubeau, Z. anorg. u. allgem. Chem. **268**, 133 (1952).

[24] H. J. Becher, Z. anorg. u. allgem. Chem. **271**, 243 (1953); **289**, 262 (1957); **291**, 151 (1957).

[25] D. R. Lide, J. Chem. Phys. **29**, 1426 (1958).

Capacitive Energy and the Ionization of Aromatic Hydrocarbons*

FELIX T. SMITH

Stanford Research Institute, Menlo Park, California

(Received April 21, 1960)

Large polynuclear aromatic molecules ionize like fragments of graphite, and their ionization potentials approach the sum of the graphite work function v_{gr} and the electrostatic work of charging a conductor the size and shape of the molecule. The capacitive work for a single charge is $u=e^2/2C$, where C is the molecular capacitance. In the limit of large size, the work to remove n electrons is $W_n=nv_{gr}+n^2u$. This limiting law implies a relation among successive ionization potentials and the electron affinity, which is well satisfied by anthracene and phenanthrene, and moderately well by naphthalene and even benzene. For larger molecules, C, and therefore u, can be estimated classically by assuming the conducting region is bounded by the carbon skeleton, and computed by analog measurements on metallic models; results are tabulated for a series of aromatics. The relation between the limiting law and more detailed quantal formulations is discussed, and the magnitude and trend of some expected deviations are explored with the help of a simple free electron picture.

INTRODUCTION

THAT many properties of large polynuclear aromatics must approach those of graphite in the limit of large size is common knowledge. Among these properties are the ionization potential and the electron affinity, which are expected to approach the work function of graphite. Although the work function itself depends upon the inevitably quantal behavior of the π-electron gas, it may be looked upon as a macroscopic property of the material, measured by experiment, and as such, it gives a classical limit for the ionization potential and electron affinity of the large aromatics. So much is well known. It seems not to have been noticed that an improved classical limit can be found by considering the electrical properties of finite particles of graphite. My purpose in this paper is: to develop this new classical limit; to show that it leads (a) to a relationship between successive ionization potentials, and (b) to an approximate, classical calculation of the ionization potentials; to demonstrate that both (a) and (b) are in reasonable agreement with experiment; to provide predictions for other unmeasured molecules for comparison with future measurements and with more detailed calculations; to estimate roughly the points at which this classical limit must diverge from the correct microscopic quantal behavior; to show how this classical limit must ultimately merge with a more detailed quantum mechanical formulation of the problem; and to point out that quantal calculations should be tested by seeing if they extrapolate properly to this classical limit.

I. CAPACITIVE ENERGY. THE CLASSICAL LIMIT AND ITS CONSEQUENCES

This approach originates from recent work on the ionization of solid conducting particles, where the potentials for successive levels of ionization differ from the work function of the solid in bulk by the classical electrostatic work required to charge up the particle. If the particle is a conductor of capacitance C, its coulombic capacitive energy when it is charged to a level of n electronic charges is $(ne)^2/2C$; to this must be added n times the work function v, which is the energy needed to raise an electron from the Fermi level in the lattice to a level where it could escape from the semi-infinite solid, for which the coulombic charging energy vanishes. The total work to remove n electrons is then

$$W_n=nv+(ne)^2/2C, \tag{1}$$

and the nth ionization potential, corresponding to the process $A^{+n-1}\rightarrow A^{+n}+e$, is[1,2]

$$\phi_n=v+(n-\tfrac{1}{2})e^2/C. \tag{2}$$

If $n<0$, electron affinities are obtained. It is often assumed that the particles are spherical, in which case $C=4\pi\epsilon_0 r$, where $\epsilon_0=8.854\cdot10^{-12}$ farad/meter is the dielectric constant of space. Another simple shape, which might be approached by graphite particles, is the thin circular disk, for which $C=8\epsilon_0 r$.

It is generally accepted that the ionization potential and electron affinity of the polynuclear aromatics approach a common limit which is close to the work function of bulk graphite. This seems justified by the fact that the layers in bulk graphite are so far apart and so weakly bound (about 1.5 kcal or 0.065 ev per atom interlayer binding energy[3]); there is also evidence

* Supported by U. S. Air Force, Air Research and Development Command.

[1] F. T. Smith, J. Chem. Phys. **28,** 746 (1958) and *Proceedings of The Third Conference on Carbon* (Pergamon Press, London, 1959), p. 419; see also T. M. Sugden and B. A. Thrush, Nature **168,** 703 (1951).

[2] H. Einbinder, J. Chem. Phys. **26,** 948 (1957), interested primarily in the average behavior of large highly charged particles, makes an approximation equivalent to neglecting a term $e^2/2C$ in Eq. (2); in this he is followed without comment by A. A. Arshinov and A. K. Musin, Doklady Akad. Nauk S.S.S.R. **118,** 461 (1958), and Yu. S. Sayasov, *ibid.* **122,** 848 (1958).

[3] H. Inokuchi, S. Shiba, T. Handa, and H. Akamatsu, Bull. Chem. Soc. Japan **25,** 299 (1952).

TABLE I. The relation between successive ionization potentials.[a]

Molecule	Experimental values			Effective work function			Effective specific potential						Estimated triple ionization potential (limits) W_3
	W_1 (A→A⁺)	W_2 (A→A⁺⁺)	$W_{-1}=-A_1$ (A→A⁻)	v_{21}	$v_{1,-1}$	$v_{2,-1}$	u_{10}	u_{20}	$u_{-1,0}$	u_{21}	$u_{1,-1}$	$u_{2,-1}$	
Benzene	9.38	26.4	(+0.54)[b]	5.55	4.42	4.0	4.99	4.40	4.96	3.8	4.96	4.58	55.5±2.7
Naphthalene	8.26	22.7	−0.65	5.15	4.46	4.2	3.87	3.48	3.81	3.1	3.80	3.57	46.2±1.8
Anthracene	7.55	21.1	−1.19	4.55	4.37	4.3	3.16	3.08	3.18	3.0	3.18	3.12	41.4±0.5
Phenanthrene	8.03	23.1	−0.69	4.50	4.36	4.3	3.64	3.58	3.67	3.5	3.67	3.62	45.8±0.4
Graphite				4.39	4.39	4.39							

[a] All values in electron volts.
[b] Extrapolated value (reference 9).

from the dielectric susceptibility that the interlayer effect on the conduction electrons is very small.[4] We may thus assume that large enough particles of a single graphitic layer will have successive ionization potentials governed by Eqs. (1) and (2) with v approximated very closely by the work function of graphite, $v_{gr}=4.39$ ev.[5] This, then, is the limiting behavior that must be approached by the ionization potentials of large fused-ring-aromatic molecules.

Two consequences can be derived from Eqs. (1) and (2) which have predictive value and can be compared with experiment. These will now be examined in turn.

A. Relationship between Successive Ionization Potentials

Besides the work function, which is known, Eqs. (1) and (2) contain only one additional parameter, the capacitance C of the molecule or particle. If this is unknown, these equations nevertheless predict a relationship between successive ionization potentials for a single molecule. It will be informative to see how closely this limiting relationship is obeyed by the molecules for which measurements are available.

Since the capacitance occurs inconveniently in the denominator, let us introduce the *specific capacitive potential* (or simply *specific potential*) by the equation

$$u=e^2/2C; \tag{3}$$

with this, Eq. (1) becomes

$$W_n=nv+n^2u. \tag{4}$$

Eliminating u between equations of this form for two different levels of ionization, n and m, we can predict successive ionization potentials (or electron affinities) from the measured value of any one of them. Equivalently, from measured values W_n and W_m, we can compute

$$v_{nm}=[mn/(m-n)][(W_n/n^2)-(W_m/m^2)]\approx v_{gr}, \tag{5}$$

and test the predicted relation by seeing how close the values v_{nm} come to each other and to v_{gr}. On the other hand, eliminating v, we can also compute

$$u_{nm}=(n-m)^{-1}[(W_n/n)-(W_m/m)], \tag{6}$$

and

$$u_{n0}=n^{-1}[(W_n/n)-v_{gr}], \tag{7}$$

and see, for a given molecule, how close these come to a common value u. Electron affinities can be used in the same comparison, since the electron affinity is

$$A_m=-W_{-m}. \tag{8}$$

A special case of Eq. (5), derived long since on other grounds,[6] is the rule that the electron affinity and the first ionization potential tend to be equidistant from the work function of graphite, $A_1+W_1=2v_{1,-1}\cong 2v_{gr}$.

The recent experiments of Wacks and Dibeler[7] make it possible for the first time to compare single and double ionization potentials for a series of polynuclear aromatics.[8] Their values of W_1 and W_2 are used for such a comparison in Table I. In addition, I have used what seem to be the only available experimental data on electron affinities for these molecules, those of Blackedge and Hush, cited by Hush and Pople[9] but apparently not yet published elsewhere; they seem to give a striking confirmation of the rule that A_1 and W_1 are balanced about the graphite work function. It is worthy of remark that v_{21}, depending on W_2, also converges rapidly to the graphite value, the deviation being only 3% for anthracene and 2% for phenanth-

[4] R. R. Haering and P. R. Wallace, *Proceedings of the Third Conference on Carbon* (Pergamon Press, London, 1959), p. 183.
[5] A. Braun and G. Busch, Helv. Phys. Acta **20**, 33 (1947).
[6] R. S. Mulliken, J. chim. phys. **46**, 497 (1949).
[7] M. E. Wacks and V. H. Dibeler, J. Chem. Phys. **31**, 1557 (1959).
[8] For benzene, the double ionization potential was observed earlier by A. Hustrulid, P. Kusch and J. T. Tate, Phys. Rev. **54**, 1037 (1938).
[9] N. S. Hush and J. A. Pople, Trans. Faraday Soc. **51**, 600 (1955).

TABLE II. Ionization potentials and the classical specific potential.

Molecule	Reference	Experimental ionization potential $W_1(A \rightarrow A^+)$	Effective specific potential $u_{10}=W_1-v_{gr}$	Classical specific potential (from metallic model) $u_0=e^2/2C_0$	Corrected classical specific potential (Eq. 39) u_{01}''
Benzene	7	9.38	4.99	8.24	6.26
Naphthalene	7	8.26	3.9	5.89	4.73
Anthracene	7	7.55	3.2	4.43	3.71
Phenanthrene	7	8.03	3.6	4.63	3.95
Tetracene	12, 11	7.71, 7.00	3.3, 2.6	3.81	
1,2-Benzanthracene	11	7.60	3.2	4.04	
3,4-Benzphenanthrene	12	8.40	4.0	3.98	
Pyrene	11	7.55	3.15	4.22	
Chrysene	11	7.8	3.4	3.81	
Perylene	11	7.15	2.75	3.67	
Coronene	11	7.6	3.2	3.34[a]	3.00

[a] 3.05 calculated for circular disk.

rene. One may confidently predict that the agreement will be even better for larger molecules, and not much worse for triple and higher ionization. Predicted values of W_3, based on Eq. (7) and the spread of values of u_{n0}, are given in Table I.

B. Classical Estimates of Molecular Capacitance

If the molecule is large enough, it should be possible to estimate its capacitance, and thus the parameter u, classically. It seems reasonable to assume that the molecule behaves as a conducting plate, bounded by the peripheral carbon skeleton of the aromatic system.

How small a particle can be treated by this model? The molecule coronene, $C_{24}H_{12}$, is sufficiently symmetric to be treated as a circular conducting disk bounded by the outer carbon atoms, for which $r=3.70$A; from this $C=8\epsilon_0 r=2.62\cdot10^{-8}$ $\mu\mu f$, $u=e^2/2C=3.05$ ev, and $W_1=v_{gr}+u=7.44$ ev. Unfortunately the ionization potential of coronene has not been measured directly, but Matsen has derived a value of 7.50 ev from a correlation of ionization potentials and electronic spectra[10] while Briegleb and Czekalla have deduced 7.6 ev from charge-transfer spectra of complexes.[11] This agreement is sufficiently encouraging to prompt similar comparisons for other molecules, even though computation is not so easy for less symmetrical configurations. However, numerical computation can be evaded by taking advantage of the fact that capacitances scale just as a linear dimension. I have, therefore, resorted to measuring the capacitances of flat metallic models composed of hexagons three inches on an edge; details of the method and necessary corrections are given in the Appendix. A comparison with available experimental values[7,11,12] is given in Table II. The computed and measured values of u appear to be converging satisfactorily for the larger of the still small molecules for which they are known; beyond phenanthrene, a considerable error no doubt resides in much of the experimental data for W_1. In general, Table II shows that the simple classical models predict values for u that come within about 30% of the experimental ones; in terms of the total ionization potential W_1 the error is reduced to about 15%. Thus, the simple classical limit gives an excellent first approximation to these ionization potentials. In the expectation that further experimental data will improve the quality of the agreement, and perhaps reveal systematic effects worth more detailed study, results of the analog computation with metallic models are given for an extensive series of molecules in Table III.

II. MOLECULE AND SOLID—THE MICROSCOPIC PICTURE

A. Molecular Capacitive Energy

How does the macroscopic, classical treatment of the last section tie in with a microscopic, quantum mechanical description of the molecular system?

Consider the molecule as an array of N more or less graphitic carbon atoms, surrounded by other atoms such as hydrogen that need not be closely specified. The total energy of the molecule, or of any of its ions, in the lowest state, can be divided uniquely into kinetic and potential energies, plus magnetic and spin

[10] F. A. Matsen, J. Chem. Phys. **24**, 602 (1956).
[11] G. Briegleb and J. Czekalla, Z. Elektrochem. **63**, 6 (1959).
[12] D. P. Stevenson (unpublished).

TABLE III. Specific potential computed classically.[a]

Molecule [b]	u_0	Molecule [b]	u_0	Molecule [b]	u_0	Molecule [b]	u_0	Molecule [b]	u_0
	8.24		2.95		2.66		3.68	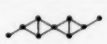	2.51
	5.89		2.95		3.41		3.22	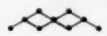	2.53
	4.43	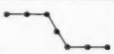	2.63		2.73		3.23		2.60
	3.81		3.98	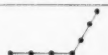	2.48		3.56		3.48
	3.30		3.33		2.72		3.17		2.79
	4.63		2.98		3.18		3.23		2.64
	4.04		3.40		3.67		2.56		3.53
	3.32		2.96		3.22		3.25		3.10
	2.98		2.61		3.21		2.56		2.80
	3.26		2.60		3.01		2.86		3.34
	2.96		3.27		2.96		2.95		3.01
	3.81		3.31		2.97		3.23		3.34
	3.28		3.53		3.00		3.23		3.00
	2.99		3.85		2.46		2.79		2.84
	2.63		3.41	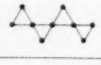	2.98		2.98		2.73
	3.41		2.98		4.22		3.05		2.28
								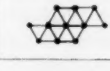	2.54

a $u_0 = e^2/2C_0$, C_0 from measurement on metallic model. Units are electron volts.

b A dot or the intersection of two lines represent a benzene hexagon, a line represents the junction of two hexagons through a common edge.

terms that can be neglected here:

$$E_0 = T_0 + U_0 + \cdots$$
$$E_{+n} = T_{+n} + U_{+n} + \cdots. \quad (9)$$

Since we need not actually compute them, we may envisage T and U as average values obtained by applying the appropriate quantal operator to the complete, accurate, wave function for the ground state of the molecule or ion. The potential energy U_{+n} includes the mutual repulsion of all the nuclei as well as the electron interactions, so it includes all the energy of the electrostatic field. The $n$fold ionization potential is given by

$$W_{+n} = E_{+n} - E_0$$
$$= (T_{+n} - T_0) + (U_{+n} - U_0) + \cdots, \quad (10)$$

and the potential energy contribution $(U_{+n} - U_0)$ includes the nuclear repulsion as well as their attraction for the electrons.

Let us now compare this with the description of a large flat graphitic sheet, in which the total energy per atom is

$$E_s = T_s + U_s + \cdots. \quad (11)$$

The work function, the energy required to remove an electron from the semi-infinite two-dimensional solid, can be formally defined by taking the limit of Eq. (10) as the number of atoms in the particle goes to infinity (in such a way that the size of the particle grows as $N^{\frac{1}{2}}$ in 2 perpendicular directions):

$$v = \lim_{N\to\infty} W_{+1}(N) = T_v + U_v + \cdots. \quad (12)$$

It is useful to consider the difference function defined by

$$\delta_{+n} = E_{+n} - (NE_s + nv). \quad (13)$$

This includes all effects due to the edge of the molecule (including the nongraphitic border atoms), and also the energy of compressing the excess positive charge into the region of the molecule. The effects around the edge (such as σ bonds to the bordering H atoms) will in large part cancel out when we subtract δ_0 from δ_{+n} to construct the quantity

$$\zeta_{n,0} = \delta_{+n} - \delta_0 = W_{+n} - nv. \quad (14)$$

Let us now look at the electrostatic energy contribution to $\zeta_{n,0}$. It is convenient to use units such that $4\pi\epsilon_0 = e = 1$. If the total electron density at any point $\mathbf{r}$, when the molecule is in the $+n$ ionized state, is $\rho_{+n}(\mathbf{r})$ and the nuclei are fixed at the positions $\mathbf{r}_i$ (their zero-point vibrations are unimportant in this context), the potential energy of the system is

$$U_{+n} = \sum_{i,j\neq i} \frac{q_i q_j}{2r_{ij}} - \sum_i q_i \int \frac{\rho_{+n}(\mathbf{r})\,d^3r}{|\,\mathbf{r}-\mathbf{r}_i\,|}$$
$$+ \left(1 - \frac{1}{M-n}\right) \iint \frac{\rho_{+n}(\mathbf{r})\rho_{+n}(\mathbf{r}')\,d^3r\,d^3r'}{2\,|\,\mathbf{r}-\mathbf{r}'\,|} + J_{+n}, \quad (15)$$

where M is the total number of electrons in the neutral molecule, and J_{+n} is a correlation term which compensates for the use of the product of densities $\rho_{+n}(\mathbf{r})$ $\rho_{+n}(\mathbf{r}')$ in the double integral instead of the correct correlated double density $\rho(\mathbf{r}, \mathbf{r}')$.

We can define the quantity

$$s_{+n}(\mathbf{r}) \equiv n^{-1}[\rho_0(\mathbf{r}) - \rho_{+n}(\mathbf{r})], \quad (16)$$

which obeys the condition

$$\int s_{+n}(\mathbf{r})\,d^3r = 1; \quad (17)$$

$ns_{+n}(\mathbf{r})$ is the distribution of electron holes, by comparison with the neutral molecule. Subtracting U_0 from U_{+n}, we find

$$U_{+n} - U_0$$
$$= n \int s_{+n}(\mathbf{r}) \left[\sum_i \frac{q_i}{|\,\mathbf{r}-\mathbf{r}_i\,|} - \left(1 - \frac{1}{M-n}\right) \int \frac{\rho_0(\mathbf{r}')\,d^3r'}{|\,\mathbf{r}-\mathbf{r}'\,|} \right] d^3r$$
$$- \frac{n}{M(M-n)} \iint \frac{\rho_0(\mathbf{r})\rho_0(\mathbf{r}')\,d^3r\,d^3r'}{2\,|\,\mathbf{r}-\mathbf{r}'\,|}$$
$$+ n^2 \left(1 - \frac{1}{M-n}\right) \iint \frac{s_{+n}(\mathbf{r})s_{+n}(\mathbf{r}')\,d^3r\,d^3r'}{2\,|\,\mathbf{r}-\mathbf{r}'\,|} + (J_{+n} - J_0). \quad (18)$$

In the limit of large N the first term in (18) becomes the potential energy contribution to the work function, U_v, the second vanishes as M^{-1}, and the third gives the classical capacitive energy. The correlation term $(J_{+n} - J_0)$ may also contribute to U_v and to the double integral that becomes the capacitive energy. However, its contribution to the latter integral is tantamount to a correlation of the holes represented by the distribution $s_{+n}(\mathbf{r})$, and must become insignificant as the density of holes diminishes with the increase in N.

For any ionized system, small or large, a capacitive energy can be defined by the third term in (18), that is, by inserting the distribution of holes $ns_{+n}(\mathbf{r})$ in the classical integral for the electrostatic energy of the system. This will make it possible to compare the results of quantum mechanical calculations with the simple classical limit, $n^2u = n^2(e^2/2C)$. Obviously, the distribution of holes s_{+n} will tend to become independent of n and will closely approach the classical distribution of charge, in order to minimize the total energy of the system.

B. The Ionization Potential as a Power Series

The character of the limiting law can be seen more clearly if one expands W_{+n} in negative powers of the average molecular radius R. In the limit, u is inversely proportional to R, and it is convenient to introduce a quantity that depends only on the shape S of the

molecule or particle and can be computed classically:

$$g_S = \lim_{R\to\infty}(Ru) = \lim_{R\to\infty}(Re^2/2C). \tag{19}$$

Since the work function v is defined by the limit (12), it may be necessary to include in the effective work function (as it appears in Eq. (5), for instance) an R^{-1} term involving another, possibly shape dependent, parameter α_S. Such a term represents, among other things, the second term on the right of Eq. (18). With these terms, the expansion is

$$W_{+n}(R, S) = n(v+\alpha_S R^{-1}) + n^2 R^{-1} g_S + R^{-2} h_S(n) + \cdots. \tag{20}$$

The form of the terms of order through R^{-1} is such as to satisfy Eq. (12) and the requirements of classical electrostatics when R is large but finite.

Using this expansion Eqs. (5)–(7) become

$$v_{nm} = v+\alpha_S R^{-1} + R^{-2}(m-n)^{-1}[(m/n)h_S(n) - (n/m)h_S(m)]\cdots, \tag{21}$$

$$u_{nm} = R^{-1}g_S + R^{-2}(n-m)^{-1}[n^{-1}h_S(n) - m^{-1}h_S(m)]\cdots, \tag{22}$$

$$u_{n0} = n^{-1}(v - v_{gr} + \alpha_S/R) + R^{-1}g_S + R^{-2}n^{-2}h_S(n)\cdots. \tag{23}$$

As we have seen, the difference $(v-v_{gr})$ is probably negligible ($\ll 0.1$); and it appears from the close convergence of the values of u_{n0} for each of the molecules in Table I that $|\alpha_S|$ is probably very small compared to g_S, so that the entire first term in Eq. (23) can usually be neglected.

In practice, one would like to use the first terms of Eq. (20) not merely as a limiting law, but to estimate ionization potentials of real, not very large, molecules. For this purpose it is desirable to have some idea, even if very rough, of the principal sources of deviation from the ideal limiting classical model. The next subsections are devoted to this question.

C. Kinetic Energy

It has so far been assumed implicitly that the kinetic energy contribution to the ionization potential W_{+n} is assignable to the work function v. In order to verify this and assess possible corrections, it is useful to assume that the kinetic energy of the π electrons that participate in the ionization behaves much like the kinetic energy of particles in a box. This permits us to use the simple considerations of the free electron theory of metals.

If one treats the molecule as a fragment of graphite containing N aromatic carbon atoms and N_π conduction electrons, and neglects edge effects and the periodicity of the lattice, the separation of variables in the dynamical problem allows one to examine the motion of the electrons parallel to the plane of the molecule as an isolated problem. (In the perpendicular direction, all π orbitals have the same structure, so the electrons behave as two-dimensional conduction electrons only.) The energy levels in a two-dimensional box of area A are

$$U = h^2k^2/2m = h^2(n_x^2+n_y^2)/2mA, \tag{24}$$

where U is measured from the bottom of the box, $-E_0$. The highest filled level is the Fermi level n_F, with energy U_F, and the total number of filled levels, with $U \leq U_F$, is roughly πn_F^2. Each level can accommodate 2 electrons, so the total number of π electrons is related to n_F and U_F by

$$N_\pi \approx 2\pi n_F^2 \tag{25}$$

and

$$U_F = h^2 n_F^2/2mA = h^2 N_\pi/4\pi mA. \tag{26}$$

In graphite, $N_\pi = N$ and

$$A = a_{gr}N = (\tfrac{3}{4})\sqrt{3}r_0^2 N, \tag{27}$$

where a_{gr} is the area per C atom in a graphite layer and $r_0 = 1.42$A is the C—C distance, so

$$U_F(\text{gr}) = \epsilon = (h^2/3)\sqrt{3}\pi r_0^2 m = 9.15 \text{ ev}, \tag{28}$$

and we can make the identification

$$v_{gr} = E_0 - \epsilon. \tag{29}$$

In the aromatic ions, the number of π electrons,

$$N_\pi = N - n, \tag{30}$$

is not very large, and the Fermi level shifts as electrons are added or removed. The work of removing an electron from the $(+n-1)$ ion is then

$$W_{n,n-1} = E_0 - U_{F,n-1} = E_0 - \epsilon\{1 - [(n-1)/N]\} = v_{gr} + (n-1)\epsilon N^{-1}. \tag{31}$$

Including the capacitive term, the $n$fold ionization potential becomes

$$W_{+n} = n(v_{gr} - \tfrac{1}{2}\epsilon N^{-1}) + n^2(u + \tfrac{1}{2}\epsilon N^{-1}). \tag{32}$$

The kinetic energy thus contributes a correction varying as N^{-1} or R^{-2} to both the effective work function and the effective specific potential. The magnitude of this correction is not reliably estimated by this simple argument (a more sophisticated metallic model would introduce the band structure and a corrected effective mass for the electron, changing the magnitude of ϵ), but taken at face value it would amount to about 0.3 ev for anthracene and phenanthrene. In this simple model, the pairing of the electrons in an orbital has been neglected insofar as it would introduce a correction of similar magnitude, alternating as n is even or odd.

Another effect of the kinetic energy term is revealed by this picture of the electron as a free particle in a box. Conditions at the edge of the molecule may give the electron an effective area for free motion different from that corresponding to N graphitic unit cells. Introducing the area $A+\delta A$ in place of $A=Na_{gr}$ in Eq. (26), one finds

$$W_{+n}=n\left(v_{gr}+\epsilon\frac{\delta A}{A+\delta A}-\frac{\epsilon}{2N}\frac{A}{A+\delta A}\right)+n^2\left(u+\frac{\epsilon}{2N}\frac{A}{A+\delta A}\right). \quad (33)$$

As an edge effect, the term $\delta A/(A+\delta A)$ varies as R^{-1}, and diminishes slowly with size. However, it is expected to be very small, since any pronounced redistribution of electrons to or from the edge will lead to a charge separation opposed by the electrostatic forces, which tend to maintain charge neutrality in each unit cell in the neutral molecule and the classical capacitive distribution in the ion.

This discussion suggests a general observation. It is often assumed, on the basis of Koopman's theorem, that ionization potentials and electronic excitation levels are linearly related. However, electronically excited molecules are still electrically neutral, and probably maintain charge neutrality very closely in each unit cell. Thus, the levels of electronic excitation can be thought of as involving mainly changes in the kinetic energy of the electrons; this would make the success of the free electron model in its various forms understandable. If this is the case, the electronic spectrum should tend to vary as R^{-2} with increase in molecular size, while we have seen that the ionization potential depends mainly on the capacitive energy which varies as R^{-1}.

D. Polarization

In the customary phenomenological discussion of the work function, it is pointed out that the electron, once it has been removed to a finite distance from the solid, exerts a polarizing influence on the conducting surface. This interaction is included in the work function, but its magnitude will depend on the size and shape of the particle, and it is worthwhile to estimate how it changes

For an ideal semi-infinite plane conductor, the interaction can be treated as being due to an image force which varies as $-e^2/16\pi\epsilon_0x^2$, where x is the distance from electron to surface. This corresponds to an effective potential energy $-e^2/16\pi\epsilon_0x$. When x is as small as atomic dimensions, the surface no longer appears as an ideal plane conductor; this is usually treated by assuming a cutoff in this image potential at some distance x_0. The work function then includes a term of the form $-v_i=e^2/16\pi\epsilon_0x_0$.

When the molecule to be ionized is not very large, the image force is reduced, and an estimate of the magnitude of the resulting change in the effective image potential can be obtained in the case of a spherical particle of radius R, for which the image force is

$$F_{i,R}=-(e^2/16\pi\epsilon_0)(x^{-2}-(x+2R)^{-2}). \quad (34)$$

This can be derived from the effective image potential

$$v_{i,R}=-e^2/16\pi\epsilon_0x+e^2/16\pi\epsilon_0(x+2R). \quad (35)$$

This will have a cutoff at the same distance x_0, and the work function then has a term

$$-v_{i,R}(x_0)=e^2/16\pi\epsilon_0x_0-e^2/16\pi\epsilon_0(x_0+2R). \quad (36)$$

The effective work function for a sphere is therefore reduced below what it is for the semi-infinite solid:

$$\Delta v_i=e^2/16\pi\epsilon_0(x_0+2R)=(e^2/8C)(1+x_0/2R)^{-1}. \quad (37)$$

It is not quite clear how the computation should be made for a nonspherical molecule, since the cutoff distance x_0 will then have to depend on the path the electron is supposed to follow. However, we can ignore x_0 in (37) and assume the correction in general to be represented roughly by $e^2/8C=u/4$. Adding this to the principal terms in the effective work function from Eq. (33), we have

$$v=v_{gr}+[(\epsilon\delta A/A)-(u/4)]-(\epsilon/2N). \quad (38)$$

The terms in parentheses are grouped together because they fall off as R^{-1}. The experimental data in Table I suggest that the polarization effect has been considerably exaggerated by this argument, and that if it exists it is much smaller than $u/4$.

E. The Classical Capacitance

The classical capacitances used in Tables II and III were obtained from metallic models which assumed the capacitive charge distribution to reside inside the carbon skeleton of the molecule. As Eq. (18) shows, the capacitive energy properly is computed from a distribution of holes in an electron cloud that may extend somewhat beyond the framework of the nuclei. Thus the capacitive energies were overestimated, and the error is worst for the smallest molecules; this is borne out by Table II. To correct for this error, the classical estimate u_{el} can be multiplied by $(1+\delta r/R)^{-1}$. Including the term from Eq. (33), the effective specific potential is

$$u=u_{el}(1+\delta r/R)^{-1}+\epsilon/2N=u_{el}+[(\epsilon/2N)-u_{el}(\delta r/R)]+u_{el}(\delta r/R)^2\cdots. \quad (39)$$

In the limit, all the correction terms vanish faster than u_{el} itself.

The requirement that the electron distribution lead to approximate charge neutrality in the region of each nucleus in the neutral molecule suggests an alternative simple model for the electrical behavior. Let us suppose that the molecule is simply cut from a sheet of graphite in such a way as to bisect all the exterior C—C bonds, leaving each nucleus surrounded by a triangular unit

cell throughout which the electrons are free to move. Metallic models constructed for this configuration would give another classical estimate for the capacitive energy. Benzene and coronene are then embedded in hexagonal figures, for which the capacitive energies are $u_{c1}'=4.76$ ev (benzene), $u_{c1}'=2.38$ ev (coronene). Alternatively, one may use Eq. (39), assuming $\delta r=0.71$A, half the C—C distance, and taking R as the geometric mean of the longest and shortest diameters of the molecular skeleton. The values of u_{c1}'' in Table II were obtained in this way, with the addition of the term $\epsilon/2N$ (which varies from 0.76 ev for benzene to 0.19 ev for coronene).

It is interesting to compare the quantal distribution of holes $s_{+n}(\mathbf{r})$ with the classical distribution in an ideal conductor. If the conductor is a circular disk, the classical distribution is well known,[13]

$$q(r)=(Q/2\pi R^2)(1-r^2/R^2)^{-\frac{1}{2}}. \tag{40}$$

Near the center of the disk, the charge density is half of what it is in a uniform distribution. Quantally, the infinity at the edge will be reduced to a high peak near the edge, and a gradual tail will remain beyond the classical edge.

F. Discussion

In a properly rigorous treatment, the argument of the last three subsections would have been based on Eq. (18) and its analog for the kinetic energy. However, such a line of argument could not have been pursued very far without introducing drastic approximations, and it seemed more fruitful at the beginning to use very simple intuitive arguments, realizing that they should be superseded later and may be wrong at some points.

The modern structure of molecular orbital theory has been quite successful in predicting some single and double ionization potentials,[9,14] and it is clear that a bridge should eventually be built between that approach and the one of this paper.

Among the points that have been neglected in this paper are spin dependent effects, which are of some importance in the smaller aromatics because the spin multiplicity changes from level to level of ionization. Also, the change in nuclear equilibrium positions has been ignored, on the double grounds that it rapidly becomes small for the larger molecules, and that we are usually confronted experimentally with "vertical" ionization potentials, in which the nuclei have not had time to move toward a new equilibrium position.

It hardly need be said that many of the considerations in this paper apply to other large systems of conjugated double bonds as well as to the fused-ring aromatics. It will be interesting, for instance, when the potentials for single and double ionization of other such systems become known, to compute the effective work function and specific potential from them, and see how the former compares with the work function of graphite. It may also be possible to estimate their molecular capacitances by classical metallic models judiciously designed. It has also been suggested to me recently by Professor D. F. Hornig that the same principles may apply to the ionization of large aliphatic systems, where the electron may be removed from the aggregate of σ electrons of the molecular skeleton; in this case, the effective work function will be quite different from that for π electrons.

[13] J. H. Jeans, *Mathematical Theory of Electricity and Magnetism* (Cambridge University Press, 1925), 5th ed., p. 249.

[14] R. M. Hedges and F. A. Matsen, J. Chem. Phys. **28**, 950 (1958).

APPENDIX

An Analog Estimate of Molecular Capacitances

Formulas are known for the capacitance of conducting objects of various simple shapes including circular and elliptic disks, and they can be used for a classical estimate of the capacitance of symmetrical molecules like coronene. For less regular shapes numerical methods would be tedious, and it is possible instead to make use of the fact that capacitances scale in proportion to a linear dimension for objects of similar shape and can be measured readily for models of reasonable size. We have therefore been able to use metallic models composed of hexagonal disks to simulate the conducting region within the C—C skeleton of polynuclear aromatic molecules. Chemical syntheses can be performed rapidly with a soldering iron, and capacitances measured with a Q-meter do the duty of appearance potentials in a mass spectrometer.

The models were made of hexagons, 3 in. on an edge, cut from brass sheet (the models of benzene, naphthalene, and anthracene were bigger, 5.635 in. on an edge). A wire running in the plane of the model and from an extremity of it connected it to the Q-meter. The wire was 73 in. long, 0.01264 in. in diameter. Measurements were made in the open, away from conductors and dielectrics; the model lay on a polyfoam support, 3 ft from the nearest wood and 6 ft from the ground. The frequency used was about 50 kc; capacitance was measured by comparison with a known impedance. The capacitance of the wire alone was $C_w=12.1$ $\mu\mu$f, and that of the model plus wire, C_{mw}. Since the capacitance of the model C_m was of about the same magnitude as that of the wire, and the charge on each influenced the other, the capacitance of the model could not be computed simply by subtraction, $C_m\neq C_{mw}-C_w$, but an approximate correction was used which will now be derived.

Consider a sphere S of radius r_s and a wire W of length h_w running normal to it, both charged to a potential V'. In this condition, the total charge on the sphere is Q_s', and the charge on an element dx of the wire is $q_w'(x)dx$, where x is measured from the center of the sphere. Compare this with the situation where the wire has been removed, the sphere is again charged

to the potential $V_s''=V'$ with a charge Q_s'', and the potential along the path of the wire is $V_w''(x)=V'r_s/x$, while $q_w''(x)=0$ everywhere on this path. The distributions of potential and charge in these two situations are connected by Green's reciprocation theorem,

$$\sum_j q_j''V_j'=\sum_j q_j'V_j'', \tag{A1}$$

so

$$Q_s''V'=Q_s'V'+V'r_s\int_{r_s}^{r_s+h_w}x^{-1}q_w'(x)\,dx. \tag{A2}$$

Since

$$Q_{sw}'=Q_s'+\int_{r_s}^{r_s+h_w}q_w'(x)\,dx, \tag{A3}$$

one finds

$$Q_s''=Q_{sw}'-\int_{r_s}^{r_s+h_w}(1-r_s/x)q_w'(x)\,dx. \tag{A4}$$

Far from the sphere the charge distribution on the wire approaches constancy, $q_w'(x)\to q_w^0$, and if end effects are neglected this constant value is related to the capacitance of the isolated wire by

$$q_w^0=Q_w^0/h_w=V'C_w/h_w. \tag{A5}$$

If one substitutes q_w^0 for $q_w'(x)$ in the integral in Eq. (A4), the error that is introduced at small values of x will be diminished by the factor $(1-r_s/x)$. With this approximation, we have

$$Q_s''\approx Q_{sw}'-Q_w^0+Q_w^0r_sh_w^{-1}\ln(1+h_w/r_s). \tag{A6}$$

The capacitance of the sphere is $C_s=Q_s''/V'$ and that of sphere plus wire is $C_{sw}=Q_{sw}'/V'$, so

$$C_s\approx C_{sw}-C_w+C_wr_sh_w^{-1}\ln(1+h_w/r_s). \tag{A7}$$

When the model is not a sphere, a further approximation is required. The potential which is used in the integrand in Eq. (A2) should now contain higher terms of a multipole expansion, but these fall off rapidly with distance and can be ignored, and the leading term in the expansion is taken to be the potential which would be created by a sphere with the same capacitance as that of the model, C_m. Since $C_s=4\pi\epsilon_0r_s=C_m$, and the wire begins at a distance r_m from the electrical center of the model, we now have instead of (A7)

$$C_m\approx C_{mw}-C_w+(C_mC_w/4\pi\epsilon_0h_w)\ln(1+h_w/r_m). \tag{A8}$$

This was used to compute the capacitance of the model C_m from the measured C_{mw} and C_w in the form

$$C_m\approx[1-(C_w/4\pi\epsilon_0h_w)\ln(1+h_w/r_m)]^{-1}(C_{mw}-C_w). \tag{A9}$$

For a symmetrical molecule, the electrical center is at the center of symmetry, and r_m was measured from there to the point of attachment of the wire. Where there was no center of symmetry, the effective center of mass was estimated by eye, and r_m measured from there.

Measurements on a sphere, a circle, and an elliptic disk, for which the capacitance could be computed exactly, gave agreement within $\pm3\%$. Results for the molecular models should be reliable to better than $\pm5\%$. Reduced to molecular dimensions, these results are tabulated as the quantity $u_0=e^2/2C_0$ in Table III.

ACKNOWLEDGMENTS

I am grateful to Dr. Robert L. Tanner for help with the capacitance measurements and advice about the correction required, and to John A. Briski for making the models and the measurements.

Vapor Pressure of Nearly Classical Liquids*

WILLIAM A. STEELE

Department of Chemistry, The Pennsylvania State University, University Park, Pennsylvania

(Received August 8, 1960)

The reduced vapor pressures of liquids which exhibit nearly classical behavior are considered. It is shown that the intermolecular quantum effects upon the parameters of the reduced vapor pressure equations of such liquids are small compared to other variations in these parameters. However, these effects can be reasonably well estimated by considering the changes in vapor pressure upon isotopic substitution in suitable simple systems. Experimental data are analyzed to give quantitative estimates of the quantum effect upon the reduced heat of vaporization, the temperature-independent term in the vapor pressure equation, and the configurational heat capacity of nearly classical liquids.

SEVERAL years ago, deBoer and Lunbeck[1] presented a quantum mechanical version of the law of corresponding states in which changes in the reduced thermodynamic variables of light molecules were given as a function of the parameter $\Lambda^*=h/\sigma(m\epsilon)^{\frac{1}{2}}$ (ϵ and σ are the parameters specifying the depth and distance scale of the intermolecular interaction curve). In their work, the magnitude of the quantum correction to the properties of substances with Λ^* small was not considered, except in the case of the reduced molar volumes of the liquids. It is of considerable theoretical and practical interest to estimate the magnitude of these quantum contributions to the properties of nearly classical liquids, since the results of many of the classical computations of liquid properties have been compared with the data on such substances (particularly, argon).[2,3] Furthermore, the results of measurements of the properties of the heavier rare gases (argon, krypton, xenon) are frequently used to illustrate the classical theorem of corresponding states.[4,5]

One of the most important physical properties of a liquid is its vapor pressure as a function of temperature. In order to obtain more detailed information about the variations in this property, the reduced vapor pressure is written as

$$\ln p^*=-\Delta H^*/T^*+A^*$$
$$p^*=p\sigma^3/\epsilon, \qquad A^*=A+\ln\sigma^3/\epsilon$$
$$\Delta H^*=\Delta H/\epsilon, \qquad T^*=kT/\epsilon, \tag{1}$$

where A is the temperature-independent term in the unreduced vapor pressure equation. As is well known, Eq. (1) actually holds over fairly short temperature ranges, but the values for these reduced constants should be comparable for simple classical fluids if the data used have been measured over the same range of reduced temperature. Here ΔH^* and A^* at $T^*=0.7$ were calculated for a number of substances with $\Lambda^*=0.1$–0.6; ΔH and A were obtained from the vapor pressure equations given in the handbooks,[6] and ϵ and σ were taken from the values given in the work cited in footnote 1, p. 1110. (In the case of methane, the configurational ΔH was estimated by subtracting the change in zero-point vibrational energy upon vaporization[7] from the experimental ΔH. This correction term is negligible for all other substances considered). When these values of ΔH^* and A^* were plotted as a function of Λ^*, it was observed that the dependence of ΔH^* and A^* upon Λ^* at small Λ^* is small compared to the other variations in these quantities. A portion of the variation may be due to errors in the values of ϵ and σ used. However, alterations in the form of the intermolecular potential energy curves will also result in changes in ΔH^* and A^*.

An alternate method of estimating the quantum effects on the reduced thermodynamic properties of nearly classical liquids can be obtained by making use of the data on isotopically substituted substances. In these systems, it is often possible to assume that the intermolecular potential energy is unchanged upon isotopic substitution. If this is indeed the case, then the differences between the properties of such fluids are primarily due to the changes in quantum mechanical parameter, and have only a second order dependence upon uncertainties in ϵ and σ or upon alterations in the potential energy curve. If the properties of the heavy and light molecules are denoted by the subscripts H and L, respectively, then the vapor pressure difference between two isotopic liquids can be written,

$$\ln p_H/p_L=-(\Delta H^*_H-\Delta H^*_L)/T^*+A_H-A_L$$
$$=-\Delta^2H^*/T^*+\Delta A. \tag{2}$$

Table I shows the values of Δ^2H^* and ΔA obtained by fitting published results for a number of substances to Eq. (2) at the listed values of T^*. The quotients $\Delta H^*/\Delta\Lambda^*$ and $\Delta A/\Delta\Lambda^*$ are given in columns 6 and 7

* This work was supported by API Project 42.

[1] J. deBoer, in *Molecular Theory of Gases and Liquids*, edited by J. O. Hirshfelder, C. F. Curtiss, and R. B. Bird (John Wiley & Sons, Inc., New York, 1954), Chap. 6.

[2] See Chap. 4 of work cited in footnote 1.

[3] T. L. Hill, *Statistical Mechanics* (McGraw-Hill Book Company, Inc., New York, 1956), Chaps. 6 and 8.

[4] J. S. Rowlinson, *Liquids and Liquid Mixtures* (Academic Press, Inc., New York, 1959), Chap. 8.

[5] J. M. H. Levelt, Physica **26**, 361 (1960).

[6] The substances considered, with the sources of the data, are: A, Kr, CH_4, CO; *Handbook of Chemistry and Physics* (Chemical Rubber Publishing Company, Cleveland, Ohio, 1959–60), 41st ed.; O_2, N_2; *Lange's Handbook of Chemistry* (Handbook Publishers, Sandusky, Ohio, 1956), 9th ed.; Ne, replotted from the data of F. Henning and J. Otto, Physik Z. **37**, 633 (1936).

[7] D. H. Rank, E. R. Shull, and D. W. E. Axford, J. Chem. Phys. **18**, 116 (1950).

TABLE I.

Substances	Ref.	T^*	Δ^2H^*	ΔA	$\Delta^2H^*/\Delta\Lambda^*$	$\Delta A/\Delta\Lambda^*$	$\Delta\Lambda^*$
$O^{16}O^{18}/O_2^{16}$	a	0.76	0.0123	0.0107	2.05	1.78	0.0060
	b	0.60	0.0131	0.0117	2.18	1.95	
$C^{13}O^{16}/C^{12}O^{16}$	a	0.80	0.0172	0.0142	4.65	3.84	0.0037
	c	0.80	0.0148	0.0105	4.00	2.84	
$C^{12}O^{18}/C^{12}O^{16}$	a	0.80	0.0128	0.0106	1.83	1.51	0.0070
$C^{13}H_4/C^{12}H_4$	a	0.68	0.0109	0.0085	1.52	1.18	0.0072
	c	0.68	0.0122	0.0153	1.69	2.12	
N_2^{15}/N_2^{14}	d	0.80	0.0191	0.0159	2.48	2.06	0.0077
	e	0.82	0.0175	0.0134	2.27	1.74	
$N^{15}N^{14}/N_2^{14}$	d	0.80	0.0097	0.0079	2.56	2.08	0.0038
Ne^{22}/Ne^{20}	f, g	0.77	0.0557	0.0355	2.00	1.28	0.0278
			Av[h]		2.1±.3	1.8±.3	

[a] T. F. Johns, in *Proceedings of the First International Conference on Isotope Separation, Amsterdam, 1957*, edited by J. Kistemacher, J. Bigeleisen, and A. O. C. Nier (North-Holland Publishing Company, Amsterdam, 1958), p. 74.
[b] W. Groth, H. Ihle, and A. Murrenhoff, Z. Angew. Chem. **68**, 644 (1956).
[c] W. Groth, H. Ihle, and A. Murrenhoff, Z. Naturforsch. **9a**, 805 (1954).
[d] K. Clusius and K. Schleich, Helv. Chim. Acta **41**, 1342 (1958).
[e] I. Kirshenbaum and H. C. Urey, J. Chem. Phys. **10**, 706 (1942).
[f] F. G. Roth and J. Bigeleisen, J. Chem. Phys. **32**, 612 (1960).
[g] W. H. Keesom and J. Haantjes, Physica **2**, 986 (1935).
[h] Signifies that CO data have been omitted from average.

of Table I. It is seen that these quantities are reasonably constant over the range $\Lambda^*=0.2$–0.6 with the exception of the values of $C^{13}O^{16}$ (data for the deuterated methanes[8] and for the nitric oxides[9] have not been included in Table I because of the large deviations from the average values of columns 6 and 7 in these systems.)

Much of the scatter in the values of $\Delta^2H^*/\Delta\Lambda^*$ and $\Delta A/\Delta\Lambda^*$ can be ascribed to the fairly large degree of uncertainty in the experimental results. However, there are several other possible reasons for the variations in these quantities. In the first place, it is not appropriate to calculate the quantum effects in this manner in systems in which the magnitude or distance scale of the intermolecular potential energy curve alters appreciably upon isotopic substitution. Other work has shown that this effect is noticeable in systems containing deuterated molecules.[10] The data on the deuteromethanes also show that the changes in physical properties of these fluids are considerably larger than the changes exhibited by systems in which the alteration in vibrational zero point energy upon isotopic substitution is less marked.

The observed changes in vapor pressure also depend upon the form of the intermolecular potential function, and, strictly speaking, the values of $\Delta^2H^*/\Delta\Lambda^*$ and $\Delta A/\Delta\Lambda^*$ obtained from data on two different substances are comparable only if the potential energy curves of the molecules are conformal. Since most of the molecules considered here are spherical or nearly so, the potential curves for the various systems should be nearly conformal with one another. However, it is interesting to note that the results for the polar liquids CO and NO do not agree very well with those for the nonpolar molecules (the dipole moments of CO and NO are 0.10 and 0.16 debyes, respectively).[11] Recently, J. Bigeleisen [J. Chem. Phys. **33**, 1775 (1960)] has pointed out that the anomalous properties of the NO system can be explained in terms of the mass effect on the equilibrium constant for the dimerization of the NO molecules in the liquid.

Graphs of $\ln p_H/p_L$ vs $1/T$ for the substances in Table I show a considerably larger curvature than is ordinarily observed in such plots. This indicates that Δ^2H^* and ΔA have a comparatively large temperature dependence, and thus it follows that the dependence of the configurational heat capacity of the liquid upon Λ^* is also relatively large. Few direct measurements have been made of the heat capacities of isotopically substituted, nearly classical liquids. However, the magnitude of the dependence of the configurational heat capacity upon Λ^* may be roughly estimated from a plot of $(C_p)_{\text{liq}}-(C_p)_{\text{gas}}$ (at $T^*=0.70$) vs Λ^{*2} for the substances mentioned in Table I. The slope of a straight line through these points is in only moderate agreement with the values of $\Delta C_p/\Delta\Lambda^{*2}$ calculated from the measurement of Clusius, *et al.*[12] on N_2^{15} and Ne^{22}. When the results of both methods of calculation are taken into account, the value of ΔC_p (configurational)$/\Delta\Lambda^{*2}$ at $T^*=0.70$ is estimated to be -11 ± 4 cal/mole deg for $\Lambda^*<0.6$.

[8] G. T. Armstrong, F. G. Brickwedde, and R. B. Scott, J. Research Natl. Bur. Standards **55**, 39 (1955).
[9] K. Clusius and K. Schleich, Helv. Chim. Acta **41**, 1342 (1958); K. Clusius, M. Vecchi, A. Fischer, and U. Piesbergen, Helv. Chim. Acta **42**, 1975 (1959).
[10] W. A. Steele, J. Chem. Phys. **33**,1619 (1960).
[11] H. E. Watson, G. G. Rao, and K. L. Ramaswamy, Proc. Roy. Soc. (London) **A143**, 558 (1934).
[12] K. Clusius, P. Flubacher, U. Piesbergen, K. Schleich, and A. Sperandio, Z. Naturforsch. **15a**, 1 (1960); K. Clusius, A. Sperandio, and U. Piesbergen, *ibid.* **14a**, 793 (1959).

Self-Diffusion in Linear Dimethylsiloxanes

DAVID W. MCCALL AND ERNEST W. ANDERSON

Bell Telephone Laboratories, Inc., Murray Hill, New Jersey

AND

CHARLES M. HUGGINS

General Electric Company, Research Laboratories, Schenectady, New York

(Received September 22, 1960)

The pressure and temperature dependences of the self-diffusion coefficients of the linear dimethylsiloxanes, containing from two to nine silicon atoms have been determined by the NMR spin-echo technique. Activation energies and volumes are presented as derived quantities; the constant-volume activation energy is estimated from these data. Extensive comparisons between the diffusion properties of the dimethylsiloxanes and equivalent hydrocarbons are made. From these comparisons, it is concluded that diffusion in siloxanes is controlled to a much larger extent by chain configurational effects. This concept is formalized by expressing the chain-size effects in an entropy of activation model.

INTRODUCTION

A LARGE number of the unusual physical properties associated with the dimethylsiloxanes $(-OSiMe_2-)_n$ are attributed to combinations of low intermolecular forces and to quite large chain flexibility.[1] These features are particularly evident in various studies of viscosity and mobility of siloxane systems. Rochow[1] discussed at length the gross dissimilarity between the viscoelastic behaviors of siloxanes and hydrocarbons of comparable chain length or even molecular weight. More recent NMR linewidth and spin-echo measurements on polydimethylsiloxane gums have demonstrated the uncommonly low microscopic viscosities of these materials.[2-5] A quantitative physical description of the diffusion process in siloxanes will require a separation of the effects of high chain flexibility and low intermolecular attraction. This paper presents some temperature and pressure dependences on the self-diffusion coefficients in a series of linear dimethylsiloxanes containing from two to nine silicon atoms. These data, while not leading to a complete understanding of the diffusion process, do provide a foundation for describing the behavior of the previously studied high polymers.

EXPERIMENTAL

The technique used to measure the self-diffusion coefficients is the nuclear magnetic resonance spin-echo method. The experimental details have been described previously[6-8] and will not be gone into here. Measurements were made over a range of temperatures, −50°C to about 100°C, and pressures, 1–700 atm.

The materials used were stock samples previously prepared and purified by the method of Patnode and Wilcock.[9] Any possible change in sample purity was checked by refractive index measurement. All samples of 2–8 Si atoms measured within ±0.0005 of the values reported by Rochow.[1] The sample of $Me_3Si-[OSi(Me)_2]_7-OSiMe_3$ was found by vapor-phase chromatography to be of greater than 95% purity ($n_D^{20}=1.3984$). Other samples, purporting to be pure compounds containing 10 or more Si atoms, were not studied since VPC analysis showed the purity to be less than 75% of the nominal constituent.

RESULTS

Figure 1 shows the dependence of the self-diffusion coefficient on chain length. The chain length is given in terms of the parameter N, the number of silicon atoms per molecule. Data for tetramethyl silane ($N=1$) are from a separate study.[10] It is seen that the decrease in D is quite marked at small N. On the other hand, D is not sensitive to N at higher molecular weights. Figure 2 compares the dimethylsiloxane data with similar data for the normal paraffins.[7] For purposes of comparison the abscissa m is taken to be the total number of atoms per molecule, excluding hydrogen. Note that the leveling off is much more apparent in the siloxane series.

The temperature-dependence data are displayed as Arrhenius plots in Fig. 3. A more detailed curve for the $N=9$ case is shown in Fig. 4. Activation energies E_p defined by $-R[\partial \ln D/\partial(1/T)]_p$, are shown in Fig. 5 together with the corresponding viscosity activation energies.[11] The activation energies for self-diffusion are uniformly about 1 kcal/mole greater than the

[1] E. G. Rochow, *Chemistry of the Silicones* (John Wiley & Sons, Inc., New York, 1951).
[2] E. G. Rochow and H. G. LeClair, J. Inorg. & Nuclear Chem. **1**, 92 (1955).
[3] C. M. Huggins, L. E. St. Pierre, and A. M. Bueche, J. Phys. Chem. (to be published).
[4] H. Kusumoto, I. J. Lawrenson, and H. S. Gutowsky, J. Chem. Phys. **32**, 724 (1960).
[5] J. G. Powles and A. Hartland, Nature **186**, 26 (1960).
[6] H. Y. Carr and E. M. Purcell, Phys. Rev. **94**, 63 (1954).
[7] D. C. Douglass and D. W. McCall, J. Phys. Chem. **62**, 1102 (1958).
[8] D. W. McCall, D. C. Douglass, and E. W. Anderson, Phys. Fluids **2**, 87 (1959).
[9] W. Patnode and D. F. Wilcock, J. Am. Chem. Soc. **68**, 358 (1946).
[10] D. C. Douglass, D. W. McCall, and E. W. Anderson, J. Chem. Phys. (to be published).
[11] D. E. Wilcock, J. Am. Chem. Soc. **68**, 691 (1946).

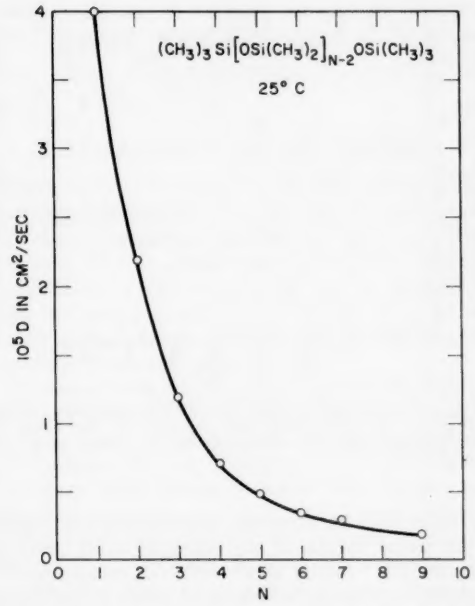

FIG. 1. Plot of D, the coefficient of self-diffusion (cm²/sec), vs N, the number of silicon atoms per molecule, for the linear dimethylsiloxane series at 25°C.

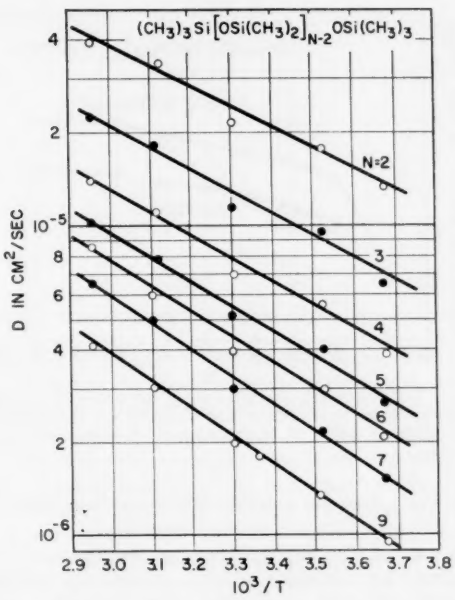

FIG. 3. Semilogarithmic plots of D, the coefficient of self-diffusion (cm²/sec), vs reciprocal temperature (°K⁻¹) for the linear dimethylsiloxane series; N is the number of silicon atoms per molecule.

activation energies for viscosity. This is in fair agreement with the Stokes-Einstein relation which predicts a difference of about 0.6 kcal/mole at room temperature.[7]

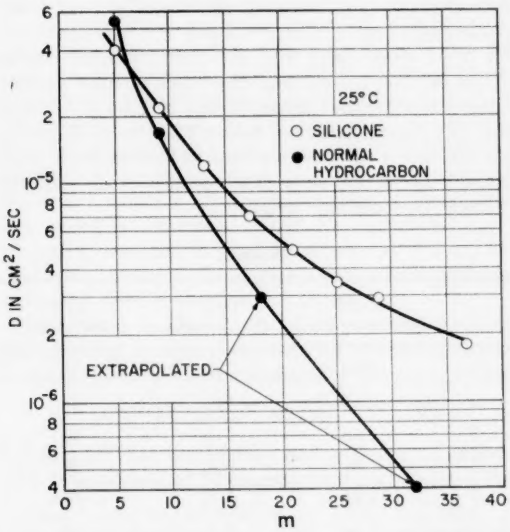

FIG. 2. Comparison of D, the coefficient of self-diffusion (cm²/sec), vs molecular size dependence (see text) for normal paraffins and linear dimethylsiloxanes at 25°C. (The two "extrapolated" points are for materials which are solids at 25°C.)

The dependence of D on pressure is shown in Fig. 6. Activation volumes $\Delta V^{\ddagger}$ defined by $-RT(\partial \ln D/\partial p)_T$, are exhibited in Fig. 7 along with the corresponding viscosity activation volumes calculated from Bridgman's data.[12] As Bridgman's points were taken in 2000-atm increments, it was necessary to extrapolate the activation volumes to lower pressures for compari-

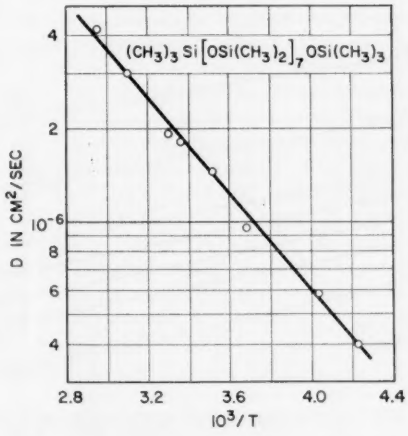

FIG. 4. Semilogarithmic plot of D, the coefficient of self-diffusion (cm²/sec), vs reciprocal temperature (°K⁻¹) for $(CH_3)_3Si[OSi(CH_3)_2]_7OSi(CH_3)_3$.

[12] P. W. Bridgman, Proc. Am. Acad. Arts Sci. 77, 115 (1949).

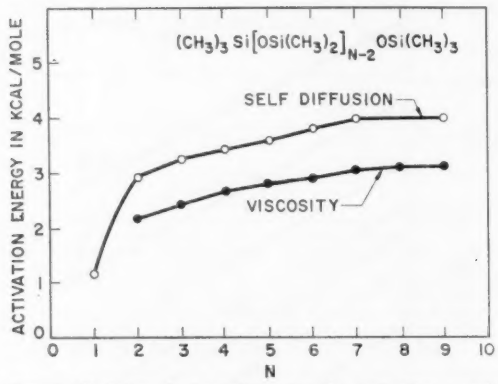

FIG. 5. Chain-length dependence for the activation energies (kcal/mole) for self-diffusion and viscosity for the linear dimethylsiloxane series; N is the number of silicon atoms per molecule.

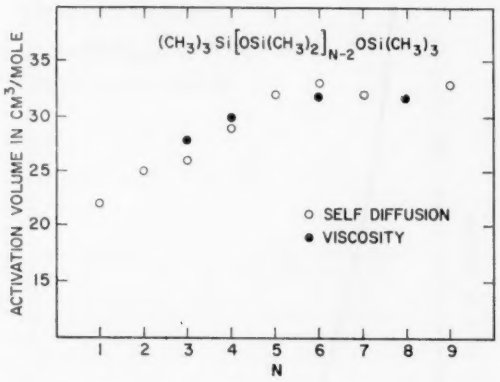

FIG. 7. Chain-length dependence for the activation volumes (cm³/mole) for self-diffusion and viscosity for the linear dimethylsiloxane series; N is the number of silicon atoms per molecule.

son. The activation volumes as derived from viscosity and diffusion data are in good agreement.

It is worth mentioning, in passing, that the activation volumes for viscosity exhibit interesting pressure dependences, first decreasing, then increasing with increasing pressure. For example, for the $N=6$ compound (MD_4M), $\Delta V_\eta^\ddagger = 68$ cm³/mole at 9000 atm, but only 21 cm³/mole at 3000 atm. The pressure range covered by the present study is insufficient to reveal the presence of such behavior in the self-diffusion experiment.

The experimental data are summarized in Table I, giving D, E_p, and $\Delta V^\ddagger$.

DISCUSSION

Perhaps the most interesting experimental findings are the small activation volumes in the range of 30 cm³/mole. This experimental value cannot correspond to the molar volume of any segment which could be considered a "unit of flow" with the exception of a methyl group having a volume of about 25 cm³/mole. These data should be compared to the typical value of about 20 cm³/mole for the normal hydrocarbons[8] which is not as unreasonable in view of the considerably smaller cross-sectional area of the methylene unit.

Another commonly used measure of "unit of flow" is the Stokes-Einstein radius, $a=kT/6\pi D\eta$. These are listed in Table II. These numbers increase uniformly with chain size, but are considered to be quite small in regard to the cross-sectional area of a dimethylsiloxane unit. For example, assuming the molecules to be close-packed spheres, an effective radius of 4 A is calculated for $N=2$ to compare with the Stokes-Einstein radius 0f 2.0 A. For comparison, the much smaller paraffin chain has a Stokes-Einstein radius of 1.9–2.0 A.[7] Note that the dimethylsiloxane Stokes-Einstein radii, unlike the activation volumes, continue to increase with chain length, albeit not at a rate commensurate with the increase in molecular weight.

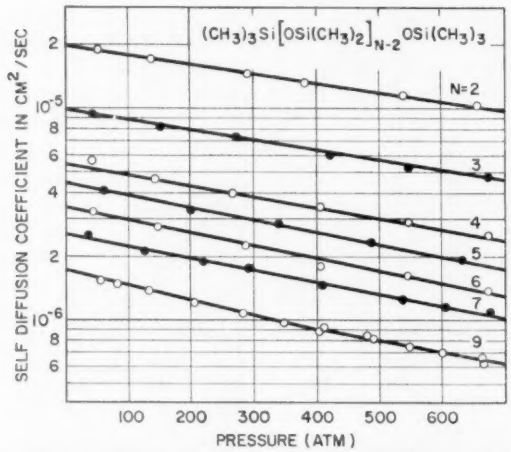

FIG. 6. Semilogarithmic plots of D, the coefficient of self-diffusion (cm²/sec), vs p, the pressure (atm), for the linear dimethylsiloxane series; N is the number of silicon atoms per molecule.

TABLE I.

N	$D\times10^6$ (cm²/sec) (25°C)	E_p (kcal/mole)	$\Delta V^\ddagger$ (cm³/mole)
1	40.0	1.1_6	22
2	22.0	2.9_4	25
3	11.8	3.2_9	26
4	7.0_7	3.4_6	29
5	4.9_2	3.6_4	32
6	3.5_2	3.8_4	34
7	2.8_8	4.0_1	32
9	1.9_0	4.0_6	33

It is of interest to estimate the energies of activation at constant volume E_v by means of the relation

$$E_v = -R[\partial \ln D/\partial(1/T)]_v = E_p - p_i \Delta V^\ddagger,$$

where

$$p_i = T(\partial p/\partial T)_v = -T(\partial V/\partial T)_p/(\partial V/\partial p)_T.$$

Unfortunately, only sparse PVT data are available; Bridgman[12] gives $(\partial V/\partial p)_T$ for $N=2$–8, with quite limited accuracy due to his 500-atm measuring intervals, and $(\partial V/\partial T)_p$ data were obtained from commercial literature.[13] Another estimate can be obtained by using the ratio of energy of vaporization to molar volume.[14] Table III lists both values of the resulting constant-volume activation energies.

Considerable significance has been attached to the ratios, $\Delta V^\ddagger/V$ and E_v/E_{vap}, as well as the comparison between them in viscosity and diffusion processes.[15] For example, McCall, Douglass, and Anderson,[8] in their study of the alkanes, found $\Delta V^\ddagger/V$ to range about 0.10–0.14, and E_v/E_{vap} to be 0.11–0.17, with a marked degree of correlation between the two sets of data. To the contrary, $\Delta V^\ddagger/V$ for the dimethylsiloxanes exhibits a uniform, sharp decline with increasing chain size, while E_v/E_{vap} shows a more gradual decline. Other than the fact that both decrease, no correlations such as those found with the alkanes is apparent. This dissimilarity in behavior can be attributed to grossly different processes controlling diffusion in the linear dimethylsiloxanes.

In the dimethylsiloxane series the ratio E_{vap}/V decreases markedly with increasing chain length. This would indicate that a large part of the total intermolecular force is being expended intrachain; that is, that the molecule has a tendency to coil or fold back on itself. By comparison, this ratio is about 2400 atm for *n*-hexane and increases mildly with increasing chain length in the paraffin series. However, the ratio $E_p/\Delta V^\ddagger$ is a constant at about 5000 atm for $N=2$ to $N=9$ in dimethylsiloxanes and varies from 5000 to 7000 atm for *n*-hexane to *n*-decane. Since E_{vap}/V is a measure of the "net" strength of the intermolecular forces and this quantity decreases while E_p increases, E_p/V remaining constant, it must be concluded that E_p for the higher members of the series becomes more strongly dependent upon configurational effects.

The Eyring model for transport processes leads to the following general expression for the self-diffusion coefficient, where λ is the elementary jump length and

$$D = (\lambda^2 kT/h) \exp(\Delta S^\ddagger/R) \exp(-\Delta H^\ddagger/RT),$$

$\Delta S^\ddagger$ and $\Delta H^\ddagger$ are the entropy and enthalpy of activation. It is convenient to consider that $\Delta H^\ddagger$ includes the energy terms associated with intermolecular forces and ΔS includes the configurational terms, both intermolecular and intramolecular. To be explicit, suppose that a long chain molecule can exist in a variety of extended and coiled configurations. It seems reasonable that molecular translation can occur more easily when the molecules are in the extended configurations, and further, it seems likely that such configurations, being lowest in energy, become less probable as the temperature is increased. The term $\exp(\Delta S^\ddagger/R)$ can be interpreted, roughly, as the probability that a molecule is in a configuration favorable for diffusion.

Table II.

N	a(A) (37°C)
2	2.0
3	2.1
4	2.2
5	2.3
6	2.4
7	2.5
9	2.7

Two features of this discussion are important, first, the entropy of activation is expected to be temperature dependent and will thus contribute to the observed activation energy E_p. In this way purely configurational terms can influence activation energies. Second, such effects can be expected to be most easily observed in polymers which have relatively flexible chains. That is, configurational terms will be most important when the energy required to bend or kink the molecular chain is small compared with kT.

The dimethylsiloxane series, having both low intermolecular forces and highly flexible chains, should be sensitive to configurational effects. This statement is intuitive but is based on the foregoing and following sequence of thoughts. Many liquids are relatively well ordered, at least on a short-range basis. For example, in the paraffin series there is evidence that the molecules tend to be extended and parallel.[7,16] The siloxanes are probably much less ordered and a wide distribution of molecular configurations is expected, at least in the longer members. Direct evidence for the marked flexibility of the dimethylsiloxane chain has been presented by Flory.[17] We are suggesting that the ease with which a molecule diffuses depends upon its particular configuration. The reason such effects are not so important in the paraffin series is that one configuration predominates.

The discussion given here is speculative and differs from Wilcock's[11] discussion of the viscosity results for

[13] Dow-Corning Silicone Notebook, ref # 2003, June, 1952.

[14] J. H. Hildebrand and R. L. Scott, *The Solubility of Nonelectrolytes* (Reinhold Publishing Corporation, New York, 1955).

[15] S. Glasstone, K. J. Laidler, and H. Eyring, *The Theory of Rate Processes* (McGraw-Hill Book Company, Inc., New York, 1941), p. 524.

[16] A. Bondi, J. Chem. Phys. **14**, 591 (1946).

[17] P. J. Flory, L. Mandelkern, J. B. Kinsinger, and W. B. Shultz, J. Am. Chem. Soc. **74**, 3364 (1952).

TABLE III.

N	$\Delta V^{\ddagger}$ cm³/mole	V cm³/mole	E_{vap}/V[a] atm	E_p[b] kcal/mole	E_v[c] kcal/mole	$\Delta V^{\ddagger}/V$	E_v/E_{vap}
2	25	210	1600	2.0	1.5	0.119	0.20
3	26	288	1350	2.4	1.8	0.090	0.21
4	29	371	1290	2.6	2.0	0.078	0.18
5	32	451	1190	2.7	2.1	0.071	0.17
6	34	515	1160	2.9	2.3	0.066	0.17
7	32	585	1140	3.1	2.6	0.055	0.17
9	33	742	1070	3.1	2.5	0.044	0.14

[a] See work cited in footnote 11.
[b] Computed from $\Delta H_{vap}/V$ (see text).
[c] Computed from PVT data (see text).

the same compounds. However, the two approaches are not mutually exclusive but rather differ in choice of emphasis; Wilcock is most concerned with the "unit of flow,"[18] while we have employed the entropy of activation.

[18] W. Kauzman and H. Eyring, J. Am. Chem. Soc. **62**, 3113 (1940).

ACKNOWLEDGMENTS

The authors wish to thank Dr. B. H. Zimm, Dr. D. C. Douglass, and Dr. W. P. Slichter for their helpful comments, and Mr. M. Hadsell, General Electric Research Laboratory, for the analyses and distillations of the materials used in this work.

Synthesis of the Cubic Form of Boron Nitride

R. H. WENTORF, JR.

General Electric Research Laboratory, Schenectady, New York

(Received September 12, 1960)

A study of the formation of cubic boron nitride shows that the alkali and alkaline earth metals and their nitrides are effective catalysts for converting hexagonal boron nitride into cubic. The pressure and temperature required varies with the catalyst, and a minimum of about 45 000 atm and 1500°C has been found to be optimum up to the present time.

SINCE the announcement in 1957 of the discovery of the cubic form of boron nitride,[1] BN (borazon) its formation has been studied further. This paper summarizes many of the additional facts now known about this synthesis.

The high-pressure, high-temperature apparatus used in this work was a double-ended conical piston device designed by H. T. Hall[2] and subsequently modified by H. P. Bovenkerk so as to improve its capacity and durability. A cross section of it is shown in Fig. 1. The

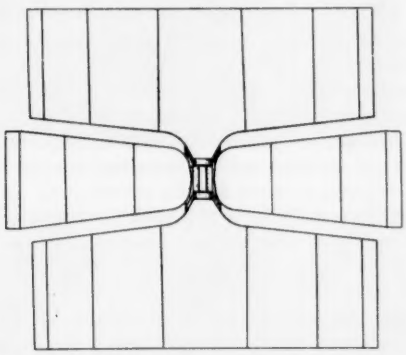

FIG. 1. "Belt" ultra high pressure, high-temperature assembly.

pressure generated inside it is calibrated by reference to electrical resistance transitions in bismuth, barium, etc., and the temperature is approximately known from the power used to heat the capsule. Routine work can be carried out at pressures and temperatures of 100 000 atm and 2500°C.

It was found that the analogy between boron nitride and carbon was quite striking. Therefore, early work was aimed at a synthesis of cubic boron nitride along lines similar to those found successful for diamond synthesis, i.e., exposure of boron-nitrogen-catalyst mixtures to a high temperature and pressure in a reaction vessel such as shown in Fig. 2, followed by a reduction in temperature to "freeze" any high-pressure modifications which might have formed, and finally, reduction of pressure to 1 atm. In this way pure boron nitride powder, borazole ($B_3N_3H_6$), and various mixtures of boron and nitrogen compounds were studied, as well as mixtures of boron nitride powder with the diamond-forming catalysts (iron, nickel, manganese). All such experiments produced only the hexagonal form of boron nitride, even at pressures as high as 100 000 atm and temperatures about 2000°C. (At this temperature the hexagonal boron nitride powder showed an increase in crystal size, from about 5 mμ to about 20 mμ.)

However, when bits of magnesium metal were buried in the hexagonal boron nitride, a chemical reaction occurred in their vicinity, and a few small hard lumps, less than 1 mm in diameter, were isolated from the mixture. These lumps were insoluble in the usual acids, easily scratched a boron carbide test plate, and gave a

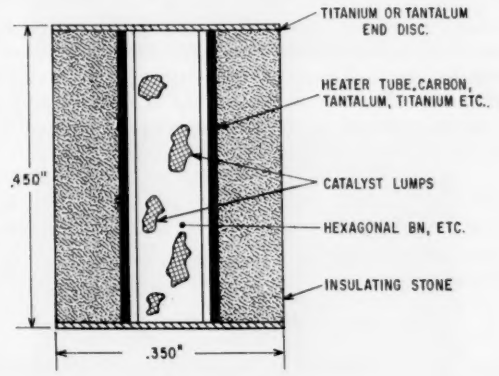

FIG. 2. Typical reaction vessel.

Debye-Scherrer pattern similar to that of diamond but with a few extra lines and a somewhat larger unit cell (3.615 A vs 3.56 A for diamond). See Fig. 3. When heated to about 2500°C at 40 000 atm, such a lump turned into a soft white powder identified as hexagonal BN from its Debye-Scherrer pattern. Thus the evidence was very strong that the hard substance was a cubic form of boron nitride. It was found difficult to determine nitrogen in the cubic boron nitride, because the ordinary Kjeldahl reagents did not attack the compound. It was necessary to dissolve it in molten NaOH

[1] R. H. Wentorf, Jr., J. Chem. Phys. **26**, 956 (1957).
[2] H. T. Hall, Rev. Sci. Instr. **31**, 125 (1960).

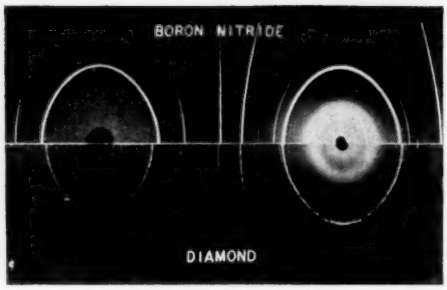

FIG. 3. Debye-Scherrer patterns for cubic BN vs diamond.

and titrate the ammonia formed, while assuming that all the N in the BN appeared as ammonia.

Any possibility that the compound was a particular one containing magnesium was dispelled when a number of other catalysts were found to transform the hexagonal boron nitride into the cubic form at various high pressures (50 000 to 90 000 atm) and temperatures (1500–2000°C). The particular pressure and temperature necessary depended upon the catalyst used; some were effective only at higher pressures and temperatures. These catalysts turned out to be the alkali metals. the alkaline-earth metals, and antimony, tin, and lead. The bulk of the chemical elements are not effective as catalysts. In general, the higher the atomic weight of a catalyst, the more pressure is required to effect the transformation. Thus, about 70 000 atm seem to be necessary for potassium or barium to be active as catalysts. At slightly lower pressures these metals react with hexagonal BN and diffuse into it, but no cubic BN forms. The effectiveness of any of these catalysts is greatly reduced by the presence of a few percent of water, boric oxide, etc., in the reaction mixture.

It was noticed that the cubic boron nitride formed with these metallic catalysts tended to be black in color, but a few tiny clear white crystals were occasionally seen. This fact suggested that perhaps the following type of reaction occurred in the mixture

$$\mathrm{Li}+3\mathrm{BN}\rightarrow\mathrm{Li_3N}+3\mathrm{B}.$$

Part of the boron could be incorporated as excess boron in the cubic BN and color it black. This prompted the use of magnesium, calcium, or lithium nitrides as catalysts, and these turned out to be the most effective of all. High yields of cubic BN could be obtained with them at pressures as low as 45 000 atm.

It was possible to form cubic boron nitride from mixtures of boron, and lithium or magnesium nitride at high pressure and temperature, but at some sacrifice in yield and crystal quality.

It was noticed that as one increased the operating temperature of the synthesis, the pressure required for forming the cubic phase also increased. Thus, the equilibrium line between the hexagonal and cubic forms rises in pressure with temperature. At a given pressure less than 100 000 atm, cubic boron nitride is stable at a higher temperature than is diamond.

The crystal size of the cubic boron nitride which is formed depends primarily on the pressure and temperature at which the reaction is carried out. The closer these lie to the cubic-hexagonal equilibrium line, the larger the resulting crystals. However, at higher temperatures the absolute reaction rate is higher, so that small variations in pressure or temperature produce large variations in crystal quality. Thus the best crystals (up to 0.5 mm average size) are grown at moderate pressures and temperatures (50 000 atm, 1700°C) in a few minutes. If the operating pressure is increased to 70 000 atm the crystal size drops to about .02 mm, i.e., the nucleation rate is much higher than at 50 000 atm.

The lithium nitride-boron nitride system has received the most study so far. It appears that at the operating conditions there is formed a loose complex of the approximate composition $\mathrm{Li_3N}\cdot 3\mathrm{BN}$. This complex then acts as a molten solvent which dissolves hexagonal BN and precipitates cubic BN by virtue of a displacement from thermodynamic equilibrium in favor of cubic BN at the operating pressure and temperature. The BN which is tied up in this complex is not entirely available for the formation of cubic BN. The complex is a white solid at room temperature and dissolves completely in dilute HCl—no hexagonal BN separates from it. It does not give a recognizable Debye-Scherrer pattern and contains neither hexagonal nor cubic BN. Debye-Scherrer d-values for this material are listed in Table I. In a mixture of this complex and hexagonal BN at operating pressure and temperature, one finds that the nucleation and growth rates of cubic BN are highest where the local complex concentration is high. However, the complex tends to diffuse, so that its concentration becomes fairly uniform after about ten minutes of heating, and the nucleation and growth rates of cubic BN then decrease markedly. This can be

TABLE I. Debye-Scherrer d-values for $\mathrm{Li_3N}$—BN high-pressure complex. (s: strong; m: medium; w: weak).

A	Intensity	A	Intensity	A	Intensity
5.60	m	1.92	w	1.16	w
3.60	s	1.85	mw	1.13	vw
3.50	mw	1.73	mw	1.10	w
3.34	mw	1.68	vw	1.08	w
3.25	w	1.64	m	1.05	w
3.08	ms	1.62	m	1.03	w
2.85	w	1.60	m	1.02	w
2.78	s	1.53	m	1.01	w
2.67	m	1.50	vw	0.990	mw
2.56	mw	1.44	w	0.965	mw
2.50	mw	1.41	w	0.945	w
2.35	w	1.38	w	0.890	w
2.25	m	1.36	w	0.880	w
2.15	ms	1.30	m	0.860	w
2.07	vw	1.275	w	0.830	w
2.03	m	1.245	w	0.820	w
1.96	w	1.17	w		

slightly offset by a slight increase in pressure, but too great a pressure increase sharply increases spontaneous nucleation.

Some photomicrographs of various crystals of cubic boron nitride are shown in Figs. 4–8. Tetrahedra and octahedra are the most common. The surfaces generally show growth marks in the form of layers or steps of various outlines. Trigons, similar to those found on diamond, can occasionally be seen. As the growth rate is increased the growth steps move closer together, so that with rapid growth the step height is about the same as the step width (about 10 mμ), and twinning becomes more likely. (Compare Figs. 7 and 8.)

The normal color of the cubic boron nitride crystals made at 50 000 atm and 1700°C with nitride catalysts is yellow. The addition of a few percent of boron changes the color to dark brown or black. By operating at 65 000 atm and 1900°C, small, white crystals of cubic boron nitride can be obtained.

No crystals having a wurtzite structure have yet been found, though this structure is almost the equivalent of the zinc-blende cubic structure possessed by

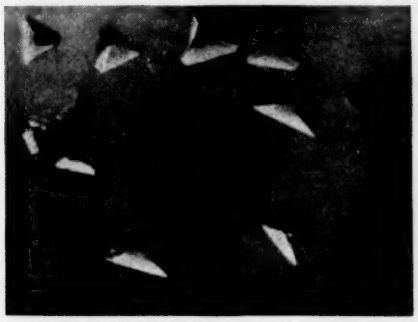

FIG. 4. Cubic BN, tetrahedral crystals.

FIG. 5. Cubic BN, octahedral crystals.

FIG. 6. Freshly grown face of cubic BN crystal.

FIG. 7. Slowly grown octahedral face of cubic BN crystal. Note trigons.

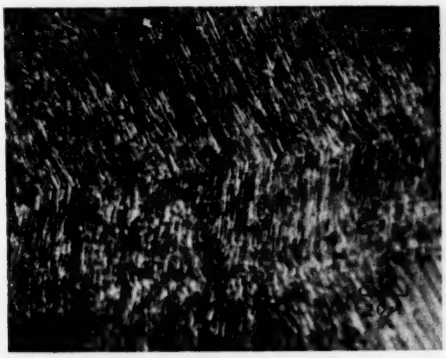

FIG. 8. Rapidly grown, twinned face of cubic BN crystal.

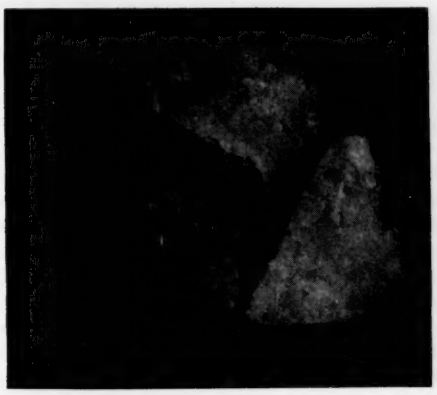

FIG. 9. Hexagonal BN flakes.

the boron nitride. (BP has the zincblende structure[3,4], but AlN and AlP have the wurtzite structure.)

If a mixture of lithium nitride and boron nitride is exposed to a high temperature and pressure appropriate for the stability of hexagonal boron nitride, white, translucent flakes of this phase form. Some of these are 1 mm or more in diam and seem to be about 0.05 mm thick. Figure 9 is a photomicrograph of some of these. Such crystals are weak and flexible and resemble graphite in their mechanical behavior.

[3] P. Popper and T. Ingles, Nature **179**, 1075 (1957).
[4] J. Perri, S. La Placa, and B. Post, Acta Cryst. **11**, 310 (1958).

ACKNOWLEDGMENTS

The author wishes to express his gratitude for the encouragement of Mr. A. J. Nerad, the chemical analyses performed by Dr. E. L. Simons, and L. B. Bronk, and the x-ray diffraction patterns prepared by R. H. Lewinski, Ann Cooper, Lucille Bruce, and Rose DeCerbo.

THE JOURNAL OF CHEMICAL PHYSICS VOLUME 34, NUMBER 3 MARCH, 1961

The Effect of Oxygen Adsorption on Photo- and Semiconduction of β-Carotene

BARNETT ROSENBERG

Department of Physics, New York University, New York

(Received June 27, 1960)

The presence of adsorbed oxygen gas increases the magnitude of the surface semiconduction currents in crystalline powder β-carotene by a factor of about 10^3. The activation energy for the surface semiconduction process is 1.52 ev in argon gas and is decreased to 1.29 ev in oxygen. The room temperature photocurrent is increased by a factor of about 25 in oxygen over the value in argon. The activation energy of the photoconduction process is not affected by oxygen. The increase in dark current in an oxygen ambient requires a time of about 2 hr to come to the equilibrium value at room temperature. Radiation is not required to cause the increase. The effect of the oxygen can be reversed completely by heating the β-carotene to 120°C in an inert atmosphere (dry nitrogen or argon). The increase in dark current is linearly proportional to the partial pressure of oxygen in the chamber. The rate of desorption of the oxygen increases with the temperature. The resulting data yield an activation energy of desorption of 0.17 ev. It is suggested that this is the binding energy for the formation of an oxygen-carotene complex, and that the decrease in semiconduction activation energy is correlated to this binding energy. An analysis is given which leads to the conclusion that the mechanism of the current increase with formation of the oxygen complex is twofold; a decrease in the activation energy for semiconduction, and an increase in the mobility of the charge carriers. There is no evidence for a change in the charge creation process. The experimental results are considered to be a partial verification of Platt's theory on the donor-carotene-acceptor complex in photosynthesis since the triplet level of chlorophyll *b* has a value of 1.43 ev, midway between the value of 1.52 ev for the free carotene semiconduction activation energy and 1.29 ev for the corresponding value of the oxygen-carotene complex. It is also suggested that a possible mechanism for the carotene protection of cells from destructive photo-oxidation may be the formation of the oxygen-carotene complex.

I. INTRODUCTION

THAT ambient oxygen gas produces a pronounced increase in the surface photoconduction and semiconduction currents of organic crystals has been known since the work of Vartanyan on phthalocyanines[1] and anthracene.[2] Since that time, a number of workers have investigated this effect and elucidated some of the details of the processes. It is now known that a number of other gases[3] can affect these currents in a reversible process, either decreasing or increasing them depending on whether the gases are electron donors or acceptors. Reversibility in these cases consists of being able to return to the previous vacuum values by gentle processes of continuous pumping on the samples with or without concomitant irradiation, or slight heating. This implies that the gases are bound to the surface molecules by weak coupling forces rather than by any high-energy chemical change in the organic molecules. Chynoweth[4] has suggested a two-stage process in the case of oxygen and anthracene: the first stage is an intermediate form of photo-oxide and the second stage is a more stable peroxide. Bree and Lyons[5] prefer to consider the formation of a biradical intermediate state which is easily dissociable. At the present time however there does not seem to be any convincing evidence in favor of any particular assumption as to the type of interaction of the gas with the substrate.

A similar situation obtains in considering the mechanism for the current increase, since this is of course contingent upon the type of interaction assumed. Chynoweth has proposed that the increase in photocurrent in anthracene with oxygen (a factor of 2 to 5)

[1] A. T. Vartanyan, Zhur. Fiz. Khim. **22**, 769 (1948).
[2] A. T. Vartanyan, Doklady Akad. Nauk. S.S.S.R. **71**, 641 (1950).
[3] W. G. Schneider and T. C. Waddington, J. Chem. Phys. **25**, 358 (1956).
[4] A. G. Chynoweth, J. Chem. Phys. **22**, 1029 (1954).
[5] A. Bree and L. E. Lyons, J. Chem. Phys. **25**, 384 (1956).

can be explained by assuming that the photo-oxidation reduces the rate of recombination of the surface charge carriers and increases their lifetime. Bree and Lyons would have the biradical intermediate dissociate into ions with a consequent liberation of positive mobile charge. Schneider and Waddington[5] have involved the surface energy levels and traps to modify the surface mobility of the charges as has been proposed for band type semiconductors like germanium.

Rosenberg[6] has shown that β-carotene exhibits both semiconduction and photoconduction. In a sandwich cell made by cooling a melt of β-carotene between two conductive glass electrodes, the semiconduction activation energy was 3.0 ev (assuming $j=j_0 \exp[-E/2KT]$). This is for the case where a glass formed on cooling due to geometrical isomerization in the melt. More recently it was found[7] that crystalline powders pressed between two electrodes exhibit the smaller activation energy of 1.5 ev which was attributed to surface conduction effects. In the material presented below, the experimental work was performed using such powdered crystalline cells in a sandwich configuration, to determine some characteristics of the effect of oxygen on the photoconduction and semiconduction surface currents. The experimental method and apparatus have been described in a previous paper.[8] The crystalline all trans β-carotene was obtained from Eastman-Kodak. This was then recrystallized four times from cold toluene solution by ethanol addition. The purity was determined by a paper chromatography technique (the criteria being a single band with no perceptible auxiliary bands) and by the less sensitive method of looking for a cis peak in the optical absorption spectra. The crystals were stored in evacuated tubes at 0°C until used.

II. EFFECT OF OXYGEN AT CONSTANT TEMPERATURE

In the past, measurements of semiconduction or photoconduction in β-carotene were made in an atmosphere of dry argon or nitrogen. The samples were first heated to 120°C and then cooled before readings were taken. This was found to be not essential in the case of β-carotene glass cells, for these were well protected from atmospheric effects, but to be quite necessary in the case of powder crystalline cells when the powder had been exposed even briefly to air after preparation.

When the powder cell had been temperature cycled (keeping the temperature below 120°C to prevent sintering) and returned to room temperature, the dark current under argon or nitrogen atmosphere was typically about 5×10^{-12} amp for an applied voltage of 22.5 v across a 3-mil thick cell of 1 cm² area. The cell was then continually flushed with dry compressed air or oxygen and the current determined as a function of time. Due to low flow rates of the gas, it usually required about 1–2 minutes to completely flush the apparatus. The results of such a measurement are shown in Fig. 1 for pure oxygen gas. In this case, the dark current increased by a factor of 3400 when the steady state was reached. The latency period at the beginning is due to the flushing time. It can be seen that the current has an initial fast rise which slows down and finally reaches a steady state value. The shape of the curve is suggestive of a relationship of $I(t)=I_{equil}[1-\exp(t/\tau)]$ which one should expect to hold on the basis of the theory of gas adsorption. However when plotted in this form, the data do not give good straight lines with a single slope and therefore only the single primitive data curve is given.

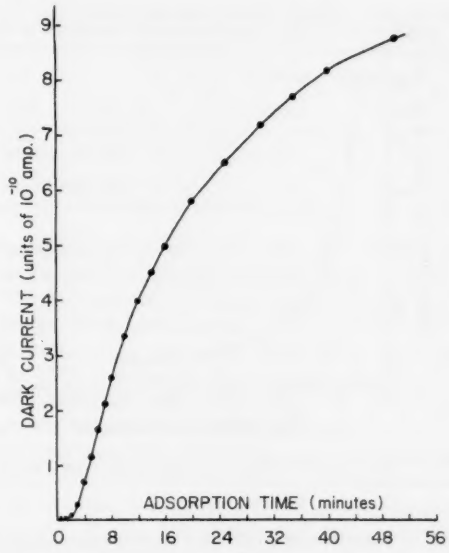

FIG. 1. Dark current increase with time in oxygen for all *trans* β-carotene.

In contradistinction to the data of Chynoweth on anthracene, irradiation with intense white light either before, during or after oxygen adsorption has no appreciable effect upon the equilibrium dark current. It is therefore concluded that in the case of β-carotene, photo-oxidation does not seem to be playing an important role. In addition, the equilibrium current is the same whether an electric field is applied during adsorption or not. These remarks hold true as well for the desorption process described below. Another variable tested was the type of electrodes used. Again, the effects were similar for metal rear electrodes of stainless steel, monel metal or aluminum. It does not seem possible, from this and other data to be presented (the desorption activation energy), to ascribe the oxygen

[6] B. Rosenberg, J. Chem. Phys. **31**, 238 (1959).
[7] B. Rosenberg, "Photoconduction and Photovoltaic Effects in Carotenoid Pigments" in *Electronic Conductivity in Organic Solids* (Interscience Publishers, Inc., New York, to be published in 1961).
[8] B. Rosenberg, J. Chem. Phys. **34**, 63 (1961).

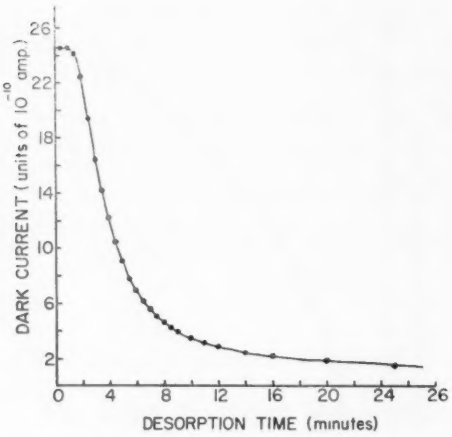

FIG. 2. Dark current decrease due to oxygen desorption for all *trans* β-carotene.

effect to a metal-semiconductor barrier phenomenon or to intergrain barrier effects.

If, after equilibrium has been reached at room temperature, the flow of oxygen gas is replaced by pure argon or nitrogen, the current decreases at a rate of a few per cent per hour. However as the temperature at which the gas change over is elevated, the current decreases at a faster rate. In Fig. 2, the decrease in dark current is shown as a function of time at the temperature of 56°C. There is an initial rapid drop followed by a much slower process. This will be discussed in more detail in Sec. V. If the sample is heated in argon or nitrogen to 120°C and cooled, the original dark current (before oxygen adsorption) is reached. We have repeated this process on a single sample as much as 12 times with no significant variation in the final dark current or the semiconduction activation energy. This indicates that the oxygen process is completely reversible with respect to changes in temperature and oxygen concentration.

Measurements were next made on the magnitude of the current increase at constant temperature as a function of the partial pressure of oxygen in the chamber. Here, the flow rate of oxygen and argon were separately monitored while the chamber was kept at normal atmospheric pressure. Each time the oxygen flow rate was increased, the current was determined after a 10-minute waiting period to allow the sample to come to a partial equilibrium (total equilibrium would require a few hours). However, it can easily be shown that if the equilibrium currents are a linear function of the partial pressure, then the nonequilibrium currents will also be a linear function of the partial pressure so long as the same relaxation time is used in each of the measurements. The same is true for nonlinear functions. At higher temperatures of course the rate of approach to equilibrium is much more rapid. In Fig. 3 the results of such measurements for two temperatures are given for all trans β-carotene. In both cases the current is linearly proportional to the partial pressure of oxygen, with the larger constant of proportionality for the higher temperature case as discussed above. The measurements cover the limited range of 0–18% oxygen concentration. These results are in agreement with Bornmann,[9] who reported a linear increase of the dark current with partial pressure of oxygen for various metal phthalocyanines. If we consider this a true Langmuir isotherm, the implication to be drawn from the linearity is a simple one, viz., that the fraction of the surface covered by the adsorbed oxygen gas which causes the current increase is a very small portion of the total surface area. Assume that the current increase (ΔI_{oxygen}) is proportional to the fractional area of surface covered by the oxygen (θ). That is

$$\Delta I_{\text{oxygen}} = K\theta. \tag{1}$$

The Langmuir isotherm equation is of the form[10]

$$\theta/(1-\theta) = bP, \tag{2}$$

where P is the partial pressure of the gas and b a constant of proportionality (at constant temperature). Then to have linearity requires that $\theta \ll 1$. We will return to this point in Sec. VI.

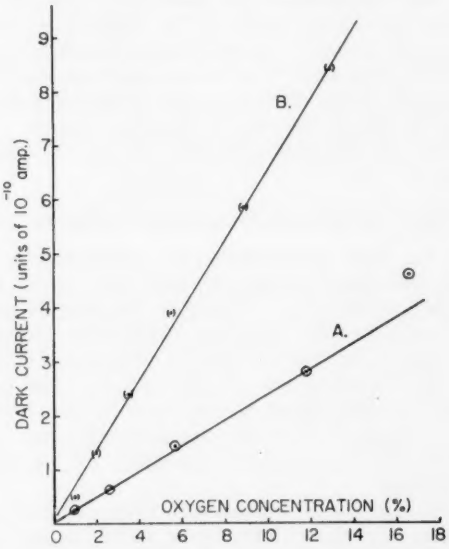

FIG. 3. Dark current increase as a function of oxygen concentration in all *trans* β-carotene: A. Temp=23°C; B. Temp=35°C.

[9] J. A. Bornmann, J. Chem. Phys. **27**, 604 (1957).

[10] More properly one should use the isotherm equation for mixed gases since nitrogen or argon is admixed with the oxygen. However this only introduces another small term in the equation which is also ignorable with respect to 1 when the experimental oxygen adsorption is linear with pressure, and the equation reduces to the above. This means that the oxygen adsorption process is independent of the presence of the inert gas.

III. EFFECT OF ADSORBED OXYGEN ON THE SURFACE SEMICONDUCTION ACTIVATION ENERGY

The surface semiconduction activation energy of powdered crystalline β-carotene is about 1.5 ev in the sandwich cell arrangement. The data of dark current vs temperature give straight lines on a semilog plot of current vs the reciprocal absolute temperature over a range of current values of 10^5 and a temperature range from −40°C to 120°C. The measurements are normally made in an atmosphere of dry argon or nitrogen, both of which give identical values. To determine the effect of oxygen on the semiconduction current, the sample is allowed to adsorb oxygen and come to equilibrium at room temperature with the gas environment containing a known and adjustable concentration of oxygen in argon. The pressure of the total gas mixture is atmospheric in all our experiments. The chamber is rapidly cooled to 0°C (or to −40°C) and then the temperature is slowly increased to 120°C. This may be done in the same oxygen containing atmosphere, or alternatively, the chamber may be flushed with pure argon after the cooling process. In the first type of measurement the chamber is flushed with pure argon after reaching 120°C for the cooling portion of the curve. The results of one such experiment are shown in Fig. 4 as illustrative of the process. Here the heating curve was started at 0°C. For the region up to 30°C (A) the curve has a straight line portion. As the temperature increases further there is gradual slowing down of the rate of current rise with temperature and then a drop off (B); and finally at temperatures above 80°C another linear portion (C). With the cooling portion of the curve, the usual straight line is obtained (D). The interpretation of these results is fairly obvious and has been corroborated in all essential details. The portion (A) is due to the association of oxygen with the surface molecules which is fairly stable below 30–40°C. At higher temperatures (B), the association breaks down at a faster rate and the oxygen molecules are desorbed from the surface, the rate of desorption increasing with temperature, and the current begins to diminish towards the normal current value in argon. In the region of (C), the oxygen is almost completely desorbed and the argon dark current is reached. This then results in the normal argon cooling curve (D).

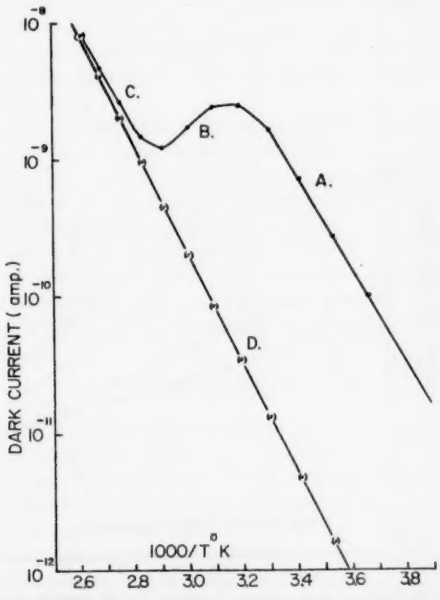

FIG. 4. The effect of oxygen on the semiconduction process in all *trans* β-carotene.

TABLE I. The effect of oxygen on the activation energies for semiconduction and photoconduction in all *trans* β-carotene.

	Activation energy (ev)	
	Argon	Oxygen
Semiconduction	1.52	1.29
Photoconduction	0.34	0.34

The points of major interest in these curves are the slopes of the regions (A) and (D) which give the activation energies of the processes; and the temperature region where rapid desorption occurs, as indicating the binding energy of the adsorbed oxygen. In all of our present measurements the slopes of the (A) portions are smaller than the (D) portions. That is the activation energy for surface conduction is less for the oxygen-carotene complex than for the pure carotene. The averages of a number of measurements give the values shown in Table I. The activation energy of semiconduction is lowered by 0.23 ev when oxygen is absorbed in sufficient quantity to greatly increase the dark current. The decrease in activation energy with adsorbed gases has been fairly well established; (in particular, see footnotes 1, 2, and 9).

The desorption process has an activation energy somewhat larger than KT, since the rate of desorption becomes rapid only above 50°C or so. The same type of curves is obtained for samples where pure argon is substituted after cooling and before heating starts, except that the desorption effect becomes noticeable at slightly lower temperatures. The desorption activation energy will be discussed in more detail in Section V.

IV. EFFECT OF ADSORBED OXYGEN ON THE PHOTOCONDUCTION ACTIVATION ENERGY

The adsorption of oxygen increases the photocurrent in β-carotene powder, but not by the same factor as the dark current increase. The results of such measurements at a constant temperature are shown in Table II. The dark current increase is larger by a factor of 44 than the photocurrent increase.

The photoconduction activation energy of all *trans* β-carotene has been reported previously[8] as 0.37 ev

TABLE II. The effect of oxygen on the dark current and photocurrent in all *trans* β-carotene at constant temperature.

Oxygen pressure = 1 atm	Temperature = 25°C	
	Dark Current (j_D)	Photocurrent (j_L)
Argon	6.0×10^{-12} amp	6.3×10^{-10} amp
Oxygen	6.6×10^{-9} amp	1.6×10^{-8} amp
Ratios:	$\frac{j_D'(\text{oxygen})}{j_D(\text{argon})}=1100$	$\frac{j_L'(\text{oxygen})}{j_L(\text{argon})}=25$

for the average of a number of measurements. We have now measured the activation energy in a sample of all *trans* β-carotene in argon and then in oxygen. The results of these measurements are given in Table I. While the magnitude of the photocurrent increases by a factor of 25, there is no perceptible difference in the activation energy in argon or oxygen.

V. DESORPTION OF OXYGEN AT CONSTANT TEMPERATURE

The data given in Fig. 4 have been interpreted as a desorption of oxygen with a temperature dependent rate. This has been tested and verified in the following manner. A previously deoxygenated sample was kept at a constant temperature and allowed to come to equilibrium (with respect to the dark current) with a gas ambient containing a known concentration of oxygen. At a given time the oxygen was flushed from the system with a continual flow of pure argon. The dark current was then measured as a function of time. Figure 2 illustrates the decrease in current. This was repeated for four different temperatures. The results are compiled in Fig. 5. The method of plotting is based upon the following analysis: We again assume as in Eq. (1) that the current increase is proportional to the fraction of the surface covered by adsorbed oxygen molecules. That is, that the total current is composed of two terms, the irreducible (argon) value and the contribution from the oxygen-carotene complex

$$I_{\text{total}}=I_{\text{argon}}+\Delta I_{\text{oxygen}}, \tag{3}$$

where ΔI_{oxygen} is given by Eq. (1). Since the second term in general is much larger than the first we will call the current increase with oxygen the total current. Therefore

$$I_{\text{total}}=\Delta I_{\text{oxygen}}=K\theta. \tag{4}$$

For the simple desorption process we have[11]

$$d\theta/dt=-\nu\theta, \tag{5}$$

where ν is the temperature dependent rate constant (when $\theta=1$) and is given by

$$\nu=A\exp(-q/KT). \tag{6}$$

[11] S. Brunauer, *The Adsorption of Gases and Vapors* (Princeton University Press, Princeton, New Jersey, 1945), Vol. I.

Integration of the expression in Eq. (5) with appropriate initial conditions gives

$$\theta(t)=\theta_{\text{equil}}\exp(-\nu t) \tag{7}$$

which on substitution of Eq. (4) yields the final equation

$$I_{\text{total}}(t)=I_{\text{equil}}\exp(-\nu t). \tag{8}$$

The data in Fig. 5 have been plotted so that straight lines would result if it followed the form of Eq. (8). Indeed, the first portion of the desorption process does give straight lines. These, however, depart from the curve after about 6 minutes decay. This is an as yet unknown slower process that has been mentioned above. The initial horizontal portions of the curves are again due to the flushing time of the sample chamber. The slopes of the curves give the values of ν. These four values of ν are then replotted to give a straight line if it follows the temperature dependence of Eq. (6). The graph is given as Fig. 6. Again a fair agreement to the expected form results. The slope of this curve then gives the value of q, the activation energy for desorption of the oxygen from the carotene surface. This value is 0.17 ev. This experimental activation energy q represents the difference in energy between the states of the gas and the bound states on the surface of the β-carotene, and apart from a small entropy factor should be the binding energy of the oxygen-carotene complex. Since there is no activation energy in forming the complex, it is certainly of great interest that this value of the binding energy should be so close to the

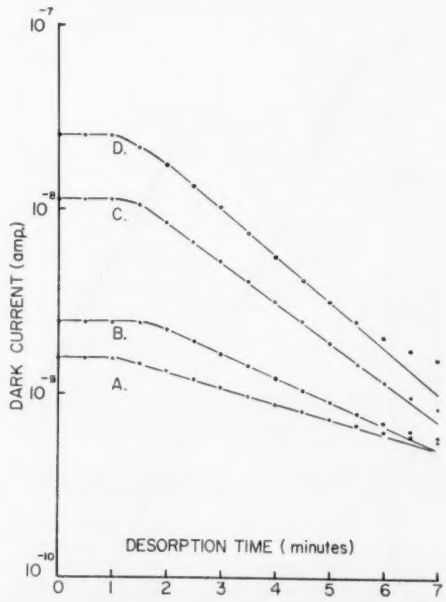

FIG. 5. Rate of dark current decrease due to oxygen desorption for all *trans* β-carotene. A. Temp = 33°C; B. Temp = 56°C; C. Temp = 86°C; D. Temp = 100°C.

value of the decrease in semiconduction activation energy (0.23 ev). We are tempted to equate the two values, consider the difference as due to experimental variation, and therefore assign the mean value of 0.20 ev to both. The general hypothesis would be, "The decrease in activation energy of surface semiconduction in organic crystals due to adsorbed acceptor gases is equal to the binding energy of the complex formed by the molecules of the gas and the surface molecules of the substrate." Unfortunately there is to our knowledge no other such comparable sets of data in the field to test this hypothesis.

VI. MECHANISMS OF CURRENT INCREASE DUE TO ADSORBED OXYGEN

We should now like to turn to considerations of the mechanisms whereby adsorbed oxygen can effect the large increases in the semiconduction and photoconduction currents. The clearest method of analysis is to write down the most simple general expressions for the semiconduction and photoconduction processes and then to determine from the experimental evidence which parameters are a function of the formation of the oxygen-carotene complex. For the semiconduction process we have the equation for the current density

$$j_D = n_0 e\mu F \exp(-E_D/2KT), \tag{9}$$

where n_0 may represent the number of molecules in the ground state, or equivalently the number of states available to the process; e is the electron charge, μ is the mobility; F is the field strength; and E_D is the experimental activation energy. (One may alternately write E_D'/KT, since there does not seem to be any general agreement on the presence or absence of the factor of 2. The writer prefers the factor of 2 since the value of E_D then for most organic substances shows a startling agreement with the energy of the lowest triplet state.)

The corresponding equation for the photocurrent cannot be so simply written. Complications of numerous sorts have arisen in determining the functional dependence on the various possible experimental parameters. In general, the photocurrents in β-carotene may follow a linear or a $\frac{3}{2}$ power dependence upon the field strength. The choice is determined by the wavelength of the exciting light and the magnitude of the applied field. The equation previously suggested by the writer is[6]

$$j_L = A\alpha_\lambda V_0 + B(\alpha_\lambda - K)V_0^{\frac{3}{2}}, \tag{10}$$

where V_0 is the applied voltage; α_λ the optical absorption coefficient; and k is a constant of the order of 10^4/cm. The constants A and B lump together other factors some of which are described in Eq. (11) below. It was pointed out in that paper that for the case of white light incident through the positive electrode the transition from the linear dependence to the higher voltage $\frac{3}{2}$ power dependence occurred at 24 v applied

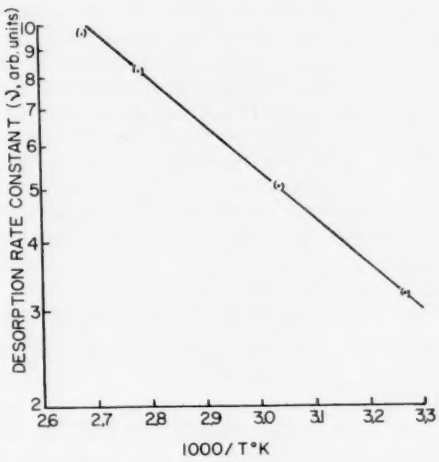

FIG. 6. The dependence of the desorption rate constant ν upon temp in all *trans* β-carotene.

across a sample 1 mil thick. In our present measurements we have the same circumstance except for the greater thickness of our sample (3 mil). The applied voltage used at present was 22.5 v and therefore we are safely within the linear region. We may then write for the restricted case of our present measurements

$$j_L = \alpha_\lambda I_\lambda \phi e\mu F \exp(-E_L/KT), \tag{11}$$

where now $\alpha_\lambda I_\lambda$ gives the intensity of absorbed light; ϕ a factor which includes, according to the triplet state theory of photoconduction suggested by the writer,[12] the lifetime of the triplet state and the ratio of the rate of intersystem crossing to the rate of other processes for depleting the excited singlet state (fluorescence and quenching); e, μ and F are as in Eq. (9) and E_L is the photoconduction activation energy described in Sec. IV. We now consider Eqs. (9) and (11) as holding for the case of an inert atmosphere (argon nitrogen etc.) and proceed to rewrite these equations with primes representing possible new values depending on the presence of adsorbed oxygen. Thus Eq. (9) becomes

$$j_D' = n_0' e\mu' F' \exp(-E_D'/2KT) \tag{12}$$

and Eq. (11) becomes

$$j_L' = \phi' \alpha_\lambda' I_\lambda e\mu' F' \exp(-E_L'/KT). \tag{13}$$

Some of these primes can be eliminated, however, from some simple considerations. The currents which are ohmic in argon remain ohmic under oxygen, and therefore $F' = F$. The absorption coefficient of β-carotene is already one of the largest known and since it has been shown that the fraction of the surface covered by the adsorbed oxygen is very small, it is not

[12] B. Rosenberg, J. Chem. Phys. **29**, 1108 (1958).

likely that α_A changes perceptibly and we set $\alpha_A'=\alpha_A$. While it is tempting, in the light of the paramagnetic nature of the oxygen ground state to assume an effect of its presence upon the factor ϕ, this does not appear likely to be important. It has been shown that oxygen decreases the lifetime of the triplet state by collisional deactivation in fluid media[13] more effectively than it enhances the transition rate of intersystem crossing (due to the fact that the lifetime of the triplet state is much longer than the excited singlet state, thus giving the oxygen more time to act). Since the oxygen is bound in this case collisional deactivation does not occur and we may set $\phi'=\phi$. We now take the ratio of the oxygen gas equations to the inert gas equations. This gives us for the semiconduction ratio [(9) and the modified (12)]

$$j_D'/j_D=(n_0'/n_0)(\mu'/\mu)\ \exp[(E_D-E_D')/2KT], \quad (14)$$

and for the photoconduction ratio [from Eq. (11) and the modified (13)]

$$j_L'/j_L=(\mu'/\mu)\ \exp[(E_L-E_L')/KT]. \quad (15)$$

These equations are now to be compared with the experimental results. The change in the semiconduction activation energy, E_D-E_D', has been given as 0.20 ev (0.23 ev by direct measurement and 0.17 by the desorption activation energy data). The photoconduction activation energy is independent of the ambient gas. Therefore $E_L-E_L'=0$. We evaluate the exponentials for room temperature and put these values in Eq. (14) and (15), giving

$$j_D'/j_D=48\times(n_0'/n_0)(\mu'/\mu) \quad (16)$$

and

$$j_L'/j_L=(\mu'/\mu). \quad (17)$$

We have thus far reduced the effect of oxygen on photoconduction to an increase of mobility of the current carriers only. The experimental value for the ratio of photocurrents at room temperature has been given in Table II as $j_L'/j_L=25$. If, as has been shown in the past, the predominant current carriers in both semiconduction and photoconduction are positive holes, then the mobilities are the same in both cases and we can put the numerical value of 25 in Eq. (16). This gives us

$$j_D'/j_D=48\times25\times(n_0'/n_0)=1200\ (n_0'/n_0). \quad (18)$$

This is to be compared with the experimental value of the ratio from Table II of $j_D'/j_D=1100$. While we should not like to put too much emphasis on the excellent agreement between the numerical values, since this is to some extent due to the choice of 0.20 ev as the decrease in semiconduction activation energy rather than the value 0.23 ev directly measured (this would change 48 to 104, a factor of about 2), it is strongly indicative that n_0' does not vary by very much from n_0. This means that we cannot consider the current increasing effect of oxygen to be a charge creation process in β-carotene. The effect of oxygen is clearly twofold: (1) it decreases the activation energy of semiconduction; and (2) it increases the mobility of the positive hole charge carriers. The product of these two factors fully account for the increase in photoconduction and semiconduction currents.

These results, while unambiguously derived in this analysis, raise some further questions. The linearity of the Langmuir Isotherm has been interpreted to mean that the fraction of the surface covered by oxygen is very small, i.e., the number of oxygen-carotene complexes is a small portion of the number of surface molecules. Yet the semiconduction activation energy is dominated by these complexes. This coupled to the result that $n_0'=n_0$, requires that the normal surface semiconduction arises similarly from only a small number of surface molecules. The question arises as to the nature of these "active" molecules on the surface. The body semiconduction activation energy of the melted glass β-carotene has been shown to be 3.0 ev.[6,7] When such a glass is crushed to a fine powder the semiconduction activation energy is reduced to 1.55 ev, in agreement with the crystalline powder values, but the magnitude of the current is not greatly increased. Since these "active" centers are the same for both the glass and crystalline states, they cannot be ascribed to any type of lattice distortions. It cannot be due to impurities since the glass shows the two different activation energies depending only on the continuous or discrete nature of the material between the electrodes.

Another difficulty is the large increase in mobility of the charge carriers if the complexes are few and far between. A partial solution to these difficulties results if we assume that the oxygen covers a large fraction of the total surface and seek another explanation for the linear isotherm. It is obvious that much more work is required to solve these problems.

VII. RELATION OF OXYGEN EFFECT TO PLATT'S "DONOR-CAROTENE-ACCEPTOR COMPLEX"

In a recent paper[14] Platt has suggested a very interesting theory concerning the involvement of carotene molecules in the photosynthetic process. This involves the dark formation of a weak donor-carotene-acceptor triple complex of a partial charge transfer type. This complex will lower the energy levels of the carotene—either the singlet or triplet levels—from the uncomplexed form. If the amount of lowering is sufficient, it could go from the values of the free carotene which are known to be higher than the corresponding electronic energy levels in chlorophyll to values below these levels. This complex would then act as an energy sink for the excited states of the whole system. The complex,

[13] G. Porter and M. W. Windsor, Proc. Roy. Soc. (London) **A245**, 238 (1958).

[14] J. R. Platt, Science **129**, 372 (1959).

upon absorption of such transferred energy, would then dissociate into neutral carotene and ionized acceptor and donor molecules. He has also suggested that bimolecular complexes may be formed which act subsequent to each other in time to accomplish the same purpose.

On the basis of the work described above we can provide an experimental verification of at least one part of this theory. While we cannot on the basis of this work confidently conclude that the oxygen-carotene complex formed is of a partial charge transfer type, it seems a plausible consideration. The value of the binding energy (0.20 ev) is of the order to be expected from such complexes—but it is also of the same order as Van der Waals binding. A complete charge transfer complex can at once be eliminated by the result given above that no positive hole injection occurs in β-carotene.

It has been shown that the surface semiconduction activation energy of the pure β-carotene has the value of 1.52 ev. The corresponding value for the oxygen-carotene complex is 1.29 ev. We can safely assume that these energies refer to a molecular level above the ground state which leads to the liberation of a mobile hole in the ground state. These two values are then to be compared with the chlorophyll molecular energy levels. Calvin and Dorough[15] and Becker and Kasha[16] have shown that the triplet level in chlorophyll *b* is 1.43 ev above the ground state. This lies almost midway between the higher value of free carotene and the lower value of the oxygen-carotene complex, in corroboration of one part of Platt's theory.

We have also attempted to find evidence for the effect of donor-carotene complexes on the semiconduction and photoconduction currents. The following gases have been tested so far: hydrogen, illuminating gas and water vapor carried by nitrogen. In all three cases there was no change in the magnitude of the currents or in the activation energies (water vapor at temperatures below 50°C, where it condenses, shorts out the insulators in the cell and causes an abnormal increase in the current, at more elevated temperatures it has no perceptible effect). We have not yet had an opportunity to extend these tests to other gases. This method of approach seems to be an eminently practical way to test the further ramifications of Platt's theory.

The formation of the weakly bound oxygen-carotene complex may be of some significance in another case. It has been proven that carotene serves to protect the living cell from a destructive chlorophyll sensitized photooxidation.[17] The above work indicates that one possible mechanism for this may be that carotene ties up the excess oxygen in the form of the weakly bound oxygen-carotene complex where it is stored, and released when the oxygen tension of the system is low, as in respiration.

ACKNOWLEDGMENTS

It is a pleasure to acknowledge a long standing debt of gratitude to Professor H. P. Kallmann of the Department of Physics, New York University, and in the present particular for helpful comments on the work described. I should like to thank Mr. R. A. Orlando for the purification of all *trans* β-carotene crystals. This work was supported by Research Grant B–1936 from the National Institute of Neurological Diseases and Blindness of the Public Health Service.

[15] M. Calvin and G. D. Dorough, Science **105,** 433 (1947).

[16] R. S. Becker and M. Kasha in *The Luminescence of Biological Systems,* edited by F. H. Johnson (A.A.A.S., Washington, D. C., 1955), p. 25.

[17] G. Cohen-Baziere and R. Y. Stanier, Nature **181,** 250 (1958).

Kinetics of Crystal Nucleation in Some Normal Alkane Liquids

DAVID TURNBULL AND ROBERT L. CORMIA
General Electric Research Laboratory, Schenectady, New York

(Received August 4, 1960)

The crystal nucleation behavior of some normal alkane liquids—$C_{16}H_{34}$, $C_{17}H_{36}$, $C_{18}H_{38}$, $C_{24}H_{50}$, and $C_{32}H_{66}$—was investigated by the droplet technique. The relative undercoolings, $1-\lambda$, (i.e., the actual undercooling in units of the absolute melting temperature) at which the crystal nucleation frequency in these liquids becomes 10^7 cm^{-3} sec^{-1} are 0.037 to 0.043, and almost an order of magnitude smaller than those for simple molecular substances. Crystal nucleation frequencies in droplets of $C_{17}H_{36}$ and $C_{18}H_{38}$ samples of very high purity were determined quantitatively. The frequencies were proportional to droplet volume and increased by a factor of 5000 to 8000 per 1° decrease in temperature. The results are satisfactorily described by the classical nucleation theory with values of the crystal nucleus - liquid interfacial tension σ, 7.2 erg-cm^{-2} for $C_{17}H_{36}$ and 9.6 erg-cm^{-2} for $C_{18}H_{38}$. The experimental pre-exponential factors in the nucleation expression agree with the theoretical values to well within the experimental uncertainty. The small relative undercooling and the weak glass-forming tendency in the high-molecular weight *n*-alkane liquids is satisfactorily explained by the hypothesis of nucleation of small segments of molecules.

INTRODUCTION

RECENTLY Cohen and one of us[1–4] developed a simple model for the glass transition according to which any liquid would form a glass at some temperature well above 0°K if crystallization does not intervene. Whether or not crystallization intervenes is determined by the magnitude of the crystallization kinetic constants (the crystal nucleation frequency I, and the crystal growth constant D_u) and the rate at which the liquid is cooled. A glass, once formed, is stable for a long time, since the rate of growth of crystals within it is very small.

In considering the glass-forming tendency it is convenient to define a reduced temperature, τ, as follows

$$\tau = kT/h_v, \tag{1}$$

where T is the ordinary absolute temperature and h_v is the molecular heat of vaporization. Certain properties of all liquids of a particular molecular type or class (e.g., simple molecular substances form one class, metallic substances another) are approximately single functions of the reduced temperature. From the meager evidence at hand it appears[3,4] that within any given class the reduced temperature τ_g at the glass transition is approximately constant, and the kinetic constant for crystal growth D_u is approximately a single function $D_u(\tau)$ of the reduced temperature. However, the reduced thermodynamic crystallization temperature τ_m varies widely within a class. As the temperature is decreased from τ_m the crystal nucleation frequency presumably increases sharply, but does not become readily measurable until τ has fallen to some value τ' proportional to τ_m, that is:

$$\tau' = \lambda\tau_m, \tag{2}$$

where λ is approximately constant for a glass. From these considerations Cohen and Turnbull[3,4] showed that the glass-forming tendency of liquids in a class should be the greater as τ_m is less.

The reduced normal boiling temperature τ_b of simple molecular substances is about 0.1. For those members of this class for which $\tau_m \gtrsim 0.06$, λ has been found[5,6] to be 0.7 to 0.75. However, when cooled at ordinary rates, the simple molecular liquids having $\tau_m < 0.05$ usually form glasses at reduced temperatures near 0.023 to 0.025.[1,3] The high molecular weight members of the normal alkane series have reduced thermodynamic crystallization temperatures around 0.045 to 0.050, but they do not form glasses when cooled at normal rates. This weak glass-forming tendency was explained[3] on the basis of the concept already developed for polymer systems[7] that crystal nucleation in long chain molecules requires aggregation not of entire molecules but only of molecular segments. Consequently, the crystal nucleation frequency and λ should be relatively large for the higher molecular weight normal alkanes. To test these ideas and also to obtain results that might be helpful in the interpretation of the mechanism of crystallization in polymer systems, we decided to measure the crystal nucleation frequency of some typical high molecular weight *n*-alkane liquids.

In order to circumvent the effects of foreign surfaces on nucleation, we have used the droplet technique described in papers by Vonnegut[8] and one of us.[9–11] The

[1] D. Turnbull and M. H. Cohen, J. Chem. Phys. **29**, 1049 (1958).
[2] M. H. Cohen and D. Turnbull, J. Chem. Phys. **31**, 1164 (1959).
[3] D. Turnbull and M. H. Cohen, *Modern Aspects of the Vitreous State*, edited by J. C. Mackenzie (Butterworths Scientific Publications, Ltd., London, 1960).
[4] D. Turnbull and M. H. Cohen, J. Chem. Phys. (to be published).
[5] D. G. Thomas and L. A. K. Stavely, J. Chem. Soc. **1952**, 4569.
[6] H. J. de Nordwall and L. A. K. Stavely, J. Chem. Soc. **1954**, 224.
[7] L. Mandelkern, *Growth and Perfection of Crystals*, edited by R. H. Doremus, B. W. Roberts, and D. Turnbull (John Wiley & Sons, Inc., New York, 1958), pp. 467–494.
[8] B. Vonnegut, J. Colloid Sci. **3**, 563 (1948).
[9] D. Turnbull, J. Appl. Phys. **20**, 817 (1949).
[10] D. Turnbull, J. Chem. Phys. **20**, 411 (1952).
[11] D. Turnbull, *Solid State Physics* (Academic Press, Inc., New York, 1956), Vol. **3**, pp. 225–306.

analysis of droplet data, which has been described fully elsewhere,[10] is outlined briefly in the following section.

ANALYSIS OF DROPLET DATA AND NUCLEATION THEORY

It is possible to determine the nucleation frequency absolutely from dilatometric measurements on droplet dispersions provided the droplet crystallization period after nucleation is negligible compared with the mean droplet nucleation time. In this method the volume of a sample of liquid in the form of droplets, kept apart by surface films, is measured during crystallization. The volume fraction $1-V$ of the sample which is still liquid after an isothermal hold for a time t is given by

$$1-V=\sum_{D=0}^{D=\infty} V_D{}^0 \exp(-k_D t), \tag{3}$$

where $V_D{}^0$ is the volume fraction of liquid droplets having diameters between D and $D+\Delta D$ (where $D \gg \Delta D$) at time zero, and k_D is the crystal nucleation frequency of a droplet having the diameter D. Also

$$\sum_{D=0}^{D=\infty} V_D{}^0 = 1. \tag{3a}$$

If nucleation occurs homogeneously (i.e., unassisted by foreign surfaces),

$$k_D = I v_D, \tag{4a}$$

where I is the nucleation frequency per unit volume and v_D is the volume of a droplet of diameter D. If nucleation is catalyzed by a film on the droplet surface,

$$k_D = I_s a_D, \tag{4b}$$

where I_s is the nucleation frequency per unit area of film and a_D is the area of the droplet.

From nucleation theory[12] the frequency of homogeneous nucleation of crystals in undercooled liquids may be written:

$$I = K_v \exp(-W^*/kT), \tag{5}$$

where $W^*=$ the work required to form a nucleus, and[13]

$$K_v = \gamma n D'/a_0{}^2, \tag{5a}$$

$$\gamma = 2(v)^{\frac{1}{3}}(\sigma/kT)^{\frac{1}{2}}. \tag{5b}$$

n = the number of molecules per unit volume;
D' = the nucleation kinetic constant in cm^2 sec^{-1};
σ is a parameter which, in classical nucleation theory, is identified with the liquid-crystal interfacial tension;
a_0 = the mean molecular diameter;
v = the molecular volume.

[12] D. Turnbull and J. C. Fisher, J. Chem. Phys. **17**, 71 (1949).

[13] In our expression for γ, Eq. (5b), the factor $n^*/i^{*\frac{1}{3}}$, where i^* is the number of molecules in the nucleus and n^* is the number of molecules in the surface of the nucleus, replaces n^* of Turnbull and Fisher's[12] expression. This modification is made to correct for Turnbull and Fisher's inadvertent failure to cancel the factor $i^{*-\frac{1}{3}}$ in arriving at their Eq. (16). Turnbull and Fisher are indebted to Professor R. Defay of the Free University of Brussels for calling this mistake to their attention.

If we assume that the liquid-crystal surface tension is independent of the orientation of the crystal surfaces it follows that

$$W^* = (16\pi/3)(\sigma^3/\Delta G_v{}^2), \tag{5c}$$

where ΔG_v is the free energy of bulk crystallization per unit volume. If ΔS_v, the entropy of crystallization per unit volume, is independent of the undercooling ΔT, we obtain

$$\Delta G_v = \Delta S_v \Delta T. \tag{5d}$$

T', the temperature at which the nucleation frequency has some specified measurable value, is easily found from this set of equations.

It is probable that σ for the high-molecular weight normal alkanes is strongly dependent upon crystal surface orientation. However, in the present analysis we shall ignore this dependence since there is no quantitative theory for it. Thus the values of σ inferred from our experiments may represent, at best, averages over the various surface orientations.

The normal alkanes of intermediate molecular weight fall into two classes according to their crystallization behavior; in one class the molecules contain an even number and in the other an odd number of carbon atoms. It has been established that the entropy of fusion per unit volume is constant for a class and it is expected from simple chemical considerations that σ should be constant as well. From these generalizations Turnbull and Cohen[3] showed that for a class [see Eq. (2)]

$$T'/T_m = \lambda = 1-(B/\lambda T_m{}^3)^{\frac{1}{3}}, \tag{6}$$

where $T_m=$ the thermodynamic crystallization temperature,

$$B = (16\pi/3)\frac{\sigma^3}{k(\Delta S_v)^2 \ln(K_v/I_r)}, \tag{6a}$$

and I_r is some constant measurable nucleation frequency. Since σ and ΔS_v are constant and K_v should vary slowly with the number of carbon atoms, B should be approximately independent of chain length. Therefore, Turnbull and Cohen[3] concluded that $1-\lambda$ should fall off with increasing chain length roughly as the reciprocal of the corresponding T_m values taken to the three-halves power.

EXPERIMENTAL

Any part of the procedure not described specifically here was just as described in the earlier paper on mercury.[10]

Compounds

The two compounds which we investigated most extensively are *n*-heptadecane ($C_{17}H_{36}$) and *n*-octadecane ($C_{18}H_{38}$). Samples of these compounds of very high purity were kindly supplied to us by the Pennsyl-

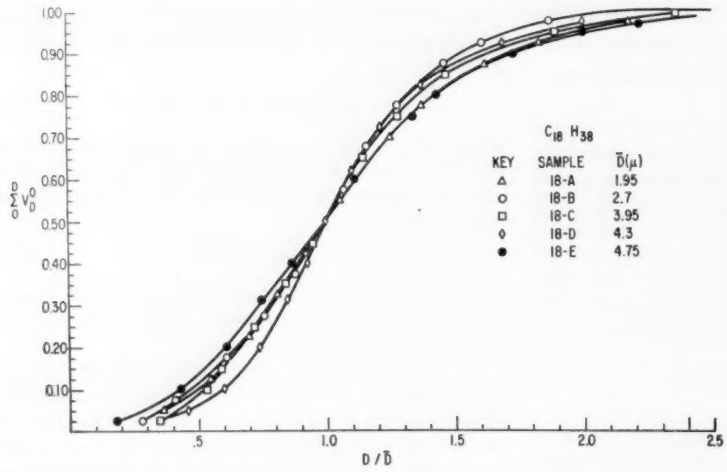

FIG. 1. Distribution of sample volume among the different droplet sizes for *n*-octadecane dispersions.

$$\sum_0^D V_D^0$$

represents the volume fraction of the droplets having diameters less than D. $\bar{D}$ is defined by Eq. (7).

vania State University and the American Petroleum Institute (A.P.I.), and were used in their as-received form.

Our other measurements were made on *n*-hexadecane ($C_{16}H_{34}$), *n*-tetracosane ($C_{24}H_{50}$), and *n*-dotriacontane ($C_{32}H_{66}$). These compounds were of ordinary CP grade and the *n*-tetracosane and *n*-dotriacontane were further purified by successive recrystallizations from sulfuric acid and diethyl ether.

Formation of Droplet Dispersions

Dispersions of hydrocarbon droplets in water, stabilized by a wetting agent, were formed by mixing the constituents in a Waring Blendor. Igepal CO-880 [C_9H_{19}–C_6H_4–$O(CH_2$–O–$CH_2)_{14}O$–C_2H_5] was used as a wetting agent. The mixture used usually consisted of 100 cc distilled water, 7 cc hydrocarbon, and 2 gm Igepal. The mean droplet size decreased with time of mixing and ranged from one to several microns. The concentration and size of the droplets in the dilatometer samples could be varied considerably by proper sampling of blended mixtures in which some gravity segregation had occurred.

Dilatometry

Our dilatometric procedures were in general similar to those described earlier,[10] except that special provision had to be made to keep the hydrocarbon droplets confined to the dilatometer bulb. This provision was a thin polyethylene diaphragm seated on a flat ground-glass joint which connected the dilatometer bulb and indicator tube. The joint was kept from leaking by pressure exerted by a clamp.

The cylindrical dilatometer bulb was 0.6 cm in inner diameter and had a capacity of 3.5 cc. The indicator tube was a long capillary of 0.02 cm inner diameter, and was filled with water during the experiments. In the isothermal experiments the dilatometer bulb was entirely immersed in a bath held at a temperature constant to within ±0.0015°. This temperature was measured with a calibrated thermometer. The amounts of hydrocarbon in the dilatometer were such that the water column in the indicator tube dropped from 2 to 8 cm during the complete course of isothermal crystallization. The crystallization rate was kept small enough so that the temperature in the dilatometer would not be raised appreciably above the bath temperature. To test the performance of the dilatometer, the coefficient of thermal expansion of water was measured over the temperature range 2 to 31°C. The results agree with published values to well within the expected errors in the cathetometer readings. Also, the measured changes in volume (about 11%) of the hydrocarbons upon solidification were in good agreement with published values.

Droplet Size Measurements

To interpret the results of droplet experiments, it is necessary to have fairly accurate knowledge of the distribution of sample volume among the different droplet sizes. To obtain this distribution, representative samples were withdrawn from the dilatometer after, and sometimes before as well, a complete set of experiments. The sample was diluted five times with an Igepal-water solution; a part of it, held in the form of a film about 25μ thick between glass plates, was examined microscopically. Photomicrographs were made of various representative regions of the film as viewed by transmitted light at magnifications of 600–700. The number of droplets in the various size ranges was then determined from these photomicrographs. About 2000 droplets were so classified in each distribution determination. The smoothed volume distribution curves for the *n*-octadecane dispersions are shown in Fig. 1. The mean droplet size $\bar{D}$ is defined by

$$\sum_{D=0}^{D=\bar{D}} V_D^0 = 0.5. \qquad (7)$$

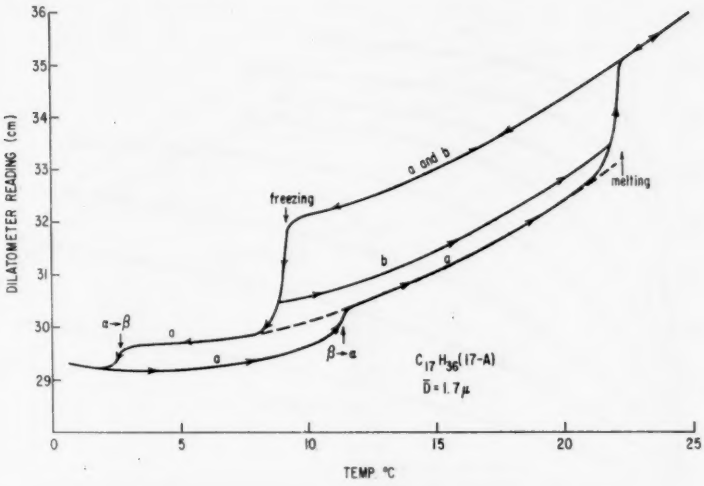

FIG. 2. Course of dilatometer readings in two continuous cooling-heating cycles [(a) and (b)] for *n*-heptadecane dispersion 17-*A*. $\alpha \rightleftarrows \beta$ represents solid state transition.

Similar distribution curves were found for the other dispersions.

We found that the volume distribution in a dispersion did not change appreciably with time, provided the dispersion was mildly agitated at least once in 48 hours and nothing evaporated from it. This conclusion is supported by the result that the solidification isotherm of a particular dispersion at a given temperature was the same, within experimental error, at widely separated times (e.g., two weeks separation).

The determination of the volume distribution of the droplets and of $\bar{D}$ is the principal source of error in our experiments. The hydrocarbon droplets could not be resolved microscopically as sharply as the mercury droplets investigated earlier.[10] We estimate the uncertainty in the droplet diameters, and in $\bar{D}$, to be $\pm 0.25\ \mu$.

RESULTS AND THEIR ANALYSIS

We shall present the description and analysis of the results for each of the hydrocarbons investigated in turn. Since the results for the different compounds are quite similar, detailed explanations will be given only for *n*-heptadecane, the first compound discussed. None of the bulk hydrocarbons undercooled more than 1 to 2° before freezing began.

n-Heptadecane

We determined first the melting and freezing range of the dispersions by continuous cooling and heating experiments. In these experiments, the temperature was changed at the rate of 0.1° per min except during freezing and melting, when the change was about 0.02° per min. The dilatometer was read at least every 5 min.

The course (within 0.02 cm) of the dilatometer readings in two cooling-heating cycles [(a) and (b)] for dispersion 17-*A* is shown in Fig. 2. In cycle (a) the melted dispersion was cooled through the freezing range, which occurred at about 13–14° undercooling (8.5–9.5°C), and then through a solid state transformation ($\alpha \rightarrow \beta$) range at 2–3°C. The dispersion was then warmed back through the solid state transformation reversal range (at 11–12°C) and on through the melting range. It is interesting that the droplets first crystallized to the α rather than the β phase. We shall not be concerned further with the solid state transformation. In the isothermal experiments the temperatures were not sufficiently low for it to occur.

We consider now the melting and freezing behavior of the dispersion. About 80% of the sample melted in the same narrow temperature range (21.9–22.1°C) as the whole of a bulk sample. However, the remaining 20% of the sample melted over the range from 1° below and upward to the bulk melting temperature T_m. It appears that the freezing range also exhibits two parts. One is a narrow range, about 13° below T_m, in which about 80% of the sample freezes, and the other a range contiguous with the first but extending about 1° below it, in which the remaining 20% of the sample freezes. These results suggested that the dispersion consists of two fractions: one fraction κ, the major one, having the melting temperature of the bulk hydrocarbon and freezing over a narrow range; the other fraction $1-\kappa$, having a 1° range of melting temperatures and a corresponding broad range of freezing temperatures. To test this hypothesis we carried out cooling-heating cycle (b), in which the freezing was interrupted by a temperature rise after going about 80% to completion. In this cycle we found (see Fig. 2) that nearly all of the frozen part of the sample exhibited the sharp melting behavior, centering at T_m, which we attributed to the fraction κ. This result confirms that the "sharply melting fraction" of the sample, κ, also freezes in a narrow temperature interval which lies above, though contiguous with, the freezing range of the "diffuse melting fraction" $1-\kappa$. Since the under-

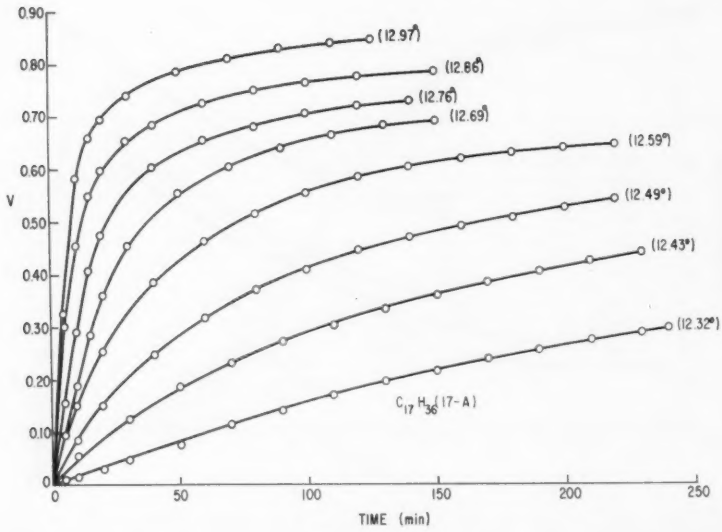

FIG. 3. Isothermal dependence of fraction of sample solidified (V) on time at several undercoolings of *n*-heptadecane dispersion 17-*A*. The numbers in parentheses represent the undercoolings. $\kappa = 0.80$.

cooling is quite large (13°) we must also conclude that the diffuse melting component freezes *in isolation* from the sharply melting component.

The amount of the diffuse melting fraction in the dispersion 17-*B*, in which the droplet size was relatively large, was found to be only one half as large ($1-\kappa \sim 0.10$) as in 17-*A*. Actually this result and those for the other hydrocarbons indicated that $1-\kappa$ is roughly proportional to $1/\bar{D}$, and hence to the specific droplet area per unit volume. This behavior suggests the possibility that the diffuse melting fraction is that part of the hydrocarbon which is affected by the surface film. It could be that in the rapid freezing, which proceeds from the interior of the droplet, elements of the liquid become completely coated by the wetting agent and occluded by the growing crystal. These occluded regions, having a higher concentration of wetting agent, might melt at temperatures lower than those at which the bulk material melts. Also, crystal nucleation within the regions will have to occur independently and because of the lower melting temperature and lesser volume of the region, it will become appreciable only at somewhat lower temperatures than in the droplet originally.

Isothermal experiments were carried out on the two dispersions at several temperatures within the first part of the freezing range as determined in the continuous cooling and heating experiments. Under these conditions freezing should be confined almost completely to the sharply melting component. The volume fraction V of this component which has solidified [see Eq. (3)] during an isothermal hold for a time t was calculated from the equation

$$V = \Delta h(t)/\kappa \Delta h(\infty), \tag{8}$$

where $\Delta h(t)$ is the fall of the dilatometer in time t, $\Delta h(\infty)$ is the fall during the entire course of solidification, and κ is the fraction of the sharply melting component estimated from the continuous cooling and heating experiments. There is an uncertainty of about 3 to 5% in our estimate of κ but this does not detract significantly from the validity of our conclusions, which are based principally on the analysis of data in which $V < 0.5$ to 0.6.

The isothermal dependence of V on t at several undercoolings (ΔT) for the dispersion 17-*A* is shown in Fig. 3. These isotherms are brought into coincidence, as shown in Fig. 4, when multiplied by the appropriate time scale factors f. In fact, just as was found for mercury,[10] the isotherms for any given hydrocarbon dispersion differ only by time scale factors.

Taking k_D to be proportional to droplet volume [Eq. (4a)] a "volume" isotherm was calculated from the volume distribution of droplets in dispersion 17-*A* and Eqs. (3) and (4a) by the procedure explained in the earlier paper.[10] This isotherm was matched with the composite experimental isotherm (Fig. 4) at $V = 0.45$, and is plotted in Fig. 4. It is seen to agree fairly well with the experimental isotherm. However, the "area" isotherm calculated similarly, but with k_D proportional to droplet area [Eq. (4b)] instead of droplet volume, deviates quite widely from the experimental isotherm. Thus these results point toward a conclusion that the nucleation frequency in the droplets is proportional to droplet volume, as expected for homogeneous nucleation.

The nucleation frequency $k_{\bar{D}}$ in the droplet of mean diameter, $\bar{D}$, is readily determined from the matched volume isotherm (see earlier paper[10]) and from it the nucleation frequency, I, per unit volume is calculated with Eq. (4a). According to nucleation theory the logarithm of I should be proportional to $1/T(\Delta T)^2$

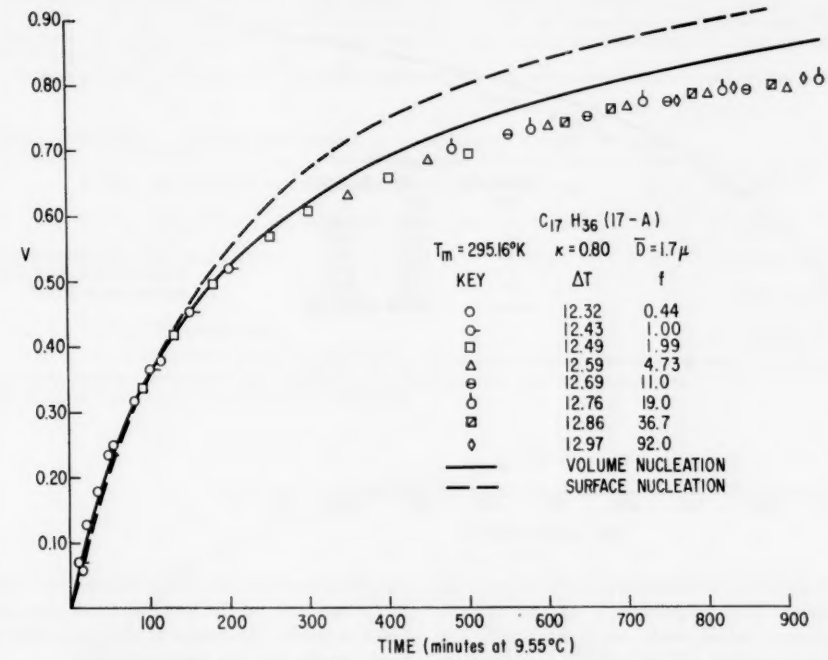

FIG. 4. Composite isotherm for *n*-heptadecane dispersion 17-*A*. This is the curve which results when the listed time scale factors, f, are applied to the individual isotherms (in this case those shown in Fig. 3). V is the fraction of the sample that has solidified. ΔT is the undercooling.

[Eqs (5), (5c) and (5d)] and it is for dispersion 17-*A*, as may be seen from Fig. 5. The magnitude of the temperature coefficient of the nucleation rate, about 5000 per degree centigrade, is astonishing but it is just as predicted by nucleation theory (see Discussion).

A set of isotherms was determined for the dispersion 17-*B*, in which the mean droplet size was much larger than in 17-*A*, and analyzed similarly. These isotherms were reduced, as before, to a composite isotherm, shown in Fig. 6, by application of the appropriate time scale factors. Again the experimental isotherm is in good agreement with the calculated "volume" isotherm. Values of the logarithm of I calculated from these data are also plotted against $1/T(\Delta T)^2$ in Fig. 5. It is seen that the linear relation for this dispersion nearly coincides with that for the smaller particle size dispersion 17-*A*. In view of the uncertainty in $\bar{D}$ the closeness to coincidence in this case is fortuitous but, since $\bar{D}^3$ differs by a factor of 13.5 in the two dispersions, we are justified in concluding that the nucleation frequency is proportional to droplet volume rather than to droplet area. From the straight line relation in Fig. 5 we have evaluated the parameters K_v and σ, in Eqs. (5) and (5c), and listed the values in Table I.

n-Octadecane

Typical results of continuous cooling-heating experiments on one of the dispersions, 18-*B*, of this hydrocarbon are shown in Fig. 7. There is no evidence from these experiments of a solid state transformation in *n*-octadecane. However, just as for *n*-heptadecane, the dispersions seem to consist of two components [com-

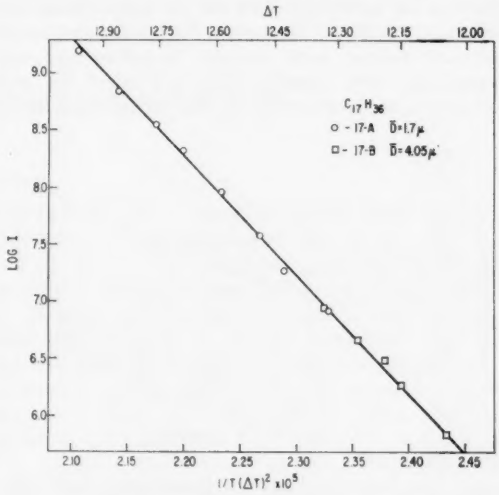

FIG. 5. Variation of $\log I$ with $1/T(\Delta T)^2$ for *n*-heptadecane dispersions 17-*A* and 17-*B*. I represents the nucleation frequency per unit volume and ΔT the undercooling. The constants which describe the curve are given in Table I.

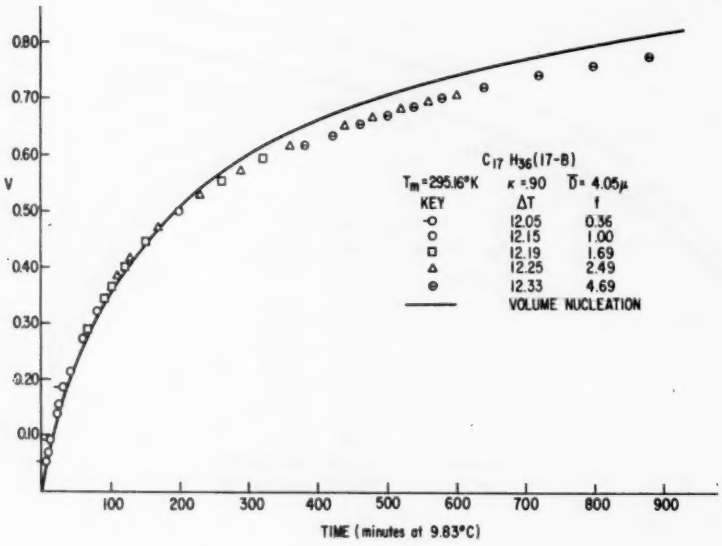

FIG. 6. Composite isotherm for *n*-heptadecane dispersion 17-*B*. Symbols are as in Fig. 4.

pare cycles (a) and (b)] differentiated by their melting-freezing behavior. The proportion κ of the sharply melting component, which melts over essentially the same temperature range (27.9–28.2°C) as the pure bulk hydrocarbon, is about the same as in *n*-heptadecane.

A set of isotherms was obtained for each of two *n*-octadecane dispersions, 18-*B* and 18-*E*, having quite different droplet size ranges. The composite experimental isotherms for the two dispersions are displayed in Figs. 8 and 9 along with the corresponding "volume" isotherm calculated as before. For both dispersions there is fair agreement between the experimental and calculated "volume" isotherms. Nucleation frequencies per unit volume were obtained as before and their logarithms vary linearly with $1/T(\Delta T)^2$ for each dispersion, as shown in Fig. 10. The straight line for the coarser dispersion 18-*E* lies higher, by a factor of 2.0 in I, than that for the fine dispersion, but this displacement is within the range of the estimated uncertainty from the droplet size measurements.

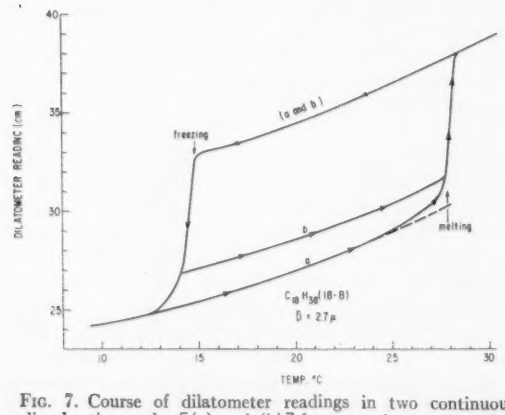

FIG. 7. Course of dilatometer readings in two continuous cooling-heating cycles [(a) and (b)] for *n*-octadecane dispersion 18-*B*.

To obtain additional information on the variation of droplet nucleation frequency with droplet size we determined single isotherms at 15.26°C and the droplet size distribution for each of three additional (18-*A*, 18-*C*, 18-*D*) *n*-octadecane dispersions. The mean droplet nucleation frequencies $k\bar{D}$ at 15.26°C for all five *n*-octadecane dispersions are plotted against $\bar{D}^2$ and $\bar{D}^3$ in Fig. 11. Although the data scatter considerably, it is evident that they are described by a $k\bar{D} \propto \bar{D}^3$ relation (corresponding to the good straight line through the origin) and not by a $k\bar{D} \propto \bar{D}^2$ relation.

We show in Fig. 10 a resultant log$I$ vs $[T(\Delta T)^2]^{-1}$ relation obtained by shifting the two straight lines for dispersions 18-*B* and 18-*E* by amounts which correspond to the displacement of the $k\bar{D}$ values for these dispersions from the $k\bar{D}$ vs $\bar{D}^3$ line in Fig. 11. The parameters σ and K_v for *n*-octadecane evaluated from the constants of the resultant line are given in Table I. The temperature coefficient of the crystal nucleation rate in *n*-octadecane is also very large, being about 7500 per degree.

n-Tetracosane

We investigated only a single dispersion, 24-*A*, of this hydrocarbon. The results of typical cooling-heating experiments are shown in Fig. 12. It is evident that the solid-state transformation behavior is quite complex and to interpret it we must suppose that three crystalline phases appear. A phase β forms in the freezing [see cycle (a)] at an undercooling of 13°, probably as a result of direct nucleation from the

TABLE I. Summary of constants [see Eq. (5)] which describe crystal nucleation frequency in some normal alkane liquids. λ is the relative temperature, in units of the absolute melting temperature, at which the nucleation frequency has the value 10^7 cm^{-3} sec^{-1}. For *n*-hexadecane and *n*-dotriacontane, λ was crudely estimated from the results of continuous cooling and heating experiments. A.P.I. means American Petroleum Institute.

Hydrocarbon	Formula	Source of hydrocarbon	σ ergs cm^{-2}	Log K_v Exptl.	Log K_v Calc.[a]	$1-\lambda$	$(1-\lambda)\lambda^{\frac{1}{2}}T_m^{\frac{1}{2}}$
n-heptadecane	$C_{17}H_{36}$	Penn State-A.P.I. (high purity)	7.2	30.5±2	32.3	0.042	208
n-octadecane	$C_{18}H_{38}$	Penn State-A.P.I. (high purity)	9.64	31.35±2	32.3	0.043	220
n-tetracosane	$C_{24}H_{50}$	CP-recrystallized	8.2[b]	24±4	32.3	0.037±0.002	212
n-hexadecane	$C_{16}H_{34}$	CP				0.041±0.004	
n-dotriacontane	$C_{32}H_{66}$	CP-recrystallized				0.042±0.005	

[a] Calculation based on assumption that segment transported in elementary nucleation step contains two carbon atoms.
[b] Becomes 9.3 if calculated using value of K_v which holds for *n*-octadecane.

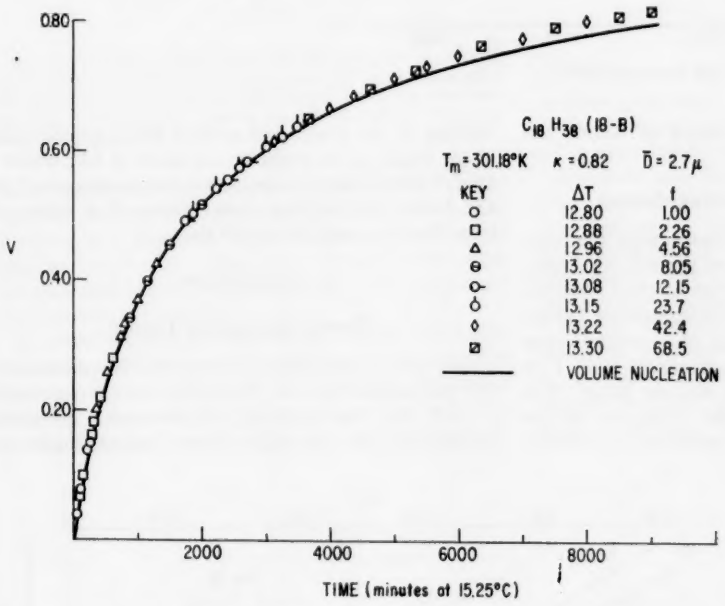

FIG. 8. Composite isotherm for *n*-octadecane dispersion 18-*B*. Symbols are as in Fig. 4.

liquid. This phase transforms[14] at 47–48°C to a phase α, which melts at 50–51°. When the phase α is cooled [cycle (b)] to a temperature 39°C, 8° below the $\alpha \rightarrow \beta$ transformation temperature, it transforms to the third phase γ. This phase reverts back to α when warmed to 43–45°C.

In *n*-tetracosane the melting range is broadened considerably by the greater amount of impurity; therefore, it was not possible to estimate κ by the procedure used for the higher purity C_{17} and C_{18} hydrocarbons. However, there is evidence for two freezing ranges, and we set $1-\kappa$ equal to the proportion of hydrocarbon that crystallized below 36.7°C in our continuous cooling experiments (see Fig. 12).

A set of isotherms was obtained and reduced to the composite isotherm, shown in Fig. 13, by application of the time scale factors given. It is seen that the composite isotherm is in close agreement with the volume isotherm calculated from the droplet size distribution of the volume. The nucleation frequency per unit volume was calculated as before, and the variation of its logarithm with $1/T(\Delta T)^2$ is shown in Fig. 14. Since the β phase apparently nucleates directly, the undercooling ΔT was calculated with reference to the thermodynamic crystallization temperature of the β, T_m^{β}, which was estimated from the thermal data given by Hoffman and Decker.[14] The parameters

[14] See J. D. Hoffman and B. F. Decker, J. Phys. Chem. **57**, 520 (1953), for discussion of this phase change.

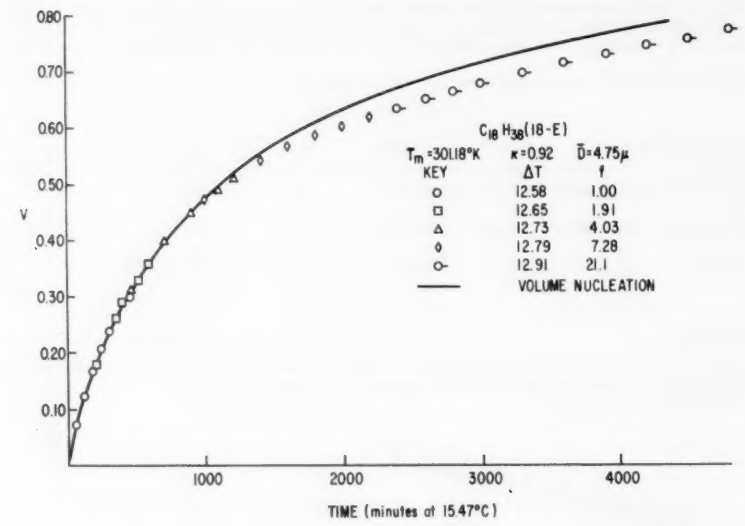

FIG. 9. Composite isotherm for *n*-octadecane dispersion 18-*E*. Symbols are as in Fig. 4.

σ and K_v for *n*-tetracosane, obtained as before, are given in the table.

n-Dotriacontane and *n*-Hexadecane

Our samples of these hydrocarbons were the least pure of any we investigated and we limited our experiments on them to the determination of their transformation behavior in continuous cooling-heating cycles. We found that the freezing range of a *n*-hexadecane dispersion, in which the droplet diameters were 1 to 10 μ, was about 12° below the melting range. The *n*-dotriacontane dispersion (droplet diameters in the range 1–10μ) exhibited a $\beta \rightarrow \alpha$ transition at 63–65°. Melting of the α occurred at 68.5–70°. Crystallization of the liquid to the β phase took place at 53°, which is 10–12° below the $\beta \rightarrow \alpha$ transition temperature and 14–15° below the melting temperature of β estimated from Hoffman and Decker's[14] data.

DISCUSSION

Test of Nucleation Theory

One test of nucleation theory would be provided by the comparison between the values of the parameter σ and the corresponding liquid-crystal interfacial tensions σ_{LS}. On the basis of the classical nucleation

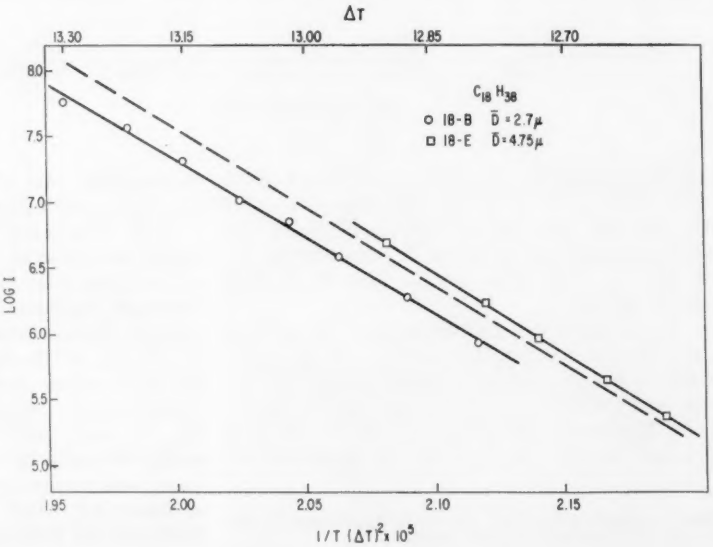

FIG. 10. Variation of log$I$ with $1/T(\Delta T)^2$ for *n*-octadecane dispersions 18-*B* and 18-*E*. The dashed curve is the resultant relation obtained by shifting the two straight lines for 18-*B* and 18-*E* by amounts which correspond to the displacement of the $k_{\bar{D}}$ values for these dispersions from the $k_{\bar{D}}$ vs $\bar{D}^3$ line in Fig. 11. The constants which describe the dashed curve are given in Table I. The symbols are the same as in Fig. 5.

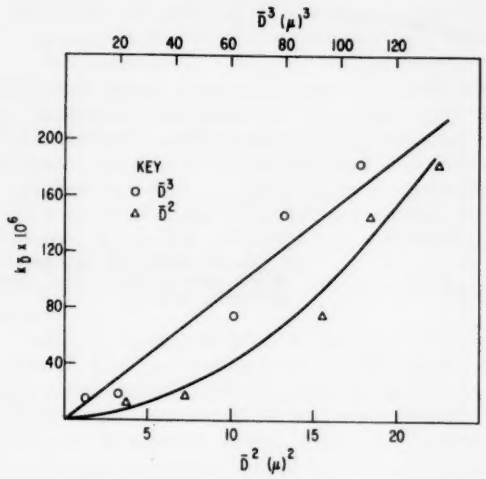

FIG. 11. Variation of $k_{\bar{D}}$ with $\bar{D}^2$ and with $\bar{D}^3$ at 15.26°C ($\Delta T = 12.79$) for *n*-octadecane dispersions. $k_{\bar{D}}$ is the nucleation frequency per droplet of diameter $\bar{D}$. The results are consistent with Eq. (4a) based on volume nucleation, but not with Eq. (4b) based on surface nucleation.

theory as modified by Cahn and Hilliard's[15] considerations on the effects of the possible diffuseness of the interface, it is expected that σ_{LS} constitutes an upper limit to the possible values of σ. Actually there seem to be no experimental determinations of σ_{LS} for any of the hydrocarbons tested.

Another test of nucleation theory which we actually can make with our present information is to compare the experimental values of K_v with those calculated from Eqs. (5a) and (5b), which are based on nucleation theory. To make this calculation, it is necessary to make some assumption about the size of the molecular segment which is transported in the elementary nucleation step. We have assumed, in line with the arguments of Douglass and McCall[16] concerning the mechanism of self-diffusion in the liquid hydrocarbons, that this segment contains two carbon atoms. We also suppose that the rate constant D' governing the movement of this segment is of the same order of magnitude as the self-diffusion coefficient of a molecule of similar size in the undercooled hydrocarbon, that is, $D' \sim 10^{-5}$ cm^2 sec^{-1}. In summary, the numbers used to calculate the K_v values which appear in the table are the following:

$$n = 1.66 \times 10^{22} \text{ segments per cm}^3$$

$$v = 6.03 \times 10^{-23} \text{ cm}^3 \text{ per segment}$$

$$a_0^2 = 10^{-15} \text{ cm}^2$$

$$D' = 10^{-5} \text{ cm}^2 \text{ sec}^{-1}.$$

Had we assumed no segmental behavior and substituted for these parameters the values for the molecule as a whole, we would have calculated K_v values about two orders of magnitude smaller, i.e., $\sim 10^{20}$ cm^{-3} sec^{-1}.

Whatever assumption is made about the segment length it is evident that, for the two hydrocarbons of highest purity, there is excellent agreement between the experimental K_v and that calculated from nucleation theory. This agreement is much closer than that found in the investigation of mercury.[10]

For the less pure hydrocarbon, *n*-tetracosane, the deviation between the experimental and calculated K_v is considerable. This deviation may be a result of impurity effects, but just what these might be we do not know at present.

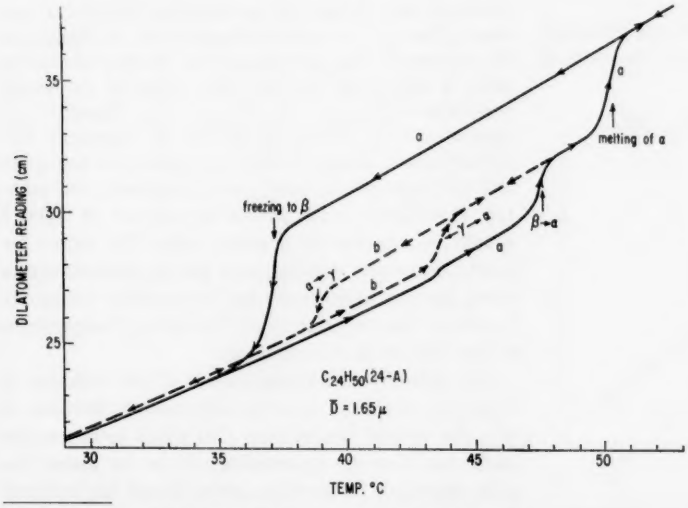

FIG. 12. Course of dilatometer readings in two continuous cooling-heating cycles [(a) and (b)] for *n*-tetracosane dispersion 24-*A*. α, β and γ represent solid phases.

[15] J. W. Cahn and J. E. Hilliard, J. Chem. Phys. **31**, 688 (1959).
[16] D. C. Douglass and D. W. McCall, J. Phys. Chem. **62**, 1102 (1958).

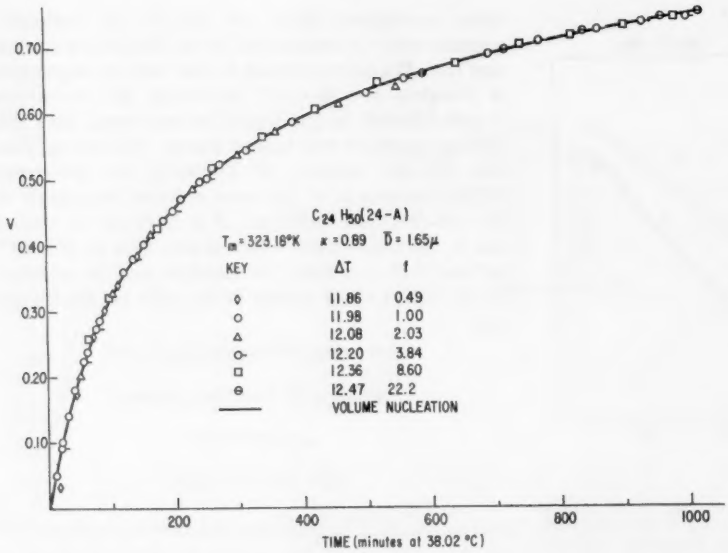

FIG. 13. Composite isotherm for *n*-tetracosane dispersion 24-*A*. Symbols are as in Fig. 4.

It was pointed out that, excepting for chain end effects, σ ought to be constant within any given (even or odd) hydrocarbon series. We have only the value, $\sigma=7.2$ erg/cm^2, for a single member of the odd series. The value for the high purity member of the even series is $\sigma=9.6$ erg/cm^2. This is somewhat larger than the nominal value $\sigma=8.2$ erg/cm^2 for the less pure *n*-tetracosane. However, the value for *n*-tetracosane becomes 9.3 erg/cm^2, in excellent agreement with that for *n*-octadecane when calculated with the value of K_v, $10^{31.3}$ cm^{-3} sec^{-1}, which holds for *n*-octadecane.

Glass-Forming Tendency in *n*-Alkanes and Linear Polymers

Also listed in Table I are the relative undercoolings $1-\lambda$ (i.e., the undercooling in units of the melting temperature) at which the crystal nucleation frequency in the various hydrocarbons has the particular value, $I_r=10^7$ cm^{-3} sec^{-1}. The values given for the high purity compounds, $C_{17}H_{36}$ and $C_{18}H_{38}$, should be quite precise, but the value for $C_{24}H_{50}$ could be in error by as much as 5–10% because of the uncertainty in the melting temperature of the β phase. Also, for *n*-hexadecane and *n*-dotriacontane the values of $1-\lambda$ are probably correct only in order of magnitude since they could only be estimated from continuous cooling-heating experiments and qualitative observations on the droplet sizes.

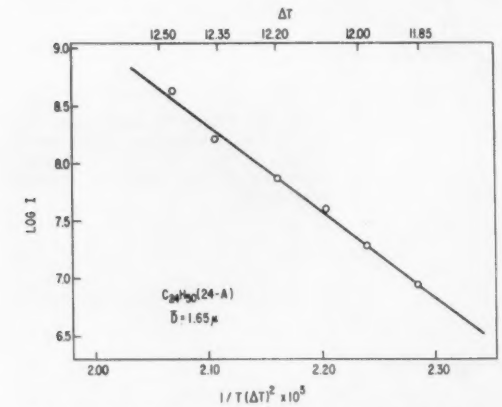

FIG. 14. Variation of log$I$ with $1/T(\Delta T)^2$ for *n*-tetracosane dispersion 24-*A*. The constants which describe the curve are given in Table I. Symbols are as in Fig. 5.

In any event, in accord with the considerations of Turnbull and Cohen[3] on nucleation of molecular segments, the relative undercoolings in the *n*-alkanes are all very small; they are about 0.04, which is almost an order of magnitude less than the values for the simple molecular substances investigated by Stavely and associates.[5,6] A further prediction of Turnbull and Cohen[3] is that, insofar as chain end effects are negligible and the segment transport rate is constant, the quantity $(1-\lambda)\lambda^{\frac{1}{2}}T_m^{\frac{1}{2}}$ given in the last column of Table I should be constant for a given series. The values for *n*-octadecane and *n*-tetracosane are in excellent agreement, but this agreement may be somewhat fortuitous in view of the uncertainty in the melting temperature of the β-phase of *n*-tetracosane.

The difficulty of forming glasses of the *n*-alkanes is caused by the small relative undercooling. Because of this, the reduced temperature τ' at which homogeneous nucleation becomes appreciable will be far above the glass transition temperature even though the reduced thermodynamic crystallization temperature is relatively low.

Since the rate constant D' for segment transport should decrease with increasing chain length, we expect that the parameter B in Eq. (6) will increase slowly with chain length. Even so, the relative undercooling for appreciable nucleation of the higher molecular weight members of the *n*-alkanes series, including the polymeric members, should be quite small. No observations seem to have been published on the crystallization behavior of linear polyethylene in droplet form. However, Mandelkern and Quinn[17] have reported that the crystal nucleation frequency in the bulk form of this polymer becomes very large at only a few degrees undercooling.

From the considerations of Turnbull and Cohen it is expected that the relative undercooling required for appreciable crystal nucleation should be quite small in any linear polymer. Yet there are several examples of polymers, presumably linear, which can be undercooled to glasses. In some of these instances, glass formation can be attributed to a thermodynamic crystallization temperature which is so low that it is at or very near the glass transition temperature.

We presume that the segments which enter into the nucleus must be at least as long as is the unit cell. If this is so, the probability of nucleation would be smaller, corresponding to a larger value of B in Eq. (6), as the unit cell is larger. It is possible that Price's observation[18] of glass formation in droplets of linear polyethylene oxide, in which the glass transition temperature is far below T_m, may be partly explained by the relatively long (seven atoms) unit cell of this material.

[17] L. Mandelkern and F. A. Quinn (unpublished).

[18] F. P. Price (private communication).

ACKNOWLEDGMENTS

We are grateful to the Pennsylvania State University and the American Petroleum Institute for making available to us the very high purity samples of *n*-heptadecane and *n*-octadecane. We are indebted to Professor J. A. Dixon of Pennsylvania State University for arranging for the gift of these samples.

We are also indebted to the following individuals: N. G. Ainslie, General Electric Research Laboratory, for assistance in the measurements on *n*-hexadecane; J. D. Hoffman, National Bureau of Standards, for valuable discussions on the stuctural and thermodynamic aspects of phase transitions in the *n*-alkanes; L. Mandelkern, National Bureau of Standards, and F. P. Price, General Electric Research Laboratory, for valuable discussions on the kinetics of crystallization in polymer systems; H. H. Marvin, C. R. Morelock, and F. P. Price, General Electric Research Laboratory, for useful advice on certain of the experimental procedures; and D. E. Sargent, now at Central Research Laboratory, Minnesota Mining and Manufacturing Company, for suggesting the wetting agent used to make the dispersions.

Alkali-Iron Group-Halogen Complexes. Dissociation Energies of $KClFeCl_2$ and $CsClFeCl_2$†

V. S. Rao and P. Kusch

Physics Department, Columbia University, New York

(Received July 22, 1960)

A number of complexes between the alkali halides and the divalent halides of the iron group metals have been observed. They are all characterized by a very large rotational magnetic moment of the order of 50 nuclear magnetons for the rotational state of most probable J. The dissociation energies at a temperature of about 1020°K of the two complexes, $KClFeCl_2$ and $CsClFeCl_2$, have been found to be 34.7 ± 1.0 and 24.7 ± 1.0 kcalM^{-1}, respectively. The data from which these results were found were obtained by measuring the relative concentrations of the alkali halide and the complex as a function of temperature while the partial pressure of $FeCl_2$ remained essentially constant. The large difference in the magnetic moments of the two detectable molecular species allows the determination of the relative concentration with considerable accuracy.

INTRODUCTION

When certain alkali halides (MX) are heated in an oven with the divalent halide of an iron group metal ($M'X_2$), the beam that issues from the slit of the oven consists of MX (as well as its polymers), $M'X_2$ and a complex $MXM'X_2$. Only the molecular species containing M are detectable on the usual hot tungsten wire, and of these species $MXM'X_2$ is the dominant one.[1] The relative abundances of the detectable species can readily be determined through the fact that the complex is characterized by a large rotational magnetic moment, and is readily deflected in an inhomogeneous magnetic field, while the alkali halide has a very small magnetic moment and is relatively slightly deflected. The fact that the complex is stoichiometrically as described has been demonstrated[1] for $KClFeCl_2$ by a velocity analysis of a molecular beam containing the species in question.

In the present paper the observation of several previously unreported molecular complexes of the indicated type, with similar properties, is reported together with a measurement of the dissociation energies of $KClFeCl_2$ and $CsClFeCl_2$. The important experimental data are the deflection properties of a beam in an inhomogeneous magnetic field.

DEFLECTION THEORY

The theory of the deflection of molecules with a rotational g value, g_J, has been previously discussed.[1] The relevant results are here given. The image of the beam in the plane of the detector is ideally a trapezoid; as usual, we approximate the trapezoidal beam with a rectangular beam of width $2b$, of the same area as the trapezoidal beam and the same intensity at half-width. A detector of width $2d$ $(2d<2b)$ is centrally placed within the beam image. A particle of mass m leaves the slit in an oven at temperature T. The particle with the most probable velocity α in the oven, $\alpha=(2kT/m)^{\frac{1}{2}}$ suffers a deflection at the detector

$$S_\alpha=(\partial H/\partial z)\mu\mu_N G/4kT=\gamma\mu i, \qquad (1)$$

where $\partial H/\partial z$ is the gradient of the magnetic field perpendicular to the plane of the beam, G is a geometrical factor, and μ is the magnetic moment of the particle in units of the nuclear magneton μ_N; $(\partial H/\partial z)$ is proportional to H and hence to the current in the coil of the magnet that produces the inhomogeneous field so that γ, for a particular apparatus and oven temperature, is a known quantity. Two approximate models (a) and (b) are assumed to develop deflection formulas appropriate to a molecule with a rotational g value. (a) We assume that a diatomic molecule with a rotational g value g_J is deflected. The distribution of molecules among the J states is determined through the quantity a where

$$a^2=h^2/8\pi^2AkT$$

and A is the moment of inertia. The most probable value of J, $\bar{J}$ is $\sqrt{2}/2a$ and the maximum value of the magnetic moment in the state of $\bar{J}$ is $\bar{\mu}=g_J\bar{J}$. The intensity of the detector is then given by

$$p=I/I_0=\pi^{\frac{1}{2}}[4d\rho(b+d)]^{-1}\times\{4bd-(b+d)^2[f(\rho)-\beta^{-2}f(\beta\rho)]\}, \qquad (2)$$

where $\rho=\gamma\bar{\mu}i/[\sqrt{2}(b+d)]$

$\beta=(b+d)/(b-d)$,

$f(\rho)=\{1-\Phi(\rho)\}\exp(\rho^2)$

$\Phi(\rho)$ is the error function, and

I_0 is the intensity for $i=0$.

(b) We assume that the molecule is spherical, i.e., that the moment of inertia about any axis through the center of mass is equal. All levels with the same J but different K coincide. We also assume that the magnetic moment about any axis through the center of mass is the same. a is defined as before and the most probable value of

† Work supported in part by a contract with the U. S. Air Force, monitored by the Air Force Office of Scientific Research of the Air Research and Development Command, and in part by a joint service contract with the U. S. Army Signal Corps, the Office of Naval Research, and the Air Force Office of Scientific Research.

[1] P. Kusch, J. Chem. Phys. **22**, 1203 (1954).

$J, \bar{J}=1/a$; $\bar{\mu}$ is as before,

$$p=I/I_0=\tfrac{1}{2}[(1+b/d)f(\rho)+(1-b/d)f(\beta\rho)], \quad (3)$$

where $\rho=\gamma\bar{\mu}i/2(b+d)$, and all other terms are as before.

In the cases under discussion there are two detectable species of molecule, the complex, with a large rotational magnetic moment, and the alkali halide, whose effective moment is principally contributed by the nuclear moments. I_0 is the intensity of the complex at $i=0$, I that of the complex at arbitrary i, I' that of the alkali halide at $i=0$ and I'' that of the alkali halide at arbitrary i. The quantity $I''/I'=\phi$ can be determined in a separate experiment. In the present work the lowest value of ϕ for the halide with the biggest nuclear moments CsCl at any field at which observations were made was 0.83. The value of I/I_0 however, is less than 0.1 at the same fields. We are interested in determining $k=I'/I_0$ from the observed quantity

$$\sigma=(I+I'')/(I_0+I')=(p+\phi k)/1+k). \quad (4)$$

The problem of finding both k and $\bar{\mu}$ is then the essentially arithmetic one of getting a good fit of the experimental curve of σ vs i with a theoretical curve whose parameters are $\bar{\mu}$ and k. It is not possible to obtain g_J without knowledge of the moment of inertia of the molecule. In view of the crudeness of the assumptions (a) and (b), $\bar{\mu}$ is only an estimate. Nevertheless it is possible to get[1] excellent fits of experimental data to the expressions just derived with the adjustment of the two parameters. The value of k obtained from a given set of experimental data does not depend significantly on the choice of model (a) or (b); indeed, the discrepancy between the result of the two models is no greater than that obtained when two independent fits of a curve are made by use of the same model.

DEFLECTION APPARATUS

Two different molecular beam deflection machines were used in this study. The first of these has been previously described[2] and has been used in earlier[1] studies of these complexes. It is essentially designed as an apparatus for studying nuclear resonances in molecules. In it are incorporated the usual A and B deflecting magnets that are essential to such an apparatus. Only one of these magnets is used in the present work, and the apparatus is thus needlessly long. Further, the deflecting power of the magnets is so great that the beams here studied are strongly deflected by residual fields in the magnets and the problem of demagnetization becomes serious. For the careful study of the present systems this apparatus is thus somewhat unsatisfactory.

The apparatus used in the determination of the dissociation energies is designed as a deflection apparatus only, and cannot be used for radio frequency spectroscopy. The ratio of gradient to field has been reduced, as compared to the earlier apparatus by a factor of about 2. The magnet gap is greater by a factor of 1.8 and these two factors greatly reduce the problem of demagnetization. The collimating slit is held fixed at a predetermined position within the gap of the deflecting field; this feature makes it possible to place the beam at a known and reproducible position in the gap with an improved precision. While the value of the magnetic field gradient along a particular trajectory in terms of the current in the field coils is not accurately known (it could, in principle, be determined from an observation of the zero moment peaks of In in the $^2P_{\frac{1}{2}}$ state, for example), experimental conditions are reproducible from run to run.

A conventional hot tungsten wire detector was used in all experiments, and the surface of the wire was oxidized when the alkali to be detected was Li or Na. The intensity of the detected beam (MX+MXM'X$_2$) was quite independent of variations in the temperature of the filament around the operating point.

Ovens

Two types of ovens were used. The conventional single-chamber model, used in the observation of the existence of the complexes and in a measurement of their rotational magnetic moments, was made of iron in the study of Fe and Co salts and of nickel in the study of Ni salts. This oven is essentially an isothermal unit and does not allow an independent variation of pressure and temperature. Such a variation was necessary in the study of the reaction of MX and M'X$_2$ with the limited data on relative concentrations that can be obtained by the present methods. Accordingly a double-chamber oven, similar, in principle, to one previously described[3] but of simpler construction, was used in the determination of dissociation energies. The two chambers were made of oxygen-free, high-conductivity copper and connected together by a nickel tube. A massive copper shield attached to the upper chamber surrounded the connecting tube within about 1 mm of the lower chamber. It was thus assured that the temperature of the tube was everywhere intermediate to that of the upper and lower chambers. If the mean free path of the molecules in the gas is small compared to the characteristic dimensions of the tube, the pressure in the upper and lower chambers is the same. In that case the temperature T_1 of the lower oven, which contains the sample, determines the pressure everywhere, while the temperature $T_2(T_2\geq T_1)$ of the upper chamber determines the temperature of the gas under study. It is thus possible, for example, to maintain a constant total pressure while varying the temperature over a considerable range. In our experiments the pressure was sufficiently high so that the

[2] H. Taub and P. Kusch, Phys. Rev. **75**, 1481 (1949); R. A. Logan, R. E. Cote, and P. Kusch, *ibid.* **86**, 280 (1952).

[3] R. C. Miller and P. Kusch, J. Chem. Phys. **25**, 860 (1956).

condition on the mean free path described above was substantially satisfied.

The temperatures were measured by use of chromel-alumel thermocouples peened into each of the two chambers. Manual monitoring of the current in the oven heaters maintained the temperatures of the lower and upper ovens constant to within about ± 0.3 and $\pm 1.0°$, respectively. These fluctuations had no significant effect on the results of the experiment.

All salts used in the present work were of reagent grade. The halides of the iron group were dehydrated by gentle heating under vacuum until the evolution of water vapor ceased. The two salts were then weighed in the desired proportion, intimately ground together, and charged into the oven.

DISSOCIATION ENERGIES. METHOD

We have a method of finding k, the relative numbers of molecules of the alkali halide and of the complex that strike the detector wire per unit time after they issue from the upper chamber at a temperature T_2. This is, except for a fixed constant, the ratio of the pressures of the two species within the upper chamber, and except for another fixed constant, the ratio of the concentrations in the chamber. If we were able to determine the pressure (or the concentration) of $FeCl_2$ in the chamber, as well as k, as a function of T_2, the enthalpy (or energy of dissociation) of the reaction could be found by the usual methods.

In the pure phase the vapor pressure of $FeCl_2$ is much greater[2,4] than that of KCl. Other vapor pressure data[5] indicate that the vapor pressures of all the alkali halides, in particular CsCl, are much less than that of $FeCl_2$. Further, our measurements of k indicate that the complex, though more abundant than the alkali halide under the conditions most favorable to the formation of the complex ($T_2=T_1$), is still much less abundant than $FeCl_2$. At our value of T_1 two distinct phases, one a liquid containing both KCl and $FeCl_2$ and the other a pure solid phase of $FeCl_2$ occur[4] when KCl is heated with a sufficient excess of $FeCl_2$, and $FeCl_2$ is then the strongly dominant species in the vapor. Even when the two phases do not exist, the vapor pressure of $FeCl_2$ far exceeds[4] that of any other component when $FeCl_2$ is in strong excess.

Suppose that T_1 is sufficiently high so that the vapor pressure in the lower chamber is also the pressure in the upper chamber. If T_2 is now varied, k will also vary. However, since $FeCl_2$ is strongly dominant, the partial pressure of $FeCl_2$ is not significantly modified by the fact that the complex is more heavily dissociated in the upper chamber of T_2 than in the lower chamber at T_1. The equilibrium constant K_p is then

$$K_p = k \times \text{constant}, \tag{5a}$$

and the equilibrium constant K_c is

$$K_c = kT_2^{-1} \times \text{constant}'. \tag{5b}$$

Application of the usual equations at once allows the determination of ΔE from a plot of $\log(k/T_2)$ vs T_2^{-1} and of ΔH from a plot of $\log k$ vs T_2^{-1}.

Dimers of both $FeCl_2$ and of KCl are known to occur.[3,4,6] In our experiments T_2 was always sufficiently greater than T_1 so that the dimers were largely dissociated and their occurrence had no significant effect on our results.

The total pressure in the ovens in the present work was of the order of 1 mm Hg. A rough estimate indicates that the molecular mean free path was much less than any dimension of the connecting tube between the two chambers. Further, a previous experiment[7] on an alkali halide (LiBr) in a similar oven, where the results had a considerable sensitivity to a lack of pressure equilibrium between the two chambers, indicated that such equilibrium was closely approached when the total pressure was about 0.5 mm Hg. It should be noted that the pressure ratio, p_2/p_1 must lie between $(T_1/T_2)^{-\frac{1}{2}}$ and 1 where $T_2 \geq T_1$. In the limiting case where the mean free path is very long and free molecular flow occurs between the two chambers, the error introduced into ΔE by the assumption of pressure equilibrium is only 1 kcal M^{-1}. For any reasonable departures from pressure equilibrium, the error introduced into ΔE by the assumption of equilibrium will be trivial.

The relative detection efficiency of the detector wire must, of course, remain constant throughout a series of measurements. It has been shown[3] that the relative detection efficiencies of the polymers of LiCl is unaffected by the over-all detection efficiency of the wire. In the present work the values of k were readily reproduced for a fixed T_1 when measurements were made for T_2, T_2', $T_2''\cdots$ and then again for T_2. In addition measurements of k were closely reproduced in measurements on two successive days at the same T_1 and T_2.

GENERAL PROPERTIES OF THE COMPLEXES

A previous report[1] showed that both $KClFeCl_2$ and $KBrFeBr_2$ have large rotational magnetic moments. With the diatomic model of the molecule, it was found that $\bar{\mu}$ was 72 nm for $KClFeCl_2$ and 46 nm for $KBrFeBr_2$. It is independent of any assumption about the molecular configuration and dimensions except that the molecule may be approximated as a diatomic molecule.

Several further experiments have been carried out on other complexes. Approximately equimolar proportions of KCl and $FeCl_2$ were heated in a single chamber iron oven and a value of $\bar{\mu}=59$ nm for the complex was found. It should be noted that there is a considerable

[4] C. Beusman, Oak Ridge Natl. Lab. Rept. ORNL-2323 (1957).
[5] G. E. Cogin and G. E. Kimball, J. Chem. Phys. **16**, 1035 (1948).
[6] R. C. Schoonmaker and R. F. Porter, J. Chem. Phys. **29**, 116 (1958).
[7] P. Kusch, J. Chem. Phys. **28**, 1075 (1958).

uncertainty in all values of $\bar{\mu}$, both because the exact path of traverse of the beam through the inhomogeneous field was not known, and also because the determination of the field in the magnet in terms of the current in the magnetizing coils is subject to considerable uncertainty. Further, the calculation of $\bar{\mu}$ is sensitively dependent on the width of the undeflected beam $2b$, in our experiments in the range from 6 to 9×10^{-3} cm, and not measurable with a high degree of precision. That part of the beam width contributed by lack of parallelism between oven slit, collimating slit, and detector, as well as that contributed by scattering of the beam, would have a somewhat different effect than the ideal image considered in the development of the earlier equations. A considerable error may, therefore, be introduced in the determination of $\bar{\mu}$ from an uncertainty in $2b$. Equimolar proportions of NaCl and $FeCl_2$ were heated in a single chamber iron oven and a value of $\bar{\mu}$ was found for the complex, identical to that found for $KClFeCl_2$. The equivalence of the two values is more significant than their values. The constants k that characterize the two systems are also approximately equal for a beam effusing from a chamber at the same temperature as that at which equilibrium between gas and melt has been established. In both cases the complex is the heavily dominant component of the detectable beam. When about 60 mole % of LiCl was heated in an iron oven with $FeCl_2$, the resulting complex was found to have $\bar{\mu}=70$ nm. The k value appears to be somewhat higher than for the other complexes just described. It should be noted, however, that LiCl is itself so heavily dimerized[3] that an important component of the vapor, over a large range of experimental conditions, is the dimer. It has also been reported[4] that several kinds of complexes of

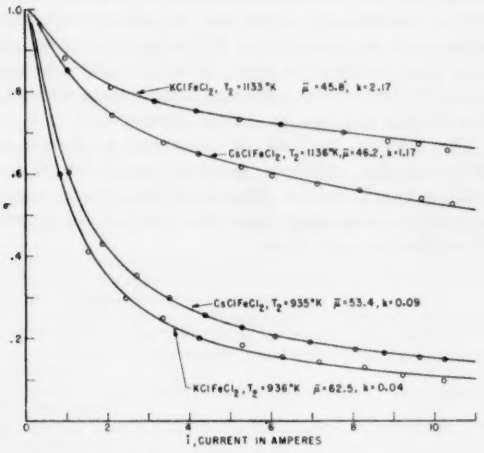

FIG. 1. Deflection curves for the KCl-$FeCl_2$ system and for the $CsCl$-$FeCl_2$ system. The quantities $\bar{\mu}$ and k are adjustable parameters required to fit the theoretical curve to the experimental points.

TABLE I. Data for the system KCl—$FeCl_2$. Composition of the charge=80 mole% $FeCl_2$. T_1 monitored at 850°K.

T_2°K	k	$\bar{\mu}$
936	0.05	62.5
978	0.16	61.6
1009	0.28	70.6
1049	0.57	52.8
1087	1.08	59.7
1133	2.17	45.8

LiCl and $FeCl_2$ exist. A thermodynamic study of the $LiCl$-$FeCl_2$ system is, therefore, difficult and the only value in our observation of the complex is to note that one exists.

Approximately equimolar proportions of KCl and $NiCl_2$ were heated in a single-chamber nickel oven. The properties of the system were closely similar to those of the complex that results from KCl and $FeCl_2$. When KCl and $NiCl_2$ were heated in an iron oven, the behavior of the system was indistinguishable from its behavior when a nickel oven was used. KCl and $CoCl_2$ heated in an iron oven also yielded a complex with properties similar to those of the KCl-$FeCl_2$ complex. It is not, of course, certain that an exchange between the Co in $CoCl_2$ and the iron in the oven did not occur.

Elsewhere in this paper, the determination of the energies of dissociation of $KClFeCl_2$ and $CsClFeCl_2$ is discussed. Incidental to this determination an extended body of data has been obtained on the value of $\bar{\mu}$ for these molecules. For $KClFeCl_2$, $\bar{\mu}=64$ nm and for $CsClFeCl_2$, $\bar{\mu}=51$ nm. We believe that the difference is a real one.

In the absence of more detailed data on the properties of the divalent halides of the iron group elements it is not possible to make an interpretation of the observed values of $\bar{\mu}$. It is, however, of interest to note that all beams that have been produced by heating an alkali halide with a divalent halide of the iron group elements contain as the dominant detectable component a complex with a very large rotational g value.

DISSOCIATION ENERGIES. RESULTS

The energies of dissociation have been measured for only two complexes, $KClFeCl_2$ and $CsClFeCl_2$. In Fig. 1 are shown two deflection curves for each of the complexes; the values of the adjustable constants are shown. For both CsCl and KCl a separate deflection curve was observed for the pure salt to find ϕ. The observed ϕ was somewhat greater than that calculated from the nuclear moments of the constituent atoms. A part of the discrepancy can be ascribed to a small shift of the collimating slit by stresses introduced when the magnet was excited. Whereas the assumption that $\phi=1$ introduces a significant error in k, it introduces a much

TABLE II. Data for the system CsCl—$FeCl_2$. Composition of the charge=80 mole% $FeCl_2$. T_1 monitored at 881°K.

T_2°K	k	$\bar{\mu}$
935	0.09	53.4
992	0.21	57.2
1040	0.40	49.4
1088	0.70	47.4
1136	1.17	46.2

smaller error in the slope of log$k$ and ϕ need not, therefore, be critically determined. It is to be noted that the values of T_2 are very nearly the same for the two complexes but that k has changed much more over the temperature interval for the KCl complex than for the CsCl complex. This at once indicates a considerably greater dissociation energy for the KCl complex and emphasizes the fact that the difference of about 10 kcal M^{-1} leads to a readily identified physical effect.

Tables I and II give the data of the experiment. Each line represents several individual observations of the deflection curve at the stated conditions. The value of $\bar{\mu}$ shows a considerable variation but not an unexpected one in view of the uncertainties in the knowledge of all constants which enter into its determination. It seems probable that $\bar{\mu}$ is less for the CsCl complex than for the KCl complex. Because the mass of Cs is greater than that of K, it is probable that the moment of inertia of the CsCl complex is greater than that of the KCl complex and hence the g_J value of the CsCl complex is rather considerably less than that of the KCl complex.

In Fig. 2 the lines are plotted relating 2+log$k$ and T_2^{-1}. The fact that the points lie along straight lines contributes to the justification of the validity of the several ssumptions here made. Only the point of lowest k, at T_2=936°K, for the KCl complex deviates badly from the straight line. The values of k are most accurately found when k is about 1. When either the alkali halide or the complex has a low abundance ($k \ll 1$, or $k \gg 1$), the fractional uncertainty in k is relatively large. Accordingly we have not used the k of the KCl-$FeCl_2$ system at T_2=936° in further calculation. The resulting least-squares fit is shown by the

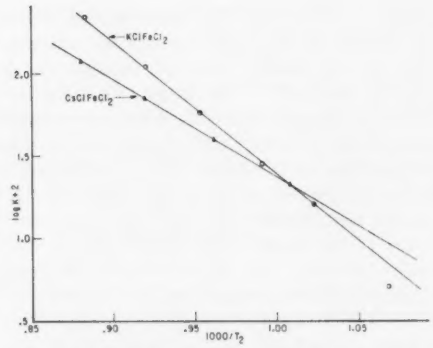

FIG. 2. A plot of 2+log$k$ vs 1000 T_2^{-1} for two complexes. The enthalpy of the reaction is found from the slopes of the straight lines.

straight lines in Fig. 2. We find

$$\Delta E(\mathrm{KClFeCl_2}) = 34.7 \text{ kcal } M^{-1} \text{ [at } T \sim 1020°\mathrm{K}]$$

and

$$\Delta E(\mathrm{CsClFeCl_2}) = 24.7 \text{ kcal } M^{-1} \text{ [at } T \sim 1020°\mathrm{K}],$$

where the statistical uncertainty in the values of ΔE are in each case 0.2 kcal M^{-1}. Two other runs on the KCl complex at different T_1 yield values of ΔE that agree with these values within the statistical errors (which were less for the runs described in Table I than for the two runs where the data are not given). In one of these cases the propertions of KCl and $FeCl_2$ in the oven were such that only a single phase, the solution of KCl in $FeCl_2$ occurred. The agreement of the values of ΔE in this case and the one in which two phases were present, suggests that the vapor pressure of $FeCl_2$ over the solution is high enough to meet the assumptions underlying the analysis. It seems to us that the statistical uncertainty gives an excessively optimistic estimate of the uncertainty of the result, and we give as a more realistic estimate ± 1.0 kcal M^{-1}, in both cases, in view of the numerous assumptions about the system that may not have been entirely met.

The present method of determining dissociation energies is not, of course, generally applicable. It does indicate how a special differential property of several molecular species may allow the study of the kinetics of reaction between them.

Problems in Perturbation Theory Calculation of Diamagnetic Susceptibility and Nuclear Magnetic Shielding in Molecules. Illustration with the Hydrogen Atom*†

LAWRENCE C. SNYDER‡§ AND ROBERT G. PARR¶

Department of Chemistry, Carnegie Institute of Technology, Pittsburgh, Pennsylvania

(Received September 12, 1960)

The perturbation theory expressions for the diamagnetic susceptibility and nuclear magnetic shielding constants of atoms and molecules may be written as sums of ground state and excited state terms. The effects of truncations in the evaluation of the excited state terms are studied through a specially contrived application of these expressions to the hydrogen atom. When the origin of the vector potential is taken $1.4a_0$ away from the proton, computations of both properties show that the excited state part is comparable with the ground state part, that the continuum excited states contribute about as much as the discrete excited states, and that the first excited discrete state accounts for about a third of the whole excited-state contribution. The inference is made, for molecules, that truncation of conventional perturbation formulas by omission of continuum contributions will result in major errors and a dependence of computed properties on the origin taken for the vector potential. The average excited state energy required to make a correct sum rule estimate of the excited state part of the nuclear magnetic shielding constant of the hydrogen atom is calculated, and it is shown to depend strongly on the distance of the shielded position from the proton.

I. INTRODUCTION

QUANTUM mechanical perturbation theory has been used by Van Vleck[1] and Ramsey[2] to derive expressions for the diamagnetic susceptibility χ and nuclear magnetic shielding constants σ_N of atoms and molecules.[3] The expressions may be written as the sum of a ground state (diamagnetic) part and an excited state (paramagnetic) part. In computations on molecules, the evaluation of the excited state part is a major obstacle, since the actual eigenfunctions are required for all discrete and continuum excited electronic states. The evaluation of the ground state part requires only the ground state eigenfunction and is thus relatively simple. In practice, one uses approximations to the electronic eigenfunctions of the unperturbed molecule. In addition one is forced to truncate the evaluation of the excited state part: one neglects the contribution of all continuum states and most excited discrete state functions. These expedients can produce errors in computed properties and cause them to depend on the choice of origin for the vector potential. A satisfactory computational procedure should give values for these molecular properties which are independent of the origin taken for the vector potential. This independence has been demonstrated by Van Vleck[1] for his perturbation theory based expression for χ, and it may be assumed for Ramsey's expression for σ_N.

In this study, the complexities of computation of these magnetic properties for molecules are deliberately made to occur for the hydrogen atom by choosing the origin of the vector potential off the proton. A complete set of eigenfunctions is available for the hydrogen atom, so all terms of the ground and excited state parts may be computed, individually and collectively. One is thus able to illustrate effects of various expedient truncations used in computations of susceptibility and shielding constants.

II. PERTURBATION THEORY

The Hamiltonian operator for the t electrons of a molecule in the presence of an applied magnetic field $\mathbf{H}^0$ and a point magnetic dipole of moment $\boldsymbol{\mu}$ is given by the formula,

$$\mathcal{H}=\sum_{j=1}^{t}\{(2m)^{-1}[(\hbar/i)\boldsymbol{\nabla}_j+(e/c)\mathbf{A}_j]^2+V_j\}+\sum_{j<j'}(e^2/r_{jj'}), \quad (1)$$

where $e=|e|$, m is the electron mass, and the jth electron with position $\mathbf{r}_j$ moves in a nuclear potential V_j. The quantity $\mathbf{A}_j$ is the vector potential representing the magnetic field at the position of the jth electron. Here $\mathbf{A}_j$ is taken to be the sum of two vector potentials, $\mathbf{A}_j=\mathbf{A}_j^0+\mathbf{A}_j^N$. The vector potential $\mathbf{A}_j^0$ represents the uniform applied magnetic field $\mathbf{H}^0$ and is given by the expression, $\mathbf{A}_j^0=\frac{1}{2}[\mathbf{H}^0\times(\mathbf{r}_j-\mathbf{r}_{0j})]$, where the vector $\mathbf{r}_{0j}$ is the origin of the vector potential for the jth electron and may be assigned arbitrarily. (Usually this origin is taken to be the same for all electrons, but one may take it to be different.)[4] The vector potential $\mathbf{A}_j^N$ represents the magnetic field at $\mathbf{r}_j$ resulting from the magnetic dipole $\boldsymbol{\mu}$ at $\mathbf{r}_N$: $\mathbf{A}_j^N=[\boldsymbol{\mu}\times(\mathbf{r}_j-\mathbf{r}_N)]/|\mathbf{r}_j-\mathbf{r}_N|^3$.

* Based on part of a thesis submitted by L. C. Snyder in partial fulfillment of the requirements for the degree of Doctor of Philosophy, Carnegie Institute of Technology, 1959.

† Presented in part at the Symposium on Molecular Structure and Spectroscopy, the Ohio State University, June 15–19, 1959. Supported in part by a research grant from the National Science Foundation.

‡ Present address: Bell Telephone Laboratories, Inc., Murray Hill, New Jersey.

§ National Science Foundation Predoctoral Fellow, 1953–1954, 1956–1958.

¶ Alfred P. Sloan Fellow, 1956–1960.

[1] J. H. Van Vleck, *The Theory of Electric and Magnetic Susceptibilities* (Oxford University Press, New York, 1932).

[2] N. F. Ramsey, Phys. Rev. **78**, 699 (1950); **86**, 243 (1952).

[3] For a recent review, see M. Karplus, Revs. Modern Phys. **32**, 455 (1960).

[4] H. F. Hameka, Mol. Phys. **1**, 203 (1958).

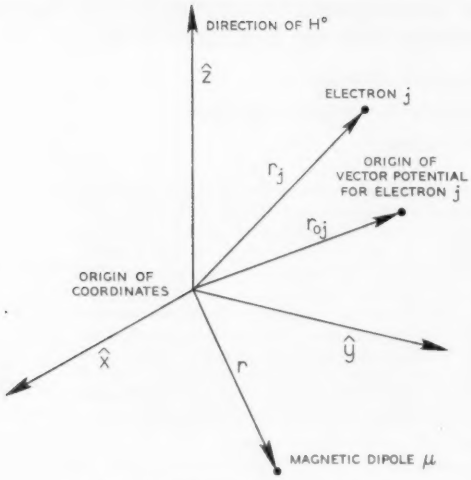

FIG. 1. Various coordinates and vectors.

Figure 1 shows the various position vectors specified. The dipole $\boldsymbol{\mu}$, which represents the magnetic moment of a nucleus, serves as a measure of the magnetic shielding field induced at $\mathbf{r}_N$ by the applied field $\mathbf{H}^0$ and thus of the magnetic shielding constant σ_N. The direct coupling of the electron magnetic moment with the applied magnetic field has not been represented in this Hamiltonian, because the part of χ or σ_N which arises from that coupling is not the subject of this study.

In liquids and gases, in which a molecule assumes all orientations with respect to the direction of $\mathbf{H}^0$ during a measurement, the magnetic susceptibility χ and magnetic shielding constant σ_N may be expressed in terms of their diagonal (tensor) components

$$\chi=\tfrac{1}{3}(\chi_{xx}+\chi_{yy}+\chi_{zz}), \quad \text{and} \quad \sigma_N=\tfrac{1}{3}(\sigma_{xx}+\sigma_{yy}+\sigma_{zz}). \tag{2}$$

For a molecular system of fixed orientation with respect to an applied magnetic field $\mathbf{H}^0$ in the z direction, on the other hand, to a good approximation $\chi=\chi_{zz}$ and $\sigma_N=\sigma_{zz}$. Only χ_{zz} and σ_{zz} are considered in the rest of this paper.

Perturbation theory expressions for the quantities χ and σ_N for atoms and molecules are derived in the conventional way.[1,2,5] The electronic Hamiltonian operator is written as the sum of an unperturbed part, which is appropriate for the molecular system isolated from both the applied field $\mathbf{H}^0$ and the magnetic dipole $\boldsymbol{\mu}$, and a perturbation which is expanded in the Cartesian components of $\mathbf{H}^0$ and $\boldsymbol{\mu}$, as are the wave function and energy $\mathcal{E}$ for the perturbed system. The quantities χ_{zz} and σ_{zz} may be defined as derivatives of $\mathcal{E}$, the energy of the perturbed system: $\chi_{zz}=-(\partial^2\mathcal{E}/\partial H_z\partial H_z)$, and $\sigma_{zz}=(\partial^2\mathcal{E}/\partial H_z\partial\mu_z)$. Convenient units of χ_{zz} are a_0^3; the quantity σ_{zz} is dimensionless. The expressions for χ_{zz} and σ_{zz} each may be conveniently written as the sum of four terms. Thus

$$\chi_{zz}=\chi^{g1}+\chi^{g2}+\chi^{ed}+\chi^{ec}, \tag{3}$$

where

$$\chi^{g1}=-(e^2/4mc^2)\,(\Psi_1^* \mid \sum_j (X_j^2+Y_j^2) \mid \Psi_1), \tag{4}$$

$$\chi^{g2}=-(e^2/4mc^2)\,(\Psi_1^* \mid \sum_j (-2X_jX_{0j}+X_{0j}^2-2Y_jY_{0j}+Y_{0j}^2) \mid \Psi_1), \tag{5}$$

$$\chi^{ed}=\sum_n{}'\chi^{ed}(n)=-(e^2/4mc^2)\,(-2\hbar^2/m)\sum_n{}'(E_n-E_1)^{-1} \mid (\Psi_n^* \mid \sum_j[(\partial/i\partial\phi_j)-X_{0j}(\partial/i\partial Y_j)+Y_{0j}(\partial/i\partial X_j)] \mid \Psi_1) \mid^2, \tag{6}$$

$$\chi^{ec}=\int_0^\infty(\partial\chi^{ec}/\partial E)\,dE$$

$$=-(e^2/4mc^2)\,(-2\hbar^2/m)\int_0^\infty(E-E_1)^{-1} \mid (\Psi_E^* \mid \sum_j[(\partial/i\partial\phi_j)-X_{0j}(\partial/i\partial Y_j)+Y_{0j}(\partial/i\partial X_j)] \mid \Psi_1) \mid^2 dE. \tag{7}$$

Similarly,

$$\sigma_{zz}=\sigma^{g1}+\sigma^{g2}+\sigma^{ed}+\sigma^{ec}, \tag{8}$$

where

$$\sigma^{g1}=(e^2/2mc^2)\left(\Psi_1^* \left| \sum_j \frac{X_j^2+Y_j^2-X_jX_N-Y_jY_N}{\mid \mathbf{r}_j-\mathbf{r}_N \mid^3} \right| \Psi_1\right), \tag{9}$$

$$\sigma^{g2}=(e^2/2mc^2)\left(\Psi_1^* \left| \sum_j \frac{-X_jX_{0j}+X_{0j}X_N-Y_jY_{0j}+Y_{0j}Y_N}{\mid \mathbf{r}_j-\mathbf{r}_N \mid^3} \right| \Psi_1\right), \tag{10}$$

[5] H. Eyring, J. Walter, and G. E. Kimball, *Quantum Chemistry* (John Wiley & Sons, Inc., New York, 1944).

$$\sigma^{ed}=\sum_n{}'\sigma^{ed}(n)$$

$$=(e^2/2mc^2)(-2\hbar^2/m)\ \mathrm{Re}\sum_n{}'(E_n-E_1)^{-1}(\Psi_n^*\mid\sum_j[(\partial/i\partial\phi_j)-X_{0j}(\partial/i\partial Y_j)+Y_{0j}(\partial/i\partial X_j)]\mid\Psi_1)^*$$

$$\times\left(\Psi_n^*\left|\sum_j\frac{[\partial/i\partial\phi_j)-X_N(\partial/i\partial Y_j)+Y_N(\partial/i\partial X_j)}{\mid\mathbf{r}_j-\mathbf{r}_N\mid^3}\right|\Psi_1\right),\quad(11)$$

and

$$\sigma^{ec}=\int_0^\infty(\partial\sigma^{ec}/\partial E)dE$$

$$=(e^2/2mc^2)(-2\hbar^2/m)\ \mathrm{Re}\int_0^\infty(E-E_1)^{-1}(\Psi_E^*\mid\sum_j[(\partial/i\partial\phi_j)-X_{0j}(\partial/i\partial Y_j)+Y_{0j}(\partial/i\partial X_j)]\mid\Psi_1)^*$$

$$\times\left(\Psi_E^*\left|\sum_j\frac{(\partial/i\partial\phi_j)-X_N(\partial/i\partial Y_j)+Y_N(\partial/i\partial X_j)}{\mid\mathbf{r}_j-\mathbf{r}_N\mid^3}\right|\Psi_1\right)dE.\quad(12)$$

In Eqs. (4) to (12), the position vectors of the electrons, their vector potential origins, and the position vector for the magnetic dipole have been in part expressed in Cartesian coordinates; $\mathbf{r}_j=[X_j,\ Y_j,\ Z_j]$, $\mathbf{r}_{0j}=[X_{0j},\ Y_{0j},\ Z_{0j}]$, and $\mathbf{r}_N=[X_N,\ Y_N,\ Z_N]$. The Cartesian coordinates are related to spherical polar coordinates as usual: $Z=r\cos\theta$, $X=r\sin\theta\cos\phi$ and $Y=r\sin\theta\sin\phi$. The symbol Re denotes the real part of a quantity. A prime on a summation indicates that $n=1$ is to be excluded. Terms of ground state parts of χ_{zz} and σ_{zz} are superscripted g. Terms of the excited state part are superscripted e.

If the origin of coordinates is taken on the nucleus of an atomic system, then the terms χ^{g1} and σ^{g1} are the values of χ and σ_N which may be computed by assuming a classical precession of the electron distribution with the Larmor angular velocity about the nucleus and applied field direction.[6] For atoms and other systems in which the electrons see a potential which is cylindrically symmetrical about an axis in the applied field direction, one has

$$\chi^{g2}+\chi^{ed}+\chi^{ec}=\sigma^{g2}+\sigma^{ed}+\sigma^{ec}=0,\quad(13)$$

where the origin of coordinates has been taken on this symmetry axis. Thus for an atom the terms χ^{g1} and σ^{g1} are the exact computed values of χ_{zz} and σ_{zz}, respectively. The individual terms entering Eq. (13) depend on the origin of the vector potential and are nonzero for most molecular systems. In a computation of χ_{zz} or σ_{zz}, the omission of one or a group of these terms can cause the computed property to depend on the origin of the vector potential.

The contributions of the discrete excited states Ψ_n are χ^{ed} and σ^{ed}. There are usually an infinite number of such contributions, and in computations on molecules it is possible to evaluate the contribution of only a few of these.[7] The contributions of the continuum excited states Ψ_E are χ^{ec} and σ^{ec}. For molecular systems the continuum contribution is never directly evaluated. It has been suggested[2] that application of a sum rule and an average excited state energy be employed to estimate the excited state part.[3]

Effects of truncations and approximations on the computed values for χ_{zz} and σ_{zz} are illustrated by the hydrogen atom computations which follow.

III. HYDROGEN ATOM COMPUTATIONS

The origin of the vector potential may be deliberately taken off the hydrogen atom proton, in order to make nonzero the usually inaccessible terms of the excited state parts of χ_{zz} and σ_{zz}. The terms of Eqs. (3) to (12)

TABLE I. Contribution of excited discrete states to χ_{zz} for the hydrogen atom.[a,b]

n	$\chi^{ed}(n)$	$\Sigma_n\chi^{ed}(n)$
2	−0.41620[b]	−0.41620[b]
3	−0.07910	−0.49530
4	−0.02899	−0.52429
5	−0.01394	−0.53823
6	−0.00780	−0.54603
7	−0.00481	−0.55084
8	−0.00318	−0.55402
9	−0.00222	−0.55624
10	−0.00161	−0.55785
∞[c]		−0.56500

[a] Units are $a_0^3(-\alpha^2/4)$, where $\alpha=e^2/\hbar c$.
[b] $(X_0^2+Y_0^2)^{\frac{1}{2}}=a_0$.
[c] First work cited in footnote 10.

[6] W. E. Lamb, Phys. Rev. **60**, 817 (1941).

[7] A. Saika and C. P. Slichter, J. Chem. Phys. **22**, 26 (1954).

TABLE II. Parts of σ_{zz} for the hydrogen atom.[a]

X_N	σ^{g1}	σ^{g2}	$\sigma^{ed}(2)$	$\sigma^{ed}(3)$	σ^{ed}
0.00	0.66667	0.00000	0.00000	0.00000	0.00000[b]
0.05	0.66279	0.06178	−0.01146	−0.00258	−0.01582
0.10	0.65277	0.11484	−0.02093	−0.00488	−0.02991
0.20	0.61797	0.19816	−0.03745	−0.00871	−0.05348
0.40	0.51714	0.29639	−0.06013	−0.01392	−0.08571
0.60	0.40589	0.33476	−0.07267	−0.01674	−0.10339
0.80	0.30370	0.33850	−0.07837	−0.01794	−0.11126
1.00	0.21802	0.32332	−0.07956	−0.01809	−0.11268[c]
1.20	0.15015	0.29881	−0.07786	−0.01758	−0.10998
1.40	0.09854	0.27069	−0.07440	−0.01667	−0.10481
1.60	0.06057	0.24222	−0.06996	−0.01554	−0.09827
1.80	0.03346	0.21520	−0.06505	−0.01433	−0.09111
2.00	0.01466	0.19047	−0.06002	−0.01311	−0.08381
2.50	−0.00886	0.14006	−0.04814	−0.01028	−0.06721
3.00	−0.01491	0.10422	−0.03822	−0.00798	−0.05257
3.50	−0.01442	0.07921	−0.03040	−0.00622	−0.04155
4.00	−0.01206	0.06164	−0.02440	−0.00490	−0.03316

[a] Here $X_0=a_0$; Y_0, Z_0, Y_N, and $Z_N=0$. Units are $\alpha^2/2$, where $\alpha=e^2/\hbar c$.
[b] Sum to $n=9$ of $\sigma^{ed}(n)$.
[c] When evaluated to $n=23$, $\sigma^{ed}=-0.114563$.

can then be evaluated with a complete set of hydrogen atom wave functions[8,9] which are eigenfunctions of the angular momentum about an axis through the proton and in the direction (z) of the applied field. The origin of the coordinate system is taken at the proton. The subscript n of wave functions Ψ_n is taken to be the principal quantum number. It is found that, of all states with the same value of n or E, only that pair of states with $l=1$ and $m=\pm1$ contribute to terms of the excited state part. The sums of these two contributions are represented by $\chi^{ed}(n)$, $\sigma^{ed}(n)$, $(\partial\chi^{ee}/\partial E)$, and $(\partial\sigma^{ee}/\partial E)$; numerical values are given in Tables I and II.[10]

The computational results for χ_{zz} are summarized in Fig. 2. Under the present assumptions, χ^{g1} must be identical with the exact computed value of χ_{zz}, and so it equals the sum of the ground and excited state parts. The magnitude of the other terms depends on the vector potential origin and is proportional to $(X_0^2+Y_0^2)^{\frac{1}{2}}$. With $(X_0^2+Y_0^2)^{\frac{1}{2}}=1.4a_0$, one hydrogen molecule bond length, both χ^{g2} and the excited state part are seen to have magnitudes comparable with χ^{g1}. Failure to compute only the excited state part would lead to an error of 100% in χ_{zz}. The contribution of the first excited discrete states $\chi^{ed}(2)$ is about 73% of the contribution of all excited discrete states χ^{ed}. The contribution of continuum states χ^{ee} has been computed in detail and is shown in Fig. 3. The lower energy continuum states are clearly most important. The continuum contribution is 43.5% of the excited state part.

In the evaluation of σ_{zz}, both the origin of the vector potential and the magnetic dipole $\boldsymbol{\mu}$ have been assumed to lie on the x axis; this facilitates computations and presentation of results. The terms σ^{g2}, $\sigma^{ed}(n)$, and $(\partial\sigma^{ee}/\partial E)$ are porportional to X_0 which is taken equal

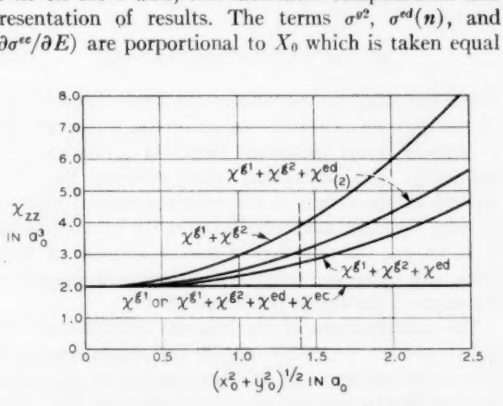

FIG. 2. Terms of perturbation theory expression for χ_{zz} of the hydrogen atom. Units are $-\alpha^2/4$, where $\alpha=e^2/\hbar c$.

[8] H. A. Bethe and E. E. Saltpeter, *Quantum Mechanics of One and Two Electron Atoms* (Springer-Verlag, Berlin, Germany, 1957).
[9] Natl. Bur. Standards Appl. Math. Circ. No. 17, (1952).
[10] Some of the numbers in Table I have been computed previously in other contexts: J. M. Harriman, Phys. Rev. **101**, 594 (1956); P. O. Löwdin, J. Chem. Phys. **30**, 617 (1959).

to a_0 in tabulated results. The contributions of discrete excited states are detailed in Table II. In this atomic case, the true value of σ_{zz} must equal σ_x^1. With the magnetic dipole one hydrogen molecule bond length from the proton, we again find both σ_x^2 and the excited state part to be comparable in magnitude with σ^{g1}. The continuum states contribute more to the excited state part than do the excited discrete states. The continuum contribution σ^{ec} has not been directly evaluated, but it has been obtained by difference with Eq. (13). The computational results for σ_{zz} are summarized in Fig. 4.

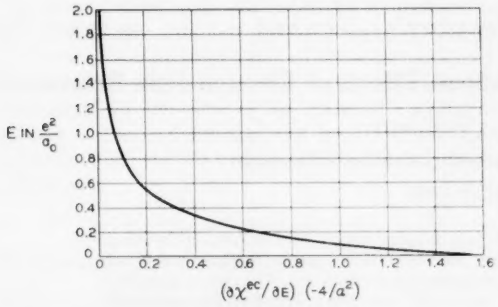

FIG. 3. Contribution of the continuum states to χ_{zz} for a hydrogen atom. $(X_0^2+Y_0^2)^{\frac{1}{2}}=a_0$.

Use of Sum Rules

Application of the quantum mechanical sum rule[11] can provide an upper limit on the magnitude of the excited state part of χ_{zz} or σ_{zz}. For the excited state part of χ_{zz}, one finds

$$\chi^{ed}+\chi^{ec}\leq(4\hbar^2a_0/m)\,(E_2-E_1)^{-1}$$
$$\times\{X_0^2(\Psi_1^*\mid-\partial^2/\partial Y^2\mid\Psi_1)+Y_0^2(\Psi_1^*\mid-\partial^2/\partial X^2\mid\Psi_1)\}. \quad (14)$$

If E_2 here is replaced by a properly chosen average excited state energy $\bar{E}$, the equality can be made to hold exactly. Evaluation of the integrals in Eq. (14) shows that the right-hand side is equal to $(32/9)\,(X_0^2+Y_0^2)\,(a_0)^3$. Equation (13) then is satisfied for any choice of vector potential origin if one takes $\bar{E}=+0.1666\ e^2/a_0$.[12]

Upon making a similar application of a sum rule, one finds that for the excited state part of σ_{zz},

$$\mid\sigma^{ed}+\sigma^{ec}\mid\leq+(2\hbar^2a_0/m)\,(E_2-E_1)^{-1}$$
$$\times\mid X_0X_N(\Psi_1^*\mid-\mid\mathbf{r}-\mathbf{r}_N\mid^{-3}\partial^2/\partial Y^2\mid\Psi_1)\mid. \quad (15)$$

[11] N. F. Mott and I. N. Sneddon, *Wave Mechanics and Its Applications* (Clarendon Press, Oxford, England, 1948), p. 94.

[12] The quantity E_1 is $-0.50\ e^2/a_0$, so that $\bar{E}=0.17\ e^2/a_0$ corresponds to an average *excitation energy* of $0.67\ e^2/a_0$. The onset of the continuum is at $E=0$, corresponding to an excitation energy of $0.50\ e^2/a_0$.

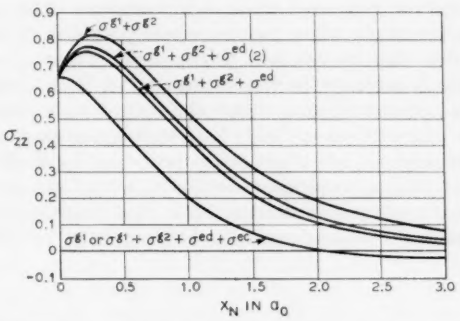

FIG. 4. Terms of perturbation theory expression for σ_{zz} of the hydrogen atom. Units are $\alpha^2/2$, where $\alpha=e^2/\hbar c$.

Again one may define an average excited state energy $\bar{E}$, which when substituted for E_2 in Eq. (15) makes the equality hold. In Table III, $\bar{E}$ is listed for a set of X_N. It depends strongly on X_N. As X_N becomes large, $\bar{E}$ approaches the value which produces the correct sum rule estimate of the χ_{zz} excited state part.

IV. SUMMARY AND CONCLUSIONS

These computations on the hydrogen atom show the considerable magnitude of errors which may be introduced by truncations and sum rule approximations in perturbation theory based calculations of the magnetic susceptibility and nuclear magnetic shielding constants of molecules. The excited state part of the perturbation theory expressions is of the same magnitude as the computed property, if the origin of the vector potential is taken but a molecular bond length from the proton. The contribution of the continuum is about equal to that of the discrete excited states. Thus major errors may result in calculations on molecules if the continuum contribution is omitted. Such an omission will also

TABLE III. Average excited-state energy required for correct sum rule estimate of excited-state part of σ_{zz} for the hydrogen atom.[a]

X_N	$(\sigma^{ed}+\sigma^{ec})$[b]	$\bar{E}$[c]
0.05	−16.172	97.52
0.10	−13.323	43.00
0.20	−9.658	17.78
0.40	−5.695	6.70
0.60	−3.641	3.58
0.80	−2.454	2.22
1.00	−1.723	1.50
1.20	−1.253	1.07
1.40	−0.939	0.80
1.60	−0.724	0.62
1.80	−0.571	0.50
2.00	−0.461	0.41
2.50	−0.291	0.28
3.00	−0.200	0.22
3.50	−0.146	0.19
4.00	−0.111	0.18

[a] $X_0=a_0$; Y_0, Z_0, Y_N, and $Z_N=0$.

[b] Upper limit is tabulated. Units are $\alpha^2/2$, with $\alpha=e^2/\hbar c$.

[c] The value of E_2 which makes Eq. (15) exact.

cause the computed value of the property to depend on the origin taken for the vector potential. It also is clear that caution must be exercised in applying sum rules to estimate the excited state parts. With a single average excited state energy the excited state part of the magnetic susceptibility for a hydrogen atom can be estimated for any origin of the vector potential. However, no single average excited state energy can give a correct sum rule estimate of the excited state contribution to the nuclear magnetic shielding for all positions of the test magnetic dipole. The presence of these difficulties in the perturbation method should encourage the continued investigation of variation or other methods[13–17] as the way to achieve quantitative computation of the magnetic properties of molecules.

[13] M. J. Stephen, Proc. Roy. Soc. (London) **A242,** 264 (1957).
[14] B. R. McGarvey, J. Chem. Phys. **27,** 68 (1957).
[15] J. A. Pople, Proc. Roy. Soc. (London) **A239,** 541 (1957).
[16] Y. Kurita and K. Ito, J. Am. Chem. Soc. **82,** 296 (1960).
[17] H. F. Hameka, Z. Naturforsh. **14***a*, 599 (1959).

THE JOURNAL OF CHEMICAL PHYSICS VOLUME 34, NUMBER 3 MARCH, 1961

Proton Relaxation Times in Paramagnetic Solutions. Effects of Electron Spin Relaxation*

N. BLOEMBERGEN AND L. O. MORGAN†

Gordon McKay Laboratory, Harvard University, Cambridge, Massachusetts

(Received August 18, 1960)

The proton relaxation time in solutions of paramagnetic ions depends, among other factors, on the relaxation time of the electron spins, τ_s. It is shown that the latter, for ions of the iron group, is determined mostly by the distortion of the hydrated complex by collisions with other water molecules. The theory provides a quantitative explanation for the decrease in T_2 in Mn^{++} (and other) solutions in very high magnetic fields. The experimentally observed field and temperature dependence of the proton relaxation times, T_1 and T_2, for ions of the iron group is compared with theory and the features which depend on τ_s are stressed.

I. INTRODUCTION

RELAXATION of protons in aqueous solutions of paramagnetic ions is dominated by interactions between the electronic spin of the ions and the spins of neighboring protons. If exchange among proton types in the solution is rapid, all protons exhibit similar relaxation behavior as a result of the mixing. The over-all relaxation observed is then a weighted average of relaxation rates in each different local proton environment. In the specific case of hydrated paramagnetic ion solutions at moderate concentrations the principal contribution occurs when the proton is within the hydration sphere of the ion.

Results of a wide variety of measurements, including both temperature and frequency dependences of proton relaxation, have been summarized in the recent literature.[1–3] In general, the most successful correlation of experimental results has been achieved through consideration of proton-electron spin dipole-dipole interaction as formulated by Solomon[4] and of isotropic proton-electron spin exchange.[5] The combined equations are

$$(1/NT_1)=(4/30)\,S(S+1)\,g^2\beta^2\gamma_I^2(n_h/N_p)r^{-6}\times[3\tau_c+7\tau_c(1+\omega_s^2\tau_c^2)^{-1}]+(2/3)\,S(S+1)\,A^2\hbar^{-2}(n_h/N_p)[\tau_e(1+\omega_s^2\tau_e^2)^{-1}] \quad (1)$$

and

$$(1/NT_2)=(4/60)\,S(S+1)\,g^2\beta^2\gamma_I^2(n_h/N_p)r^{-6}\times[7\tau_c+13\tau_c(1+\omega_s^2\tau_c^2)^{-1}]+(1/3)\,S(S+1)\,A^2\hbar^{-2}(n_h/N_p)[\tau_e+\tau_e(1+\omega_s^2\tau_e^2)^{-1}] \quad (2)$$

for $\omega_I\tau_c\ll 1$ and $\omega_I\ll\omega_s$. These conditions are not severe since τ_c is expected to be of the order of 10^{-11} sec, or shorter, and $\omega_s=650\,\omega_I$.

In Eqs. (1) and (2) indexes I and S refer to proton and electron spins, respectively; ω is the Larmor precessional frequency; γ, the gyromagnetic ratio; r, the ion-proton internuclear distance; A, the spin exchange constant; τ_c and τ_e, the correlation times for dipolar and spin exchange interactions respectively; n_h, the number of protons in the hydration sphere of the ion; N_p, the molar concentration of H (in any form) in the

* The research reported in this paper was made possible through support extended Cruft Laboratory, Harvard University, jointly by the Navy Department (Office of Naval Research), the Signal Corps of the U. S. Army, and the U. S. Air Force.

† On leave from the University of Texas, Austin, Texas, 1960, with support from the University Research Institute.

[1] R. Hausser and G. Laukien, Z. Physik **153,** 394 (1959).
[2] R. A. Bernheim, T. H. Brown, H. S. Gutowsky, and D. E. Woessner, J. Chem. Phys. **30,** 950 (1959).
[3] L. O. Morgan and A. W. Nolle, J. Chem. Phys. **31,** 365 (1959).
[4] I. Solomon, Phys. Rev. **99,** 559 (1955).
[5] N. Bloembergen, J. Chem. Phys. **27,** 572, 595 (1957).

solution; and N, the molar concentration of paramagnetic ions. All other symbols have their usual meanings.

Temperature dependence of the dipolar part of T_1 and T_2 is attributable to variation of τ_c, which for a number of paramagnetic ions, e.g., Mn^{++}, Cu^{++}, Gd^{3+},[2,3] has been shown to be related to the ion tumbling time τ_r. Thus, τ_c should have an exponential temperature dependence[2]

$$\tau_c = \tau_c^{\circ} \exp(V_c/RT). \tag{3}$$

This is well confirmed experimentally.[1,2,6] However, the exponential dependence does not necessarily follow for the spin exchange contribution, nor for the dipolar contribution when τ_c is not primarily determined by tumbling of the complex, but also by the time dependence of the magnetization of the electron spin τ_s. The time dependence of the scalar interaction is determined by the time τ_h for chemical exchange of protons in the complex and also by τ_s.[5] If the interaction between the ith proton and jth electron spin is written as

$$\mathcal{H}_{ij} \exp(t) = A_{ij}(t)\, \mathbf{I}_i \cdot \mathbf{S}_j(t), \tag{4}$$

the correlation function may be written

$$\begin{aligned} &\langle A_{ij}(t)\, S_{zj}(t)\, A_{ij}(t+\tau)\, S_{zj}(t+\tau) \rangle \\ &\quad = \langle A_{ij}(t)\, A_{ij}(t+\tau) \rangle \langle S_{zj}(t)\, S_{zj}(t+\tau) \rangle \\ &\quad = A^2 \exp(-\tau/\tau_H) \tfrac{1}{3} S(S+1) \exp(-\tau/\tau_s) \end{aligned} \tag{5}$$

because the motion of the protons in and out of the complex is not correlated with the motion of the electron spin. This is shown in more detail in the following section where the electron spin relaxation time is discussed. A similar relation holds for the transverse components of the electron spin, in the limit of rapid motion for electron spin relaxation. One has therefore

$$\tau_e^{-1} = \tau_h^{-1} + \tau_s^{-1}. \tag{6}$$

Similarly one has for the dipolar interaction

$$\tau_c^{-1} = \tau_r^{-1} + \tau_s^{-1} \tag{7}$$

because it will be shown that the electron spin motion is—to a good approximation—not correlated with the rotation of the complex. For the Mn^{++} ion one has at low temperature

$$\tau_h > \tau_s \gg \tau_r.$$

In general, τ_s will be a function of the temperature and the magnetic field. In fact, τ_s can be expected to increase if the precession period of the electron spin becomes comparable with the characteristic time for motions leading to electron spin relaxation in the solution. Accordingly, the transverse relaxation time for the protons should decrease. This is in qualitative agreement with the data of Bernheim, Brown, Gutowsky, and Woessner[2] and of Morgan and Nolle.[3] A quantitative discussion requires a more careful analysis of electron spin relaxation, when the motion in the liquid is not fast compared to the electronic Larmor precession. In general, several relaxation times τ_s will then have to be considered.

Kivelson[7] has developed a theory of electron spin resonance linewidths for free radicals and paramagnetic ions in magnetically dilute crystals and in dilute liquid solutions which includes consideration of nuclear quadrupole moments, zero field splittings, anisotropic Zeeman terms and intramolecular electron-nuclear dipolar interactions, motional and exchange effects. The theory has been applied by Rogers and Pake[8] to explain the variation in linewidth with m_I in the hyperfine ESR spectrum of VO^{++} in aqueous solution. Spin-orbit coupling was specifically excluded in both considerations. It is shown in the following section that the latter is the principal mechanism leading to electron spin relaxation in dilute aqueous solutions of iron group ions. A comparison with experimental data in the last section of this paper shows that it is sufficient to explain satisfactorily the observed features of the contribution of electron spin relaxation to proton spin relaxation in many such solutions.

II. THEORY OF THE ELECTRON SPIN RELAXATION TIME

The data of Tinkham, Weinstein, and Kip[9] show that the interaction between Mn^{++} ions plays a negligible role in the relaxation mechanism in dilute solutions ($<0.05N$). In such solutions the dominant mechanism is undoubtedly via the spin-orbit coupling, first considered by Kronig.[10] Van Vleck[11] has made an elaborate model of this relaxation mechanism considering the coupling of the spins with the normal modes in a complex, which in turn are modulated by the Debye waves of the crystalline lattice. This model has been adopted by Russian workers[12–15] to discuss the relaxation time of ions in crystals and solutions.

In a liquid one considers the modulation of the crystalline field splitting, the g-tensor, and the hyperfine coupling by the Brownian motion. In a similar way the Kronig-Van Vleck mechanisms could be described in terms of a modulation of the coefficients in

[5] P. F. Cox and L. O. Morgan, J. Am. Chem. Soc. **81**, 6409 (1959).

[7] D. Kivelson, J. Chem. Phys. **33**, 1094 (1960).

[8] R. N. Rogers and G. E. Pake, J. Chem. Phys. **33**, 1107 (1960).

[9] M. Tinkham, R. Weinstein, and A. F. Kip, Phys. Rev. **84**, 848 (1951).

[10] R. deL. Kronig, Physica **6**, 33 (1939).

[11] J. H. Van Vleck, Phys. Rev. **57**, 426 (1940).

[12] S. A. Al'tshuler and K. A. Valiev, J. Exptl. Theoret. Phys. (U.S.S.R.) **35**, 947 (1958) [translation: Soviet Phys. JETP **8**, 661 (1959)].

[13] A. A. Kokin, J. Exptl. Theoret. Phys. (U.S.S.R.) **36**, 508 (1959) [translation: Soviet Phys. JETP **9**, 353 (1959)].

[14] G. V. Skrotskii and A. A. Kokin, J. Exptl. Theoret. Phys. (U.S.S.R.) **36**, 169, 481 (1959) [translation: Soviet Phys. JETP **9**, 116, 335 (1959)].

[15] Sh. Sh. Bashkirov, Phys. Metals and Metals Research (U.S.S.R.) **6**, 2 (1958).

a spin-Hamiltonian by the lattice vibrations. For free radicals with spin $S=\frac{1}{2}$ and a g value close to the free electron value modulation of the isotropic and/or anisotropic hyperfine coupling is important. For Ti^{3+} and Cu^{++} ions, with $S=\frac{1}{2}$ but an anisotropic g different from 2, modulation of the g tensor is probably dominant. McConnell,[16] Kivelson[7] and Rogers and Pake[8] have discussed these effects. For ions with $S\geq 1$, such as Ni^{++}, Cr^{3+}, V^{++}, Fe^{3+}, and Mn^{++}, modulation of the crystalline field parameters will be the most important mechanism, as was first discussed by McGarvey.[17] His equations are only qualitatively correct. Al'tshuler and Valiev[12] have given a very interesting discussion of electron spin relaxation in paramagnetic solutions. They arrive at the conclusion that for ions such as Cu^{++} and Co^{++}, which have some closely spaced low orbital levels, the transverse electron spin relaxation time may be considerably shorter than the longitudinal one. For other ions they reach conclusions similar to those presented here. Our work considers in more detail the various motions in the liquid and the different relaxation times that may result when the motion in the liquid is not very fast compared to the splitting of the electron spin levels. It is also shown that the proton spin relaxation times provide a check on the details of the electron spin relaxation mechanism.

Since the motion is random and isotropic, one has for tensor components in irreducible form, T [compare, e.g., Rose,[18] Eq. (4.32)].

$$\langle \mathsf{T}_{lm}(\theta,\phi,t)\,\mathsf{T}_{l'm'}(\theta,\phi,t+\tau)\rangle = c_l^2\delta_{ll'}\delta_{mm'}\exp(-\tau l(l+1)/\tau_r), \quad (8)$$

where τ_r is the correlation time for the rotation of the complex with an orientation described by spherical angles θ and ϕ. For a sphere of radius a in a viscous medium,

$$\tau_r/2=4\pi\eta a^3/3kT. \quad (9)$$

The constants c_l should be determined from the trace relationship

$$Tr\mathcal{K}_{cr,l}^2=\sum_{m_s}\mathcal{K}_{cr,l}^2=(2l+1)c_l^2, \quad (10)$$

where $\mathcal{K}_{cr,l}$ is the lth power polynomial in the crystalline field potential with zero average. In the case of a cubic Mn^{++} complex, e.g., only c_4 is nonvanishing. The left-hand side of (10) is then equal to $\frac{4}{3}\delta^2$, where δ is the energy separation between the doublet and quartet state of the $S=\frac{5}{2}$ ion in a cubic field. In terms of the constant a of the spin-Hamiltonian $a(S_x^4+S_y^4+S_z^4)$ one has $c_4=3^{-\frac{1}{2}}\times 48a$. The relaxation times can now be determined in the usual way from the equation of motion for the spin density matrix σ in the rotating coordinate system in the Schrödinger representation.

$$\dot{\sigma}_{\alpha\alpha'}=\sum_{\beta,\beta'}R_{\alpha\alpha'\beta\beta'}(\sigma_{\beta\beta'}-\sigma_{\beta\beta}{}^0\delta_{\beta\beta'}), \quad (11)$$

where the notation of Redfield[19] [his Eq. (2.19)] has been adopted and where the indexes refer to the m_s- states with values from $-\frac{5}{2}$ to $+\frac{5}{2}$. The relaxation coefficients can readily be expressed in terms of spectral densities which are Fourier transforms of Eq. (8). For the longitudinal relaxation times one is interested in the diagonal terms $R_{\alpha\alpha\beta\beta}$. For the transverse relaxation time one needs terms with $\alpha-\alpha'=\beta-\beta'=\pm 1$. One finds [Redfield,[19] Eqs. (2.16) and (2.24)]

$$R_{m_sm_sm_s'm_s'}=\hbar^{-2}\sum_l 2\tau_r l^{-1}(l+1)^{-1}c_l^2C^2(Sl\,S;\,m_sm_s')\times[1+\omega_s^2(m_s-m_s')^2\tau_r^2l^{-2}(l+1)^{-2}]^{-1}. \quad (12)$$

In the limit of extreme narrowing the last factor may be put equal to unity. One then has a single relaxation time. Following the method of Abragam and Pound[20] for the solution of the rate equations in this case, one obtains for the relaxation time of the longitudinal component

$$\tau_s^{-1}=4\tau_r\hbar^{-2}\sum_l[c_l^2/l(l+1)]\times[1-(2S+1)W(Sl1,\,S,\,SS)], \quad (13)$$

where W is a Racah coefficient, tabulated by Rose,[18] in his Appendix I. On substituting its value into Eq. (13), one finds

$$\tau_s^{-1}=2\tau_r\hbar^{-2}\sum_l c_l^2/S(S+1). \quad (14)$$

For the cubic Mn^{++} complex $\sum_l c_l^2=16\times 48a^2$. It is easy to show that the same relaxation time also applies to a transverse component in this limit.

To explain the field variation of τ_s one has of course to go back to the set of rate equations (11), because one is then interested in the deviations from the extreme narrowing case. In general, there are $2S=5$ characteristic longitudinal relaxation times. Because of the symmetry property of the matrix elements, the relaxation coefficients in (11) satisfy the relation $R_{mm',m'm'}=R_{-m-m,-m'-m'}$. The magnetic moment operator decays with only $S+\frac{1}{2}=3$ characteristic times[21] which may be obtained by solving the three simultaneous equations for $\dot{\sigma}_{5/2,5/2}-\dot{\sigma}_{-5/2,-5/2}$, $\dot{\sigma}_{3/2,3/2}-\dot{\sigma}_{-3/2,-3/2}$, and $\dot{\sigma}_{1/2,1/2}-\dot{\sigma}_{-1/2,-1/2}$. The eigenvectors $v_{m,\lambda}(m=\frac{5}{2},\frac{3}{2},\frac{1}{2})$ corresponding to the three relaxation times $\tau_{l,\lambda}(\lambda=1,2,3)$ are then found. The correlation function for the z component of magnetization is then

$$\langle S_z(t)\,S_z(t+\tau)\rangle=\sum_m\sum_{\lambda=1,2,3}mv_{m,\lambda}\times\exp\{-\tau/\tau_\lambda\}\tfrac{1}{3}S(S+1)/\sum_m\sum_\lambda mv_{m,\lambda}. \quad (15)$$

[16] H. McConnell, J. Chem. Phys. **25**, 709 (1956).
[17] B. R. McGarvey, J. Phys. Chem. **61**, 1232 (1957).
[18] M. E. Rose, *Elementary Theory of Angular Momentum* (John Wiley & Sons, Inc., New York, 1957).
[19] A. G. Redfield, IBM J. Research Develop. **1**, 19 (1957).
[20] A. Abragam and R. V. Pound, Phys. Rev. **92**, 943 (1953).
[21] F. Lurcat, Compt. rend. **240**, 2402, 2517 (1955).

A similar program could be carried through for the transverse components of the magnetization, starting from the rate equations for the off-diagonal elements of the density matrix.[18,19]

$$\dot{\sigma}_{m,m+1}=\sum_{m'}R_{m,m+1,m',m'+1}\sigma_{m',m'+1} \tag{16}$$

with

$$R_{m,m+1,m',m'+1}=2(-1)^{m'-m}C(SlS;\,m,\,m'-m)$$
$$C(SlS;\,m+1,\,m'-m)\frac{2\hbar^{-2}\tau_r l^{-1}(l+1)^{-1}c_l^2}{1+\omega_s^2(m-m')^2\tau_r^2 l^{-2}(l+1)^{-2}}$$
$$-2\delta_{m,m'}\sum_q C^2(SlS;\,mq)$$
$$\times\{2\hbar^{-2}\tau_r l^{-1}(l+1)^{-1}c_l^2/[1+\omega_s^2 q^2\tau_r^2 l^{-2}(l+1)^{-2}]\}. \tag{17}$$

This will lead to three transverse relaxation times, which are in general not equal to the longitudinal times.

Thus one will have six different times τ_s and consequently six different times τ_e to substitute in Eq. (2), three in the first term, and three others in the second term. The experimental data do not warrant such a computational effort. When T_2 is much shorter than T_1 the difference is due primarily to the term in Eq. (2) which is linear in τ_e. Therefore, T_2^{-1} increases with τ_e for large values of $\omega_s\tau_r$.

A qualitative idea about this increase may be obtained in the following way. There is a situation in which there is only one longitudinal relaxation time even for slow motion $\omega_s\tau_r\geq 1$. If thermodynamic equilibrium is assumed at all times within the spin system one has the single relaxation time[11,22]

$$\tau^{-1}{}_{s'}=2\sum_m\sum_{m'}R_{mnm'n'}(E_m-E_{m'})^2/\sum_m\sum_{m'}(E_m-E_{m'})^2. \tag{18}$$

This assumption is clearly not valid in our case. It supposes an infinitely short transverse relaxation time. In a solid with rapid dipole-dipole flip-flops between the various m-states it is applicable. Let us nevertheless evaluate Eq. (18) for our case

$$\frac{1}{\tau_s}=\frac{2\sum_{m=-s}^{+s}\sum_{m'=-s}^{+s}C^2(SlS;\,mm')(m-m')^2[1+\omega_s^2(m-m')^2\tau_r^2 l^{-2}(l+1)^{-2}]^{-1}\hbar^{-2}c_l^2 2\tau_r}{\frac{2}{3}(2S+1)S(S+1)}. \tag{19}$$

The numerator may be evaluated as follows

$$\sum_m\sum_{m'}C^2(SlS,\,mm'-m)(m-m')^2=\sum_\mu\sum_m\sum_{m'}C^2(SlS;\,m\mu m')\mu^2$$
$$=[(2S+1)/(2l+1)]\sum_\mu\sum_m\sum_{m'}C^2(SSl,\,mm'\mu)\mu^2=[(2S+1)/(2l+1)]\sum_{m'}\sum_\mu\mu^2=(2S+1)^2\tfrac{1}{3}l(l+1).$$

In the extreme narrowing limit this expression reduces properly to the previous result Eq. (14). There it was shown that magnetization decays with a single exponential, regardless of the initial distribution over the various spin states. In particular, the same value should be obtained for an initial Boltzmann distribution. It is believed that τ_s as evaluated from Eq. (19) gives a fair indication of how T_2^{-1}, given by Eq. (2), increases with increasing ω_s. Note that the decrease in T_2 should begin for $\omega_s(4/20)\tau_r\sim 1$, with $m-m'=4$ and $l=4$, whereas the increase in T_1 due to reduced dipole-dipole relaxation should begin for $\omega_s(2/6)\tau_r\sim 1$, with $m-m'=2$ and $l=2$.

The experimental data for Mn^{++} solutions indicate that the important decrease in T_2 occurs for much higher values of ω_s than the increase in T_1. The probable reason is that the main relaxation mechanism of the Mn^{++} ion is not the modulation of the 16-pole interaction by rotation of the cubic complex [term with $l=4$ in Eq. (19)], but rather the distortion from cubic symmetry by the water molecules outside the complex which dart rapidly in and out and deform the complex[12] with a characteristic time, $\tau_v<\tau_r/l(l+1)$. Although this motion is much more complex and cannot be treated rigorously, one may add, in analogy with the case of rotational motion a term with $l=2$ in the various Eqs. (11)–(18) with $\tau_r/6$ replaced by τ_v, and the constant c_2 determined by

$$5c_2^2=Tr\{D[S_z^2-\tfrac{1}{3}S(S+1)]+E[S_x^2-S_y^2]\}^2. \tag{20}$$

This is the only term in Eq. (14) present for Ni^{++} and Cr^{3+} with $S<2$. It should be emphasized once more that the correct way to calculate the decrease in T_2 is by using the solutions of the rate Eqs. (11), rather than (18) which is strictly valid only in a solid with strong interaction between neighboring ions.

Finally the possibility of interference with other electron spin relaxation mechanisms should be considered. In the following enumeration **I** will denote the nuclear spin of the paramagnetic ion, not as heretofore the spin of the protons. The interaction of the latter with the electron spin determines their relaxation time

[22] L. C. Hebel and C. P. Slichter, Phys. Rev. **113**, 1504 (1959).

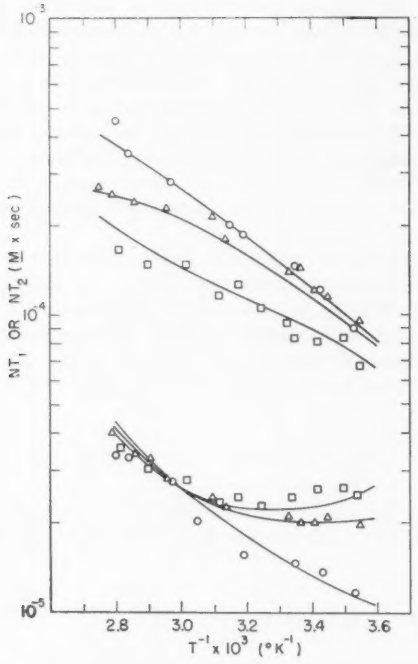

FIG. 1. Proton NT_1 and NT_2 for Mn^{++} solutions as functions of $1/T$. □—14 Mc, Δ—30 Mc, ○—60 Mc. Upper curves—NT_1, lower curves—NT_2. Solid lines were calculated using the constants given in the text.

according to Eqs. (1) and (2), but it can be ignored in the calculation of τ_s. The following processes can be distinguished:

(a) Relaxation by modulation of the isotropic hyperfine interaction $A(t)\,\mathbf{I}\cdot\mathbf{S}$;

(b) Relaxation by modulation of the anisotropic hyperfine interaction $\mathbf{I}\cdot\mathbf{B}(t)\cdot\mathbf{S}$;

(c) Relaxation by modulation of the anisotropic g-factor $\mathbf{H}_0\cdot\Delta\mathbf{g}(t)\cdot\mathbf{S}$;

(d) Relaxation by modulation of the quadratic crystalline field splitting $\mathbf{S}\cdot\mathbf{D}(t)\cdot\mathbf{S}$;

(e) Relaxation by modulation of crystalline 16-pole interaction, etc.

The modulation of the scalar $A(t)$ is caused only by impinging of molecules outside the complex. The wave function at the nucleus is thus distorted with a correlation time τ_v. The modulation of the second-order traceless tensors $\mathbf{B}(t)$, $\Delta\mathbf{g}(t)$, and $\mathbf{D}(t)$, has two causes. The rotation of the complex as a whole modulates the angular factors with correlation time τ_r, describing the orientation of the tensor axes with respect to the laboratory coordinate system. If the complex had perfect cubic symmetry and this were the only motion, the interactions would vanish and no relaxation would result. The ratio of the axes of these tensors may, however, be modulated by molecular distortions of the complex with correlation time τ_v. This was shown to be the most important mechanism for the tensor $\mathbf{D}(t)$. Although the modulation of the dipolar hyperfine structure and anisotropic g-value is usually considered to arise from a rotating rigid complex, it should be emphasized that this model is adopted mainly for mathematical elegance. The dipolar interaction has only three independent elements rather than five for a general traceless second order tensor, but one is the radial factor, which may be modulated by distortion of the complex from outside. The same motion can also modulate $\Delta\mathbf{g}$ in the same way as it modulates D, E and the Eulerian angles of the tensor $\mathbf{D}(t)$.

There is no interference term between process (a) and any other mechanism. When the statistical average over all orientations in space of the tensors is taken in the isotropic liquid, a vanishing result for the cross term is obtained as A itself does not depend on the angle.

In the same way the cross term between mechanism (e) and any other mechanism vanishes, since the orders of the spherical harmonics involved are different.

It remains to investigate the cross-effects between (b), (c), and (d). McConnell[16] and Kivelson[7] have shown the existence of cross terms between (b) and (c), and in principle similar cross terms should arise with (d). The interest is here, however, centered on paramagnetic ions which have no resolved fine or hyperfine splittings in aqueous solution. Therefore, averages over all m_I and m_s states should be taken. Then all interference terms between (b), (c), and (d) vanish, because $\langle\mathbf{I}\rangle=\langle\mathbf{S}\rangle=\langle I_k S_l\rangle=0$, etc.

III. COMPARISON WITH EXPERIMENTAL RESULTS

Mn^{++} Solutions: ($S=\frac{5}{2}$; $3d^5$ ^6S)

In addition to data reported previously[1–3] for proton relaxation in aqueous Mn^{++} solutions, results have been obtained at proton resonance frequencies of 14, 30, and 60 Mc over the temperature range 5° to 80°C,[23] and are shown graphically in Fig. 1 as a function of T^{-1}. The solid curves indicated for NT_1 are those expected for $\tau_c(300°\text{K})=3.0\times10^{-11}$ sec and $V_c=4.5$ kcal/mole, using the first term (dipolar) of Eq. (1) and Eq. (3); with $r=2.8$ A, $\mu=5.9\beta$, and $n_h=12$.

Following the suggestion of Bernheim, Brown, Gutowsky, and Woessner,[2] we assume that τ_c at high temperatures is essentially τ_h, and that

$$\tau_h=\tau_h^0\exp(V_h/RT), \tag{21}$$

while at low temperatures τ_s contributes heavily to τ_c[Eq. (6)]. According to Eq. (19), for $l=2$

$$\frac{1}{\tau_s}=\frac{12c_2^2\hbar^{-2}}{5S(S+1)}\left[\frac{\tau_v}{1+\omega_s^2\tau_v^2}+\frac{4\tau_v}{1+4\omega_s^2\tau_v^2}\right] \tag{22}$$

[23] Experimental methods used were those given in detail in footnote 3. Temperature control was obtained using a flowing gas thermostat. Reported temperatures are probably accurate to within ±1°C.

and according to Eq. (20)

$$c_2^2 = 2/225(2S+1)S^2(S+1)^2 \times\{1-[3/4S(S+1)]\}[2\langle D^2\rangle_{Av}+3\langle E^2\rangle_{Av}]. \quad (23)$$

From the experimental data shown in Fig. 1 the spin exchange contribution to $(NT_2)^{-1}$ may be calculated as a function of temperature and frequency. At low temperatures, where $\tau_e \approx \tau_s$, τ_v may then be evaluated from the frequency dependence of $(NT_2)_{ex}$ predicted by Eqs. (2) and (22). The results of this calculation are given in Table I. Noting that τ_v is the correlation time for the impact of water molecules of the solvent upon the hydrated ion, we expect that

$$\tau_v = \tau_v^0 \exp(V_v/RT). \quad (24)$$

The observed exponential temperature dependence of τ_v gives $V_v = 3.9$ kcal/mole.

Bleaney and Ingram[24] found $D = 0.018$ cm^{-1} and $E = 0$ for $MnSiF_6 \cdot 6H_2O$ crystals and $D = 0.024$ cm^{-1} and $E \approx 0.01$ cm^{-1} for the Tutton salt, $(NH_4)_2Mn(SO_4)_2 \cdot 6H_2O$, from the ESR spectrum at room temperature. In these substances the Mn^{++} ion is surrounded by an octahedron of water molecules in a manner similar to that proposed for the hydrated ion in solution. Assuming that the effect on D of fields external to the hydrated ion in the crystal is small, we use the value $D = 0.018$ cm^{-1} in Eq. (22). Then, taking $\tau_v = 2.4\times10^{-12}$ sec, τ_s at 300°K and 30 Mc is found to be 4.5×10^{-9} sec. This corresponds to a low-field value of 3.5×10^{-9} sec, which is in good agreement with $\tau_s = 3\times10^{-9}$ sec estimated[5] from the ESR linewidth data of Tinkham, Weinstein, and Kip.[9] The values of D and τ_v used here are considerably smaller than those obtained by Kokin,[13] whose value for D (0.08 cm^{-1}) is much larger than that expected on the basis of results for hydrated ions in crystals. Since the pertinent motion is not rotation of the complex, our shorter value for the correlation time appears to be more reasonable and is consistent with the high field behavior of the proton T_2.

At high temperatures ($\tau_e \approx \tau_h$) the best fit of Eq. (2) to experimental data is obtained with $\tau_h(300°K) = 2.3\times10^{-8}$ sec and $V_h = 8.1$ kcal/mole, which are comparable to the values reported by Bernheim, *et al.*[3] Thus, $\tau_e(300°K) \cong 3.8\times10^{-9}$ sec and $(A/h) = 1.0\times10^6$ sec^{-1}.

TABLE I. Temperature dependence of τ_v in Mn^{++} solutions.

T(°C)	T^{-1}(°K^{-1})	$(\omega_s)_c$[a](Mc)	τ_v(sec)
12	3.5	72	3.4×10^{-12}
21	3.4	89	2.8×10^{-12}
30	3.3	105	2.3×10^{-12}
40	3.2	127	1.9×10^{-12}

[a] Frequency at which $\omega_s\tau_v = 1$.

[24] B. Bleaney and D. J. E. Ingram, Proc. Roy. Soc. (London) **A205**, 336 (1951).

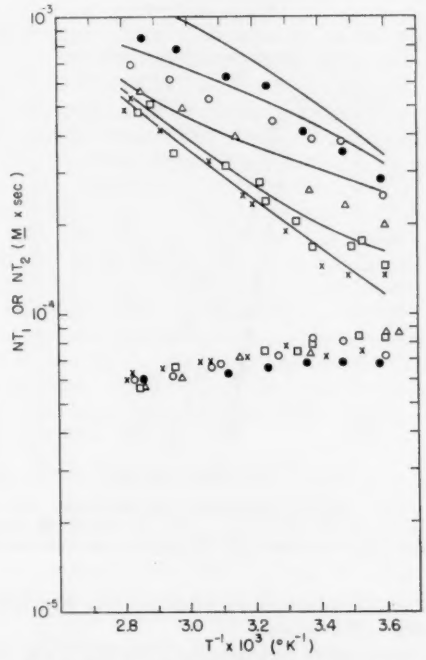

FIG. 2. Proton NT_1 and NT_2 for V^{++} solutions as functions of $1/T$. ×−2.7 Mc, □−6 Mc, Δ−14 Mc, ○−30 Mc, ●−60 Mc. Upper curves−NT_1, lower curves−NT_2. Solid lines were calculated for NT_1 using the constants given in the text. To avoid confusion the calculated curves for NT_2 are shown in Fig. 3 for the spin exchange contribution.

The solid curves drawn in for NT_2 in Fig. 1 represent Eq. (2), taking all contributions into account according to the preceding discussion. The agreement is well within the expected experimental error and must be considered satisfactory. The behavior of T_1 and T_2 clearly indicates that two distinct motions in the solutions, described by τ_r and τ_v, are important in the relaxation mechanism, and corroborate the assumption that proton chemical exchange becomes important if electron spin relaxation times are sufficiently long.

V^{++} Solutions: ($S = \frac{3}{2}$; $3d^3\ ^4F$; Orbital Singlet Lowest in a Cubic Field)

Proton relaxation times for solutions of VSO_4 in dilute H_2SO_4 are presented in Fig. 2. These data were obtained using samples maintained in a reducing atmosphere and containing an excess of solid zinc amalgam. Other experimental details have been given previously.[3] It was verified that both T_1 and T_2 are independent of concentration to at least 0.01 M VSO_4 and 0.1 M H_2SO_4. The predominant ionic species in such solutions is usually assumed to be the hydrated

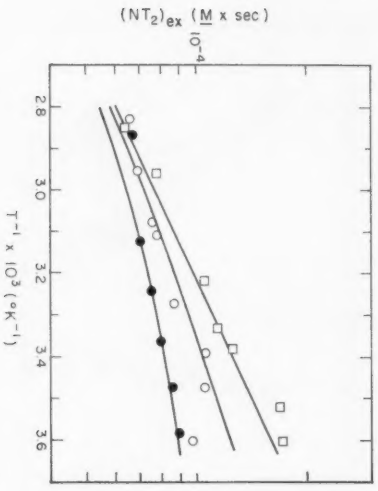

FIG. 3. Spin exchange contribution to proton NT_2 for V^{++} solutions as a function of $1/T$. □ −6 Mc, ○ −30 Mc, ● −60 Mc. Solid lines were calculated using the constants given in the text.

vanadium(II) ion and no evidence was obtained in this work to the contrary.

The solid curves representing T_1 in Fig. 2 are those expected for the several proton resonance frequencies employed according to the first term (dipole-dipole) of Eq. (1). The constants used were the same as those for Mn^{++} solutions except $\mu_s=3.83$, $V_c=4.3$ kcal/mole, and $\tau_c(300°K)=2.0\times10^{-11}$ sec. It should be noted that in each case the curves give essentially the correct temperature dependence. However, the expected 10/3 increase in T_1 at high fields relative to the low-field values is not entirely realized. A similar situation in Cu^{++} and Gd^{3+} solutions has been previously noted.[3] The cause of the discrepancy is not known, but may be the contribution of relaxation occurring in the second and more remote layers of water molecules around the paramagnetic ions. There the effective correlation time may be considerably shorter than for protons in the primary hydration sphere so that the important increase in that part of T_1 occurs at higher frequency.

Certain features of the transverse proton relaxation behavior are apparent even in the unresolved data shown in Fig. 2: (1) T_2 is considerably less than T_1 at all frequencies, (2) there is no gross frequency dependence, and (3) in general, T_2 decreases with increasing temperature. These observations suggest that $\tau_s<\tau_h$ and $\tau_s>\tau_c$, so that $\tau_e=\tau_s$ and $\omega_s\tau_e\gg1$. The spin exchange contributions to NT_2 are shown in Fig. 3. Application of Eqs. (2) and (22) to the observed frequency dependence of $(NT_2)_{ex}$ gives the values of τ_v listed in Table II, from which $V_v=2.8$ kcal/mole. The value of V_v calculated from the temperature variation of $(NT_2)_{ex}$ at 2.7 Mc is 2.6 kcal/mole, assuming that τ_s [and $(NT_2)_{ex}$] is an explicit function of τ_v and is essentially equal to its zero field value at that frequency.

A value of D for the hydrated V^{++} ion in solution may be estimated from data reported for the vanadium(II) Tutton salt, $(NH_4)_2V(SO_4)_2\cdot6H_2O$, by Bleaney, Ingram, and Scovil[25] for which $D=0.158\pm0.01$ cm^{-1} and $E=0.049\pm0.005$ cm^{-1}. Assuming that D for the ion in solution is approximately $\frac{2}{3}$ of that for the solid Tutton salt and $E=0$ as in the case of Mn^{++}, we obtain $\tau_s(300°K)=5\times10^{-10}$ sec at low fields and 6×10^{-10} sec at 30 Mc. On that basis Eq. (2) yields $(A/h)=2\times10^6$ sec^{-1}. In the temperature range 0°–100°C $\tau_s^{-1}\ll\tau_r^{-1}$ and $\tau_c=\tau_r$.

Cr^{3+} Solutions: ($S=\frac{3}{2}$; $3d^3$ ^4F)

Among hydrated ions of the iron group Cr^{3+} is unique in that the mean lifetime τ_h for protons in the hydration sphere of the ion is sufficiently long that the rate of proton exchange with those of bulk solvent determines the overall proton relaxation time in the solution. Although this has not been recognized previously, it is perhaps not surprising in view of the very long (of the order of hours) characteristic lifetime for water molecules in the hydration sphere.[26]

A similar case of slow proton exchange has been examined in detail for solutions of the bisethylenediaminecopper(II) ion[6] and general relaxation rate equations were used in connection with that work of the type introduced by McConnell.[27] Pearson, Palmer, Anderson, and Allred[28] have made essentially the same application in a recent publication. The pertinent relation for this case is

$$(T_1)^{-1}=(T_{1w})^{-1}+Nn_hN_p^{-1}(T_{1c}+\tau_h)^{-1}, \qquad (25)$$

in which T_{1w} is the relaxation time in pure water and T_{1c} is the relaxation time in the hydration sphere of the paramagnetic ion. This relation applies for $Nn_hN_p^{-1}\ll1$ and $T_1>\tau_h$. The latter condition is valid in our experiments. It is necessary in order to have a homogeneous system, and not two distinct groups of protons with different relaxation times as discussed in

TABLE II. Temperature dependence of τ_v in V^{++} solutions.

T(°C)	T^{-1}(°K^{-1})	$(\omega_s)_e$	τ_v(sec)
5	3.6×10^{-3}	112	2.17×10^{-12}
12	3.5×10^{-3}	130	1.87×10^{-12}
21	3.4×10^{-3}	152	1.60×10^{-12}
30	3.3×10^{-3}	170	1.43×10^{-12}

[25] B. Bleaney, D. J. E. Ingram, and H. E. D. Scovil, Proc. Phys. Soc. (London) **A64**, 601 (1951).
[26] J. P. Hunt and H. Taube, J. Chem. Phys. **18**, 757 (1950).
[27] H. McConnell, J. Chem. Phys. **28**, 430 (1958).
[28] R. G. Pearson, J. Palmer, M. M. Anderson, and A. L. Allred, Z. Elektrochem. **64**, 110 (1960).

detail by Broersma.[29] A similar equation applies to T_2 in this case.

Proton T_1 and T_2 as functions of temperature are shown in Fig. 9 of footnote 1 for Cr^{3+} solutions. At low temperatures T_1 and T_2 decrease with increasing temperature because the rate of proton exchange increases and a proton remains in the hydration sphere of an ion for a time, τ_h, long compared to its relaxation time in that environment. At higher temperatures just the reverse is true so that $(T_1)^{-1} \cong (T_{1w})^{-1} + N n_h N_p^{-1} (T_{1c})^{-1}$ and Eqs. (1) and (2) apply. Eq. (25) provides a natural explanation for these observations. τ_h is found to be 4×10^{-6} sec at 300°K and $V_h = 10$ kcal/mole. Results are the same for resolution of both T_1 and T_2 data.

Equation (25) can also explain quantitatively the frequency dependence of T_1 and T_2 for Cr^{3+} solutions reported previously.[3] With the value of τ_h in the foregoing, the revised τ_c for dipolar interaction in such solutions is then 8×10^{-11} sec at 300°K. The same value is obtained from both the low frequency T_1 and the break in the T_1 vs frequency curve.

At temperatures well above 300°K T_2 continues to decrease with increasing temperature, but with somewhat smaller slope. Assuming that this is attributable to the increase in τ_s in the second term of Eq. (2), $V_v \approx 2.5$ kcal/mole and $(NT_2)_{ex} \approx 8\times10^{-5}$ at 300°K.

The ESR linewidth at x band for hydrated Cr^{3+} in solutions of violet $Cr(NO_3)_3$ is about 150 gauss at 300°K, so that $\tau_s \approx 5\times10^{-10}$ sec at low fields. Eqs. (22) and (23) then give $D = 0.08$–0.11 cm^{-1} depending upon the choice of τ_v in the range 2×10^{-12} to 2.5×10^{-11} sec. $(A/\hbar)$ may then be evaluated from Eq. (2) and is found to be 2×10^6 sec^{-1}.

$Cu^{++}(S=\frac{1}{2}; 3d^9\ ^2D)$ and $Gd^{3+}(S=\frac{7}{2}; 4f^7\ ^8S)$ Solutions

The dipole-dipole mechanism appears to account satisfactorily for observed T_1 and T_2 for protons in Cu^{++} and Gd^{3+} solutions.[1–3,6] The calculated τ_c's are consistent with the ion tumbling process (2×10^{-11} sec) although that value may be somewhat lower than expected for hydrated Gd^{3+}, around which the solvent stiffening would be expected to be greater than in the case of hydrated Cu^{++}.

On that basis, it is expected that τ_s for both ions is of the order of 10^{-9}–10^{-10} sec. If it were shorter, so that $\tau_s \leq \tau_r$, T_1 and T_2 would decrease with increasing temperature, at least at low temperatures. That does not seem to be the case.[1,2,6] If τ_s were much longer than 10^{-9} sec, it is probable that there would be some spin exchange contribution to T_2^{-1}, although that also depends upon the magnitude of A, which could be very small.

McConnell[16] has estimated $\tau_{s,1}$ and $\tau_{s,2}$ for the various hyperfine components of the Cu^{++} spectrum in aqueous solution on the basis of anisotropy of the g- and hyperfine interaction tensors modulated by rotation of the hydrated ion. The calculated values fall within the range 3×10^{-8} to 2×10^{-9} sec for $\tau_r \sim 3\times10^{-11}$ sec. The actual relaxation time is probably an order of magnitude shorter, because Cu^{++} solutions do not exhibit a resolved hyperfine structure in microwave spectra.

For Gd^{3+}, Weger and Low[30] report $D = 0.04$ cm^{-1} and $E = 0.004$ in $LaCl_3 \cdot 7H_2O$. Using that value of D in Eqs. (22) and (23), the value of τ_s is found to be $4-7\times10^{-10}$ sec at 30 Mc, depending upon the choice of τ_v in the range 2×10^{-12} to 2.5×10^{-11} sec. The minimum calculated τ_s is found at $\tau_v = 8\times10^{-12}$ sec. A complete calculation of τ_s would require consideration of the 16-pole and 64-pole interactions, as well as those of lower order. However, since we expect that terms in D are the most important, the estimate of τ_s given above is probably satisfactory.

$Ni^{++}(S=1; 3d^8\ ^3F)$, $Co^{++}(S=\frac{3}{2}; 3d^5\ ^4F)$, and $Fe^{++}(S=2; 3d^6\ ^5D)$ Solutions

Proton relaxation times in solutions of these ions are much longer than in solutions of comparable concentration of the ions discussed before. In each case for Ni^{++}, and Co^{++}, and Fe^{++} one finds $T_1 \simeq T_2$ with no frequency dependence up to 60 Mc, and with a very slight increase or decrease (Ni^{++}) with increasing temperature.[1,2]

If one determines, without justification, τ_c from the observed T_1 with Eq. (1), very short times $\tau_c = 3\times10^{-12}$ sec for Ni^{++}, 5×10^{-13} sec for Co^{++}, and 10^{-12} sec for Fe^{++} would be obtained. It should be emphasized that the theory of Sec. II breaks down, if it leads to values of τ_s shorter than the correlation time of the motion in the liquid τ_v [compare Eq. (2.20) of Redfield[19]]. This implies that the instantaneous values of the crystalline field interactions D and E are larger than $\hbar\tau_v^{-1}$. For Ni^{++} and Fe^{++} this is quite reasonable. One has nearly complete quenching of the electron spin angular momentum at each instant. The true relaxation time of Fe^{++} solution may even be longer than the experimental value quoted in the foregoing, if a few percent of Fe^{3+} had been present in the experiment.[1]

A simple theoretical argument shows that the factor between square brackets in Eqs. (1) and (2) should be replaced by $10\tau_v(1+\omega_{cr}^2\tau_v^2)^{-1}$ when quenching occurs because $\hbar^{-1}D\tau_v = \omega_{cr}\tau_v \gg 1$. The nuclear spin relaxation time is increased by a factor $(\omega_{cr}\tau_v)^2$ and is independent of the external field because ω_{cr} is very large compared to the circular Zeeman frequency ω_s.

In the case of the Co^{++} ion with an odd number of electrons, the quenching will never be complete since the Kramers degeneracy remains. The dominant relaxation mechanism, however, will be that resulting from transitions between different Kramers doublets connected by the modulated crystalline potential of the kind introduced by Al'tshuler and Valiev.[12] The argu-

[29] S. Broersma, J. Chem. Phys. **24**, 153 (1956); **27**, 484 (1957).

[30] M. Weger and W. Low, Phys. Rev. **111**, 1526 (1958).

ment for Fe^{++} and Ni^{++} may therefore also be applied to Co^{++}.

A problem related to the quenching of the electron-spin angular momentum, is the quenching of rotational angular momentum J of a molecule in a liquid. In most discussions of nuclear spin relaxation, the spin-orbit coupling $c\mathbf{I}\cdot\mathbf{J}$ has been ignored. This is justifiable in the case of liquid HF because of quenching of J, although the coupling constant c is actually quite large. Baker and Ramsey[31] found $h^{-1}c_p=71$ kc for the proton and $h^{-1}c_F=320$ kc for F^{19} in HF. If the spin-rotational coupling were a dominant factor the relaxation time of F^{19} in pure liquid HF should be 25 times shorter than that of hydrogen. Actually the two relaxation times are found to be about equal.[32]

In other molecules, however, the spin-rotational coupling may not be quenched as completely and may contribute significantly to the relaxation mechanism. It would be of considerable interest to extend the theories of relaxation to include the cases in which the interactions with electron spin or molecular rotation have a magnitude comparable to $\hbar\tau_r^{-1}$.

IV. DISCUSSION

In those cases in which data are available for the estimation of D according to Eq. (23) the values obtained are comparable to those reported for crystals containing the appropriate hydrated ions. This indicates that the instantaneous values of the distortion of the water octahedron about the ion have the same order of magnitude as in crystals.

Values of τ_v cannot be obtained with any precision from Eqs. (22) and (23) on the basis of the temperature dependence of τ_s alone in the range of magnetic field strengths utilized in the experimental work considered here. A broad maximum is observed for $[\tau_v(1+\omega_s^2\tau_v^2)^{-1}+4\tau_v(1+4\omega_s^2\tau_v^2)^{-1}]$ as a function of τ_v centering about $\tau_v=8\times10^{-12}$ sec for $\omega_s=1.2\times10^{11}$ sec^{-1}. On the other hand, variation of ω_s at a given temperature (and τ_v) provides the necessary sensitivity. Values of $\tau_v(300°\text{K})$ calculated for Mn^{++} and V^{++} solutions, 2.4×10^{-12} and 1.5×10^{-12} sec, respectively, from the frequency dependence of τ_s are entirely consistent with the proposed molecular impact process.

ACKNOWLEDGMENTS

We are indebted to Miss Joye Murphy and Dr. Paul Cox of the University of Texas for making many of the experimental measurements (with support from the Robert A. Welch Foundation) reported in this paper which had not previously been published. One of us (L.O.M.) wishes to thank the University of Texas Research Institute for support of a research leave during the Spring Term, 1960, and the Division of Engineering and Applied Physics, Harvard University, for the courtesies extended to him during his tenure as a Research Fellow in the Division.

[31] M. R. Baker and N. F. Ramsey, Bull. Am. Phys. Soc. Ser. II **5**, 344 (1960).

[32] I. Solomon and N. Bloembergen, J. Chem. Phys. **25**, 261 (1956).

Microwave Spectrum of Acetyl Chloride*

K. M. SINNOTT†

Mallinckrodt Chemical Laboratory, Harvard University, Cambridge Massachusetts

(Received September 21, 1960)

The microwave spectrum of ten isotopic species of acetyl chloride are reported. Internal rotation of the methyl group splits some of the rotational transitions into doublets in addition to the chlorine hyperfine structure. Analysis of the internal rotation splitting gives a barrier to internal rotation of the methyl group of 1296±30 cal/mole. From the hyperfine structure, the chlorine nuclear quadrupole coupling constants for Cl^{35} along the C−Cl bond axis and perpendicular to the plane of symmetry of the molecule were determined to be −58.5 and 21.5 Mc, respectively. The corresponding values for Cl^{37} were −46.4 and 17.2 Mc. These coupling constants have been interpreted to give information about the double bond and ionic character of the C−Cl bond. The following structural parameters have been determined from the rotational constants of CH_3COCl^{35}, CH_3COCl^{37}, $C^{13}H_3COCl^{35}$, $CH_3C^{13}OCl^{35}$, $CH_3CO^{18}Cl^{35}$, and CD_3COCl^{35}:

C—H	1.083±0.005 A	<CCH	110°21′±10′
C—C	1.499±0.010	<CCO	127°5′ ±10′
C=O	1.192±0.010	<CCCl	112°39′±30′
C—Cl	1.789±0.005		

The observed rotational constants of CH_2DCOCl^{35} show that the equilibrium configuration of acetyl chloride has a methyl hydrogen atom opposite the oxygen atom.

INTRODUCTION

THE present work on acetyl chloride represents part of a systematic investigation of the potential barrier hindering internal rotation of the methyl group in the series CH_3COZ. This series includes acetaldehyde,[1] acetyl fluoride,[2] acetyl cyanide,[3] acetic acid,[4] and acetyl bromide.[5] The variation of the barrier with the group Z in this series of closely related molecules should yield some information about the origin of the potential barrier.

EXPERIMENTAL

The normal mixture of CH_3COCl^{35} and CH_3COCl^{37} used was a commercial sample. The other isotopic species were prepared by the reaction of PCl_3 with the appropriate acetic acid species. Malonic acid was exchanged with D_2O and then heated to give CD_3COOD from which CD_3COCl was prepared. CH_2DCOCl was obtained from CH_2DCOOD prepared by the reaction of ketene with D_2O. The C^{13} and O^{18} species were prepared from samples of the corresponding acids kindly provided by Dr. Louis Pierce who has described their preparation elsewhere.[2]

The microwave spectrometer used was a conventional Hughes-Wilson instrument employing 100 kc square-wave Stark modulation. Frequency measurements were made with multiples of a 5-Mc signal monitored with the 5-Mc standard from Station WWV. The frequencies of individual lines were reproducible to within ±0.2 Mc and the splittings of the fine structure to within ±0.1 Mc.

OBSERVED FREQUENCIES

The frequencies of the assigned lines of all the species, except the monodeuterated, are given in Table I. The spectra of the nondeuterated species is complicated to a certain extent by the presence of both the chlorine nuclear quadrupole hyperfine structure and the splitting due to internal rotation. In the case of the transitions involving J values less than 4 the internal rotation splitting could not be resolved and, therefore, only the chlorine hyperfine splitting was observed. With J values greater than 8, only the internal rotation splitting was resolvable. At intermediate J values, both the chlorine hyperfine structure and the internal rotation splitting were observed. In these cases approximate values of the chlorine nuclear quadrupole splittings were calculated from the coupling constants obtained from the low J transitions and these were used to assign the individual components. After this assignment, the observed splittings were used in the final calculation of the chlorine nuclear quadrupole coupling constants.

STRUCTURE

The rotational constants and moments of inertia for the normal molecule, and the C^{13}, O^{18}, and the fully deuterated species are given in Tables II and III, respectively. The rotational constants were obtained from a least-squares treatment using the low J transitions and those intermediate ones in which the centrifugal distortion correction was small. In some isotopic species the use of high J transitions could not be avoided as insufficient low J transitions were observed. In the case of the O^{18} species, no R-branch transitions were observed due to the low concentration of this isotope. Therefore, the moments of inertia were cal-

* The research reported in this paper was made possible by support extended Harvard University by the Office of Naval Research.

† Present address: Polychemicals Department, E. I. du Pont de Nemours and Company, Washington Laboratory, P. O. Box 1217, Parkersburg, West Virginia.

[1] R. W. Kilb, C. C. Lin, and E. B. Wilson, Jr., J. Chem. Phys. **26**, 1695 (1957).

[2] L. Pierce and L. C. Krisher, J. Chem. Phys. **31**, 875 (1959).

[3] L. C. Krisher and E. B. Wilson, Jr., J. Chem. Phys. **31**, 882 (1959). See Errata, J. Chem. Phys. **33**, 304 (1960).

[4] W. J. Tabor, J. Chem. Phys. **27**, 974 (1957).

[5] L. C. Krisher, J. Chem. Phys. (to be published).

TABLE I. Observed frequencies (Mc).

J	J'	F_i	F_f	Torsional level	CH_3COCl^{35}	CH_3COCl^{37}
1_{01}	2_{12}	1/2	3/2	A and E	20 327.30	
		1/2	1/2	A and E	20 332.60	
		5/2	5/2	A and E	20 334.80	
		5/2	7/2	A and E	20 340.25	
		3/2	5/2	A and E	20 349.25	
		3/2	3/2	A and E	20 353.25	
2_{02}	3_{13}	7/2	7/2	A and E	26 467.75	
		1/2	3/2	A and E	26 471.05	26 165.30
		3/2	5/2	A and E	26 476.55	26 169.10
		7/2	9/2	A and E		
		5/2	7/2	A and E	26 481.53	26 172.95
		3/2	3/2	A and E	26 485.20	
		5/2	5/2	A and E		
2_{12}	3_{03}	5/2	7/2	A and E	19 926.80	
		3/2	5/2	A and E	19 928.25	
		5/2	5/2	A and E	19 932.10	
		7/2	9/2	A and E	19 934.00	
		1/2	3/2	A and E	19 936.00	
		3/2	3/2	A and E	19 941.80	
3_{13}	4_{04}	7/2	9/2	E	28 278.10	27 492.96
		5/2	7/2	E		
		7/2	9/2	A	28 278.78	27 493.69
		5/2	7/2	A		
		9/2	11/2	E	28 281.08	27 495.40
		3/2	5/2	E		
		9/2	11/2	A	28 281.76	27 496.12
		3/2	5/2	A		
4_{14}	4_{23}	5/2	5/2	E	26 181.00	
		11/2	11/2	E	26 182.60	
		5/2	5/2	A		
		11/2	11/2	A	26 183.95	
		7/2	7/2	E	26 185.50	
		9/2	9/2	E	26 186.80	
		7/2	7/2	A		
		9/2	9/2	A	26 188.30	
5_{05}	5_{14}	11/2	11/2	E	23 090.50	
		9/2	9/2	E		
		13/2	13/2	E	23 092.30	
		7/2	7/2	E		
		11/2	11/2	A	23 095.25	
		9/2	9/2	A		
		13/2	13/2	A	23 097.14	
		7/2	7/2	A		
5_{23}	5_{32}	7/2	7/2	A and E	25 150.65	25 962.30
		13/2	13/2	A and E	25 153.00	25 964.05
		9/2	9/2	A and E	25 159.20	25 969.00
		11/2	11/2	A and E	25 161.60	25 970.85
6_{15}	6_{24}	13/2	13/2	E	19 125.31	18 695.28
		11/2	11/2	E		
		15/2	15/2	E		
		9/2	9/2	E		
		13/2	13/2	A	19 128.55	18 697.87
		11/2	11/2	A		
		15/2	15/2	A		
		9/2	9/2	A		
6_{24}	6_{33}	9/2	9/2	A and E	23 260.30	24 014.90
		15/2	15/2	A and E	23 261.50	24 015.90
		11/2	11/2	A and E	23 265.75	24 019.20
		13/2	13/2	A and E	23 267.00	24 020.20
7_{16}	7_{25}	15/2	15/2	E	24 086.30	23 172.22
		13/2	13/2	E		
		17/2	17/2	E	24 087.55	
		11/2	11/2	E		
		15/2	15/2	A	24 091.40	23 176.50
		13/2	13/2	A		
		17/2	17/2	A	24 092.65	
		11/2	11/2	A		

TABLE I.—Continued

J	J'	F_i	F_f	Torsional level	CH_3COCl^{35}	CH_3COCl^{37}
7_{25}	7_{34}	11/2	11/2	E	22 344.40	22 846.60
		17/2	17/2	E	22 345.20	22 847.27
		11/2	11/2	A		
		17/2	17/2	A	22 346.02	22 848.00
		13/2	13/2	E	22 347.65	22 849.41
		15/2	15/2	E	22 348.40	22 850.10
		13/2	13/2	A		
		15/2	15/2	A	22 349.23	22 850.83
8_{17}	8_{26}	17/2	17/2	E		29 342.20
		15/2	15/2	E		
		19/2	19/2	E		29 343.42
		13/2	13/2	E		
		17/2	17/2	A		29 348.80
		15/2	15/2	A		
		19/2	19/2	A		29 350.15
		13/2	13/2	A		
8_{26}	8_{35}	13/2	13/2	E	23 073.27	23 120.90
		19/2	19/2	E		
		15/2	15/2	E	23 074.50	
		17/2	17/2	E		
		13/2	13/2	A	23 075.56	23 122.25
		19/2	19/2	A		
		15/2	15/2	A	23 076.80	
		17/2	17/2	A		
9_{27}	9_{36}	19/2	19/2	E		
		17/2	17/2	E	25 860.85	25 279.18
		21/2	21/2	E		
		15/2	15/2	E		
		19/2	19/2	A		
		17/2	17/2	A	25 865.30	25 282.92
		21/2	21/2	A		
		15/2	15/2	A		
10_{28}	10_{37}	21/2	21/2	E	30 836.85	29 521.30
		19/2	19/2	E		
		23/2	23/2	E	30 837.95	29 522.04
		17/2	17/2	E		
		21/2	21/2	A	30 843.67	29 527.40
		19/2	19/2	A		
		23/2	23/2	A	30 844.77	29 528.13
		17/2	17/2	A		
11_{38}	11_{47}	19/2	19/2	E	29 817.85	30 067.30
		25/2	25/2	E		
		21/2	21/2	E	29 819.00	30 068.48
		23/2	23/2	E		
		19/2	19/2	A	29 820.30	30 069.05
		25/2	25/2	A		
		21/2	21/2	A	29 821.40	30 070.27
		23/2	23/2	A		
					$C^{13}H_3COCl^{35}$	$C^{13}H_3COCl^{37}$
3_{12}	4_{04}	7/2	9/2	E	27 813.90	27 044.25
		5/2	7/2	E		
		7/2	9/2	A		
		5/2	7/2	A		
		9/2	11/2	E	27 816.80	27 046.88
		3/2	5/2	E		
		9/2	11/2	A		
		3/2	5/2	A		
5_{23}	5_{32}	7/2	7/2	A and E	24 179.60	
		13/2	13/2	A and E	24 181.90	
		9/2	9/2	A and E	24 188.08	
		11/2	11/2	A and E	24 190.08	
6_{15}	6_{24}	13/2	13/2	E	18 816.30	
		11/2	11/2	E		
		15/2	15/2	E		
		9/2	9/2	E		
		13/2	13/2	A	18 819.38	
		11/2	11/2	A		
		15/2	15/2	A		
		9/2	9/2	A		

TABLE I.—Continued

J	J'	F_i	F_f	Torsional level	$C^{13}H_3COCl^{35}$	$C^{13}H_3COCl^{37}$
6_{24}	6_{33}	9/2	9/2	A and E	22 371.19	
		15/2	15/2	A and E		
		11/2	11/2	A and E	22 376.50	
		13/2	13/2	A and E		
7_{16}	7_{25}	15/2	15/2	E	23 841.25	22 908.0
		13/2	13/2	E		
		17/2	17/2	E	23 842.59	
		11/2	11/2	E		
		15/2	15/2	A	23 846.17	22 912.1
		13/2	13/2	A		
		17/2	17/2	A	23 847.47	
		11/2	11/2	A		
8_{26}	8_{35}	13/2	13/2	E	22 491.47	
		19/2	19/2	E		
		15/2	15/2	E	22 492.59	
		17/2	17/2	E		
		13/2	13/2	A	22 493.90	
		19/2	19/2	A		
		15/2	15/2	A	22 495.00	
		17/2	17/2	A		
9_{27}	9_{36}	19/2	19/2	E		
		17/2	17/2	E	25 466.03	24 822.00
		21/2	21/2	E		
		15/2	15/2	E		
		19/2	19/2	A		
		17/2	17/2	A	25 470.35	24 825.58
		21/2	21/2	A		
		15/2	15/2	A		
10_{28}	10_{37}	21/2	21/2	E		
		19/2	19/2	E		29 932.42
		23/2	23/2	E		
		17/2	17/2	E		
		21/2	21/2	A		
		19/2	19/2	A		29 938.48
		23/2	23/2	A		
		17/2	17/2	A		
					$CH_3C^{13}OCl^{35}$	$CH_3C^{13}OCl^{37}$
3_{13}	4_{04}	7/2	9/2	E		
		5/2	7/2	E	28 196.8	
		7/2	9/2	A		
		5/2	7/2	A		
		9/2	11/2	E		
		3/2	5/2	E	28 199.6	
		9/2	11/2	A		
		3/2	5/2	A		
5_{23}	5_{32}	7/2	7/2	A and E	25 223.87	
		13/2	13/2	A and E	25 227.20	
		9/2	9/2	A and E	25 230.51	
		11/2	11/2	A and E	25 232.97	
7_{16}	7_{25}	15/2	15/2	E	23 989.95	
		13/2	13/2	E		
		17/2	17/2	E	23 991.05	
		11/2	11/2	E		
		15/2	15/2	A	23 995.15	
		13/2	13/2	A		
		17/2	17/2	A	23 996.28	
		11/2	11/2	A		
8_{26}	8_{35}	13/2	13/2	E	23 066.35	
		19/2	19/2	E		
		15/2	15/2	E	23 067.67	
		17/2	17/2	E		
		13/2	13/2	A	23 068.63	
		19/2	19/2	A		
		15/2	15/2	A	23 069.90	
		17/2	17/2	A		

TABLE I.—Continued

J	J'	F_i	F_f	Torsional level	$CH_3C^{13}OCl^{35}$	$CH_3C^{13}OCl^{37}$
9_{27}	9_{36}	19/2	19/2	E		
		17/2	17/2	E	25 791.85	
		21/2	21/2	E		
		15/2	15/2	E		
		19/2	19/2	A		
		17/2	17/2	A	25 796.17	
		21/2	21/2	A		
		15/2	15/2	A		
10_{28}	10_{37}	21/2	21/2	E	30 696.01	29 390.91
		19/2	19/2	E		
		23/2	23/2	E	30 697.15	
		17/2	17/2	E		
		21/2	21/2	A	30 702.86	29 396.97
		19/2	19/2	A		
		23/2	23/2	A	30 703.99	
		17/2	17/2	A		
					$CH_3CO^{13}Cl^{35}$	
9_{27}	9_{36}	19/2	19/2	E		
		17/2	17/2	E	25 411.05	
		21/2	21/2	E		
		15/2	15/2	E		
		19/2	19/2	A		
		17/2	17/2	A	25 414.85	
		21/2	21/2	A		
		15/2	15/2	A		
10_{28}	10_{37}	21/2	21/2	E		
		19/2	19/2	E	30 988.90	
		23/2	23/2	E		
		17/2	17/2	E		
		21/2	21/2	A		
		19/2	19/2	A	30 995.70	
		23/2	23/2	A		
		17/2	17/2	A		
11_{38}	11_{47}	19/2	19/2	E		
		25/2	25/2	E	28 338.33	
		21/2	21/2	E		
		23/2	23/2	E		
		19/2	19/2	A		
		25/2	25/2	A	28 341.10	
		21/2	21/2	A		
		23.2	23.2	A		
12_{39}	12_{48}	21/2	21/2	E		
		27/2	27/2	E	31 811.40	
		23/2	23/2	E		
		25/2	25/2	E		
		21/2	21/2	A		
		27/2	27/2	A	31 817.55	
		23/2	23/2	A		
		25/2	25/2	A		
					CD_3COCl^{35}	CD_3COCl^{37}
1_{01}	2_{12}	1/2	1/2	A and E	18 048.30	
		5/2	5/2	A and E	18 049.90	
		5/2	7/2	A and E	18 055.36	
		3/2	5/2	A and E	18 062.50	
2_{02}	3_{13}	1/2	3/2	A and E	23 662.10	
		3/2	5/2	A and E	23 666.35	
		7/2	9/2	A and E	23 667.22	23 382.73
		5/2	7/2	A and E	23 671.50	23 386.40
		3/2	3/2	A and E	23 674.50	23 388.60
3_{03}	4_{14}	3/2	5/2	A and E	29 066.43	
		5/2	7/2	A and E	29 068.51	28 667.02
		9/2	11/2	A and E		
		7/2	9/2	A and E	29 070.50	28 668.73
		7/2	7/2	A and E	29 074.00	

TABLE I.—Continued

J	J'	F_i	F_f	Torsional level	CD_3COCl^{35}	CD_3COCl^{37}
3_{13}	4_{04}	5/2	7/2	A and E	26 125.90	25 441.10
		7/2	9/2	A and E		
		3/2	5/2	A and E	26 128.35	25 443.15
		9/2	11/2	A and E		
4_{14}	4_{23}	5/2	5/2	A and E	22 441.05	
		11/2	11/2	A and E		
		7/2	7/2	A and E	22 444.25	
		9/2	9/2	A and E		
5_{23}	5_{32}	7/2	7/2	A and E	20 171.82	
		13/2	13/2	A and E	20 173.96	
		9/2	9/2	A and E	20 179.30	
		11/2	11/2	A and E	20 181.40	
5_{24}	5_{33}	7/2	7/2	A and E	27 010.3	
		13/2	13/2	A and E	27 011.9	
		9/2	9/2	A and E	27 016.2	
		11/2	11/2	A and E	27 017.7	
6_{24}	6_{33}	9/2	9/2	A and E	18 724.40	
		15/2	15/2	A and E		
		11/2	11/2	A and E	18 725.55	
		13/2	13/2	A and E		
7_{16}	7_{25}	11/2	11/2	A and E	22 027.80	21 123.0
		17/2	17/2	A and E		
		13/2	13/2	A and E	22 028.93	
		15/2	15/2	A and E		
7_{25}	7_{34}	11/2	11/2	A and E	18 427.00	18 730.03
		17/2	17/2	A and E		
		13/2	13/2	A and E	18 429.23	18 732.27
		15/2	15/2	A and E		
8_{26}	8_{35}	13/2	13/2	A and E	19 836.38	19 667.25
		19/2	19/2	A and E		
		15/2	15/2	A and E	19 837.06	
		17/2	17/2	A and E		
9_{27}	9_{36}	19/2	19/2	A and E		
		17/2	17/2	A and E	23 242.90	22 470.92
		21/2	21/2	A and E		
		15/2	15/2	A and E		
9_{28}	9_{45}	15/2	15/2	A and E	24 862.10	25 827.40
		21/2	21/2	A and E		
		17/2	17/2	A and E	24 865.15	25 829.70
		19/2	19/2	A and E		
10_{37}	10_{46}	17/2	17/2	A and E	24 235.00	24 725.0
		23/2	23/2	A and E		
		19/2	19/2	A and E	24 236.35	
		21/2	21/2	A and E		
11_{38}	11_{47}	19/2	19/2	A and E	25 585.28	25 356.28
		25/2	25/2	A and E		
		21/2	21/2	A and E		25 357.04
		23/2	23/2	A and E		

culated from the values of $(A-C)/2$ and κ and the average value of $I_a+I_b-I_c$ determined in the other nondeuterated species. The rotational constants for $CH_3CO^{18}Cl^{35}$ were then calculated from the moments of inertia.

An isotopic substitution has been made in every position in the molecule. The structure can, therefore, in principle be completely determined with only two assumptions. These are that the molecule has a plane of symmetry and that the CH_3 group is symmetrical about the C—C axis. The coordinates of the two carbon atoms and the oxygen and chlorine atoms were first obtained directly by the method of Kraitchman[6] using the observed changes in the moments of inertia of normal CH_3COCl^{35} on substitution of these atoms. The out-of-plane hydrogen coordinate was obtained using the difference between the average value of $I_a+I_b-I_c$ for the nondeuterated and fully deuterated species, respectively, as suggested by Laurie.[7] The remaining hydrogen coordinates were obtained from the differences between the moments of inertia of CH_3COCl^{35} and CD_3COCl^{35}.

[6] J. Kraitchman, Am. J. Phys. **21**, 17 (1953).
[7] V. W. Laurie, J. Chem. Phys. **28**, 704 (1958).

TABLE II. Rotational constants (Mc).

	A	B	C
CH_3COCl^{35}	10 162.39	4946.66	3393.07
CH_3COCl^{37}	10 160.60	4808.74	3327.40
$C^{13}H_3COCl^{35}$	9894.47	4868.35	3326.21
$C^{13}H_3COCl^{37}$	9889.14	4731.58	3261.38
$CH_3C^{13}OCl^{35}$	10 159.49	4932.06	3385.97
$CH_3CO^{18}Cl^{35}$	9623.48[a]	4841.02[a]	3282.56[a]
CD_3COCl^{35}	8758.77	4532.73	3098.77
CD_3COCl^{37}	8753.45	4408.08	3039.17

[a] Assuming $I_a+I_b-I_c=2.9524$ amu A^2.

This determination of the structure showed that both the chlorine atom and the carbonyl carbon atom lie very close to the "a" axis. As a result, the Kraitchman method does not yield accurate values of the "b" coordinates. Therefore, the structure was calculated in two other ways; (a) without using the CH_3COCl^{37} moments and (b) without using the $CH_3C^{13}OCl$ moments, using the first moment equations in each case to obtain the coordinates of the chlorine and carbon atoms, respectively. The average values of the structural parameters obtained in these three ways are given in Table IV. The limits of error given are based on the differences in the coordinates obtained by the three methods described and on the estimated experimental errors. The structure of acetyl chloride is illustrated in Fig. 1, which also shows the position of the principal axes.

A comparison and discussion of the structures of acetaldehyde, acetyl chloride, acetyl fluoride, and acetyl cyanide has been given elsewhere.[3]

BARRIER TO INTERNAL ROTATION

The value of the barrier hindering internal rotation of the methyl group was determined using the treatment of Kilb, Lin, and Wilson[1] and Herschbach.[8] This assumes a model of a rigid asymmetric framework (—COCl) attached to a symmetric rotor (—CH_3). The potential barrier is taken to be of the form,

$$V=(V_3/2)(1-\cos 3\alpha)+(V_6/2)(1-\cos 6\alpha)+\cdots, \quad (1)$$

where α is the angle describing the relative orientation of the rotor and the framework. This potential converges rapidly[9,10] and only the first term was considered in the present work.

In the case of an infinite barrier, each torsional state v is triply degenerate. With lower barriers, tunneling of the methyl group splits this degeneracy giving a nondegenerate "A" level and a doubly-degenerate "E" level. The transitions between the "A" levels resemble those of a pseudo-rigid rotor. The E transitions have different effective rotational constants and also contain odd-order perturbation terms. In the present work the odd-order terms were negligible and both the A and E series of transitions followed a rigid rotor pattern. The barrier to internal rotation can be determined from the difference in the rotational constants for the A and E types of transitions. However this procedure is not convenient if the differences in the rotational constants are small as in acetyl chloride. In this case it is preferable to determine the barrier di-

TABLE III. Moments of inertia[a] (amu A^2).

	I_a	I_b	I_c	$I_a+I_b-I_c$
CH_3COCl^{35}	49.7453	102.1965	148.9893	2.9525
CH_3COCl^{37}	49.7540	105.1275	151.9297	2.9518
$C^{13}H_3COCl^{35}$	51.0923	103.8403	151.9841	2.9485
$C^{13}H_3COCl^{37}$	51.1198	106.8419	155.0052	2.9565
$CH_3C^{13}OCl^{35}$	49.7595	102.4989	149.3060	2.9524
$CH_3CO^{18}Cl^{35}$	52.5310	104.4265	154.0051	2.9524[b]
CD_3COCl^{35}	57.7171	111.5290	163.1392	6.1069
CD_3COCl^{37}	57.7522	114.6828	166.3391	6.0959

[a] Conversion factor$=5.05531\times10^5$ Mc/amu A^2.
[b] Assumed (no R-branch transitions observed).

TABLE IV. Molecular structure of acetyl chloride.

C—H	1.083±0.005 A	∠CCH	110°21′±10′
C—C	1.499±0.010	∠CCO	127°5′ ±10′
C=O	1.192±0.010	∠CCCl	112°39′±30′
C—Cl	1.789±0.005		

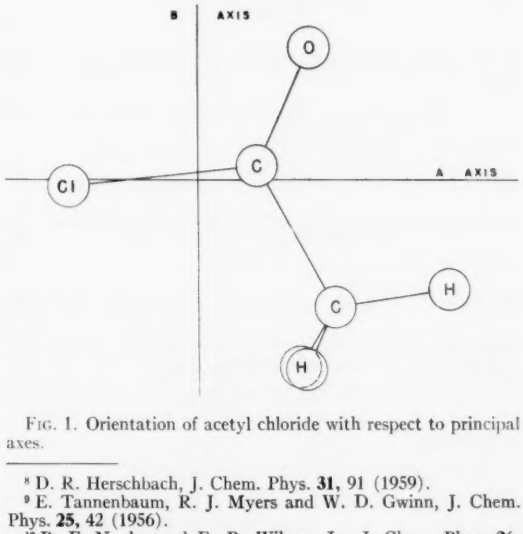

FIG. 1. Orientation of acetyl chloride with respect to principal axes.

[8] D. R. Herschbach, J. Chem. Phys. **31**, 91 (1959).
[9] E. Tannenbaum, R. J. Myers and W. D. Gwinn, J. Chem. Phys. **25**, 42 (1956).
[10] R. E. Naylor and E. B. Wilson, Jr., J. Chem. Phys. **26**, 1057 (1957).

TABLE V. Observed internal rotation splittings (Mc) and corresponding barrier (cal/mole).

Transition		CH_3COCl^{35}		CH_3COCl^{37}		$C^{13}H_3COCl^{35}$		$C^{13}H_3COCl^{37}$		$CH_3C^{13}OCl^{35}$		$CH_3C^{13}OCl^{37}$		$CH^3CO^{18}Cl^{35}$	
J	J'	$\Delta\nu$	V_3	$\Delta\nu$	V_3	$\Delta\nu$	V_3	$\Delta\nu$	V_3	$\Delta\nu$	V_3	$\Delta\nu$	V_3	$\Delta\nu$	V_3
3_{13}	4_{04}	0.68	1338	0.73	1304										
5_{05}	5_{14}	4.80	1277												
6_{15}	6_{24}	3.24	1282	2.59	1306	3.08	1288								
7_{16}	7_{25}	5.10	1285	4.28	1300	4.90	1283	4.10	1308	5.22	1277				
7_{25}	7_{34}	0.80	1302	0.71	1296										
8_{17}	8_{26}			6.67	1274										
8_{26}	8_{35}	2.30	1286			2.42	1287			2.26	1281				
9_{27}	9_{36}	4.45	1286	3.74	1288	4.32	1291	3.58	1306	4.32	1287			3.80	1340
10_{28}	10_{37}	6.82	1294	6.10	1281			6.06	1288	6.85	1287	6.06	1296	3.20	1309
11_{38}	11_{47}	2.43	1303	1.77	1311									2.77	1313
12_{39}	12_{48}													6.15	1296

rectly from the splitting of each transition using Eqs. (13) to (16) of Swalen and Herschbach.[11]

In this method, the energy level differences are expanded as

$$\Delta W = W_A - W_E = (\partial W/\partial A)\Delta A + (\partial W/\partial B)\Delta B + (\partial W/\partial C)\Delta C \quad (2)$$

$$\Delta A = A_A - A_E = (h\lambda_\alpha I_\alpha/8\pi^2 r I_\alpha^2)\Delta(1+4F\rho_v) \quad (3)$$

and similarly for ΔB and ΔC, where I_α is the moment of inertia of the methyl group about its symmetry axis, λ_g are the direction cosines of the top axis with respect to the principal axes, I_g are the principal moments of inertia of the entire molecule, and

$$r = 1 - \sum_g \lambda_g^2 I_\alpha / I_g.$$

If the rigid-rotor energy levels are written in the usual form

$$W = \tfrac{1}{2}(A+C)J(J+1) + \tfrac{1}{2}(A-C)E(\kappa), \quad (4)$$

then

$$\partial W/\partial A = \tfrac{1}{2}\{J(J+1) + E(\kappa) + (\kappa+1)[\partial E(\kappa)/\partial\kappa]\} \quad (5)$$

$$\partial W/\partial B = \frac{\partial E(\kappa)}{\partial \kappa} \quad (6)$$

$$\partial W/\partial C = \tfrac{1}{2}\{J(J+1) - E(\kappa) + (\kappa-1)[\partial E(\kappa)/\partial\kappa]\}. \quad (7)$$

With these expressions, ΔA, ΔB, and ΔC can be calculated from the observed splittings. The barrier $V_3 = 9Fs/4$ is then determined from the structure and the value of s corresponding to the observed value of $\Delta(1+4F\rho_v)$.

In the present case ΔC is zero since the axis of rotation of the methyl group is perpendicular to the "c" axis. The ratio $\Delta B/\Delta A$ can be determined from the structure of the molecule and the moments of inertia. Equation (2) can, therefore, be written

$$\Delta W = \Delta A\{(\partial W/\partial A) + d(\partial W/\partial B)\}, \quad (8)$$

where $d = \Delta B/\Delta A$. ΔA and, hence, V_3 can thus be calculated from each splitting.

The barrier corresponding to each resolvable splitting was calculated in this way. The results are given in Table V. Table VI gives the average values for the different species together with the structural factors used. The agreement among the values obtained for a given species and between the average values is very satisfactory. In view of possible uncertainties in the structure which would affect these values, it is felt that the average barrier for all species should be expressed as 1296±30 cal/mole. This value is remarkably close (−9 cal) to that found in acetyl bromide[5] and only 86, 146, and 216 cal/mole greater than the values for the barrier in acetyl cyanide,[3] acetaldehyde,[1] and acetyl fluoride,[2] respectively. This small variation in the barrier with large changes in the size and electronegativity of the group Z in this series (CH_3COZ) suggests that the barrier cannot be primarily due to steric repulsion or electrostatic interaction.

EQUILIBRIUM CONFORMATION

The moments of inertia of the nondeuterated and fully deuterated species are independent of the relative orientation of the methyl group and the rigid COCl framework. However, in a species having an asymmetric methyl group, for example, CH_2D, the over-all moments of inertia will depend upon the orientation of this group with respect to the framework. The spectrum of CH_2DCOCl was, therefore, studied in order to determine the equilibrium conformation of acetyl chloride.

[11] J. D. Swalen and D. R. Herschbach, J. Chem. Phys. **27**, 100 (1957).

TABLE VI. Internal barrier and structural constants.

	CH_3COCl^{35}	CH_3COCl^{37}	$C^{13}H_3COCl^{35}$	$C^{12}H_3COCl^{37}$	$CH_3C^{13}OCl^{35}$	$CH_3C^{13}OCl^{37}$	$CH_3CO^{18}Cl^{35}$
F	1.6867×10^5 Mc	1.6854	1.6874	1.6853	1.6866	1.6853	1.6825
λ_a	0.48659	0.48379	0.51104	0.50729	0.48532	0.48252	0.44437
λ_b	0.87363	0.87518	0.85955	0.86148	0.87433	0.87589	0.89584
I_α	3.1158 amu A² used for all species						
V_3	1295	1295	1287	1301	1283	1296	1315

The moments of inertia of this isotopic species were calculated for two different possible equilibrium conformations: Case I, in which a methyl hydrogen eclipses the oxygen atom, and case II, in which a methyl hydrogen eclipses the chlorine atom. For each case two isomers exist. In one the deterium atom is in the plane of the framework and in the other it is out of the plane. These two isomers are designated as sym- and asym-CH_2DCOCl.

Table VII gives the observed spectra of the CH_2DCOCl^{35}. No lines of CH_2DCOCl^{37} were assigned. In most cases the chlorine nuclear quadrupole hyperfine splitting could not be resolved due to insufficient concentration of the isotopic species. In these cases, the frequency of the strongest central component is given. Where more than one line was resolved, the hyperfine splitting was corrected for using coupling constants estimated from those given in the next section. Although in either case, the two equivalent asymmetric forms possible could have given rise to doublets in the rotational spectrum of asym-CH_2DCOCl, none were observed.

TABLE VII. Observed transitions[a] of CH_2DCOCl^{35} (Mc).

J	J'	sym-CH_2DCOCl^{35}	asym-CH_2DCOCl^{35}
2_{02}	3_{12}	25 623.0	
2_{12}	3_{03}	18 758.5	
3_{03}	4_{14}		31 065.70
3_{13}	4_{04}	26 822.75	27 897.37
5_{05}	5_{15}	21 697.58	22 784.10
5_{23}	5_{32}	25 657.85	21 844.75
6_{15}	6_{24}	18 275.45	18 577.95
6_{24}	6_{33}	23 737.50	
7_{16}	7_{25}	22 573.58	24 015.28
7_{25}	7_{34}	22 546.25	19 988.0
8_{17}	8_{26}	28 514.05	
8_{26}	8_{35}	22 727.54	21 565.5
9_{27}	9_{36}	24 722.25	25 324.9
9_{36}	9_{45}		26 911.43
10_{28}	10_{37}	28 739.25	
10_{37}	10_{46}		26 281.5

[a] Frequencies listed are those obtained after correction for the chlorine hyperfine structure.

The moments of inertia obtained from these transitions are given in Table VIII. The values calculated from the structure for the symmetric and asymmetrical isomers of cases I and II in the foregoing are also given. Comparison of the experimental and calculated values shows conclusively that case I, methyl hydrogen eclipses oxygen atom, is correct. This equilibrium conformation is the same as that found in acetaldehyde, acetyl fluoride and acetyl cyanide.

CHLORINE NUCLEAR QUADRUPOLE COUPLING CONSTANTS

The analysis of the chlorine nuclear quadrupole hyperfine structure was carried out in terms of the coupling constants, χ_{aa}, χ_{bb}, and χ_{cc}. These are defined as $\chi_{aa}=eQ(\partial^2V/\partial a^2)$ etc., where Q is the chlorine nuclear quadrupole moment and $\partial^2V/\partial a^2$ is the field gradient along the "a" principal axis. Only two of the coupling constants are independent, but it is convenient for discussion to retain the three constants.

For the purposes of computation the expression for the first-order interaction energy[12] was written in the form

$$E_Q(J,F)=\left\{(\chi_{aa}+\chi_{cc})\left[J(J+1)-3\left(\frac{\partial E(\kappa)}{\partial\kappa}\right)\right]+(\chi_{aa}-\chi_{cc})\left[E(\kappa)-\kappa\left(\frac{\partial E(\kappa)}{\partial\kappa}\right)\right]\right\}\frac{Y(F)}{J(J+1)}. \quad (9)$$

TABLE VIII. Comparison of observed and calculated moments of inertia[a] of CH_2DCOCl^{35} (amu A²).

	Observed	Calculated Case I	Calculated Case II
I_a-sym	50.6867	50.6805	53.7490
I_b-sym	107.7482	107.7153	102.6333
I_c-sym	155.4390	155.2800	153.2664
I_a-asym	53.5241	53.4938	51.9689
I_b-asym	103.8676	103.9828	106.7161
I_c-asym	153.0461	152.9047	154.2726

[a] Conversion factor: 5.05531×10^5 Mc/amu A².

[12] J. K. Bragg and S. Golden, Phys. Rev. **75**, 735 (1949).

TABLE IX. Chlorine nuclear quadrupole coupling constants (Mc).[a]

	CH_3COCl^{35}	CD_3COCl^{35}	CH_3COCl^{37}	CD_3COCl^{37}
χ_{aa}	−58.0	−53.2	−45.5	−42.9
χ_{bb}	36.4	31.7	28.5	25.4
χ_{cc}	21.6	21.5	17.0	17.5
χ_{xx}	−59.2	−57.7	−46.4	−46.3
χ_{yy}	37.6	36.2	29.4	28.8
χ_{zz}	21.6	21.5	17.0	17.3
θ	6°28′	12°36′	6°17′	12°13′

[a] χ_{aa} etc. are the observed values along the principal axes a, b, and c. χ_{xx} etc. are the values obtained after transformation to the system x, y, z, where the x axis coincides with the C—Cl bond and the z axis is perpendicular to —COCl plane. θ is the angle between the "a" and "x" axes.

The values of χ_{aa} and χ_{cc} were then obtained by a least-squares treatment of the resolved hyperfine structure of the low J transitions. The hyperfine splittings of transitions involving J values greater than 5 were not used in this calculation as they are not very sensitive to χ_{aa} and χ_{cc}. For this reason also the coupling constants for the C^{13} and O^{18} species could not be determined.

In order to relate the coupling constants to properties of the carbon-chlorine bond, it is necessary to obtain the values of the constants along the bond axis. These values were obtained by transformation from the principal axes a, b, and c to the system x, y, and z, where the x axis coincides with the C—Cl bond and the z axis is perpendicular to the plane of the framework, using the equations

$$\chi_{xx}\cos^2\theta+\chi_{yy}\sin^2\theta=\chi_{aa}$$

$$\chi_{xx}\sin^2\theta+\chi_{yy}\cos^2\theta=\chi_{bb}, \qquad (10)$$

where θ is the angle between the a and x axis; χ_{cc} is invariant to this transformation. The observed values of χ_{aa} etc. and the values calculated for χ_{xx} etc. are given in Table IX. The error in χ_{aa}, χ_{bb} and χ_{cc} is estimated to be ±1 Mc.

The ratio between the average χ_{xx} for CH_3COCl^{35} and CD_3COCl^{35}, and the average χ_{xx} for CH_3COCl^{37} and CD_3COCl^{37} is 1.26. The corresponding χ_{yy} ratio is 1.27. The ratio of the published values[13] of the quadrupole moments of Cl^{35} and Cl^{37} is 1.2688.

The transformation discussed in the foregoing assumes that the principal axis of the quadrupole tensor coincides with the bond axes. Since the coupling constants have been determined for both the CH_3COCl and CD_3COCl species, it is possible to check this assumption.

It can be shown that

$$\tan 2\phi = (\sin 2\Delta)^{-1}\{K'[(\chi_{aa}-\chi_{bb})/(\chi'_{aa}-\chi'_{bb})]-\cos 2\Delta\}, \qquad (11)$$

where ϕ is the angle between the principal axis of the nuclear quadrupole tensor and the "a" axis in the deuterated species, Δ is the rotation of the inertial axes in going from the nondeuterated to the deuterated species, χ_{aa} and χ_{bb} are the coupling constants along the "a" and "b" axes and are unprimed for the nondeuterated and primed for the deuterated species and K' is the ratio which converts the nuclear moment of the chlorine species in the unprimed form to that occurring in the primed form. The angle ϕ obtained using this expression can be compared with the angle between the bond direction and the "a" axis for the appropriate species. If the quadrupole tensor axis coincides with the C—Cl bond axis then these two angles will be the same.

The average value of ϕ obtained for CD_3COCl^{35} using the data for this molecule and CH_3COCl^{35} and CH_3COCl^{37} is 15°48′. In the case of CD_3COCl^{37} the average value is 13°54′. The corresponding angles between the C—Cl bond and the "a" axis are 12°36′ and 12°13′. The estimated errors (±1 Mc) in the coupling constants introduce an error of between +4° and −5° in the calculated value of ϕ. Thus it can only be concluded that, in the present case, the principal axis of the quadrupole tensor is within about 5° of the bond axis.

The effect of this uncertainty in the direction of the quadrupole tensor axis on the calculated values of the coupling constants along the bond axis has been determined. In the case of the nondeuterated species an uncertainty of ±5° results in an error of −3 and +1 Mc, respectively, in χ_{xx}. In the deuterated species the corresponding error is ±3.5 Mc.

It is clear from the difference between the values of χ_{yy} and χ_{zz} that there is not axial symmetry about the C—Cl bond as would be expected for an unperturbed σ bond. The departure of the field gradient from axial symmetry is in the direction expected for electron loss from the $3p_z$ chlorine orbital. Such a loss can be represented by the contribution to the ground state by the resonance structure I shown in the following. If the electron loss from the $3p_z$ orbital contributes χ_{zz}^z to χ_{zz}, then it makes a contribution of $-\frac{1}{2}\chi_{zz}^z$ to each of χ_{xx} and χ_{yy}. Thus, $\chi_{zz}^z=\frac{2}{3}(\chi_{zz}-\chi_{yy})$ may be evaluated as 10.2±3 Mc using the average values of χ_{zz} and χ_{yy} for CH_3COCl^{35} and CD_3COCl^{35} and taking into account the possible errors in χ_{zz} and χ_{yy}. Since complete removal of an electron from a $3p_z$ atomic orbital for the chlorine atom leads to a coupling constant of −109.74 Mc,[14] the value of χ_{zz}^z can be interpreted as indicating 9.3±3% electron deficit for the chlorine $3p_z$ orbital. This corresponds to 9.3±3% double-bond character in the C—Cl bond.

The low negative value of χ_{xx} indicates that on a time average the chlorine $3p_z$ orbital contains more than one electron, or the presence of considerable s character in the chlorine atomic orbital used in bond formation.

[13] C. H. Townes and A. L. Schawlow, *Microwave Spectroscopy* (McGraw-Hill Book Company, Inc., New York, 1955).

[14] C. H. Townes and B. P. Dailey, J. Chem. Phys. **23**, 118 (1955).

The electron gain can be represented by the contribution of the resonance structure II.

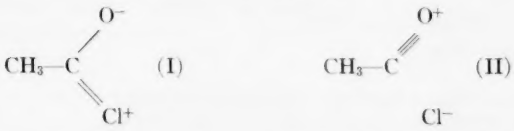

In order to estimate the amount of this ionic or s character, it is necessary to correct χ_{xx} for the contribution arising from the electron deficit in the $3p_z$ orbital. This electron deficit results in a contribution χ_{zz}^z along the z axis and $-\frac{1}{2}\chi_{zz}^z$ along the x and y axes. Therefore, $\chi_{xx}(\text{corr.})=\chi_{xx}(\text{obs})+\frac{1}{2}\chi_{zz}^z$. From χ_{zz}^z obtained in the foregoing and the average value of χ_{xx} for CH_3COCl^{35} and $CD\,COCl^{35}$, $\chi_{xx}(\text{corr.})=-63.6\pm4.5$ Mc, taking into account possible errors in χ_{zz}^z and χ_{xx}. If the chlorine orbital is taken to be a pure p orbital, this value of 63.6 ± 4.5 Mc corresponds to $42\pm4\%$ ionic character. It is probable that the bond contains a certain amount of s character but the amount cannot be determined.

The value of χ_{xx} in acetyl chloride may be compared with -74.77 Mc in methyl chloride,[15] -70.07 Mc in ethyl chloride,[16] and -70.16 Mc in vinyl chloride.[17] In the case of vinyl chloride, the observed coupling constants indicated about 6% double-bond character in the C—Cl bond. The present work, therefore, shows that there is a greater conjugation between the carbon-chlorine bond and the carbon-oxygen double bond in acetyl chloride than between the carbon-chlorine bond and the carbon-carbon double bond in vinyl chloride. In addition, the amount of ionic character is also greater in acetyl chloride than in methyl chloride, ethyl chloride or vinyl chloride.

The C—Cl bond length in acetyl chloride is 1.789 A which is 0.008 A greater than the value in methyl chloride.[18] One would expect the contribution of resonance structure I to shorten the C—Cl bond. Apparently the contribution of structure II must cancel out any shortening due to conjugation.

ACKNOWLEDGMENTS

The author wishes to express his appreciation to Professor E. Bright Wilson, Jr., for his help and many discussions during the course of this work. Discussions with the members of Professor Wilson's group were also greatly appreciated, particularly those with Dr. R. W. Kilb and Dr. J. D. Swalen.

[15] J. Kraitchman and B. P. Dailey, J. Chem. Phys. **22**, 1477 (1954).
[16] R. S. Wagner and B. P. Dailey, J. Chem. Phys. **26**, 1592 (1957).
[17] D. Kivelson, E. B. Wilson, Jr., and D. R. Lide, Jr., J. Chem. Phys. **32**, 205 (1960).
[18] S. L. Miller, L. C. Aamodt, G. Dousmanis, C. H. Townes, and J. Kraitchman, J. Chem. Phys. **20**, 1112 (1952).

Electrochromism, a Possible Change of Color Producible in Dyes by an Electric Field*

JOHN R. PLATT

Physics Department, University of Chicago, Chicago, Illinois

(Received March 4, 1960)

Theoretical considerations suggest that the absorption and emission spectra of certain dyes may be shifted by hundreds of angstroms upon application of a strong electric field. The effect could be called "electrochromism," in analogy to "thermochromism" and "photochromism." The theory of the effect is outlined and is discussed in terms of compounds which might be expected to show it most strongly.

THEORETICAL considerations suggest that the absorption and emission spectra of certain dyes may be shifted by hundreds of angstroms upon application of a strong electric field.

This effect could be called "electrochromism," in analogy to "thermochromism" and "photochromism" which describe changes of color produced by heat and by light. The present paper is intended to outline the theory of this effect, to show how large it might be expected to be and what kinds of compounds might exhibit it most strongly, and to suggest that an experimental search for it might be desirable.

Electrochromic effects are expected in conjugated organic dyes of the dipolar linear-chain type, like the merocyanines studied by Brooker and co-workers.[1] The spectra and excited states of these compounds can often be shifted thousands of angstroms by solvent and polarization effects. The qualitative theory of these shifts has been given by Brooker and Simpson[2] and the quantitative prediction of the peak wavelengths and shape of the absorption curves has been given by Platt.[3]

The merocyanine dyes are of the general type

$$O{=}CH{-}CH{=}CH{-}\cdots{-}CH{=}CH{-}NH_2. \quad (I)$$

Their formulas can also be written with a second, dipolar-ionic, structure,

$$^{-}O{-}CH{=}CH{-}CH{=}\cdots{=}CH{-}CH{=}NH_2^{+}. \quad (II)$$

Their spectral shifts depend on the fact that a conjugated chain of N atoms has a maximum wavelength of its first absorption peak when it can be written with two extreme resonance structures that are equivalent.[1] This "isoenergetic wavelength," λ_I, is near $\lambda_I = N(500\ \text{A})$, or at about 7500 A for a 15-atom chain. The exact wavelength also depends somewhat on the terminal groups, commonly aromatic ring systems, of which the N and O atoms are a part; but this need not concern us here. When the extreme resonance structures are nonequivalent, the peak is shifted to shorter wavelengths and higher energies, reaching its shortest position (commonly at 5000 A or less) for molecules such as polyenes, $H_2C{=}CH{-}CH{=}CH{-}\cdots{-}CH{=}CH_2$, where a single resonance structure dominates the ground state. H. Kuhn[4] showed that this increase of energy is due physically to the alternation of single and double bond lengths, which produces a Brillouin gap when one resonance structure is dominant.

In a given solvent, the formula for the spectral energy E of the first absorption peak is

$$E^2 = E_I^2 + (b_L - b_R)^2, \quad (1)$$

where E_I is the spectral energy of the isoenergetic wavelength of a given chain length, and b_L and b_R are the basicities of the terminal groups on the left and right ends of the chain, expressed in energy units. The difference $(b_L - b_R)$ measures quantitatively the stabilization of one of the two extreme resonance structures relative to the other.

The merocyanine dyes are unusual in that one of the structures, the nonpolar one, may be the most stable one in a nonpolar solvent such as benzene or hexane; while the other structure, the polar one, may be the most stable one in a polar solvent such as water, which reduces the Coulomb energy of charge-separation. In a series of mixed solvents of increasing polarity, the $(b_L - b_R)$ value of some of these dyes can therefore be changed essentially continuously from a negative value in a nonpolar solvent through a zero value to a positive value in a polar solvent. As Eq. (1) shows, the peak wavelength of absorption (or emission) is then shifted from a short wavelength (high energy) in nonpolar solvents to progressively longer wavelengths until it reaches the isoenergetic wavelength and energy E_I where $(b_L - b_R)$ is zero, and then it is shifted back toward short wavelengths again in the polar solvents. In those molecules that are fluorescent, the emission peak should be at slightly longer wavelengths than the absorption peak and should shift correspondingly.

The greatest wavelength shifts are obtained when $(b_L - b_R)$ is nearly zero in one of the extreme solvents,

* Based in part on work done at Bell Telephone Laboratories, Murray Hill, New Jersey, Summer of 1958.

[1] L. G. S. Brooker, G. H. Keyes, R. H. Sprague, R. H. Van Dyke, E. Van Lare, G. Van Zandt, F. L. White, H. W. J. Cressman, and S. G. Dent, Jr., J. Am. Chem. Soc. **73**, 5332 (1951); L. G. S. Brooker, G. H. Keyes, and D. W. Heseltine, *ibid.* 5350 (1951).

[2] L. G. S. Brooker and W. T. Simpson, Ann. Rev. Phys. Chem. **2**, 121 (1951).

[3] J. R. Platt, J. Chem. Phys. **25**, 80 (1956).

[4] H. Kuhn, Chimia (Switz) **2**, 1 (1948); J. Chem. Phys. **17**, 1198 (1949).

say a nonpolar one, and when this quantity grows steadily to very large positive or negative values in the other extreme solvent, the polar one. Cases of this type are the dyes

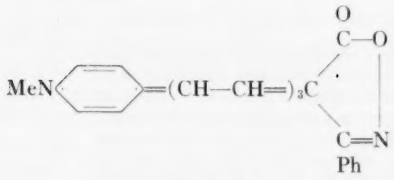

(III)

[designated (22)–(24), $n=3$, in the works cited in footnotes 1 and 3], and

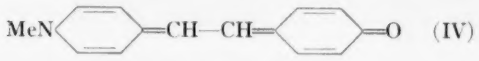

(IV)

[designated (22-HS) in the work cited in footnote 3 and (II) in the work cited in footnote 1b].

The peak absorption wavelength of Dye III shifts from 7100 A in pyridine to 4875 A in water. [The (b_L-b_R) values are 4000 cm^{-1} and 16 000 cm^{-1}, respectively, and E_I is 13 500 cm^{-1}, with λ_I at 7200 A]. The peak of Dye IV shifts from 6000 A in pyridine to 4450 A in water. [The (b_L-b_R) values are 3800 cm^{-1} and 16 000 cm^{-1}, respectively, and E_I is 16 000 cm^{-1}, with λ_I at 6250 A.] In both cases, the (b_L-b_R) values change by about 12 000 cm^{-1}, that is, by about 1.5 ev, between the two solvents. Dyes such as Indophenol Blue (V)

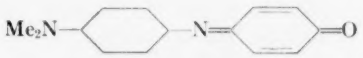

(V)

also show large shifts.[5]

The electrochromic effect anticipated here is the possible production of similar spectral shifts by changing the relative energy of the two resonance structures of such a dye by use of an electric field instead of a polar solvent. The obvious generalization of Eq. (1) for an applied electric field is

$$E^2=E_I^2+(b_L-b_R+V_{LR})^2, \qquad (2)$$

where V_{LR} is the potential difference between the left and right ends of the chain, representing an added energy difference between the two resonance structures.

In a fluid medium, even small electric fields will tend to orient the chains, as in the Kerr effect, producing double refraction; but there is then no change of color except in polarized light. The size of this effect is, of course, dependent on temperature as well as on dipole moment and field strength. The electrochromic effect described here would be an additional change of color produced in the most oriented chains. In rigid media, molecules oriented with their dipoles along the field will have their dipolar structures stabilized; those oriented with their dipoles against the field will be destabilized; the spectral shifts should be opposite in these two cases. In fluid media, most of the molecules will of course tend to be oriented with the field rather than against it.

Presumably the electrochromic spectral shifts for Dyes such as III and IV in a nonpolar solvent should become comparable to the solvent shifts just quoted for these dyes, when the electric field reaches strengths of the order of the maximum solvent-induced basicity difference, that is, about 1.5 v per molecular length. In Dyes III and IV, this would be about 10^7 v/cm. Indeed for Dye IV in pyridine, judging by Brooker's data, fields only 1/100 this large should produce an easily detectable wavelength shift of about 100 A and a peak intensity change of about 20%. [Because of the quadratic nature of Eq. (2), the dyes most sensitive to small fields should be those where (b_L-b_R) is large in the nonpolar solvents and small in polar ones; but Brooker does not describe any particularly favorable cases of this kind]. These expected field strengths for producing a detectable effect appear to be below the breakdown strength of clean nonpolar solvents and plastic insulating materials. The spectral shifts in transparent dielectrics might have considerable value for studying local fields inside these materials.

Some of Brooker's later papers[6] describe the so-called "cruciform dyes" which have two steric configurations with different spectra, one configuration having a large dipole moment and one having a small one. The equilibrium between these two forms could again be shifted by an electric field to produce a change of color in either absorption or emission. The electrochromic effect in this case might have some technical applications, but it promises to be of somewhat less fundamental interest because it involves a geometrical rearrangement and is not a pure electronic shift; the rearrangement would probably also be hindered in rigid media.

All these electrochromic effects should have very fast time constants, no more than about 10^{-9} sec for geometrical rearrangements in low-viscosity systems, and much faster than this for pure electronic shifts.

It appears that an experimental search for electrochromic effects on the absorption and emission spectra of such dyes and other organic and inorganic compounds might turn up phenomena of considerable interest and value.

[5] L. G. S. Brooker and R. H. Sprague, J. Am. Chem. Soc. **63**, 3214 (1941).

[6] L. G. S. Brooker, F. L. White, D. W. Heseltine, G. H. Keyes, S. G. Dent, Jr., and E. J. Van Lare, J. Photographic Sci. **1**, 173 (1953) and patents.

Electron Spin Relaxation in Metal-Ammonia Solutions* †

VICTOR L. POLLAK‡

Department of Physics, Washington University, Saint Louis, Missouri

(Received August 8, 1960)

The pulsed magnetic resonance technique was employed to measure the electron spin relaxation times T_1 and T_2 in solutions of sodium and potassium in liquid ammonia. Measurements were carried out over a range of temperatures from $-50°C$ to $+30°C$, and for the concentration range of 10^{-4} to 10^{-2} mole metal per mole NH_3. It was found that T_1 and T_2 are equal at all measured concentrations and temperatures, these times ranging from 1 to 3 μsec. For dilute solutions, the data are shown to be quantitatively consistent with the assumption that the relaxation is owing to the contact hyperfine interaction of the electrons with the N^{14} nuclei of ammonia. This interaction is modulated by the relative motion of the electrons and the ammonia molecules, the spin relaxation time being proportional to the modulation rate, as is typical in cases of extreme motional narrowing. An electron tunneling mechanism is proposed as a possible source of the modulation. That the electron-nitrogen hyperfine interaction is largely responsible for the spin relaxation in dilute solutions is verified by measurements on a sample prepared from isotopically substituted ammonia ($N^{15}H_3$). A qualitative explanation of the variation of the electron spin relaxation time with concentration is proposed.

INTRODUCTION

THE alkali metals, and to a lesser extent certain of the alkaline earth metals, dissolve readily in liquid NH_3. The solutions thus formed have many interesting and remarkable physical properties and hence have been the subject of research over a period of almost 100 years. However, the explanation of the unusual properties of metal-ammonia solutions is still a matter of considerable controversy. A variety of models have been proposed, but none of these has escaped valid objection based upon experimental evidence.[1]

With the invention of the magnetic resonance technique, a powerful tool for experimental investigation of these solutions became available. The resonance method provides detailed information about the microscopic environment of electrons and nuclei within the sample being studied; such data naturally put previous models to a severe test, and provide an excellent basis for new theoretical development of an improved model. It would not be surprising if magnetic resonance data will eventually lead to a satisfactory theory of metal-ammonia solutions.

The most crucial question in the theory of metal-ammonia solutions concerns the fate of the alkali-metal valence electron upon solution. It is generally conceded that in the most dilute solutions the electron is dissociated from its parent ion, and is trapped in some kind of bound structure or cavity among the ammonia molecules. This conclusion is based largely upon electromotive force and electrical conductance studies. The most recent detailed theory of such a cavity model is due to Jortner.[2]

The properties of concentrated metal-ammonia solutions resemble those of a liquid metal—e.g., a saturated solution of K in NH_3 has a conductivity about half that of liquid mercury. Here it is agreed that the electrons occupy energy levels in a conduction band.

The electron spin resonance in metal-ammonia solutions has been observed and measured by a number of workers, using various solute metals and working at temperatures ranging from below the ammonia melting point ($-78°C$) to room temperature.[3–6] The nature of the spin relaxation mechanism has, however, not been previously established. The outstanding feature of the resonance is its extraordinary sharpness—in dilute sodium and potassium solutions at room temperature the ESR line is closely Lorentzian in shape, and has a width (δH) of about 0.02 oe between points of maximum slope. The relaxation time T_2 corresponding to this width is

$$T_2 \approx 2[\sqrt{3}\gamma(\delta H)]^{-1} \approx 3\ \mu\text{sec},$$

the quantity γ being the gyromagnetic ratio of the electron, and having the value of 17.6×10^6 oe^{-1} sec^{-1}.

The purpose of the work reported herein is to establish the source of the observed linewidths, i.e., to identify the dominant spin relaxation mechanisms. To this end, precise measurements of transverse relaxation time T_2 as well as of the spin-lattice relaxation time T_1 were carried out as a function of temperature and concentration for dilute and moderately dilute solutions of sodium and potassium metal. The pulsed

* This work was supported by the U. S. Air Force through the Air Force Office of Scientific Research of the Air Research and Development Command, and by an equipment loan contract with the Office of Naval Research. Some of the apparatus was provided by a grant from the Alfred P. Sloan Foundation.

† Most of the results reported herein are taken from the author's Ph.D. thesis, Washington University, St. Louis, Missouri, 1960.

‡ Now at Schlumberger Well Surveying Corporation, Houston, Texas.

[1] The most recent review article on this subject is by M. C. R. Symons, Quart. Rev. (London) **13**, 99 (1959).

[2] J. Jortner, J. Chem. Phys. **30**, 839 (1959).

[3] C. A. Hutchison and R. C. Pastor, J. Chem. Phys. **21**, 1959 (1953); Revs. Modern Phys. **25**, 285 (1953).

[4] D. E. O'Reilley, Ph.D. thesis, University of Chicago, Chicago, Illinois, 1955, microfilm order No. T-2964.

[5] R. A. Levy, Phys. Rev. **102**, 31 (1956).

[6] R. J. Blume, Phys. Rev. **109**, 1867 (1958).

magnetic resonance technique[7,8] was employed, using a frequency of 30 Mc and a field H_0 of 11 oe. Our data overlap, at certain points, the earlier data,[3–6] and in the section on experimental results we compare the various results.

Our interpretation of the experimental data in dilute solutions follows the method of Kaplan and Kittel,[9] but differs from the latter in that the relaxation mechanism is assumed to be the contact hyperfine interaction of the electrons with the nitrogen nuclei of ammonia. We then verify this hypothesis experimentally by relaxation time measurements on a sample prepared from $N^{15}H_3$ in place of ordinary ammonia. An electron tunneling process is suggested as a possible mechanism for modulation of the interaction, and is shown to be consistent with the known electrical conductivity.

Finally, for solutions of higher concentration, a qualitative explanation of the variation of spin relaxation times with concentration is given.

EXPERIMENTAL APPARATUS AND TECHNIQUE

By and large our experimental method is similar to that of Blume.[6] We have refined Blume's technique so as to increase the precision and widen the scope of the relaxation time measurements. We shall limit ourselves in this section to describing briefly those features of our experimental method which differ from that of Blume.

Samples

Various methods of preparing and analyzing metal-ammonia samples have been described in the literature.[3,5,6,10] All samples used in the present work were prepared and analyzed for us under the direction of Professor S. I. Weissman of the Washington University Department of Chemistry. Their procedure is as follows.

Alkali metal is forced into glass capillaries of known diameter. The desired amount is then obtained by breaking off a piece of the capillary having the appropriate length. This metal-filled piece is then introduced into a vacuum system. The metal is now triply distilled, the last distillation taking the metal up into the high-pressure glass tube which is to contain the metal-ammonia sample. The bottom of this sample tube is sealed, and liquid ammonia from a reservoir in another part of the vacuum system is distilled over into the sample tube, filling it to the desired level. The liquid ammonia in the reservoir has itself been purified by dissolving alkali metal therein. Finally, the top end of the sample tube is sealed, while the end containing the metal-ammonia solution is held at liquid nitrogen temperature.

The high-pressure glass tubing has an outside diameter of $\frac{1}{2}$ in. (nominal), a wall thickness of 5/64 in., and is rated as being capable of withstanding pressures up to 500 psi. The vapor pressure of NH_3 at $+30°C$ is only 170 psi; however, experience showed that the inevitable strains developed in the glass at the sealed ends make the sample tubes considerably less pressure resistant than the manufacturer's rating indicates. Some experience is required on order to make sealoffs that are consistently safe at room temperature.

Solutions of metals in liquid ammonia are metastable. The reaction

$$2Me+2NH_3 \rightarrow 3MeNH_2+H_2$$

eventually goes to completion, and renders the solutions diamagnetic. The metal-amide is not very soluble in NH_3, and after sufficient deterioration has taken place, its presence can be detected visually as a white precipitate. Certain impurities catalyze the above reaction,[10] making it necessary to prepare the solutions with considerable care. Deterioration was minimized by storing samples at dry-ice temperature and by taking data as soon after sample preparation as possible. Samples were visually inspected for the presence of the amide precipitate before and after taking data.

Precise sample concentration was determined after all other data had been completed. First the sample and its container were weighed. The glass container was then broken, the ammonia allowed to evaporate, and the amount of residual alkali metal measured by a chemical method, ending with a titration. This information, plus the weight of the empty container then allow the concentration to be calculated.

Our sample of Na-$N^{15}H_3$ was prepared using ammonia gas containing $95^+\%$ $N^{15}H_3$.[11]

Static Field

A homogeneous static magnetic field H_0 of about 11 oe was provided by a set of Helmholtz coils of 12 in. radius. A current-regulated power supply was designed to supply a stable coil current of about 0.9 amp at 16 v. The homogeneity of the H_0 field over the volume of the sample, as well as its stability, were both good to better than one part in 10^4, as required for this experiment.

Pulsed Radiofrequency Field

A pulsed alternating 30 Mc magnetic field, perpendicular to H_0 and about 1 oe in amplitude, was produced by sending a pulsed rf current of about 3.5 amp (peak) through an appropriate configuration of conductors (see Fig. 1). The relaxation time T_2 was measured as the time constant of the deacy of the electron free-precession signal following a 90° pulse.[7] The 90° rotation of the magnetization is achieved by adjusting the amplitude of an rf pulse having a duration

[7] E. L. Hahn, Phys. Rev. **80**, 580 (1950).
[8] H. Y. Carr and E. M. Purcell, Phys. Rev. **94**, 630 (1954).
[9] J. Kaplan and C. Kittel, J. Chem. Phys. **21**, 1429 (1953).
[10] F. J. Dewald and G. Lepoutre, J. Am. Chem. Soc. **76**, 3369 (1954).

[11] Purchased from Isomet Corporation, Palisades Park, New Jersey.

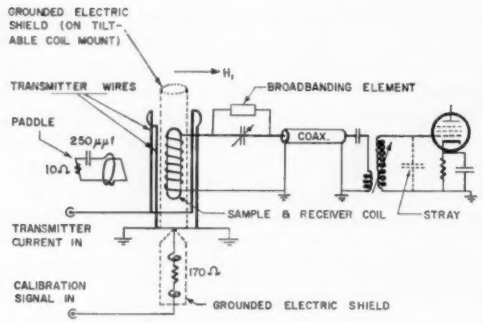

FIG. 1. Schematic diagram of crossed coil assembly and receiver input circuit.

of 0.2 μsec, corresponding to about 6 cycles. In measuring the longitudinal relaxation time T_1, the 180°–90° pulse method[8] was used, as in Blume's work. A 0.4 μsec variable duration pulse served to produce the 180° rotation of the magnetization.[12] The time interval between the two pulses was varied by making use of the precision variable-time-delay circuit of a Tektronix type 535 cathode-ray oscilloscope. Calibration of this time base was occasionally checked against a crystal-controlled Tektronix type 181 time-mark generator.

The experiment was performed at a repetition frequency of 400 cps.

Receiver System

Figure 1 shows a semischematic representation of the crossed coil assembly and receiver input circuit. The receiver coil, in which the emf resulting from the precessing magnetization of the sample is induced, is shown in the figure as a small coil with axis parallel to the transmitter wires. The combination of a grounded electric shield[13] and "paddle"[14] serve to eliminate electric coupling between transmitter and receiver. Magnetic coupling is minimized by mechanical adjustment of the receiver coil axis.

It will be noted that a double-tuned input circuit is employed. This circuit was adjusted to critical coupling and has a bandwidth of about 2 Mc. The bandwidth of the succeeding amplifier is 4.4 Mc. The double-tuned input circuit has, in general, two advantages: (1) the impedance presented to the input stage of the amplifier can be made optimum, even though a low-impedance connecting cable is used, thus achieving an amplifier noise figure approaching unity, and (2) a nonlinear broadbanding element can be introduced in the position shown in Fig. 1 without deleterious capacitive loading. Considerable success was, in fact, achieved by use of a (selected) Raytheon type 1N307 diode as the broadbanding element. For small signals, this diode was equivalent to a resistance of about 4000 ohms at room temperature. For the undesired large-amplitude signals picked up from the transmitter, the low forward resistance of the diode served to broadband the input circuit further, thus reducing the duration of the input circuit ringing. Unfortunately, the diode is not suited for making measurements as a function of temperature, since its small-signal resistance is temperature dependent. At room temperature, however, the input circuit ringing time was reduced by about 1 μsec when the diode was used in place of a resistor. This constituted an appreciable improvement in the measurement of relaxation times in the microsecond range.

The 30 Mc amplifier is a standard broadband radar i.f. amplifier and will not be described further. It is followed by a diode detector and video catode follower. Figure 2 shows some typical output waveforms.

In order to attain further improvement in signal-to-noise ratio, a boxcar integrator[15] was employed. A gating pulse is provided that can be set to occur at any instant of time during a free-precession signal, and the integrator gives a dc output voltage proportional to the

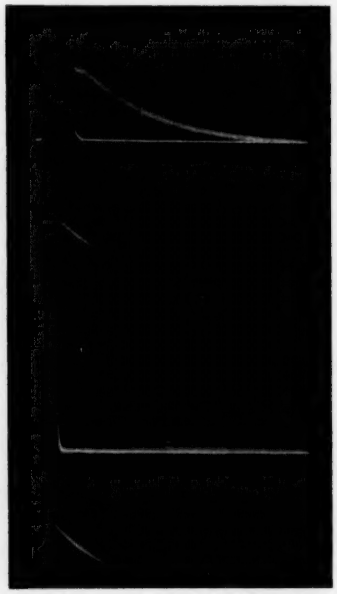

FIG. 2. Typical receiver output waveforms. The upper oscillogram is a double exposure showing receiver output waveforms in a T_2 experiment with the H_0 field on and off. Horizontal time scale is 1 μsec per division. The lower oscillogram is a multiple exposure, showing free-precession signals following the second pulse in a T_1 experiment, for various pulse separations. Time scale is 2 μsec per division.

[12] Blume has shown that this method of measuring T_1 is applicable even though the pulse durations are not negligibly short compared to the relaxation times, provided the Bloch equations are obeyed.[8]

[13] F. E. Terman, *Radio Engineer's Handbook* (McGraw-Hill Book Company, Inc., New York, 1943), p. 134.

[14] A broadband tuned circuit (Fig. 1) was used as a "paddle." This is a modification of the design used by H. E. Weaver, Phys. Rev. **89**, 923 (1953).

[15] D. H. Holcomb and R. E. Norberg, Phys. Rev. **98**, 1074 (1955).

amplitude of the signal at the time of the gate and averaged over many repetitions of the experiment. Setting the gate pulse to occur at various instants of time then gives the signal amplitude as a function of time. The integrator output voltage was displayed on a chart recorder, allowing further (visual) time averaging to be performed, and making it easy to compare signal amplitudes with calibration signals. The calibration signals were obtained by pulsing a Hewlett-Packard type 608-D signal generator and attenuating its output signal by means of a Tektronix type B170-A precision switch attenuator. The output of the attenuator was terminated so as to give weak magnetic coupling between the termination and the receiver coil (see Fig. 1). Thus, the calibration signals traverse the whole receiver system, allowing precise amplitude comparison to be made with free-precession signals.

Temperature Control System

Provision was made in the design of the crossed coil to allow for the passage of precooled nitrogen gas past the sample. The gas temperature was regulated by allowing a controlled portion of the gas flow to pass through a heat exchanger coil immersed in liquid nitrogen. By varying the proportion of direct and cooled flow, the temperature of the sample was continuously variable over the range of interest. The temperature was monitored by placing a thermocouple junction into the gas flow next to the sample coil. A small capacitor, from one of the thermocouple leads to ground, served to bypass any induced rf currents and preserved the shielding of the receiver input circuit. Temperature stability was maintained by manual adjustment of the flow rates.

EXPERIMENTAL RESULTS

Spin relaxation times T_1 and T_2 of electrons in Na–NH_3 and K–NH_3 were measured at 30.5 Mc over the range of concentrations 10^{-4} to 10^{-2} moles metal per mole NH_3,[16] and at temperatures ranging from -50°C to $+30$°C. All free precession signals were found to decay exponentially. It was found that T_1 equals T_2 at all concentrations and temperatures, and that these relaxation times range from 1.0 to 3.3 μsec.

Measurements on a dilute solution of sodium in $N^{15}H_3$ gave considerably longer relaxation times than would be expected for a sample of the same concentration made with ordinary ammonia ($N^{14}H_3$).

Variation of T_2 with Temperature

For dilute samples, the relaxation times were observed to increase with increasing temperature. In samples of higher concentration, with increasing temperature, the relaxation time passes through a maximum; the higher the concentration, the lower the temperature at which this maximum occurs. Several typical curves of T_2 vs temperature are shown in Fig. 3. In interpreting the variation of T_2 with temperature, it must be kept in mind that the paramagnetic susceptibility, and therefore the concentration of unpaired electrons, increases with increasing temperature. That the increase in T_2 with temperature does not continue monotonically is most likely because of the increase in the unpaired-electron concentration, rather than being a *direct* result of the increase in temperature.

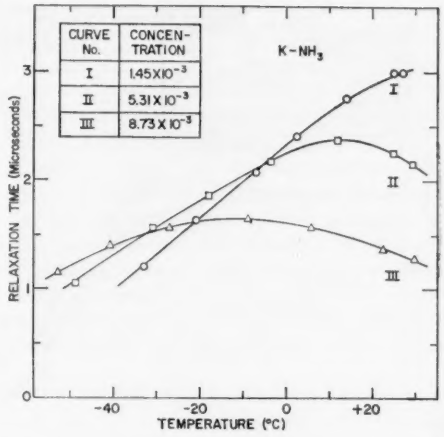

FIG. 3. Typical variation of electron spin relaxation times with temperature in K-NH_3 solutions. Concentrations are in moles metal per mole NH_3.

Variation of T_2 with Concentration

At any given temperature, T_2 exhibits a small gradual increase as concentration is increased, until, above a certain critical concentration, T_2 begins to decrease sharply. This critical concentration becomes higher the lower the temperature. The initial increase in T_2 is most pronounced at low temperature.

In Fig. 4 we have plotted T_2 vs concentration at $+25.0$°C and -33.5°C. The data points shown were obtained by interpolation of our T_2 vs temperature data. The temperatures $+25$°C and -33.5°C were chosen for display because they lie near the extremes of the temperature range investigated, and because there exist other data on T_1 and T_2 at these temperatures, allowing comparison between our results and these others.

Variation of T_2 with Metal Solute

The relaxation times in Na–NH_3 are found to be either somewhat longer or about the same as those in K–NH_3 at comparable temperatures and concentrations.

[16] Expressed as moles per liter, the given range of concentrations corresponds approximately to 0.01–0.4M. Unless otherwise indicated, concentrations will be given as moles metal per mole NH_3.

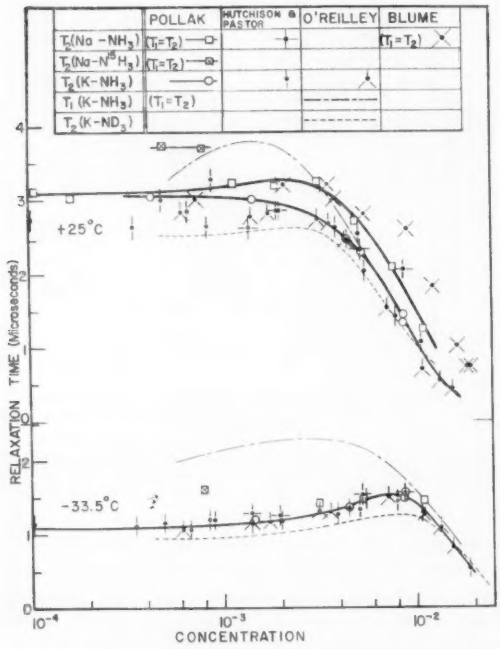

FIG. 4. Electron spin relaxation times vs concentration for various types of metal-ammonia solutions. Concentrations are in moles metal per mole NH_3.

The difference is most pronounced at high temperatures where it can amount to as much as 30% (see Fig. 4).

Variation of T_2 with Sample Deterioration

A fairly concentrated Na–NH_3 sample was allowed to remain at room temperature for several days. The relaxation time was occasionally measured as the reaction $2Na+2NH_3 \rightarrow 2NaNH_3+H_2$ proceeded to completion. It was found that the relaxation time varied as though the metal concentration were being continually decreased.

Variation of T_2 with Isotopic Substitution

O'Reilley[4] has measured T_1 and T_2 in K–ND_3 at room temperature, 0°C, and −33.5°C as a function of potassium concentration using the continuous wave (cw) method. In dilute deuterated solutions, he finds T_2 to be somewhat shorter than in the ordinary solutions (see Figs. 4 and 5).

We measured T_1 and T_2 in a single dilute sample of Na–$N^{15}H_3$, as a function of temperature and deterioration. Unfortunately, this sample exploded after having been allowed to remain at room temperature for about three days, and its exact concentration is therefore not known. However, we were able to estimate the concentration to be 0.8×10^{-3} from signal amplitude considerations. Two sets of data had been taken on this sample—the first with the sample fresh, and the second after the sample had suffered partial deterioration. From signal amplitude considerations, the equivalent concentration of the partly deteriorated sample was estimated to be 0.5×10^{-3}. The relaxation time data for this sample are shown in Figs. 4 and 5. As in all other samples, it was found that T_1 and T_2 are equal. Comparison of the Na-$N^{15}H_3$ data with that from the ordinary solutions (Fig. 3) shows that the change in relaxation times with deterioration is, qualitatively, as expected.

Comparison with Earlier Data

Hutchison and Pastor[3] and O'Reilley[4] have measured T_1 and T_2 in K-NH_3 at +25°, 0°, and −33.5°C, using the continuous wave (cw) technique and working at 8 Mc. Blume[6] has measured T_1 and T_2 in Na-NH_3 at +24°C by the pulse method, at 17 Mc.

As can be seen from Fig. 4, the agreement between our T_2 data in K-NH_3 at 25° and −33.5°C and the cw data is excellent. At 0°C, however, our results for T_2 differed somewhat. An error in measurement of temperature is indicated; the cw results at 0°C agree closely with our T_2 data at about −7°C.

Our measurements in Na-NH_3 at room temperature agree with those of Blume for concentrations below about 4×10^{-3} ($\approx0.15M$), but for higher concentrations Blume obtains considerably longer relaxation times than we do (see Fig. 4). Blume also finds that T_1 equals T_2 for those samples on which he was able to measure T_1.

The cw measurements[4] give T_1 greater than T_2 in certain regions of concentration and temperature, and

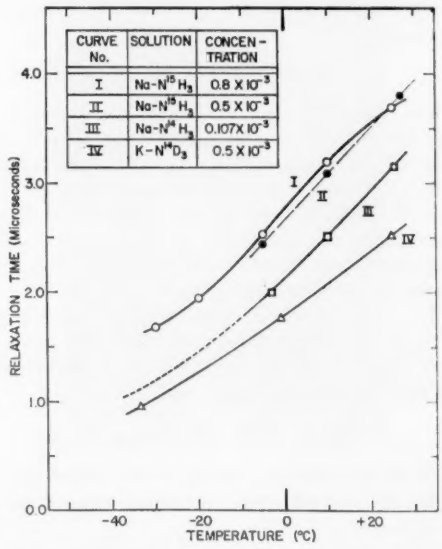

FIG. 5. Electron spin relaxation time vs temperature for dilute solutions having different isotopic constitution. Data for curve IV are due to O'Reilley.[4]

$T_1 = T_2$ in others (see Fig. 4). As mentioned earlier, we measured $T_1 = T_2$ everywhere. We have not attempted to account for this discrepancy. It is well known that the cw method for obtaining T_1 (saturation method) is far less direct than the pulse method; both the experimental procedure and the analysis of the data are beset with complications, and errors can easily creep in.[17] Before discrediting O'Reilley's T_1 results, however, it would be necessary either to repeat his measurements or to make a detailed critique of his analysis and procedure. Moreover, O'Reilley's data look very convincing, particularly in view of the fact that for certain concentrations and temperatures he gets T_1 different from T_2, whereas for other concentrations and temperatures, for which the *same* T_2 is measured, he finds T_1 equal to T_2.

Precision of Measurement

Measurements of T_1 and T_2 on any given sample were found to be reproducible to 5% or better. Systematic errors in the relaxation time data are expected to be worst for the weakest signals and the shortest relaxation times, i.e., at the lowest and highest concentrations, and especially at the lowest temperatures. However, the excellent agreement of our T_2 data with the cw results suggests the absence of systematic errors in the measurement of T_2.

No systematic difference between T_1 and T_2 was found. Calculating the quantity

$$100(T_1 - T_2)/T_2$$

averaged indiscriminately over all the data, as well as the standard deviation of this quantity from its average, we obtained $-1.6 \pm 4.1\%$.

THEORY

Method of Kaplan and Kittel

Thus far, the only attempt to give a quantitative interpretation of the observed electron spin relaxation times in metal-ammonia solutions appears to be that of Kaplan and Kittel (KK).[9] These authors proposed that in dilute solutions, the relaxation proceeds via the motionally modulated contact hyperfine interaction of the electrons with ammonia protons. More recently, however, measurements of the Knight shift by McConnell and Holm[18] revealed that the dominant nuclear spin density at the unpaired electron is that of the nitrogen nuclei, the proton and sodium densities being negligible by comparison. Using the KK model, it is easily shown that the observed N^{14} spin density at the electron is of the right order of magnitude to account for the electron spin relaxation time in dilute solutions.

Following KK, the ESR linewidth is given by

$$\delta H = \gamma_e (\Delta H)^2 \tau_c, \tag{1}$$

where γ_e is the electron's gyromagnetic ratio (17.6×10^6 oe^{-1} sec^{-1}), ΔH is the rigid-lattice linewidth, and τ_c is the correlation time, i.e., the reciprocal of the frequency at which the interaction is modulated. Equation (1) is valid so long as τ_c is short compared to the electron Larmor period, this condition being generally referred to as the case of "extreme motional narrowing," and being characterized by Lorentzian line shapes or exponentially-decaying free precession signals. The rigid-lattice width, ΔH, is given by[19]

$$(\Delta H)^2 = (64\pi^2/27) \sum_i \mu_i^2 [(I_i+1)/I_i] \, |\psi(i)|^2. \tag{2}$$

Here μ_i and I_i are the magnetic moment and spin of the ith nucleus and $|\psi(i)|^2$ is the hyperfine contact density of nucleus i at the unpaired electron. Assuming that the electron is in equal contact with each of $\mathfrak{N}$ identical nuclei, Eq. (2) becomes

$$(\Delta H)^2 = (64\pi^2/27) \mu_n^2 [(I+1)/I] P^2(n) \mathfrak{N}^{-1}. \tag{3}$$

The quantity $P(n)$ is the total nuclear density at the electron, and is defined by $P(n) = \mathfrak{N} |\psi(n)|^2$. The electron spin relaxation time T_2 is related to the linewidth by

$$(T_2)^{-1} \approx \gamma_e \delta H. \tag{4}$$

Combining Eqs. (1) through (4) gives

$$T_2^{-1} \approx (64\pi^2/27) \gamma_e^2 \mu_n^2 [(I+1)/I] P^2(n) (\tau_c/\mathfrak{N}) \tag{5}$$

as the basic formula for the calculation of T_2. For the nucleus N^{14} we have $I = 1$, $\mu_n = 2.04 \times 10^{-24}$ erg/oe. The quantity $P(N^{14})$ is reported to have the value 4.5×10^{24} cm^{-3} and to be independent of concentration.[18] Inserting these data into Eq. (5) gives

$$T_2 \approx 0.82 \times 10^{-18} \mathfrak{N} (\tau_c)^{-1} \text{ (cgs)}. \tag{6}$$

If we follow KK's method, we take τ_c to be the Debye dipolar relaxation time

$$\tau_c \approx 3\eta V/kT.$$

Here η is the viscosity of the liquid and kT is Boltzmann's constant into the absolute temperature. V is the volume per ammonia molecule, and is given by

$$V = W(L_0 \rho)^{-1},$$

where W is the molecular weight of ammonia (17 g/mole), ρ is the density, and L_0 is Avogadro's number. Hence,

$$\tau_c \approx (3W/L_0 k)(\eta/\rho T), \tag{7}$$

[17] N. Bloembergen, E. M. Purcell, and R. V. Pound, Phys. Rev. **73**, 679 (1948).

[18] H. M. McConnell and C. H. Holm, J. Chem. Phys. **26**, 1517 (1957).

[19] A. F. Kip, C. Kittel, R. A. Levy, and A. M. Portis, Phys. Rev. **91**, 1066 (1953).

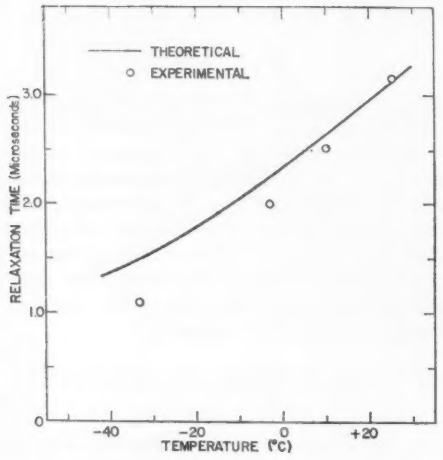

FIG. 6. Electron spin relaxation time vs temperature for very dilute solutions of metal in $N^{14}H_3$. Theoretical curve is calculated from Eq. (8) using O'Reilley's data on density and viscosity[4] and assuming a temperature-independent N^{14} hyperfine density at the electron. Three of the experimental points are from our data on a sodium-ammonia sample having concentration 0.107×10^{-3}. The low temperature point is read from Fig. 4.

and, from Eq. (6),

$$T_2\approx 0.82\times 10^{-18}(L_0k\mathfrak{N}/3W)(\rho T/\eta)=2.3\times 10^{-11}(\rho T/\eta). \tag{8}$$

In Eq. (8) we have put $\mathfrak{N}=17$—i.e., one-third KK's value for $\mathfrak{N}$—since there are one third as many N^{14} nuclei per molecule as protons. At $+20$°C, O'Reilley[4] gives $\eta=0.14$ centipose, and $\rho=0.611$ g/cm^3 for the viscosity and density of pure NH_3. Inserting these values into the above relations gives $\tau_c=4.8\times 10^{-12}$ sec, and $T_2=2.9\times 10^{-6}$ sec, in agreement with the experimental value.

We can also compare the KK theory with our experimental results at other temperatures, if we assume that the number of N^{14} nuclei that are in contact with the electron, and their hyperfine contact density at the electron $P(N^{14})$, are both temperature independent. Density and viscosity data at various temperatures are given by O'Reilley.[4] Figure 6 shows a plot of T_2 vs temperature according to Eq. (8), together with the best experimental values at the lowest measured concentrations. The agreement with experiment is obviously much better than this approximate theory can justify.

Kaplan and Kittel suggested that spin relaxation time measurements using *deuterated* metal-ammonia solutions would constitute a test of their theory, the small deuteron moment leading to a much longer electron relaxation time. Such measurements have been performed by O'Reilley,[4] who found, however, that the relaxation times using ND_3 are not much different than in the NH_3 solutions, and correctly concluded that KK's theory of the spin-relaxation is in error. The error is, presumably, that the relaxation proceeds via the contact with N^{14} nuclei and not with the protons or deuterons. When applied to relaxation via the N^{14} hyperfine coupling, KK's theory predicts that the only difference between relaxation times in NH_3 and ND_3 solutions will arise from the difference in the correlation times. Quantitatively we expect, from Eqs. (5) and (7),

$$\frac{T_2(NH_3)}{T_2(ND_3)}=\frac{\tau_c(ND_3)}{\tau_c(NH_3)}=\left(\frac{\eta W}{\rho}\right)_{\text{deut}}\Big/\left(\frac{\eta W}{\rho}\right)_{\text{normal}}. \tag{9}$$

Using O'Reilly's density and viscosity data,[4] one finds that in dilute solutions the above ratio is temperature independent, and amounts to a factor of 1.2, in agreement with experiment.[20]

For the case of dilute solutions of metal in $N^{15}H_3$, application of Eq. (5) gives

$$\frac{T_2(N^{15}H_3)}{T_2(N^{14}H_3)}=1.35\frac{\tau_c(N^{14}H_3)}{\tau_c(N^{15}H_3)}, \tag{10}$$

the factor 1.35 arising from the different magnetic moment and spin of nitrogen-15 ($\mu=-1.43\times 10^{-24}$ erg/oe; $I=\frac{1}{2}$). Our data on the Na—$N^{15}H_3$ sample show the ratio $T_2(N^{15}H_3)/T_2(N^{14}H_3)$ to vary from 1.20 at room temperature to 1.26 at -5°C (see Fig. 5). Increasing the mass of the ammonia molecule will, at a given temperature, *increase* the correlation time—as in the case of ND_3—because of equipartition of energy. Hence we expect the ratio of relaxation times [Eq. (10)] to be somewhat *less* than 1.35.[21] The fact that the relaxation times in the $N^{15}H_3$ solution are *longer at all* than in the ordinary solutions is by itself convincing evidence of the role played by the nitrogen hyperfine interaction. The possibility of the presence of a competing relaxation mechanism is, however, not ruled out by our data.

Modulation of the Hyperfine Interaction by Electron Tunneling

Kaplan and Kittel's use of the Debye dipolar relaxation time as the correlation time in the calculation given in the foregoing is based upon their model of metal-ammonia solutions. In this model one pictures the electron as being located in a cavity in the liquid, surrounded by randomly rotating ammonia dipoles with which the electron interacts via the hyperfine coupling.

An alternative source of modulation of the hyperfine coupling suggests itself when one remembers that the electrons in metal-ammonia solutions have a high mobility. Even in dilute solutions, the mobility of the

[20] See Fig. 4. The right side of Eq. (9) may as well be written $\eta_{\text{deut}}/\eta_{\text{normal}}$, since the molar volumes of NH_3 and ND_3 are (experimentally) equal.

[21] The presence of 5% $N^{14}H_3$ would lower the coefficient in Eq. (10) to 1.33.

negative charge carriers has been measured to be from 5 to 7 times greater than that of the positive carriers, the metal ions.[22] Without making any detailed assumptions about the instantaneous "state" of the electron, one can easily estimate a correlation time from the available electrical conductivity data.

Before making this estimate, we mention that several writers have proposed that the correct description of the electronic motion in the liquid may be via a tunneling mechanism. This idea was first suggested by Farkas, who used it as the basis for a theory of electrical conductivity of metal-ammonia solutions.[23] The expression for the conductivity derived by Farkas is in moderately good agreement with experiment for concentrated solutions ($1M$ to $5M$). More recently, Dewald and Lepoutre have been led independently to the conclusion that barrier tunneling is the important conduction mechanism in *dilute* solutions by their extensive measurements of the thermoelectric properties of such solutions.[24] The possibility of a tunneling mechanism is also mentioned by O'Reilley.[4] We shall therefore adopt this point of view, although it is not essential to the arguments which follow.

Since the direction of tunneling is random, one can describe the tunneling process by a diffusion-type equation, the diffusion coefficient D being connected with the mobility m by the Einstein relation

$$eD=mkT. \tag{11}$$

The mobility is, in turn, related to the equivalent conductance λ by

$$\lambda=eL_0m. \tag{12}$$

The connection between the correlation time for translational diffusion and the diffusion coefficient may be obtained, as in the analogous nuclear resonance problem,[25] from the theory of Brownian motion—i.e.,

$$d^2=2D\tau_c, \tag{13}$$

where we take d to be the mean distance of tunneling. Combining Eqs. (11), (12), and (13) gives

$$\tau_c=e^2L_0d^2/2kT\lambda. \tag{14}$$

Inserting this into Eq. (6) gives

$$T_2\approx 0.82\times 10^{-18}(2kTv\mathfrak{N}/e^2L_0d^2) \tag{15}$$

for the relaxation time. With increasing dilution at -33°C, the equivalent conductance is reported by Kraus[26] to approach the limiting value of 1000 cm^2/ohm-mole. If we take d equal to the mean separation among ammonia molecules ($\approx$3.4 A), then Eq. (15) gives $T_2\approx 0.3\times 10^{-6}\mathfrak{N}$ seconds.[27] Recalling that the experimental value is 1.1×10^{-6} sec, we see that the agreement is quite adequate. Note that although $\mathfrak{N}$ and d in Eq. (15) depend upon the details of the model, $\mathfrak{N}$ will in general be approximately proportional to d^3, and hence the model details enter essentially by way of a single parameter.

Equation (14) for the correlation time gives $\tau_c\approx 4\times 10^{-12}$ sec, which is of the same order as the Debye rotation time calculated from Eq. (7). It is possible that this is merely a coincidence; on the other hand it is quite likely that there should be a correlation between the tunneling and the dipolar kinetic motion—i.e., that conditions favorable for tunneling will require a time of the order of the Debye time for their establishment. Thus, one may picture the electronic charge as tending to orient the ammonia dipoles, while the response of these, in turn, produces the strong local electric field required to precipitate the tunneling. This would mean that the electrical conductivity depends upon the Debye rotation time and ought to vary with isotopic substitution. Now, in his cw experiments, O'Reilley[4] observed that the Q values of the sample-containing circuit were higher for K–ND_3 samples than for K–NH_3 samples of the same concentration at the same temperature, and concluded that the electrical conductivity in the deuterated solutions is about 20% lower than in the ordinary solutions. O'Reilley's explanation—that the electron is somewhat more tightly bond in the deuterated solvent—is difficult to justify. The explanation given above seems more plausible, and ties in both the conductivity and the electron spin relaxation time with the Debye time characteristic of the liquid motion.

Solutions of Medium Concentration

Thus far our discussion of the KK theory has been restricted to the very dilute range of concentrations. KK suggest that the observed decrease in the electron spin relaxation time with increasing concentration may plausibly be ascribed to dipolar interaction among unpaired electrons, in which case the theory of motional narrowing applied to this interaction gives[28]

$$T_1=(5/6\pi^2)(kT/\gamma_e^4\hbar^2\eta N_p) \tag{16}$$

for the relaxation time in the presence of translational diffusion. Here N_p is the concentration of paramagnetic centers and η their effective viscosity. It turns out that Eq. (16) gives a relaxation time comparable to that which is measured in the range of concentrations 5 to 10×10^{-3} mole metal per mole NH_3, the bulk viscosity being used for η. As KK point out, that is just the concentration range in which T_1 begins to decrease. The

[22] C. A. Kraus, J. Am. Chem. Soc. **30**, 1197 (1908); **36**, 864 (1914).
[23] L. Farkas, Z. physik. Chem. (Leipzig) **A161**, 355 (1932).
[24] F. J. Dewald and G. Lepoutre, J. Am. Chem. Soc. **78**, 2953 (1956).
[25] A. Abragam, *Cours sur les Phenomenes Lies a la Resonance Magnetique* (Centre d'Etudes Nucleaires de Saclay, Gif-sur-Yvette, Seine et Oise, France, 1955).
[26] C. A. Kraus, J. Franklin Inst. **212**, 537 (1931).
[27] It should be kept in mind that the value for the contact density at room temperature has been used here, while the other quantities are for -33°C. Conductivity data above the boiling point are not available.

observed decrease is, however, much sharper than the behavior predicted by Eq. (16). In any case, it is not clear that the theory developed for nuclear resonance in liquids can be applied directly to the present problem, since this theory does not take into account the demands of the Pauli principle.[28] We must therefore conclude that the suggested mechanism, if effective, is either incorrectly described by Eq. (16), or is accompanied by another, more effective, mechanism which comes into play in approximately the same concentration range.

The observed variation of the electron-spin relaxation time with increasing concentration can be accounted for qualitatively as follows.

As the metal concentration is increased, interactions between electrons and metal ions and among the electrons themselves become increasingly important. The Knight shift results[18] indicate that the density of metal nuclei at the unpaired electron increases with increasing concentration. That the metal ions play a role is also evident from the observed variation of the spin relaxation time with metal solute (Fig. 4).

As the density of the paramagnetic centers increases, the contribution to the linewidth from the contact hyperfine interaction will tend to diminish due to the additional modulation by electron exchange; i.e., the gradual increase in T_2 with concentration shown in Fig. 4 can be attributed to *exchange narrowing*.[29]

The onset of exchange effects is associated with the formation of conduction bands; the concentration at which the spin relaxation time begins to drop off sharply are, indeed, those at which the electrical conductivity increases sharply. We expect, however, that as the electron mobility increases, the electrons will no longer respond adiabatically to the molecular motion in the liquid—i.e., the electric and magnetic fields at an electron will be time-modulated. In particular, any existing spin-orbit interaction will now be modulated, and therefore becomes an effective mechanism for spin relaxation.[30] Since the electron's orbit at the position of an ion core will differ for different metal ions, the spin relaxation rate arising from spin-orbit coupling will depend upon the solute metal. This mechanism, then, competes against the effect of exchange, and very likely accounts for the observed sharp decrease in the relaxation time at the higher concentrations. Since the character of the electronic wave function at the position of an ion core remains fairly independent of the surroundings, one expects that the *relative* effectiveness of different ion cores in bringing about spin relaxation will be the same in metal solutions as in solid metals. That the relaxation time in sodium solutions is longer than in potassium solutions is therefore consistent with the experimental results for electron spin relaxation in metals.[31] Another point of (qualitative) consistency is the temperature dependence of the relaxation time. At high concentrations the relaxation time *decreases* with increasing temperature, just as in metals, and opposite to the low concentration behavior.

The study of electron spin relaxation in lithium-ammonia solutions suggests itself as a possible test of these ideas, since lithium *metal* behaves anomalously in this respect.[31]

ACKNOWLEDGMENTS

The author is indebted to Professor S. I. Weissman and members of his staff for their preparation and analysis of the metal-ammonia samples. Helpful discussions with Professor R. E. Norberg, Dr. T. E. Das, Richard Blume, and Jonathan Reichert regarding various aspects of this work are gratefully acknowledged.

[28] For the case of a metal, the analogous spin relaxation mechanisms, referred to as the spin-spin and spin-current interactions, have been investigated theoretically by A. W. Overhauser, Phys. Rev. **89**, 689 (1953).

[29] J. H. Van Vleck, Phys. Rev. **74**, 1168 (1948).

[30] The conditions under which spin-orbit coupling provides an effective spin relaxation mechanism are discussed by D. Pines, J. Bardeen, and C. P. Slichter, Phys. Rev. **106**, 489 (1957).

[31] G. Feher and A. F. Kip, Phys. Rev. **98**, 337 (1955).

Structure of Alkali Metals in the Liquid State*

N. S. GINGRICH† AND LEROY HEATON

Argonne National Laboratory, Lemont, Illinois

(Received December 16, 1959)

Neutron diffraction patterns have been obtained for the alkali metal liquids; lithium (180°C), sodium (100°C), potassium (65°C), rubidium (40°C, 160°C, 240°C, and 360°C), and cesium (30°C, 300°C, and 575°C). It was found necessary to correct intensities for scattering by a free atom for lithium and sodium but not for the heavier atoms. Atomic distribution curves were computed for all the above cases, and compared with results from x-ray diffraction. Just above melting temperatures the nearest-neighbor distances are for lithium 3.15 A, sodium 3.82 A, potassium 4.64 A, rubidium 4.97 A, and cesium 5.31 A, the number of nearest neighbors is, within one-half atom, about 9.0 to 9.5 atoms in each case. At elevated temperatures with rubidium and cesium, a weak subsidiary concentration of atoms appears between the usual first and second neighbor concentration.

INTRODUCTION

THE structures of some alkali metals in the liquid state have been determined[1] from x-ray diffraction studies, but others have remained undetermined largely due to their prohibitive absorption of x rays. These materials do not strongly absorb neutrons of suitable wavelengths and hence a study of them by neutron diffraction offers a promising means of obtaining their structures. In this way the structures of liquid rubidium and liquid cesium have been obtained for the first time in the work reported here. The x-ray determination of the structure of liquid lithium[2] in 1941, suffered from difficult and somewhat inadequate experimental conditions, results from similar work with sodium[3] and potassium,[4] though taken under more favorable conditions, are limited in their validity by limitations in the available experimental techniques of some years ago. An attempt was made in the present work to use neutron diffraction to determine the liquid structures of all the alkali metals, using similar techniques and procedures for each one so as to facilitate intercomparison.

The structures of a number of elements in the liquid state have been determined from neutron diffraction studies.[5–11] In most cases, absorption of the neutrons was so small that the absorption correction was considered negligible or at least it was considered to be essentially independent of scattering angle for samples approximately 1 cm thick. An attractive feature of neutron patterns is due to the essentially isotropic nature of the scattering of thermal neutrons by an atomic nucleus. At large angles where interference effects in coherent scattering from different atoms fade away, the intensity approaches a constant value rather than approaching a rapidly falling atomic structure factor curve as in the case of x rays. This provides higher intensities at large angles of scattering and eliminates dependence upon a knowledge of the exact form of the structure factor of the atom. Corrections for effects such as incoherent scattering, inelastic scattering and multiple scattering are assumed to be or sometimes have been calculated to be isotropic. In the cases of liquid helium[9] and liquid neon[11] correction was made for scattering by free atoms. In all cases it was assumed that the atomic distribution function can be obtained by applying the usual Fourier integral transformation to the coherently scattered intensity pattern. Results from this kind of procedure have been reported for helium, nitrogen, oxygen, sulphur, neon, argon, mercury, lead, and bismuth.

EXPERIMENTAL PROCEDURES

Neutrons of wavelength $\lambda = 1.09$ A were selected from the CP-5 reactor operated at 2 meg by reflection from the (111) planes of a copper single crystal. (Work with cesium was done at $\lambda = 1.03$ A and 1 meg.) The samples were contained in a cylindrical vanadium cell with inside dimensions $\frac{7}{16}$ in. (diameter) and 2 in. (length). Walls of the cells were 0.004 in. thick in the region upon which the monochromatic neutrons were incident. Cells were nearly filled with sample material of high chemical purity in a dry box flooded with dry argon, capped, removed from the box and hermetically sealed by heliarc welding in an argon atmosphere. A loaded cell was then mounted over the center of the diffractometer table in a large evacuated furnace. Incident and scattered neutron beams passed through thin aluminum windows. The samples were heated by means of a cylindrical heater of thin sheet vanadium

* Work performed under the auspices of the United States Atomic Energy Commission.

† Resident research associate on leave from the University of Missouri.

[1] N. S. Gingrich, Revs. Modern Phys. **15**, 90 (1943).
[2] C. Gamertsfelder, J. Chem. Phys. **9**, 450 (1941).
[3] F. H. Trimble and N. S. Gingrich, Phys. Rev. **53**, 278 (1938).
[4] C. D. Thomas and N. S. Gingrich, J. Chem. Phys. **6**, 411 (1938).
[5] O. Chamberlain, Phys. Rev. **77**, 305 (1950).
[6] P. C. Sharrah and G. P. Smith, J. Chem. Phys. **21**, 228 (1953).
[7] D. G. Henshaw, D. G. Hurst, and N. K. Pope, Phys. Rev. **92**, 1229 (1953).
[8] G. H. Vineyard, J. Chem. Phys. **22**, 1665 (1954).
[9] D. G. Hurst and D. G. Henshaw, Phys. Rev. **100**, 994 (1955).
[10] D. G. Henshaw, Phys. Rev. **105**, 976 (1957).
[11] D. G. Henshaw, Phys. Rev. **111**, 1470 (1958).

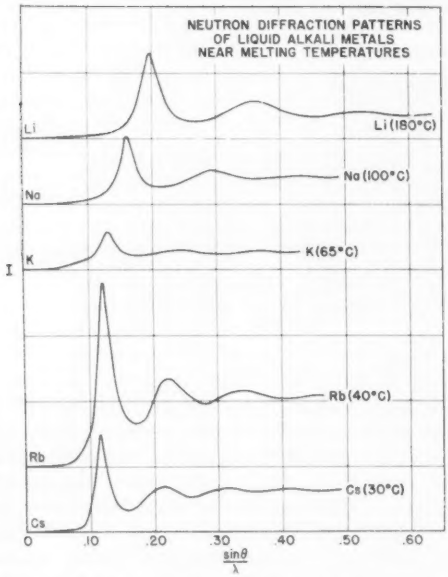

FIG. 1. Neutron diffraction patterns of liquid alkali metals near melting temperatures.

surrounding the sample. Temperatures up to 575°C were maintained and recorded continuously for runs as long as 72 hrs.

The incident beam of monochromatic neutrons was monitored with a fission counter and the number of scattered neutrons for a preset number of monitor counts was counted with a BF_3 detector. Automatic operation gave a chart record of the number of scattered neutrons per monitor neutron, as a function of scattering angle up to about 100° with approximately eight readings per degree. Correction for scattering from material other than the sample was made by taking runs with an empty cell of identical construction and subtracting this empty-cell intensity from the loaded-cell intensity at each scattering angle. This background correction was almost entirely lacking in prominences, since it was primarily due to the thin vanadium walls of the cell and heater. Measured values of the linear absorption coefficients of all sample materials agreed satisfactorily with published values, where available, and the product of linear absorption coefficient and sample radius varied between 0.002 to 0.08, for which there is no appreciable angular variation of absorption correction.

EXPERIMENTAL RESULTS

Figure 1 shows the observed intensity curves of the alkali metals at temperatures just above their melting points. These patterns have been corrected for empty-cell background and changed from laboratory to center-of-mass coordinates. While the ordinates are plotted to an arbitrary scale, the graph does indicate the relative scattering powers of the various alkali metals in the liquid state. The counting rate of the main peak of the rubidium pattern was 1600 counts/min giving nearly 13 000 counts/point. The cesium data which was obtained with 1 megawatt of reactor power has been normalized to 2 megawatts power to facilitate comparison with the other elements in this figure. In all the curves the experimental data commenced at approximately $(\sin\theta)/\lambda = 0.056$ A^{-1} where θ is one-half the scattering angle, and from this point to the origin, the intensity curve is drawn as an estimate in this unobservable region.

Lithium

Natural lithium contains isotopes of mass numbers 6 and 7. Since the absorption of neutrons by Li-6 is prohibitive, Li-7 was chosen for the present study. The linear absorption coefficient of Li-7 was measured and found to be 0.09 cm^{-1}, giving a small absorption correction that is essentially independent of scattering angle. Diffraction patterns of liquid Li-7 were taken at 180°C (melting point 179°C) and at 400°C. After correction for empty-cell scattering, these patterns showed marked depressions from constant intensity at large angles, but as in the case of liquid helium[9] when the experimental points were corrected for scattering by a free atom, i.e., changed from laboratory to center-of-mass coordinates, the large-angle scattering approached essentially constant intensity, as directly observed with the heavier atoms such as rubidium or cesium. This is evidence that in these diffraction experiments with light atoms, recoil of the target nucleus is significant and that scattering of neutrons by light atoms in the liquid state appears to be as if the atoms were free. Figure 1 shows the pattern for liquid Li-7 at

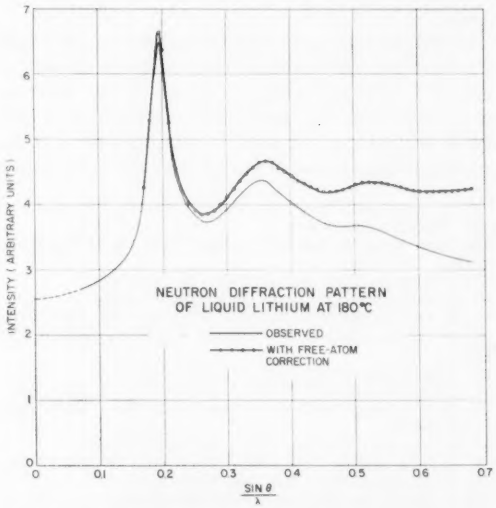

Fig. 2. Neutron diffraction pattern of liquid lithium at 180°C.

180°C along with other patterns for comparison, and Fig. 2 shows the Li-7 pattern before and after the correction for free-atom scattering.

Sodium

Diffraction patterns were taken of liquid sodium at 100°C (melting point 97.8°C). Figure 1 shows the 100°C sodium pattern. When corrected for empty-cell scattering alone, intensities at large scattering angles fell along a line slightly depressed below that for isotropic scattering, but correction for scattering from free atoms, raised the large-angle scattering to essentially constant intensity as had been found for liquid helium[9] and liquid lithium. Peak positions were found at $(\sin\theta)/\lambda$ of 0.163 A^{-1}, 0.295 A^{-1}, and the pattern is generally similar to what is expected from the early work with x rays.[3]

Potassium

Of all the alkali metals, liquid potassium gave the weakest pattern of coherent intensity and it was studied at only one temperature, 65°C, just above the melting point of 63.7°C. Figure 1 shows the corrected intensity pattern for potassium at 65°C, the free-atom correction for potassium amounts to only a few percent at the maximum observed value of $(\sin\theta)/\lambda$ and was neglected for the heavier atoms. Intensity peaks for potassium were found at $(\sin\theta)/\lambda=0.130$ A^{-1}, 0.24 A^{-1}, and 0.36 A^{-1}, the intensity beyond 0.405 A^{-1} was assumed to be essentially constant. Peak positions are in approximate agreement with those obtained[4] with x rays.

Rubidium

This material proved to be the most intense neutron scatterer of all the alkali metal liquids and it was chosen as the subject of an intensive study of the effect of temperature on its diffraction pattern. Patterns were obtained at ten different temperatures from 40°C to 575°C and Fig. 3 shows patterns at 40°C (melting point 39°C), 160°C, 240°C, and 360°C, plotted to an intensity scale in arbitrary units. At 40°C, peaks occur at $(\sin\theta)/\lambda=0.122$ A^{-1}, 0.223 A^{-1} and 0.34 A^{-1}. No reproducible intensity fluctuations could be found beyond $(\sin\theta)/\lambda=0.46$. Corrections to the patterns were made for empty-cell scattering. These patterns show that as the temperature is increased the innermost diffraction peak shifts slightly toward smaller $(\sin\theta)/\lambda$ values while the outermost peak, though somewhat diffuse, shows a definite shift to larger values of $(\sin\theta)/\lambda$.

Cesium

Figure 4 shows the observed intensity curves corrected for empty-cell background for cesium (melting point 28.5°C) at 30°C, 300°C, and 575°C. At 30°C,

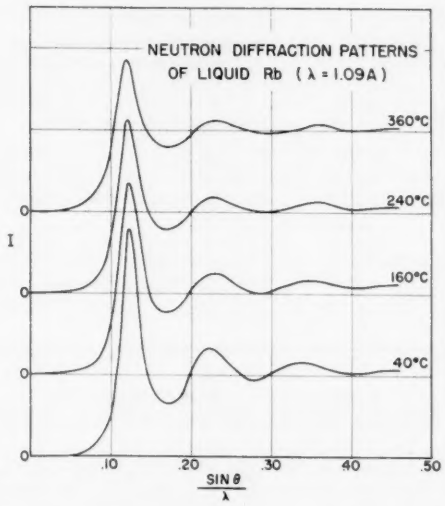

FIG. 3. Neutron diffraction patterns of liquid rubidium ($\lambda=1.09$ A).

peaks occur at $(\sin\theta)/\lambda$ values of 0.117 A^{-1}, 0.213 A^{-1}, 0.31 A^{-1}, and 0.41 A^{-1}. Beyond $(\sin\theta)/\lambda=0.50$ A^{-1} no reproducible fluctuation in intensity could be found, and it was therefore assumed that beyond this point the intensity was constant. The fourth peak was very weak but repeated runs established it as shown. At 300°C, intensity peaks were found at $(\sin\theta)/\lambda=0.113$ A^{-1}, 0.215 A^{-1}, 0.31 A^{-1} and approximately 0.4 A^{-1}. The pattern at 575°C has weak peaks at $(\sin\theta)/\lambda=$ 0.109 A^{-1} and 0.22 A^{-1} and a trace of a very weak rise just beyond 0.4 A^{-1}. These data show the same type of peak-position temperature-dependence for cesium, as was observed for rubidium.

ANALYSIS OF DIFFRACTION PATTERNS

The experimental patterns were analyzed to determine the atomic distributions as in previous analyses,[5–11] using the method worked out by Zernike and Prins,[12] and Debye and Menke.[13] The form of the equation used is

$$4\pi r^2\rho(r)=4\pi r^2\rho_0+(2r/\pi)\int_0^{s_0} si(s)\sin(rs)ds\ldots, \qquad (1)$$

where r is the distance from any atom-center within the liquid, $\rho(r)$ is the actual density of atoms, in atoms/A^3, at distance r from the origin atom. The average density of atoms is ρ_0, $s=4\pi(\sin\theta)/\lambda$ and $i(s)$ is a function of the corrected experimental intensity. For neutron patterns,

$$i(s)=[I(s)-c]/(k-c)-1,$$

[12] F. Zernike and J. Prins, Z. Physik **41**, 184 (1927).
[13] P. Debye and H. Menke, *Ergebnisse der Techische Rontgenkunde*. II (Akademische Verlagsgesellshaft, Leipzig, 1931), p. 1.

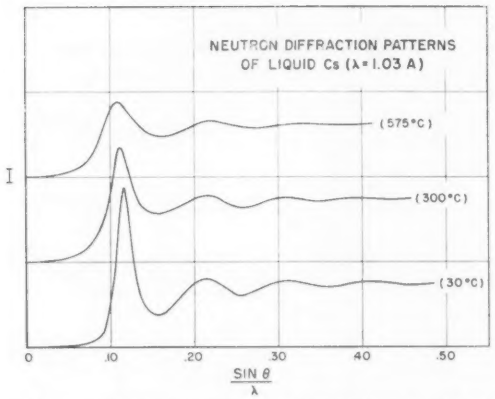

FIG. 4. Neutron diffraction patterns of liquid cesium ($\lambda = 1.03$ A).

where $I(s)$ is the observed intensity corrected for effects for which corrections are known, k is the constant intensity at large angles where interference effects can no longer be observed, and c is a factor which is introduced for the purpose of allowing for effects which are independent of angle, but which cannot be easily calculated. Assuming $I(s)$, k and c have been found, it is then a matter of straightforward calculation to determine $4\pi r^2\rho(r)$, the atomic distribution function, which was done with the Argonne National Laboratory computer, GEORGE.

In all these determinations it is recognized that the correctness of the results is limited by the precision of the experimental data and the validity of the corrections and the analyses. One source of uncertainty arises from the fact that in Eq. (1), the upper limit of the integral should be infinity, but for obvious practical reasons, it must be some finite value, which is designated s_0. In practice, scattering was observed to as large an angle as possible and successive runs were made in an attempt to establish the upper limit of s beyond which no reproducible fluctuations of intensity could be observed. Beyond this point $I(s)=k$ and $i(s)=0$. To determine the constant c, the experimental data were taken to as small angles of scattering as could be made without encountering the incident beam, and the curve was extended arbitrarily to zero angle. The intensity at zero angle was taken to be the constant c which represents angularly independent intensity such as that from incoherent scattering. Since this constant was not assigned with assurance of its correctness, in a number of cases, several values were tried in an attempt to learn how sensitive the results were to the choice of c. In all cases tried, changing c did affect the shapes of the distribution curves but for changes in c that appeared reasonably possible, alterations in the resulting curves were not severe.

The assignment of k is more straightforward except for the fact that it is often difficult to determine from the last weak observable oscillations of intensity, exactly where the intensity is to be considered to have reached a constant value. A guide to the choice of this curve-fitting is available in the criterion that

$$\int_0^{s_0} s^2 i(s)\,ds = -2\pi^2\rho_0,$$

and in a number of cases this condition was used to help in finding satisfactory fittings.

Since the ratio $(k-c)/c$ is a measure of the ratio of coherent to incoherent neutron scattering for the liquids studied, this ratio is useful to know and for the liquids at temperatures just above melting, it is as follows: 0.7 for Li^7; 1.5 for Na; 1.0 for K; 22 for Rb, and 3.7 for Cs.

Atomic Distributions

Figure 5 shows the atomic distributions for all the alkali metals at temperatures slightly above their melting temperatures and Table I lists data for these metals, some taken from the curves of Fig. 5. These five atomic distribution curves are similar in their general features, all showing that the nearest neighbors are not discrete or permanent. The numbers of nearest neighbors, measured similarly and rounded off to the closest one-half atom, vary between 9.0 and 9.5. The differences are probably due to errors in the experimental data or in the analyses. Positions of the first

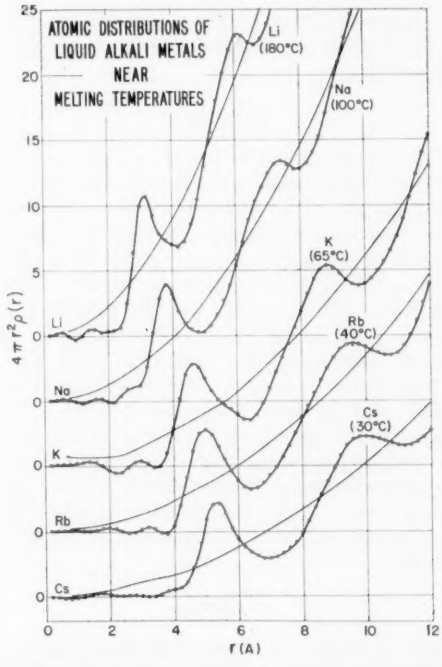

FIG. 5. Atomic distributions of liquid alkali metals near melting temperatures.

TABLE I.

Element	Melting point (°C)	Density (atoms/A³)	First intensity peak $(\sin\theta)/\lambda$	Nearest-neighbor distance A	Number of nearest neighbors
Lithium	179	0.04373 (180°C)	0.195	3.15	9.5
Sodium	97.8	0.02430 (100°C)	0.163	3.82	9.0
Potassium	63.7	0.01276 (65°C)	0.131	4.64	9.0
Rubidium	39.0	0.01078 (40°C)	0.122	4.97	9.5
Cesium	28.5	0.00813 (30°C)	0.117	5.31	9.0

peak are in general agreement with corresponding values obtained for the liquids by x rays.

The present results obtained with liquid lithium are considered to be much more reliable than those from the early work using x rays in which case uncertainties were introduced by using an unusually large sample, by the large incoherent correction, by the use of the photographic method, and perhaps by products of corrosive effects of the sample material upon the cell. In the case of liquid sodium, the position of the first peak in the distribution curve as determined here is, within experimental error, the same as found in the early x ray work. The weak diffraction pattern from potassium was nevertheless sufficiently well-determined to give a distribution curve whose appearance is generally similar to those for the other alkali metals. It seems probable that in the case of potassium, x-ray work using modern techniques can supply results that are more reliable than those reported here. Figure 6 shows the atomic distributions for liquid rubidium at temperatures of 40°C, 160°C, 240°C, and 360°C. The first peak has its maximum value at 4.97 A. If a discrete peak is constructed with the slope of the curve above 4.97 A, drawn symmetrically with that below 4.97 A, the area under the curve represents a concentration of about 9.5 atoms as nearest neighbors. Early attempts to determine the effect of temperature on the distribution curves for rubidium gave, at intermediate and high temperatures, an indication of what appeared to be the gradual introduction of a secondary peak at distances just beyond the first peak. To check on this effect, diffraction patterns were taken at several temperatures without altering other experimental conditions. At 80°C and at 120°C, the distribution curves (not shown) are essentially the same as at 40°C except for slight suppression of prominences. However, at 160°C, 240°C, and 360°C, Fig. 6 shows what appears to be the progressive development of a subsidiary peak in the neighborhood of just under 6 A. If this weak subsidiary peak is due to finite termination of the integral in Eq. (1), one would normally expect each major peak in the curve to be bracketed by one or more pairs or ripples, but the points between $r=0$ and the first peak do not show ripples large enough to account for this extra peak as the result of termination errors. An attempt was made to see whether less emphasis on the relatively poorly determined, last weak peak of the diffraction pattern, might reduce the prominence of this subsidiary peak on the distribution curve. This was done by applying to the $i(s)$ function, a modifying factor of the form $\exp-(A\sin^2\theta)$ where A was chosen to reduce the height of the last peak to one-third of its experimentally determined value. This factor was tried with several sets of data and in all

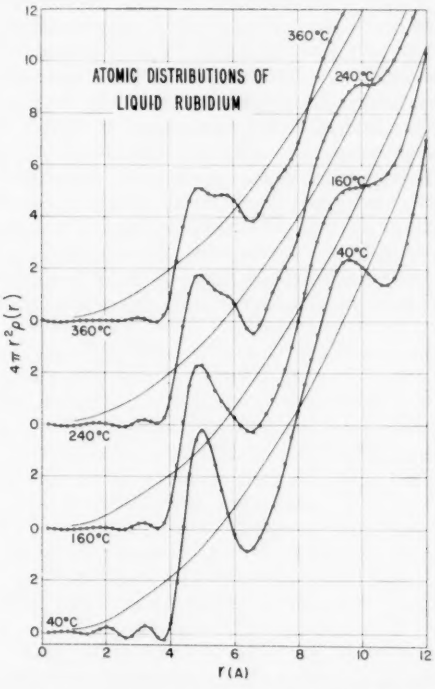

FIG. 6. Atomic distributions of liquid rubidium.

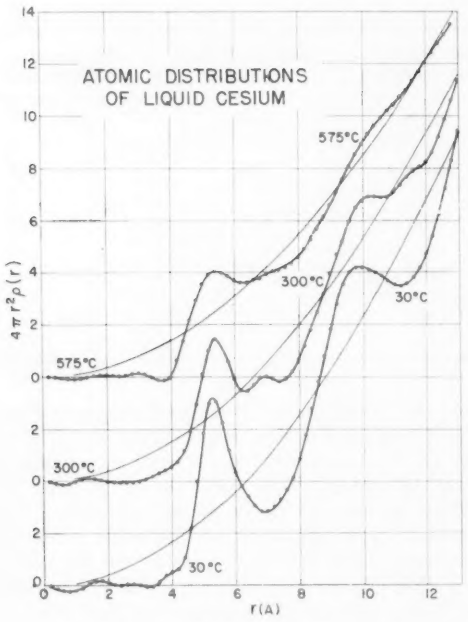

FIG. 7. Atomic distributions of liquid cesium.

cases the subsidiary peak remained in about the same amount relative to the first peak. Repeated runs sometimes gave slight differences in the form of the extra peak, but it always appeared at temperatures above 160°C. Fig. 7 shows the curve of $4\pi r^2\rho(r)$ as a function of r for cesium at 30°C, 300°3, and 575°C. The concentration of nearest neighbors is represented by the first peak whose maximum value occurs at 5.31 A and whose area represents approximately 9.0 atoms. At 300°C this first peak has shifted to about 5.4 A and at 575°C it is a little higher than 5.4 A. As in previous work with liquids of this kind, elevated temperatures tend to produce distribution curves with peaks and valleys that are less prominent than those at lower temperatures. The 300°C distribution curve for cesium also shows the introduction of a subsidiary peak at distances just beyond the first peak as did the rubidium curves.

SUMMARY

Neutron diffraction patterns have been obtained for the alkali metals lithium, sodium, potassium, rubidium, and cesium in the liquid state at temperature just above melting in each case, and at selected elevated temperatures for some of them. To facilitate intercomparison of patterns from these similar liquids, the experimental technique was nearly identical in all cases, including sample containment, temperature heating and control, neutron beam monochromatization and collimation, and detection and measurement of diffracted intensities. Corrections were found necessary and satisfactory for free-atom recoil in the cases of lithium and sodium, but negligible for heavier atoms. From these corrected patterns, atomic distribution curves were computed showing general agreement with earlier work with x rays for those materials which had been studied. Consideration of advantages and disadvantages of neutrons compared to x rays, leads to the estimate that of those elements studied with both radiations, neutrons are definitely superior in the case of lithium, x rays are superior with potassium, and for sodium, either radiation leads to results whose reliability is roughly equivalent. With the best coherent scatterer for neutrons, rubidium, patterns taken at several temperatures gave distribution curves which showed at elevated temperatures what appears to be a progressive development of a weak subsidiary peak in the distribution curves at distances between the first and second peaks. A similar effect was observed with cesium but not for the lighter elements in the range of temperature studied.

ACKNOWLEDGMENTS

We wish to express our appreciation to Dr. S. S. Sidhu, in whose laboratory this work was performed, for his interest in this problem and to D. D. Zauberis for his assistance with instrumentation and data collection.

Transients in the Blue and Green Luminescence of ZnS:Cu:Cl Crystals

A. HALPERIN AND H. ARBELL

Department of Physics, The Hebrew University of Jerusalem, Jerusalem, Israel

(Received June 9, 1960)

Upon exciting the investigated ZnS crystals by the light of two wavelengths, 0.37 and 0.33 μ, in succession, their blue luminescence at low temperatures was found to rise to a maximum I_m from which it decayed to its normal steady value I_∞. The green luminescence band showed a similar effect above 170°K. A reduction in the degree of filling of the "blue" traps was found to take place during the decay of the transients at low temperatures. Results are discussed using a previously proposed energy model.

I. INTRODUCTION

SOME results of an investigation of the optical properties of ZnS crystals carried out in this laboratory, were described in previous communications.[1,2] The investigation included the blue and green luminescence, the thermoluminescence, and the photoconductivity of ZnS crystals activated with low concentrations of copper and chlorine. An energy scheme was then proposed,[2] which fitted the variety of experimental observations.

It is the aim of the present communication to report the observation of transient phenomena in the blue and green luminescence of the investigated crystals. The additional information may help towards a better understanding of the processes involved in the luminescence of sulfide phosphors.

II. EXPERIMENTAL AND RESULTS

The crystals used and the experimental arrangements, were the same as described previously.[1,2] Thus, only specific data regarding the experimental procedure will be given while describing the results.

A. Transitents

Upon exciting the crystal successively with the light of two suitably chosen wavelengths, λ_1 and λ_2, its luminescence upon the second excitation was found to rise steeply to a maximum, followed by a decay to the stationary value obtained by a single excitation with λ_2 light alone.

The effect obtained at liquid-air temperature with the blue component of the luminescence of ZnS is shown in Fig. 1. The curves describe the luminescence intensity as a function of time. Monochromatic light of about 20 A spectral half-width was used for the excitations, and by suitable attenuation of the light beam (using wire gauges), the intensity of the exciting light was made constant for the different excitations. The crystal in the vacuum cryostat was heated prior to the first excitation to about 600°K to remove any possible effects of former excitations. It was then cooled to liquid-air temperature and exposed to $\lambda_1=0.37\mu$ light (at time t_1, Fig. 1). The exciting light was kept on long enough for the luminescence to reach saturation. At time t_2 the 0.37-μ light was cut off and the crystal was kept for a constant time in the dark. At time t_3 it was exposed to $\lambda_2=0.331\mu$. The luminescence now reached a maximum I_m, after which it decayed to a value I_∞, equal to that obtained at saturation upon excitation with 0.331μ light alone. The ratio I_m/I_∞ was in this case 2.3. The recorded value of I_m was possibly somewhat limited by the slow response of the recorder ($\sim$1 sec). At t_4 (Fig. 1) the 0.331μ light was cut off. Upon now exciting the crystal again with 0.331μ, even after keeping it for a long period in the dark, the luminescence showed the usual saturation curve, rising gradually to the saturation value I_∞.

The rate of decay from I_m to I_∞ was found to depend on the intensity of the exciting light λ_2, being faster with more intense excitation. The ratio I_m/I_∞, however, was almost independent of the intensity of excitation.

All the investigated ZnS crystals exhibited this effect at low temperatures. The pair of wavelengths $\lambda_1=0.37\mu$, $\lambda_2=0.331\mu$, being the most effective. Other pairs, however, also showed the transient effect as shown in Fig. 2. Curve a gives the ratio I_m/I_∞ for different wavelengths λ_2, after the first excitation with $\lambda_1=0.37\mu$. It shows a sharp peak at 0.331μ with about 50 A half-width. Figure 2(b) shows the effect of different wavelengths λ_1, i.e., it describes the ratio I_m/I_∞ obtained upon excitation with $\lambda_2=0.331\mu$ after the first excitation with different wavelengths λ_1.

The effect becomes stronger at somewhat higher temperatures, and for the same crystal a value $I_m/I_\infty\sim7$ was reached at 200°K. At still higher temperatures this ratio decreases, and the blue transients disappear at below room temperature.

The wavelength $\lambda_2=0.331\mu$ was the most effective in producing the transients at 80°K [Fig. 2(a)]. At higher temperatures there is a shift towards longer wavelengths. This is shown in Fig. 3, where the transients after excitation with $\lambda_1=0.366\mu$ are given for various wavelengths λ_2 at 80°K (curve a) and at 200°K (curve b). There is a shift of about 0.5 A/deg which seems to

[1] A. Halperin and H. Arbell, Phys. Rev. **113**, 1216 (1959).
[2] H. Arbell and A. Halperin, Phys. Rev. **117**, 45 (1960); also H. Arbell, Ph.D. thesis, The Hebrew University, Jerusalem, 1960.

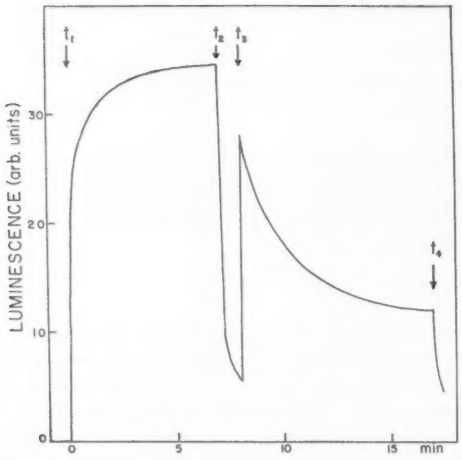

FIG. 1. Transients in the blue luminescence of ZnS at 80°K. First excitation, 0.37μ; second excitation, 0.331μ.

follow the shift with temperature of the absorption edge of the crystal.[3]

The green luminescence of the same crystal did not show the transients at liquid-air temperature. At higher temperatures the green component of most of the investigated crystals showed similar transients. Fig. 4 is similar to Fig. 2, but this time with regard to the green luminescence at 290°K. Curve a gives the ratio I_m/I_∞ as a function of λ_2 after excitation with $\lambda_1=0.40\mu$, while curve b describes this ratio as a function of λ_1 with $\lambda_2=0.342\mu$.

The transients in the green band appear at about 170°K and were even observed at above room temperature.

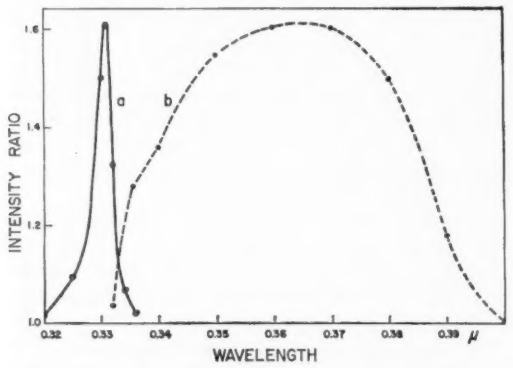

FIG. 2. Effect of different wavelengths on the transients in the blue luminescence at 80°K. (a) The ratio I_m/I_∞ as a function of wavelength of the second excitation, after first excitation with 0.37μ. (b) Effect of different wavelengths of the first excitation, with second excitation by 0.331μ.

[3] See for example C. K. Coogan, Proc. Phys. Soc. (London) **B70**, 845 (1957).

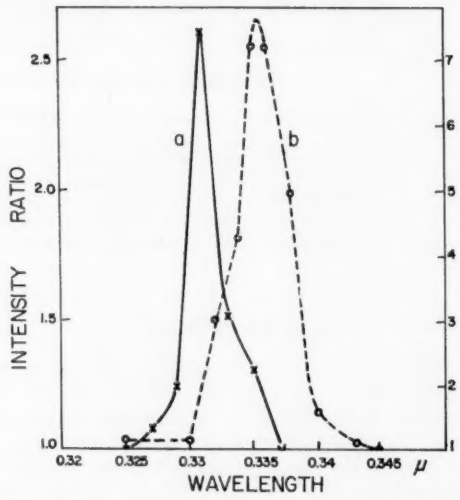

FIG. 3. Curve a (left scale), like curve a in Fig. 2 (at 80°K), curve b (right scale), the same at 200°K.

Some crystals which exhibited the described phenomenon in the blue component at low temperatures, showed at temperatures above 150°K, an inversed effect, i.e., transients appeared upon excitation with longer wavelengths ($\sim$0.37μ) after previous excitation with shorter wavelengths ($\sim$0.33μ). This inversed effect was comparatively weak, and was observed mainly in the green luminescence. The decay from I_m was very fast in this case, and the stationary value (I_∞) was usually reached within a few seconds.

B. Effects on the Thermal Glow

The glow curve of the investigated crystals is composed[2] of a blue peak at about 120°K, a green one at about 160°K, and another very weak, green, peak at above room temperature.

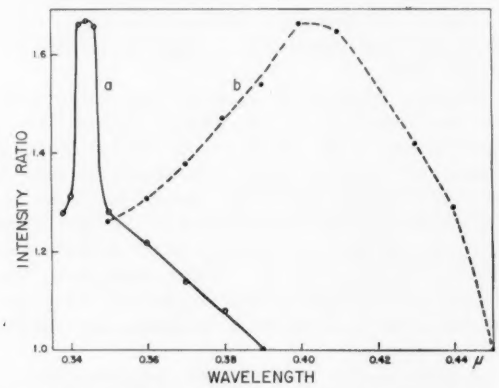

FIG. 4. Same as Fig. 2 except for the green luminescence band at 290°K. First excitation in curve a, 0.40μ; second excitation in curve b, 0.342μ.

More information on the processes involved in producing the transients was obtained from measurements of the intensities of the glow peaks produced by excitation with various wavelengths.

In one set of experiments the crystal was excited to saturation: (a) with 0.37μ alone, (b) with 0.331μ light of the same intensity, (c) with 0.37μ followed by a second excitation with 0.331μ light.

For the 160°K green peak, the light sums were found to be equal for the excitations a–c. For the blue peak, however, the light sums depended upon the manner of excitation. Upon excitation with 0.37μ (case a) the blue glow was three times as intense as that obtained with 0.331μ (case b). It is interesting to note that upon repeated excitation with 0.37 and 0.331μ (case c), the intensity of the blue peak was found to be reduced to the value corresponding to excitation with 0.331μ alone. It seems, therefore, that the second excitation does not affect the occupation of the green traps established by the first excitation. It changes, however, the occupation of the blue traps. The transients are thus obtained while the concentration of carriers in the blue traps, is changed from the state reached on the first excitation, to that corresponding to saturation by the second excitation. The factor 3 in the relative glow intensities obtained with 0.37μ and 0.331μ fits fairly well with the ratio $I_m/I_\infty = 2.3$, obtained for the same crystal and at the same conditions. The difference should be attributed partly to the slow response of the recorder, which tends to reduce the measured I_m value, and partly to self-decay which takes place at the time from the cutoff of the first excitation, to the exposure of the crystal to the second excitation.

At short exposures (far from saturation) the thermoluminescence excitation spectra were found (both for the blue and green components) to follow very closely,

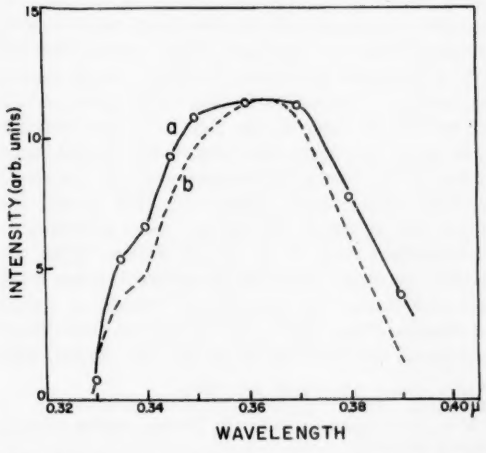

FIG. 5. Excitation spectra at saturation for the blue band. (a) For the 120°K thermoluminescence peak; (b) for the steady luminescence at 80°K.

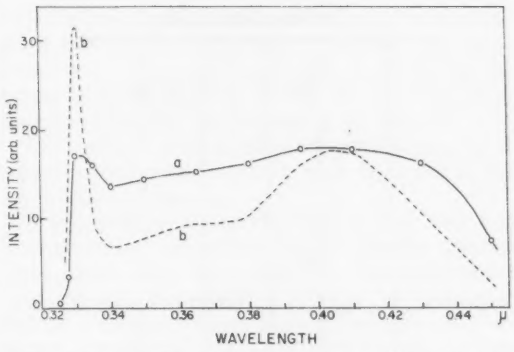

FIG. 6. Same as Fig. 5 for the green band. (a) For the 160°K peak; (b) for the steady luminescence at 80°K.

the corresponding steady luminescence excitation spectra.[2] The experiment described here indicated that this is not the case with the thermoluminescence excitation spectra obtained at saturation. Such spectra for the blue and green peaks were now taken with exposures about 10 times those needed to obtain saturation of the 120°K blue peak with 0.37μ, and of the 160°K green peak with 0.40μ light. The results are given in Figs. 5 and 6 for the 120 and 160°K peaks, respectively. The steady luminescence excitation spectra at 80°K are given for comparison.[4] The ordinates for the luminescence intensity were chosen to enable the two curves to fit at 0.365μ for the blue component (Fig. 5) and at 0.40μ for the green one (Fig. 6).

The thermoluminescence excitation spectrum for the blue peak [Fig. 5(a)] still closely follows that for the blue luminescence (curve b), except for some flattening near the maximum of the curve, which becomes more pronounced upon further prolongation of the exposures. Near the absorption edge at about 0.33μ, however, longer exposures do not seem to enhance the glow, which remains at this region much weaker than near the maximum at 0.365μ. The curve [Fig. 5(a)] very closely follows that obtained for the excitation of the transients in the luminescence [Fig. 2(b)].

For the green component, the thermoluminescence excitation spectrum upon saturation [Fig. 6(a)] is more greatly flattened. In fact it is nearly flat for the whole spectral range between 0.33 and 0.43μ. It is interesting to note the behavior at 0.33μ. At this wavelength, the crystal absorbs quite strongly, and the exciting light is practically wholly absorbed in a thin surface layer of the crystal. Nevertheless, the luminescence at this wavelength is much stronger than that at 0.40μ. The glow intensity at this wavelength, however, very nearly approaches the saturation value obtained for the longer wavelengths. This point will be further discussed later.

[4] The fine structure in the excitation spectra near the absorption edge (see footnotes 1 and 2) has been omitted in Figs. 5 and 6.

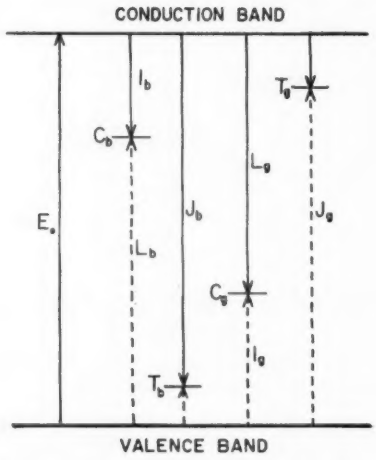

FIG. 7. Energy band model for the ZnS:Cu:Cl crystals.

III. DISCUSSION

In previous work[2] we came to the conclusion that the blue and green bands arise from two separate sets of traps and centers. It has also been shown that the excitation spectra for thermoluminescence were identical with those for the steady luminescence. This means that the intensity of luminescence changes parallel to the filling up of the related traps. One can understand this correlation only by assuming that the number of empty centers changes with that of full traps, so that the luminescence intensity depends, in fact, on the number of empty centers. This view fits the results obtained in the present work, and the transients can be explained as due to a reduction in the number of the empty centers which accompanies the reduction in the number of full traps during the second excitation.

We shall start discussing the transients in the blue luminescence at low temperatures. One of the two models proposed in the previous work (footnote 2, Fig. 8) seems a simpler way of explaining the present results. It is given in Fig. 7 with the additional transitions needed for the present discussion.

It consists essentially of an electron trapping level and a luminescence center for the green band (T_g and C_g, respectively), and a similar pair of a hole trapping level (T_b) and center (C_b) for the blue band. Electron transitions are indicated in Fig. 7 by full lines, and hole transitions by dashed lines.

Ultraviolet radiation of 0.365μ is assumed to produce mainly transitions $-L_b$, by which holes in the centers, C_b, are excited into the valence band (or levels near it). This radiation proves very effective for emptying the centers, and in subsequent trapping of the holes at T_b. Exposure now, of the well-excited crystal to 0.33μ radiation, results in the formation of free holes and free electrons (transition E_0 across the forbidden gap). The high mobility of electrons compared to that of holes,[5,6] makes the electron transitions J_b more probable than the hole transitions J_g. The former cause the number of holes trapped at T_b to be reduced. The balance between the number of trapped holes and that of the empty centers (see the foregoing), seems to be restored by transitions L_b, which give the blue luminescence during excitation, and by the competition between transitions J_b and I_b, of which only the latter add to the blue luminescence upon excitation across the gap (0.33μ). As a result the luminescence is reduced from I_m to I_∞, the value established by dynamic equilibrium, taking into account all the mentioned transitions.

The slow migration of the holes prevents similar effects (due to transitions I_g, J_g) in the green luminescence at low temperatures. This fits our experimental results, which show that the "green" traps (T_g) tend to be filled up to saturation by any wavelength between 0.33–0.43μ. The blue traps and centers seem to be in close connection, probably through excited levels very close to the valence band. This causes practically all the holes excited thermally from T_b, to recombine at the blue centers.[2] The existence of such levels was also indicated by the structure in the absorption[7] and in the excitation spectra[1] in this region.

The sharp drop in the thermoluminescence upon excitation below 0.33μ should be expected, as at these wavelengths, the excitation penetrates only a thin surface layer of the crystal, and thus only traps at that layer may contribute to the thermoluminescence. The drop in the steady luminescence is again, in accordance with the general behavior by which the luminescence intensity changes parallel to the thermoluminescence.

It is interesting to note at this point, that the green glow peak obtained by excitation with 0.33μ approaches the same saturation limit as that obtained upon excitation with longer wavelengths (see Fig. 6). This seems difficult to understand, remembering that 0.33μ radiation penetrates only a thin layer, which is small compared with the thickness of the crystal. The light sum of the green glow peak should be proportional to the number of traps contributing to the glow, and this can not be the same in the thin layer penetrated by 0.33μ, as it is in the whole bulk of the crystal, unless we assume that most of the green traps are located in the thin surface layer. Zalm *et al.* have shown[8] that copper-rich layers on the surface were necessary for electroluminescence. Such surface layers might also provide the main source for the green trapping levels. This proposition, however, is not enough to explain our results. First, light penetrating the bulk should activate all the outer layers around the crystal, while

[5] E. A. Kroger, Physica **22**, 637 (1956).
[6] J. Lambe and C. C. Klick, Phys. Rev. **98**, 959 (1955).
[7] V. A. Arkhangelskaya and P. P. Feofilov, Optika i Spectroskopia **2**, 107 (1957).
[8] P. Zalm, G. Diemer, and H. A. Klasens, Philips Research Repts. **9**, 81 (1954).

0.33μ can activate only the layer at the surface of incidence. Second, the fall in the blue luminescence and thermoluminescence upon excitation near the edge, indicates a bulk effect. It would then be difficult to see how 0.33μ which penetrates only a thin layer, can empty blue traps in the bulk, previously filled up by 0.37μ (see Results B). We therefore assume some mechanism of energy transfer. This should not necessarily involve a diffusion of carriers into the crystal. The short wavelength tail of blue luminescence which is effective in exciting the green band, penetrates into the bulk, and at very long exposures might fill up the green traps and partly empty the blue ones by the transitions described above (Fig. 7).

The transients at higher temperatures can not be related to the glow peaks at low temperatures. Those in the green luminescence may be related to the green glow above room temperature. This glow was, however, too weak for changes in its intensity to be measured. Similarly, the transients in the blue luminescence at higher temperatures, might be connected with a glow peak near room temperature. Such a glow was not observed, probably because of temperature quenching, which is strong for the blue luminescence near room temperature. It should be stressed that the transients at higher temperatures show a much faster decay compared to those at low temperatures, indicating that only a small number of traps are involved.

The appearance of transients in the green luminescence indicates that transitions J_g become more pronounced upon raising the temperature. This might be explained by the increase in the free hole migration upon increasing the temperature of the crystal.[9]

The inversed transient effect observed in the present work appeared rarely and in a weak form, and it will not be discussed now.

Transients also appear in other forms. The well known infrared stimulation and quenching of luminescence, often show initial bursts in the luminescence upon exposing the crystal to infrared, in addition to the uv radiation. Another form of transients was observed by Tolstoi and Feofilof.[10,11] These authors describe the so called "light flashes" obtained upon repeated excitation of certain phosphors with the *same* wavelength. The mechanism of these flashes seems to differ from that of the transients described in the present work, and our crystals did not show the light flashes either in the blue or in the green component of the luminescence.

---

[9] See, for example, G. F. J. Garlick, *Luminescent Materials* (Oxford University Press, New York, 1949), p. 103.

[10] N. A. Tolstoi and P. P. Feofilov, Doklady Akad. Nauk S.S.S.R. **68**, 285 (1949).

[11] N. A. Tolstoi, Doklady Akad. Nauk. S.S.S.R. **111**, 582 (1956). (English translation, Soviet Phys. Doklady **1**, 698 (1956–7).

Calculation of the Lower Excited Energy Levels of Helium

H. F. Hameka

Department of Chemistry, The Johns Hopkins University, Baltimore, Maryland

(Received July 7, 1960)

The energies of the 1^1S, 2^1S, 2^3S, 2^1P, and 2^3P states of helium have been calculated according to a method due to Pluvinage. It was shown that the Coulomb electronic repulsion term may be replaced by an effective potential function that accounts for first-order electronic repulsion effects on the wave functions. The deviations between calculated and experimental energy values vary between 0.01 and 0.06 a.u.

INTRODUCTION

ONE of the main difficulties for describing atomic systems is to find a suitable method to account for electron correlation effects. An interesting contribution to this problem was supplied by Pluvinage's calculation of the ground-state energy of helium.[1] In this case, it is known that the wave function depends only on the distances of the two electrons from the nucleus, r_1 and r_2, and on the interelectron separation u. Pluvinage observed that the Schrödinger equation (in atomic units) may be rewritten in this case as

$$(H^{(0)}+H^{(1)})\psi(r_1, r_2, u)=E\psi(r_1, r_2, u),$$

$$H^{(0)}=-(2r_1^2)^{-1}(\partial/\partial r_1)[r_1^2(\partial/\partial r_1)]$$
$$-(2r_2^2)^{-1}(\partial/\partial r_2)[r_2^2(\partial/\partial r_2)]$$
$$-(1/u^2)(\partial/\partial u)[u^2(\partial/\partial u)]$$
$$-(2/r_1)-(2/r_2)+u^{-1},$$

$$H^{(1)}=-\tfrac{1}{2}\left(\frac{r_1^2-r_2^2+u^2}{u r_1}\frac{\partial^2}{\partial r_1\partial u}+\frac{r_2^2-r_1^2+u^2}{u r_2}\frac{\partial^2}{\partial r_2\partial u}\right). \quad (1)$$

It is now profitable to treat $H^{(1)}$ as a perturbation since it is to be expected that the contribution of $H^{(1)}$ to the total energy is small. The ground-state eigenfunction and eigenvalue of the operator $H^{(0)}$ are

$$\Phi_0^{(0)}=F(1+\tfrac{1}{2}ik, 2, 2iku)\exp(-2r_1-2r_2),$$
$$E_0^{(0)}=-4+k^2, \quad (2)$$

where F denotes the confluent hypergeometric series.

By taking the function $\Phi_0^{(0)}$ as a trial function with parameter k for a variational calculation of the ground state energy of He, Pluvinage[1] obtained a value that is 0.026 a.u. higher than the experimental value.

A disadvantage of the Pluvinage method is the fact that it is difficult to evaluate integrals containing the confluent hypergeometric function F. In two recent papers,[2,3] it was pointed out that it is possible to set the parameter k of Eq. (2) equal to zero without affecting the result for the ground-state energy very seriously. In fact, the deviation in the energy value increased only from 0.026 to 0.029 a.u. If k is set equal to zero, the function $F(1+\frac{1}{2}ik, 2, 2iku)$ reduces to a Bessel function $J_1(2i\sqrt{u})/i\sqrt{u}$. The evaluation of the various integrals is now greatly facilitated and it may be possible to extend the method to more complicated systems.[3,4]

AN EFFECTIVE POTENTIAL

In the present paper a few changes in the mathematical formulation of the Pluvinage method will be suggested. It will be shown that this will lead to the introduction of a new effective potential function for the electron repulsion.

If, in the Hamiltonian of the He atom, the electron repulsion term is omitted, the solutions of this simplified system are

$$\psi_{n,m}^{(0)}=2^{-\frac{1}{2}}\{\psi_n(1)\psi_m(2)\pm\psi_m(1)\psi_n(2)\}\zeta(1, 2), \quad (3)$$

where $\zeta(1, 2)$ denotes the proper spin functions and ψ_n and ψ_m are hydrogenlike wave functions of nuclear charge 2. According to the works cited in footnotes 2 and 3, we assume that the various states of the He atom are described by the approximate wave functions

$$\psi_{n,m}=\psi_{n,m}^{(0)}J_1(2i\sqrt{u})/i\sqrt{u}. \quad (4)$$

The corresponding energy is

$$\frac{\langle\psi_{n,m}\,|\,H\,|\,\psi_{n,m}\rangle}{\langle\psi_{n,m}\,|\,\psi_{n,m}\rangle}=E_n+E_m+\frac{\langle\psi_{n,m}\,|\,G\,|\,\psi_{n,m}\rangle}{\langle\psi_{n,m}\,|\,\psi_{n,m}\rangle},$$

$$G=-u^{-1}\{(x_1-x_2)[(\partial/\partial x_1)-(\partial/\partial x_2)]$$
$$+(y_1-y_2)[(\partial/\partial y_1)-(\partial/\partial y_2)]$$
$$+(z_1-z_2)[(\partial/\partial z_1)-(\partial/\partial z_2)]\}(\partial/\partial u), \quad (5)$$

[1] P. Pluvinage, Ann. Phys. **5**, 145 (1950).

[2] L. Spruch and M. Kelly, Phys. Rev. **116**, 911 (1959).

[3] P. Walsh and S. Borowitz, Phys. Rev. **115**, 1206 (1959).

[4] P. Walsh and S. Borowitz, Phys. Rev. **119**, 1274 (1960).

TABLE I. Formulas of matrix elements of u^n.

$\langle(1s)_1(1s)_2 \mid u^n \mid (1s)_1(1s)_2\rangle$	$(1/3.4^{n+2})(n^2+10n+24)(n+2)!$
$\langle(1s)_1(2s)_2 \mid u^n \mid (1s)_1(2s)_2\rangle$	$\frac{1}{2}(n+1)!/81\{2^{-n+1}(9n^3+9n^2+114n-64)+2^{-2n-1}(45n+418)\}$
$\langle(1s)_1(2s)_2 \mid u^n \mid (2s)_1(1s)_2\rangle$	$(1/5.3^{n+9})32(n-2)n(n+4)(n+6)(n+2)!$
$\langle(1s)_1(1s)_2 \mid u^n \mid (1s)_1(2s)_2\rangle$	$(2048\sqrt{2}/2401)(n+1)!\{3^{-n-4}(-49n^2+406n-1944)+2^{-2n-2}(7n+96)\}$
$\langle(1s)_1(2p)_2 \mid u^n \mid (1s)_1(2p)_2\rangle$	$3^{-5}(n+1)!\{2^{-n+1}(9n^3+45n^2+162n+80)+2^{-2n-2}(30n+332)\}$
$\langle(1s)_1(2p)_2 \mid u^n \mid (2p)_1(1s)_2\rangle$	$-(32/5.3^{n+10})n(n+4)(n^2+14n+48)(n+2)!$

where the partial derivative operators act explicitly on the coordinates indicated. Integration by parts of each term with respect to the coordinate (x_1, x_2, etc.) occurring in the partial derivative operators of the matrix element G yields

$$\langle\psi_{n,m} \mid G \mid \psi_{n,m}\rangle = \langle\psi_{n,m}{}^{(0)} \mid V(u) \mid \psi_{n,m}{}^{(0)}\rangle$$

$$\langle\psi_{n,m} \mid \psi_{n,m}\rangle = \langle\psi_{n,m}{}^{(0)} \mid U(u) \mid \psi_{n,m}{}^{(0)}\rangle, \qquad (6)$$

where

$$U(u) = \{J_1(2i\sqrt{u})/i\sqrt{u}\}^2$$

$$V(u) = [\tfrac{1}{2}(\partial^2/\partial u^2)+u^{-1}(\partial/\partial u)]U(u). \qquad (7)$$

From the properties of Bessel functions[5] it follows easily that

$$U(u) = \sum_{n=0}^{\infty} \frac{(2n+2)!}{n!(n+1)!(n+1)!(n+2)!}u^n,$$

$$V(u) = \sum_{n=-1}^{\infty} \frac{(2n+5)!}{(n+1)!(n+2)!(n+2)!(n+4)!}u^n. \qquad (8)$$

In treating two-electron systems it is thus possible to account for electron repulsion by replacing the Coulomb potential function $(1/u)$ by $V(u)$ if the normalization operator 1 is simultaneously replaced by $U(u)$.

LOWER EXCITED STATES OF HELIUM

These results may now be applied to a calculation of the lower energy levels of helium. The wave functions that will be used are all defined by Eq. (4) and the orbital parts of the functions $\psi_{n,m}{}^{(0)}$ are, in the cases that will be considered,

$$(1s)_1(1s)_2$$

$$2^{-\frac{1}{2}}\{(1s)_1(2s)_2 \pm (2s)_1(1s)_2\}$$

$$2^{-\frac{1}{2}}\{(1s)_1(2p_z)_2 \pm (2p_z)_1(1s)_2\}, \qquad (9)$$

where the expressions between brackets denote hydrogenlike wave functions of nuclear charge 2 and the subscripts denote the coordinates.

The calculation of the various terms does not present serious difficulties. For example, let us outline the calculation of a matrix element containing $2p$ functions:

$$\int (1s)_1(2p_z)_2 u^n (1s)_1(2p_z)_2 d\tau_1 d\tau_2$$

$$= \int (1s)_1(2p_z)_2 u^n (1s)_1(2p_z)_2 r_1^2 r_2^2 \sin\theta_2 \sin\theta_{12} dr_1 dr_2 \times d\theta_2 d\theta_{12} d\phi_2 d\phi_{12}.$$

The integrations over θ_2, ϕ_2, and ϕ_{12} are performed first. The next step is to replace the integration over θ_{12} by an integration over u and substitute $s=r_1+r_2$ and $t=r_1-r_2$. The integral is then reduced to

$$(2/3)\int_0^{\infty} u^{n+1}du \int_{-u}^{u} e^{-t}dt \int_u^{\infty} (s^2-2st+t^2)(s^2-t^2)e^{-3s}ds,$$

which yields an explicit expression in n.

According to this procedure, all matrix elements of

TABLE II. Calculated and experimental energy levels of helium. The quantities E' are obtained by mixing 1^1S and 2^1S states.

State	E_{calc}	E'_{calc}	E_{exp}
1^1S	−2.87462	−2.88926	−2.90372
2^1S	−2.14033	−2.09163	−2.14599
2^3S	−2.14285	...	−2.17525
2^1P	−2.06777	...	−2.12385
2^3P	−2.07905	...	−2.13318

[5] G. N. Watson, *A Treatise on the Theory of Bessel Functions* (Cambridge University Press, New York, 1945), p. 147.

TABLE III. Comparison with other calculations in which no adjustable parameters are employed. The differences between theoretical and experimental results are reported. ΔE_1 and $\Delta E'_1$ are obtained from Table II. ΔE_2 and $\Delta E'_2$ were obtained from hydrogenlike wave functions for nuclear charge 2 but containing no u, and ΔE_3 were obtained by Heisenberg.[a]

	ΔE_1	$\Delta E'_1$	ΔE_2	$\Delta E'_2$	ΔE_3
1^1S	0.02910	0.01446	0.15372	0.07328	...
2^1S	0.00566	0.05436	0.10964	0.15008	0.02585
2^3S	0.03240	...	0.05111	...	0.04747
2^1P	0.05608	...	0.14359	...	0.00158
2^3P	0.05413	...	0.08464	...	0.00319

[a] See footnote 6.

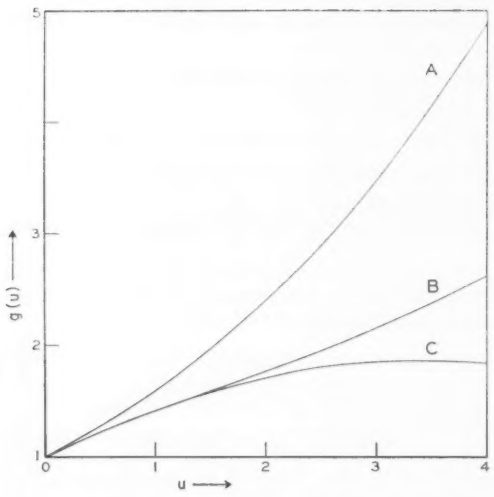

FIG. 1. Comparison of various correlation functions. Curve A represents the function $J_1(2i\sqrt{u})/i\sqrt{u}$, curves B and C are the numerical correlation functions obtained by Green *et al.* and by Roothaan and Weiss, respectively.

the functions $U(u)$ and $V(u)$ may be obtained as fairly rapidly converging infinite sums. For the states considered the formulas are relatively simple and are reported in Table I. The various energy levels, together with the experimental values, are listed in Table II. For the sake of completeness, the ground-state energy has been included also; it is equal to the value previously obtained by Walsh and Borowitz.[3]

The relatively good result for the 2^1S state is fortuitous and is due to the fact that the wave function is not orthogonal to the ground-state wave function. This defect may be removed by constructing a trial wave function as a linear combination of wave functions describing the 1^1S and 2^1S states. In evaluating the two roots of the corresponding secular equation, it has to be borne in mind that

$$\langle\psi_{n,m} \mid H \mid \psi_{n',m'}\rangle + \langle\psi_{n',m'} \mid H \mid \psi_{n,m}\rangle = (E_{n,m}+E_{n',m'})\langle\psi_{n,m}{}^{(0)} \mid U(u) \mid \psi_{n',m'}{}^{(0)}\rangle + 2\langle\psi_{n,m}{}^{(0)} \mid V(u) \mid \psi_{n',m'}{}^{(0)}\rangle. \quad (10)$$

The results of this calculation are reported in the third column of Table II.

DISCUSSION

In order to judge the relative merits of the present work, it may be helpful to make a comparison with other calculations where no adjustable parameters are employed. Such a comparison is made in Table III. On comparing the ΔE_1 and ΔE_2 values one may conconclude that the introduction of the function $J_1(2i\sqrt{u})/i\sqrt{u}$ in the wave function improves the accuracy of the calculations by a factor varying roughly between 2 and 5. On the other hand, the present results for P states seem to be less reliable than those obtained by Heisenberg[6] as early as 1926.

On the other hand, it is not entirely fair to base our comparisons only on the number of adjustable parameters in the wave functions, because the amount of work involved in computing the matrix elements of $U(u)$ and $V(u)$ is not much less than introducing a few parameters in the wave functions and minimizing with respect to the energy.

It may be interesting to compare the behavior of the function $J_1(2i\sqrt{u})/i\sqrt{u}$ (compare the work cited in footnote 7) with other correlation functions, in particular with the numerical correlation functions obtained by Green *et al.*[8] and by Roothaan and Weiss.[9] The three different functions are presented graphically in Fig. 1. It follows that for small u the three functions are quite similar whereas for larger u they start to diverge. However, the behavior of the correlation functions for large u is relatively unimportant since for that case the orbital functions become very small, so that the total wave function, which is a product of orbital and correlation functions, also becomes small.

Our results show that the modified Pluvinage method offers a relatively simple way to obtain moderately accurate energy values for the helium atom without the use of any adjustable parameters. It may prove to be useful to calculate quantities that depend strongly on u, such as spin orbit and spin-spin interactions. On the other hand, a significant improvement of the accuracy would involve very tedious calculations. A simple fashion for extending the method to more complicated systems has not yet been found, although promising attempts in that direction have been made in the works cited in footnotes 3 and 4.

By introducing an appropriate value for the nuclear charge Z, the formulas of Table I may easily be extended to calculations on He-like ions.

---

[6] W. Heisenberg, Z. Physik **39**, 499 (1926).

[7] M. Abremowitz, *Tables of Bessel-Clifford Functions of Orders Zero and One*, National Bureau of Standards, Applied Mathematics Series 28 (U. S. Government Printing Office, Washington, D. C., 1953).

[8] L. C. Green, C. Stephens, E. K. Kolchin, C. C. Chen, and P. P. Rush, J. Chem. Phys. **30**, 1061 (1959).

[9] C. C. J. Roothaan and A. W. Weiss, Revs. Modern Phys. **32**, 194 (1960).

Dimensional Change of Polypeptide Molecules in the Helix-Coil Transition Region. II

KAZUO NAGAI

The Osaka Industrial Research Institute, Daini-Nishi-2 Chome, Oyodoku Osaka, Japan

(Received August 29, 1960)

The mean-square end-to-end distance $\langle R^2 \rangle$ and radius of gyration $\langle S^2 \rangle$ are calculated for polypeptide molecules in the helix-coil transition region. The helical content, the sequence length distributions of helical and randomly coiled sections, etc., are also calculated for illustration. The statistical mechanical model on which the present calculation is based, is essentially equal to the second models in Gibbs-DiMarzio's and Zimm-Bragg's theories, respectively, though formulation is made on a more general model for the two purposes, i.e., for some convenience in calculating various quantities and for an examination of the degree of approximation of the above model. As a result, this model is found to be very satisfactory in spite of its simplicity. In order to calculate chain dimensions, two configurational models are examined. The one (model I), is somewhat rigorous, account being taken of the effects of bond lengths, bond angles, and hindered rotations. Two kinds of residues, i.e., those involved in helical sections, and those in randomly coiled sections, are distinguished by assigning different internal rotational potentials. The other (model II), is more approximate but more tractable. It can be obtained by replacing a helical section by a rod with an appropriate length and a randomly coiled section by an appropriate random flight chain. Numerical computations show that the two models give very close results for the infinitely long chain in the region where essential dimensional change occurs. By using model II, the effects of statistical mechanical parameters on $\langle R^2 \rangle$ are examined in detail. As a result, for example, it is shown that the larger the mean number of residues involved in a helical section becomes, the larger $\langle R^2 \rangle$ becomes, even if the helical content remains unchanged. For large N (e.g., $N>300$), as chain configurations go from randomly coiled to rodlike, $\langle R^2 \rangle$ and $\langle S^2 \rangle$ first decrease, pass through a minimum, and then increase until they reach the values for the perfect α helix. The appearance of this minimum is due to the considerably extended local configuration of randomly coiled residues. Namely, the appearance of a short helical section, turns the extended configuration to the folded one of the α helix and hence the polymer chain shrinks.

I. INTRODUCTION

FOLLOWING the announcement in the previous paper[1] (I) of this series, theoretical curves are drawn for the mean-square end-to-end distances of polypeptide molecules in the helix-coil transition region. In addition, the scope of the theory is considerably broadened by including more general cases and by calculating several other quantities which are required for full understanding of results and experimental test of the theory. First, the theory is extended to take into account the effect of degree of polymerization (D.P.) or the end effect, by using a simple configurational model (we shall refer to this as model II) introduced in the Note of I. Although the importance of this effect on statistical mechanical behaviors of polypeptide chains has been well known experimentally[2] and theoretically,[3,4] and further, that on chain dimensions was already pointed out in I (p. 414), it was neglected in I because of mathematical difficulty in calculating the mean-square end-to-end distance by using the more rigorous configurational model (model I) on which the calculation of I was based. This effect is found to be serious and especially so, as can be anticipated, when the transition inclines to the helix side where essential dimensional change occurs. The two configurational models for polypeptide chains are numerically compared with each other for the infinitely long chain, by using reasonable values for parameters involved, in order to examine the usefulness and the range of validity of model II and hence justify our succeeding results and discussions derived using model II.

Second, it is obvious that in some range of the helix side of the transition region, polypeptide chains possess a configuration which is neither randomly coiled nor rodlike, and which therefore does not obey, of course, Gaussian statistics or any other simple one. The mean-square end-to-end distance, though it is nevertheless possible to calculate it, cannot then be compared with experimental data, since any simple relation does not hold between it and $P(\theta)$ in light scattering (or the mean-square radius of gyration), in contrast with the cases of a random coil and a perfect rod. The mean-square radius of gyration, therefore, is also calculated, since it appears in the coefficient of $(2\sin\theta/2)^2$ in $P(\theta)$, in the special case where the refractive index increments of helical and randomly coiled residues happen to be equal. When this is not the case, the coefficient, though it is still also not impossible to calculate it, becomes more complicated and also loses its definite physical meaning.

A few other quantities such as the helical content, the sequence length distribution, etc., are also calculated for comparison and full understanding of results obtained. The mechanism of the helix-coil transition has been one of the main objects of current theories[3–10]

[1] K. Nagai, J. Phys. Soc. Japan **15**, 407 (1960), hereafter referred to as I.
[2] P. Doty and J. T. Yang, J. Am. Chem. Soc. **78**, 498 (1956).
[3] J. H. Gibbs and E. A. DiMarzio, J. Chem. Phys. **30**, 271 (1959).
[4] B. H. Zimm and J. K. Bragg, J. Chem. Phys. **31**, 526 (1959).
[5] J. A. Schellman, Compt. rend. trav. lab. Carlsberg, Sér. chim. **29**, No. 15 (1955); J. Phys. Chem. **62**, 1485 (1958).
[6] T. L. Hill, J. Polymer Sci. **23**, 549 (1957).
[7] S. A. Rice, A. Wada, and E. P. Geidushek, Discussions Faraday Soc. **25**, 130 (1958).
[8] S. A. Rice and A. Wada, J. Chem. Phys. **29**, 233 (1958).
[9] A. Miyake, Busseiron Kenkyu **2–4**, 271 (1958).
[10] L. Peller, J. Phys. Chem. **63**, 1194, 1199 (1959).

and the discussion of itself does not need to be repeated here. However, between the mechanism of the transition and chain dimensions, there exist, as can be anticipated, very intimate relations, which is what we wish to elucidate in this paper.

Some overlap with I in some early parts should be allowed in order to make this paper self-contained. Further, some similarity with Zimm and Bragg's theory (Z–B's theory) in the construction of partition function, is inevitable since the method employed here is the matrix method, which was used in the development of their theory.

II. THEORY

Statistical Mechanical Model

First, we present the statistical mechanical model briefly since details have been already given in I. The repeating unit of a polypeptide chain is regarded as an amino acid residue (—CO—CHR—NH—). All the residues of a molecule are numbered as 1, 2, $\cdots$, N from the end, with a free carboxyl group. The state of the ith residue is described perfectly by the symbol μ_i, which is assumed to be one if the residue is *distorted* so as to form a helical section, and zero if it is *undistorted* or involved in a randomly coiled section. More precisely speaking, the term "distorted" means that the rotational angles around the three consecutive bonds N—C, C—C, and C—N of a residue, are equal to those characteristic of the α helix. The peptide nitrogen atom of the ith residue is assumed to be hydrogen bonded to the peptide oxygen atom of the $(i+4)$th residue, if and only if, all the three residues put between them are *distorted* (See Fig. 1 of I). Then, an arrangement of the digits, zero and one, corresponds to a state of a polypeptide molecule. Here, we exclude two kinds of sequences, 010 and 0110, since these states are, though not impossible, physically unreasonable. Namely, only one or only two consecutive *distorted* residues do not cause any intramolecular hydrogen bond and, hence, there is no reason for these residues to be *distorted* in the loss of freedom. In the present model, we have also neglected the possibility of breaking of only one or only two consecutive hydrogen bonds, which does not disrupt the α helix. This approximation would be fairly good for the following reason. The helix-coil transition does not occur when a hydrogen bond breaks without any other decrease in free energy, but does occur when the increase in energy on the breaking of a hydrogen bond is balanced with some other decreases in free energy, e.g., the increase in entropy due to the increase in freedom of the skeletal chain and the decrease in free energy due to exchange reactions of hydrogen bonds with solvent molecules. These two affairs do not appear to occur if the structure of the α helix is tightly held.

Partition Function

We now construct the partition function by the matrix method. Generally speaking, when we wish to take into account the interaction among (at most) m consecutive (say) ith, $\cdots$, $(i+m-1)$th residues by this method, it is convenient to construct a transition probability matrix, each element of which denotes the probability ofo ccurrence of the affair that one of all states, $\mu_i \cdots \mu_{i+m-2}$, possible for the ith, $\cdots$, $(i+m-2)$th residues, is followed by one of all states, $\mu_{i+1} \cdots \mu_{i+m-1}$, possible for the $(i+1)$th, $\cdots$, $(i+m-1)$th residues. In our problem m equals four, since the sequence 0110 is the longest one among those within which the interaction must be taken into account. Seven possible sequences of $\mu_i\ \mu_{i+1}\ \mu_{i+2}$ to be considered are given by

111	α
101	γ_3
011	α_2
001	γ_1
110	α_1
100	γ_2
000	1.

The remaining one, 010, is omitted for the aforementioned reason. Our transition matrix, therefore, is of order seven.

It is found to be convenient to consider separately, the contributions to the partition function from the first and Nth residues and the rest put between them. As for the latter group, we assume the contributions to the parrition function (or the statistical weights) from the middle residues of the sequences, 111, 101, 011, 001, 110, 100, and 000, to be α, γ_3, α_2, γ_1, α_1, γ_2, and 1, respectively, as shown in the foregoing list; 1, assigned for the middle residue of the sequence 000, arises merely from the fact that the free energy of the perfect random coil is chosen as the standard of free energy. Here α measures the decrease in configurations of chain skeleton, accompanying the instance when a residue is *distorted* or brought from a perfect coiled section to the middle parts of a helical section. Here too, α_1 and α_2 are similar to α, except that they are assumed to include all unusual effects encountered at both ends of a helical section. They will appear in the pair, $\alpha_1\alpha_2$, in solutions of the present problem, since one helical section always has two ends. Further γ_1 and γ_2 are the contributions from two *undistorted* residues adjacent to both sides of a helical section, respectively, and γ_3 is the contribution from an *undistorted* residue adjacent to helical sections at both sides. These are probably smaller than unity because of various steric hindrances. Further, β is assumed to be

the contribution from the formation of an intramolecular hydrogen bond, including the effect on solvent molecules. Since three consecutive *distorted* residues always bring about one hydrogen bond, β appears always in the pair with α.

Our aim of adopting a somewhat complicated statistical mechanical model in this state, as compared with other authors,[3,4] is not a refinement of the models themselves but is of some convenience in calculation and in an examination of the degree of approximation of a simpler model, which will be employed in this paper soon and which has already been employed in those of other authors.[3,4]

The matrix associated with a residue belonging to the latter group can be chosen as

$$\mathbf{p}(\alpha, \cdots, \gamma_3) = \begin{pmatrix} \sigma & 0 & 0 & 0 & \alpha_1 & 0 & 0 \\ 0 & 0 & \alpha_2 & 0 & 0 & 0 & 0 \\ \sigma & 0 & 0 & 0 & 0 & 0 & 0 \\ 0 & 0 & \alpha_2 & 0 & 0 & 0 & 0 \\ 0 & \gamma_3 & 0 & 0 & 0 & \gamma_2 & 0 \\ 0 & 0 & 0 & \gamma_1 & 0 & 0 & 1 \\ 0 & 0 & 0 & \gamma_1 & 0 & 0 & 1 \end{pmatrix}, \tag{1}$$

where

$$\sigma = \alpha\beta. \tag{2}$$

The (k, l) element of the matrix, except for the (3, 5) element, equals the probability of occurrence of the lth state (numbered from the top in the foregoing list) among the seven sequences possible for three consecutive residues when the second and third digits of the kth sequence equal to the first and second digits of the lth sequence, respectively, and equals zero otherwise. The (3, 5) element, which produces the prohibited sequence 0110, is taken as zero.

We assume the contribution from the first residue, which can never be involved in a helical section, to be γ_c' when the second residue is *distorted*, or γ_c when it is *undistorted*. Then, the matrix associated with this residue is found to be

$\mathbf{p}_c(\gamma_c, \gamma_c')$ = the matrix whose (7, 4) element equals γ_c', (7, 7) element equals γ_c, and all other elements are zero. (3)

Similarly, the matrix associated with the Nth residue is

$\mathbf{p}_a(\gamma_a, \gamma_a')$ = the matrix whose (5, 6) element equals γ_a', (6, 7) and (7, 7) elements equal γ_a, and all other elements are zero. (4)

The meaning of γ_a and γ_a' is now obvious.

The partition function is given by

$$Z_N(\alpha, \cdots, \gamma_a') = SAE[\mathbf{p}_c(\gamma_c, \gamma_c')\{\mathbf{p}(\alpha, \cdots, \gamma_3)\}^{N-2} \times \mathbf{p}_a(\gamma_a, \gamma_a')], \tag{5}$$

where the symbol "SAE" denotes the sum of all elements of a matrix in the succeeding bracket.

To evaluate Eq. (5), it is convenient to expand $\mathbf{p}(\alpha, \cdots, \gamma_3)$ by its eigenvalues and eigenvectors. The characteristic equation of this matrix is found to be

$$\lambda^3(\lambda-\sigma)(\lambda-1) - \sigma\alpha_1\alpha_2\{\gamma_1\gamma_2 + \gamma_3(\lambda-1)\} = 0. \tag{6}$$

The five roots of this equation, or the eigenvalues, are denoted by $\lambda_1, \lambda_2, \cdots, \lambda_5$ in their order of magnitude, i.e., $\lambda_1 > \lambda_2 > \cdots > \lambda_5$. The doubly degenerate eigenvalue, zero, of the matrix, does not enter into our problem. On solving the relations

$$\mathbf{p}(\alpha, \cdots, \gamma_3)\mathbf{u}(\lambda) = \lambda\mathbf{u}(\lambda),$$

and

$$\mathbf{v}(\lambda)\mathbf{p}(\alpha, \cdots, \gamma_3) = \lambda\mathbf{v}(\lambda),$$

where

$$\lambda = \lambda_1, \lambda_2, \cdots, \lambda_5, \tag{7}$$

and

$$\mathbf{v}(\lambda_k)\mathbf{u}(\lambda_l) = \delta_{kl}, \qquad k, l = 1, 2, \cdots, 5, \tag{8}$$

where δ_{kl} is Klonecher's delta, we have, for normalized right-hand side and left-hand side eigenvectors,

$$\mathbf{u}(\lambda) = \left(1 \frac{\sigma\alpha_2}{\lambda^2} \frac{\sigma}{\lambda} \frac{\sigma\alpha_2}{\lambda} \frac{\lambda-\sigma}{\alpha_1} \frac{\sigma\alpha_2\gamma_1}{\lambda^2(\lambda-1)} \frac{\sigma\alpha_2\gamma_1}{\lambda^2(\lambda-1)}\right)^T, \tag{9}$$

and

$$\mathbf{v}(\lambda) = c(\lambda)\left(1 \frac{\alpha_1\gamma_3}{\lambda^2} \frac{\lambda-\sigma}{\sigma} \frac{\alpha_1\gamma_1\gamma_2}{\lambda^2(\lambda-1)} \frac{\alpha_1}{\lambda} \frac{\alpha_1\gamma_2}{\lambda^2} \frac{\alpha_1\gamma_2}{\lambda^2(\lambda-1)}\right), \tag{10}$$

where $\lambda = \lambda_1, \lambda_2, \cdots, \lambda_5$, and

$$c(\lambda) = \lambda^3(\lambda-1)\{5\lambda^4 - 4(1+\sigma)\lambda^3 + 3\sigma\lambda^2 - \sigma\alpha_1\alpha_2\gamma_3\}^{-1}. \tag{11}$$

Then the matrix $\mathbf{p}(\alpha, \cdots, \gamma_3)$ and hence $\{\mathbf{p}(\alpha, \cdots, \gamma_3)\}^{N-2}$ may be expanded as

$$\mathbf{p}(\alpha, \cdots, \gamma_3) = \sum_{\lambda} \lambda\mathbf{u}(\lambda)\mathbf{v}(\lambda), \tag{12}$$

and

$$\{\mathbf{p}(\alpha, \cdots, \gamma_3)\}^{N-2} = \sum_{\lambda} \lambda^{N-2} \mathbf{u}(\lambda)\mathbf{v}(\lambda), \quad (13)$$

where the summation must be taken over $\lambda = \lambda_1, \cdots, \lambda_5$. Since

$$SAE[\mathbf{p}_c(\gamma_c, \gamma_c')\mathbf{u}(\lambda)\mathbf{v}(\lambda)\mathbf{p}_a(\gamma_a, \gamma_a')] = \sigma\alpha_1\alpha_2\lambda^{-3}(\lambda-1)^{-1}\{\gamma_c'(\lambda-1)+\gamma_c\gamma_1\} \times \{\gamma_a'(\lambda-1)+\gamma_a\gamma_2\}c(\lambda), \quad (14)$$

we have, on inserting Eq. (13) into Eq. (15),

$$Z_N(\alpha, \cdots, \gamma_a') = \sum_{\lambda} \sigma\alpha_1\alpha_2\lambda^{N-2}(\lambda-1)^{-1}\{\gamma_c'(\lambda-1)+\gamma_c\gamma_1\} \times \{\gamma_a'(\lambda-1)+\gamma_a\gamma_2\}\{5\lambda^4-4(1+\sigma)\lambda^3+3\sigma\lambda^2-\sigma\alpha_1\alpha_2\gamma_3\}^{-1}. \quad (15)$$

Now we show how a quantity determined by states of some or all of the residues can be averaged over this partition function. All of the quantities encountered in the following have the form

$$f(\mu_1, \mu_2, \cdots, \mu_N) = f_1(\mu_1, \mu_2)\{\prod_{i=2}^{N-1} f_i(\mu_{i-1}, \mu_i, \mu_{i+1})\} f_N(\mu_{N-1}, \mu_N). \quad (16)$$

Remembering that each element of $\mathbf{p}(\alpha, \cdots, \gamma_3)$ represents the relative probability of a given residue being in a certain specified state, we find, for the required average

$$\langle f(\mu_1, \mu_2, \cdots, \mu_N)\rangle = \{Z_N(\alpha, \cdots, \gamma_a')\}^{-1} \times SAE[\mathbf{f}_1(\gamma_c, \gamma_c')\{\prod_{i=2}^{N-1} \mathbf{f}_i(\alpha, \cdots, \gamma_3)\}\mathbf{f}_N(\gamma_a, \gamma_a')], \quad (17)$$

where $\mathbf{f}_i(\alpha, \cdots, \gamma_3)$'s are given by

$$\mathbf{f}_i(\alpha, \cdots, \gamma_3) = \begin{vmatrix} \sigma f_i(1,1,1) & 0 & 0 & 0 & \alpha_1 f_i(1,1,0) & 0 & 0 \\ 0 & 0 & \alpha_2 f_i(0,1,1) & 0 & 0 & 0 & 0 \\ \sigma f_i(1,1,1) & 0 & 0 & 0 & 0 & 0 & 0 \\ 0 & 0 & \alpha_2 f_i(0,1,1) & 0 & 0 & 0 & 0 \\ 0 & \gamma_3 f_i(1,0,1) & 0 & 0 & 0 & \gamma_2 f_i(1,0,0) & 0 \\ 0 & 0 & 0 & \gamma_1 f_i(0,0,1) & 0 & 0 & f_i(0,0,0) \\ 0 & 0 & 0 & \gamma_1 f_i(0,0,1) & 0 & 0 & f_i(0,0,0) \end{vmatrix}$$

$$i = 2, \cdots, N-1, \quad (18)$$

and

$\mathbf{f}_1(\gamma_c, \gamma_c') = \mathbf{p}_c(\gamma_c, \gamma_c')$ with $\gamma_c f_1(0, 0)$ and $\gamma_c' f_1(0, 1)$ instead of γ_c and γ_c', respectively, and $\mathbf{f}_N(\gamma_a, \gamma_a') = \mathbf{p}_a(\gamma_a, \gamma_a')$ with $\gamma_a f_N(0, 0)$ and $\gamma_a' f_N(1, 0)$ instead of γ_a and γ_a', respectively. (19)

Though $f(\mu_1, \mu_2, \cdots, \mu_N)$ in Eq. (16) is a product of functions determined by states of three consecutive residues, we can, if necessary, average a product of functions of states of (at most) four consecutive residues.

Although $Z_N(\alpha, \cdots, \gamma_a')$ is a function of $\alpha, \beta, \cdots, \gamma_a'$, it is very troublesome to indicate this fact on $Z_N(\alpha, \cdots, \gamma_a')$, as we have done until now. Since we are, ultimately, only interested in the case where

$$\alpha_1 = \alpha_2 = \alpha,$$
$$\gamma_1 = \gamma_2 = \gamma_3 = \gamma_c = \gamma_c' = \gamma_a = \gamma_a' = 1, \quad (20)$$

let us introduce the following rule, i.e., α and β are not indicated explicitly since they are always involved; α_1 and α_2 are indicated explicitly only when they differ from α; $\gamma_1, \gamma_2, \cdots$, and γ_a' are indicated only when

they differ from unity. This rule is assumed to hold for $\mathbf{p}(\alpha, \cdots, \gamma_3)$, $\mathbf{p}_c(\gamma_c, \gamma_c')$, $\mathbf{p}_a(\gamma_a, \gamma_a')$, $\mathbf{f}_i(\alpha, \cdots, \gamma_3)$, $\mathbf{f}_1(\gamma_c, \gamma_c')$, and $\mathbf{f}_N(\gamma_a, \gamma_a')$.

In the special case described by Eq. (20), the eigenvalue equation, Eq. (6), reduces to

$$\lambda^2(\lambda-\sigma)(\lambda-1)=\sigma\alpha^2, \tag{21}$$

whose four roots are denoted newly by λ_1, λ_2, λ_3, and λ_4, in their order of magnitude. One root of Eq. (6) becomes zero, and hence does not again enter into our problem. Equations (9)–(11) and (15) become

$$\mathbf{u}(\lambda)=\left(1\frac{\sigma\alpha}{\lambda^2}\frac{\sigma}{\lambda}\frac{\sigma\alpha}{\lambda^2}\frac{\lambda-\sigma}{\alpha}\frac{\lambda-\sigma}{\alpha}\frac{\lambda-\sigma}{\alpha}\right)^T, \tag{22}$$

$$\mathbf{v}(\lambda)=c(\lambda)\left(1\frac{\alpha}{\lambda^2}\frac{\lambda-\sigma}{\sigma}\frac{\lambda-\sigma}{\sigma\alpha}\frac{\alpha}{\lambda}\frac{\alpha}{\lambda^2}\frac{\lambda-\sigma}{\sigma\alpha}\right), \tag{23}$$

$$c(\lambda)=\lambda(\lambda-1)\{4\lambda^2-3(1+\alpha)\lambda+2\sigma\}^{-1} \tag{24}$$

with $\lambda=\lambda_1$, λ_2, λ_3, λ_4, and

$$Z_N=\sum_{\lambda}\lambda^N(\lambda-\sigma)\{4\lambda^2-3(1+\alpha)\lambda+2\sigma\}^{-1}. \tag{25}$$

This simple statistical mechanical model is essentially equivalent to the second models in Gibbs and DiMarzio's (G–D's) and Z–B's theories, respectively. It seems to be the most reasonable one among those containing less parameters than three and hence is also adopted in this paper dealing with chain dimensions. We shall confine ourselves only to this model throughout, except where the degree of approximation to it will be examined.

Helical Content and Fraction of Intact Hydrogen Bonds

These quantities, although having been fully discussed by many authors, are again calculated here, since they bear a close relationship to our main subject in many respects, as will be seen in the following. These quantities can be expressed in two alternative forms, which we shall show first for the fraction of intact hydrogen bonds.

Since the number of intact hydrogen bonds may be expressed as

$$\sum_{i=2}^{N-1}\mu_{i-1}\mu_i\mu_{i+1},$$

and its maximum value is $N-4$, the fraction of intact hydrogen bonds, c_N, is given by

$$c_N=(N-4)^{-1}\sum_{i=2}^{N-1}\langle\mu_{i-1}\mu_i\mu_{i+1}\rangle. \tag{26}$$

On applying Eq. (17) to each term, we have

$$\langle\mu_{i-1}\mu_i\mu_{i+1}\rangle=Z_N^{-1}SAE[\mathbf{p}_c\mathbf{p}^{i-2}\sigma(\partial\mathbf{p}/\partial\sigma)\mathbf{p}^{N-i-1}\mathbf{p}_a], \tag{27}$$

or, on inserting $\mathbf{p}$ given by Eq. (12) into Eq. (27) and noticing the relations

$$\mathbf{v}(\lambda_k)\sigma(\partial\mathbf{p}/\partial\sigma)\mathbf{u}(\lambda_l)=\lambda_k c(\lambda_k), \tag{28}$$

and

$$SAE[\mathbf{p}_c\mathbf{u}(\lambda_k)\mathbf{v}(\lambda_l)\mathbf{p}_a]=(\sigma\alpha^2)^{-1}\lambda_k(\lambda_k-\sigma)\lambda_l^2(\lambda_l-\sigma)c(\lambda_l), \tag{29}$$

$$\langle\mu_{i-1}\mu_i\mu_{i+1}\rangle=Z_N^{-1}(\sigma\alpha^2)^{-1}\sum_{k,l}c(\lambda_k)c(\lambda_l)\lambda_k^2(\lambda_k-\sigma)\times\lambda_l^2(\lambda_l-\sigma)\lambda_k^{i-2}\lambda_l^{N-i-1}. \tag{30}$$

One form of c_N can be obtained by noticing

$$c_N=(N-4)^{-1}Z_N^{-1}\sum_{i=2}^{N-1}SAE[\mathbf{p}_c\mathbf{p}^{i-2}\sigma(\partial\mathbf{p}/\partial\sigma)\mathbf{p}^{N-i-1}\mathbf{p}_a]$$

$$=(N-4)^{-1}Z_N^{-1}\sigma(\partial Z_N/\partial\sigma)=(N-4)^{-1}(\partial\ln Z_N/\partial\ln\sigma). \tag{32}$$

On performing the calculation involved, we have

$$c_N=(N-4)^{-1}Z_N^{-1}\sum_{\lambda}\lambda^N\{Nc(\lambda)\zeta(\lambda)-I_1(\lambda)\}, \tag{33}$$

with

$$\zeta(\lambda)=(\lambda-\sigma)\{4\lambda^2-3(1+\sigma)\lambda+2\sigma\}^{-1} \tag{34}$$

and

$$I_1(\lambda)=2\lambda(\lambda-1)(\lambda-\sigma)(2\lambda^2-\sigma)\{4\lambda^2-3(1+\sigma)\lambda+2\sigma\}^{-3}. \tag{35}$$

The other form is obtained by inserting Eq. (30) into Eq. (26) and performing the summation over i,

$$c_N=(N-4)^{-1}Z_N^{-1}(\sigma\alpha^2)^{-1}\sum_{k,l}c(\lambda_k)c(\lambda_l)\lambda_k^2(\lambda_k-\sigma)\times\lambda_l^2(\lambda_l-\sigma)(\lambda_l-\lambda_k)^{-1}(\lambda_l^{N-2}-\lambda_k^{N-2}), \tag{36}$$

where the summation extends over k, $l=1, 2, 3, 4$. For the same k and l, $(\lambda_l-\lambda_k)^{-1}(\lambda_l^{N-2}-\lambda_k^{N-2})$ should be replaced by its limiting value, i.e.,

$$(\lambda_l-\lambda_k)^{-1}(\lambda_l^{N-2}-\lambda_k^{N-2})=(N-2)\lambda_k^{N-3}, \text{ when } k=l.$$

This promise is assumed to hold throughout this paper. For the infinitely large N, we have

$$c_\infty = c(\lambda_1). \tag{37}$$

The two expressions for c_N, Eqs. (33) and (36), are of course equal to each other, in spite of considerable difference in their superficial forms. The two methods described have merits and demerits, respectively. As is easily seen, for example, Eq. (36) has more systematic form, on the one hand, but contains more terms, on the other hand, than does Eq. (33). An essential advantage of the second method, however, is its wider applicability. Whereas the mean-square end-to-end distance can be calculated by both methods, the mean-square radius of gyration can be calculated, only by the second method.[21] Generally speaking, the first forms are useful for simple quantities such as c_N, but the second forms are preferable for complicated quantities, because of their compactness when both methods are applicable.

The helical content (or the fraction of *distorted* residues) is given by

$$\xi_N = (N-2)^{-1}\sum_{i=2}^{N-1}\langle\mu_i\rangle, \tag{38}$$

$\langle\mu_i\rangle$ is given by

$$\langle\mu_i\rangle = Z_N^{-1} SAE[\mathbf{p}_c\mathbf{p}^{i-2}\alpha(\partial\mathbf{p}/\partial\alpha)\,\mathbf{p}^{N-i-1}\mathbf{p}_a], \tag{39}$$

or, on using Eq. (29) and the relation

$$\mathbf{v}(\lambda_k)\alpha(\partial\mathbf{p}/\partial\alpha)\,\mathbf{u}(\lambda_l) = \lambda_l^{-1}\{\lambda_l\lambda_k+\lambda_k(\lambda_k-\sigma)+\lambda_l(\lambda_l-\sigma)\}c(\lambda_k), \tag{40}$$

$$\langle\mu_i\rangle = Z_N^{-1}(\sigma\alpha^2)^{-1}\sum_{k,l} c(\lambda_k)c(\lambda_l)\lambda_k(\lambda_k-\sigma)\lambda_l(\lambda_l-\sigma) \times\{\lambda_l\lambda_k+\lambda_k(\lambda_k-\sigma)+\lambda_l(\lambda_l-\sigma)\}\lambda_k^{i-2}\lambda_l^{N-i-1}. \tag{41}$$

After the same procedure as used for c_N, we find

$$\xi_N = (N-2)^{-1}(\partial\ \ln Z_N/\partial\ \ln\alpha) = (N-2)^{-1}Z_N^{-1}\sum_{\lambda}\lambda^N\{N\xi(\lambda)\zeta(\lambda)-I_2(\lambda)\}, \tag{42}$$

with

$$\xi(\lambda) = (\lambda-1)(3\lambda-2\sigma)\{4\lambda^2-3(1+\sigma)\lambda+2\sigma\}^{-1}, \tag{43}$$

and

$$I_2(\lambda) = 2\lambda(\lambda-1)(\lambda-\sigma)(6\lambda^2-8\sigma\lambda+3\sigma^2) \times\{4\lambda^2-3(1+\sigma)\lambda+2\sigma\}^{-3}, \tag{44}$$

or alternatively,

$$\xi_N = (N-2)^{-1}Z_N^{-1}(\sigma\alpha^2)^{-1} \times\sum_{k,l} c(\lambda_k)c(\lambda_l)\lambda_k(\lambda_k-\sigma)\lambda_l(\lambda_l-\sigma) \times\{\lambda_k\lambda_l+\lambda_k(\lambda_k-\sigma)+\lambda_l(\lambda_l-\sigma)\} \times(\lambda_l-\lambda_k)^{-1}(\lambda_l^{N-2}-\lambda_k^{N-2}). \tag{45}$$

For the infinitely large N, we have

$$\xi_\infty = \xi(\lambda_1). \tag{46}$$

Frequency of Alternations of Helical and Randomly Coiled Sections, and Sequence Length Distributions

First we calculate the former quantity. The mean number of alternations can be expressed as

$$\sum_{i=2}^{N-1}\langle\mu_{i-1}(1-\mu_i)\rangle$$

or

$$\tfrac{1}{2}\sum_{i=2}^{N-1}\langle\mu_{i-1}(1-\mu_i)+\mu_i(1-\mu_{i+1})\rangle. \tag{47}$$

On noticing the relation

$$\alpha(\partial\mathbf{p}(\alpha_2)/\partial\alpha_2)+\alpha(\partial\mathbf{p}(\alpha_1)/\partial\alpha_1) = \alpha(\partial\mathbf{p}/\partial\alpha) -\sigma(\partial\mathbf{p}/\partial\sigma), \tag{48}$$

we have, for the mean frequency of alternations, η_N,

$$\eta_N = \tfrac{1}{2}\{(\partial\ \ln Z_N/\partial\alpha)-(\partial\ \ln Z_N/\partial\sigma)\}, \tag{49}$$

which, according to Eqs. (32) and (42), becomes

$$\eta_N = \tfrac{1}{2}\{(N-2)\xi_N-(N-4)c_N\}. \tag{50}$$

It can be found that

$$\lim_{N\to\infty}\eta_N/N = (\lambda-1)(\lambda-\sigma)\{4\lambda^2-3(1+\sigma)\lambda+2\sigma\}^{-1}. \tag{51}$$

Next we proceed to calculate the distribution in numbers of residues involved in a helical section. Since the probability that the ith, $(i+1)$th, $\cdots$, and jth residues constitute just a $\nu_1(=j-i+1)$-helical section (i.e., a helical section containing just ν_1 residues) can be given by

$$\langle(1-\mu_{i-1})\mu_i\mu_{i+1}\cdots\mu_{i+\nu_1-1}(1-\mu_{i+\nu_1})\rangle,$$

the mean number of ν_1-helical sections, $L_N(\nu_1)$, is

written as

$$L_N(\nu_1)=\sum_{i=2}^{N-\nu_1}\langle(1-\mu_{i-1})\mu_i\mu_{i+1}\cdots\mu_{i+\nu_1-1}(1-\mu_{i+\nu_1})\rangle, \quad (52)$$

which, on remembering that μ_1 and μ_N are always zero, may be written as

$$L_N(\nu_1)=\sum_{i=2}^{N-\nu_1+2}\langle\mu_{i-1}\mu_i\cdots\mu_{i+\nu_1-2}\rangle$$

$$-2\sum_{i=2}^{N-\nu_1+1}\langle\mu_{i-1}\mu_i\cdots\mu_{i+\nu_1-1}\rangle+\sum_{i=2}^{N-\nu_1}\langle\mu_{i-1}\mu_i\cdots\mu_{i+\nu_1}\rangle. \quad (53)$$

The quantity $\langle\mu_{i-1}\mu_i\cdots\mu_{i+\nu_1-2}\rangle$, on the other hand, is given by

$$\langle\mu_{i-1}\mu_i\cdots\mu_{i+\nu_1-2}\rangle$$

$$=Z_N^{-1}SAE[\mathbf{p}_c\mathbf{p}^{i-2}\sigma^{\nu_1-2}(\partial\mathbf{p}/\partial\sigma)^{\nu_1-2}\mathbf{p}^{N-\nu_1-i+2}\mathbf{p}_a]$$

$$=Z_N^{-1}\sigma^{\nu_1-3}SAE[\mathbf{p}_c\mathbf{p}^{i-2}\sigma(\partial\mathbf{p}/\partial\sigma)\,\mathbf{p}^{N-\nu_1-i+2}\mathbf{p}_a]. \quad (54)$$

The first sum in Eq. (53), therefore, becomes

$$\sum_{i=2}^{N-\nu_1+2}\langle\mu_{i-1}\mu_i\cdots\mu_{i+\nu_1-2}\rangle=Z_N^{-1}\sigma^{\nu_1-2}(\partial Z_{N-\nu_1+3}/\partial\sigma). \quad (55)$$

The second and third sums are merely equal to Eq. (55) with ν_1+1 and ν_1+2, instead of ν_1, respectively. Thus we have

$$L_N(\nu_1)=Z_N^{-1}\{\sigma^{\nu_1-2}(\partial Z_{N-\nu_1+3}/\partial\sigma)-2\sigma^{\nu_1-1}(\partial Z_{N-\nu_1+2}/\partial\sigma)$$

$$+\sigma^{\nu_1}(\partial Z_{N-\nu_1+1}/\partial\sigma)\}$$

$$=Z_N^{-1}\alpha^2\sigma^{\nu_1-2}\sum_\lambda\lambda^{N-\nu_1}\{(N-\nu_1+1)(\zeta(\lambda))^2-I_3(\lambda)\}, \quad (56)$$

with

$$I_3(\lambda)=2\zeta(\lambda)\{4\lambda^2-3(1-\sigma)\lambda+2\sigma\}^{-1}$$

$$\times\{\zeta(\lambda)(6\lambda^2-3\lambda-3\sigma\lambda+\sigma)-2\lambda+\sigma\}. \quad (57)$$

It can be found that

$$\lim_{N\to\infty}\nu_1L_N(\nu_1)/N=\nu_1c(\lambda_1)(1-\sigma/\lambda_1)^{\nu_1-3}. \quad (58)$$

The expression for randomly coiled sections can be obtained similarly. On noticing the relation

$$\mathbf{v}(\lambda_k)(\partial\mathbf{p}(\gamma_2)/\partial\gamma_2)\{\mathbf{p}-\alpha(\partial\mathbf{p}/\partial\alpha)-(\partial\mathbf{p}(\gamma_1)/\partial\gamma_1)$$

$$-(\partial\mathbf{p}(\gamma_2)/\partial\gamma_2)-(\partial\mathbf{p}(\gamma_3)/\partial\gamma_3)\}^{\nu_0-2}(\partial\mathbf{p}(\gamma_1)/\partial\gamma_1)\mathbf{u}(\lambda_l)$$

$$=\mathbf{v}(\lambda_k)(\partial\mathbf{p}(\gamma_3)/\partial\gamma_3)\mathbf{u}(\lambda_l), \quad (59)$$

we have, for the mean number of ν_0-coiled sections,

$$M_N(\nu_0)=Z_N^{-1}[\partial Z_{N-\nu_0+1}(\gamma_3)/\partial\gamma_3]_{\gamma_3\to1}$$

$$=Z_N^{-1}\sum_\lambda\lambda^{N-\nu_0}\{(N-\nu_0+1)(\lambda-1)^2[(\zeta(\lambda)]^2$$

$$-I_4(\lambda)\}, \quad (60)$$

with

$$I_4(\lambda)=2(\lambda-1)^2(\zeta(\lambda))^2\{4\lambda^2-3(1+\sigma)\lambda+2\sigma\}^{-1}$$

$$\times\{10\lambda^2-6(1+\sigma)\lambda+3\sigma\}. \quad (61)$$

Also we have

$$\lim_{N\to\infty}\nu_0M_N(\nu_0)/N=\nu_0c(\lambda_1)\sigma\alpha^2(1/\lambda_1)^{\nu+3}. \quad (62)$$

Equations (60) and (62), although having been derived for $\nu_0\geq3$, are found to be valid for all ν_0's.

Equations (58) and (62) are similar to sequence length distributions encountered frequently in statistical theories of copolymers.[11] Now $\sigma/\lambda_1(1/\lambda_1)$ might be regarded as the probability of finding one *distorted* (*undistorted*) monomer being followed by another monomer of the same kind.

Finally, the mean values of ν_1 and ν_0 are given by

$$\langle\nu_1\rangle=(N-2)\xi_N/\eta_N, \quad (63)$$

and

$$\langle\nu_0\rangle=\{N-(N-2)\xi_N\}/(\eta_N+1), \quad (64)$$

which reduce to (in the limit of $N\to\infty$),

$$\langle\nu_1\rangle=(3\lambda_1-2\sigma)/(\lambda_1-\sigma), \quad (65)$$

and

$$\langle\nu_0\rangle=\lambda_1/(\lambda_1-1). \quad (66)$$

Mean-Square End-to-End Distances

Now we proceed to deal with our main subject, i.e., the calculation of mean-square end-to-end distances. For this purpose, two configurational models are used in the following.

Model I

In this model, account is taken of the effects of bond lengths, bond angles, and hindered rotations of skeletal polypeptide chains. The most useful method for describing end-to-end distances of any macromolecule by basic quantities characterizing its local configurations, is the one proposed first by Eyring,[12] which has recently been followed by many authors[13–16] for studying the

[11] See, for example, T. Alfrey, Jr., J. I. Bohrer, and H. Mark, *Copolymerization* (Interscience Publishers, Inc., New York, 1952).

[12] H. Eyring, Phys. Rev. **39**, 746 (1932).

[13] T. M. Birshtein and O. B. Ptitsyn, J. Tech. Phys. (U.S.S.R.) **29**, 1048 (1959). See also the many works of Russian researchers cited in this paper.

[14] S. Lifson, J. Chem. Phys. **29**, 80, 89 (1958); **30**, 964 (1959).

[15] K. Nagai, J. Chem. Phys. **30**, 660 (1959); **31**, 1169 (1959).

[16] C. A. J. Hoeve, J. Chem. Phys. **32**, 888 (1960).

chain dimensions of stereospecific polymers in solutions. Our point of view in applying this method to the present problem is that, for transformation matrices of *distorted* and *undistorted* residues (not the matrices appeared in the preceding sections, but the ones appearing in the expression for the end-to-end distance[1,15]) we should assign some different average matrices because of considerable differences in their mean configurations. We give here only the final expression for this model and the definition of symbols; its derivation has already been given in I.

The bond lengths of N—C, C—C, and C—N in each repeating unit, —NH(—CO—CHR—NH—)CO—, are represented by b_1, b_2, and b_3, and the supplements of the bond angles, ∠NCC, ∠CCN, and ∠CNC, by ω_1, ω_2, and ω_3, respectively. Here θ_1, θ_2, and θ_3 are assumed to be the internal rotational angles around N—C, C—C, and C—N, and are measured from the *trans* position in a direction such that the chain skeleton is twisted in the right-handed sense (see Fig. 2 in I).

For simplicity, rotations around all bonds are assumed to be independent. Then, the mean-square end-to-end distance $\langle R^2 \rangle$ can be expressed[1] as a sum of products of appropriate averages of such matrices as

$$\mathbf{A}(\theta_k, \omega_k) = \begin{pmatrix} \cos\omega_k & \sin\omega_k & 0 \\ \sin\omega_k \cos\theta_k & -\cos\omega_k \cos\theta_k & \sin\theta_k \\ \sin\omega_k \sin\theta_k & -\cos\omega_k \sin\theta_k & -\cos\theta_k \end{pmatrix}$$

$$k=1, 2, 3. \quad (67)$$

Averages of these matrices, of course, depend on whether a residue is *distorted* or *undistorted*, and hence are denoted as

$$\langle \mathbf{A}(\theta_k, \omega_k) \rangle = \mathbf{A}_{\mu,k}, \qquad k=1, 2, 3, \quad (68)$$

where μ has the same meaning as μ_i's. From $\mathbf{A}_{\mu,k}$'s we define furthermore:

$$\mathbf{A}_\mu = \mathbf{A}_{\mu,1}\mathbf{A}_{\mu,2}\mathbf{A}_{\mu,3}, \quad (69)$$

$$\mathbf{X}_\mu = (b_1^2+b_2^2+b_3^2)\mathbf{E} + 2b_1b_2\mathbf{A}_{\mu,1} + 2b_2b_3\mathbf{A}_{\mu,2} + 2b_1b_3\mathbf{A}_{\mu,1}\mathbf{A}_{\mu,2}, \quad (70)$$

$$\mathbf{Y}_\mu = b_3\mathbf{A}_{\mu,3} + b_2\mathbf{A}_{\mu,2}\mathbf{A}_{\mu,3} + b_1\mathbf{A}_{\mu,1}\mathbf{A}_{\mu,2}\mathbf{A}_{\mu,3}, \quad (71)$$

and

$$Z_\mu = b_1\mathbf{E} + b_2\mathbf{A}_{\mu,1} + b_3\mathbf{A}_{\mu,1}\mathbf{A}_{\mu,2}. \quad (72)$$

For the infinitely long chain, we find

$$\langle R^2 \rangle / N = [\xi(\lambda_1)\mathbf{X}_1 + \{1-\xi(\lambda_1)\}\mathbf{X}_0 + 2 \times \{\mathbf{Y}_1\mathbf{S}_{11}\mathbf{Z}_1 + \mathbf{Y}_1\mathbf{S}_{10}\mathbf{Z}_0 + \mathbf{Y}_0\mathbf{S}_{01}\mathbf{Z}_1 + \mathbf{Y}_0\mathbf{S}_{00}\mathbf{Z}_0\}]_{1,1}, \quad (73)$$

where

$$\mathbf{S}_{11} = c(\lambda_1)[\{\mathbf{A}_1^{-3} + (1-\sigma/\lambda_1)(\mathbf{A}_1^{-1}+\mathbf{A}_1^{-2})\}\mathbf{K} \times \{\mathbf{A}_1^{-3} + (1-\sigma/\lambda_1)(\mathbf{A}_1^{-1}+\mathbf{A}_1^{-2})\} - (\mathbf{A}_1^{-1}+\mathbf{A}_1^{-2}+\mathbf{A}_1^{-3}) - (1-\sigma/\lambda_1)(2\mathbf{A}_1^{-1}+\mathbf{A}_1^{-2})],$$

$$\mathbf{S}_{10} = c(\lambda_1)(\lambda_1-\sigma)\{\mathbf{A}_1^{-3} + (1-\sigma/\lambda_1)(\mathbf{A}_1^{-1}+\mathbf{A}_1^{-2})\}\mathbf{K} \times (\lambda_1\mathbf{E}-\mathbf{A}_0)^{-1},$$

$$\mathbf{S}_{01} = c(\lambda_1)(\lambda_1-\sigma)(\lambda_1\mathbf{E}-\mathbf{A}_0)^{-1}\mathbf{K} \times \{\mathbf{A}_1^{-3} + (1-\sigma/\lambda_1)(\mathbf{A}_1^{-1}+\mathbf{A}_1^{-2})\},$$

$$\mathbf{S}_{00} = c(\lambda_1)(\lambda_1-\sigma)(\lambda-1)^{-1} \times \{\mathbf{A}_1^{-3} - (\sigma/\lambda_1)\mathbf{A}_1^{-2} + (\sigma\alpha^2/\lambda_1^3)\mathbf{E}\}\mathbf{K}(\lambda_1\mathbf{E}-\mathbf{A}_0)^{-1}, \quad (74)$$

with

$$\mathbf{K} = \{\mathbf{A}_1^{-3} - (\sigma/\lambda_1)\mathbf{A}_1^{-2} - (\sigma\alpha^2/\lambda_1^3)\mathbf{A}_0(\lambda_1\mathbf{E}-\mathbf{A}_0)^{-1}\}^{-1}. \quad (75)$$

When α becomes zero, β being finite, then $\lambda_1 \to 1$, $\xi(\lambda_1) \to 0$, $\mathbf{K} \to \mathbf{A}_1^3$, $\mathbf{S}_{11}$, $\mathbf{S}_{10}$, $\mathbf{S}_{01} \to \mathbf{0}$, and $\mathbf{S}_{00} \to (\mathbf{E}-\mathbf{A}_0)^{-1}$. Hence, Eq. (73) reduces to

$$\langle R_0^2 \rangle / N = [\mathbf{X}_0 + 2\mathbf{Y}_0(\mathbf{E}-\mathbf{A}_0)^{-1}\mathbf{Z}_0]_{1,1}, \quad (76)$$

which is the expression for the perfect random coil.

Since in the preceding calculation any kind of end effects is neglected, Eq. (73) ceases to be valid for a finite chain when the transition inclines to the helix side and molecular configurations approach very near to the α helix. It is not an easy task to take these effects into account in this model, and consequently we shall introduce a new, simpler model.

Model II.[17]

This model is defined as follows. A helical section containing ν_1 residues is replaced by a rod of $\nu_1 l_1$ in length; a randomly coiled section containing ν_0 residues is replaced by a random flight chain consisting of ν_0 steps of l_0 in length, and they are combined alternatively at ends by a universal joint so as to form a interrupted helix. The degree of approximation accompanying this replacement depends on $\langle \nu_1 \rangle$ and $\langle \nu_0 \rangle$; it becomes better as these quantities become larger. Detailed discussion on this point will be given in the next section by comparing numerical results obtained for these two models.

Now let $\mathbf{r}_i (i=1, \cdots, N)$ be the vector from the starting point of the ith residue [or the end point of the $(i-1)$th residue] to the end point of the residue. The mean-square end-to-end distance, $\langle R^2 \rangle$ can then

[17] This model was first suggested to the author by Dr. A. Wada.

be expressed as

$$\langle R^2\rangle=\sum_{i=1}^{N}\langle \mathbf{r}_i^2\rangle+2\sum_{i<j}\langle \mathbf{r}_i\cdot\mathbf{r}_j\rangle, \qquad (77)$$

where $\langle \mathbf{r}_i\cdot\mathbf{r}_j\rangle$ is the scalar product of $\mathbf{r}_i$ and $\mathbf{r}_j$. To average R^2, we shall use the second method since the first method, although also applicable, leads to a very lengthy and unsystematic expression.[21] It is convenient to calculate the following three kinds of terms separately:

(i) $$J_1=\sum_{i=1}^{N}\langle \mathbf{r}_i^2\rangle. \qquad (78)$$

Since $\langle \mathbf{r}_i^2\rangle$ may be written as

$$\langle \mathbf{r}_i^2\rangle=\langle \mu_i l_1^2+(1-\mu_i)l_0^2\rangle$$
$$=l_0^2\{1-(1-l_1^2/l_0^2)\langle\mu_i\rangle\}, \qquad (79)$$

it follows that

$$J_1=Nl_0^2\{1-(1-l_1^2/l_0^2)N^{-1}(N-2)\xi_N\}. \qquad (80)$$

(ii) $$J_2=\sum_{i=2}^{N-2}\langle \mathbf{r}_i\cdot\mathbf{r}_{i+1}\rangle. \qquad (81)$$

$\langle \mathbf{r}_i\cdot\mathbf{r}_{i+1}\rangle$ may be expressed as

$$\langle \mathbf{r}_i\cdot\mathbf{r}_{i+1}\rangle=l_1^2\langle\mu_i\cdot\mu_{i+1}\rangle$$
$$=l_1^2Z_N^{-1}SAE\{\mathbf{p}_c\mathbf{p}^{i-2}\alpha[\partial\mathbf{p}(\alpha_1)/\partial\alpha]_{\alpha_1=\alpha}\mathbf{p}^{N-i-1}\mathbf{p}_a\}, \qquad (82)$$

which becomes, on inserting the relation

$$\mathbf{v}(\lambda_k)\alpha[\partial\mathbf{p}(\alpha_1)/\partial\alpha]_{\alpha_1=\alpha}\mathbf{u}(\lambda_l)=\lambda_l^{-1}\lambda_k(\lambda_k+\lambda_l-\sigma)c(\lambda_k), \qquad (83)$$

$$\langle \mathbf{r}_i\cdot\mathbf{r}_{i+1}\rangle=l_1^2Z_N^{-1}(\sigma\alpha^2)^{-1}\sum_{k,l}c(\lambda_k)c(\lambda_l)\lambda_k^2(\lambda_k-\sigma)$$
$$\times\lambda_l^2(\lambda_l-\sigma)(\lambda_k+\lambda_l-\sigma)\lambda_k^{i-2}\lambda_l^{N-i-2}. \qquad (84)$$

Now we have

$$J_2=l_1^2Z_N^{-1}(\sigma\alpha^2)^{-1}\sum_{k,l}c(\lambda_k)c(\lambda_l)\lambda_k^2(\lambda_k-\sigma)\lambda_l^2(\lambda_l-\sigma)$$
$$\times(\lambda_k+\lambda_l-\sigma)(\lambda_l-\lambda_k)^{-1}(\lambda_l^{N-3}-\lambda_k^{N-3}). \qquad (85)$$

(iii) $$J_3=\sum_{2\le i<j-1\le N-2}\langle \mathbf{r}_i\cdot\mathbf{r}_j\rangle. \qquad (86)$$

$\langle \mathbf{r}_i\cdot\mathbf{r}_j\rangle$ may be expressed as

$$\langle \mathbf{r}_i\cdot\mathbf{r}_j\rangle=l_1^2\langle\mu_i\mu_{i+1}\cdots\mu_j\rangle, \qquad (87)$$

which, according to Eqs. (54), (27), and (28), becomes

$$\langle \mathbf{r}_i\cdot\mathbf{r}_j\rangle=l_1^2Z_N^{-1}(\sigma\alpha^2)^{-1}\sum_{k,l}c(\lambda_k)c(\lambda_l)\lambda_k^3(\lambda_k-\sigma)$$
$$\times\lambda_l^3(\lambda_l-\sigma)(\lambda_k/\sigma)^{i-2}(\lambda_l/\sigma)^{N-j-1}\sigma^{N-3}. \qquad (88)$$

On inserting Eq. (88) into Eq. (86), and performing the summation over i and j, we find

$$J_3=Z_N^{-1}(\sigma\alpha^2)^{-1}\sum_{k,l}c(\lambda_k)c(\lambda_l)\lambda_k^3(\lambda_k-\sigma)\lambda_l^3(\lambda_l-\sigma)$$
$$\times(\lambda_l-\lambda_k)^{-1}\{\lambda_l(\lambda_l-\sigma)^{-1}(\lambda_l^{N-4}-\sigma^{N-4})$$
$$-\lambda_k(\lambda_k-\sigma)^{-1}(\lambda_k^{N-4}-\sigma^{N-4})\}. \qquad (89)$$

Now for the required quantity we have

$$\langle R^2\rangle=J_1+2(J_2+J_3). \qquad (90)$$

In the limit of $N\to\infty$, J_1/N, J_2/N, and J_3/N reduce to

$$l_0^2\{1-(1-l_1^2/l_0^2)\xi(\lambda_1)\}, \qquad c(\lambda_1)(2\lambda_1-\sigma)/\lambda_1,$$

and

$$c(\lambda_1)\lambda_1/(\lambda_1-\sigma),$$

respectively, therefore $\langle R^2\rangle$ reduces to

$$\langle R^2\rangle/Nl_0^2=\langle R^2\rangle/\langle R_0^2\rangle$$
$$=1-\xi(\lambda_1)+[\xi(\lambda_1)+2c(\lambda_1)\{3+\sigma^2/\lambda(\lambda-\sigma)\}](l_1^2/l_0^2). \qquad (91)$$

This equation should be compared with Eq. (73) for model I.

$P(\theta)$ in Light Scattering and Mean-Square Radius of Gyration

We attempt to calculate these quantities for the reason mentioned in the introduction. Rigorously speaking, polypeptide molecules composed of one kind of amino acid residue, although being indeed homopolymers chemically, might be considered as copolymers physically, in the transition region, in the sense that *distorted* and *undistorted* residues have very different configurations and environments. Therefore, it seems likely that intensities of light scattered from these are somewhat different.

It can be shown that the intensity of scattered light (so normalized as to become unity at $\theta=0$) from a molecule composed of two kinds of components, 1 and 0, is given generally by[18]

$$P(\theta)=\{\sum_i m_{\mu_i}(\partial n/\partial c)_{\mu_i}\}^{-2}$$
$$\cdot\sum_{i<j}m_{\mu_i}m_{\mu_j}(\partial n/\partial c)_{\mu_i}(\partial n/\partial c)_{\mu_j}$$
$$\times\langle(\sin\kappa s r_{ij})/\kappa s r_{ij}\rangle_{\mu_i,\mu_j}. \qquad (92)$$

Here μ_i is assumed to be 1 when the ith element (residue in our case) is the component 1, and assumed to be 0 otherwise. Here m_1 and m_0 are element (residue) weights of the components, 1 and 0, respectively, and $(\partial n/\partial c)_1$ and $(\partial n/\partial c)_0$ are refractive index increments. κ and s have their usual meanings, i.e., $\kappa=2\pi/\lambda$ and $s=2\sin(\theta/2)$. Here r_{ij} is the distance between the ith and jth elements, $\langle(\sin\kappa s r_{ij})/\kappa s r_{ij}\rangle_{\mu_i,\mu_j}$ is the average of

[18] From discussion with Dr. H. Yamakawa.

$(\sin\kappa s r_{ij})/\kappa s r_{ij}$ in the case where the two elements are in the states specified by μ_i and μ_j. It can be seen that $P(\theta)$ reduces to its usual form

$$P(\theta)=\sum_{i<j}\langle(\sin\kappa s r_{ij})/\kappa s r_{ij}\rangle$$

rigorously, only when $m_1(\partial n/\partial c)_1=m_0(\partial n/\partial c)_0$, and approximately, when the distribution of the two components on a chain is nearly random and

$$\langle(\sin\kappa s r_{ij})/\kappa s r_{ij}\rangle$$

does not depend on μ_i and μ_j. The latter case seems to apply to some synthetic copolymers.[19] However, this is not the case in our problem. Namely, most of the theories already published[3,4,10] have shown that the distribution of the two kinds of residues is highly blocked rather than random. Furthermore

$$\langle(\sin\kappa s r_{ij})/\kappa s r_{ij}\rangle$$

depends strongly on μ_i and μ_j for small $j-i$, as can be easily presumed. Under this circumstance, it is the following quantity that we can obtain experimentally from the coefficient of $(\kappa s)^2$ in $P(\theta)$,

$$N^{-2}\{\sum_i m_{\mu_i}[\partial n/\partial c)_{\mu_i}\}^{-2}$$
$$\times\sum_{i<j}m_{\mu_i}m_{\mu_j}(\partial n/\partial c)_{\mu_i}(\partial n/\partial c)_{\mu_j}\langle r_{ij}^2\rangle_{\mu_i,\mu_j}. \tag{93}$$

Only in the special case where $m_1(\partial n/\partial c)_1=m_0(\partial n/\partial c)_0$ or $(\partial n/\partial c)_1=(\partial n/\partial c)_0$ (because $m_1=m_0$ in our case), can we obtain the mean-square radius of gyration

$$\langle S^2\rangle=N^{-2}\sum_{i<j}\langle r_{ij}^2\rangle_{\mu_i,\mu_j}. \tag{94}$$

Since the calculation of Eq. (93), although not impossible, is very tedious, we give here only the expression for $\langle S^2\rangle$. When we cannot find any system in which $(\partial n/\partial c)_1=(\partial n/\partial c)_0$ we will be obliged to calculate Eq. (93) for comparison with experiment.

Since $\mathbf{r}_{ij}=\mathbf{r}_{i+1}+\mathbf{r}_{i+2}+\cdots+\mathbf{r}_j$ Eq. (94) may be written as

$$\langle S^2\rangle=N^{-2}\{\sum_{0\le i<i'\le j\le N}\langle\mathbf{r}_{i'}^2\rangle+2\sum_{0\le i<i'<j'\le j\le N}\langle\mathbf{r}_{i'}\cdot\mathbf{r}_{j'}\rangle\}. \tag{95}$$

Just as we have done in the preceding section, we shall calculate the following three kinds of terms separately.

$$\text{(i)}\quad J_1^*=\sum_{0\le i<i'\le j\le N}\langle\mathbf{r}_{i'}^2\rangle=\sum_{i=1}^{N}i(N-i+1)\langle\mathbf{r}_i^2\rangle. \tag{96}$$

On inserting Eq. (79) with $\langle\mu_i\rangle$ given by Eq. (41), and performing the summation over i,[20] we have

$$J_1^*=l_0^2[\tfrac{1}{6}N(N+1)(N+2)-(1-l_1^2/l_0^2)Z_N^{-1}(\sigma\alpha^2)^{-1}$$
$$\times\sum_{k,l}c(\lambda_k)c(\lambda_l)(\lambda_k-\sigma)(\lambda_l-\sigma)$$
$$\times\{\lambda_k\lambda_l+\lambda_k(\lambda_k-\sigma)+\lambda_l(\lambda_l-\sigma)\}$$
$$\times(\lambda_l-\lambda_k^-)^3\{N(\lambda_l^{N+2}-\lambda_k^{N+2})-(N+2)\lambda_k\lambda_l(\lambda_l^N-\lambda_k^N)\}. \tag{97}$$

$$\text{(ii)}\qquad J_2^*=\sum_{i=1}^{N-1}i(N-i)\langle\mathbf{r}_i\cdot\mathbf{r}_{i+1}\rangle. \tag{98}$$

On inserting Eq. (84) we have

$$J_2^*=l_1^2Z_N^{-1}(\sigma\alpha^2)^{-1}$$
$$\times\sum_{k,l}c(\lambda_k)c(\lambda_l)\lambda_k(\lambda_k-\sigma)\lambda_l(\lambda_l-\sigma)(\lambda_k+\lambda_l-\sigma)$$
$$\times(\lambda_l-\lambda_k)^{-3}\{(N-1)(\lambda_l^{N+1}-\lambda_k^{N+1})$$
$$-(N+1)\lambda_k\lambda_l(\lambda_l^{N-1}-\lambda_k^{N-1})\}. \tag{99}$$

$$\text{(iii)}\quad J_3^*=\sum_{1\le i<j-1\le N-1}i(N-j+1)\langle\mathbf{r}_i\cdot\mathbf{r}_j\rangle. \tag{100}$$

Similarly we have

$$J_3^*=l_1^2Z_N^{-1}(\sigma\alpha^2)^{-1}\sum_{k,l}c(\lambda_k)c(\lambda_l)\lambda_k^2(\lambda_k-\sigma)\lambda_l^2(\lambda_l-\sigma)$$
$$\times(\lambda_l-\lambda_k)^{-3}[(\lambda_l-\lambda_k)\{\lambda_l^2(\lambda_l-\sigma)^{-1}$$
$$\times((N-2)\lambda_l^{N-1}-(N-1)\sigma\lambda_l^{N-2}+\sigma^{N-1})$$
$$+\lambda_k^2(\lambda_k-\sigma)^{-2}((N-2)\lambda_k^{N-2}-(N-1)\sigma\lambda_k^{N-2}+\sigma^{N-1})\}$$
$$-2\lambda_k\lambda_l\{\lambda_l(\lambda_l-\sigma)^{-1}(\lambda_l^{N-2}-\sigma^{N-2})$$
$$-\lambda_k(\lambda_k-\sigma)^{-1}(\lambda_k^{N-2}-\sigma^{N-2})\}]. \tag{101}$$

[19] W. H. Stockmayer, L. D. Moore, Jr., M. Fixman, and B. N. Epstein, J. Polymer Sci. **16**, 517 (1955).

[20] In the procedure of summation over i used for deriving Eqs. (45), (97), etc., there remain some questions to be clarified. Equation (41) for $\langle\mu_i\rangle$, derived from Eq. (39), has been verified to be valid only for i, being in the range $3<i<N-2$, since the relation $\mathbf{p}^i=\Sigma_\lambda\lambda^i\mathbf{u}(\lambda)\mathbf{v}(\lambda)$ is defined only for i larger than 1. On deriving Eq. (45), however, we have considered Eq. (41) to be valid also for $i=2$ and $N-1$, assuming implicitly that $\Sigma_\lambda\mathbf{u}(\lambda)\mathbf{v}(\lambda)$ is the unit matrix. This is not so since, of seven eigenvalues of $\Sigma_\lambda\mathbf{u}(\lambda)\mathbf{v}(\lambda)$, four are unity, but the remaining three are zero. We shall show that our formal treatment, nevertheless, is correct. Here $\mathbf{p}_c$ and $\alpha(\partial\mathbf{p}/\partial\alpha)$ may be written as $\mathbf{p}_c=\mathbf{p}_c'\mathbf{p}$ and $\alpha(\partial\mathbf{p}/\partial\alpha)=\mathbf{p}\mathbf{p}'$, where $\mathbf{p}_c'=(\partial\mathbf{p}(\gamma_c)/\partial\gamma_c)$ and $\mathbf{p}'$ is a matrix whose (1,1), (3,3), and (5,5) elements are 1, and all other elements are zero. Now Eq. (39) is expressed as

$$\langle\mu_i\rangle=Z_N^{-1}SAE[\mathbf{p}_c'\mathbf{p}^i\mathbf{p}'\mathbf{p}^{N-i-1}\mathbf{p}_a].$$

On inserting $\mathbf{p}^i=\Sigma_\lambda\lambda^i\mathbf{u}(\lambda)\mathbf{v}(\lambda)$, $(i\gtrless1)$, we find Eq. (41) again. Thus Eq. (41) now has been verified to be valid also for $i=2$, and even for $i=1$. Similarly, it can be verified to be valid also for $i=N-1$, and N. (In fact, $\langle\mu_1\rangle$ and $\langle\mu_N\rangle$ are identically zero.) Consequently Eq. (41) is valid for all i. This circumstance is found to be true also for Eqs. (30), (54), (84), and (88). The reason for including the two insignificant terms $\langle\mu_1\rangle$ and $\langle\mu_N\rangle$ (being equal to zero) is merely because, by doing so, J_1^* becomes somewhat brief. Also for J_2^* and J_3^*, a similar procedure will be used for the same reason.

Thus we obtain[21]

$$\langle S^2\rangle = J_1^* + 2(J_2^* + J_3^*). \tag{102}$$

When $k=l$, the quantity

$$(\lambda_l-\lambda_k)^{-3}\{N(\lambda_l^{N+2}-\lambda_k^{N-2}) - (N+2)\lambda_k\lambda_l(\lambda_l^N-\lambda_k^N)\},$$

appearing in Eq. (97) is found to reduce to

$$(\tfrac{1}{6})N(N+1)(N+2)\lambda^{N-1}.$$

Consequently J_1^* reduces to

$$J_1^* = (\tfrac{1}{6})N^3 l_0^2\{1-(1-l_1^2/l_0^2)\xi(\lambda_1)\}$$

in the limit of $N\to\infty$. Similarly J_2^* reduces to $J_2^* = (\tfrac{1}{6})N^3 l_1^2 c(\lambda_1)(2\lambda_1-\sigma)/\lambda_1$ in the same case. When $k=l$, the quantity $(\lambda_l-\lambda_k)^{-3}[\ \ ]$ in Eq. (101) reduces to

$$\begin{aligned}\tfrac{1}{6}(\lambda_1-\sigma)^{-4}\{&6\sigma^{N+1} - (N-1)N(N+1)\sigma^3\lambda_1^{N-2}\\ &+3(N-2)N(N+1)\sigma^2\lambda_1^{N-1}\\ &-3(N-2)(N-1)(N+1)\sigma\lambda_1^N\\ &+(N-2)(N-1)N\lambda_1^{N+1}\}.\end{aligned} \tag{103}$$

Consequently J_3^* reduces to $J_3^* = \tfrac{1}{6}l_1^2N^3c(\lambda_1)\lambda_1/(\lambda_1-\sigma)$ in the limit of $N\to\infty$. Thus for the infinitely long chain we find the relation

$$\langle S^2\rangle = \tfrac{1}{6}\langle R^2\rangle, \tag{104}$$

which manifests that the chain behaves essentially Gaussian in this case.

It should be noted that no mathematical approximations have been made in deriving all expressions in this section.

III. RESULTS AND DISCUSSION

We wish to start from an examination of statistical mechanical behaviors of the simple model described by Eqs. (20)–(25). The physical character of this model is expressed by the following two points. First the minimum helical section allowed is made of three consecutive *distorted* residues supported by one intramolecular hydrogen bond (i.e., one turn of the α helix). Second, the breakdown of the α-helical structure at some middle parts of the α helix takes place when and only when three or more consecutive hydrogen bonds break. The conspicuous sharpness of the helix-coil transition experienced in this model is due on one hand to the difficulty of forming the minimum helical section, but, if once formed, it grows easily to a long helical section; the other hand, the breaking of three consecutive hydrogen bonds occurs rarely, but if it ever does, it gives rise to a rapid spread of both sides of the chain. As already pointed out, this model is equivalent to the second models in G–D's and Z–B's theories. Respective characteristic equations (Eq. (21) in the present theory, Eq. (16) in G–D's, and Eq. (19) with $\mu=3$ in Z–B's) coincide with each other if we replace $(xu)^{-1}$, Z^{-1}, x^{-1} in G–D's, and λ, $\sigma^{\frac{1}{2}}$, s in Z–B's by λ, α, σ in the present, respectively. The relations among various parameters of these theories now become clear. The dependence of the fraction of intact hydrogen bonds on α, σ, and D.P. N has been fully discussed. Though stress, therefore, is not laid upon it here, it seems worthy to add a few remarks.

If one wishes to do some quantitative (rather than illustrative) discussion, it is desirable to determine α from experimental data since a quantitative estimate of numbers of possible configurations of *distorted* and *undistorted* residues from purely theoretical consideration is very difficult, just as that of entropy of fusion of low molecular weight substances is difficult. Zimm and Bragg[4] assigned $\alpha = 2^{\frac{1}{2}}\times10^{-2}$ for poly-γ-benzyl-L-glutamate in the mixed solvent system ethylene dichloride-dichloroacetic acid (1:4) by comparison of their theoretical results with the experimental data of Doty and Yang,[2] and Doty and Iso,[22] on optical rotations of the two specimens different in D.P., i.e., $N=1500$ and 26. We also shall use this value mainly in the following calculation, although results for a few other α's will be included in order to examine the effect of α on chain dimensions.

In all respects, it is worthwhile to know well the behavior of four roots of Eq. (21), which have been entering into all the expressions derived, and their relative weights, which they occupy in the partition function, in the transition region. It can be seen from Eq. (21) that as σ goes from zero to ∞, or the transition goes from the perfect random coil to the perfect α helix, the largest eigenvalue λ_1 goes monotonously from 1 to ∞ [in the order of $O(\sigma)$], λ_2 from 0 [$O(\sigma)$] to about $1-\alpha^2$, λ_3 from 0 to α, and λ_4 from 0 to $-\alpha$. For a sufficiently small α, such as that described previously, the transition, however, is practically completed within very narrow ranges of σ and hence λ_1, λ_2, λ_3, and λ_4. This becomes especially so, as α becomes smaller. For example, whereas for $\alpha=4\times10^{-2}$ the change in σ from approx. 0.72 to 1.05 is required to bring $\xi(\lambda_1)$, the helical content of the infinitely long chain, from 22 to 78%, for $\alpha=2^{\frac{1}{2}}\times10^{-2}$ the change from 0.98 to 1.03 suffices to bring $\xi(\lambda_1)$ from 21 to 78%. From this fact it

[21] Note the following point. J_2 and J_3 can be written, alternatively, as

$$J_2 = \sum_{i=0}^{N-2}\langle \mathbf{r}_i\cdot\mathbf{r}_{i+1}\rangle = l_1^2 Z_N^{-1}\alpha\left[\frac{\partial Z_N(\alpha_1)}{\partial\alpha}\right]_{\alpha_1\to\alpha}$$

and

$$J_3 = l_1^2 Z_N^{-1}\sum_{2\le i<j\le N-2}\sigma^{j-i-2}SAE[\mathbf{p}_s\mathbf{p}^{i-1}\sigma(\partial\mathbf{p}/\partial\sigma)\mathbf{p}^{N-j}\mathbf{p}_a],$$

$$= l_1^2 Z_N^{-1}\sum_{r=0}^{N-5}\sigma^{r+1}(\partial Z_{N-r}/\partial\sigma).$$

$\langle R^2\rangle$ therefore, is obtainable also by the first method. Since this procedure is not applicable to J_1^*, J_2^*, and J_3^*, $\langle S^2\rangle$ is unobtainable by the first method.

[22] P. Doty and K. Iso (unpublished).

can be also found that the smaller α is, the sharper the transition becomes. For small α and hence σ near unity, four roots are obtained as follows. Since Eq. (21) may be solved as $\sigma=\lambda^3(\lambda-1)\{\alpha^2+\lambda^2(\lambda-1)\}^{-1}$, we first calculate σ for an appropriate λ_1 larger than unity by this relation instead of solving directly λ_1 for a given σ. Here λ_3 and λ_4 are given approximately by $\lambda_3\simeq\alpha+\frac{1}{2}\alpha^2\sigma^{-1}(1+\sigma)$ and $\lambda_4\simeq-\alpha+\frac{1}{2}\alpha^2\sigma^{-1}(1+\sigma)$. Therefore, λ_2 is given approximately by $\lambda_2=1+\sigma-\lambda_1-\lambda_3-\lambda_4\simeq1+\sigma-\lambda_1-\alpha^2\sigma^{-1}(1+\sigma)$. Starting from this value and using Newton's method two or three times repeatedly, we can reach sufficiently accurate λ_2 (having significant numbers of ten). It is unnecessary to calculate λ_3 and λ_4 since together they practically do not enter into our problem as will presently be seen. Let us estimate numerically the contribution of each eigenvalue to the partition function, i.e., $\zeta(\lambda)\lambda^N$ in the case of $\alpha=2^{\frac{1}{2}}\times10^{-2}$. As σ increases from 0 to ∞, $\zeta(\lambda_1)$ decreases from 1 to 0, keeping the relation $\zeta(\lambda_1)+\zeta(\lambda_2)\simeq1.001$, and $\zeta(\lambda_3)$ and $\zeta(\lambda_4)$ are always approx. $\frac{1}{2}$. Since λ_3 and λ_4 are of orders of α and $-\alpha$, respectively, $\zeta(\lambda_3)\lambda_3^N$ and $\zeta(\lambda_4)\lambda_4^N$ are negligible for N larger than 4, i.e., practically for all N. As σ goes from zero to ∞, λ_2/λ_1 increases from zero, passes through a maximum (0.972 at approx. $\sigma=1$), and then decreases monotonously. Therefore, when N is small (e.g., <30) the leading term in Z_N is $\zeta(\lambda_1)\lambda_1^N$ for small σ and $\zeta(\lambda_2)\lambda_2^N$ for large σ. For σ near 1, relative weights of both terms are given approximately by λ_1^N and λ_2^N. On the other hand for large N (e.g., >100), the leading term is always $\zeta(\lambda_1)\lambda_1^N$, the maximum contribution of $\zeta(\lambda_2)\lambda_2^N$ occurring at $\sigma=1$. For very large N (>600), the contribution of the latter becomes always negligible. The contributions of λ_2 to the helical content, the mean-square end-to-end distance, etc., are found to be somewhat more sensitive, details varying from case to case. The relative weight of $\zeta(\lambda_1)$ in $\zeta(\lambda_1)\lambda_1^N$ is found not to be negligible for all cases examined. For example, the difference [seen in Fig. 5(c)] between the helical contents for two specimens of $N=1500$ and ∞ is arising not from the contribution of λ_2 but from that of $\zeta(\lambda_1)$.

Now we are in a good position to examine the degree of approximation of the present statistical mechanical model. One way for this is to estimate errors in λ_1 and λ_2, accompanying the simplification described by Eq. (20). If $\alpha_1\alpha_2\gamma_1\gamma_2$ is replaced by α^2, Eq. (6) becomes

$$\lambda^3(\lambda-\sigma)(\lambda-1)-\sigma\alpha^2\{1+(\gamma_3/\gamma_1\gamma_2)(\lambda-1)\}=0. \quad (105)$$

This equation reduces to Eq. (21) only when $\gamma_3/\gamma_1\gamma_2=1$. Owing to steric hindrances γ_1 and γ_2 seem to be somewhat smaller than unity. Furthermore γ_3 seems to be smaller than $\gamma_1\gamma_2$ due to the interaction between two neighboring helical sections, perhaps $0\leq\gamma_3/\gamma_1\gamma_2\leq1$. An error which might arise from this circumstance was already pointed out by Zimm and Bragg[4] but an estimate of it has remained unexamined. The maximum error occurs at the extreme case, $\gamma_3/\gamma_1\gamma_2=0$. In this case Eq. (105) reduces to

$$\lambda^3(\lambda-\sigma)(\lambda-1)-\alpha^2\sigma=0. \quad (106)$$

Numerical computations show that the differences between the two largest eigenvalues λ_1's of Eq. (21) and (106), and the two next largest λ_2's are of the order of $\sigma\alpha^2\simeq2\times10^{-4}$ near $\sigma=1$ and smaller than it elsewhere. For intermediate $\gamma_3/\gamma_1\gamma_2$ this is found to be true. Numerical computations for several special cases show that the effect on the helical content is also negligible in the range of σ in which we are interested. From these facts it follows that the degree of approximation of this model is very satisfactory, provided that α^2 is considered to contain not only the contribution from the decrease in freedom of two *distorted* residues but that from all unusual effects occurring at both ends of a helical section. The difficulty of determining α from purely theoretical consideration arises, in part here.

At the early time when the helix-coil transition was first discovered it was not clear whether the transition proceeded in the all-or-none fashion or through the disruption of the α helix from some middle parts as well as both ends. Current theories[3,4,10] and experiments[23] have shown that the latter is the case. In this connection it seems of interest to calculate the three probabilities that the chain is in the three forms, the first being the perfect random coil, the second being disrupted only from the ends, and the third being disrupted from some middle parts as well as the ends, respectively. Since the statistical weights of a perfect random coil and of all states equal 1 and Z_N, respectively, the probability for the first form is given simply by $1/Z_N$. The statistical weight of the state where only the ith, $(i+1)$th, $\cdots$ and jth residues are *distorted* is given by $\alpha^2\sigma^{j-i-1}$. The probability for the second form q_e therefore, is given by

$$q_e=Z_N^{-1}\sum_{2\leq i<j-1\leq N-2}\alpha^2\sigma^{j-i-1}$$

$$=Z_N^{-1}\alpha^2\sigma(1-\sigma)^{-2}\{\sigma^{N-2}-(N-2)\sigma+N-4\}. \quad (107)$$

Now the probability for the third form becomes

$$q_i=1-q_e-Z_N^{-1}. \quad (108)$$

In Fig. 1, q_e (solid curves) and q_i (broken) for $\alpha=2^{\frac{1}{2}}\times10^{-2}$ and a few N's are plotted against $\ln\sigma$. For $N=100$, the first form is preponderant and in equilibrium mainly with the second when $\sigma<1$, but the second becomes so and in equilibrium the third when $\sigma>1$. When $\sigma\simeq1$, the three forms are mixed. On the contrary for $N=1000$ the third is always preponderant in the calculated range of σ. [Concerning the helical

[23] Unpublished works of Doty's laboratory.

contents in this range of σ, see Fig. 5(c).] Furthermore the probability of finding the perfect α helix, i.e., $Z_N^{-1}\alpha^2\sigma^{N-4}$ is found to be small in the same range of σ for all N's examined here. Consequently it is proved that the helix-coil transition experienced in polypeptides of moderate D.P. does not proceed in the all-or-none fashion but does proceed through the disruption of the α-helical structure from some middle parts as well as both ends.

We proceed to calculate chain dimensions. Parameters involved in model I can be determined as follows. The bond lengths and the supplements of bond angles of the skeleton of polypeptide molecules are chosen, following Corey and Pauling,[24] as

$$b_1=\mathrm{NC}=1.32\ \mathrm{A},\quad b_2=\mathrm{CC}=1.53\ \mathrm{A},\quad b_3=\mathrm{CN}=1.47\ \mathrm{A},$$
$$\omega_1=\pi-\angle\mathrm{NCC}=66^\circ,\quad \omega_2=\pi-\angle\mathrm{CCN}=70^\circ,$$
$$\omega_3=\pi-\angle\mathrm{CNC}=57^\circ, \tag{109}$$

for both *distorted* and *undistorted* residues. Internal rotational angles of *distorted* residues are assumed to equal those of the α helix. Since the peptide linkage has been found not to be rotatable because of its partial double-bond character,[25,26] we assume $\theta_1=0^\circ$ for both *distorted* and *undistorted* residues. According to Pauling and Corey,[27] the α helix is produced by the rotation of 100° per residue around the helical axis and the translation of 1.5 A along the axis. It can be shown that, having assumed the above values for the bond lengths and the supplements of bond angles, internal rotational angles consistent with this requirement must be

$$\theta_1\ (\text{around NC})=0^\circ,\qquad \theta_2(\mathrm{CC})=133^\circ,$$
$$\theta_3(\mathrm{CN})=122^\circ, \tag{110}$$

provided that the sense of the α helix of L-polypeptides is assumed to be right-handed, as has been supposed for a long time.[28]

Little has been known of local configurations of polypeptide molecules being in the state referred to as randomly coiled. From rather hasty consideration one might suppose that it would be just such a state that each of the rotational angles around two rotatable bonds of a residue takes nearly equiprobably the six

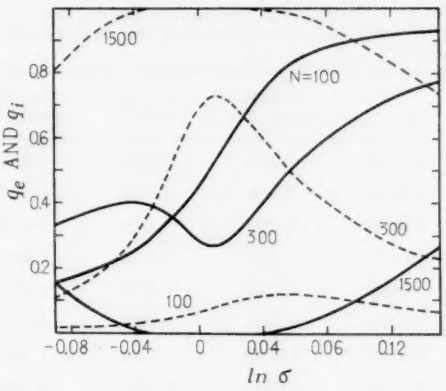

FIG. 1. The two probabilities of finding the α helices disrupted from only both ends (q_e, solid curves), and disrupted from some middle parts as well as both ends (q_i, broken). Consequently $1-q_e-q_i$ denotes the probability of finding the perfect random coil. N: *D.P.*; $\alpha=2^{\frac{1}{2}}\times10^{-2}$.

values proposed by Pauling and Corey,[29] or the three values proposed by Mizushima *et al.*[30] This, however, would hardly be the case as will be seen presently, for poly-γ-benzyl-L-glutamate in dichloroacetic acid, and perhaps for all polypeptides being in the state referred to as randomly coiled. Under this circumstance it seems best to determine it from experimental data in such a manner that the calculated $\langle R_0^2\rangle$ for the perfect random coil, i.e., Eq. (76), fits observed values. For hindered rotational potentials we shall adopt the following sinusoidal function[15]

$$E(\theta_k)=\tfrac{1}{2}E_{k*}\{1-\cos(\theta_k-\theta_{k*})\},\qquad k=2,3, \tag{111}$$

where E_{k*} is the maximum height of the potential barrier and θ_{k*} is the most probable value of θ_k. Even if this very simple form is assumed, two parameters are still required in order to describe the state of rotation around one bond. However it is impossible to determine uniquely four parameters required in the present case only from one observed value of $\langle R_0^2\rangle$, and hence some of them must be chosen somewhat arbitrarily. Doty *et al.*[31] observed $\langle R_0^2\rangle=(890)^2\mathrm{A}^2=7.92\times10\ \mathrm{A}^2$ for a specimen of poly-γ-benzyl-L-glutamate of $N=1500$ in dichloroacetic acid at 25°C. We shall use this value. After several trials, $E_{2*}=E_{3*}=8$ kcal and $\theta_{2*}=-\theta_{3*}=20^\circ$ are found to be appropriate, giving $\langle R_0^2\rangle=7.51\times10^5\ \mathrm{A}^2$. Our intention in having selected these values for θ_{2*} and θ_{3*} rather than $\theta_{2*}=\theta_{3*}=0$ is that by doing so, we might be capable of taking into account the asymmetric structure in L-polypeptides. Namely, a bulky side group would force the two skeletal bonds,

[24] R. B. Corey and L. Pauling, Rend. ist. lombardo Sci. P. I. **89**, 10 (1955).
[25] S. Mizushima, T. Simanouti, S. Nagakura, K. Kuratani, M. Tsuboi, H. Baba, and O. Fujioka, J. Am. Chem. Soc. **72**, 3490 (1950).
[26] R. M. Badger and H. Rubalcava, Proc. Natl. Acad. Sci. U. S. **40**, 12 (1954).
[27] L. Pauling, R. B. Corey, and H. R. Branson, Proc. Natl. Acad. Sci. U. S. **37**, 205, 241 (1951).
[28] From theoretical calculation of the rotatory dispersion of the α helix I. Tinoco, Jr. and R. W. Woody, [J. Chem. Phys. **32**, 461 (1960)] have recently proposed an opposing opinion i.e., that the left-handed sense is preferable for poly-γ-benzyl-L-glutamate and polypeptides with similar rotatory behaviors. The difference in the sense of the helix, however, would not influence our following result very significantly.
[29] L. Pauling and R. B. Corey, Proc. Natl. Acad. Sci. U. S. **37**, 729 (1951).
[30] See work cited in footnote 33.
[31] P. Doty, J. H. Bradbury, and A. M. Holtzer, J. Am. Chem. Soc. **78**, 947 (1956).

TABLE I. Comparison of the two expressions, Eqs. (73) and (91), of $(\langle R^2\rangle/\langle R_0^2\rangle)^{\frac{1}{2}}$ for the infinitely long chain; α is chosen as $\alpha=2^{\frac{1}{2}}\times10^{-2}$.

$\ln\sigma$	Helical content, $\xi(\lambda_1)$	Eq. (73) (model I)	Eq. (91) (model II)
−0.07410	0.0374	0.9656	0.9834
−0.04442	0.0845	0.9393	0.9650
−0.02082	0.2111	0.8926	0.9259
−0.01263	0.3033	0.8742	0.9073
−0.00422	0.4332	0.8720	0.8990
0.00383	0.5741	0.9096	0.9246
0.01309	0.7173	1.0141	1.0134
0.02330	0.8252	1.1780	1.1658
0.03460	0.8940	1.3769	1.3597
0.05530	0.9506	1.7287	1.7130
0.07505	0.9721	2.0360	2.0272
0.09367	0.9822	2.3156	2.3161

which combine the α carbon atom bearing the side group to the rest of the chain, to rotate, on an average, to such a direction that the group becomes separate from the rest of the chain. Such an effect has been observed experimentally.[32] It is worthy to remark that the value of E_{k*} selected is considerably larger than those observed in other simple substance,[33] i.e., rotations around the two bonds are by no means freely rotatable nor are those which are mentioned at the beginning of this paragraph. After all, the observed value of $\langle R_0^2\rangle$ is much larger than those which would be expected if the former were the case.[34] This extremely limited flexibility is perhaps not intrinsic property of polypeptide chains but due to various steric effects between skeletal atoms and/or solvent molecules adsorpted on NH and CO groups by hydrogen bonds. From the foregoing discussion it appears preferable to consider the local configuration of the randomly coiled chain as being rather similar, although of course not being as definite, as that of the β extended configuration, than those which one might be liable to suppose from the term "randomly coiled." This suggestion is also supported by the experimental evidence[35] that some polypeptides are obtainable in the β form by, e.g., evaporation of solvents from solutions in which polypeptide chains are in the randomly coiled configuration.

Parameters in model II can be determined rather easily. Without any hesitation, l_1 is taken as 1.5 A, that is the helical pitch per residue. Here l_0 is calculated by the relation $(\langle R_0^2\rangle/N)^{\frac{1}{2}}=(7.51\times10^5\div1500)^{\frac{1}{2}}$ A$=$ 22.4 A, where for $\langle R_0^2\rangle$ we use the value calculated above rather than Doty *et al.*'s experimental value in order to compare the two configurational models. Now all parameters contained in the two models have been determined.

On adopting $\alpha=2^{\frac{1}{2}}\times10^{-2}$ and using Eqs. (73) and (91), expansion ratios of chain dimensions from the perfect random coil, $(\langle R^2\rangle/\langle R_0^2\rangle)^{\frac{1}{2}}$ for $N=\infty$ are calculated and given in Table I, those in the third column corresponding to model I and those in the fourth to model II. Agreement between two corresponding $(\langle R^2\rangle/\langle R_0^2\rangle)^{\frac{1}{2}}$'s is considerably good and especially so for $\sigma>1$, where essential dimensional change occurs. This seems due to the following circumstance. In order that model II is significant, mean numbers of residues involved in a helical and randomly coiled sections, i.e., $\langle\nu_1\rangle$ and $\langle\nu_0\rangle$ must be suitably large, or alternatively the mean frequency of alternations of helical and randomly coiled sections must be small. As can be seen from Fig. 2, where the mean number of helical sections per chain divided by N is plotted against $\ln\sigma$, this is the case for $\sigma\simeq1$, $\langle\nu_1\rangle$ and $\langle\nu_0\rangle$ indeed being nearly equal to $\alpha^{-1}=71$ in the present case. However as σ becomes larger, $\langle\nu_0\rangle$ becomes smaller until it reaches unity in the limit of $\sigma\to\infty$. Although extremely small ν_0 indeed makes it insignificant to replace a ν_0-coiled section by

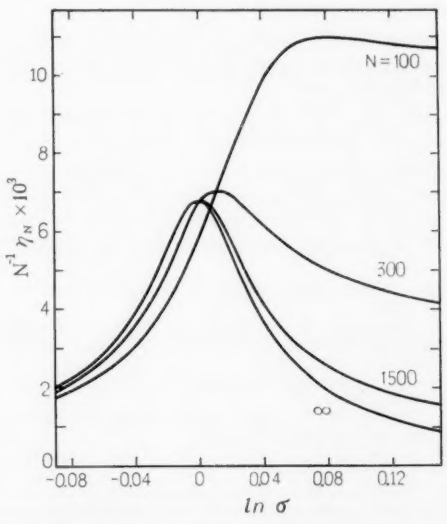

FIG. 2. N (*D.P.*) dependence of the mean number of helical sections per chain divided by N. $\alpha=2^{\frac{1}{2}}\times10^{-2}$.

[32] M. Tsuboi, T. Shimanouchi, and S. Mizushima, J. Am. Chem. Soc. **81**, 1406 (1959).

[33] S. Mizushima, *Structure of Molecules and Internal Rotation* (Academic Press, Inc., New York, 1954).

[34] Note that $\langle R_0^2\rangle$'s equal each other for two cases, one in which rotations around two bonds are free, and the other in which each of the rotational angles takes equiprobably some symmetrically distributed values, e.g., such as 0°, 120°, and −120°.

[35] See, for example, C. H. Bamford, A. Elliott, and W. E. Hanby, *Synthetic Polypeptides* (Academic Press, Inc., New York, 1956), Chap. X.

the corresponding random flight chain, but the agreement seen in Table I shows that the error accompanying this, nevertheless, is eventually negligible at least for the σ examined, and justifies our following results and discussion, which will be derived by using model II. Furthermore it might be possible even to guess that $\langle R^2 \rangle$ in the transition region would not be affected very seriously by any specific form assumed for internal rotational potentials of *undistorted* residues in Model I, provided that it is so chosen as to give the same $\langle R_0^2 \rangle$.

In order to see the effect of α on chain dimension as clearly as possible, it appears convenient to compare $\langle R^2 \rangle$'s at an equal helical content rather than at equal σ. For a while we shall confine our discussion to the infinitely long chain. We can write σ as

$$\ln\sigma = -\Delta F/RT = -\Delta H/RT + \Delta S/R, \quad (112)$$

where ΔF, ΔH, and ΔS are free energy, enthalpy, and entropy changes, respectively, accompanying the formation of one intramolecular hydrogen bond. If we choose suitably ΔH and ΔS, for different α's we can make the helical contents approximately equal at the same temperature. In Fig. 3(b), the helical content for the case of $\alpha = 2^{\frac{1}{2}} \times 10^{-2}$, $\Delta H = 1$ kcal, and $\Delta S = 5.92$ eu,[36] are plotted against temperature, T°C. Curves for $\alpha = 4 \times 10^{-2}$, $\Delta H = 2.83$ kcal, and $\Delta S = 7.92$ eu $\alpha = 10^{-2}$, $\Delta H = 0.721$ kcal, and $\Delta S = 5.80$ eu, and $\alpha = 5 \times 10^{-3}$, $\Delta H = 0.357$ kcal, and $\Delta S = 5.89$ eu, are found to be, although being not rigorously equal, very close to that of $\alpha = 2^{\frac{1}{2}} \times 10^{-2}$. Corresponding curves for $(\langle R^2 \rangle / \langle R_0^2 \rangle)^{\frac{1}{2}}$ are calculated by Eq. (91) and plotted in Fig. 3(a), from which it can be seen that the smaller α becomes, the larger the chain dimension does at the same helical content. This is understandable for the following reason.

Since, as we have seen, α^2 is the statistical weight associated with such an alternation as randomly coiled section→helical section→randomly coiled section on the chain, smaller α has the effects of not only making the transition sharper but making the mean frequency of alternations fewer or making more the numbers of residues involved in a helical and randomly coiled sections. This is illustrated in Fig. 4(a), where $\nu_1 L_\infty(\nu_1)/N$, i.e., the fraction of residues involved in ν_1-helical sections, are plotted against ν_1 for different α's but almost equal helical contents [rigorously, $\xi(\lambda_1) = 0.5086$, 0.5097, and 0.5049 for $\alpha = 2^{\frac{1}{2}} \times 10^{-2}$, 10^{-2}, and 5×10^{-3}, respectively].

The contribution of a ν_0-coiled section and a ν_1-helical section to $\langle R^2 \rangle$ are equal to $\nu_0 l_0^2$ and $\nu_1^2 l_1^2$, respectively. Therefore, total contributions of all randomly coiled sections are determined simply by total numbers of *undistorted* residues. On the contrary those of all helical sections depend on the helical sequence length distribution; they become larger as $\langle \nu_1 \rangle$ does so even if the total helical content remains unchanged. Thus we have been able to understand the effect of α on $\langle R^2 \rangle$.

The effect of σ on $\langle R^2 \rangle$ is also understandable in a similar way. It is of interest to note that the contribution of a helical section containing less residues than a critical value, $l_0^2/l_1^2 (= 222$ in the present case) is smaller than that of a randomly coiled section containing the same number of residues. The decrease from unity in $(\langle R^2 \rangle / \langle R_0^2 \rangle)^{\frac{1}{2}}$ near $\sigma = 1$, seen in Fig. 3(a) and Table I, is due to the fact that most of the helical sections appearing, contain less residues than this critical value. This means physically that by the appearance of a short helical section the residues involved in it gather

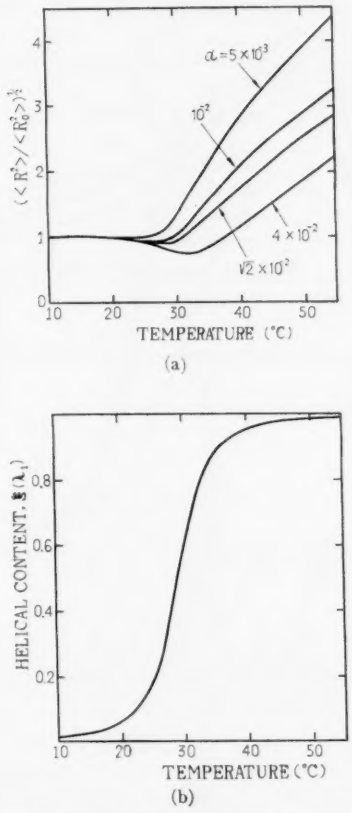

FIG. 3. Effect of α on chain dimensions. (a) $(\langle R^2 \rangle / \langle R_0^2 \rangle)^{\frac{1}{2}}$ of the infinitely long chain for various α's [calculated from Eq. (91)] are plotted against temperature, °C. Equation (112) is assumed between $\ln\sigma$ and temperature, °K; ΔH and ΔS are chosen as:

α	ΔH (kcal)	ΔS (eu)
4×10^{-2}	2.83	7.92
$2^{\frac{1}{2}} \times 10^{-2}$	1	5.92
10^{-2}	0.721	5.80
5×10^{-3}	0.357	5.89.

(b) The helical content for $\alpha = 2^{\frac{1}{2}} \times 10^{-2}$. The curves of helical contents for other α's are very close to it and are hence omitted here to avoid confusion.

[36] These values for ΔH and ΔS are chosen somewhat arbitrarily.

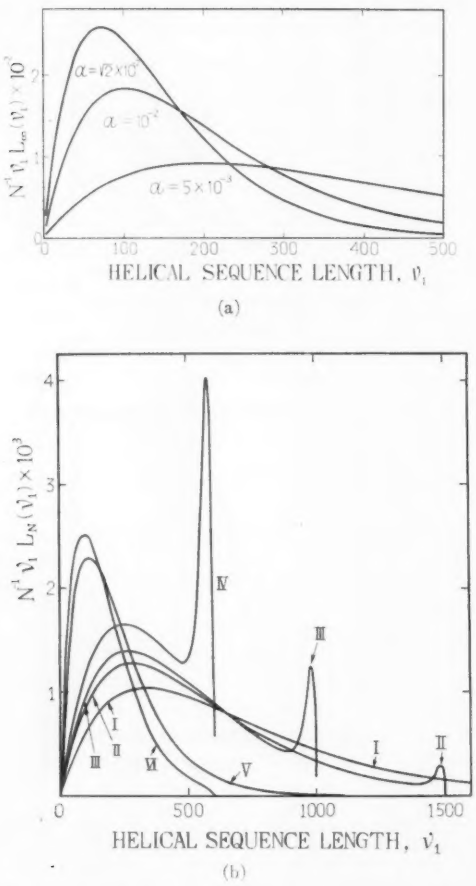

FIG. 4. (a) Effect of α on the helical sequence length distribution in the infinitely long chain. A comparison is made at almost equal helical content, approx. 50%. (b) Effect of N (*D.P.*) and σ. Curve I: $\ln\sigma=0.0553$, $N=\infty$; II: $\ln\sigma=0.0553$, $N=1500$; III: $\ln\sigma=0.0553$, $N=1000$; IV: $\ln\sigma=0.0553$, $N=600$; V: $\ln\sigma=0.0131$, $N=\infty$; VI: $\ln\sigma=0.0131$, $N=600$. $\alpha=2^{\frac{1}{2}}\times10^{-2}$ for all cases.

together and hence the polymer chain shrinks. This fact is consistent with our understanding that while the α-helical configuration has been considered as the folded one, the randomly coiled configuration should preferably be considered as being similar to the β extended one. Although the minimum in $\langle R^2\rangle$ appears always when $l_0>l_1$, its degree becomes small as α decreases, becoming practically imperceptible for $\alpha=5\times10^{-3}$. This is also understandable if we remember the clarified effect of α on the sequence length distribution. As σ increases, the number of residues involved in a helical section increase and further exceed the critical value; hence the polymer chain begins to expand. The effect of σ on the helical sequence length distribution can be seen clearly by comparing the curves I ($\ln\sigma=0.0560$, $N=\infty$) and IV ($\ln\sigma=0.0560$, $N=600$) with V ($\ln\sigma=0.01311$, $N=\infty$) and VI ($\ln\sigma=0.01311$, $N=600$) in Fig. 4(b).

$(\langle R^2\rangle/\langle R_0^2\rangle)^{\frac{1}{2}}$ and $(\langle S^2\rangle/\langle S_0^2\rangle)^{\frac{1}{2}}$ are calculated[37] by using Model II for $\alpha=2^{\frac{1}{2}}\times10^{-2}$ and various N's, and shown in Figs. 5(a) and (b). For comparison the curves for the helical contents are also shown in Fig. 5 (c).[38] The small circles shown in the right-hand sides of Figs. 5(a) and (b) denote the corresponding values for the perfect α helices, i.e., $N^{\frac{1}{2}}l_1/l_0$ and $(N/2)^{\frac{1}{2}}l_1/l_0$, to which $(\langle R^2\rangle/\langle R_0^2\rangle)^{\frac{1}{2}}$ and $(\langle S^2\rangle/\langle S_0^2\rangle)^{\frac{1}{2}}$ tend, respectively, in the limit of $\sigma\to\infty$. As is done in Fig. 5(c), we may choose temperature as the abscissa instead of $\ln\sigma$. In this case $\Delta H=1.08$ kcal and $\Delta S=6.06$ eu have been chosen so as to fit the curve ($N=1500$) for the helical content with the experimental data of Doty and Yang.[2] General features of dimensional changes accompanying the helix-coil transition can be understood immediately from these figures and hence need no explanation here. However, it seems of considerable interest to remark the following point. As σ increases, chain dimensions (and probably also configurations) of specimens of smaller N, approach more rapidly those of the α helices than do those of specimens of larger N, in spite of less helical contents of the former specimens. For example, at $\ln\sigma=0.14$ the helical content of the specimen of $N=1500$ remains approx. 98%, which seems indistinguishable from 100% experimentally, but $(\langle R^2\rangle/\langle R_0^2\rangle)^{\frac{1}{2}}$ becomes smaller than the corresponding value of the α helix by as much as 21%. On the contrary, the helical content of $N=100$ falls 86%, but $(\langle R^2\rangle/\langle R_0^2\rangle)^{\frac{1}{2}}$ exceeds the corresponding value by no more than 3%. This is due to the fact that dimensions of the α helices are much more affected by the disruption of the α-helical structure from some middle parts than by that from both ends. This has been pointed out by Rice and Wada.[8] As has already been seen, the distruption of specimens of smaller N takes place mainly from both ends but that of larger N occurs from some middle parts as well as from both ends. (See Fig. 1.)

IV. SOME CONCLUDING REMARKS

Whether the present theory is quantitative or not (i.e., merely illustrative) depends, in part, on whether $\alpha=2^{\frac{1}{2}}\times10^{-2}$ and $l_0=22.4$ A[39] used, are so or not. As

[37] In the course of numerical computations of Eqs. (85), (89), (97), (99), and (101), it has been found that contributions of terms containing λ_3 and λ_4 are negligible for almost all cases. Therefore, we are required to calculate only three kinds of terms, i.e., those with $k=l=1$, $k=l=2$, and $k=1$ and $l=2$, which are essentially different.

[38] We have assumed optical rotation to be in the linear relation with helical content rather than mean fraction of intact hydrogen bonds. Difference, however, is found to be small for such small α as $\alpha=2^{\frac{1}{2}}\times10^{-2}$. For example, $\xi(\lambda_1)$ and $C(\lambda_1)$ equal 0.5086 and 0.4951 for $\alpha=2^{\frac{1}{2}}\times10^{-2}$ and $\ln\sigma=0.0001$, and 0.5844 and 0.5373 for $\alpha=1/18$ and $\ln\sigma=0.0135$, respectively.

[39] Curves of $(\langle R^2\rangle/\langle R_0^2\rangle)^{\frac{1}{2}}$ and $(\langle S^2\rangle/\langle S_0^2\rangle)^{\frac{1}{2}}$ can be converted comparatively easily to those for different l_0, but not so for different α.

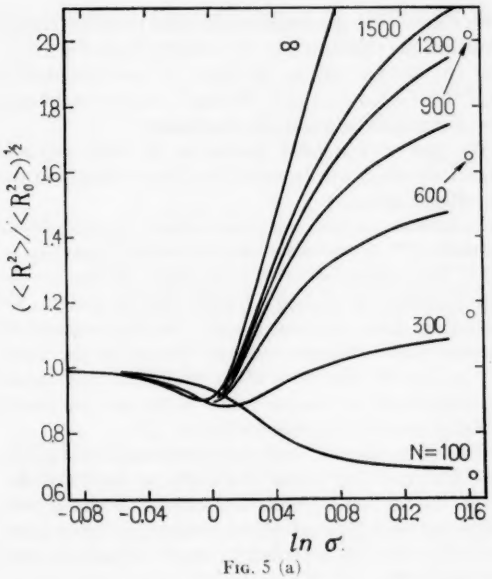

FIG. 5 (a)

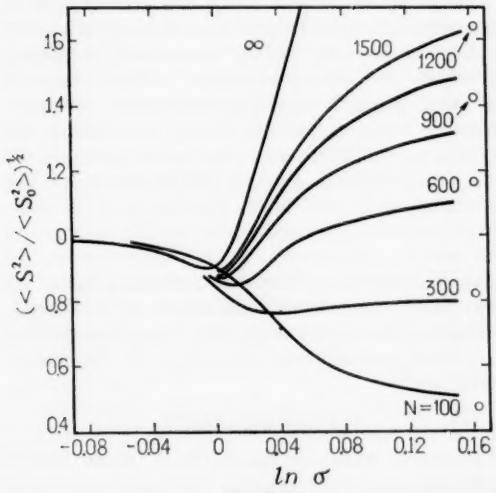

FIG. 5 (b)

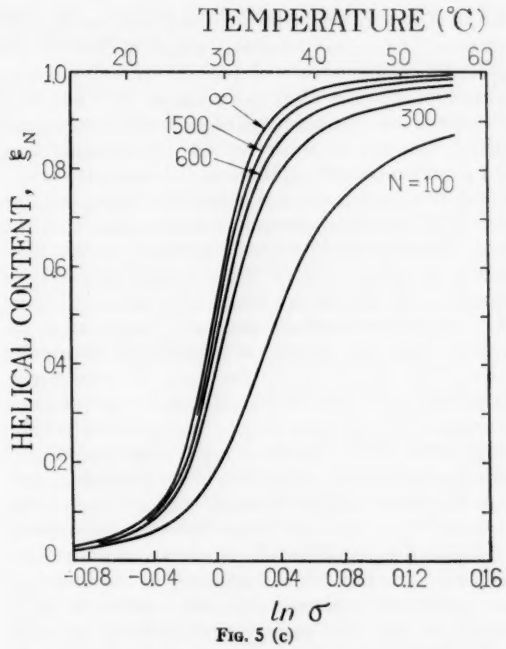

FIG. 5 (c)

FIG. 5. (a) $(\langle R^2\rangle/\langle R_0^2\rangle)^{\frac{1}{2}}$ and (b) $(\langle S^2\rangle/\langle S_0^2\rangle)^{\frac{1}{2}}$ for various N's (*D.P.*). The small circles shown in the right-hand sides of the figures denote the corresponding values for the perfect α helices. The parameters in Eqs. (90) and (102) are chosen as $\alpha=2^{\frac{1}{2}}\times10^{-2}$, $l_1=1.5$ A, and $l_0=22.4$ A. (c) Helical contents. Equation (112) is assumed between $\ln\sigma$ and temperature, °K. The temperature in the upper abscissa is graduated in °C (not in °K). $\Delta H=1.08$ kcal and $\Delta S=6.06$ eu are chosen so as to fit the curve of $N=1500$ with the experimental data of Doty and Yang[2] on optical rotations of poly-γ-benzyl-L-glutamate in the solvent system ethylene dichloride-dichloroacetic acid (1:4).

has been described, Zimm and Bragg[4] chose the preceding value of α from the experimental data of Doty *et al.*[2,22] on optical rotations of the two specimens, i.e., $N=1500$ and 26, of poly-γ-benzyl-L-glutamate. The helical content of a specimen of small N such as 26, as is well known, is very sensitive to N and hence is much affected by polydispersity. Errors which may arise from it can be excluded by careful fractionations. Even if this is done, there remains a question whether or not a linear interpolation of observed optical rotations between the two values corresponding to the perfect α helix and the perfect random coil gives correctly the helical content for a specimen of such small N. Tinoco and Woody[40] have warned of this point, although it has still remained unclarified how long a helical section contributes to the optical rotation by the essentially same amount as does the equal number of residues in the infinitely long α helix. This point appears to need further investigation.

In the present calculation we have neglected all long-range interactions between residues being distant by more than five residues along the chain. Of these the most important is the so-called excluded volume effect, with which we are always inevitably haunted when we wish to discuss chain dimension in solutions. Most of the solvent or solvent systems in which a polypeptide chain is in the randomly coiled configuration or in which the transition occurs are good solvents for corresponding polypeptides. Therefore the chain appears to behave as non-Gaussian and hence the relation, $\langle R_0^2\rangle=Nl_0^2$, which we have assumed for the perfect random coil, does not hold. Though current

[40] See work cited in footnote 28.

theories[41] of dilute polymer solutions teach us that the relation $\langle R_0^2\rangle = Na^2(1+N^{\frac{1}{2}}b)$, where a and b are quantities characteristic of polymer-solvent systems, is appropriate near Flory temperature, it is not clear whether or not this expression is still valid for such good solvent systems as those we are encountering now (e.g., poly-γ-benzyl-L-glutamate-dichloroacetic acid). Under this circumstance it seems best to replace the real chain by a hypothetical Gaussian chain with the same mean-square end-to-end distance, as we have done in the present theory. When l_0 is determined from experimental data in this way, it inevitably has some D.P. dependence, perhaps becoming larger as N increases. From this respect it is preferable to use l_0's determined experimentally for each N respectively, rather than a l_0 determined from data on one specimen throughout (as we have done). The excluded volume effect in interrupted helices is much more complicated and even qualitative estimation is not possible at present. For these reasons it seems safe to consider the curves in Figs. 5(a) and (b) to be rather illustrative.

In spite of the considerable importance of the present problem, there has not yet appeared in the literature any systematic experimental result capable of being compared with the theory quantitatively or even qualitatively. A critical test of the theory, therefore, must be postponed till it becomes available. Instead we wish to remark the following fragmental but interesting point.

In order to clarify the question whether or not the transition occurs in the all-or-none fashion, Doty and his co-workers[42,43] carried through the transition a specimen of polypeptide, which has the same intrinsic viscosity in the perfect helical form and the perfect random coil form. If the all-or-none were the case, any change would not occur in intrinsic viscosity during the transition. Results showed that this was not the case (although what did happen had not been described). If, following this procedure, we carry through the transition specimens which have the same $\langle R^2\rangle$ or $\langle S^2\rangle$ in both forms (the specimens of $N=222$ or 444,[43] respectively, in the present case) it is evident from Figs. 5(a) and (b) though curves for these N's are not drawn, that these quantities pass through a shallow minimum near the middle point of the transition.

We now give a brief discussion of other physical quantities which are expected to change sharply in the transition region.

As is well known, the mean-square electric dipole moment $\langle U^2\rangle$ is the same kind of physical quantity as $\langle R^2\rangle$. The expression of this for model II can be obtained merely by replacing l_1 and l_0 by ju_1 and ju_0, respectively. Here, ju_1 and ju_0 are electric moments of *distorted* and *undistorted* residues defined in the same way as l_1 and l_0. The curve of $\langle U^2\rangle$, although not drawn because of lack of reliable values of ju_1 and ju_0, would probably show a behavior similar to $\langle R^2\rangle$.

General features, as seen for dimensional changes in Figs. 5(a) and (b), would also apply, at least qualitatively, to frictional properties such as intrinsic viscosity and translational diffusion constant, since these quantities may be assumed to vary in parallel with $\langle R^2\rangle$ and $\langle S^2\rangle$.

Though in the present theory only the changes in dimensions have been treated, those in shape are also of considerable interest, varying from nearly symmetric (spherical) to highly asymmetric (rodlike) shape. It will affect gradient dependence of intrinsic viscosity, streaming birefringence, etc. Yang[44] has already observed a marked difference in the former quantities for both extreme forms. One of the measures for this asymmetry is the ratio of the component of the mean square radius of gyration parallel to the direction of both ends to that vertical to it. Unfortunately, this quantity cannot be obtained in functional form. We might select, instead, the quantity, $(\langle R^2\rangle/\langle S^2\rangle - 1)$, which varies from 0 to 1 as chain configurations do from the perfect random coil (Gaussian) to the perfect α helix (rodlike).

ACKNOWLEDGMENT

The author wishes to thank Dr. A. Wada for his helpful suggestions and valuable discussions concerning this and related problems.

[41] See, for example, the recent review concerning this problem by W. H. Stockmayer, Makromol. Chem. **35,** 54 (1960).

[42] P. Doty, Revs. Modern Phys. **31,** 107 (1959).

[43] It seems noteworthy that these values of N's are comparable with about $N=300$, a specimen which has been found to have the same intrinsic viscosity in both forms. Here this value of N is read from Fig. 2 in footnote 31.

[44] J. T. Yang, J. Am. Chem. Soc. **81,** 3902 (1959).

High-Speed Computations in Diffusion Kinetics. III. Solute Depletion in the Cylindrical One Radical-One Solute Model*

HUGO FRICKE AND DAVID L. PHILLIPS

Chemistry and Applied Mathematics Divisions, Argonne National Laboratory, Argonne, Illinois

(Received August 24, 1960)

The earlier study [D. A. Flanders and H. Fricke, J. Chem. Phys. **28**, 1126 (1958)] of the kinetic properties of a cylindrically symmetric one radical-one solute model was extended by taking account of the transient dilution of the solute which occurs during the reaction. The results of the computations are collected in a table from which, by interpolation I_R the fraction of radicals recombining, can be obtained for any experimentally important values of the four dimensionless parameters which define the problem. Under conditions of practical interest the effect of solute depletion on I_R is (a) appreciable only when the ratio of the rate constants of radical-solute and radical-radical reactions is above 0.1, and (b) only slightly affected by the diffusion coefficient of the solute. The role played by solute depletion is elucidated by graphs representing the transient course of the reactions.

THE treatment of the one radical-one solute model, described in the first paper of this series,[1] was simplified by ignoring the transient dilution of the solute, which occurs owing to its reaction with the radical. In the second paper[2] this so-called "depletion effect" was taken into account in the spherically symmetric version of the model. The object of the present work was to carry out a similar study of the cylindrically symmetric model. The problem was accordingly studied by adding Eqs. (3b) and (4b) to the system of equations solved in I using $\epsilon=1$. The notation is the same as used before,

$$\partial C/\partial t = D_1\partial^2 C/\partial r^2 + (D_1/r)\partial C/\partial r - \beta C n \qquad (3b)$$

$$C=C_0, \qquad t=0, \qquad r=0-\infty. \qquad (4b)$$

The computations were carried out as in II on the Argonne computer GEORGE, in terms of the earlier used parameters: $E=N_0\alpha/2\pi D$, $B=b^2\beta C_0/4D$, β/α, and D_1/D. The values for I_R are believed accurate to the third significant figure.

Calculations were made for five different values of E from 0.707 to 10.61. When the model is applied to water treated with charged material particles, the corresponding range of linear energy transfer (LET) values is approximately 2 to 30 ev/A [as calculated by using $\alpha=10^{-11}$ molecules^{-1} cm^3 sec^{-1}, $D=4.5\times10^{-5}$ cm^2 sec^{-1}, $G(-H_2O)=5.2$].[3,4] In particle tracks of LET below 2 ev/A, the spatial distribution of the radicals along the track is too far from being uniform to use the model. The values of E studied include 1.35 and 2.58, for which computations were not made in I. Practical applications [5-7] of the model have shown that the values of E used in I were spaced too far apart to allow data for intermediate values of E to be interpolated with sufficient accuracy.

As expressed in I_R, which represents the fraction of recombining radicals, the depletion effect increases with increasing E and β/α and with decreasing D_1/D. No computations were made above $\beta/\alpha=2$, which is the largest value expected to be encountered experimentally.[2] The computations were limited, moreover, to values of D_1/D below 0.4, the range of chief practical interest.

The computed values of I_R are presented in Table I. From these data, by interpolation, sufficiently accurate values of I_R can be obtained for any given values of the parameters of experimental interest. In using the table, the following features should be noted.

(1) The transient change in concentration of the solute becomes negligible when $\beta/\alpha\to0$ or $D_1/D\to\infty$; I_R then depends only on E and B. This was the case calculated in I, but the calculation was repeated with greater accuracy and the values obtained are shown under $\beta/\alpha=0$.

(2) The radical-radical reaction is so fast that, under practical conditions, the amount of solute diffusing into the reaction zone from the environment is relatively small during the time of this reaction. That this is the situation can be shown by examining the transient stage of the reactions (compare with the following). Further evidence is obtained from the fact that, within the range of D_1/D values studied, I_R is only slightly affected by the value of D_1/D (Fig. 1). This slight effect of D_1/D on I_R can be readily taken into account by using the table, but for practical purposes one may use for I_R the values given for $D_1/D=0.2$.

* Based on work performed under the auspices of the U. S. Atomic Energy Commission.

[1] D. A. Flanders and H. Fricke, J. Chem. Phys. **28**, 1162 (1958), hereafter referred to as I.

[2] H. Fricke and D. L. Phillips, J. Chem. Phys. **32**, 1183 (1960), hereafter referred to as II.

[3] $G(-H_2O)$ represents the number of water molecules initially decomposed per 100 ev of absorbed radiation energy.

[4] H. Fricke, Ann. N. Y. Acad. Sci. **59**, 567 (1955).

[5] C. B. Senvar and E. J. Hart, *Proceedings of the Second United Nations International Conference on the Peaceful Uses of Atomic Energy* (United Nations, New York, 1958), Vol. 29, p. 19.

[6] C. N. Trumbore and E. J. Hart, J. Phys. Chem. **63**, 867 (1959).

[7] A. R. Anderson and E. J. Hart, Radiation Research Society Meeting, San Francisco, May, 1960.

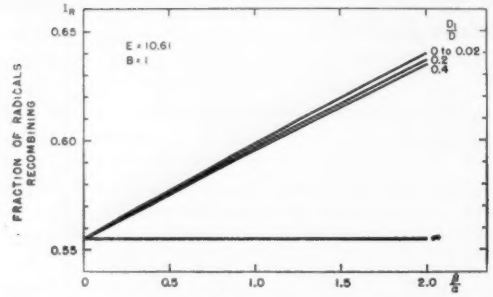

FIG. 1. I_R as a function of β/α, for $E=10.61$, $B=1$, and different values of D_1/D.

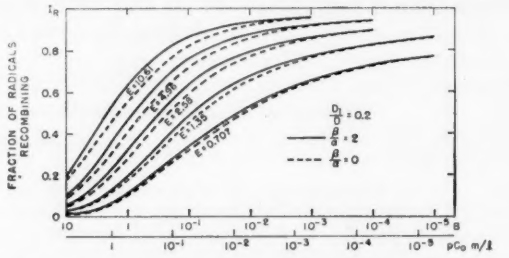

FIG. 2. I_R as a function of B, for different values of E, $\beta/\alpha=2$ and 0, $D_1/D=0.2$. Also shown is the approximate scale of pC_0 values in moles/liter to be used when the model is applied to water ($p=\beta/2\alpha$).

(3) Since the relation of I_R to β/α is nearly linear (Fig. 1), I_R for any desired β/α can be interpolated with good accuracy from the data for I_R given in Table I. For the values of D_1/D of practical interest, the depletion effect is negligible when $\beta/\alpha \leq 0.1$; in this range one may use for I_R the values given for $\beta/\alpha=0$.

Plots useful for analyzing experimental data may be prepared from Table I. Figure 2 represents I_R as a function of B, for different values of E. Figure 3 represents I_R as a function of E, for different values of B. In both cases data are shown for $\beta/\alpha=2$ and 0, $D_1/D=0.2$. To facilitate the physical understanding of these plots, we include scales for LET (LET$=2.7\times E$ ev/A) and for pC_0 ($pC_0=0.56\times B$ moles/liter, $p=\beta/2\alpha$) which are computed for water. On examining Fig. 2, it will be seen that solute depletion affects the I_R-B curve in two ways: The curve becomes steeper over its central section and is shifted horizontally towards larger B's. For $E=10.61$, $\beta/\alpha=2$, $D_1/D=0.2$, the shift at the center of the curve is approximately equivalent to a 40% decrease in the calculated value of β.

Figures 4 and 5(a)–(c) show for some typical cases, the transient drop in concentration of the solute in the reaction zone and its chronological relation to the radical-radical and radical-solute reactions. Time and length are given in seconds and centimeters, calculated for application of the model to water ($D=4.5\times10^{-5}$ cm^2 sec^{-1}, $b=18\times10^{-8}$ cm).[2]

TABLE I. Fraction of radicals recombining (I_R) for different values of parameters ($E=N_0\alpha/2\pi D$; $B=b^2\beta C_0/4D$).

E	D_1/D	β/α log $B\rightarrow$	1	0	−1	−2	−3	−4	−5
					I_R				
10.61	0	2		0.640					
	0.02	2		0.640	0.863				
	0.2	2	0.204	0.637	0.862	0.933	0.959		
	0.4	2		0.635	0.860				
	0.2	1	0.191	0.597	0.846	0.929			
	0–∞	0[a]	0.181	0.555	0.822	0.922	0.956		
4.96	0.02	2		0.466	0.761				
	0.2	2	0.1066	0.463	0.759	0.874	0.920	0.943	
	0.4	2		0.461	0.757				
	0.2	1	0.1026	0.433	0.740	0.868			
	0–∞	0[a]	0.0989	0.404	0.715	0.859	0.916	0.941	
2.58	0.02	2			0.637				
	0.2	2	0.0582	0.315	0.634	0.792	0.862	0.899	
	0.4	2			0.632				
	0.2	1	0.0570	0.297	0.615	0.784			
	0–∞	0[a]	0.0558	0.281	0.593	0.774	0.856	0.897	
1.35	0.02	2			0.488				
	0.2	2	0.0313	0.195	0.486	0.676	0.774		0.863
	0.4	2			0.485				
	0.2	1	0.0309	0.188	0.472	0.668			
	0–∞	0[a]	0.0305	0.180	0.455	0 658	0 766		0.861
0.707	0.02	2			0.339				
	0.2	2	0.0166	0.113	0.338	0.532	0.650		0.771
	0.4	2			0.337				
	0.2	1	0.0165	0.110	0.329	0.525			
	0–∞	0[a]	0.0164	0.107	0.320	0.517	0.643		0.769

[a] No depletion.

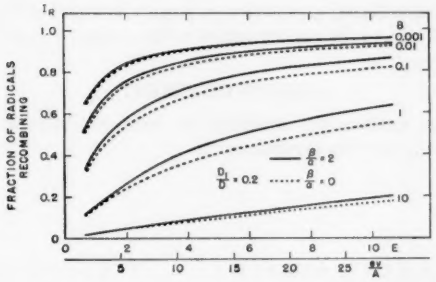

FIG. 3. I_R as a function of E, for different values of B, $\beta/\alpha=2$ and 0, $D_1/D=0.2$. Also shown is the approximate scale of LET values in ev/A to be used when the model is applied to water.

For values of the parameters stated in the legend, Fig. 4 shows the spatial distribution of the solute at different times during the reaction. The inserted table records the fractions of radicals which have combined with each other $[I_R(t)]$ and with the solute $[I_S(t)]$ at these different times. Note the initial rapid reaction controlled drop in concentration of the solute and the subsequent slow diffusion controlled recovery to the initial condition. In the center of the reaction zone, the maximal drop in concentration of the solute is 85%, reached after 0.6×10^{-9} sec, at which time the radical recombination reaction is within 10% of completion. After 10^{-8} sec, both reactions are practically completed, but the concentration of the solute in the center of the zone is only 46% of its original value.

Figures 5(a)–(c) show as function of time (1) the relative concentration of solute at the axis of the cylinder $[C(t)/C_0]$, (2) the fraction of radicals which have recombined $[I_R(t)]$, and (3) the fraction of radicals which have combined with the solute $[I_S(t)]$. Data are shown for three different values of the dif-

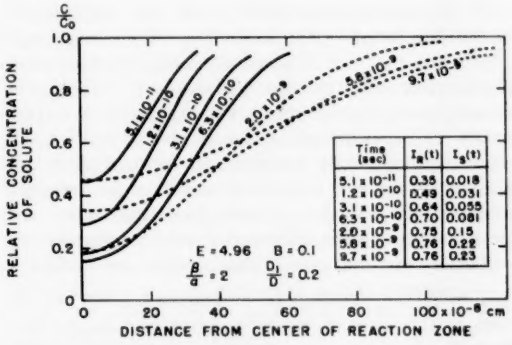

Time (sec)	$I_R(t)$	$I_S(t)$
5.1×10^{-11}	0.35	0.018
1.2×10^{-10}	0.49	0.031
3.1×10^{-10}	0.64	0.055
6.3×10^{-10}	0.70	0.081
2.0×10^{-9}	0.75	0.15
5.8×10^{-9}	0.76	0.22
9.7×10^{-9}	0.76	0.23

FIG. 4. Spatial distribution of solute at different times during the reaction, for $E=4.96$, $B=0.1$, $\beta/\alpha=2$, $D_1/D=0.2$. The solid lines represent the concentration of the solute during the initial period in which the concentration is decreasing; the dashed lines represent the concentration during the period of recovery. The scales of time (sec) and length (cm) are calculated for application of the model to water. The inserted table records the fractions of radicals which have recombined $[I_R(t)]$ and combined with the solute $[I_S(t)]$ at the times stated.

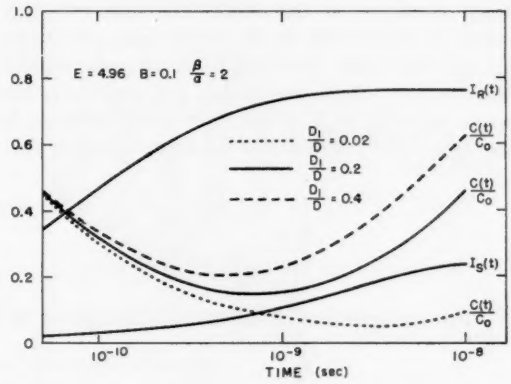

(a)

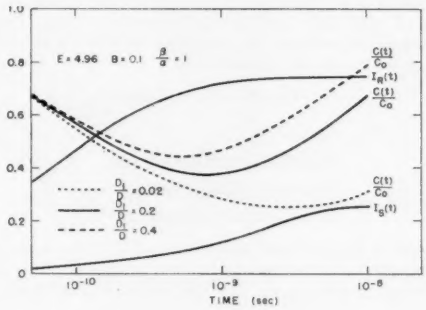

(b)

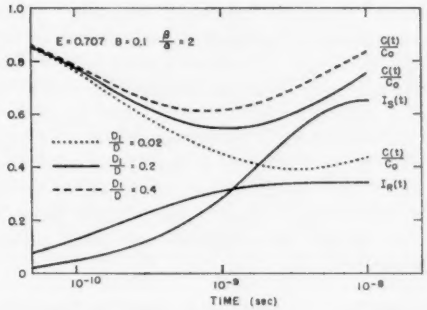

(c)

FIG. 5. Time curves for (1) the relative concentration of solute at the axis of the cylinder $[C(t)/C_0]$, (2) the fraction of radicals which recombined $[I_R(t)]$, and (3) the fraction of radicals which combined with the solute $[I_S(t)]$. The $I_R(t)$ and $I_S(t)$ curves are shown only for $D_1/D=0.2$. The curves for the other values of D_1/D practically coincide with these. (a) $E=4.96$, $\beta/\alpha=2$; (b) $E=4.96$, $\beta/\alpha=1$; (c) $E=0.707$, $\beta/\alpha=2$; (a)–(c) $B=0.1$, $D_1/D=0.4$, 0.2, and 0.02. The time scale (in seconds) is calculated for application of the model to water.

fusion coefficient of the solute. The $I_R(t)$ and $I_S(t)$ curves are shown only for $D_1/D=0.2$, since the curves for the two other values of D_1/D are only slightly different from these. As pointed out previously, the reason the value of D_1/D has such a small effect on I_R and I_S is that the diffusion of the solute is so slow that the recombination reaction is largely completed before D_1/D affects the concentration of the solute to a marked degree.

ACKNOWLEDGMENT

The authors are indebted to Anthony Strecok for carrying out the programming.

THE JOURNAL OF CHEMICAL PHYSICS VOLUME 34, NUMBER 3 MARCH, 1961

Paramagnetic Resonance Absorption in Naphthalene in Its Phosphorescent State*

CLYDE A. HUTCHISON, JR., AND BILLY W. MANGUM† ‡

Enrico Fermi Institute for Nuclear Studies and Department of Chemistry, University of Chicago, Chicago, Illinois

(Received August 18, 1960)

Paramagnetic resonance absorption has been observed in naphthalene in solid solution in a single crystal of durene when irradiated with light from an A-H6 mercury lamp. The fine structure of the spectrum at a frequency of $\sim 22.7\times10^9$ cps may be described by the spin-Hamiltonian

$$\mathcal{H}=|\beta|\,\mathbf{H}\cdot g\cdot\mathbf{S}+DS_z^2+E(S_x^2-S_y^2),$$

with

$$S=1,$$
$$g=2.0030\pm0.0004 \text{ (isotropic)},$$
$$D/hc=\pm0.1003\pm0.0006 \text{ cm}^{-1},$$
$$E/hc=\mp0.0137\pm0.0002 \text{ cm}^{-1}.$$

Observations at a different frequency, $\sim 9.7\times10^9$ cps, and also measurements on perdeuteronaphthalene are described by essentially the same parameters. The fine structure data identify the spectrum as arising from a triplet state and leave no doubt as to the triplet character of the phosphorescent state of naphthalene. The zero-field splitting of the triplet has its origin in the magnetic dipole-dipole interaction between the two unpaired electrons in the triplet state. These experimental results are in agreement with the theoretical estimates. Hyperfine structure has been observed and is interpretable on the basis of the anisotropic hyperfine interaction constants for a C-H fragment given by McConnell. The π-electron spin density on the α-carbons is found to be 0.209. The hyperfine structure results identify the spectrum as arising from naphthalene. In addition they show that the triplet state is ${}^3B_{2u}{}^+$ and that the naphthalene molecules are oriented in the crystals such that they are not only coplanar with the durene molecule which they replace but also have their long and short twofold axes in this plane parallel, respectively, to the long and short axes of durenes.

INTRODUCTION

IT was suggested by Lewis, Lipkin, and Magel[1] and by Terenin[2] that the relatively long-lived phosphorescence emission of complex organic molecules at low temperatures might come from a triplet-singlet transition. The extensive investigations of Lewis and Kasha[3,4] served to establish the fact that quite generally the upper state involved in the phosphorescence of organic molecules in rigid solvents is the lowest triplet state into which the molecule falls after being optically excited to a higher singlet state. There have been extensive optical investigations of these phosphorescent states.[5]

Detailed investigations of the phosphorescence in the case of naphthalene have been made by McClure,[6–8] by Ferguson, Iredale and Taylor,[9] and by Williams.[10]

It was realized by Lewis[3,4] that the triplet-state mechanism for phosphorescence implied photomagnetic effects and that the demonstration of photomagnetism in phosphorescing systems would afford striking confirmation of this interpretation. Exploratory experiments were performed by Lewis and Calvin[11] and a more thorough study was made by Lewis, Calvin, and Kasha[12] of the effect of illumination on the magnetic susceptibility of the system fluorescein-boric acid glass, confirming the existence of photomagnetism.

Earlier photomagnetic experiments by Fröhlich,

* This work has been supported by the U. S. Atomic Energy Commission.

† National Science Foundation Predoctoral Fellow, 1956–1959.

‡ Present address: The Clarenden Laboratory, Parks Road, Oxford, England.

[1] G. N. Lewis, D. Lipkin, and T. T. Magel, J. Am. Chem. Soc. **63**, 3005 (1941).

[2] A. Terenin, Acta Physicochim. U.R.S.S. **18**, 210 (1943).

[3] G. N. Lewis and M. Kasha, J. Am. Chem. Soc. **66**, 2100 (1944).

[4] G. N. Lewis and M. Kasha, J. Am. Chem. Soc. **67**, 994 (1945).

[5] M. Kasha and S. P. McGlynn, Ann. Rev. Phys. Chem. **7**, 403 (1956).

[6] D. S. McClure, J. Chem. Phys. **17**, 905 (1949).

[7] E. H. Gilmore, G. E. Gibson, and D. S. McClure, J. Chem. Phys. **20**, 829 (1952).

[8] E. H. Gilmore, G. E. Gibson, and D. S. McClure, J. Chem. Phys. **23**, 399 (1955).

[9] J. Ferguson, T. Iredale, and J. A. Taylor, J. Chem. Soc. **1954**, 3610.

[10] R. Williams, J. Chem. Phys. **30**, 233 (1959).

[11] G. N. Lewis and M. Calvin, J. Am. Chem. Soc. **67**, 1232 (1945).

[12] G. H. Lewis, M. Calvin, and M. Kasha, J. Chem. Phys. **17**, 804 (1949).

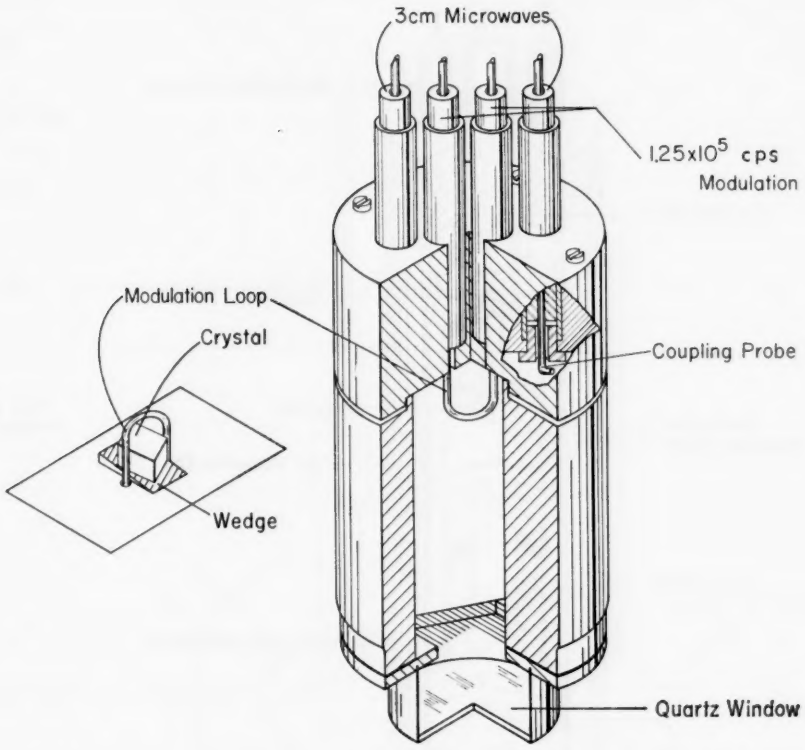

FIG. 1. Cavity used in 3-cm experiments.

Szalay, and Ször[13] had revealed photomagnetic effects, and the magnetic dichroism observed by Yamamoto[14] was in agreement with the photomagnetism studies. The experiments of Evans[15] have given the most detailed results, and he has measured the decay times for the paramagnetism accompanying phosphorescence, finding them to be in agreement with the observed decay times for the phosphorescence emission. Kortum[16] has also investigated the photomagnetism accompanying phosphorescence.

At about the same time that the triplet-state mechanism for phosphorescence was proposed by Lewis, paramagnetic resonance was first observed by Zavoisky.[17] Microwave paramagnetic resonance techniques appeared to be ideally suited to the investigation of the photomagnetic effects accompanying phosphorescence. Efforts[18] to observe paramagnetic resonance in the systems which had been used in the static field susceptibility experiments gave negative results.

It was first pointed out to us by Weissman[19] that the inability to observe resonance in these systems probably had its origin in a splitting of the triplet state in zero magnetic field which would lead to a large anisotropy of the high field resonance. He suggested that inasmuch as the attempts to observe resonance were made on randomly oriented molecules the anisotropy broadening was responsible for the failure.

Optical investigations had been made using oriented molecules, particularly by McClure.[20,21] It was believed that dilute solutions of oriented phosphorescent molecules in an optically nonabsorbing material were required for the resonance experiments because of the self-quenching processes and other complications which might interfere in the case of pure crystalline substances. McClure,[22] Sidman,[23] and others suggested various such systems to us, in particular, McClure's[20,22] single-crystal solution of naphthalene in durene. We were finally encouraged to make such experiments by K. H. Hausser, who supplied us with naphthalene-durene crystals grown by H. C. Wolf.

We express our appreciation for all the help and advice mentioned above which served to revive our

[13] P. Frohlich, L. Szalay, and P. Szor, Acta Chem. Phys. Univ. Szeged (Hungary) **2**, 96 (1948).
[14] D. Yamamoto, J. Chem. Soc. Japan **72**, 693, 782 (1951); Bull. Chem. Soc. Japan **24**, 211, 214 (1951).
[15] D. F. Evans, Nature **176**, 777 (1955).
[16] G. Kortum, Angew. Chem. **70**, 14 (1958).
[17] E. Zavoisky, J. Phys. U.S.S.R. **9**, 211, 245, 447 (1945); **10**, 170, 197 (1946).
[18] See for example, J. A. Weil, "Search for the paramagnetic resonance absorption of an organic dye in its triplet state," thesis, University of Chicago, 1955, p. 2.
[19] S. I. Weissman (private communication).
[20] D. S. McClure, J. Chem. Phys. **22**, 1668 (1954).
[21] D. S. McClure, J. Chem. Phys. **24**, 1 (1956).
[22] D. S. McClure (private communication).
[23] J. W. Sidman (private communication).

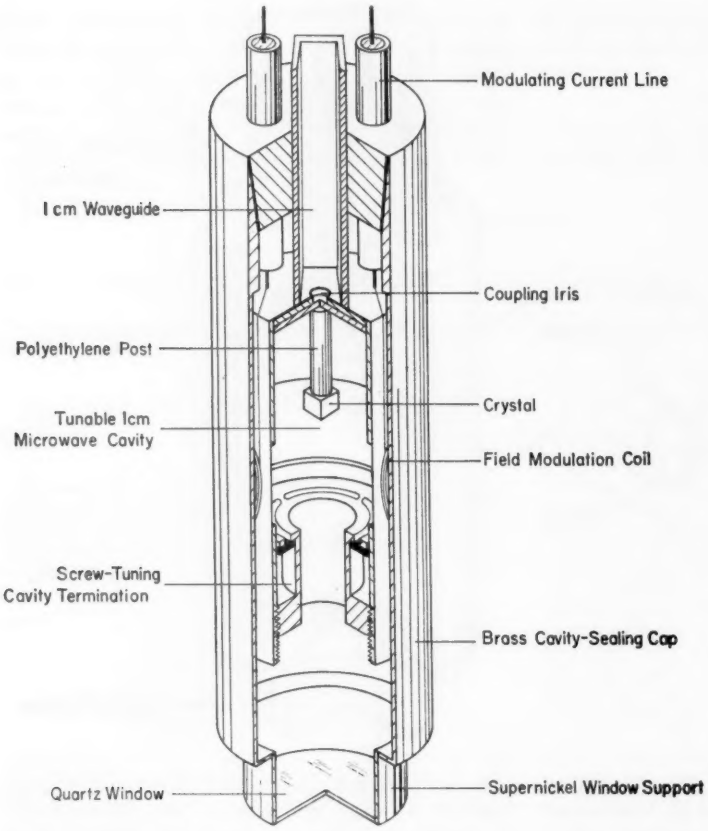

FIG. 2. Cavity used in 1-cm experiments.

interest in this problem after several years of discouraging results[18] and which led to the experiments described in this paper.

A preliminary account of these results has been given by Hutchison and Mangum.[24]

EXPERIMENTAL DETAILS

The measurements have been made using microwave frequencies of $\sim 9.7\times10^9$ cps (3 cm) and $\sim 22.7\times10^9$ cps (1 cm). Magnetic fields were determined from proton resonance frequencies. In some cases the proton resonance signal and the triplet-state signal were superposed on a dual beam scope and in others proton frequencies were measured at the fields for center of resonance as determined from recorder charts. Diphenylpicryl hydrazyl was placed in the cavity at the position of the crystal being studied. The value of the magnitude $|\mathbf{H}|$ of the field strength measured in gauss was taken to be

$$|\mathbf{H}| = 3.5658\times10^{-7}\times(\nu_{\mathrm{mic}}/\nu_P{}^{\mathrm{DPPH}})\times\nu_P,$$

where ν_{mic} = microwave frequency, $\nu_P{}^{\mathrm{DPPH}}$ = proton resonance frequency with magnetic field adjusted to center of hydrazyl resonance, ν_P = proton resonance frequency with proton signal superposed on that part of resonance being investigated.

Light for the irradiation of the crystals was supplied from an A–H6 high-pressure Hg arc. The sample was placed in a resonant cavity provided with a quartz window at the bottom. The two cavities used in these experiments are shown in Figs. 1 and 2. The 3-cm cavity was rectangular and operated in the TE–101 mode. The 1-cm cavity was cylindrical and operated in the TE-011 mode. The cavities were immersed in a quartz Dewar which contained liquid N_2. The light entered at an unsilvered window on the Dewar and was reflected into the cavity as shown in Fig. 3. The microwave magnetic field $\mathbf{H}_{RF}$ in the 1-cm cavity was polarized perpendicular to the static magnetic field $\mathbf{H}$ for all angles of rotation of the cavity about its axis. In the 3-cm cavity the direction of the microwave field rotated with the cavity. The magnetic field $\mathbf{H}$ was modulated at a frequency of 1.25×10^5 cps using a loop inside the cavity in the 3-cm case and coils outside the cavity in the 1-cm case.

[24] C. A. Hutchison, Jr., and B. W. Mangum, J. Chem. Phys. **29**, 952 (1958).

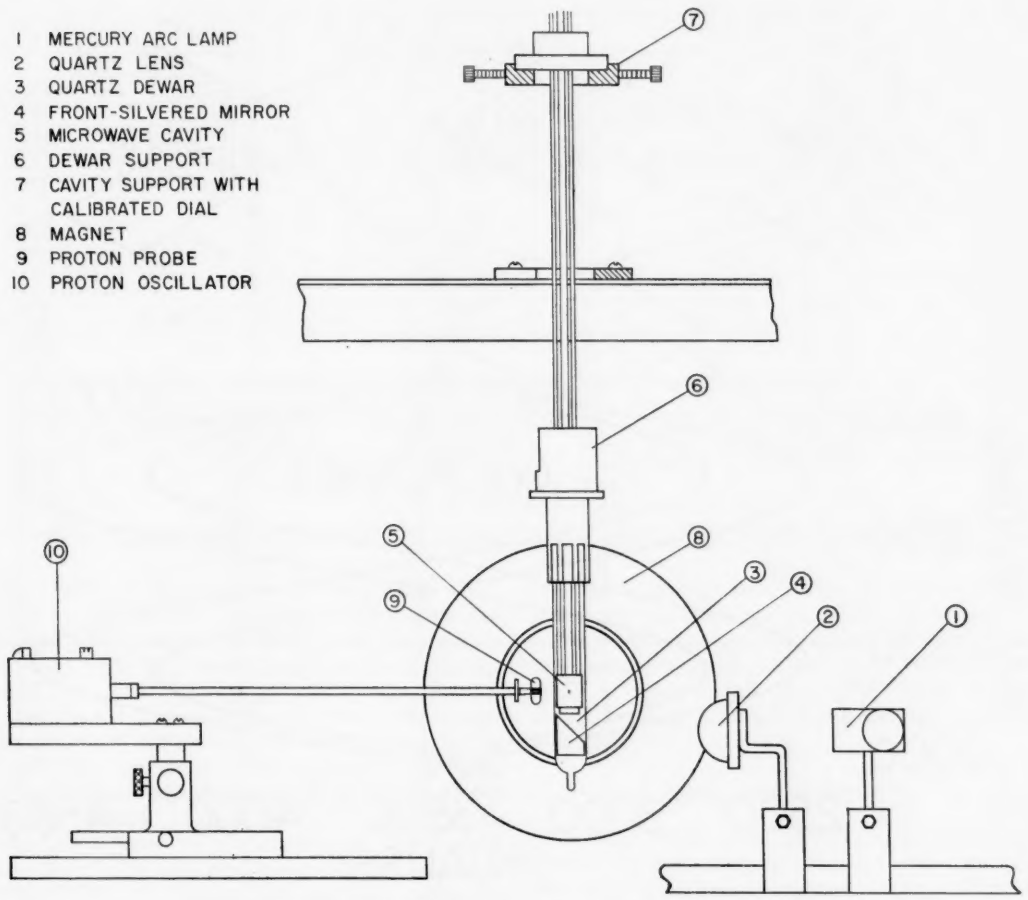

FIG. 3. Schematic diagram of apparatus.

The crystals were mounted and oriented in the cavities so that when the cavities were rotated about their long axes these axes of rotation were normal to a principal magnetic plane of a durene molecule. The axis systems used for describing the durene and naphthalene molecules are shown in Fig. 4. The durene crystal[25] is monoclinic with $\beta = 1.977$ rad (113.3°) (angle between a and c axes). There are two durene molecules per unit cell as shown in Fig. 5. The angles which the x axis (long axis) of one durene molecule makes with the a, b, c'-(c' is perpendicular to the ab

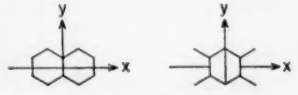

FIG. 4. Axis systems for naphthalene and durene molecules.

[25] J. M. Robertson, Proc. Roy. Soc. (London) **A141**, 594 (1933); **A142**, 659 (1933).

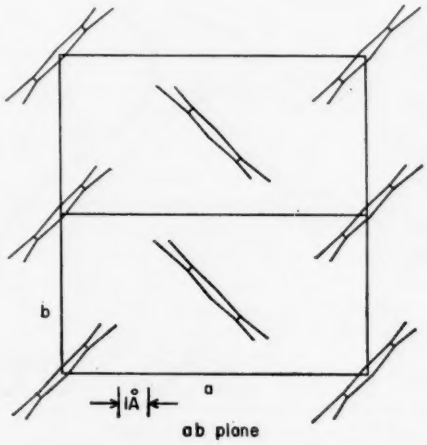

FIG. 5. Arrangement of molecules in the durene structure.

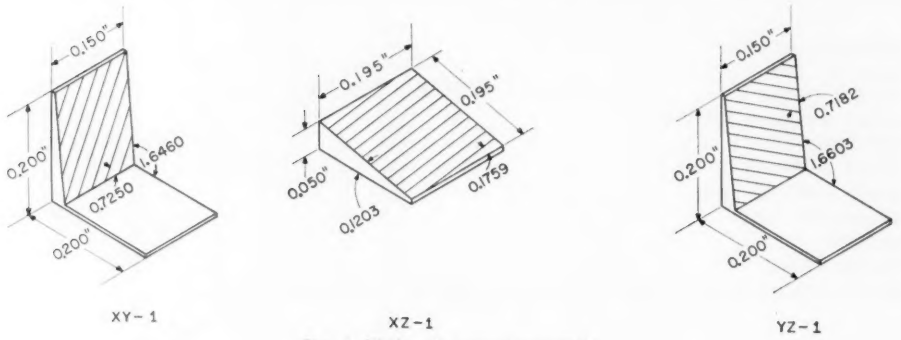

FIG. 6. Wedges for mounting crystals.

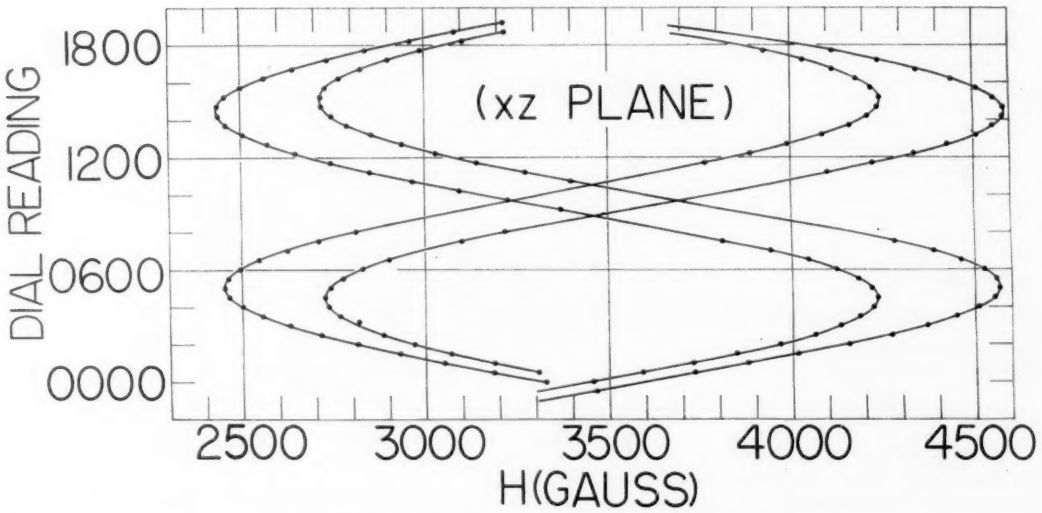

FIG. 7. Magnitude of **H** at which resonance was observed vs rotation of **H** in *xz* plane of one type of durene molecule.

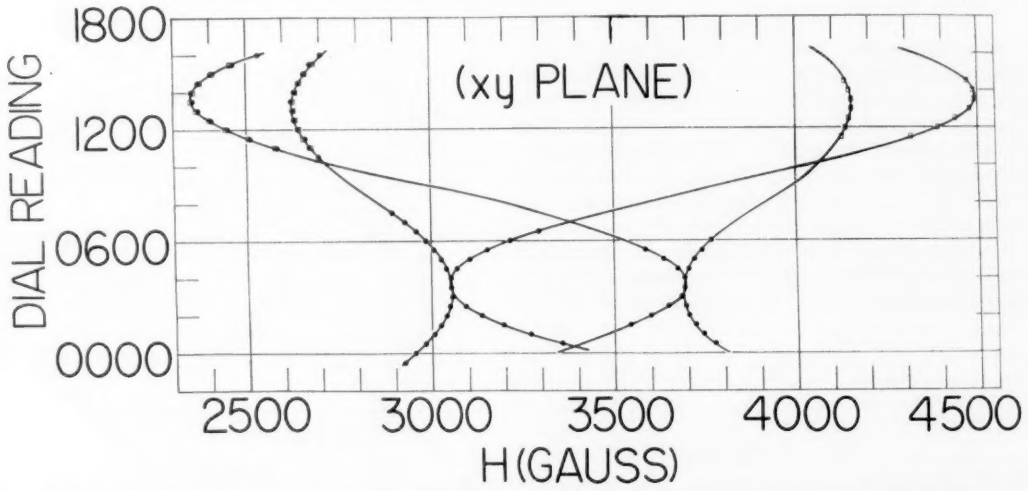

FIG. 8. Magnitude of **H** at which resonance was observed vs rotation of **H** in *xy* plane of one type of durene molecule.

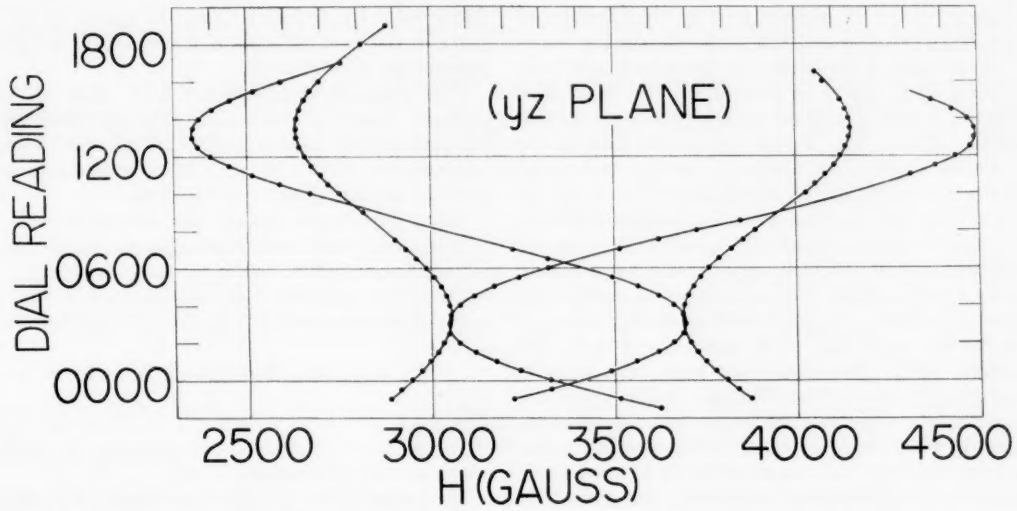

FIG. 9. Magnitude of **H** at which resonance was observed vs rotation of **H** in yz plane of one type of durene molecule.

plane) axes of the crystal are, respectively, 0.857, 0.723, and 1.475. The y axis (short axis) makes the angles 1.690, 1.592, and 0.120. The two molecules go into each other by a twofold screw rotation about the b axis.

The crystal cleaves in the ab plane. Microscopic examination of surface striations served to identify the b axis. This identification was confirmed by J. Fisher by microscopic examination using polarized light and the optical and cleavage data of Groth[26] (Groth's information must be transformed to Robertson's[25] axis choice). Crystals were mounted using Apiezon N grease with their cleavage surfaces flat against the ruled surfaces of the polystyrene wedges of the type shown in Fig. 6. They were mounted so that their b axes were parallel to the ruled lines. It will be seen that the angles of these wedges and of their rulings were such that when the wedges were mounted with their bases against the top of the cavity (3 cm), or on a post with their bases parallel to the top of the cavity (1 cm), the rotation of the cavity about an axis normal to **H** caused an effective motion of **H** in the xy, yz, or xz planes of one of the two types of durene molecules, depending on which wedge was used. Actually there was an ambiguity of an angle π with respect to the alignment of the crystals against the rulings on the wedges. It was therefore necessary to do two resonance experiments with each new crystal examined. The resonance results served to show which alignment was the correct one.

The crystals were grown by lowering a melt through a temperature gradient. To prepare the melt 2 mole % of naphthalene was added to durene, but the actual naphthalene concentrations in the crystals which were used in the resonance experiments are not known.

The naphthalene used in the experiments was carefully purified material given to us by M. Kasha and by H. S. Jarrett and G. Sloan. The durene was purchased from the Eastman Kodak Company and was vacuum sublimed before use.

EXPERIMENTAL RESULTS

In Figs. 7–9 are shown typical results for the magnitudes of field strength $|\mathbf{H}|$ at which resonance was observed for various angles of rotation of **H** in the principal magnetic planes of one type of durene molecule. On the vertical axis 1000 divisions on the dial is an angle of $\pi/2$. The assumption is made, and will be seen later to be verified, that the naphthalene molecules are oriented with their x, y, and z axes parallel, respectively, to the x, y, and z axes of the durene molecules (see Fig. 4). Therefore the vertical scale gives the angle through which **H** is rotated in a principal magnetic plane of the naphthalene molecules. Inasmuch as the $\mathbf{H}_{RF}$ was perpendicular to **H** the transitions for which $\Delta M=\pm 1$ (M is the strong field quantum number) were observed. Two absorptions were found for each type of naphthalene molecule because of the aforementioned zero field splitting of the triplet state. In general, then, four peaks are expected at arbitrary orientations, i.e., two peaks for each of the two crystallographically inequivalent naphthalene molecules. Stationary points of $|\mathbf{H}|$ vs angle of rotation are reached when **H** passes through the x, y, or z axes of naphthalene molecules. It should be noted from Fig. 5 that the plane of one type of naphthalene will be nearly perpendicular to that of the other type but not exactly so. Also, the y axes of both types are nearly parallel.

[26] P. H. Groth, *Chemische Krystallographie* (W. Englemann, Leipzig, 1906).

Consequently, if **H** is moving in the xz plane of one type of naphthalene molecule, it is also moving nearly in the xz plane of the other, but the pattern is $\pi/2$ out of phase with respect to that of the first type. This behavior is very clearly shown in Fig. 8 where the two 2-peak patterns (one 2-peak pattern for each of the 2 types of naphthalene molecule) are seen to be very closely the same but displaced from each other by $\pi/2$ in dial reading. The mounting wedges shown in Fig. 6 were constructed for only one of the two types of molecules, so the data from only one of the two 2-peak patterns were utilized. For a given 2-peak pattern the larger separation corresponds to **H** along the z axis and the smaller separation to **H** along the x axis. The molecule which gives the larger z-axis separation is the correctly oriented one. Similarly in Fig. 9 (for the yz plane) one recognizes the large z-axis separation as being the same as in Fig. 8 and the smallest separation as being therefore that corresponding to **H** along the y axis. One sees, as described previously, that when **H** is along the y axis of one molecule it is also simultaneously almost along the y axis of the other. The intermediate 2-peak separation in this figure is, of course, almost the x-axis separation of the molecule for which the wedge was not designed. When **H** moves in the yz plane of the first molecule it moves nearly in the xy plane of the other molecule.

Fine structure measurements were made on nine crystals. A total of 19 measurements were made along principal axes at ~ 9.6 to $\sim 9.9\times 10^9$ cps and 16 measurements at $\sim 22.7\times 10^9$ cps. All measurements were made at the boiling point of liquid N_2.

When illumination ceased this resonance decayed, as will be described later. Resonance was unobservable in pure durene crystals under the same conditions.

These fine structure data are described within the errors of the measurements by the spin-Hamiltonian

$$\mathcal{H}=|\beta|\,\mathbf{H}\cdot g\cdot\mathbf{S}+DS_z^2+E(S_x^2-S_y^2),$$

with $S=1$.

The data are, of course, too numerous to publish here but they are available in tabulated form.[27]

The parameters in the spin-Hamiltonian were determined from the experimental results obtained with **H** along the various principal axes and the detailed results are summarized in Table I.

Here g_{xx} was calculated from the relation

$$g_{xx}=\frac{2h\nu-\frac{1}{2}[(D+E)/2]\{[(D+E)/2g_{xx}\beta H_{10}{}^x]+[(D+E)/2g_{xx}\beta H_{0\bar{1}}{}^x]\}+\cdots}{\beta(H_{10}{}^x+H_{0\bar{1}}{}^x)}$$

where the subscripts 10 and $0\bar{1}$ refer to the two peaks observed for a given molecule and the superscript denotes the axis which was parallel to **H** and H is used for $|\mathbf{H}|$. The values of the left-hand side of this equation are very insensitive to the values used for D, E, and g_{xx} on the right. The values of Hutchison and Mangum[24] were used for D and E and a self-consistent value for g_{xx} was easily found. Higher terms in the expansion have a negligible effect on the value found for g_{xx}.

In a similar manner g_{yy} was calculated from the relation

$$g_{yy}=\frac{2h\nu-\frac{1}{2}[(D-E)/2]\{[(D-E)/2g_{yy}\beta H_{10}{}^y]+[(D-E)/2g_{yy}\beta H_{0\bar{1}}{}^y]\}+\cdots}{\beta(H_{10}{}^y+H_{0\bar{1}}{}^y)}$$

and g_{zz} from the relation

$$g_{zz}=\frac{2h\nu-[(E^2/2g_{zz}\beta H_{10}{}^z)+(E^2/2g_{zz}\beta H_{0\bar{1}}{}^z)]+\cdots}{\beta(H_{10}{}^z+H_{0\bar{1}}{}^z)}.$$

The values of D/hc labeled z axis were calculated from the relation

$$D=-\tfrac{1}{2}\left[g_{zz}\beta(H_{10}{}^z-H_{0\bar{1}}{}^z)+\frac{E^2}{2g_{zz}\beta H_{10}{}^z}-\frac{E^2}{2g_{zz}\beta H_{0\bar{1}}{}^z}\right]+\cdots$$

using the Hutchison and Mangum[24] value for E and the previously calculated g_{zz}. Values of D and E labeled x, y axes were calculated from the relation

$$D-3E=g_{xx}\beta(H_{10}{}^x-H_{0\bar{1}}{}^x)+\tfrac{1}{2}(D+E)/2\left[\frac{D+E}{2g_{xx}\beta H_{10}{}^x}-\frac{D+E}{2g_{xx}\beta H_{0\bar{1}}{}^x}\right]+\cdots,$$

and a similar relation along the y axis.

The relations just given, and used in finding the parameters which describe the data, follow from the expressions given in the next section for the eigenvalues of the spin-Hamiltonian.

The values given after the $\pm$ signs in Table I were obtained by (i) calculating two values of $|\mathbf{H}|$ for the two resonances with **H** along a given axis from the parameters of Table I for that direction and frequency; (ii) averaging the deviations of the measured $|\mathbf{H}|$ from the calculated $|\mathbf{H}|$; (iii) multiplying these

[27] For supplementary material, order Document 6573 from ADI Auxiliary Publications Project, Photoduplication Service, Library of Congress, Washington 25, D. C. A copy may be secured by citing the Document number and by remitting $6.25 for photoprints, or $2.50 for 35-mm microfilm. Advance payment is required. Make checks or money orders payable to: Chief, Photoduplication Service, Library of Congress.

TABLE I. Parameters in the spin-Hamiltonian.

System	Frequency, cps	g_{xx}	g_{yy}	g_{zz}	D/hc, cm^{-1}	E/hc, cm^{-1}
Light naphthalene, $C_{10}H_8$, in light durene, $(CH_3)_4C_6H_2$		(6)[a]	(6)[a]	(7)[a]	±0.1008	∓0.0138
		2.0044	2.0020	2.0029	±0.0007	±0.0002
	~9.7×10^9	±0.0018	±0.0026	±0.0017	x, y axis	x, y axis
					±0.1005	
					±0.0003	
					z axis	
		(3)[a]	(2)[a]	(3)[a]	±0.1003	∓0.0137
		2.0030	2.0030	2.0029	±0.0006	±0.0002
	~22.7×10^9	±0.0004	±0.0012	±0.0004	x, y axes	x, y axes
					±0.1003	
					±0.0001	
					z axis	
Perdeutero naphthalene, $C_{10}D_8$ in perdeutero durene, $(CD_3)_4C_6D_2$		(2)[a]	(4)[a]	(4)[a]	±0.1012	∓0.0134
		2.0030	2.0031	2.0023	±0.0003	±0.0001
	~22.7×10^9	±0.0004	±0.0003	±0.0006	x, y axes	x, y axes
					±0.1009	
					±0.0002	
					z axis	

[a] The number of experimental measurements is given in parentheses in each case.

average deviations by $\partial g/\partial|\mathbf{H}|$, $(\partial D/hc)/\partial|\mathbf{H}|$, or $(\partial E/hc)/\partial|\mathbf{H}|$ to get the ± values given in the table.

These parameters give a good fit not only along the principal axes but in the other directions also. This is illustrated in Fig. 10. In this figure the open circles are experimental points (the same points as plotted in Fig. 9) and the filled circles are calculated from the appropriate values of the parameters in Table I. In this figure 1000 dial divisions correspond to an angle of $\pi/2$. The experimental points were obtained in two separate experiments, one in which the points in the vicinity of the y axis were obtained and another in which the points in the vicinity of the z axis were obtained. The crystal was remounted between these two experiments (by visual alignment with respect to the cavity walls) and rotated with respect to the dial by a visually estimated angle of $\pi/2$ in order to obtain maximum field modulation in each case. The dial readings for the one experiment were shifted by 1000 when the graph was plotted. The double solid circles at the point half-way between y and z represent the error introduced in assuming that the crystal was rotated with respect to the dial by exactly $\pi/2$.

It should be noted that these experiments do not give the signs of either D or E but do determine the fact that these two parameters have opposite signs.

Hyperfine structure was investigated at ~22.7×10^9 sec^{-1}. Proton resonance signals were superposed on triplet-state resonance signals using a dual-beam oscilloscope. A typical signal with $\mathbf{H}$ parallel to the x axis is shown in Fig. 11 for light naphthalene in completely deuterated durene. The 5-peak hyperfine pattern along the x axis had average widths between maximum and minimum slopes for each component equal to 3.6, 3.8, 3.8, 3.8, and 3.5 gauss and the average intervals between crossover points were 7.7, 7.5, 7.5, and 7.7 gauss for light naphthalene in light durene. The figures are the averages of from 30 to 40 measurements with an average deviation from the average equal to 0.3 gauss. For light naphthalene in completely deuterated durene the widths were 3.1, 3.9, 4.0, 3.9, and 3.1 gauss and the intervals were 7.5, 7.2, 7.2, and 7.5 gauss on the basis of a single measurement. Only single peaks were observed with $\mathbf{H}$ parallel to the y or the z axes of the naphthalene molecules. The single peak along the y axis is Gaussian with a width of 9.2±0.6 gauss between points of maximum slope in light durene. This was the average of 39 measurements and the average deviation from the average is given. The single peak with $\mathbf{H}$ along the z axis had a width of 13.0±0.6 gauss between points of maximum slope in light durene. This was the average of 22 measurements and the average deviation from the average is given. A single measurement in perdeutero durene gave 13.1 gauss. The peak was somewhat non-Gaussian and showed some indication of structure when perdeutero durene was used.

In the case of perdeutero naphthalene only a single peak was observed along each of the three axes. The widths between points of maximum slope along the x, y, and z axes were, respectively, 6.4, 4.7, and 5.9 gauss on the basis of 1 or 2 measurements on each peak.

Along the x-axis the spectrum of mono-α-deuteronaphthalene was a 4-line pattern with intensities in approximately the ratios 1:3:3:1 and of 1,4 -dideuteronaphthalene was a 3-line pattern with intensities in approximately the ratios 1:2:1.

Lifetimes of the paramagnetic resonances were

measured by timing the decays of the oscilloscope signal. The detection system was calibrated by measuring the decreases in oscilloscope signal resulting from decreases of the 1.25×10^5 cps field modulation amplitude by known amounts, the modulation amplitude being always relatively small compared with the width of the triplet-state signal. Some of these results have been reported by Hutchison and Mangum.[28]

DISCUSSION OF RESULTS

Fine Structure

Inasmuch as the system which is being investigated consists of molecules held together by relatively weak van der Waals forces we neglect all crystalline fields and consider only the perturbation of the triplet state by the magnetic field plus a molecular field with the symmetry of the free naphthalene molecule, namely orthorhombic. It has been shown by Stevens[29] that the most general expressions for the energies and states corresponding to the lifting of the degeneracy of a state with $S=1$ by a magnetic field and an electric field of orthorhombic symmetry are given by the eigenvalues and eigenstates of the spin-Hamiltonian

$$\mathbf{H}=|\beta|\,\mathbf{H}\cdot g\cdot\mathbf{S}+DS_z^2+E(S_x^2-S_y^2).$$

The eigenvalues and eigenvectors of this Hamiltonian with $\mathbf{H}$ along the three principal axes are

$$\begin{aligned}
\mathbf{H}\,||\,z:\quad & W_1=D+g_{zz}|\beta||\mathbf{H}|+E\tan\theta_z, && \cos\theta_z|1\rangle+\sin\theta_z|\bar{1}\rangle,\\
& W_0=0, && |0\rangle,\\
& W_{\bar{1}}=D-g_{zz}|\beta||\mathbf{H}|-E\tan\theta_z, && \sin\theta_z|1\rangle-\cos\theta_z|\bar{1}\rangle,
\end{aligned}$$

where $\tan 2\theta_z=E/g_{zz}\beta|\mathbf{H}|$;

$$\begin{aligned}
\mathbf{H}\,||\,x:\quad & W_1=\frac{D+E}{2}+g_{xx}|\beta||\mathbf{H}|-\frac{D+E}{2}\tan\theta_x, && \cos\theta_x|1\rangle+\sin\theta_x|\bar{1}\rangle,\\
& W_0=D-E, && |0\rangle,\\
& W_{\bar{1}}=\tfrac{1}{2}(D+E)-g_{xx}|\beta|\mathbf{H}||+\tfrac{1}{2}(D+E)\tan\theta_x, && \sin\theta_x|1\rangle-\cos\theta_x|\bar{1}\rangle,
\end{aligned}$$

where $\tan2\theta_x=-(D+E)/2g_{xx}|\beta||\mathbf{H}|$;

$$\begin{aligned}
\mathbf{H}\,||\,y:\quad & W_1=\tfrac{1}{2}(D-E)+g_{yy}|\beta||\mathbf{H}|+\tfrac{1}{2}(D-E)\tan\theta_y, && \cos\theta_y|1\rangle+\sin\theta_y|\bar{1}\rangle,\\
& W_0=D+E, && |0\rangle,\\
& W_{\bar{1}}=\tfrac{1}{2}(D-E)-g_{yy}|\beta||\mathbf{H}|-\tfrac{1}{2}(D-E)\tan\theta_y, && \sin\theta_y|1\rangle-\cos\theta_y|\bar{1}\rangle,
\end{aligned}$$

where $\tan2\theta_y=(D-E)/2g_{yy}|\beta||\mathbf{H}|$.

Energy level diagrams with $\mathbf{H}$ along x, y, and z are shown in Fig. 12 with the 9.7×10^9 and 22.7×10^9 cps transitions indicated. It will be seen that at zero field the triplet is split into three levels. Two of these are separated by $2|E|$ and the mean of these two is separated from the third by $|D|$. These experiments do not give the signs of either D or E but they do show that the signs of these two parameters are opposite. In an axial or hexagonal field (benzene) the E term would be zero and the triplet would be split into a singlet and a doublet. In naphthalene the ratio, $|D|/|E|$, is 7.29.

It will be seen that this zero-field splitting results in an anisotropy sufficient to obscure the observation of the $\Delta M=\pm1$ transitions in a system of randomly oriented molecules.

It is also clear that the spectrum originates in a triplet state. The hyperfine structure to be discussed later unambiguously identifies the triplet state as being a triplet state of the naphthalene molecule. It will also be seen that the principal axes of the naphthalene molecule coincide with the principal axes of the durene molecule. The crystals were oriented with respect to the axes of the durene molecules, i.e., the orientations were based on their external morphology and the data of Robertson,[25] and the stationary points in the spectrum of naphthalene correspond within the errors of measurement to the principal axes of the durene molecules. It is of course not clear from these measurements that the x, y, and z axes of naphthalene are along the x, y, and z axes, respectively, of durene as labeled in Fig. 4. The hyperfine structure data to be discussed later do, however, show that this is the case.

The observed zero-field splitting has its origin in the magnetic dipole-dipole interaction between the two π electrons of the triplet state which may be represented by

$$\mathbf{H}_{ij}=(g^2\beta^2/r_{ij}^3)\{\mathbf{S}_i\cdot\mathbf{S}_j-3[(\mathbf{S}_i\cdot\mathbf{r}_{ij})(\mathbf{S}_j\cdot\mathbf{r}_{ij})/|\mathbf{r}_{ij}|^2]\}.$$

[28] C. A. Hutchison, Jr., and B. W. Mangum, J. Chem. Phys. **32**, 1261 (1960).

[29] K. W. H. Stevens, Proc. Roy. Soc. (London) **A214**, 237 (1952).

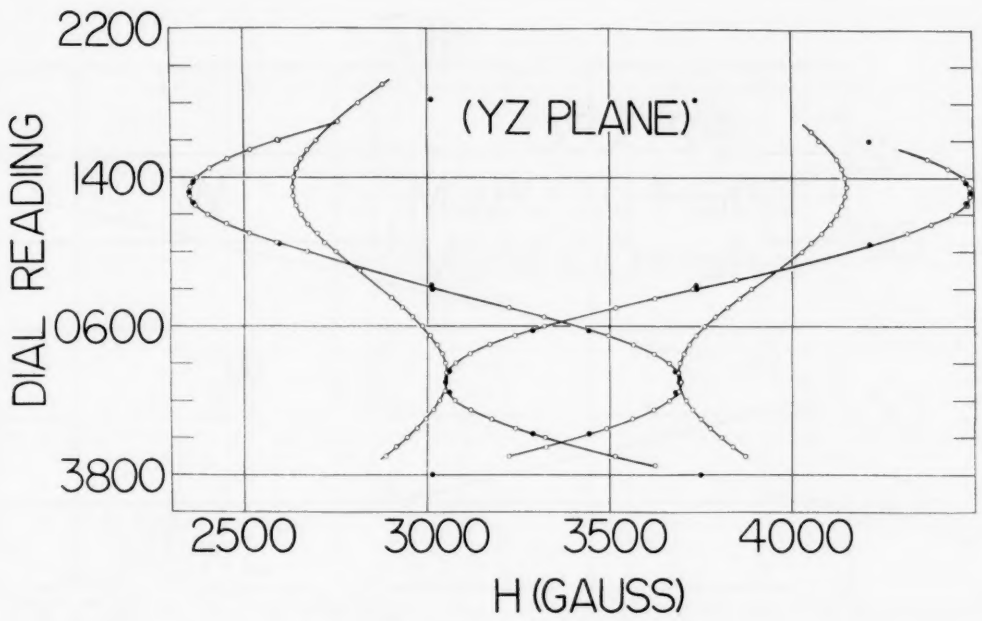

FIG. 10. Fit of spin-Hamiltonian to experimental data.

The zero-field splitting of the triplet thus arises from the same source as in the case of the ground triplet state of the O_2 molecule.[30]

The very weak crystalline field of the durene molecules would be expected to give negligible perturbing effects relative to the effects internal to the naphthalene molecule. The spin-orbit coupling which is responsible in inorganic ions for splittings of the order observed here, i.e., 0.1 cm^{-1}, clearly produces only a very small splitting in this case on the basis of (i) theoretical calculations[31–33] of spin-orbit energies; (ii) experimental observations[34] on lifetimes of triplet states; and (iii) the observed deviation of g from the free-electron value. The spin-orbit coupling perturbation mixes singlets and triplets and thus limits the lifetime in the triplet state. The long lifetimes which are observed are inconsistent with sufficient spin-orbit coupling to produce the measured zero-field splittings. On the other hand, the magnetic dipole-dipole interaction does not mix singlets and triplets and may be as large as observed without resulting in any inconsistency with respect to lifetimes.

Calculations of the zero-field splittings of the triplet states of organic molecules have been made by Gouterman and Moffitt,[35] Gouterman,[36] Hameka,[37] and Bersohn.[38] One might expect the problem of calculating the dipole-dipole interaction between two electron spins distributed over π-orbitals to be especially

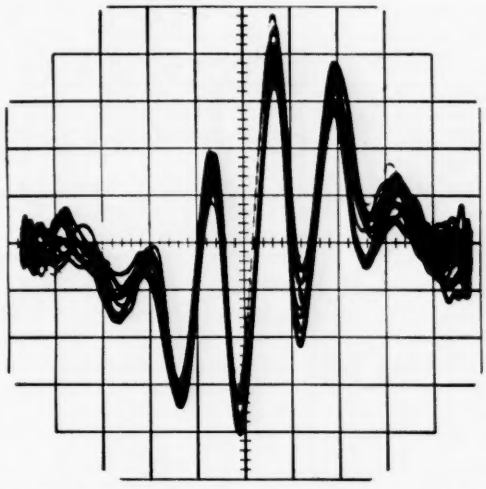

FIG. 11. Hyperfine structure with **H** parallel to the x axis.

[30] M. Tinkham and M. W. P. Strandberg, Phys. Rev. **97,** 937 (1955).
[31] D. S. McClure, J. Chem. Phys. **20,** 682 (1952).
[32] M. Mizushima and S. Koide, J. Chem. Phys. **20,** 765 (1952).
[33] H. F. Hameka and L. J. Oosterhoff, Mol. Phys. **1,** 358 (1958).
[34] D. P. Craig, J. M. Hollas, and G. W. King, J. Chem. Phys. **29,** 974 (1958).
[35] M. Gouterman and W. Moffitt, J. Chem. Phys. **30,** 1107 (1959).
[36] M. Gouterman, J. Chem. Phys. **30,** 1369 (1959).
[37] H. F. Hameka, J. Chem. Phys. **31,** 315 (1959).
[38] R. Bersohn (unpublished results).

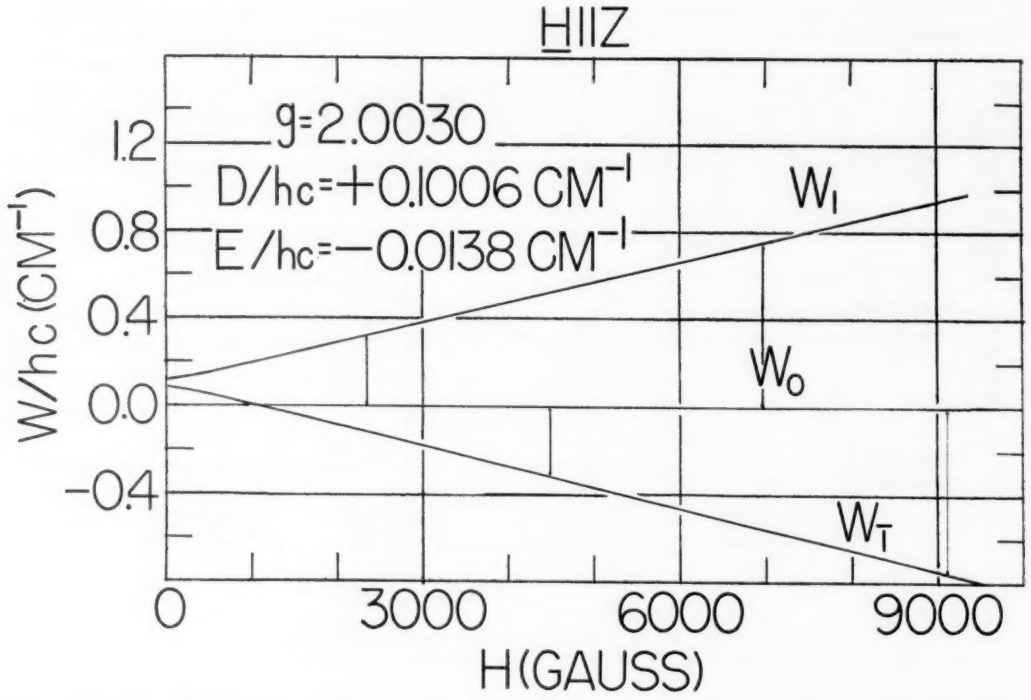

FIG. 12 (a)

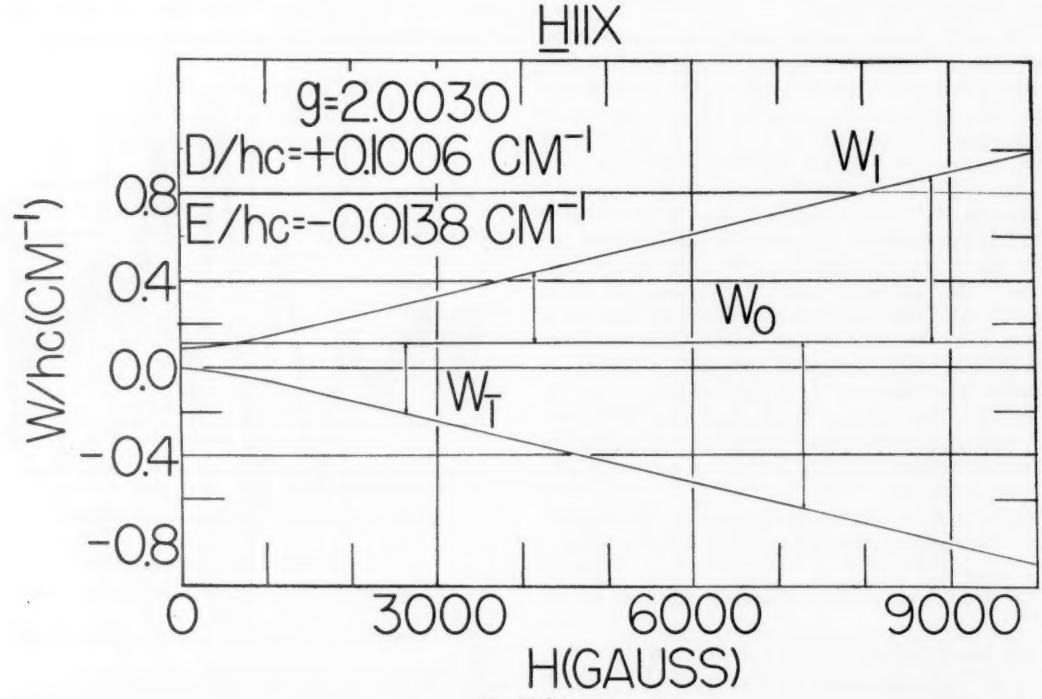

FIG. 12 (b)

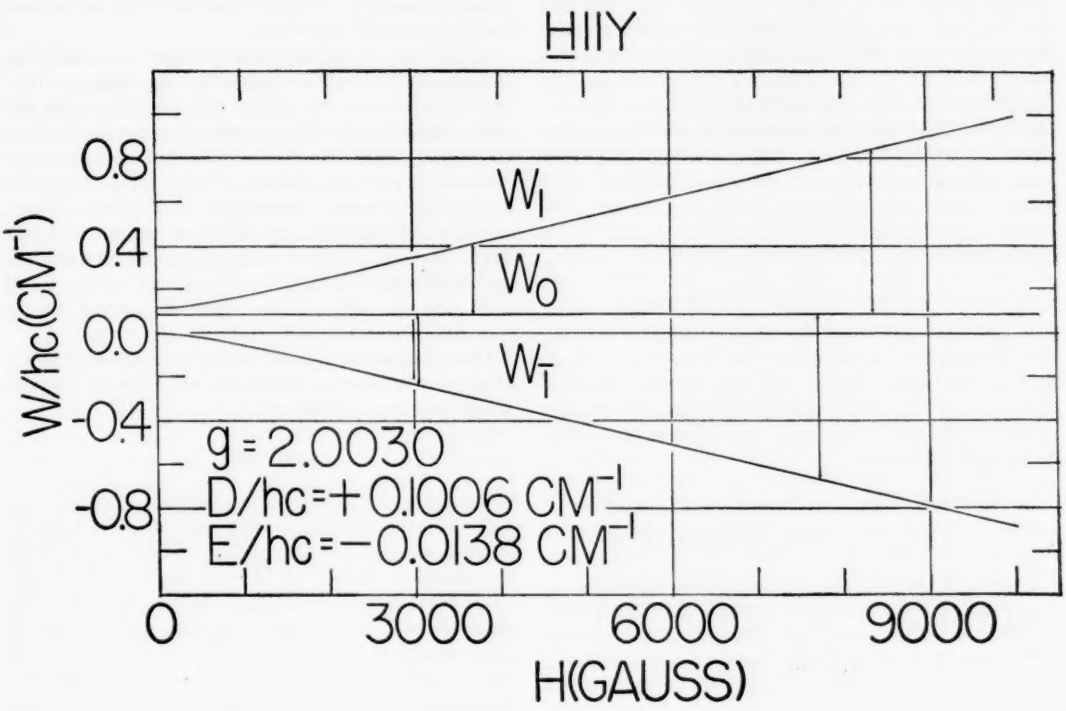

FIG. 12 (c)

FIG. 12. Energy level diagrams for **H** along x, y and z axes.

difficult because of the dependence on the inverse cube of the distance coupled with the inability of approximate molecular wave functions to deal with the problem of close approaches. However, because one is dealing with a triplet state the antisymmetric orbital factors of the simplest approximate functions result in a correlation of the electronic motions preventing their being in the same place at the same time; e.g., in the case of ethylene discussed by Moffitt and Gouterman[35] the orbital factor $a(1)b(2)-a(2)b(1)$, where a, b are $2p$ orbitals on the two C atoms of course has this property. McConnell[39] has pointed out that quite generally the differences in energy corresponding to zero-field splittings produced by magnetic dipole-dipole interaction do not involve terms arising from close approaches of the two spins. This is a result of an antisymmetry requirement on the space part of the exact triplet state wave function. Thus one can have considerable confidence in the results of the calculations based on approximate molecular wave functions.

It should also be remarked that within the π-electron approximation using only $2p\pi$ atomic orbitals it is not possible to place the two electrons on the same C atom at the same time without violating the Pauli principle. In the O_2 molecule[30] this is of course not the case because two orthogonal π orbitals are available on each atom and then, because of the inverse cube dependence of the magnetic dipole-dipole interaction on distance, the largest part of the zero field splitting arises from contributions when both electrons are on the same atom.

Therefore, it is not purely a coincidence that the dipole-dipole energy of two electron spins at the C—C distance in naphthalene is quite close to the observed value of D, 0.1 cm^{-1}.

The calculations of Gouterman[36] give the values of D and E in terms of the values of these parameters which were calculated by Gouterman and Moffitt[35] for ethylene ($D/hc=0.195$ cm^{-1}, $E/hc=0.23$ cm^{-1} for ethylene) using Gaussian functions. Considering only the two highest filled orbitals, 4 and 5, and the two lowest unfilled orbitals, 5′ and 4′, he finds that a good fit of our D and E values in Table II (magnitudes and relative signs) is obtained only for the L_a state,[40]

$$L_a=\sin\phi(5,5')+\cos\phi(4,4').$$

Gouterman[41] has found, using Hückel orbitals, that for

[39] H. McConnell, Proc. Natl. Acad. Sci. U. S. **45**, 172 (1959).

[40] J. R. Platt, J. Chem. Phys. **17**, 484 (1949).

[41] M. Gouterman (private communication).

$\phi=1.01$ (58°), $D/hc=0.104$ cm^{-1} and $E/hc=0.0136$ cm^{-1} which is in very good agreement with our results. For the L_b state, which is a mixture of configurations (4, 5′) and (5, 4′) no reasonable fit to our data is possible as is also the case for the B states which are the other two linear combinations of the four configurations already mentioned. The L_a state is the one that had been assigned theoretically[42] and these magnetic resonance experiments afford in principle a method for determining the particular configuration mixing which obtains in this case. The best fit is given by the mixture

$$L_a=0.85(5, 5')+0.53(4, 4').$$

Pariser[43] has calculated the wave functions for the excited states of naphthalene. He finds that a $^3B_{2u}{}^+$ state is the lowest triplet state for naphthalene and that it is 2.16 ev above the ground state; the experimental value is 2.64 ev. For this state he finds the configuration mixture,

$$0.92(5, 5')+0.21(4, 4')+0.27(3, 3')+0.03$$
$$(4, 1'+1, 4')+0.17(2, 2')+0.09(1, 1').$$

There can be no doubt, in view of our experimental data, that (i) the observed paramagnetic resonance arises from a triplet state and that (ii) the source of the zero-field splitting is the magnetic dipole-dipole interaction between the two electrons of this triplet state.

Hyperfine Structure

The isotropic component of the proton hyperfine interaction with the π-electron system of aromatic free radicals, observed in liquid solutions, is well understood due to the extensive investigations which have followed the original theoretical work of McConnell,[44] Bersohn,[45] Weissman,[46] and Venkataraman and Fraenkel.[47] In such cases only the isotropic component is observed because of the tumbling of the molecules in the liquid. The isotropic interaction occurs because (i) the magnetization of the π-system of electrons produces, through exchange interaction, a small magnetization of the σ-system; (ii) the σ-system spin is paired with the H s electrons in the C—H bonds, thus imparting a negative magnetization to the H s electrons; and (iii) these s electrons interact with the protons through the Fermi-Segre contact interaction. It has been shown by McConnell[44] that to a good approximation the isotropic hyperfine interaction between the π-system and a given ring proton may be expected to be proportional to the electron spin density on the carbon adjacent to that proton. The proportionality constant is found experimentally to be close to 22.5 gauss or 63×10^6 cps.

In the case of naphthalene in durene in which the paramagnetic aromatic molecules are oriented in a crystal, we have the opportunity of observing the anisotropic magnetic dipole-dipole interaction between the π-system and the protons which averages to zero in the case of the liquid solutions. The electron spin which is distributed over a π-orbital on a given C atom interacts mainly with the adjacent proton and this dipole-dipole interaction is of course strongly dependent on the direction of **H** with respect to the C—H bond and the axis of the π-orbital (normal to the molecular plane).

This interaction is of course also approximately proportional to the spin density on the adjacent C atom. Therefore we may write

$$a_N=\rho_N K,$$

where a_N is the hyperfine interaction, ρ_N is the spin density on the adjacent C atom normalized to 1 for the entire molecule, $K=\{A^2\alpha^2+B^2\beta^2+C^2\gamma^2\}^{\frac{1}{2}}$, α, β, γ are the direction cosines of **H** with respect to (i) the C—H bond direction (A axis), (ii) the normal to the plane of the ring, (B axis), and (iii) a third axis (C axis) normal to both (i) and (ii), respectively. A, B, and C are the isotropic plus anisotropic hyperfine interactions per unit normalized spin density on the adjacent atom when **H** is parallel to the A axis, B axis, or C axis, respectively.

In order to calculate the dipole-dipole contributions A_d, B_d, and C_d to the hyperfine splittings one must integrate the interaction,

$$g_e g_N \beta_e \beta_N \{[(\mathbf{s}\cdot\mathbf{I})/|\mathbf{r}|^3]-3[(\mathbf{r}\cdot\mathbf{s})(\mathbf{r}\cdot\mathbf{I})/|\mathbf{r}|^5]\},$$

(where **r** is distance from the electron spin to the proton) over the π-orbital on the C atom, with **H** along the A axis, B axis, and C axis, respectively. McConnell and Strathdee[48] have evaluated these magnetic dipole-dipole interactions, and find $A_d\cong+30$ Mc, $B_d\cong0$ Mc, and $C_d\cong-30$ Mc. The well-known isotropic hyperfine interaction is -63 Mc giving for the sum of these two interactions the values $A\cong-33$ Mc, $B\cong-63$ Mc, and $C\cong-93$ Mc.

In the case of aromatic free radicals this anisotropic proton hyperfine interaction has been observed by McConnell *et al.*,[49,50] Ghosh and Whiffen,[51] and by Miyagawa and Gordy.[52] Experimental measurements[49] of the hyperfine interaction with the proton on the

[42] N. S. Ham and K. Ruedenberg, J. Chem. Phys. **25**, 13 (1956).
[43] R. Pariser, J. Chem. Phys. **24**, 250 (1956).
[44] H. M. McConnell, J. Chem. Phys. **24**, 764 (1956).
[45] R. Bersohn, J. Chem. Phys. **24**, 1066 (1956).
[46] S. I. Weissman, J. Chem. Phys. **25**, 890 (1956).
[47] B. Venkataraman and G. K. Fraenkel, J. Chem. Phys. **24**, 737 (1956).
[48] H. M. McConnell and J. Strathdee, Mol. Phys. **2**, 129 (1959).
[49] T. Cole, C. Heller, and H. M. McConnell, Proc. Natl. Acad. Sci. U. S. **45**, 525 (1959).
[50] H. M. McConnell, C. Heller, T. Cole, and R. W. Fessenden, J. Am. Chem. Soc. **82**, 766 (1960).
[51] D. K. Ghosh and D. H. Whiffen, Mol. Phys. **2**, 285 (1959).
[52] I. Miyagawa and W. Gordy, Bull. Am. Phys. Soc. Ser. II, **4**, 260 (1959); J. Chem. Phys. **30**, 1590 (1959).

central C atom in CH $(COOH)_2$ radical gave $A=-30.0$ Mc, $B=-61.5$ Mc, and $C=-92.5$ Mc, in excellent agreement with the calculated values.

In considering the proton hyperfine interaction in the case of the naphthalene triplet state we will consider the molecule to be a collection of 8 C—H fragments, each with the anisotropic hyperfine interactions described. A simple Hückel orbital for the configuration (5, 5′) would give a normalized spin density 0.18 on the α C's, 0.07 on the β C's, and 0.00 on the 9, 10 C's. Pariser's[43] wave function for the $^3B_{2u}{}^+$ state of naphthalene gives 0.168 on the α C's, 0.074 on the β C's and 0.015 on the 9, 10 C's.

It is clear that qualitatively a result such as is shown in Fig. 11 for **H** along the x axis of the molecule is to be expected on the basis of the model which we have assumed. With this orientation **H** is along the C axis of the α C's which is the direction of largest proton hyperfine interaction, -93 Mc, per unit spin density on the adjacent C atom, and the adjacent C atom is the one with large spin density, 0.17, giving a splitting of 16 Mc. For the β C's **H** is in a direction of much smaller splitting, 53 Mc per unit spin density and the spin density is lower by a factor 2.3, namely, 0.07 leading to a splitting of 3.9 Mc. Hence the four equivalent α C's produce a 5-line pattern with intensities in the ratio 1:4:6:4:1. Each of these components consists of 5 lines with a binomial distribution of intensities which arise from the β C's and which are much more closely spaced and not resolved. The lack of resolution may perhaps be due to crystal imperfections. In the y direction a single line which is very accurately Gaussian is observed. In this direction the splitting is 30 Mc for the α C's and 81 Mc for the β C's per unit spin density on the adjacent C's. When the spin densities are taken into account the splittings become 5.0 and 6.0 Mc, respectively. All eight protons are therefore approximately equivalent and this leads to a 9-line spectrum with a Gaussian envelope. The structure is not resolved. The peak which was observed in the z direction is also qualitatively in agreement with expectation. Only the one interaction constant B is involved in this direction.

Values of A, B, and C were calculated on the basis of the observed patterns and the spin density distribution given by Pariser's[43] wave function. Assuming the correctness of the model just proposed, which will later be seen to be justified, the peak observed along the y axis may be regarded to a first approximation as a superposition of nine absorptions; this leads to the conclusion that the individual peaks could not be narrower than 4.0 to 4.5 gauss with a spacing of $\sim$2.9 gauss, because the observed width is 9.2 gauss. (The word, width, will be used to denote the separation of the points of maximum and minimum slope. Nine superposed Gaussians with widths less than about 1.5 times their spacing show structure whereas the observed peak is smooth. Nine superposed Gaussians with this minimum width give a resultant with a width 3.2 times the spacing of the individual peaks.) It is therefore clear that most of the width of each of the five main peaks of the pattern which is observed along the x axis arises from this $\sim$4.5-gauss width of the five individual components of which the five main peaks in turn are composed, and not from their spacing, which is given by

$$(\rho_\beta/2.80)\{\tfrac{3}{4}A^2+\tfrac{1}{4}C^2\}^{\frac{1}{2}}.$$

If five Gaussians are superposed, the ratio of indivisual width to spacing which best simulates the observed pattern is very close to 0.67. On defining the first crossover distance as the distance from the center of the pattern to that field right of center which is half-way between the first minimum and the second maximum in the derivative, such a superposition gives a first crossover distance 1.06 times the spacing of the five Gaussians. The observed average crossover interval is 7.35 ± 0.15 gauss on the basis of the measurement in heavy durene and 7.6 ± 0.3 from the measurement in light durene, and hence the observed pattern corresponds to a spacing of 6.9 ± 0.2 gauss in the first case and 7.2 ± 0.3 gauss in the second. This spacing is determined solely by the hyperfine constant C and the spin density, $\rho_\alpha=0.168$, and is given by $(\rho_\alpha/2.80)C$. Thus $|C|$ is found to be 115 ± 3 Mc from the heavy durene data and 119 ± 5 Mc from the light durene data. This result is very insensitive to the ratio of width to spacing which is assumed for five Gaussians whose superposition is observed.

For the z-axis peak only the constant B is involved. Here we have one 5-peak superposition with spacing $\rho_\alpha{}^B/2.80=(0.168/2.80)B$, each peak of which is a superposition of five peaks with spacing $\rho_\beta{}^B/2.80=(0.074/2.80)B$. For $\rho_\beta{}^B/2.80\cong2.00$ gauss, $\rho_\alpha{}^B/2.80=4.56$ gauss. If each of the 25 peaks is 4.3 gauss wide, which is the minimum width as inferred from the smoothness of the y-axis curve, then their superposition will give an absorption that is 12.8 gauss wide from maximum to minimum slope. The observed width is 13.0 ± 0.6 gauss. This fit is insensitive to the width that is assumed for the individual peaks. Thus $|B|$ is found to be 76 ± 4 Mc.

It will be seen that the value of A cannot be inferred with any reliability from either the measurements along the y axis or the measurements along the x axis, because the constant C is also involved in each of these cases in a way that obscures the effect of the A constant. The results are quite consistent however with a value of A in the vicinity of -30 Mc.

If we assume that the experimental values, $B=-61.5$ Mc and $C=-92.5$ Mc obtain in our case also, we may then infer that $\rho_\alpha=0.209$ from the x-axis data. It is not possible to get a quantitative idea of the value of ρ_β from our results because the effects of ρ_α are always involved and in fact dominate. It is to be noted that the value of ρ_α is close to that observed by Carrington,

Dravnieks and Symons,[53] namely, 0.218, in the naphthalene negative ion. There is undoubtedly a negative spin density on the 9, 10 C's which will need to be investigated by means of C^{13} effects. The complete elucidation of the hyperfine structure effects must await further studies on isotopically substituted molecules.

The hyperfine structure data permit (i) the unambiguous conclusion that it is the paramagnetic resonance spectrum of naphthalene which is being observed in these experiments and not the spectrum of durene or some impurity. In addition, the observed hyperfine structure patterns show (ii) that the naphthalene molecules go into the durene structure substitutionally with their x, y, and z axes parallel, respectively, to the x, y, and z axes of durene molecules (see Fig. 4), and also (iii) that the triplet state which is being observed, which is presumably responsible for the phosphorescence, is the ${}^3B_{2u}{}^+$ state and not the ${}^3B_{3u}{}^+$ state as suggested by Williams.[10] The fact that with $H \| x$ (x, of course, here denotes the axis of the durene since the crystals were oriented according to the durene structure) the light naphthalene gave a 5-line pattern is interpretable only on the basis of (i) a ${}^3B_{2u}{}^+$ state with axes of naphthalene and durene respectively parallel or of (ii) a ${}^3B_{3u}{}^+$ state (which would put larger spin densities on the β positions than on the α positions) with a rotation of the naphthalene molecule by $\pi/2$ about its z axis with respect to the durene molecule which it replaces and with which it is coplanar. (ii) is eliminated by the facts that the mono-α-deuteronaphthalene gave a 4-line pattern and the 1,4-dideuteronaphthalene gave a 3-line pattern.

[53] A. Carrington, F. Dravnieks, and M. C. R. Symons, J. Chem. Soc. **1959**, 947.

Other Investigations

The paramagnetic resonance of randomly oriented molecules in their triplet states has been investigated by van der Waals and de Groot.[54,55] They have investigated the $\Delta M_s=2$ transition which is permitted by the dipole-dipole interaction and which is much less anisotropic than the $\Delta M_s=1$ transitions studied in our experiments. Their results for naphthalene are in essential agreement with ours.

ACKNOWLEDGMENTS

In addition to the acknowledgments given in the Introduction, we acknowledge the invaluable help of Edward Bartal, J. S. D. Danielson, and Winifred M. Y. Huo in the execution of the experiments and calculations.

[54] J. H. van der Waals and M. S. de Groot, Mol. Phys. **2**, 333 (1959).

[55] M. S. de Groot and J. H. van der Waals, Mol. Phys. (to be published).

New Determinations of the Vibrational Constants of Li^6F and Li^6Cl^{35} by the Molecular Beam Electric Resonance Method*

T. I. Moran and J. W. Trischka

Department of Physics, Syracuse University, Syracuse, New York

(Received August 4, 1960)

New measurements of the vibrational constants of LiF and LiCl were stimulated by the hypothesis of Klemperer and Herschbach that disagreement between infrared and previous molecular beam values of these constants could be explained by a variation in the efficiency of the molecular beam detector with vibrational state. The new molecular beam results rule out this hypothesis because of their agreement with infrared results. These new values are 930 ± 19 cm^{-1} for Li^6F and 705 ± 14 cm^{-1} for Li^6Cl^{35}. The agreement of these values with the infrared results leads to the conclusion that the vibrational states of molecules in the molecular beam source have a Boltzmann distribution. The relative detector efficiency for the vibrational states $v=0$ and $v=1$ did not vary when the total efficiency was changed over a range from 0.2 of the maximum value to the maximum. The ratio of the vibrational constants of Li^6F and Li^7F was found to be 1.06 ± 0.01, in agreement with the value calculated from the ratio of the reduced masses. A rough measurement of the vibrational decay constant between the $v=1$ and $v=0$ states gave 65 ± 40 sec^{-1}.

INTRODUCTION

VALUES of the vibrational constant, ω_e, obtained by the molecular beam electric resonance method[1,2] and from infrared absorption measurements[3,4] for LiF and LiCl, disagree by amounts well beyond the stated limits of experimental error. To explain the disagreement in the case of LiCl, Klemperer and Herschbach[5] have suggested that in the molecular beam apparatus the hot wire detector, which makes use of the process of surface ionization, has an efficiency which depends on the vibrational state of the neutral molecules striking it. We believed that their suggestion was interesting enough to warrant new measurements for both LiF and LiCl by the molecular beam method, which is indirect and subject, as will be seen in the following pages, to difficulties of a type not encountered in the direct method of infrared spectroscopy.

At this point we give a detailed description of the molecular beam method in order that the reader may understand the general nature of our experiments as well as the details given in the following sections. Figure 1 shows a schematic diagram of the electric resonance apparatus.[6] A molecular beam of LiF or LiCl emanates from a hot oven and passes through a chamber evacuated to a pressure of $2\text{–}3\times10^{-7}$ mm of Hg. At the end of this chamber it strikes a hot, oxygenated W wire on whose surface Li ions are formed. These ions, after passage through a mass spectrometer, are detected with a secondary emission multiplier.[7] Following the multiplier is an amplifier and a pen recorder.

Molecules, a few per thousand, in the lowest rotational states are sufficiently deflected by the inhomogeneous electric fields, A and B, to follow a sigmoid path similar to that shown in Fig. 1. Most molecules, because of their insignificant deflections by the A and B fields, are stopped by the knife edge in the B field. Transitions between rotational substates, $(J, m_J)\rightarrow(J, m_J')$, take place in the C field, a homogeneous field

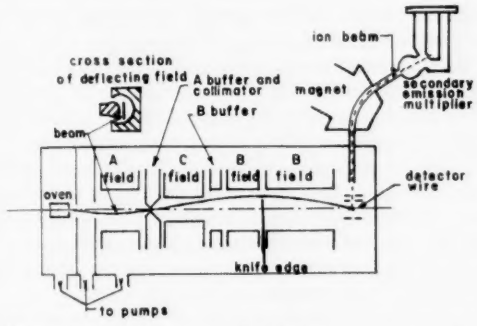

FIG. 1. Schematic diagram of electric resonance apparatus.

with a superposed radio-frequency field. Transition frequencies are determined by the quantum numbers of the molecular states, by the magnitude of the electric field, and by the vibrationally averaged molecular constants μ and A, where μ is the dipole moment and A the moment of inertia. The apparatus in the present experiment is so designed that when no transitions occur no molecules can reach the detector, but molecules in the $(1, \pm1)$ state in the A field will reach the detector if they undergo a transition to the $(1, 0)$ state in the C field.

* Supported in part by the Office of Naval Research.

[1] R. Braunstein and J. W. Trischka, Phys. Rev. **98**, 1092 (1955).

[2] D. T. F. Marple and J. W. Trischka, Phys. Rev. **103**, 597 (1956).

[3] G. L. Vidale, J. Phys. Chem. **64**, 314 (1960).

[4] W. Klemperer, W. G. Norris, A. Büchler and A. G. Emslie, J. Chem. Phys. **33**, 1534 (1960).

[5] W. Klemperer and D. Herschbach, Proc. Natl. Acad. Sci. U. S. **43**, 429 (1957).

[6] Figure 1 is the same as Fig. 1 in footnote 2, where some of the details of the apparatus are given. Other references describing the apparatus will also be found in footnote 2.

[7] D. T. F. Marple, Rev. Sci. Instr. **26**, 1205 (1955).

The measurement of ω_e is made possible by the ability of the apparatus to make a spectral discrimination between molecules in different vibrational states. Because μ and A change with vibrational state, the spectral lines from molecules in these states occur at different frequencies. Ideally, the ratio of line intensities for molecules in two adjacent vibrational states is given by[8]

$$R = e^{-\omega_e/kT}, \quad (1)$$

where k is the Boltzmann constant and T is the absolute temperature of the molecules in the oven.

We selected for study molecules in the two lowest adjacent vibrational states; i.e. those for which the vibrational quantum numbers are $v=0$ and $v=1$. These are the most populated states and although higher states could be observed, the population of these higher states was too low to permit observations of useful accuracy.

There are several reasons why, in practice, R may not be given by Eq. (1). To list and discuss these reasons it is convenient to consider the events occurring in four different places in the apparatus; viz., the oven, the region between the oven and the detector wire, the surface of the detector wire, and the region from the wire surface to the recorded data.

Equation (1) rests on the assumption, never tested directly for molecular beam ovens, that the distribution of vibrational states for the molecules in the oven is a Boltzmann distribution. A correct measurement of ω_e requires that the distribution of vibrational states in the beam be the same as it is in the oven.

In the region between the oven and the detector wire two processes can bring about changes in the population of the beam molecules in the $v=0$ and $v=1$ states. First, molecules in the excited, $v=1$, state undergo spontaneous radiative transitions to the $v=0$ state, with a resultant depletion of the excited state population. Secondly, the different values of μ and A for molecules in the two vibrational states will result in different deflections for these molecules; hence, in different fractions passing by the knife-edge.

Equation (1) will be incorrect if the ionization efficiency of the detector wire varies with vibrational state, as suggested by Klemperer and Herschbach.[5] The magnitude of this effect will, however, depend on the ionization efficiency. For example, if the ionization efficiency is, for all practical purposes, 100%, the vibrational effect on ionization efficiency will not be important. We believe it reasonable, therefore, to assume that the vibrational effect will vary with the ionization efficiency and will be most noticeable for low efficiencies.

It is important to the validity of Eq. (1) that the deflection of the pen-recorder be proportional to the ion current leaving the surface of the hot wire; hence, that no nonlinear effects on the ion current exist in the ion acceleration process, in the mass spectrometer, in the secondary emission multiplier, in the amplifier, or in the pen recorder itself. Hereafter the symbol R will stand for the ratio of intensities of lines in different vibrational states as they appear on the pen recorder. A detailed analysis of the corrections to the measured quantity R will be given later.

The results of four different experiments are presented in this paper. In the first, measurements were made of R and the oven temperature for molecular beams of Li^6F and Li^6Cl^{35}, under the condition that the detector wire had its maximum obtainable ionization efficiency. With suitable corrections this experiment led to values of ω_e. In the second, we wished to determine the effect of the ionization efficiency on R, and therefore made measurements at a fixed oven temperature when the detector wire was at its maximum efficiency and when at a much reduced efficiency. The third was prompted by the unexpected result of a previous molecular beam experiment in which it was found that the isotope shift in ω_e, as evidenced by $\omega_e(Li^6F)/\omega_e(Li^7F)$, did not agree with the theoretical value predicted from the ratio of the reduced masses of these molecules. To check this earlier experiment we decided to measure R for Li^6F and Li^7F at a fixed oven temperature. The fourth experiment, to be described in detail later, was used to determine one of the corrections to R. However, from it we have been able to determine a rough value of the lifetime of the excited vibrational state, $v=1$, of LiF.

APPARATUS AND TECHNIQUES

A. The Oven; Temperature Measurements

The oven was designed with particular attention paid to the need for an accurate knowledge of the beam temperature and the need to achieve, both in the oven and in the beam, a Boltzmann distribution of the vibrational states. The oven, with two separately heated chambers, was of the style developed by Ochs, Cote, and Kusch,[9] but the slit arrangement on the front chamber was similar to that developed by Miller and Kusch,[10] who found that very thin slits were necessary in order to achieve the velocity distribution theoretically predicted for the beam coming from an ideal oven. We made no effort to see if slit thickness affected the distribution of vibrational states, but, following the practice of Miller and Kusch, used slit material 0.0025 cm thick. The slit opening was 0.0075 cm wide by 0.8 cm high. The slit material was held to the front chamber by Cu clamps 0.47 cm thick. The oven had steel and Ta slits, respectively, for the formation of beams of LiF and LiCl. Slits of either steel or Zr were rapidly

[8] G. Herzberg, *Spectra of Diatomic Molecules* (D. Van Nostrand Company, Inc., Princeton, New Jersey, 1950), 2nd ed., p. 122.

[9] S. A. Ochs, R. E. Coté, and P. Kusch, Phys. Rev. **21**, 459 (1953).

[10] R. C. Miller and P. Kusch, Phys. Rev. **99**, 1314 (1955).

corroded by LiCl. Two different ovens were used, one of Ni, the other of K-monel.

The value of a two-chamber oven came from two features: (1) the beam temperature was dependent only on the temperature of the front chamber and was therefore independent of the beam intensity which was determined by the temperature of the rear chamber; (2) polymerization was reduced when the front chamber was at a higher temperature than the rear chamber.

The second feature was of particular importance for LiCl beams because beam intensity was at a premium. When the front chamber was 75°C to 100°C hotter than the rear chamber, the LiCl line intensities increased by a factor of between 2 and 3 over their intensities when the two chambers were at the same temperature. This increase represented an actual improvement in the ratio of signal to noise because no change in the background intensity of the beam occurred when the temperature of the front chamber increased. No improvement in the intensity of LiF lines resulted from an increase in the temperature differential between the two chambers. The above results are in general accord with beam polymerization data tabulated by Kusch and Hughes.[11]

The beam temperature was determined from temperature measurements made in two places in the front chamber of the oven. Chromel and alumel wires, peened, each in a different place, into the Cu clamps on the front of the oven, formed one thermocouple. The second thermocouple consisted of Chromel-Alumel wires peened together into a Cu plug, which, in turn, was clamped into a hole in the side of the front chamber.

The reliability of the temperature measurements was assured in ways now to be described. First, the accuracy of the Chromel-Alumel thermocouples was confirmed through simultaneous measurements made with a Pt-Pt and 10% Rh thermocouple. The agreement was within ±2°C. Secondly, it was noted that the thermocouples were altered by use. The temperature difference between them (the Cu plug always had the lower temperature) showed a steady increase, an increase which was evidently caused in part by poor thermal contacts because after several days they became noticeably loose. The larger changes in temperature difference were accompanied by changes in the ratio R, in such a direction as to indicate that after a time the beam temperature was higher than the temperature of either thermocouple. To assure the reliability of their readings the thermocouples were replaced after three or four days of operation. We did not accept any data for which the temperature difference was greater than 18°C (the difference was never less than 5°C). We assigned to the beam a temperature, estimated to be accurate to ±1%, equal to the average of the temperatures of the two thermocouples in the front chamber.

[11] P. Kusch and V. W. Hughes, "Atomic and Molecular Beam Spectroscopy," *Handbuch der Physik*, S. Flugge, editor (Springer-Verlag, Berlin, Germany, 1959), Vol. 37–1.

B. Ratio Measurements

The detection and current measuring systems will be discussed first. The molecular beam detector was an oxygenated W wire, 0.012 cm in diameter, which had its maximum efficiency at 1220°K (wire temperatures were measured with an optical pyrometer). Measurements made by Trischka and Kurtz[12] show that, when such a wire is operated at its maximum efficiency, about 80% of the Li atoms in an incident neutral beam of LiCl are converted into positive ions at the surface of the wire. The ionization efficiency of the wire was a function of its temperature. For example, a 75°C rise above the optimum temperature caused the efficiency to fall to about 50% of its maximum value, and the maximum efficiency was restored when the wire was returned to the lower temperature. However, the process could not be reversed when the temperature increase was greater than 75°C. Then the wire required a new oxygenation to restore it to maximum efficiency.[13]

It has been mentioned earlier that for accurate measurements of the ratio R, the deflection of the pen recorder must be proportional to the ion current leaving the detector wire. Calibration of the amplifier-recorder system showed it to be linear to ±0.2% of full scale deflection. The mass spectrometer-multiplier system was not calibrated, but was assumed to be linear because of the small currents present, at most 10^{-13} amp in the mass spectrometer and at most 10^{-8} amp at the output of the secondary emission multiplier.

The method for measuring R will now be described. First, with the oscillator frequency fixed, the maximum intensity of the selected $v=1$ line was measured after the line had been recorded by adjustment of the C-field voltage. By further adjustment of the C-field voltage the corresponding $v=0$ line was recorded and its maximum intensity measured. The $v=1$ line was then remeasured. This method enhanced the accuracy with which the $v=1$ line was measured (this line had about one-third the intensity of the $v=0$ line) and also provided a check on the constancy of apparatus conditions. The three operations described above will hereafter be called a "measurement" and a series of "measurements," on the average about ten in these experiments, will be called a "run."

Runs were made for Li^6F, Li^7F, and Li^6Cl^{35}. The strong field spectrum of Li^6F, consisting of two resolved lines, was observed at a field such that the $v=1$ lines

[12] In unpublished work done in this laboratory J. Kurtz and J. W. Trischka studied the efficiency of ionization of LiCl on oxygenated tungsten wire by observing the intensity of neutral particles leaving the wire when they struck a second, hot, oxygenated tungsten wire.

[13] The efficiency of the wire also decreased when its temperature was lowered below 1220°K. However, this method was impractical because the time required to take a reading increased from about 1/10 sec at 1220°K to about 10 sec at 1140°K. Moreover, the efficiency at the lower temperature was a function of beam strength, being about 50% (relative to a wire at maximum efficiency) at a beam current of 10^{-9} amp and 100% at a beam current of 10^{-12} amp.

TABLE I. Uncorrected experimental values of the vibrational constants ω_e of Li^6F and Li^6Cl^{35}. T is the oven temperature. R is the ratio of line intensities for molecules in the $v=1$ and $v=0$ states.

Molecule	T(°K)	R	ω_e(cm^{-1})
Li^6F	1074	0.281	947
	1092	0.288	944
	1106	0.290	951
	1112	0.292	951
	1116	0.294	948
	1147	0.303	951
			uncorrected $\bar{\omega}_e=949\pm10$
Li^6Cl^{35}	972	0.343	722
	977	0.348	725
	981	0.330	756
	1031	0.360	731
	1033	0.350	753
	1034	0.361	731
			uncorrected $\bar{\omega}_e=736\pm11$

and the $v=0$ lines were clearly resolved.[14] For Li^7F individual lines were not resolved in the spectrum of a given vibrational state; however, the spectrum of the $v=1$ state was clearly separated from the spectrum of the $v=0$ state. The intensity for each vibrational state was taken to be the maximum value of the unresolved spectrum. The lack of resolution, in this case a result of inhomogeneities in the brass C field,[15] resulted in a useful enhancement of spectral intensity. The lines used in the Li^6Cl^{35} spectrum were the resolved lines in the strong-intermediate field spectrum designated by Marple and Trischka in Table III of their paper as 35–0–1 and 35–1–1.[2] These two lines are corresponding lines for the $v=0$ and $v=1$ states and were chosen because they are quite distinct from one another and from all other lines in the spectrum.

Table I gives the results of a number of runs, arranged in order of increasing temperature, for Li^6F and Li^6Cl^{35}. These runs were made with the detector wire adjusted to give maximum efficiency. The values of ω_e were computed with the use of Eq. (1), and because, as mentioned in the Introduction, the measured R is not the same as the ideal R the values of ω_e in Table I are called "uncorrected." Corrections will be discussed in the next section. The results of runs made with Li^7F will be discussed later.

CORRECTIONS

Table II lists and gives the magnitudes of the three corrections which must be made to the values of ω_e, given in Table I. The first correction is a consequence of the fact that the $v=0$ and $v=1$ lines were not observed at the same C-field voltage. The beam molecules, while moving into and out of the C field, pass through regions of spatially varying field where they may undergo nonadiabatic changes of state. The fraction of molecules which undergo such changes varies with the C-field voltage, becoming smaller as the voltage increases. Hence, the number of molecules available for radiofrequency induced transitions varies with the C-field voltage, and the same line observed at two different voltages will show an apparent change in intensity. The corrections given as item 1 of Table II were deduced from the experimentally determined variation in the number of nonadiabatic transitions with C-field voltage.

The second correction shown in Table II is determined by the velocity selecting properties of the knife-edge region of the apparatus. For an ideally thin beam the knife-edge position will determine the upper limit to the velocity of the molecules reaching the detector; whereas, the B-field electrode opposite the knife-edge will set the lower velocity limit. If these velocity limits are designated by $u_{\min}$ and $u_{\max}$ and the quantity $y=u/\alpha$, where α is the most probable molecular velocity in the oven, then the observed line intensity for an ideally thin beam, will be[16]

$$I=2I_0\int_{y_{\min}}^{y_{\max}} y^3 \exp(-y)^2 \sin^2(bl/\alpha y)dy, \qquad (2)$$

where I_0 is the total intensity of the molecules, with velocities from $u=0$ to $u=\infty$, which are available for the particular transition under observation; b is proportional to the matrix element for the transition, and l is the length of the transition region.

The integral given by Eq. (2) will not be the same for the two vibrational states for the following reasons: (a) the difference in the molecular constants μ and A for the two states leads to a difference in the forces on the molecules in the A and B fields and hence to a difference in the band of velocities selected at the knife-edge; (b) the quantity b is not the same for molecules in the two states because of the differences in μ and A, and (c) because b depends on the C-field voltage. The effects of the differences listed in (b) and (c) are negligible; i.e. $\leqslant 0.1\%$.

The effect noted under (a) is important, but not

TABLE II. Percentage Corrections to the values of $\bar{\omega}_e$ given in TABLE I.

Kind of correction	Li^6F (%)	Li^6Cl^{35} (%)
1. Changes in nonadiabatic transitions	0.0	−0.7
2. Change in velocity bands	+1.7	−1.2
3. Decay of $v=1$ state	−3.6±1.8	−2.3±1.2
Net correction	−1.9±1.8	−4.2±1.2

[14] J.-C. Swartz and J. W. Trischka, Phys. Rev. **88**, 1085 (1952).
[15] R. C. Luce and J. W. Trischka, J. Chem. Phys. **21**, 105 (1953).
[16] For a discussion of transition probabilities cf. N. F. Ramsey, *Molecular Beams* (Oxford University Press, New York, 1956), pp. 118 ff. The origin of Eq. (2) is easily seen from Ramsey's Eq. (Vol. 19), p. 123.

easily calculated theoretically because the beam does not have a zero width, and its position in the fields is not accurately known. The correction for this effect was made by means of a simplified theory whose adequacy was attested to by a special series of experiments, now to be described.

The effect on the beam molecules of differences in vibrational state is a change in force; but, a change in force can also be brought about through a change in the field strengths of the A and B fields. Hence, the effects of a change in the vibrational state can be compensated by a change in electric field strengths. Such a compensation can be made exactly (and hence, independently of beam width and position) at sufficiently weak fields in which the force is proportional to μ^2AE^2, where E is the electric field intensity. In LiF the quantity μ^2A increases by 4% from the $v=0$ state to the $v=1$ state.[14] The effect of this increase can, therefore, be compensated for by a decrease in E of 2%. Table III shows the result of an experiment in which such a compensation was made. The field parameter λ_B, characteristic of the B field and defined by $\lambda=\mu E/(\hbar^2/2A)$, is given in column (1). (The A field is set to produce refocusing of the beam.) Column (2) shows the result of a measurement of R without any compensation; i.e. R was determined in the same way as were the values in Table I. On the other hand, column (3) shows the values of R determined with compensation made as described above. At $\lambda_B=0.6$ the fields were weak enough for complete compensation to be effective, and column (3) should have a value of R which is the same as the value obtained by making a correction to column (2) for the change in vibrational state. Such a correction was made theoretically under the simplifying assumptions that the beam was of negligible width and was accurately located in the apparatus at the position optically determined for it before the apparatus was set into operation. Column (4) shows this theoretically corrected value and column (5) shows the calculated velocities of molecules which succeeded in passing beyond the knife-edge region to the detector.

Although columns (3) and (4) are in good agreement for $\lambda_B=0.6$, thereby confirming the usefulness of the theory, we believed it important to make a further test at stronger fields and picked $\lambda_B=1.4$, the strongest field condition available. For this value of λ_B column (3) cannot show the result of a complete compensation for vibrational effects, however, it is still possible to make a theoretical calculation of column (3) based on the figure in column (2), with the result shown in column (4), for comparison with column (3). Since columns (3) and (4) agree for such widely different field conditions, we felt justified in using the simplified theory to make corrections to the values of ω_e in Table I. The small corrections in Table II, item 2, are consistent with the small differences at $\lambda_B=1.4$ between columns (2) and (3) in Table III, because nearly the same value of λ_B, namely, $\lambda_B=1.33$, was used for the measurements whose results are recorded in Table II.

TABLE III. Measurements and calculations used to determine the effect on R of deflecting forces and small changes in deflecting forces. R is the ratio of measured line intensities from molecules in the $v=1$ and $v=0$ states. Li^7F beam.

(1)	(2)	(3)	(4)	(5)
λ_B	R, At λ_B	R: Field voltage reduced by 2% for $v=1$ molecules	R, Calculated	Calculated ideal velocity band; v/α
0.6	0.325±0.007	0.303±0.004	0.304±0.007	0.4 to 0.7
1.4	0.313±0.003	0.315±0.003	0.310±0.003	0.8 to 1.6

A note on the errors in Table III is necessary. The errors in the figures in columns (2) and (3) are the probable errors calculated from the standard deviations for runs containing ten measurements. Each number in column (3) is the result of a single run, whereas each number in column (2) is the average of two runs, one performed before the run represented by column (3) and the other performed afterward. The agreement of these "before" and "after" runs was used as a criterion of the constancy of conditions during the experiment. The errors listed in column (4) are the same as those in column (2) because the latter was used as a basis for determining the former.

The third correction listed in Table II is required because of the spontaneous decay of molecules in the $v=1$ state during their flight through the apparatus. If f is the fraction of molecules which do not decay, then

$$f=e^{-t/T} \tag{3}$$

where T is the lifetime, determined by the rate of spontaneous emission for a radiative transition from the $v=1$ to the $v=0$ state, and t is the effective transit time of the molecule; i.e., the time in which the molecule must decay in order not to be detected as in the $v=1$ state.

There are no experimental values for T, but Klemperer and Herschbach[5] have calculated a theoretical value for LiCl, finding $T=3.6\times10^{-2}$ sec. Their method of calculation, applied to LiF, gives a theoretical value of $T=1.6\times10^{-2}$ sec. There is no way of estimating the errors in these values, but it is fortunately possible to use some of the information in Table III to obtain a rough value of the lifetime of LiF and thereby check on the order-of-magnitude correctness of the theoretical calculations.

The ratios given in column (3) of Table III are intended to be values of R which require no correction for effects due to the differences between the molecular constants μ and A for molecules in the $v=1$ and $v=0$ states. The actual absence of need for such a correction is accurately true at $\lambda_B=0.6$, and, though not so true for the stronger field represented by $\lambda_B=1.4$, the small

TABLE IV. Effect of detector wire ionization efficiency on ratio, R, of line intensities for molecules in $v=1$ and $v=0$ states. Three runs were made for each molecule.

Molecule	Lower efficiency (fraction of maximum efficiency)	R_{Hi}/R_{Lo}
Li^6F	0.2 to 0.3	1.00±0.01
Li^7F	0.3 to 0.5	1.00±0.01
Li^6Cl^{35}	≲0.5	0.99±0.01

differences among the numbers in columns (2), (3), and (4) under these conditions show that the lack of compensation is very probably less than the experimental error. Hence, within the stated experimental errors, the two numbers in column (3) should agree with one another unless there is a vibrational decay of molecules in flight, and their failure to agree is positive evidence of such a decay.

The nonzero width of the beam and its somewhat undetermined position in the apparatus makes it difficult to estimate the accuracy of any calculation of the lifetime from the figures in Table III. To make such a calculation, which requires finding the average value of $1/v$ for the molecules in the detectable beam, we have assumed an ideally thin beam and have used the velocity limits given in column (5) of Table III. We believe that the error in this method is less than the rather large error in the difference between the two numbers in column (3). This difference is the principle experimental quantity entering into the calculation. The lifetime, so calculated, is best expressed by

$$1/T=65\pm40 \text{ sec}^{-1}.$$

Thus the probable range of T is from 1.0×10^{-2} sec to 4.0×10^{-2} sec, which includes the theoretical value given above. The stated error comes from the errors in the numbers in column (3) of Table III.

The corrections for decay of the excited vibrational state were calculated as follows: for Li^6F the experimental lifetime with the experimental limits of error was used; for Li^6Cl^{35} the theoretical lifetime was used and the limits of error arbitrarily set at 50% to indicate an uncertainty similar to the uncertainty in the value used for LiF. The sizes of these corrections are shown in Table II.

RESULTS AND DISCUSSION

In Table IV are presented the results of experiments dealing with the effect on the ratio R of the ionization efficiency of the detector wire. In all cases R was the same when the wire was run at maximum efficiency and at the fraction of this efficiency shown in column (2). We believe these results provide strong evidence that the detector wire does not discriminate between vibrational states in the process of surface ionization, because it is unlikely that the nature of such discrimination would remain unchanged for a large change in the efficiency of ionization. This evidence is important for the interpretation of the results of the measurement of the vibrational constants.

TABLE V. Comparison of present results with those obtained from infrared spectra.

Molecule	ω_e (cm^{-1}) This paper	Infrared
Li^6F	930±19	961±2[a]
Li^6Cl^{35}	705±14	685±3[b]

[a] G. L. Vidale, J. Phys. Chem. **64**, 314 (1960).
[b] W. Klemperer, W. G. Norris, A. Büchler, and A. G. Emslie, J. Chem. Phys. **33**, 1534 (1960).

Table V gives the corrected values of the vibrational constants ω_e and, for comparison, values determined from infrared absorption experiments. Although the present results and the infrared results disagree by amounts slightly outside the limits of experimental error, the disagreement is less than twice the probable error in the present experiments. There is apparently no systematic disagreement, because the present result is higher than the infrared result in one case and lower in the other. We believe, therefore, that the agreement is good enough to warrant the conclusion that the hypothesis of Klemperer and Herschbach has no validity for the present experiments. The conclusions drawn from Table IV are thus re-enforced.

If the presence of the vibrational phenomenon hypothesized by Klemperer and Herschbach[5] is ruled out in the present experiment, then it is possible to conclude from the agreement between the present results and the infrared results that the distribution of vibrational states in the oven must be a Boltzmann distribution. This is the first time this distribution has been verified by such direct observations.

The present molecular beam results for the vibrational constants disagree markedly with the previous molecular beam measurements made by one of the authors (JWT) and others. The previous results were $\omega_e=756\pm38$ cm^{-1} for Li^6F and $\omega_e=536\pm60$ cm^{-1} for Li^6Cl^{35}.[1,2] We can give no certain explanation for this disagreement, but because of the thoroughness of the present investigation, we believe the new results should replace the old ones. We suspect that the low values of the old results are a consequence of inaccurate temperature measurements.

There is one other molecular beam result which cannot be compared with either infrared measurements or with the present measurements; this is the vibrational constant of CsF.[17] In the light of our present experience with these measurements we believe this value should be highly suspect and is very probably too low.

The ratio of the vibrational constants for Li^6F and Li^7F was measured in four separate runs on four different days and found to be 1.06±0.01, in agreement with the theoretical value expected on the basis of the difference in reduced masses of the two molecules.

[17] J. W. Trischka, Phys. Rev. **74**, 718 (1948).

Interpretation of the Appearance Potentials of Secondary Ions

M. B. WALLENSTEIN AND M. KRAUSS

National Bureau of Standards, Washington, D. C.

(Received August 29, 1960)

The statistical theory of mass spectra assumes that the excitation energy in a molecule-ion is essentially equipartitioned prior to unimolecular decomposition. Some of the consequences of this assumption have been deduced and the results have been used in interpreting the observed appearance potentials of secondary and tertiary ions of neopentane, *n*-butane, and *1*-butene. Although the results are not quantitative, it is evident that considerable vibrational energy is removed with the neutral fragment. The problem of the detailed interpretation of appearance potentials is complicated by the fluctuation of the vibrational energy distribution in the products of a decomposition from the most probable value, i.e., equipartition. Some general considerations with regard to determination of minimum-energy decomposition paths and the significance of this study in relation to the statistical theory of mass spectra are also presented.

I. INTRODUCTION

IT is now generally accepted that most of the fragment ions in hydrocarbon and other large molecule mass spectra are formed by successive and competing decompositions of isolated, excited molecular ions. Rosenstock *et al.*[1] have developed a rate expression for such a system in which the excited molecular ions are represented as a collection of harmonic oscillators and internal rotors. Decomposition is assumed to occur from some stable electronic state which is energized, after a Franck-Condon transition to some higher state, by the transfer of part or all of the initial electronic excitation energy into vibrational energy through a large number of radiationless transitions.

We must note here that there may be one or several terminal states from which decompositions may occur, each corresponding to a "band" of levels, wherein radiationless transitions are possible and within which the energy rapidly is transformed into vibrational energy of the "ground" state, or to a single electronic level. There is evidence that this situation is very prevalent; some important examples occur in the mass spectrum of benzene and ethyl alcohol with indications that the situation also occurs in the larger paraffins such as *n*-heptane and *n*-octane. This can be deduced from rate considerations governing metastable ion production, which is discussed more fully elsewhere.[2] The existence of such bands or single electronic levels will require marked modification of the assumptions of the statistical theory. For a single level, the problem reduces to the usual requirement of calculating the kinetics of unimolecular decomposition from a set of specified initial vibrational states. For the elucidation of the kinetics of decomposition from a band of levels, we are faced initially with the formidable task of determining the energy distribution among levels of the band. In either case we must know the probabilities for finding an ion in any of the bands or single levels.

There is some possibility of determining the initial excitation at low energies for certain molecules as the resolution of the vibrational structure of acetaldehyde and propanol indicate.[3] However, in more highly excited molecule-ions there is no knowledge of the initial distribution of excitation and, more important, little information on the detailed process of the relaxation of the energy. Because of this situation, it is necessary to make admittedly simplified assumptions, deduce the consequences thereof and compare these with experiment.

The statistical theory of Rosenstock *et al.* requires the energy to be randomized in the vibrational degrees of freedom of the ground state of the ion. Friedman *et al.*,[4] Chupka,[5] and Steiner *et al.*,[6] have discussed, at length, the consequences of the statistical theory with respect to primary dissociations of the parent ion. These authors have concluded that, near threshold, the theory is either not applicable or requires quantitative modification.

Friedman *et al.* have observed that a considerable amount of excess energy should be required in large molecules over the minimum required for dissociation in order to attain rates of dissociation fast enough to be observed in the mass spectrometer. This observation is taken to indicate a basic deficiency in the theory on the basis of the assumption that dissociation energies computed from appearance potentials are generally correct. We do not feel that this question has been completely resolved for there seem to be many instances where computed dissociation energies are incorrect. This problem will be pursued further in Sec. II.

Chupka accepted the thesis that large amounts of excess energy are not found. He deduced, from a study of metastable ions, that only a fraction of the total number of oscillators seem to be accessible to provide the activation energy for decomposition. He then found that, for primary decompositions, inclusion of the

[1] H. M. Rosenstock, M. B. Wallenstein, A. L. Wahrhaftig, and H. Eyring, Proc. Natl. Acad. Sci. U. S. **38**, 667 (1952).

[2] H. M. Rosenstock, and C. E. Melton (unpublished work).

[3] H. Hurzeler, M. G. Inghram, and J. D. Morrison, J. Chem. Phys. **28**, 76 (1958).

[4] L. Friedman, F. A. Long, and M. Wolfsberg, J. Chem. Phys. **27**, 613 (1957).

[5] W. A. Chupka, J. Chem. Phys. **30**, 191 (1959).

[6] B. Steiner, C. F. Giese, and M. G. Inghram, presented at 1960 ASTM meeting.

thermal energy already present in the molecule coupled with the decreased number of oscillators could account for the apparent lack of excess energy which would otherwise be required to give suitably large rate constants. There is an additional uncertainty introduced, when using electron impact values for appearance potentials as usually measured, resulting from the electron energy spread. This may obscure differences between actual dissociation energies and those observed if the curvature in the probability curve is not properly considered.

There are certain difficulties with Chupka's analysis of photoionization metastable ions. The assumption of a reduced number of degrees of freedom does not predict the low maximum and wide half-width observed but the contrary. Chupka obtains agreement with experiment if the predicted shape is averaged over the thermal distribution. It is necessary at this point to examine in more detail the validity of Chupka's analysis.

The rate expression is derived by considering all the *accessible* states lying in a certain energy range. The expression $[1-\epsilon_0/E)]^{N-1}$ can be interpreted as the chance, in an equilibrium distribution, that more than ϵ_0 of the total energy E is in one particular degree of freedom. E is the total energy available to the group of interacting degrees of freedom and is not necessarily equal to the total energy of the molecule. Chupka requires that, during the relaxation of the excited molecule-ion, all the energy is funneled into a restricted number of oscillators since he does not change E when reducing the number of vibration degrees of freedom N by a factor of $\frac{1}{3}$ or $\frac{1}{2}$. It would seem that this is a too stringent requirement and that, in addition to any excess energy required to achieve a sufficient rate of dissociation, there must be energy "frozen" in non-accessible modes.[7]

We must note that accessibility of a mode of vibration with respect to energy transfer and rapid randomization does not necessarily imply an active role in the dissociation process. On the other hand, it is to be expected that those inaccessible modes are either removed in space or of such symmetry that their vibrations do not contribute to extension of any critical coordinate. The initial equilibrium distribution of thermal energy will, of course, be distorted during the relaxation and will contribute in an unknown way to the various groups of finally noninteracting modes.

A similar situation to that described has been discussed in great detail by Gill and Laidler[8] and Slater.[9] However, it should be noted that in Slater's theory there is an equilibrium distribution which is maintained by collisions. In this theory they are not interested in the accessibility of energy interchange among groups of oscillators.

In this paper we adopt the viewpoint of the statistical theory in a heuristic fashion with respect to the energetics of secondary ion formation. Although the difficulties in interpreting primary processes at threshold are not as yet solved, it is not necessary to have complete information on the primary process in order to begin an investigation into secondary and higher-order decompositions. Since the primary ions are formed at energies much above threshold in these processes, the statistical theory is assumed to be applicable to a higher approximation than seems to be the case at threshold. In particular, we shall assume that primary ions are formed such that the vibrational energy in the activated state is randomly distributed in a time short compared to the decomposition of the parent. As a result, the total energy available for the primary ion and the neutral fragment will be equilibrated between the ion and the neutral fragment and may be easily calculated. The consequences of these assumptions are examined in Secs. III and IV, where it is found that they are capable of providing a reasonable explanation for the magnitudes of the observed appearance potentials. It should be noted that several authors[10] have observed that excess energy is carried off by the neutral fragment and that the appearance potentials for secondary ions may be high. However, in all cases this situation was not their prime consideration and little or no detailed discussion was given.

II. HEATS OF FORMATION OF RADICALS AND IONS

The assumption that mass spectra of polyatomic molecules result from the unimolecular decompositions of excited molecules and ions immediately makes it necessary to know the energetics of the possible decompositions. The original hypothesis upon which the present statistical theory of mass spectra is founded is that the processes which lead to the formation of a given ion at threshold will be those which require the minimum amount of energy. Although there is some reason to doubt this hypothesis now, it is still the best starting point in view of the deficiency of experimental information. One assumes, therefore, that correlations, if they exist, between heats of reaction and apparent heats of activation derived from appearance potentials will appear when heats of reaction are calculated from heats of formation for the stable species.

We have constructed a table of values which are derived solely from thermal or kinetic data and from directly measured ionization potentials. A complete discussion of the sources and probable errors for the values given in Table I will be published elsewhere.

[7] R. A. Marcus, J. Chem. Phys. **20**, 359 (1952).
[8] E. K. Gill and K. J. Laidler, Proc. Roy. Soc. (London) **A250**, 121 (1959).
[9] N. B. Slater, Phil. Trans. Roy. Soc. (London) **A246**, 57 (1953).
[10] S. Wexler, G. R. Anderson, and L. A. Singer, J. Chem. Phys. **32**, 417 (1960); H. M. Rosenstock, Ph.D. thesis, University of Utah; A. Kropf, E. M. Eyring, A. L. Wahrhaftig, and H. Eyring, J. Chem. Phys. **32**, 149 (1960); and footnote 5.

Here it is sufficient to note that the heat of formation values shown are taken mainly from the compilations of Roberts and Skinner,[11] Szwarc,[12], and Cottrell,[13] augmented where necessary and possible by approximation methods used by Franklin.[14] The free radical ionization potential data used are almost exclusively those determined by direct measurement by Lossing *et al.*[15] The required ionization potentials of molecules were taken from the tabulation by Field and Franklin,[16] while all relevant thermal data for molecular species have been taken from Rossini *et al.*[17]

In using the data of Table I to calculate heats of the reactions considered in the next section, one can be reasonably certain that the values found will be in error by no more than perhaps 1 to 5 kcal depending upon the specific case.[18] This assumes that Lossing's values are very close to the adiabatic ionization potentials. In all of the reactions considered here, the reverse heats of activation are relatively small for radical—radical-ion recombinations and are probably not large, i.e., not more than about 10 kcal,[19] for the molecule—radical-ion and radical—molecule-ion recombinations. Entropy factors are probably more significant in the latter cases in determining the decomposition rates. It may be noted that Taubert[20] has found reverse heats of activation that fall in the vicinity of 10 kcal for processes of this kind. We shall find, in studying secondary and tertiary ions, that no serious error will be introduced by simply estimating the reverse heats of activation since they constitute only a small part of the total energy of activation for a series of consecutive unimolecular decompositions.

TABLE I.[a]

Molecule or radical	$\Delta H_f(R)$	I^b	$\Delta H_f(R^+)$
CH_3	32.2	229.7	262.9
C_2H_5	24.0	201.1	225.1
C_2H_3**	71.2	217.9	289.1
n-C_3H_7	18.7	200.4	219.1
s-C_3H_7	15.3	182.2	197.5
$CH_2{=}CH{-}CH_2$	30.0	188.2	218.2
$CH{\equiv}C{-}CH_2$[b]	66.1	190.2	256.3
n-C_4H_9	13.8	199.2	213.0
s-C_4H_9	10.4	182.9	193.3
i-C_4H_9	12.4	192.6	205.0
t-C_4H_9	5.0	171.1	176.1

[a] All values in kcal at 300°K.

[b] Ionization potentials of these species have been measured by Lossing. There are no data for heats of formation of the ions or radicals except appearance potentials. The values given for $\Delta H_f(R+)$ have been corrected to approximate thermal values by estimating and removing any reverse activation energies involved.

TABLE II.

Process	Thermal heat of reaction	Appearance potential[a] heat of reaction
$C_2H_6^+ \rightarrow C_2H_5^+ + H$	26.6	28.8
$C_3H_8^+ \rightarrow C_3H_7^+ + H$	15.9	12.0
n-$C_4H_{10}^+ \rightarrow$ *s*-$C_4H_9^+ + H$	26.5	30.0
n-$C_4H_{10}^+ \rightarrow$ *n*-$C_3H_7^+ + CH_3$	32.5	2.8
n-$C_4H_{10}^+ \rightarrow$ *s*-$C_3H_7^+ + CH_3$	10.7	2.8
n-$C_5H_{12}^+ \rightarrow$ *n*-$C_3H_7^+ + C_2H_5$	34.8	7.4
n-$C_5H_{12}^+ \rightarrow$ *s*-$C_3H_7^+ + C_2H_5$	21.3	7.4
n-$C_4H_{10}^+ \rightarrow C_2H_5^+ + C_2H_5$	35.3	30.0
$C_3H_6^+ \rightarrow C_3H_5^+ + H$	39.4	49.6
1-$C_4H_8^+ \rightarrow C_3H_5^+ + CH_3$	23.6	45.6

[a] All values of appearance potentials used for these calculations are the "best values" tabulated by Field and Franklin, footnote 15.

An immediate consequence of using the thermal heats of formation of Table I to compute heats of reaction for process occurring in the mass spectrometer is the observation that, even for single bond breaks, differences in measured appearance potentials do not always yield thermal values for heats of formation of the fragment ions. In Table II a comparison is made between thermal and appearance potential values for a number of processes involving single bond breaks.

The values calculated for loss of a hydrogen atom from ethyl, propyl, and *n*-butyl ions are all within the expected experimental errors in the data. The dissociations of $C_4H_{10}^+$ and $C_5H_{12}^+$ to give the $C_3H_7^+$ ion are not easily understood. The differences are too large even if one assumes a rearrangement to form *s*-C_3H_7 and are in the wrong direction for interpretation as a reverse activation energy. The heats of formation and ionization potentials of H, CH_3, C_2H_5 can be assumed correct to

[11] J. S. Roberts and H. A. Skinner, Trans. Faraday Soc. **45**, 339 (1949).

[12] M. Szwarc, Chem. Revs. **47**, 75 (1950).

[13] T. L. Cottrell, *The Strengths of Chemical Bonds* (Butterworths Scientific Publications, Ltd., London, 1958), 2nd ed.

[14] J. L. Franklin, Ind. Eng. Chem. **41**, 1070 (1949); J. Chem. Phys. **22**, 1304 (1954).

[15] F. P. Lossing, Ann. N. Y. Acad. Sci. **67**, 499 (1957); *Mass Spectrometry* (Institute of Petroleum, London, 1959).

[16] F. H. Field and J. L. Franklin, *Electron Impact Phenomena* (Academic Press, Inc., New York, 1957).

[17] F. D. Rossini, K. S. Pitzer, R. L. Arnett, R. M. Braun, and G. C. Pimentel, *Selected Values of Physical and Thermodynamic Properties of Hydrocarbons and Related Compounds* (Carnegie Press, Carnegie Institute of Technology, Pittsburgh, Pennsylvania, 1953).

[18] For example, recent work by A. G. Harrison and F. P. Lossing [J. Am. Chem. Soc. **82**, 519 (1960)] agrees with the value for the ΔH_f of $C_3H_3^+$ to within 6 kcal.

[19] H. M. Rosenstock, Ph.D. thesis, University of Utah.

[20] A. R. Taubert, presented at ASTM meeting, Atlantic City, New Jersey, June, 1960.

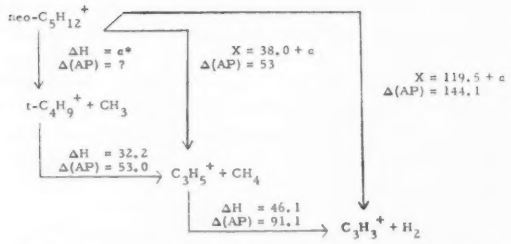

FIG. 1. Formation of $C_3H_5^+$ from neo-C_5H_{12}. *Neither ΔH nor A(neo-$C_5H_{12}^+$) is known. If the reasonable value of 15 kcal is assumed for ΔH in this process, then the X values are all in quite good agreement with $\Delta(AP)$'s.

within 1 or 2 kcal. Less reliance may be placed on the C_3H_7 and C_4H_9 heats of formation. Whatever the errors may be, comparison of the first eight entries in Table II shows that no choice of heats of formation for these ions and radicals can be made which will make all of these reactions consistent with the apparent dissociation energies calculated from appearance potentials. It seems that, in these cases, one can only conclude that the methods used in measuring the appearance potentials do not yield energies that are simply interpretable in terms of thermal values.

In view of these results, it is apparent that a much closer inspection must be made of the way in which appearance potentials are measured and interpreted. It is equally clear that an unambiguous set of thermal and ionization data would provide a most desirable basis for determining the lower limits of expected appearance potentials.

III. ENERGIES OF DISSOCIATION PROCESSES

The minimum energies for the formation of $C_3H_5^+$ and $C_3H_3^+$ from neo-C_5H_{12}, n-C_4H_{10}, and 1-C_4H_8 are given in Figs. 1–3. These values include the estimated reverse heats of activation. Figures 4 and 5 present the same information for the formation of $C_2H_5^+$ and $C_2H_3^+$ from neo-C_5H_{12} and n-C_4H_{10}. Also shown in these figures are the differences between appearance potentials of the ions formed by successive decomposition. That the processes indicated by each of the decomposition sequences actually occur has been shown in each case by the existence of mestable ion peaks corresponding to each of the decompositions. As we shall show later, these sequences are not necessarily the only ones by which a given ion might be produced. If the differences in appearance potentials, $\Delta(AP)$, represent only thermal plus activation energies, and if they have been correctly assigned, they should at least be approximately equal to the sums of the corresponding thermal plus activation energies already calculated. This is obviously not the case. Unless the processes to which the $\Delta(AP)$ values are attached have been completely misassigned, as seems unlikely in view of the metastable ion spectrum, we must account for some large excess energies.

We have seen that at threshold, presumably, certain degrees of freedom are "frozen" or inactive and do not contribute to the dissociation energy. There is little evidence as to the amount of energy at threshold which remains in the frozen modes. However, when more energy is available, the probability of energy transfer increases. It is then more reasonable to assume that the energy is essentially randomly distributed among all degrees of freedom. We may still assume that for the primary break a restricted number of modes are active. This number may or may not equal the number of active modes at threshold. Lacking any specific information, we have assumed that the total excess energy both in the active and inactive modes, is equilibrated between the neutral and ionic fragments during the dissociation of the parent ion.

However, as we will show in Sec. IV, equilibration does not mean a high occupancy of vibrational states corresponding to equipartition of the energy although equipartition is still the most probable distribution. For the purposes of the present section, we shall nevertheless assume that the energy is equipartitioned between the vibrational degrees of freedom of the neutral and ionic species. We are required to make such a simplification since we are ignorant of the sensitivity of our mass spectrometers and of the over-all shapes of the probability curves for the formation of the ion. The corrections due to fluctuations about the most probable distribution at decomposition will be dealt with briefly in Sec. IV. In this section we shall find that the assumption of equipartition provides interesting correlations with experimental appearance potentials but is too

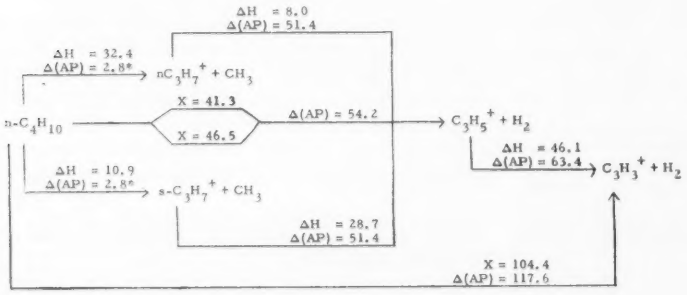

FIG. 2. Formation of $C_3H_3^+$ from n-C_4H_{10}. *This $\Delta(AP)$ value is probably incorrect. All X values were calculated using ΔH values for these two reactions.

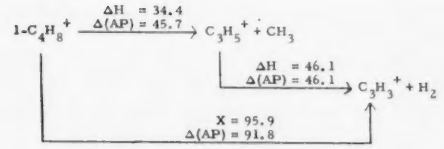

FIG. 3. Formation of $C_3H_3^+$ from 1-$C_4H_8^+$.

crude to allow quantitative prediction of appearance potentials of secondary and tertiary ions.

The examples in Figs. 1–5 were chosen because considerable confidence may be placed in the precision of the "conventional" appearance potentials for these molecules. We define a "conventional" appearance potential as one obtained by any of the semiempirical or empirical techniques described by Field and Franklin,[16] which do not consider any theory determining the rate of decomposition of the excited ions. We have computed the total energy X required for secondary ions from

$$f_1(X-\epsilon_1)=\epsilon_2, \tag{1}$$

and for the tertiary ions

$$f_2\{f_1(X-\epsilon_1)-\epsilon_2\}=\epsilon_3. \tag{2}$$

In these equations f_1 and f_2 are the fraction of normal modes associated with the fragment ions in the primary and secondary dissociations. We have required that the excess energy in the primary (or secondary) ion finds its way exclusively into the "active" modes for the secondary (or tertiary) dissociation to occur with no excess energy in the inactive modes. In order to compute f_i it is necessary to assume either all modes are active or that the f_i's are not very different if fewer modes are active.

The energy changes associated with the relative translation of the neutral and ionic species and with their rotational energies have been ignored in the foregoing calculation. Two reasons dictate this simplification. In the first place the energies associated with these degree of freedom, except for translational energy caused by the reverse heat of activation, are small and, considering the gross approximations involved in our calculations, do not warrant detailed consideration. Secondly, the rate theory used here does not include conservation of linear and angular momentum in its formulation.

It is evident from Figs. 1–3 that the computed thermal activation energies are far smaller than the appearance potential differences and the computed X values. More encouraging, we do not find that the appearance potential differences are ever appreciably small than the X values and are, in fact, usually somewhat larger. Such a conditions hould exist, of course, in order to allow for the additional excess energy required to obtain a rate of 10^5–10^6 sec^{-1} or larger if there are several competitive processes preceding this one.

In Figs. 4 and 5 we present the results of similar considerations for the $C_2H_5^+$ and $C_2H_3^+$ ions from neo-C_5H_{12} and n-C_4H_{10}. It should be noted that the process for the production of $C_2H_3^+$ that is indicated by metastable ions, i.e., through the $C_2H_5^+$ ions, has X's much larger than the appearance potential differences. Therefore, we have investigated several other possibilities which give better agreement between the X's and the appearance potential differences. We have included the direct production of $C_2H_3^+$ from the t-$C_4H_9^+$ in the neo-C_5H_{12} scheme even though the competitive production of $C_3H_5^+$ from t-$C_4H_9^+$ would reduce the number of $C_2H_3^+$ ions formed to very

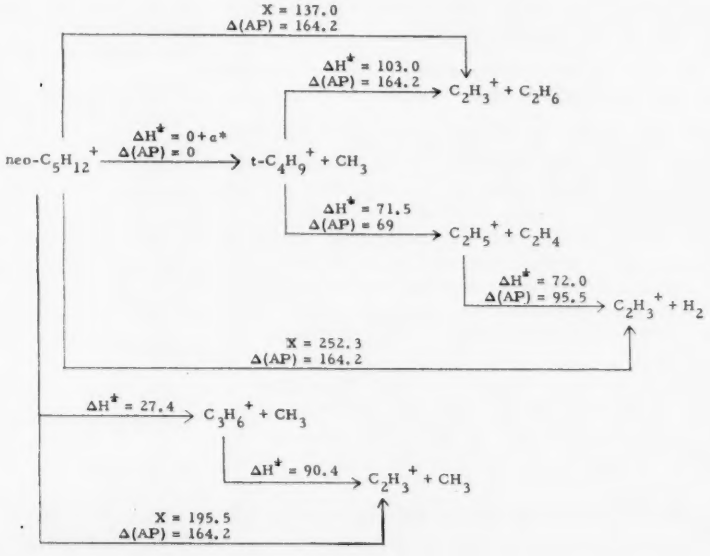

FIG. 4. Possible modes of formation of $C_2H_3^+$ from neo-pentane. *α is assumed to be 15 kcal.

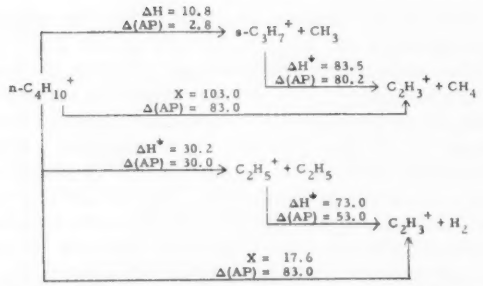

FIG. 5. Possible modes of formation of $C_2H_3^+$ from *n*-butane.

negligible proportions. We must emphasize that the X's offer only an approximate guide to the interpretation of secondary appearance potentials. Consideration of fluctuations about equipartition and the over-all shape of the probability curves including competition is fundamental to an improved understanding. This will be discussed in the next section.

IV. DETERMINATION OF MINIMUM ENERGY PATHS

In discussing the decomposition patterns of neo-$C_5H_{12}^+$ ion, Lampe and Field[21] observed that the metastable ion at $m^+=25.1$ implies that $C_2H_3^+$ is formed by the following reaction sequence:

$$\text{neo-}C_5H_{12}^+ \rightarrow t\text{-}C_4H_9^+ + CH_3$$
$$\quad\quad\quad

vibrational degrees of freedom of the dissociating ions, and that the most probable distribution of this excess at the time of decomposition is that corresponding to equipartition of the energy among the vibrational degrees of freedom. This last assumption implies the expectation of a sharpness of the energy distribution about the most probable equipartition value, which is not justified in systems having such a small number of degrees of freedom. To see this we can investigate the properties of a simplified harmonic oscillator molecule in which all of the oscillators are equivalent. We wish to calculate the number of ways in which n quanta (of size $h\nu$) of excess energy in the ion at the time of dissociation are distributed over the vibrational degrees of freedom of the two dissociating parts of the original ion. If s_1 and s_2 represent the numbers of vibrational degrees of freedom in the two parts, then the number of ways in which n_1 and $n_2(n_1+n_2=n=E/h\nu)$ quanta can be distributed in these two groups of oscillators is, for a particular choice of n_1 and n_2:

$$N_{n_1,n_2}=\frac{(n_1+s_1-1)!}{n_1!(s-1)!}\cdot\frac{(n_2+s_2-1)!}{n_2!(s_2-1)!}. \tag{5}$$

If we assume complete freedom of interchange of quanta among the oscillators, then the probability of a particular value of n_1+n_2 appearing is just

$$P_{n_1,n_2}=N_{n_1,n_2}/\sum_{n_1,n_2}N_{n_1,n_2}, \tag{6}$$

where

$$\sum N_{n_1,n_2}=\frac{(n+s-1)!}{n!(s-1)!}$$

with

$$n_1+n_2=n. \tag{7}$$

It can easily be shown that, subject to the condition $n_1+n_2=n$, the most probable distribution is $n_1/s_1=n_2/s_2$ corresponding to equipartition. Unfortunately, the distribution of P_{n_1,n_2} values is not at all sharply peaked around this most probable value. The probability, for example, in which n_1 and n_2 deviate by as much as 50% from the most probable values is only slightly less than that of the most probable distribution. This situation is illustrated for a model system in Fig. 6. The implication of this result is that primary ions will be formed with a very broad distribution in energy. The appearance of secondary ions then will depend on the number of primary ions formed with a given energy times the rate of formation of secondary ions from primary ions having this excitation energy.

The model curves shown here are calculated by the following scheme. A fourteen-atom parent ion is assumed to decompose into a nine-atom primary ion plus a five-atom neutral fragment. The kinetics employed are described in the following set of equations:

$$n_1 \xrightarrow{k_1} n_2 \xrightarrow{k_2} n_3$$

$$n_1=n_0\exp(-k_1t)$$

$$n_2=n_0\frac{k_1}{k_2-k_1}\{\exp(-k_1t)-\exp(-k_2t)\}$$

$$n_3=n_0\left\{1-\frac{k_2}{k_2-k_1}\exp(-k_1t)+\frac{k_1}{k_2-k_1}\exp(-k_2t)\right\}$$

$$k_1=10^{13}\left[\frac{E-\epsilon_1}{E}\right]^{N-1}\qquad k_2=10^{13}\left[\frac{E'-\epsilon_2}{E'}\right]^{N'-1}, \tag{8}$$

where n_i = number of ions at time t and $N=36$ or 12 and $N'=21$ or 7. In all cases t has been taken to be 10^{-5} sec.

The result of this type of analysis is shown in Fig. 7. As can be seen in the figure, a very long low energy tail is to be expected for the appearance potential curves of secondary ions. If the number of degrees of freedom are reduced by a factor of 3, a considerable, though reduced, low energy tail is calculated for the secondary ions. The experimental curves do exhibit such behavior.[22] There is also a corresponding high-energy tail on the respective primary ions which may be obscured by the effects of competition among the primaries. The experimentally measured appearance potentials will be determined largely by the sensitivity and noise level of the instrument. Thus no particular significance in terms of thermal activation energies (i.e., the activation energy that would presumably be obtained for a system in which the time for reaction approaches infinity) can be attached to secondary ion appearance potentials without detailed information as to the kinetics of the formation process. The agreement of the X's with the differences in the appearance potentials is indicative of the inadequacy of conventional techniques for measuring appearance potentials and is due to the lack of detection of the extreme length of the tails on secondary ions measured on low sensitivity instruments. The larger the neutral fragment that is obtained in the primary process, the longer and flatter will be the tail for the secondary ion and the higher the apparent appearance potential that would be measured using conventional techniques.

V. DISCUSSION

We wish to emphasize two intimately connected considerations. The first is the lack of any real agreement between dissociation energies calculated from appearance potentials and those obtained thermally. There are as many differences as agreements. In the second place, the use of the appearance potentials of secondary and tertiary ions must be handled with great caution. We believe that all the values which have been ob-

[22] A. B. King and F. A. Long, J. Chem. Phys. **29**, 374 (1958).

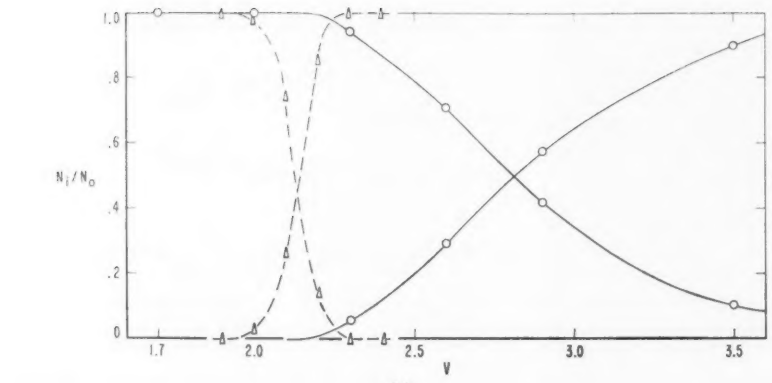

(a)

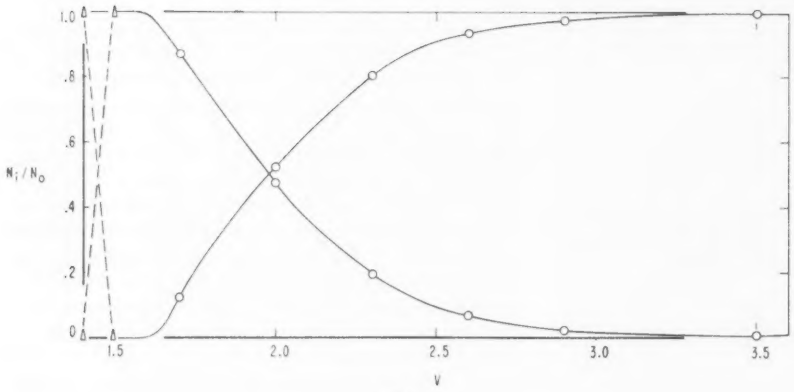

(b)

FIG. 7. Calculated breakdown pattern of secondary ions. (a) N oscillators in parent (primary ion); (b) $N/3$ oscillators in parent (primary ion).

tained by treating ionization efficiency curves in a conventional manner must be reevaluated in the light of consequences of the statistical theory although much of the primary data may be satisfactory. Unfortunately, all the points that have been raised by Chupka and Friedman *et al.* have not been resolved. It is difficult to make quantitative predictions from the statistical theory due to the uncertainties which exist in certain of the important parameters. This is in addition to any more fundamental difficulties that arise when the energy is not equilibrated.

Quantitative consideration of the energy excess for the secondary and tertiary ion appearance potentials founders in the difficulties discussed above. In this case the conventional treatments for handling the data are less adequate than for primary ions. We feel, therefore, that the mere fact of an energy excess does not warrant any conclusions as to the fact or degree of randomization. A careful study of the problem of the secondary ion appearance potentials will have to await at least the results of the investigations suggested by Friedman *et al.* and Chupka. The most that can be said is that the evidence does not rule out the assumption of energy randomization in the accessible degrees of freedom or the assumption that the accessible modes subsume all the internal modes of the molecule.

Effect of Pressure on the Spectra of Five Nickel Complexes*

D. R. STEPHENS AND H. G. DRICKAMER

Department of Chemistry and Chemical Engineering, University of Illinois, Urbana, Illinois

(Received August 22, 1960)

The effect of pressure to 150 kbars has been measured on the absorption spectra of five nickel complexes. The results are discussed in terms of the change of 10 Dq and of the Racah parameter B, with pressure. In general 10 Dq, the crystal field strength, increased with pressure, but the increase noted was not the same when calculated for the different peaks of a given complex. This discrepancy may be described in terms of changes of covalency as measured by changes of the Racah parameter B. In general B decreased with increasing pressure showing increased covalency at high pressure. There were some discrepancies in the value of B obtained from different transitions. These may be the result of experimental error, but may also be associated with distortions of the field, or with weaknesses in the assumption of point charges or dipoles.

THE effect of pressure on crystal field peaks of five octahedral Ni(II) complexes has been measured to 150 kbars. The high-pressure spectroscopic techniques have been discussed elsewhere,[1-3] except that the pressure calibration in the range above 140 kbars has been modified. This will be discussed in another paper.

Parsons and Drickamer[2] have studied the effect of pressure on several spin-allowed crystal field peaks in octahedral complexes. They found that pressure increased the crystal field parameter Dq as expected from the theory, although the increase in Dq for two transitions in the same complex was not equal, in disagreement with the simple theory. Using the equations of Tanabe and Sugano,[4] they calculated the effect of pressure on B, a measure of covalency, to give the same change in Dq for the two transitions. Where possible, this same technique is applied, again using Tanabe and Sugano's calculations. Liehr and Ballhausen[5] have more detailed calculations for this case, but values of B are not obtainable from their work.

The complexes studied include Ni(o-phen)$_3$(NO_3)$_2$, Ni($\alpha-\alpha'$dip)$_3$ Br_2, and Ni(en)$_2$(SCN)$_2$, all obtained from Dr. T. S. Piper, KNi(Gly)$_3$, obtained from A. D. Mackay Company, and NiO, obtained from Dr. W. B. Wilson from the Battelle Memorial Institute. Here, o-phen=o-phenanthroline, ($\alpha-\alpha'$ dip=$\alpha-\alpha'$ dipyridyl, and en=ethylenediamine. All of these complexes are octahedral and their spectra can be explained by crystal field theory. The ground state for Ni(II) in an octahedral field is (using Mulliken's nomenclature $^3A_2$(F), with three spin-allowed transitions, $^3A_2$(F)$\rightarrow$ $^3T_2$(F), $^3A_2$(F)$\rightarrow$$^3T_1$(F), and $^3A_2$(F)$\rightarrow$$^3T_1$(P). The lowest-lying transition, $^3A_2$(F)$\rightarrow$$^3T_2$(F), was obtained for all five complexes. The next higher transition, $^3A_2$(F)$\rightarrow$$^3T_1$(F), was obtained for KNi(Gly)$_3$, NiO, and Ni(en)$_2$(SCN)$_2$ while the highest transition, $^3A_2$(F)$\rightarrow$$^3T_1$(P), was obtained only for KNi(Gly)$_3$ and NiO. Pressure effects on other peaks were not obtained due to experimental difficulties. The shifts in energies of these absorption peaks are shown in Figs. 1 to 10. The change in 10 Dq with pressure, is the same as the energy shift for the $^3T_2$(F) transition and is indicated as such. Figure 10 shows the rather anomalous, but reproducible, pressure effect in Ni($\alpha-\alpha'$ dip)$_3$ Br_2. In this complex Dq does not seem to increase with pressure above about 80 kbars. For KNi(Gly)$_3$, NiO, and Ni(en)$_2$(ScN)$_2$, the change in 10 Dq with pressure for each transition is shown in Figs. 11 through 13. These changes were obtained from Tanabe and Sugano's calculations, assuming B=constant=1030 cm^{-1}. It can be seen that Δ10 Dq is not equal for each transition in the same complex, and at high pressures, the difference is larger than experimental error, which was 50 to 100 cm^{-1}. This discrepancy could be due to a number of factors, one of which might be the increase in covalency. This can be discussed in terms of the Racah parameter B which is determined by the repulsion

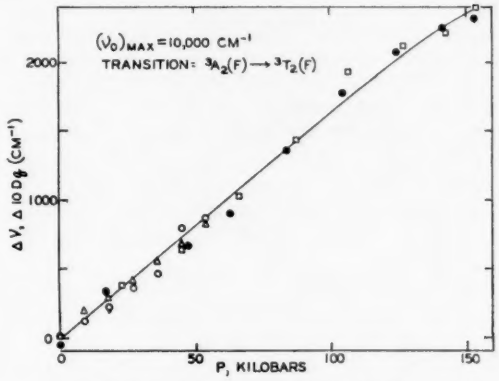

FIG. 1. $\Delta\nu$, Δ10Dq vs pressure. KNi(Gly)$_3$.

* This work was supported in part by U. S. Atomic Energy Commission, Chemical Engineering Project 5.

[1] R. A. Fitch, T. E. Slykhouse, and H. G. Drickamer, J. Opt. Soc. Am. **47**, 1015 (1957).

[2] R. W. Parsons and H. G. Drickamer, J. Chem. Phys. **29**, 930 (1958).

[3] T. E. Slykhouse and H. G. Drickamer, J. Phys. Chem. Solids **7**, 207 (1958).

[4] Y. Tanabe and S. Sugano, J. Phys. Soc. Japan **9**, 753, 766 (1954).

[5] A. D. Liehr and C. J. Ballhausen, Ann. Phys. **6**, 134 (1959).

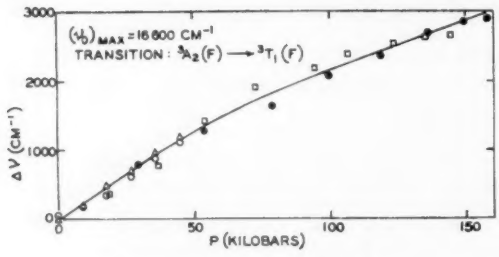

FIG. 2. $\Delta\nu$ vs pressure. $KNi(Gly)_3$.

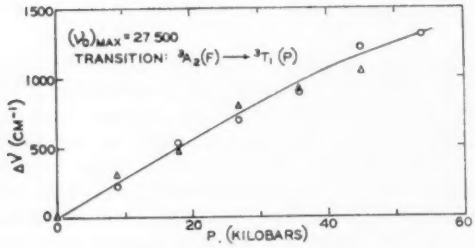

FIG. 3. $\Delta\nu$ vs pressure. $KNi(Gly)_3$.

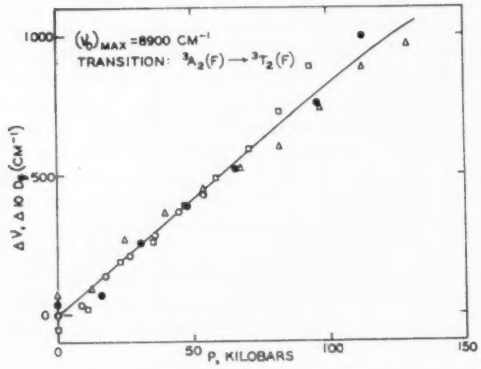

FIG. 4. $\Delta\nu$, $\Delta 10Dq$ vs pressure. NiO.

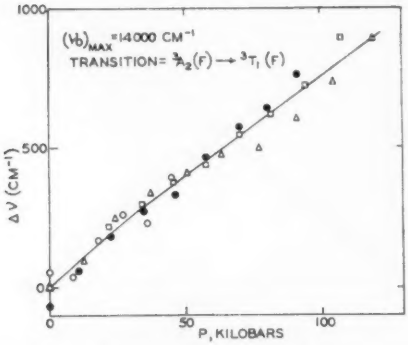

FIG. 5. $\Delta\nu$ vs pressure. NiO.

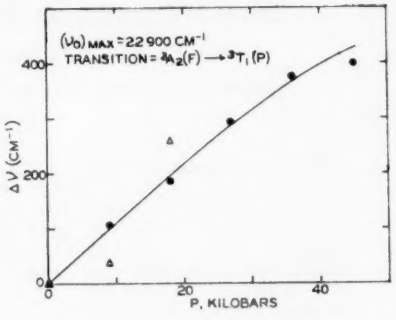

FIG. 6. $\Delta\nu$ vs pressure. NiO.

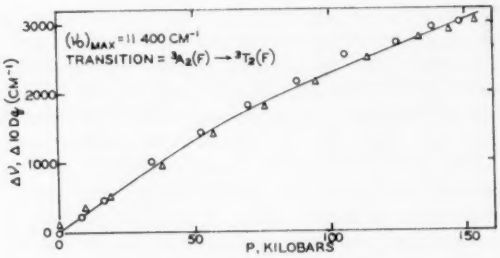

FIG. 7. $\Delta\nu$, $\Delta 10Dq$ vs pressure. $Ni(en)_2(SCN)_2$.

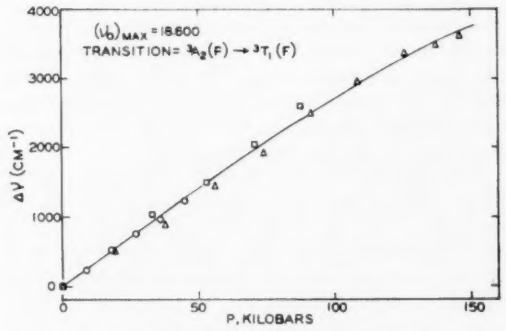

FIG. 8. $\Delta\nu$ vs pressure. $Ni(en)_2(SCN)_2$.

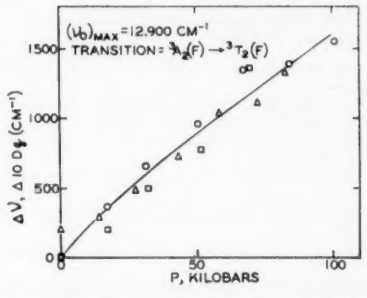

FIG. 9. $\Delta\nu$, $\Delta 10Dq$ vs pressure. $Ni(O\text{-}phen)_3(NO_3)_2$.

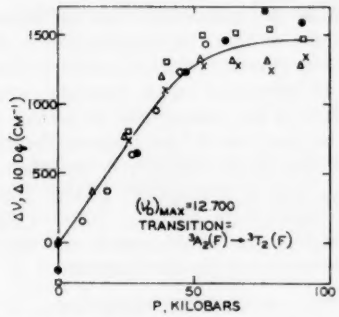

FIG. 10. $\Delta\nu$, $\Delta 10Dq$ vs pressure. $Ni(\alpha-\alpha'\ dip)_3Br_2$.

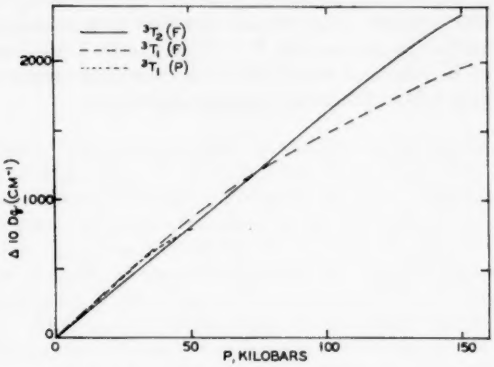

FIG. 11. $\Delta 10Dq$ vs pressure. $KNi(Gly)_3$.

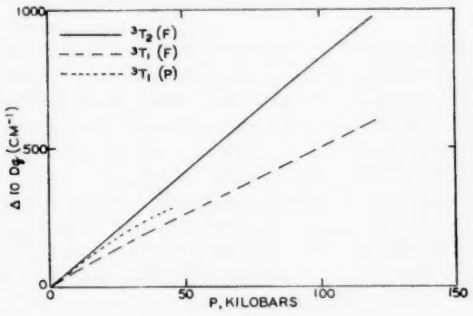

FIG. 12. $\Delta 10Dq$ vs pressure. NiO.

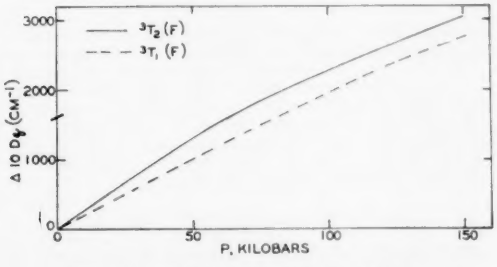

FIG. 13. $\Delta 10Dq$ vs pressure. $Ni(en)_2(SCN)_2$.

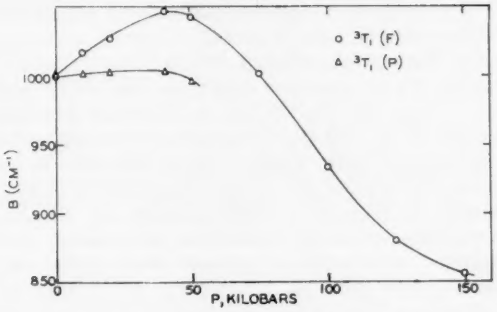

FIG. 14. B vs pressure. $KNi(Gly)_3$.

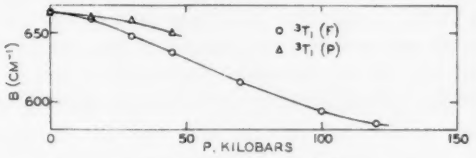

FIG. 15. B vs pressure. NiO.

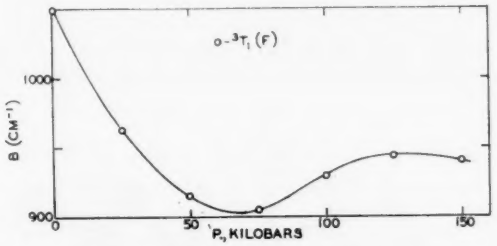

FIG. 16. B vs pressure. $Ni(en)_2(SCN)_2$.

between electrons on a given atom. An increase in the degree of covalency between a metal atom and its ligands, would be accompanied by a spreading out of the charge cloud and therefore a reduction of the repulsion and thus of B. Even if this is a somewhat oversimplified view of a complex situation, calculation of B as a function of pressure, is a convenient means of classifying deviations from simple crystal field theory. Therefore, the change in B was calculated for each complex, using $\Delta 10\,Dq$ obtained from the $^3T_2(F)$ transition. The value of B used for atmospheric pressure was the average one that best fitted the $^3T_1(F)$ and $^3T_1(P)$ transitions. The change in B with pressure for the $^3T_1(F)$ and $^3T_1(P)$ transitions are shown in Figs. 14 through 16. The equations used are[4]:

$$E[^3A_2(F)\rightarrow{}^3T_2(F)]=10\,Dq \quad (1)$$

$$E(^3A_2(F)\rightarrow{}^3T_1(F))=\tfrac{3}{2}(10\,Dq+15/2B-\tfrac{1}{2}[(10\,Dq-9B)^2+144B^2]^{\frac{1}{2}} \quad (2)$$

$$E(^3A_2(F)\rightarrow{}^3T_1(P))=\tfrac{3}{2}(10\,Dq)+\tfrac{1}{2}[(10\,Dq-9B)^2+144B^2]^{\frac{1}{2}}. \quad (3)$$

The change in B is quite sensitive to the energy shift of the transition and is probably only of qualitative value. For example, although B for $KNi(Gly)_3$ increases for the $^3T_1(F)$ transition during the first 40 kbars, it can be seen from Fig. 11 that the difference in $\Delta 10\,Dq$ for the $^3T_2(F)$ and $^3T_1(F)$ transitions is almost within experimental error. Thus, a small difference in the energy shifts could give a rather large change in B. In general, B decreases at high pressure for all three complexes, indicating an increase in covalency with pressure. At atmospheric pressure B was quite small for NiO and decreased steadily for both transitions, indicating a large amount of covalency in this complex.

It may be noted that there is a discrepancy in the change in B for the $^3T_1(F)$ and $^3T_1(P)$ transitions in $KNi(Gly)_3$ and NiO. Aside from the sensitivity of B to the energy shifts, calculating B in this manner does not take into account other possibilities of error in the theory, such as the effect of distortion of the octahedron of ligands, or the assumption that the ligands act as point charges, so that the disagreement in B may not be surprising. However, the qualitative evidence for an increase in covalency with pressure seems valid.

The effect of the assumption of perfect symmetry may not be great, as at high pressure the discrepancy in $\Delta 10\,Dq$ for $Ni(en)_2(SCN)_2$ is no larger than for $KNi(Gly)_3$ and is appreciably smaller than $\Delta 10\,Dq$ for NiO. Since there are two different ligands for $Ni(en)_2(SCN)_2$, we would expect a distortion from octahedral symmetry for this complex.

ACKNOWLEDGMENTS

The authors would like to thank Dr. W. B. Wilson of the Battelle Memorial Institute for furnishing the NiO crystals. They would also like to acknowledge fruitful discussions with T. S. Piper and D. S. McClure. D. R. Stephens would like to acknowledge assistance from a Dow Chemical Company Fellowship.

Infrared Spectrum of Single Crystals of LiOH, LiOD, and LiOH·LiOD†

R. M. HEXTER

Mellon Institute, Pittsburgh, Pennsylvania

(Received March 23, 1960)

High-resolution infrared absorption spectra of single crystals of LiOD and of the solid solution LiOH·LiOD are reported. These are compared with each other and with the spectrum of monocrystalline LiOH. Comparisons with the spectra of $Mg(OH)_2$ and $Ca(OH)_2$ are also made. The differences in selection rules for the two types of hydroxides are discussed together with differences in spectra to be expected upon changing the mass of the cation and upon deuterium substitution. The discussion is in terms of the current theory of the spectra of such crystals. It is concluded that the complex spectrum of these minerals in the high-frequency region (2000–5000 cm^{-1}) is entirely due to OH^- (or OD^-) ion motion. The motion is quite localized; the motions of the several OH^- ions of the crystal are poorly coupled. Difficulties with previous assignments due to unusual temperature dependencies of intensities are also discussed. The restricted rotational character of the localized motion of the OH^- ions, previously proposed, may be used to rationalize these difficulties and to qualitatively account for the existence and similarity of the spectra of all three materials. Finally, the "rotational" model accounts well for the frequency shifts consequent on deuteration.

INTRODUCTION

THE problem of exploring the vagaries of the spectra of $Mg(OH)_2$ and $Ca(OH)_2$ has been set forward many times previously.[1–3] The problem is not, however, restricted to these minerals. It undoubtedly encompasses the hydroxides of Cd, Fe(II), Ni(II), Co(II), and Mn(II), as they are isostructural with those of Mg and Ca. In all of these the space group is D_{3d}^3, with the OH ions situated on sites of symmetry C_{3v}. As pointed out before,[1] the infrared spectrum of the pseudo-alkaline earth hydroxide LiOH is remarkably similar to those of $Mg(OH)_2$ and $Ca(OH)_2$. Indeed, one of the principal purposes of this article is to account for this similarity.

The crystal structure of LiOH was first elucidated by Ernst,[4] using x-ray techniques. It has been recently refined by Dachs,[5] who used neutron diffraction. The relationship of its structure to that of $Mg(OH)_2$ and $Ca(OH)_2$ may be appreciated by examination of Fig. 1. The unit cell of LiOH contains two formula units. Using the standard procedures of factor group analysis,[6] Wickersheim[7] has proposed an assignment of the spectrum of a single crystal of LiOH in which various pairs of lines are described as additive and subtractive combinations of the OH fundamentals with lattice frequencies. Some of these are associated with unit cell modes which involve cation motion; such assignments will be discussed below in detail.

In previous reports[1,2] we have attempted partial analyses of the spectra of $Mg(OH)_2$, $Ca(OH)_2$, and LiOH in terms of models which view these spectra as originating solely in the localized motion (librational or hindered rotational) of the hydroxide ion. Another purpose of this article is to report the results of high-resolution studies of single crystals of LiOD and of LiOH·LiOD which seem to leave little doubt of the latter view.

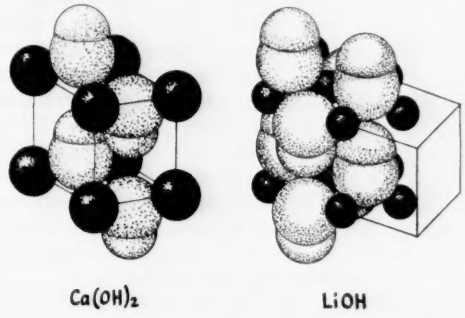

FIG. 1. Crystal structures of $Ca(OH)_2$ and LiOH, to the same scale.

EXPERIMENTAL

LiOD single crystals were prepared by two methods. One of these was that used in our prior preparation of LiOH single crystals[1] and also used by Wickersheim[7] in his study. LiOD crystals so produced were quite suitable for use in our double-beam instrument (to be described later in this article). However, for single-beam higher-resolution studies, the isotope effect on the intensities was so marked that considerably thicker crystals than those produced by this method were required. This was accomplished by the slow cooling of a melt in an induction furnace and in an argon atmosphere. No special drying of the argon was attempted.

† This research was supported in part by the United States Air Force through the Air Force Office of Scientific Research of the Air Research and Development Command.

[1] R. M. Hexter, J. Opt. Soc. Am. **48,** 770 (1958).
[2] R. M. Hexter and D. A. Dows, J. Chem. Phys. **25,** 504 (1956).
[3] R. T. Mara and G. B. B. M. Sutherland, J. Opt. Soc. Am. **43,** 1100 (1953); R. T. Mara, dissertation, University of Michigan (1954) (published as Tech. Rept. 2, Signal Corps Project 152B-O); R. T. Mara and G. B. B. M. Sutherland, J. Opt. Soc. Am. **46,** 465 (1956).
[4] T. Ernst, Z. physik. Chem. (Leipzig) **B20,** 65 (1933).
[5] H. Dachs, Z. Krist. **112,** 60 (1959).
[6] H. Winston and R. S. Halford, J. Chem. Phys. **17,** 607 (1949).
[7] K. A. Wickersheim, J. Chem. Phys. **31,** 863 (1959).

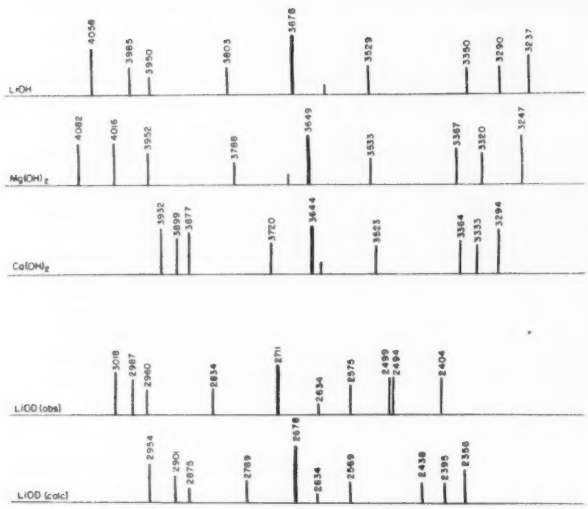

FIG. 2. Comparison of spectra of LiOH, $Mg(OH)_2$, and $Ca(OH)_2$ plus comparison of observed and calculated spectra of LiOD. For method of calculation, see text.

The power supplied to the coils of this furnace was so controlled that the melt was allowed to supercool until nucleation occurred. Immediately after nucleation, the temperature of the sample was raised to a temperature still below the melting point such that one of the several nuclei survived the demise of the others. When a temperature was found that maintained this nucleus at a constant size, the power input to the furnace was held constant for 2 hr, during which time this nucleus grew into a large platelet. Following this the power was twice reduced, and after each reduction the crystal was permitted to grow in thickness, presumably isothermally, for 2-hr periods. After a total of 7 hr the entire sample appeared to be singular, and the heating was terminated. Upon cooling to room temperature, the sample was removed from its silver crucible and cleaved parallel to the (001) face. By this method a single crystal $\sim 750\ \mu$ thick was produced.

As indicated by the infrared measurements themselves, crystals of LiOD stored over silica gel do not exchange their deuterium perceptibly in a period of at least a month. Nevertheless, the crystal prepared by the second method described above was observed to demonstrate features of the spectra of both LiOH and LiOD, as will be described in detail below. Apparently, in the several remeltings preparatory to nucleation, probably due to the lack of special drying of the argon, exchange occurred while the sample was in the liquid state. Taking into account the isotope effect of intensity, the spectra qualitatively suggest that the exchange proceeded 50% to completion. We assume that no segregation occurred upon nucleation and subsequent crystal growth, as such would be unlikely on thermodynamic grounds. We shall refer to this crystal as a 1:1 solid solution of LiOD in LiOH, or as LiOH·LiOD. In the interpretations of the spectra presented later the exact isotopic dilution of this sample is of little consequence.

The double-beam spectrometer mentioned previously was the same Perkin-Elmer model 13 used in our previous study of LiOH.[1] As in earlier investigations[8–10] it was modified by the substitution of a 7500-line/in. Merton-NPL diffraction grating for the Littrow mirror, with a KBr prism left in place. This grating is blazed for 3-μ radiation. The purity of this radiation was insured by the use of a Lucite chopper and an LiF filter.

The single-beam highest-resolution instrument was a Perkin-Elmer model 112G modified by the use of a regulated Nernst glower source and a PbTe detector. In each instrument the sample was mounted before the monochromator such that only "normal-incidence" spectra were recorded.

Frequency Calibrations

Disagreement of several frequencies reported by Wickersheim[7] with those previously reported by us[1] suggested greater care with spectral calibration. In our previous study of LiOH, calibration was accomplished using the method of Friedel and McKinney[11] as discussed by Downie *et al.*[12] The basic calibration points used were those of the 2.7-μ band of atmospheric water vapor, precise frequency values for which are tabulated by Benedict and Plyler.[13] The values of $\tilde{\nu}_0$ and B were found to be, respectively, 100 cm^{-1} and 3.87×10^{10} cm^{-2}.

[8] D. A. Dows and R. M. Hexter, J. Chem. Phys. **24,** 1117 (1956).
[9] R. M. Hexter, Spectrochim. Acta **10,** 281 (1958).
[10] R. M. Hexter, Spectrochim. Acta **10,** 291 (1958).
[11] D. S. McKinney and R. A. Friedel, J. Opt. Soc. Am. **38,** 222 (1948).
[12] A. R. Downie, M. C. Magoon, T. Purcell, and B. Crawford, J. Opt. Soc. Am. **43,** 941 (1953).
[13] W. S. Benedict and E. K. Plyler, J. Research Natl. Bur. Standards **46,** 246 (1951).

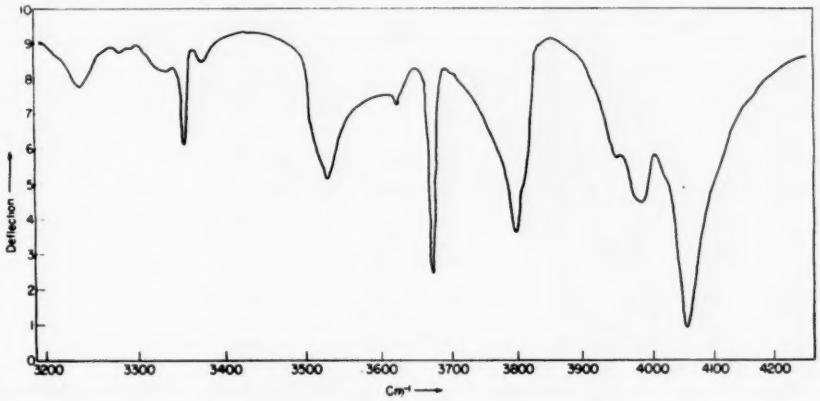

FIG. 3. Infrared spectrum of a single crystal of LiOH, normal incidence upon (001) face.

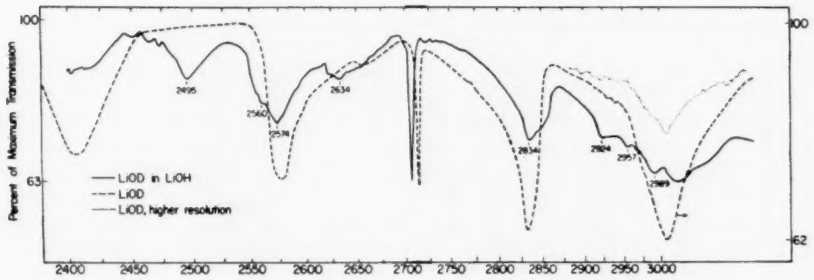

FIG. 4. Infrared spectra of single crystals of LiOD and of LiOD in LiOH, normal incidence upon (001) faces.

The resultant plot of T_0 vs $\tilde{\nu}$, over the range 4000 cm^{-1} to 3500 cm^{-1} had no discernible curvature, indicating the correctness of $\tilde{\nu}_0$. The extrapolation of this empirical straight line was apparently in error, however, and a recalibration has been made using ν_1 of NH_3 as well as the water-vapor lines. This new calibration yields frequencies for some LiOH bands still in disagreement with those tabulated by Wickersheim (see Fig. 2).

Calibrations of the LiOD spectra were accomplished using 10-cm cells of HCl and HBr gas, at pressures of 60 cm and 40 cm, respectively, plus atmospheric carbon dioxide.

Spectra

The spectrum of LiOH is presented in Fig. 3. This is the same spectrum cited earlier.[1] We include it because of the aforementioned calibration refinements and because it demonstrates a reflection maximum, also observed with the solid solution, which was not observed by Wickersheim. This reflection maximum will be discussed below.

The spectra of LiOD and LiOD in LiOH are presented in Fig. 4. Higher-resolution spectra of the 2950–3030 cm^{-1} and 2480–2640 cm^{-1} regions of the LiOD region in the solid solution are illustrated in Figs. 5 and 6, re-

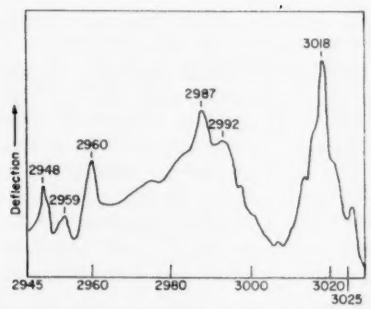

FIG. 5. Infrared spectrum of single crystal of LiOH·LiOD, 2950–3030 cm^{-1} region.

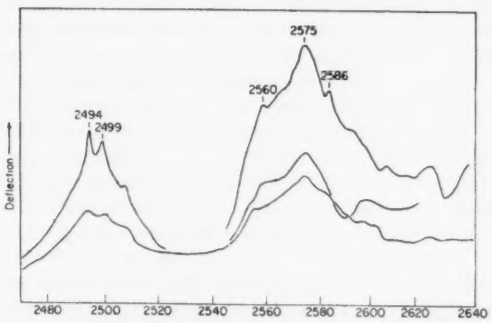

FIG. 6. Infrared spectrum of single crystal of LiOH·LiOD, 2480–2640 cm^{-1} region.

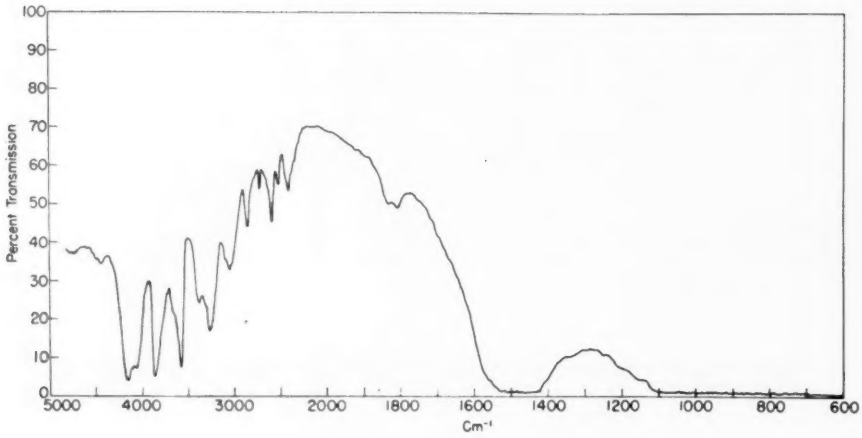

FIG. 7. Infrared spectrum of single crystal of LiOH·LiOD, 600–5000^{-1} region, low resolution.

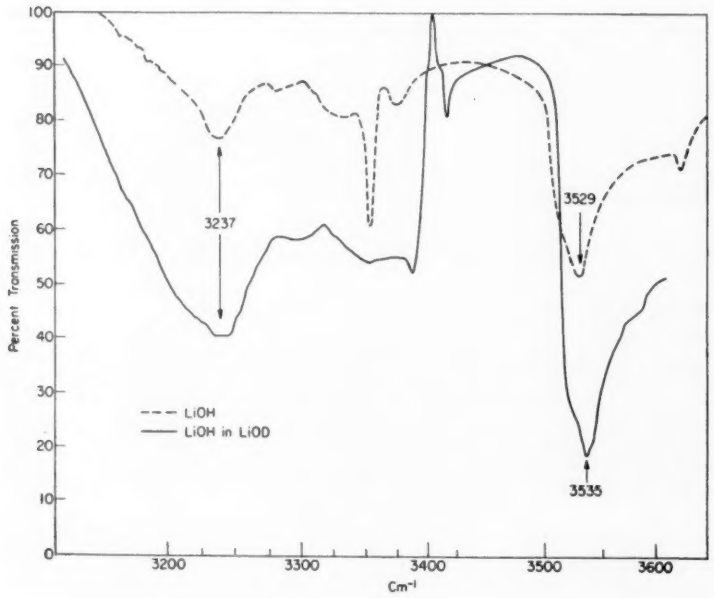

FIG. 8. Infrared spectrum of single crystal of LiOH·LiOD, 3200–3600 cm^{-1} region.

spectively. Figure 7 is a low-resolution spectrum of the LiOH·LiOD crystal covering the entire rock salt region. Figure 8 illustrates the lower-frequency side of the spectrum of the LiOH region in the solid solution and includes the same region in the spectrum of pure LiOH, for purposes of comparison. The reflection maximum referred to above is found in the spectrum of solid solution, shifted to slightly higher frequency. The significance of this shift will be discussed below.

Of the spectra illustrated here, those of Figs. 3, 4, and 8 were recorded using the grating-modified Perkin-Elmer model 13, while those of Figs. 5 and 6 were obtained with the Perkin-Elmer model 112G. The spectrum illustrated in Fig. 7 was recorded on a Beckman IR-4 instrument.

DISCUSSION

While our principle purpose here is to contrast the spectra of LiOH and LiOD, we also hope to show that there is great and essential similarity between the spectra of these substances and those of $Mg(OH)_2$[3] and $Ca(OH)_2$.[14] In order to understand better the possible differences in the spectra of all of these materials, it is of value to contrast both their structures and the form of the normal coordinates of their possible lattice modes. The procedures of constructing the latter make use of well-known techniques[15] and have been amply illustrated by others. The contrasting structures

[14] H. W. Morgan and W. R. Busing, J. Chem. Phys. **28,** 998 (1958).

[15] D. F. Hornig, J. Chem. Phys. **16,** 1063 (1948).

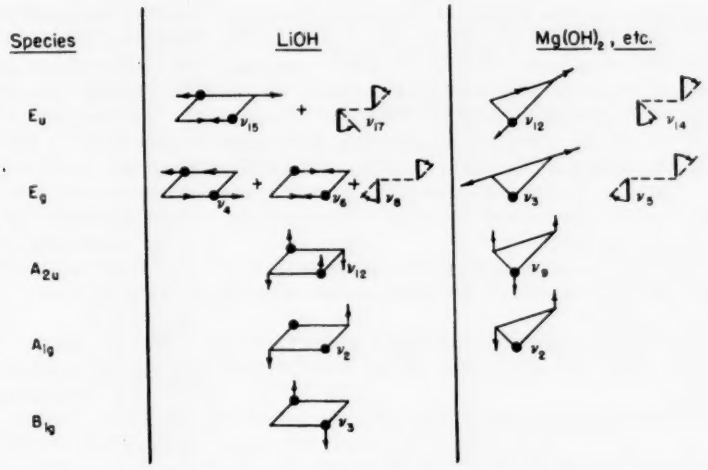

FIG. 9. Form of normal coordinates of LiOH and $Mg(OH)_2$, etc.

are shown in Fig. 1. In Fig. 9, the lattice modes are indicated by the form of the unit cell modes; in each case it suffices to illustrate these with a figure possessing as many formula units as there are in the primitive unit cell. The figure used, however, is not a primitive unit cell, but has a sufficient number of the elements of symmetry of that cell to serve the present purpose. In degenerate species only one member of each degenerate pair is illustrated.

Figure 1 emphasizes at least two important differences in the two structures. These differences are simply in the populations of the unit cells, essentially related to the difference in stoichiometry, and in the coordination numbers of the hydroxide ions. In one case [$Mg(OH)_2$, $Ca(OH)_2$] the hydroxide ions are located at sites of symmetry C_{3v} and in the other (LiOH) the site symmetry with respect to OH^- is C_{4v}. Thus, in the alkaline-earth hydroxide the anions sit atop trigonal pyramids, while in LiOH the OH^- ion is at the pinnacle of a tetragonal pyramid.

The consequences of the first of these differences are manifested in Fig. 9. In this figure we have identified the lattice modes of LiOH using Wickersheim's numbering system. The lattice modes of $Mg(OH)_2$ are numbered in a consistent manner.

As the vibrational species are identical, so will be the selection rules. Nevertheless, it is to be noted that if this procedure is valid, because of the differences in the masses of Mg, Ca, and Li, and because of the differences in charges and geometry, it would be considerably accidental to find near coincidences in the spectra of LiOH and, say, $Mg(OH)_2$. Furthermore, because of the difference in the number of lattice modes of species E_g there should be, according to this approach, one fewer fundamental active in $Mg(OH)_2$, in additive and subtractive combination.

Finally, Fig. 9 enables us to make the prediction that of all the absorption bands of LiOH, only those involving ν_2, ν_8, and ν_{17} will be simply affected by deuterium substitution. As the first of these has the character of translation and the last two of rotation, the frequency ratios of each type with the new frequency produced by deuterium substitution should be approximately $(17/18)^{\frac{1}{2}}$ and $(9/17)^{\frac{1}{2}}$, respectively. These are sufficiently different to provide a basis for assignment. [The internal modes' frequency ratio ν_{OH}/ν_{OD} will also be given by $(9/17)^{\frac{1}{2}}$.] If there is considerable mode-mixing within any species, few of these numbers will have any validity. Because of the great difference between the frequencies of the internal and lattice modes, the last frequency ratio will probably not be changed. Finally, deuterium substitution may well affect the frequencies of all the remaining lattice modes (except the inactive ν_{2_1}) but in no simple manner.

The spectrum of the monocrystalline solid solution will not be easy to predict, from this point of view. If, as we believe, the solution is approximately 1:1, each unit cell should then be populated with an average of one OH^- ion and one OD^- ion. To a first approximation, the degeneracies of ν_4, ν_6, ν_8, ν_{15}, and ν_{17} should be removed, with the greatest effects concentrated in ν_8 and ν_{17}. Nevertheless, this is a poor approximation, and we should rather recognize that such gross substitution constitutes a severe rendering of the translation group of the crystal, with broadened bands as a consequence. Where removal of degeneracy does result in the appearance of new bands, these two will be broad.

We now summarize the results of Figs. 3–6, together with a comparison of the results of spectra of $Mg(OH)_2$ and $Ca(OH)_2$, in order to judge the outcome of the contrasts anticipated above, all of which were based upon the predictions of the factor group, i.e., upon the assumption of extensive coupling of the motions of all the ions throughout the crystal.

This summary is best appreciated by inspection of Fig. 2. In this figure, the frequencies of the most in-

tense bands of the spectra of $Mg(OH)_2$, $Ca(OH)_2$, LiOH, and LiOD are plotted to the same scale. We have also incluced a "calculated" LiOD spectrum, obtained from the observed LiOH spectrum by the simple application of the $\rho=(9/17)^{\frac{1}{2}}$ rule throughout.

Perusal of Fig. 2 leads to the following conclusions about the spectra of $Mg(OH)_2$, $Ca(OH)_2$, and LiOH):

1. There are near coincidences in these spectra even with changes in mass and charge of cation, stoichiometry, and geometry.

2. Taking into account similarities in disposition of bands, there are apparently the same number of bands in each spectrum.

Comparison of those parts of Fig. 2 which have to do with LiOH and LiOD leads to the following conclusions:

All frequencies are shifted approximately according to the $\rho=(9/17)^{\frac{1}{2}}$ rule. Mitra[16] has found the same result using powdered $Mg(OD)_2$. Therefore, the motions giving rise to these spectra have only to do with OH ions.

The final point of summary may be gained by inspection of Figs. 4, 7, and 8. In the solid solution there are no new bands; indeed, the spectra are hardly displaced from their positions in the pure compounds, and they are not broadened. Indeed, OH^- and OD^- seem to undergo all their motions without knowledge of each other's presence.

Thus the basic point of the factor group approach cannot be assumed in further discussions of the motions of OH^- in these substances. We must, rather, concentrate on the localized character of the motions of OH^-.

It has been suggested[1] that these spectra may originate in the restricted rotation of the OH^- ion in the external field imposed by the remainder of the crystalline lattice. We shall now contrast the predictions of this model with the interpretations of the spectrum of LiOH, as derived from the factor group selection rules.

It is first necessary to point out that there are few differences between the spectra reported here and that reported by Wickersheim which are not accounted for by reason of differences in resolution or calibration accuracy (discussed previously). There is little question of the reality of the weak band at $\sim$3630 cm^{-1}. Analogous bands are found in the spectra of both $Mg(OH)_2$ and $Ca(OH)_2$. The sharp line at $\sim$3350 cm^{-1} has earlier been ascribed to part of a reflection maximum, only slightly shifted and modified in shape upon dilution in LiOD. We believe this reflection maximum is associated with the OH internal funamental, in the manner discussed by Haas and Hornig.[17] The high-frequency side of the reflection band associated with this fundamental is located closest to the absorption maximum.[16] The internal OH fundamental has an extremely large absorption coefficient, some 300 times that of the other bands in the spectrum.[18] The low-frequency side of a reflection band is separated from its high-frequency side by an amount proportional to the quantity $(\partial\mu/\partial Q)^2$, which in turn is proportional to the absorption coefficient. It is therefore to be expected that a reflection maximum may be found at frequency much lower than that of the absorption maximum of an intense transition. It would take only a slight diminution in $\partial\mu/\partial Q$ or more probably, in the index of refraction or even the number of absorbers (see Haas and Hornig[17]) to cause the shift in this reflection maximum caused by the deuterium substitution (Fig. 8).

We next discuss the effect of temperature on these spectra. Wickersheim notes that the fifth band *above* the OH fundamental increased in intensity with increasing temperature. In the study of $Ca(OH)_2$ by Morgan and Busing[14] one of the outstanding observations was the decrease in intensity of a high-frequency "combination" (3720 cm^{-1}) upon lowering the temperature from 20°C to −196°C. Similar behavior of a band of $Mg(OH)_2$ (3788 cm^{-1}) was reported by Mara.[3] Such thermal behavior is characteristic of an "upper-stage" band; to account for such in terms of the "internal-vibration coupled with lattice-vibrations" model used by Wickersheim, the lattice modes must be endowed with rather unusual anharmonicities. As has been pointed out previously,[1] "upper-stage" bands may be easily rationalized by the "rotational" model. Indeed, they may even serve as starting points in the "rotational" analysis.

In making his assignments of the low-frequency fundamentals Wickersheim uses, for the most part, the "difference bands." There seems to be no reason for choosing these over the "summation bands." Indeed, Wickersheim comments on the "strong symmetry" of his spectrum about the OH stretching fundamental. In Table I we contrast the extent of symmetry among the more intense bands, using his assignments and the frequencies obtained in both studies. Examination of this table leads to the conclusion that whatever symmetry there was using Wickersheim's calibration is diminished in using ours. If the lattice-frequency model is used, there is reason to expect extensive symmetry; the effects of anharmonicity ought to be the same on both summation and difference bands. The rotational model has no such requirement.

In addition to the $V=V_0(1-\cos 2\theta)$ potential we have proposed that for the field in which the rotating OH^- ions move,[1] there should be added a feature which reflects the threefold symmetry of $V(\phi)$ in $Mg(OH)_2$ and its four-fold symmetry in LiOH. Mitra[16] has initiated such considerations, but they are incomplete. We can, however, come to the conclusion that there should be few differences in the spectra as a result of the different "folded-ness" of these fields. As

[16] S. S. Mitra, dissertation, University of Michigan, Ann Arbor, Michigan (1957).

[17] C. Haas and D. F. Hornig, J. Chem. Phys. **26,** 707 (1957).

[18] H. A. Benesi, J. Chem. Phys. **30,** 852 (1959).

indicated in our earlier article,[1] each level of the restricted rotator is denoted by two quantum numbers, n and m, where $m=0, \pm1, \pm2, \cdots \pm n$. Each level with $m \neq 0$ is doubly degenerate in the azimuthal field $V(\phi)=0$. If $V(\phi)$ is finite and has symmetry C_{3v}, these degeneracies are respectively removed for the levels $m=3, 5\cdots$, while if the field has symmetry C_{4v}, these degeneracies are removed for $m=2, 4\cdots$. Nevertheless, upon comparing the possible transitions in the two manifolds, according to the selection rules $\Delta n=0, \pm2, \pm4, \pm6\cdots$; $\Delta m=0$ and $\Delta n=\pm1, \pm3, \pm5, \cdots$; $\Delta m=\pm1$, we find that the ultimate multiplicities of the transitions are identical for the two point groups. The similarity of the spectra of LiOH and of $Mg(OH)_2$ and $Ca(OH)_2$ is completely consistent with this finding.

In summary, taking into account the temperature dependence and asymmetry of the spectra of all of these substances, together with the apparent identity of multiplicities found in the spectra, we find them more compatible with the "rotational" model than with the "lattice-vibration" model. The latter model fails to account for the similarities among the spectra of LiOH, $Mg(OH)_2$, and $Ca(OH)_2$; the fact that the deuterium isotope effect is simple and affects all of the spectrum; and the fact that partial deuterium substitution does not in any way change either the LiOH or LiOD spectra. These observations have all been well rationalized on the basis of the highly localized "rotational" model.

TABLE I.

	Wickersheim's study		Present investigation	
	From "summation bands"	From "difference bands"	From "summation bands"	From "difference bands"
ν_6	125±3	143±4	125±1	143±1
ν_{17}	286±7	291±6	286±1	314±1
ν_8	320±4	343±6	307±2	388±1
ν_{15}	420±4	419±4	394±3	427±2

ACKNOWLEDGMENTS

The author wishes to express his thanks to Dr. Herman R. Leider for a small supply of LiD from which the LiOD was prepared and to Dr. Wartan A. Jemian for help in growing the LiOD crystal. Preliminary results were obtained while the author was a visitor at the Lawrence Radiation Laboratories, University of California, Livermore, California. The hospitality of the staff of those laboratories is gratefully acknowledged.

Evidence of Multiple Trapping Sites for Excited Nitrogen Atoms in Solid Molecular Nitrogen

R. A. HEMSTREET AND J. R. HAMILTON

Research Laboratory, Linde Company, Division of Union Carbide Corporation, Tonawanda, New York

(Received August 8, 1960)

A study of glow curves and thermal effects indicates that both ground state and excited nitrogen atoms are trapped in discharged nitrogen condensed at 4.2°K. At elevated temperatures the recombination of ground state atoms is apparently governed by a single activation energy. The excited atoms are found in two types of traps; one associated with the ordered and the other with the disordered regions in the matrix and each has a distribution of energies.

A NUMBER of publications have reported the properties of nitrogen atoms trapped in solid molecular nitrogen at low temperatures. Spectroscopic studies[1–7] indicate that the prominent features of the condensation and subsequent warm-up glows are due to the $^2D-^4S$ and $^2P-^2D$ atomic nitrogen transitions and the $^1S-^1D$ system of atomic oxygen present as an impurity. Weaker features are attributed to the $^2P-^4S$ atomic nitrogen transition and radiation from excited molecular states. Electron spin resonance studies[8–13] demonstrate the presence of ground state nitrogen atoms in condensed nitrogen discharge products. Fontana[14] has measured a minimum nitrogen atom concentration of 0.03% and states that the initiation of atom recombination occurs at 9°K and that the upper limit of atom stabilization is the molecular nitrogen transition temperature of 35°–36°K. Fontana suggests that, if the recombination of atoms is diffusion controlled, the process has an unusual temperature dependence.

The occurrence of bright glows is the most spectacular aspect of the trapped nitrogen atom system, but there does not appear to be any satisfactory explanation of the origin of the excited states causing these glows. In many publications it has been tacitly assumed that the glow and atom recombination are related. It is evident that either excited atoms are trapped in the molecular nitrogen matrix and become free to radiate at elevated temperatures, or the excited atoms are formed during the process of recombination of ground state atoms. The latter explanation has been expressed by Edwards.[15] Experimental support of either mechanism is weak.

The present work is a study of the temperature dependence of the glow caused by trapped nitrogen atoms and was undertaken to determine which of the afore-mentioned mechanisms is the more likely to be correct. The specific glow frequencies studied were the $\alpha(^2D-^4S)$ of atomic nitrogen at 5229 A and the $\beta(^1S-^1D)$ of atomic oxygen at 5549 A.

EXPERIMENTAL METHOD

The technique of dissociating gaseous nitrogen and condensing the discharge products is similar to that used by Broida[1] and Fontana.[14] A 10 Mc discharge is used instead of the 2450-Mc cavity. Power is supplied from a Westinghouse Industrial R.F. Generator having a maximum output of 1 kw. The electrodes are metal straps around a Pyrex tube. Nitrogen flows from a vessel of calibrated volume, through the discharge tube, directly to the condensation surface. The flow rate is varied with a needle valve. Flow rates are reported in terms of the number of moles of N_2 per minute deposited in the low-temperature cell. The total mass of nitrogen deposited varied between 0.01 and 0.03 mole.

A single cylinder of nitrogen was used for all the work reported here. Analysis showed the following impurities: 21 ppm H_2O, <7 ppm H_2, <1 ppm hydrocarbons, <1 ppm CO_2, <1 ppm O_2.

Because of radiation losses, it is not possible to specify the electrical power delivered to the discharge tube. However, all discharges were run at the same value of the plate current of the generator. The power output was approximately 100 w.

Figure 1 is a diagram of the low-temperature cell. The Dewars have been omitted. Basically, the apparatus consists of a copper cup sealed at the end of a

[1] A. M. Bass and H. P. Broida, Phys. Rev. **101**, 1740 (1956).
[2] H. P. Broida and M. Peyron, J. phys. radium **19**, 480 (1958).
[3] M. Peyron, E. Hörl, H. W. Brown, and H. P. Broida, J. Chem. Phys. **30**, 1304 (1959).
[4] H. P. Broida and M. Peyron, J. phys. radium **18**, 593 (1957).
[5] C. M. Herzfeld, Phys. Rev. **107**, 1239 (1957).
[6] C. M. Herzfeld and H. P. Broida, Phys. Rev. **101**, 606 (1956).
[7] E. Hörl, J. Mol. Spectroscopy **3**, 425 (1959).
[8] T. Cole, J. T. Harding, J. R. Pellam, and D. M. Yost, J. Chem. Phys. **27**, 593 (1957).
[9] S. N. Foner, C. K. Jen, E. L. Cochran, and V. A. Bowers, J. Chem. Phys. **28**, 351 (1958).
[10] C. K. Jen, S. N. Foner, E. L. Cochran, and V. A. Bowers, Phys. Rev. **112**, 1169 (1958).
[11] T. Cole and H. M. McConnell, J. Chem. Phys. **29**, 451 (1958).
[12] L. A. Wall, D. W. Brown, and R. E. Florin, J. Chem. Phys. **30**, 602 (1959).
[13] L. A. Wall, D. W. Brown, and R. E. Florin, J. Phys. Chem. **63**, 1762 (1959).
[14] B. J. Fontana, J. Appl. Phys. **29**, 1668 (1958).
[15] J. W. Edwards in *Formation and Trapping of Free Radicals*, edited by A. M. Bass and H. P. Broida (Academic Press, Inc., New York, 1960).

glass tube which extends up and out of the top of the cryostat. A Housekeeper seal is used to bond the copper to the glass. The discharge products are brought in through a central glass tube which may be heated electrically.

The copper cup is 40 mm long, 20 mm in diameter, and has a wall thickness of 0.25 mm. The mass of the copper is 11 g exclusive of thermometers and heater. Two thermometers are used to cover the range of 1.2° to 90°K. A copper resistance thermometer (No. 40 AWG) is close wound in a double layer over the outside of the cup, exclusive of the bottom, and has a room temperature resistance of 150 ohms. It is used in the range of 20° to 90°K. The windings are cemented in place with a thin film of 9574 General Electric clear baking varnish. A 100 ohm, ½ w Ohmite carbon resistor is used in the 1.2° to 20°K range. The ceramic insulation was ground off and the resistor was sealed in a thin, close fitting copper sheath with baking varnish. This unit was soldered with Woods metal into a hole running through the base of the cup. Each thermometer is equipped with four leads; two for current and two for voltage measurements.

A 100-ohm manganin heater is wound around the outside wall of the cup over the copper thermometer. The windings are spaced to cover the entire wall and still permit the refrigerant to directly contact the underlying copper. All electrical leads (No. 40 AWG copper) are spiralled along the outside surface of the glass tube supporting the copper cup and are cemented in place with baking varnish.

A gold plated copper radiation shield surrounds the copper cup and is extended to the bottom of the Dewar by means of a ¼ in. diameter copper post. In this manner the shield is held at the refrigerant temperature as long as any liquid remains in the cryostat. The shield has a single hole in the bottom and a ring of holes around the top to permit circulation of refrigerant and also to allow escape of gas formed during a condensation. A gold-cobalt vs copper[16] thermocouple is attached to the base of the shield. All condensations were carried out at the normal boiling point of helium.

The copper thermometer was calibrated at the boiling point of hydrogen[17] and the argon triple point[18] using the data of Dauphinee and Preston-Thomas.[19] The copper thermometer is believed to have an accuracy of ±0.05°K.

The copper resistance was recorded directly on a Leeds and Northrup, 60 000 Series, Recorder having a range of 0 to 100 ohms. The carbon thermometer was calibrated at the boiling points of hydrogen[17] and helium[20] and the hydrogen triple point.[17] Liquid hydrogen having a para content of 95% or higher was used. Calibration of the carbon thermometer was repeated each time after the apparatus was warmed to room temperature. The following equation, taken from Clement and Quinnell,[21] was used to relate resistance and temperature

$$\log R + K/\log R = A + B/T. \quad (1)$$

A constant measuring current of 7.5 μa was used and voltages across the thermometer were measured with a Rubicon B potentiometer, or recorded directly on a Leeds and Northrup Adjustable Range Recorder. Typical values of the constants in Eq. (1) are $A=3.687$, $B=2.931$, and $K=3.343$. Temperature measurements with the carbon thermometer are accurate to at least ±0.05°K under static conditions and ±0.1°K under conditions where the temperature is slowly varying (<1°K/min) subject to the validity of Eq. (1).

A direct light path exists from the surface of the condensed nitrogen, up the inlet tube, and through a quartz window. Intensity measurements were made with a 931-A phototube or, when a particular wavelength was desired, the phototube was replaced by a mirror which reflected the light onto the slit of a

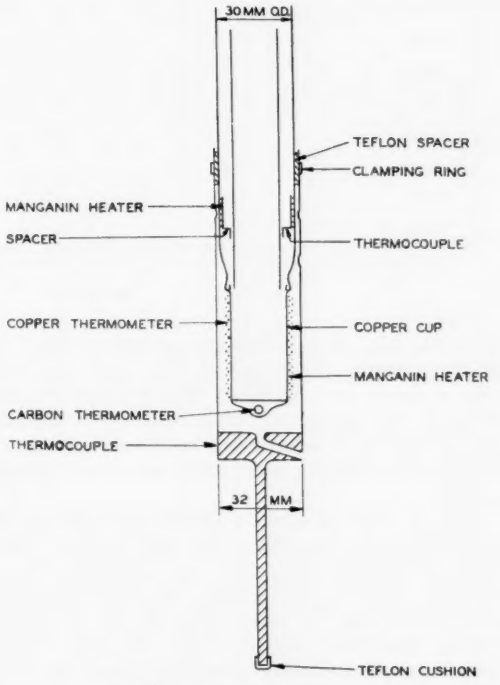

FIG. 1. Diagram of the low-temperature cell.

[16] N. Fuschillo, J. Phys. Chem. **61**, 644 (1957).
[17] C. T. Linder, Westinghouse Research Laboratories, Research Rept. R-94433-2-A (1950).
[18] A. Michels, T. Wassenaar, Th. Sluyters, and W. de Graaff, Physica **23**, 89 (1951).
[19] T. M. Daughinee and H. Preston-Thomas, Rev. Sci. Instr. **25**, 884 (1954).
[20] H. Van Dijk and M. Durieux, Physica **24**, 1 (1958).
[21] J. R. Clement and E. H. Quinnell, Rev. Sci. Instr. **23**, 219 (1952).

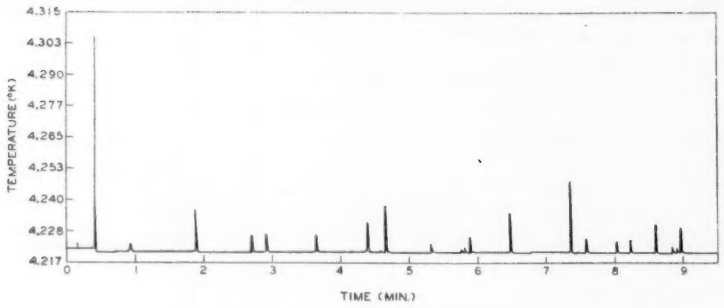

FIG. 2. Thermal releases (spikes) during the deposition of undischarged nitrogen. Only a portion of the deposition is shown. 0.00008 mole/min deposition rate.

Jarrel-Ash Ebert Spectrometer using either a 931-A or IP–21 phototube. Phototube outputs were amplified with a Leeds and Northrup 9836-A amplifier and recorded. The phototube voltage was 810 v. Intensities are reported in arbitrary units. However, a unit of 1 is equivalent to a current of 0.01 μa phototube output current.

Prior to condensation, approximately 200 cc of liquid helium are introduced into the cryostat. This leaves the cup and shield immersed in 6 inches of refrigerant. After the condensation, the liquid helium is pumped, reducing the temperature to 1.2° to 1.3°K, and the liquid level gradually drops. When the liquid level is at the bottom of the shield, about 60 cc of helium remain, and the apparatus may be manipulated in two ways. In each case the helium pumping is continuous. The cup may be heated electrically to any desired temperature and held there by balancing the heat input against the loss to the bath. Any temperature between 3.5° and 30°K may be held constant as long as the helium bath lasts. Temperature control is manual and the heater current is varied so as to keep the voltage across the carbon thermometer constant. Any temperature between 3.5° and 30°K may be reached and stabilized within one minute after heating commences. The duration of constant temperature is approximately $1\frac{1}{2}$ hr at 15°K and 20 min at 25°K. Below 20°K temperature fluctuations during a run can be kept within ± 0.005°K calculated from the galvanometer deflections using Eq. (1). Above 20°K the fluctuations increase, but in no case do they exceed ± 0.05°K.

A continuous warmup is carried out by increasing the heater current linearly with time after the helium level has dropped to the base of the shield. This gives a warming rate in which the temperature increases nearly linearly with time. The operation may be done manually or by means of a variable speed motor drive. At any temperature the system may be quenched by bubbling helium gas through the liquid helium causing a sudden evolution of cold gas which cools the cup from temperatures as high as 30° down to 5°K within 30 to 45 sec.

The term "discharged" refers to nitrogen condensed after dissociation in the electric discharge. "Ordinary" nitrogen refers to nitrogen that was not passed through the discharge prior to condensation.

EXPERIMENTAL RESULTS

Deposition and Warmup of Ordinary Nitrogen

During the slow deposition of ordinary nitrogen frequent heat releases are sensed by the carbon thermometer, but when the deposition rate is rapid, these heat releases are not observed. Figure 2 demonstrates the heat releases during a slow deposition. Because the low-temperature cell and thermometer are in direct contact with the refrigerant, the indicated temperatures and temperature rises are much lower than the actual temperatures of the solid nitrogen. Fontana[14] has shown that the solid temperature may be as high as 20°K depending on the flow rate. However, the terms "fast" and "slow" deposition rates are relative and care must be used when comparing results obtained with other apparatus since the surface temperature of the solid will not only depend on the gas temperature and flow rates, but also on the condensing area, thickness, and thermal conductivity of the condensing surface.

The heat releases suggest that there are frequent changes in the structure of the solid nitrogen during a slow (low-temperature) deposition. It is not known whether this process is localized in the deposit.

Figure 3 shows a series of warming curves of condensed nitrogen. An exothermal process occurs between 15° and 17°K in slowly deposited nitrogen, but is absent or undetected in rapidly deposited samples. The heat release is estimated to be approximately 3 cal/mole and does not appear to be strongly dependent on the deposition rate as long as it is less than about 0.005 mole/min. The mass of the copper cup, but not the thermometers or heater, has been entered into the calculations of all heat releases. The copper heat capacity was taken from Kelly[22] and the nitrogen heat capacity from Giauque and Clayton.[23] The calculated heat releases are low because the principal errors are

[22] K. K. Kelly, Bulletin No. 477, U. S. Dept. of the Interior, Bureau of Mines, 1948 (Revised 1950).

[23] W. F. Giauque and J. O. Clayton, J. Am. Chem. Soc. **55**, 4875 (1933).

unmeasured heat losses, i.e., to the helium bath and glass supports of the cup.

The 15°K heat release is reproducible in slowly deposited samples and probably is an annealing process. The fact that the annealing process is not observed in rapidly deposited nitrogen is consistent with the absence of thermal pulses during rapid deposition. However, it has not been established whether the exothermal processes at 15°K and during deposition are of the same type. Very likely they are not. The 15°K event occurs rather slowly while the heat releases during deposition appear to occur suddenly. Perhaps the deposition process is a localized change from amorphous to short range order and the 15°K process is a change from short to long range order; e.g., a sintering of small crystals. At sufficiently high deposition rates these ordering processes do not occur because the surface temperature is high enough to permit sufficient diffusion to form a well ordered solid. These results are to be contrasted with x-ray studies[24] which indicate that "nitrogen deposited at 20°K shows more disorder than that deposited at 4.2°K and subsequently annealed at 13°K."

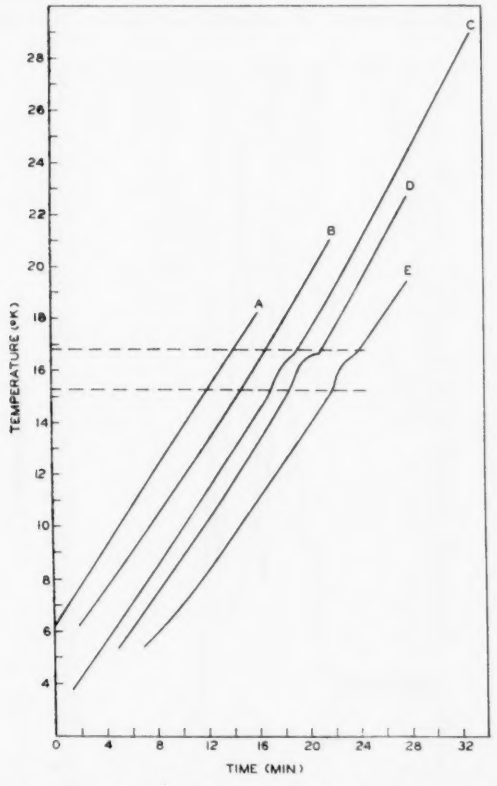

FIG. 3. Warming curves of solid undischarged nitrogen. The deposition rates are: A—0.0177 mole/min, B—empty cell, C—0.00547 mole/min, D—0.00167 mole/min, E—0.00296 mole/min.

[24] L. H. Bolz, M. E. Boyd, F. A. Mauer, and H. S. Peiser, Acta Cryst. **12**, 247 (1959).

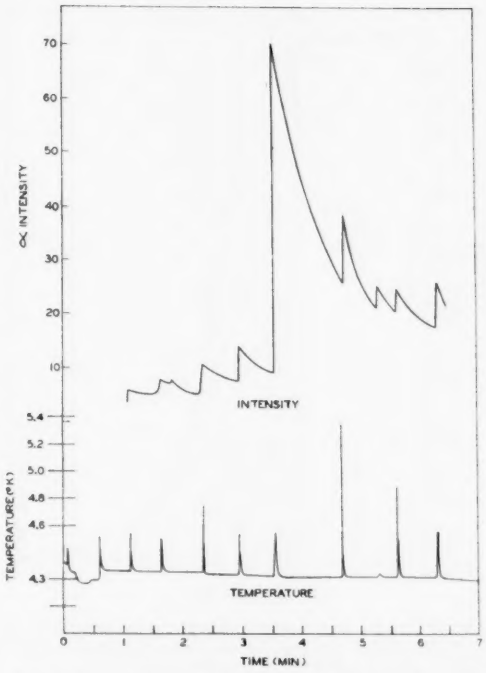

FIG. 4. Temperature and α intensity during deposition of discharged nitrogen. The zero on the intensity scale is arbitrary. 0.003 mole/min deposition rate.

Sometimes, after the termination of the deposition, an additional thermal spike is observed when the helium bath pumps are started. Vibration from the pumps probably initiates the process. Also, it may be initiated by illuminating the nitrogen with a light although the light alone is not sufficient to cause the observed temperature rise. In general, this "after spike" is most likely to be observed if there has been no thermal spike immediately prior to the termination of the deposition and likely the effect is due to ordering initiated by shock or a slight temperature rise caused by illumination.

Deposition and Very Low Temperature Activity of Discharged Nitrogen

The deposition of discharged nitrogen at 4.2°K is accompanied by a strong green glow and frequent bright yellow flashes. This process has been described by Fontana,[25] who states that the flashes consist of simultaneous increases in the β and B-band intensity and decrease in the α intensity. Sudden increases in temperature and decrease in magnetic susceptibility also accompany these flashes. The thermal observations are confirmed as is the behavior of the β and B

[25] B. J. Fontana, J. Chem. Phys. **31**, 148 (1959).

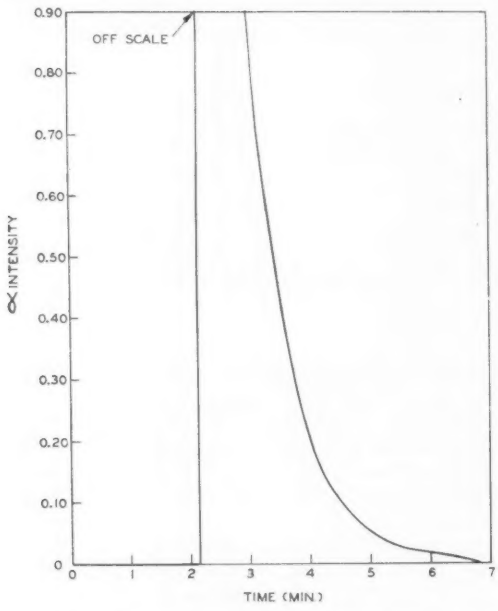

FIG. 5. Very low temperature activity in solid discharged nitrogen. This activity occurred 83 min after termination of the deposition and reduction of the temperature to 1.3°K.

frequencies, but in the work reported here, the α intensity always increases. Figure 4 shows the temperature during a discharged nitrogen deposition with the α intensity recorded simultaneously. Each thermal spike is accompanied by an increase in the α intensity which decays exponentially. The half-life of the decay is 30.4 sec.

No correlation exists between the magnitude of the α intensity and temperature spikes because the process is known from visual observations to be localized in the deposit. The thermal effects are very similar to those observed during the deposition of ordinary nitrogen, but the magnitude and frequency is greater in the case of discharged nitrogen.

Following deposition the α intensity decays exponentially with a half-life of 31 sec. This number is an average of five runs. This half-life is not affected by rapid cooling to 1.2°K during the decay.

One final phenomenon associated with the deposition should be noted. Before a nitrogen sample can be warmed, the liquid helium level must be pumped down to the base of the shield. This requires about 2 to 4 hr, during which time the temperature of the solid nitrogen is 1.2° to 1.3°K. During this period occasional activity has been observed in the form of sudden initiation of the glow. This has been observed six times out of seventy and does not appear to be simply related to conditions of discharge, flow rate, or quantity of nitrogen deposited. In some cases the process has occurred an hour after the temperature was reduced, so there is no question about the solid still being "hot." Figure 5 shows a record of one such occurrence. The decay is exponential with a half-life of 29.8 sec. We have been unable to determine whether this phenomenon is localized and no thermal effects have been observed. However, the high thermal conductivity of the super-fluid helium may account for the absence of measurable thermal effects. Because the phenomenon is rare, only the α intensity has been successfully recorded. The initiation of this post-deposition "flash" is probably related to the same ordering phenomena observed after the deposition of ordinary nitrogen initiated by shock or illumination.

Warmup of Condensed Discharged Nitrogen

Figure 6 shows the α-glow intensity and temperature during controlled warming of solid discharged nitrogen. Although not shown on Fig. 6, the first traces of glow are detected at 4.5° to 4.7°K. The onset of glow activity is not accompanied by any sudden heat release and the intensity increases smoothly as the temperature is raised. The most interesting aspects of the glow curve are the occurrence of a shoulder at 14° to 15°K and

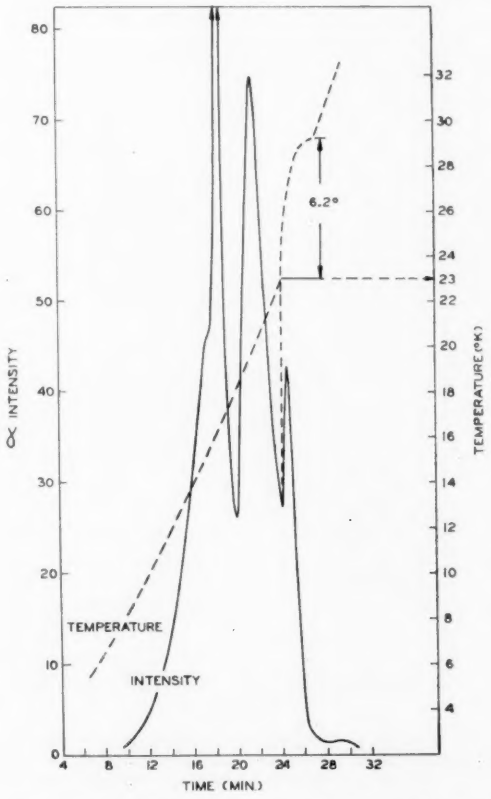

FIG. 6. α intensity and temperature during controlled warming of solid discharged nitrogen. 0.0043 mole/min deposition rate.

two maxima, one at 16°K and the other at 19.7° to 20°K. Following the 20°K glow maximum there is a sudden heat release at 23°K. The heat release is accompanied by a momentary increase in glow activity. This heat release does not occur in ordinary nitrogen. Figure 6 is replotted in Fig. 7 as intensity vs temperature.

The features in the glow curve are reproducible, but the heat release does not always occur at the same temperature. It may occur anywhere between 14° and 23°K, although, under the condition of discharge and flow rate used, it is usually found between 20° and 21°K following the second maximum in the glow curve. Figure 8 shows a case where the heat release occurred at 18.2°K.

If the deposition rate is rapid, the glow curve is markedly changed, as shown in Fig. 9. The 14°–15°K shoulder and 16°K maximum are missing, while the 20°K maximum is still observed. In this case the heat release occurred at 20.5°K. The low-temperature (<17°K) glow features are obviously dependent on the deposition rate and occur under conditions where the annealing process is observed in ordinary nitrogen. The 16°K glow peak covers exactly the same temperature range as the annealing event and a slight temperature rise is measurable over this range when the discharged nitrogen is deposited slowly (see Fig. 8).

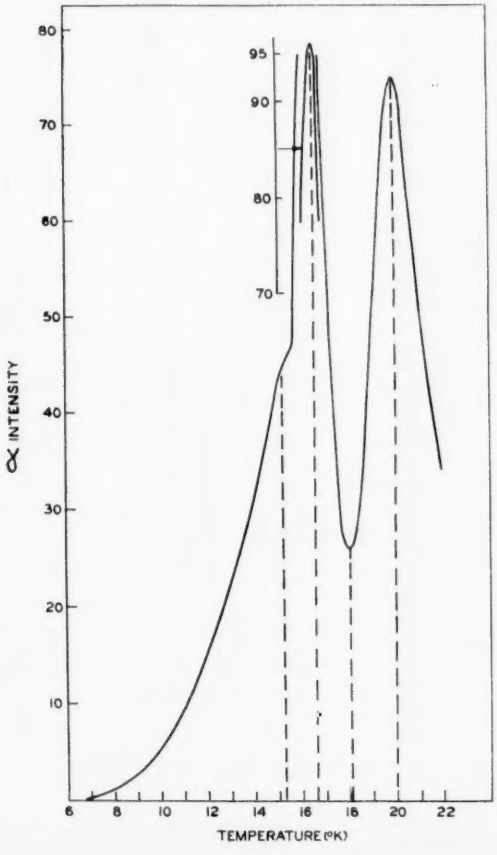

FIG. 7. α intensity as a function of temperature. Same data as Fig. 6.

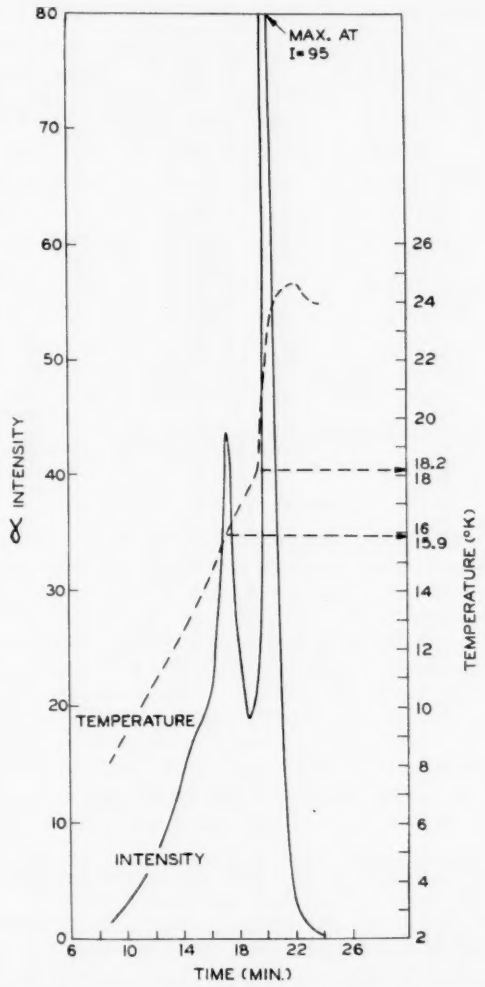

FIG. 8. α intensity and temperature during controlled warming of solid discharged nitrogen. 0.0012 mole/min deposition rate.

The fact that the heat releases appear abruptly is a characteristic of the experimental procedure. A heat release is observed when the rate of heat production exceeds the rate of loss to the liquid helium heat sink. If a discharged nitrogen sample is permitted to warm up without restraint (by complete removal of the refrigerant) no sudden heat release is observed. Comparison of discharged and undischarged nitrogen during unrestrained warming shows that the heat release becomes measurable at 5° to 6°K and proceeds

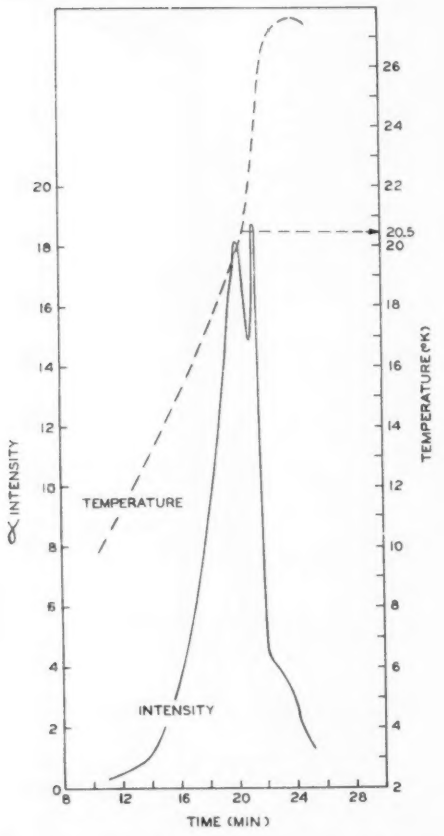

FIG. 9. α intensity and temperature during controlled warming of solid discharged nitrogen. 0.0366 mole/min deposition rate.

continuously as the temperature rises. With this in mind, we will continue to use the terms "initiation" of the heat release. This experimental situation is fortunate because it allows one to distinguish between the glow and heat producing processes. Although the heat releases here are relative to balances of heat fluxes, they do represent the major portion of the heat producing process.

The nitrogen deposit has been observed with a telescope during warming and there is no visual evidence of localized glow activity.

Although Figs. 6, 8, and 9 indicate termination of glow activity soon after the heat release, use of maximum phototube sensitivity shows the glow to persist to temperatures as high as 40°K. There is an abrupt intensity increase (α and β) at the molecular nitrogen transition temperature. The 35.85°K transition is observed in all runs on both discharged and undischarged nitrogen.

The behavior of the β intensity is similar to, but much weaker than the α intensity on warming. See Figs. 10 and 11. The B bands were detected on warming, but were too weak to determine their temperature dependence.

Figures 6 through 11 indicate that there are two types of traps for the glow process, one associated with the disordered regions in the nitrogen matrix and the other associated with ordered regions. It is also evident that the glow process is rather sensitive to structural changes in the solid. The 15°K annealing and 35.85°K phase change cause large increases in the glow activity.

Table I compares the heat release temperature, ΔH, the calculated nitrogen atom concentration, integrated α intensity, and flow (or deposition) rate. The dissociation energy of N_2 was taken as 225 kcal/mole.[26]

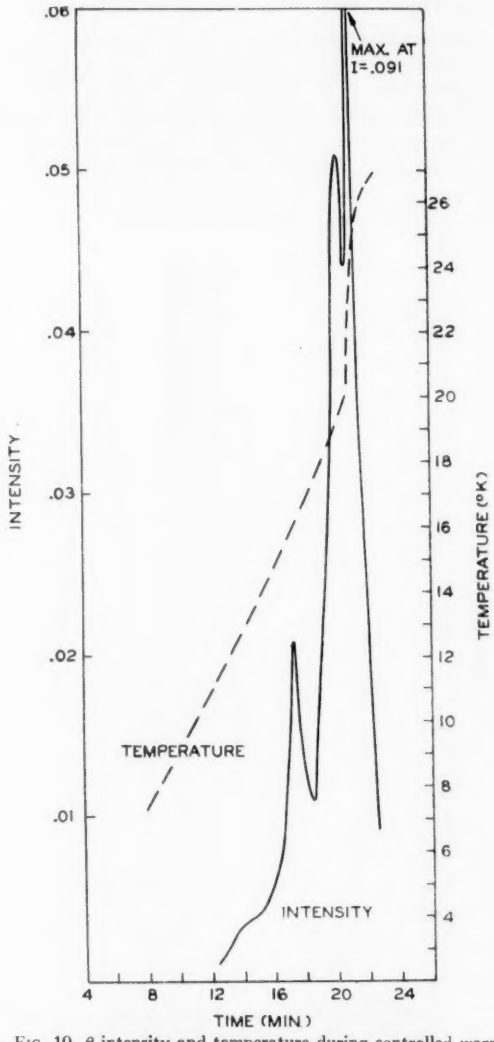

FIG. 10. β intensity and temperature during controlled warming of solid discharged nitrogen. 0.0026 mole/min deposition rate.

[26] D. C. Frost and C. A. McDowell, Proc. Roy. Soc. (London) **A236**, 278 (1956).

The nitrogen atom concentration was calculated on the assumption that the heat release results from the recombination of ground state atoms. Because these concentrations are based on measurements made during restrained warming, the values will be low compared to other published values, but they still are useful as relative measures. Concentrations calculated from unrestrained warming experiments indicate nitrogen atom concentrations of the order of magnitude of 0.1%. Assuming that the magnitude of the heat release is a proper measure of the ^4S nitrogen atom concentration and the integrated α intensity is a correct measure of the total number of radiating ^2D atoms, several generalizations can be made. Neither the concentration of ^4S atoms, nor the total number of radiating ^2D atoms is dependent on the deposition rate. However, it is apparent that, as the ^4S atom concentration increases, the total number of radiating ^2D atoms decreases. The lack of dependence of atom concentrations on deposition rate is surprising and probably indicates that the conditions of discharge are critical in determining trapped atom concentrations.

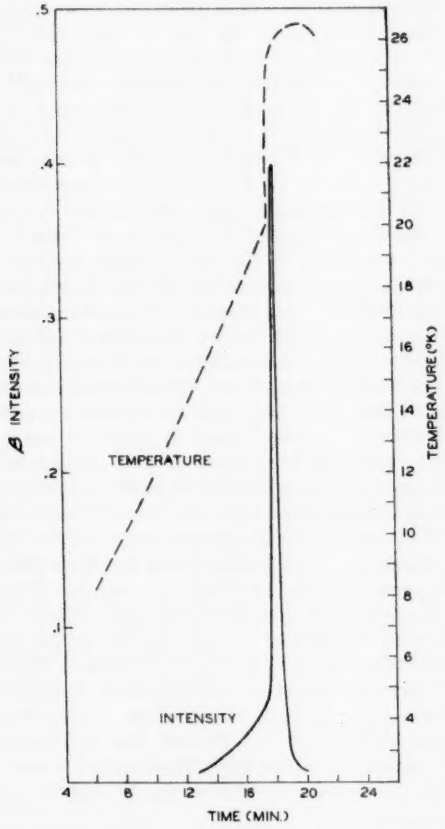

FIG. 11. β intensity and temperature during controlled warming of solid discharged nitrogen. 0.0138 mole/min deposition rate.

TABLE I. Comparison of ^4S atom concentrations and integrated α intensity.

T,°K[a]	ΔH[b]	%N	I[c]	*Deposition rate*[d]
14.5	87.5	0.0078	*ND*[e]	0.0064
17.6	117	0.010	631	0.0113
18.0	44.5	0.0039	3500	0.0198
18.2	40.7	0.0036	*ND*	0.0012
19.7	40.2	0.0036	*ND*	0.0026
20.2	32.3	0.0029	8850	0.0366
20.4	37.4	0.0033	8940	0.00234
23.0	27.2	0.0023	29,300	0.0043

[a] Temperature at which the heat release is initiated. See text.
[b] Cal/mole.
[c] Integrated α intensity per mole. Only data are included which were obtained with the same phototube under identical operating conditions.
[d] Mole/min.
[e] No data.

Several experiments were performed in which a discharged nitrogen sample was heated to temperatures of 14°, 20°, and 27°K and then quenched rapidly to 4°–6°K. In each case, upon quenching, the α intensity decayed exponentially with a half-life of 30–31 sec. Here it should be noted that the decay assumes an exponential form as soon as the temperature reduction is started. The rate at which the temperature is reduced does not affect the exponential form or the half-life. On reheating, the α glow reappeared at approximately the temperature from which the sample was quenched suggesting that a distribution of activation energies control the glow process.

Qualitative information about the activation energies of the process causing the heat release was obtained with interrupted warming experiments. The temperature of a discharged nitrogen sample was raised slowly until the heat release just begins, at which point the temperature is held constant for 15 to 20 min. If the temperature is raised after this period, no further heat release is detected. Thus, the process causing the heat release, when initiated, will go to completion. This should be contrasted with the behavior of the glow during an interrupted warming. At constant temperature the glow decays, but when the temperature is again increased, the glow intensity increases, frequently becoming as large or larger than before the interruption.

DISCUSSION

The experimental work gives several significant results with which any model for the origin of the glow in solid discharged nitrogen must be consistent, namely:

1. The maximum glow and thermal activity do not necessarily occur at the same temperature.

2. If the thermal and glow activity are attributed to ^4S and ^2D atoms respectively, then high concentrations

of ^4S atoms are associated with a small number of radiating ^2D atoms.

3. The activation energies of the thermal and glow processes are different in the sense that the thermal process behaves as though it is controlled by a single activation energy, while the glow process appears to be controlled by a distribution of energies.

4. Regardless of the nature of the cause of the initiation of the glow activity, the decay of the $^2D-^4S$ intensity is always the same following cessation of the stimulus. The decay is exponential with a half-life of approximately 30 sec. The half-life is independent of temperature.

There are two alternative explanations for the origin of the glow activity (origin of ^2D and ^2P nitrogen states). They are:

1. The ^2D and ^2P states are formed in the solid nitrogen during condensation and at elevated temperatures. They would be formed by the excitation of ^4S atoms.

2. The ^2D and ^2P states are formed in the discharge and become trapped in the solid nitrogen such that they are not free to radiate except at elevated temperatures.

If the first alternative is accepted, then an energy source for the excitation of ^4S atoms must be found. The only reasonable source is the recombination of ^4S atoms. This cannot result directly in excited atoms so a second step is necessary. The ^2D or ^2P atoms could be formed by an energy exchange between ^4S atoms and excited nitrogen molecules resulting from recombination. These steps are illustrated in Eqs. 2 through 6.

$$N(^4S)+N(^4S)\rightarrow N_2 \text{ (excited state)} \tag{2}$$

$$N(^4S)+N_2 \text{ (excited state)}\rightarrow N(^2P, \text{ or } ^2D)+N_2 \tag{3}$$

$$N(^2P)\rightarrow N(^2D)+h\nu(\delta) \tag{4}$$

$$N(^2P)\rightarrow N(^4S)+h\nu(\mu) \tag{5}$$

$$N(^2D)\rightarrow N(^4S)+h\nu(\alpha). \tag{6}$$

Part of the recombination energy is radiated while the remainder is transferred to the lattice as heat. The usual restrictions concerning collisions of the second kind apply, particularly the requirement that the excited molecules have a reasonably long lifetime.

This mechanism has been proposed by Edwards[15] and the authors.[27] However, such a mechanism seems very unlikely in view of the fact that thermal and glow processes do not necessarily coincide, and it is not obvious how the maximum glow activity can precede the process causing it (recombination of ^4S atoms). Even more significantly it is noted that the inverse relation between the ^4S and ^2D atom concentrations is completely inconsistent with the energy exchange mechanism.

The only reasonable way of preserving the energy exchange mechanism would be by assuming that the thermal effects are not caused by atom recombinations but by something like annealing of defects engendered by the presence of free atoms. Obviously, this situation would lower the free atom concentration estimates to an almost insignificant value and would be contrary to published thought on the subject. At present it is preferable to accept the thermal effects as representative of atom recombination and reject the exchange mechanism as causing the excited atomic states. This leads to the hypothesis that excited nitrogen atoms are trapped such that they are stable with respect to emission at sufficiently low temperatures.

Two assumptions will be made concerning the trapping of ground state and excited atoms. First, assume that the ^4S atoms are stable in a solid molecular nitrogen matrix only by inhibition of diffusion, and all the atoms have the same diffusion constant (same activation energy). At sufficiently low temperatures recombination is prevented because the diffusion constant is very small. As the temperature is raised the recombination rate will increase smoothly. In the type of experiments reported in this paper, recombination will become evident when the rate of heat production (taken as proportional to the reaction rate) exceeds the rate of heat transfer to the liquid helium heat sink. The temperature at which this occurs will depend on the initial atom concentration and the warming rate. If the warming rates are the same in a series of experiments (as was the case in Table I) the heat release temperature will decrease as the atom concentration increases. This picture is consistent with the data of Table I.

The explanation of the glow process involves the assumption that excited atoms (^2D and ^2P) originating in the discharge are trapped within the molecular nitrogen matrix. However, the inhibition of diffusion is not by itself sufficient to stabilize the ^2P and ^2D atoms, and the excited atoms are not stable for long periods by being at sites where their radiative lifetimes approach the lifetime in vacuum (about 20 hr for ^2D and 4 sec for ^2P). Storage of these solids for 10 to 20 hr at 4.2°K shows no measurable loss of ^2D atoms on warm-up, and it is unreasonable to expect sites which will extend the ^2P lifetime sufficiently long to be observable hours after deposition. The excited atoms would be trapped in the sense that they are held by some sort of weak complex with the molecular nitrogen matrix. This complex would have to be such that the excited atom is stable with respect to spontaneous emission. Milligan *et al.*[28] have postulated the existence of an N_3 radical to explain certain infrared observations. The triatomic nitrogen of Herzfeld[5] and Peyron[3] does not represent the complex postulated here. Their model is used to explain the emission spectra of the ^2P and ^2D states

[27] R. A. Hemstreet and J. R. Hamilton, Fourth International Symposium on Free Radical Stabilization, August 31–September 2, 1959, Washington, D. C.

[28] D. E. Milligan, H. W. Brown, and G. C. Pimentel, J. Chem. Phys. **25**, 1080 (1956).

and thus refers to a situation where the excited atoms are unstable.

It is impossible, from the results of this paper, to specify the nature of the traps causing stabilization of excited states, but the results do demonstrate that there are two types of traps. One of these is associated with the ordered and the other with the disordered regions in the nitrogen matrix. Each of these trap types probably has a distribution of energies which appears to be continuous within the experimental resolution. This means that at any given temperature, only a certain fraction of excited atoms are free to radiate while the remainder are stable for rather long periods of time. The possibility of multiple trapping sites for nitrogen atoms has been noted by Jen.[29]

The concept of a distribution of trapping energies for excited atoms is consistent with the observation that the ^4S and excited atom concentrations are inversely related. At any given temperature there are four reactions to consider. The first is the recombination of ^4S atoms which by postulate is only diffusion controlled.

$$N(^4S)+N(^4S)\rightarrow N_2. \quad (7)$$

Secondly, excited atoms will leave their traps and radiate

$$N(\text{trapped, excited})\rightarrow N(\text{free, excited})\rightarrow N(^4S)+h\nu. \quad (8)$$

The third and fourth reactions are recombinations between ^4S atoms and excited atoms, both trapped and free.

$$N(^4S)+N(\text{trapped, excited})\rightarrow N_2 \quad (9)$$

$$N(^4S)+N(\text{free, excited})\rightarrow N_2. \quad (10)$$

Reactions (9) and (10) will destroy excited atoms before they can radiate thus reducing the intensity. Thus, the higher the mobile ^4S atom concentration, the greater the probability that excited atoms will be destroyed before they are out of their traps and free to radiate. Equation (10) will be significant only if the excited state has a reasonably long lifetime.

Because the decay of the $^2D-^4S$ transition during a quench and following deposition is independent of temperature, the half-lite is representative of the free, radiating ^2D atom in the solid matrix. Since the quenched decays are not compound processes, i.e., simultaneous emission and retrapping of the ^2D atoms, once the ^2D atom is untrapped it remains that way. Thermal quenching does not retrap these atoms. This is contrary to the process whereby the atoms were trapped in the first place, i.e., rapid quenching in a very cold molecular nitrogen matrix. In order that the decay be unaffected by temperature changes (cooling from 4° to 1.2°K or from 14°, 20°, or 27°K to 5°K) it would be necessary to distinguish between two types of ^2D atoms; those which are trapped so they may not radiate, and those which are immobilized but still free to radiate. This situation could occur if there are only a few sites at which an excited atom is stabilized with respect to emission. At elevated temperatures ^2P and ^2D atoms would be ejected from their traps and be free to radiate. When the temperature is reduced, it will be impossible for all the excited atoms to return to their traps before they are immobilized by virtue of the reduction in their diffusion constant. Those excited atoms that do not get back to traps would continue radiating in spite of the thermal quench.

An alternative to the problem of two types of ^2D atoms may be made by assuming that only the ^2P atoms are trapped so as to be stable with respect to radiation and both the ^2D and ^4S atoms are subject only to diffusion laws. At a given temperature a portion of the ^2P atoms would leave their traps and very quickly become ^2D atoms by emission. Since the ^2D atoms may not be stabilized radiatively they decay to ^4S atoms and this decay would not be dependent on temperature. The other consideration of recombinations between excited and ground state atoms still apply.

The limited data on the β lines indicate that much the same considerations apply to the behavior of excited oxygen atoms. A detailed discussion of the oxygen atoms will not be attempted, but it should be noted that, from the positions of the maxima in the glow curves, the oxygen atoms are trapped very similarly to the nitrogen atoms.

ACKNOWLEDGMENTS

The authors would like to thank Dr. J. T. Mullhaupt, Dr. S. A. Stern, and Dr. C. J. Ultee for valuable discussions during the course of this work. We are particularly indebted to Dr. J. A. Krumhansl of Cornell University for his interest and constructive suggestions concerning the interpretation of the experimental results.

[29] C. K. Jen, in *Formation and Trapping of Free Radicals*, edited by A. M. Bass and H. P. Broida (Academic Press, Inc., New York, 1960).

Interaction of a Triplet and a Normal Helium Atom*

G. H. BRIGMAN

Convair, Forth Worth, Texas

AND

S. J. BRIENT AND F. A. MATSEN

Departments of Chemistry and Physics, The University of Texas, Austin, Texas

(Received August 15, 1960)

The electronic energy of the system He(^1S) and He(^3S) was calculated as a function of nuclear separation. This calculation differs from an earlier one by R. A. Buckingham and A. Dalgarno [Proc. Roy. Soc. (London) **A213**, 327 (1952)] in three ways: (1) the use of a nodeless $2s$ function, (2) the use of an open-configuration wavefunction ($1s1s'$) for He(^1S) and (3) the use of orbital exponents optimized for each internuclear distance. The energy obtained lies approximately one volt below the earlier calculation but confirms it in all qualitative aspects including the presence of a "hump" at $R \cong 4a_0$.

I. INTRODUCTION

THE potential energy curve between a normal helium atom and a triplet helium atom He(^3S, $1s2s$) has considerable influence on the "actual" half-life of the triplet helium atom. The triplet helium atom is doubly metastable ($\Delta L=0$, $\Delta S=1$) and its natural half-life has been estimated at 10^5 sec.[1] However, in any actual environment its half-life is much less than 10^5 sec as a result of other destructive processes. The destruction is due mainly to diffusion to the wall and to metastable compound formation, e.g., $He_2\,{}^3\Sigma(1s^2, 1s2s)$. These processes are governed in the main by the singlet helium-triplet helium interaction energy.

Several lines of evidence suggest that the potential energy curve between a normal and a triplet helium atom may have a hump in it.

(1) A hump in the closely related $He_2\,{}^1\Sigma(1s^21s2s)$ curve was postulated by Nickerson[2] in 1935 to account for a band with a sharp head lying 385 cm^{-1} to the blue of the forbidden 602 A ($1s2s \rightarrow 1s^2$) line in atomic helium.

(2) In 1952 Buckingham and Dalgarno[3] calculated the interaction energy for $He_2\,{}^1\Sigma_u$ and $He_2\,{}^3\Sigma_u$ and found humps of 0.26 and 0.29 ev, respectively, at $R=4a_0$. When van der Waals interaction was introduced these values were reduced to 0.146 and 0.178 ev, respectively, at $R=4.25a_0$.[4]

(3) Buckingham and Dalgarno calculated[5] the collision and diffusion cross sections from their potential curve for the ^3S atom in normal helium. In 1955 Phelps[6] obtained a value for the diffusion coefficient which was in substantial agreement with that calculated by Buckingham and Dalgarno. In 1957 Stebbings[7] measured the scattering cross section for triplet helium in normal helium and obtained a value which agreed with that calculated by Buckingham and Dalgarno.

(4) In 1953 Phelps and Molnar[8] observed a large temperature dependence in both the diffusion coefficient and in the three-body combination coefficient [$2\,\mathrm{He}+\mathrm{He}(^3S_1) \rightarrow \mathrm{He}+\mathrm{He}_2(^3\Sigma_u)$] which suggests the existence of a hump. In 1954 Burhop[9] estimated the height of the hump from Phelps and Molnar's work to be 0.115 ev at $R=4.17a_0$ for He_2 ($^3\Sigma$).

(5) In 1955 Phelps[6] observed that the three-body combination coefficient for helium was significantly lower than was observed in other cases.

(6) The suggestion of Phelps and Molnar that there exists a hump in the potential energy curve for neon between the normal atom and the $^3P_2$ metastable atom that is greater than 0.0517 ev, provides a lower limit for the helium hump, since Phelps'[10] observation of the three-body collision coefficient of neon, indicates that the height of the hump in neon is less than that for helium.

Because the existence of a hump in the potential curve is in itself surprising and because of the importance of the potential curve in the several phenomena discussed, it was of interest to repeat the Buckingham and Dalgarno calculation with an improved wavefunction.

* This research was supported in part (G. H. Brigman) by Convair as a corporate-sponsored project, and in part (S. J. Brient and F. A. Matsen) by the Advanced Research Projects Agency, monitored by the Air Force Office of Scientific Research, of the Air Research and Development Command.

[1] J. S. Mathis, Astrophys. J. **125**, 318 (1957).

[2] J. L. Nickerson, Phys. Rev. **47**, 707 (1935).

[3] R. A. Buckingham and A. Dalgarno, Proc. Roy. Soc. (London) **A213**, 327 (1952).

[4] R. A. Buckingham and A. Dalgarno calculated two values of the proportionality constant in the van der Waal energy expression, -20 and -30×10^{60} erg cm^6. They used the arbitrary values -10.6 and -21.2×10^{60} erg cm^6 in their computation. However, the value -30×10^{60} erg cm^6 agrees closely with one calculated by Dalgarno and Kingston [Proc. Phys. Soc. (London) **72**, 1053 (1958)] from a modified sum of oscillator strengths. This suggests that the hump may not be as large as estimated by Buckingham and Dalgarno.

[5] R. A. Buckingham and A. Dalgarno, Proc. Roy. Soc. (London) **A213**, 506 (1952).

[6] A. V. Phelps, Phys. Rev. **99**, 1307 (1955).

[7] R. F. Stebbings, Proc. Roy. Soc. (London) **A241**, 270 (1957).

[8] A. V. Phelps and J. B. Molnar, Phys. Rev. **98**, 120 (1953).

[9] E. H. S. Burhop, Proc. Phys. Soc. (London) **A67**, 276 (1954).

[10] A. V. Phelps, Phys. Rev. **114**, 1011 (1959).

TABLE I. Open-shell calculation for the $^3\Sigma_u^+$ state of the helium molecule, using a valence-bond function and Slater orbitals.

Internuclear separation in a.u.	Total energy in ev[a]	Interaction energy in ev[a]	Optimized orbital exponents			
			a	b	c	d
1.5	−136.02259	+1.287406	2.0044	1.6520	1.9714	0.5431
1.9	−138.36365	−1.053652	2.1473	1.3823	1.9817	0.5019
2.13	−138.55284	−1.242841	2.1540	1.3201	1.9846	0.4889
2.5	−138.29658	−0.986582	2.1632	1.2581	1.9865	0.4772
3.5	−137.35845	−0.048454	2.1775	1.1868	1.9910	0.5045
4.0	−137.16973	+0.140265	2.1804	1.1804	1.9923	0.5323
4.39	−137.11984	+0.190158	2.1800	1.1799	1.9929	0.5461
4.5	−137.11561	+0.194390	2.1801	1.1817	1.9929	0.5542
5.0	−137.12761	+0.182384	2.1815	1.1828	1.9929	0.5671
∞	−137.31000	0.0	2.183125	1.188601	1.9940298	0.56479711

[a] The conversion used was 1 a.u. = 27.2 ev.

II. CALCULATION

The Buckingham and Dalgarno (B and D) calculation was based on the atomic functions of Morse, Young, and Haurwitz[11] (MYH). The MYH $2s$ function is orthogonal to $1s$ on the same atom. MYH determined their exponents by minimizing the atomic energies for the separated atoms $He(^1S, 1s^2)$ and $He(^3S, 1s2s)$. Buckingham and Dalgarno employed these same orbital exponents for all internuclear separations.

The present calculation differs from that of B and D in three respects, (a) the use of nodeless orbitals, (b) the use of an open-configuration wavefunction for singlet helium, and (c) the use of orbital exponents optimized for each internuclear distance.

The wavefunction used is

$$\psi = (1/\sqrt{2})[(\phi_1 - \phi_2) - (\phi_3 - \phi_4)]$$

$$\phi_1 = \begin{pmatrix} a_A b_A c_B d_B \\ \alpha\ \beta\ \alpha\ \alpha \end{pmatrix}, \qquad \phi_2 = \begin{pmatrix} a_A b_A c_B d_B \\ \beta\ \alpha\ \alpha\ \alpha \end{pmatrix}$$

$$\phi_3 = \begin{pmatrix} a_B b_B c_A d_A \\ \alpha\ \beta\ \alpha\ \alpha \end{pmatrix}, \qquad \phi_4 = \begin{pmatrix} a_B b_B c_A d_A \\ \beta\ \alpha\ \alpha\ \alpha \end{pmatrix},$$

where

$$a_A = (a^3/\pi)^{\frac{1}{2}} \exp(-a r_A)$$
$$a_B = (a^3/\pi)^{\frac{1}{2}} \exp(-a r_B)$$
$$b_A = (b^3/\pi)^{\frac{1}{2}} \exp(-b r_A)$$
$$b_B = (b^3/\pi)^{\frac{1}{2}} \exp(-b r_B)$$
$$c_A = (c^3/\pi)^{\frac{1}{2}} \exp(-c r_A)$$
$$c_B = (c^3/\pi)^{\frac{1}{2}} \exp(-c r_B)$$
$$d_A = (d^5/3\pi)^{\frac{1}{2}} r_A \exp(-d r_A)$$
$$d_B = (d^5/3\pi)^{\frac{1}{2}} r_B \exp(-d r_B).$$

[11] P. M. Morse, L. A. Young, and E. S. Haurwitz, Phys. Rev. **48**, 948 (1935).

The exchange integrals were evaluated on the IBM 650 at the University of Texas from programs developed by J. Miller and J. M. Gerhauser. The remaining integrals and assembly program were run on the IBM 704 at Convair, Fort Worth, Texas. First the orbital exponents were optimized at Convair, using approximate values for exchange integrals by the Mulliken[12] approximation or by simply inserting accurate values as input data. The final calculations

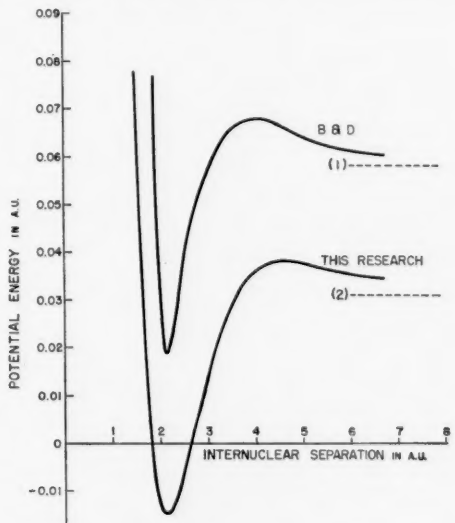

FIG. 1. Calculated potential energy curves as a function of internuclear separation. The zero of energy corresponds to the sum of the atomic energies of $He(^1S_0)$ and $He(^3S_1)$. C. E. Moore, *Atomic Energy Levels* (National Bureau of Standards, U. S. Government Printing Office, Washington 25, D. C., 1949). Here (1) and (2) correspond to the sum of the atomic energies as calculated by MYH[11] and in this research, respectively.

[12] R. S. Mulliken, J. chim. phys. **46**, 500, 521 (1949).

at each internuclear separation were made with accurate values of the exchange integrals using the optimized values of the orbital exponents.

III. DISCUSSION

The results are given in Table I and Fig. 1. The present calculation shows a hump of 0.19 ev, in the potential curve at $R=4.5a_0$, similar to that of Buckingham and Dalgarno. Because the wave function we used is more flexible than that of Buckingham and Dalgarno, since it allows for radial correlation and since the orbital exponents were optimized for each internuclear separation, it provides further support for the existence of the hump. Neither this calculation nor that of Buckingham and Dalgarno made explicit allowance for distortion polarization (i.e., p orbitals were not included) so that each calculation may lie relatively too high in the neighborhood of the hump. See footnote 4 for a discussion of a polarization correction.

The dissociation energy $[E(\infty)-E(R_{eq})]$ from this calculation is 1.24 ev compared to 1.09 ev estimated by Buckingham and Dalgarno from their calculation. At equilibrium separation the present calculation lies 0.41 ev below the sum of the experimental atomic energies. This represents a lower limit to the experimental binding energy.

ACKNOWLEDGMENT

We wish to acknowledge the help of Ronald D. Poshusta in the preparation of this paper.

THE JOURNAL OF CHEMICAL PHYSICS VOLUME 34, NUMBER 3 MARCH, 1961

Theoretical Investigations on the Light Scattering of Colloidal Spheres. IX. Lateral Scattering at 90° from Incident Natural and Linearly Polarized Light*

WILLIAM J. PANGONIS, WILFRIED HELLER, AND NICOLAOS A. ECONOMOU

Department of Chemistry, Wayne State University, Detroit 2, Michigan

(Received July 14, 1960)

The Mie quantities $i_{||}, i_{\perp}$ and their sum are calculated for nonabsorbing spheres for the parameters $\gamma=90°$, $m=1.05$ (0.05) 1.30 and $\alpha=0.2$ (0.2) 25.6. The experimentally important specific scattered intensity $(I_u/I_0c)_0$ is derived from $(i_{||}+i_{\perp})/2$. The periodicities in the prominent (secondary) i (α) oscillations and in the less pronounced primary and tertiary oscillations are briefly discussed.

I. INTRODUCTION

THE intensity of light scattered by nonabsorbing colloidal and microscopic spheres, evaluated on the basis of the Mie theory, has been treated in several preceding publications for the angles γ of 0°,[1] 45°,[2] 135°,[2] and 180°[2] with respect to the reverse direction of the primary beam. The present paper is concerned with lateral scattering at $\gamma=90°$. Observations at this practically convenient angle are favored by many authors. In the great majority of instances, the R-G-D equation[3] has been and is being used for the interpretation of the data. This is unquestionably permissible as long as $(m-1)\to 0$ and α[4] is not too large ($\leqslant 10$). Except for these limiting cases, the Mie theory must be applied. The present paper is concerned with the theoretical evaluation of 90° scattering on the basis of this theory. The parameters considered are $\alpha=0.2(0.2)25.6$ and $m=1.05(0.05)1.30$.[5] This covers all possible contingencies which may arise with suspensions or emulsions of nonabsorbing spheres with a diameter between the limits of 0–3.3 μ (assuming the use of the Hg-vacuum wavelength λ_0 of 5460.73 a.u.) and with any relative refractive index conceivable in dispersions except for special very highly refractive materials.

II. THEORETICAL QUANTITIES TO BE CONSIDERED

The primary theoretical quantities to be considered are $i_{||}$, $i_{\perp}$, and i_u. They have been defined previously.[3,6] From these, the practically important quantities

$$(I_{\perp}/I_0c)_0=(3\rho_{12}/2\lambda\alpha^3\rho_2)i_{\perp}\times 10^{-2} \quad (1a)$$

$$(I_{||}/I_0c)_0=(3\rho_{12}/2\lambda\alpha^3\rho_2)i_{||}\times 10^{-2} \quad (1b)$$

$$(I_u/I_0c)_0=(3\rho_{12}/2\lambda\alpha^3\rho_2)i_u\times 10^{-2} \quad (1c)$$

were derived. Here, c is the concentration in $g\times 100g^{-1}$ and $i_u=(i_{\perp}+i_{||})/2$.

The quantity on the left-hand side is the intensity

* This work was supported by the Office of Naval Research.

[1] M. Nakagaki and W. Heller, J. Chem. Phys. **30**, 783 (1959).

[2] W. Heller and M. Nakagaki, J. Chem. Phys. **31**, 1188 (1959).

[3] See W. Heller, M. Nakagaki, and M. Wallach, J. Chem. Phys. **30**, 444 (1959).

[4] $\alpha=\pi D/\lambda$, where D is the diameter of the scattering spherical particle; and λ is the wavelength in the medium; m is the relative refractive index μ_2/μ_1, where μ_2 is the refractive index of the particles and μ_1 is the refractive index of the medium.

[5] All data up to $\alpha=7.0$ were hand computed, the primary data $(i_{\parallel}, i_{\perp})$ for $\alpha>7.0$ were electronically computed at the Wayne State University Computation laboratory.

[6] W. Heller and W. J. Pangonis, J. Chem. Phys. **26**, 498 (1957).

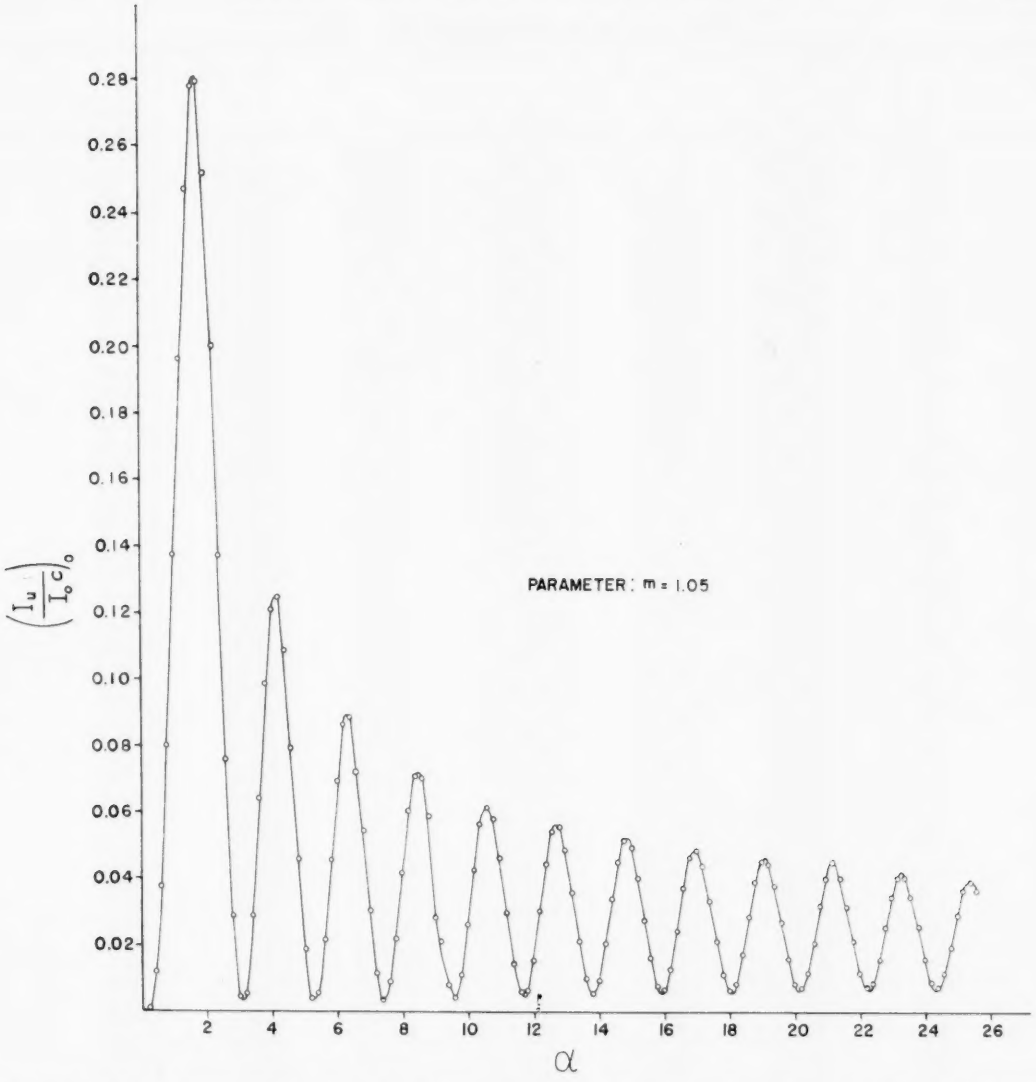

FIG. 1. Specific intensity, per unit solid angle, of light scattered at 90° from incident unpolarized light. I. Relative refractive index, $m = 1.05$. (Dispersing medium: water at 25°C; vacuum wavelength, = 5460.73 A.)

scattered, per unit solid angle, unit path length, and unit intensity of the incident beam from a system containing 1 g of scattering material per 100 g of system; ρ_2 and ρ_{12} are the densities of the scattering material and of the entire system, respectively. The subscript 0 outside the bracket indicates that these data are to be compared with experimental I/I_0c data extrapolated to $c \to 0$. The subscripts $\perp$, $\parallel$ indicate that the incident beam is linearily polarized and vibrates perpendicular and parallel respectively to the plane of observation. The subscript u applies to incident unpolarized light. In all three instances, the intensities calculated represent the total intensities scattered at $\gamma = 90°$. The data of Eqs. (1a) and (1b) are applicable also to the case that the intensity of the scattered light is recorded after its passage through a Glan-Thompson prism, on using an incident unpolarized beam. In that case, the subscripts $\perp$ and $\parallel$ indicate the direction of polarization of the scattered component selected.

The results given here for $(I/I_0c)_0$ apply to the green Hg line ($\lambda_0 = 5460.73$ a.u.) and to water at 25°C as the medium. For another wavelength λ' the specific scattered intensities of the same system

$$(I/I_0c)_0' = (I/I_0c)_0(\lambda/\lambda')\text{cm}^{-1} \qquad (2)$$

if the dispersion corrections are negligible.

TABLE I. i Values for an angle of observation γ of 90°.

α	$m=1.05$			$m=1.10$		
	$i_\perp$	$i_\parallel$	$(i_\perp+i_\parallel)$	$i_\perp$	$i_\parallel$	$(i_\perp+i_\parallel)$
0.2	0.0_76864		0.0_76864	0.0_62720		0.0_62720
0.4	0.0_44227		0.0_44227	0.0_41670	$0.0_{10}2916$	0.0_41670
0.6	0.0_44476	0.0_81000	0.0_44476	0.0_81739	0.0_81783	0.0_81783
0.8	0.0_52255	0.0_55290	0.0_52255	0.0_59096	0.0_73374	0.0_59096
1.0	0.0_77477	0.0_71743	0.0_77477	0.003031	0.0_62980	0.003031
1.2	0.001856	0.0_61084	0.0018561	0.007552	0.0_51876	0.007553
1.4	0.003709	0.0_65023	0.0037095	0.01507	0.0_58886	0.015078
1.6	0.006210	0.0_51855	0.0062185	0.02500	0.0_43392	0.02503
1.8	0.008893	0.0_55703	0.0088987	0.03521	0.0_51068	0.03531
2.0	0.010983	0.0_41491	0.0109979	0.04241	0.0_52853	0.04269
2.2	0.011640	0.0_43349	0.011673	0.04339	0.0_56496	0.04403
2.4	0.010276	0.0_46526	0.0103412	0.03657	0.001261	0.03783
2.6	0.007230	0.0_31103	0.0072403	0.02282	0.002093	0.02491
2.8	0.003340	0.0_31641	0.003504	0.008845	0.002990	0.00183
3.0	0.000493	0.0_22148	0.0007070	0.001707	0.003705	0.005412
3.2	0.000821	0.0_22474	0.0010684	0.01134	0.004053	0.01539
3.4	0.005970	0.0_22560	0.0062260	0.04333	0.004034	0.04736
3.6	0.01613	0.0_22442	0.0163742	0.09430	0.003853	0.09815
3.8	0.02941	0.0_22300	0.0296400	0.15032	0.003848	0.15416
4.0	0.04216	0.0_22361	0.0423961	0.19112	0.004416	0.19553
4.2	0.05010	0.0_22852	0.050385	0.20218	0.005815	0.20799
4.4	0.05012	0.0_33940	0.050514	0.18037	0.008442	0.18881
4.6	0.04162	0.0_55624	0.042182	0.13032	0.01203	0.14235
4.8	0.02714	0.0_57833	0.027923	0.06877	0.01618	0.08495
5.0	0.01180	0.001017	0.012817	0.02220	0.02011	0.04231
5.2	0.00203	0.001221	0.003251	0.01845	0.02292	0.04137
5.4	0.00363	0.001353	0.004983	0.07669	0.02405	0.10074
5.6	0.01955	0.001386	0.02093	0.19501	0.02370	0.21871
5.8	0.047454	0.001342	0.04879	0.34252	0.02283	0.36535
6.0	0.080853	0.001271	0.08212	0.47273	0.02286	0.49559
6.2	0.11142	0.001272	0.11269	0.53178	0.02544	0.55722
6.4	0.12545	0.001425	0.12687	0.49898	0.03110	0.53008
6.6	0.11841	0.001761	0.12017	0.38400	0.03971	0.42371
6.8	0.09175	0.002265	0.09401	0.23076	0.05014	0.28090
7.0	0.05459	0.002920	0.05751	0.09881	0.06009	0.15890
7.2	0.02072	0.003450	0.02417	0.04774	0.06804	0.11578
7.4	0.00435	0.003783	0.00813	0.12069	0.07200	0.19269
7.6	0.01491	0.003945	0.01885	0.32568	0.07262	0.39830
7.8	0.05379	0.003881	0.05767	0.61171	0.07136	0.68307
8.0	0.1140	0.003730	0.1177	0.88784	0.07096	0.95880
8.2	0.1789	0.003615	0.1825	1.05539	0.07458	1.12997
8.4	0.2267	0.003768	0.2304	1.04747	0.08455	1.13202
8.6	0.2400	0.004279	0.2442	0.86543	0.10114	0.96657
8.8	0.2131	0.005251	0.2183	0.57585	0.12133	0.69718
9.0	0.1538	0.006447	0.1602	0.29171	0.14181	0.43352
9.2	0.0828	0.007493	0.0903	0.13607	0.15875	0.29482
9.4	0.0277	0.008437	0.0361	0.19976	0.16764	0.36740
9.6	0.0122	0.008903	0.0211	0.49964	0.16965	0.66929
9.8	0.0489	0.009018	0.0579	0.95884	0.16633	1.12517
10.0	0.1330	0.008651	0.1417	1.43931	0.16393	1.60324
10.2	0.2400	0.008204	0.2482	1.77747	0.16871	1.94618
10.4	0.3383	0.008059	0.3464	1.85205	0.18447	2.03652
10.6	0.3952	0.008595	0.4038	1.62936	0.21189	1.84124
10.8	0.3906	0.009811	0.4005	1.18312	0.24954	1.43266
11.0	0.3234	0.011285	0.3347	0.68268	0.28845	0.97113
11.2	0.2149	0.013586	0.2285	0.34574	0.32055	0.66629
11.4	0.1036	0.015731	0.1193	0.35081	0.33835	0.68916
11.6	0.0336	0.017265	0.0508	0.74491	0.34154	1.08645
11.8	0.0406	0.018044	0.0586	1.42213	0.33443	1.75656
12.0	0.1303	0.017659	0.1479	2.16180	0.32638	2.48818
12.2	0.2813	0.016941	0.2982	2.72429	0.32792	3.05221
12.4	0.4464	0.016138	0.4626	2.93014	0.34485	3.27499
12.6	0.5728	0.016014	0.5888	2.70368	0.38789	3.09157
12.8	0.6177	0.016069	0.6338	2.10289	0.44994	2.55283
13.0	0.5659	0.01820	0.5841	1.34272	0.51904	1.86176
13.2	0.4318	0.02123	0.4531	0.74505	0.58054	1.32559
13.4	0.2577	0.02499	0.2827	0.61074	0.61835	1.22909
13.6	0.1100	0.02853	0.1385	1.07601	0.62745	1.70346
13.8	0.0490	0.03099	0.0800	2.02051	0.61435	2.63486
14.0	0.1095	0.03167	0.1412	3.11270	0.59368	3.70638
14.2	0.2855	0.03119	0.3167	3.98522	0.57946	4.56468

TABLE I.—*Continued.*

α	$m=1.05$			$m=1.10$		
	$i_\perp$	$i_\parallel$	$(i_\perp+i_\parallel)$	$i_\perp$	$i_\parallel$	$(i_\perp+i_\parallel)$
14.4	0.5254	0.03005	0.5554	4.36529	0.59809	4.96338
14.6	0.7514	0.02709	0.7784	4.14046	0.65274	4.79320
14.8	0.8874	0.02686	0.9142	3.37764	0.74197	4.11961
15.0	0.8868	0.02852	0.9153	2.32448	0.85076	3.17524
15.2	0.7447	0.03234	0.7770	1.38159	0.95257	2.33416
15.4	0.5133	0.03730	0.5506	1.01396	1.02533	2.03929
15.6	0.2735	0.04269	0.3162	1.49245	1.05702	2.54947
15.8	0.1110	0.04724	0.1582	2.72041	1.04683	3.76724
16.0	0.0955	0.05011	0.1456	4.26882	1.01450	5.28332
16.2	0.2514	0.05068	0.3021	5.60328	0.97858	6.58186
16.4	0.5432	0.05012	0.5933	6.28767	0.98758	7.27525
16.6	0.8822	0.04656	0.9287	6.12133	1.04741	7.16874
16.8	1.1544	0.04411	1.1985	5.15112	1.16281	6.31453
17.0	1.2596	0.04478	1.3044	3.69949	1.30840	5.00789
17.2	1.1699	0.04864	1.2186	2.30586	1.46154	3.76740
17.4	0.9055	0.05473	0.9603	1.59595	1.58091	3.17686
17.6	0.5661	0.06191	0.6280	1.99371	1.64238	3.63609
17.8	0.2693	0.06896	0.3382	3.47078	1.64853	5.11931
18.0	0.1295	0.07369	0.2032	5.54769	1.60708	7.15477
18.2	0.2116	0.07623	0.2878	7.51772	1.56673	9.08445
18.4	0.5062	0.07251	0.5787	8.73311	1.56780	10.30091
18.6	0.9336	0.06958	1.0032	8.79236	1.63482	10.42718
18.8	1.3509	0.06716	1.4181	7.64317	1.76853	9.41117
19.0	1.6288	0.06650	1.6953	5.68788	1.95380	7.64168
19.2	1.6603	0.07011	1.7304	3.66877	2.15134	5.82011
19.4	1.4344	0.07761	1.5120	2.45224	2.31545	4.76769
19.6	1.0250	0.08731	1.1123	2.63845	2.41411	5.05256
19.8	0.5786	0.09786	0.6764	4.27766	2.42294	6.70060
20.0	0.2656	0.10668	0.3723	6.86805	2.39525	9.26330
20.2	0.2088	0.10591	0.3147	9.61236	2.35655	11.96891
20.4	0.4491	0.10419	0.5533	11.59597	2.35979	13.95576
20.6	0.9209	0.10103	1.0219	12.14842	2.44288	14.59130
20.8	1.4760	0.09571	1.5717	10.97488	2.61112	13.58600
21.0	1.9385	0.09308	2.0316	8.47246	2.84703	11.31949
21.2	2.1498	0.09527	2.2420	5.65177	3.09553	8.74730
21.4	2.0405	0.10388	2.1444	3.72836	3.30055	7.02891
21.6	1.6339	0.11718	1.7511	3.55328	3.39680	6.95008
21.8	1.0699	0.13185	1.2017	5.26606	3.43290	8.69896
22.0	0.5547	0.14651	0.7012	8.35546	3.40510	11.76056
22.2	0.2929	0.15085	0.4437	11.87424	3.36842	15.24266
22.4	0.3970	0.14766	0.5446	14.76120	3.38450	18.14570
22.6	0.8473	0.14337	0.9906	16.02552	3.48783	19.51335
22.8	1.5154	0.13520	1.6506	15.05992	3.70661	18.76653
23.0	2.1793	0.12959	2.3089	12.12378	4.00953	16.13331
23.2	2.6179	0.12817	2.7460	8.41241	4.33535	12.74776
23.4	2.6839	0.13499	2.8188	5.56499	4.56447	10.12938
23.6	2.3463	0.14851	2.4948	4.83794	4.73460	9.57254
23.8	1.7262	0.16875	1.8959	6.54721	4.76413	11.31134
24.0	1.0288	0.18240	1.2112	10.12403	4.72473	14.84876
24.2	0.5170	0.19534	0.7123	14.52500	4.67115	19.19615
24.4	0.3845	0.19954	0.5840	18.40087	4.67335	23.07422
24.6	0.7281	0.19673	0.9248	20.45165	4.79457	25.24622
24.8	1.4483	0.18860	1.6369	19.76440	5.05842	24.82282
25.0	2.3133	0.18106	2.4943	16.44723	5.44206	21.88929
25.2	3.0260	0.17568	3.2016	11.83821	5.85247	17.69068
25.4	3.3478	0.17798	3.5258	7.96878	6.18275	14.15153
25.6	3.1679	0.19085	3.3587	6.51798	6.40304	12.92102
		$m=1.15$			$m=1.20$	
0.2	$0.0_6 5968$		$0.0_6 5968$	$0.0_5 1039$	$0.0_{11} 1000$	$0.0_5 1039$
0.4	$0.0_4 3705$	$0.0_5 1638$	$0.0_4 3705$	$0.0_4 6482$	$0.0_5 5062$	$0.0_4 6482$
0.6	$0.0_5 3989$	$0.0_6 9178$	$0.0_5 3989$	$0.0_5 7036$	$0.0_7 2979$	$0.0_5 7036$
0.8	0.002051	$0.0_4 1656$	0.002051	0.003665	$0.0_6 5432$	0.003665
1.0	0.006892	$0.0_5 1595$	0.006893	0.012350	$0.0_5 5279$	0.012355
1.2	0.017227	$0.0_4 1009$	0.017228	0.03094	$0.0_4 3494$	0.030974
1.4	0.034258	$0.0_4 4983$	0.03430	0.06124	$0.0_5 1748$	0.061414
1.6	0.056219	$0.0_5 1876$	0.05640	0.09919	$0.0_5 7062$	0.099896
1.8	0.077697	$0.0_5 6345$	0.07833	0.13432	0.002364	0.13668
2.0	0.091145	0.001732	0.09287	0.15334	0.006570	0.15991
2.2	0.089924	0.003967	0.09389	0.14587	0.01500	0.16087

TABLE I.—*Continued.*

α	$m=1.15$			$m=1.20$		
	$i_\perp$	$i_\parallel$	$(i_\perp+i_\parallel)$	$i_\perp$	$i_\parallel$	$(i_\perp+i_\parallel)$
2.4	0.071764	0.007592	0.07935	0.10925	0.02783	0.13708
2.6	0.041573	0.012127	0.05370	0.05829	0.04204	0.10033
2.8	0.013728	0.016392	0.03012	0.02131	0.05301	0.07432
3.0	0.010693	0.019087	0.02978	0.04561	0.05785	0.10346
3.2	0.054796	0.019808	0.07460	0.16709	0.05754	0.22463
3.4	0.151749	0.019252	0.17100	0.36862	0.05498	0.42360
3.6	0.277719	0.018890	0.29660	0.57392	0.05787	0.63179
3.8	0.38639	0.02551	0.41190	0.70223	0.06946	0.77169
4.0	0.43866	0.026140	0.46480	0.72602	0.09672	0.82274
4.2	0.42011	0.037264	0.45737	0.64209	0.14392	0.78601
4.4	0.33578	0.054438	0.39021	0.47281	0.20846	0.68127
4.6	0.211954	0.075963	0.28791	0.26936	0.27726	0.54662
4.8	0.095485	0.097543	0.19302	0.13972	0.33130	0.47102
5.0	0.054607	0.113821	0.16842	0.23083	0.35405	0.58488
5.2	0.154403	0.121189	0.27559	0.61753	0.35293	0.97046
5.4	0.40799	0.119989	0.52797	1.17969	0.33718	1.51687
5.6	0.74547	0.115617	0.86108	1.66400	0.33254	1.99654
5.8	1.042209	0.115377	1.15758	1.88491	0.36092	2.24583
6.0	1.174956	0.126762	1.30171	1.81463	0.43946	2.25409
6.2	1.106980	0.154384	1.26136	1.52350	0.57180	2.09530
6.4	0.875155	0.198668	1.07382	1.09596	0.74118	1.83714
6.6	0.563488	0.253916	0.81740	0.64909	0.91045	1.55954
6.8	0.28481	0.28465	0.56946	0.42739	1.03607	1.46346
7.0	0.1769	0.3514	0.5283	0.7362	1.0871	1.8233
7.2	0.3671	0.3730	0.7401	1.6044	1.0729	2.6773
7.4	0.8769	0.3750	1.2519	2.6544	1.0265	3.6809
7.6	1.5446	0.3665	1.9111	3.4205	1.0033	4.4238
7.8	2.1174	0.3629	2.4803	3.6803	1.0590	4.7393
8.0	2.3807	0.3819	2.7626	3.4417	1.2252	4.6669
8.2	2.2558	0.4345	2.6903	2.8244	1.4964	4.3208
8.4	1.8006	0.5210	2.3216	1.9882	1.8250	3.8132
8.6	1.1812	0.6302	1.8114	1.1986	2.1363	3.3349
8.8	0.6352	0.7359	1.3711	0.9604	2.3464	3.3068
9.0	0.4276	0.8187	1.2463	1.7049	2.4081	4.1130
9.2	0.7628	0.8596	1.6224	3.1803	2.3447	5.5250
9.4	1.6211	0.8629	2.4840	4.6853	2.2426	6.9279
9.6	2.7155	0.8466	3.5621	5.6999	2.2046	7.9045
9.8	3.6451	0.8415	4.4866	6.0262	2.3131	8.3393
10.0	4.0973	0.8773	4.9746	5.6481	2.6062	8.2543
10.2	3.9352	0.9714	4.9066	4.6265	3.0672	7.6937
10.4	3.2122	1.1232	4.3354	3.1641	3.6310	6.7951
10.6	2.1724	1.3050	3.4774	1.8850	4.1110	5.9960
10.8	1.2361	1.4836	2.7197	1.7546	4.3553	6.1099
11.0	0.9014	1.6132	2.5146	3.0015	4.3377	7.3392
11.2	1.4354	1.6679	3.1033	4.9781	4.1505	9.1286
11.4	2.7070	1.6616	4.3686	6.9402	3.9712	10.9114
11.6	4.2555	1.6272	5.8827	8.4060	3.9471	12.3531
11.8	5.5874	1.6183	7.2057	9.0602	4.1698	13.2300
12.0	6.3168	1.6798	7.9966	8.6500	4.6935	13.3435
12.2	6.1955	1.8427	8.0382	6.9674	5.4438	12.4112
12.4	5.1941	2.0966	7.2907	4.3802	6.2382	10.6184
12.6	3.6328	2.4026	6.0354	2.4922	6.7784	9.2706
12.8	2.1731	2.6668	4.8399	2.5692	6.8936	9.4628
13.0	1.6541	2.8366	4.4907	4.2147	6.6561	10.8708
13.2	2.4432	2.8828	5.3260	6.5868	6.3148	12.9016
13.4	4.1837	2.8385	7.0222	9.2631	6.0983	15.3614
13.6	6.1991	2.7703	8.9694	11.7864	6.1557	17.9421
13.8	7.9390	2.7527	10.6917	13.3285	6.6399	19.9684
14.0	9.0159	2.8535	11.8694	12.7460	7.5541	20.3001
14.2	9.0526	3.1121	12.1647	9.3258	8.6982	18.0240
14.4	7.8239	3.5193	11.3432	4.8091	9.5578	14.3669
14.6	5.5741	3.9857	9.5598	2.5498	9.7792	12.3290
14.8	3.4252	4.3737	7.7989	3.0234	9.4477	12.4711
15.0	2.6709	4.5828	7.2537	5.0214	8.9588	13.9802
15.2	3.7362	4.5812	8.3174	8.0412	8.5988	16.6400
15.4	5.9950	4.4509	10.4459	12.1259	8.4901	20.6160
15.6	8.5654	4.3126	12.8780	16.6846	8.8595	25.5441
15.8	10.8399	4.2833	15.1232	19.5016	9.8488	29.3504
16.0	12.3667	4.4482	16.8149	17.0956	11.3049	28.4005
16.2	12.6170	4.8575	17.4745	9.6705	12.5519	22.2224
16.4	10.9853	5.4569	16.4422	3.7045	12.8592	16.5637

TABLE I.—*Continued.*

α	$m=1.15$			$m=1.20$		
	$i_\perp$	$i_\parallel$	$(i_\perp+i_\parallel)$	$i_\perp$	$i_\parallel$	$(i_\perp+i_\parallel)$
16.6	7.8231	6.1043	13.9274	2.0149	12.2856	14.3005
16.8	4.7980	6.6067	11.4047	2.9866	11.5074	14.4940
17.0	3.7900	6.8221	10.6121	5.5055	11.0020	16.5075
17.2	5.1601	6.7561	11.9162	9.9604	10.8444	20.8048
17.4	8.0228	6.5331	14.5559	16.8831	11.2350	28.1181
17.6	11.3578	6.3264	17.6842	24.5446	12.3530	36.8976
17.8	14.4846	6.2869	20.7715	26.2523	14.0840	40.3363
18.0	16.7736	6.5288	23.3024	17.2715	15.5572	32.8287
18.2	17.0984	7.1042	24.2026	6.8104	15.7652	22.5756
18.4	14.5411	7.9201	22.4612	1.9412	14.8040	16.7452
18.6	9.8963	8.7290	18.6253	1.3099	13.6783	14.9882
18.8	5.8815	9.2789	15.1604	2.7285	13.0334	15.7619
19.0	4.6851	9.4424	14.1275	6.2957	12.8791	19.1748
19.2	6.4497	9.3077	15.7574	13.8854	13.3741	27.2595
19.4	10.1395	9.0407	19.1802	25.9692	14.8402	40.8094
19.6	14.7060	8.8385	23.5445	34.1379	16.9965	51.1344
19.8	19.3052	8.8555	28.1607	25.8621	18.5906	44.4527
20.0	22.6001	9.2345	31.8346	11.6033	18.2708	29.8741
20.2	22.5976	9.9593	32.5569	3.3616	16.5577	19.9193
20.4	18.0999	10.8845	28.9844	0.6796	14.9701	15.6497
20.6	11.3633	11.6839	23.0472	0.7335	14.2764	15.0099
20.8	6.4028	12.1494	18.5522	2.7670	14.3023	17.0693
21.0	5.1714	12.2555	17.4269	9.0167	15.2048	24.2215
21.2	7.4137	12.1319	19.5456	23.2142	17.3398	40.5540
21.4	12.2389	11.9612	24.2001	38.5563	20.1519	58.7082
21.6	18.7861	11.9098	30.6959	33.1283	21.5615	54.6898
21.8	25.7404	12.1160	37.8564	16.7411	20.0369	36.7780
22.0	30.2753	12.6671	42.9424	6.1809	17.1857	23.3666
22.2	28.6556	13.4633	42.1189	1.8032	15.1237	16.9269
22.4	20.8178	14.2366	35.0544	0.3706	14.4452	14.8158
22.6	11.8993	14.7187	26.6180	0.5611	14.7239	15.2850
22.8	6.3836	14.9251	21.3087	4.4041	16.3237	20.7278
23.0	5.3229	15.0212	20.3441	18.0665	19.6708	37.7373
23.2	8.1744	15.1382	23.3126	39.0037	23.7284	62.7321
23.4	14.5423	15.3026	29.8449	36.9576	24.8529	61.8105
23.6	24.0521	15.6041	39.6562	20.2659	21.0380	41.3039
23.8	34.3328	16.1563	50.4891	9.2766	16.3578	25.6344
24.0	39.2890	16.8123	56.1013	4.6333	13.7796	18.4129
24.2	33.9650	17.3536	51.3186	2.5845	13.3435	15.9280
24.4	22.1853	17.5561	39.7414	1.0637	14.0948	15.1585
24.6	11.6965	17.5162	29.2127	1.6543	16.5214	18.1757
24.8	6.0642	17.5099	23.5741	12.3230	21.4749	33.7979
25.0	5.3287	17.7844	23.1131	36.8179	27.6628	64.4807
25.2	9.0606	18.3145	27.3751	38.0883	28.6408	66.7291
25.4	17.7901	19.1112	36.9013	21.6418	21.5342	43.1760
25.6	31.3147	20.0814	51.3961	10.8393	14.4952	25.3345
		$m=1.25$			$m=1.30$	
0.2	$0.0_5$1585	0.0_{11}1000	$0.0_5$1585	$0.0_5$2228		$0.0_5$2228
0.4	$0.0_4$9948	$0.0_8$1296	$0.0_4$9948	$0.0_4$1405		$0.0_4$1405
0.6	0.001089	$0.0_7$7398	0.001089	$0.0_3$1552		$0.0_3$1552
0.8	0.005702	$0.0_5$1373	0.005703	$0.0_3$8187	$0.0_5$2940	0.008189
1.0	0.019406	$0.0_4$1364	0.019419	0.02804	$0.0_4$2980	0.028069
1.2	0.048688	$0.0_4$9205	0.048780	0.07038	$0.0_3$2062	0.07058
1.4	0.095741	$0.0_3$4746	0.096215	0.13732	$0.0_3$1097	0.13841
1.6	0.15283	0.001982	0.15481	0.21572	$0.0_4$4744	0.22046
1.8	0.20255	0.006828	0.20937	0.27965	0.01681	0.29646
2.0	0.22499	0.019223	0.24421	0.30238	0.04751	0.34989
2.2	0.20647	0.043151	0.24962	0.26787	0.10289	0.37076
2.4	0.14766	0.076081	0.22374	0.18183	0.16889	0.35072
2.6	0.07310	0.10684	0.17994	0.08977	0.21825	0.30802
2.8	0.04239	0.12497	0.16736	0.09692	0.23769	0.33461
3.0	0.13604	0.12871	0.26475	0.31580	0.23421	0.55001
3.2	0.38292	0.12487	0.50779	0.70083	0.22508	0.92591
3.4	0.69094	0.12419	0.81513	1.04696	0.23660	1.28356
3.6	0.92437	0.13923	1.06360	1.24793	0.29178	1.53971
3.8	1.02592	0.18492	1.21084	1.32346	0.42569	1.74915
4.0	0.99876	0.27612	1.27488	1.26739	0.65796	1.92535
4.2	0.84508	0.41483	1.25991	1.04010	0.95197	1.99207
4.4	0.58512	0.57399	1.15911	0.68613	1.21200	1.89813

TABLE I.—*Continued.*

α	$m=1.25$			$m=1.30$		
	$i_\perp$	$i_\parallel$	$(i_\perp+i_\parallel)$	$i_\perp$	$i_\parallel$	$(i_\perp+i_\parallel)$
4.6	0.32865	0.70536	1.03401	0.47423	1.35507	1.82930
4.8	0.31621	0.76843	1.08464	0.81947	1.36154	2.18101
5.0	0.75797	0.76365	1.52162	1.67130	1.27998	2.95128
5.2	1.51172	0.72013	2.23185	2.41525	1.21539	3.63064
5.4	2.15993	0.70009	2.86002	2.76348	1.26388	4.02736
5.6	2.46161	0.74769	3.20930	2.90712	1.50432	4.41144
5.8	2.46072	0.90528	3.36600	3.02218	1.96200	4.98418
6.0	2.26834	1.18581	3.45415	2.92741	2.57689	5.50430
6.2	1.88101	1.55336	3.43437	2.33698	3.22010	5.55708
6.4	1.29662	1.92354	3.22016	1.54668	3.69327	5.23995
6.6	0.85495	2.18100	3.03595	1.58243	3.81521	5.39764
6.8	1.16608	2.27264	3.43872	2.62159	3.57427	6.19586
7.0	2.2737	2.1803	4.4540	3.6241	3.2320	6.8561
7.2	3.4642	2.0231	5.4873	4.1709	3.1004	7.2713
7.4	4.1974	1.9553	6.1527	4.5978	3.3345	7.9323
7.6	4.4460	2.0868	6.5328	5.3025	3.9119	9.2144
7.8	4.3879	2.4592	6.8471	6.0541	4.8212	10.8753
8.0	4.0880	3.0443	7.1323	5.7087	6.0079	11.7166
8.2	3.3443	3.7473	7.0916	3.7291	7.1025	10.8316
8.4	2.2102	4.3917	6.6019	2.3364	7.5072	9.8436
8.6	1.7288	4.7251	6.4539	2.8536	6.9881	9.8417
8.8	2.6577	4.6405	7.2982	3.8364	6.0734	9.9098
9.0	4.2003	4.2887	8.4890	4.6570	5.5010	10.1580
9.2	5.4746	3.9707	9.4253	5.7811	5.5011	11.2822
9.4	6.3201	3.8716	10.1917	7.9006	5.9916	13.8922
9.6	6.8945	4.1553	11.0498	10.7404	7.2150	17.9554
9.8	7.2268	4.8539	12.0807	11.3391	9.2377	20.5768
10.0	6.7830	5.9484	12.7314	6.5611	11.3143	17.8754
10.2	4.8217	7.1714	11.9931	2.3034	11.9342	14.2376
10.4	2.6191	7.9521	10.5712	1.9534	10.6088	12.5622
10.6	2.4262	7.9162	10.3424	2.8520	8.8295	11.6815
10.8	3.8234	7.2603	11.0837	3.9273	7.8551	11.7824
11.0	5.6020	6.5387	12.1407	6.0303	7.4669	13.4972
11.2	7.2948	6.1373	13.4321	10.6380	7.8242	18.4622
11.4	9.0502	6.1573	15.2075	17.5994	9.6097	27.2091
11.6	10.9413	6.7911	17.7324	18.9018	12.9549	31.8567
11.8	11.8445	8.2190	20.0635	7.7981	16.1710	23.9691
12.0	9.0425	10.1638	19.2063	1.3453	15.8857	17.2310
12.2	3.9422	11.5782	15.5204	0.5140	12.8637	13.3777
12.4	1.7345	11.5098	13.2443	1.2356	10.4923	11.7279
12.6	2.3244	10.3723	12.6967	2.4255	9.5401	11.9656
12.8	4.1774	9.1945	13.3719	5.3986	9.0232	14.4218
13.0	6.7994	8.4766	15.2760	13.5488	9.8357	23.3845
13.2	10.1875	8.2178	18.4053	27.4516	12.7433	40.1949
13.4	14.5852	8.8014	23.3866	23.7336	17.7740	41.5076
13.6	18.3324	10.5847	28.9171	6.4933	20.6934	27.1867
13.8	14.6104	13.2230	27.8334	1.2267	17.1801	18.4068
14.0	5.4578	14.9953	20.4531	0.1130	12.6136	12.7266
14.2	1.1280	14.4903	15.6183	0.0670	10.9183	10.9853
14.4	0.6817	12.7533	13.4350	0.8534	10.3043	11.1577
14.6	1.8559	11.3253	13.1812	4.4900	10.7389	15.2289
14.8	4.6297	10.4621	15.0918	17.6606	13.0999	30.7605
15.0	9.6957	10.1047	19.8004	38.3730	18.1660	56.5390
15.2	17.7463	10.9102	28.6565	18.5127	24.3225	42.8352
15.4	26.1052	13.2898	39.3950	6.2987	21.6304	27.9291
15.6	20.1733	16.5666	36.7399	3.5527	14.0615	17.6142
15.8	6.6066	17.8286	24.4352	1.9410	10.6562	12.5972
16.0	1.2216	15.9007	17.1223	0.6339	10.4119	11.0458
16.2	0.1189	13.4259	13.5448	0.1939	10.8559	11.0498
16.4	0.1814	12.2780	12.4599	4.1384	13.5326	17.6710
16.6	1.8855	11.7654	13.6509	26.6469	18.9753	45.6222
16.8	7.4172	11.8550	19.2722	33.4138	27.9071	61.3209
17.0	19.6898	13.4173	33.1071	11.5878	29.2558	40.8436
17.2	34.6939	16.8324	51.5263	9.1363	15.6197	24.7560
17.4	23.9081	20.3820	44.2901	8.4528	8.8842	17.3370
17.6	7.2875	19.4043	26.6918	6.3163	8.7862	15.1025
17.8	2.3971	15.1264	17.5235	3.8325	9.5221	13.3546
18.0	1.5396	12.2478	13.7874	1.5601	12.3447	13.9048
18.2	0.6462	11.7755	12.4217	6.4362	18.1960	24.6322
18.4	0.3667	12.0420	12.4087	37.9519	29.1621	67.1140
18.6	4.5661	13.4961	17.9622	14.5854	42.0098	56.5952

TABLE I.—*Continued.*

α	$m=1.25$			$m=1.30$		
	$i_\perp$	$i_\parallel$	$(i_\perp+i_\parallel)$	$i_\perp$	$i_\parallel$	$(i_\perp+i_\parallel)$
18.8	20.4464	16.8595	37.3059	9.8148	21.8814	31.6962
19.0	41.3149	22.1088	63.4237	13.1157	7.5725	20.6882
19.2	23.4432	24.6063	48.0495	14.7524	5.8966	20.6490
19.4	7.9396	18.5894	26.5290	13.4154	6.8906	20.3060
19.6	4.6097	12.1024	16.7121	9.9748	9.5687	19.5435
19.8	4.8491	9.7779	14.6270	6.3142	15.1488	21.4630
20.0	4.1357	10.1274	14.2631	17.0358	25.7719	42.8077
20.2	1.8454	11.5153	13.3607	15.7157	47.3757	63.0914
20.4	3.0697	15.0361	18.1058	6.2431	41.1024	47.3455
20.6	21.5203	21.4679	42.9882	9.7700	8.7705	18.5405
20.8	40.6475	29.8746	70.5221	16.0380	4.3831	20.4211
21.0	18.9420	28.1382	47.0802	20.7438	5.0106	25.7544
21.2	8.4095	15.0259	23.4354	23.0384	6.5468	29.5852
21.4	7.4561	7.9592	15.4153	19.8871	10.8548	30.7419
21.6	9.2793	6.8960	16.1753	18.0780	19.5256	37.6036
21.8	10.1136	7.8841	17.9977	12.0463	38.9780	51.0243
22.0	7.2451	10.7336	17.9787	2.9758	71.9577	74.9335
22.2	5.0311	16.7255	21.7566	3.1654	14.7853	17.9507
22.4	23.2541	27.5509	50.8050	8.7533	5.3796	14.1329
22.6	29.0482	39.9672	69.0154	16.7645	6.0384	22.8029
22.8	13.0441	27.3515	40.3956	25.7406	6.0561	31.7967
23.0	8.3539	9.7978	18.1517	32.6064	8.2197	40.8261
23.2	9.9737	4.6081	14.5818	37.8366	13.5129	51.3495
23.4	13.9134	4.5640	18.4774	14.0870	26.6022	40.6892
23.6	17.4849	5.9141	23.3990	3.6012	68.7152	72.3164
23.8	16.2592	10.0989	26.3581	0.8338	30.7952	31.6290
24.0	11.9525	18.8586	30.8111	1.3435	7.9714	9.3149
24.2	19.8386	35.8549	55.6935	5.9747	9.6031	15.5778
24.4	14.1205	49.6449	63.7654	15.0307	8.7466	23.7773
24.6	7.0364	20.0817	27.1181	30.0538	9.4696	39.5234
24.8	7.4977	5.3773	12.8750	44.3483	11.6951	56.0434
25.0	11.4768	3.3038	14.7806	75.7612	18.4599	94.2211
25.2	17.4146	3.4321	20.8467	7.6612	42.6280	50.2892
25.4	24.5994	5.2170	29.8164	7.2460	69.4909	76.7369
25.6	28.4880	10.3580	38.8460	1.5290	10.0795	11.6085

III. RESULTS

1. General

Table I gives the individual values of $i_\perp$, $i_{||}$ and the sum $(i_\perp+i_{||})$. One-half of the latter value, i_u, is used in the calculations of the practically important quantity $(I_u/I_0c)_0$. The variation of $(I_u/I_0c)_0$ with α is considered in Figs. 1–3 for various m values. It is, at the limiting m values of 1.05 and 1.30, monotonic up to an α value of nearly 1.70 ± 0.05 and 1.60 ± 0.05, respectively. At these α values, the first maximum occurs. On using the green Hg line for the incident beam (5461 a.u.), the limiting particle size above which answers become multivalued is, therefore, defined by a diameter of slightly more than $\frac{1}{5}\ \mu$. At larger α values the scattering spectra or additional light scattering quantities must be considered in order to obtain single-valued answers on particle size. Although the monotonic section of the curves resembles the curve expected on the basis of the Rayleigh theory (where i is proportional to α^6), a satisfactory quantitative agreement is limited to α values<1.0. The α value at which the difference between the Rayleigh i values and the Mie i values has reached 5% is given, for various m values, in Table II.[7]

[7] These data were calculated by Mr. Herbert Doppke in this laboratory.

The α values at which the error in α reaches 5% is of course somewhat higher. (This will be discussed in more detail elsewhere in connection with a special scrutiny on the practical limits of applicability of the Rayleigh theory.)

Numerical and graphical data of $(I_{||}/I_0c)_0$ and $(I_\perp/I_0c)_0$ may readily be calculated from the primary data given in Table I. Their consratideion, in addition to that of $(I_u/I_0c)_0$ is helpful in reducing the multivaluedness of answers on particle size at α values larger than those specified above.

TABLE II. Limiting α value, α_l, at which i_u computed from the Rayleigh equation differs by 5% from the true (Mie) i_u value. (m: relative refractive index.)

m	α_l
1.05	0.373
1.10	0.400
1.15	0.435
1.20	0.478
1.25	0.529
1.30	0.595

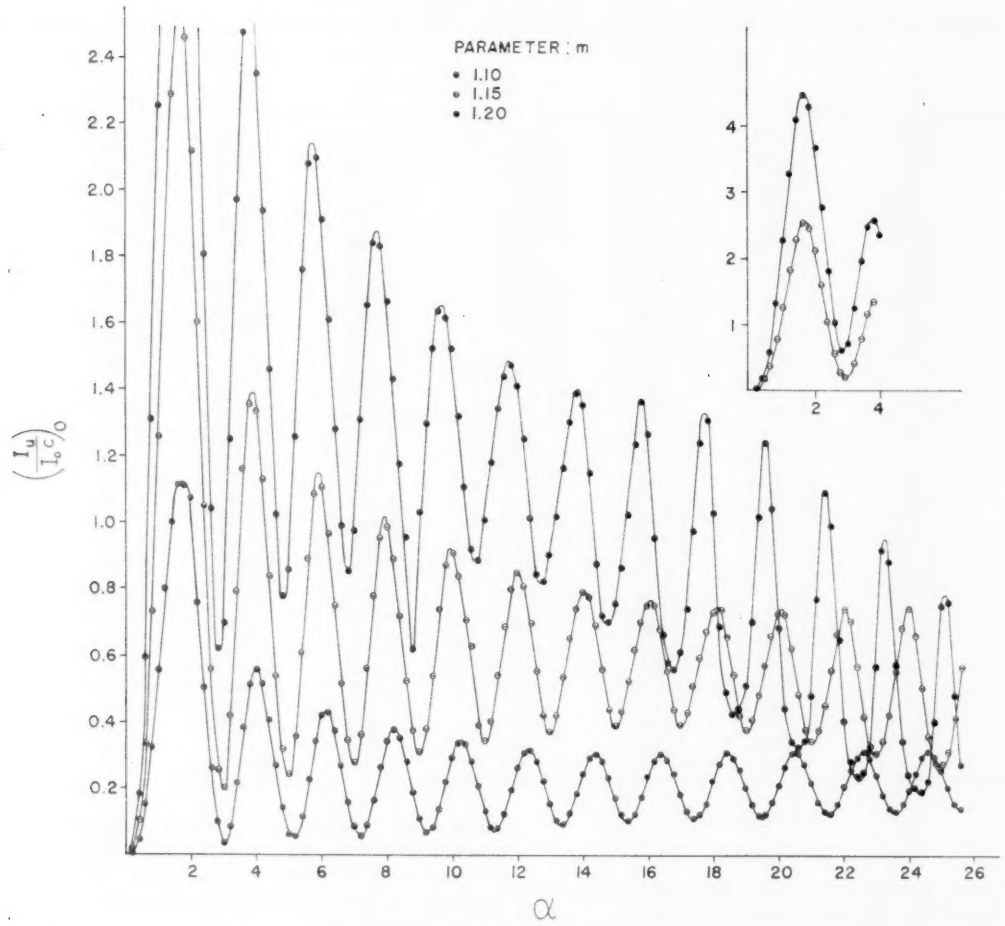

FIG. 2. Specific intensity, per unit solid angle, of light scattered at 90° from incident unpolarized light. II. Relative refractive indices 1.10, 1.15, 1.20.

2. Remarks on the Periodicities in the $i(\alpha)$ and $(I/I_0c)_0(\alpha)$ curves

The most striking feature of the $i(\alpha)$ curves and of the derived curves in Figs. 1–3 is the periodic variation of the light-scattering quantities between maxima and minima. As already stated previously,[8] the period is surprisingly constant. The $\Delta\alpha$ interval between successive maxima and also between successive minima of i_u is 2.22, 2.16, 1.96, and 1.92 at $m=1.00$, 1.05, 1.20, and 1.30, respectively. The interval is virtually the same for $i_\perp$, but slightly different for $i_\parallel$.[8] Both the location, in terms of α, of the first maximum and the intervals are numerically the same for the experimentally observed quantity, the intensity of the scattered beam relative to that of the incident beam, $(I/I_0)_c$, provided that the concentration c is small enough to exclude minor shifts in the characteristic values due to multiple scattering. Except for the first three maxima, this identity applies also to the derived limiting quantity $(I/I_0c)_0$[9] which is free from complications due to multiple scattering. Considering for example $m=1.20$, the first maximum in $(I/I_0c)_0$ occurs at $\alpha=1.60$ while that of i occurs at $\alpha=2.1$. At the fourth maximum ($\alpha=7.7$ as compared to $\alpha=7.8$), the difference has already become inconsequential and is practically nonexistent at still higher orders.

[8] M. Nakagaki and W. Heller, J. Chem. Phys. **32**, 835 (1960).

[9] A mathematical identity between i maxima and $(I/I_0c)_0$ maxima is, of course, not possible since the latter quantity varies in direction proportion to α^3, while i and I/I_0 are proportional to α. However, the rate of change of i with α is so strong, even in the immediate neighborhood of a maximum and minimum, that the differences are too small to exceed the $\Delta\alpha$ interval of 0.2 used for the computations except for the maxima of the first, second, and third orders. (Because of the smallness of i at the minima, the differences are not detectable for the minima of any order including the first-order minimum.)

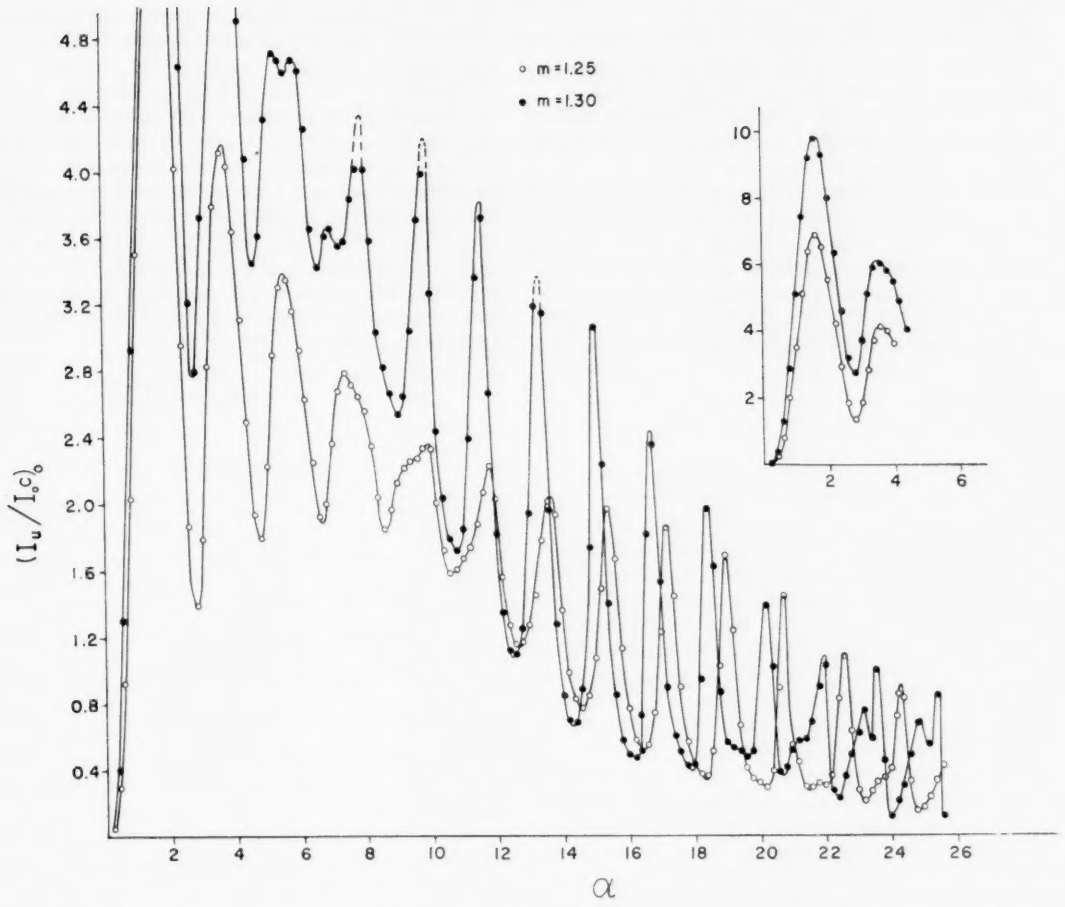

FIG. 3. Specific intensity, per unit solid angle, of light scattered at 90° from incident unpolarized light. III. Relative refractive indices: 1.25, 1.30.

While the periodicities just discussed are the most striking, they are not the only ones to occur in the i (α) and $(I/I_{0c})_0(\alpha)$ curves. The average values of i, per period, should increase with α and those of $(I/I_{0c})_0$ should decrease with increasing α approaching the value zero as $\alpha \to \infty$. This general trend is quite unmistakable from the tabular and graphical material presented. It is equally apparent, however, that this general trend is complicated by oscillations or undulations of comparatively large period. Such oscillations of comparatively long periods have previously been observed also for scattering at an angle γ of 0°[1] and 45°[2]. The long period oscillations in the present case may best be discussed by means of the $(I/I_{0c})_0(\alpha)$ figures remembering that the same conclusions could be drawn from the i (α) data in spite of the difference in aspect of such alternate curves. It is convenient and sufficient to consider, instead of the average values per period, the variation of the maximal and minimal values, respectively, as a function of α. The former decrease steadily with increasing α, if $m=1.05$, but—in view of the following—there is little doubt that they will reach a minimum at $\alpha>25$. This minimum is actually found for $m=1.10$ at $\alpha=15\pm2$. At m values in excess of 1.15, these minima degrade into curve inflections at still lower α values. The minimal values of $(I/I_{0c})_0$ exhibit similar oscillations or undulations. At $m=1.05$, the minimal values increase very slightly with increasing α and, most likely, reach a maximum at $\alpha>25$. At higher m values, these maxima in the minimal values are actually observed within the α range investigated. They are located at the α values 16 ± 1, ~7 and ~4 for an m of 1.15, 1.20, and 1.30, respectively. Like the minimal values of the maxima, the maximal values of the minima shift therefore rapidly towards smaller α values as m increases. It is significant that the maximal values of the minima and the minimal values of the maxima occur at the same α values. Associated with the

long period oscillation or undulation is, therefore, a periodic change in the amplitude of the short period oscillations discussed in the preceding paragraph (see particularly the curve for $m=1.15$ and $m=1.20$).

At m values >1.20, a third ("tertiary") type of structuration (oscillation or undulation of ultra-short period) is indicated although not clearly revealed in addition to the prominent short period oscillation of large amplitude (secondary structure) and the comparatively long period oscillation or undulation of rather small amplitude (primary structure). This third type of structuration is indicated particularly at $5<\alpha<10$ and at $\alpha>18$ provided $m>1.20$. While it gives to the prominent secondary oscillations merely the appearance of unharmonicity of nonrepeating pattern, if $m=1.25$, the resolution at $m=1.30$ is sufficient to reveal shallow "tertiary" maxima and minima. The compilation of the light scattering functions at $\Delta\alpha$ intervals of 0.2, while sufficient for all other purposes, was clearly not sufficient in order to resolve the details of this tertiary structure. The presence of this tertiary structure had not been found in the previous investigations of lateral light scattering functions as reported within this series (1–3). This, however, may be due only to the fact that m values larger than 1.20 had not been considered for the other angles. It is apparently only at higher m values that the tertiary structure becomes apparent.

Theoretical Investigations on the Light Scattering of Colloidal Spheres. X. "Scattering Ratio" and Depolarization of Light Scattered at an Angle of Observation of 90°*

WILFRIED HELLER, WILLIAM J. PANGONIS,† AND NICOLAOS A. ECONOMOU‡

Department of Chemistry, Wayne State University, Detroit 2, Michigan

(Received July 25, 1960)

The scattering ratio σ for nonabsorbing spheres and for an angle of observation γ of 90° is calculated from data given in the preceding publication [J. Chem. Phys. **34**, 960 (1961), Paper IX, this issue], for $m=1.05$ (0.05) 1.30 and $\alpha=0.2$ (0.2) 25.6. The scattering ratio represents the ratio of the total intensities scattered from a linearly polarized incident beam vibrating once parallel and, subsequently, perpendicular to the plane of observation. In the present instance of spheres, the results are identical with the depolarization in infinitely dilute systems. The experimentally attractive features of σ measurements are pointed out and the precautions to be observed for useful application of the theoretical data are enumerated. The periodicities in the σ (α) curves due to the primary, secondary, and tertiary undulations in the basic $i(\alpha)$ functions are briefly discussed with particular emphasis upon selecting conditions of optimum sensitivity of the method for particle size determinations, characterized by an error of not more than 1−3 A in particle diameter in monodisperse systems.

INTRODUCTION

MEASUREMENTS, at a single angle γ[1] and at a single vacuum wavelength λ_0 of the light scattered from an incident unpolarized beam, can be translated into particle weights or molecular weights after converting the experimental data into absolute data by means of an instrument constant. This constant depends on and varies with (a) the reflectivity losses of primary and scattered beam at and in the scattering cell, respectively, (b) the geometrically effective part of the irradiated volume, (c) the effective solid angle of the scattered radiation received by the recording device, and (d) the anisotropy of the photosensitive surface of the recording photocell. The need for this instrument constant is a practical inconvenience although its empirical determination by various available methods[2] is relatively easy. Light scattering measurements at two (dissymmetry measurements) or more angles, in the form of ratios, require far smaller "corrections" since the instrument constant is here defined by the angular variation of the first three factors. Still, it is large enough so that it cannot be neglected. By contradistinction, the measurements of intensity ratios at a single angle γ may eliminate the need for an empirical instrument constant entirely and thus provide a theoretically attractive means of absolute particle size (molecular weight) determinations from light scattering. There are two possibilities: (1) the measurement of scattering at two or more wavelengths, (2) the determination of scattering obtained from a linearly polarized beam whose electric vector forms, in successive experiments, two (or more) angles with the plane of observation. (Very powerful, for analytical reasons, is a combination of these two methods, i.e., the spectral investigation of intensity ratios.) In these ratios, factor (b) cancels out completely in a well-constructed scattering apparatus. Factor (a) can here be neglected since its ratio will have the value 1.0 for $\gamma=90°$. Factor (c) enters only if, and to the extent as, the rate of change of the two light scattering quantities with solid angle differs. Factor (d), finally, if consequential, can be determined easily or eliminated by selecting the proper azimuth in the installation of the recording device. Ratio measurements have, in addition, quite generally, the following advantages: (1) The concentration of the dispersed system or solution does not enter explicitly. This eliminates an important source of error which, in general, overshadows the error introduced by the measurement of a second optical quantity; (2) the concentration dependence of scattering is reduced to the much smaller concentration dependence of ratios, which, in general, leads to far more secure extrapolations to zero concentration.

The spectral method referred to will be discussed in a later paper. This paper deals with intensity ratios obtained with monochromatic polarized light. In view of the general preference of $\gamma=90°$ for particle size and molecular weight determinations in "single angle" measurements, this angle will be considered. There are two possibilities of approach. An unpolarized incident beam is used and an analyzing prism is inserted in the scattered beam. The first measurement is carried out with the plane of polarization parallel to the plane of observation and the second with the former perpendicular to the latter. This is the classical method of depolarization measurements. An alternate possibility is the use of a linearly polarized incident beam vibrating once parallel to the plane of observation and, in a second experiment, perpendicular to it. No analyzing prism is inserted in the scattered beam. This method

* This work was supported by the Office of Naval Research.

† Present address: Film Dept., E. I. DuPont de Nemours & Company, Experimental Station, Wilmington, Delaware.

‡ Present address: Physics Department, University of Thessaloniki, Greece.

[1] γ is the angle between the direction of observation and the reverse direction of the incident beam.

[2] They are briefly reviewed by R. Tabibian and W. Heller, J. Coll. Sci. **12**, 25 (1957).

yields the "scattering ratio."[2] The latter arrangement deserves preference for experimental reasons discussed elsewhere.[3] The theoretical data are, as will be seen, applicable to both procedures if the scattering particles are isotropic spheres. The data to be reported here are derived from the individual Mie-data given previously[4] for $\gamma=90°$, $\alpha=0.2(0.2)$ 15.2 and $m=1.05(0.05)$ 1.30, α and m having been defined previously (e.g., footnote 4).

I. DEFINITIONS

The depolarization of light scattered at $\gamma=90°$, as defined by Gans,[5] is

$$\theta=0.5\,J_u/(J_\perp-J_{||}). \tag{1}$$

Here, J is the intensity, in ergs cm^{-2} sec^{-1}, of the radiation scattered by one sphere from *incident unpolarized light*. The subscripts $\perp$ and $||$ indicate that the electric vector of the scattered light vibrates perpendicular and parallel, respectively, to the plane of observation and the subscript u identifies that portion of the scattered light which represents natural (unpolarized) light. The quantity θ, therefore, represents the intensity of the "depolarizing" component in the scattered light relative to that of the excess polarized light. The term depolarization was introduced in order to express numerically the deviation of scattered light in a given system from the state of complete polarization expected at $\gamma=90°$ from Rayleigh spheres ($J_{||}=0$) in absence of multiple scattering. On considering $J_{||}$ as the depolarizing component which is customary and justified, without qualification, as long as $J_{||}<J_\perp$:

$$\theta=J_{||}/(J_\perp-J_{||}) \tag{1a}$$

Another definition of depolarization, also introduced by Gans,[5]

$$\Delta=J_{||}/J_\perp=\theta/(\theta+1), \tag{2}$$

has found more general acceptance. An alternate designation of the latter ratio is "polarization ratio," a term introduced by LaMer and associates.[6] The latter term is preferable if this ratio is used as a criterion of particle size at angles γ other than 90°, as done by these authors, since the ratio is then finite even for Rayleigh spheres.

Since it is, for many purposes, more interesting to have a quantitative measure for the excess of polarized light rather than the excess of unpolarized light[7] in the laterally scattered beam, it is useful to recall the definition of the "degree of polarization,"

$$P_{90°}=(J_\perp-J_{||})/(J_\perp+J_{||}), \tag{4}$$

introduced by Mie.[8] The quantities defined are, of course, easily interconvertible:

$$P_{90°}=J_{||}/J_t\theta=[(1/\Delta)-1](J_{||}/J_t) \tag{5}$$

where the total scattered light $J_t=(J_\perp+J_{||})$.

The scattering ratio is, by definition,[3,9]

$$\sigma=J_{||}/J_\perp, \tag{6}$$

where, this time, the subscripts refer to the direction of the electric vector of the *linearly polarized incident beam* with respect to the plane of observation and J represents the *total* intensity scattered from the respective component of the incident beam. The difference in meaning of the subscripts to J in Eqs. (6) and (2) can lead to ambiguity unless it is clearly stated, or follows from the context, as to which of the two quantities is meant in a given instance.[10] This ambiguity is avoided by the use of two subscripts of which the first refers to the incident beam and the second, joined to the first by an arrow, refers to the scattered beam. Thus, $J_{\perp\to||}$ identifies the component vibrating parallel to the plane of observation, which is scattered from an incident linearly polarized beam vibrating perpendicular to the plane of observation. On applying this symbolism

$$\Delta=J_{u\to||}/J_{u\to\perp} \tag{2a}$$

$$\sigma=J_{||\to t}/J_{\perp\to t}. \tag{6a}$$

In the case of isotropic spheres

$$J_{\perp\to||}=J_{||\to\perp}=0 \tag{7}$$

---

[2] W. Heller and R. Tabibian (to be published elsewhere).

[3] W. J. Pangonis, W. Heller, and N. A. Economou, J. Chem. Phys. **34**, 960 (1961).

[4] R. Gans, Phys. Z. **28**, 661 (1927).

[5] G. Mie, Ann. Physik **25**, 377 (1908).

[6] D. Sinclair and V. K. LaMer, Chem. Revs. **44**, 245 (1949), and a series of later papers by La Mer and co-workers; see also M. Kerker, J. Colloid Sci. **5**, 165 (1950), and later papers.

[7] The most direct formulation of this excess would be the "degree of naturalization"

$$N=2J_{||}/(J_{||}+J_\perp) \tag{3}$$

representing the ratio of unpolarized to total scattered light.

[8] W. Heller and M. Nakagaki, J. Chem. Physics **31**, 1188 (1959).

[9] A precedent to this situation arose during Krishnan's interesting work [R. S. Krishnan, Proc. Ind. Acad. Sci. **1A**, 782 (1935), and later papers] concerned with the four components of light scattered from nonisotropic particles of a size not negligible with the dimensions of the wavelength: the components vibrating parallel and perpendicular, respectively, to the plane of observation if the electric vector of the incident linearly polarized beam is perpendicular to the plane of observation and the corresponding components if the electric vector of the incident beam is parallel to the plane of observation. Krishnan resolved this problem by introducing for the four components, in the order named, the following symbols: H_v, V_v, H_h, V_h. On applying this to Eq. (2):

$$\Delta=(H_v+H_h)/(V_v+V_h). \tag{2a}$$

This symbolism has generally been accepted. Although it eliminated the risk of ambiguity, it suffers from two disadvantages: (1) The symbols $H(h)$ and $V(v)$, which stand for horizontal and vertical, respectively, presuppose that the plane of observation is horizontal which is often, but not always true; (2) it is necessary to memorize that the capital letters refer to the scattered beam and the small ones to the incident beam. A further disadvantage is that the symbolism does not indicate which light scattering quantity is involved (i, I, I, etc.). This is immaterial only if ratios are considered.

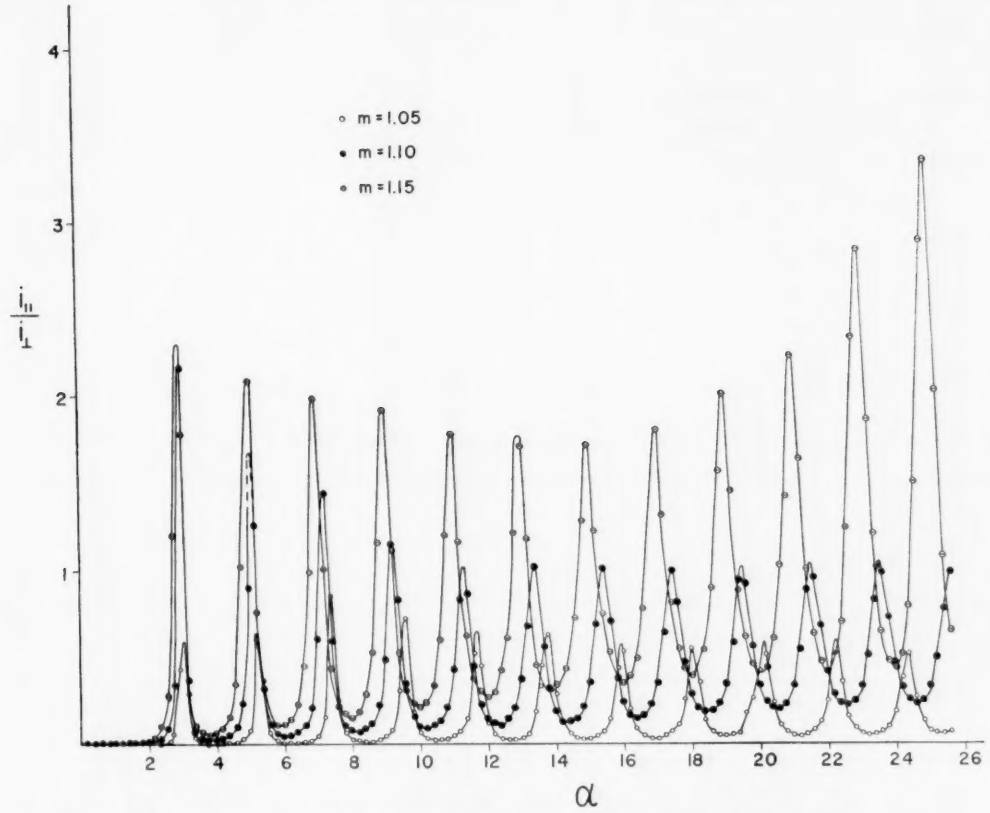

FIG. 1. Scattering ratio and depolarization at an angle of observation γ of 90°. I. relative refractive indices, m: 1.05, 1.10, 1.15.

at any α and m and, therefore,

$$\sigma = \Delta. \tag{8}$$

The results reported here represent, therefore, both depolarization and scattering ratio.

The primary theoretical data obtained from the Mie theory are the values of the dimensionless quantity $i(\alpha, m, \gamma)$.[11] The quantity J is directly proportional to i. The same applies to the experimental quantities I/I_0 and I/I_0c.[11] Their ratio is, therefore, identical with the theoretical ratio

$$\sigma_0 = \Delta_0 = i_{\parallel}/i_{\perp} \tag{9}$$

provided the necessary extrapolations, discussed in Sec. III, have been carried out. This condition of identity is symbolized by the subscript 0.

II. RESULTS

The numerical values of $i_{\parallel}/i_{\perp}$ are given in Table I. The results are illustrated by Figs. 1–3. The α value associated with a given $i_{\parallel}/i_{\perp}$ value ceases to be single-valued beyond the first maximum of $i_{\parallel}/i_{\perp}$ which occurs at $\alpha = 3.0$ and 2.7 if $m = 1.05$ and 1.30, respectively. This corresponds to a particle diameter of 390 and 350 mμ, respectively, on operating with the green Hg line (λ_0: 5460.7 A). On carrying out measurements at two wavelengths so as to differentiate between the first ascending and first descending branches of the $\sigma(\alpha)$ curve, the range of single-valuedness can be extended to approximately 530 and 450 mμ, respectively. This single-valuedness presupposes, of course, that it is *a priori* certain that the particle size in the systems to be investigated, while unknown numerically, is not in excess of the limits stated. If this information is not available, measurements at three widely spaced wavelengths are necessary and generally sufficient[3] in order to obtain single-valued results. More conclusive, and more elegant but also more time consuming, is the compilation of the spectra of σ.

The optimum resolving power of σ, at α values midway between a minimum and a maximum, is quite remarkable. Thus, at the intermediate m value of 1.20, the resolving power, in terms of $\Delta\alpha$, is at midheight of

[11] For a definition of these symbols see W. Heller, M. Nakagaki, and M. L. Wallach, J. Chem. Phys. **30**, 444 (1959); or W. Heller and W. J. Pangonis, *ibid.* **26**, 498 (1957).

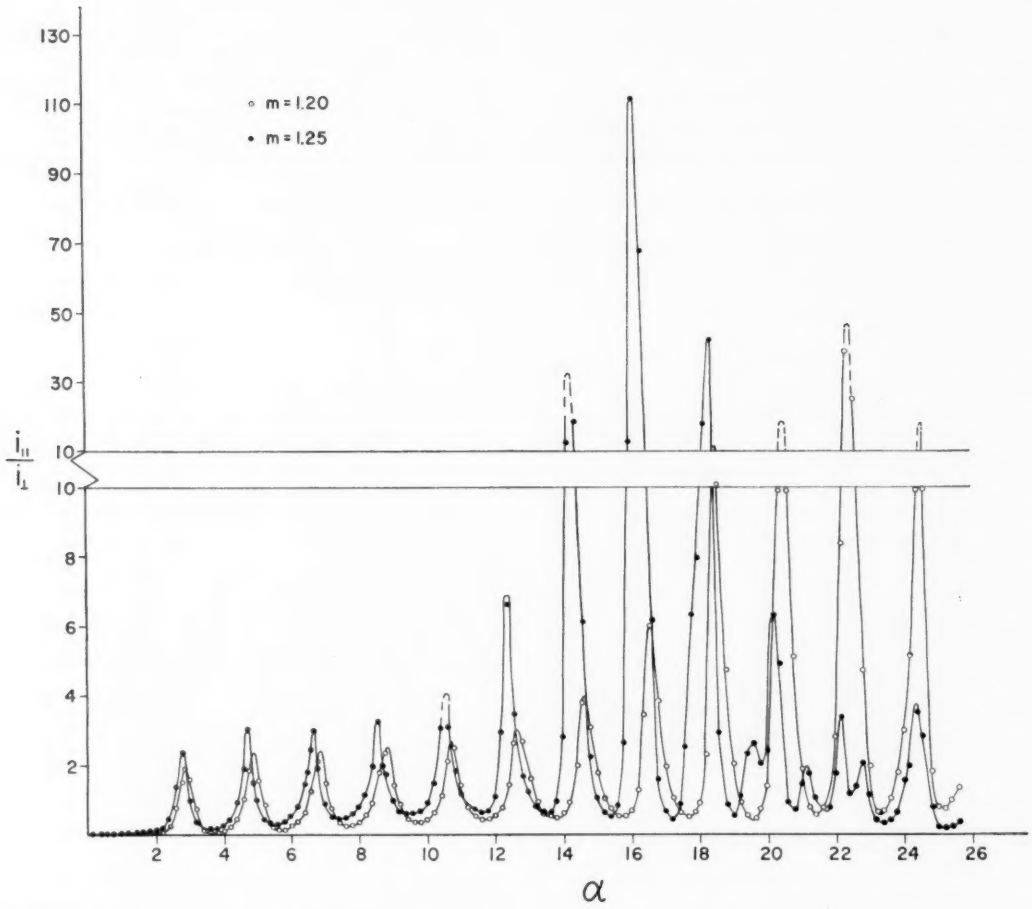

FIG. 2. Scattering ratio and depolarization at an angle of observation γ of 90°. II. relative refractive indices: 1.20, 1.25.

the first-order wave ($\alpha \sim 2.6$) 0.001, corresponding to a particle diameter differential of slightly less than 1 A if $\lambda_0 = 5461$ A on assuming a conservative uncertainty in σ determinations of 1%. This optimum resolving power changes fairly little with either m or the order of the wave. Thus one obtains, for instance, for the seventh-order wave at $m = 1.30$, whose amplitude is very large, an optimum resolving power of approximately 2.5 A under the conditions stated. Since proper choice of the wavelength should allow one to use always the midheight of the pertinent wave, extremely accurate particle size determinations are possible (in strictly monodisperse systems) once the problem of multivaluedness of answers is eliminated. The only restriction to this generalization is that the range of very small particle sizes defined by α values of less than approximately 2 at $m = 1.05$ and of less than approximately 1.5 at $m = 1.30$ must be excluded. Here the absolute value of $J_{\parallel}$ becomes so small that precise experimental determination is difficult or even impossible.[12]

Rayleigh scattering ($\alpha \to 0$) is characterized by perfect polarization. The inverse statement, often found, to the effect that absence of appreciable depolarization indicates a small particle size, is not true. This is immediately apparent from the figures given. An example may illustrate this: the degree of polarization is 98.9% at the first minimum, if $m = 1.05$, (particle diameter of 5200 A if $\lambda_0 = 5460.7$ A). Equally interesting is the fact that at sufficiently large α and m values an almost perfect negative degree of polarization may be obtained. Thus, $-P_{\parallel}$ has the value of 98.9% at the seventh maximum if $m = 1.30$. Negative values of P approach-

[12] Individual measurements of the experimental quantities corresponding to $i_{\perp}$ or $i_{\parallel}$ can, of course, also be made very sensitive to changes in particle size by adopting the method of midheight measurement here proposed; however, the sensitivity of σ is superior since the near coincidence of $i_{\perp}$ and $i_{\parallel}$ minima (footnote 4) leads to larger maximal $d\sigma/d\alpha$ values.

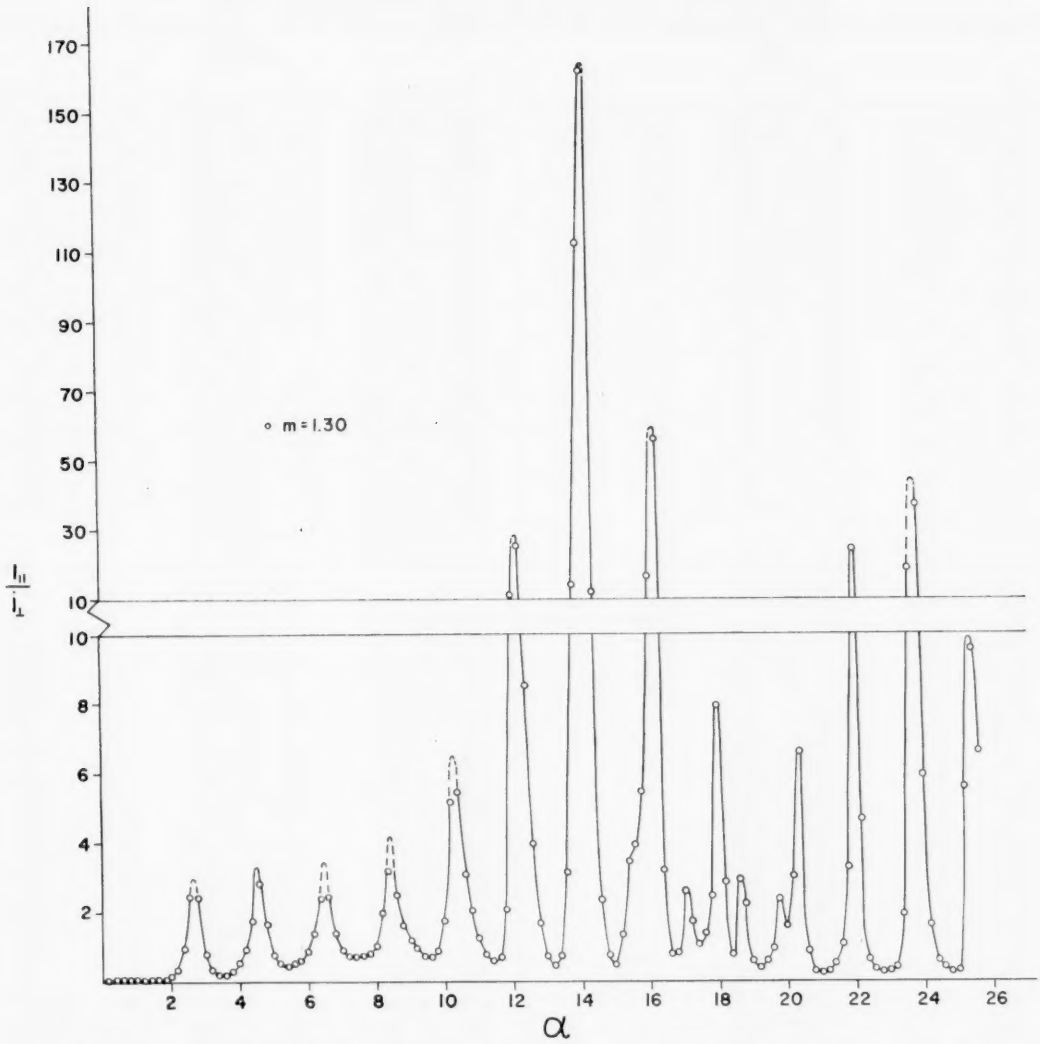

FIG. 3. Scattering ratio and depolarization at an angle of observation γ of 90°. III. relative refractive index: 1.30.

ing 1.0 even more closely can be anticipated at the proper maximum if $m>1.30$.

The $\sigma(\alpha)$ curves reflect, except for obvious quantitative differences, the same general features found previously[4] for the individual quantities $i_{||}$, $i_{\perp}$, and i_u. In addition to the prominent secondary maxima and minima of very regular periodicity, one finds, again, primary and tertiary maxima and minima.

The primary maxima essentially coincide with the secondary maxima of largest amplitude. Thus, according to Figs. 1–3, the first primary maximum occurs at $\alpha\gg25$, $\gg25$, >25, ~22.5, ~16.2, and ~14.0 if $m=1.05$, 1.10, 1.15, 1.20, 1.25, and 1.30, respectively. For the latter m value, a second primary maximum is indicated at $\alpha\sim24$. The period of recurrence of these primary maxima, $\Delta\alpha$, is very large. It is about 10 for $m=1.30$ and undoubtedly appreciably larger (see curve for $m=1.25$) at lower m values. It is noteworthy that at low m values the rise to the first primary maximum is preceded by a decline to a minimum.[13] This minimum, like the primary maximum, shifts to lower α values as m increases. It vanishes between $m=1.15$ and $m=1.20$.

The primary undulations may be followed also by considering, instead of the amplitude changes in the

[13] The $m=1.05$ curve shows even a shallow maximum at $\alpha\sim7$ which, however, is not pronounced enough to affirm its existence positively.

TABLE I. Scattering ratio and depolarization for nonabsorbing spheres ($\gamma=90°$).

$m=1.05$

α	σ	α	σ	α	σ
0.6	0.0_6223	10.0	0.0650	19.4	0.0541
0.8	0.0_5235	10.2	0.0341	19.6	0.0851
1.0	0.0_4236	10.4	0.0238	19.8	0.1691
1.2	0.0_4584	10.6	0.0217	20.0	0.4015
1.4	0.0_3135	10.8	0.0251	20.2	0.5072
1.6	0.0_3299	11.0	0.0348	20.4	0.2319
1.8	0.0_3641	11.2	0.0632	20.6	0.1097
2.0	0.00136	11.4	0.1517	20.8	0.0648
2.2	0.00288	11.6	0.5132	21.0	0.0480
2.4	0.00635	11.8	0.4443	21.2	0.0443
2.6	0.0152	12.0	0.1354	21.4	0.0509
2.8	0.0491	12.2	0.0602	21.6	0.0717
3.0	0.4356	12.4	0.0361	21.8	0.1232
3.2	0.3013	12.6	0.0279	22.0	0.2640
3.4	0.0428	12.8	0.0260	22.2	0.5150
3.6	0.0151	13.0	0.0321	22.4	0.3719
3.8	0.00782	13.2	0.0491	22.6	0.1692
4.0	0.00560	13.4	0.0969	22.8	0.0892
4.2	0.00569	13.6	0.2592	23.0	0.0594
4.4	0.00786	13.8	0.6317	23.2	0.0489
4.6	0.0135	14.0	0.2889	23.4	0.0503
4.8	0.0289	14.2	0.1092	23.6	0.0633
5.0	0.0861	14.4	0.0572	23.8	0.0977
5.2	0.6010	14.6	0.0360	24.0	0.1772
5.4	0.3725	14.8	0.0302	24.2	0.3777
5.6	0.0709	15.0	0.0321	24.4	0.5189
5.8	0.02828	15.2	0.0434	24.6	0.2701
6.0	0.01573	15.4	0.0726	24.8	0.1302
6.2	0.0114	15.6	0.1560	25.0	0.0782
6.4	0.0114	15.8	0.4251	25.2	0.0580
6.6	0.0149	16.0	0.5247	25.4	0.0531
6.8	0.0247	16.2	0.2015	25.6	0.0602
7.0	0.05349	16.4	0.0922		
7.2	0.1664	16.6	0.0527		
7.4	0.8687	16.8	0.0382		
7.6	0.2644	17.0	0.0355		
7.8	0.0721	17.2	0.0415		
8.0	0.0327	17.4	0.0604		
8.2	0.0202	17.6	0.1093		
8.4	0.0166	17.8	0.2560		
8.6	0.0178	18.0	0.5686		
8.8	0.0246	18.2	0.3602		
9.0	0.0419	18.4	0.1432		
9.2	0.0904	18.6	0.0745		
9.4	0.3043	18.8	0.0497		
9.6	0.7277	19.0	0.0408		
9.8	0.1840	19.2	0.0422		

$m=1.10$

α	σ	α	σ	α	σ
0.4	0.0_5175	4.2	0.02876	8.0	0.07993
0.6	0.0_4975	4.4	0.0468	8.2	0.07066
0.8	0.0_4371	4.6	0.0923	8.4	0.08072
1.0	0.0_3983	4.8	0.2353	8.6	0.11686
1.2	0.0_3248	5.0	0.9057	8.8	0.21070
1.4	0.0_3590	5.2	1.2421	9.0	0.48612
1.6	0.00135	5.4	0.3136	9.2	1.16668
1.8	0.00304	5.6	0.12153	9.4	0.83920
2.0	0.00673	5.8	0.06665	9.6	0.33955
2.2	0.0150	6.0	0.04836	9.8	0.17347
2.4	0.0345	6.2	0.04784	10.0	0.11390
2.6	0.09172	6.4	0.0623	10.2	0.09492
2.8	0.3380	6.6	0.1034	10.4	0.09960
3.0	2.1707	6.8	0.2173	10.6	0.13004
3.2	0.3575	7.0	0.60816	10.8	0.21091
3.4	0.0931	7.2	1.42534	11.0	0.42253
3.6	0.0409	7.4	0.59659	11.2	0.92715
3.8	0.0256	7.6	0.22299	11.4	0.96449
4.0	0.02311	7.8	0.11666	11.6	0.45850

$m=1.10$

α	σ	α	σ	α	σ
11.8	0.23516	16.6	0.17110	21.4	0.88525
12.0	0.15097	16.8	0.22573	21.6	0.95596
12.2	0.12036	17.0	0.35367	21.8	0.65189
12.4	0.11769	17.2	0.63383	22.0	0.40753
12.6	0.14346	17.4	0.99057	22.2	0.28367
12.8	0.21396	17.6	0.82378	22.4	0.22928
13.0	0.38655	17.8	0.47497	22.6	0.21764
13.2	0.77920	18.0	0.28968	22.8	0.24612
13.4	1.01247	18.2	0.20840	23.0	0.33071
13.6	0.58313	18.4	0.17952	23.2	0.51535
13.8	0.30405	18.6	0.18593	23.4	0.82021
14.0	0.19072	18.8	0.23138	23.6	0.97863
14.2	0.14540	19.0	0.34350	23.8	0.72765
14.4	0.13701	19.2	0.58639	24.0	0.46668
14.6	0.15764	19.4	0.94421	24.2	0.32159
14.8	0.21967	19.6	0.91497	24.4	0.25397
15.0	0.36600	19.8	0.56641	24.6	0.23443
15.2	0.68947	20.0	0.34875	24.8	0.25593
15.4	1.01120	20.2	0.24515	25.0	0.33088
15.6	0.70824	20.4	0.20350	25.2	0.49437
15.8	0.38480	20.6	0.20108	25.4	0.77587
16.0	0.23765	20.8	0.23791	25.6	0.98236
16.2	0.17464	21.0	0.33603		
16.4	0.15706	21.2	0.54770		

$m=1.15$

α	σ	α	σ	α	σ
0.4	0.0_5442	9.0	1.9147	17.6	0.5570
0.6	0.0_4230	9.2	1.1268	17.8	0.4340
0.8	0.0_4808	9.4	0.5323	18.0	0.3892
1.0	0.0_3231	9.6	0.3117	18.2	0.4154
1.2	0.0_3586	9.8	0.2308	18.4	0.5446
1.4	0.00145	10.0	0.2141	18.6	0.8820
1.6	0.00334	10.2	0.2468	18.8	1.5776
1.8	0.00817	10.4	0.3496	19.0	2.0154
2.0	0.01900	10.6	0.6007	19.2	1.4431
2.2	0.0441	10.8	1.2002	19.4	0.8916
2.4	0.1058	11.0	1.7896	19.6	0.6010
2.6	0.2917	11.2	1.1619	19.8	0.4587
2.8	1.1941	11.4	0.6138	20.0	0.4086
3.0	1.7850	11.6	0.3823	20.2	0.4407
3.2	0.3615	11.8	0.2896	20.4	0.6013
3.4	0.1269	12.0	0.2659	20.6	1.0282
3.6	0.0680	12.2	0.2974	20.8	1.8975
3.8	0.05319	12.4	0.4036	21.0	2.3698
4.0	0.05959	12.6	0.6613	21.2	1.6364
4.2	0.08870	12.8	1.2271	21.4	0.9773
4.4	0.16212	13.0	1.7148	21.6	0.6339
4.6	0.3583	13.2	1.1799	21.8	0.4707
4.8	1.0216	13.4	0.6784	22.0	0.4183
5.0	2.0844	13.6	0.4468	22.2	0.4698
5.2	0.7849	13.8	0.3467	22.4	0.6838
5.4	0.2941	14.0	0.3165	22.6	1.2369
5.6	0.15509	14.2	0.3437	22.8	2.3380
5.8	0.1070	14.4	0.4498	23.0	2.8219
6.0	0.1078	14.6	0.7150	23.2	1.8519
6.2	0.1395	14.8	1.2769	23.4	1.0522
6.4	0.2270	15.0	1.7158	23.6	0.6487
6.6	0.4506	15.2	1.2261	23.8	0.4705
6.8	0.99946	15.4	0.7424	24.0	0.4279
7.0	1.9866	15.6	0.5034	24.2	0.5109
7.2	1.0160	15.8	0.3951	24.4	0.7913
7.4	0.4276	16.0	0.3596	24.6	1.4975
7.6	0.2373	16.2	0.3849	24.8	2.8873
7.8	0.1714	16.4	0.4967	25.0	3.3374
8.0	0.1604	16.6	0.7802	25.2	2.0213
8.2	0.1926	16.8	1.3769	25.4	1.0742
8.4	0.2893	17.0	1.8000	25.6	0.6412
8.6	0.5334	17.2	1.3092		
8.8	1.1586	17.4	0.8143		

TABLE I.—*Continued.*

$m = 1.20$

α	σ	α	σ	α	σ
0.2	0.0_6963	8.8	2.4431	17.4	0.6654
0.4	0.0_5781	9.0	1.4124	17.6	0.5032
0.6	0.0_4424	9.2	0.7372	17.8	0.5364
0.8	0.0_3148	9.4	0.4786	18.0	0.9007
1.0	0.0_3427	9.6	0.3867	18.2	2.3148
1.2	0.00112	9.8	0.3838	18.4	7.6258
1.4	0.00285	10.0	0.4614	18.6	10.4420
1.6	0.00712	10.2	0.6629	18.8	4.7766
1.8	0.0176	10.4	1.1475	19.0	2.0456
2.0	0.0428	10.6	2.1808	19.2	0.9632
2.2	0.1028	10.8	2.4821	19.4	0.5714
2.4	0.25474	11.0	1.4451	19.6	0.4978
2.6	0.7212	11.2	0.8337	19.8	0.7188
2.8	2.487	11.4	0.5722	20.0	1.5746
3.0	1.268	11.6	0.4695	20.2	4.9255
3.2	0.3443	11.8	0.4602	20.4	22.0252
3.4	0.14915	12.0	0.5426	20.6	19.4616
3.6	0.1008	12.2	0.7813	20.8	5.1688
3.8	0.09891	12.4	1.4241	21.0	1.6862
4.0	0.1332	12.6	2.7197	21.2	0.7469
4.2	0.2241	12.8	2.6831	21.4	0.5226
4.4	0.4409	13.0	1.5792	21.6	0.6508
4.6	1.0293	13.2	0.9587	21.8	1.1968
4.8	2.3712	13.4	0.6583	22.0	2.7804
5.0	1.53381	13.6	0.5222	22.2	8.3870
5.2	0.5715	13.8	0.4981	22.4	38.9778
5.4	0.2858	14.0	0.5926	22.6	26.2399
5.6	0.1998	14.2	0.9327	22.8	3.7064
5.8	0.1915	14.4	1.9874	23.0	1.0888
6.0	0.2422	14.6	3.8352	23.2	0.6083
6.2	0.37532	14.8	3.1248	23.4	0.6724
6.4	0.6763	15.0	1.7841	23.6	1.0381
6.6	1.4026	15.2	1.0693	23.8	1.7633
6.8	2.42417	15.4	0.7001	24.0	2.9740
7.0	1.4766	15.6	0.5304	24.2	5.1628
7.2	0.6687	15.8	0.5050	24.4	13.2497
7.4	0.3867	16.0	0.6612	24.6	9.9866
7.6	0.2933	16.2	1.2979	24.8	1.7426
7.8	0.2877	16.4	3.4712	25.0	0.7513
8.0	0.3560	16.6	6.0972	25.2	0.7519
8.2	0.5298	16.8	3.8530	25.4	0.9950
8.4	0.9179	17.0	1.9983	25.6	1.3372
8.6	1.7822	17.2	1.0887		

$m = 1.25$

α	σ	α	σ	α	σ
0.2	0.0_6631	5.0	1.0075	9.8	0.6716
0.4	0.0_4130	5.2	0.4764	10.0	0.8770
0.6	0.0_4679	5.4	0.3241	10.2	1.4873
0.8	0.0_3241	5.6	0.3037	10.4	3.0362
1.0	0.0_3703	5.8	0.3679	10.6	3.2627
1.2	0.00189	6.0	0.5228	10.8	1.8988
1.4	0.00496	6.2	0.8258	11.0	1.1672
1.6	0.01297	6.4	1.48354	11.2	0.8413
1.8	0.0337	6.6	2.5510	11.4	0.6803
2.0	0.0854	6.8	1.94896	11.6	0.6206
2.2	0.2089	7.0	0.95896	11.8	0.6939
2.4	0.5152	7.2	0.5840	12.0	1.1240
2.6	1.462	7.4	0.4658	12.2	2.9369
2.8	2.948	7.6	0.46936	12.4	6.6355
3.0	0.9461	7.8	0.56047	12.6	4.4623
3.2	0.3261	8.0	0.74469	12.8	2.2010
3.4	0.1797	8.2	1.12047	13.0	1.2466
3.6	0.1506	8.4	1.98697	13.2	0.8066
3.8	0.1802	8.6	2.7332	13.4	0.6034
4.0	0.2765	8.8	1.7460	13.6	0.5773
4.2	0.49088	9.0	1.0210	13.8	0.9050
4.4	0.9810	9.2	0.7216	14.0	2.7474
4.6	2.1462	9.4	0.6126	14.2	12.8451
4.8	2.4301	9.6	0.6027	14.4	18.7080

$m = 1.25$

α	σ	α	σ	α	σ
14.6	6.1022	18.4	32.8368	22.2	3.3244
14.8	2.2597	18.6	2.9557	22.4	1.1847
15.0	1.0421	18.8	0.8245	22.6	1.3758
15.2	0.6147	19.0	0.5351	22.8	2.0968
15.4	0.5090	19.2	1.0496	23.0	1.1721
15.6	0.8212	19.4	2.3413	23.2	0.4620
15.8	2.6985	19.6	2.6253	23.4	0.3280
16.0	13.0159	19.8	2.0164	23.6	0.3382
16.2	112.8375	20.0	2.4487	23.8	0.6211
16.4	67.6751	20.2	6.2398	24.0	1.5777
16.6	6.2399	20.4	4.8981	24.2	1.8073
16.8	1.5483	20.6	0.9975	24.4	3.5158
17.0	0.6814	20.8	0.7349	24.6	2.8539
17.2	0.4851	21.0	1.4854	24.8	0.7171
17.4	0.8525	21.2	1.7867	25.0	0.2878
17.6	2.6626	21.4	1.0674	25.2	0.1970
17.8	6.3102	21.6	0.7431	25.4	0.2120
18.0	7.9547	21.8	0.7795	25.6	0.3635
18.2	18.2215	22.0	1.4814		

$m = 1.30$

α	σ	α	σ	α	σ
0.2	0.0_5101	10.0	1.7244	19.8	2.3991
0.4	0.0_4185	10.2	5.1809	20.0	1.5128
0.6	0.0_3102	10.4	5.4308	20.2	3.0145
0.8	0.0_3359	10.6	3.0959	20.4	6.5835
1.0	0.00106	10.8	2.0000	20.6	0.8976
1.2	0.00293	11.0	1.2382	20.8	0.2732
1.4	0.00799	11.2	0.7354	21.0	0.2415
1.6	0.0220	11.4	0.5460	21.2	0.2841
1.8	0.0601	11.6	0.6853	21.4	0.5458
2.0	0.1571	11.8	2.0736	21.6	1.0800
2.2	0.3841	12.0	11.8075	21.8	3.2356
2.4	0.9288	12.2	25.0256	22.0	24.1803
2.6	2.4312	12.4	8.4913	22.2	4.6708
2.8	2.4524	12.6	3.9331	22.4	0.6145
3.0	0.7416	12.8	1.6713	22.6	0.3601
3.2	0.32116	13.0	0.7259	22.8	0.2352
3.4	0.2260	13.2	0.4642	23.0	0.2520
3.6	0.2338	13.4	0.7488	23.2	0.3571
3.8	0.3216	13.6	3.1868	23.4	1.8884
4.0	0.5191	13.8	14.0046	23.6	19.0808
4.2	0.915	14.0	111.5484	23.8	36.9299
4.4	1.766	14.2	162.7494	24.0	5.9331
4.6	2.857	14.4	12.0737	24.2	1.6072
4.8	1.662	14.6	2.3917	24.4	0.5819
5.0	0.766	14.8	0.7417	24.6	0.3150
5.2	0.50322	15.0	0.4734	24.8	0.2637
5.4	0.45735	15.2	1.3138	25.0	0.2436
5.6	0.51746	15.4	3.4341	25.2	5.5641
5.8	0.64920	15.6	3.9579	25.4	9.5901
6.0	0.88026	15.8	5.4900	25.6	6.5920
6.2	1.37789	16.0	16.4364		
6.4	2.38787	16.2	55.9754		
6.6	2.41098	16.4	3.2700		
6.8	1.36340	16.6	0.7121		
7.0	0.8917	16.8	0.8351		
7.2	0.7433	17.0	2.5247		
7.4	0.7252	17.2	1.7096		
7.6	0.7377	17.4	1.0510		
7.8	0.7963	17.6	1.3910		
8.0	1.0524	17.8	2.4845		
8.2	1.9046	18.0	7.9127		
8.4	3.2131	18.2	2.8271		
8.6	2.4488	18.4	0.7683		
8.8	1.5831	18.6	2.8802		
9.0	1.1812	18.8	2.2294		
9.2	0.9515	19.0	0.5773		
9.4	0.7583	19.2	0.3997		
9.6	0.6717	19.4	0.5136		
9.8	0.8146	19.6	0.9592		

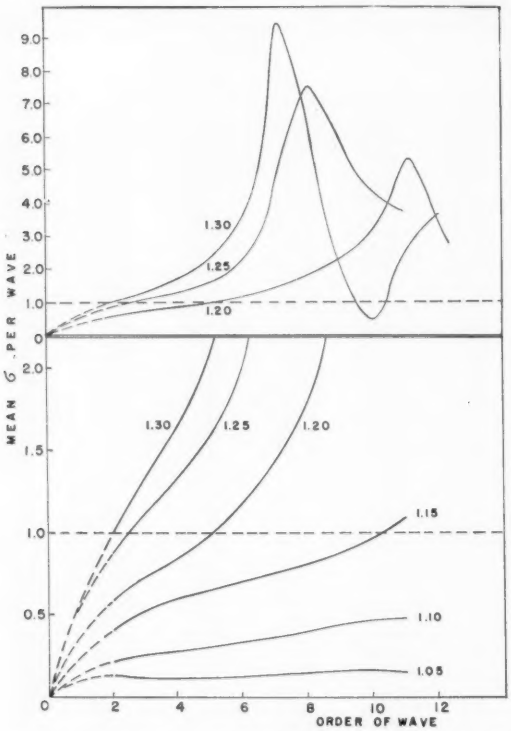

FIG. 4. Variation of the mean scattering ratio and depolarization, per wave, with α. Parameter: relative refractive index.

prominent secondary structure, rather the average $i_{||}/i_{\perp}$ values per secondary wave, of order n,

$$\langle\sigma\rangle_n=\langle\Delta\rangle_n=(\langle i_{||}\rangle/\langle i_{\perp}\rangle)_n.$$

They may be obtained from the $i_{||}$ and $i_{\perp}$ values directly, or, more simply, from the relationship

$$\langle\sigma\rangle_n=(\bar{\sigma}_{\min_n}\sigma_{\max_n})^{\frac{1}{2}},$$

where $\bar{\sigma}_{\min_n}$ refers to the average minimal σ value at the inception and upon completion of the nth wave and $\sigma_{\max_n}$ refers to the peak value of σ for the same wave. The results thus obtained are illustrated by Fig. 4. These averages are of particular interest with regard to the prospective behavior of polydisperse systems (see the following).

The existence of insufficiently resolved tertiary maxima and minima is indicated at α values >18 and >15 if $m=1.25$ and 1.30, respectively, (see Figs. 1–3). At lower α and m values the amplitude of these short period oscillations seems to be too small to be detectable. It would be of interest to ascertain as to whether and to what extent there is a relationship between the "frequency" (oscillations per unit α) of undulations in the primary, secondary, and tertiary structure such as exists between fundamentals and overtones. The period of the primary structure, unfortunately, is too large and the tertiary structure too little resolved in order to allow a definite statement on the basis of the results computed thus far.

The data given can be strictly applied only to monodisperse systems. In view of the large amplitude of the oscillations of the $\sigma(\Delta)$ values compared to that of the individual quantities, $i_{\perp}$ and i_u, it is *a priori* clear that the scattering ratio (depolarization) is particularly sensitive to heterodispersion. A comparison of the curves in Fig. 4 with the corresponding curves in Figs. 1–3 shows the change in $\sigma(\Delta)$ to be expected in shifting from a monodisperse system defined by α to a moderately heterodisperse system, defined by $\bar{\alpha}$, whose particle size distribution approximates in its contour that of the σ oscillation in the $\Delta\alpha$ interval of the nth wave. Because of this particularly high sensitivity of the scattering ratio (depolarization) to heterodispersion, this light scattering quantity was selected for the determination of size distribution curves from light scattering. The theoretical background of this method—which in the meantime has been applied successfully[14]—will be discussed in a following paper.

III. REQUIREMENTS FOR A PRACTICAL APPLICATION OF THE THEORETICAL DATA ON LATERAL SCATTERING

The relative intensity of light scattered by one sphere in a particular direction of observation, defined by γ, is, at a given α and m,

$$J_{\gamma}=(\lambda^2/4\pi^2r^2)i_{\gamma}, \tag{10}$$

if the incident unpolarized beam has unit intensity and if the photometric distance, $r\gg\lambda$. The dimensionless quantity J represents, therefore, the scattered radiant energy which passes, at γ, per unit time and unit area through a differential surface element of a sphere of radius r, the center of which contains the scattering sphere exposed to an influx of radiant energy of 1 erg/cm^2 and per sec. If the incident beam is linearly polarized, i and, therefore, J depend also on the azimuthal angle, Φ, i.e., the angle between the direction of observation and the electric vector of the former. For the general case, therefore,

$$J_{\gamma,\Phi}=(\lambda^2/4\pi^2r^2)i_{\gamma,\Phi}. \tag{10a}$$

The values of Φ considered here and in preceding investigations of this series, are either 0° or 90° ($i_{||}$ and $i_{\perp}$, respectively). Experiments are carried out with a system containing many spheres, with an incident beam whose intensity is not unity and one measures the scattered radiation which goes, at r, through a finite surface section ΔS of the photometric sphere. (Except for minor corrections necessary for curvature, ΔS is identical with the area of the entrance pupil of

[14] A. F. Stevenson, W. Heller, and M. Wallach (to be published).

the photometric device used for the measurements, provided that the photosensitive area of the device $\geqslant \Delta S$.) While, therefore, under idealized conditions, the experimentally determined intensity

$$I' = JNI_0 dS, \tag{11}$$

where I_0 is the intensity of the incident beam and N is the number of spheres per ml, Eq. (11) becomes an inequality on replacing dS by ΔS. The quantity J is then no longer uniquely defined, but represents an integral value which should be obtained between the limits $\gamma+\Delta\gamma$, $\gamma-\Delta\gamma$, $\Phi+\Delta\Phi$ and $\Phi-\Delta\Phi$. Simple multiplication of $J_{\gamma,\Phi}$ by ΔS would be permissible only if the radiation diagram were spherically symmetrical (proportionality between I' and ΔS) which is not the case. In addition, the scattered radiation of N spheres is not additive on account of multiple scattering which vanishes only as $N \to 1$. In order to obtain experimental data which are strictly comparable with the simple theoretical data, computed for a specific value of γ and Φ, a suitable twofold extrapolation of the former is, therefore, necessary. Double extrapolation yields finite scattering data on considering the experimentally obtained scattering intensity per unit concentration, unit ΔS and unit intensity of the primary beam. Since the concentration is conveniently expressed in terms of the volume fraction of the scattering spheres

$$\phi = N\alpha^3\lambda^3/6\pi^2, \tag{12}$$

the quantities to be compared are

$$(I'/I_0\Delta S\phi) \underset{\phi\to 0}{\overset{\Delta S\to 0}{=\!=}} (6\pi^2/\alpha^3\lambda^3)J. \tag{13}$$

It is, practically, more convenient to consider the solid angle $\omega_0 = \Delta S/r^2$ instead of ΔS. The doubly extrapolated quantity (on the left-hand side) strictly comparable to the theoretical quantity (on the right-hand side) follows then, on setting

$$(I'/\omega) = I$$

as

$$(I/I_0\phi)_0 = (6\pi^2/\lambda^3\alpha^3)Jr^2 = (3/2\lambda\alpha^2)i, \tag{14}$$

where the subscript 0 symbolizes the value obtained by extrapolation to $\phi \to 0$ and $\omega_0 \to 0$.[15]

The preceding discussion is of primary importance, of course, only for the practical utilization of individual light scattering data reported in preceding publications of this series. Nevertheless, the same arguments apply for the determination of intensity ratios, such as dissymmetry, scattering ratio and depolarization. Failure to extrapolate the experimentally determined ratios to zero concentration will lead here to smaller but still appreciable errors[16] since the effect of multiple scattering is, at constant α and m, different for the two components of the ratio. The same applies, although to a far lesser extent,[16] to the effect of the solid angle. The error resulting from the use of data obtained at a finite solid angle is caused here by the fact that the contours of the sectional radiation diagram defined by ω_0 are different for the two components. This may be neglected only if $\omega_0 \leqslant 15\times10^{-4}$ sr. At these very small angles, σ is within the limits of minimum experimental errors, proportional to ω_0.[16]

[15] Extrapolation of light scattering quantities to zero solid angle is quite generally not carried out. In fact, none of the available commercial instruments allows one to do this. Consequently, the great majority of published experimental data is affected by the resulting error since it varies with α and m and is, therefore, not fully eliminated by the use of a single empirical instrument constant. In very many of these cases, though, the error is most likely smaller than the cumulative error due to other sources. A detailed discussion of the experimental "solid angle error" has been given on the basis of systematic experimentation by R. Tabibian and W. Heller [J. Colloid Sci. **13**, 6 (1958)].

[16] W. Heller and R. Tabibian (to be published elsewhere).

NMR Spectra of Glycidaldehyde

C. A. REILLY AND J. D. SWALEN
Shell Development Company, Emeryville, California

(Received July 15, 1960)

The NMR spectra of glycidaldehyde were measured at 40 and 60 Mc/sec.

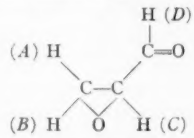

These complicated spectra of four interacting protons were analyzed by two methods: the $ABKY$ approximation and the iterated $ABCD$ solution. The various mathematical techniques developed should prove useful in the analyses of other complicated spin resonance spectra.

The following spin-spin coupling constants, J_{ij} in cycles per second and chemical shifts, δ_i in parts per million (relative to tetramethylsilane) were found:

	J_{AB}	J_{AC}	J_{BC}	J_{AD}	J_{BD}	J_{CD}	δ_A	δ_B	δ_C	δ_D
40 Mc/sec	5.54	2.04	4.90	−0.03	−0.32	6.36	3.096	3.158	3.356	8.922
60 Mc/sec	5.54	2.09	4.87	+0.03	−0.31	6.24	3.098	3.166	3.356	8.922

The first three coupling constants are very close in magnitude to those obtained in other epoxides (in most cases to within 0.5 cps).

The magnitude of the coupling constant between the aldehyde proton (D) and the adjacent proton (C) indicates that the D proton of the aldehyde group is probably on a time average, mainly in a plane perpendicular to the epoxide ring. The proton (D) could be either *cis* or *trans* to proton (C), but from a consideration of internal rotation interactions, it is probably in the *trans* configuration. The J_{AC} and J_{BC} coupling constants are consistent with an "eclipsed-ethanelike" model rather than with an "ethylenelike" one. The coupling constants across the molecule, J_{AD} and J_{BD}, are an order of magnitude smaller than the other constants. This is in agreement with the approximate attenuation factor of 1/10 for spin-spin coupling through a single bond.

INTRODUCTION

THE usual methods[1] for analyzing NMR spectra in detail are not adequate unless the spectra are relatively simple. For more complex spectra more powerful methods are needed. Recently, iterative methods[2] were developed and applied to the analysis of the NMR spectra of the three interacting protons attached to an epoxide ring. In the present paper these methods are further developed and applied to the analysis of the NMR spectra of four interacting spins. It is found that both the intensities and the positions of *all* lines in the NMR spectra of glycidaldehyde can be accounted for satisfactorily. Reliable NMR parameters can be derived and used, e.g., for the purpose of extending our understanding of the relation between NMR spectra and molecular structure.

The nuclear magnetic resonance spectra of glycidaldehyde

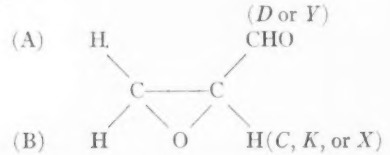

arise from the three ring protons (labeled A, B, and C, K or X) and an aldehyde proton (labeled D or Y). The spins of these four nuclei interact so strongly that complicated spectra are observed. The aldehyde proton gives rise to resonance lines that are well separated from those of the three ring protons, but this proton is strongly spin-spin coupled to the adjacent ring proton and weakly coupled to the other ring protons. The resonance lines from the A and B protons appear with considerable overlapping and even some of the C resonances overlap the AB pattern at 40 Mc/sec.

The assignment of the various lines presents a major problem in the derivation of the various spin-spin coupling constants and the magnetic screening parameters. In the next section we shall give the matrix elements of the general four spin system ($ABCD$). Two methods of analysis will then be discussed. These are the $ABKY$ approximation and an iteration method on the general four spin system ($ABCD$).

In order to aid in the making of an unequivocal assignment, spectra of glycidaldehyde were observed at both 40 and 60 Mc/sec. The 60-Mc/sec spectrum was analyzed by the $ABKY$ approximation followed by the $ABCD$ solution. The 40-Mc/sec spectrum was too highly perturbed (and hence too complicated) to analyze by the $ABKY$ approximation so that the iterative $ABCD$ method was used directly.

[1] See J. A. Pople, W. G. Schneider, and H. J. Bernstein, *High Resolution Nuclear Magnetic Resonance* (McGraw-Hill Book Company, Inc., New York, 1959).
[2] C. A. Reilly and J. D. Swalen, J. Chem. Phys. **32**, 1378 (1960).

TABLE I. Basis functions for a four-spin system.

	A	B	C	D	
1.	α	α	α	α	$F_Z=+2$
1.	β	α	α	α	$F_Z=+1$
2.	α	β	α	α	
3.	α	α	β	α	
4.	α	α	α	β	
1.	β	β	α	α	$F_Z=0$
2.	β	α	β	α	
3.	α	β	β	α	
4.	β	α	α	β	
5.	α	β	α	β	
6.	α	α	β	β	
1.	β	β	β	α	$F_Z=-1$
2.	β	β	α	β	
3.	β	α	β	β	
4.	α	β	β	β	
1.	β	β	β	β	$F_Z=-2$

THEORETICAL BASIS

Matrix for Four-Spin System

The products of spin functions for a four-spin system are used as the basis functions. These are given in Table I where they are sorted by the total Z component of the spin angular momenta (denoted F_Z).

The matrix elements of the Hamiltonian calculated for this system

$$\mathcal{H}=\sum_i h_i I_Z(i)+\sum_{\substack{i,j\\ i<j}} J_{ij}\mathbf{I}_i\cdot\mathbf{I}_j$$

with the aid of angular momentum properties[1]) are presented in Table II. The basis functions of Table I and the matrix elements of Table II are appropriate for any system ($ABCD$) of four nonequivalent spins. The superscript on each diagonal element is the F_Z value for the submatrix to which this element belongs. Furthermore, the ordering of the basis functions of Table I is such that the diagonal matrix elements in

TABLE II. Matrix for a four-spin system.

4×4 Submatrix ($F_Z=+1$)

$$\begin{pmatrix} H_{11}^{+1} & \frac{1}{2}J_{AB} & \frac{1}{2}J_{AC} & \frac{1}{2}J_{AD} \\ \frac{1}{2}J_{AB} & H_{22}^{+1} & \frac{1}{2}J_{BC} & \frac{1}{2}J_{BD} \\ \frac{1}{2}J_{AC} & \frac{1}{2}J_{BC} & H_{33}^{+1} & \frac{1}{2}J_{CD} \\ \frac{1}{2}J_{AD} & \frac{1}{2}J_{BD} & \frac{1}{2}J_{CD} & H_{44}^{+1} \end{pmatrix}$$

4×4 Submatrix ($F_Z=-1$)

$$\begin{pmatrix} H_{11}^{-1} & \frac{1}{2}J_{CD} & \frac{1}{2}J_{BD} & \frac{1}{2}J_{AD} \\ \frac{1}{2}J_{CD} & H_{22}^{-1} & \frac{1}{2}J_{BC} & \frac{1}{2}J_{AC} \\ \frac{1}{2}J_{BD} & \frac{1}{2}J_{BC} & H_{33}^{-1} & \frac{1}{2}J_{AB} \\ \frac{1}{2}J_{AD} & \frac{1}{2}J_{AC} & \frac{1}{2}J_{AB} & H_{44}^{-1} \end{pmatrix}$$

6×6 Submatrix ($F_Z=0$)

$$\begin{pmatrix} H_{11}^{0} & \frac{1}{2}J_{BC} & \frac{1}{2}J_{AC} & \frac{1}{2}J_{BD} & \frac{1}{2}J_{AD} & 0 \\ \frac{1}{2}J_{BC} & H_{22}^{0} & \frac{1}{2}J_{AB} & \frac{1}{2}J_{CD} & 0 & \frac{1}{2}J_{AD} \\ \frac{1}{2}J_{AC} & \frac{1}{2}J_{AB} & H_{33}^{0} & 0 & \frac{1}{2}J_{CD} & \frac{1}{2}J_{BD} \\ \frac{1}{2}J_{BD} & \frac{1}{2}J_{CD} & 0 & H_{44}^{0} & \frac{1}{2}J_{AB} & \frac{1}{2}J_{AC} \\ \frac{1}{2}J_{AD} & 0 & \frac{1}{2}J_{CD} & \frac{1}{2}J_{AB} & H_{55}^{0} & \frac{1}{2}J_{BC} \\ 0 & \frac{1}{2}J_{AD} & \frac{1}{2}J_{BD} & \frac{1}{2}J_{AC} & \frac{1}{2}J_{BC} & H_{66}^{0} \end{pmatrix}$$

Diagonal matrix elements

$$\begin{aligned}
H_{11}^{+2} &= h_A+h_B+h_C+h_D+J+j_C+j_D \\
H_{11}^{+1} &= -h_A+h_B+h_C+h_D-J'-j_C'-j_D' \\
H_{22}^{+1} &= h_A-h_B+h_C+h_D-J'+j_C'+j_D' \\
H_{33}^{+1} &= h_A+h_B-h_C+h_D+J'-j_C+j_D \\
H_{44}^{+1} &= h_A+h_B+h_C-h_D+J'+j_C-j_D \\
H_{11}^{0} &= -h_A-h_B+h_C+h_D+J-j_C-j_D \\
H_{22}^{0} &= -h_A+h_B-h_C+h_D-J+j_C'-j_D' \\
H_{33}^{0} &= h_A-h_B-h_C+h_D-J-j_C'+j_D' \\
H_{44}^{0} &= -h_A+h_B+h_C-h_D-J-j_C'+j_D' \\
H_{55}^{0} &= h_A-h_B+h_C-h_D-J+j_C'-j_D' \\
H_{66}^{0} &= h_A+h_B-h_C-h_D+J-j_C-j_D \\
H_{11}^{-1} &= -h_A-h_B-h_C+h_D+J'+j_C-j_D \\
H_{22}^{-1} &= -h_A-h_B+h_C-h_D+J'-j_C+j_D \\
H_{33}^{-1} &= -h_A+h_B-h_C-h_D-J'+j_C'+j_D' \\
H_{44}^{-1} &= h_A-h_B-h_C-h_D-J'-j_C'-j_D' \\
H_{11}^{-2} &= -h_A-h_B-h_C-h_D+J+j_C+j_D
\end{aligned}$$

where:

$$\begin{aligned}
h_i &= \tfrac{1}{2}\eta H_0(1-\sigma_i) \\
J &= \tfrac{1}{4}(J_{AB}+J_{CD}) \\
J' &= \tfrac{1}{4}(J_{AB}-J_{CD}) \\
j_C &= \tfrac{1}{4}(J_{AC}+J_{BC}) \\
j_C' &= \tfrac{1}{4}(J_{AC}-J_{BC}) \\
j_D &= \tfrac{1}{4}(J_{AD}+J_{BD}) \\
j_D' &= \tfrac{1}{4}(J_{AD}-J_{BD})
\end{aligned}$$

TABLE III. *ABKY* submatrices for a four-spin system.

$F_Z=+1$

$$\begin{pmatrix} (H_{11}')^{+1} & 0 & \delta_{13}^{+1} & 0 \\ 0 & (H_{22}')^{+1} & \delta_{23}^{+1} & 0 \\ \delta_{13}^{+1} & \delta_{23}^{+1} & H_{33}^{+1} & 0 \\ 0 & 0 & 0 & H_{44}^{+1} \end{pmatrix}$$

$F_Z=-1$

$$\begin{pmatrix} H_{11}^{-1} & 0 & 0 & 0 \\ 0 & H_{22}^{-1} & \delta_{23}^{-1} & \delta_{24}^{-1} \\ 0 & \delta_{23}^{-1} & (H_{33}')^{-1} & 0 \\ 0 & \delta_{24}^{-1} & 0 & (H_{44}')^{-1} \end{pmatrix}$$

where,

$$\delta_{13}^{+1}=(\tfrac{1}{2}J_{AK}\cos\phi_{+1}+\tfrac{1}{2}J_{BK}\sin\phi_{+1})$$
$$\delta_{23}^{+1}=(-\tfrac{1}{2}J_{AK}\sin\phi_{+1}+\tfrac{1}{2}J_{BK}\cos\phi_{+1})$$
$$\delta_{23}^{-1}=(\tfrac{1}{2}J_{AK}\sin\phi_{-1}+\tfrac{1}{2}J_{BK}\cos\phi_{-1})$$
$$\delta_{24}^{-1}=(\tfrac{1}{2}J_{AK}\cos\phi_{-1}-\tfrac{1}{2}J_{BK}\sin\phi_{-1})$$

$F_Z=0$

$$\begin{pmatrix} H_{11}^{0} & \delta_{12}^{0} & \delta_{13}^{0} & 0 & 0 & 0 \\ \delta_{12}^{0} & (H_{22}')^{0} & 0 & 0 & 0 & 0 \\ \delta_{13}^{0} & 0 & (H_{33}')^{0} & 0 & 0 & 0 \\ 0 & 0 & 0 & (H_{44}')^{0} & 0 & \delta_{46}^{0} \\ 0 & 0 & 0 & 0 & (H_{55}')^{0} & \delta_{56}^{0} \\ 0 & 0 & 0 & \delta_{46}^{0} & \delta_{56}^{0} & H_{66}^{0} \end{pmatrix}$$

where,

$$\delta_{12}^{0}=(\ \tfrac{1}{2}J_{AK}\sin\phi_{+0}+\tfrac{1}{2}J_{BK}\cos\phi_{+0})$$
$$\delta_{13}^{0}=(\ \tfrac{1}{2}J_{AK}\cos\phi_{+0}-\tfrac{1}{2}J_{BK}\sin\phi_{+0})$$
$$\delta_{46}^{0}=(\ \tfrac{1}{2}J_{AK}\cos\phi_{-0}+\tfrac{1}{2}J_{BK}\sin\phi_{-0})$$
$$\delta_{56}^{0}=(-\tfrac{1}{2}J_{AK}\sin\phi_{-0}+\tfrac{1}{2}J_{BK}\cos\phi_{-0})$$

(For definition of H_{ii}' see Table IV.)

Table II are listed in order of decreasing energy if $h_A \ll h_B \ll h_C \ll h_D$.

Diagonalization of the submatrices of Table II by appropriate methods will lead to a determination of their eigenvalues (energy levels) and eigenvectors (wave functions). The various observed transitions are between these eigenvalues with the restriction $\Delta F_Z=\pm 1$. The relative intensities depend on the eigenvectors for the corresponding states in the manner shown in a later section.

ABXY and *ABKY* Approximations

The *ABXY* approximation is merely an extension of the *ABX* approximation.[1] In both cases all off-diagonal matrix elements, except those equal to $\frac{1}{2}J_{AB}$, are neglected and two-by-two rotations are performed in order to diagonalize the resulting matrices. The coupling constants J_{ij} and the shielding parameters h_i can be obtained from the energy levels derived from the observed spectrum (to be described later).

In the *ABKY* approximation all off-diagonal matrix elements are included except those coupling to the *Y* proton, i.e., J_{AY}, J_{BY}, and J_{KY}. The two-by-two rotations are now applied to these matrices.[3] Upon the completion of this procedure the transformed submatrices of Table III are obtained. Second-order perturbation theory is now applied in order to determine the energy levels given in Table IV. The wave functions could also be found by perturbation theory, but these rather complicated expressions will not be given here. (Generally it is easier to find the eigenvectors, if they are needed, with the aid of an electronic computer, e.g., the Bendix G-15). The transition energies in this approximation can easily be found, if desired, from the levels of Table IV. The spin-spin coupling constants J_{ij} and magnetic shielding parameters h_i can readily be found by equating these energies to the energy levels derived from the observed spectrum. If an off-diagonal element δ_{ij} in the matrices of Table III becomes comparable with the difference between the energy levels that it connects, e.g., if $\delta_{23}^{+1}\approx(H_{22}')^{+1}-H_{33}^{+1}$, then the corresponding perturbation term Δ_{ij} will be relatively large. In this case the *J*'s and *h*'s derived with this approximation should be used to recalculate the matrices and the above procedure repeated until a convergent solution is found.

The *ABXY* energy levels can be obtained from Table IV by setting the Δ_{ij}'s to zero.

ABCD Method of Solution

If the spectrum from four spins cannot be analyzed satisfactorily with the aid of either the *ABXY* or the *ABKY* approximation, then the matrices, the elements of which are given in Table II, can be diagonalized on an electronic computer, e.g., the Bendix G-15, IBM 650, or 704. However, one must first have approximate values for J_{ij} and h_i in order to calculate the numerical values for the matrix elements. An iteration procedure can then be used to refine the fit to the energy levels determined experimentally.

[3] Cf. the *ABK* approximation in footnote 2.

TABLE IV. Energy levels in the *ABKY* approximation.

Level no.	Energy
2_1	$h_A+h_B+h_X+h_Y+J+j_X+j_Y$
1_1	$h_X+h_Y-J'+D_{+1}+\Delta_{13}{}^{+1}=(H_{11}')^{+1}+\Delta_{13}{}^{+1}$
1_2	$h_X+h_Y-J'-D_{+1}+\Delta_{23}{}^{+1}=(H_{22}')^{+1}+\Delta_{23}{}^{+1}$
1_3	$h_A+h_B-h_X+h_Y+J'-j_X+j_Y-\Delta_{13}{}^{+1}-\Delta_{23}{}^{+1}$
1_4	$h_A+h_B+h_X-h_Y+J'+j_X-j_Y$
0_1	$-h_A-h_B+h_X+h_Y+J-j_X-j_Y+\Delta_{12}{}^{0}+\Delta_{13}{}^{0}$
0_2	$-h_X+h_Y-J+D_{+0}-\Delta_{12}{}^{0}=(H_{22}')^{\circ}-\Delta_{12}{}^{0}$
0_3	$-h_X+h_Y-J-D_{+0}-\Delta_{13}{}^{0}=(H_{33}')^{0}-\Delta_{13}{}^{0}$
0_4	$h_X-h_Y-J+D_{-0}+\Delta_{46}{}^{0}=(H_{44}')^{0}+\Delta_{46}{}^{0}$
0_5	$h_X-h_Y-J-D_{-0}+\Delta_{56}{}^{0}=(H_{55}')^{0}+\Delta_{56}{}^{0}$
0_6	$h_A+h_B-h_X-h_Y+J-j_X-j_Y-\Delta_{46}{}^{0}-\Delta_{56}{}^{0}$
-1_1	$-h_A-h_B-h_X+h_Y+J'+j_X-j_Y$
-1_2	$-h_A-h_B+h_X-h_Y+J'-j_X+j_Y+\Delta_{23}{}^{-1}+\Delta_{24}{}^{-1}$
-1_3	$-h_X-h_Y-J'+D_{-1}-\Delta_{23}{}^{-1}=(H_{33}')^{-1}-\Delta_{23}{}^{-1}$
-1_4	$-h_X-h_Y-J'-D_{-1}-\Delta_{24}{}^{-1}=(H_{44}')^{-1}-\Delta_{24}{}^{-1}$
-2_1	$-h_A-h_B-h_X-h_Y+J+j_X+j_Y$

where,

$$\Delta_{13}{}^{+1}=\frac{(\delta_{13}{}^{+1})^2}{(H_{11}'-H_{33})^{+1}} \qquad \Delta_{23}{}^{-1}=\frac{(\delta_{23}{}^{-1})^2}{(H_{22}-H_{33}')^{-1}}$$

$$\Delta_{23}{}^{+1}=\frac{(\delta_{23}{}^{+1})^2}{(H_{22}'-H_{33})^{+1}} \qquad \Delta_{24}{}^{-1}=\frac{(\delta_{24}{}^{-1})^2}{(H_{22}-H_{44}')^{-1}}$$

$$\Delta_{12}{}^{0}=\frac{(\delta_{12}{}^{0})^2}{(H_{11}-H_{22}')^{0}} \qquad \Delta_{46}{}^{0}=\frac{(\delta_{46}{}^{0})^2}{(H_{44}'-H_{66})^{0}}$$

$$\Delta_{13}{}^{0}=\frac{(\delta_{13}{}^{0})^2}{(H_{11}-H_{33}')^{0}} \qquad \Delta_{56}{}^{0}=\frac{(\delta_{56}{}^{0})^2}{(H_{55}'-H_{66})^{0}}$$

$$D_{+1}\cos 2\phi_{+1}=(h_B-h_A)-j_X'-j_Y' \qquad D_{+1}\sin 2\phi_{+1}=D_{+0}\sin 2\phi_{+0}$$
$$=D_{-0}\sin 2\phi_{-0}=D_{-1}\sin 2\phi_{-1}=\tfrac{1}{2}J_{AB}$$

$$D_{+0}\cos 2\phi_{+0}=(h_B-h_A)+j_X'-j_Y'$$

$$D_{-0}\cos 2\phi_{-0}=(h_B-h_A)-j_X'+j_Y'$$

$$D_{-1}\cos 2\phi_{-1}=(h_B-h_A)+j_X'+j_Y'$$

The first task in the iteration procedure is the assignment of the various transitions. If the pattern is well spread out, then an assignment is naturally easy. However, as the resonances from various protons move together and start overlapping, the intensities of the various components change radically and "forbidden" or "combination" lines start appearing. Up to a point the *ABKY* approximation can be used to give an assignment and to calculate approximate constants. However, when the perturbation becomes too large for second-order theory to be adequate, a different procedure should be tried. Third- or fourth-order perturbation leads to extremely complicated formulas which are too unwieldy to be of much practical use. If the approximate treatment outlined in the last section cannot be used, then the only method left seems to be to calculate spectra on a computer with various reasonable values for J_{ij} and h_i. Here a knowledge of the spectra of similar compounds is extremely helpful. For example, it was shown[2] that the coupling constants in four epoxides are fairly constant from molecule to molecule. If reasonable values for the parameters are chosen, some of the lines observed can be definitely assigned to transitions. After a sufficient number of lines has been assigned, experimental values for the energy levels can be determined. It may then be possible to assign further lines with the aid of these energy levels and to repeat the process until all lines have been assigned.

A sum rule that we have found very useful for the determination of the energy levels states that $\nu(i\leftarrow j)+\nu(j\leftarrow k)+\cdots\nu(s\leftarrow t)=E_i-E_t$, i.e., the energy difference between two levels is the sum of the transition energies connecting these levels. If more than one set of transitions connected the levels, then each such set must give the same resultant sum.

The principle of spectroscopic stability[4] may also be of use in working out assignments. This principle states that

$$\sum_{i,j} |\,(\psi_i{}^a \,|\, \alpha \,|\, \psi_i{}^b)\,|^2 = \sum_{i,j} |\,(\phi_i{}^a \,|\, \alpha \,|\, \phi_i{}^b)\,|^2$$

for any operator α. If $\alpha=F_X$, the X component of the spin angular momentum, then this principle as applied to NMR spectra states that the sum of the intensities of all transitions between $F_Z=a$ and $F_Z=b$ is independent of the wave functions used for the matrix representation. The application of these interpretative aids will be illustrated in the detailed analyses of the glycidaldehyde spectra to follow.

If the correct parameters had been chosen then the eigenvalues of the diagonalized matrix would be the energy levels derived from the observed transitions as outlined above. However, in general, the eigenvalues will not agree exactly with the energy levels but an iteration procedure can be used to reach the desired solution.

[4] E. U. Condon and G. Shortley, *The Theory of Atomic Spectra* (Cambridge University Press, New York, 1957).

The computer diagonalization of the Hamiltonian matrix H can be symbolized as the similarity transformation

$$S^{-1}HS=\Lambda,$$

where S is the unitary matrix ($S^{-1}=\tilde{S}$), the columns of which are the eigenvectors found by the computer and Λ is a diagonal matrix, the elements of which are the eigenvalues, λ_i, of H. Since the S matrix varies in a higher order than the eigenvalues, e.g., a first-order correction to the wave function leads to a second-order correction in the energy, this matrix can be used to derive more accurate values for the elements $(H_{\text{exp}})_{nn}$ from the (diagonal) matrix of the experimental energy levels Λ_{exp}, as follows: $S\Lambda_{\text{exp}}S^{-1}=S\Lambda_{\text{exp}}\tilde{S}=H_{\text{exp}}$. Then it follows that $(H_{\text{exp}})_{nn}=\sum_i S_{ni}{}^2\lambda_i$. (The off-diagonal elements $(H_{\text{exp}})_{nn}$ could also be used, but these are not necessary. In fact it is inadvisable to use them because because they are subject to much larger fluctuations during the iterative process.) The matrix elements $(H_{\text{exp}})_{nn}$ so found can then be used together with the equations of Table II to find new values for the spin-spin coupling constants and the screening parameters, i.e., a set of linear equations is solved. These in turn lead to a new Hamiltonian matrix which is diagonalized to give the new matrices S' and Λ'. S' instead of S is then applied to Λ_{exp} and the foregoing process repeated until a consistent set of parameters is obtained. Schematically the whole process can be represented as

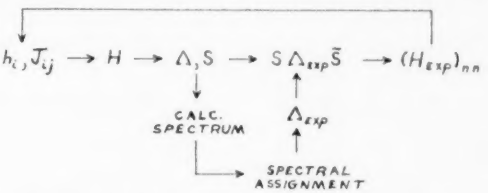

The intensities of the various transitions are proportional to $|\,(\psi_i \,|\, I_x \,|\, \psi_j)\,|^2$ and can be found directly from the final S matrices found in the iteration procedure previously described.

$$I(F_Z, i\leftarrow F_Z-1, j) \propto |\,(\tilde{S}_{F_Z} T_{F_Z,F_Z-1} S_{F_Z-1})_{ij}\,|^2,$$

where T_{F_Z,F_Z-1} is proportional to the I_X matrix between the states with spin angular momenta F_Z and F_Z-1. The latter matrices are given in Table V for an *ABCD* system.

EXPERIMENTAL

General

A freshly distilled sample of glycidaldehyde together with a small amount of tetramethylsilane (TMS) as an internal reference contained in a standard Wilmad precision tube was degassed by a standard freeze-pump-thaw technique. The NMR spectrum at 40 Mc/sec was obtained immediately and that at 60 Mc/sec was obtained at a later date. Additional 40

Mc/sec spectra were obtained at this time and the measurements combined with the earlier ones at 40 Mc/sec. No obvious differences in the two sets of spectra were noted. The spectra were calibrated in the usual way by a sideband technique.

The 60-Mc/sec spectrum is shown in Fig. 1 and the 40-Mc/sec spectrum in Fig. 3. It is evident that the spectrum at 40 Mc/sec is considerably more complicated than the one at 60 Mc/sec. In each case the "aldehyde proton" is at highest energy and the proton on the same carbon atom as the aldehyde group is at next highest energy. However, at 40 Mc/sec some of the lines from this proton appear to overlap with those from the remaining two protons. It is the this overlap that makes the analysis of the 40-Mc/sec spectrum difficult.

Analysis of 60-Mc/sec Spectrum

The 60-Mc/sec spectrum with the line assignment is shown in Fig. 1. The experimental line positions with respect to the TMS are given in cycles per second (cps) in the third column of Table VI. Because of variations in sweep rates through the spectrum, it was necessary to average the results of several such sweeps. The positions of transitions 11, 12, and of transition 24 were first established to ±0.3 cps with respect to TMS. The separation of 12.78 cps between these resonances was then used for determining the positions of the remaining lines in the spectrum. At least 5 tracings were used to obtain the average positions listed in Table VI. The standard deviations are shown in column 4. The separation of 0.26 cps between transitions 25, 27 and 26, 28 was obtained from the separation in time of the two "beats" following the resonance consisting of these transitions.[5]

TABLE V. T matrices for four-spin system.

$$T_{21}=[1\ \ 1\ \ 1\ \ 1]$$

$$T_{10}=\begin{bmatrix}1&1&0&1&0&0\\1&0&1&0&1&0\\0&1&1&0&0&1\\0&0&0&1&1&1\end{bmatrix}$$

$$T_{-1,-2}=\begin{bmatrix}1\\1\\1\\1\end{bmatrix}$$

$$T_{0,-1}=\begin{bmatrix}1&1&0&0\\1&0&1&0\\1&0&0&1\\0&1&1&0\\0&1&0&1\\0&0&1&1\end{bmatrix}$$

Note that $T_{-1,-2}=\tilde{T}_{21}$

$(T_{0,-1})_{i,j}=(T_{10})_{5-j,\,7-i}$

[5] C. A. Reilly, J. Chem. Phys. **25**, 604 (1956).

TABLE VI. Glycidaldehyde line positions at 60 Mc/sec.

Transition No.	Origin	Obs	σ	Calc from *ABCD* soln.	Obs-Calc
1	$-1_4\leftarrow-2_1$	180.19 cps	0.49 cps	180.28 cps	−0.09 cps
2	$0_3\leftarrow-1_1$	180.19	0.49	180.30	−0.11
3	$0_5\leftarrow-1_2$	182.85	0.38	182.75	+0.10
4	$+1_2\leftarrow\ 0_1$	182.85	0.38	182.77	+0.08
5	$0_6\leftarrow-1_3$	185.83	0.18	185.79	+0.04
6	$+1_3\leftarrow\ 0_2$	185.83	0.18	185.75	+0.08
7	$+1_4\leftarrow\ 0_4$	188.21	0.11	188.26	−0.05
8	$+2_1\leftarrow+1_1$	188.21	0.11	188.32	−0.11
9	$-1_3\leftarrow-2_1$	185.53	0.23	185.59	−0.06
10	$0_2\leftarrow-1_1$	185.53	0.23	185.69	−0.16
11	$0_4\leftarrow-1_2$	190.20	...	190.12	+0.08
12	$+1_1\leftarrow\ 0_1$	190.20	...	190.09	+0.11
13	$0_6\leftarrow-1_4$	...		191.10	
14	$+1_2\leftarrow\ 0_5$	...		191.24	
15	$+1_4\leftarrow\ 0_3$	195.52	0.15	195.63	−0.11
16	$+2_1\leftarrow+1_2$	195.52	0.15	195.64	−0.12
17	$-1_2\leftarrow-2_1$	195.52	0.15	195.49	+0.03
18	$0_4\leftarrow-1_3$	200.07	0.25	200.01	+0.06
19	$0_5\leftarrow-1_4$	198.09	0.22	197.95	+0.14
20	$+1_4\leftarrow\ 0_6$	202.49	0.24	202.48	+0.01
21	$0_1\leftarrow-1_1$	201.43	0.24	201.42	+0.01
22	$+1_1\leftarrow\ 0_2$	205.66	0.11	205.81	−0.15
23	$+1_2\leftarrow\ 0_3$	203.95	0.20	203.98	−0.03
24	$+2_1\leftarrow+1_3$	208.30	...	208.38	−0.08
25	$-1_1\leftarrow-2_1$	532.25	0.06	532.40	−0.15
26	$0_2\leftarrow-1_3$	532.51	0.06	532.50	+0.01
27	$0_3\leftarrow-1_4$	532.25	0.06	532.32	−0.07
28	$+1_3\leftarrow\ 0_6$	532.51	0.06	532.46	+0.05
29	$0_1\leftarrow-1_3$	538.38	0.01	538.33	+0.05
30	$+1_1\leftarrow\ 0_4$	538.38	0.01	538.30	+0.08
31	$+1_2\leftarrow\ 0_5$	538.38	0.01	538.35	+0.03
32	$+2_1\leftarrow+1_4$	538.38	0.01	538.35	+0.03

After many tries and preliminary calculations both on the 40- and the 60-Mc/sec spectra, the assignment shown in Fig. 1 was finally taken to be the most reasonable. On the basis of this assignment, the energy level diagram of Fig. 2 was constructed. The sum rule discussed in the theoretical part above was used to find the most consistent values for the energy levels. For example, assuming level -2_1 to be zero, the sum of the observed positions for transitions 8, 12, 21, and 25 gives 1112.09 cps for level 2_1. Averaging this with the sums for the other 11 possible paths between these two levels gives 1112.131 cps as the "best" numerical value for level 2_1. Similarly for the various paths connecting -2_1 to each of the other levels. The position thus found for each energy level relative to -2_1 is shown in column 2 of Table VII. The average position for all 16 levels is 551.449 cps. Since this average position must be zero (i.e., Trace $H=0$, see Table II), 551.449 was subtracted from the values in column 2 to give those in column 3 of Table VII. These are the numerical values $(\lambda_i)_{exp}$ of the experimental NMR energy levels for glycidaldehyde at 60 Mc/sec. With these "best" values for $(\lambda_i)_{exp}$ the line positions riven for all transitions, except 22, are within ±0.1 cps of the observed positions. Transition 22 is observed to be at 0.21 cps lower frequency and must

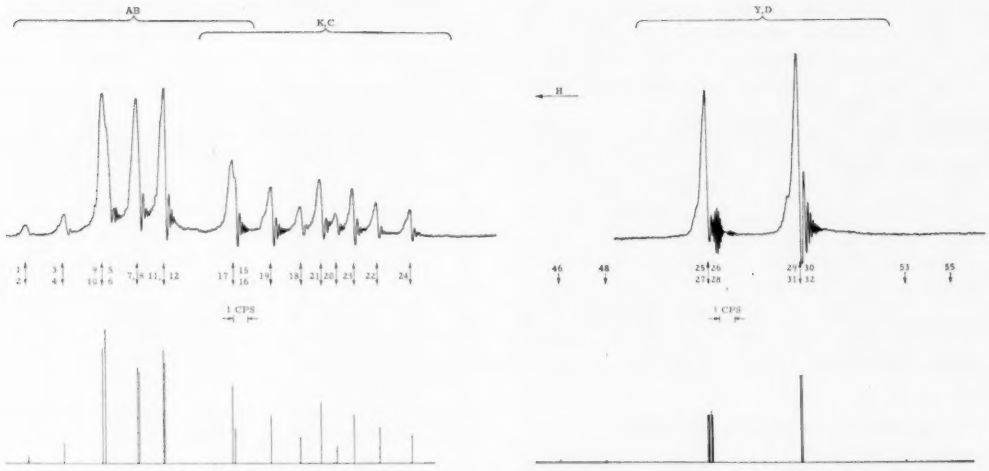

FIG. 1. 60-Mc/sec NMR spectrum of glycidaldehyde.

be in error by about this amount. A better fit of the observed spectrum might have been obtained if the line positions had been weighted according to the estimated precision and a least squares criterion had been used in deriving the energy levels. Such an extension of the present scheme for analyzing NMR spectra will be postponed until a later date.

ABXY Approximation

With the transitions assigned as in Fig. 1, approximate values for the coupling constants J_{ij} and the screening parameters h_i were first determined from a simple $ABXY$ approximation, i.e., the energy correction terms needed for the $ABKY$ approximation were assumed to be zero.

Because of the four intervening bonds between the Y proton and either the A or the B proton, it is expected that both J_{AY} and J_{BY} will be small. Thus it was tentatively assumed that $J_{AY}=J_{BY}=0$. This means that j_Y and j_Y' as defined in Table II will both be zero. Consequently, in this approximation the D's and ϕ's as defined in Table IV will be related to one another as

TABLE VII. Numerical values for NMR energy levels of glycidaldehyde at 60 Mc/sec.

Level	Position (relative to -2_1)	(λ_i)exp	From *ABCD* soln.	Diff.
2_1	1112.131 cps	560.682 cps	560.724 cps	−0.04 cps
1_1	923.874	372.425	372.408	0.02
1_2	916.578	365.129	365.089	0.04
1_3	903.795	352.346	352.348	0.00
1_4	573.835	22.386	22.372	0.01
0_1	733.745	182.296	182.319	−0.02
0_2	718.000	166.551	166.598	−0.05
0_3	712.503	161.054	161.107	−0.05
0_4	385.610	−165.839	−165.887	0.05
0_5	378.283	−173.166	−173.260	0.09
0_6	371.333	−180.116	−180.110	−0.01
-1_1	532.338	−19.111	−19.096	−0.02
-1_2	195.433	−356.016	−356.007	−0.01
-1_3	185.515	−365.934	−365.900	−0.03
-1_4	180.210	−371.239	−371.213	−0.03
-2_1	0	−551.449	−551.492	0.04
avg	551.449 cps			

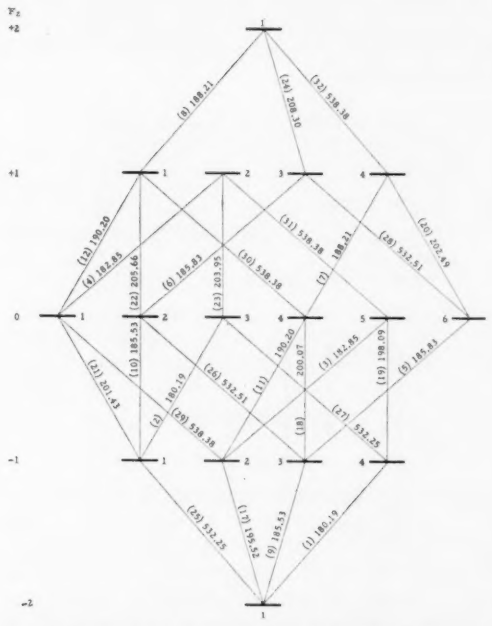

FIG. 2. Energy level diagram for 60-Mc/sec NMR spectrum of glycidaldehyde. Not to scale.

follows:

$$D_{+1}=D_{-0} \quad \text{and} \quad D_{+0}=D_{-1}$$

$$\phi_{+1}=\phi_{-0} \qquad \phi_{+0}=\phi_{-1}.$$

The detailed calculations of the remaining coupling constants and screening parameters in this approximation give

$$J_{AB}=5.50 \text{ cps} \qquad h_A=\ 93.11 \text{ cps}$$

$$J_{XY}=5.90 \text{ cps} \qquad h_B=\ 94.33 \text{ cps}$$

$$J_{AX}=1.02 \text{ cps} \qquad h_X=100.97 \text{ cps}$$

$$J_{BX}=5.90 \text{ cps} \qquad h_Y=267.69 \text{ cps.}$$

$$J_{AY}=0 \text{ cps}$$

$$J_{BY}=0 \text{ cps}$$

These numbers were now used as starting parameters for carrying out the *ABKY* approximation.

ABKY Approximation

The parameters found in the *ABXY* approximation were next used as initial data for the first *ABKY* calculation. This approximation led to new values for the parameters, which were then used for the second *ABKY* approximation. The process was repeated until eight iterations had been completed. It was found that convergence to a consistent solution was quite slow, particularly for J_{AK} and J_{BK}. Hence, the value derived for each parameter was plotted as a function of the iteration number and extrapolated to an estimated asymptotic final value. Such values were then used for a further *ABKY* iteration. Still another one was then required to reach a nearly convergent solution. The following values for the parameters were obtained:

$$J_{AB}=\ 5.54 \text{ cps} \qquad h_A=\ 92.97 \text{ cps}$$

$$J_{KY}=\ 6.24 \text{ cps} \qquad h_B=\ 94.79 \text{ cps}$$

$$J_{AK}=\ 2.09 \text{ cps} \qquad h_K=100.68 \text{ cps}$$

$$J_{BK}=\ 4.87 \text{ cps} \qquad h_Y=267.67 \text{ cps.}$$

$$J_{AY}=+0.03 \text{ cps}$$

$$J_{BY}=-0.31 \text{ cps}$$

Since $\nu_0=60.00$ Mc/sec, the shielding parameters in dimensionless units become

$$\delta_A=2h_A/\nu_0\times10^6=3.098$$

$$\delta_B=2h_B/\nu_0\times10^6=3.166$$

$$\delta_K=2h_K/\nu_0\times10^6=3.356$$

$$\delta_Y=2h_Y/\nu_0\times10^6=8.922.$$

ABCD Solution

The parameters derived via the *ABKY* approximation were next used to calculate the matrices of Table II. The Bendix computer (model G-15) was then used to find their eigenvalues and eigenvectors. The eigenvalues are listed in the fourth column of Table VII. The differences to the nearest hundredth of a cycle per second between these eigenvalues and the experimental energy level are shown in the last column of this table. In no case does a difference exceed 0.1 cps; in fact only one difference (for level 0_5) exceeds 0.05 cps. The line positions calculated from these eigenvalues are shown in column 5 of Table VI. Their differences from the observed positions are shown in the last column of this table. All calculated positions are within 0.2 cps of the observed ones and hence, in view of the somewhat large standard deviations of each observed position, are considered to be in good agreement with them. Therefore, no iteration was done.

A more sensitive criterion of the adequacy of the solution comes from a comparison of the calculated and observed intensities. The intensity of each line was calculated by the method outlined in the theoretical part of this paper. The matrices S_{F_Z} were formed from the eigenvectors and the matrix products

$$|\,(\tilde{S}_{F_Z}T_{F_Z,F_Z-1}S_{F_Z-1})_{ij}\,|^2$$

were found from these and the T matrices shown earlier Table V. The results are summarized in Table VIII.

TABLE VIII. Calculated line intensities for 60-Mc/sec NMR spectrum of glycidaldehyde.

	Lower Level					
Upper level	1_1	1_2	1_3	1_4		
2_1	2.047	0.338	0.633	0.982	$\Sigma=4.000$	
	0_1	0_2	0_3	0_4	0_5	0_6
1_1	2.255	0.797	0.012	0.980	0	0
1_2	0.218	0.073	1.065	0	0.965	0.019
1_3	0	1.604	0.011	0.002	0.018	0.996
1_4	0	0	0	2.142	0.446	0.394
Σ	2.473	2.474	1.088	3.124	1.429	1.409
	$\Sigma=11.997$					
	-1_1	-1_2	-1_3	-1_4	Σ	
0_1	1.492	0.971	0.011	0	2.474	
0_2	1.456	0.013	1.005	0	2.474	
0_3	0.069	0	0	1.018	1.087	
0_4	0	2.534	0.586	0.004	3.124	
0_5	0	0.235	0.127	1.069	1.431	
0_6	0	0	1.410	0	1.410	
					$\Sigma=12.000$	
	-2_1					
-1_1	1.018					
-1_2	1.753					
-1_3	1.138					
-1_4	0.091					
Σ	4.000					

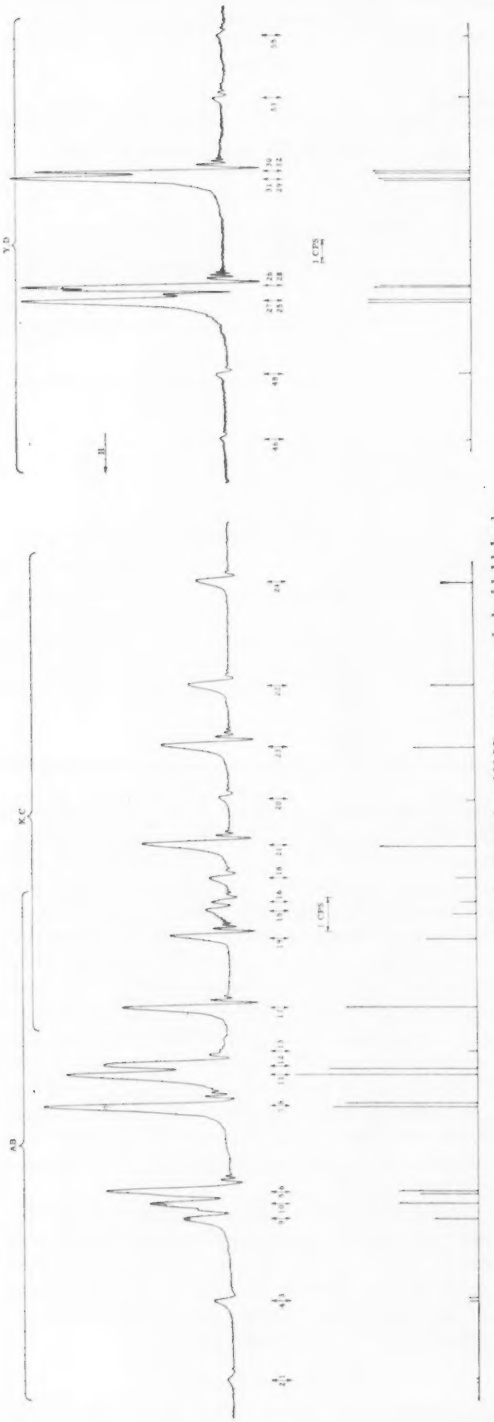

FIG. 3. 40-Mc/sec NMR spectrum of glycidaldehyde.

(The common factor $\eta^2/4$ has been omitted from all these numbers.) The principle of spectroscopic stability was used to check for arithmetic errors in these calculations as follows. In zeroth order, i.e., all J_{ij} neglected (set equal to zero), it can easily be shown that there will be four transitions of equal intensity between levels with $F_Z=+2$ and $F_Z=+1$ giving a total intensity (un-normalized) of 4. Similarly for the transitions between levels with $F_Z=-1$ and $F_Z=-2$. Between levels with $F_Z=+1$ and 0 as well as between those with $F_Z=0$ and $F_Z=-1$ there will be 12 transitions of equal intensity for a total intensity (un-normalized) of 12 in each case. These intensity sums will be the same for any degree of perturbation introduced by the J_{ij} couplings. It is seen from Table VIII that this is so in the present case. The agreement between the calculated and observed spectra is indicated in Fig. 1. It is about as good as could be expected for spectra obtained with the present instrumentation.

Analysis of 40-Mc/sec Spectrum

The 40-Mc/sec spectrum is shown in Fig. 3. The line assignments were made on the basis of comparisons with the 60-Mc/sec spectrum and of intensity calculations with approximate coupling constants and shielding parameters. The line positions given in Table IX were obtained by averaging the results of at least 18 or 19 recordings the spectrum. The standard deviations for most lines are considerably smaller than for the lines

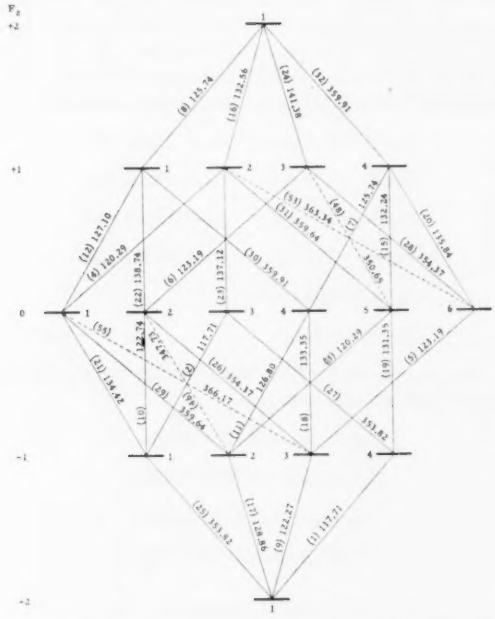

FIG. 4. Energy level diagram for 40-Mc/sec NMR spectrum of gycidaldehyde.

in the 60-Mc/sec spectrum. For all the 40-Mc/sec lines these deviations are ≤ 0.05 cps.

With the assignment of Fig. 3 and the line positions of Table X, the energy level diagram of Fig. 4 was constructed, the dashed lines being combination transtions (not observed at 60 Mc/sec). The energy levels $(\lambda_i)_{exp}$ of Table X were then found in the same way as were those for the 60-Mc/sec spectrum.

The parameters found from the 60-Mc/sec data were next used to calculate the matrices of Table II, the field-dependent parameters h_i having been first reduced by the factor $\frac{2}{3}$ (the conversion factor from 60 to 40 Mc/sec). The eigenvalues and eigenvectors for these matrices were found with the Bendix G-15 computer. The values of $(\lambda_i)_{exp}$ were then used together with the eigenvectors from this diagonalization to calculate "better" values of the diagonal elements $(H_{exp})_{nn}$ by the relation

$$(H_{exp})_{nn}=\sum_i S_{ni}^2\lambda_i.$$

TABLE IX. Line positions in 40-Mc/sec spectrum of glycidaldehyde.

Transition No.	Origin	Observed position	σ	Calc from *ABCD* soln.	Obs-Calc
1	$-1_4\leftarrow-2_1$	117.71 cps	0.04 cps	117.76 cps	−0.05 cps
2	$0_5\leftarrow-1_1$	117.71	0.04	117.64	0.07
3	$0_5\leftarrow-1_2$	120.29	0.04	120.40	−0.11
4	$1_2\leftarrow 0_1$	120.29	0.04	120.32	−0.03
5	$0_6\leftarrow-1_3$	123.19	0.03	123.11	0.08
6	$1_3\leftarrow 0_2$	123.19	0.03	123.18	0.01
7	$1_4\leftarrow 0_4$	125.74	0.03	125.75	−0.01
8	$2_1\leftarrow 1_1$	125.74	0.03	125.87	−0.13
9	$-1_3\leftarrow-2_1$	122.27	0.04	122.29	−0.02
10	$0_3\leftarrow-1_1$	122.74	0.04	122.73	0.01
11	$0_4\leftarrow-1_2$	126.80	0.05	126.78	0.02
12	$1_1\leftarrow 0_1$	127.10	0.05	126.98	0.12
13	$0_6\leftarrow-1_4$	...	...	127.64	...
14	$1_3\leftarrow 0_5$	...	...	128.27	...
15	$1_4\leftarrow 0_5$	132.24	0.05	132.13	0.11
16	$2_1\leftarrow 1_2$	132.56	0.05	132.52	0.04
17	$-1_3\leftarrow-2_1$	128.86	0.04	128.82	0.04
18	$0_4\leftarrow-1_3$	133.35	0.05	133.32	0.03
19	$0_5\leftarrow-1_4$	131.35	0.05	131.45	−0.10
20	$1_4\leftarrow 0_6$	135.84	0.04	135.95	−0.10
21	$0_1\leftarrow-1_1$	134.42	0.04	134.51	−0.09
22	$1_1\leftarrow 0_2$	138.74	0.03	138.77	−0.03
23	$1_2\leftarrow 0_3$	137.12	0.03	137.19	−0.07
24	$2_1\leftarrow 1_3$	141.38	0.02	141.45	−0.07
25	$-1_1\leftarrow-2_1$	353.82	0.04	353.91	−0.09
26	$0_2\leftarrow-1_3$	354.37	0.04	354.35	0.02
27	$0_3\leftarrow-1_4$	353.82	0.04	353.79	0.03
28	$1_3\leftarrow 0_6$	354.37	0.04	354.42	0.05
29	$0_1\leftarrow-1_2$	359.64	0.05	359.60	0.04
30	$1_1\leftarrow 0_4$	359.91	0.05	359.80	0.11
31	$1_2\leftarrow 0_5$	359.64	0.05	359.52	0.12
32	$2_1\leftarrow 1_4$	359.91	0.05	359.92	−0.01
46	$0_2\leftarrow-1_2$	347.73	0.04	347.82	−0.09
48	$1_3\leftarrow 0_5$	350.65	0.04	350.60	0.05
53	$1_2\leftarrow 0_6$	363.34	0.05	363.34	0.00
55	$0_1\leftarrow-1_3$	366.17	0.03	366.13	0.04

TABLE X. NMR energy levels of glycidaldehyde at 40 Mc/sec.

Level	Position (relative to -2_1)	(λ_i)exp	From *ABCD* soln.	Obs-Calc
2_1	741.219 cps	375.228 cps	375.252 cps	−0.02
1_1	615.438	249.447	249.392	0.06
1_2	608.700	242.709	242.728	−0.02
1_3	599.791	233.800	233.807	−0.01
1_4	381.343	15.352	15.335	0.01
0_1	488.386	122.395	122.409	−0.01
0_2	476.618	110.627	110.627	0.00
0_3	471.547	105.556	105.539	0.02
0_4	255.603	−110.388	−110.410	0.02
0_5	249.102	−116.889	−116.795	−0.09
0_6	245.435	−120.556	−120.612	0.06
-1_1	353.878	−12.113	−12.100	−0.01
-1_2	128.822	−237.169	−237.190	0.01
-1_3	122.248	−243.743	−243.725	−0.02
-1_4	117.730	−248.261	−248.247	−0.01
-2_1	0	−365.991	−366.010	0.02
av	365.991	0		

These numerical values for $(H_{exp})_{nn}$ were then substituted in the 16 defining equations for the diagonal elements (Table II) and better values for the coupling constants J_{ij} and the screening constants h_i found by solving these equations. These new values were now used to calculate new submatrices and the above procedure repeated. After the third iteration the eigenvalues given in the fourth column of Table X were obobtained. It will be noted that, as in the 60-Mc/sec spectrum, these eigenvalues agree with the experimental values $(\lambda_i)_{exp}$ to better than ± 0.1 cps. The positions calculated for the transitions from these eigenvalues are given in column 5 of Table IX. The agreement between the observed and calculated positions is somewhat better than for the 60-Mc/sec spectrum-undoubtedly because the experimental data are more precise.

The intensity of each line was next calculated in the same way as for the 60-Mc/sec spectrum with the results presented in Fig. 3.

The values derived for the coupling constants and the shielding parameters from this solution are

$$J_{AB}=5.54 \text{ cps} \qquad h_A=61.914 \text{ cps}$$

$$J_{CD}=6.36 \text{ cps} \qquad h_B=63.163 \text{ cps}$$

$$J_{AC}=2.04 \text{ cps} \qquad h_C=67.120 \text{ cps}$$

$$J_{BC}=4.90 \text{ cps} \qquad h_D=178.434 \text{ cps.}$$

$$J_{AD}=-0.03 \text{ cps}$$

$$J_{BD}=-0.32 \text{ cps}$$

Since the measured value of ν_0 for our spectrometer is 39.996 Mc/sec the shielding parameters in dimen-

TABLE XI.

R	J_{AB}	J_{AC}	J_{BC}	$(J_{AC}+J_{BC})$	δ_A	δ_B	δ_C
—CHO	5.54	2.06	4.89	6.95	3.096	3.160	3.356
—ϕ	5.65	2.49	4.04	6.53	2.510	2.810	3.608
—CN	5.54	2.48	4.26	6.74	3.109	3.002	3.503
—$COCH_3$	5.78	1.95	5.21	7.16	2.942	3.001	3.366
—COOH	6.28	1.86	5.01	6.87	2.934	2.988	3.478
av	5.76	2.17	4.67	6.84	2.918	2.922	3.462
σ	0.14	0.14	0.22	0.10	0.112	0.054	0.046
%	2.4	6.4	4.7	1.5	3.8	1.8	1.3

sionless units are

$$\delta_A = 2h_A/\nu_0 \times 10^6 = 3.096$$

$$\delta_B = 2h_B/\nu_0 \times 10^6 = 3.158$$

$$\delta_C = 2h_C/\nu_0 \times 10^6 = 3.356$$

$$\delta_D = 2h_D/\nu_0 \times 10^6 = 8.922.$$

A comparison of these values with those previously derived from the *ABKY* solution of the 60-Mc/sec spectrum shows that the agreement is quite good for all parameters except $J_{CD}(J_{KY})$. The reason for this discrepancy is not known. The following "best" values for the glycidaldehyde parameters were obtained by averaging the two sets of results, with the 40-Mc/sec ones being given double weight:

$J_{AB}=$ 5.54 cps $\quad \delta_A=3.096.$

$J_{CD}=$ 6.32 cps $\quad \delta_B=3.160$

$J_{AC}=$ 2.06 cps $\quad \delta_C=3.356$

$J_{BC}=$ 4.89 cps $\quad \delta_D=8.922.$

$J_{AD}=$ 0.01 cps

$J_{BD}=-0.32$ cps

DISCUSSION

The *ABKY* approximation is a definite improvement over the simpler *ABXY* approximation, but we have found it is certainly necessary to iterate the *ABKY* solution to a consistent solution. Usually it will be advantageous to iterate the trial values at least twice and then extrapolate these values to their approximate asymptotic value. This process can then be continued by two more iterations leading to a better asymtotic value and finally to a consistent solution. This procedure was used to advantage on the 60-Mc/sec spectrum, but the 40-Mc/sec spectrum was too perturbed to justify the *ABKY* approximate method.

In both the *ABKY* method and the *ABCD* method, the use of the energy levels was found to be far superior to the usual direct use of the line positions. In this procedure the effects of an error in the measurement of a line position has a minimal influence in the determination of the constants. In addition, it is easier to analyze the 16 energy levels than the 30 or more observed transitions. An iterative program based on the transitions themselves would be much more difficult.

The agreement between the parameters for the 40 and the 60-Mc/sec spectra is rather remarkable. It certainly points out the necessity of measuring the spectrum a large number of times in order to obtain accurate values for the line positions. Unless this is done, magnetic field drifts may cause undesirably large errors in the position of a given line (see σ in Table VI).

It is interesting to compare the various parameters determined for glycidaldehyde with those of other epoxides.[2] (See Table XI.) It is indeed surprising that the shielding of the *C* proton, i.e., the proton nearest the *R* group, is least affected by changes in this group. Also the sum of its coupling constants to protons *A* and *B* is subject to relatively small variations.

In glycidaldehyde the magnitude of the spin-spin coupling between the aldehyde proton and the adjacent proton (*C*) gives us an indication of the average dihedral angle. Valence bond calculations by Karplus[6] gave approximately 8 to 9 cps for a dihedral angle of 0° and 180°, 2 cps for an angle of 60° and ~0(−0.3) cps for an angle of 90°. Experimentally, values of 5 to 8 cps have been found for angles of 180° and values of 2 to 4 cps have been found for 60° angles. In glycidaldehyde with the rapid internal rotation of the aldehyde groups with respect to the epoxide ring (see below) the spin-spin coupling will be an average value weighted over the various configurations. Our value of 6.3 cps indicates that a configuration with a dihedral angle of 0° and/or 180° must represent a sizable contribution to the average.

The barriers to internal rotation have been determined for a number of related molecules.[7–10] These are

ethane CH_3-CH_3	2750−3150	cal/mole
acetaldehyde CH_3CHO	1150	cal/mole
propylene oxide	2560	cal/mole.

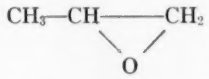

If group interactions dominate, i.e., if the changes in bond lengths and angles are small and if the potential energy is not some complicated function of the two groups, then we should estimate that the potential barrier hindering internal rotation in glycidaldehyde is about 1050±150 cal/mole. This barrier leads essentially to free rotation on the NMR time scale.

In acetaldehyde a methyl proton eclipses the aldehyde oxygen atom and the other two methyl protons straddle the aldehyde proton. In propylene[11] one methyl

[6] M. Karplus, J. Chem. Phys. **30**, 11 (1959).

[7] (a) J. D. Kemp and K. S. Pitzer, J. Chem. Phys. **4**, 749 (1936); J. Am. Chem. Soc. **59**, 276 (1936); (b) G. B. Kistiakowsky, J. R. Lacher, and F. Stitt, J. Chem. Phys. **6**, 407 (1938); **7**, 289 (1939).

[8] R. W. Kilb, C. C. Lin, and E. B. Wilson, Jr., J. Chem. Phys. **26**, 1695 (1957).

[9] J. D. Swalen and D. R. Herschbach, J. Chem. Phys. **27**, 100 (1957).

[10] D. R. Herschbach and J. D. Swalen, J. Chem. Phys. **29**, 761 (1958).

[11] D. R. Herschbach and L. C. Krisher, J. Chem. Phys. **28**, 728 (1958).

proton eclipses the double bond. We should predict that in glycidaldehyde, the aldehyde oxygen probably eclipses the adjacent proton (C), which is approximately *trans* to proton D. The aldehyde group is probably in the same plane as proton C and this plane is perpendicular to the plane of the epoxide ring.

The epoxide ring spin-spin coupling constants J_{AC} and J_{BC} are consistent with an eclipsed ethane type model according to Karplus' calculations for these constants as a function of the angle. The J_{AB} coupling

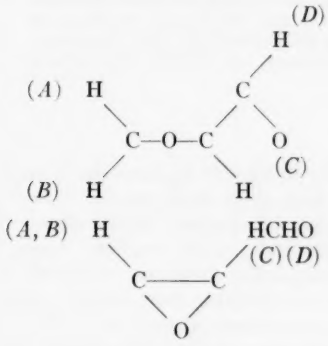

constant is similar to that found in other epoxides so we should expect an HCH angle approximately the same, i.e., 116°15′±2°.

The coupling constants across the molecule, J_{AD} and J_{BD}, are much smaller than the other constants. The attentuation in passing through one more bond is approximately 1/20, i.e.,

$$\tfrac{1}{2}(J_{AD}+J_{BD}) \approx \tfrac{1}{20}\left[\tfrac{1}{2}(J_{AC}+J_{BC})\right].$$

This is consistent with the finding for other molecules where the attenuation is usually about $\frac{1}{10}$. It is interesting that J_{AD} is essentially zero and that J_{BD} is negative. In spin propagation the role of *cis* and *trans* have been reversed, i.e., $|J_{AD}| < |J_{BD}|$ compared with $|J_{BC}| > |J_{AC}|$. This may be a result of the additional 120° bond angle change.

ACKNOWLEDGMENTS

We are indebted to G. B. Payne of these laboratories for supplying the sample of glycidaldehyde and to Roy Johnson of Varian Associates for obtaining the NMR spectrum at 60 Mc/sec.

Geometric Basis of Phase Change

ROBERT GINELL*

Department of Chemistry, Brooklyn College, Brooklyn, New York

(Received August 25, 1960)

A consideration of the higher j-mers by association theory shows that starting with the 7-mer and going up to 19-mer, spherically symmetric atoms can pack in an unsymmetrical arrangement in which more bonds exist among the atoms in the array than if the atoms were packed symmetrically. The asymmetric pattern is then the model for the liquid while the symmetric array yields the crystal. The transition from the liquid to the crystal is difficult by homogeneous nucleation because it requires a cooperative effort of, in the neighborhood of 12–15 atoms. Heterogeneous nucleation is, however, simple since by this mechanism the region where the liquid j-mers are more stable than the crystal j-mers is bypassed. Methods of calculating the equilibrium constants and the concentrations of the various species are derived from association theory. The critical value where the formation of higher close-packed j-mers becomes important is when the value of the equilibrium constant exceeds 1.

IN the general theory of association[1] the aggregation of 1-mers (also called clusters) of various sizes is described in general, and equations for calculating their concentrations are given. Since liquids and solids consist essentially of large j-mers, it seems appropriate to examine these higher j-mers in greater detail to see what light can be shed on the solid and liquid states and especially on the transitions between such states. It is with this aim that this paper is written. This problem has been the subject of many papers which are ably summarized by Hirschfelder, Curtiss, and Bird,[2] and Hill[3] among others.

In order to simplify the discussion, we shall assume first, that the shape of the 1-mer is spherical, and second, that the force field surrounding the 1-mer (that is, the attractive and repulsive forces) that gives rise to these higher j-mers is also spherically symmetric. Naturally, these assumptions limit the scope of the conclusions, especially the quantitative ones, but they an be modified at a later date without sacrificing the basic concepts that will emerge. The third assumption that we shall make is that the bonding process is a stepwise procedure; that is, that the bonding process proceeds wherever geometrically possible by the formation of one bond at one time. The process of forming a multiple bond consists then of the successive formation of single bonds which are separated in time, although the time lapse may be very short. This is a logical assumption since, if bonding can occur by a single bond process, the likelihood of its proceeding by the formation of two bonds simultaneously, is exceedingly remote due to the stringent geometric requirements for such simultaneous bonding. However, in certain transformations it is geometrically impossible (at least for a static model) to proceed by a single bond process; in such cases we shall consider the simplest bond process which can occur. Nonetheless, these multiple bond processes between close-packed forms are equivalent to single-bond processes involving more loosely packed forms. With these assumptions, we shall start with a consideration of the structure of the higher j-mers. The conclusions are summarized in Table I and in the text there are comments on the various steps and their interpretations.

THE 2-MER

. There is little new to be said about the formation of the 2-mer. The equations are from an earlier publication.[1]

THE 3-MER

There are two forms of the 3-mer possible, the linear form and the close-packed (cp) form. The concentration of the two species depends entirely on the value of the equilibrium constants. The formation of the linear 3-mer from the 2-mer and the 1-mer involves the formation of a single bond; because we have postulated a spherically symmetric force field, undoubtedly the energy requirements for forming this single bond are the same as the energy requirements for forming a single bond between two 1-mers. However, the probabilities are different since there are two ends on the 2-mer where the 1-mer can combine and break off. Hence, as a first and probably good approximation, $K_{1,2}=2k_{1,2}/2l_{1,2}=K$. We take $k_{1,2}=k_{1,1}$ and $l_{1,2}=l_{1,1}$, where $k_{1,1}$ is the specific-rate constant of aggregation of two 1-mers to a 2-mer, and $l_{1,1}$ is the specific-rate constant of degradation of a 2-mer to two 1-mers. Correspondingly, the subscripts 1, 2 refer to the process between a 1-mer and a 2-mer to form a 3-mer.

For the concentration of the close-packed 3-mer, the problem is a little more complex. According to our assumptions the cp form is formed from and decom-

* On leave 1960–61; Present address: 207 Park Building, University of Utah, Salt Lake City, Utah.

[1] R. Ginell, Ann. N. Y. Acad. Sci. **60**, 521 (1955).

[2] J. O. Hirschfelder, C. F. Curtiss and R. B. Bird, *Molecular Theory of Gases and Liquids* (John Wiley & Sons, Inc., New York 1954).

[3] T. L. Hill, *Statistical Mechanics* (McGraw-Hill Book Company, Inc., New York, 1956).

TABLE I.

Species	Reaction	Equilibrium constant	Concentration	Number of bonds	Number of forms
2-mer	$n_1+n_1 \underset{l_{1,1}}{\overset{k_{1,1}}{\rightleftarrows}} n_2$	$K_2=k_{1,1}/2l_{1,1}=K/2$	$C_2=\frac{1}{2}KVC_1^2$	1	1
3-mer	$n_2+n_1 \underset{m'=2}{\overset{m=2}{\rightleftarrows}} n_1-n_1$ (linear n_1)	$K_3(\text{lin})=K_2\cdot(2k/2l)=K^2/2$	$C_3(\text{lin})=\frac{1}{2}K^2V^2C_1^3$	2	2
	$n_1-n_1 \underset{m'=3}{\overset{m=1}{\rightleftarrows}} n_1-n_1$ (n_1, n_1)	$K_3(\text{cp})=K_3(\text{lin})\cdot(k/3l)=K^3/6$	$C_3(\text{cp})=1/6K^3V^2C_1^3$	3	
4-mer	$n_3+n_1\rightleftarrows n_4$ (see Fig. 1)	$K_{4\text{I}}=K_3(\text{lin})\,2k/2l=K^3/2$	$C_{4\text{I}}=(K^3/2)\,V^3C_1^4$	3	6 total 1 cp)
		$K_{4\text{II}}=K_3(\text{lin})\,k/3l=K^3/6$	$C_{4\text{II}}=(K^3/6)\,V^3C_1^4$	3	
		$K_{4\text{III}}=K_3(\text{cp})\,3k/l=K^4/2$	$C_{4\text{III}}=(K^4/2)\,V^3C_1^4$	4	
		$K_{4\text{IV}}=K_3(\text{lin})\,(2k\cdot k)/(2l\cdot 4l)=K^4/8$	$C_{4\text{IV}}=(K^4/8)\,V^3C_1^4$	4	
		$K_{4\text{V}}=K_3(\text{cp})\,[(3k\cdot 2k)/l\cdot 4l)]=K^3/4$	$C_{4\text{V}}=(K^5/4)\,V^3C_1^4$	5	
		$K_{4\text{VI}}=K_3(\text{cp})\,[(3k\cdot 2k\cdot 2k)/(l\cdot 4l\cdot 6l)]=K^6/12$	$C_{4\text{VI}}=(K^6/12)\,V^3C_1^4(\text{cp})$	5	
5-mer	$n_4+n_1\rightleftarrows n_5$ (see Fig. 2)	$K_5(\text{cp})=K_4(\text{cp})\,[(4k\cdot 3k\cdot 2k)/(l\cdot 2l\cdot 6l)]=K^9/6$	$C_5(\text{cp})=(K^9/6)\,V^4C_1^5$	9	20 total (1 cp)
6-mer	$n_5+n_1\rightleftarrows n_6$ (see Fig. 3)	$K_{6a}(\text{cp})=K_5(\text{cp})\,[(2k\cdot 3k\cdot 2k)/(l\cdot l\cdot 4l)]=\frac{1}{2}K^{12}$	$C_{6a}(\text{cp})=\frac{1}{2}K^{12}V^5C_1^6$	12	1 (cp)
		$K_{6t}(\text{cp})=K_{6a}(\text{cp})\,[(k\cdot l)/(12l\cdot k)]=K^{12}/24$	$C_{6t}(\text{cp})=1/24K^{12}V^5C_1^6$	12	1 (cp) Total (2 cp)
7-mer	$n_6+n_1\rightleftarrows n_7$ (see Fig. 4)	$K_{7a}(\text{cp})=K_{6a}[(2k\cdot 2k\cdot k\cdot k')/(l\cdot l\cdot 2l\cdot l')]=K^{15}K'$	$C_{7a}=6K^{15}K'V^6C_1^7$ (all forms) (?)	15+1	6 forms (?) (5 degenerate)
		$K_{7bD}=K_{6a}\cdot(4k^3/2l^3)=K^{15}$	$C_{7bD}=K^{15}V^6C_1^7$	15	1
		$K_{7bL}=K_{6a}\cdot(4k^3/2l^3)=K^{15}$	$C_{7bL}=K^{15}V^6C_1^7$	15	1
		$K_{7c}=K_{6a}\cdot(4k^3/6l^3)=\frac{1}{3}K^{15}$	$C_{7c}=\frac{1}{3}K^{15}V^6C_1^7$	15	1
		$K_{7t}=K_{6t}\cdot(48k^3/6l^3)=\frac{1}{3}K^{15}$	$C_{7t}=\frac{1}{3}K^{15}V^6C_1^7$	15	1 10 forms (cp)
8-mer	$n_7+n_1\rightleftarrows n_8$ (see Fig. 5)	$K_{8a}=60K^{18}K'$	$C_{8a}=60K^{18}K'V^6C_1^8$ (all forms)	18+1	6 (?)
		$K_{8b}=K^{18}$	$C_{8b}=K^{18}V^6C_1^8$	18	1
		$K_{8c}=\frac{1}{3}K^{18}$	$C_{8c}=\frac{1}{3}K^{18}V^6C_1^8$	18	1
		$K_{8d}=K^{18}$	(D&L) $C_{8d}=2K^{18}V^6C_1^8$	18	2 (D&L)
		$K_{8e}=K^{18}$	$C_{8e}=K^{18}V^6C_1^8$	18	1
		$K_{8ta}=\frac{1}{2}K^{18}$	$C_{8ta}=\frac{1}{2}K^{18}V^6C_1^8$	18	1
		$K_{8tb}=K^{18}$	$C_{8tb}=K^{18}V^6C_1^8$	18	1
		$K_{8tc}=\frac{1}{3}K^{18}$	$C_{8tc}=\frac{1}{3}K^{18}V^6C_1^8$	18	1
		$K_{8td}=K^{18}$	$C_{8td}=K^{18}V^6C_1^8$	18	1 15 forms (cp)

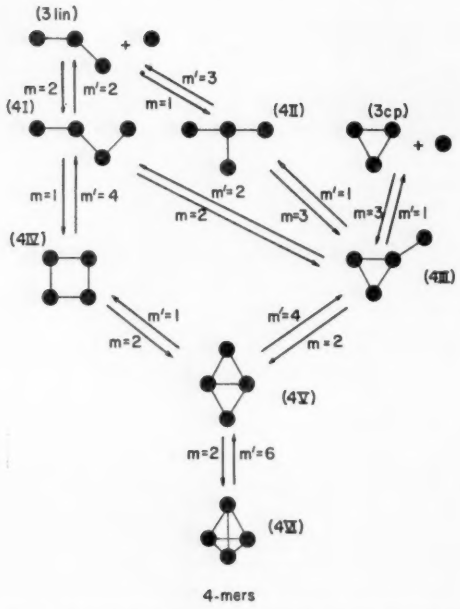

FIG. 1. Schematic diagram of all possible 4-mers and the multiplicities involved in their transformations.

poses into the linear form. We can write the equilibrium constants elementarily in the following way:

$$K_3(\text{linear}) = K_2 \cdot K_{1,2(3\text{lin})} = \tfrac{1}{2}K \cdot (2k_{1,2}/2k_{1,1}) = \tfrac{1}{2}K^2$$

$$K_3(\text{cp}) = K_{3\text{lin}} \cdot [k_{3\text{lin}(3\text{cp})}/l_{3\text{cp}(3\text{lin})}], \tag{1}$$

and

$$k_{3\text{lin}(3\text{cp})} = ma \exp(-\epsilon/RT) \tag{2}$$

$$l_{3\text{cp}(3\text{lin})} = m'a' \exp(-\epsilon'/RT), \tag{2'}$$

where m or m' = the multiplicity = the number of ways in which the particular step can be done, ϵ or ϵ' = energy of activation of the particular step, and a or a' = the probability that the process will occur given the requisite energy conditions. The primed quantities refer to the backward step (breaking bonds), the unprimed, the forward step (making bonds). Here, $k_{n(j)}$ is the specific rate constant of the formation of a j-mer from an n-mer, $j=n$ (the j-mer has more bonds than the n-mer), $k_{1,n(j)}$ is the specific-rate constant of the formation of a j-mer from an n-mer and a 1-mer; $j=n+1$, l in general is used in a sense opposite to k. Whereas k denotes the formation of a bond, l denotes the breaking of bonds.

To a first approximation we can take the energy factors ϵ to be identical for all formation steps, and ϵ' to be separately identical for all degradation steps. (ϵ is not however equal to ϵ'.) The multiplicity of the various steps can be calculated and we have done so later. The factors a and a' are however, difficult to specify exactly. While in the case of the formation of a bond from a 1-mer and an n-mer, the a factor is probably equal or close to equal, to the a factor in the 1-mer-1-mer reaction; in the formation of the second or close-packing bonds, they are probably not equal. However, in this paper we shall assume that the a and a' factors in all cases are, respectively, equal. While this is undoubtedly a poor approximation, it will simplify our results without disturbing their qualitative significance. The exact quantitative evaluation which is possible pragmatically, will be reserved for a later paper where an analysis of the values in a real substance will be undertaken.

The result of this assumption is that

$$k_{n(j)} = m_{n(j)}k_{1,1} = m_{n(j)}k \tag{3}$$

and

$$l_{j(n)} = m'_{j(n)}l_{1,1} = m'_{j(n)}l. \tag{3'}$$

This is equivalent to stating that all bonds are alike and are the same as a single bond. The values for the 3-mer in Table I were calculated using this assumption.

THE 4-MER AND SHORT CALCULATION OF THE CONCENTRATION

As can be seen from Fig. 1, the 4-mer process is more complex. There are six forms possible, of which one is close packed. Following the process described in a previous publication[1] of writing the differential equations describing the growth and degradation of the various species, summing the equations, and equating to zero (since this is an equilibrium process), we arrive at the following set of equations:

$$\begin{aligned}
&k_{1,3\text{lin}(4\text{I})}n_1n_{3\text{lin}} - l_{4\text{I}(1,3\text{lin})}n_{4\text{I}} - k_{4\text{I}(4\text{IV})}n_{4\text{I}} + l_{4\text{IV}(4\text{I})}n_{4\text{IV}} \\
&\qquad - k_{4\text{I}(4\text{III})}n_{4\text{I}} + l_{4\text{III}(4\text{I})}n_{4\text{III}} = 0 \\
&k_{1,3\text{lin}(4\text{II})}n_1n_{3\text{lin}} - l_{4\text{II}(1,3\text{lin})}n_{4\text{II}} - k_{4\text{II}(4\text{III})}n_{4\text{II}} \\
&\qquad + l_{4\text{III}(4\text{II})}n_{4\text{III}} = 0 \\
&k_{1,3\text{cp}(4\text{III})}n_1n_{3\text{cp}} - l_{4\text{III}(1,3\text{cp})}n_{4\text{III}} + k_{4\text{II}(4\text{III})}n_{4\text{II}} \\
&\qquad - l_{4\text{III}(4\text{II})}n_{4\text{III}} + k_{4\text{I}(4\text{III})}n_{4\text{I}} - l_{4\text{III}(4\text{I})}n_{4\text{III}} \\
&\qquad - k_{4\text{III}(4\text{V})}n_{4\text{III}} + l_{4\text{V}(4\text{III})}n_{4\text{V}} = 0 \\
&k_{4\text{I}(4\text{IV})}n_{4\text{I}} - l_{4\text{IV}(4\text{I})}n_{4\text{IV}} - k_{4\text{IV}(4\text{V})}n_{4\text{IV}} + l_{4\text{V}(4\text{IV})}n_{4\text{V}} = 0 \\
&k_{4\text{III}(4\text{V})}n_{4\text{III}} - l_{4\text{V}(4\text{III})}n_{4\text{V}} + k_{4\text{IV}(4\text{V})}n_{4\text{IV}} - l_{4\text{V}(4\text{IV})}n_{4\text{V}} \\
&\qquad - k_{4\text{V}(4\text{VI})}n_{4\text{V}} + l_{4\text{VI}(4\text{V})}n_{4\text{VI}} = 0 \\
&k_{4\text{V}(4\text{VI})}n_{4\text{V}} - l_{4\text{VI}(4\text{V})}n_{4\text{VI}} = 0.
\end{aligned} \tag{4}$$

On using Eqs. (3) and (3′) and the multiplicities shown on Fig. 1, the values of the rate constants are

$$\begin{aligned}
&k_{1,3\text{lin}(4\text{I})}=2k; && l_{4\text{I}(1,3\text{lin})}=2l\\
&k_{4\text{I}(4\text{IV})}=k; && l_{4\text{IV}(4\text{I})}=4l\\
&k_{4\text{I}(4\text{III})}=2k; && l_{4\text{III}(4\text{I})}=2l\\
&k_{1,3\text{lin}(4\text{II})}=k; && l_{4\text{II}(1,3\text{lin})}=3l\\
&k_{4\text{II}(4\text{III})}=3k; && l_{4\text{III}(4\text{II})}=l\\
&k_{4\text{IV}(4\text{V})}=2k; && l_{4\text{V}(4\text{IV})}=l\\
&k_{1,3\text{cp}(4\text{III})}=3k; && l_{4\text{III}(1,3\text{cp})}=l\\
&k_{4\text{III}(4\text{V})}=2k; && l_{4\text{V}(4\text{III})}=4l\\
&k_{4\text{V}(4\text{VI})}=2k; && l_{4\text{VI}(4\text{V})}=6l. \qquad (5)
\end{aligned}$$

On substituting the values from Eq. (5) into Eq. (4), dividing by l, and solving the resulting set of equations simultaneously, we get values for the concentrations shown in Table I.

There is a simpler method possible for arriving at the concentrations of the various species, which avoids the necessity of solving simultaneous equations and also obviates the necessity of considering all possible species. This method is to follow any path of reaction desired to the final product. The concentration of the final product will then be the product of the equilibrium constants along the chosen path. By this method identical answers are obtained. For instance by this method,

$$n_{4\text{cp}}=K_{3\text{cp}}(3k\cdot 2k\cdot 2k/l\cdot 4l\cdot 6l)n_1{}^4=\tfrac{1}{6}K^3\cdot\tfrac{1}{2}K^3\cdot n_1{}^4=\tfrac{1}{12}K^6n_1{}^4, \qquad (6)$$

which result is the same as that obtained via the simultaneous equations. This method has further utility especially in the consideration of the more complex species since varying the paths by which one obtains a particular species should always yield the same final concentration. If one obtains differing answers, then it is obvious that somewhere one has chosen the wrong multiplicities.

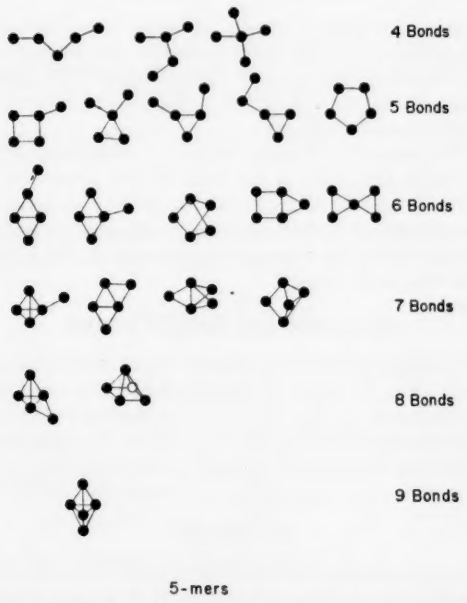

FIG. 2. Schematic diagram of all possible 5-mers.

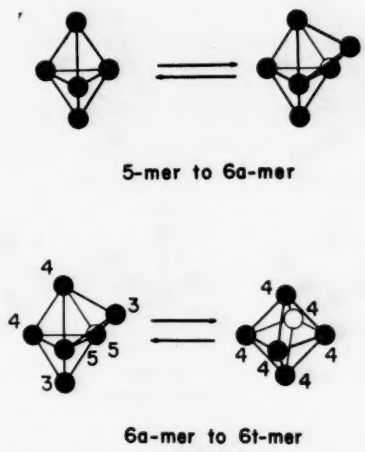

FIG. 3. Schematic diagram showing conversion of cp 5-mer to the 6*a*-mer and the transition of a 6*a*-mer to a 6*t*-mer. (Numbers give the number of bonds of each atom.)

THE 5-MER PROCESS

As can be seen from Fig. 2 there are 20 different 5-mers. All these forms are loose mobile forms, able to move forward or back a generation by breaking or making one bond. The concentrations of the various forms can be easily calculated, although in Table I only the concentration of the close-packed form is given.

THE 6-MER PROCESS

In the 6-mer there are many more forms than in the 5-mer. However, most important are the two close-packed forms (Fig. 3). The route chosen to calculate the concentration of the 6*t*-mer is by a transition from the 6*a*-mer, however, it can be formed directly from the loose forms of the 5-mer. The numbers attached to the component atoms in the 6-mer denote the number of bonds each atom has.

THE 7-MER PROCESS

The 7-mer, in addition to many loose forms, has a number of close-packed forms. Four of these forms are straightforward and unambiguous, the 7*b*-mer which has both *D* and *L* forms, the 7*c*-mer and the 7*t*-mer (see

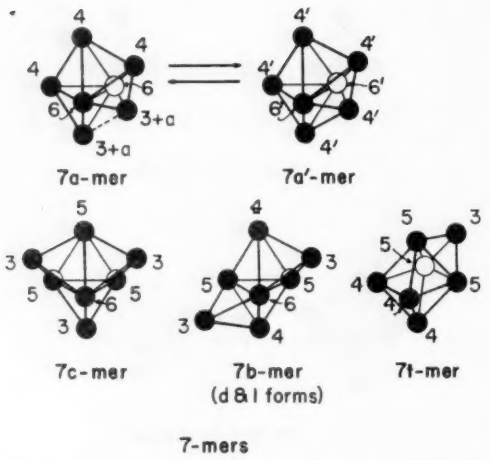

FIG. 4. Schematic diagram showing all possible close-packed 7-mers. (Numbers indicate the number of bonds of each atom.)

Fig. 4). These forms have 15 bonds each and can transform from one to another. The 7*a*-mer, however, is unusual. Owing to the geometric relationships, when one makes the 15th bond, the final atom comes extremely close to another atom; that is, one simultaneously makes a 16th bond. This 16th bond is about 10.9% longer than the other 15 bonds as derived from actual measurements on a static model. In addition, this bond can move from its original position to any position around the five ring, since the activation energy is very slight. This can be readily seen from models. (See Fig. 6.) While the potential barrier to be surmounted in order to transform a 7*b*-mer to a 7*c*-mer is relatively high, the barrier existing in the 7*a*-mers is much lower. This means that the weak bond can wander around the ring. It can also go to the central atoms so that the 6′—6′ bond becomes the weak bond; here there is no activation energy barrier. Hence, the equilibrium form that this form probably assumes is either the 7*a*′-mer, or a 7*a*-mer, where all the bonds are a little longer, the extra 10.9% being distributed over all the bonds. This of course makes the concentration calculation a little more difficult. We have assumed that there are six forms, five of which are degenerate by the following reasoning: We assume that the weak bond can occupy any of the 4′—4′ positions giving five identical (degenerate forms) and that the 6th form is where the weak bond is the 6′—6′ bond. However, as previously discussed, if all the bonds loosen to some extent so as to get a form intermediate between all these forms then the concentration calculation is probably not correct and the concentration is still higher than that given; hence, the factor 6 should be replaced by a factor w of undetermined magnitude.

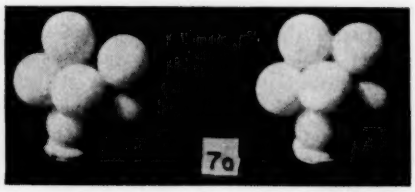

FIG. 6. Photograph of a model of 7*a*-mer is on the left showing the *a* bond. On the right is a model of a 7*a*′-mer.

The result of this much higher concentration of the 7*a*-mer is that most of the close-packed 7-mer will be in the 7*a*-mer form. However, as can be seen from an examination of models, the 7*a*-mer cannot give rise to a regular crystalline array; the only form in the 7-mers that will, is the 7*t*-mer.

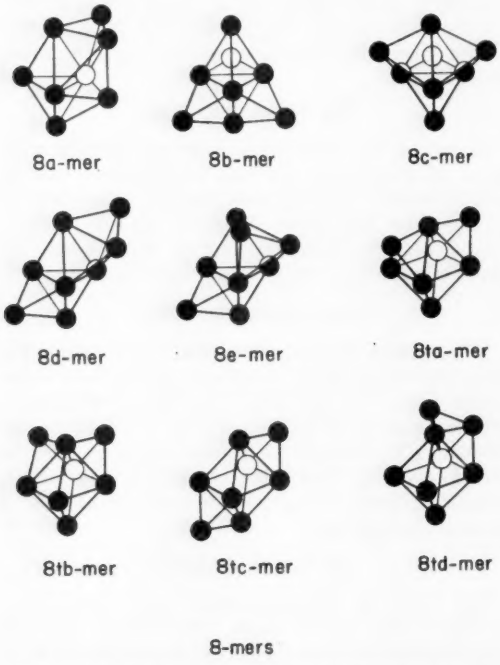

FIG. 5. Schematic diagram of all possible close-packed 8-mers.

THE 8-MER AND HIGHER FORMS

Pursuing this trend of thought we can see that in the 8-mer (Fig. 5), where 15 close-packed forms exist, the concentration of the 8*a*-mer is predominant. In the higher *j*-mers as can be seen from Table II, the process of forming these weaker *a* bonds is further carried on in the *a* forms, while the *t* forms only make regular bonds.

GAS PHASE

For quantitative and qualitative predictions we must consider the absolute value of K. If K is substantially less than 1, then the substance is in the gas phase. This

TABLE II. Number of bonds for most close packed species (*t* & *a* series).

Species	*a* form				*t* form (cp)	
	No. regular bonds	No. weaker bonds	total No. bonds	No. atoms 3 bonds	total No. regular bonds	No. 3 bonds
3-mer	3	...	3			
4-mer	6	...	6	4		
5-mer	9	...	9	2		
6-mer	12	...	12	2	12	0
7-mer	15	1	16	0	15	1
8-mer	18	1	19	1	18	2
9-mer	21	2	23	0	21	1
10-mer	24	3	27	0	25	0
11-mer	27	4	31	0	28	1
12-mer	30	6	36	0	32	0
13-mer	33	7	40	0	36	0
14-mer	36	7	43	1	39	1
15-mer	39	8	47	0	43	0
16-mer	42	9	51	0	48	0
17-mer	45	10	55	0	52	0
18-mer	48	11	59	0	56	0
19-mer	51	12	63	0	60	0

can be seen from a consideration of the following equations,

$$\sum_{i=1}^{m} iC_i = C_1 + 2C_2 + 3C_3 + \cdots mC_m, \tag{7}$$

where C_m is the concentration of the mth species, the largest present in the system. Substituting the values for C_x in the right-hand side of Eq. (7) gives

$$\sum_{i=1}^{m} iC_i = C_1 + 2K_2C_1^2 + 3[K_3]C_1^3 + 4[K_4]C_1^4 + \cdots m[K_m]C_1^m, \tag{8}$$

where $[K_j]$ is equal to the sum of the K_j for the various species. Inverting[4] Eq. (8) we get

$$C_1 = \sum_{x=1}^{\infty} d_x \Big(\sum_{1}^{m} iC_i\Big)^x, \tag{9a}$$

where

$$d_1 = 1$$

$$d_2 = -2K_2$$

$$d_3 = 8K_2^2 - 3[K_3]$$

$$d_4 = -40K_2^3 + 30K_2[K_3] - 4[K_4]$$

$$d_5 = 224K_2^4 - 252K_2^2[K_3] + 48K_2[K_4] + 27[K_3]^2 - 5[K_5], \quad \text{etc.} \tag{9b}$$

[4] R. Ginell, J. Chem. Phys. **23**, 2395 (1955).

Although Eq. (8) is for a finite series, it can be inverted just as an infinite series to give Eq. (9) if one discards in the coefficients of d_x, all the K_j where $j > m^{(1)}$. Now

$$\sum_{i=1}^{m} iC_i = g/M^{(0)}V,$$

where g is the weight of sample in a volume V and $M^{(0)}$ is the weight in grams of an Avogadro number of the 1-mer. Hence, this is an experimental quantity.

If one substitutes the values of K from Table I[5] in $[K_j]$, one gets

$$[K_3] = (K^2/2 + \tfrac{1}{6}K^3)V^2$$

$$[K_4] = [K^3/2 + K^3/6 + K^4/2 + K^4/8 + K^5/4 + K^6/12]V^3 = (4/6K^3 + 5/8K^4 + K^5/4 + K^6/12)V^3, \quad \text{etc.}$$

One can readily see that when K is small and less than 1, the species that are present in greatest abundance are the lower forms (j small) and the loose forms. (Since the loose forms have fewer bonds, K is raised to a lower power.) For instance, in helium[6] at about 200°K, K_2 is approximately 10^{-4}. This means that the system will consist mainly of 1-mers to the extent of about 99.9991% and the greater part of the rest will be 2-mers. This is essentially the classical picture we have of

[5] The K's in Eqs. (8) and (9) are K_ϵ while the K's from Table I are K_N hence the necessity of inserting the V^n which are the conversion factors.

[6] R. Ginell (to be published).

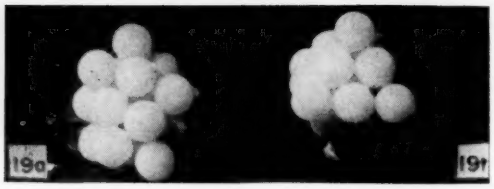

FIG. 7. Photograph of model at left is a 19*a*-mer which is a liquid array, model at right is a 19*t*-mer which is a crystal array.

a gas. As the temperature decreases K_2 increases in value.

LIQUID AND SOLID STATES

As the value of K increases, the number of higher j-mers increases. However in the 7-mer the form having the preponderant concentration is the 7*a*-mer. This preponderance increases in the 8*a*-mer and higher j-mers. When the value of K exceeds 1, then the concentration of the close packed forms exceeds the concentration of the loose packed forms. The great majority of these forms are however in the *a* state. (The power to which K is raised is equal to the number of bonds). However, the *a* state is not regular in the sense that they cannot give rise to a regular crystal form. The only way to go to a regular crystal is through the *t* forms, which however are very few in number and which have fewer bonds. As a result a liquid consisting of *a* forms condenses from the gas.

These *ja*-mers would correspond to the solid like phase postulated by Eyring[7] and co-workers in their treatment of the liquid state and also would fulfill the criteria of Bernal's[8] prenuclei. The internal particles in the *ja*-mers have a coordination number of 12 but exhibit fivefold symmetry.

MECHANISM OF THE GROWTH PROCESS

If the rate of growth is slow and K is greater than 1, then a 1-mer when it strikes a j-mer, loses its freedom of translation relative to the j-mer and now has 1° of vibrational freedom and 2° of rotational freedom. It is, however, at the crest of a potential energy hill and falls down making a second bond and further down making a third bond. It is now in a 3-hole where it is at a potential energy minimum. The only degrees of freedom that it has are vibrational degrees. It can escape from this 3-hole by breaking one bond going over a potential energy barrier and falling into another hole (potential energy minimum). If this is a 3-hole, the particle continues to move over the surface in a series of jumps from one 3-hole to another 3-hole. Occasionally it may fall into a 4-hole. Here it has formed two new bonds and is at a lower energy level than in a three hole and needs twice as much energy to escape because from the geometry, it can no longer break one bond at a time but must break two bonds simultaneously. The process could also proceed through one of the looser forms breaking several bonds, one at a time, successively but this is also a difficult process. The result is that a 4-hole is a relatively stable position. Similarly, escape from a 5-hole or higher is progressively more difficult.

In Table II we exhibit the results obtained by taking the 7*a*-mer and the 7*t*-mer and growing them in this way (using models) and for each step figuring the most close-packed system. (See Fig. 7.) The number of bonds resulting are given in the table. For the *ja*-mer, this is an exceedingly difficult process since the *ja*-mer must in reality be quite mobile, while the actual models are static. However, it can be seen that the growth is not quite regular and that while the number of bonds in *jt*-mers is equal to the number of regular bonds in the *ja*-mer till the 9-mer, the *ja*-mer contains a number of extra bonds (weaker bonds). The number of bonds in the *jt*-mers, which are all normal bonds, increase and after the 9-mer exceed the number of regular bonds in the *ja*-mer. But up to the 19-mer the *ja*-mer still has a greater number of bonds (counting both weak and regular). However, the *a*-series does not give rise to a regular structure while the *t*-series does. This means that when a gas condenses slowly it goes to form a liquid.

To convert this liquid to a crystal means that the value of K must be such that the high *jt*-mers are stable compared to the *a* forms and a cooperative endeavor involving in the neighborhood of 12 to 15 atoms must ensue. These 12 to 15 atoms must rearrange themselves to an unstable *jt*-mer that can then grow to a size that is stable compared to *ja*-mers of corresponding size. This is naturally a difficult process and hence homogeneous nucleation occurs only with great difficulty and then only at lower temperatures where K is greater.

Heterogeneous nucleation is however comparatively easy. If one seeds the liquid (whose K is in the right range) with micro crystals or with a foreign substance whose interatomic distances are correct, then one has effectively bypassed the region where the *jt*-mers are unstable. Hence crystal growth proceeds readily and can be extremely rapid.

ACKNOWLEDGMENT

The author wishes to acknowledge the help resulting from many stimulating discussions with Dr. Albert E. Sobel.

[7] H. Eyring, T. Ree, and N. Hirai, Proc. Natl. Acad. Sci. U. S. **44**, 683 (1958); E. J. Fuller, T. Ree, and H. Eyring, *ibid.* **45**, 1594 (1959); C. M. Carlson, H. Eyring, and T. Ree, *ibid.* **46**, 333 (1960); T. R. Thomson, H. Eyring, and T. Ree, *ibid.* **46**, 336 (1960); C. M. Carlson, H. Eyring, and T. Ree, *ibid.* **46**, 649 (1960).

[8] J. D. Bernal, Nature **185**, 68 (1960).

Shock Tube Study of Vibrational Relaxation in the $A\ ^2\Sigma^+$ State of NO†

W. Roth

Armour Research Foundation, Physics Research Division, Chicago, Illinois

(Received May 10, 1960)

Nonequilibrium NO γ-band emission has been observed behind incident shock waves in rare gas-air mixtures in the approximate temperature range, 5000–10 000°K. Vibrational relaxation times for collisional de-excitation of NO($A\ ^2\Sigma^+$) were measured. The measured relaxation times were used to calculate P_{10}, the probability for collisional de-excitation of the $v'=1$ level of the $A\ ^2\Sigma^+$ state; P_{10} ranges from about 3×10^{-5} at 5000°K to 3×10^{-4} at 10 000°K.

THE study of nonequilibrium emission of radiation behind shock waves has been receiving increasing attention. When a molecule is formed by recombination of atoms, the upper vibrational energy levels have an initial population in excess of that at equilibrium. If the electronic state involved is not the ground state, then electronic transitions originating from the highly populated upper vibrational levels will result in visible or ultraviolet band emission which exceeds the same band emission in intensity under conditions of thermal equilibrium. In addition, the relative intensities of the emitted bands during the approach to an equilibrium distribution of vibrational energy will be different from those observed when equilibrium is finally attained. Since vibrational equilibration is slow compared to translational and rotational equilibration, it is possible, with rather simple techniques, to observe a changing intensity distribution in the bands emitted by electronically excited molecules behind strong shock waves. This has been observed, for the violet band system of CN.[1]

It is known that the NO concentration behind strong shock waves in air overshoots its equilibrium value during the approach to chemical equilibrium.[2] Thus, it may be expected that the population of excited electronic states of NO also exceeds an equilibrium population and that vibrational relaxation effects in the upper electronic states will be observed. Vibrational relaxation of NO in its ground electronic state has been measured[3] but no attempt had been made to observe this phenomenon in any of the excited electronic states.

EXPERIMENTAL

A 1-in. i.d. glass and quartz shock tube with high and low pressure sections 1 and 2 m long, respectively, was used to produce shock waves in pure Xe or Ar and in these same gases containing up to 5% of room air. The rare gases used were Airco Assayed reagent grade contained in Pyrex break-seal vessels. One batch of Xe contained 0.04 mole % of Kr but all other batches of Xe and Ar used contained no mass spectrometrically detectable impurities. Incident shocks in the Mach number range, $M_s \approx 8$–11 were produced in Xe, with and without air, using a He driver, and for Ar a H_2 driver was used to produce $M_s \approx 8$–10.

The shock tube was instrumented as described earlier[1,4] with velocity stations consisting of a series of reflecting surfaces cut into a Lucite rod leading to an unfiltered 1P21 photomultiplier tube. A grating monochromator-1P28 photomultiplier combination was used to observe the emitted light, and its $\frac{1}{2}$-mm entrance slit was exactly opposite the slit of one of the velocity stations located 37 cm from the downstream end of the shock tube. Velocity records with nine photomultiplier stations, spaced 20 cm apart, indicated that in the M_s range produced in this work, the shock velocity remained constant in a region from 25 to 75 cm from the downstream end of the shock tube and decreased on either side of this region.

The entrance and exit slit widths of the monochromator resulted in a spectral half-width of 55 A. With a monochromator setting of 2250 A it was possible to observe the combined temporal behavior of $\gamma(1, 1)$ and $\gamma(0, 0)$ emission at 2244 and 2269 A, respectively. In order to observe depopulation of the $v'=1$ level of the $A\ ^2\Sigma^+$ state, uncomplicated by any superimposed emission from $v'=0$, it was found convenient to use a monochromator setting of 2810 A thus isolating the $\gamma(1, 6)$ band.

The temporal behavior of γ-band emission with respect to the shock front was observed by displaying both the velocity station and monochromator signals on the oscilloscope while chopping the sweep at 100 kc.

Spectra of incident shocks were photographed with a Hilger Medium Quartz Prism spectrograph using a 103-0 uv sensitive plate. The spectrum of a Hg germi-

† This work supported by the Bendix Corporation under contract to the Army Rocket and Guided Missile Agency, Huntsville, Alabama.

[1] W. Roth, J. Chem. Phys. **31**, 720, 1683 (1959). This paper indicated incorrectly that the ratio of equilibrium populations, N_1/N_0 in the $B\ ^2\Sigma^+$ state was 0.8. The correct statement should be: "the ratio of equilibrium intensities I_{11}/I_{00} in the $B\ ^2\Sigma^+$ state is about 0.6."

[2] J. J. Allport, Bull. Am. Phys. Soc. Ser. II, **4**, 328 (1959).

[3] F. Robben, J. Chem. Phys. **31**, 420 (1959).

[4] W. Roth and P. Gloersen, J. Chem. Phys. **29**, 820 (1958).

TABLE I. Bands observed in spectrum of 25 incident shock waves in Xe containing up to 5% air.

N_2^+ — 1st negative		CN-violet		NO-γ	
λ, A	(v', v'')	λ, A	(v', v'')	λ, A	(v', v'')
4652	(1, 3)	3883	(0, 0)	2479	(0, 2) P
4600	(2, 4)	3871	(1, 1)	2471	(0, 2) Q
4167	(3, 4)	3862	(2, 2)		
		3855	(3, 3)		
		3584	(3, 2)		

cidal lamp was superimposed for wavelength calibration.

RESULTS

Xenon

The spectrum of 25 incident shocks of various strengths in Xe containing up to 5% air was photographed by multiple exposure of the shocks as they swept by the spectrograph slit. The slit was positioned sufficiently far from the end of the shock tube to avoid exposure by radiation behind the reflected shock wave. This radiation was quenched by intersection of the reflected shock front and contact surface at a point far closer to the end of the tube. The bands observed are listed in Table I. In conformance with an earlier observation,[1] the relative intensities of the CN-violet bands were in reverse order from that observed in flames and discharges, and from that which could be calculated from known transition probabilities assuming equilibrium emission at any of the temperatures attained behind the shock fronts.

Figure 1 indicates the type of oscilloscope record obtained when a shock wave was produced in pure Xe. The upper trace represents the visible light signal from one of the velocity stations. The first peak is associated with impurity emission at the shock front. The second peak is continuum emission from Xe.[4] The lower trace is the simultaneously recorded signal from the monochromator set at 2250 A. Figure 2 is a similar record obtained for Xe+2.5% air. The upper trace here exhibits a series of peaks following the shock front which was identified earlier as CN-violet band emission.[1]

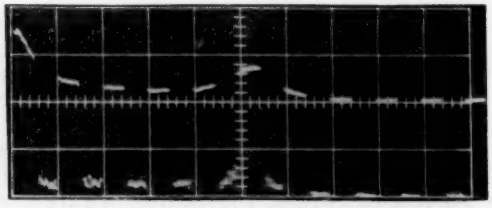

FIG. 1. Radiation from incident shock in pure Xe. Upper trace, visible radiation; Lower trace, 2250-A radiation; Sweep speed, 10 μsec/cm, chopped sweep.

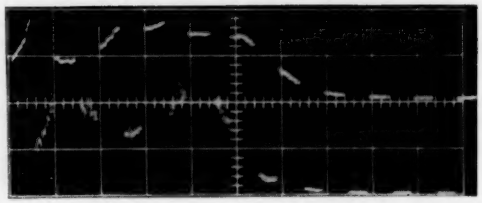

FIG. 2. Radiation from incident shock in Xe+2.5% air. Upper trace, visible radiation; Lower trace, 2250-A radiation; Sweep speed, 10 μsec/cm, chopped sweep.

In the lower trace, NO γ-band emission [(1,1) and (0, 0)] is seen to peak about 8 μsec (uncorrected for flow behind the shock) after passage of the shock front and this is followed by a peak in Xe continuum emission. When the sweep speed is increased and not chopped, the NO γ emission is resolved into two peaks as shown in Fig. 3 and these are followed by the peak in Xe continuum emission. The first peak represents $\gamma(1, 1)$ and the second is $\gamma(0, 0)$.

The following sequence of reactions, modified somewhat from that proposed earlier for nonequilibrium CN emission,[1] is employed to account for the observed results:

$$N+O \underset{M}{\overset{k_7}{\longrightarrow}} NO(A\,^2\Sigma^+)_{v'=3} \underset{k_8'}{\overset{k_8}{\rightleftarrows}} NO(X^2\pi)_{v''=i}+h\nu. \quad (1)$$

$$NO(A^2\,\Sigma^+)_{v'=3} \underset{M}{\overset{k_5}{\longrightarrow}} NO(A\,^2\Sigma^+)_{v'=2} \underset{k_6'}{\overset{k_6}{\rightleftarrows}} NO(X^2\pi)_{v''=i}+h\nu. \quad (2)$$

$$NO(A\,^2\Sigma^+)_{v'=2} \underset{M}{\overset{k_3}{\longrightarrow}} NO(A\,^2\Sigma^+)_{v'=1} \underset{k_4'}{\overset{k_4}{\rightleftarrows}} NO(X^2\pi)_{v''=i}+h\nu. \quad (3)$$

$$NO(A\,^2\Sigma^+)_{v'=1} \underset{M}{\overset{k_1}{\longrightarrow}} NO(A\,^2\Sigma^+)_{v'=0} \underset{k_2'}{\overset{k_2}{\rightleftarrows}} NO(X^2\pi)_{v''=i}+h\nu. \quad (4)$$

In (1) we assume that the $NO(A\,^2\Sigma^+)$ is initially formed in $v'=3$ inasmuch as no γ-band transitions originating from $v'>3$ have ever been observed. If our observations are restricted to $\gamma(1, 1)$ and $\gamma(0, 0)$

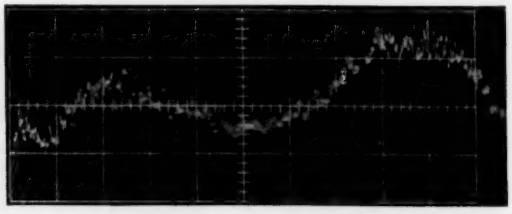

FIG. 3. 2250 A radiation from incident shock in Xe+2.5% air. Peaks represent $\gamma(1,1)$, $\gamma(0,0)$ and Xe continuum radiation, respectively. Sweep speed, 5 μsec/cm.

only, and if we choose the peak of $\gamma(1, 1)$ as our time origin, then we are concerned only with (3) and (4) and this is case, $i=0$. It is assumed that, at the peak of $\gamma(1, 1)$, the population of $v'=1 \gg v'=z$. The reverse reaction

$$\mathrm{NO}(A\,^2\Sigma^+)_{v'=0} \xrightarrow[M]{k'_1} \mathrm{NO}(A\,^2\Sigma^+)_{v'=1} \qquad (5)$$

is neglected inasmuch as the fully allowed electronic transition rate constant k_2 is very much greater than the vibrational transition rate constant k'_1, and the equilibrium

$$\overset{k_1}{\underset{k'_1}{\rightleftarrows}}$$

is not attained. Similarly, $k_2 \gg k_1$, and it can be shown[1] that the time between $\gamma(1, 1)$ and $\gamma(0, 0)$ peaks, which is equivalent to the period between the time origin and steady state $\gamma(0, 0)$ emission, is given by

$$t=[k_1(M)]^{-1} \ln \frac{[\mathrm{NO}(A\,^2\Sigma^+)_{v'=1}]_0}{[\mathrm{NO}(A\,^2\Sigma^+)_{v'=1}]_t} = \tau \ln R, \qquad (6)$$

where t is corrected for gas flow behind the shock, τ is the density dependent vibrational relaxation time for $v'=1 \rightarrow v'=0$ and the concentration ratio R is equivalent to the ratio of the intensity of $\gamma(1, 1)$ at its peak to that at the time of steady state in $\gamma(0, 0)$ emission. This is simply a function of the depopulation rate of the $v'=1$ state and can be measured by observing the decay rate of any electronic transition originating in $v'=1$. It has been found most convenient in these experiments to isolate the $\gamma(1, 6)$ emission at 2810 A for this purpose. A typical record is shown in Fig. 4. Each shock condition for which t was measured was duplicated as closely as possible for a measurement of R in this way. Relaxation times τ calculated from measurements of t and R are given in Table II for a range of temperatures and Xe densities behind the shock and for initial air concentrations of 2.5 and 5.0 mole %. T was calculated to the nearest 25°, from the measured incident shock Mach numbers. The sound velocities in Xe+2.5 % air and Xe+5.0 % air were taken as 0.181 and 0.185 mm/μsec, respectively, and an averaged specific heat ratio γ was used for each case.

FIG. 4. 2810 A radiation from incident shock in Xe+2.5% air. Decay rate of $\gamma(1,6)$ radiation. Sweep speed, 5 μsec/cm.

TABLE II. Relaxation times for $v'=1 \rightarrow v'=0$ in the $A\,^2\Sigma^+$ state of NO.

T, °K	ρ_{Xe}[a] 10^{17} cm^{-3}	Mole% air	τ, μsec
9900	1.25	2.5	34
8875	1.30	5.0	32
8875	1.30	5.0	49
8825	1.24	2.5	31
8275	1.24	2.5	39
7975	1.29	5.0	49
7400	1.29	5.0	91
7125	2.47	2.5	56
6950	2.47	2.5	41
6700	2.46	2.5	46
6650	2.56	5.0	64
6375	2.55	5.0	56
5425	2.54	5.0	106

[a] Initial pressures in the low pressure section of the shock tube were 1 mm and 2 mm for ρ_{Xe} equal to $\sim 1.25 \times 10^{17}$ cm^{-3} and $\sim 2.5 \times 10^{17}$ cm^{-3}, respectively.

The air was assumed to be undissociated since the extent of dissociation relaxation during vibrational equilibration was unknown and changing.

P_{10}, the probability of the radiationless transition $v'=1 \rightarrow v'=0$, was calculated from τ for each temperature and density in Table II. This is simply the reciprocal of the number of collisions during the life τ of the $v'=1 \rightarrow v'=0$ process. In calculating the collision frequency, the kinetic cross section of the NO($A\,^2\Sigma^+$) molecule was taken as 2.86 A. This value was obtained by adding 1.8 A to the spectroscopically determined equilibrium internuclear distance.[5] Theoretical treatments by Landau and Teller[6] and Schwartz and Herzfeld[7] both indicate an approximate $T^{-\frac{1}{3}}$ dependence of $\log P_{10}$. A plot of this type, of the results of this work, is shown in Fig. 5. It will be noted that P_{10} is apparently independent of ρ_{Xe} and initial air concentration, as expected. Widom[8] has suggested that $\log P_{10}$ is more properly a linear function of $T^{-\frac{1}{3}}$ or T. While a plot of the data as a function of $T^{\frac{1}{3}}$ appeared about as good as the $T^{-\frac{1}{3}}$ plot, the variation with T exhibited more scatter than shown in Fig. 5, particularly at high values of T.

[5] J. O. Hirschfelder and M. A. Eliason, Ann. N. Y. Acad. Sci. **67**, 451 (1957).
[6] H. A. Bethe and E. Teller, Ballistic Research Labs. Rept. X117 (1941).
[7] K. E. Herzfeld, "Relaxation phenomena in gases" in *Thermodynamics and Physics of Matter* (Princeton University Press, Princeton, New Jersey, 1955), p. 646.
[8] B. Widom, J. Chem. Phys. **27**, 940 (1957).

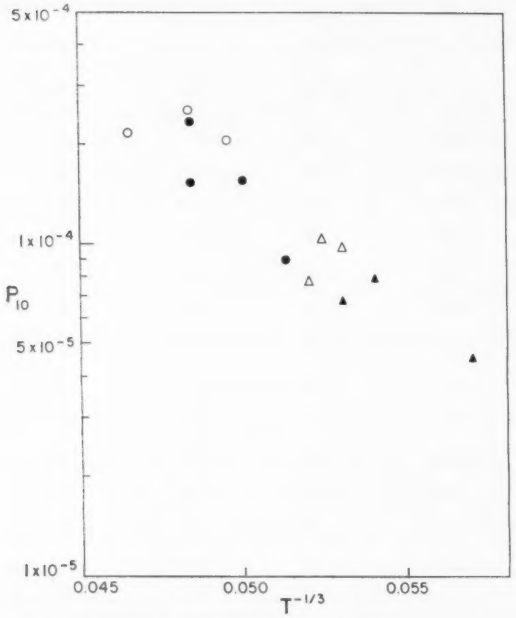

FIG. 5. Temperature dependence of the probability of a $v'=1\rightarrow v'=0$ transition in NO($A\ ^2\Sigma^+$). Open symbols refer to 2.5% initial air. Circles refer to ρ_{Xe} of about 1.25×10^{17} cm^{-3}. Triangles refer to ρ_{Xe} of about 2.5×10^{17} cm^{-3}.

Argon

Definitive results were unobtainable in Ar. It was immediately apparent that the intensity ratio $I_{0,0}/I_{1,1}$ was twice that observed in Xe and that the $\gamma(0, 0)$ emission was much broader in time and had a much flatter peak than the same emission in Xe. These effects were so pronounced that it was not possible to resolve $\gamma(1, 1)$ and $\gamma(0, 0)$ peaks when the initial air concentration was less than 5%. Furthermore, it proved impossible to isolate any γ-band emission originating in $v'=1$ from emission originating in $v'=0$. Emission from $v'=0$ appeared to have broadened. Presumably, however, isolation could have been effected if a smaller spectral half-width had been employed.

Despite the observational difficulties, a number of measurements were made of the time between $\gamma(1, 1)$ and $\gamma(0, 0)$ emission peaks in Ar containing 5% air. These gross results appeared to fall within the experimental scatter of the results obtained in Xe so that Xe and Ar do not appear to differ greatly in their ability to remove vibrational energy from NO($A\ ^2\Sigma^+$).

DISCUSSION

Rough estimates, based on the work of Mirels[9] and Duff,[10] indicated that, for the experimental conditions reported here, the boundary layer thickness at distances behind the shock fronts corresponding to the measured relaxation times, was always less than 2 mm. This estimate, together with the reported constancy of the shock velocity in the region of measurement, is considered sufficient evidence to justify the assumption of constant conditions in the relaxation region. Furthermore, while the boundary layer thickness could affect emission intensities, it could have no effect on the time to steady-state emission. Only the latter quantity was measured in this work.

A straight line was drawn, by eye, through the points in Fig. 5 and extrapolated slightly at each end to cover the range 5000–10 000°K. P_{10} values, thus obtained at 1000° intervals, were used to compute relaxation times at densities referred to a pressure of 1 atm for comparison with other relaxation times reported in the literature in this manner. The results are given in Table III.

Unfortunately, data on the relaxation time to equilibrium NO formation do not extend above about 3500°K,[11] but a further extrapolation of the results in Table III suggests that NO($A\ ^2\Sigma^+$) has relaxed to vibrational equilibrium before NO formation has reached equilibrium. This reduces the magnitude of the error in the calculated T in Table II and Fig. 5.

The vibrational frequency and anharmonicity constant of the $A\ ^2\Sigma^+$ state of NO indicate a dissociation level at about 14 ev above the zero level of the ground electronic state. However, γ-band emission originating from $v'>3$ has never been observed and this has been attributed to a crossing of the $A\ ^2\Sigma^+$ and $B^2\pi$ states at a point between the $v'=3$ and the $v'=4$ level of the former state.[12] This, and a further perturbation of $B^2\pi$ by other states, allows NO($A\ ^2\Sigma^+$) to be formed by inverse predissociation from normal atoms having relative velocities equivalent to about 6.5 ev. This relatively low-energy requirement explains why γ-band emission is so readily stimulated in the temperature range considered here. On the other hand, similar arguments can be used to show that β-band emission should also be easy to produce and this emission could possibly interfere with measurements at wavelengths where the two band systems overlap. However, it has been found that, at these high temperatures, the β-band system is smeared out into a continuum with no apparent structure[13] and therefore, in the small wavelength interval

TABLE III. Relaxation times referred to density at 1 atm pressure for $v'=1\rightarrow v'=0$ in NO ($A\ ^2\Sigma^+$).

T, °K	5000	6000	7000	8000	9000	10 000
τ, μsec	28	18	12	8	6	5

[9] H. Mirels, NACA TN-3401 (1955); NACA TN-3712 (1956).
[10] R. E. Duff, Phys. Fluids **2**, 207 (1959).
[11] W. E. Gibson and F. K. Moore, Cornell Aeronautical Lab., Rept. No. HF-1056-A-2 (1958).
[12] Y. Tanaka, J. Chem. Phys. **22**, 2045 (1954); J. T. Vanderslice, E. A. Mason, and W. G. Maisch, *ibid.* **31**, 738 (1959).
[13] J. C. Keck, J. C. Camm, B. Kivel, and T. Wentink, Ann. Phys. N. Y. **7**, 1 (1959).

in which relaxation was measured here, β-band emission was probably insignificantly weak.

The change in intensity ratio of $\gamma(0, 0)$ and $\gamma(1, 1)$ when Ar was used instead of Xe and the apparent broadening of $\gamma(0, 0)$ is consistent with some recent observations[14] in which addition of He to the NO afterglow caused a change in intensity distribution in the γ bands. This was attributed to the formation of excited NO in the three-body reaction,

$$N(^4S)+O(^3P)+M\rightarrow NO^*+M,$$

where the nature of the third body affects the distribution of vibrational energy during the formation of an intermediate state of NO. It is possible, therefore, that Ar and Xe are sufficiently different as third bodies to have produced the observed effect. However, in view of the paucity of experimental results on this effect at the present time, there are other equally valid explanations. For example, the intensity of the aforementioned β-band continuum radiation may be enhanced when Ar is the third body involved in formation of NO*.

It has been shown[6] that for vibrational levels whose end points are not far removed from the equilibrium internuclear distance (i.e., small v), $P_{v,v-1}=vP_{10}$. Thus since $NO(A^2\Sigma^+)$ is apparently formed at $v'=3$, for any T and ρ, the total relaxation time from the time of formation is only about 1.83 τ_{10}.

The results reported here and in an earlier publication[1] appear to indicate that for relatively nonpolar molecules, the predicted temperature dependence of the vibrational relaxation time[6–8] is the same for excited electronic states as it is for ground states.

[14] C. A. Barth, W. J. Schade, and J. Kaplan, J. Chem. Phys. **30**, 347 (1959).

THE JOURNAL OF CHEMICAL PHYSICS VOLUME 34, NUMBER 3 MARCH, 1961

Vacuum Ultraviolet Absorption Spectrum and Dipole Moment of Nitrogen Trifluoride*

S. R. La Paglia and A. B. F. Duncan

Department of Chemistry, University of Rochester, Rochester, New York

(Received August 29, 1960)

The electronic absorption spectrum of NF_3 was investigated for the first time. At the lowest pressures, the long wavelength limit of absorption is at about 960 A in agreement with the lowest ionization potential of the molecule (939 A). Quantitative intensity measurements showed a smooth decrease of the absorption coefficients to effectively zero at about 1800 A, with no indication of even partly resolved electronic transitions. Comparisons with the electronic spectrum of ammonia are discussed. The molecular dipole moment is used to obtain an equivalent orbital representation of the NF_3 wave function.

INTRODUCTION

THE absorption spectrum and excited electronic states of ammonia have been extensively studied,[1] but we have no information on the excited electronic states of nitrogen trifluoride. It was expected that the lower excited states of NF_3 are associated with excitation of an electron from a lone-pair orbital on the nitrogen atom, as in ammonia. It was further expected that the lowest electronic transition and lowest ionization energy would have values similar to the values for ammonia.

The molecular dipole moment of NF_3 is 0.234 debye and was first reported by Watson *et al.*[2] It has since been confirmed several times.[3,4] However, this small value of the moment does not necessarily indicate an almost planar structure. According to the electron diffraction work of Schomaker and Lu,[5] the F–N–F angle is 102° 5′, and the N—F bond length is 1.37 A. The structural data have been confirmed by Wilson,[6] Pace, and Pierce,[7] from infrared spectra, and by Gordy,[8] with microwave measurements.

In order to account for the unexpectedly small dipole moment, later authors have unanimously ascribed it to an almost perfect cancellation of the bond moment by an atomic moment of opposite sign which arises from $s-p$ hybridization of the nitrogen lone pair.

* Part of a dissertation submitted by S. R. La Paglia to the Graduate School of the University of Rochester in partial fulfillment of the requirements for the degree of Doctor of Philosophy. This research was supported in part by the Office of Naval Research.

[1] A. B. F. Duncan, Phys. Rev. **47**, 822 (1935).

[2] H. E. Watson, G. P. Kane, and K. L. Ramaswamy, Proc. Roy. Soc. (London) **A156**, 130, 144 (1936).

[3] W. Gordy and S. N. Ghosh, J. Chem. Phys. **21**, 308 (1953).

[4] O. R. Gilliam, H. D. Edwards, and W. Gordy, Phys. Rev. **75**, 1014 (1949).

[5] V. Schomaker and C. S. Lu, J. Am. Chem. Soc. **72**, 1182 (1950).

[6] M. Wilson and S. Polo, J. Chem. Phys. **20**, 1716 (1952).

[7] E. Pace and L. Pierce, J. Chem. Phys. **23**, 1248 (1955).

[8] W. Gordy and J. Sheridan, Phys. Rev. **79**, 513 (1950).

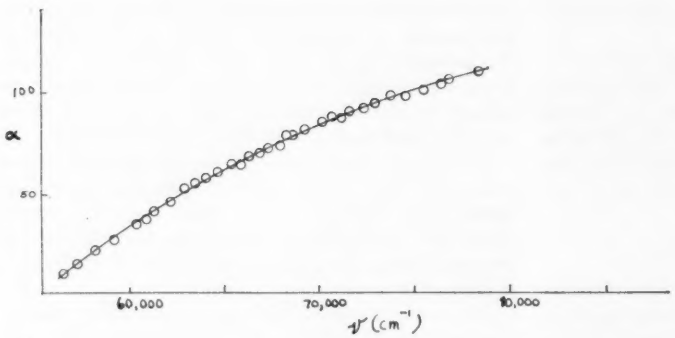

FIG. 1. Absorption coefficients (α) for NF_3.

EXPERIMENTAL PROCEDURE AND RESULTS

The absorption spectra were photographed in the first order of a 2-m radius of curvature grating ruled 30 000 lines/in. on a 4-in. ruled surface. For investigation of the region 2000–1500 A, the NF_3 was contained in a fused quartz cell, 10 cm in length, with plane-end windows, placed in front of the slit of the spectrograph. A hydrogen discharge furnished a good continuum to 1700 A. At shorter wavelengths a Lyman source was used and the NF_3 was contained in the spectrograph itself. Kodak SWR plates were used in most of the work, but Kodak II-O and III-O UV sensitized plates were used for quantitative measurements of absorption coefficients.

NF_3 was obtained from a commercial source and contained about 2% air, which led initially to absorption by NO. However, this impurity was completely removed by pumping the sample through a train of traps at 90°K, 77°K, and 63°K. A second sample[9] was purified in the same way. Infrared and mass spectroscopic analysis showed no detectable impurities in the two samples used after this treatment.

The absorption was apparently continuous, with no visual indication of resolved electronic transitions. Quantitative measurements were therefore made in an effort to observe incompletely resolved, electronic transitions on a plot of absorption coefficient vs wavelength. In these measurements, NF_3 was confined in the spectrograph and was separated from the hydrogen-discharge background source by a LiF window which transmitted to about 1250 A. The pressure of NF_3 was measured by calibrated-thermocouple and cold-cathode ionization gauges. Eastman Spectroscopic II-O and III-O ultraviolet sensitized plates were used and special precautions were taken to insure constant operating conditions of the light source. On each plate were four or five accurately timed exposures of the source alone and one or more timed exposures through the gas. The photographic density was then determined from the calibration spectra and the H and D curves were constructed at a large number of known frequencies. The photographic density corresponding to exposure through the gas was read from the straight-line portions of the curves, and the ratios (t/t_0) so determined were assumed equal to (I_0/I). The absorption coefficient used here (α) is defined as

$$\alpha=(1/l_0)\ \ln(I_0/I),$$

where l_0 is the path length in centimeters at 0°C and 76 cm Hg pressure. In previous experience we found that reciprocity-law failure was not serious for these plates; however, the over-all error in the absolute values of α is probably not less than 20%. The principal interest in absorption coefficients here lies in their change with frequency, which is subject to a smaller error.

No indication of shallow maxima or minima could be found; instead, the absorption coefficients increased in a perfectly regular way with increasing frequency. The absorption curve between 55 000 and 80 000 cm^{-1} is shown in Fig. 1. No accurate measurements of absorption coefficients could be made above about 80 000 cm^{-1}.

At the lowest pressure of NF_3, below 0.008 mm, very strong absorption is apparent below 960 A (104 170 cm^{-1}). This wavelength limit is believed to correspond to the lowest(vertical) ionization potential of the molecule, and is in qualitative agreement with the electron bombardment value 939.1 A (10 6480 cm^{-1}) reported by Reese and Dibeler.[10] To accurately locate the spectroscopic ionization potential, it is necessary to observe the Rydberg-like series of transitions converging to the ionization limit. No such series was found for NF_3.

The lowest ionization potential of NF_3 is about 2 ev higher than that of NH_3, and there is a corresponding shift of the first electronic transition of NF_3 toward higher frequencies, relative to ammonia. However, it is still probable that the excitation from the lone-pair

[9] Obtained through the courtesy of Dr. Cohen and Dr. Schoenfelder of Reaction Motors.

[10] R. Reese and V. Dibeler, J. Chem. Phys. **24**, 1175 (1956).

orbital of nitrogen is responsible for absorption in both molecules. It was considered possible that the observed difference in ionization potentials could be accounted for by a difference in hybridization in this orbital. This possibility was explored in the approximate calculations reported in the following section.

Approximate Wave Functions for NF_3 and Application to the Dipole Moment and Ionization Potential

The present calculation had two purposes. Primarily we wished to find similarities and differences between LCAO functions, determined in the same way, which might prove helpful in comparing the spectra and ionization potentials of NH_3 and NF_3. Secondly, we wished to show that the dipole moment of NF_3 can be explained in terms of LCAO functions which allow substantial $s-p$ hybridization of the nonbonding electrons on both nitrogen and fluorine.

The LCAO wave functions have the properties of localization and direction. For example, the seven electrons of fluorine (excluding $1s$) are assigned to three equivalent orbitals (nonbonding) localized on the side of the F atom away from the bond. The remaining F electron is assigned to the bond orbital localized along the bond. This gives a trigonal symmetry about each F atom which is a part of the over-all trigonal symmetry of the molecule formed by the three equivalent bond orbitals and the lone-pair orbital on nitrogen. The latter is directed along the molecular axis in a direction defined as $+z$.

Specifically, the 26 electrons of the molecule ($1s$ excluded) are assigned to these three types of orbitals:

$$\chi_L{}^N = \cos\epsilon_L{}^N s_N + \sin\epsilon_L{}^N p_N{}^L \qquad (2 \text{ electrons})$$

$$\chi_{L_i}{}^{F_k} = \cos\epsilon_L{}^F s_F + \sin\epsilon_L{}^F p_F{}^{L_i} \qquad (18 \text{ electrons})$$

$$\chi_{B_j} = \lambda(\cos\epsilon_B{}^N s_N + \sin\epsilon_B{}^N p_N{}^{B_i}) + \mu(\cos\epsilon_B{}^F s_F + \sin\epsilon_B{}^F p_F{}^{B_i}), \qquad (6 \text{ electrons})$$

where $i=1, 2, 3$ $k=1, 2, 3$, $p_N{}^L$ is a $2p$ function on N in the lone-pair direction, $p_F{}^{L_i}$ is a $2p$ function on F in the nonbonding direction i, $p_N{}^{B_i}$ and $p_F{}^{B_i}$ are $2p$ N and F functions directed towards each other along a bond (σ functions), and s_N and s_F are $2s$ N and F functions.

The explicit forms of these functions are determined by the parameters ϵ which specify the normalized $s-p$ hybrids, and the parameters λ and μ, which allow for polarity in the bond function. In the present method of calculation, all but one of the parameters are determinable. The remaining parameter is determined by the requirement that the wave functions give the experimentally observed dipole moment. The basic atomic functions used are analytical approximations (Slater functions) of the form

$$s_i = (Z_i{}^5/3\pi)^{\frac{1}{2}} r \exp(-Z_i r) \quad \text{and} \quad p_i = (Z_i{}^5/\pi)^{\frac{1}{2}} r \times \cos\theta \exp(-Z_i r),$$

where $Z_N = 1.95$ and $Z_F = 2.60$.

If $\chi_{L_i}{}^F$ and $\chi_{L_j}{}^F$ are nonbonding functions on the same F atom, orthogonality between the two gives,

$$\int \chi_{L_i}{}^F \chi_{L_j}{}^F d\tau = 0$$

$$\cos^2\epsilon_L{}^F + \sin^2\epsilon_L{}^F \int p_{L_i}{}^F p_{L_j}{}^F d\tau = 0 = \cos^2\epsilon_L{}^F + \sin^2\epsilon_L{}^F \cos\beta,$$

where $\cos\beta$ is the cosine of the angle between the nonbonded pairs; β is related to δ the external angle between the nonbonded pair and the bond through the geometric relation,

$$(2/\sqrt{3}) \sin\beta/2 = \sin\delta.$$

From these relations, we are immediately able to calculate the hybridization of the nonbonded F electrons if the angle δ is known. However, the angle δ is not directly known, so the calculation is to be repeated for several values of δ, and therefore hybridization of $\chi_L{}^F$, in order to test the sensitivity of the results to the value of δ chosen.

If we now impose the condition that the functions $\chi_L{}^N$ and $\chi_{L_i}{}^F$ be orthogonal, we may calculate the hybridization of $\chi_L{}^N$ for any hybridization of $\chi_{L_i}{}^F$. This procedure finds justification in the fact that by the use of the $\chi_L{}^N$ so determined, we can immediately calculate the dipole moment component due to the lone pair on N, called $M_L{}^N$, for each value of the angle δ, and compare this to the corresponding component of the moment for NH_3. Using N as the center of coordinates,

$$M_L{}^N = -2ea_H R_L{}^N \times 10^{18} \quad \text{Debye units}$$

$$R_L{}^N = \int \chi_L{}^N z \chi_L{}^N d\tau,$$

where $e = 4.8025 \times 10^{-10}$ esu, $a_H = 0.5292 \times 10^{-8}$ cm. Table I presents the results of this calculation. We see that $M_L{}^N$ is essentially independent of the angle δ and compares favorably with the component of the moment found by Duncan and Pople[11] for the NH_3 molecule $M_L{}^N = -3.667D$.

[11] A. B. F. Duncan and J. A. Pople, Trans. Faraday Soc. **49**, 217 (1953).

TABLE I.

M_L^N	δ	M_L^F
$-3.7620\ D$	110°	$55.336\ D$
-3.7623	112	55.542
-3.7623	113	55.625
-3.7623	114	55.682
-3.7623	115	55.741
-3.7622	117	55.770
-3.7622	118	55.674

We can also compute the component of the total moment due to the nonbonded orbitals on the F atom M_L^F,

$$M_L^F = -18ea_H(\cos\gamma)\,R_L^F \times 10^{18},$$

where $\cos\gamma$ is the cosine of the external angle between the bond and the molecular axis; it is included since the integral

$$R_L^F = \int \chi_L^F r \chi_L^F d\tau,$$

is evaluated along the bond. The results have been included in Table I. It is interesting to note that without hybridization of the nonbonding F electrons, R_L^F equals just r_{NF}, and M_L^F is a constant independent of δ with value 52.054 D or 5.784 per pair. With hybridization, M_L^F is about $55.7D$ or about $6.2D$ per pair. This is very significant in view of the small total moment and reemphasizes the importance of $s-p$ hybridization in the computation of dipole moments.

It is now possible to calculate an approximate bond wave function. For the total dipole moment we have

$$M_{exp} = M_L^N + M_L^F + M_P + M_B,$$

where $M_P = -60.730D$ is the proton moment, $M_{exp} = 0.234$ is the experimental moment, and $M_B = \cdots$ is the bond moment. It is clear that for a given value of δ, M_B is known,

$$M_B = M_{exp} - M_L^F - M_L^N - M_P.$$

Hence, in order to find an approximate bond wave function, we can impose the conditions that it give the above bond moment. We also have the relations,

$$\int \chi_L^N \chi_{B_i} d\tau = 0 \qquad (1)$$

$$\int \chi_{L_i}^F \chi_{B_i} d\tau = 0 \qquad (2)$$

$$\int \chi_{B_i} \chi_{B_i} d\tau = 1. \qquad (3)$$

From (1) and (2),

$$\sin\epsilon_B^N = \mu/\lambda(A\cos\epsilon_B^F + B\sin\epsilon_B^F),$$

$$\cos\epsilon_B^N = -\mu/\lambda(C\cos\epsilon_B^F + D\sin\epsilon_B^F),$$

where A, B, C, and D are complicated sums and products of overlap integrals and molecular parameters. Then, since $\sin^2\epsilon_B^N + \cos^2\epsilon_B^N = 1$,

$$(\lambda/\mu)^2 = (A^2+C^2)\cos^2\epsilon_B^F + (B^2+D^2)\sin^2\epsilon_B^F + 2(AB+CD)\cos\epsilon_B^F \sin\epsilon_B^F. \qquad (4)$$

Equation (4) was solved by trial on the IBM 650, giving a ratio λ/μ, the ϵ_B^N and the ϵ_B^F. Then (3) was used to normalize the bond and give values of λ and μ. The bond moment could then be calculated. This process was repeated many times until the calculated bond moment agreed with the required bond moment to within $0.02D$. The bond moment is

$$M_B = -6ea_H(\cos\gamma)\,R_B \times 10^{18}$$

$$R_B = \int \chi_B r \chi_B d\tau.$$

The results are ambiguous since there are two solutions giving the same M_B as in Eq. (4). However, we can use the results obtained from previous calculations on H_2O, NH_3, and other molecules, to choose a bond function containing more p_F than s_F as being the more realistic. The complete LCAO wave functions are, then,

$$\chi_L^N = 0.705s_N + 0.709p_N$$

$$\chi_L^F = 0.418s_F - 0.908p_F$$

$$\chi_B = 0.262s_N - 0.503p_N - 0.371s_F + 0.768p_F.$$

In order to test the sensitivity of the bond wave function to the assumed value of δ, the calculations were repeated at $\delta = 110°$ and 117°. The nitrogen part of the bond function was found to be relatively insensitive to δ as was the N lone pair. Also, in spite of the fact that the bond moment must change by approximately $0.4D$ to compensate for the new orientations of the F nonbonding pairs, the bond function as a whole does not change radically.

The calculation indicates that the ratio λ/μ is about 0.66, with a polarity N^+F^-. This is the polarity taken for the experimental moment and the polarity usually ascribed to this bond. The results also indicate that both the polarity of the bond and the hybridization of the nonbonding orbitals contribute to the total moment

in a logical manner for NF_3. From the value of $\lambda/\mu=0.66$, the N—F bond in NF_3 appears to be more polar than the N—H bond of NH_3 for which $\lambda/\mu=0.84$. The similarity in hybridization of the N lone pair indicates very little change in this essentially atomic orbital in going from fluoride to hydride. The similarity in the N part of the bond orbital is a reflection of the fact that the bond angles are not radically different in NF_3 and NH_3. Mashima[12] has made a similar calculation for NF_3. He wished to show that the dipole moment could be accounted for in terms of hybridization of lone pair and bonding functions. His method lacks the generality of the present calculation. Although the wave function was to be determined by the dipole moment, an arbitrary amount of s character (17.4%) was chosen for the N part of the bond orbital. More importantly, Mashima assumed $\lambda=\mu=1$. The F—N electronegativity difference indicates that the bond should be somewhat polar.[8,13]

The lone-pair functions in NH_3 and NF_3 have very similar hybridization according to the dipole calculations. If these functions are essentially atomic in nature (as written here they are purely atomic), then to a crude approximation we may ignore their interaction with other atoms and electrons. In that case, the energy difference between the orbitals in the two molecules may be calculated from an atomic Hamiltonian,

$$H=-\nabla^2/2-7/r_N+\sum_i(2J_i-K_i),$$

where the kinetic and nuclear potential operators are recognized, and J_i, K_i are the coulomb and exchange operators. If the lone-pair function $\chi_L{}^N$ were an eigenvector of this Hamiltonian, its energy would be the eigen value $E_L{}^N$, the orbital energy. The orbital ionization potential is taken as the negative of the orbital energy;

$$E_L{}^N=\int\chi_L{}^N H\chi_L{}^N d\tau.$$

However, we merely wish to attach significance to the quantity

$$(E_L{}^{NF_3}-E_L{}^{NH_3})=1.12 \text{ ev}.$$

This result was obtained with the wave functions,

$$\chi_L{}^{NH_3}=0.624s_N-0.782p_N,$$

$$\chi_L{}^{NF_3}=0.705s_N-0.709p_N.$$

The kinetic, nuclear-attractive, coulomb and exchange integrals over AO's were taken from Duncan.[14] If, as stated previously, the ionization potential of NF_3 refers to removal of a nitrogen lone-pair electron, the corresponding experimental quantity is

$$(I.P.{}^{NF_3}-I.P.{}^{NH_3}=13.2\pm0.2-11.3\pm0.2 \text{ ev}$$

$$=1.9\pm0.4 \text{ ev}.$$

The closeness of agreement does reinforce our concept of the lone pair as an atomic function perturbed to some extent by the presence of substituents.

[12] M. Mashima, J. Chem. Phys. **24**, 489 (1956).
[13] L. Pauling, *Nature of the Chemical Bond* (Cornell University Press, Ithaca, New York, 1940).
[14] A. B. F. Duncan, J. Chem. Phys. **27**, 423 (1957).

Growth of Whiskers by Chemical Reactions

C. R. MORELOCK AND G. W. SEARS

General Electric Research Laboratory, Schenectady, New York

(Received May 23, 1960)

In the present paper the general conditions for the growth of whiskers by vapor deposition is considered. If several reactions are available to grow a given crystal phase, that reaction with the lowest entropy of reaction will allow the growth of near-perfect crystals, at the largest temperature difference between source crystals and growing crystals.

NEAR-PERFECT whiskers[1–4] grow at low supersaturations of their own vapor by the action of axial screw dislocations. Likewise, near-perfect platelets may grow at low supersaturations by the action of a twist boundary[5] or a single screw dislocation[6] in the parent nucleus. A twist boundary is represented by a planar grid[7] of screw dislocations.

In practice[8] the supersaturation[3,4] is usually maintained by holding the source crystals and the growing whiskers or platelets at slightly different temperatures. It is the purpose of the present paper to describe a general procedure for whisker and platelet growth allowing much larger temperature differences between the source crystal and the whisker growth region.

The supersaturation in the vapor phase over a growing whisker may not exceed that value at which two-dimensional nucleation occurs at an appreciable rate. The relation between saturation ratio α and the two-dimensional nucleation rate $\dot{N}$ is given by[3]

$$\ln\alpha=\pi a\sigma^2M/\rho kRT^2\ln B/\dot{N}, \tag{1}$$

where $B\sim10^{20}$ sec^{-1}, a is the interlayer spacing, ρ is the density of the crystal phase, σ is the surface free energy, M is the molecular weight of the vapor species, k and R are the molecular and molar gas constants, respectively, and T is the absolute temperature. Since the nucleation rate is such a sensitive function of saturation ratio, the critical ratio α_c, below which whisker growth can occur, is obtained by solving Eq. (1) for $\dot{N}=1$. It is written

$$\alpha_c=\exp\{\pi a\sigma^2M/\rho RkT^2\ln B\}. \tag{2}$$

The free energy of deposition corresponding to Eq. (1) is written

$$\Delta F=-RT\ln\alpha, \qquad \alpha=P/Po, \tag{3}$$

for growth from the pure vapor. In the case of a more general reaction, the saturation ratio α, will be defined

$$\alpha=K/Ko, \tag{3a}$$

where Ko is the equilibrium constant for the transport reaction at the temperature of the growing crystal, and K is the reaction constant of the transport reaction for pressures of reactants and products over the growing crystal.

The first derivative of the free energy of a deposition reaction with respect to temperature is given by

$$(\partial\Delta F/\partial T)_p=-\Delta S, \tag{4}$$

where ΔS is the entropy of reaction. To a first approximation for a general deposition reaction

$$\Delta F=-\Delta S\cdot\Delta T, \tag{5}$$

where ΔT is the temperature difference between the source and growth regions. When a crystal grows by a vapor transport reaction,

$$\Delta S=\Delta H/T, \tag{6}$$

where ΔH is the heat of the reaction at the temperature in question. On combining Eqs. (2), (5), and (6), it is seen that

$$\Delta T_c=\pi a\sigma^2M/\rho k\cdot\Delta H\cdot\ln B, \tag{7}$$

where ΔT_c is the largest temperature difference at which whisker or platelet growth can occur.

Of all the possible vapor-phase reactions leading to a given solid phase, that reaction having the smallest enthalpy of reaction will have the largest value of ΔT_c.

From the point of view of temperature control during whisker growth, the most suitable reaction will have the smallest enthalpy of reaction. Since enthalpy need not have the same algebraic sign as free energy, it is quite possible to use chemical reactions at a low temperature as evaporation processes, which will reverse at a higher temperature to deposit crystals. An obvious example of this type of reaction is given by[9]

$$Pb+4CH_3\rightleftarrows Pb(CH_3)_4,$$

[1] G. W. Sears, Acta. Met. **1**, 457 (1953).
[2] G. W. Sears, Acta. Met. **3**, 361 (1955).
[3] G. W. Sears, Acta. Met. **3**, 367 (1955).
[4] C. R. Morelock (to be published).
[5] J. B. Newkirk and G. W. Sears, Acta. Met. **3**, 110 (1955).
[6] G. W. Sears, J. Chem. Phys. **25**, 637 (1956).
[7] F. C. Frank, Discussions Faraday Soc. **5**, 33 (1949).
[8] U. S. Patent #2,813,811 issued November 17, 1957, to G. W. Sears, assigned to General Electric Company, Schenectady, New York.
[9] F. Paneth and W. Hofeditz, Ber. deut. chem. Ges. **62**, 1335 (1929).

where lead is volatized at room temperature and is redeposited at about 250°C.

Implicit in all of the preceding discussion is the assumption that equilibration occurs in the gas phase as the temperature varies from the source region to the growth region. Recent work on the growth of alumina whiskers[10–12] shows that a less restrictive assumption is sufficient, that equilibration need not occur in the gas phase if it occurs in the adsorbed phase on a perfect surface of a growing crystal. The next step of equilibration occurring only at the growth or evaporation step is not sufficient for the application of the conclusions of the preceding discussion. The growth of copper whiskers by the hydrogen reduction of cuprous iodide[13] illustrates the effects of step-catalyzed reactions.

Since whiskers and platelets can be grown by many other phase transformations than vapor deposition, it is pertinent to remark that the general principles stated are valid for any crystal growth process that involves the screw-dislocation mechanism.

[10] R. C. DeVries and G. W. Sears, J. Chem. Phys. **31**, 1256 (1959).
[11] G. W. Sears and R. C. DeVries, J. Chem. Phys. **32**, 93 (1960).
[12] G. W. Sears and R. C. DeVries (to be published).
[13] C. R. Morelock and G. W. Sears, J. Chem. Phys. **31**, 926 (1959).

THE JOURNAL OF CHEMICAL PHYSICS VOLUME 34, NUMBER 3 MARCH, 1961

Infrared Spectroscopic Evidence for the Rotation of the Ammonia Molecule in Solid Argon and Nitrogen*

DOLPHUS E. MILLIGAN AND ROBERT M. HEXTER
Mellon Institute, Pittsburgh, Pennsylvania
AND
KURT DRESSLER
Princeton University Observatory, Princeton, New Jersey

(Received December 21, 1959)

High-resolution infrared spectra (of the symmetric bending mode) of ammonia suspended at high dilution in solid argon and nitrogen have been obtained. More than a half dozen extremely sharp bands have been observed in the 950–1040 cm^{-1} region (in the spectrum of ammonia) in these materials under conditions where there should be little if any absorption due to polymeric species. The frequency separations of the bands, their temperature dependence, and their extreme sharpness appear to be compatible with a model in which the ammonia molecule executes quantized rotation in these solids.

INTRODUCTION

DURING the past few years considerable attention has been devoted to the spectroscopic study of various atomic and small molecular species suspended in inert solids. In some of these studies it has been common practice to condense on a cold window (77–4.2°K) a gaseous binary solution in which one of the components is present to the extent of only 1% or less. Under these conditions it seems reasonable to assume that if the condensate is crystalline, its crystal structure is virtually the same as that of the pure inert gas. Behringer[1] has shown that for a variety of crystal structures, when the solute is present to the extent of $\leq 1\%$, the probability of a particular solute molecule having a nearest neighbor of its own kind is vanishingly small. At these low concentrations the solute molecules are in a force field created primarily by interactions with their nearest neighbors. Furthermore, as these neighbors are rare gas atoms, and the matrix is, with considerable probability, of the crystal structure of the rare gas atoms, many of the orientation-dependent forces are averaged to zero. One would expect that in those cases where the dimensions of the solute molecule are comparable to those of the inert gas, there would be little hindrance to rotation of the solute species. There have already been several reports of visible,[2] infrared,[3] and electron spin resonance[4] spectra in which effects arising from the rotation of small solute species have been observed in rare gas matrices.

We have been concerned recently with the infrared spectroscopic study of a number of systems involving small molecules suspended in inert solids. In the work

* This research was supported in part by the U. S. Air Force through the Air Force Office of Scientific Research of the Air Research and Development Command.
[1] R. E. Behringer, J. Chem. Phys. **29**, 537 (1958).
[2] G. W. Robinson and M. McCarty, Jr., J. Chem. Phys. **30**, 999 (1959).
[3] E. Catalano and D. E. Milligan, J. Chem. Phys. **30**, 45 (1959).
[4] H. M. McConnell, J. Chem. Phys. **29**, 1422 (1958).

reported here we shall be primarily concerned with the high-resolution spectroscopic study of the symmetric bending mode (ν_2) of ammonia suspended in solid argon and nitrogen.

Becker and Pimentel[5] have previously reported on the infrared spectrum of ammonia suspended at relatively low dilutions in solid argon, xenon, and nitrogen. These workers observed four bands in the 970–1040 cm^{-1} region, using argon as a matrix and six bands in this region in a xenon matrix. Five bands were observed in the 900–1150 cm^{-1} region using nitrogen as the matrix material, some of which were thought to be due to an ammonia-water compound. Becker and Pimentel concluded on the basis of concentration studies that the bands observed in all three matrices were due to monomeric and polymeric species of ammonia.

Recently, Catalano and Milligan[3] have obtained infrared spectroscopic results which indicate that the water molecule executes quantized rotation in solid argon, xenon, and krypton. In view of these results and the fact that the dimensions of the water and ammonia molecules are comparable, it was considered to be worthwhile to reinvestigate the ammonia-argon and ammonia-nitrogen systems under conditions of greater dilution and higher spectral resolution. The experimental procedures were identical to those described by Catalano and Milligan[3] except for the use of a grating spectrometer (Perkin-Elmer 112G) and liquid He deposition temperatures.

RESULTS AND DISCUSSION

Spectra of ammonia suspended at 4.2°K in solid argon were obtained at Ar/NH_3 mole ratios of 350, 500, 800, 1000, and 1200 and nitrogen at N_2/NH_3 mole ratios of 500, 1200, and 1700. Spectra of ammonia suspended in these materials are shown in Fig. 1. In addition to the bands shown in the NH_3–N_2 spectrum, much weaker bands are observed at 1014, 1026, and 1033 cm^{-1}. The spectral features shown in Fig. 1 show little if any dependence on concentration in the ranges involved. The concentration dependence of the weaker bands in the NH_3–N_2 spectra is not clear.

Spectra recorded during the slow warmup of the ammonia-argon deposits from 4°K to approximately 30°K, indicate that the bands at 1000 and 1015 cm^{-1} increase in peak intensity whereas the 974 cm^{-1} complex decreases in peak intensity with very little if any change in bandwidth. The relatively weak and broad bands centered at 992 and 1012 cm^{-1} sharpen with increasing temperature in the range 4.2–30°K. On several occasions the 992 cm^{-1} band has been observed to split into three extremely sharp components at temperatures near 30°K. The spectral changes occurring in the temperature range 4.2–30°K appear to be reversible with temperature. On raising the temperature of the deposit above about 35°K and recooling to 4.2°K,

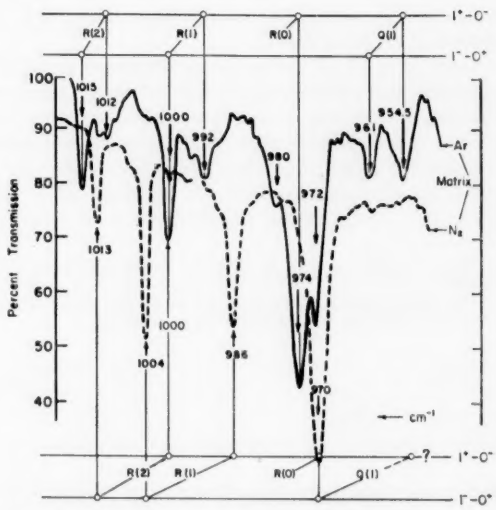

FIG. 1. ν_2 of ammonia in argon and nitrogen matrices ($T=4.2°K$), $Ar/NH_3=1200$, $N_2/NH_3=1700$.

all of the bands with the exception of the band at 1015 cm^{-1} are found to decrease in peak intensity. However, the percentage decrease in intensity of the 1000 cm^{-1} band is approximately one-half that of the other bands. The band at 1015 cm^{-1} is observed to increase in peak intensity, and a broad band centered at approximately 1045 cm^{-1} develops on warming the deposit to approximately 35°K and recooling to 4.2°K. The 1045 cm^{-1} band in all probability corresponds to a band observed previously[6] in the spectrum of solid ammonia. The growth of the 1045 cm^{-1} band at temperatures near 35°K appears to indicate that the spectral changes observed in this temperature range are due to diffusion.

The bands observed in the spectrum of ammonia in nitrogen are somewhat sharper and show no evidence of structure under the maximum spectral resolution obtainable in this region. On raising the temperature the bandwidths are observed to increase with little or no change in peak height.

The spectral features under consideration here are due to the symmetric bending mode (ν_2) of ammonia. In the gas phase this vibration is split due to inversion. The Q branches are located at 932 and 968 cm^{-1}; likewise, each line in each sub-band (except for $K=0$) is double. The average separation between neighboring lines in the composite spectrum for all K is of the order of 20 cm^{-1}. In the spectrum of crystalline ammonia there is no evidence for either inversion doubling or free rotation, as only a single broad band is observed in the region appropriate for ν_2 (1050 cm^{-1}).

The absence of any detectable concentration dependence of the spectra suggests that we are concerned with spectral features arising from the motion of monomeric

[5] E. D. Becker and G. C. Pimentel, J. Chem. Phys. **25**, 224 (1956).

[6] F. P. Reding and D. F. Hornig, J. Chem. Phys. **19**, 594 (1951).

species of ammonia. The multiplicity, extreme sharpness of the lines, and their thermal behavior, can be most easily explained on the basis of a model in which the NH_3 molecule possesses some degree of rotational freedom.

The rare gases (with the exception of helium) are known to crystallize in face-centered cubic structures. The internuclear distance in solid argon is approximately 3.83 A. Nitrogen is known to exhibit two crystalline forms, a face-centered cubic form stable below 35°K and a hexagonal close-packed structure stable above 35°K. Using appropriate values for the nitrogen-nitrogen bond distance and the van der Waals radius of nitrogen, the diameter of the cavity formed by the removal of a nitrogen molecule from the crystalline solid can be estimated to be of the order of 4 A. The diameter of the minimum cavity in which the ammonia molecule may freely rotate varies from 3.1 to 5.7 A. Thus rotation of ammonia molecules situated at substitutional sites in solid argon and nitrogen should be possible about the principal axis or about some axis slightly inclined to it. Our discussion of the spectrum will therefore begin by the assumption of the possibility of such rotation.

Most of the lines in the Ar-NH_3 spectrum may be grouped into two series (Table I) in which successive lines are separated by an increment of the order of the rotational separation observed in the gas phase. Those lines neglected in this tabulation occur as shoulders and will not be discussed. By comparing the argon matrix spectrum with that of the gas (Table II), it is seen that there is a near coincidence of frequencies of the 1^+-0^- lines through $J=3$ with the italicized frequencies of Table I. This correspondence is probably fortuitous.

If the temperature of the sample was indeed 4.2°K, only the $J=0$ level would have been appreciably populated. Accordingly, we should expect the $R(0)$ line of the 1^+-0^- transition to be the strongest feature

TABLE I. Lines observed in the spectrum of NH_3 in argon and nitrogen matrices at $T=4.2$°K.

	(1^+-0^-)	$(1^--0^+$
	Ar: NH_3	
$Q(1)$	954.5 cm^{-1}	961 cm^{-1}
$R(0)$	974	...
$R(1)$	992	1000
$R(2)$	1012	1015
	N_2: NH_3	
$Q(1)$	?	970
$R(0)$	970	...
$R(1)$	986	1004
$R(2)$	1000	1013

TABLE II. Low $J=K$ transitions in R branches of symmetric bending mode of gaseous ammonia.[a]

$R(J)$	$0^s\rightarrow1^s$ (1^+-0^-)	$0^s\rightarrow1^a$ (1^--0^+)
0	952	...
1	971.90	1007.48
2	991.84	1026.92
3	1011.24	1046.27
4	1030.36	1065.46

[a] Frequencies identified in this table are from S. Mizushima *et al.*, *Report on Perkin-Elmer Grating Spectrophotometer Model 112G* (Nankodo Company, Ltd., Tokyo, 1957).

of the ν_2 band. Lines originating in $J=1$ and $J=2$ levels would then be progressively weaker. Furthermore, if most of the molecules are in the lowest rotational level, we should expect to observe very little intensity in the Q-branch, for this is forbidden from the $J=0$ level. We shall therefore assign the strong line 974 cm^{-1} in Ar-NH_3 to the $R(0)$ transition of the 1^+-0^- band. The related line of the 1^--0^+ band does not occur in NH_3. With this origin, the other assignments at the top of Fig. 1 follow quite naturally. The two series of Table I have been factored by this logic.

A similarly derived assignment for the N_2-NH_3 spectrum is also presented in Table I and at the bottom of Fig. 1. We are here forced to conclude that the $Q(1)$ line of the (1^--0^+) band and the $R(0)$ line overlap at 970 cm^{-1}. From the separations of the $R(1)$ lines in the (1^+-0^-) and (1^--0^+) bands, we derive inversion splittings for NH_3 of 8 cm^{-1} and 18 cm^{-1} in the Ar and N_2 matrices, respectively. This is to be compared with the value of 35.58 cm^{-1} observed in the gaseous state (Table II). The decrease in the inversion doubling (gas→matrix) is consistent with the observed increase in the height of the barrier to inversion indicated by the increase in the frequency of the bending vibration. In the gas phase this frequency is approximately $(932+968)/2$ cm^{-1} (Q-branch frequencies). In Ar and N_2 matrices, the corresponding frequencies are approximately $(954+961)/2$ cm^{-1} and $(950+970)/2$ cm^{-1}.[7] These solvent shifts of approximately $+8$ and $+10$ cm^{-1} are usual for bending vibrations.

It is of interest to estimate the increase in height of the barrier to inversion due to the matrix environment. If it is assumed that the inversion splitting of ν_2 depends exponentially on the height of the potential barrier above the ν_2 level,[8] the barrier height can be estimated to increase by approx 400 and 800 cm^{-1} in the N_2 and Ar matrices, respectively. These estimates have been made using the relationship $\Delta\nu/\nu_2=\pi^{-1}\exp[-(V_0-\nu_2)/528\text{ cm}^{-1}]$, where $\Delta\nu$ is the inversion doubling and V_0 is the height of the barrier above the vibrational ground

[7] These are estimated positions of the Q branches in the N_2 matrix.

[8] Compare D. M. Dennison and G. E. Uhlenbeck, Phys. Rev. **41**, 313 (1932).

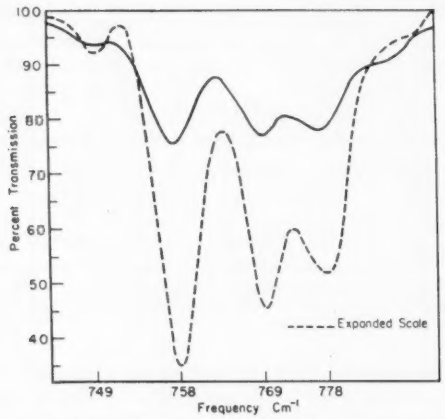

FIG. 2. ν_2 of ND_3 in solid argon ($Ar/ND_3=500$; $T=4.2°K$).

state. Upon substituting the parameter 528 cm^{-1} into this relationship, together with the known value of V_0 in the gaseous state (2070 cm^{-1}), the experimentally established value of $\Delta\nu=36$ cm^{-1} is obtained. The values of ν_2 used in the calculation were 950 cm^{-1} in the gaseous state and 960 cm^{-1} in the solid matrices.

If, as is implied here, the inversion splitting of NH_3 is reduced from 36 cm^{-1} in the gas phase to less than 10 cm^{-1} in solid argon, one would predict that only a single series or a double series of lines with spacings of the order of 1 cm^{-1} would be observed in the spectrum of ND_3 in argon.[9] This prediction is strikingly confirmed by the spectrum of ND_3 in solid argon. As can be seen in Fig. 2, only a single series of lines with spacings of the order of 9 cm^{-1} is observed. The rotational spacing in this mode of gaseous heavy ammonia is of the order of 10 cm^{-1}, which is within experimental error of the spacings observed in solid argon-ND_3. The assignments proposed for the Ar-ND_3 spectrum are 749 $cm^{-1}=Q$ branches, 758 $cm^{-1}=R(0)$, 769 $cm^{-1}=R(1)$, and 778 $cm^{-1}=R(2)$.

A puzzling feature of the NH_3-Ar and NH_3-N_2 spectra is the absence of any lines of frequency less than 950 cm^{-1}. Some rationalization of the absence of P branches can be made on the basis of the small populations of the $J>0$ states. Nevertheless, according to the assignments of Fig. 1 and Table I, $R(1)$ and $R(2)$ transitions were observed. Further rationalization of this phenomenon is pursued as follows. If the ammonia molecule is constrained to rotate only about its principal axis ($J=K$), or about axes close to the principal axis ($J\approx K$), then levels with $J-K>0$ will be shifted to progressively higher energies with respect to the $J=K$ levels. Thus the population of such levels becomes even less probable on thermal grounds and we should concentrate primarily (as we have) on levels with $J=K$. If we retain all selection rules appropriate for this ($\|$) band ($\Delta K=0$, $\Delta J=0$, ±1 except when $K=0$, when $\Delta K=0$, $\Delta J=\pm1$), and consider that only $K=J$ rotational levels are accessible in the vibrational ground level, we should expect only lines in the Q and R branches.

On the basis of the experimental results and the analysis given here it would appear that isolation of the ammonia molecule in solid argon or nitrogen produces little if any change in the architecture of the molecule. The effect of these matrices seems to be apparent only through a rather sizable increase in the frequency of this vibration (relative to the singlet at about 950 cm^{-1}, the mean frequency of the two Q branches, which would be observed in the absence of rotation) and a reduction in the inversion splitting. It should also be noted that in the matrix which by its geometry offers the greater restriction to the motion of the NH_3 molecule (Ar), the reduction of the inversion splitting is the greater.

Note added in proof. Since the submission of this manuscript, we have succeeded in obtaining a spectrum of a $\sim0.1\%$ solid solution of NH_3 in N_2 at 27°K, using liquid neon as a refrigerant. The intensity distribution of the spectrum of this sample differed from that obtained with similar samples deposited at 4°K, but otherwise the spectra were identical. When the temperature of the sample deposited at 27°K was decreased to 4°K, the intensity distribution of the sample closely approximated that of samples deposited at 4°K. This temperature dependence is consistent with our hypothesis of rotation of NH_3 in solid N_2 and Ar.

[9] In the gas phase of ND_3, the inversion splitting of ν_2 is only 2.4 cm^{-1}.

Photochemical Studies in Flash Photolysis. II. Photolysis of Acetone with Filtered Light*

N. SLAGG† AND R. A. MARCUS‡

Department of Physical Chemistry, Polytechnic Institute of Brooklyn, Brooklyn, New York

(Received August 8, 1960)

Flash photolysis was studied in the absence of wavelengths below 200 mμ. Effects of acetone pressure, light intensity, added biacetyl, temperature, and wavelength were investigated. The results are consistent with primary acts postulated previously on the basis of low-intensity studies, but with the absence of complicating first-order secondary reactions at these high radical concentrations. Deactivation of excited molecules explains the pressure effect on the C_2H_6/CO ratio, for wall effects are absent under flash conditions. A hot radical mechanism is suggested by the data for methane formation. The effect of wavelength on C_2H_6/CO ratio in regions centered near 260, 280, and 295 mμ is rather striking, and the results are compared with trends in low-intensity studies in the same pressure region.

INTRODUCTION

THE photolysis of acetone has been extensively investigated at low light intensities,[1,2] and several studies[3–5] have been made at extremely high intensities under flash conditions. Khan, Norrish, and Porter[3] flash-photolyzed acetone in the presence of a large amount of inert gas (carbon dioxide) using unfiltered light and found a C_2H_6/CO ratio of unity. Oster and Marcus[4] also used unfiltered light and observed ratios of about 1.25 in the absence of, but unity in the presence of, excess carbon dioxide. They observed that traces of biacetyl had the same effect and found, too, from the pressure dependence of the CO quantum yield, that light below 200 mμ was contributing effectively to their photolysis and, it may be presumed, to that of Khan *et al.*

In the present work these wavelengths are removed and the effects of pressure, intensity, temperature, added biacetyl, and wavelength are described. Where feasible, these data are compared with those obtained at 280 mμ by Roebber, Rollefson, and Pimentel,[5] who used a monochromatic (magnesium spark) source. The latter authors' results showed one major apparent difference from low intensity ones—an increased quantum yield of CO with increased pressure. At low intensities little or no such effect has been found.[6–8]

EXPERIMENTAL

Apparatus, Materials, and Analysis

The flash apparatus was described previously,[9] the flashing voltage here being 8000 v. A cylindrical quartz vessel was used, 2.3 cm i.d. and 20 cm long, closed at one end and attached to the vacuum system by a graded seal at the other. The exploding wire[4] was 32 cm long, placed parallel to the cylindrical vessel and, except where specified in Table I, 2.15 cm distant from the latter's axis. In several experiments, so indicated in Table I, a 7910 Vycor vessel, with an i.d. of 2.6 cm and a length of 20 cm, was used instead. The wire length employed was then 22 cm. Throughout, the analytical apparatus, procedures, and purification of acetone and biacetyl were the same as in Part I.

Filters

To effectively eliminate light of wavelengths of 200 mμ and less when the quartz reaction vessel was used, the vessel was surrounded with a single layer of du Pont cellophane 450-PD. The vessel plus the cellophane was enclosed in a closefitting protective concentric quartz tube of 2-mm wall thickness. The effectiveness of the cellophane was established from results with two layers of cellophane, which showed essentially no further change in ratios of reaction products. Using the Vycor vessel, which cuts off wavelengths below 220 mμ, rather similar product ratios were obtained. To obtain wavelengths centered near 260 mμ, 280 mμ, and 295 mμ, a suitable concentration of 1,4-diphenylbutadiene in ethanol, one of CS_2 in CCl_4, and a single layer of 88-CA-48 du Pont cellophane, respectively, were used. Transmission curves for these filters are shown in Fig. 1. After the cellophane transmission is multiplied by the extinction coefficient of acetone in this weakly absorbing spectral region, the cellophane is seen, in effect, to provide a wavelength band of about 25 mμ, centered near 295 mμ. The filters were placed in a cylindrical Vycor jacket, 5 cm i.d., and concentric with the 3 cm o.d. Vycor reaction vessel.

* Abstracted from the doctoral dissertation of Norman Slagg, Polytechnic Institute of Brooklyn, June, 1960. (Available on microfilm from University Microfilms, Ann Arbor, Michigan.) Presented in part at the 132nd Meeting of the American Chemical Society, New York City, September, 1957.

† Present Address, Thiokol Corporation, Denville, New Jersey.

‡ Alfred P. Sloan Research Fellow.

[1] Cf. review by E. W. R. Steacie, *Atomic and Free Radical Reactions* (Reinhold Publishing Corporation, New York, 1954).

[2] Cf. review by W. A. Noyes, G. B. Porter, and J. E. Jolley, Chem. Revs. **56,** 49 (1956).

[3] M. A. Khan, R. G. W. Norrish, and G. Porter, Proc. Roy. Soc. (London) **A219,** 312 (1953).

[4] G. K. Oster and R. A. Marcus, J. Chem. Phys. **27,** 472 (1957) (Part I of this series); cf. R. A. Marcus, Can. J. Chem. **36,** 102 (1958), which summarizes several of the results reported in the present paper.

[5] J. L. Roebber, G. K. Rollefson, and G. C. Pimentel, J. Am. Chem. Soc. **80,** 255 (1958).

[6] D. S. Herr and W. A. Noyes, J. Am. Chem. Soc. **62,** 2052 (1940).

[7] D. E. Hoare, Trans. Faraday Soc. **53,** 791 (1957).

[8] J. Heicklen and W. A. Noyes, J. Am. Chem. Soc. **81,** 3858 (1959).

[9] G. K. Oster and R. A. Marcus, J. Chem. Phys. **27,** 188 (1957).

TABLE I. Flash photolysis of acetone with filtered light.

a. Effect of acetone pressure

Exptl	p_{acet} (mm)	No. of flashes	CO/flash (μ moles)	C_2H_6/CO	CH_4/CO	$CO/p_{acet} \times 10^3$
100[a]	243	3	0.51	1.21	0.10	2.1
97[a]	150	3	0.37	1.49	0.10	2.3
73[a]	100	3	0.24	1.66	0.11	2.4
56	160	2	0.46	1.31	0.11	2.8
48	100	2	0.30	1.62	0.10	3.0
49	100	2	0.28	1.65	0.11	2.8
57	50	4	0.16	1.61	0.12	3.2
37	25	10	0.085	1.83	0.11	3.4
39	9.1	25	0.026	2.26	0.11	2.9
59	6.7	30	0.021	2.32	0.12	3.1

b. Effect of incident intensity, I_0, at 100 mm acetone[b]

Exptl.	Wire distance (cm)	No. of flashes	CO/flash (μ moles)	C_2H_6/CO	CH_4/CO
48	2.15	2	0.30	1.62	0.10
49	2.15	2	0.28	1.65	0.11
41	5.75	7	0.13	1.52	0.12
34	10.25	15	0.073	1.64	0.09
42	18.25	20	0.035	...	0.11
43	18.25	20	0.036	1.67	0.11
44	28.25	25	0.020	1.63	0.11

c. Effect of temperature at 100 mm acetone

Exptl.	T (°C)	No. of flashes	CO/flash (μ moles)	C_2H_6/CO	CH_4/CO
114	26	4	0.15	1.64	0.11
116	25	4	0.13	1.62	0.12
113	90	4	0.15	1.77	0.10
115	90	4	0.14	1.81	0.11
141[c]	185	1	0.68	1.86	0.09
140[c]	26	1	0.78	1.70	0.12

d. Effect of added biacetyl at 100 mm acetone

Exptl.	Biacetyl (mm)	No. of flashes	CO/flash (μ moles)	C_2H_6/CO	CH_4/CO
49	...	2	0.28	1.65	0.11
77	0.28	2	0.30	1.64	0.10
78	0.54	3	0.28	1.58	0.09
11[d]	...	1	1.13	1.28	0.11
102[d]	0.58	1	1.37	1.03	0.07

e. Effect of wavelength[e]

Exptl.	λ (mμ)	Acetone (mm)	No. of flashes	CO/flash (μ moles)	C_2H_6/CO	CH_4/CO
153	260	100	25	0.047	2.83	0.21
163	260	100	25	0.052	2.67	0.17
154	260	200	14	0.105	1.93	0.10
136	280	100	15	0.046	2.26	0.11
137	280	100	15	0.047	2.33	0.10
162	280	200	8	0.089	1.41	0.09
138	295	100	16	0.037	1.23	0.12
147	295	100	16	0.036	1.27	0.11
166	295	200	8	0.084	1.11	0.21

[a] Experiments 73–116 were performed with a new sample of cellophane 450-PD.

[b] The intensity is approximately inversely proportional to the distance between wire and vessel axis noted in Table Ib (cf. footnote 9). Some deviation would be expected from this "infinite length line source" law at the larger distances because of the finite length effect. For this reason, no CO/I_0 ratios were computed.

[c] Vycor reaction vessel, wire 2.5$_0$ cm from vessel axis.

[d] Quartz vessel without cellophane, 450-PD filter.

[e] Vycor reaction vessel, wire 3.2$_0$ cm from vessel axis.

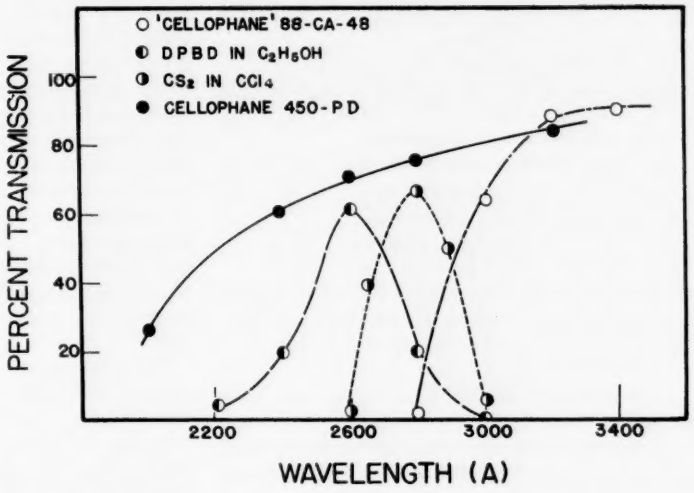

FIG. 1. Percent transmission of various filters vs wavelength (liquids have a 1 cm path length). The transmission curve for the CS_2 solution is sensitive to impurities. (A narrower transmission band having the same maximum has been found with purer reagents.) The acetate film 88–CA–48 is 0.00088 in. thick and the cellophane 450–PD is 0.0013 in.

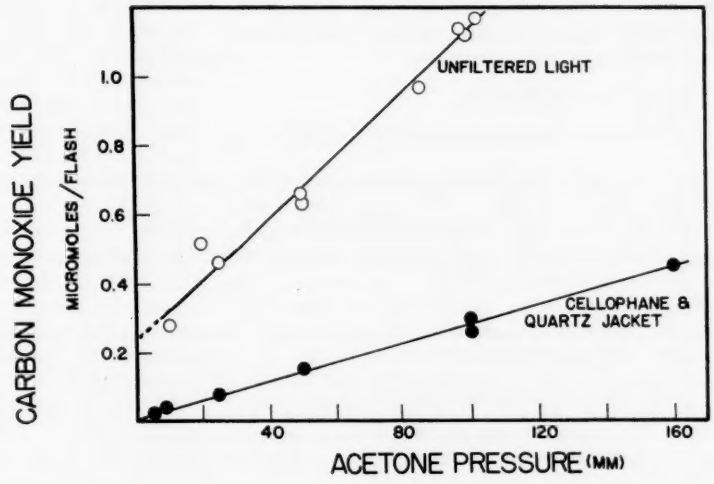

FIG. 2. Plot of CO vs acetone pressure, illustrating the importance of wavelengths near 190 mμ using unfiltered light.

Temperature

Almost all experiments were performed at room temperature. A temperature of about 90°C was obtained with a heated beaker of water and one of 185°C with an easily removable asbestos-covered heating coil which jacketed the vessel. At the desired temperature, determined by a thermocouple, the acetone pressure was adjusted, the heating device removed, and the wire moved quickly into place and flashed. The resultant maximum gas temperature drop before flashing, inferred from any gas pressure drop, was less than 8°C.

RESULTS

Results obtained at various acetone pressures, intensities, temperature, added biacetyl, and wavelength are given in Table I and Fig. 2. The results may be summarized as follows:

1. When the wavelengths shorter than 200 mμ are removed, CO is directly proportional to the acetone pressure. Hence, because of the small percent light absorption in this region,[10] CO is directly proportional to the absorbed light intensity. However, when wavelengths shorter than 200 mμ are not removed, the CO vs p plot in Fig. 2 does not extrapolate to the origin, a consequence of the intense acetone absorption near 190 mμ. The remaining results shown here were obtained in the absence of these short wavelengths.

[10] R. G. W. Norrish, H. G. Crone, and O. D. Saltmarsh, J. Chem. Soc. **1934**, 1456; W. A. Noyes, A. B. F. Duncan, and W. M. Manning, J. Chem. Phys. **2**, 717 (1934).

2. CO was essentially independent of temperature and of traces of added biacetyl.

3. The C_2H_6/CO ratio decreased markedly with increasing pressure. It was independent of incident light intensity, of added biacetyl (unlike the 190 mμ data[4]), and almost independent of temperature.

4. The C_2H_6/CO ratio increased with decreasing wavelength in the three regions studied (260, 280, 295 mμ), in the pressure range investigated.

5. The CH_4/CO ratio was independent of all the preceding variables, except perhaps of wavelength.

6. Two experiments with equal mixtures of acetone and acetone-d_6 were performed. The ratio $(CD_4)(CH_4)/(CD_3H)(CH_3D)$ was found to be 1.08 and 1.12.[11]

DISCUSSION

Comparison of the C_2H_6/CO ratios in Table Ia and b with the corresponding ratios at various wavelengths suggests that our major photochemical contribution is centered near 290 mμ.

The independence of CO quantum yield of absorbed light intensity is in agreement with step (1), first suggested by low intensity studies, this step being followed now by radical recombinations only.

$$(CH_3)_2CO+h\nu\rightarrow 2CH_3+CO$$
$$\text{or } \rightarrow CH_3+CH_3CO'\rightarrow 2CH_3+CO. \qquad (1)$$

CH_3CO' denotes a hot CH_3CO whose only fate is to dissociate. At low intensities, CO is also formed from dissociation of thermally equilibrated CH_3CO radicals, a step which can readily be shown to be unimportant here because of the huge radical concentration and the resulting predominance of radical recombinations. (Similarly, reaction of thermal CH_3's with acetone to form CH_4 can be excluded here.)

The independence of C_2H_6/CO ratio and, hence, of biacetyl/CO ratio[12] of light intensity, and the decrease in C_2H_6/CO ratio with increasing pressure are consistent with steps (1) and (2), (2a) having been established by low-intensity studies.

$$(CH_3)_2CO+h\nu\rightarrow(CH_3)_2CO^*\rightarrow CH_3+CH_3CO \qquad (2a)$$
$$\xrightarrow{M}(CH_3)_2CO, \qquad (2b)$$

where M is any colliding molecule.

This trend of ratio with pressure was also found at low intensities,[6] the study being performed at constant absorbed intensity to counteract the intensity effect on thermal reactions noted earlier but absent here. However, under low-intensity conditions wall effects can occur, and one explanation previously offered for the pressure trend was based on an increased acetone pressure's causing a decreased diffusion of acetyl radicals to the wall. At the wall they were assumed to recombine to form biacetyl. Wall effects are absent under flash conditions, so such an explanation is not applicable here: The radical concentration is so high at flash intensities that the radical may be estimated to diffuse only about 0.01 cm at 100 mm gas pressure before it recombines.[13] It therefore has a negligible chance of reaching the wall. Another complicating pressure effect sometimes present at low intensities but absent here involves diffusion of radicals out of the light beam, thereby decreasing their average concentration and increasing the relative importance of first-order processes.[14]

The independence of CH_4/CO of incident light intensity[15] and acetone pressure shows that the CH_4, too, arises either in a primary act or from one species which does not undergo competitive reactions of different orders. The first possibility, an intramolecular formation of CH_4 and CH_2CO, was eliminated by the results of our acetone-acetone-d_6 experiments, whose random mixing results established a free radical origin of the methanes. (In an intramolecular formation, only CH_4 and CD_4 would be formed.) Again, we believe that we have established that the bulk of the methane does not arise here from a disproportionation between thermally equilibrated CH_3's and CH_3CO's, for in that case the CH_4/CO would decrease appreciably with increasing acetone pressure, which it does not.[5,16] Accordingly, we infer that the CH_4 arises from a hot methyl radical (or hot acetyl reacting with methyl). This mechanism is easily shown to be consistent with a $(CH_4)(CD_4)/(CH_3D)(CD_3H)$ ratio of about unity in the absence of isotopic effects. Even including isotopic effects some cancellation of the effects would be expected in this overall ratio, with a result which would approach unity.

The wavelength effect on the C_2H_6/CO ratio is striking. The ratio increases with decreasing wavelength in the pressure range studied. Data in the literature obtained in this pressure range at the higher low intensities and at two different wavelengths are summarized in Table II. The same trend appears to exist,[17] though not unequivocally. The maximum intensity in

[11] We are greatly indebted to Professor H. I. Schiff of McGill University for these analyses.

[12] In unpublished studies in this laboratory, A. Shilman has found this ratio to equal approximately $(C_2H_6/CO-1)$. See footnote 5.

[13] The distance, x, is $(2D\tau)^{\frac{1}{2}}$, and τ, the lifetime of a radical, $=1/(kR/l)^{\frac{1}{2}}$ so that $x=(4Dl^2t/kR)^{1/4}$ where R is the biacetyl formation per unit volume, l is the flash time, 3×10^{-4} sec[4], and k is the recombination constant, assumed here as a first approximation to be of the order of that[1] for CH_3 radicals.

[14] W. A. Noyes and L. Dorfman, J. Chem. Phys. **16**, 788 (1948); A. J. C. Nicholson, J. Am. Chem. Soc. **73**, 3981 (1951).

[15] Cf. same independence of ratio on I_0 and same value of ratio at high "low intensities," P. Ausloos and E. W. R. Steacie, Can. J. Chem. **33**, 47 (1955).

[16] $(CH_3)\propto(C_2H_6)^{\frac{1}{2}}$ and $(CH_3CO)\propto(C_2H_6\text{–}CO)^{\frac{1}{2}}$, therefore R_{CH_4}/R_{CO} would be proportional to

$$\{(C_2H_6/CO)[(C_2H_6/CO)-1]\}^{\frac{1}{2}},$$

where C_2H_6 denotes the ethane formed, etc.

[17] An opposite trend at this pressure has been observed under different conditions (e.g., lower intensities). See work cited in footnote 6.

TABLE II. Acetone photolysis at low intensities and approximately 150 mm acetone.

Authors	Relative[a] intensity	250–270 mμ C_2H_6/CO	Relative[a] intensity	300+ mμ C_2H_6/CO
Steacie and Darwent[b]	20	2.2	3	1.4
Spence and Wild[c]	10	2.4		
	2	2.2	2	1.2±0.2
Howland and Noyes[d]	3, 0.3	1.4	1	1.2

[a] Rounded figures.
[b] E. W. R. Steacie and B. de B. Darwent, J. Chem. Phys. **16**, 230 (1948).
[c] R. Spence and W. Wild, J. Chem. Soc. **1941**, 590.
[d] J. J. Howland and W. A. Noyes, J. Am. Chem. Soc. **66**, 974 (1944).

Table II is about 10^5 less than ours in the same wavelength range.

The present data may be compared with those obtained by Roebber *et al.*[5] Their C_2H_6/CO ratio was intensity-dependent, as here. The C_2H_6/CO ratio decreased with increasing pressure, as here, and their C_2H_6/CO approximately equals ours in the 280 mμ range. A major difference, however, is that their CO quantum yield increased with increasing pressure while ours in Table Ia does not, a point which merits further investigation.

ACKNOWLEDGMENT

The authors are pleased to acknowledge the support of this research by the United States Air Force WADC and Office of Scientific Research.

Note added in proof. In subsequent work by Mr. A. Shilman in this laboratory, an extensive investigation has been made of pressure effects near 260, 280, and 300 mμ. Near 260 mμ and near 300 mμ, the CO quantum yield was pressure-independent. Near 280 mμ, it was pressure-dependent in agreement with Roebber *et al.*[5] Thus, the difference between Roebber's results at 280 mμ and those obtained at low light intensities[6–8] (usually at 254 and 313 mμ) appear to represent wavelength effects.

THE JOURNAL OF CHEMICAL PHYSICS VOLUME 34, NUMBER 3 MARCH, 1961

Electrical Conductivity of Near-Stoichiometric α-Nb_2O_5†

E. H. GREENER,* D. H. WHITMORE, AND M. E. FINE

Department of Materials Science, Northwestern University, Evanston, Illinois

(Received June 29, 1960)

The electrical conductivity of α-Nb_2O_5 monocrystalline and sintered specimens, measured under a constant ambient oxygen pressure and over the temperature range 300 to 900°C, exhibits an exponential temperature dependence with an activation energy of 1.65 ev. The isothermal conductivity, σ, of near-stoichiometric α-Nb_2O_5 is related to the ambient oxygen partial pressure, P_{O_2}, by the power law expression $\sigma = \text{const}\ P_{O_2}^{-0.21\pm0.01}$. Both sets of observations may be rationalized on the basis that slightly-reduced α-Nb_2O_5 becomes a metal-excess, *n*-type semiconducting oxide containing oxygen vacancies capable of trapping electrons. A detailed analysis of the relation between conductivity and ambient oxygen pressure has indicated that the conductivity dependency may be ascribed to a mechanism whereby defect levels (due to oxygen ion vacancies with either one or two trapped electrons) are created and electrons are thermally excited from these levels into the conduction band.

INTRODUCTION

THE potential use of niobium for high temperature service has focused attention on its oxides since these make up the barrier layer between the metal and gas phase during oxidation. Unfortunately little is known about the properties of these materials. Brauer[1] found that α-Nb_2O_5 could exist as a single phase with departures from stoichiometry up to $Nb_2O_{4.8}$. He also indexed the first x-ray powder patterns of this material, but was unable to solve the crystal structure. Later investigators[2,3] found α-Nb_2O_5 to be monoclinic, but were not able to agree on lattice dimensions. While Nb_2O_5 may be prepared with two or more structures by transformation at different temperatures, the transformation to the α modification occurs on heating to 1100°C and is irreversible on cooling below this temperature. The lattice parameters of α-Nb_2O_5 according to Holtzberg *et al*[2] are listed in Table I.

† This research was supported by the Department of Navy, Office of Naval Research.

* Present address: Assistant Professor of Mathematical Engineering, Marquette University, Milwaukee, Wisconsin.

[1] G. Brauer, Z. anorg. u. allgem. Chem. **248**, 1–34 (1941).

[2] F. Holtzberg, A. Reisman, M. Berry, and M. Berkenblit, J. Am. Chem. Soc. **79**, 2039–2041 (1957).

[3] M. W. Shafel and R. Roy, Z. Krist. **110**, 241 (1951).

TABLE I. Lattice parameters of α-Nb_2O_5 (after Holtzberg[2]).

$a=21.34$ A
$b=3.816$ A
$c=19.47$ A
$\beta=120°\ 20'$

Kling[4] measured the conductivity of fused Nb_2O_5 as a function of oxygen partial pressure and reported an increase in conductivity with a decrease in partial pressure of oxygen. This behavior is indicative of a metal-excess semiconductor, but Kling failed to give values for any of the important parameters of his measurements. The present study was initiated for the purpose of relating the observed electrical properties of near-stoichiometric α-Nb_2O_5 to both the electronic band structure and the defect structure present in this material.

EXPERIMENTAL DETAILS

Both pressed and sintered and single crystalline specimens were used. Concerning the former, high-purity Nb_2O_5 powder[5] which was a mixture of the α and β modifications was cold-pressed without addition of any binder at pressures of 40 000 psi and sintered at temperatures between 1300 and 1350°C for two hours. After this treatment, the Nb_2O_5 existed entirely as the α modification. The apparent densities of the sintered compacts were measured pycnometrically and were found to be within 80 to 90% of the theoretical density of 4.55 g/cm³ reported by Holtzberg *et al.*[2] Rectangular parallelpipeds $\frac{1}{2}$ in.$\times\frac{1}{4}$ in. $\times$0.05 in. and disks 0.65 in. in diameter and 0.10 in. thick were cut from the sintered compacts and used for conductivity specimens, the surfaces being polished with 420 grit carborundum paper.

Small single crystals approximately 2 mm in diameter were kindly furnished by the Linde Air Products Company. Flat surfaces were ground and polished with 420 grit carborundum on the crystals for electrical contact. No analysis of the Linde crystals or knowledge of their perfection was available.

During measurement the specimen was held in a Lavite jig and platinum electrodes were placed against the specimen by means of stainless steel screws bearing against Lavite pressure plates (see Fig. 1). Resistance measurements were made by both the two- and the four-probe methods, with both methods yielding essentially identical results. The potential drop across the specimens was measured with a Keithley model 610 electrometer, while that across a standard resistance (either 10^3 or 10^4 ohms) was measured with a Rubicon type B potentiometer. To avoid any contribution to the measured potential from thermally generated emf's, readings were taken in both forward and reverse directions and averaged. Furthermore, the resistance was evaluated at several different potentials to be certain that the specimen behaved ohmically. The specimen jig was placed either in a Vycor tube surrounded by an electrical resistance furnace or else in a vacuum bell jar arrangement containing a small nichrome furnace. The furnace temperatures were held to ±1°C by means of a saturable reactor controller. Both the Vycor tube and vacuum bell jar were connected to the same vacuum-atmosphere system illustrated in Fig. 2. The

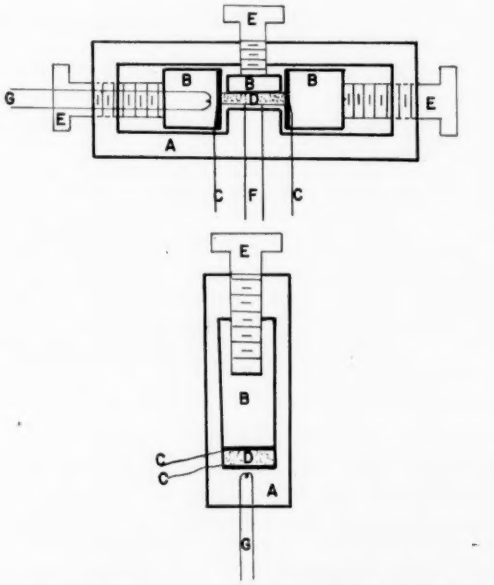

FIG. 1. Specimen jig.

[4] H. Kling, *The Technology of Columbium* (John Wiley & Sons, Inc., New York, 1958), p. 87.

[5] The high-purity Nb_2O_5 powder used in this investigation was kindly furnished by the Fansteel Metallurgical Corp., North Chicago, Illinois. A typical analysis, as furnished by Fansteel, is as follows:

By x-ray

Ta_2O_5	0.06
TiO_2	<0.005
Fe	<0.005
ZnO	<0.05
Ni	0.06

By emission

Al	0.007	Cr	<0.001
Ni	0.003	Co	<0.001
Mg	0.008	Mo	<0.002
Fe	0.005	V	<0.001
Si	0.03	Sn	<0.005
W	<0.01	Mn	<0.001
Zr	<0.02	Be	<0.0005
Yb	<0.01	Zn	<0.0005
Pb	<0.001	B	<0.0001
Ti	<0.01	Cd	<0.0001

specimen chamber was evacuated and oxygen admitted to a known partial pressure which was measured with the aid of either an open or closed tube mercury manometer. The tank oxygen used was purified by passing it over activated charcoal at liquid nitrogen temperatures. The criterion for equilibrium following a pressure change was a constant specimen resistance over a period of thirty minutes.

The electrical conductivity of sintered specimens referred to in the present paper should, in reality, be thought of as an "effective" conductivity since in specimens of varying density it is difficult to evaluate an absolute conductivity. For example, in air at a temperature of 727°C, the conductivity of sintered α-Nb_2O_5 varied from 1 to 3×10^{-4} ohm^{-1} cm^{-1}, with the specimens of greater density, as expected, having the greater values. In all cases, conductivity is given in terms of the reciprocal of the measured resistance multiplied by the appropriate geometrical constant. Because of their irregular geometry, the results for the small single crystals are expressed as the reciprocal of the measured resistance.

RESULTS AND DISCUSSION

In Fig. 3, the temperature dependence of the electrical conductivity is given for sintered α-Nb_2O_5 specimens and Nb_2O_5 single crystals heated in air over the temperature range 300 to 900°C. It is seen that the conductivity of both sintered specimens and single crystals has a positive temperature coefficient and that the change may be expressed by the well-known relationship

$$\sigma=\sigma_0 \exp -E/kT, \qquad (1)$$

where E is related to the activation energy for the creation of charge carriers in either the conduction or valence band. From the analysis of the slope of the

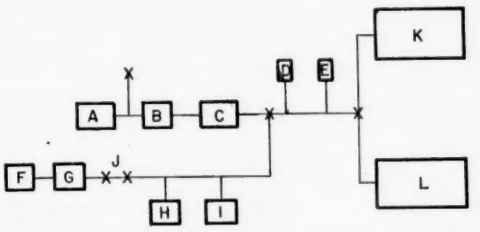

A. MECHANICAL PUMP
B. MERCURY DIFFUSION PUMP
C. LIQUID NITROGEN TRAP
D. THERMOCOUPLE GAGE
E. COLD CATHODE ION GAGE
F. GAS SUPPLY
G. ACTIVATED CHARCOAL TRAP
H. OPEN MANOMETER
I. CLOSED MANOMETER
J. DOSING SYSTEM
K. BELL JAR
L. VACUUM MUFFLE FURNACE
X. STOPCOCK

FIG. 2. Schematic diagram of vacuum atmosphere system.

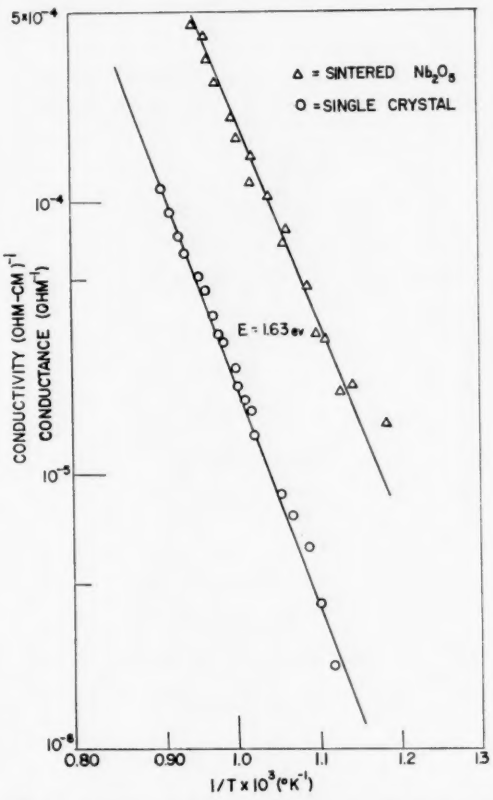

FIG. 3. Electrical conductivity of sintered α-Nb_2O_5 and electrical conductance of Nb_2O_5 single crystal versus $1/T$ for specimens heated in air.

logσ versus $1/T$ plot (Fig. 3), a value of 1.65 ± 0.01 ev was obtained for E.

Incorporated in the pre-exponential term σ_0 is the temperature dependence of the carrier mobility. This is probably not significant in comparison with the temperature dependence of the charge carrier concentration. The temperature variation of the Hall mobility for compounds like Nb_2O_5 has been accounted for on the basis of scattering by the acoustical vibrational modes of the lattice ($\mu\sim T^{-\frac{3}{2}}$ mobility law[6]) or scattering by the optical lattice vibrations ($\mu\sim[\exp\theta/T-1]$ mobility law).[7,8] In the polar semiconductors PbS, PbSe, PbTe,[9] and TiO_2,[10] the temperature behavior of the mobility can be approximated by the equation $\mu=\mu_0 T^{-n}$, in which n is a constant of magnitude 2 to 3.5. It is noteworthy that all of the foregoing mobility laws

[6] J. Bardeen and W. Shockley, Phys. Rev. **80,** 72 (1952).
[7] H. Frölich and N. F. Mott, Proc. Roy. Soc. (London) **A171,** 496 (1939).
[8] H. Fröhlich, H. Pelzer, and S. Zienau, Phil. Mag. **41,** 221 (1950).
[9] W. W. Scanlon in *Solid State Physics*, F. Seitz and D. Turnbull, editors (Academic Press, Inc., New York, 1959), Vol. 9, p. 83.
[10] F. A. Grant, Revs. Modern Phys. **31,** 646 (1959).

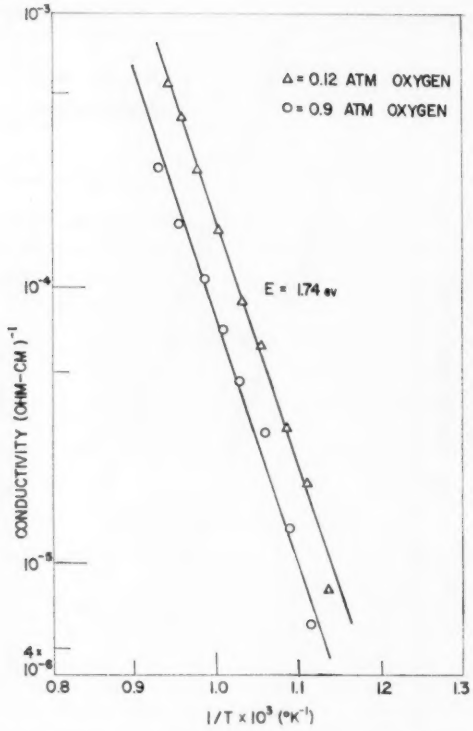

FIG. 4. Electrical conductivity versus $1/T$ for sintered α-Nb_2O_5.

yield a negative temperature coefficient for the mobility.

Recent experiments on rutile (TiO_2) have indicated that it is difficult to decide whether the temperature dependence of the Hall mobility may be rationalized better on the basis of a power law $\mu \sim T^{-n}$ with $2.5 \leq n \leq 3.5$ or by assuming a polar scattering law with a Debye temperature Θ in the range from 670 to 810°K.[11] In either instance, the resultant variation in the mobility of near-stoichiometric rutile over a given temperature range is not significant when compared with the change occurring in the carrier concentration.[12]

Because the electrical properties of Nb_2O_5 appear quite similar to those of rutile, it seems reasonable to expect the carrier mobility in Nb_2O_5 to behave analogously to that of rutile. If the power law holds, the temperature change in mobility would obviously be much smaller than the exponential term involving number of change carriers; whereas if polar scattering were assumed to hold and Θ for Nb_2O_5 lies between 500 and 1500°K, then the mobility would change by, at most, a factor of six in the temperature range investigated. Reference to Fig. 3 and Fig. 4 indicates that the conductivity changes by at least a factor of one hundred in the same temperature interval.

The electrical conductivity of a sintered α-Nb_2O_5 specimen at oxygen pressures of 0.9 atm and 0.12 atm is given as a function of temperature in Fig. 4. The temperature behavior of the conductivity for this specimen can be expressed by Eq. (1) with essentially the same E; however, the values of the conductivity are uniformly higher at the lower oxygen pressure.

The isothermal conductivity of a sintered α-Nb_2O_5 specimen was also measured as a function of oxygen partial pressure at different temperatures. The oxygen pressures ranged from 0.95 atm to 0.002 atm in these measurements. The results are given in Fig. 5 in which the logarithm of the conductivity was plotted against the logarithm of the oxygen partial pressure. The following empirical relation holds for these data:

$$\sigma = P_{O_2}^{-0.24 \pm 0.01}. \tag{2}$$

It is interesting to observe that linear plots were obtained at all three temperatures.

Because the conductivity increases with decreasing oxygen partial pressure, α-Nb_2O_5 can be classified as a metal-excess, n-type semiconductor. The metal-excess may arise from either oxygen ion vacancies or from cation interstitials. Since both of these mechanisms create an excess of positive charge, quasi-free electrons, in concentrations sufficient to balance this charge, must be postulated in order to maintain electroneutrality in the sample.

Pure stoichiometric α-Nb_2O_5 is considered to be an insulator since all the electrons are bound tightly in the closed shell of either the Nb^{5+} or O^{2-} ions. The allowable electron states may be divided up into a full valence band representing the anion states and an empty conduction band representing the cation states. This is shown in Fig. 6(a). The hypothesis of a cation excess and associated quasi-free electrons in α-Nb_2O_5 serves to introduce a new set of discrete levels below the conduction band as is shown in Fig. 6(b). These quasi-free electrons would be bound in the field of the centers

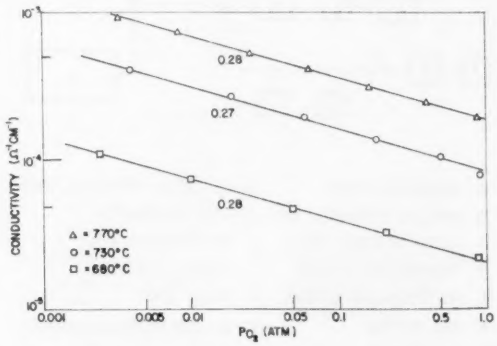

FIG. 5. Electrical conductivity of sintered α-Nb_2O_5 versus oxygen partial pressure.

[11] H. P. R. Frederikse and W. R. Hosler (private communication).

[12] D. C. Cronemeyer, Phys. Rev. **87**, 876 (1952).

of positive charge (oxygen ion vacancies or Nb^{5+} interstitials) and would need to acquire additional energy, equal to E_1 or E_2 in Fig. 6(b), in order to be excited into the conduction band.

On the basis of the exponent in Eq. (2) and the amount of thermal energy available in the temperature range 500 to 900°C, it is possible to decide whether oxygen ion vacancies or cation interstitials are responsible for the metal excess existing in near-stoichiometric α-Nb_2O_5.

The equation for the creation of the oxygen ion vacancy and the two trapped electrons constituting the metal excess may be written[13]

$$O_l^{2-} \rightleftharpoons O\square^{X} + \tfrac{1}{2}O_2, \tag{3}$$

where O_l^{2-} is an oxygen ion in a normal lattice position and $O\square^{X}$ is an oxygen vacancy which has trapped 2 electrons in its field.

The two electrons trapped at the oxygen ion vacancy may be excited into the conduction band according to

$$O\square^{X} \rightleftharpoons O\square\cdot \ominus \tag{4}$$

$$O\square\cdot \rightleftharpoons O\square\cdot\cdot + \ominus \tag{5}$$

where $O\square\cdot$ is an oxygen ion vacancy which has trapped one electron in its field, $O\square\cdot\cdot$ is an oxygen ion vacancy from which both electrons have been excited, and $\ominus$ is an electron in the conduction band.

If the concentrations of defects produced are small and the defects do not interact, the equilibrium constants for Eqs. (3) to (5) may be written in terms of the concentrations, represented by square brackets, and P_{O_2}, the partial pressure of oxygen.

$$K_1 = P_{O_2}^{\frac{1}{2}}[O\square^{X}] \tag{6}$$

$$K_2 = \frac{[\ominus][O\square\cdot]}{[O\square^{X}]} \tag{7}$$

$$K_3 = \frac{[\ominus][O\square\cdot\cdot]}{[O\square\cdot]}. \tag{8}$$

Substitution of the expressions into the condition of electroneutrality

$$[\ominus] = 2[O\square\cdot\cdot] + [O\square\cdot] \tag{9}$$

leads to the following expression for the change in conduction band carrier concentration (and hence conductivity) with oxygen partial pressure

$$[\ominus]^2 - [\ominus]K_1K_2P_{O_2}^{-\frac{1}{2}} - 2K_1K_2K_3P_{O_2}^{-\frac{1}{2}} = 0. \tag{10}$$

Consider the following two possible limiting cases

$$[\ominus] \gg 2K_3 \tag{11a}$$

$$[\ominus] \gg 2K_3. \tag{11b}$$

[13] The development presented here follows from the general ideas of F. A. Kroger and H. J. Vink in *Solid State Physics*, F. Seitz and D. Turnbull, editors (Academic Press, Inc., New York, 1956), Vol. 3, p. 307.

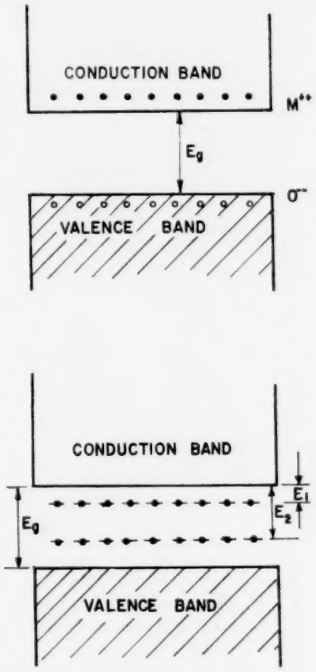

FIG. 6. Hypothetical band model for metal-excess semiconductors.

If Eq. (11a) is limiting, then Eq. (10) reduces to

$$[\ominus]^2 = K_1K_2P_{O_2}^{-\frac{1}{2}}$$

or

$$[\ominus] = (K_1K_2)^{\frac{1}{2}}P_{O_2}^{-1/4}, \tag{12a}$$

whereas if Eq. (11b) is limiting, Eq. (10) reduces to

$$[\ominus]^3 = 2K_1K_2K_3P_{O_2}^{-\frac{1}{2}}$$

or

$$[\ominus] = (2K_1K_2K_3)^{1/3}P_{O_2}^{-1/6}. \tag{12b}$$

According to Eq. (8), K_3 is expressed as

$$K_3 = \frac{[\ominus][O\square\cdot\cdot]}{[O\square\cdot]}.$$

Therefore, if $[O\square\cdot] \gg 2[O\square\cdot\cdot]$, then $[\ominus] \gg 2K_3$ and Eq. (12a) will hold; whereas if $2[O\square\cdot\cdot] \gg [O\square\cdot]$ then $[\ominus] \ll 2K_3$ and Eq. (12b) will hold.

Since Eq. (12a) gives agreement with experimental observations as expressed by Eq. (2), this indicates that $[O\square\cdot] \gg 2[O\square\cdot\cdot]$. Such a situation would occur if $E_2 \gg E_1$, and $E_2 \gg kT$ [see Fig. 6(b)], where E_1 and E_2 are, respectively, the energies necessary to excite the first and second electrons from an oxygen vacancy trap and kT is the available thermal energy.

Unpublished work on reduced specimens of Nb_2O_5 by Greener[14] indicates that for relatively dilute con-

[14] E. H. Greener, Ph.D. thesis, Northwestern University (1960).

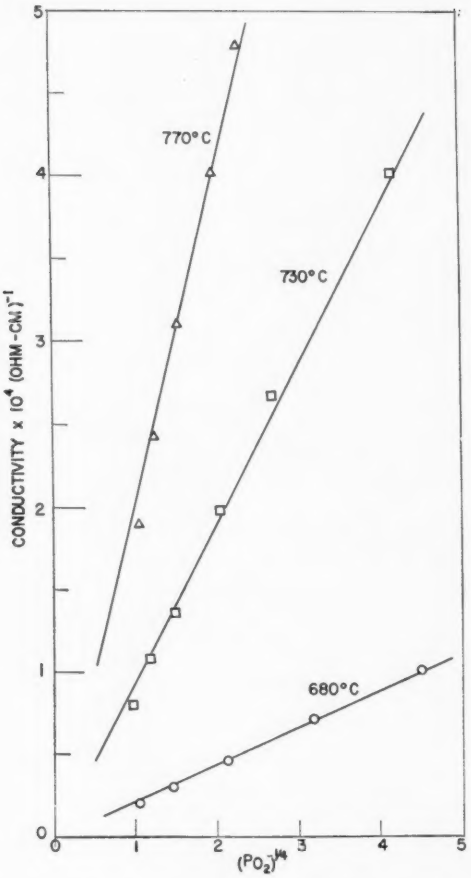

FIG. 7. Electrical conductivity of sintered α-Nb_2O_5 versus $P_{O_2}^{-1/4}$.

centrations of defects an activation energy of 0.1 ev might be necessary to excite the first electron, and one of from 0.5 to 1.0 ev might be necessary to completely ionize the oxygen vacancy; however, the thermal energy available in the range 500 to 900°C is only about 0.09 ev.

A similar analysis to that presented above for oxygen ion vacancies has been made for the hypothetical case of Nb^{5+} interstitials. The equations are a great deal more cumbersome since there are five equations for the excitation of the five electrons from the pentavalent interstitial cation. The analysis indicates that it would be possible for this model to give Eq. (2) only if the excitation of the last two electrons from interstitial cations were responsible for the observed change in conductivity. This is not likely since the energy required to excite the fourth and fifth electrons should be very large compared with the available thermal energy.

Any model which explains the isothermal change in conductivity with oxygen partial pressure must also account for its temperature dependence, given in Eq. (1). In near-stoichiometric polar materials with only electronic conductivity, there can be two sources of conduction band carriers:

(1) Those arising from intrinsic semiconduction. The absorption by an electron in the valence band of energy equal to E_G [Fig. 6(a)] excites the electron into the conduction band, leaving an electron hole behind in the valence band. The concentration of conduction band charge carriers as a function of temperature may be expressed as[15]

$$[\ominus]=[\ominus]_0 \exp(-E_G/2kT) \tag{13}$$

where E_G is the gap energy, k is Boltzmann's constant, and T is the absolute temperature.

(2) Those arising from the excitation of carriers trapped at defect levels. If it is assumed that the defect consists of an oxygen ion vacancy and two trapped electrons and that Eq. (12a) holds, then the number of conduction band carriers may be expressed as a function of partial pressure according to

$$[\ominus]=K_1K_2P_{O_2}^{-1/4}. \tag{13a}$$

However, K_1 and K_2 are temperature-dependent according to

$$K_1=K_{O_1}\exp(-W_D/kT)$$
$$K_2=K_{O_2}\exp(-E_1/kT), \tag{14}$$

where W_D is the energy to create the defect level and E_1 is the energy to excite the first electron from the oxygen ion vacancy into the conduction band [Fig. 6(b)].

Assuming that both processes are responsible for the conduction band carrier concentration at thermal equilibrium, it seems reasonable to represent that concentration by the sum of Eqs. (12a) and (13). Thus,

$$[\ominus]_{total}=[\ominus]_0\exp(-E_G/2kT)$$
$$+K_{O_1}K_{O_2}\exp[-W_D+E_1)/2kT]P_{O_2}^{-1/4}. \tag{15}$$

Since the conductivity is experimentally observed to be a function of the oxygen partial pressure, the second term on the right-hand side of Eq. (15) must be at least equal in magnitude to the first term, or, in fact, larger. Accordingly, a plot of the conductivity against the $(-\frac{1}{4})$ power of the oxygen partial pressure should be a linear one of slope equal to

$$(K_{O_1}K_{O_2})^{\frac{1}{2}}\exp-(W_D+E_1)/2kT$$

and of intercept equal to $[\ominus]_0\exp-E_G/2kT$. Therefore, if the intrinsic contribution is not appreciable, the curve should pass through the origin.

The data presented in Fig. 5 were replotted in this fashion in Fig. 7 and it is apparent that extrapolations to zero pressure do pass through the origin. Therefore any significant contribution from intrinsic semicon-

[15] See, for example, N. F. Mott and R. W. Gurney, *Electronic Processes in Ionic Crystals* (Oxford University Press, London, 1940), p. 152.

duction in the temperature and pressure range investigated may be ruled out and the variation of the conduction band carrier concentration with pressure and temperature may be represented by the relation

$$[\ominus]=(K_{O_1}K_{O_2})^{\frac{1}{2}}\exp[-(W_D+E_1)/2kT]P_{O_2}^{-1/4} \quad (15a)$$

where $(W_D+E_1)/2$ is the same quantity as the empirical E of Eq. (1) and assumes the value 1.65 ev for the present case.

A further check on the proposed mechanism can be obtained from an analysis of the slopes of Fig. 7. By taking the slopes at two different temperatures [as in Eq. (14a)], it is possible to calculate a value for $(W_D+E_1)/2$. Analysis of the three possible combinations represented in Fig. 7 yields a value of 2.0 ev. Considering that only three temperatures were used, the agreement in comparing this with the isobaric value of 1.65 ev is satisfactory. Thus two experiments, one at constant temperature and the other at constant pressure, yield approximately the same value for the total energy necessary for the defect creation (oxygen ion vacancy+trapped electrons) plus the excitation of one of the trapped electrons into the conduction band.

Since the value of E_1 is probably very small the majority of the measured activation energy is associated with W_D. It is interesting to note that the assumption of a value of 0.15 ev for E_1 in Eq. (15a) yields a value of 3.16 ev for W_D. This value is in close agreement with the enthalpy of the reaction

$$Nb_2O_5 \rightleftharpoons Nb_2O_4+\tfrac{1}{2}O_2; \quad \Delta H=3.15 \text{ ev at } 1000^\circ\text{K}$$
$$=3.12 \text{ ev at } 1200^\circ\text{K} \quad (16)$$

calculated from the data given by Coughlin[16] for the free energies and enthalpies of formation of Nb_2O_4 and Nb_2O_5.

Data presented by Earle[17] on the pressure dependence of the conductivity of sintered rutile (TiO_2) specimens can be successfully interpreted by the method outlined above for Nb_2O_5 which led to Eq. (15a) (see Fig. 8 for a typical plot). It appears that in the temperature range 600 to 900°C the conductivity of near-stoichiometric TiO_2 is also entirely defect-controlled.

Thus, the authors feel it would be of value to reexamine much of the previous work pertaining to the electrical conductivity of nonstoichiometric compound semiconductors to determine to what extent the creation of defect levels and their ionization is responsible for the observed conductivity.

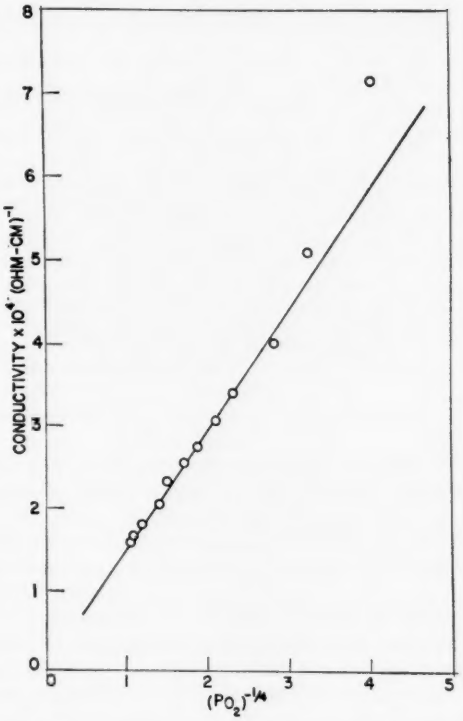

FIG. 8. Electrical conductivity of sintered TiO_2 versus $P_{O_2}^{-1/4}$ (after Earle[17]).

[16] J. P. Coughlin, Bulletin 542, Bureau of Mines, Washington, D. C. (1954).
[17] M. P. Earle, Phys. Rev. **61**, 56 (1942).

Monte Carlo Computations on the Ising Model. The Body-Centered Cubic Lattice

LESTER GUTTMAN*

General Electric Research Laboratory, Schenectady, New York

(Received March 1, 1960)

The Monte Carlo method of computation has been used to obtain some equilibrium properties of bcc binary solid solutions whose atoms interact according to the Ising model. Four cases have been treated: (a) $N=128$, $c=\frac{1}{2}$, (b) $N=1024$, $c=\frac{1}{2}$, (c) $N=1024$, $c=3/8$, and (d) $N=1024$, $c=\frac{1}{4}$ (N being the total number of atoms and c the fraction of one kind.) In all cases the heat capacity has a well-defined maximum. At the equiatomic composition, the height of this maximum is greater in the larger crystal. Discontinuities in thermodynamic properties were not observed, and it seems reasonable that the order-disorder transition in an infinite crystal would be characterized by an infinite heat capacity as calculated by Onsager and others for two-dimensional crystals. Comparison of the results with experimental properties of β-CuZn suggests a remarkable applicability of the Ising model to this system. The potentialities and limitations of the Monte Carlo method for systems with phase transitions are discussed.

IT is widely believed that the Ising model provides a useful framework for the understanding of order-disorder phenomena in metallic solid solutions. When the basis for this belief is examined in detail,[1] it is found that there is rather poor quantitative agreement between experiment and the properties calculated from the model by various mathematical approximations. However, the extent to which these discrepancies point to defects in the model is ambiguous, since the approximate results are known to differ considerably, and even qualitatively, from the exact solutions for plane lattices.[2] As the analytical solution to the statistical mechanical problem for three-dimensional lattices may still be far away, there is an immediate interest in reliable estimates of the properties of Ising systems. The Monte Carlo method[3] using digital computers is a natural one to apply for this purpose, in view of the discrete nature of the coordinates and spectrum. This has occurred to a number of people, and calculations have been carried through for the two-dimensional case by Salsburg *et al.*[4] and by Fosdick[5]; the three-dimensional case has been treated by Fosdick,[6] for the fcc lattice, and by Flinn *et al.*,[7] for the bcc lattice. The last investigation[7] was of interest to me in connection with the behavior of the iron-aluminum system, but it seemed that to obtain useful results it would be necessary to change certain details of the computation, and of course to extend it to include compositions other than the ideal 1:1. The results of this extension are described below.

COMPUTATIONAL METHOD

In the general Monte Carlo method of Metropolis *et al.*,[3] the equilibrium properties of a system are estimated by averaging over a sequence of microscopic states generated as follows: With the system in some state, a tentative transition to a nearby state is selected by a random process. The corresponding energy change ΔE is calculated and the next state of the sequence is the new state or the old one according to whether or not $\exp(-\Delta E/kT)>\zeta$, where ζ is a number chosen at random in the interval $(0, 1)$. The taking of averages begins when it is judged, essentially subjectively, that the influence of the starting configuration is negligible; the sequence is terminated when it is judged, again subjectively, that the gain in precision of including more states is not worth the computational cost. It has been shown[3,8] that averages so taken converge in the limit of infinitely long sequences to the equilibrium properties of the system, provided that the random process is capable of leading to all possible microscopic states. Since the systems that can now be handled by computers are very small, there is an altogether separate problem of extrapolating their properties to the macroscopic limit.

The specific system under consideration contains N atoms of two kinds, A and B, in fixed numbers, N_A and N_B, located on the lattice sites of a bcc crystal. A microscopic state is completely described by giving the kind of atom occupying each site, and its energy is taken to be

$$E=-vn_{AB},$$

where v is a constant and n_{AB} is the number of pairs of unlike nearest-neighbor atoms. Four cases have been

* Present address: Solid State Science Division, Argonne National Laboratory, Argonne, Illinois.

[1] L. Guttman, in *Solid State Physics* (Academic Press, Inc., New York, 1956), Vol. 3, p. 146.

[2] G. F. Newell and E. W. Montroll, Revs. Modern Phys. **25**, 353 (1953).

[3] N. Metropolis, A. W. Rosenbluth, M. N. Rosenbluth, A. H. Teller, and E. Teller, J. Chem. Phys. **21**, 1087 (1953).

[4] Z. W. Salsburg, J. D. Jacobson, W. Fickett, and W. W. Wood, J. Chem. Phys. **30**, 65 (1959).

[5] L. D. Fosdick (private communication).

[6] L. D. Fosdick, Phys. Rev. **116**, 565 (1959).

[7] P. A. Flinn, G. M. McManus, and F. J. O'Meara (private communication).

[8] W. W. Wood and F. R. Parker, J. Chem. Phys. **27**, 720 (1957).

considered:

(a) $N_A = N_B = 128$.

(b) $N_A = N_B = 512$.[9]

(c) $N_A = 384$, $N_B = 640$.

(d) $N_A = 256$, $N_B = 768$.

In all cases the crystal is a cube, containing n^3 unit cells, with $n=4$ in (a), and $n=8$ in (b)–(d). To minimize surface effects, periodic boundary conditions are used, i.e., the system is surrounded on all sides with copies of itself.

Each lattice site is represented by a location in the memory of a digital computer (here an IBM 704). The location is assigned a one or a zero, corresponding to occupation of the site by an A or a B atom. A pair of lattice sites is chosen at random; if the sites contain identical atoms, another pair is selected. When the two sites are differently occupied, the eight nearest neighbor sites of each are examined. Suppose there are m_{AA} A atoms neighbor to the A atom, and m_{AB} A atoms neighbor to the B atom. Then interchanging this pair of atoms would effect an increase Δn_{AB} in the number of unlike pairs given by

$$\Delta n_{AB} = 2(m_{AA} - m_{AB} + \delta),$$

where δ is unity if the sites in question are themselves nearest neighbors, and zero if they are not. If $\Delta n_{AB} \geq 0$, the interchange is carried out. If Δn_{AB} is <0, the Boltzmann factor

$$f = \exp[(v/kT)\Delta n_{AB}]$$

is compared with a random number ζ, $0<\zeta<1$; if $f \geq \zeta$, the interchange is carried out; if $f<\zeta$, the original state is retained.

At the very beginning of the computation, the system is assigned a configuration of known energy $-n_{AB}{}^{\circ}v$. The energy E_j of any subsequent state is known from the cumulative effects of the allowed interchanges. Account is thus kept of

$$-E_j/v = (n_{AB})_j = n_{AB}{}^{\circ} + \sum^{j} \Delta n_{AB},$$

from which one can compute

$$m\langle -E/v\rangle_m = \sum_1^m (n_{AB})_j,$$

and

$$m\langle (-E/v)^2\rangle_m = \sum_1^m (n_{AB})_j^2,$$

where m is the number of states in a sequence. Certain other properties are also counted: The long-range order is measured by R, the number of A atoms on unit cell corners; this number is known initially, and the cumulative effects of allowed interchanges are easily counted. It is also possible to measure the average number of *triplets* of sites occupied in either of two ways. The three sites are in the form of an isosceles triangle, two of whose sides are nearest-neighbor bonds, the third being a cube edge. The apex site may be either one of the pair involved in a tentative interchange; if it is found that two of its neighbors separated by a cube edge are both A atoms, a counter is increased by unity. There are two such counters, one of them being incremented if the central atom is an A, the other if it is a B. In this way, one counts triplets of the type A-A-A or of the type A-B-A. This counting is incomplete, in that for each state only two atoms are examined, and even for these only one triplet is tested of the 12 in which the atom is central. Nevertheless, it seems obvious that the average values of these counters, suitably normalized, are equal to the probabilities of finding the corresponding triplet configurations at equilibrium, since the atoms are chosen at random, and since the 12 triplets are equivalent in a crystal of cubic symmetry.

At the beginning of a computation the computer memory contains the stored program, an initial lattice configuration, its energy (actually $n_{AB}/2$) and its long-range order, a series of "temperatures" at which computing is to take place, and a short table of nine-decimal random numbers. The (pseudo) random numbers needed for ζ and for selection of sites are generated by the middle-square process[3]; occasionally this process produces a number identical to the preceding number, and this number would then repeat indefinitely; whenever this occurs, the program starts a new sequence using one of the numbers in the table.

The table of "temperatures" is actually a table of Boltzmann factors

$$f_1 = \exp(-2v/kT)$$

for the loss of two unlike pairs. At each value of v/kT, the program computes and stores the first eight powers of f_1; computation of the factor

$$f = \exp[(v/kT)\Delta n_{AB}]$$

for $0 > 1/2(\Delta n_{AB}) \geq -8$ reduces simply to selection of the corresponding power of f_1.

The generation of states proceeds at the first temperature until a predetermined number of interchanges, usually 1000, has been attempted. A record is then made of the instantaneous values of $\frac{1}{2}n_{AB}$ and R, and of the various totals

$$\tfrac{1}{2}\sum_1^{1000}(n_{AB})_j, \qquad \tfrac{1}{4}\sum_1^{1000}(n_{AB})_j^2, \qquad \sum_1^{1000} R_j,$$

and the triplet counters. The totals are then reset to zero, and another sequence of 1000 attempted inter-

[9] Owing to an error in the input configuration, N_A was actually 510 and N_B 514; in the following, it has been assumed that the results for this case differ negligibly from those for $N_A = N_B = 512$.

changes is started. When a predetermined number (usually 16 or 25) of such sequences has been completed, an image of the last configuration is recorded, the next value of f_1 is selected, and the whole computation begins anew. By arranging the temperatures in a rising or falling series, and by using the last configuration at one temperature as the first configuration at the next temperature, the effect of the starting configuration is minimized. The computation stops automatically when the table of "temperatures" is exhausted.

For equal numbers of A and B atoms, a pair of sites contains like atoms as often as unlike, so that on the average only every other pair selected is examined further. The average time to select two pairs and attempt the interchange of one of them is about 12 msec. This time includes only three multiplications, most of the remainder consisting of logical and control operations. The IBM 704 operation called AND ("logical sum") is particularly useful in determining the state of occupancy of individual sites.

TREATMENT OF DATA

The presentation of the results of the computation must be prefaced by some discussion of how to proceed from the raw computer output to estimates of equilibrium properties. It will be seen that the present results are subject to considerable imprecision, which could be reduced substantially only by a costly increase in total computation time.

The averages of properties over a number of states as small as 10^3 show appreciable fluctuations. Generally, these fluctuations are superimposed, near the start of computation at a given temperature, on a transient drift whose duration is greater the larger the system, the larger the temperature difference from the previous temperature, and the lower the temperature. Moreover, ordering is observed to proceed more slowly than disordering, other conditions being equal. The first subjective judgment that arises, therefore, is to decide at what point in the computation the effects of the initial state have become small compared to the random fluctuations; if this point is taken too early, the averages over the subsequent states are not entirely typical of equilibrium; if it is taken too late, the averages will include too few states and precision will be lost. The problem of separating the initial trend from the equilibrium fluctuations is complicated by the fact that the fluctuations themselves vary in size with temperature. This is readily seen from the relation[10]

$$C=(1/kT^2)\left(\langle E^2\rangle_{Av}-\langle E_{Av}\rangle^2\right), \qquad (1)$$

where C is the heat capacity. In the present case, the heat capacity has a steep maximum at the order-disorder transition temperature, so that the energy is subject to the greatest fluctuations in the most interesting range. In this range one cannot hope to evaluate equilibrium properties merely by averaging over a few states after the decay of the initial transient.

On the other hand, the heat capacity can be estimated independently from the energy fluctuations and by differentiation of the average energy. Agreement between these values indicates that the sampling of states has been adequate. This is the reason for including a calculation of the energy variance in the program.

In the present computations, preliminary runs gave some idea of the length of time to reach equilibrium and of the most interesting temperature region in each of the four cases. The temperatures and the numbers of interchanges to be attempted were selected accordingly. For a fixed total computation time, it seemed more economical to approach equilibrium from only one direction at each temperature. Therefore, there are no duplications of temperatures in the "heating" and "cooling" series, reliance being put instead on the general agreement between the results of the series of both kinds.

The decision of how many states to discard at the start of each temperature was made as follows. The last one-fourth to one-half of the states were assumed to be typical of equilibrium, and from them estimates were made of average properties and, crudely, of their variances. The initial states were then discarded up to a point at which the energy was safely within one standard deviation of the later average, and the other properties appeared also to have reached equilibrium values. In the smaller crystal [case (a)], these criteria were satisfied very quickly; even the biggest drop in temperature (30%) was established after less than 2000 interchanges. The results for this case are based on samples ranging from 31 000 to 62 000 states. In the larger crystals [cases (b)–(d)], many more interchanges were needed, of course, to erase the effects of the initial state, the number of states discarded being at least 5000 and sometimes as large as 30 000. The results for these crystals are based on samples ranging from 35 000 to 100 000 states at each temperature.

RESULTS

Averages of n_{AB}, n_{AB}^2, of R, and of the triplet probabilities, denoted by P_{AAA} and P_{ABA} (P_{AAA} is, in the limit, the fraction of all triplets which are made up of three A atoms; P_{ABA}, $P_{ABB}\cdots$ are similarly defined), were calculated at a number of temperatures for each of the four systems investigated.

A. Thermal Properties

Since only nearest-neighbor interactions are being considered, the *energy* is given by the number of nearest-neighbor pairs n_{AB}, or more conveniently, since it is independent of the size of the system, by the short-range order parameter for nearest neighbors σ

[10] E. Schrödinger, *Statistical Thermodynamics* (Cambridge University Press, New York, 1952).

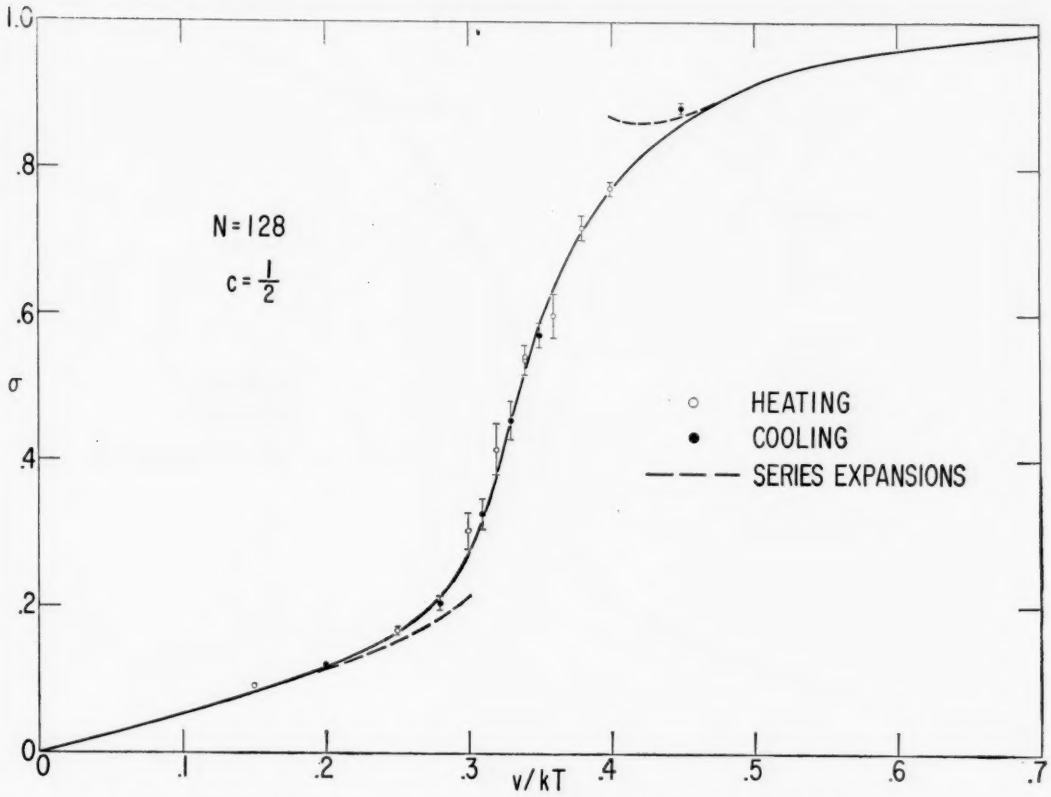

FIG. 1. Short-range order parameter σ vs reduced inverse temperature v/kT, case (a) ($N=128$, $c=\frac{1}{2}$).

defined by[1]

$$\sigma=\frac{n_{AB}-n_{AB}(\text{random})}{n_{AB}(\text{perfect order})-n_{AB}(\text{random})},$$

which varies from unity at $T=0$ to zero at $T=\infty$. For N atoms in the ratio $c:1-c$,

$$n_{AB}(\text{random})=zNc(1-c),$$

(z, the coordination number, is 8 for the bcc lattice), and

$$n_{AB}(\text{perfect order})=zNc, \qquad c\leq\tfrac{1}{2}.$$

The values of σ for the four cases considered are shown in Figs. 1–4, with curves intended to represent their over-all behavior. The statistical errors[11] in these values allow a rather large latitude in drawing these curves. They have been drawn as smoothly as possible, with no intentional discontinuities in slope. In addition to the results of the Monte Carlo calculation, use was made of the series expansions,[2] valid at extreme temperatures for $c=\frac{1}{2}$. For other compositions, there is available only the quasi-chemical expression valid at very high temperatures,

$$d\sigma/dx=2(1-c)^2 \qquad (x=v/kT).$$

The *heat capacity* can be calculated from the expression

$$C/Nk=zc^2x^2(d\sigma/dx).$$

Values of σ were read from the curves of Figs. 1–4 at intervals of 0.01 in x, and a table of differences was prepared. Here and there the values were adjusted by one or two units in the third decimal place to give smooth second differences, and the derivative $d\sigma/dx$ was calculated from the central-difference formula. Figures 5 and 6 show the heat capacity for the four cases.

The *entropy* difference between two temperatures is given by

$$(\Delta S/Nk)=(1/Nk)\int_{T_1}^{T_2}(dE/T)=-zc^2\int_{\sigma_1}^{\sigma_2}xd\sigma$$

$$=zc^2\left\{x_1\sigma_1-x_2\sigma_2+\int_{x_1}^{x_2}\sigma dx\right\},$$

[11] The error limits in Fig. 1 are standard deviations, estimated from the observed inverse proportionality of the variance of the mean to the sample size. In the larger crystals, the correlations between states persist too long to enable this estimate to be made, and the precision of σ in these cases can be judged by the deviations from the smooth curves.

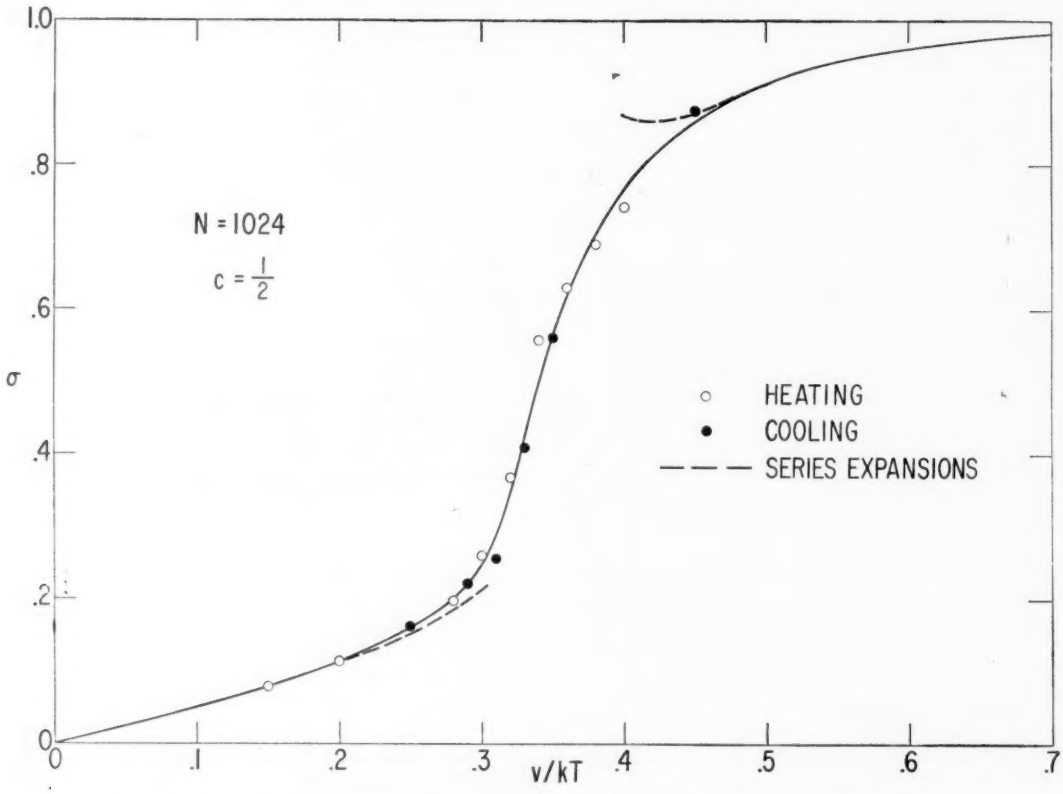

FIG. 2. Short-range order parameter σ vs reduced inverse temperature v/kT, case (b) ($N=1024$, $c=\frac{1}{2}$).

so that the entropy at a given temperature can be calculated if it is known at any other temperature. The entropy is known exactly at $T=\infty$ ($x=0$), since the solutions are random, and

$$S(T=\infty)=k\ln(N!/N_A!N_B!),$$

which is, for large N,

$$S=-Nk[c\ln c+(1-c)\ln(1-c)];$$

for $N=128$, Stirling's formula in the form

$$\ln N!=N\ln N-N+\tfrac{1}{2}\ln 2\pi N$$

gives, for $c=\frac{1}{2}$, a value of the entropy about 3.0% less than $Nk\ln 2$.

At $T=0$, and $c=\frac{1}{2}$, a perfectly ordered state of zero entropy is attained. At any other composition, the ground state is degenerate. For compositions not too far from $c=\frac{1}{2}$, most of the states of lowest energy are obtained by filling one sublattice with the majority atoms and distributing the other half of the atoms randomly on the other sublattice. The entropy is then

$$S(T=0)=k\ln[(N/2)!/N_A!(\tfrac{1}{2}N-N_A)!]$$
$$=-\tfrac{1}{2}Nk[2c\ln(2c)+(1-2c)\ln(1-2c)].$$

The difference between $S(\infty)$ and $S(0)$ is a further check on the curves of Figs. 1–4, as shown in Table I. The agreement is satisfactory in all but case (d), where the discrepancy of about 0.02 suggests that the heat capacity does not fall at low temperatures as rapidly as the extrapolation in Fig. 6.

Values of the entropy at intermediate temperatures were computed by numerical integration, assigning the theoretical value to $S(T=\infty)$. Figure 7 shows the results for cases (b)–(d); those for case (a) are not different enough from those for (b) to be worth exhibiting.

B. Distribution Functions

The long-range order parameter S was calculated from

$$S=|\,(2R/Nc)-1\,|,$$

where R is the number of A atoms on corner sites. This function is symmetrical about the point $R=Nc/2$, reflecting the symmetry between cell corners and cell centers. One would expect the equilibrium values of R to be distributed symmetrically about $Nc/2$, with a single central maximum in the disordered state, and two maxima in the ordered state. When the degree of

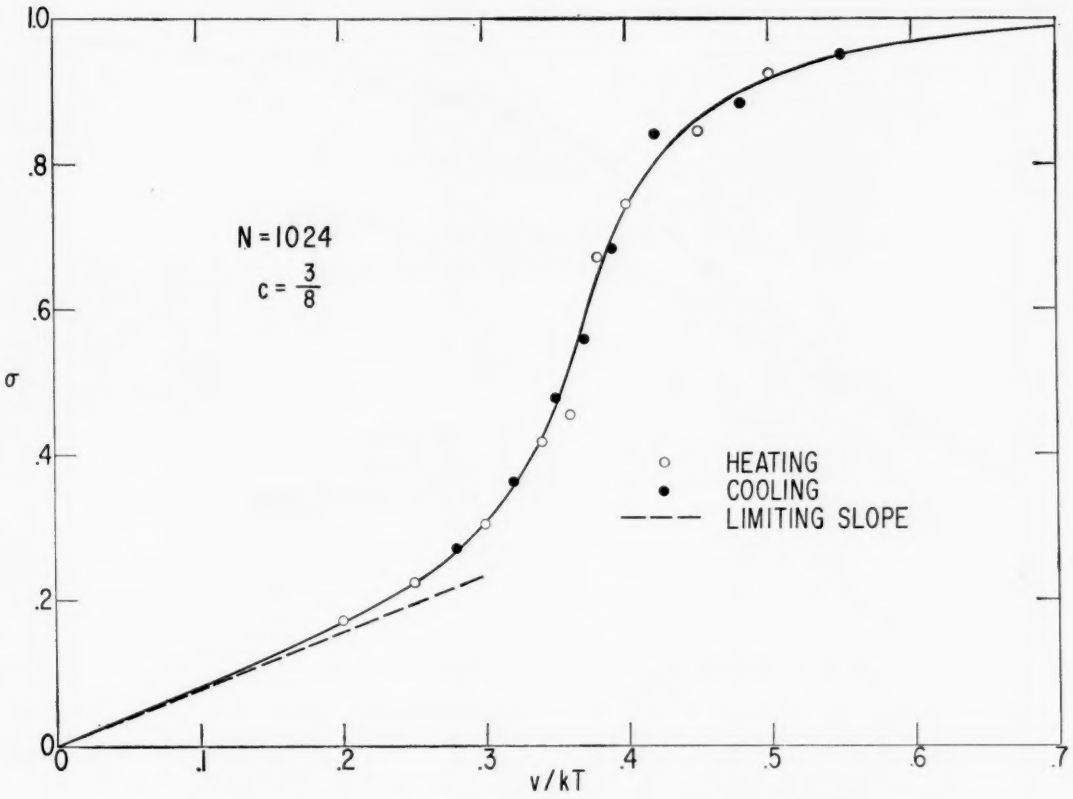

FIG. 3. Short-range order parameter σ vs reduced inverse temperature v/kT case (c) ($N=1024$, $c=3/8$).

long-range order was high, it was found that the systems remained for long times in states with R on one side of $Nc/2$, so that S_{Av} could unambiguously be calculated from R_{Av}. At higher temperatures, and especially for case (a), more and more frequent transitions were observed between the region of high R and that of low R, so that a simple average of R would have led to an underestimate of S. It was sometimes possible, however, to select sequences of 1000 states in which R was clearly different from its random value, and to estimate S from these states. The value so obtained is obviously an overestimate, but not a bad one for the larger crystals over an interesting temperature range.

The results for case (b) shown in Fig. 8 are typical of those for other systems.

The distribution of *pairs* of two kinds of atoms is completely specified by the composition c and a single probability, conveniently given in terms of a short-range order parameter σ_n. The parameter for nearest neighbors $\sigma_1=\sigma$ has been discussed in the previous section. The parameter for next-nearest neighbors σ_2 was not sampled directly, but can be calculated from the triplet probabilities P_{ABA} and P_{AAA} using the relation

$$\sigma_2=(P_{AA}'/c^2)-1=[(P_{ABA}+P_{AAA})/c^2]-1,$$

where P_{AA}' is the probability of finding two A atoms separated by a cube edge. Although these results are available, it did not seem worth the space necessary to give them in detail.

There are six different ways[12] of filling *three* sites with two kinds of atoms, but only two of the probabilities are independent if the composition and one short-range order parameter, say σ, are known. One can easily derive the four conditions:

$$P_{AAA}+P_{AAB}+P_{BAB}=c,$$

$$P_{BBB}+P_{BBA}+P_{ABA}=1-c,$$

$$P_{ABA}-P_{BAB}=\tfrac{1}{2}(P_{AAB}-P_{BBA}),$$

$$2P_{ABA}+P_{AAB}+2P_{BAB}=2P_{AB}=4c^2[\sigma+(1-c)c^{-1}],$$

which suffice to determine the entire triplet distribution from measurements of any two probabilities, e.g., the observed values of P_{ABA} and P_{AAA}. However, as

[12] Neglecting the existence of long-range order; see the following.

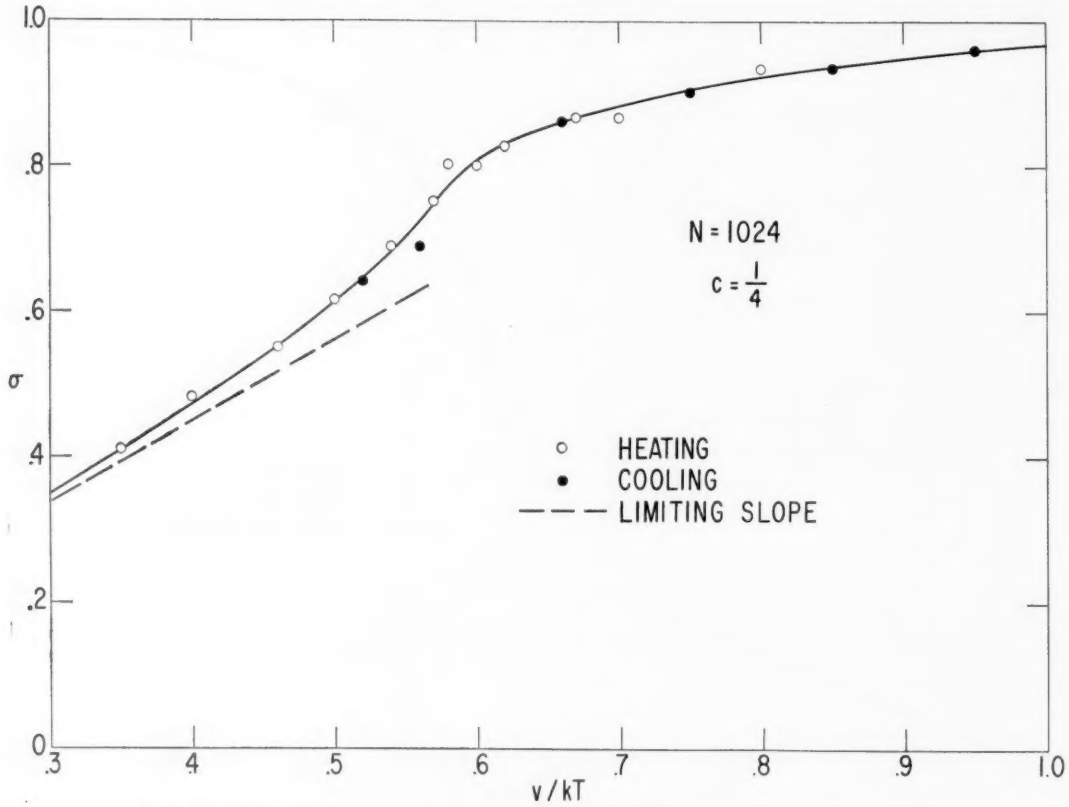

FIG. 4. Short-range order parameter σ vs reduced inverse temperature v/kT case (d) ($N=1024$, $c=\frac{1}{4}$).

for σ_2, it was not thought worth taking the necessary space to present all these values. A partial discussion is given in the next section.

In the special case $c=\frac{1}{2}$, the symmetry between A and B gives another relationship between the triplet probabilities. The observations can then be checked through the equation

$$\sigma/2=P_{\mathrm{ABA}}-P_{\mathrm{AAA}};$$

the mean deviation from this equality was 0.0036 in σ in case (a) and 0.005 in case (b).

DISCUSSION

A. Thermodynamic Properties

The most important thermodynamic questions relate to the behavior of the energy at the order-disorder transition. The author has been influenced in this respect by the exact results in two dimensions[2] and by Wakefield's conjecture[13] for the simple cubic lattice, which agree in pointing to the specific heat becoming infinite at the transition temperature. The energy (or short-range order) as a function of temperature for an *infinite* crystal then has a vertical tangent at one point, but no finite vertical portion (giving a latent heat as in a classical first-order transition) or discontinuity in slope (as in a classical second-order transition).[14] The smoothness of the curves in Figs. 1–4 reflects in part this prejudice about the behavior of infinite crystals; however, there is no evidence in the Monte Carlo results of any discontinuities whatever, and this in itself is sufficient reason for plotting the energy function in this way.

In any event, discontinuous behavior is a property of infinite crystals, and intimations of it should appear only in very much larger systems than those investigated here. This can be seen in the results of Onsager[15] who has obtained some properties of finite plane crystals, as well as those for the limit of $N\to\infty$; for the maximum heat capacity he finds

$$C_{\max}/Nk=0.495\ \ln n+0.188,$$

where n^2 is the number of unit cells. Assuming the same

[13] A. J. Wakefield, Proc. Cambridge Phil. Soc. **47**, 419, 799 (1951).

[14] G. H. Wannier, Revs. Modern Phys. **17**, 50 (1945).

[15] L. Onsager, Phys. Rev. **65**, 117 (1944).

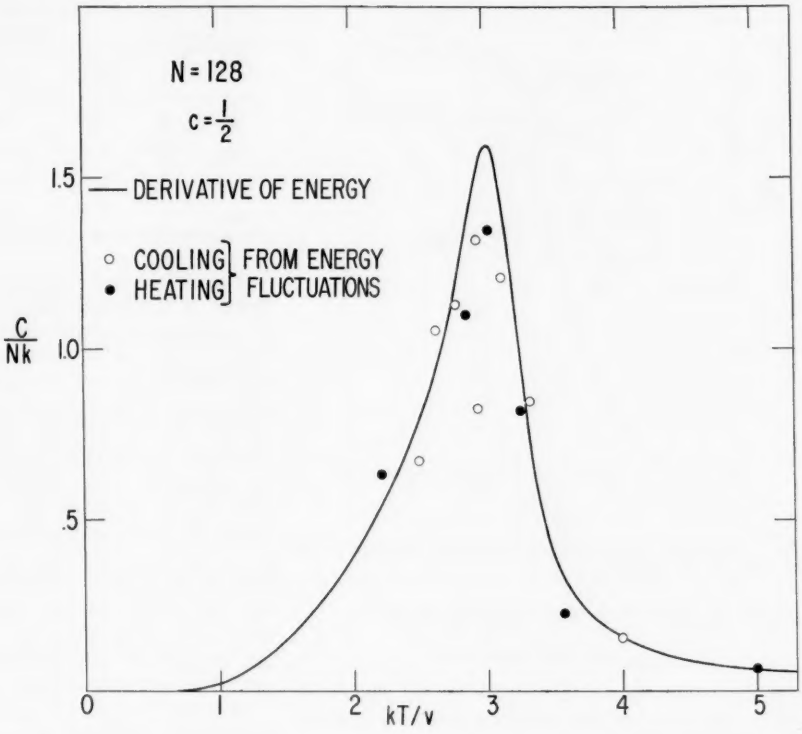

FIG. 5. Reduced heat capacity C/Nk vs reduced temperature kT/v, case (a) ($N=128, c=\frac{1}{2}$). Solid curve obtained by numerical differentiation of average energy. Points obtained from observed energy fluctuations at equilibrium.

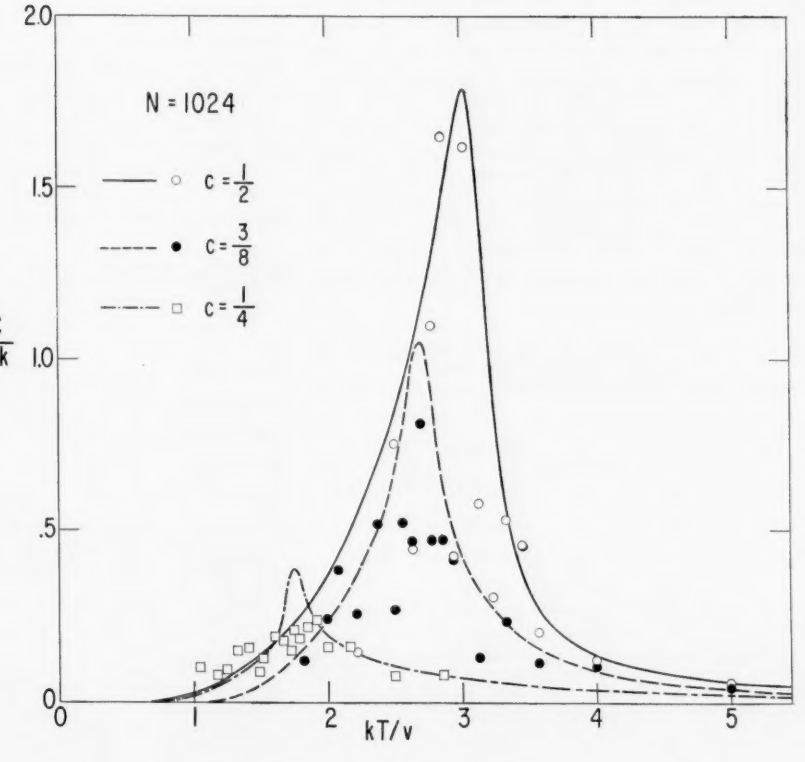

FIG. 6. Reduced heat capacity C/Nk vs reduced temperature kT/v, cases (b)–(d) ($N=1024$, $c=\frac{1}{2}, \frac{3}{8}, \frac{1}{4}$). Curves obtained by numerical differentiation of average energy. Points obtained from observed energy fluctuations at equilibrium.

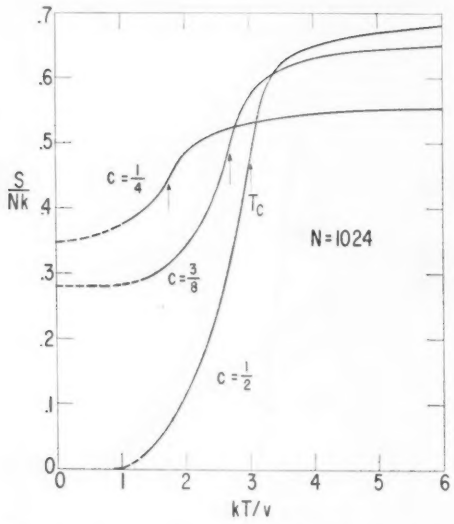

FIG. 7. Reduced entropy S/Nk vs reduced temperature kT/v, cases (b)–(d) ($N=1024$, $c=\frac{1}{4}, \frac{3}{8}, \frac{1}{2}$).

form for the three-dimensional case, one finds

$$C_{\max}/Nk=0.29\ln n+1.19$$

from the values $C_{\max}/Nk$ of 1.59 ($n=4$) and 1.79 ($n=8$). The constants are, of course, not very precise, and there is no check on the functional dependence, but their values are not unreasonable.[16] A graphical comparison of the Monte Carlo results at the equiatomic composition with those of Onsager[15] for the *infinite*, plane Ising crystal is made in Fig. 9. The ordinate for the two-dimensional case has been multiplied by the appropriate factor to make the total energy increment the same as for the bcc case. Allowing as well as one can for the effect of finite crystal size, it seems that in the three-dimensional case the bulk of the anomalous heat capacity lies below the critical temperature, rather than above it as in the two-dimensional case.

TABLE I. Comparison between theoretical entropy increment and value from numerical integration.

Case	N	c	$\Delta S/Nk$ Theoretical	$\Delta S/Nk$ Numerical
a	128	$\frac{1}{2}$	0.676	0.685
b	1024	$\frac{1}{2}$	0.693	0.693
c	1024	$\frac{3}{8}$	0.380	0.377
d	1024	$\frac{1}{4}$	0.214	0.195

[16] By analogy with two-dimensional crystals, one would expect a linear dependence on $\ln n$ only for rather larger n, and only a somewhat slower increase in the range $n=4$ to 8. [See H. A. Kramers and G. H. Wannier, Phys. Rev. **60**, 263 (1941); also S. Katsura, Progr. Theoret. Phys. (Kyoto) **11**, 476 (1954)].

TABLE II. Summary of thermodynamic properties at the critical temperature.

N	c	kT_c/v	σ_c	$C_{\max}/Nk$	S_c/Nk
128	$\frac{1}{2}$	3.03	0.454	1.59	0.451
1024	$\frac{1}{2}$	3.03	0.425	1.79	0.486
1024	$\frac{3}{8}$	2.70	0.580	1.04	0.497
1024	$\frac{1}{4}$	1.76	0.749	0.39	0.446

The individual points plotted in Figs. 5 and 6 are the values of the heat capacity obtained from Eq. (1). The agreement between these and the derivative of the energy in case (a) indicates that equilibrium had been substantially reached, and that the important range of microscopic states was adequately sampled for this system. This was clearly not the case for $N=1024$, the fluctuations being generally too small. The fact that the number of states sampled for crystals containing 1024 atoms was too few for a proper estimate of the energy fluctuations means that the average energy of these crystals is also not quite as well estimated as that of the crystal containing 128 atoms. In spite of this, the results for the larger crystals are useful to indicate the effect of crystal size, at $c=\frac{1}{2}$, and because the "transition" temperatures at other compositions are better defined the larger the system.

In cases (b)–(d), attention should be drawn to the rapid fall in the maximum heat capacity with increasing deviation from the ideal composition, and the simultaneous decrease in the transition temperature. The values of kT_c/v for all compositions are much lower than those calculated from the quasi-chemical approximation,[17] and the ratios $T_c(c)/T_c(\frac{1}{2})$ are also lower, i.e., the ordered region of the phase diagram is narrower than calculated from this approximation.

The "critical properties" of the various systems are summarized in Table II, and in Table III the Monte

TABLE III. Comparison of Monte Carlo values for infinite crystal ($c=\frac{1}{2}$) at the critical temperature with various approximations.

Source	kT_c/v	σ_c	$C_{\max}/Nk$	S_c/Nk
Monte Carlo	3.03	0.418	(∞)	0.495
Bragg-Williams[a,b]	4	0	1.50	0.693
Quasi-chemical[a,b]	3.48	0.144	1.78	0.652
Kurata *et al.*[c]	3.28	...	...	...
Domb[d]	3.08	0.311	(∞)	0.548

[a] F. C. Nix and W. Shockley, Revs. Modern Phys. **10**, 1 (1938).
[b] T. Muto and Y. Takagi, in *Solid State Physics* (Academic Press, Inc., New York, 1955), Vol. 1, p. 194.
[c] M. Kurata, R. Kikuchi, and T. Watari, J. Chem. Phys. **21**, 434 (1953).
[d] C. Domb, Compt. rend. reunion ann. avec comm. thermodynam. union intern. phys. (Paris). Changements de phases, 177 (1952).

[17] R. Fowler and E. A. Guggenheim, *Statistical Thermodynamics* (Cambridge University Press, New York, 1949); Eq. 1318, 5, p. 582.

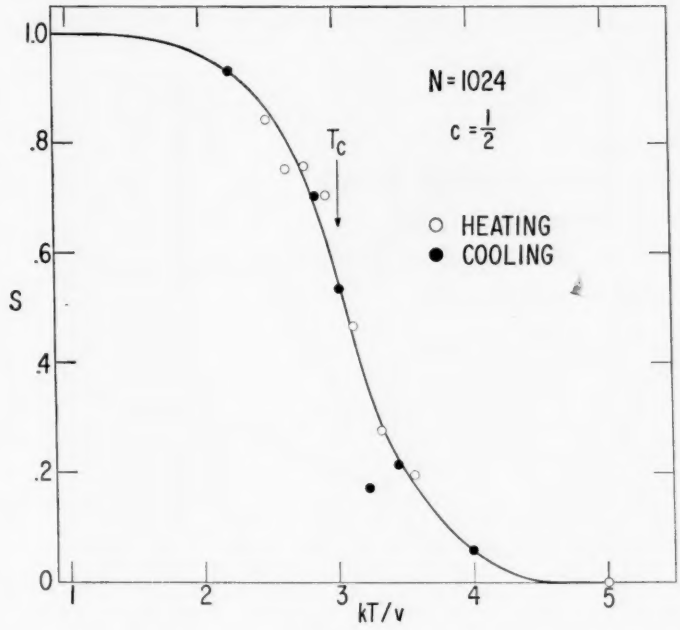

FIG. 8. Long-range order parameter S vs reduced temperature kT/v, case (b) ($N=1024$, $c=\frac{1}{2}$).

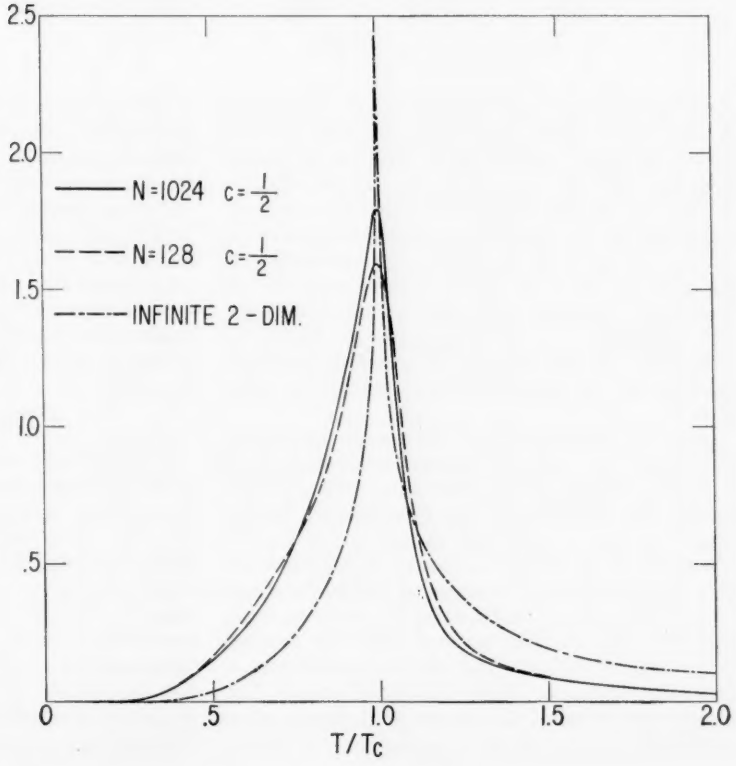

FIG. 9. Reduced heat capacity C/Nk vs reduced temperature T/T_c for bcc crystals at ideal composition [cases (a) and (b)], compared to that of infinite square two-dimensional crystal (Onsager[18]). Ordinate in last case is adjusted so that the total energy increment is the same as in the other two.

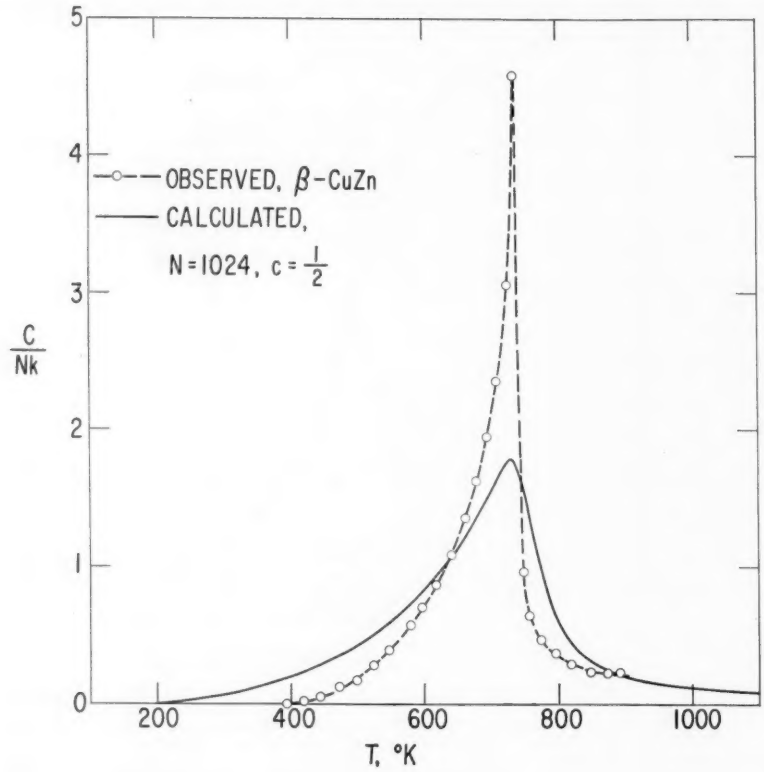

FIG. 10. Experimental reduced heat capacity C/Nk of β-CuZn (Moser[18]) vs absolute temperature T (points and broken curve) compared with Monte Carlo results, case (b) (solid curve). The two curves have the same areas up to their respective maxima.

Carlo values at the ideal composition, extrapolated to $N=\infty$, are compared to those calculated for this case by various approximate methods. The assumption has been made that kT_c/v, σ_c and S_c/Nk vary linearly with $N^{-1}\ln N$, as Onsager[15] found for the first of these in the two-dimensional case. The values in the last line of this table were obtained by Domb by estimating the asymptotic behavior of the exact series expansions of the partition function, and should be the most accurate. The agreement with the Monte Carlo results is fairly good, and would be improved if the critical properties varied faster with crystal size than has been assumed here.

Quantitative comparison of the present results with experiment may be of some value if one keeps in mind that the properties in the limit $N=\infty$ are quite uncertain. The experimental[18] heat capacity of β-CuZn (in excess of that of $\frac{1}{2}$Cu+$\frac{1}{2}$Zn) is shown in Fig. 10, together with the Monte Carlo heat capacity for case (b). The absolute temperature scale for the latter was determined so that the areas under the curves up to T_c were the same; this gives a v/k of 241°K, or $Nv=480$ cal/g atom for β-CuZn. The ordering temperature is then calculated to be 730°K (737°K, observed). The experimental value of S_c/Nk, viz., 0.51, is also close to the extrapolated Monte Carlo value of 0.495 (independent of v.) The concordance of these values, and the similarity shown in Fig. 10 (when allowance is made for the sharpening of the Monte Carlo curve with increasing crystal size) indicate either a nearly incredible applicability of the Ising model to β-CuZn, or, much more likely, a fortuitous cancellation of other influences on the behavior of the real system.

It does not seem useful to compare the Monte Carlo results with the observed[19] short-range order coefficients of β-AgZn because the latter are not known to better than 25%.

B. Distribution Functions

As mentioned earlier, the long-range order parameter S is somewhat overestimated at high temperatures. Nevertheless, it seems certain, as shown in Fig. 8, that the "long"-range order is nonvanishing even somewhat above the temperature at which the heat capacity is greatest. This phenomenon is undoubtedly a property of small systems; when, as here, the maximum possible distance between sites is less than ten times the distance between neighbors, there is still some correlation between the ways distant sites are occupied at $T/T_c\cong 1.2$. Presumably, with increasing size of crystal,

[18] H. Moser, Physik. Z. **37**, 737 (1936).

[19] E. Suoninen and B. E. Warren, Acta Met. **6**, 172 (1958).

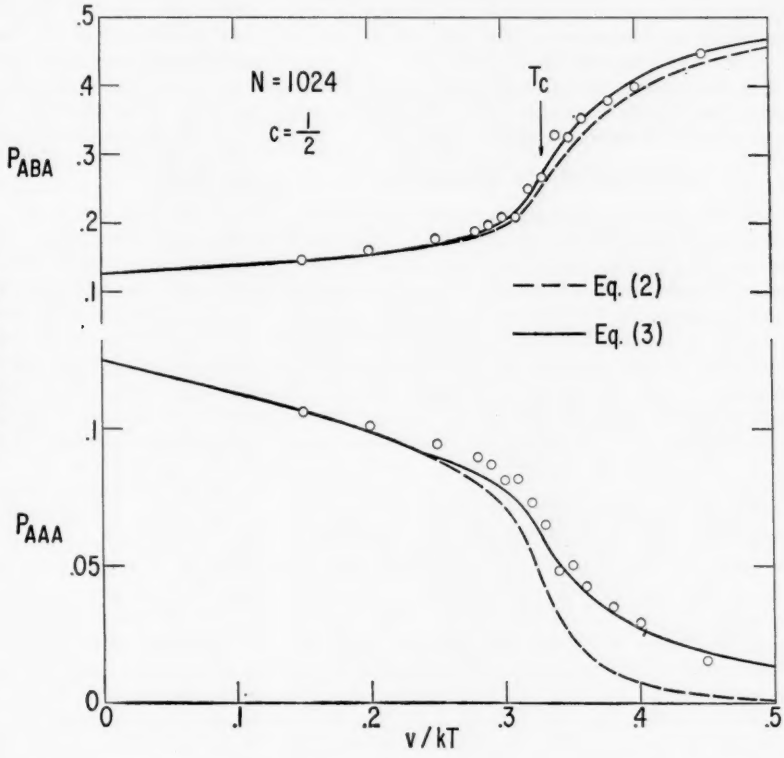

FIG. 11. Triplet probabilities P_{AAA} and P_{ABA} vs reduced inverse temperature v/kT, case (b), ($N=1024$, $c=\frac{1}{2}$). Points are Monte Carlo results, curves are calculated from "superposition approximation" from observed short-range order, Eqs. (2), or observed short-range and long-range order, Eqs. (3).

the range above T_c where S is nonvanishing would shrink, and, in the limit $N\to\infty$, the long-range order would vanish just at the temperature of infinite heat capacity. Local properties, such as the energy, are presumably much less sensitive to crystal size, and are therefore more nearly comparable with experimental measurements, within the limitations emphasized previously.

The *triplet* probabilities, P_{ABA} and P_{AAA}, being local properties, could profitably be compared with experimental values if they existed. Regrettably, no way of measuring them has yet been devised. An instructive comparison is that between the Monte Carlo values and those computed on the assumption of independent pairs ("superposition approximation.") The simplest assumption, namely, that all AB pairs are equivalent, leads to the equations

$$P_{ABA}=[c^4/(1-c)][\sigma+(1-c)/c)]^2 \qquad (2a)$$

$$P_{AAA}=c^3(1-\sigma)^2. \qquad (2b)$$

If the existence of long-range order is taken into account, there are two kinds of AB pairs, and the expressions for the triplet probabilities become much more involved. For $c=\frac{1}{2}$, Eqs. (2a) and (2b) are replaced by

$$P_{ABA}=[(1+\sigma)^2-4S^2\sigma]/8(1-S^2) \qquad (3a)$$

$$P_{AAA}=(1-\sigma)^2/8(1-S^2), \qquad (3b)$$

which reduce to the preceding expressions for $S=0$. These expressions are plotted in Fig. 11, for comparison with the Monte Carlo results for case (b). Clearly, recognizing the presence of long-range order does much to improve the superposition approximation. The Monte Carlo results are generally higher than the values computed from either Eqs. (2) or (3) for P_{AAA} and P_{ABA}. This means that an atom has two neighbors *unlike* itself more often than would happen if the distribution of *pairs* were random; in other words, there is a "clustering" of order. Similarly, every atom has two neighbors *like* itself more often than would be expected from a random distribution of pairs, and there is a "clustering" of disorder. It follows directly that triplets like ABB, in which there are one "right" pair and one "wrong" pair, occur less frequently than expected. This is just what would be anticipated in view of the cooperative nature of the transition. The use of an additional parameter (the long-range order), in the ordered state, supplies nearly all the information needed to describe the clustering. Actually the dis-

ordered state is nearly as complicated, especially near the transition temperature; this was pointed out by Wannier[14] and is evident from Fig. 11.

The short-range order parameter for nearest neighbors σ, has already been sufficiently discussed in connection with the thermodynamic properties.

CONCLUSIONS AND PROSPECTS

The Monte Carlo computations point to the existence of an order-disorder transformation in binary solid solutions of the kind treated, namely, those following the Ising model and based on a bcc lattice. The transition temperature is $T_c=3.03\ v/k$ at the ideal composition, and the heat capacity has an asymmetrical maximum whose height increases with crystal size. At this composition, the crystal still has about 42% of its nearest-neighbor order at the transition, and its entropy is about 0.5 Nk. The small three-dimensional crystals treated seem to differ from infinite square planar crystals in having a larger fraction of their total energy increase below the transition temperature.

The heat capacity of β-CuZn resembles qualitatively the computed heat capacity of these small crystals, and the resemblance may be expected to grow with increasing crystal size. There is good agreement between the values of v computed from the transition temperature on the one hand, and from the energy increment up to T_c, on the other. The *simplest* Ising model therefore seems to be adequate as a description of β-CuZn, although caution is indicated in this respect by the knowledge that further influences ought to be considered (cf. the next paragraph but one).

The utility of the Monte Carlo method is well exemplified by the present work, but so are its limitations. With moderate effort it is possible to compute the properties of small systems fairly precisely. Many of the present results could have been predicted qualitatively, but it is nevertheless instructive to see them emerge from the simple model. The systems treated here are large enough to show cooperative behavior, but only just large enough. Faster computers will allow larger systems to be handled, of course, but it is at least questionable whether this would lead to much better understanding. For example, one of the motivations for the present work was the hope of calculating the form of the iron-aluminum equilibrium diagram (in which system there must be also next-nearest neighbor interactions on the Ising model), with special attention to the order of the transitions. In the light of the experience described the prospects for this program are rather dim: the diffuseness of the transition at compositions other than the ideal one, and the obvious effect of size on the long-range order, would make it hard even to locate transition temperatures as a function of composition. To go further and predict whether infinite crystals would have first or higher order transitions seems hopeless at present. Only in very much larger crystals would one expect a well-defined latent heat with an attendant discontinuity in long-range order and coexistence of ordered and disordered phases, since these effects will only appear when the interfacial free energy is a small enough perturbation.

Neither does it seem profitable to refine the Monte Carlo computations merely by the introduction of interactions with more distant neighbors, in an attempt to get quantitative agreement with experiment in particular systems,[6] unless at the same time the effects of crystal size are somehow included. It should also be kept in mind that the variations of interatomic distances in real solid solutions with temperature, composition and state of order lead to easily measurable changes in the vibrational spectrum and presumably to corresponding effects on the cooperative behavior.[1] It is therefore somewhat academic to go very far in improving the precision of Monte Carlo computations on the Ising model with constant interactions.

The usefulness of the Monte Carlo method seems therefore to be not so much in the precise numerical results that it provides, as in the physical insight it affords into the behavior of systems with strong interactions. These insights are not only immediately satisfying, but may also suggest directions for improvements in theoretical treatments.

ACKNOWLEDGMENTS

Miss Marilyn Rogers, under the supervision of Gordon K. Carter, supplied the input and output routines needed to complete my symbolic program. She also checked the program for errors and operated the computer. I am grateful to M. B. Webb for giving me many chances to test my ideas in an informal way. The late Donald Flanders taught me the elements of computer programming. My wife read the manuscript critically, and discussed numerous questions with me.

THE JOURNAL OF CHEMICAL PHYSICS VOLUME 34, NUMBER 3 MARCH, 1961

Theory of the Two- and One-Dimensional Rigid Sphere Fluids

E. HELFAND AND H. L. FRISCH

Bell Telephone Laboratories, Incorporated, Murray Hill, New Jersey

AND

J. L. LEBOWITZ*

Graduate School of Mathematical Sciences, Yeshiva University, New York, New York

(Received August 26, 1960)

The approximate theory of the three-dimensional hard sphere fluid developed by Reiss, Frisch, and Lebowitz has given astonishingly good predictions with little labor. In an attempt to investigate the reason for this result we adduce, in this paper, further evidence for the internal consistency of the approximations of this theory. Thus it is noted that the same equation of state of hard sphere fluid is obtained when one used the "integral condition" as when the "infinity condition" is used. We have then applied the theory to study the thermodynamic properties, in particular the equation of state, of the rigid sphere fluid in two and one dimensions. The approximate equation of state of the two-dimensional rigid sphere fluid is in good agreement over the range of fluid densities with the results of the machine Monte Carlo calculations by Jacobson and Wood and dynamical machine calculations of Wainwright and Alder. The exact Tonks' equation of state of the one-dimensional rigid sphere fluid is derived in a particularly simple manner.

I. INTRODUCTION

THE thermodynamic properties of systems of particles interacting only with rigid core repulsive forces are determined completely by the value of certain contact correlation functions. Reiss, Frisch, and Lebowitz[1] (hereinafter referred to as I) have recently made significant progress in the theory of such systems by focusing attention on these required unknowns, rather than attempting to determine all the information contained in the full radial distribution function. The theoretical basis of I has been viewed in a somewhat different manner and extended to provide the basis for the treatment of real fluids in a paper by Helfand, Reiss, Frisch, and Lebowitz.[2] Unfortunately these investigations do not seem to supply the complete reason why these simple theories make as accurate predictions as they do. A very partial answer to this question, which we obtain in the first part of this paper, is that there exists further evidence of the inner consistency of the theory as developed for three-dimensional fluids. In the attempt to investigate further this question we consider in the main part of this paper the extension of the theory to two and one dimensions to see how well and possibly why it works in these cases.

The basic technique is to define a function $G(\lambda, \rho)$ such that $\rho G(\lambda, \rho)$ is the density of rigid sphere molecules of diameter a in contact with a single "solute" sphere (this single particle may, alternatively, be viewed as a hole) of diameter b, where $\lambda a=\frac{1}{2}(a+b)$ and ρ is the particle number density (N/V in three dimensions, N/A in two dimensions, and N/L in one dimension). The significance of λ is that if the normal molecule-molecule potential function is $u(r)$, the molecule-solute interaction potential is $u(r/\lambda)$. Thus, even for more general potentials, the solute is essentially a size-scaled version of the normal molecules. We have termed such a scaled particle a λ-cule. The value of λ may range from zero to infinity. When $\lambda=0$ the λ-cule can completely penetrate all molecules so that it is a free particle. The value $\lambda=\frac{1}{2}$ plays a role of central importance since it is the first point at which the λ-cule can interact with more than one molecule at a time. When $\lambda=1$ we see that $b=a$, so that the λ-cule is identical with the other molecules. Thus $G(1, \rho)$ is the contact radial distribution function for a pure system of diameter a particles. Finally, when $\lambda=\infty$ the λ-cule may be regarded as a plane rigid wall.

The method of determining the G function for a three-dimensional system as developed in I is reviewed in the next section, and a new observation relating to the consistency of the assumed form of G is made. We then extend this technique to allow for the treatment of a two-dimensional hard sphere system, where some additional complications enter. An equation of state in close agreement with machine calculations is derived. Next we show that the method may be simply applied to a one-dimensional system to yield the exact equation of state. Finally, in appendices, we consider the application of the theory to the simplest cases of the perfect gas and the hard sphere lattice gas.

II. THREE DIMENSIONS

In three dimensions the equation of state of a hard sphere fluid is

$$p/\rho kT=1+\tfrac{2}{3}\pi\rho a^3 G(1, \rho), \tag{2.1}$$

* Supported by the Air Force Office of Scientific Research.

[1] H. Reiss, H. L. Frisch, and J. L. Lebowitz, J. Chem. Phys. **31**, 369 (1959).

[2] E. Helfand, H. Reiss, H. L. Frisch, and J. L. Lebowitz, J. Chem. Phys. **33**, 1379 (1960).

while the chemical potential is

$$\mu/kT=\ln\rho\Lambda^3+4\pi\rho a^3\int_0^1\lambda^2G(\lambda,\rho)d\lambda, \tag{2.2}$$

where $\Lambda^3=h^3/(2\pi mkT)^{\frac{3}{2}}$. As a generalization of (2.2) one has for the work of introducing a λ-cule at a fixed point in a system of molecules

$$W(\lambda)=4\pi\rho a^3kT\int_0^\lambda\lambda'^2G(\lambda',\rho)d\lambda', \tag{2.3}$$

(W is also ρ-dependent but here and at various other points later we will leave the functional dependence on ρ implicit when it is obvious), from which one obtains by differentiating

$$G(\lambda,\rho)=(4\pi\rho a^3\lambda^2kT)^{-1}[\partial W(\lambda)/\partial\lambda]. \tag{2.4}$$

A relation exists between the work of introducing a λ-cule (or equivalently the work of creating a hole of radius λa) and the probability of finding a hole of at least size λa as a result of a spontaneous fluctuation, $p_0(\lambda)$; it is

$$p_0(\lambda)=\exp[-W(\lambda)/kT]. \tag{2.5}$$

This allows the discussion to be carried through in terms of certain physically defined probabilities. The probability of a vacant hole of radius λa is equal to

$$p_0=1-p_1-p_2-p_3-\cdots, \tag{2.6}$$

where p_k is the probability of finding exactly k molecules in this region. Equation (2.6) may be rearranged as

$$p_0=1-(p_1+2p_2+3p_3+\cdots)+(p_2+3p_3+6p_4)-(p_3+4p_4+\cdots)+\cdots, \tag{2.7}$$

where the first sum in parentheses represents the average number of individual particles in the region of radius λa, the second sum represents the average number of pairs, the third the average number of triplets, etc. (See Appendix A for the case of the ideal gas.) The series (2.7) may be written in terms of m-particle correlation functions,[3] $g^{(m)}$, as

$$p_0(\lambda)=1+\sum_{m=1}^{\infty}[(-1)^m\rho^m/m!]\int_{[\text{region of radius }\lambda a]}g^{(m)}(\mathbf{r}_1,\cdots,\mathbf{r}_m)d\mathbf{r}_1\cdots d\mathbf{r}_m. \tag{2.8}$$

The convenience of Eq. (2.8) arises from the fact that the series on the right-hand side terminates at a value m equal to the number of molecules which may be packed into the region of radius λa. For $\lambda\leq\frac{1}{2}$ the only term is $m=1$; i.e., the center of only one molecule may be in a cavity of radius less than $\frac{1}{2}a$, and the probability of a molecule being there is the density times the cavity volume.[4] Therefore we have

$$p_0(\lambda)=1-\tfrac{4}{3}\pi\rho a^3\lambda^3, \qquad \lambda\leq\tfrac{1}{2}, \tag{2.9}$$

which leads through Eqs. (2.4)–(2.5) to

$$G(\lambda)=1/(1-\tfrac{4}{3}\pi\rho a^3\lambda^3), \qquad \lambda\leq\tfrac{1}{2}. \tag{2.10}$$

By examination of the series (2.8) it is also shown in I that both $G(\lambda)$ and $\partial G(\lambda)/\partial\lambda$ are continuous for all λ and that the discontinuity of the second derivative of G at $\lambda=\frac{1}{2}$ is given by

$$(\partial^2G/\partial\lambda^2)_{\lambda=\frac{1}{2}+}-(\partial^2G/\partial\lambda^2)_{\lambda=\frac{1}{2}-}=-\frac{8\pi\rho a^3}{1-(\pi\rho a^3/6)}G(1). \tag{2.11}$$

A further condition which $G(\lambda)$ must satisfy arises from the fact that from the chemical potential of Eq. (2.2) one may calculate a pressure which must be equal to that given by Eq. (2.1). Explicitly, the thermodynamic equality

$$p=\int_0^\rho\rho'(\partial\mu/\partial\rho')_T d\rho', \tag{2.12}$$

leads to

$$\tfrac{2}{3}\pi\rho^2G(1,\rho)=\rho^2\int_0^1 4\pi\lambda^2G(\lambda,\rho)d\lambda-\int_0^\rho\rho'd\rho'\int_0^1 4\pi\lambda^2G(\lambda,\rho')d\lambda. \tag{2.13}$$

Because of the definite limits on the λ integration this is not a deterministic equation but rather a condition on G. It relates the value of G at $\lambda=1$ to an integral over the range $0<\lambda<1$. The fact that G is known exactly for $\lambda\leq\frac{1}{2}$ makes this an even narrower range.

A condition on $G(\lambda)$ exists for large values of λ. Under these circumstances the surface of the cavity may be considered as a hard flat wall. The density near such a wall $\rho G(\infty)$ is proportional to the pressure,

$$p/kT=\rho G(\infty), \tag{2.14}$$

so that $G(\infty)$ may be related to $G(1)$ by Eq. (2.1):

$$G(\infty)=1+\tfrac{2}{3}\pi\rho a^3G(1). \tag{2.15}$$

In this limit, as the size of the system goes to infinity, the density of the system remains constant and is unaffected by the presence of the cavity. Equation (2.14) may then also be derived by treating the cavity as a system of volume $v=\frac{4}{3}\pi\lambda^3a^3$ in contact with a particle bath (represented by the rest of the system). This system is then represented by a grand canonical ensemble

$$p_n=z^nQ_n/\Xi,$$

[3] T. L. Hill, *Statistical Mechanics* (McGraw-Hill Book Company, Inc., New York, 1956), Section 29.

[4] For $\lambda=1$, $m=12$, the number of molecules in contact with a given one at close packing, while for $\lambda\gg1$, $m(\lambda)\sim(\frac{4}{3}\pi\sqrt{2})\lambda^3+0(\lambda^2)$.

where z is the activity, Ξ the grand partition function, and Q_n the canonical partition function of n particles in the cavity. This yields

$$p_0=\Xi^{-1}=\exp(-pv/kT),$$

which combined with (2.4) and (2.5) leads to (2.15).

In summary one has the following exact information about the function $G(\lambda)$: (a) the value of $G(\lambda)$ for $\lambda\leq\frac{1}{2}$, Eq. (2.10); (b)–(c) the continuity of $G(\lambda)$ and its first derivative; (d) the magnitude of the discontinuity of $G''(\lambda)$ at $\lambda=\frac{1}{2}$; (e) the integral condition (2.13); (f) the infinity condition (2.15).

A quasi-thermodynamic argument is used in I to determine the form of $G(\lambda)$ for large values of the argument λ. The work of expanding a cavity in a fluid is given by a pressure-volume and a surface tension-surface area term:

$$dW=pdV+\sigma dS. \tag{2.16}$$

As a first approximation to the Gibbs-Tolman-Koenig[5] relation for the surface tension of a surface of radius of curvature λa, one has

$$\sigma=\sigma_0[1-(2\delta/\lambda)], \tag{2.17}$$

where δa is the distance between the surface for which the superficial density vanishes and the surface of tension. Equation (2.16) may thus be written

$$dW=[4\pi pa^3\lambda^2+8\pi\sigma_0a^2\lambda+16\pi\sigma_0\delta a^2]d\lambda, \tag{2.18}$$

so that by Eq. (2.4) the suggested form for $G(\lambda)$ is

$$G(\lambda,\rho)=A(\rho)+[B(\rho)/\lambda]+[C(\rho)/\lambda^2], \tag{2.19}$$

where A, B, C may be written in terms of p, σ, and δ.

By examining the properties of mixtures of molecules and λ-cules Reiss, Frisch, and Lebowitz show how further insight into G may be gained. Their considerations suggest the form (2.19) for G is a good, analytic approximation over the entire range $\frac{1}{2}<\lambda<\infty$, and is in fact exact not only at the upper limit as indicated in the previous paragraph but also at the lower limits. Details of this argument as applied to the two-dimensional fluid are presented in the following section.

The three unknown functions of density which appear in Eq. (2.19) may be determined from a combination of any three of the five exact conditions (b) to (f) in combination with (a). In I the continuity of G and G' conditions, and the infinity condition are used to derive the three-dimensional equation of state

$$p/\rho kT=(1+y_3+y_3^2)/(1-y_3)^3, \tag{2.20}$$

where $y_3=\pi\rho a^3/6$ (y_3 ranges from 0 to 0.740 for close packing). This is in remarkably good agreement with the machine calculations of Wood and Jacobson[6] and Wainwright and Alder.[7] Equation (2.20) has the virial development

$$p/\rho kT=1+4y_3+10y_3^2+19y_3^3+31y_3^4+\cdots, \tag{2.21}$$

which compares well with the exact virial series[8]

$$p/\rho kT=1+4y_3+10y_3^2+18.36y_3^3+(29.4\pm1.3)y_3^4+\cdots. \tag{2.22}$$

We have tried also to calculate G using the continuity of G and G' and the integral condition (2.13). The same equation of state is found, so that with the three coefficient form (2.19) the four conditions (b), (c), (e), and (f) are compatible. This lends further weight to (2.19) as an analytic approximation for G since with this form the theory possesses added internal consistency.

On the other hand when one of the four conditions used above is replaced by the discontinuity condition (d) the resulting virial series is in poor agreement with the exact virial expansion.

III. TWO DIMENSIONS

The pressure and chemical potential of a two-dimensional fluid of rigid spheres are given, respectively, by

$$p/\rho kT=1+\tfrac{1}{2}\pi\rho a^2G(1,\rho), \tag{3.1}$$

$$\mu/kT=\ln\rho\Lambda^2+2\pi\rho a^2\int_0^1\lambda G(\lambda,\rho)d\lambda. \tag{3.2}$$

The contact correlation function of molecules touching a λ-cule is related to the work of expanding the λ-cule by

$$G(\lambda,\rho)=(2\pi\rho a^2\lambda kT)^{-1}[\partial W(\lambda)/\partial\lambda]. \tag{3.3}$$

The work is given by the series (2.8) in conjunction with (2.5) so that we can show that for $\lambda\leq\frac{1}{2}$, where the series terminates after $m=1$, $G(\lambda,\rho)$ is given exactly by

$$G(\lambda,\rho)=1/(1-\pi\rho a^2\lambda^2), \qquad \lambda<\tfrac{1}{2}. \tag{3.4}$$

Furthermore, $G(\lambda)$ and $[\partial G/\partial\lambda]$ may again be shown through examination of (2.8) to be continuous. The second derivative, however, diverges this time as $(\lambda-\frac{1}{2})^{-1}$ as $\lambda\to\frac{1}{2}$. The second derivative condition was not used in three dimensions and likewise in two dimensions we will not find that there is a necessity to employ it. (The final solution will not have the correct second derivative at $\lambda=\frac{1}{2}$ but this does not seem to greatly affect the equation of state.)

[5] J. O. Hirschfelder, C. F. Curtiss, and R. B. Bird, *Molecular Theory of Gases and Liquids* (John Wiley & Sons, Inc., New York, 1954), p. 351.

[6] W. W. Wood and J. D. Jacobson, J. Chem. Phys. **27**, 1207 (1957).

[7] T. E. Wainwright and B. J. Alder, U. S. Atomic Energy Commission Report Contract No. W-7405-eng-48, Lawrence Radiation Laboratory, Livermore, University of California.

[8] Reference 5, p. 157.

The condition on G arising from the thermodynamic relation (2.12) between p and μ is [cf. (2.13)]

$$\tfrac{1}{2}\pi\rho^2 G(1,\rho)=\rho^2\int_0^1 2\pi\lambda G(\lambda,\rho)\,d\lambda - \int_0^\rho \rho'\,d\rho'\int_0^1 2\pi\lambda G(\lambda,\rho')\,d\lambda. \quad (3.5)$$

This equation may be put into a more useful form by inserting (3.4) and differentiating with respect to ρ:

$$\rho^2\left[\partial G(1,\rho)/\partial\rho\right]+2\rho G(1,\rho)=\tfrac{1}{2}\{\rho/[1-(\pi\rho/4)]\} +4\rho\int_{\frac{1}{2}}^1 \lambda G(\lambda,\rho)\,d\lambda+4\rho^2\int_{\frac{1}{2}}^1 \lambda\left[\partial G(\lambda,\rho)/\partial\rho\right]d\lambda. \quad (3.6)$$

Finally, we again find an infinity condition by equating Eq. (3.1) to Eq. (2.14) which holds also in two dimensions. This yields

$$G(\infty)=1+\tfrac{1}{2}\pi\rho a^2 G(1). \quad (3.7)$$

These conditions may be used to determine the equation of state if we have a form of G in λ. As in three dimensions we may obtain some information by a consideration of mixtures. By the technique presented in I, G may be related to a function Q by the equation

$$Q(\lambda,\rho)=-\rho a^2\int_0^\lambda 2\pi\lambda' G(\lambda',\rho)\,d\lambda' - \rho^2 a^2\int_0^\lambda 2\pi\lambda'\left[\partial G(\lambda',\rho)/\partial\rho\right]d\lambda'+\pi\rho a^2\lambda^2 G(\lambda,\rho). \quad (3.8)$$

Q is given by

$$Q(\lambda,\rho)=-\tfrac{1}{2}\pi\rho^2 a^2\left[\partial G(1,\rho,\rho_\lambda)/\partial\rho_\lambda\right]_{\rho_\lambda}=0, \quad (3.9)$$

where $G(1,\rho,\rho_\lambda)$ in this definition is the contact radial distribution function between two normal molecules in a system with molecule density ρ and λ-cule density ρ_λ. We see that Eq. (3.6) is the special case of (3.8–9) with $\lambda=1$. From the properties of p_0 it follows, as in I, that

$$Q=\partial Q/\partial\lambda=0, \qquad \lambda\leq\tfrac{1}{2}. \quad (3.10)$$

Furthermore for large λ we find from Eq. (3.8) that the dominant term of Q is

$$Q_{\text{dom}}=-\pi\rho^2 a^2\lambda^2\left[\partial G(\infty,\rho)/\partial\rho\right],$$

which varies as λ^2.

The functions G and Q have discontinuities in certain of their derivatives with respect to λ but the indications of I are that these functions may be approximated closely by analytic functions. A form which interpolates the $\lambda=\frac{1}{2}$ and $\lambda\to\infty$ limiting behavior of Q is

$$Q(\lambda,\rho)=\omega_2(\rho)\,(\lambda-\tfrac{1}{2})^2. \quad (3.11)$$

Using Eq. (3.8) such a Q may be shown to be compatible with a G of the form

$$G=\phi(\rho\lambda^2)+A(\rho)+[B(\rho)/\lambda]. \quad (3.12)$$

As in I the function $\phi(\rho\lambda^2)$ must vanish, since it vanishes in the limit $\lambda\to\infty$, $\rho\lambda^2\to$const. In two dimensions, therefore, the indicated form for G is

$$G=A(\rho)+[B(\rho)/\lambda]. \quad (3.13)$$

This form may also be arrived at by the quasi-thermodynamic argument. The three-dimensional considerations may be employed directly if we regard the two-dimensional fluid as a system of infinite cylinders with parallel axes and take the properties for unit length in the axial direction. Equation (2.16) for the work of expanding a λ-cule becomes

$$dW=2\pi pa^2\lambda d\lambda+2\pi\sigma a d\lambda. \quad (3.14)$$

With a surface tension σ independent of λ this, by Eq. (3.3), goes over into the form (3.13) for λ. For large λ the surface tension should have the form $\sigma_0[1-(\delta/\lambda)]$ which would add a C/λ^2 term to (3.13) but since such a term is not applicable to the small λ limits, as indicated by the Q function argument, and since C/λ^2 is small for large λ, it is not appropriate to include a curvature term.

The parametric functions of ρ, $A(\rho)$ and $B(\rho)$, may be determined by using the continuity of G to match (3.13) to (3.4) at $\lambda=\frac{1}{2}$, and by employing the infinity condition, (3.7). Instead of the infinity condition the integral equation, (3.5), may be used as a second condition. As in three dimensions the result is the same, which again adds weight to this form for G.[9]

The equation of state found in this way is

$$p/\rho kT=1/(1-y_2)^2, \quad (3.15)$$

where $y_2=\pi\rho a^2/4$ (y_2 ranges from 0 to 0.907 for close packing). This has as a virial development

$$p/\rho kT=1+2y_2+3y_2^2+4y_2^3+5y_2^4+\cdots, \quad (3.16)$$

to be compared with the exact virial series

$$p/\rho kT=1+2y_2+3.128y_2^2+4.262y_2^3 +(4.95\pm0.25)\,y_2^4+\cdots. \quad (3.17)$$

In Fig. 1 the equation of state over the entire range of accessible fluid densities is compared with the results of machine Monte Carlo calculations by Jacobson and

[9] We have not found any other functional forms which exhibit this property. For instance if one uses $G=A+B/\lambda+C/\lambda^2$ with the continuity of G and G' at $\lambda=\frac{1}{2}$ and either the infinity condition or the integral condition, one obtains two different answers, both poor.

Wood[10,11] and dynamical machine calculations by Wainwright and Alder.[11,12] The agreement is good. For comparison the results of the simple Lennard-Jones-Devonshire cell theory are included on the same graph. Various extended cell calculations, such as Cohen and Rethmeier's[13] double cell cluster theory with exact cell shape, do not substantially better the agreement over the entire range of densities. The cell theories, however, seem to be in agreement with the low pressure ordered phase which is observed[10,12] at densities greater than $\rho a^2 \approx 0.8$. Close packing corresponds to $\rho a^2 = 2/\sqrt{3} = 1.15$.

The complete $G(\lambda, \rho)$ determined in the above calculation is

$$G(\lambda,\rho)=[(1-y_2)^2]^{-1}+\tfrac{1}{2}\{(1-y_2)^{-1}-[(1-y_2)^2]^{-1}\}\lambda^{-1}. \tag{3.18}$$

By Eqs. (3.3), (3.13), and (3.14) this corresponds to a surface tension

$$\sigma/\rho akT=\tfrac{1}{2}[(1-y_2)^{-1}-(1-y_2)^{-2}]. \tag{3.19}$$

IV. ONE DIMENSION

An extremely simple treatment of the properties of a one-dimensional system of rigid spheres may be achieved by application of the Reiss, Frisch, and Lebowitz techniques. The thermodynamic properties of the system are derivable from the equation of state,

$$p/\rho kT=1+\rho aG(1,\rho), \tag{4.1}$$

and the chemical potential

$$\mu/kT=\ln\rho\Lambda+2\rho a\int_0^1 G(\lambda,\rho)\,d\lambda. \tag{4.2}$$

The pressure is also related to the density at the wall by [cf. Eq. (2.14)]

$$p/\rho kT=G(\infty,\rho). \tag{4.3}$$

We can derive the equation of state in essentially one step by realizing that since no two particles on opposite sides of a λ-cule with $\lambda>\frac{1}{2}$ can ever interact, molecules cannot tell what size λ-cule they are next to for $\lambda>\frac{1}{2}$. Thus $G(\lambda,\rho)$ must be independent of λ for $\lambda>\frac{1}{2}$, and as a special case the molecule-molecule contact density must equal the wall density, i.e.,

$$G(1,\rho)=G(\infty,\rho). \tag{4.4}$$

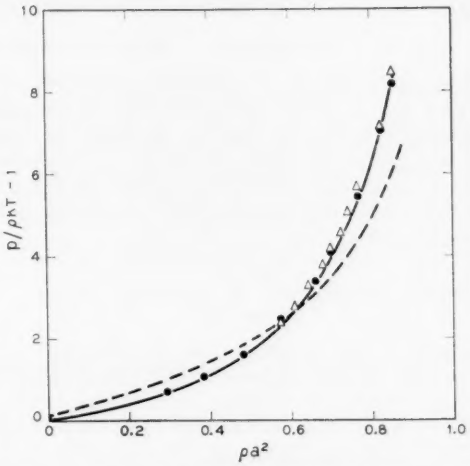

FIG. 1. The equation of state of a two-dimensional hard sphere fluid: ——— this work; ● Monte Carlo calculations of Wood; Δ dynamical calculations of Alder and Wainwright; ------ Lennard-Jones-Devonshire cell theory.

This equation in conjunction with Eqs. (4.1) and (4.3) yields the well-known Tonks' equation of state[14] for a one-dimensional hard sphere system

$$p/\rho kT=1/(1-\rho a), \tag{4.5}$$

which is exact.

Equation (4.5) may be derived in another simple manner. For $\lambda\leq\frac{1}{2}$, at most one molecule can be in a cavity. The probability that the cavity is vacant is, therefore, one minus the density times the cavity volume, or

$$p_0(\lambda)=1-\rho(2a\lambda), \qquad \lambda\leq\tfrac{1}{2}. \tag{4.6}$$

The work of forming such a cavity is again [cf. (2.5)]

$$W(\lambda)=-kT\ln p_0, \tag{4.7}$$

and G is related to this work by

$$G(\lambda,\rho)=(2\rho akT)^{-1}[\partial W(\lambda)/\partial\lambda], \tag{4.8}$$

so that

$$G(\lambda,\rho)=1/(1-2\rho a\lambda), \qquad \lambda\leq\tfrac{1}{2}. \tag{4.9}$$

For $\lambda>\frac{1}{2}$ we saw in the last paragraph that G is constant so using the continuity of G, which is easily established as in I or previous sections, we have

$$G(\lambda\geq\tfrac{1}{2},\rho)=G(1,\rho)=G(\infty,\rho)=1/(1-\rho a). \tag{4.10}$$

By Eq. (4.1) or (4.3) this leads immediately to the Tonks' equation, (4.5).

The fact that G is constant for $\lambda>\frac{1}{2}$ follows also from Eq. (4.8). For $\lambda>\frac{1}{2}$ the work of expanding a

[10] J. D. Jacobson and W. W. Wood, Los Alamos Scientific Laboratory of the University of California, Report GMX-10-37.

[11] We thank Dr. Jacobson, Dr. Wood, Dr. Wainwright, and Dr. Alder for making available and allowing us to include the results of their calculations which are not fully completed. These authors have cautioned us that there may be some changes in individual points upon further refinement. Nevertheless we have felt that it is worthwhile to include these data in order to provide an indication of the degree of reliability of the present calculation.

[12] T. E. Wainwright and B. J. Alder, private communication.

[13] E. G. D. Cohen and B. C. Rethmeier, Physica **24**, 959 (1958).

[14] L. Tonks, Phys. Rev. **50**, 955 (1936).

cavity (or λ-cule) is all pressure-volume work so that

$$dW = p(2ad\lambda), \qquad \lambda > \tfrac{1}{2} \tag{4.11}$$

which implies $G(\lambda > \frac{1}{2}, \rho) = \text{constant} = p/\rho kT$.

In I it was shown how a knowledge of the cavity probability p_0 could be used to determine the radial distribution function over part of the range. To develop this theory for one dimension we must write the series (2.8) for p_0 in the range $\frac{1}{2} < \lambda < 1$, wherein the series terminates at $m = 2$:

$$p_0(\lambda) = 1 - 2\rho a\lambda + \tfrac{1}{2}\rho^2 a^2 \int_{-\lambda a}^{\lambda a} \int_{-\lambda a}^{\lambda a} g(|r_1 - r_2|)\, dr_1 dr_2,$$

$$= 1 - 2\rho a\lambda + \rho^2 a^2 \int_0^{2\lambda} (2\lambda - x) g(ax)\, dx, \quad \lambda \leq 1. \tag{4.12}$$

Differentiating twice with respect to λ, one finds that

$$\partial^2 p_0 / \partial \lambda^2 = 4\rho^2 a^2 g(2\lambda a), \qquad \lambda < 1. \tag{4.13}$$

The function p_0 is related to G through Eqs. (4.7)–(4.8) and is given by

$$p_0(\lambda) = \exp\left[-2\rho a \int_0^{\lambda} G(\lambda', \rho)\, d\lambda' \right]$$

$$= (1 - \rho a)\, \exp[-\rho a(2\lambda - 1)/(1 - \rho a)], \qquad \lambda > \tfrac{1}{2}. \tag{4.14}$$

The combination of Eqs. (4.13) and (4.14) allow us to write for the radial distribution function in the range $a < r < 2a$

$$g(r) = (1 - \rho a)^{-1} \exp[-\rho(r - a)/(1 - \rho a)], \qquad a < r < 2a, \tag{4.15}$$

in agreement with other theories of the pair correlation function.[15] The range of r may be extended by considering further terms in the p_0 series, (2.8). The higher order correlation functions which enter may be written in terms of products of pair correlations exactly in one dimension.[15]

Interestingly enough Eq. (4.15) can be extended, partly at least, to the case where the molecules have in addition to their hard cores also a soft potential ϕ_s. When ϕ_s has a finite range γa, $\gamma > 1$, then for $\lambda > \frac{1}{2}\gamma$ the molecules will again be unable to "feel" across the cavity and we will have

$$dW = p2ad\lambda, \qquad \lambda > \tfrac{1}{2}\gamma$$

$$G(\lambda) = p/\rho kT, \qquad \lambda > \tfrac{1}{2}\gamma. \tag{4.16}$$

If further $\gamma < 2$ then the above arguments yield

$$g(r) = (p/\rho kT)^2 p_0(\gamma a/2)\, \exp[-(p/kT)(r - \gamma a)], \qquad \gamma a < r < 2a, \tag{4.17}$$

where $g(r)$ is the radial distribution function between two molecules in the fluid. The nature of the soft potential ϕ_s enters here only through the value of the pressure p and the work necessary to make a hole of size $(\gamma a/2)$:

$$p_0(\gamma a/2) = \exp[-W(\tfrac{1}{2}\gamma a)/kT]. \tag{4.18}$$

ACKNOWLEDGMENT

We would like to express our appreciation to Howard Reiss for several valuable discussions and suggestions in relation to this work.

APPENDIX I. IDEAL GAS

We give a simple illustration of the ideas discussed in Sec. 2 by considering the case of an ideal gas. For this gas it is well known that p_N satisfies the Poisson distribution[16]

$$p_n = (\nu^n/n!)e^{-\nu}, \tag{A.1}$$

where $\nu = \frac{4}{3}\pi\rho a^3\lambda^3 = \langle n \rangle$. In particular

$$p_0 = \exp(-\tfrac{4}{3}\pi\rho a^3\lambda^3) = \exp[-W(\lambda)/kT], \tag{A.2}$$

and

$$dW = \rho kT dV = p dV.$$

APPENDIX II. RIGID LATTICE GAS

Another simple illustration of our ideas can be obtained by considering a lattice of η sites on which N particles are to be placed. The volume per site is taken to be unity. The particles behave like rigid spheres in that not more than one particle can be placed on one site and that otherwise the particles do not interact. A hole will now mean an empty lattice site and according to Eqs. (2.5)–(2.7) we find

$$p_0 = \exp(-W/kT) = 1 - \rho, \tag{B.1}$$

with $\rho = N/\eta$. This yields for the chemical potential μ in accordance with Eqs. (2.2) and (2.3)

$$\mu = kT \ln(\rho\Lambda^3) + W = kT \ln\{[\rho/(1 - \rho)]\Lambda^3\}, \tag{B.2}$$

while the pressure is given by

$$p = \int_0^{\rho} \rho(\partial\mu/\partial\rho)\, d\rho = -kT \ln(1 - \rho). \tag{B.3}$$

[15] Z. W. Salsburg, R. W. Zwanzig, and J. G. Kirkwood, J. Chem. Phys. **21**, 1098 (1953).

[16] S. Chandrasekhar, Revs. Modern Phys. **15**, 1 (1943).

Proton Magnetic Resonances of Some Borazole Derivatives

KAZUO ITO, HARUYUKI WATANABE, AND MASAJI KUBO

Chemistry Department, Nagoya University, Chikusa, Nagoya, Japan

(Received August 1, 1960)

The proton magnetic resonance spectra of ten borazole derivatives were recorded and assignments were carried out. The chemical shifts of BH and NH protons are close to each other, the values being nearly equal to the sum of the contribution of a diamagnetic ring current and the chemical shift of C=CH−C protons. The signals of NH and BH protons showed the partial collapse of multiplet structures due to quadrupole relaxation. BC_2H_5 protons gave a single sharp line instead of showing both methyl and methylene signals each split by I–I coupling. An explanation is given in terms of electronegativity considerations.

BORAZOLE and its derivatives present an interesting group of compounds, because they are unique in having a borazole ring, which simulates a benzene ring in many ways, although the analogy is by no means complete. In a series of physical investigations, the present authors have obtained information on the molecular structure[1,2] and electronic state[1] of these compounds. The present investigation has been undertaken in order to obtain further knowledge on the electronic state of a borazole ring from the observation of chemical shifts and splittings. The proton and B^{11} magnetic resonances of borazole have already been reported.[3,4] Borazole is distinct from benzene in that each proton is bonded to boron or nitrogen having a nuclear spin and also an electric quadrupole moment capable of affecting through its spin-lattice relaxation the relative broadening of multiplet components. Therefore, a systematic study was carried out on the proton magnetic resonances of a number of borazole derivatives.

EXPERIMENTAL

The method of synthesis and purification has already been described elsewhere[1,2,4] for seven borazole derivatives used in the present investigation. The identification was made by means of their melting points, boiling points, infrared absorption spectra, freezing point depressions, etc. *N*-Trimethylborazole was prepared by Hohnstedt and Haworth's method,[5] i.e., by the reduction of *B*-trichloro-*N*-trimethylborazole with sodium borohydride $NaBH_4$ in triethylene glycol dimethyl ether solution. It was purified by distillation under reduced pressure, bp 133°C, mp −7.5°C as compared with 133°C and −7.8°C reported in the literature. *B*-trichloro-*N*-triethylborazole was synthesized from boron trichloride and ethylamine in accordance to Turner and Warne's method,[6] dehydrochlorination being promoted by means of triethylamine. The identification was made by the determination of its mp (57°C) and the infrared spectra and also by the derivation from it of hexaethylborazole, which was already identified.[1] *B*-Trimethyl-*N*-triethylborazole was prepared by the reaction of *B*-trichloro-*N*-triethylborazole with a suitable Grignard reagent and purified by fractionation. The resulting liquid was a new compound. Therefore, there are no physical data available in the literature for comparison.

The proton magnetic resonance spectra were recorded at room temperature by means of a JNM-3 high-resolution NMR spectrometer of Japan Electron Optics Laboratory Company operating at 40 Mc. Chemical shifts defined by

$$\delta = 10^6(H_s - H_r)/H_r$$

were evaluated using cyclohexane as an internal standard. Here, H_s denotes the applied magnetic field for the proton signal of the sample and H_r is that for the reference signal.

ASSIGNMENTS

B-Trichloroborazole (Fig. 1) shows a single unresolved broad peak at -3.9_3 ppm due to protons bonded to nitrogen. The spectrum of *B*-trichloro-*N*-trimethylborazole (Fig. 2) has a single sharp absorption at -1.7_5 ppm attributable to methyl groups. *B*-Trichloro-*N*-triethylborazole (Fig. 3) gives rise to a triplet centered at $+0.3_8$ ppm originating from methyl groups in ethyl groups and a quartet centered at -2.2_0 ppm attributable to methylene groups. The quartet has a slightly complicated structure due to the presence of nitrogen directly bonded to methylene groups.

N-Trimethylborazole (Fig. 4) shows a sharp intense absorption peak at -1.6_0 ppm attributable to methyl protons, in addition to fairly broad quartet lines

[1] H. Watanabe and M. Kubo, J. Am. Chem. Soc. **82,** 2428 (1960); H. Watanabe, K. Ito, and M. Kubo, *ibid.* **82,** 3294 (1960).
[2] H. Watanabe, M. Narisada, T. Nakagawa, and M. Kubo, Spectrochim. Acta **16,** 78 (1960); H. Watanabe, T. Totani, T. Nakagawa, and M. Kubo, *ibid.* (to be published).
[3] K. Ito, H. Watanabe, and M. Kubo, J. Chem. Phys. **32,** 947 (1960).
[4] K. Ito, H. Watanabe, and M. Kubo, Bull. Chem. Soc. Japan **33,** 1588 (1960).
[5] L. Hohnstedt and D. T. Haworth, J. Am. Chem. Soc. **82,** 89 (1960).
[6] H. S. Turner and R. J. Warne, Chem. & Ind. (London) **18,** 526 (1958).

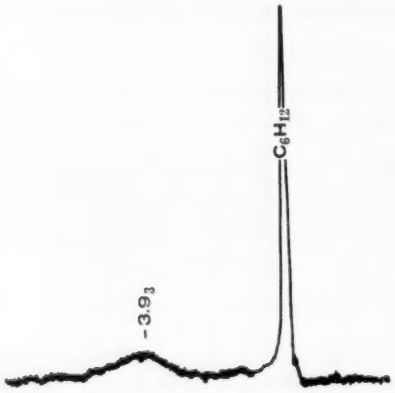

FIG. 1. NMR spectrum of *B*-trichloroborazole in 10% carbon tetrachloride solution.

centered at -3.0_5 ppm due to protons bonded to B^{11} having a nuclear spin equal to $\frac{3}{2}$. The effect of the less abundant isotope B^{10} was hardly discernible. A component line of the quartet could not be located exactly, because it was masked by the intense line of

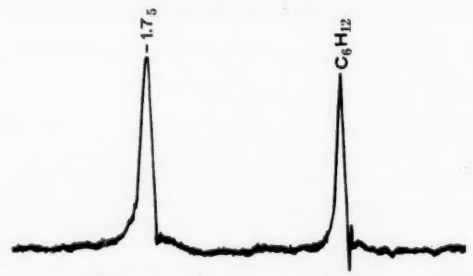

FIG. 2. *B*-Trichloro-*N*-trimethylborazole in 10% carbon tetrachloride solution.

methyl protons. Hexamethylborazole (Fig. 5) shows two sharp lines of equal intensity at -1.5_8 and 1.0_0 ppm. Considering the spectrum of *B*-trichloro-*N*-trimethylborazole, the former was assigned unequivocally to protons in methyl groups bonded to nitrogen, while the latter to those bonded to boron. *B*-Trimethyl-*N*-triethylborazole (Fig. 6) shows a sharp line at $+0.9_3$ ppm due to BCH_3 protons and also a characteristic three-four pattern of ethyl groups centered at $+0.4_0$ and -1.9_8 ppm.

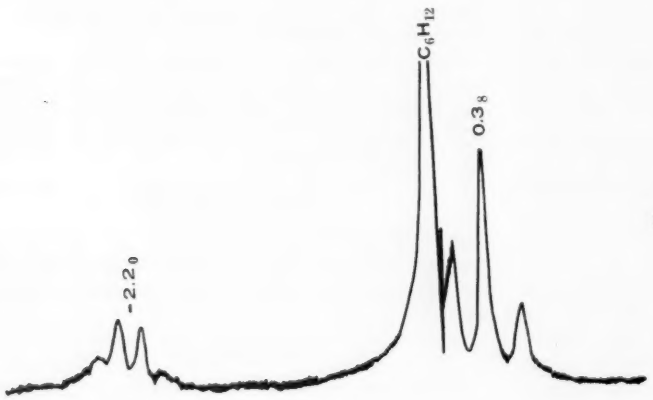

FIG. 3. *B*-Trichloro-*N*-triethylborazole in 25% carbon tetrachloride solution.

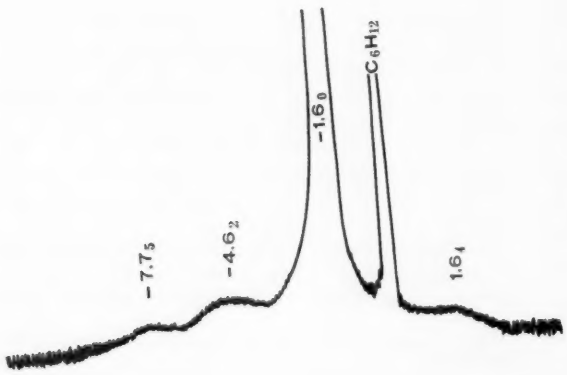

FIG. 4. *N*-Trimethylborazole.

B-Triethyl-*N*-trimethylborazole (Fig. 7) shows a sharp absorption at $+0.4_5$ ppm and a composite one at -1.5_0 ppm. The former was interpreted as an unresolved peak arising from protons in ethyl groups bonded to boron, while the latter was presumed to be a triplet attributable to NCH_3 protons, although the triplet structure was not very convincing. Mention should be made here that this compound underwent gradual decomposition, as has already been reported.[1] The spectrum of hexaethylborazole (Fig. 8) is comprised of a typical quartet centered at -2.1_7 ppm and three other prominent peaks. The former was assigned unequivocally to methylene protons in ethyl groups bonded to nitrogen. The highest peak at $+0.5_2$ ppm was presumed to be the unresolved signal of protons in ethyl groups attached to boron. A hump on its higher magnetic field side and the remaining two peaks constitute a triplet centered at $+0.4_0$ ppm. This triplet was attributed to methyl protons in ethyl groups bonded to nitrogen.

FIG. 5. Hexamethylborazole in 5% carbontetrachloride solution.

B-Trimethyl-*N*-triphenylborazole (Fig. 9) shows a peak at $+1.6_0$ ppm attributable to BCH_3 protons and another peak at -5.7_5 ppm having a structure to some extent. Although the resolution of the latter peak is open to suspicion, this peak was interpreted as the proton signal of phenyl groups. *B*-Triethyl-*N*-triphenylborazole (Fig. 10) yields two lines at $+1.0_5$ and -5.7_5 ppm. The former was assigned to the unresolved signal of BC_2H_5 protons while the latter to that of phenyl protons.

The numerical values of chemical shifts δ and spin coupling constants J are shown in Table I.

DISCUSSION

BH and NH Proton Chemical Shifts

The BH proton signals of *N*-trimethylborazole and the NH proton signal of *B*-trichloroborazole are very broad owing to the quadrupole relaxation arising from the presence of B^{11} and N^{14} nuclei, respectively. It has already been reported that, in the proton magnetic resonance spectrum of borazole, the multiplet structure

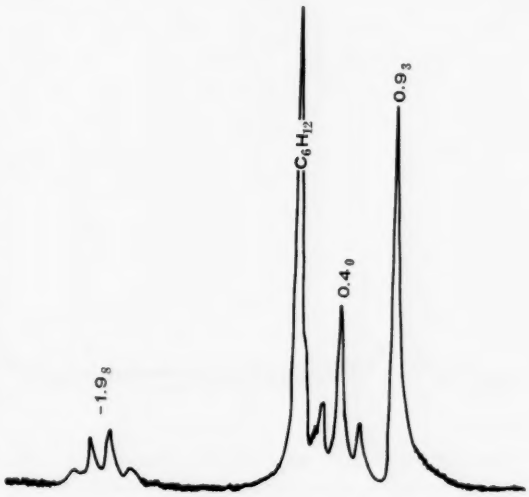

FIG. 6. *B*-Trimethyl-*N*-triethylborazole in 22% carbon tetrachloride solution.

of an NH triplet is well resolved[3,4] with its central line slightly stronger than the two outer ones. The corresponding triplet of *B*-trichloroborazole is collapsed to such an extent that the multiplet structure is hardly discernible. It is interesting to note that chlorine atoms bonded to boron affect the electric field gradient at N^{14} nuclei.

The chemical shifts, -3.0_5 and -3.9_3 of BH and NH protons (chemical shifts are expressed in ppm units) in these two compounds are close to those in borazole, -3.0_7 and -4.0_6, respectively. According to studies on the ultraviolet spectra of borazole and its derivatives,[7] a methyl group bonded to nitrogen and also a chlorine atom bonded to boron are known to

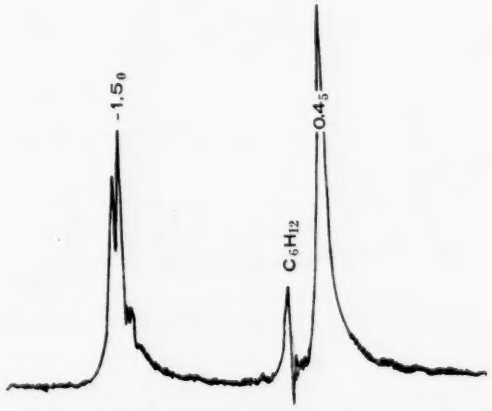

FIG. 7. *B*-Triethyl-*N*-trimethylborazole in 22% carbon tetrachloride solution.

[7] C. W. Rector, G. W. Schaeffer, and J. R. Platt, J. Chem. Phys. **17**, 460 (1949).

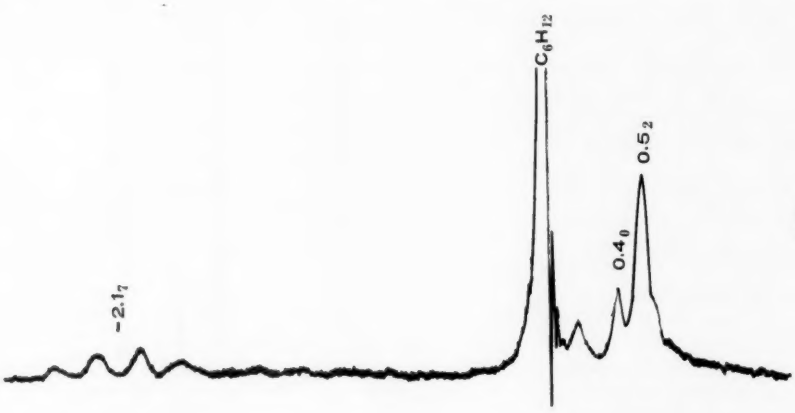

FIG. 8. Hexaethylborazole in 10% carbon tetrachloride solution.

affect the electronic state of the borazole ring: the former increases while the latter decreases the donor-acceptor double bond character of BN bonds in the ring. However, the chemical shifts seem to be insensitive to this effect.

The chemical shifts of BH and NH protons in borazole and its derivatives are fairly close to each other, despite a considerable difference between the electronegativities of boron and nitrogen. As in a benzene ring,[8] the diamagnetic ring current induced by the external magnetic field in a borazole ring is presumed to contribute to the chemical shifts of BH and NH protons. This contribution is estimated from the diamagnetic anisotropies of a borazole ring and a benzene ring,[1] the molceular dimensions of these rings,[9] and the contribution, -1.50, of the diamagnetic ring current to the chemical shift of protons in benzene[10] as -0.9 and -1.1 for BH and NH protons, respectively. Subtracting this value from the observed BH and NH proton chemical shifts, one has -2.2 and -2.9 respectively, as referred to cyclohexane, or $+1.2$ and $+0.5$ as referred to water as a standard. The latter values are close to the chemical shift of protons in a C=CH—C group ranging from -0.9 to $+1.0$,[11] as observed for various compounds, rather than, for instance, to the NH proton chemical shift ranging over 1.9–2.0 in secondary amines. The result is plausible, since BN bonds in a borazole ring, which are isoelectronic with CC bonds in a benzene ring, are known to have a partial double-bond character.[1,2,7,12]

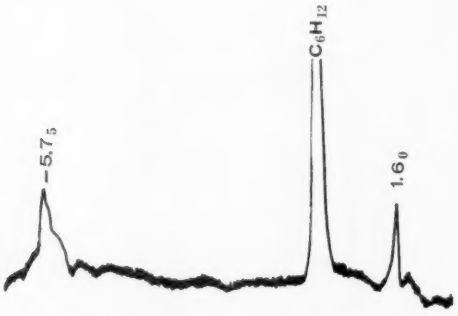

FIG. 9. *B*-Trimethyl-*N*-triphenyl borazole in 5% carbon tetrachloride solution.

BCH_3 and NCH_3 Proton Chemical Shifts

The proton chemical shift, 1.6_0, of BCH_3 in *B*-trimethyl-*N*-triphenylborazole is greater by about 0.6 ppm than those in hexamethylborazole and *B*-trimethyl-*N*-triethylborazole, 1.0_0 and 0.9_3. As has already been pointed out by the present authors,[1] phenyl groups are bonded to a borazole ring with their planes perpendicular to the borazole ring. Accordingly, the diamagnetic ring current induced by the external field in the phenyl rings will shift the BCH_3 proton signal to a higher magnetic field. A calculation similar to that employed for the proton signal of benzene[8] has led to a shift of about 0.5 ppm in good agreement with 0.6 ppm mentioned above. A similar relation holds for the proton signals of the corresponding *B*-triethyl-*N*-triY-compounds. Accordingly, the chemical

[8] H. J. Bernstein, W. G. Schneider, and J. A. Pople, Proc. Roy. Soc. (London) **A236,** 515 (1956).

[9] S. H. Bauer, J. Am. Chem. Soc. **60,** 524 (1938); B. P. Stoicheff, Can. J. Phys. **32,** 339 (1954); K. Kimura and M. Kubo, J. Chem. Phys. **32,** 1776 (1960).

[10] J. S. Waugh and R. W. Fessenden, J. Am. Chem. Soc. **79,** 846 (1957).

[11] J. A. Pople, W. G. Schneider, and H. J. Bernstein, *High-resolution Nuclear Magnetic Resonance* (McGraw-Hill Book Company, Inc., New York, 1959), pp. 242, 245.

[12] Electron diffraction: A. Stock and R. Wierl, Z. anorg. u. allgem. Chem. **203,** 228 (1931); S. H. Bauer, J. Am. Chem. Soc. **60,** 524 (1938); K. P. Coffin and S. H. Bauer, J. Phys. Chem. **59,** 193 (1955). X-ray: D. L. Coursen and J. L. Hoard, J. Am. Chem. Soc. **74,** 1742 (1952). uv spectra: C. C. J. Roothaan and R. S. Mulliken, J. Chem. Phys. **16,** 118 (1948). IR and Raman spectra: B. L. Crawford, Jr., and J. T. Edsall, J. Chem. Phys. **7,** 223 (1939); W. G. Price, R. D. B. Fraser, T. S. Robinson, and H. C. Longuet-Higgins, Discussions Faraday Soc. **9,** 131 (1950). Dipole moments: K. L. Ramaswamy, Proc. Indian Acad. Sci. **A2,** 364 (1935).

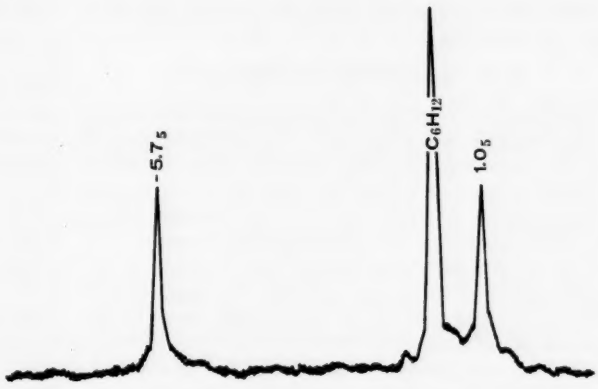

FIG. 10. *B*-Triethyl-*N*-triphenylborazole in 25% carbon tetrachloride solution.

shift of BCH_3 protons devoid of the effect of ring currents in phenyl groups is about 0.9–1.1 as referred to cyclohexane, or 4.3–4.5 as referred to water. The latter value is higher than the chemical shift, 3.6–4.4, of CCH_3 protons as expected from the electronegativity of boron.

The dependence of the chemical shift of NCH_3 in *B*-triX-*N*-trimethylborazoles on the *B*-substituents is related to the inductive effect rather than to the electromeric effect of the substituents. In other words, both the chemical shift of NCH_3 and the $-I$ effect[13] of the *B*-substituents increase progressively in the order of *B*-trichloro-*N*-trimethylborazole, *N*-trimethylborazole, hexamethylborazole, and *B*-triethyl-*N*-trimethylborazole, in agreement with a prediction from electronegativity considerations. The observed chemical shifts of NCH_3 protons ranging over 1.7–1.9 as referred to water are close to those of OCH_3 protons, 1.3–1.7, rather than to those of typical NCH_3 protons, 2.1–2.9.[14] The result can be explained, because the electronegativity of nitrogen in a borazole ring is closer to that of oxygen than to that of nitrogen in ordinary nitrogen compounds, as described below.

BC_2H_5 and NC_2H_5 Proton Chemical Shifts

The proton signal of NC_2H_5 shows a normal three-four pattern, whereas that of BC_2H_5 is a single peak having no *I-I* splittings. Dailey and Shoolery[15] have studied the proton magnetic resonance spectra of an ethyl group in C_2H_5X type compounds and found that the difference between the chemical shift of methyl protons and that of methylene protons is in linear rela-

TABLE I. Chemical shifts δ (in ppm) and spin coupling constants J (in cps) of *B*-triX-*N*-triY-borazoles. For borazole, J_{NH} denotes the spin coupling constant between nitrogen and hydrogen atoms directly bonded to each other. In *B*-triethyl-*N*-trimethylborazole, the same notation is used for the same pair of atoms separated by two chemical bonds.

					NCH_3		BCH_3	
X	Y	C_6H_5	NH	BH	NCH_2	CCH_3	BC_2H_5	J
Cl	H		-3.9_3					
Cl	CH_3				-1.7_5			
Cl	C_2H_5				-2.2_0	$+0.3_8$		$J_{HH}=8.0$
H	H		-4.0_5	-3.0_7				$J_{NH}=56$, $J_{BH}=138$
H	CH_3			-3.0_5	-1.6_0			$J_{BH}=125$
CH_3	CH_3				-1.5_8		$+1.0_0$	
CH_3	C_2H_5				-1.9_8	$+0.4_0$	$+0.9_3$	$J_{HH}=7.2$
C_2H_5	CH_3				-1.5_0		$+0.4_5$	$J_{NH}=3.0$
C_2H_5	C_2H_5				-2.1_7	$+0.4_0$	$+0.5_2$	$J_{HH}=8.1$
CH_3	C_6H_5	-5.7_5					$+1.6_0$	
C_2H_5	C_6H_5	-5.7_5					$+1.0_5$	

[13] M. J. S. Dewar, *The Electronic Theory of Organic Chemistry* (Oxford University Press, New York, 1949). See also R. W. Taft, Jr., J. Am. Chem. Soc. **79**, 1045 (1957).
[14] L. H. Meyer, A. Saika, and H. S. Gutowsky, J. Am. Chem. Soc. **79**, 4567 (1953).
[15] B. P. Dailey and J. N. Schoolery, J. Am. Chem. Soc. **77**, 3977 (1955).

tion to the electronegativity of an atom directly linked to the ethyl group.

$$\text{E.N.} = 0.695[\delta(CH_3) - \delta(CH_2)] + 1.71.$$

This empirical equation first proposed for electronegativity values ranging over 2.6–3.9 was found by Baker[16] to be valid approximately even for electronegativity values as small as 1.7 for lead and 1.4 for aluminum. According to this relation, the chemical shift difference $\Delta\delta$ vanishes for the electronegativity equal to 1.71. It has been shown theoretically[17] that in this case *I-I* splittings also disappear leading to a single sharp signal for ethyl protons, as was actually found in the present investigation.

Introducing $\Delta\delta$ equal to zero and 2.4–2.6 for BC_2H_5 and NC_2H_5 proton signals, respectively, into the aforementioned equation, one has 1.7 and 3.4–3.5 for the electronegativities of boron and nitrogen in a borazole ring. The frequency of the symmetric bending vibration of a methyl group is known to depend on the electronegativity of an atom directly bonded to the methyl group.[18] The infrared absorption band of *N*-trimethylborazole[19] at about 1470 cm^{-1}, which is assigned to this mode of vibration, leads to the electronegativity of nitrogen equal to 3.5 in good agreement with 3.4–3.5 mentioned above. The deviation of these values beyond all conceivable errors from the accepted electronegativities of boron and nitrogen, 2.0 and 3.0 can be accounted for at least qualitatively by the electronic structure[1,2,7,12] involving resonance among

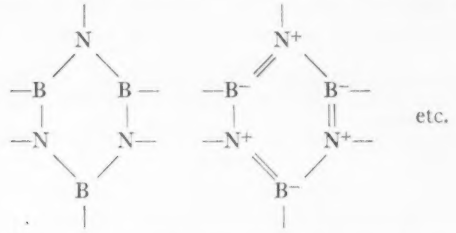

Owing to the partial formation of donor-acceptor double bonds, the boron atoms and the nitrogen atoms of a borazole ring are presumed to be less electronegative and more electronegative, respectively.

NC_6H_5 Proton Chemical Shifts

The chemical shifts at -5.7_5 of phenyl protons in *B*-trimethyl-*N*-triphenylborazole and *B*-triethyl-*N*-triphenylborazole are practically identical with that in benzene, -5.77. Although not all protons in a phenyl group are equivalent, the proton signals of ortho, meta, and para hydrogen atoms were not resolved in the present investigation. According to a study on the proton magnetic resonances of monosubstituted benzines,[20] the proton signals are not resolved unless the substituent is NO_2, CHO, COOH, NH_2, etc., having a strong $\pm E$ effect or the phenyl group is bonded to fluorine showing a strong *I* effect. Since the phenyl groups are at right angles to the borazole ring as mentioned above, and hence π conjugation between the rings is inappreciable, and also because nitrogen is much less electronegative than fluorine, it is reasonable that the proton signals of these *B*-trialkyl-*N*-triphenylborazoles were not resolved.

Spin Coupling Constants

The spin coupling constant $J(B^{11}H) = 125$ cps was observed for *N*-trimethylborazole as compared with 134 cps evaluated by Phillips *et al.*[21] from the B^{11} magnetic resonance spectrum of the same compound. The value is close to 138 cps in borazole[3,4] and also to 125 cps for the terminal protons of diborane.[22] In general, the spin coupling constant $J(XH)$ in a molecule changes with the isotopic substitution of the atom X in proportion to the nuclear *g* factor of the nucleus X.[23] It is noteworthy that $J(B^{11}H)/g(B^{11})$ equal to 69.6 cps is considerably smaller than the corresponding ratios, 86–180 cps for C^{13}, 113 cps for N^{14}, 117 cps for F^{19}, 190 cps for Si^{29}, and 81–150 cps for P^{31}.

Muller and Pritchard[24] have measured spin coupling constants between protons and C^{13} nuclei for a number of hydrocarbons and interpreted the results on the basis of a simple semiempirical equation relating the coupling constant with the amount of *s* character of the carbon orbitals involved in the bonds. According to their theoretical calculations as well as experimental results, the ratio of the spin coupling constant J_{CH} between hydrogen and carbon directly bonded by the sp^2 hybridized atomic orbital of carbon and that between the same pair of atoms bonded by the sp^3 orbital is approximately 1.33 irrespective of the polarity of the CH bonds. The same relation holds surprisingly well also for boron compounds. The spin coupling constants J_{BH} in borazole and *N*-trimethylborazole involving sp^2 hybridization gives the mean value of 132 cps, whereas those in $(CH_3)_2NHBH_3$ and $(CH_3)_3NBH_3$ equal to 94 and 97 cps, respectively,[21] leads to

[16] E. B. Baker, J. Chem. Phys. **26**, 960 (1957).
[17] See work cited in footnote 11, p. 116.
[18] W. J. Lehmann, C. O. Wilson, Jr., and I. Shapiro, J. Chem. Phys. **28**, 777 (1958); L. J. Bellamy, *The Infra-red Spectra of Complex Molecules* (John Wiley & Sons, New York, 1958), 2nd ed., p. 25.
[19] W. C. Price, R. D. B. Fraser, T. S. Robinson, and H. C. Longuet-Higgins [Discussions Faraday Soc. **9**, 131 (1950)] have reported the spectrum of this compound which is different from that recorded by the present authors [H. Watanabe, Y. Kuroda, and M. Kubo (to be published)].
[20] P. L. Corio and B. P. Dailey, J. Am. Chem. Soc. **78**, 3043 (1956).
[21] W. D. Phillips, H. C. Miller, and E. L. Muetterties, J. Am. Chem. Soc. **81**, 4496 (1959).
[22] R. A. Ogg, Jr., J. Chem. Phys. **22**, 1933 (1954).
[23] See work cited in footnote 11, p. 188.
[24] N. Muller and D. E. Pritchard, J. Chem. Phys. **31**, 768 (1959).

the mean value of 96 cps for J_{BH} involving sp^3 hybridization. The ratio of the two mean values, 1.37, agrees excellently with 1.33 mentioned above.

The coupling constant $J(N^{14}H)$ was 3.0 cps across two chemical bonds in *B*-triethyl-*N*-trimethylborazole. $J(HH)$ ranged over 7.2–8.1 cps between methyl protons and methylene protons in an ethyl group bonded to nitrogen in *B*-substituted *N*-triethylborazoles. These values are of the right order of magnitude.

ACKNOWLEDGMENT

The present authors wish to thank Dr. T. Seki of Japan Electron Optics Laboratory Company for recording the high-resolution NMR spectra.

THE JOURNAL OF CHEMICAL PHYSICS VOLUME 34, NUMBER 3 MARCH, 1961

Proton Magnetic Resonance Spectra of Compounds of the Type $X(C_2H_5)_n$. Relative Signs of the X-H Spin Coupling Constants

P. T. NARASIMHAN* AND MAX T. ROGERS

Kedzie Chemical Laboratory, Michigan State University, East Lansing, Michigan

(Received August 15, 1960)

The high-resolution proton magnetic resonance spectra of phosphorus triethyl, tin tetraethyl, and lead tetraethyl have been studied at both 40 Mc and 60 Mc. The various spin-spin coupling constants (J) and the proton internal chemical shift (δ) values for these molecules have been obtained by an analysis of the spectra as A_3B_2 and A_3B_2X systems. (A denotes CH_3 group protons, B the CH_2 group protons, and X is a nucleus other than the proton with spin $\frac{1}{2}$ such as P^{31}, Sn^{117}, Sn^{119}, or Pb^{207}.) In phosphorus triethyl it is found that J_{AX} and J_{BX} have opposite signs. The proton magnetic resonance spectrum of tin tetraethyl is a complex A_3B_2 type spectrum even at 60 Mc with "satellite" lines from naturally present $Sn^{117}(C_2H_5)_4$ (7.67%) and $Sn^{119}(C_2H_5)_4$ (8.68%) in the sample. Analysis of the satellite spectrum as an A_3B_2 type shows that J_{AX} and J_{BX} have opposite signs (here $X=Sn^{117}$ or Sn^{119}). The proton resonance spectrum of lead tetraethyl has been reinvestigated and it is found that the satellite lines due to $Pb^{207}(C_2H_5)_4$ do not show any asymmetry, in contrast with earlier observations of Baker. Probable causes for Baker's results are given and it is shown theoretically and experimentally that such an asymmetry does not truly exist. The coupling constants J_{AX} and J_{BX} are found to have opposite signs in lead tetraethyl also.

I. INTRODUCTION

IN a previous communication[1] it was shown by an analysis of the "satellite" lines in the proton magnetic resonance spectrum of mercury diethyl that J_{AX} and J_{BX} ($X=Hg^{199}$) have opposite signs. (As before, we denote the protons of the CH_3 group by A and those of the CH_2 group by B.) It was further pointed out that by a study of the proton resonance spectra of compounds of the type $X(C_2H_5)n$, where the nucleus X has a spin of $\frac{1}{2}$, it might be possible to obtain the relative signs of J_{AX} and J_{BX} in favorable cases. In the present paper, we wish to deal with proton resonance spectra of three compounds of this type—$P(C_2H_5)_3$, $Sn(C_2H_5)_4$, and $Pb(C_2H_5)_4$—to determine the relative signs of the X-H spin coupling constants in these molecules. P^{31} (natural abundance = 100%) has a nuclear spin of $\frac{1}{2}$, while tin has three naturally occurring isotopes with spin $\frac{1}{2}$. Of these three, only two isotopes, Sn^{117} (7.67%) and Sn^{119} (8.68%), occur in appreciable abundance. Pb^{207}, the isotope of lead with a spin of $\frac{1}{2}$, has a natural abundance of 21.11%. Assuming that in these molecules there is no spin interaction between protons of one ethyl group and those of another, in other words considering the ethyl groups in a given molecule to be equivalent, one might expect the proton resonance spectra of the three compounds investigated here to have the following features.

(a) Phosphorus triethyl: since the P^{31} nucleus has a spin of $\frac{1}{2}$ and since its natural abundance is 100% the proton resonance spectrum would be of the A_3B_2X type.

(b) Tin tetraethyl: the proton resonance spectrum of tin tetraethyl would be of the A_3B_2 type but the lines for $Sn^{117}(C_2H_5)_4$ and $Sn^{119}(C_2H_5)_4$ may show up due to the appreciable abundance of these tin nuclei. The spectra of these two species would fall under the A_3B_2X category.

(c) Lead tetraethyl: the spectrum of this compound would be of the A_3B_2 type and that due to $Pb^{207}(C_2H_5)_4$ would be of the A_3B_2X type. Earlier, Baker[2]

* Present address: Noyes Chemical Laboratory, University of Illinois, Urbana, Illinois.

[1] P. T. Narasimhan and M. T. Rogers, J. Chem. Phys. **31**, 1431 (1959).

[2] E. B. Baker, J. Chem. Phys. **26**, 960 (1957).

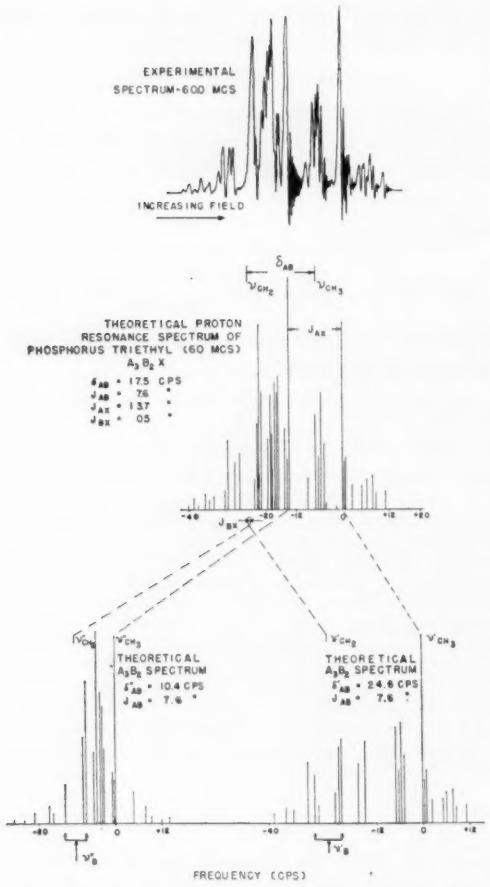

FIG. 1. Proton magnetic resonance spectrum of phosphorus triethyl at 60 Mc (top). The theoretical spectrum, calculated by use of the indicated constants, is shown in the center. The two A_3B_2 spectra which make up this calculated spectrum are also shown separated (bottom).

investigated the proton magnetic resonance spectrum of lead tetraethyl at 30 Mc and found the satellite lines (A_3B_2X) due to spin-spin interaction between Pb^{207} and the protons of the ethyl group. He also noted that the internal chemical shift ($\delta_{AB}=\nu_A-\nu_B$) between CH_3 and CH_2 group protons at 30 Mc is less than 1 cps with the result that the A_3B_2 part of the spectrum is almost a single broad line ($J_{AB}=8.2$ cps).

Since we are concerned here mainly with the determination of the magnitude and relative signs of J_{AX} and J_{BX} in these three compounds it is clear that a method for the analysis of A_3B_2X spectra is essential. By means of a simple extension of the theory for A_3B_2C systems outlined by us elsewhere,[3] it is possible to obtain expressions for the transition frequencies and relative intensities for the A_3B_2X case. Alternatively, since we are interested only in the proton magnetic resonance spectra, we can use the concept of "effective" internal chemical shifts, δ'_{AB} and δ''_{AB}, corresponding to the two spin states of the X nucleus, and thus treat the A_3B_2X spectrum as a combination of two A_3B_2-type spectra, In this case, we have

$$\delta'_{AB}=(\delta_{AB}+\tfrac{1}{2}J_{AX}-\tfrac{1}{2}J_{BX}) \quad (1a)$$

and

$$\delta''_{AB}=(\delta_{AB}-\tfrac{1}{2}J_{AX}+\tfrac{1}{2}J_{BX}). \quad (1b)$$

This alternative method was also indicated in our earlier communication[1] and in the present work use has been made of this method. Details of the analysis of A_3B_2-type spectra have been published.[4,5] By following these procedures we have been able to calculate theoretically the proton magnetic resonance spectra of phosphorus triethyl, tin tetraethyl, and lead tetraethyl. The magnitudes and relative signs of the X-H coupling constants have also been obtained. In the course of the present investigation, it was noted that the satellite spectrum of lead tetraethyl at both 40 Mc and 60 Mc has a high degree of symmetry about the central intense line. This observation is in contrast to an earlier report by Baker[2] who studied this compound at 30 Mc and found "extra" lines on only one side of the spectrum. A theoretical calculation of the satellite spectrum in this compound conclusively shows that such an asymmetry is not truly present.

II. EXPERIMENTAL

The proton magnetic resonance spectra were obtained with a 40-Mc Varian Associates high resolution NMR spectrometer (V-4300B) equipped with a V-4311 rf unit for operation at 60 Mc also. The compounds were studied as liquids and were degassed and sealed in 5 mm o.d. Pyrex tubes. Sample spinning and audio modulation techniques were employed.

III. ANALYSIS OF THE SPECTRA

A. Phosphorus Triethyl

Figure 1 shows the proton NMR spectrum of phosphorus triethyl at 60 Mc (top) along with the theoretically calculated spectrum (center). The theoretical spectrum was obtained by proper superposition of two A_3B_2-type spectra calculated using two effective internal chemical shifts of 24.6 cps and 10.4 cps (see Fig. 1, bottom). J_{AB} for this case is 7.6 cps. These data were obtained in the following manner. An inspection of the experimental spectrum shows two intense and narrow lines, one on the high-field side and another at about the center. These two lines may be identified as due to the CH_3 protons split into a doublet by spin

[3] P. T. Narasimhan and M. T. Rogers, J. Chem. Phys. **33,** 727 (1960).

[4] B. R. McGarvey and G. Slomp, J. Chem. Phys. **30,** 1586 (1959).

[5] P. T. Narasimhan and M. T. Rogers, J. Am. Chem. Soc. **82,** 34 (1960).

interaction with P^{31}. The separation between these two lines, which is 13.7 cps, is then the value of J_{AX}. The constancy of this separation at 40 Mc confirmed this assignment. Next, using the high-field line of this doublet as ν_A' we set out to fit the lines lying on the high-field side by means of a suitable A_3B_2-type spectrum. A value of $|J_{AB}/\delta_{AB}'|=0.25$ was estimated at the outset by comparison with a set of theoretical A_3B_2 spectra obtained earlier. Further refinements yielded a good fit for $|J_{AB}/\delta_{AB}'|=0.309$. By means of this calculation, it was possible to fit well not only lines on the high-field side but many on the low-field side also. It was then clear that the rest of the lines in the experimental spectrum should fit another A_3B_2-type spectrum but now with a different effective chemical shift, δ_{AB}''. This was confirmed and the value of $|J_{AB}/\delta_{AB}''|=0.731$ was thus obtained. δ_{AB}' and δ_{AB}'' could then be obtained directly from the experimental spectrum by locating two important lines for each case (see Fig. 1, bottom). It can be shown that the center of these two lines corresponds to the position of ν_B' or ν_B'', as the case may be. In this manner, δ_{AB}' and δ_{AB}'' were found to be 24.6 cps and 10.4 cps, respectively. From the two J/δ ratios obtained above a consistent value of $J_{AB}=7.6$ cps was arrived at.

It will be seen from Fig. 1 that for a satisfactory superposition of the two A_3B_2 spectra the value of $J_{BX}=0.5$ cps and it will be noted that J_{AX} and J_{BX} have opposite signs. δ_{AB}, the internal chemical shift between A and B protons (unmodified by spin interactions with X), is found to be 17.5 cps at 60 Mc; the protons of the CH_3 group are more shielded than those of the CH_2. The spectrum of $P(C_2H_5)_3$ at 40 Mc showed that these assignments are essentially correct, but owing to the decreased internal chemical shifts and the consequent overlapping of several lines, many significant features of the spectrum that were useful in the analysis at 60 Mc were lost at 40 Mc.

B. Tin Tetraethyl

The main multiplet part of the spectrum of this compound at 60 Mc (Fig. 2) can be fitted by means of a theoretically calculated A_3B_2 spectrum with $|J_{AB}/\delta_{AB}|=0.350$. The value of δ_{AB} obtained by the direct method[6] from the experimental spectrum is -23.4 cps at 60 Mc, the minus sign indicating that the CH_3 protons are less shielded than the CH_2 protons. J_{AB} is found to be 8.2 cps. In addition to this A_3B_2-type spectrum, "satellite" lines are noticeable in the experimental spectrum of tin tetraethyl, particularly when the rf power is increased to a reasonably high level (see Fig. 3). On the extreme low-field side of the spectrum a triplet pattern is noticeable. The center of this triplet is separated from ν_A of the main A_3B_2 spectrum by 34.8 cps, and on the high-field side a more complex

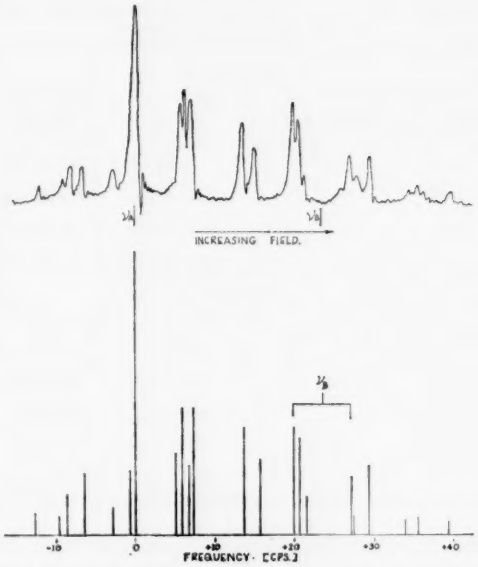

FIG. 2. Proton magnetic resonance spectrum of tin tetraethyl at 60 Mc (main multiplet only). The theoretical spectrum (bottom) is the theoretical A_3B_2 spectrum with $|J_{AB}/\delta_{AB}|=0.350$.

pattern is noticeable with a peak separated from ν_A by the same amount. Identifying these lines as the CH_3 part of $Sn^{117/119}(C_2H_5)_4$, the value of J_{AX} is found to be 71.2 cps for $Sn^{119}(C_2H_5)_4$ and 68.1 cps for $Sn^{117}(C_2H_5)_4$. It will be noticed that the satellite lines are rather broad because the lines due to $Sn^{117}(C_2H_5)_4$ and $Sn^{119}(C_2H_5)_4$ fall close together. Since the ratio of the magnetogyric ratios, $\gamma(Sn^{117}):\gamma(Sn^{119})$, is 1:1.048, the values of J_{AX} ($X=Sn^{117}$) and J_{AX} ($X=Sn^{119}$) are also in the same ratio. The spacing between the triplet lines of the satellite spectrum on the low-field side is 8.2 cps and agrees well with the value of J_{AB} obtained directly from the A_3B_2 part of the spectrum.

The location of the CH_2 part of the $Sn^{117/119}(C_2H_5)_4$ spectrum is also indicated in Fig. 3 (bottom). This was identified as follows: since the CH_3 part is a triplet pattern on the low-field side, thus indicating a first-order-type spin interaction[7] with the CH_2 protons for this case, one would expect the CH_2 group lines to be a quartet and also fairly well removed from the CH_3 group lines. But in the experimental spectrum there is no clear-cut indication of a group of quartet lines, apparently due to overlap with the main A_3B_2 spectrum as well as with other satellite lines. This fact is further substantiated by two broad lines of low intensity falling on the extreme high-field side. These two lines may be identified as part of the CH_2 group and the separation between these two lines is also 8.2 cps. In this manner, the theoretical spectrum of the CH_2 satellite

[6] P. T. Narasimhan and M. T. Rogers, J. Am. Chem. Soc. **82** (1960).

[7] H. S. Gutowsky, D. W. McCall, and C. P. Slichter, J. Chem. Phys. **21**, 279 (1953).

TABLE I. Values of the "effective" internal chemical shifts for protons in tin tetraethyl (60 Mc).

$Sn^{117}(C_2H_5)_4$			
Sign of J_{AX}	Sign of J_{BX}	δ_{AB}'	δ_{AB}''
+	+	4.75 cps	42.05 cps
+	−	26.05 cps	72.85 cps
−	+	72.85 cps	26.05 cps
−	−	42.05 cps	4.75 cps
$SN^{119}(C_2H_5)_4$			
Sign of J_{AX}	Sign of J_{BX}	δ_{AB}'	δ_{AB}''
+	+	3.9 cps	42.9 cps
+	−	28.3 cps	75.1 cps
−	+	75.1 cps	28.3 cps
−	−	42.9 cps	3.9 cps

lines in the high-field region has been constructed. The value of J_{BX} for Sn^{199} $(C_2H_5)_4$ is found to be 32.2 cps. The corresponding value of Sn^{117} $(C_2H_5)_4$ was deduced from the known magnetogyric ratios of Sn^{117} and Sn^{119} to be 30.8 cps for J_{BX}.

With the values of J_{AX}, J_{BX}, and δ_{AB} obtained above, we can calculate the effective internal chemical shifts for Sn^{117} $(C_2H_5)_4$ and Sn^{119} $(C_2H_5)_4$ from Eqs. (1a) and (1b). Table I summarizes these data for various combinations of signs for J_{AX} and J_{BX}. It will be seen that both δ' and δ'' for Sn^{117} $(C_2H_5)_4$ and Sn^{119} $(C_2H_5)_4$ are very much alike. As a consequence, satellite lines of these two species fall close together and the lines appear broadened out.

An inspection of Table I shows that if J_{AX} and J_{BX} have the same sign in tin tetraethyl then the ratios of $|J/\delta|$ will be about 0.2 and 1.9, respectively, for the two spin states of X. Theoretical spectra calculated with these values do not fit the experimental one satisfactorily, particularly on the high-field side. On the other hand, the high-field lines as well as the low-field lines agree better with the calculated spectra using $|J/\delta|$ values of about 0.1 and 0.3 (see Fig. 3) thus indicating that J_{AX} and J_{BX} have opposite signs. The theoretical spectrum shown in Fig. 3 was obtained by using first-order approximation[7] for $|J/\delta|=0.1$ and solving the general A_3B_2 case[5] for $|J/\delta|=0.3$.

The spectrum of the compound obtained at 40 Mc confirms the assignments made above from the 60-Mc spectrum. The high-field quartet satellite lines assigned to the CH_2 group are shifted towards low field by about 7.8 cps at 40 Mc as would be expected on the present basis.

C. Lead Tetraethyl

The proton resonance spectrum of this compound was recorded earlier by Baker[2] at 30 Mc using a swept-frequency spectrometer. Baker noticed splittings of the satellite lines due to Pb^{207} $(C_2H_5)_4$ on only one side of the spectrum and so far no explanation of these unusual splittings has been offered. Our investigations on this compound were initiated primarily to determine the relative signs of J_{AX} and J_{BX} in the Pb^{207} $(C_2H_5)_4$ molecule. The spectra that we obtained at both 40 Mc and 60 Mc turned out to be very similar to Baker's—a broad but intense central peak accompanied by the satellite "ethyl group" lines on either side of this central line. However, it was noticed that the satellite lines in our spectra had a high degree of symmetry with "splittings" on both sides. These splittings in the "ethyl group" lines can be shown to be due to higher-order spin-spin interaction between the protons. Figure 4 shows a typical 40 Mc spectrum of lead tetraethyl obtained in the present work. We shall discuss the probable causes for Baker's results and the question of asymmetry in the satellite spectrum after dealing with the relative signs of J_{AX} and J_{BX} in Pb^{207} $(C_2H_5)_4$.

The values of J_{AX} and J_{BX} obtained by locating the centers of the CH_2 and CH_3 lines in the satellite spectrum are 125.0 cps and 41.0 cps, respectively, in good agreement with the data obtained from the published spectrum (30 Mc) of Baker. The value of J_{AB} is found to be 8.2 cps from the "ethyl group" multiplet separations. Using Eqs. (1a) and (1b), the values of δ' and δ'' can be calculated for various combinations of signs of J_{AX} and J_{BX}. Table II summarizes these data. The value of δ_{AB} is not known exactly but is very likely to be less than 1 cps at 40 Mc judging from the width of the central intense lines at low rf power.

The theoretical A_3B_2 spectra calculated using the above values of δ' and δ'' along with $J_{AB}=8.2$ cps are shown in Fig. 4. It will be seen that better agreement with the experimental spectrum is obtained when J_{AX} and J_{BX} are assigned opposite signs ($\delta'\sim\delta''\sim84$ cps). δ' and δ'' do not differ appreciably since δ_{AB} is very small. The "effective" internal chemical shifts are determined in this case almost solely by the magnitudes and signs of J_{AX} and J_{BX}. This feature is noticeable by the near constancy in the appearance of the satellite spectrum up to 60 Mc. This point brings us now to the question of asymmetry in the satellite spectrum. Since δ' and δ'' are very nearly equal, the two A_3B_2

TABLE II. Values of the "effective" internal chemical shifts for protons in lead tetraethyl (40 Mc).

Signs of J_{AX}	Sign of J_{BX}	δ_{AB}''	
$\left\{\begin{matrix}+\\-\end{matrix}\right\}$	$\left\{\begin{matrix}+\\-\end{matrix}\right\}$	~42 cps	~42 cps[a]
$\left\{\begin{matrix}+\\-\end{matrix}\right\}$	$\left\{\begin{matrix}-\\+\end{matrix}\right\}$	~84 cps	~84 cps[a]

[a] δ' and δ'' are estimated to be accurate to within 2 cps. Note that the sign of δ_{AB} is not known. However, this does not give rise to any serious error since δ_{AB} is very small compared to J_{AX} and J_{BX}.

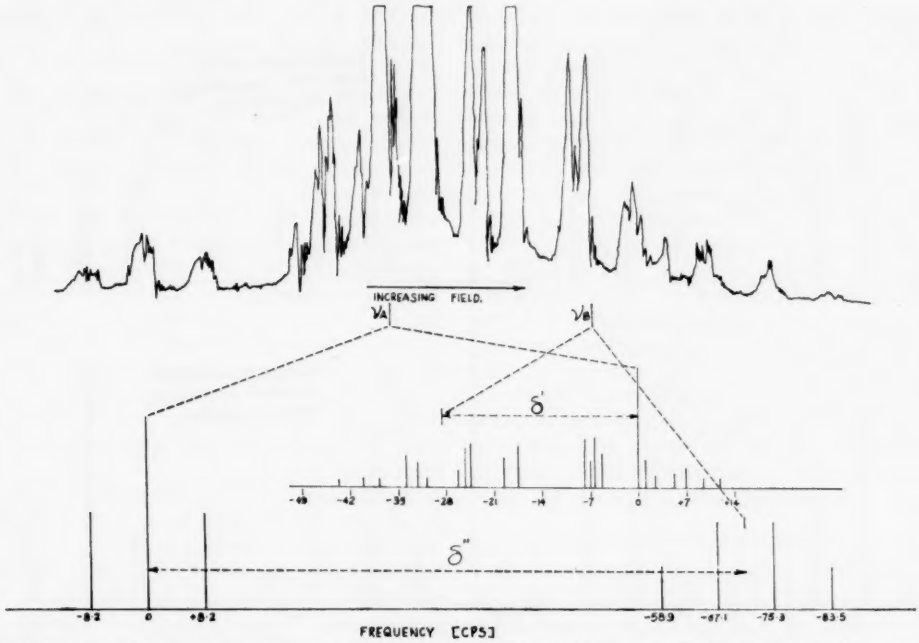

FIG. 3. Proton magnetic resonance spectrum of tin tetraethyl at 60 Mc at higher power (top). The theoretical spectrum for the satellite lines arising from Sn^{119} $(C_2H_5)_4$ only are shown (bottom); the constants employed are given in the text.

spectra corresponding to the two spin states of X should resemble each other closely, and since δ_{AB} is very small, the two spectra should be centered at the intense line. Thus, there is no theoretical reason for any marked asymmetry to be present in this system. Our own experimental findings confirm the absence of any asymmetry and hence we may conclude that the reported asymmetry[2] in the satellite spectrum is not a truly inherent feature. The calculated spectra bring out very well the higher order splittings in the multiplets on both sides. Again this feature is observed in our experimental spectra and therefore the presence of "extra" lines on only one side of the spectrum recorded by Baker probably indicates loss of resolution on one side of his spectrum.

A few possible explanations for Baker's results may not be out of place here. Of these, the one that comes first to mind is the possibility of saturation of the protons with the fairly high rf power used in recording the satellite lines. Saturation will take place also predominantly during the time when the central intense peak is traversed. This peak then broadens out and lines recorded immediately after this peak may not be well resolved. In our own experiments we have been able to reproduce some spectra somewhat similar to the one obtained by Baker by using slow sweep rates and fairly high rf power. In these spectra (magnetic field sweep increasing from left to right) lines falling to the right of the central line show a tendency to smear out and in these the higher order splittings seem to be absent. A similar situation might have prevailed during the recordings of Baker. Saturation of the receiver is another possibility. Yet another is the loss of resolution in the spectrometer (through magnetic field in homogeneity or other similar causes) after passing through the intense central line.

IV. DISCUSSION

By means of the present analysis of the proton magnetic resonance spectra of phosphorus triethyl, tin tetraethyl, and lead tetraethyl, it has been possible to show that J_{AX} and J_{BX} have opposite signs in P^{31} $(C_2H_5)_3$, Sn^{117} $(C_2H_5)_4$, Sn^{119} $(C_2H_5)_4$, and Pb^{207} $(C_2H_5)_4$. This result is similar to that found[1] for Hg^{199} $(C_2H_5)_2$. In all these molecules it is observed that the absolute value of J_{AX} is greater than that of J_{BX} (for a summary of results see Table III). This phenomenon is interesting since the A nuclei are separated from X by three bonds while the B nuclei are separated by only two bonds.

It may be worthwhile to see how these data may be interpreted on the basis of the current concepts of nuclear spin-spin coupling in molecules. The theory of nuclear spin coupling in $^1\Sigma$ molecules has been developed by Ramsey[8] and applied by several authors.[9–11] Since

[8] N. F. Ramsey, Phys. Rev. **91**, 303 (1953).
[9] H. M. McConnell, J. Chem. Phys. **24**, 460 (1956).
[10] G. A. Williams and H. S. Gutowsky, J. Chem. Phys. **30**, 717 (1959).
[11] H. S. Gutowsky, M. Karplus, and D. M. Grant, J. Chem. Phys. **31**, 1278 (1959).

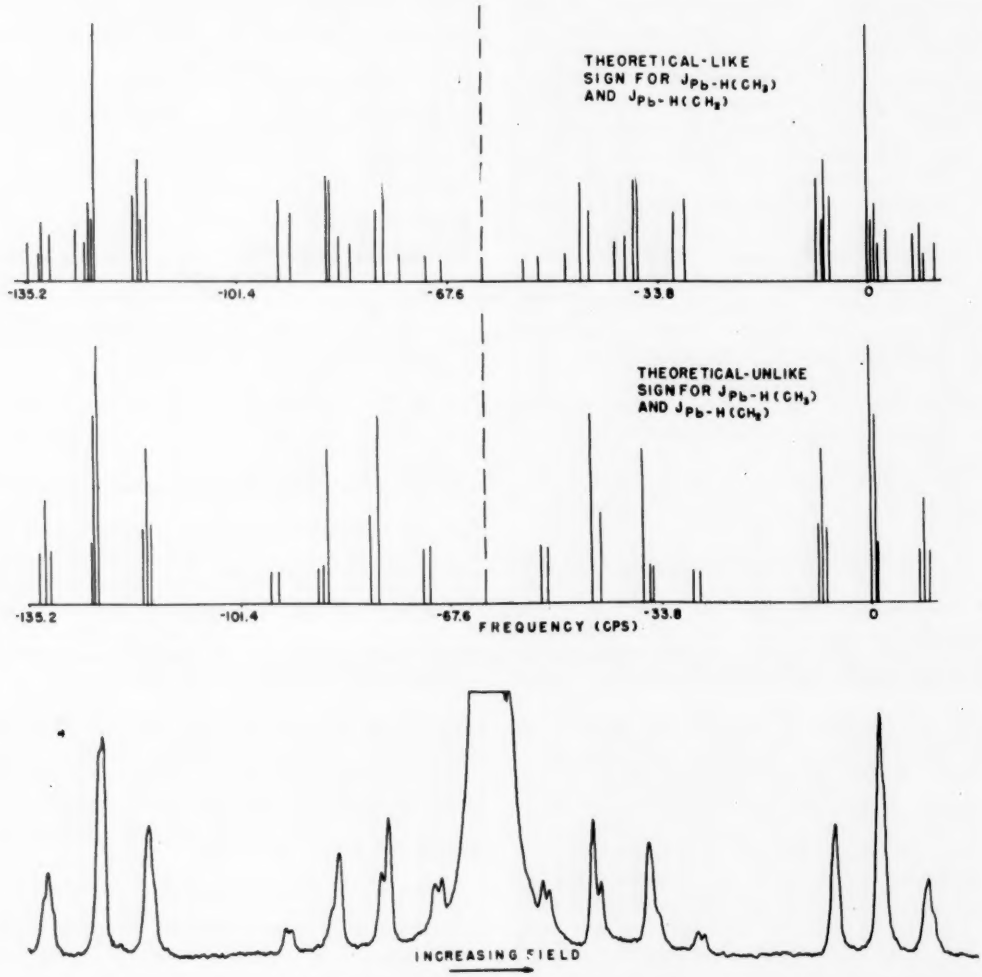

FIG. 4. Proton magnetic resonance spectrum of lead tetraethyl at 40 Mc (bottom). The theoretical spectrum computed for unlike signs of J_{Pb-CH_3} and J_{Pb-CH_2} are given (center), along with the spectrum computed for like signs of these coupling constants (top). Note the high degree of symmetry of the satellite spectrum with respect to the central intense line.

TABLE III. Proton internal chemical shifts and various spin coupling constants in some compounds of the type $X(C_2H_5)_n$.

Compound	δ_{AB}[a]	J_{AB}	Atomic No. of X	J_{AX}	J_{BX}	Relative sign of J_{AX} and J_{BX}
(1) $P^{31}(C_2H_5)_3$	+0.292 ppm	7.6 cps	15	13.7 cps	0.5 cps	Opposite
(2) $Sn^{117}(C_2H_5)_4$	−0.390 ppm	~8.2 cps	50	~68.1 cps	~30.8 cps	Opposite
(3) $Sn^{119}(C_2H_5)_4$	−0.390 ppm	8.2 cps	50	71.2 cps	32.2 cps	Opposite
(4) $Hg^{199}(C_2H_5)_2$[b]	−0.240 ppm	7.0 cps	80	115.2 cps	87.6 cps	Opposite
(5) $Pb^{207}(C_2H_5)_4$[c]	~0	8.2 cps	82	125.0 cps	41.0 cps	Opposite

[a] Values in the absence of spin coupling with the X nucleus.
[b] See references 1 and 5 of text; also R. E. Dessy, T. J. Flautt, H. H. Jaffé, and G. F. Reynolds, J. Chem. Phys. **30**, 1422 (1959).

the coupling nuclei in all the cases studied here are separated by two or more bonds, we may interpret the data, at least qualitatively, on the basis of the "long-range" molecular orbital approximation outlined by McConnell.[9] Following McConnell, the various contributions to the spin coupling constant $J_{NN'}$, for two nuclei N and N' separated by two or more bonds in a molecule, can be written as a sum of one- and two-electron terms. An examination of the expression for the various one-electron terms shows that these are dependent on $1/r_{NN'}^3$, where $r_{NN'}$, is the distance between the coupling nuclei. It is perhaps reasonable then to conclude that the significant contributions, to J_{AX} at least, arise from two-electron terms.[12] Since one of the coupling nuclei is a proton in all these cases, the large J_{AX} couplings may be ascribed to the Fermi-contact term.[13] In fact, semiquantitative calculations made by Narasimhan and Karplus[12] support this view. In this connection, it is of interest to note the increase in J_{AX} values with the increase in the atomic number of X. However, no such regularity is observed with regard to the J_{BX} values, apparently due to significant contributions from other terms. The dominance of these terms over the contact term may also perhaps account for the different sign of J_{BX}.

The analysis of the proton magnetic resonance spectra of compounds of the type $X(C_2H_5)_n$ (spin of $X=\frac{1}{2}$) is perhaps in general more easily carried out by means of "effective" internal chemical shifts, thus reducing the problem to the solution of the A_3B_2 case. On the other hand, if one proceeds in the general manner one has to obtain four quantities—δ_{AB}, J_{AB}, J_{AX}, and J_{BX}—directly from the experimental spectrum. In complicated cases the situation will be almost hopeless. Double irradiation[14] techniques may be used advantageously in these systems for simplification of the experimental spectra as well as identification of the various lines. It will be highly desirable to perform these experiments on the systems studied here and thus check the assignments made above. For instance, if P^{31} nuclei are saturated in $P(C_2H_5)_3$ and one looks at the proton resonance spectrum simultaneously, this spectrum should be of the A_3B_2 type with δ_{AB} and J_{AB} values given in Table III. Baker[2] has performed the double irradiation experiment with $Pb(C_2H_5)_4$ and has noticed the absence of satellite lines due to Pb^{207} $(C_2H_5)_4$ when Pb^{207} is irradiated. Similar experiments on the other compounds of the $X(C_2H_5)n$ type would be interesting.

ACKNOWLEDGMENTS

We wish to thank the staff of the MISTIC computer laboratory of Michigan State University for their valuable cooperation. This work was supported by the U. S. Atomic Energy Commission. We are indebted to the Research Corporation for a grant which made possible the purchase of necessary equipment.

[12] A more detailed treatment of these couplings on the basis of both M. O. and V. B. theories has been given by P. T. Narasimhan and M. Karplus (unpublished).

[13] E. Fermi, Z. Physik **60**, 320 (1930).

[14] J. A. Pople, W. G. Schneider, and H. J. Bernstein, *High Resolution Nuclear Magnetic Resonance* (McGraw-Hill Book Company, Inc., New York, 1959), pp. 160 and 229.

Fractionation of Nitrogen Isotopes between Nitrosonium Salt Solutions and Nitrogen Oxides*

ALFRED NARTEN

Department of Chemistry, Columbia University, New York, New York

(Received October 19, 1960)

Single stage enrichment factors α for the isotope exchange reaction of N^{15} between oxides of nitrogen and solutions of nitrosylsulphuric and nitrosylphosphoric acid have been determined. Single stage equilibration resulted in values of α that decrease from 1.046 for 1*M* to 1.013 for 10.2*M* sulphuric acid in the nitrosylsulphuric acid system, and from 1.042 for 4.7*M* to 1.005 for 14.8*M* phosphoric acid in the nitrosylphosphoric acid system.

INTRODUCTION

THE nitrosonium salts of sulphuric acid ($NO^+HSO_4^-$, "nitrosylsulphuric acid") and phosphoric acid ($NO^+H_2PO_4^-$, "nitrosylphosphoric acid"), when dissolved in aqueous solutions of the acids undergo partial hydrolysis according to the simplified reactions:

$$2NOHSO_4+H_2O\underset{\text{cool}}{\overset{\text{heat}}{\rightleftharpoons}}N_2O_3+2H_2SO_4 \qquad (1a)$$

$$2NOH_2PO_4+H_2O\underset{\text{cool}}{\overset{\text{heat}}{\rightleftharpoons}}N_2O_3+2H_3PO_4. \qquad (1b)$$

The decomposition of the nitrosonium salts is small at low temperatures and low water concentrations of the solutions. Data on the nitrosylsulphuric acid system are available[1] in connection with the lead chamber process for the production of sulphuric acid; no data on the nitrosylphosphoric acid system could be found in the literature.

If the fractionation factor α for the exchange of the nitrogen isotopes, according to

$$2N^{14}OHSO_4+N_2{}^{15}O_3\rightleftharpoons 2N^{15}OHSO_4+N_2{}^{14}O_3 \qquad (2a)$$

$$2N^{14}OH_2PO_4+N_2{}^{15}O_3\rightleftharpoons 2N^{15}OH_2PO_4+N_2{}^{14}O_3, \qquad (2b)$$

is favorable and if the exchange rate of (2a) and (2b) is great enough, an attractive process for the separation of the nitrogen isotopes could be based on reactions (2a) and (2b). Reactions (1a) and (1b) are reported to be reversible, at least at higher acid concentrations[1]; a thermal reflux technique would make the process even more attractive. It is for these reasons that this study has been undertaken.

EXPERIMENTAL

Known amounts of 99% $NOHSO_4$(NOH_2PO_4) were introduced into an equilibration flask (1000 ml). After the flask had been carefully evacuated, measured amounts of aqueous H_2SO_4(H_3PO_4) were added. The equilibration vessel was kept at constant temperature, and the solution was agitated by a magnetic stirrer to provide good contact of the gas and liquid phases. The pressure in the equilibration vessel was read with a Bourdon-type gauge made of glass. After one hour, samples of the gas (2 ml) and liquid (0.5 ml) were collected and processed for mass spectrometer analysis. The nitrogen in the liquid phase was converted to nitric oxide by reduction with mercury[2]; the gas phase was reduced to nitric oxide using selenium.[3] The N^{15}/N^{14} ratio was determined using the 31/30 peaks of nitric oxide.[4] The results are given in Tables I and II.

Experiments were also done to determine the reflux efficiency of a possible exchange unit according to reaction (1a). Equation (1a) is only a rough description of the actual hydrolysis reaction of nitrosylsulphuric acid. At high concentrations of H_2SO_4, NO is oxidized giving NO_2 which will then constitute most of the gas phase. At low acid concentrations, N_2O_3 will react with water to give nitric acid and NO. Nitric acid cannot be converted to gaseous nitrogen oxides by a thermal reflux technique. Even nitrosonium salt solutions in 96% H_2SO_4 will contain appreciable amounts of HNO_3 which cannot be removed from the solution by simply heating the system. Of course, a chemical reflux technique according to[5]

$$2HNO_3+SO_2\rightleftharpoons 3H_2SO_4+2NO \qquad (3)$$

could be employed.

RESULTS AND DISCUSSION

The single stage separation factor α ranges from 1.046 for 1*M* to 1.013 for 10.2*M* sulfuric acid in the nitrosylsulphuric acid system, and from 1.042 for 4.7*M* to 1.005 for 14.8*M* phosphoric acid in the nitrosylphosphoric acid system at room temperature. The heavy isotope will concentrate in the liquid phase.

* Supported in part from a grant from the U. S. Atomic Energy Commission.

[1] L. Gmelin, *Handbuch der Anorganischen Chemie* (Verlag Chemie GMBH, Berlin, Germany, 1936), Syst. No. 4(N), Syst. No. 9(S); F. Seel, in Chemical Society Special Publication No. 10, London, England (1957), p. 7.

[2] G. Lunge and E. Berl, *Chemisch-Technische Untersuchungsmethoden* (Springer-Verlag, Berlin, Germany, 1932), Vols. 1 and 2.

[3] E. Barnes, J. Indian Chem. Soc. **9**, 330 (1932).

[4] W. Kuhn, A. Narten, and M. Thürkauf, Helv. Chim. Acta **42**, 1433 (1959).

[5] T. I. Taylor and W. Spindel, in *Proceedings of the International Symposium on Isotope Separation* (North Holland Publishing Company, Amsterdam, 1958), p. 158.

TABLE I. Single stage separation factors for the nitrosylsulphuric acid system.

H_2SO_4[a]	$NOHSO_4$[a] (moles/liter)	$NOHSO_4$[b]	Temperature (°C)	Pressure (mm Hg)	$\alpha = \frac{(N^{15}/N^{14})\text{liquid}}{(N^{15}/N^{14})\text{gas}}$
10.2	1.0	0.3	21	60	1.014±0.001
			30	100	1.013±0.001
			50	260	1.013±0.001
8.9	1.0	0.08	20	200	1.023±0.001
			30	300	1.021±0.001
			50	550	1.017±0.001
5.0	1.0	0.00	23	700	1.044±0.0005
			35	720	1.043±0.0005
			50	720	1.040±0.0005
1.0	0.02	0.00	25	580	1.044±0.003
			35	600	1.046±0.0005
			50	670	1.045±0.001

[a] Before equilibration.
[b] After equilibration. [See G. A. Hantzsch and K. Berger, Z. anorg. Chemie **190,** 321 (1930).]

TABLE II. Single stage separation factors for the nitrosylphosphoric acid system.

H_3PO_4[a] (moles/liter)	NOH_2PO_4[a]	Temperature (°C)	Pressure (mm Hg)	$\alpha = \frac{(N^{15}/N^{14})\text{liquid}}{(N^{15}/N^{14})\text{gas}}$
14.8	2.0	30	730	1.005±0.001
4.7	1.0	30	730	1.042±0.001

[a] Before equilibration.

The high α at low acid concentrations occurs because most of the gas phase is NO, whereas the low α at high acid concentrations can be ascribed to the fact that most of the gas phase is $NO_2(N_2O_4)$. The same phenomenon was also observed with the HNO_3–NO exchange system of Taylor and Spindel[5] to which the systems discussed in this paper show many analogies. In fact, at low acid concentrations the amount of nitric acid in the liquid phase will be so high that one could speak of an HNO_3–NO system containing sulphuric (phosphoric) acid.

No experiments on the rate of the exchange reaction (2a) have been done. From the mentioned analogy with the HNO_3-NO system the assumption is justified that the exchange will be slow at low acid concentrations and rapid at high acid concentrations. Taylor and Spindel found an optimum concentration of approximately 10*M* HNO_3 for their system; at this concentration the height equivalent to a theoretical plate (HETP) of an HNO_3–NO exchange column packed with 3013 HELIPAK (Podbielniak Inc., Chicago, Ill.) is reported to be 3 cm at a flow rate of 1.6 ml liquid/cm² min.[5] It is highly probable that similar column stage heights can be expected for the systems under consideration.

Since a simple, and therefore desirable, thermal reflux technique cannot be used with the nitrosylsulphuric (nitrosylphosphoric) acid systems, these do not seem to offer any advantages as compared with the HNO_3–NO system, unless the exchange rate is found to be greater (the column stage height lower) than in the HNO_3–NO system. However, the consumption of chemicals for a reflux mechanism according to (3) would be considerably lower than for the HNO_3–NO system, since the major part of the nitrogen in the liquid phase (the nitrosonium part) could still be refluxed by passing the solution through a thermal decomposer. Only the HNO_3 part of the nitrogen would have to be refluxed chemically.

Still, the enrichment of N^{15} in a countercurrent unit of $NOHSO_4/H_2SO_4$ and NO/NO_2 would be an attractive process if the N^{15} cascade were attached to a lead chamber plant for the production of sulphuric acid. In this case, all the chemicals needed for the N^{15} production could be taken from and recycled to the chamber units. The cost of the enriched N^{15} would only be determined by the construction and maintenance costs of the N^{15} cascade. Such a process is, of course, limited by the production capacity of the lead chamber plant.

ACKNOWLEDGMENT

The author is indebted to Professor T. I. Taylor for helpful discussions and for his continued interest in this work.

Letters to the Editor

THE Letters to the Editor section is subdivided into three parts entitled Communications, Comments and Errata, and Notes. These three sections are all subject to the same limitations on length. The textual material of each Letter is limited to a number of words equal to 950 minus the following; (a) 200 words for each average-sized figure; (b) 50 words for each displayed equation; (c) 7 words for each line of table including headings and horizontal rulings. No proof will be sent to the authors of "Communications" and "Comments and Errata." Proof will be sent to the authors of "Notes." The publication charge for Letters is $30 per page, with a minimum of $30 per Letter. If honored, the Institution will be entitled to 100 reprints without covers. See issues of May–September, 1957, for descriptions of categories.

Communications

Energy Transfer between Triplet States Detected by Electron Spin Resonance Spectroscopy

J. B. FARMER, C. L. GARDNER, AND C. A. MCDOWELL

Department of Chemistry, University of British Columbia, Vancouver, B. C., Canada

(Received January 16, 1961)

ELECTRON spin resonance due to a triplet state of a molecule was first detected by Hutchison and Mangum.[1] They observed the resonance due to the triplet state of naphthalene in a uv-irradiated single crystal of solid solutions of this compound in durene. More recently van der Waals and de Groot[2] confirmed these results but also were able to observe a magnetic resonance due to the triplet state of naphthalene in a uv-irradiated rigid glass solution in glycerol at 77°K. The resonance which van der Waals and de Groot observed was at a much lower magnetic field than that studied by Hutchison and Mangum. These latter workers observed the resonance corresponding to transitions between neighboring sublevels of the triplet. That observed by van der Waals and de Groot was due to transitions between the highest and lowest sublevels and corresponded to the $\Delta m=2$ transition. De Groot and van der Waals[3] have also observed the electron spin resonance due to the triplet states of quite a number of other polynuclear hydrocarbons in uv-irradiated rigid glass solutions at 77°K. They were able to determine the zero-field splittings from the spectra. In the case of naphthalene they found good agreement between their value for the zero-field splitting and that obtained by Hutchison and Mangum[1] from experiments on orientated single crystals.

These new results of de Groot and van der Waals[3] open up many possibilities. We have recently studied the magnetic resonance of molecules in triplet states in glassy solutions at 77°K and have used this technique to study the exchange of energy between the triplet states of benzophenone and naphthalene in a rigid E.P.A. solution at 77°K.

In our experiments the solutions of benzophenone and naphthalene ($10^{-2}-10^{-1}$ M) in E.P.A. were outgassed and sealed in thin walled 4 in. diameter quartz tubes. The rigid glass solutions at 77°K were photolysed with the tube in a quartz Dewar vessel inserted in a resonant cavity operating in the TE_{012} mode. The experiments were performed using what was essentially a Varian 100 kc modulation esr spectrometer employing a 6-in. magnet. Light of ~366-mμ wavelength from a water cooled G.E.C. AH6 mercury arc was used for the uv-irradiation. A Schott & Company UV-JL interference filter with a 9-mμ half-width and a 38% transmission coefficient at 365 mμ was used to isolate the desired radiation wavelength. Light of this wavelength lies outside the absorption band of naphthalene and also is beyond the longest wavelength which can excite the naphthalene fluorescence and phosphorescence.[4] We were unable to observe any resonance due to the triplet state when a 5×10^{-2} M solution of naphthalene was irradiated at 77°K with light of wavelength 366 mμ. Using the unfiltered radiation from the AH 6 lamp, the resonance due to the triplet state of the naphthalene molecule under the same conditions could be readily observed.

The phosphorescence spectrum of benzophenone which is attributed to transitions from the first triplet state to the ground state is readily excited by radiation of 366 mμ wavelength. Gilmore, Gibson, and McClure[5] determined the quantum yield of the benzophenone phosphorescence at 77°K in E.P.A. (when excited by light of wavelength 366 mμ) to be 0.8. Electron spin resonance due to the triplet state of the benzophenone could not be detected when rigid solutions of this compound in E.P.A. were irradiated at 77°K. We did, however, detect the resonance which in earlier work[6] was attributed to the benzophenone ketyl radical, presumably formed by the triplet state of the benzophenone abstracting a hydrogen atom from one of the components of the E.P.A. solvent.

When mixtures of benzophenone and naphthalene in E.P.A. at 77°K were irradiated with light transmitted by the above filter at 366 mμ, we were readily able to observe the electron spin resonance due to the triplet state of naphthalene. At the same time a much reduced esr spectrum due to the benzophenone ketyl radical was also observed.

These results, therefore, prove conclusively that there is a transfer of energy from the benzophenone molecules which have been excited to their triplet states by the radiation of wavelength 366 mμ, to the naphthalene molecules, thereby exciting these to their triplet states. Furthermore, our work confirms the views of Terenin

and Ermalov[7] who concluded from studies of the phosphorescence spectra of mixtures of benzophenone (and other donors) and naphthalene in ether plus ethanol at 77°K that there was a transfer of energy between the triplet states of these molecules in the rigid glass solutions.

Our results also suggest a possible explanation of the observations of Ferguson and Tinson[8] who found that the phosphorescence spectrum of benozphenone in petroleum ether at −180°C is replaced by another at longer wavelengths when the concentration is increased from 10^{-4} to $10^{-2}M$. These workers attributed their results to energy transfer to the triplet state of benzophenone. As we have shown that the triplet state of this molecule reacts very rapidly at 77°K with the components of E.P.A. to form a ketyl radical, it is possible that the second phosphorescence spectrum observed by Ferguson and Tinson comes from the ketyl radical or some resulting compound.

We wish to thank the National Research Council of Canada for generous grants in support of this research.

[1] C. A. Hutchison, Jr., and B. W. Mangum, J. Chem. Phys. **29,** 952 (1958); **34,** 908 (1961).
[2] J. H. van der Waals and M. S. de Groot, Mol. Phys. **2,** 233 (1959).
[3] M. S. de Groot and J. H. van der Waals, Mol. Phys. **3,** 190 (1960).
[4] E. Clar, Spectrochim. Acta **4,** 116 (1950).
[5] E. H. Gilmore, G. E. Gibson, and D. S. McClure, J. Chem. Phys. **20,** 829 (1950); **23,** 399 (1955).
[6] D. H. Henderson and C. A. McDowell (unpublished).
[7] A. Terenin and V. Ermalov, Doklady Akad. Nauk S.S.S.R. **85,** 547 (1952); Trans. Faraday Soc. **52,** 1042 (1956).
[8] J. Ferguson and H. J. Tinson, J. Chem. Soc. **1952,** 3083.

Sixth Virial Coefficients for Gases of Parallel Hard Lines, Hard Squares, and Hard Cubes

WILLIAM G. HOOVER* AND ANDREW G. DE ROCCO

Department of Chemistry, University of Michigan, Ann Arbor, Michigan

(Received January 9, 1961)

THE virial equation of state can be written as

$$\beta p = \sum_{1}^{\infty} B_n \rho^n,$$

where $\beta = 1/kT$, ρ is the number density, and the set of coefficients $\{B_n\}$ are the virial coefficients. The topological graphs are known which permit the calculation of $\{B_n\}$ up to B_7,[1] if the related integrals of the f_{ij} products can be accomplished. Because the integrals are formidable for realistic choices of the potential, simpler models have been introduced to effect the integrals. The simplest nontrivial case is that of parallel hard lines, squares, and cubes.[2] The hard-cube potential has the property that any integral I_n of a product πf_{ij} can be written as $I_1|I_1|^{n-1}$, where n is the dimensionality of the interacting figures; this feature of the problem was clearly noted by Zwanzig.[3] To compute the set $\{B_n\}$ one need only evaluate the pertinent set of integrals in one dimension; the extension to higher dimensions involves only mechanical effort. To calculate B_2 and B_3, only one integral must be done. For B_4, B_5, and B_6 one needs to accomplish three, 10, and 56 integrals, respectively.

We have succeeded in computing B_6 by a straightforward but tedious method, the details of which will be published. We present in Table I the results for B_6

TABLE I. Virial coefficients for lines, squares, and cubes.

	Lines	Squares	Cubes
B_1	1	1	1
B_2	1	2	4
B_3	1	3	9
B_4	1	11/3	34/3
B_5	1	67/18	455/144
B_6	1	121/40	−2039/108
B_1	1.0000	1.0000	1.0000
B_2	1.0000	1.0000	1.0000
B_3	1.0000	0.7500	0.5625
B_4	1.0000	0.4583	0.1771
B_5	1.0000	0.2326	0.0123
B_6	1.0000	0.0945	−0.0184

and the lower coefficients (previously known), for lines of length σ, squares of area σ^2, and cubes of volume σ^3. The first set of values corresponds to the choice of σ^n for the n-dimensional B_2; the second set uses $2^{n-1}\sigma^n$ for the corresponding B_2 (both sets are employed in the literature). It is interesting to note that B_6 is negative in three dimensions, a result anticipated by Temperley on the basis of his extension of the Zwanzig calculations to higher dimensions.[4] At this point the earlier work deserves some further comment:

(1) Tonks[5] calculated the equation of state for the one-dimensional case, but the fact that Tonks did not employ the cluster expansion prevents any extension of his results to higher dimensions.

(2) Geilikman[2] obtained B_2, B_3, and B_4 for cubes, although, as he later pointed out, the result for B_4 was incorrect.

(3) Zwanzig,[3] using the results of Riddell and Uhlenbeck,[6] computed the first five coefficients for the case described in this letter. Zwanzig agrees that the inequalities in Helmholtz energy for systems of cubes and spheres used in his paper[3] to limit the virial coefficients for spheres do not seem sufficient for this purpose.[7] If his treatment had been rigorous our result would imply a negative B_6 for hard spheres, in contrast to the suggestion of Alder and Wainwright[8] that both B_6

and B_7 for hard spheres are positive. Whether or not B_n° and $B_n^{\square}$ have the same sign is still an open question.

(4) As noted earlier Temperley found that B_4 was negative in five dimensions and B_5 negative in four dimensions. It is clear that B_5 will eventually become positive again if a sufficient number of dimensions is employed. His later statement[9] that Ford found B_4 and B_7 as negative for spherical molecules is without foundation, since the Gaussian model employed by Ford does not correspond to any potential.

(5) Domb[10] presented equations of state for "squares" and "cubes" in which B_4, B_5, and B_6 were negative. These were presumably approximations derived from an Ising model, but none of the coefficients beyond the first agree with the exact results for hard squares and hard cubes.

We will present the detailed calculation of B_6 in the near future. We are now actively concerned with the calculation of B_7 and the analog of the radial distribution function for such systems.

* Proctor and Gamble Predoctoral Fellow, 1960–1961.

[1] G. W. Ford, unpublished dissertation, University of Michigan, Ann Arbor, Michigan, 1954; $n=7$.
[2] B. T. Geilikman, Proc. Acad. Sci. U.S.S.R. **70,** 25 (1950).
[3] R. W. Zwanzig, J. Chem. Phys. **24,** 855 (1956).
[4] H. N. V. Temperley, Proc. Phys. Soc. (London) **70B,** 536 (1957).
[5] L. Tonks, Phys. Rev. **50,** 955 (1936).
[6] R. J. Riddell, Jr. and G. E. Uhlenbeck, J. Chem. Phys. **21,** 2056 (1953).
[7] R. W. Zwanzig (private conversation).
[8] B. J. Alder and T. E. Wainwright, J. Chem. Phys. **33,** 1439 (1960).
[9] H. N. V. Temperley, Nuovo cimento Suppl. **9,** Ser. 10, 163 (1958).
[10] C. Domb, Nuovo cimento Suppl. **9,** Ser. 10, 9 (1958).

Infrared Spectrum of Diimide*

EDMUND J. BLAU, BERNARD F. HOCHHEIMER, AND HILBERT J. UNGER

Applied Physics Laboratory, The Johns Hopkins University, Silver Spring, Maryland

(Received December 27, 1960)

BANDS belonging to the infrared spectrum of the diimide (N_2H_2) molecule have been observed. This molecule has been previously identified by Foner and Hudson[1] by mass spectrometry as a product of a radio-frequency discharge though gaseous hydrazine. We have used the method of preparation of Foner and Hudson. Our experimental arrangement permits deposition of the discharge products on a cold infrared-transparent window and simultaneous sampling of the discharge products for analysis on the mass spectrometer. A dry-ice trap immediately follows the discharge to remove hydrazine. The cryostat is very similar to one described by Wagner and Hornig.[2] It has a clear aperture of 35 mm and fits easily into the sample space of the modified Perkin-Elmer model 12B spectrometer used in these experiments. With liquid nitrogen as coolant, a calcium fluoride window reached a steady temperature of 82°K in 15 min and a sodium chloride window 86°K in a similar time.

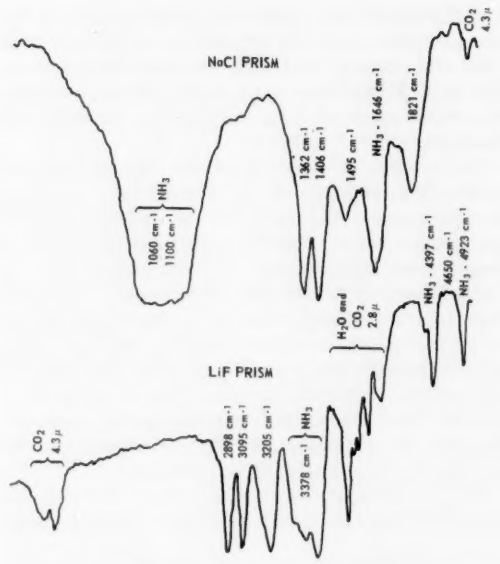

FIG. 1. Infrared spectrum of diimide.

If hydrazine vapor is admitted into the evacuated system, it condenses completely in the dry-ice trap and nothing deposits on the cold window of the cryostat. When the discharge is started, the pressure following the dry-ice trap increases to between 100 and 1000 μ, depending on the discharge power. A yellow deposit, which is stable at least 2 to 3 hr at temperatures below 120°K, forms on the cold window.

Analysis of the discharge products with the mass spectrometer shows the presence of nitrogen, ammonia, and diimide. The undecomposed hydrazine is completely collected in the dry-ice trap as indicated by its absence in the mass spectrometer. In some experiments a trace of mass 45 (N_3H_3) was detected. By varying the hydrazine flow rate and the discharge power, it was possible to vary the ratio of diimide to ammonia from below 1% to about 20%.

The spectrum of the deposit as recorded with the NaCl and LiF prisms is shown in Fig. 1. The rock salt region was examined as far as 15 μ, but no bands were found beyond those shown in the tracing. In addition to the bands of solid ammonia,[3] the spectrum includes

several bands which cannot be correlated with any known compound likely to be present (including hydrazine, hydrazoic acid, ammonium azide, dihydrazonium ion, ammonium ion, nitric oxide, nitrous oxide, dinitrogen trioxide, dinitrogen tetroxide, dinitrogen pentoxide, or nitrite ion). These bands, which are attributed to diimide, occur at 1362, 1406, 1495, 1821, 2898, 3095, 3205, and 4650 cm^{-1}, those at 1495, 1821, and 4650 cm^{-1} being the weakest. Under varying conditions, the intensities of the bands in the LiF region (2898, 3095, and 3205 cm^{-1}) relative to the ammonia band at 3378 cm^{-1} agree qualitatively with the diimide-ammonia ratios obtained with the mass spectrometer. When either hydrazine or ammonia is deposited, the deposit is white and the bands listed above do not appear.

The conclusion that the new bands are associated with diimide is strengthened by the behavior of the deposit when the cryostat warms up. Above 120°K the color of the deposit gradually changes from yellow to white; at the same time the pressure rises. The diimide and ammonia absorption bands disappear and are replaced by bands of solid hydrazine. These bands persist almost up to room temperature and are the only spectral feature observed above 180°K. During warmup, diimide and ammonia are detected in the mass spectrometer (with a maximum rate of evolution at about 160°K and 170°K, respectively). In addition, nitrogen is evolved and, above 220°K hydrazine. Since nitrogen and hydrazine are not present in the original deposit, they must have been formed during warmup from the materials present on the window. Any reasonable reaction which can be written to account for the formation of hydrazine from diimide would also lead to the production of nitrogen.

The identification of at least some of the observed bands with diimide is not unreasonable. The band at 3205 cm^{-1} almost certainly indicates a compound containing an NH bond, and the band at 1406 cm^{-1} can be assigned to the NN stretching mode, in agreement with the conclusions of Lefevre and Werner[4] that the stretching frequency of the azo group occurs in this region. Work is continuing on this investigation, and a detailed analysis of the spectrum will accompany a later report.

The authors express their appreciation to R. L. Hudson for carrying out the mass spectrometer measurements and to S. N. Foner and J. T. Massey for helpful discussions. A. I. Mahan participated in some of the early work on optical problems.

* Work supported by Bureau of Naval Weapons, Department of the Navy.

[1] S. N. Foner and R. L. Hudson, J. Chem. Phys. **28**, 719 (1958).
[2] E. L. Wagner and D. F. Hornig, J. Chem. Phys. **18**, 296 (1950).
[3] F. P. Reding and D. F. Hornig, J. Chem. Phys. **19**, 594 (1951).
[4] R. J. Lefevre and R. L. Werner, Australian J. Chem. **10**, 26 (1957).

Measurement of Absolute Infrared Absorption Intensities in Crystals

J. L. Hollenberg and David A. Dows

Department of Chemistry, University of Southern California, Los Angeles, California

(Received December 27, 1960)

VERY few measurements of absolute absorption intensities have been made on the infrared spectra of crystals because the small sample thicknesses required are difficult to prepare and to measure. We are developing a method of measuring sample thickness which is of sufficient accuracy for infrared intensity work, and are applying it to the study of intensities in molecular crystals.

The method is based on the observation of interference fringes in the transmitted light as the sample is condensed in a thin film on a substrate. Our low-temperature cell is of conventional design, and contains a silver chloride window which can be cooled to any convenient low temperature. The optical transmission of the cell and cold silver chloride window is recorded as a function of time (at a known fixed wave number ν_0) while the compound to be studied is sublimed into the cell, where it condenses to form a solid film. The choice of silver chloride is dictated by its refractive index of 2.0. Since most molecular crystals have indices of refraction roughly 1.5, they act as efficient antireflection coatings for the silver chloride, giving intense fringes. If N is the number of fringes recorded and n_0 the index of refraction of the sample at the observation wave number ν_0 (in the near infrared), then the usual thin-film interference formula gives the thickness of the film as $d=N/(2n_0\nu_0)$.

The absolute intensities are defined by the formula

$$B=(1/nd)\int_{\text{band}} \ln(T_0/T)\,d\nu,$$

where n is the number of millimoles of sample per cubic centimeter, d is the thickness, T and T_0 are the transmissions with and without the sample, and ν is the frequency (wave number units).

In using this method one must know the values of n_0 and of the density of the film. We feel that the films we prepare are normally characteristic of the bulk material (they are about 1 to 10 μ thick) and that surface effects are not important. Thus densities are commonly available, and the index of refraction can be estimated by applying corrections for dispersion and density to any values (usually for the liquid in the visible region) available. These corrections are usually less than 10%, so they introduce less error than the necessary integrations.

To illustrate the results obtainable with this method, we give in Table I the intensities of the (687, 1036, and 3036–3067–3090) wave number bands of benzene,

measured near 77°K. For comparison we also show the results of Person and Swenson for these bands.[1] Our results are based on 12 and 6 independent measurements, respectively, for the 1036 and 3067 regions, in which the sample thickness ranged from 0.70–3.82 μ (1036 region) and 1.58 to 3.81 μ (3067 region). The 680 wave number value is the result of only three measurements thus far. The errors assigned are the maximum scatter of our data. Person and Swenson's errors are their estimates of their accuracy.

TABLE I. Absolute intensities in crystalline benzene. Entries are in darks=cm mM^{-1}.

Mode	B (P and S)	B (this work)	B (liquid)[a]	B (gas)[b]
ν_{11} (687)	3500±650	9100±1200	9500	8780
ν_{20} (1036)	670±90	1390±140	1090	880
ν_{13} (3067)	200	278±30	550	
ν_{18} (3036+) (3090)	950±200	1950±385	4440	5980
ν_{13} (3036+) (3067+) $+\nu_{18}$ (3090)	1150	2230±400	4990	7560

[a] I. C. Hisatsune and E. S. Jayadevappa, J. Chem. Phys. **32,** 565 (1960).
[b] H. Spedding and D. H. Whiffen, Proc. Roy. Soc. (London) **A238,** 245 (1956).

The relative values of our results agree with those of Person and Swenson, but the absolute values are higher by a factor of about two. Recent data of Person[2] on reflection intensities are in reasonable agreement with our values.

There is some question as to whether annealing the sample prepared by sublimation onto a cold window will change the intensity. We have made several temperature-dependence studies on the 1036 cm^{-1} band, and one on the 687 cm^{-1} band and find an indication that warming and cooling again to 77°K may change the intensity, though probably not by as much as 10%. The temperature-dependence results themselves are of interest; the intensities at 63°, 77°, and 160°K are the same to within about 5%. This result is in disagreement with the conclusions of Mair and Hornig[3] and of Olsen[4] and of Fordemwalt,[5] all of whose results were for a larger temperature range up to about 0°C. Our resolution in the 1036 cm^{-1} region is about 1–1.5 wave numbers, considerably better than that of previous investigators, and we observed changes in linewidths with temperature which may have affected apparent intensities. It is probable, too, that changes in intensity *do* occur in the temperature region between 160°K and the melting point, since the band contour is known[4] to change greatly in this region.

We are making further measurements on benzene and on several other compounds in an effort to better estimate the reliability and accuracy of these intensities and to check the many variables involved. The results of these studies will be published at a later date in complete form.

We wish to thank the National Science Foundation for a fellowship to one of us (JLH) and for support of the project which includes this work. Professor W. B. Person has kindly communicated results from theses under his direction.

[1] W. B. Person and C. A. Swenson, J. Chem. Phys. **33,** 233 (1960).
[2] W. B. Person (private communication).
[3] R. D. Mair and D. F. Hornig, J. Chem. Phys. **17,** 1236 (1949).
[4] D. A. Olsen, thesis, State University of Iowa, Ames, Iowa, 1960.
[5] J. N. Fordemwalt, thesis, State University of Iowa, Ames, Iowa, 1960.

Comments and Errata

Solvent Effects in Nuclear Magnetic Resonance

R. J. ABRAHAM

National Physical Laboratory, Teddington, Middlesex, England

(Received October 28, 1960)

BUCKINGHAM *et al.*,[1] have discussed the variation of the proton chemical shifts of methane and acetonitrile in various solvents, in terms of Van der Waals, anisotropic, and polar interactions.

The chemical shifts were measured using an external reference and then correcting for the solvent bulk susceptibility. This procedure is completely rigorous, but a more comprehensive way of examining these results is to compare directly the chemical shifts of methane and acetonitrile in the same solvents. This is shown in Table I. The first two columns give the results of the work cited in footnote 1 for all the solvents in which both solutes were measured. The third column shows the results of subtracting the methane shift from the acetonitrile, and in the fourth column this difference is adjusted to zero for the solvent *n*-hexane, i.e., we assume that the difference of the chemical shifts of acetonitrile and methane in *n*-hexane is due to only the different chemical nature of the solute protons. The remaining results in column four thus show the influence of the solvent on the solute shifts. The obvious explanation for these low-field shifts is that these are due to the reaction field[2] of the solvent when acetonitrile is the solute.

Using the value of 1.34 for the refractive index of

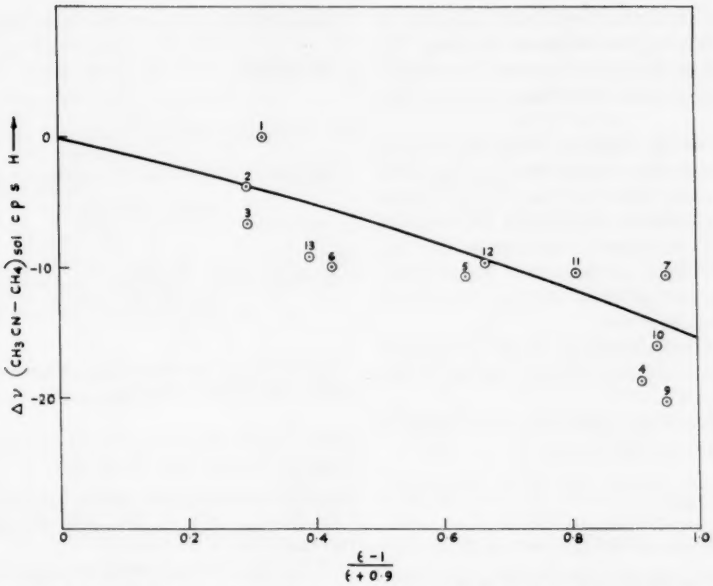

FIG. 1. The difference in the chemical shift values of acetonitrile and methane in various solvents (relative to the difference in *n*-hexane) against $(E-1)/(E+0.9)$.

acetonitrile Eqs. (13) and (14) of the work cited in footnote 1 give

$$E^{\text{cps}} = -11[(E-1)/(E+0.9)] - 4.3[(E-1)/(E+0.9)]^2.$$

In Fig. 1 the values in the last column of the table are plotted against $(E-1)/(E+0.9)$, with the line shown calculated from the above equation.

The agreement is reasonably good for all the solvents, except benzene. Thus when one removes the specific solvent fields by referring to the methane chemical shift in that solvent, halogenated compounds, strongly anisotropic nitro compounds, and aromatic compounds all behave as expected on the reaction field theory picture. The "normal" behavior of the halogenated solvents on this picture may be contrasted with their anomalous behavior as discussed in the work cited in footnote 1. This suggests that the very large bulk susceptibility corrections may be the least accurate part of the corrected chemical shift values in these compounds. The "normal" behavior of the anisotropic nitro compounds is also a reasonable result, as the magnetic field due to the solvent anisotropy would be expected, for these similar solutes, to be independent of the solute. This has been demonstrated to be the case for aromatic solvents.[3]

However the benzene result on this picture is completely anomalous. Here there is a shift of approximately 1 ppm *in excess* of the normal high field shift due to the aromatic ring current.[3] Such a shift can only be accounted for by a specific solvent-solute interaction. Very similar behavior has been observed for chloroform in aromatic solvents, e.g., the chloroform signal moves approximately 1.5 ppm to high field on dissolving chloroform in mesitylene.[4] This has been explained as due to association of the chloroform with

TABLE I. Proton chemical shifts (in cps at 60 Mc) of acetonitrile and methane in various solvents (relative to chloroform external reference).[a]

Solvent	Chemical shift: Acetonitrile	Methane	Ac-Me	
1. *n*-Hexane	358.7	452.9	−94.2	0
2. *trans*-Butene 2	371.3	469.4	−98.1	−3.9
3. *cis*-Butene 2	367.3	468.2	−100.9	−6.7
4. Acetone	357.0	469.9	−112.9	−18.7
5. Ethyl ether	353.2	458.1	−104.9	−10.7
6. Triethylamine	344.8	449.0	−104.2	−10.0
7. Acetonitrile	344.8	449.6	−104.8	−10.6
8. Benzene	434.2	470.5	−36.3	+57.9
9. Nitrobenzene	364.8	479.3	−114.5	−20.3
10. Nitromethane	366.6	476.8	−110.2	−16.0
11. CH_2Cl_2	320.9	425.5	−104.6	−10.4
12. $CHCl_3$	319.2	423.1	−103.9	−9.7
13. CCl_4	323.8	427.2	−103.4	−9.2

[a] See work cited in footnote 1.

the benzene ring in which the C—H bond is normal to the benzene ring with the proton nearest the ring. This suggests strongly that the methyl protons in acetonitrile are in a similar position with respect to the benzene ring.

This breakdown of the chemical shift results does show that the problem of explaining the chemical shifts of this particular polar solute in the solvents given becomes merely the problem of explaining the methane shift in the same solvent, plus the reaction field effect, and in one case specific solvent-solute interactions. It would be of interest to know whether this result applies to other polar molecules.

I would like to acknowledge the many discussions with Dr. T. Schaefer and Dr. P. Diehl, out of which this note originated.

This paper is published by permission of the Director of the National Physical Laboratory.

[1] A. D. Buckingham, T. Schaefer, and W. G. Schneider, J. Chem. Phys. **32,** 1227 (1960).
[2] A. D. Buckingham, Can. J. Chem. **38,** 300 (1960).
[3] A. A. Bothner-By and R. E. Glick, J. Chem. Phys. **26,** 1651 (1957).
[4] J. A. Pople, W. H. Schneider, and H. J. Bernstein, *High-Resolution Nuclear Magnetic Resonance* (McGraw-Hill Book Company, Inc., New York, 1959), p. 430.

Solvent Effects in Nuclear Magnetic Resonance

A. D. Buckingham,* T. Schaefer,† and W. G. Schneider

Division of Pure Chemistry, National Research Council, Ottawa, Canada

(Received December 21, 1960)

THE modification suggested by Dr. Abraham[1] for analyzing the data reported in footnote 2 is a very useful one and does serve to isolate the "reaction field" effects in a straightforward manner. In practice this method can be applied directly by using the nonpolar solute, in this case CH_4, as an internal reference in the same solution containing the polar solute. One of the present authors has employed this method in a recent investigation of the proton shifts of methyl acetylene in various solvents, in the course of which several measurements on CH_3CN were also carried out. In these measurements (at a fixed frequency of 60 Mc) neopentane, in a concentration of 2 mole %, was added to the 5 mole % acetonitrile solutions. The proton resonance shifts of the acetonitrile in neopentane, benzene, and acetone solutions are shown in Fig. 1. On the assumption that neopentane may be regarded as an inert solvent, it is apparent that in the benzene solution there is an excess shift of the acetonitrile

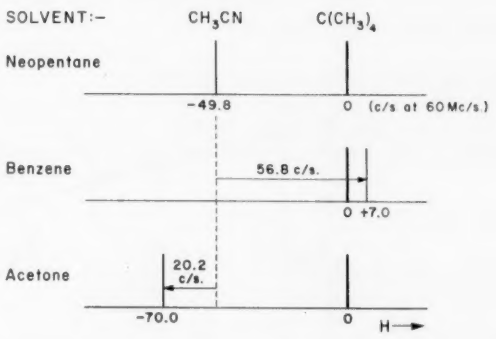

FIG. 1. Proton resonance shifts of acetonitrile in neopentane, benzene, and acetone solutions.

proton resonance to *high* field of 56.8 cps and in the acetone solution an excess shift to *low* field of 20.2 cps. This confirms the results obtained relative to the CH_4 proton shift by the previous method using an external $CHCl_3$ reference.[1,2]

If the nonpolar reference solute molecule neopentane is assumed to have approximately the same molecular volume as the CH_3CN solute molecule, and if differences in shape are ignored, the two solutes may be expected to experience the same magnetic environment in a common solvent. Effects due to the bulk diamagnetic susceptibility of the solvent, as well as effects due to its diamagnetic anisotropy would then be absent. The "van der Waals shift" for the neopentane and acetonitrile molecules is probably comparable in magnitude and hence the residual observable shift might be considered to constitute the "reaction-field" effect. The large residual positive shift oberved in benzene clearly must have another origin. A specific molecular interaction between acetonitrile and benzene, as suggested by Abraham, is a possible explanation. But if the nature of this interaction is of the hydrogen-bonding type similar to that of chloroform,[3] then in addition to the excess shift to high field in benzene, a low-field shift in acetone may be anticipated. In this case the low-field shift in acetone actually observed could not be attributed solely to a "reaction-field" shift. Another possible explanation of the observed anomaly in the benzene solvent may be in terms of the molecular shape of the solute molecule. The possibility exists that in a medium of disk-shaped benzene molecules, the acetonitrile molecules experience a different magnetic environment from that of a spherical neopentane reference molecule. In this connection it may be relevant to mention that we have also observed proton shifts in propionitrile and acrylonitrile in benzene whose magnitudes (~50 cps) are comparable to those of acetonitrile. The question of molecular shape also enters in these examples, but the possibility of a specific molecular interaction, either of a hydrogen

bonding or charge-transfer type, cannot be excluded at present. Further investigations on the nature of the solvent effects in these and related systems are in progress.

* Permanent address: Inorganic Chemistry Laboratory, University of Oxford, Oxford, England.
† Permanent address: Chemistry Department, University of Manitoba, Winnipeg, Canada.

[1] R. J. Abraham, J. Chem. Phys. **34,** (1961).
[2] A. D. Buckingham, T. Schaefer, and W. G. Schneider, J. Chem. Phys. **32,** 1227 (1960).
[3] J. A. Pople, W. G. Schneider, and H. J. Bernstein, *High-Resolution Nuclear Magnetic Resonance* (McGraw-Hill Book Company, Inc., New York, 1959), pp. 402, 428.

Coupled Anharmonic Vibrations and Spectral Band Broadening

ROBIN S. MCDOWELL*

Spectroscopy Laboratory, Massachusetts Institute of Technology, Cambridge, Massachusetts

(Received December 27, 1960)

RECENTLY Frisch and Vidale[1] proposed a classical model for hydrogen-bonded systems according to which the observed broadening of the vibrational spectral bands of such systems arises from the precession of coupled anharmonic vibrations. The substitution of reasonable parameters for O—H···O bonds in their expressions led to an estimated broadening of 32 cm^{-1} for the O—H stretching vibration. It has been pointed out[2] that this value is sufficiently less than the amount of broadening observed for such systems to suggest that this mechanism makes only a slight contribution to bandwidth. Unfortunately two-dimensional errors in Frisch and Vidale's paper make coupling seem less important than it is.

In their model of the A—H···B bond, where B is held fixed, the weak bond connecting H and B is described by the anharmonic potential $V_{HB}=(k_{HB}/2)y_H^2+(\alpha/3)y_H^3$, where y_H is the displacement of the proton and k_{HB} is the force constant associated with the H···B bond. (The anharmonic force constant α is difficult to evaluate properly; Frisch and Vidale obtain an approximate value by requiring the cubic potential function to give a reasonable value for the dissociation energy of the hydrogen bond. This approximation depends upon the behavior of the curve at some distance from the potential minimum, however, and not too much reliance should be placed on the value of α obtained.) The Hamiltonian of this system is

$$H=\tfrac{1}{2}[\dot{x}_A^2+\dot{x}_H^2+\nu_A^2x_A^2+\nu_H^2x_H^2-2Cx_Ax_H+\tfrac{2}{3}\gamma x_H^3],$$

where $x_i^2=m_iy_i^2$, $\nu_A^2=k_{AH}/m_A$, $\nu_H^2=(k_{AH}+k_{HB})/m_H$, $C=k_{AH}/(m_Am_H)^{\frac{1}{2}}$ and $\gamma=\alpha/(m_H)^{\frac{1}{2}}$. The equations of motion of the coupled oscillators are then given correctly by Frisch and Vidale's Eqs. (2); in obtaining these equations, however, the authors erroneously made the substitution $\gamma=\alpha/m_H$.

Solution of the equations of motion by the methods of nonlinear mechanics[1] gives a broadening $\Delta\bar{\nu}_H=2|\gamma\beta_2^2\beta_1|A_1/2\pi c\omega_H$ [cf. Eq. (21) of work cited in footnote 1] where the β_i are the normalized coefficients of the unperturbed normal coordinates $\xi(t)$, $\eta(t)$: $x_H(t)=\beta_1\xi+\beta_2\eta$; ω_H is the harmonic frequency ($\alpha=0$) of the A—H vibration; and A_1 is the amplitude of the normal coordinate $\xi(t)$. It is important to note that A_1 has the units of ξ and x ($g^{\frac{1}{2}}$ cm) rather than of y(cm), as is assumed by Frisch and Vidale; to a good approximation, $A_1=A_1'(m_A)^{\frac{1}{2}}$, where A_1' is the linear amplitude of vibration of the H···B bond, which Frisch and Vidale calculate to be 0.26 a.u. Correction of these two errors will change their numerical result by the factor $(m_A/m_H)^{\frac{1}{2}}=4.25$, giving a bandwidth of 136 cm^{-1}. This numerical result is in better agreement with the observed bandwidths of hydrogen-bonded compounds and suggests that this approach[1] may have some merit. Quantitative application to particular hydrogen-bonded systems is limited, however, by its classical nature and by the difficulty of evaluating α.

It should be noted that Gross and Val'kov[3] have found evidence for strong anharmonicity of the low-frequency vibration in the Raman spectra of a number of hydrogen-bonded compounds.

* Present address: Los Alamos Scientific Laboratory, University of California, Los Alamos, New Mexico.

[1] H. L. Frisch and G. L. Vidale, J. Chem. Phys. **25,** 982 (1956).
[2] C. G. Cannon, Spectrochim. Acta **10,** 341 (1958).
[3] E. F. Gross and V. I. Val'kov, Izvest. Akad. Nauk S.S.S.R., Ser. Fiz. **14,** 426 (1950); Doklady Akad. Nauk S.S.S.R. **67,** 619 (1949); **68,** 473, 1013 (1949); **74,** 453 (1950).

Comment on the Calculation of Zero-Field Splittings

R. MCWEENY

Quantum Chemistry Group, University of Uppsala, Uppsala, Sweden
and
Departments of Mathematics, Physics, and Chemistry, University College of North Staffordshire, England

(Received November 28, 1960)

A RECENT note[1] dealt with the general theory of electron spin-spin coupling and concluded with a brief numerical application to the phosphorescent triplet state of naphthalene, in which the integrals were reduced using crude approximations. Dr. J. H. van

der Waals has drawn my attention to the difficulty of evaluating such integrals more rigorously owing to the occurence of singularities. It was pointed out[1] that the integral

$$I_x=\int (x_{12}^2/r_{12}^5)Q_{ca}(1,2;1,2)dv_1dv_2,$$

where Q_{ca} is the "coupling anisotropy function,"[2] is without singularities because of the double antisymmetry which makes Q_{ca} vanish like r_{12}^2 for $r_{12}\to 0$. This property is completely general but is lost in the LCAO reduction of the integral unless the terms are suitably grouped. It may be preserved by writing the LCAO approximation in the form [see Eq. (9) and (11) of the work cited in footnote 1]

$$Q_{ca}(1,2;1',2')=\tfrac{1}{2}\sum_{ijkl}Q_{1ik}Q_{1jl}\times[\phi_i(1)\phi_j(2)-\phi_j(1)\phi_i(2)]\times[\phi_k(1')\phi_l(2')-\phi_l(1')\phi_k(2')]^*.$$

In the most general LCAO form (configuration interaction admitted) $Q_{1ik}Q_{1jl}$ would simply be replaced by the more general coefficient μ_{ijkl}. *Every term* in the expansion then has the required double antisymmetry, which is characteristic of Q_{ca} not only for triplet states but whenever the function exists (i.e., $S\neq 0$).

Reduction along the lines of the work cited in footnote 1 leads to identical results [see Eq. (11)] provided AO integrals such as $\gamma_{i\mathfrak{g}}{}^{\beta}{}_{7}$ are reinterpreted as

$$\gamma_{ik}{}^{(x)}=\tfrac{1}{2}\int (x_{12}^2/r_{12}^5)[\phi_i(1)\phi_k(2)-\phi_k(1)\phi_i(2)]^2dv_1dv_2.$$

This is no longer singular for $r_{12}\to 0$ (singularities in the separate terms "cancelling") and the main contributions arise from regions where ϕ_i^2 and ϕ_k^2 are large: the point charge approximation used in the work cited in footnote 1 then remains reasonable. Van der Waals (private communication) has obtained more satisfactory results by direct (six-dimensional) numerical integration on an electronic computer.

[1] R. McWeeny, J. Chem. Phys. **34**, 399 (1961).
[2] R. McWeeny, Proc. Roy. Soc. (London), to be published.

Spin Dependence of the First-Order Transition Density Matrix

WERNER A. BINGEL

Max-Planck-Institut für Physik und Astrophysik, Munich, Germany

(Received October 24, 1960)

IN a previous paper[1] the properties of the first-order density matrix $\gamma(\mathbf{x}'|\mathbf{x})$ were discussed. Especially, the dependence of γ on the spin variables was given [Eqs. (A6–8) of the work cited in footnote 1] for a pure spin state with quantum numbers S, M_S. This result can be generalized to *transition* densities between two *different* states with spin quantum numbers, S, M_S and S', M_S'. Instead of (A6)[1] one now has[2]

$$\gamma(\mathbf{x}'|\mathbf{x})=\gamma_{++}(\mathbf{r}'|\mathbf{r})\cdot\alpha(s')\alpha(s)+\gamma_{+-}(\mathbf{r}'|\mathbf{r})\cdot\alpha(s')\beta(S)+\gamma_{--}(\mathbf{r}'|\mathbf{r})\cdot\beta(S')\beta(s)+\gamma_{-+}(\mathbf{r}'|\mathbf{r})\cdot\beta(s')\alpha(s), \quad (1)$$

where for
$S'=S$:

$$\gamma_{\pm\pm}=\delta(M_S,M_S')[\tfrac{1}{2}\gamma\pm(M_S/S)\gamma_S]$$

$$\gamma_{\pm\mp}=\delta(M_S,M_{S\pm1})[(S\pm M_S)(S+1\mp M_S)/S^2]^{\frac{1}{2}}\gamma_S$$

$S'=S+1$:

$$\gamma_{\pm\pm}=\pm\delta(M_S,M_S')\times[(S+1-M_S)(S+1+M_S)/(2S+1)]^{\frac{1}{2}}\gamma_S$$

$$\gamma_{\pm\mp}=\pm\delta(M_S,M_{S\pm1})\times[(S+1\mp M_S)(S+2\mp M_S)/(2S+1)]^{\frac{1}{2}}\gamma_S \quad (2)$$

$S'=S-1$:

$$\gamma_{\pm\pm}=\pm\delta(M_S,M_S')[(S-M_S)(S+M_S)/(2S-1)]^{\frac{1}{2}}\gamma_S$$

$$\gamma_{\pm\mp}=\mp\delta(M_S,M_{S\pm1}')\times[(S-1\pm M_S)(S\pm M_S)/(2S-1)]^{\frac{1}{2}}\gamma_S,$$

other values of S' give a zero result.

Here $\gamma\equiv\gamma(\mathbf{r}'|\mathbf{r})$ is the spinless first-order *transition* density and $\gamma_S\equiv\gamma_S(\mathbf{r}'|\mathbf{r})$ is the *transition* spin density. For $S'=S$, $M_S'=M_S$, one regains the former results. Equation (2) shows that for given S and S' all four components of γ in (1) can be expressed, *for all* $(2S+1)(2S'+1)$ *values of* M_S *and* M_S', in terms of the two quantities γ and γ_S. The derivation of Eqs. (1) and (2) is very similar to that given in the appendix of the work cited in footnote 1 [Eqs. (A1–A8)], the only difference is that now the two space functions Ψ in (A4) are $\Psi_{S,k}{}^{(m)}$ and $\Psi_{S',k'}{}^{(m')}$ and the two spin-spin functions in (A5) are $\Theta_{S,M_S;k}{}^{N}$ and $\Theta_{S',M_S';k'}{}^{N}$.

The same results have been obtained by McWeeny[3] using the theory of irreducible tensor operators.

[1] W. A. Bingel, J. Chem. Phys. **32**, 1522 (1960); The following misprints should be corrected: Eq. (24) = ··· $\exp(iM\Phi)$ Table I, sp^3, second line: ${}^{1,3}D$, p. 1528, right column, second line: the letter $\mathfrak{D}$ should carry a tilde on top, Eq. (A5): the arguments of the first Θ should be lower case s, p. 1528, right column, third line from the bottom: the exponent of the round bracket should be $\frac{1}{2}$ instead of 2, and p. 1529, left column, seventh line from the bottom: the arguments of $\gamma-$ should be boldface $\mathbf{r}$'s.
[2] For simplicity, the subscripts SM_S, $S'M_S'$ on all γ's in (1) and (2) have been omitted.
[3] R. McWeeny and Y. Mizuno, Special Technical Report No. 2 (1960) University College of North Staffordshire (England); Proc. Roy. Soc. (to be published).

Erratum: Distribution Functions of a Fluid in an External Potential Field. Application to Physical Adsorption

[J. Chem. Phys. **33**, 464 (1960)]

WILLIAM A. STEELE AND MARVIN ROSS

Department of Chemistry, The Pennsylvania State University, University Park, Pennsylvania

(Received January 4, 1961)

A FACTOR of $\frac{1}{2}$ was omitted from one of the terms in Eq. (5.2). This equation should read

$$A_c - A_0 = \omega_1 - \omega_2/2kT + 0/(kT)^2. \qquad (5.2)$$

This error was carried over into several following equations. In particular, the last terms on the right-hand sides of Eqs. (5.9), (6.9), and (6.10) should be multiplied by $\frac{1}{2}$, and Eq. (6.11) should be altered to read

$$\mu_{ac} - \mu_{lc} = \bar{u}_s(L_z)[1 + \rho_0 \kappa_0 \bar{u}_s(L_z)/2 + \cdots]. \qquad (6.11)$$

This error thus invalidates the conclusion that the effect of the first-order change in the density of an adsorbed film in a weak external field upon the chemical potential is cancelled by the second-order change in the configurational free energy.

Erratum: Optical and Other Electronic Properties of Polymers

[J. Chem. Phys. **33**, 1332 (1960)]

IGNACIO TINOCO, JR.

Chemistry Department, University of California, Berkeley, California

(Received January 16, 1961)

PROFESSOR R. Feynman, California Institute of Technology, has pointed out that Eq. (24) of this paper cannot be substituted into Eqs. (22) or (23) to give the correct oscillator strength or polarizability for a polymer. Instead of an expression for $\boldsymbol{\mu}_{0A} \cdot \boldsymbol{\mu}_{A0}$ we need one for $\nu_{0A} \boldsymbol{\mu}_{0A} \cdot \boldsymbol{\mu}_{A0}$. The new equation is given below, together with some corrected typographical errors. An analogous correction in a previous paper (J. Am. Chem. Soc. **1960**, 4785) leads to the deletion of the second term in Eqs. (1) and Eq. (A11) of that paper.

The last term in Eq. (4) should be

$$\cdots \sum_{j \neq i} [(V_{ia;\, j0}) \psi_0^0 / h\nu_{0a}]. \qquad (4)$$

Equation (5) should read

$$(V)_{ia;\, ja'} = \int \psi_{ia}^0 V_{si,tj} \psi_{ja'}^0 d\tau. \qquad (5)$$

The third term in Eq. (14) should have a prime on the subscript of (V); it should read

$$(V)_{ia;\, ja'}{}^2. \qquad (14)$$

The first sum in Eq. (20) is over capital K; the second to the last term in Eq. (20) should have

$$\mathbf{q}_{i0a'} \quad \text{replace} \quad \mathbf{q}_{j0a'}.$$

Equation (24) should read

$$\sum_K \nu_{OAK} \boldsymbol{\mu}_{OAK} \cdot \boldsymbol{\mu}_{AOK} = \nu_{OA} \boldsymbol{\mu}_{OA} \cdot \boldsymbol{\mu}_{AO} = N \mu_{0a} \cdot \mu_{a0} \nu_{0a}$$

$$- \sum_{i=1}^{N} \sum_{j \neq i} \sum_{a' \neq a} \frac{4(V)_{ia;\, ja'} \boldsymbol{\mu}_{i0a} \cdot \boldsymbol{\mu}_{j0a'} \nu_{j0a'} \nu_{0a}}{h(\nu_{j0a'}{}^2 - \nu_{0a}{}^2)}$$

$$- 2 \sum_{i=1}^{N} \sum_{j \neq i} (V)_{ia;\, j0} \boldsymbol{\mu}_{i0a} \cdot (\boldsymbol{\mu}_{iaa} - \boldsymbol{\mu}_{i0})/h$$

$$- 2 \sum_{i=1}^{N} \sum_{j \neq i} \sum_{a' \neq a} \frac{(V)_{iaa';\, j0} \boldsymbol{\mu}_{i0a} \cdot \boldsymbol{\mu}_{i0a'} \nu_{0a}}{h(\nu_{0a'} - \nu_{0a})}$$

$$+ \sum_{i=1}^{N} \sum_{j \neq i} [(V)_{iaa;\, j0} - (V)_{i00;\, j0}] \boldsymbol{\mu}_{i0a} \cdot \boldsymbol{\mu}_{i0a}/h. \qquad (24)$$

Erratum: Infrared Detection of the Formyl Radical HCO

[J. Chem. Phys. **32**, 927 (1960)]

GEORGE E. EWING, WARREN E. THOMPSON, AND GEORGE C. PIMENTEL

Department of Chemistry, University of California, Berkeley, California

(Received December 19, 1960)

AN error in our calculations of the thermodynamic functions of HCO has been brought to our attention.[1] We have omitted the statistical weight factor associated with the doublet character of the ground electronic state of this free radical. A temperature independent term of $R \ln 2 = +1.38$ cal/deg mole must be added to every number in the columns headed $-(F^\circ - H_0^\circ)/T$ and S° in Table IX. The enthalpy function and heat capacity computations are unchanged.

[1] Dr. J. Gordon, private communication.

Notes

Radial Distribution Function from the Percus-Yevick Equation*

A. A. BROYLES

Department of Physics, University of Florida, Gainesville, Florida

(Received October 10, 1960)

PERCUS and Yevick[1] have applied their collective coordinate techniques to the problem of determining the radial distribution function $g(r)$ for a classical fluid in thermal equilibrium. They have derived an integral equation given as Eq. (64) of the work cited in footnote 1. In order to indicate the validity of their assumptions and the accuracy of results obtained from their techniques, a numerical solution to the Percus-Yevick (PY) equation is presented here for a case where $g(r)$ is available from the Monte Carlo (MC) and Born-Green (BG) methods.

Monte Carlo radial distribution functions have been obtained by Wood and Parker[2] for the Lennard-Jones (LJ) type potential. Comparisons between these MC functions and solutions to the BG equation are presented in footnotes 3 and 4. Our Fig. 1 compares the PY function with the MC and BG functions[4] for $na^3=10/9$ where na^3 is the number of particles per unit volume when the unit of length is the parameter a in the LJ potential ϕ in Eq. (1),

$$\phi(r)=4\epsilon[(a/r)^{12}-(a/r)^{6}]. \tag{1}$$

In these calculations, kT/ϵ was taken to be 2.74.

The techniques for solving the PY integral equation were similar to those described in the work cited in footnote 3. Checks were made on the accuracy of the solution by decreasing the interval and by comparing the g's substituted under the integral sign with those produced by the integration (one iteration), and it is believed that the PY solution presented in Fig. 1 is known to within ± 0.003.

One manner of comparing these functions is to substitute them into Eq. (2),

$$4\pi a^{-3}\int_0^\infty (1-g)r^2dr=n^{-1}a^{-3}\{1-kT(\partial p/\partial n)_T^{-1}\} \tag{2}$$

and to observe the difference.[5] The integral in this equation converges so slowly that it is helpful to use the asymptotic form of g at large r. For the PY equation, this form is given by

$$g\sim 1+b\exp(-\alpha r)\sin(mr-c), \tag{3}$$

where the parameters are listed in Table I for r measured in units of a. The parameters for the same form

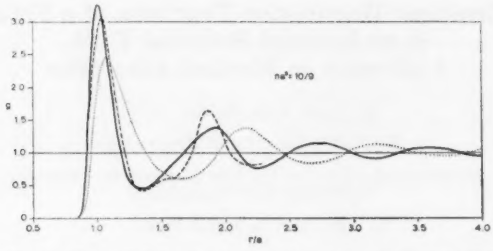

FIG. 1. The radial distribution function g vs r/a for $na^3=10/9$ from the Percus-Yevick integral equation (solid curve), the Monte Carlo method (dashed curve), and the Born-Green integral equation (dotted curve).

obtained by fitting the BG solution are also listed, as well as the left-hand side of Eq. (2) evaluated with the aid of Eq. (3). For the PY solution, Eq. (3) approximates g to within 0.1 for r's greater than $1.9a$ and to within 0.01 for r's greater than $2.9a$.

Table I also lists pv/RT and E'/RT evaluated with

TABLE I. Thermodynamic functions and parameters for Eq. (3).

	b	α	m	c	Left side of Eq. (2)	pv/RT	E'/RT
PY	3.79	1.163	7.357	5.989	0.93	10.10	−1.42
BG	9.276	1.383	2π	2.928	0.10	3.82	−2.56
MC						7.70	−1.90

the aid of[6] Eqs. (24) and (25) of the work cited in footnote 2 for the PY and BG solutions.

We see from Table I that pv/RT and E'/RT computed from the PY solution are closer to the MC value than are the same quantities computed from the BG solution. Figure 1 shows that the entire curve of the PY solution is much closer to the MC than to the BG solution. The PY solution behaves as though it is unable to follow some of the smaller twists and turns of the MC curve but tries to smooth them out in a reasonable fashion. It is clear that the PY techniques have yielded some very interesting results in this case and warrant further study for improvement and other applications.

The computations presented here were carried out on the IBM 650 of the University Statistical Laboratory with the aid of Frank Vickers who programmed the problem introducing several ingenious innovations to speed up the solution.

* This work was supported in part by the National Science Foundation.

[1] J. K. Percus and G. J. Yevick, Phys. Rev. **110**, 1 (1958).
[2] W. W. Wood and F. R. Parker, J. Chem. Phys. **27**, 720 (1957).
[3] A. A. Broyles, J. Chem. Phys. **33**, 456 (1960).
[4] A. A. Broyles, J. Chem. Phys. (to be published).
[5] Terrell L. Hill, *Statistical Mechanics* (McGraw-Hill Book Company, Inc., New York, 1956), 1st ed., p. 185, Eq. (29.35).
[6] A minus sign was apparently omitted from the right side of Eq. (25) of the work cited in footnote 2.

Low-Energy Process for F^- Formation in SF_6

R. K. CURRAN

Westinghouse Research Laboratories, Pittsburgh, Pennsylvania

(Received November 23, 1960)

A RECENT electron impact experiment using the RPD[1] method in a mass spectrometer has revealed a low-energy process for the formation of F^- in SF_6. The appearance potential is measured as being in the range 0 to 0.05 ev. The cross section for the process closely resembles that for SF_6^- formation.[2] That is, the F^- current has the width of the electron distribution and the cross section is thus close to a delta function at zero energy. The maximum cross section for F^- formation is about 0.01 of the SF_6^- cross section. The F^- current vs electron energy is shown in Fig. 1. The electron retarding curve is used to determine the zero of the electron energy scale. Zero electron energy corresponds to the foot of the electron retarding curve.

The kinetic energy of the F^- ions has been measured as 0.20 ± 0.05 ev which yields a total kinetic energy of 0.23 ± 0.05 ev for the process. There is no dependence of the ion energy on electron energy because of the sharp energy dependence of the cross section. The total kinetic energy of the process is taken as 146/127 times the kinetic energy of the F^- fragment ion.

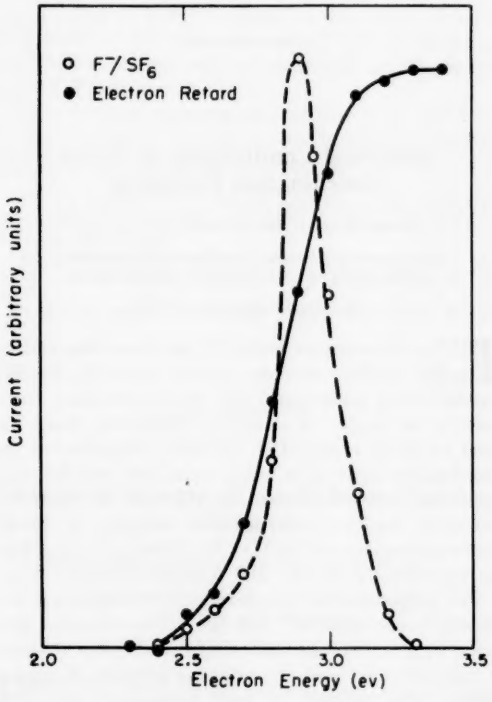

FIG. 1. F^- current vs electron energy.

The dissociation energy of the SF_5 and F bond, $D(SF_5-F)$ may be determined from

$$AP(F^-)+EA(F)\leq D(SF_5-F)+KE_{\text{Total}}. \quad (1)$$

Using the appearance potential of F^-, $AP(F^-)=0+0.05$ or -0 ev and the total kinetic energy, $KE_{\text{Total}}=0.23\pm0.05$ ev as measured, along with the electron affinity of fluorine,[3] $EA(F)=3.62\pm0.09$, one obtains from Eq. (1) that $D(SF_5-F)\leqslant 3.39\pm0.15$ ev. The inequality holds since nothing definite may be said of the internal energy of the SF_5 fragment. It should be noted that by taking[4] $\Delta H_f(F)=18.5$ kcal/mole and $\Delta H_f(S)=57$ kcal/mole together with[5] $\Delta H_f(SF_6)=-262$ kcal/mole one has $[D(S-6F)]/6=71.7$ kcal/mole or 3.11 ev. Considering the uncertainty[4] in the value of $\Delta H_f(S)$, there is no disagreement between the electron impact value for $D(SF_5-F)$ and the thermochemical value for $[D(S-6F)]/6$. It thus appears that there is a constant S—F bond energy in SF_5 and SF_6.

The work of Hickam and Fox[2] has shown the appearance potential of SF_5^- from SF_6 to be 0 ev. This result, in the light of the present work, suggests that a value of about 3.39 ev be placed on the electron affinity of SF_5.

[1] R. E. Fox, W. M. Hickam, D. J. Grove, and T. Kjeldaas, Jr., Rev. Sci. Instr. **26**, 1101 (1955).
[2] W. M. Hickam and R. E. Fox, J. Chem. Phys. **25**, 642 (1956).
[3] H. O. Pritchard, Chem. Revs. **52**, 529 (1953).
[4] T. L. Cottrell, *The Strengths of Chemical Bonds* (Butterworth Scientific Publications, Ltd., London, 1958).
[5] F. D. Rossini, D. D. Wagman, W. H. Evans, S. Levine, and I. Jaffe, Natl. Bur. Standards (U. S.) Circ. No. 500 (1952).

Gaseous Detonations. XIV. The CH Radical in Acetylene Oxygen Detonations

RICHARD K. LYON AND PAUL H. KYDD

Gibbs Chemical Laboratory, Harvard University, Cambridge, Massachusetts

(Received September 6, 1960)

WITH the apparatus described previously[1] we have observed the time-resolved absorption spectrum of a detonation in an equimolar mixture of acetylene and oxygen at an initial pressure of 6 mm. The over-all spatial resolution of the apparatus is 9 mm. Since the detonation wave velocity (measured over 10-cm intervals) under these conditions is stable to $\frac{1}{2}\%$, the mean displacement of the front from its average position during the light flash should be only 0.5 mm. Hence the resolution of the detonation wave structure is

chiefly determined by the spatial apparatus resolution. Unfortunately the absorption spectra change in a distance comparable to or less than our resolution, so that quantitative measurement of the time variation of the spectra could not be made. However qualitative observation was possible, and is described in full detail in the work cited in footnote 2.

The 3143 band of CH appears directly behind the shock front, then the OH absorption appears, and the CH absorption disappears. Due to limited resolution we cannot say whether OH appears before or after CH disappears. The region of the detonation wave in which CH is observed and OH is not, is between 3 and 8 mm wide.[3] The f number for the 3143 transition is unknown, but is necessarily less than one. On this basis we calculate a lower limit for the CH concentration of 4×10^{11} molecules/cc. This would require a conversion of 4×10^{-5}% of the original C_2H_2 to CH radicals.

Bennett and Wedaa[4] have observed the light emission of the acetylene-oxygen detonation as a function of time. They found a zone of intense luminosity directly behind the shock front of the detonation. The width of this zone varied inversely with initial pressure. At an initial pressure of 6 mm the luminous zone had a width of 5.5 mm.

It seems probable that the luminous zone and the reaction zone coincide. If this is assumed, then the zone in which we have observed CH is the same as the reaction zone, within a large experimental error. This might be taken to mean that the CH radical disappears when the oxidation is complete, i.e., when the acetylene is exhausted.

The temperature immediately behind the shock front is readily calculated from the observed detonation wave velocity and is 2078°K. At this temperature the reaction $C_2H_2\rightleftharpoons2CH$ would give an equilibrium concentration of 1.2×10^{10} molecules of CH per cc, less by a factor of 33 than the lower limit of the observed concentration. Further, since the reaction is 230 kcal/mole endothermic, it must be very slow. On this basis we conclude that CH is not formed by acetylene dissociation but by some oxidation reaction.

Gaydon,[5] in discussing the chemiluminescent emission of CH in flames, has proposed the reaction $C_2+OH\rightarrow CH+CO$. He suggests that the C_2 might be formed by oxidation of diacetylene[6] via

$$C_4H_2+O_2\rightarrow C_4H_2O_2\rightarrow C_2+H_2+2CO.$$

Using the best available values for the heats of formation of C_2[7] and diacetylene[8] this reaction is calculated to be about 40 kcal endothermic. This would make it too slow to explain the present observation, but the difficulty might be removed if one postulates the sequential reactions $C_4H_2+H\rightarrow H_2+C_4H$ and $C_4H+O_2\rightarrow CO+C_2+CHO$, which we estimate to be 22 kcal endothermic, using 6 kcal as the heat of formation of CHO.[9]

Recent studies by Kistiakowsky and Richards[10] strongly indicate that the rate-determining step in the high-temperature oxidation of acetylene is $H+O_2\rightarrow O+OH$, although the rest of the chain reaction is not completely certain. In the authors' opinion this justifies postulating that OH is present when CH is formed, even though it is not detected.

[1] G. B. Kistiakowsky and F. D. Tabbutt, J. Chem. Phys. **30**, 577 (1959).
[2] R. K. Lyon, thesis, Harvard University, 1960.
[3] It should be noted that the CH spectrum is very close packed while that of OH is open. With the spectrograph we used (a Hilger E-1 Littrow type, 6.8 A/mm dispersion) the structure of the OH was well resolved, but the CH appeared as a broad line. Hence the method of detection is much more sensitive to CH than OH; OH could have been present in higher concentration than CH and still have escaped detection.
[4] A. L. Bennett and H. W. Wedaa, J. Chem. Phys. **23**, 1359 (1955).
[5] A. G. Gaydon, *The Spectroscopy of Flames* (Chapman and Hall, Ltd., London, 1959).
[6] Recent studies by J. N. Bradley and G. B. Kistiakowsky, J. Chem. Phys. (to be published) have shown that diacetylene is probably formed during the oxidation of acetylene.
[7] R. L. Altman, J. Chem. Phys. **32**, 615 (1960).
[8] F. H. Coats and R. C. Anderson, J. Am. Chem. Soc. **79**, 1340 (1957).
[9] A. Trotman-Dickenson, *Gas Kinetics* (Butterworth Scientific Publications, Ltd., London, 1955).
[10] G. B. Kistiakowsky and L. W. Richards (to be published); also see L. W. Richards, thesis, Harvard University, 1960.

Electrical Conductivity of Some Coordination Polymers

SEIICHI KANDA AND SHINICHI KAWAGUCHI

Department of Chemistry, Institute of Polytechnics, Osaka City University, Kita-ku, Osaka, Japan

(Received November 2, 1960)

THE semiconductor behavior has been observed by earlier workers on some organic materials, notably aromatic ring compounds[1] and those containing metal ions in the center of structure.[2] However, there has been no study reported on electrical properties of the coordination polymer in which metal ions and chelating agents are arrayed alternately. We wish to report the electrical conductivities of solid samples of 1,6-dihydroxyphenazinato-Cu(II) (A), 2,5-dihydroxy-*p*-benzoquinonato-Cu(II) (B) and rubeanato-Cu(II) (C).

The preparation of the former two compounds has already been reported,[3] and the latter was also prepared by a similar method using the alcoholic solution of rubeanic acid and the aqueous solution of copper sulfate. Fine powder of each compound was compressed into a disk (12 mm in diameter and 2~3 mm

thick) under pressure of about 5×10^3 kg/cm². To avoid the effect of grain boundary contributions, the measurement of resistivity was carried out mainly with ac by means of a Q meter (Mita Radio Laboratory, model 29-5). In addition, the dc measurement was performed employing a vibrating condenser type voltmeter or a dc microammeter. These electrical measurements were usually made under a reduced pressure of approx 10^{-3} mm Hg.

The resistivity of the sample C was found to be represented by the formula $R=R_0\exp(\Delta E/kT)$ in the temperature range of -10 to 80°, and with ac: R(at 30°) $=5\times10^4$ ohm cm, $\Delta E=0.2$ ev, with dc: R(at 30°) $=2.5\times10^5$ ohm cm, $\Delta E=0.3$ ev. At higher temperatures above 90° the compound tends to decompose gradually, resulting in an increase of resistivity, but the ΔE value is not altered.

The dc measurement of the sample A gave the following results: R(at 60°) $=10^{13}$ ohm cm, $\Delta E=1$ ev (60∼160°). These data are reproducible showing no hysteresis. This ac measurement at the same temperature range gave a small positive value of dR/dT and R (at 60°) $=10^7$ ohm cm, but at lower temperatures of dry ice, and liquid nitrogen dR/dT turned either to zero or to a small negative value.

The compound B gave no reproducible value of resistivity either with dc or ac measurement. With dc the R value at 100° was found to be of the order of magnitude of 10^{10} ohm cm and $dR/dT<0$. With ac, R at 20° was of the order of magnitude of 10^7 ohm cm and $dR/dT<0$.

More detailed investigation of electrical properties of the compound C, such as rectifying and thermoelectric properties, is now in progress.

[1] Cf., for example, H. Inokuchi, Bull. Chem. Soc. Japan **29**, 131 (1956); A. G. Chynoweth and W. G. Schneider, J. Chem. Phys. **22**, 1021 (1954).
[2] D. D. Eley and G. D. Parfitt, Trans. Faraday Soc. **51**, 1529 (1955); A. Epstein and B. S. Wildi, J. Chem. Phys. **32**, 324 (1960).
[3] S. Kanda and Y. Saito, Bull. Chem. Soc. Japan **30**, 192 (1957).

Infrared Spectra of the Lithium Halide Dimers

WILLIAM KLEMPERER* AND WILFRED G. NORRIS†

Department of Chemistry, Harvard University, Cambridge, Massachusetts

(Received November 18, 1960)

EARLIER work on the infrared spectra of the gaseous alkali halides revealed only one absorption in each system.[1] This absorption was assigned to the vibrational transition of the diatomic monomer. A reinvestigation of this absorption in the lithium halides using a grating spectrometer has completely confirmed this assignment.[2] On the basis of the observation of only one absorption in the alkali halide spectra one of us (W.K.) stated that the chemical composition of the vapor in equilibrium with the condensed phase consists entirely of monomeric species. The fact that Friedman[3] and Miller and Kusch[4] had observed that the vapor effusing from Knudsen cells was highly dimerized, was interpreted to indicate that these workers did not have equilibrium conditions inside the beam source. This conjecture has been amply disproven by Kusch and co-workers.[5]

The lithium halides are the most highly dimerized alkali halides. Furthermore, the vibration frequencies of the lithium halides are the highest in frequency, which is of great convenience experimentally. We have therefore reinvestigated the infrared spectra of these systems. The present study has extended the wavelength range to 220 cm^{-1}. This limit is considerably below that of the earlier work, which extended to only about 200 cm^{-1} past the absorption of the monomer. For each system two new absorptions were observed below the frequency region examined earlier. The frequencies of the absorption maxima are listed in Table I. For lithium fluoride the bands were considerably broader than those of the other three halides and the maxima are uncertain to about 15 cm^{-1}. A spectrogram of lithium chloride is shown in Fig. 1. This is typical of the observation for LiCl, LiBr, and LiI systems.

TABLE I. Absorption maxima of the lithium halide dimers in cm^{-1}.

LiF	640	460
LiCl	460	335
LiBr	413	295
LiI	375	248

On the basis of a planar rhomboid structure there are expected to be three infrared-active normal modes of vibration in the alkali halide dimers. Two of these B_{2u} and B_{3u} are in-plane bond-stretching motions. The third is the B_{1u} out-of-plane bending motion. In view of the fact that only two absorptions have been presently observed the assignment of these bands to normal vibrations is somewhat arbitrary.

We tentatively assign the two observed vibrations as the B_{2u} and B_{3u} bond-stretching motions. The high frequency vibration corresponds to the oscillation of atoms parallel to the long axis of the rhombus. The

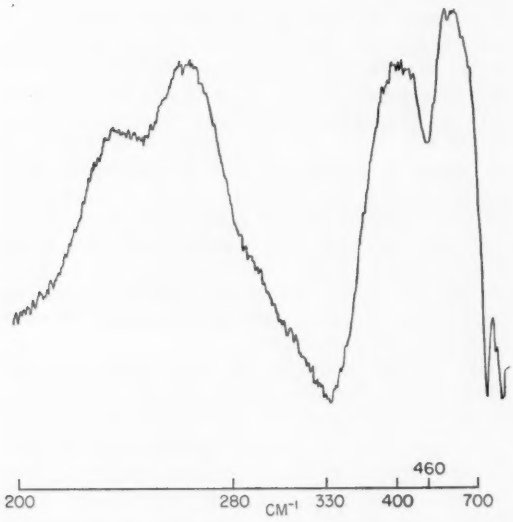

FIG. 1. Infrared spectrum of gaseous lithium chloride. The spectrum is observed with cesium-iodide optics using a mechanically driven slit to maintain somewhat constant light intensity. The absorption at 700 cm^{-1} is due to polyethylene while the band at $\sim$260 cm^{-1} is due to atmospheric water which remained after strong flushing with nitrogen.

reasons for this choice are twofold. First, this assignment fits well the ratio of the frequencies expected on the basis of a simple valence force field with small potential constants for in-plane angle deformations. The geometry, which effects the splitting of the vibrations in this model, has been recently measured for LiCl, LiBr, and LiI.[6,7] Second, if the intensities of the three infrared-active modes are estimated from a polarizable-ion model, the out-of-plane bending motion is expected to be much weaker than the two stretching motions.

This research has been aided by grants from the National Science Foundation and the Research Corporation.

* Alfred P. Sloan Fellow.

† Present address: Department of Physics, Juniata College, Huntingdon, Pennsylvania.

[1] W. Klemperer and S. A. Rice, J. Chem. Phys. **26**, 618; **27**, 573 (1957).

[2] W. Klemperer, W. G. Norris, A. Buchler, and A. G. Emslie, J. Chem. Phys. **33**, 1534 (1960).

[3] L. Friedman, J. Chem. Phys. **23**, 477 (1955).

[4] R. C. Miller and P. Kusch, J. Chem. Phys. **25**, 680 (1956); **27**, 981 (1957).

[5] G. M. Rothberg, M. Eisenstadt, and P. Kusch, J. Chem. Phys. **30**, 517 (1959); M. Eisenstadt, V. S. Rao, and G. M. Rothberg, *ibid.* **30**, 604 (1959).

[6] P. A. Akischin and N. G. Rambidi, Z. physik. Chem. **213**, 111 (1960).

[7] S. H. Bauer, R. F. Porter, and T. Ino, J. Chem. Phys. (to be published).

Bis-Liganded Nitrosyl as a Reaction Intermediate

JAMES R. COX, JR., AND JAMES D. RAY

School of Chemistry, Georgia Institute of Technology, Atlanta, Georgia

(Received November 2, 1960)

INVESTIGATION of the kinetics and equilibrium of the gas-phase reaction of nitrosyl chloride and methanol has revealed that, while the equilibrium constant K for the reaction is given by the expression

$$K=[\mathrm{MeONO}][\mathrm{HCl}]/[\mathrm{NOCl}][\mathrm{MeOH}], \qquad (1)$$

the forward reaction is second order in methanol and first order in nitrosyl chloride. The obverse criterion deduced from transition state theory that the reverse reaction be first order in methanol as well as in methyl nitrite and hydrogen chloride has been experimentally confirmed; thus the stoichiometry of the reaction is properly represented by Eq. (2)

$$2\mathrm{MeOH}+\mathrm{NOCl}\underset{k_{-1}}{\overset{k_1}{\rightleftharpoons}}\mathrm{MeONO}+\mathrm{HCl}+\mathrm{MeOH}. \qquad (2)$$

Determination of the kinetic constants was made by quantitative infrared spectroscopy; the initial reaction rate in each direction was evaluated as a function of the partial pressure of each component of the system in order to establish the kinetic orders. At $25\pm2°$ $k_1=6.2\times10^{-5}$ mm Hg^{-2} sec^{-1} and $k_{-1}=8.9\times10^{-5}$ mm Hg^{-2} sec^{-1}. $K=k_1/k_{-1}=0.69$. Independent evaluation of K by quantitative infrared spectroscopy of the equilibrium mixtures led to a value of 0.73, in good agreement with the above, and with the published value.[1]

Although several reaction paths are consistent with

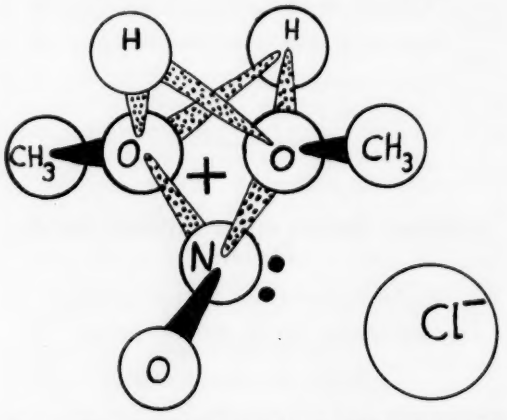

FIG. 1. Three-dimensional sketch of the *bis*-liganded reaction intermediate (I). The dotted bonds are being made and broken during progress along the reaction coordinate in either direction.

the available experimental data, consideration of the geometry and symmetry of the reactants leads to the following sequence, which has many interesting implications:

$$2\,\mathrm{MeOH} \rightleftharpoons (\mathrm{MeOH})_2 \quad (3)$$

$$(\mathrm{MeOH})_2 + \mathrm{NOCl} \rightleftharpoons I \rightleftharpoons \mathrm{MeOH \cdot HCl} + \mathrm{MeONO} \quad (4)$$

$$\mathrm{MeOH \cdot HCl} \rightleftharpoons \mathrm{MeOH} + \mathrm{HCl}. \quad (5)$$

In support of the above formulation the following facts may be noted. (a) Chemically stable species in which a nitrosyl ion is coordinated to two electron-donor groups have been well characterized[2]; their resemblance to I is obvious. (b) Methanol is known to be in equilibrium with a hydrogen-bonded dimer (as well as a tetramer) in the gas phase,[3] and evidence has been adduced by infrared[4] and nuclear magnetic resonance[5] methods that a cyclic structure is likely for such alcohol dimers. In the cyclic dimer the two electron pairs which become coordinated to nitrogen in I are spatially oriented so that little, if any, reorganization of atoms would be required in order to form the new bonds. (c) The chloride ion probably requires little solvation[6]; since in I it is internally "solvated" by interactions with the more positive parts of the molecule which are at least in part covalent, and since in passing along the reaction coordinate in either direction from I free ions do not form, at worst any species in the sequence which possesses ionic character may be thought of as a very tight gaseous ion pair. (d) The C—Cl bond in NOCl is exceptionally long, and is considered to possess considerable "ionic character."[7] In addition the electron density of nitrogen in methyl nitrite is similar to that in NOCl, both being unusually low as judged by NMR chemical shifts.[8] (e) The compound MeOH·HCl is well established.[9]

Alternative pathways by which formation of the activated complex takes place are, of course, possible. A methanol dimer having a single hydrogen bond, a methyl nitrite—hydrogen chloride adduct, and a methyl alcohol—nitrosyl chloride adduct, are all possible substitutes in reactions (3), (4), and (5).

[1] J. A. Leermakers and H. C. Ramsperger, J. Am. Chem. Soc. **54**, 1837 (1932).
[2] C. C. Addison and J. Lewis, Chem. Soc. London Quart. Revs. **9**, 132 (1955).
[3] W. Weltner and K. S. Pitzer, J. Am. Chem. Soc. **73**, 2606 (1951).
[4] M. Van Thiel, E. D. Becker, and G. C. Pimentel, J. Chem. Phys. **27**, 95 (1957).
[5] E. D. Becker, U. Liddel, and J. N. Shoolery, J. Mol. Spectroscopy **2**, 1 (1958).
[6] P. A. H. Wyatt, Discussions Faraday Soc. **24**, 162 (1957); A. B. Burg and G. W. Campbell, Jr., J. Am. Chem. Soc. **70**, 1964 (1948).
[7] J. A. A. Ketelaar and K. J. Palmer, J. Am. Chem. Soc. **59**, 2629 (1937).
[8] Private communication from Dr. Lawrence H. Piette, Varian Associates, Palo Alto, California.
[9] J. Russell and O. Maass, Can. J. Research **5**, 436 (1931).

Heat Capacity Anomaly in Solid Air*

WILLIAM H. LIEN AND NORMAN E. PHILLIPS

Department of Chemistry and Lawrence Radiation Laboratory, University of California, Berkeley, California

(Received December 12, 1960)

WE have recently had occasion to make heat capacity measurements on several "empty" calorimeters, made almost entirely of copper and weighing approx 180 g. In two separate sets of measurements between 1°K and 4°K unexpectedly high results were obtained; below 3°K the heat capacity was 40% to 80% higher than estimated. Investigation showed that the high heat capacity was caused by the presence of approximately 0.1 g of air sealed into the calorimeters. After the second of these runs the calorimeter seal was cracked to permit the escape of the air and the measurement repeated without otherwise changing the apparatus. The heat capacity was then found to be close to that estimated for the calorimeter. The heat capacity of the air is shown in Fig. 1. There is an uncertainty of perhaps 5% in the amount of air present and therefore in the values plotted in the figure. In this temperature range the heat capacity of solid air is as much as 400 times greater than that of solid oxygen.[1]

It seems probable that the large heat capacity is associated with an antiferromagnetic ordering of the electron spins of the oxygen molecules at about 3°K. From a comparison of the spectroscopic entropy of oxygen gas with calorimetric measurements on the condensed phases, Giauque and Johnston[2] showed that in

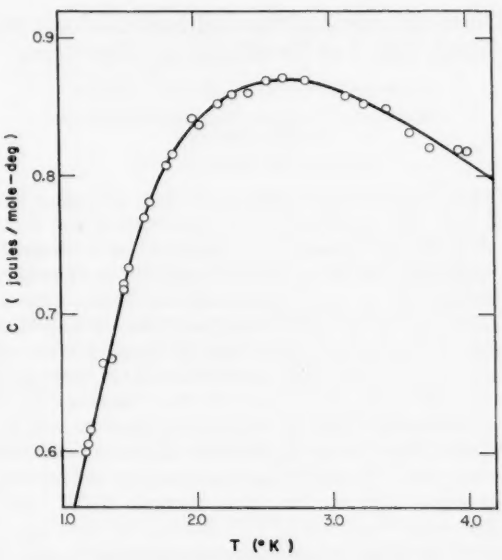

FIG. 1. The heat capacity of solid air.

pure solid oxygen the spins are largely aligned at liquid hydrogen temperatures. Calorimetric[2,3] and magnetic[3,4] susceptibility data suggest that a transformation to an antiferromagnetic state is coincident with the γ-β crystallographic transition at 43.8°K. Dilution of an antiferromagnet with a diamagnetic material reduces the mean energy of interaction between the spins. Consequently, the alignment of the spins in solid air can be expected to take place at a lower temperature than in pure oxygen. Further support for this point of view comes from magnetic susceptibility measurements on liquid oxygen-nitrogen solutions. Between 64°K and 77°K these solutions follow a Curie-Weiss law with antiferromagnetic Weiss constants.[5] The Weiss constant for a composition corresponding to the present sample would be about 7°K, within the usual range of values that might be expected for a material with a Neel temperature of 3°K. The fact that the heat capacity does not have the sharp peak characteristic of antiferromagnetic transitions in pure compounds is to be expected on general grounds and also by comparison with magnetic measurements on solutions.[6]

* This work was performed under the auspices of the U. S. Atomic Energy Commission.

[1] M. O. Kostriukova and P. G. Strelkov, Doklady Akad. Nauk S.S.S.R. **90,** 525 (1953).
[2] W. F. Giauque and H. L. Johnston, J. Am. Chem. Soc. **51,** 2300 (1929).
[3] A. S. Borovik-Romanov, M. P. Orlova, and P. G. Strelkov, Doklady Akad. Nauk S.S.S.R. **99,** 699 (1954).
[4] E. Kanda, T. Haseda and A. Otsubo, Physica **20,** 131 (1954).
[5] A. Perrier and H. K. Onnes, Communications from the Physical Laboratory of the University of Leiden, No. 139d (1914).
[6] H. Bizette and B. Tsai, Compt. rend. **217,** 444 (1943).

Dipole Moment of the OH Radical from the Stark Effect of Its Microwave Spectrum*

RICHARD T. MEYER† AND ROLLIE J. MYERS
Department of Chemistry, University of California, Berkeley, California

(Received November 28, 1960)

THE electric dipole moment of the OH radical has been the subject of recent experimental and theoretical studies. Madden and Benedict[1] have obtained a value of 1.54 debye from a study of the emission spectrum of an oxyacetylene flame. Their value is based upon the relative intensities of the OH and H_2O rotational lines and on a tentative determination of the ratio of OH and H_2O in the flame. It is very close to the OH bond moment of 1.53 D[2] as found in water. The theoretical determinations stem from interest in the wave functions of the first row diatomic hydrides. Krauss and Wehner[3] have summarized the recent theoretical work on the dipole moment of OH. The values range from 0.8–2.7 D; however, the most complete calculations including the best correlation corrections give values in the range 2.1–2.7 D.

The purpose of this paper is to report the initial value that we have obtained from the Stark effect of the OH microwave transitions near 23 820 Mc. Our value is subject to a greater uncertainty than are most microwave dipole moment determinations, but it is probably comparable in accuracy to the Madden and Benedict value. An estimate of our experimental uncertainties indicates that the OH dipole moment must be close to the bond moment in water or perhaps slightly larger than this value, but the theoretical estimates of 2.1–2.7 D are outside of our experimental error.

The Stark effect measurements were made in a parallel-plate wave guide cell constructed of aluminum sheet. The parallel plates were mounted in a 3-ft length of 4-in. diameter "Pyrex" pipe. They were flared at each end nearly to the diameter of the pipe in order to facilitate microwave excitation by dielectric rods.[4] The plates were spaced about 6 mm apart and square-wave Zeeman modulation at 5 kc was applied to the center part of the cell to facilitate the detection of the relatively weak microwave absorptions. The OH radicals were produced by a microwave discharge through a H_2 and O_2 mixture.[5]

Because of experimental limitation on pressure and maximum electric field before gaseous breakdown occurred, it was not possible to resolve individual Stark components. It was possible, however, to measure the shift in the frequency of the maximum of the microwave absorption of each of the two hyperfine components of the $N=4$ transition. At a field of 775 ± 15 v/cm a shift toward higher frequency of 1.13 ± 0.3 Mc and 1.20 ± 0.3 Mc were observed for the $F=4$ and $F=5$ components, respectively.

Because of the large rotational constant of OH the Stark effect is almost entirely due to second-order terms between the Λ doublets. Penny[6] has given the equations for Hund's case (a) [see G. Herzberg, *Molecular Spectra and Molecular Structure.* I. *Spectra of Diatomic Molecules* (D. Van Nostrand Company, Inc., Princeton, New Jersey, 1950), 2nd ed.] and without hyperfine interaction. The intermediate coupling can be taken into account by a very simple procedure. If one removes ϵ, the major off-diagonal element in the molecular Hamiltonian,[5,7] by a transformation corresponding to a two-by-two rotation through an angle ϕ, then this angle has a simple vector-model significance for the two $^2\Pi$ states of OH,

$$\langle\Omega\rangle = (1\pm\tfrac{1}{2})\cos^2\phi + (1\mp\tfrac{1}{2})\sin^2\phi.$$

The use of the above $\langle\Omega\rangle$ in Penny's equations corrects them for intermediate coupling.

The hyperfine interaction in OH is considerably larger than the possible Stark perturbations so that the weak field case for the J, I, F, M representation is the

appropriate one. This can either be done exactly or by perturbation through the technique of Townes and Schawlow.[8] The final equation for the Stark effect of each level in its simplest form is

$$W_1(F=J-\tfrac{1}{2})=\frac{\langle\Omega\rangle^2\mu^2E^2}{J^2(J+1)^2(W_1^0-W_2^0)}$$

$$\times\{[(2J+3)/(2J+1)]M^2+\tfrac{1}{4}\},$$

where the equation for $F=J+\frac{1}{2}$ can be obtained by replacing $(2J+3)$ by $(2J-1)$.

Since we did not resolve individual Stark components some type of averaging procedure must be used. In the parallel plate guide the microwave and dc electric fields were parallel, thus the selection rule $\Delta M=0$. In the weak-field case the intensities of each Stark component should be proportional to M^2. A value for the dipole moment was calculated from the frequency shift for every M value and an average value was determined using M^2 as a weighting factor. Burris[9] has found this to be a satisfactory method when individual Stark components are not resolved. From the two frequency shifts we obtain 1.63 and 1.68 D for the $F=4$ and $F=5$ components, respectively. We have selected an average value of 1.65 ± 0.25 D. The stated error is larger than the direct experimental one and it should be generous enough to include the errors introduced by the necessity of averaging the Stark components. Work is continuing on this problem and we hope to be able to resolve individual Stark components and to reduce the errors in the determination.

We would like to thank Professor W. D. Gwinn for his personal assistance and encouragement during this work, and Dr. L. C. Allen for helpful discussions.

* This research was supported by a grant from the Petroleum Research Fund administered by the American Chemical Society. Grateful acknowledgment is hereby made to the donors of this fund.

† National Science Foundation Predoctoral Fellow 1956–59; Present address: Physical Sciences Research Department, Sandia Corporation, Albuquerque, New Mexico.

[1] R. P. Madden and W. S. Benedict, J. Chem. Phys. **23,** 408 (1955). Note: these authors make no final estimate of the error in their dipole moment determination.

[2] Based on a total dipole moment of 1.88 D and an angle of 104.45°.

[3] M. Krauss and J. F. Wehner, J. Chem. Phys. **29,** 1287 (1958).

[4] E. B. Brackett, P. H. Kasai, and R. J. Myers, Rev. Sci. Instr. **28,** 699 (1957).

[5] G. C. Dousmanis, T. M. Sanders, Jr., and C. H. Townes, Phys. Rev. **100,** 1735 (1955).

[6] W. G. Penny, Phil. Mag. **11,** 602 (1931). Note: Eq. (2) of the work cited in footnote 5 is incorrect and it should be multiplied by $(2J+1)/J$.

[7] J. H. Van Vleck, Phys. Rev. **33,** 467 (1929).

[8] C. H. Townes and A. L. Schawlow, *Microwave Spectroscopy* (McGraw-Hill Book Company, Inc., New York, 1955), p. 260.

[9] C. A. Burris, J. Chem. Phys. **31,** 1270 (1959).

Spin Inversion Operator in Nuclear Magnetic Resonance

ROBERT L. FULTON AND JOHN D. BALDESCHWIELER

Department of Chemistry, Harvard University, Cambridge, Massachusetts

(Received November 14, 1960)

CORIO[1,2] has used the operator λ_j defined by

$$\lambda_j\,|\,I_j,m_j\rangle=|\,I_j,-m_j\rangle, \tag{1}$$

to prove a number of important properties of the NMR spin Hamiltonian. From the definition of λ_j the commutation rules are[3]

$$[\lambda_j,I_{xj}]=\lambda_jI_{yj}+I_{yj}\lambda_j=\lambda_jI_{zj}+I_{zj}\lambda_j=0. \tag{2}$$

The fact that the commutators $[\lambda_j,I_{xj}]$ and $[\lambda_j,I_{yj}]$ are different is not important for the usual NMR problem since

$$[\Lambda,\ \sum_{j<k}J_{jk}I_j\cdot I_k]=0, \tag{3}$$

where $\Lambda=\prod_j\lambda_j$, regardless of whether λ commutes or anticommutes with I_x and I_y.

For some NMR problems, however, the difference in commutation properties of λ with I_x and I_y is significant. For example, the Hamiltonian operator for a nuclear magnetic double resonance experiment is[4–6]

$$\mathcal{H}=\sum_jA_jI_{zj}+\sum_{j<k}J_{jk}I_j\cdot I_k+\sum_jv_{2j}I_{xj}, \tag{4}$$

where

$$A_j=v_{0j}+\omega_2/2\pi,$$

ω_2 = frequency of second radio frequency field,

$$v_{0j}=-\gamma_jH_0/2\pi,$$

$$v_{2j}=-\gamma_jH_2/2\pi,$$

and

H_2 = amplitude of second radio frequency field.

The appearance of I_{xj} or I_{yj} in the last term of Eq. (4) depends simply on the choice of the phase of the rotating field ω_2 or on the definition of the axis of the oscillating field commonly used in NMR experiments. Since the commutators $[\lambda_j,I_{xj}]$ and $[\lambda_j,I_{yj}]$ differ, $[\Lambda,\mathcal{H}]$ depends on the definition of the axis of the radio frequency field.

This result suggests that a somewhat different definition of the spin inversion operator would be more appropriate

$$\bar{\lambda}_j\,|\,I_j,m_j\rangle=\exp(i\phi_{mj})\,|\,I_j,-m_j\rangle, \tag{5}$$

where ϕ_{mj} is a real constant depending on m_j, and $|\,I_j,m_j\rangle$ is an eigenfunction of I^2 and I_z. For the

operator $\tilde{\Lambda}_j$,

$$\tilde{\Lambda}_j I_{zj}+I_{zj}\tilde{\Lambda}_j=0. \tag{6}$$

If it is required that $\tilde{\Lambda}_j$ anticommute with the other components of the angular momentum,

$$\tilde{\Lambda}_j I_{xj}+I_{xj}\tilde{\Lambda}_j=\tilde{\Lambda}_j I_{yj}+I_{yj}\tilde{\Lambda}_j=0, \tag{7}$$

it follows that $i\tilde{\Lambda}_j=-\tilde{\Lambda}_j i$. Furthermore, ϕ_{mj} must be equal to $m_j\pi+\phi'$, where ϕ' is some real constant independent of m. The constant ϕ' can be conveniently set equal to zero.

Using these properties of $\tilde{\Lambda}_j$ and Eq. (5), it is easily shown that $[\tilde{\Lambda}_j, I_j^2]=0$, $\tilde{\Lambda}_j^2=1$, if m_j is an integer, and $\tilde{\Lambda}_j^2=-1$ if m_j is a half integer. It should be noted that these properties of $\tilde{\Lambda}_j$ are just those found for a time reversal operator.

The operator $\tilde{\Lambda}=\prod_j\tilde{\Lambda}_j$ can be used, for example, to show the invariance of a nuclear magnetic double resonance spectrum to change in the sign of the coupling constant J. If $\mathcal{H}'$ is the Hamiltonian of Eq. (4) with the signs of all the coupling constants changed ($J_{jk}\rightarrow -J_{jk}$), then

$$\mathcal{H}+\mathcal{H}'=2A+2C, \tag{8}$$

where $A=\sum_j A_j I_{zj}$, and $C=\sum_{j>i} v_{ij} I_{zj}$.

Since $[\mathcal{H}, \tilde{\Lambda}]=-2\tilde{\Lambda}A-2\tilde{\Lambda}C$,

$$\pm\tilde{\Lambda}\mathcal{H}\tilde{\Lambda}-\mathcal{H}=-2A-2C, \tag{9}$$

where the sign of $\tilde{\Lambda}\mathcal{H}\tilde{\Lambda}$ depends on whether $\sum_j m_j$ is integer or half integer. Combining Eqs. (8) and (9) gives

$$\tilde{\Lambda}\mathcal{H}=-\mathcal{H}'\tilde{\Lambda}. \tag{10}$$

The proof from Eq. (10) that the eigenvalues and transition probabilities between eigenstates of $\mathcal{H}$ and $\mathcal{H}'$ are equal is identical to that given by Corio.[7]

The spin inversion operator $\tilde{\Lambda}_j$ displays rotational symmetry, and thus $[\mathcal{H}, \tilde{\Lambda}]$ does not depend on the choice of the x or y axis for the direction of the radio frequency field. However it must be noted that $\tilde{\Lambda}_j$ has the special properties that $i\tilde{\Lambda}_j=-\tilde{\Lambda}_j i$, and $\tilde{\Lambda}_j^2=\pm 1$ depending on whether m_j is integer or half integer.

[1] P. L. Corio, Chem. Revs. **60**, 363 (1960).
[2] P. L. Corio, J. Chem. Phys. **29**, 682 (1958).
[3] The commutation rules given in the work cited in footnote 1, p. 372 are in error. However $[\Lambda, \mathcal{H}]$ is correctly given, and all theorems based on this commutator are valid. (P. L. Corio, private communication).
[4] A. L. Bloom and J. N. Shoolery, Phys. Rev. **97**, 1261 (1955).
[5] J. D. Baldeschwieler, J. Chem. Phys. **34**, 718 (1961).
[6] $\mathcal{H}$ is given in a coordinate system rotating at frequency ω_2.
[7] Work cited in footnote 1, p. 406, Eqs. (5) to (7).

Identification of Perinaphthene Radical in Petroleum Product

FERDINAND C. STEHLING AND KENNETH W. BARTZ

Research and Development Division, Humble Oil and Refining Company, Baytown, Texas

(Received November 21, 1960)

THE existence of free radicals in petroleum[1–3] and in some products derived from petroleum[4] has been determined by electron spin resonance (ESR). Although these radicals are believed to be condensed, aromatic ring structures, the specific identification of a free radical in petroleum or related products has not been reported. In most previous cases the ESR spectra have consisted of a single peak with no resolved fine structure. A spectrum of a free radical with extensive fine structure has now been obtained from the aromatic fraction of catalytic cycle stock; this radical has been identified as the perinaphthene radical [see diagram (1)].

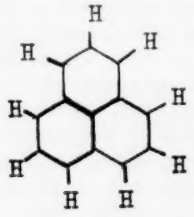

DIAGRAM 1.

The history of the sample was as follows: a fraction of crude oil boiling between 320 and 670°C was successively hydrodesulfurized, catalytically cracked, and distilled. The high boiling residue was phenol extracted and the extract was examined by ESR after removing the phenol. A spectrometer operating at 9.2 kMc with 100-kc single modulation and phase-sensitive detection was used to obtain the spectrum which is shown in Fig. 1. The g value, the number of peaks, and the splitting between peaks appear to be identical to those reported for the perinaphthene radical by Sogo, *et al.*[5] The rela-

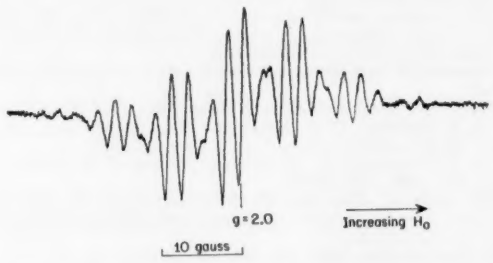

FIG. 1. ESR spectrum of phenol extract of catalytic cycle stock.

tive intensities of the peaks are also similar; exact correspondence of the relative intensities is not to be expected because of differences in resolution. Thus, the radical species in the phenol extract of catalytic cycle stock is undoubtedly the perinaphthene radical. The concentration determined by numerical double integration of the first harmonic of the absorption mode and comparison with a diphenylpicrylhydrazyl sample of known concentration was about 10^{-4} moles/liter.

An investigation of the origin of the perinaphthene radical will be conducted shortly.

[1] H. S. Gutowsky, B. R. Ray, R. L. Rutledge, and R. R. Unterberger, J. Chem. Phys. **28,** 744 (1958).
[2] D. E. O'Reilly, J. Chem. Phys. **29,** 1188 (1958).
[3] T. H. Brown, H. S. Gutowsky, and K. E. Van Holde, J. Chem. Eng. Data **5,** 181 (1960).
[4] R. B. Williams and F. C. Stehling, unpublished work.
[5] P. B. Sogo, M. Nakazaki, and M. Calvin, J. Chem. Phys. **26,** 1343 (1957).

Solvent Effects on the Spectra of Halide Ions*

S. J. Strickler† and M. Kasha

Department of Chemistry, Florida State University, Tallahassee, Florida

(Received December 14, 1960)

It has been known for many years that halide ions in solution show strong absorption bands in the ultraviolet region.[1] The first interpretations of these bands were as "electron affinity spectra" in which it was proposed that an electron was transferred from the halide ion to one or several solvent molecules.[2,3] More recent theories regard the excited state in these solvated systems as having the electron bound in the average field of the oriented solvent dipoles,[4] or in a spherical infinite potential-well defined approximately by the first solvation shell.[5] Recently it has been suggested that this may be true for water and alcohols, but that a specific transfer takes place in solvents such as acetonitrile.[6] None of these theories seems to us to be entirely satisfactory.

However, regardless of the exact nature of the excited state, it seems well established that solutions of I^-, Br^-, and Cl^- show a distinct type of transition, which cannot be regarded as any internal electronic transition for the free ion. Indeed, no internal electronic transition is believed possible in these ions. Whichever theory of the excited state is considered most nearly correct, the solvent molecules must be intimately involved in it. This suggests that the solvent effects on the spectra might be large and characteristic of this type of transition.

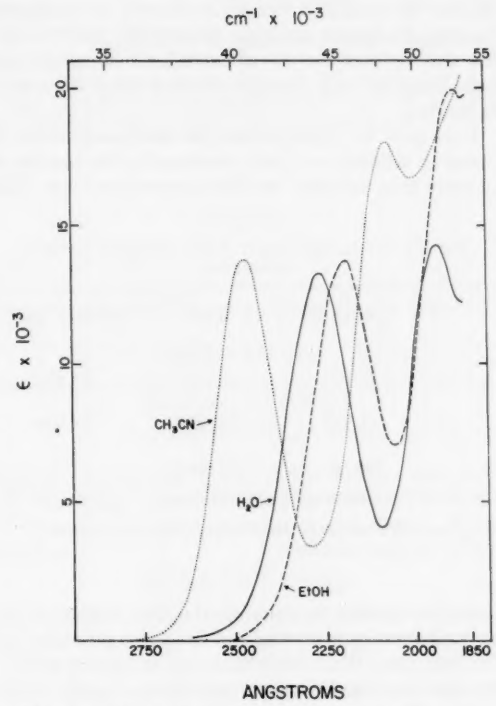

Fig. 1. Spectra of sodium iodide in acetonitrile, water, and absolute ethanol.

With this in mind we have studied the spectra of iodide, bromide, and chloride ions in several solvents. The compounds used were sodium iodide, tetraethylammonium bromide, and tetraethylammonium chloride. (The latter two were chosen for solubility reasons.) The solvents used were acetonitrile, water, and absolute ethanol. All spectra were measured using a 0.1-mm cell in a Cary model 14 spectrophotometer, with the entire light path flushed with nitrogen.

Figure 1 shows the spectra of iodide ion in the three solvents. Two peaks corresponding to the $^2P_{3/2}$ and $^2P_{1/2}$ states of the halogen atoms[2] appear in the spectra of I^- and Br^-. The doublet splitting in the case of Cl^- is so small (<900 cm^{-1}) that the peaks could not be resolved. Table I summarizes the frequencies of the transitions of the ions in the three solvents. For I^- and Br^- only the value for the low-frequency peak is given.

Spectra of NaI were also run in mixtures of absolute ethanol and acetonitrile. The bands were slightly broader than in pure solvents. Both bands of the doublet shifted smoothly to the blue with increasing proportions of ethanol and neither band showed any indication either of splitting into two distinct components or of abnormal broadening. This is evidence

against the model in which an electron is transferred to a specific solvent molecule, since if this were the case one would expect two sets of bands in the mixed solvent corresponding to a transfer to each kind of solvent molecule.

It is seen in Table I that the frequency shifts in changing solvents are fairly uniform in the spectra of all three ions, and that the shifts are rather large. This

TABLE I. Frequencies (cm^{-1}) of first absorption peaks of halide ions.

	Acetonitrile	Water	Ethanol (abs.)
I^-	40 500	44 150	45 520
Br^-	45 930	51 000[a]	52 000[a]
Cl^-	50 760	(55 200)[b]	

[a] The spectrum is not well resolved, so these values are approximate.
[b] This value taken from Scheibe.[1]

regularity appears in spite of the fact that there is a large difference in the size and ionization potential for the three ions. We believe that any transition of this type should show similar solvent effects. A study of the solvent effects on any strong ultraviolet transition could then be used as a test for a transition of this type.

It has been suggested that the ultraviolet spectra of a large number of anions are due to such electron transfer transitions.[3,7] Although solubility is a problem, the test for similar solvent effects could be applied to many of these ions. Such a study has been carried out for the strong transitions in the spectra of the ions NO_3^- and NO_2^-. The solvent shifts are qualitatively different from those observed for halide ions, and must therefore be assigned to internal transitions in these molecules. The spectra of nitrate and nitrite ions will be discussed in another place.[8]

* This work was supported in part by a contract between the Physics Branch, Office of Naval Research, U. S. Navy and the Florida State University.

† National Science Foundation Predoctoral Fellow, 1956-60. Present address: Department of Chemistry, University of California, Berkeley, California.

[1] G. Scheibe, Z. Elektrochem. **34**, 497 (1928); Z. physik. Chem. (Leipzig) **B5**, 355 (1929).
[2] J. Franck and G. Scheibe, Z. physik. Chem. (Leipzig) **A139**, 22 (1928).
[3] E. Rabinowitch, Revs. Modern Phys. **14**, 112 (1942).
[4] R. Platzman and J. Franck in *L. Farkas Memorial Volume*, edited by A. Farkas and E. P. Wigner (Research Council of Israel, Jerusalem, 1952), p. 21; Z. Physik **138**, 411 (1954).
[5] M. Smith and M. C. R. Symons, Discussions Faraday Soc. **24**, 206 (1957).
[6] E. M. Kosower, J. Am. Chem. Soc. **80**, 3253, 3261 (1958).
[7] H. L. Friedman, J. Chem. Phys. **21**, 319 (1953).
[8] S. J. Strickler and M. Kasha, to be published.

Core Polarization in Li_2

OKTAY SINANOĞLU* AND EARL M. MORTENSEN†

Department of Chemistry and Lawrence Radiation Laboratory, University of California, Berkeley, California

(Received November 23, 1960)

RECENTLY, a theory was given[1] to show how a molecule can be built up from separate groups of electrons. Each group includes electron correlation, yet the separation takes the Pauli exclusion principle fully into account. The method justifies, e.g., the separate treatment of σ and π electrons.

In Li_2 the energy separates into the energies of two (Li^+) ion cores interacting with dispersion forces, the correlated $(\sigma_g 2s)^2$ shell, and the correlation energy between the outer electrons and cores.[1] The latter is referred to as "core polarization" and has not been considered in previous configuration interaction calculations.[2] It is the entire correlation effect and not just the "orbital average polarization," or single excitations part which would vanish after a complete SCF calculation. This core-valence electron correlation energy can be obtained as the expectation value of a (Li^+) correlation or "fluctuation" potential[1] over outer MO's.

We use Callaway's[3] potential V_p resulting from the instantaneous polarization of (Li^+) by a slow electron, the main part coming from the dipole terms. We shall examine the contribution of core polarization to the small binding energy of Li_2 and its sensitivity to the crudeness of the outer MO's used.

For Li atom, $\langle 2s, V_p 2s\rangle$ is calculated with an analytic Hartree-Fock SCF orbital $2s_R$ and also with a Slater orbital $2s^0$ Schmidt-orthogonalized to the core. The SCF $2s_R$ is the 6-term "best compromise" orbital given by Roothaan, Sachs, and Weiss[4] in their Table Vb. The $2s^0$ is for Slater exponents $\delta_{1s}=2.65$ and $\delta_{2s}=0.65$,

$$2s^0=[1/(4\pi)^{\frac{1}{2}}][0.39915r\exp(-0.65r) - 1.5030\exp(-2.65r)]. \quad (1)$$

For $Li_2\langle\sigma_g 2s, V_p\sigma_g 2s\rangle$ is calculated for one core and one outer MO the result being multiplied by four for the total core polarization.[1] Two different approximate outer MO's are used: (1) The analytic "best limited" SCF MO of Ransil[5]:

$$(2\sigma_g)_R=0.52979(2s_a+2s_b)+0.11438(2p\sigma_a+2p\sigma_b) - 0.14397(1s_a+1s_b), \quad (2)$$

with Slater exponents $\delta_{2s}=0.6335$, $\delta_{2p\sigma}=0.7609$, and $\delta_{1s}=2.6894$. (2) An MO formed from $2s$ Slater AO's Schmidt-orthogonalized to *both* cores

$$(2\sigma_g)_{OMO}=0.57222(2s_a+2s_b)-0.13748(1s_a+1s_b), \quad (3)$$

with $\delta_{2s}=0.65$, $\delta_{1s}=2.65$. Both MO's are for the equilibrium internuclear distance of $R_e=5.051$ a.u.

The lowering of the total energies of Li and Li_2 due to core polarization is shown in Table I. Numerical integrations were carried out on IBM 704. The value obtained for Li with the analytic[4] HF SCF $2s_R$ agrees

TABLE I. Core polarization energies in electron volts.

	ev
Li atom	
(a) HF SCF $2s_R$	0.1018
(b) OAO (Eq. 1) $2s^0$	0.1066
Li_2 molecule (R_e=5.051 a.u.)	
(c) SCF MO [Eq. (2)] $(2\sigma_g)_R$	0.2473
(d) OMO [Eq. (3)] $(2\sigma_g)_{OMO}$	0.2520
Contribution to Li_2 binding energy	
(c) −2 (a)	0.0436
(d) −2 (b)	0.0387

with that of Callaway; he used[3] an earlier numerical HF orbital. The total energy of Li_2 is lowered by approx 0.25 ev. This should be compared to the "orbital average polarization" energy which should be less[6] than 0.019 ev as found by Ishiguro, *et al.*[2] The latter is not a correlation energy and arises as the difference between a complete SCF and a fixed core outer electron SCF calculation.[1,2]

Penetration effects are neglected in V_p. They were estimated previously[1] for Li to be less than 0.035 ev for the $1s_\beta 2s_\alpha$ interaction and 0.001 ev for $1s_\alpha 2s_\alpha$. The "exclusion effect"[1] of other electrons on the core-polarization energy of one, as well as three or more electron Coulomb correlations which may be small are also left out.

The contribution to the binding energy (1.03 ev) of Li_2 is also shown in Table I. We note that the energy is not very sensitive to the crudeness of the orbitals used. Thus where SCF MO's are not available, e.g., for Na_2, K_2, etc., it would suffice to use OMO's. Note also that though core polarization contributes quite appreciably to the total energies of Li and Li_2, the effects on the two almost cancel and yield a small contribution to the binding energy. Such a cancellation has often been assumed in semiempirical theories.

We are most thankful to Professor K. S. Pitzer for encouraging this research. The work was done under the auspices of the United States Atomic Energy Commission.

* Present address: Sterling Chemistry Laboratory, Yale University, New Haven, Connecticut.

† National Science Foundation Postdoctoral Fellow.

[1] O. Sinanoğlu, J. Chem. Phys. **33,** 1212 (1960); Proc. Roy. Soc. (to be published); Phys. Rev. (to be published); Bull. Am. Phys. Soc. **5,** 433 (1960).

[2] E. Ishiguro, K. Kayama, M. Kotani, and Y. Mizuno, J. Phys. Soc. (Japan) **12,** 1355 (1957).

[3] J. Callaway, Phys. Rev. **106,** 868 (1957); V_p given in his Table I is in Rydbergs.

[4] C. C. J. Roothaan, L. M. Sachs, and A. W. Weiss, Revs. Modern Phys. **32,** 186 (1960).

[5] B. J. Ransil, Revs. Modern Phys. **32,** 245 (1960); Table I.

[6] The value 0.019 ev is too high for "orbital average polarization" in Li_2, because it results from a very crude approximation[2] to outer MO's in the field of fixed cores.

Vaporization of Several Rare Earth Oxides*

MORTON B. PANISH

Research and Advanced Development Division, Avco Corporation, Wilmington, Massachusetts

(Received November 18, 1960)

THE vaporization of two of the lightest rare earth oxides, La_2O_3 and Nd_2O_3 has been shown by several workers[1,2] to proceed principally by means of the reaction

$$M_2O_{3(s)} \rightarrow 2MO_{(g)} + O_{(g)}. \quad (1)$$

The work of Chupka, Inghram, and Porter was a mass spectrometric study of the La–La_2O_3 system, and that of Walsh, Goldstein, and White was a simple effusion study of La_2O_3 and Nd_2O_3 vaporizing from tungsten effusion cells.

In this work, the vaporization of Pr_2O_3, Nd_2O_3, Sm_2O_3, and Eu_2O_3 has been studied at temperatures ranging from 1950°K to 2350°K by analyzing the species effusing from a Knudsen effusion cell with a Bendix time-of-flight mass spectrometer. Experimental details of the heating and temperature measuring techniques will be described elsewhere.[3]

The effusion cells were lined with either iridium or thoria. Studies in which iridium liners were used were principally to determine the relative amounts of the various species in equilibrium with the oxide with a minimum of chemical interference from the container. The ratio $I_M{}^+/I_{MO}{}^+$ of ion currents due to the metal and monoxide when 20-ev electrons were used are given in the last column in Table I. For each of the compounds studied, a search for effusing species was made at several temperatures and electron bombardment energies.

If the ion current ratios in Table I represent the ratios of the equilibrium species with the effusion cell, it is obvious that among the oxides studied there is a change in the vaporization mode from that shown in Eq. (1) to that shown in Eq. (2), with increasing atomic number of the rare earth metal

$$M_2O_{3(s)} \rightarrow 2M_{(g)} + 3O_{(g)}. \quad (2)$$

Spurious results would be expected if the observed ions did not originate from simple ionization of neutral

species, but from dissociative ionization of a parent molecule or by ion molecule combination in the ion source. In all the cases presented here, ion molecule combination is highly improbable because of the low concentration of ions and molecules in the ion source. If the MO^+ ions were due to dissociative ionization, ions of higher mass would be present in appreciable amounts. This is not the case.

The M^+ ions observed when vaporizing Sm_2O_3 and Eu_2O_3 could have derived from dissociative ionization. In order to determine which process led to the formation of these ions, Sm_2O_3 and Eu_2O_3 were vaporized from ThO_2 effusion cells containing a small amount of SiO_2. The vaporization thus occurred in an oxidizing atmosphere. Under these conditions, the MO^+ ions, rather than M^+ ions, were the major species observed. It follows that the M^+ ions observed as the major, or as an important species under neutral conditions, were due principally to simple ionization of the parent M atoms in the effusion beam.

TABLE I. Equilibrium vaporization data at 2000°K.

Oxide	P_M (atm)	P_{MO} (atm)	P_{MO_2} (atm)	$I_M{}^+/I_{MO}{}^+$
Pr_2O_3	$<1\times10^{-8}$	1×10^{-7}	$<5\times10^{-9}$	<0.1
Nd_2O_3	$<5\times10^{-9}$	5×10^{-8}	...	<0.1
Sm_2O_3	$\approx3\times10^{-9}$	$\approx3\times10^{-9}$	...	0.5–1.0
Eu_2O_3	7×10^{-8}	9×10^{-9}	...	8.0±2

The vaporization of the oxides under neutral conditions appeared to be stoichiometric. X-ray analyses of the oxides after heating indicated that only M_2O_3 was present at the end of the run.

In order to determine the approximate equilibrium pressures of the vaporizing species, mixtures of the oxide and rhodium powder were effused from thoria-lined cells. The rhodium provided an internal calibration by which the pressure of the species could be calculated from

$$P_X = (I_X{}^+\sigma_{Rh}/I_{Rh}{}^+\sigma_X)\,P_{Rh}, \qquad (3)$$

where P, σ, and I^+ are the vapor pressures, electron cross sections, and ion currents of the species X and rhodium. Iridium vaporizing from the liner in the first experiments could not be used for calibration because of its low vapor pressure.[3] The vapor pressures of rhodium estimated by Stull and Sinke,[4] and confirmed in this laboratory,[3] were used.

The electron cross sections of rhodium, the rare earth metals, and oxygen were taken as 40.6, 73, and 3.3, respectively, on the basis of the work of Otvos and Stevenson.[5] It was assumed that the electron cross sections of the oxides were equal to the sums of the cross sections for the metals and oxygen. The uncertainties included in the extrapolation of the data of Otvos and Stevenson and in the assumption that electron cross sections are additive could, of course, have led to errors as large as a factor of 2 or 3 in the absolute pressure data. The values reported in Table I can, therefore, only be considered to be approximate.

It is assumed that the predegassed thoria liners did not interfere with these measurements. No condensed phase interaction was noted and the equilibrium vapor pressure of $ThO_{(g)}$ and $ThO_{2(g)}$ with $ThO_{2(s)}$ was several orders of magnitude lower than that of the gaseous species of the least volatile of the compounds studied.[6] The ratios of the various species effusing from the thoria lined cells were not markedly different from those obtained with the iridium cells.

* This work was supported by Avco Corporation, by the Advanced Research Projects Agency and by the Materials Central Wright Air Development Division, Wright-Patterson Air Force Base, Ohio.

[1] W. A. Chupka, M. G. Inghram, and R. F. Porter, J. Chem. Phys. **24**, 792 (1956).

[2] P. N. Walsh, H. W. Goldstein, and D. White, J. Am. Ceram. Soc. **43**, 229 (1960).

[3] M. B. Panish and L. Reif (to be published).

[4] J. Otvos and D. Stevenson, J. Am. Chem. Soc. **78**, 546 (1956).

[5] D. R. Stull and G. C. Sinke, *Thermodynamic Properties of the Elements* (American Chemical Society, Washington, D. C., 1956).

[6] M. B. Panish and L. Reif, unpublished results.

Density Measurements in Reflected Shock Waves

W. C. GARDINER, JR.,* AND G. B. KISTIAKOWSKY

Gibbs Chemical Laboratory, Harvard University, Cambridge, Massachusetts

(Received November 7, 1960)

THE state of experimental gas behind reflected shock waves is usually calculated from the velocity of the incident wave using the simple theory of plane shock wave reflection. Recent results have indicated, however, that the reflected waves may actually be substantially weaker than calculated, even in a pure monatomic gas.[1–3] We have carried out a number of experiments using the technique of soft x-ray absorption to see if the density behind reflected shock waves in pure xenon would be significantly lower than calculated.

The apparatus described previously[4] was rebuilt to enable shock wave experiments to be done under clean vacuum conditions. The shock tube is of 3-in. i.d. steel tubing, with a 10-ft driver section and an 11-ft expansion section. It can be evacuated to less than 10^{-5} mm Hg and has an outgassing rate of about 1–3 μ/hr. Shock velocities were measured using platinum resistance gauges and a raster-sweep oscilloscope. Attenuation was less than 0.2% in 50 cm. Beryllium slits 1.5 mm wide define the x-ray beam. The intensity of the

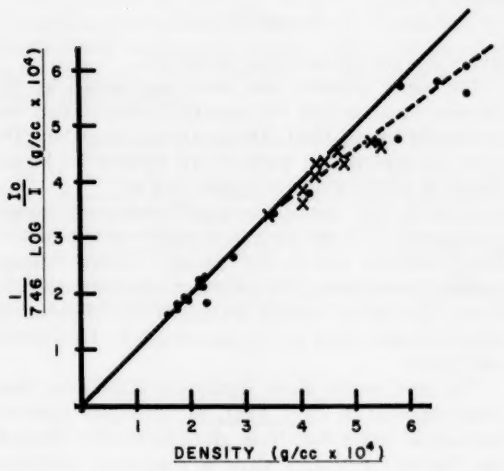

FIG. 1. Density measurements. ●=incident shocks, ×=reflected shocks.

x-ray signal and hence the accuracy of the density measurements have been increased. Xenon of greater than 99.995% purity (determined mass-spectroscopically) was used as the experimental gas. Static calibration at densities up to 3.5×10^{-4} g/cc indicated that Beer's Law was obeyed, with an extinction coefficient $\epsilon=746$ cc/g. Calibration was extended above 3.5×10^{-4} g/cc with density measurements in incident shocks.

Figure 1 summarizes the experimental results on incident and reflected shocks. The abscissa is gas density calculated from incident shock velocities, the ordinate is gas density measured from oscilloscope records[4] using $\epsilon=746$ cc/g. The densities measured in incident shocks show the extent to which Beer's Law is no longer obeyed above 3.5×10^{-4} g/cc.

Densities were measured in reflected shocks at distances of 0.5 to 5 cm from the reflecting plate. The calculated reflected shock temperatures were from 3000 to over 7000°K. Within the experimental accuracy the densities measured immediately after the passage of the reflected shocks agree with those calculated from incident shock velocities. No correlation of the scatter of the points above or below the dashed line either with shock strength or with distance from the reflecting plate was found. These measurements indicate, therefore, that densities immediately behind reflected shocks in a monatomic gas are not substantially different from those calculated from incident shock velocities.

After passage of the reflected shock the density was observed to increase in an approximately linear fashion as long as the gas remained undisturbed. The rate of increase was temperature dependent, approximately doubling over the range of reflected shock temperatures studied. The upper limit to this range was marked by the occurrence, after an induction period, of sudden increases in density which we attribute to ionization. Sample experimental data: incident shock velocity 688 m/sec, calculated reflected shock temperature 3500°K, calculated reflected shock density 3.47×10^{-4} g/cc, measured reflected shock density at the wave front $3.4_2\times10^{-4}$ g/cc, measured density after 350 μsec $3.5_6\times10^{-4}$ g/cc. These particular data refer to a density range where the deviation from Beer's Law is not appreciable and therefore do not have to be corrected for this effect.

The steady increase in density is of course disturbing insofar as it confirms that more is involved in the gas dynamics of reflected shock propagation than the simple theory admits. For chemical kinetic studies in reflected shock waves the temperature history of the gas is the matter of primary concern, and the significance of the present results in this respect is not certain. It might seem a reasonable assumption to say that the compression that we observe after the shock must be an adiabatic one. If this is so, then the sample data above would indicate that the temperature of the gas has risen to 3591°K after 350 μsec. But the adiabatic assumption also predicts that the pressure would have increased by 7% in this same interval, a value which is higher than the results of Skinner[2] suggest. If the pressure increases at the same rate as the density (4% in 350 μsec) then the compression is isothermal. Since Skinner's experiments were done at lower shock strengths than the ones reported here a direct comparison is not possible. It would seem, however, that the reflected shock temperature is subject to less variation than the adiabatic assumption predicts.

This work was supported by the Office of Naval Research.

* Present address: Department of Chemistry, The University of Texas, Austin, Texas.

[1] R. A. Strehlow and A. Cohen, J. Chem. Phys. **30**, 257 (1959).
[2] G. B. Skinner, J. Chem. Phys. **31**, 268 (1959).
[3] T. A. Brabbs, S. A. Zlatarich, and F. E. Belles, J. Chem. Phys. **33**, 307 (1960).
[4] G. B. Kistiakowsky and P. H. Kydd, J. Chem. Phys. **25**, 824 (1956); J. P. Chesick and G. B. Kistiakowsky, *ibid.* **28**, 956 (1958).

Entropies of Vaporization of Hydrocarbons and the Hildebrand Rule

R. W. HERMSEN AND J. M. PRAUSNITZ

Department of Chemical Engineering, University of California, Berkeley, California

(Received November 21, 1960)

OVER 40 years ago Hildebrand[1] reported the observation that the entropies of vaporization of nonpolar fluids are essentially equal when comparison

is made, not at the same reduced temperature or at the same vapor pressure, but rather at the same saturated vapor volume. In 1939 Hildebrand[2] reported calculations for entropies of vaporization for several hydrocarbons and claimed that deviations from the Hildebrand rule could be explained in terms of liquid structure. When mercury was used as a reference, the observed entropies for benzene, *n*-hexane, *n*-heptane, and cyclohexane were significantly larger than those predicted by the Hildebrand rule; the larger entropy was believed to be due to additional liquid order in excess of that for a simple liquid such as methane.

Since Hildebrand's 1939 article, highly accurate vapor pressure data for hydrocarbons have been published by Rossini and associates[3]; further, a reliable correlation for volumetric properties of gases, reported by Pitzer and Curl,[4] now makes it possible to compute saturated vapor volumes without assuming ideal gas behavior as was done by Hildebrand. It appeared worthwhile, therefore, to repeat Hildebrand's calculations using more recent information on the thermal and volumetric properties of hydrocarbons.

Table I shows entropies of vaporization for 21 hydrocarbons at a saturated vapor volume of 49.5 liter/g mole, the volume previously used by Hildebrand. The entropies were calculated from the vapor pressure data

TABLE I. Entropies of vaporization of hydrocarbons at saturated vapor volume of 49.5 liter/g mole in cal/g mole, °K.[a]

Substance	Temp., °K	ΔS	ΔS (excess)[b]	ΔS[c]
Methane	92.6	22.5	0	
Ethane	163.2	22.7	+0.2	
Propane	209.3	22.6	+0.1	
n-Butane	251.2	22.3	−0.2	
Isobutane	239.5	22.2	−0.3	
n-Pentane	288.6	22.3	−0.2	20.7
Isopentane	279.8	22.1	−0.4	20.2
Neopentane	260.8	21.8	−0.7	20.1
n-Hexane	323.1	22.2	−0.3	21.5
n-Heptane	353.3	22.4	−0.1	21.5
n-Octane	381.9	22.4	−0.1	21.2
2-Methylheptane	373.3	22.3	−0.2	
2,2-Dimethylhexane	361.7	22.0	−0.5	
n-Decane	432.9	22.5	0.0	
n-Eicosane	611.9	22.6	+0.1	
Cyclopentane	302.3	22.4	−0.1	
Cyclohexane	334.7	22.2	−0.3	21.1
Methylcyclohexane	355.4	21.7	−0.8	
1-Butene	245.4	22.6	+0.1	
1,3-Butadiene	247.5	22.4	−0.1	
Benzene	334.6	22.7	+0.2	21.2
Mercury				20.1

[a] ΔS is accurate to ±0.1 entropy unit.
[b] $\Delta S(\text{excess}) = \Delta S - \Delta S(\text{methane})$.
[c] See work cited in footnote 2.

according to

$$dP/dT = \Delta S/(V-v),$$

where P is the vapor pressure at temperature T, and V and v are, respectively, the saturated vapor and liquid volumes. The relationship between P and V is given by

$$V = (RT/P) + B,$$

where B is the second virial coefficient.

The vapor pressure data were represented by the Antoine equation and the numerical computation was performed by an IBM 704 electronic computer. The entropies reported in Table I are believed to be accurate to within ±0.1 cal/g mole/deg K.

Table I also shows the equilibrium temperature corresponding to the saturated vapor volume of 49.5 liter/g mole as well as the "excess" entropy relative to that for methane. The column at the extreme right shows the earlier results published by Hildebrand[2] which are also given in the monograph by Hildebrand and Scott.[5]

The new results show significant differences from those reported in 1939. First, the entropies reported here are all larger than those given previously. Second, the "excess" entropies show a completely different pattern from that observed earlier. The results in Table I show that all normal paraffins from C_1 to C_{20} appear to have essentially the same entropy within the accuracy now available. However, branched

TABLE II. Entropies of vaporization of isomeric heptanes at saturated vapor volume of 49.5 liter/g mole in cal/g mole, °K[a]

Substance	Temp., °K	ΔS	ΔS (excess)[b]	v, cc/g mole
n-Heptane	353.3	22.4	−0.1	159
3-Ethylpentane	347.9	22.1	−0.4	154
2,4-Dimethylpentane	334.3	22.0	−0.5	158
2,2-Dimethylpentane	332.8	21.8	−0.7	157
3,3-Dimethylpentane	339.7	21.7	−0.8	153
2,2,3-Trimethylbutane	334.2	21.5	−1.0	153

[a] ΔS is accurate to ±0.1 entropy unit.
[b] $\Delta S(\text{excess}) = \Delta S - \Delta S(\text{methane})$.

paraffins show negative "excess" entropies which increase with the extent of branching. It is interesting that neopentane, which because of its approximately spherical shape was thought to be very similar in its properties to methane, actually shows one of the largest negative "excess" entropies.

The effect of branching is brought out even more clearly in the results shown in Table II which gives entropies for six isomeric heptanes. "Excess" entropies are also shown and the last column gives the saturated liquid molar volumes.

Since the Hildebrand rule is a reasonable but essentially empirical relationship it is difficult to interpret the exact meaning of the "excess" entropies in terms of liquid structure. However, the results in Table I and especially those in Table II suggest that the free volumes of irregularly shaped molecules are larger than those for molecules which have a smooth and regular shape.

The authors are grateful to the National Science Foundation and to the donors of the Petroleum Research Fund for financial support, and to the Computing Center of the University of California for the use of their facilities.

[1] J. H. Hildebrand, J. Am. Chem. Soc. **37**, 970 (1915).
[2] J. H. Hildebrand, J. Chem. Phys. **7**, 233 (1939).
[3] F. D. Rossini, K. S. Pitzer, R. L. Arnett, R. M. Braun, and G. C. Pimentel, *Selected Values of the Physical and Thermodynamic Properties of Hydrocarbons and Related Compounds* (Carnegie Press, Pittsburgh, Pennsylvania, 1953).
[4] K. S. Pitzer and R. F. Curl, Jr., J. Am. Chem. Soc. **79**, 2369 (1957).
[5] J. H. Hildebrand and R. L. Scott, *Solubility of Nonelectrolytes* (Reinhold Publishing Corporation, New York, 1950), p. 79.

Transient Dimer Formation by 2,5-Diphenyloxazole*

ISADORE B. BERLMAN

Radiological Physics Division, Argonne National Laboratory, Argonne, Illinois

(Received November 16, 1960)

EMISSION spectrograms and measurements of the lifetime of solutions of paraxylene and large concentrations of 2,5-diphenyloxazole (PPO) indicate that transient excited dimers are formed according to the concept postulated by Forster and Kasper.[1] The evidence for this assumption is as follows:

(1) The shape of the emission spectrum from xylene-PPO solutions excited with 3130-A radiation changes progressively with increasing concentration of PPO as shown in Fig. 1. That these observations were not the result of absorption and reemission processes can easily be demonstrated by varying the thickness of the solution sample at constant concentration.

(2) Absorption measurements were made using a variable light-path cell,[2] and the results indicate that the shape of the absorption spectrum does not change with concentration. These observations negate the possibility of permanent dimers.

(3) The measured mean fluorescent lifetime of PPO in xylene as measured by the initial slope of the fluorescent lifetime curve remains essentially 2.65 ± 0.10 nsec irrespective of the solute concentration. A second and longer component makes its appearance and becomes progressively more prominent as the solute concentration is increased, as shown in Fig. 2. Interposing a Wratten 2B series VI filter between the solution and the detecting equipment to eliminate the shorter wavelengths of the emission spectrum, results in the elimination of the short component of the recorded lifetime curve, leaving only the longer component; the mean lifetime of which was experimentally determined to be 14.0 ± 1.5 nsec. The presence of a possible third and even longer component in the emission lifetime could not be established with the present equipment.

(4) The effect of viscosity of the solvent on the formation of the dimers was investigated by the above

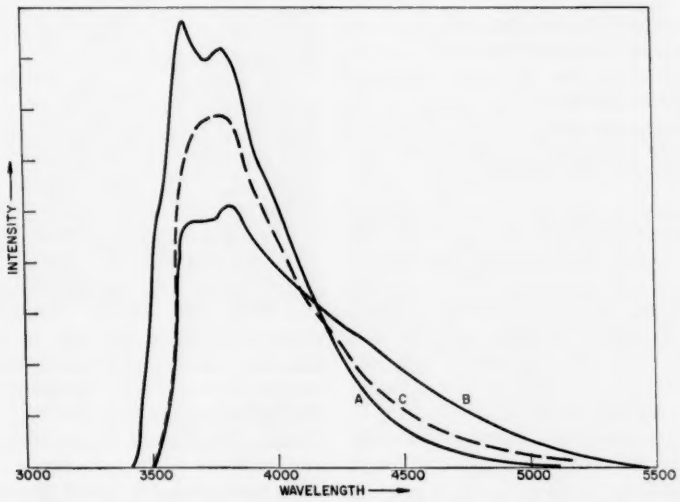

FIG. 1. Relative emission spectra from PPO-xylene solutions under static illumination of 3130-A radiation for the concentrations of 1 g/liter using a 1-mm sample, curve *A*, 100 g/liter, using a 0.2-mm sample, curve *B*, and 100 g/liter, heated, curve *C*.

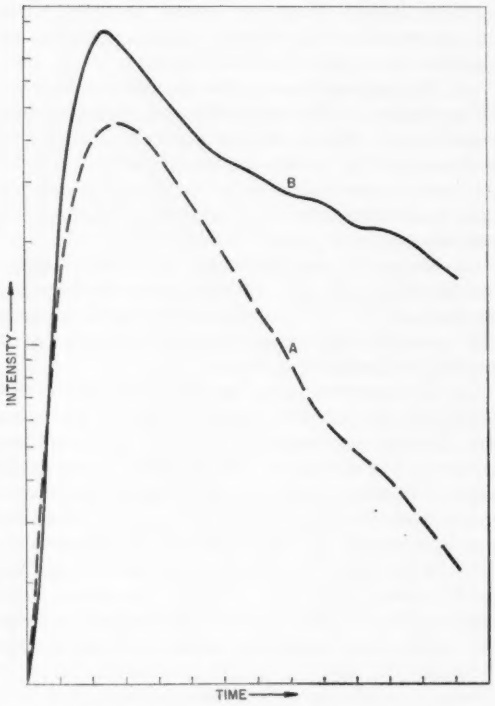

FIG. 2. Semilog plots of the fluorescent lifetime of a PPO-xylene solution at concentrations of 4 g/liter, curve *A*, and 100 g/liter, curve *B*. Intensities are arbitrary.

methods. In aliphatics (methylcyclohexane, paraffin oil) and in alcohol (ethyl alcohol) at the same solute concentration the results disclose that the larger the viscosity the smaller the dimerization. Although the same is true also for the aromatics (benzene, toluene, xylene, isopropyl biphenyl), for the same concentration of PPO and for relatively similar values of the viscosity, dimers occur much less readily in the aromatics. This later result eliminates the possibility that an impurity in PPO is the cause of the spectrum shift.

(5) It is commonly recognized that, generally, cooling enhances dimerization whereas heating deactivates the dimers.[3,4] The same is true in the present experiment. Heating a solution of 100 g/liter of PPO in xylene dramatically affects the emission spectrum as shown by curve *C* in Fig. 1; whereas heating a solution of 1 g/liter of PPO in xylene to the same temperature does not change the magnitude or shape of the emission spectrum. Cooling a solution of 100 g/liter of PPO in toluene below room temperature increases the long wavelength portion of the spectrum at the expense of the shorter wavelengths.

The apparatus and the experimental procedure have been described in an earlier report.[5] Unless otherwise specified, the experiments were performed at room temperature and under nitrogenated conditions.

In conclusion, our observations have been that in each solvent tested the decrease in quantum yield at high PPO concentrations is accompanied by the formation of transient dimers. Those solvents which exhibit the most *self-quenching* also display the most dimerization.

The author would like to thank Dr. Arye Weinreb and Dr. Harvey A. Schultz for helpful discussions.

[1] T. Forster and K. Kasper, Z. Electrochem. **59,** 976 (1955).
[2] Research and Industrial Instrument Company, England.
[3] P. Pringsheim, *Fluorescence and Phosphorescence* (Interscience Publishers, Inc., New York, 1949), p. 359.
[4] V. L. Levshin, Bull. Acad. Sci. U.S.S.R. Phys. Ser. **20,** 362 (1956).
[5] I. Berlman, J. Chem. Phys. **33,** 1124 (1960).

Density versus Chemical Shift in NMR Spectra*

SIDNEY GORDON AND B. P. DAILEY

Department of Chemistry, Columbia University, New York, New York

(Received November 14, 1960)

RECENT studies of solvent effects in NMR spectra[1] have suggested that the observed chemical shifts in nonhydrogen bonded systems should be made up of the following contributions: σb the contribution due to bulk magnetic susceptibility, σa arising from anisotropy in the magnetic susceptibility, $\sigma\omega$ due to van der Waals forces between neighboring molecules, and σE the polar effect caused by the perturbation of the electronic structure of the molecule by an electric field arising from the surrounding molecules.

The presence of a van der Waals shift should be demonstrated clearly by a study of the chemical shift of nonpolar molecules over a range of densities in the gaseous and liquid state. Using a technique of measurement suggested by Dr. Akira Okaya, we have studied the proton chemical shifts of gaseous methane and ethylene as a function of density at room temperature. Pressures up to 300 atm were investigated.

Both gases were commercial samples (CH_4 purity was 99%; C_2H_4, 99.5%). Samples were prepared by condensing known amounts of gas from a vacuum line into tubes whose volume-length ratios were accurately known. After vaporizing at room temperature the corresponding gas density could be calculated directly. For samples whose pressure was less than 20 atm, ordinary 5-mm o.d., 3-mm i.d. cylindrical Pyrex tubes were used. For higher pressures, 5-mm o.d., 0.5-mm i.d. thick-walled capillary Pyrex tubes were used. The measurements were made using a Varian high-

resolution NMR spectrometer operating at 60 Mc. The shifts were measured for the lower pressure samples, by the usual sideband technique, using an internal capillary filled with cyclohexane as a reference. For high pressure samples, the measurements were performed using a substitution technique and had a mean deviation of less than 1.5 cycles.

For both substances, an increase in density produced a shift toward lower fields. The data for ethylene (4 points) and methane (11 points) indicate a linear variation of chemical shift with density.

For both substances the shift to lower field with an increase in density is in excess of the value predicted from the diamagnetic susceptibility. This suggests the existence of a van der Waals shift which has linear dependence on density. The derived values of the van der Walls shift coefficient are given in Table I, where ρ is the density in g/ml.

TABLE I.

Substance	$-\chi_m \times 10^6$	Exptl. (cps) shift	Susc. (cps) shift	van der Waals (cps) shift
Ethane (l)	26.8[a]	141.1ρ	111.8ρ	29.3ρ
Ethylene (l)	18.8[a]	115.0ρ	84.1ρ	30.9ρ
Methane (g)	17.4[a]	164.9ρ	136.03ρ	28.9ρ
Ethylene (g)	18.8[a]	107.7ρ	84.1ρ	23.6ρ

[a] C. Barter, R. G. Meisenheimer, and D. P. Stevenson, J. Phys. Chem. **64**, 1312 (1960).

To investigate the dependence of the chemical shift on density in the liquid phase, a Varian variable-temperature probe was used at low temperatures, which were obtained by boiling liquid nitrogen from a 25-l metal Dewar. Temperatures could be held constant to better than ± 0.5°C. To measure the chemical shifts of the liquid samples, using the sideband technique, a secondary reference liquid was required. Acetyl chloride (mp of 112°C) was chosen for this purpose. The shift of acetyl chloride from gaseous methane was determined in a separate series of measurements. Here it was assumed that the chemical shift of gaseous methane as a function of temperature is negligible. The resulting slopes for these liquid-phase measurements are also given in Table I. The van der Waals shift coefficients are of similar magnitude to those obtained from the gas phase data. The difference in slope for gaseous and liquid ethylene is barely outside the experimental limits of error.

TABLE II. δ in ppm from gaseous methane.

Substance	Gas at zero density	Gas at liquid density	Liquid (temp.)	Association shift
Methane	0	0.888	0.908 (−106.1°C)	0.020
Ethane	0.750	1.998	1.995 (−76.7°C)	−0.003
Ethylene	5.167	6.120	6.188 (−78.0°C)	0.068

The data thus obtained, plus a determination of the chemical shift of liquid methane at one temperature (−106.1°C) and of gaseous ethane permit a calculation of corrected "association shifts" using empirical slopes to calculate the necessary extrapolation to a common density for the two phases. These "association shifts" are given in Table II. Within their probable errors, they are all zero.

While the above evidence seems to rule out a role for any type of molecular interaction which takes place only in the liquid state, it is still theoretically possible that these molecules are undergoing some type of association common to the gas and liquid phase. Measurements of the chemical shift of methane in solutions of methane in xenon, in a series of measurements being carried out at the present time, show that the van der Waals shift of methane produced by xenon is two or three times larger than that of pure methane. This is strong evidence for the dependence of chemical shifts on van der Waals interactions between molecules.

* Supported in part by a grant from the National Science Foundation and by the Sloan Foundation.

[1] A. D. Buckingham, T. Schaefer, and W. G. Schneider, J. Chem. Phys. **32**, 1227 (1960).

Hyperfine Splittings in the (HOOC)C^{13}H(COOH) Radical

T. COLE AND C. HELLER

Scientific Laboratory, Ford Motor Company, Dearborn, Michigan

(Received November 10, 1960)

STUDIES of proton hyperfine structure in the electron magnetic resonance (EMR) spectra of the radical (HOOC)ĊH(COOH) have indicated[1–3] that the unpaired electron occupies essentially a $2p\pi$ orbital, centered on the methylene carbon, as shown in Fig. 1(A). Further information regarding the radical and its unpaired electron wave function can be obtained from the hyperfine tensors of C^{13} in the methylene position of the carbon skeleton of the radical. Previous investigations[4,5] using C^{13} in natural abundance (1.1%) have shown the maximum value for the hyperfine splitting of 210±5 Mc to be along the x axis. Splittings along the y and z directions could not be measured due to the very low intensity of the C^{13} lines.

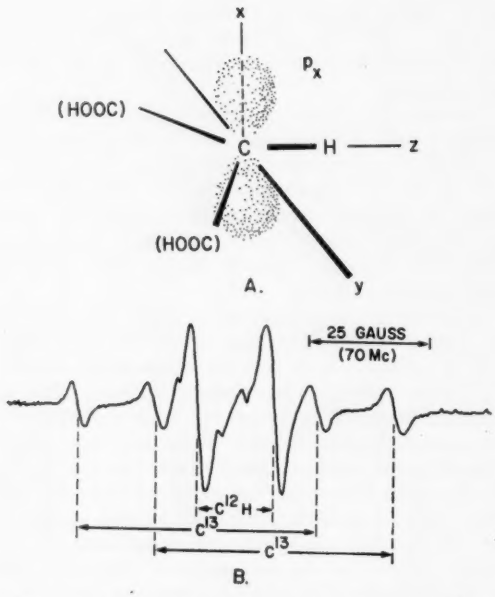

FIG. 1. (A) Cartesian molecular axis system. (B) X band EMR spectrum of the radicals HOOC$-$C^{12}H$-$COOH (two strong lines) and HOOC$-$C^{13}H$-$COOH (four weaker satellites).

We have prepared malonic acid containing 39% C^{13} in the methylene position (HOOC—$C^{13}H_2$—COOH) from CH_3I (39% C^{13}) by conventional methods.[6] Single crystals of malonic acid were grown from ether solutions by slow evaporation. Crystals were x-irradiated and annealed according to the procedure described previously.[2] EMR spectra were taken at room temperature with a conventional X-band spectrometer employing 100-kc field modulation. The polarizing magnetic field was continuously controlled and monitored by an NMR servo system.

Spectra were taken every 10° in the $x-z$ and $x-y$ quadrants. A typical spectrum is shown in Fig. 1(B). The observed C^{13} splittings in all the spectra can be accounted for by a hyperfine tensor $\mathbf{A}^C$, diagonal in the x, y, z coordinate system of Fig. 1A, and having principal values $A_{xx}^C=212.7\pm0.5$ Mc, $A_{yy}^C=22.8\pm1.5$ Mc, and $A_{zz}^C=42.2\pm1$ Mc. The isotropic part of the hyperfine tensor $a^C=\frac{1}{3}\mid Tr\mathbf{A}^C\mid$ is found to be 92.6 ± 0.7 Mc.

The corresponding principal values of the hyperfine tensor $\mathbf{A}^H$ for the methylene proton have been shown[2] to be $A_{xx}^H=-58\pm1$ Mc,[7] $A_{yy}^H=-91\pm1$ Mc, and $A_{zz}^H=-29\pm1$ Mc; a^H is equal to -59 ± 1 Mc, and indicates a negative electron spin density at the proton.

Several remarks may be made about the C^{13} data. First, using the value[8] of 115 ± 10 Mc for a^C in $C^{13}H_3$, we obtain the unpaired spin density on the methylene carbon, $\rho_c=a^C(\text{HOOC—C}^{13}\text{HCOOH})/a^C(C^{13}H_3)=0.8\pm0.08$. This is in close agreement with the value of $\rho_c=0.9$ obtained by the semiempirical relationship $a^H=Q\rho_c$, using $Q=-23$ gauss. Second, the dipolar hyperfine interaction for a C^{13} nucleus with a $2p\pi$ electron has been calculated[10] to be $64(3\cos^2\theta-1)\mid\rho_c\mid$, where θ is the angle between the *x axis* and the magnetic field direction. If we take $\rho_c=0.8$ and $a^C=+93$ Mc we obtain $A_{xx}^C=+93+102=+195$ Mc, and $A_{zz}^C=A_{yy}^C=+93-51=+42$ Mc. On the other hand, for $a^C=-93$ Mc, we have $A_{xx}^C=+9$ Mc, and $A_{zz}^C=A_{yy}^C=-144$ Mc, respectively. Our data strongly supports the positive value of a^C and, therefore, a positive electron spin density at the carbon nucleus. This confirms previous theoretical predictions.[9,11]

Finally, we note the asymmetry of the hyperfine tensor in the $y-z$ plane. If the $2p\pi$ orbital has cylindrical symmetry about x and the three σ bonds are identical, we expect $A_{zz}^C=A_{yy}^C$. Instead, however, we find $A_{zz}^C-A_{yy}^C=19$ Mc. The three σ bonds of course have different distributions of spin polarization, due to the differing bond lengths and atomic orbitals involved for the C—C and C—H bonds. A calculation of $A_{zz}^C-A_{yy}^C$, assuming a spin density of 0.05 in each of the three bonds,[9] and using the distributed dipole formulas of McConnell and Strathdee,[12] gives a maximum $A_{zz}^C-A_{yy}^C=0.3$ Mc. Even such drastic changes in the σ structure as assigning the values $\rho_{C-H}=0.05$, $\rho_{C-C}=0$ give an anisotropy of only 10 Mc. To obtain a 20-Mc anisotropy would require the center of gravity of the π orbital to be moved ~0.15 A from the C^{13} nucleus along the z direction. It is hoped that a study of the hyperfine tensors of the radical (HOOC)$\dot{C}$H(C^{13}OOH) will further elucidate the electronic structure of this radical. This work is now in progress.

We wish to thank C. Bayer of this Laboratory for assisting with the preparation of the labeled malonic acid.

[1] T. Cole, C. Heller, and H. M. McConnell, Proc. Natl. Acad. Sci. U. S. **45,** 525 (1959).
[2] H. M. McConnell, C. Heller, T. Cole, and R. W. Fessenden, J. Am. Chem. Soc. **82,** 766 (1960).
[3] H. M. McConnell, D. D. Thompson, and R. W. Fessenden, Proc. Natl. Acad. Sci. U. S. **45,** 1600 (1959).
[4] H. M. McConnell and R. W. Fessenden, J. Chem. Phys. **31,** 1688 (1959).
[5] C. Giuliano and H. M. McConnell, unpublished work.
[6] A. Murray, III, and D. L. Williams, *Organic Syntheses with Isotopes* (Interscience Publishers, Inc., New York, 1958), Vol. I, p. 40, 119.
[7] Many recent EMR measurements on HOOC$-\dot{C}$H$-$COOH radical performed in this laboratory indicate that the value of 61 Mc reported for $A_{xx}^H(=B)$ in the work cited in footnote 2 is too large and should be changed to 58 Mc.
[8] T. Cole, H. O. Pritchard, N. R. Davidson, and H. M. McConnell, Mol. Phys. **1,** 406 (1958).
[9] H. M. McConnell and D. B. Chesnut, J. Chem. Phys. **28,** 107 (1958).
[10] W. V. Smith, P. P. Sorokin, I. L. Gelles, and G. J. Lasher, Phys. Rev. **115,** 1546 (1959); R. G. Barns and W. V. Smith, *ibid.* **93,** 95 (1954).
[11] A. D. McLachlan, H. H. Dearman, and R. Lefebvre, J. Chem. Phys. **33,** 65 (1960).
[12] H. M. McConnell and J. Strathdee, Mol. Phys. **2,** 129 (1959).

THE JOURNAL OF CHEMICAL PHYSICS

Radiolysis of Aqueous Solutions

Kinetics of Coordinate Bond Formation

Kinetics of Coordinate Bond Formation

Quadrupole Relaxation Effects in

Oxygen Isotope Fractionation

Studies in Molecular Structure. III.

Intramolecular Energy Transfer in

Crystal Field Splitting and

Anomalous Relaxation of Hyperfine

Electrical Resistivity of Liquid

Analysis of Specific Heat Data for

Infrared Spectra of Alkylidiborons

Capacitive Energy and the

Vapor Pressure of Nearly

Self-Diffusion in Linear

Synthesis of the Cubic Form of

The Effect of Oxygen Adsorption

Kinetics of Crystal Nucleation in

Alkali-Iron Group-Halogen

Problems in Perturbation Theory

in Molecular Illustration

Proton Relaxation Times in

Microwave Spectrum of Acetyl

Electrochromism, a Possible

Electron Spin Relaxation in

Structure of Alkali Metals in the

Transients in the Blue and Green

Calculation of the Lower Limit

Dimensional Change of Polymer

High-Speed Computations in

Solute Model

Paramagnetic Resonance Absorption

New Determinations of the

nance Method

Interpretation of the Appearance

Effect of Pressure on the Spectra of

Infrared Spectrum of Single Crystal

Evidence of Metastable Trapping

Interaction of a Triplet and a

Theoretical Investigations on the

Incident Natural and Linearly

Theoretical Investigations on the

tion of Light Scattered at an

NMR Spectra of Alkylaldehydes